Final Report

Advanced MEA's for Enhanced Operating Conditions, Amenable to High Volume Manufacture

Cooperative Agreement No. DE-FC36-02AL67621

Submitted to

U. S. Department of Energy
Office of Transportation Technologies

September 30, 2007

By
3M Fuel Cell Components Program
3M Company, St. Paul, MN 55144

Prime Contractor: 3M Company, St. Paul, MN 55144

Project Title: Advanced MEA's for Enhanced Operating Conditions, Amenable to High Volume Manufacture

Principal Investigator: Dr. Mark K. Debe, 3M Fuel Cell Program

Team Members: Case Western Reserve University
Colorado School of Mines
Dalhousie University
University of Illinois, Urbana- Champaign
University of Miami
University of Minnesota
VAIREX Corporation

(This page left blank intentionally)

Foreword and Acknowledgements

This report documents the work performed by 3M Company under the Cooperative agreement No. DE-FC36-02AL67621, "Advanced MEA's for Enhanced Operating Conditions, Amenable to High Volume Manufacture." The period of performance for this contract was from January 1, 2002 until June 30, 2007.

The principal objectives of the program were to develop high performance, lower cost membrane electrode assemblies (MEA's), fabricatable by high volume manufacturing methods, that could meet the demanding system operating conditions of higher temperature and low humidification for automotive applications.

A substantial portion of the work completed in this contract was an extension of the developments under two preceding cooperative agreements Nos. DE-FC-02-97EE50473, and DE-FC-99EE50582, which investigated catalyzed membrane electrode assemblies for PEM fuel cells based on a fundamentally new, nanostructured thin film catalyst and support system, and demonstrated the feasibility for high volume manufacturability. The remainder of the work completed in this contract focused on membrane development, including PFSA ionomers for improved durability and performance at hotter and drier operating conditions, as well as new materials research for very higher (> 120^{o}C) temperature fuel cell operation.

All MEA materials, process development and stack fabrication work were carried out by 3M Co., at its St. Paul, MN, 3M Center campus and its Menomonie, WI, pilot plant. The 3M team included primarily members from the Fuel Cell Components Program, but significant assistance was received over varying periods of time from members of 3M's Corporate Materials Rearch Laboratory, Process Technology Center, Analytical Technology Center, and Software Electronics and Mechanical Systems. Dr. Mark Debe was the Principal Investigator and Technical Team Leader, Dr. Steven Hamrock and Dr. Radoslav Atanasoski Co-P.I.'s, Dr. Judith Hartmann the Program Manager, and Mr. Steven Kays of 3M Government R&DContracts department was the contract administrator.

Significant recognition is due the 3M Fuel Cell Components Program technical team members who were most responsible for completing the work represented in this final report, including several who contributed major sections of this report. We are all very appreciative of the support of 3M management.

Subcontractors included Case Western Reserve University, Cincinatti, OH; Colorado School of Mines, Golden CO; Dalhousie University, Nova Scotia, CA; University of Illinois-Urbana Champaign; University of Miami, University of Minnesota, Minneapolis; and VAIREX Corporation, Boulder, CO.

From our subcontractors' organizations we are particularly indebted to Prof. Thomas Zawodzinski, Dr. Derek Lebzelter, Thomas Kalapos and Dr. Hayley Every of CWRU; Prof. Andrew Herring, Dr. Steven F. Dec, Dr. Fanqin Meng, James Horan, Niccolo Aieta, Mei-Chen Kuo, and Dana Lipfert of CSM; Prof. Jeffrey Dahn, Dr. David Stevens and Dr. Arman Bonakdarpour of Dalhousie U.; Prof. Hongtan Liu and Dr. Tianhong (Amy) Zhou of U. of Miami; Dr. Lajos Gancs and Prof. Andrzej Wieckowski of U. ILL-Urbana; Prof. Woods Haley, Lingling Jia, and Dat Nguyen of U. of MN; and Dr. Ski Milburn and Bill Butler of VAIREX Corp.

We are also highly appreciative of the contributions from our collaborators at Argonne National Laboratory including Dr. Ira Bloom, Mr. Lee Walker, Mr. John Basco, Dr. Rajesh Ahluwalia and Dr. Xiaohua Wang; and at Lawrence Berkeley National Laboratory including Drs. Breslau Blizanac, Karl J. J. Mayrhofer, Nenad M. Markovic, Philip N. Ross, and Vojislav R. Stamenkovic.

This work was funded in part by the U. S. DOE, Energy Efficiency and Renewable Energy Office of Transportation Technologies and advanced Automotive Technologies. DOE technical oversight of the project was provided by Technology Development Managers Valri Lightner and Amy Mannheim, of the Dept. of Energy Hydrogen, Fuel Cells and Infrastructure Technologies Program, DOE Technical Advisor Thomas Benjamin (Argonne National Laboratory), and DOE Project Officer David Peterson (Golden, CO).

Executive Summary

Today the world faces increasingly serious environmental challenges. The solutions to these challenges must come from the proper balance of often conflicting public policy and socioeconomonic drivers with the availability of appropriate new technology. The development of hydrogen fueled vehicles for transportation is one example of new technology seriously being considered to replace the internal combustion engine (ICE) in order to reduce our dependence on fossil fuels and lower emissions of greenhouse gases.

The polymer electrolyte membrane fuel cell (PEMFC) is the most promising technology being developed to replace the ICE. By electrochemically combining hydrogen and oxygen from air to produce water, electricity is generated by the fuel cell for powering electric motors that drive the vehicle without polution or carbon emissions. Although the concept of a fuel cell is over a century old, only in the last decade have sufficiently significant advances been made in the PEMFC technology to warrant substantial investments in the development of practical systems. Many materials and process challenges remain to be overcome before cost effective, fuel cell powered vehicles can be successfully commercialized. This report summarizes the work completed over the past five and one-half years under a 3M Company/U. S. Department of Energy Cooperative Agreement directed specifically at advancing the key fuel cell components most critical for overcoming the PEMFC performance, durability and cost barriers.

The heart of a working PEMFC, where the electrochemical reactions convert the hydrogen and air to electricity, heat and water, is called the membrane electrode assembly, or MEA. The MEA is a multi-layered article comprising two key components: the ion exchange membrane at its center, and the Pt based electrocatalysts on either side of the membrane. These are the most expensive components of the fuel cell for reasons related to the materials necessary to obtain the performance and durability. The industry standard catalyst materials consist of nanometer sized particles of Pt dispersed onto the surfaces of high surface area carbon black particles. The industry standard membrane material uses a perfluorinated sulfonic acid polymer for the ion conducting membrane, a commercial example of which is DuPont's Nafion.^{TM} The work of this contract focused on the development of advanced ion exchange membranes and electrocatalysts for PEMFCs that will enable operation under ever more demanding automotive operating conditions, and the use high volume compatible processes for their manufacture.

Higher performing and more durable electrocatalysts must be developed for PEMFCs to meet the power density and lifetime hours required for fuel cell vehicles. This means the catalyst activities for reducing the oxygen to water must be improved. At the same time the amount of expensive Pt catalyst must be reduced to lower the MEA costs. And while these two properties are met, the catalyst must be made more resistant to multiple degradation mechanisms to reach the necessary operating lifetimes. Today's commercialized catalysts consist of nanometer sized particles of Pt dispersed onto carbon black support particles. They are formed into "inks" and applied to the surfaces of the ion exchange membranes. Within the real life automotive fuel cell environment, the carbon support particles can be rapidly corroded by the Pt particles they support, the Pt particles can dissolve into the adjacent membranes, or they can cluster together to lose effective surface area. Very important, the smaller the Pt particles are made in order to increase their surface area, the lower their fundamental activity for converting

the oxygen to water. In this report, we present a body of work focused on the development of a completely new approach to PEMFC electrocatalyts, called nanostructured thin film (NSTF) catalysts that eliminate many of the issues identified above with current catalyst technology. The carbon black supports are eliminated with this new approach and that eliminates the carbon corrosion issue. The thin film nature of the catalyst significantly improves its robustness against dissolution and grain growth, preserving the surface area. Most important, the fundamental activity of the NSTF for oxygen reduction is improved by over 500% compared todispersed Pt catalyts. Finally, the process for fabricating the NSTF catalysts is consistent with high volume roll-good manufacturing, and extremely flexible towards the introduction of new catalyst compositions and structures. In this report we document the work done to develop new multi-element NSTF catalysts with properties that exceed pure Pt, that are optimized for use with the membranes discussed below, and significantly advance the state-of-the-art towards meeting the DOE Hydrogen Fuel Cells and Infrastructure Technology program's 2010 targets for PEMFC electrocatalysts. The body of work completed advances the fundamental understanding of the NSTF catalyt technology, identifies new NSTF-ternary catalyst materials for higher performance, documents enhanced durability under multiple types of accelerated tests by factors of 10x to 50x over conventional catalysts, and demonstrates their performance and durability in large area MEA fuel cell stack tests.

The PEMFC ion exchange membrane is the other key functioning fuel cell component on which significant work was completed during this contract. While many improvements have been made to standard PFSA type membranes in the past few years, they still require humidification to achieve adequate proton conductivity, and so their use at elevated temperatures and drier operating conditions is limited. Membranes with increased durability and conductivity are critical. Towards this goal, two approaches were pursued in the membrane development work reported here.

The first part of the membrane work, designed for immediate application at drier conditions, and fuel operating temperatures between 85 and 120^{o}C, focused on the development of a membrane based on a low equivalent weight (EW), perfluorinated sulfonic acid (PFSA) ionomer for good ionic conductivity at low humidification, and the use of stabilizing additives for improved oxidative stability. The ionomer used was developed at 3M and has a shorter acid containing side-chain than the Nafion™ ionomer. This ionomer also has a higher Tα and higher modulus than that of a Nafion™ membrane of the same EW, allowing lower EW ionomers to be prepared with very good mechanical properties. In addition, more than 50 stabilizing additives were evaluated in *ex-situ,* Fenton's tests and more than 10 of these were incorporated into membranes and evaluated in accelerated fuel cell tests. This work led to thin (25-30 micron), cast membranes with substantially improved conductivity and durability under simulated automotive conditions, compared to membranes currently available.

The second body of membrane work completed under this contract was focused on developing and characterizing three major approaches for making new proton exchange membranes for operation under hot ($\geq$ 120°C) and dry (dew point $\leq$ 80°C) fuel cell conditions: inorganic materials with enhanced proton conductivity, polymer matrices swollen with low molecular weight fluorinated acids and proton conducting ionic liquids. New materials developed in this part of the program show the promise of the development of new membranes with even better characteristics under demanding fuel cell operating conditions, further improving the efficiency and viability of fuel cell systems.

Report Organization

Due to the length of this report, the Table of Contents following this introduction gives a high level view of the report contents. Each major section and some subsections have a more detailed table of contents defining its organization, as well as its own list of figures, tables and references. A list of abbreviations and acronyms for the entire report is contained in this introductory section, immediately after the high level table of contents. A final Appendix contains all the appendices for all sections.

This report is divided into five major Sections. In addition to defining the major project Tasks, Section 1 contains an introduction and background, defines the project objectives and goals, identifies the subcontractors and collaborators and their primary contribution areas. It concludes with a summary of the project accomplishments and comparison to the project goals.

The body of work completed under this contract is reported in Sections 2, 3 and 4 which contain all the research results for the majorTasks 1, 2 and 3 defined in Section 1.

Section 2 addresses the work completed towards development, down-selection and integration of the catalyst and membrane components used for the advanced MEA's for operation in the range of $85 \leq T \leq 120^{o}C$. This is the largest section and encompasses all the NSTF catalyst work for activity enhancement and durability testing, the 3M PFSA membrane development for enhanced durability and higher temperature/drier operation, integration of those catalysts and membranes for down-selection, down-selection and screening of the GDL, investigation of air management strategies, and advanced modeling of MEA's.

Section 3 summarizes all the research completed on the new materials and conceptual approaches for development of membranes designed for operation above $120^{o}C$ that do not rely on aqueous proton conduction.

Section 4 summarizes all the work on the MEA scale-up and short stack testing completed in fulfillment of the contract requirements.

Section 5 concludes with a summary of the technology transfer activities, including lists of all the publications, presentations and patent applications resulting from the contract.

Finally, the appendix contains related subcontractor and national laboratory reports and publications.

High Level Table of Contents

List of Abbreviations

ADF-STEM	annular dark field scanning transmission electron microscopy
ANL	Argonne National Laboratory
BETI	perfluoroethyl bissulfonyl imide
CCM	catalyst coated membrane
CSM	Colorado School of Mines
CV	cyclic voltammograms
DMA	dynamic mechanical analysis
DOE	Department of Energy
E_a	activation energy for surface area loss
EC-IRAS	electrochemical infrared reflection-absorption spectroscopy
ECSA	electrochemical surface area
EMI	ethyl methyl imidazolium
EPR	electron paramagnetic resonance
EW	equivalent weight, polymer molecular weight per mol of acid groups
FC	fuel cell
GDL	gas diffusion layer
HFCIT	Hydrogen, Fuel Cells and Infrastructure Technologies
HFR	high frequency resistance
HPA	heteroopoly acid
HOR	hydrogen oxidation reaction
HRTEM	high resolution transmission electron microscopy
H_{upd}	hydrogen under-potential deposition
IEC	ion exchange capacity
IRAS	infrared reflection absorption spectroscopy
k	Arrhenius rate constant
LBNL	Lawrence Berkeley National Laboratory
MEA	membrane electrode assembly
NMR	nuclear magnetic resonance
NSTF	nanostructured thin film catalyst
OCV	open circuit voltage
OFR	oxygen free radicals
ORR	oxygen reduction reaction
p	influence parameter in linear regression analysis
PDS	potentiodynamic polarization scan
PEFC	polymer electrolyte fuel cell
PEM	proton exchange membrane, polymer electrolyte membrane
PEMFC	proton exchange membrane fuel cell
PFGSE	pulse-field gradient spin-echo
PFSA	perfluorinated sulfonic acid
PA	phosphoric acid
PBI	polybenzamidazole
PSS	potentiostatic scans
Pt/C	Pt on carbon catalysts
PTA	phosphotungstic acid
PTMOS	phenyltrimethoxysilane
R^2	least squares fitting parameter
RH	relative humidity
RHE	reversible hydrogen electrode
RPT	reference polarization test

RRDE	rotating ring disc electrode
SEF	surface area enhancement factor
S_{min}	minimum normalized surface area
SOD	superoxide dismutases
STA	silicotungstic acid
STR	Stark tuning rate
STS	surfactant-templated silica
TEM	transmission electron microscopy
TFE	tetrafluoroethylene
TEOS	tetraethylorthosilane
TFSI	trifluoromethyl bissulfonyl imide
TM	transition metal
XRD	x-ray diffraction

Section 1

Project Overview

Section 1 Project Overview

1.1 Introduction and Background

Motivation

The development and commercialization of affordable hydrogen fuel cells are necessary for the realization of a hydrogen-based economy. Proton exchange membrane fuel cells (PEMFC's) or polymer electrolyte fuel cells (PEFC's) represent a promising technology for automotive, small stationary and portable power applications. PEMFC's are energy conversion devices that process a fuel gas (e.g., hydrogen) and an oxidant gas (e.g., air) and generate electricity with only water and heat as byproducts. Fig. 1 gives a schematic representation of the PEMFC. Half cell reactions on the anode (hydrogen oxidation) and cathode (oxygen reduction) catalyst electrodes are separated by a polymeric membrane that serves to isolate the reactant gases and to transport protons from the anode to the cathode.

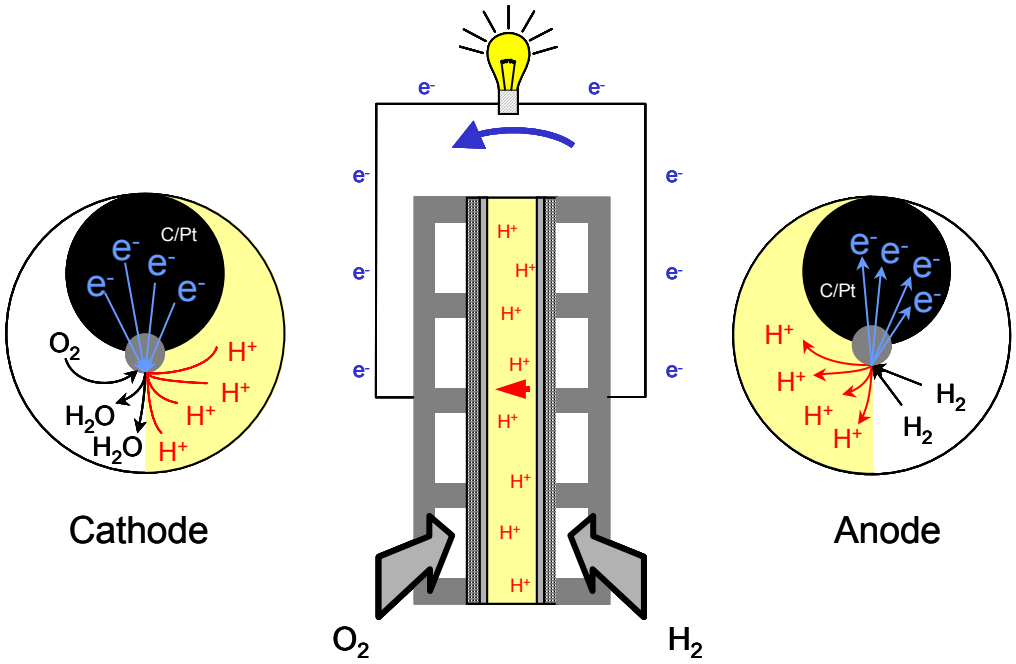

Fig. 1. Schematic representation of a PEMFC, including anode and cathode half-cell reactions.

Secure and controllable sources of primary energy which do not exacerbate the impending consequences of global warming from atmospheric CO_2 are currently stressed by the U.S. Dept. of Energy and most major automotive suppliers as a driving force for the development of hydrogen/air polymer electrolyte fuel cells for automotive applications [1]. In contrast to the other two major application areas of PEFC's, portable electronic devices and stationary/back-up/forklift etc. power, where the fuel cell competes for customer preference with alternative battery technologies such as lithium ion or lead acid respectively, PEFC's for automotive traction applications offer a real solution to an increasing need for sustainable mobility for the world's future generations. With roughly twice the fuel efficiency of internal combustion engines, and zero emissions of environmental pollutants, they pose a near ideal solution if the hydrogen can be

obtained from fully renewable sources. Significant challenges remain however before it will become cost-competitive and consumer accepted.

Critical Barriers

A number of critical barriers specific to the fuel cell components must be overcome to meet the HFCIT goals for hydrogen-based fuel cells suitable for automotive applications. These barriers relate to cost (initial and operating), performance (operating efficiency and power density) and durability (lifetime and end-of-life performance). Some associated 2010 targets for an integrated fuel cell system operating on direct hydrogen are $45/kWe, 50% efficiency at rated power, 650 W/L power density for the stack, and 5000 hours durability. The fuel cell membrane electrode assembly (MEA) components directly affect these barriers. The amount of Pt precious metal required and cost of the ion exchange membrane materials are the largest stack cost elements at high volumes, assuming efficient, high yield manufacturing processes can be used to fabricate the MEA's. The cathode catalyst activity is the key-determining factor of the Pt loading required (initial cost) and is strongly related to the stack fuel efficiency (operating cost), since the operating voltage at a required current density determines fuel efficiency. Maintaining high membrane conductivity, particularly at low humidity and higher temperatures, is also critical to achieving high operating potentials and thereby fuel cell efficiencies. The cathode catalyst activity and membrane conductivity also contribute to determining the stack power density, which in turn determines the physical size of the stack and its cost. The ability to operate the fuel cell stack under drier conditions is a key requirement for reducing parasitic power loss (and increasing efficiency) associated with water management. Supplying and recovering humidity to the fuel and oxidant gases can be highly energy intensive, so developing MEA's that can be operated drier is a critical need. Similarly, cooling high power stacks is a significant issue under ambient conditions. In contrast to internal combustion engines (ICE), a much larger fraction of the waste heat of a fuel cell stack must be extracted by a coolant and radiator system. Keeping the size of parasitic power demand for coolant circulation low and the size of the condenser/radiators reasonable demands a higher stack temperature for maximum power generation in hot environments. Hence, MEA's are required that can operate effectively at higher temperatures (up to 120^{o}C) with minimal additional water.

Degradation processes acting on the MEA materials become worse at higher temperatures and drier operating conditions, requiring the development of more stable membrane materials and catalysts that more effectively reduce oxygen to water without intermediate peroxide production or catalyst support oxidation. Designing MEA's for hot, dry reactant conditions require development of new membranes, catalysts and GDL's that are stable and durable under those conditions. The components must be matched to each other and integrated with a flow field design and air management strategy.

Membranes that are stable against peroxide induced decomposition, catalysts which produce less peroxide and have stable surface areas and activities under realistic, demanding operating conditions are critical requirements for meeting the DOE long-term technical targets for durability. In addition, the processes for making the MEA components must be consistent with high volume production to meet the quality and cost targets.

For these basic reasons, this project has focused on development of advanced MEA components, particularly catalysts and membranes that allow for higher performance

operation with less precious metal catalyst under hotter, drier conditions which can be fabricated using cost-effective, high-volume processes.

Approach

The approach taken in this project to research and develop such advanced MEA's has two thrusts: the development of full MEA's for the temperature range of 85ºC ≤ T ≤ 120ºC, and development of new electrolytes for operation at or above 120ºC. For the lower temperature range, PEM's were developed based on modifications of 3M's novel PFSA type membrane that still utilizes water for proton conduction [2]. The 3M PEM's Tα is 25ºC higher than the perfluorinated sulfonic acid (PFSA) standard membrane (such as Nafion™) of similar equivalent weight, and the dry membrane modulus is over ten times higher at 120ºC. These attributes provide improved mechanical properties. Shorter side-chain lengths of the basic 3M ionomer add stability at lower equivalent weights enabling higher conducting membranes under both wet and dry conditions. The modifications developed in this project included incorporation of additives to the membrane to facilitate peroxide decomposition for better oxidative stability and enhanced water retention for higher conductivity under low humidification. It also included development of different membrane processing conditions to facilitate better integration with the NSTF catalyst system (discussed below).

The upper operating temperature for an MEA made with a PFSA type membrane is about 120ºC, due to performance and stability considerations. For the higher temperature range, new membrane materials and low-water based proton conduction methods were investigated in this project. They utilized 3M perfluorinated acids, various proprietary ionic liquids, and inorganic additives. Work included fundamental characterization and understanding how to incorporate those materials into polymer matrices to form effective membranes.

The approach to the development of advanced cathode catalysts having less precious metal than current state-of-the-art constructions was based on the novel 3M nanostructured thin film (NSTF) catalyst support and deposition system [3]. The approach builds on previous work completed under two prior 3M/DOE cooperative agreements (DE-FC-02-97EE50473, DE-FC02-99EE50582)**.** The NSTF catalyst approach represents the third and newest class of electrocatalysts, after carbon supported dispersed Pt and Pt blacks. The original NSTF concept is a thin film consisting of an oriented array of high-aspect ratio (length to width ratio greater than 3) particles of arbitrary geometrical cross-sectional shape, composition and coatings. As currently fabricated for fuel cell applications, the current NSTF catalysts consist of magnetron sputter-deposited thin films of catalyst applied over a nanostructured thin film monolayer of oriented crystalline whiskers of an organic pigment material, designated PR149 (CAS number), a perylene dicarboximide derivative. It differs in several fundamental ways from the class of Pt/C dispersed catalysts, which together eliminate or significantly reduce the corrosion, dissolution and low specific activity issues intrinsic to Pt/C catalysts. The NSTF process easily generates new compositions and structures via a dry, roll-goods process amenable to high volume manufacturing. New multi-element cathode catalysts were found that significantly outperformed pure Pt-coated NSTF supports. The 3M NSTF catalysts exhibit 5x to 10x higher specific activity, significantly reduced F^- release and much greater surface area stability under highly oxidative conditions than commercially available carbon supported dispersed catalysts.

References for Section 1.1

1. "Multi-Year Research, Development and Demonstration Plan," Hydrogen, Fuel Cells and Infrastructure Technologies Program, Energy Efficiency and Renewable Energy, U. S. Dept. of Energy, 2003-2010, http://www.eere.energy.gov.
2. S. J. Hamrock and M. A. Yandrasits, J. of Macromolecular Science, Part C: Polymer Reviews **46**, 219 (2006).
3. M.K. Debe, Chapter 45 in Handbook of Fuel Cells – Fundamentals, Technology and Applications, W. Vielstich, A. Lamm, H. A. Gasteiger, Editors, Vols. 1-4, John Wiley & Sons, 2003.

1.2 Project Objectives and Goals

The overall objective of this project was development of high performance, lower cost membrane electrode assemblies (MEA's) qualified to meet demanding automotive system operating conditions of higher temperature and little or no humidification, using less precious metal, higher stability catalysts, and higher durability membranes than current state-of-the-art constructions. It included development of MEA component fabrication processes amenable to high volume, cost-effective production and capable of meeting quality targets. It also included research into new membrane material strategies for operation at very high temperatures.

The project directly addressed the three most critical barriers identified for MEA's in the DOE HFCIT "Multi-Year Research, Development and Demonstration Plan"; A. Durability, B. Stack Material and Manufacturing Cost, and C. Electrode Performance. High level technical targets for overcoming these barriers by 2010, identified in the above HFCIT Multi-year Plan include > 5000 hour durability with cycling, costs of $15/kW, and precious group metal total loadings of 0.5 g/kW-rated. More specific targets for the membranes and electrocatalysts, to be reached by 2010 and 2015, are summarized in Tables 3.4.11 and 3.4.12 of the HFCIT Multi-year Plan, and are reproduced below in subsection 1.5.

The technical plan to meet this objective included three basic tasks:

Task 1: Durable MEA's for operation in the temperature range of 85 $\leq$ T $\leq$ ~ 120ºC, while operating on low humidification with PFSA based ionomer and lower cost materials and catalysts.

Task 2: Research and development of MEA's for the higher temperature range of 120 $\leq$ T $\leq$ 150ºC, based on non-aqueous proton conduction mechanisms, using lower cost materials and fabrication processes.

Task 3: Matched MEA materials and processes scaleable to high volumes, for testing in a fuel cell stack.

These tasks are defined more explicitly in the next section.

1.3 Task Descriptions

Task 1

Task 1 was directed at advancing the state-of-the-art in cathode structures and durable PFSA based membranes to stretch the limits of current MEA technology toward more stability at hotter, drier operating conditions (85 $\leq$ T $\leq$ 120ºC) with lower cost materials and high volume compatible processes. Task 1 had five principal subtasks.

By far the majority work under Task 1 focused on three subtasks. The first of these was development of advanced cathode catalysts, based on the 3M NSTF electrocatalyst technology. It included development of ternary Pt alloy catalysts, using combinatorial and standard screening methods, multiple accelerated durability tests, and down-selection by various metrics. The second major subtask under Task 1 focused on development of more durable membranes based on 3M's PFSA ionomer. It involved

using a low EW PFSA ionomer developed at 3M having improved mechanical properties, and combining it with additives that stabilize the membrane towards decomposition by hydrogen peroxide and associated radicals. The third major subtask under Task 1 focused on down-selection of the catalysts and membranes for scale-up (Task 3) and their integration into catalyst coated membranes (CCMs) with gas diffusion layers (GDL's), for optimized performance at 85 $\leq$ T $\leq$ 120ºC. Work under this task included screening and down-selection of the GDL.

Two smaller subtask efforts included first, advanced modeling of MEA's nominally for flow field and gas diffuser optimization, using code developed at the U. of Miami and adapted to the ultra-thin layer NSTF electrocatalysts. It involved applying a three dimensional modeling capability for predicting the local reactant, temperature and flow conditions within the fuel cell active area and within the catalyst electrode areas and membrane. The second smaller subtask focused on investigation of an optimized air management strategy for operation under hotter, drier conditions, using two types of air compressors developed by Vairex, Corp.

Task 2

Task 2 was directed at development of very high temperature PEM membranes that ideally do not rely on water for proton transport. As originally proposed it included development of stable catalysts and supports with matching gas diffusion and flow field components to take the MEA into an operating range of 120 $\leq$ T $\leq$ 150°C and nearly dry operation. Subtasks as originally proposed included: development of a high temperature electrolyte membrane and appropriate catalysts; optimization of the catalyst membrane interfaces; advanced materials characterization and modeling with subcontractors; and short stack testing (if warranted). As work progressed on these newer, longer range material systems, the research was focused on characterization, study and fabrication of the basic membrane elements only, and not on the composite MEA (membrane, catalyst and GDL) since identification of catalysts and MEA integration were not warranted until the membrane approach could be identified.

Task 3

Task 3 was directed at the scale-up and optimization of MEA component fabrication processes amenable to high volume, high quality, low cost production for selected components from Tasks 1 or 2. The first subtask included: scale-up and optimization of the fabrication processes for the NSTF -catalyst, membrane, catalyst coated membrane (CCM), and GDL. The focus of the second subtask was characterization of the down-selected MEA's in full-scale short stacks.

1.4 Subcontractors and Collaborators

The subcontractor institutions, national laboratory and their principals participating on this contract are listed below in alphabetical order with their areas of contribution.

Case Western Reserve University
Prof. T. Zawodinski,
Fundamental experimental studies of proton transport in liquid and solid proton conductors, and fundamental studies of catalyst/electrolyte ORR

Colorado School of Mines
Prof. Andrew Herring,
Synthesis of heteropolyacids additives for fabrication of composite membranes.

Dalhousie University
Prof. Jeffrey Dahn, Dr. David Stevens, and Dr. Arman Bonakdarpour,
Combinatorial fabrication of multi-element sputter deposited catalysts on 3M NSTF supports and their materials characterization by multiple methods.

U. of Illinois, Urbana
Prof. Andrzej Wieckowski and Dr. Lajos Gancs,
Use of electrochemical, infrared spectroscopy and transmission electron microscopy to study the fundamental material properties of the NSTF catalyst structure.

U. of Miami
Prof. H. Liu and Dr. Tianhong (Amy) Zhou,
Adapting three dimensional, mixed phase modeling codes for simulating operating MEAs to be able to treat ultra-thin electrode layers.

U. of Minnesota
Prof. W. Halley,
Theory and simulation studies for non-aqueous membrane based proton conduction.

Vairex Corp., Boulder, CO.
Dr. Ski Milburn (CEO),
Development of air compressor technology.

Argonne National Laboratory
Dr. Ira Bloom, Mr. Lee Walker, and Mr. John Basco,
Final stack testing protocol development and oversight.

Lawrence Berkeley National Laboratory
Drs. Berislav B. Blizanac, Karl J.J. Mayrhofer, Nenad M. Markovic, Phillip N. Ross, and Vojislav R. Stamenkovic
Fundamental RRDE cyclic voltammetry characterization of the NSTF-Pt and ternary alloy catalyst electrochemical properties.

1.5 Summary of Accomplishments and Comparisons with Project Goals

Technology transfer activities

Significant efforts were expended to disseminate the results of the research and development findings from this contract to the wider fuel cell community. In total thirty-six presentations were made over the period of 2003 to 2007 at national and international meetings and conferences, fourteen of which were invited. Twenty-six publications were prepared for journal publications or conference proceedings, and four for annual DOE progress reports. Ten patent applications were generated in part from this work and all have published. Finally, close interactions with six universities and three national laboratories during the contract have also enabled transfer of the technology and concepts in both directions. One PhD thesis was also completed under research towards the goals of this contract. MEA's containing the NSTF PtCoMn catalyst and 3M PFSA based membrane, and the 3M membrane with enhanced durability, as developed in part under this contract, have been and continue to be sold and sampled to customers for evaluation.

Summary of project's impact

Today's commercialized catalysts consist of nanometer sized particles of Pt dispersed onto carbon black support particles. They are formed into "inks" and applied to the surfaces of the ion exchange membranes. Within the real life automotive fuel cell environment, the carbon support particles can be rapidly corroded by the Pt particles they support, the Pt particles can dissolve into the adjacent membranes, or they can cluster together to lose effective surface area. Very important, the smaller the Pt particles are made in order to increase their surface area, the lower their fundamental activity for converting the oxygen to water. In this report, we present a body of work focused on the development of a completely new approach to PEMFC electrocatalysts, called nanostructured thin film (NSTF) catalysts that eliminate many of the issues identified above with current catalyst technology. The carbon black supports are eliminated with this new approach and that eliminates the carbon corrosion issue. The thin film nature of the catalyst significantly improves its robustness against dissolution and grain growth, preserving the surface area. Most important, the fundamental activity of the NSTF for oxygen reduction is improved by over 500% compared to dispersed Pt catalysts. Finally, the process for fabricating the NSTF catalysts is consistent with high volume roll-good manufacturing, and extremely flexible towards the introduction of new catalyst compositions and structures. In this report we document the work done to develop new multi-element NSTF catalysts with properties that exceed pure Pt, are optimized for use with the membranes discussed below, and significantly advance the state-of-the-art towards meeting the DOE Hydrogen Fuel Cells and Infrastructure Technology program's 2010 targets for PEMFC electrocatalysts. The body of work completed advances the fundamental understanding of the NSTF catalyst technology, identifies new NSTF-ternary catalyst materials for higher performance, documents enhanced durability under multiple types of accelerated tests by factors of 10x to 50x over conventional catalysts, and demonstrates their performance and durability in large area MEA fuel cell stack tests.

Membranes with increased durability and conductivity under hotter, drier conditions are critical to allow the use of fuel cells in many applications, including automotive. The approach described here is to develop a membrane base on a low equivalent weight (EW), perfluorinated sulfonic acid (PFSA) ionomer for good ionic conductivity at low humidification, and to use stabilizing additives for improved oxidative stability. The ionomer used was

developed at 3M and has a shorter acid containing side-chain than the Nafion™ ionomer. This ionomer also has a higher Tα and higher modulus than that of a Nafion™ membrane of the same EW. This allows lower EW ionomers to be prepared with very good mechanical properties, providing a stronger membrane at high temperature. The conductivity, performance and physical properties of this ionomer at several EW's were evaluated. The water absorption properties and conductivity as a function of humidification show trends which are somewhat different than Nafion™. In addition, more than 50 stabilizing additives were evaluated in ex-situ, Fenton's tests and more than 10 of these were incorporated into membranes and evaluated in accelerated fuel cell tests. Many of these showed significant membrane stabilization. Further evaluation of some of these additives using EPR spectroscopy was undertaken to attempt to elucidate the mechanism of the stabilizing effect.

This work led to thin (25-30 micron), cast membranes with conductivity as high as 25 mS/cm at 120ºC and 25% RH. MEA's made with these membranes had increase performance and lifetimes at 90ºC and 44% RH that were in excess of 4,000 hours, compared to about 230 hours for a Nafion™ 112 membrane a (50 micron, extruded PFSA membrane). The hydrogen fluoride content of the water coming from fuel cells with these new membranes was about 100 times lower as well.

While many improvements have been made to PEMFC membranes they still require humidification to achieve adequate proton conductivity and so their use under elevated temperature and drier operating conditions is limited. Three major approaches for proton exchange membranes for hot ($\geq 90°C$) and dry (dew point $\leq 80°C$) fuel cell conditions were evaluated:

Inorganic materials for enhanced proton conductivity: The heteropoly acids, HPAs, are a large class of inorganic super acids that have been shown to give interesting properties to composite PFSA ionomers containing them. In this work we investigated the effect of doping the 3M ionomer with HPAs 12-phospho, silico or zinco tungstic acid. It was shown that under dry condition that the HPA lowered the Ea for proton transport, the opposite was true for wet conditions below 100°C. These HPAs were added to the 3M ionomer membrane and in some cases an increase in conductivity and/or fuel cell performance was observed, although the water soluble HPAs are not stable in the membranes under fuel cell operating conditions. Because of their ability to enhance the proton conductivity in the ionomer under dry conditions considerable effort was placed in trying to immobilize them in the ionomer. Three approaches were taken: 1. the formation of HPA silica particles ex-situ, 2. attempts to bind the HPA to pre-formed silica particles, and 3. the formation of silica particles in-situ in the ionomer. All of these approaches used silicon based lacunary HPA and silica derived from TEOS and other precursors. While considerable progress was made the robustness of the silica linkage under hot acidic conditions was called in to question. Anion-immobilizing interactions in PFSA medium between heteropolyacid anions and colloidal silica were discovered. In addition, organosulfonic acid-functionalized silica, or zirconium oxide-based additives were evaluated, and some small improvements in membrane performance were seen in some cases, although proton conductivity or fuel cell performance was usually reduced.

Polymer matrices swollen with low molecular weight fluorinated acids: Three approaches were evaluated. For ionic liquids imbibed into silica-filled expanded PTFE, conductivity or 10 mS/cm was achieved but fuel cell performance was very poor. For polymer-silica matrices formed by solvent induced phase separation followed by imbibition

of fluorinated acids, 20 mS/cm was achieved but fuel cell performance was poor due to poor retention of acid. For a polybenzimidazole polymer filled with silica and fluorinated acid, 9.3 mS/c, was achieved and good fuel cell performance was achieved relative to conventional polybenzimidazole-phosphoric acid membrane despite the fact that conductivity for the latter was much better. Comparison of resistance-corrected fuel cell polarization results to conductivity results showed clearly that the poorer fuel cell performance for polybenzimidazole-phosphoric acid membrane was due to catalyst poisoning, whereas performance for the polybenzimidazole polymer filled with silica and fluorinated acid membrane was limited primarily by conductivity of the membrane.

Proton conducting ionic liquids: Fundamental conductivity experiments were done for fluorinated ionic liquids with the conjugate acid of the fluorinated portion of the ionic liquid, and with addition of water as well as candidates for replacement of water. Conductivity of these liquid electrolytes was measured using a custom liquid cell that was developed and cast solid membranes were tested using two or four-point conductivity probes. Selected electrolytes were incorporated into PFSA or into polybenzimidazole based membranes. Good ionic conductivities from membranes and proton conductivities from new liquid electrolytes were obtained under dry conditions. The highest conductivity for a liquid electrolyte was 0.04 S/cm at 120 °C under bone dry conditions. For polymer membranes with ionic liquid electrolytes, conductivities were in the range of 10^{-2} S/cm under bone dry conditions. Leaching of these liquid electrolytes was believed to be the reason for poor results in fuel cell evaluations.

Summary of accomplishments meeting project objectives

The following Tables I and II compare the status of the various electrocatalyst and membrane performance and durability characteristics, as developed under this contract, with the DOE targets for 2010 and 2015 specified in the most recent DOE HFCIT Multi-Year Research, Development and Demonstration Plan.

Tables III and IV provide summary lists of the key accomplishments, as judged by the 3M investigators, towards development and understanding of advanced electrocatalysts and membranes for PEM fuel cells, resulting from this project.

As the body of this report should make clear, every task and subtask of this cooperative agreement was executed along lines very close to the original proposal. Only in a few cases, with smaller subtasks and because it made practical sense, did the research and development efforts depart from the planned methodology in order to focus on more critical areas rather than extend beyond what was practical. For example, in Task 2, research continued to focus on the high temperature membrane materials characterization and development strategies alone, rather than dilute the focus by including high temperature catalysts and MEA integration before the membranes were ready. Another example was in Task 1 where the development of an air compressor technology for a specific pressure turn-down profile most beneficial to MEA operation was limited to the compressor development and testing itself, with only limited integration with a stack for testing, since the available fuel cell stack was not well matched to the compressor.

Table I. Technical Targets: Electrocatalysts for Transportation Applications *

Characteristic	Units	2010/2015 Stack Targets	3M 2007 Status (volume mfg'd roll-good)
PGM Total Content	g/kW rated in stack	0.3 / 0.2	**0.47** (in 22 cell stack)
PGM Total Loading	mg PGM/cm^2 electrode area	0.3 / 0.2	**0.25 – 0.4**
Durability with cycling At operating T ≤ 80°C At operating T > 80°C	Hours	5000 / 5000 2000 / 5000	**< 20 μ V/hr-cell non-reversible loss over 550 hrs** (DOE-3 5kW stack, 3380 load cycles at 90°C)
Mass Activity (150kPa H_2/O_2 80°C. 100% RH)	A/mg-Pt @ 900 mV	0.44 / 0.44	**0.18 – 0.25** (≤ 0.2 mg/cm^2)
Specific Activity (150 kPa H_2/O_2 at 80°C, 100% RH)	μA/cm^2-Pt @ 900 mV	720 / 720	**2,930** (0.2 mg/cm^2)
ECSA loss by Stop/Start	% ECSA loss	< 40 / 40	**< 30**
Electrochemical support loss at high potentials	mV after 100 hrs @ 1.2 V	< 30 / 30	**< 10**

Table II. Technical Targets: Membranes for Transportation Applications **

Characteristic	Units	2010/2015 Target	3M 2006 Status (50 cm^2 cell)
Membrane Conductivity at: Operating Temperature Room Temperature -20 °C	 S/cm S/cm S/cm	0.10 / 0.10 0.07 / 0.07 0.01/ 0.01	**0. 10** @ 120°C 61% RH, 250 kPa, 730 EW **0.10** saturated TBD
Operating Temperature	°C	≤ 120	≤ 120
Inlet water vapor partial pressure	kPa (absolute)	1.5 / 1.5	
Oxygen cross-over	mA/cm^2	2 / 2	Expected to be similar to PFSA
Hydrogen cross-over	mA/cm^2	2 / 2	**< 2** @ 70 °C, saturated
Durability with load cycling	Hours, T ≤ 80 °C Hours, T > 80 °C	5000 2000 / 5000	**> 5,000 (90°C)** **> 4,000 (90°C)**

* Based on Table 3.4.12. Technical Targets: Electrocatalysts for Transportation Applications, In DOE HFCIT Multi-Year Research, Development and Demonstration Plan.
**Based on Table 3.4.11. Technical Targets: Membranes for Transportation Applications, In DOE HFCIT Multi-Year Research, Development and Demonstration Plan.

Table III. Principal Accomplishments: Catalyst Components

- Developed new high performance NSTF PtCoMn ternary electrocatalyst with 250% gain in specific activity over NSTF Pt.
- Demonstrated a factor of two improvement in specific power density, lowering Pt loading to less than 0.3 gPt/kW in 50 cm^2 single cell tests at 0.7V.
- Achieved oxygen reduction specific activity of 2000-3000 microA/cm^2-Pt, five to ten times higher than conventional catalysts, and already far above the 2010 target of 720 microA/cm^2-Pt.
- Demonstrated the ability to tailor the NSTF support whisker to the catalyst coating in order to optimize the catalyst mass activity.
- Demonstrated the relationship between electrode ultra-thinness and zero-mass transfer overpotential up to 2 A/cm^2 with the NSTF thin layer electrodes.
- Demonstrated the NSTF PtCoMn ternary is the world's first highly durable and robust electrocatalyst that eliminates carbon corrosion at 1.5V, minimizes Pt dissolution and agglomeration, significantly reduces (> tenfold) F^- ion release due to membrane degradation, and lengthens MEA lifetimes under accelerated testing by over an order of magnitude.
- Demonstrated one to two orders of magnitude greater resistance to corrosion, Pt dissolution and agglomeration than traditional catalysts in cyclic voltammetry, constant voltage, and stop/start fuel cell tests run at high temperatures and potentials.
- Integrated the NSTF ternary catalysts with the 3M low EW membrane, establishing feasibility for CCM roll-good manufacture achieving improved performance, start-up and water management.
- Qualified the manufacturing process for the critical MCTS roll-good substrate for NSTF catalysts to achieve yields above 96%.
- Adapted a full 3-D mathematical modeling program for simulating MEA functional performance and internal MEA reactant and current distributions, to accommodate ultra-thin electrodes for the first time.
- Demonstrated non-reversible performance loss rates of less than 10 microvolts/hour in 312 cm^2, 22-cell, 5 kW stack under load-cycling conditions at 90°C for over 550 hours.
- Developed catalyst coated membrane product for sale and evaluation at multiple customer sites.
- Extended new NSTF catalyst technology and knowledge to new3M/ DOE Grant No. DE- DE-FG36-07GO17007, "Advanced Cathode Catalysts and Supports for PEM Fuel Cells."

Table IV. Principal Accomplishments: Membrane Components

- Extended the lifetime of a 3M PFSA-type membrane by a factor of 15 under load-cycling accelerated tests.
- Evaluated new, low EW PFSA membranes with improved performance under hot, dry conditions, having improved mechanical properties compared to other commercially available membranes.
- Developed new membranes stabilizing additives that allowed a more than tenfold increase in MEA lifetime under accelerated durability tests, and 5000 hour lifetimes under simulated automotive conditions.
- Evaluated new inorganic materials which can increase proton conductivity under hotter, drier conditions, finding some with enhanced conductivity under hotter, drier conditions, and some with lower levels of fluoride generation, indicating a decrease in the rate of membrane degradation in MEA durability testing.
- Developed fluorinated acid/polymer composite membranes which showed good mechanical properties and improved performance in MEA's at very high temperatures compared to current (PBI-Phos acid) high temperature membranes.
- Studied ionic liquids/acid blends having proton conductivity of 37 mS/cm **without water** at 80°C.
- Met the DOE target for a membrane with an area specific resistance below 100 mohm-cm^2 at 120°C (~25 mohm-cm^2 at 120°C with 0.5 atm water vapor pressure, 250 kPa total, 1 mil membrane).
- Extended new membrane/additive technology and knowledge to two other 3M/DOE Contracts: DE-FC36-03GO13098 "MEA and Stack Durability for PEM Fuel Cells," and new Grant No. DE-FG36-07GO17006, "Membranes and MEA's for Dry, Hot Operating Conditions."
- New 3M membranes w/additive are currently used in products for two customers and being qualified at others.
- Obtained a more basic understanding of the critical issues affecting membrane, and therefore MEA durability, and the role of catalytically active metals in stabilizing or destabilizing MEA components towards degradation, allowing further improvements in MEA durability.

Section 2

MEA Component Development for 85 ≤ T ≤ 120°C

Section 2.1 NSTF Catalyst Development

This section reviews the work done under the first major subtask of **Task 1** discussed in section 1.2, to develop durable MEAs for operation in the temperature range of 85 ≤ T ≤ ~ 120°C while operating on low humidification with PFSA based ionomers and lower cost catalysts. The focus of this section is on the catalyst development.

Table of Contents for Section 2.1

2.1.0 Introduction

As polymer electrolyte membrane (PEM) fuel cells move towards commercialization for various markets, required improvements in performance, durability and cost are becoming better defined. The fuel cell membrane electrode assemblies (MEAs) are key to achieving many of these targeted improvements for automotive applications [1], and durability is perhaps the most critical at this stage of technology development. However, the required performance and durability must ultimately be achieved with MEA materials and process costs consistent with the pricing required for successful commercialization. Considering just one of the MEA components, the electrocatalyst electrodes, there are many properties that need to be met simultaneously before a robust, high-volume automotive-capable system can be realized. These include high catalyst mass activity and utilization, low mass transport losses, high tolerance to multiple surface area loss mechanisms, tolerance of a wide humidity and temperature operating window, tolerance of internally and externally generated impurities, cold start and freeze tolerance, and the ability to be fabricated by robust high volume-compatible, low cost processes.

Carbon supported, finely dispersed Pt electrocatalysts have been under extensive development and the work-horse electrode in PEM fuel cells for two decades. The primary rationalization for development of Pt/C electrocatalysts was that the Pt catalyst particles must be as small as possible, in the nanometer size range, to obtain as much surface area per unit mass of Pt, in order to achieve the maximum mass activity for the oxygen reduction reaction (ORR). This high dispersion required then an electrically conductive support for which carbon blacks seemed ideal as well. As is often the case, however, these advantages were balanced by equally important negative consequences.

It has become increasingly clear that the concept of using an electrochemical-corrosion-susceptable support is fundamentally limiting for achieving robust durability[1-4] in applications where fuel cell start-ups and shut-downs occur frequently. Similarly, the price paid for using highly dispersed nanometer particles to maximize the mass specific surface area are a) the specific activities (A/cm^2-Pt) are proportionately smaller, due in part to the particle size effect, and b) the required resistance to Pt dissolution is worsened due to the basic instability of nano-sized particles.

For more than ten years, we have been developing an alternative supported catalyst electrode concept for PEM fuel cell MEA's, the nanostructured thin film (NSTF) catalyst.[5]The 3M nanostructured thin film (NSTF) catalyst is called such because the form of the catalyst is essentially a polycrystalline thin film conformally coating a nanostructured layer of high aspect ratio, oriented crystalline whiskers made of an organic pigment molecule. It contains neither carbon nor additional ionomer in the electrode layers that are 20-30 times thinner than conventional dispersed Pt/carbon based MEA's. Fig. 1 shows SEM images of the NSTF catalyst coated whiskers, roll-good fabricated by a vacuum coating process, prior to incorporation onto the surfaces of a PEM to form a catalyst-coated membrane. Fig. 2 shows an SEM cross-section of one side of the catalyst-coated membrane, also fabricated by a dry roll-good process, illustrating the extreme thinness of the electrode layer. Other images of NSTF catalysts as a function of down-web position, and the advantages of the much simplified process for producing catalyst coated membranes compared to wet-chemical methods for making and coating conventional dispersed catalysts, are discussed in reference.[6]

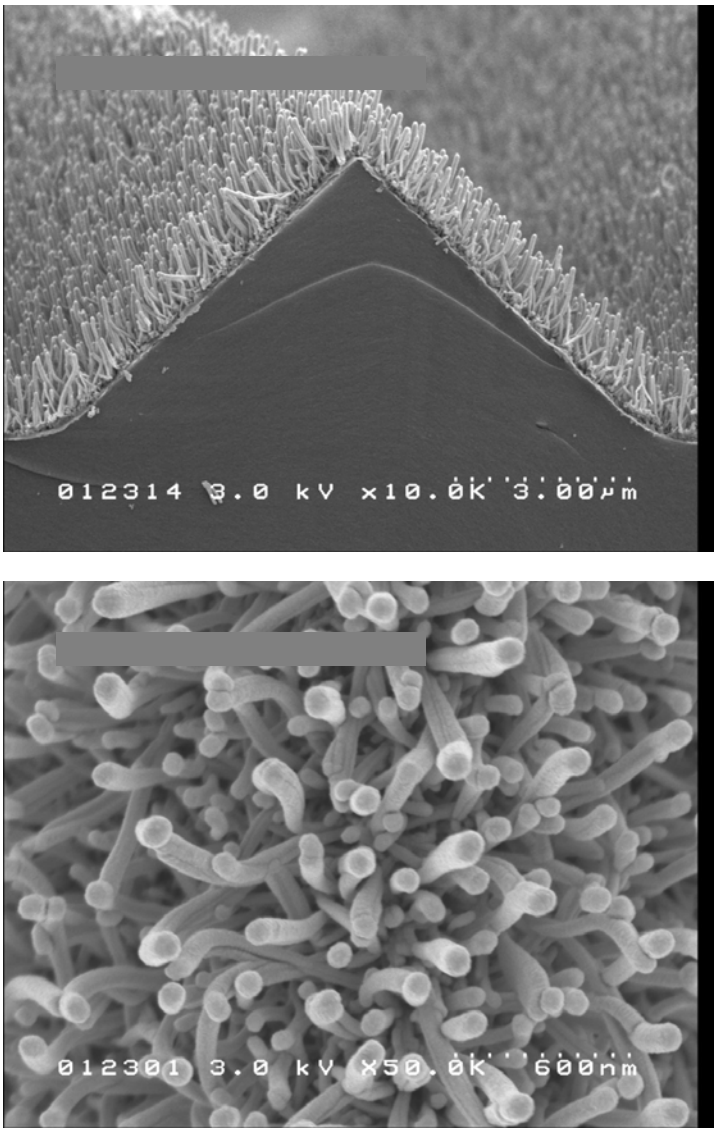

Fig. 1. SEM images at 50,000 original magnification, of the PtCoFe coated NSTF whiskers.

The organic pigment whiskers are highly inert thermally, chemically, and extremely resistant to electrochemical corrosion.[7] The thin film catalyst coatings consist of relatively large, contiguous crystallite domains or nanoscopic catalyst particles. This morphology endows NSTF catalysts with a high level of resistance to loss of surface area by Pt dissolution and agglomeration resulting from stop/start cycling.[7-9] Significantly reduced fluoride ion release rates are also measured under identical comparative experiments with the NSTF versus Pt/C catalyst electrodes, translating to ten-fold increases in lifetimes under various types of single cell tests compared to MEA's having identical membranes and gas diffusion layers but Pt/C electrodes. [10]

The extreme thinness of the electrode allows significant reduction in mass transfer overpotentials at high current densities (see Section 2.1.5.3). The role of the crystalline

support whisker is also understood now to play an important role by influencing the growth morphology of some thin film catalysts, as discussed in section 2.1.2.2.

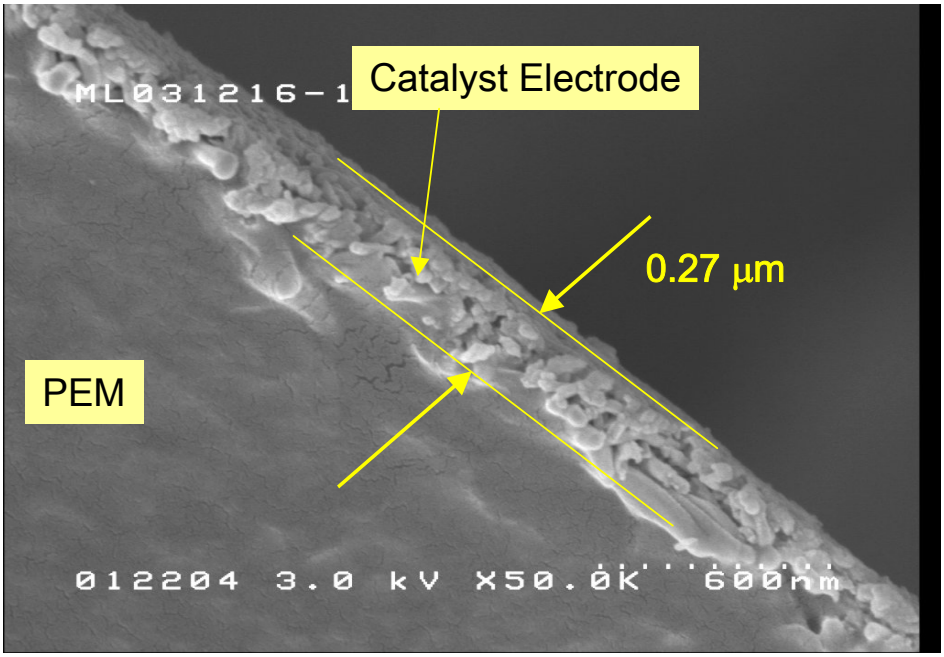

Fig. 2. SEM cross-section of one side of the catalyst-coated membrane, fabricated by a dry roll-good process, illustrating the extreme thinness of the electrode layer.

The Pt and Pt alloy films comprise nanometer scale whiskerettes that grow off the sides of the organic whiskers forming closely packed pillars with [111] side and base facets and truncated pyramidal [100] tops. Their axes grow at a uniform angle of 70^{o} with respect to a whisker's axis, suggesting the cubic [111] side planes of the whiskers are in effect epitaxial substrates for the basal fcc [111] facet of the whiskerette pillars

Most notable however, the NSTF-Pt and Pt alloy catalysts exhibit a five to ten fold gain in specific activity compared to high surface area dispersed Pt/Carbon, measured in either 50 cm^2 fuel cells, or rotating ring disc electrode (RRDE) apparatus [see section 2.1.2.3 and Appendix II], in which the absolute values of the specific activity measured in RRDE agree very well with those from bulk polycrystalline Pt surfaces. This gain in specific activity compensates for the lower electrochemical surface area of the NSTF catalysts so that equivalent performances to high surface area carbon supported catalysts are achieved with reduced loadings. By optimizing the surface area of the whisker support to match the volume of the NSTF catalyst over-coating, the mass activities can be made equivalent to the highest values currently attributed to carbon supported dispersed Pt-alloys[11,12]. Finding ways to increase the specific activity of Pt catalysts is a key strategy for obtaining enhanced fuel cell performance.

Increasing the specific activity of Pt electrocatalysts, (A/cm^2-Pt actual) through the use of Pt alloys has been an active area of electrocatalyst development beginning with phosphoric acid fuel cells[13]. Various mechanisms to explain the factors affecting specific activity have been proposed over the years including electronic structure effects (d-band center and vacancies), site-blocking spectator species, surface faceting, Pt-Pt spacing,

"particle size" effects, near surface alloying, surface defects, and impurities. New concepts for controlling the physical and electronic structure of near-surface alloys to obtain enhanced activity continue to be generated for model systems and DFT calculations are getting closer to explaining the fundamental basis for the enhancements.[14,15] The issue is translating these concepts into practical catalyst systems that can be cost effectively scaled-up to the volumes and quality required for fuel cell commercialization.

This section summarizes the work done in this project to develop the NSTF catalysts to achieve enhanced activity for ORR and durability. The results are summarized in five subsections, beginning with 2.1.1 with results obtained in collaboration with Dalhousie University to screen new catalyst compositions applied to the 3M NSTF support whiskers by sputter deposition to make compositional spreads for characterization in 64 channel segmented cells.

Section 2.1.2 summarizes the fundamental studies of the NSTF catalysts done in collaboration with The University of Illinois, Urbana-Champagn, and Lawrence Berkeley National Laboratory. These are three different investigations of the nature of the NSTF catalyst at a basic surface science level. In 2.1.2.1, CO adsorption and IR reflection absorption spectroscopy are used with *in-situ* electrochemcial characterization of the NSTF catalysts. In 2.1.2.2 the first in-depth high resolution transmission electron microscopy study is reported describing the nature of the Pt crystallites on the NSTF whisker supports and a growth model for how they develop the crystal habit exhibited. Finally, 2.1.2.3 describes the first rotating ring disc electrode characterization of the NSTF catalysts, and compare the fundamental activities measured by RRDE to those from in large area fuel cells for the first time.

Section 2.1.3 summarizes the new alloy catalyst fabrication done in 50 cm^2 fuel cells at the 3M laboratories, and results of mutiple characterization methods completed to evaluate the effects of catalyst composition, layered construction, loading and support structure have on fuel cell performance and ORR specific and mass activities.

Section 2.1.4 summarizes six types of durability tests applied to the down-selected NSTF PtCoMn catalysts, with comparisons, in all but one case, with commercially available carbon supported dispersed Pt. In all the tests, the durability enhancement observed for the NSTF catalysts was one to two orders of magnitude improvement. These basic advantages come because of the elimination of the carbon black support, and the thin film nature of the NSTF catalyst coating.

Section 2.1.5 summarizes the considerations used for down-selection of the NSTF PtCoMn ternary catalyst for scale-up and stack testing, including the composition selection for best ORR activity, minimization of mass transfer overpotential, minimal fluoride release rates and optimum break-in conditioning.

References for 2.1.0

1. H.A. Gasteiger, S. S. Kocha, B. Sompalli, and F. T. Wagner, Applied Catalysis B:Environmental 56, (2005) 9-35.
2. Robert M. Darling and Jeremy P. Meyers, J. of Electrochem. Soc. 150(11) (2003) A1523-A1527, J. of The Electrochemical Society **152**(1) (2005) A242-A247.
3. L. M. Roen, C. H. Paik and T. D. Jarvi, Electrochemical and Solid-State Lett., **7**(1) (2004) A19-A72.
4. S. D. Knights, K. M. Colbow, J. St-Pierre, and D. P. Wilkinson, J. of Power Sources **127**, (2004) 127-134.
5. M. K. Debe, in Handbook of Fuel Cells –Fundamentals, Technology and Applications, W. Vielstich, A. Lamm, H. A. Gasteiger, Editors, John Wiley & Sons, 2003, Ch. 45.
6. M. Debe, A. Hester, G. Vernstrom, A. Steinbach, S. Hendricks, A. Schmoeckel, R. Atanasoski, D. McClure and P. Turner, "Nanostructured Thin Film Catalysts for PEM Fuel Cells by Vacuum Web Coating," in press, 50th Annual Technical Conference Proceedings of the Society of Vacuum Coaters, Louisville, KY, April 30-May 3, 2007.
7. M. K. Debe, A. K. Schmoeckel, G. D. Vernstrom and R. Atanasoski, "High Voltage Stability of NanoStructured Thin Film Catalysts for PEM Fuel Cells," J. Power Sources **161**, 1002-1011 (2006).
8. M. K. Debe, A. K. Schmoeckel, S. M. Hendricks, G. D. Vernstrom, G. M. Haugen and R. T. Atanasoski, "Durability Aspects of Nanostructured Thin Film Catalysts for PEM Fuel Cells," presented at Symposium on Durability and Reliability of Low-Temperature Fuel Cell Systems, 208th ECS meeting, Oct. 16 - 21, 2005, Los Angeles, CA and published in ECSTransactions, Vol.1(8), 51-66 (2006).
9. K. Noda, A. Steinbach and M. Debe, " Start-stop durability testing of 3M's Nanostructured Thin Film Catalysts for PEM Fuel Cells, presented at the 210th ECS meeting, Oct. 29-Nov. 3, 2006, Cancun, Mexico, and published in ECS Transactions, Volume 3(1), 835 (2006).
10. "VII.A.2 Advanced MEA's for Enhanced Operating Conditions," in DOE Hydrogen, Fuel Cells and Infrastructure Technologies Program FY 2005 Progress Report, page 672; and in DOE Hydrogen Program FY 2004 Progress Report, page 301.
11. K. C. Neyerlin, W. Gu, J. Jorne and H. A. GAsteiger, J. Electrochem. Soc. **153**(10)A1955 (2006)
12. F. T. Wagner, H. A. Gasteiger, R. Makharia, K. C. Neyerlin, E. L Thompson, S. G. Yan, ECS Trans. **3**(1) 19 (2006)
13. D. Thompsett, in *Handbook of Fuel Cells: Fundamentals, Technology and Applications*, W. Vielstich, A. Lamm, and H. A. Gasteiger, Editors, p. 467, Chap. 37, Wiley, New York (2003).
14. V. R. Stamenkovic, B. S. Mun, M. Arenz, K. J. Mayrhofer, C. A. Lucas, G. Wang, P. N. Ross and N. M. Markovic, Nature Materials **6** (2007) 241-247.
15. Y. Xu, A.V. Ruban and M. Mavrikakis, J. Am. Chem.Soc. **2004**, 126, 4714-4725.

2.1.1 Compositional Screening of Advanced Electrocatalysts

2.1.1.1 Introduction

This section reviews the work done by subcontractor Dalhousie University, specifically within the laboratory of Prof. Jeffrey Dahn, utilizing their unique combinatorial fabrication and characterization technology to screen advanced multi-element electrocatalysts coated onto the 3M NSTF whisker support films.

The main goal of this subcontract was to utilize the combinatorial materials science capability at Dalhousie University in order to produce and characterize a wide spectrum of platinum-based binary and ternary electrocatalysts, including corrosion stability and catalyst activities.

The subcontract encompassed four main tasks:

1. *Materials fabrication* via generating combinatorial type arrays of sputter deposited binary and ternary metal mixtures and alloys.
2. *Materials characterization* by rapid XRD for structural and Electron microprobe analysis for compositional determination.
3. *Materials stability evaluation* of catalysts after testing in FC and in vitro (acid wash) by XRD and Electron microprobe analysis.
4. *Functional properties evaluation* of catalysts in configurations amenable to the combinatorial fabrication method and subsequent correlation with 50-cm^2 FC performance.

An important aspect of these tasks is that the substrates onto which the Dalhousie catalyst materials were deposited, were the 3M NSTF whisker support films discussed throughout this report and basic to the fundamental activity and durability advantages documented herein. A second important aspect is that the Dalhousie method for coating the catalysts, multi-layer sputter deposition, is the same methodology used by 3M in its preparation of NSTF catalysts, albeit on a much smaller scale and as a batch process Nevertheless, this goes far in assuring that the Dalhousie fabricated materials and understanding would translate well to the larger scale, roll-good processes employed at 3M.

It is essential to point out that the characteristically close interaction between 3M and its subcontractors on this contract was taken a step further in this particular case. Namely, the participants on both sides acted as a single team. Daily interactions were necessary because what was shared and jointly addressed were not only the positives results but most of the time the day-to-day problems that had to be overcome. Moreover, under 3M's guidance a fuel cell laboratory capability at Dalhousie was established.

While multi-component catalyst systems have been studied by others, it is difficult to directly compare one system to another because of differences between sample preparation methods and experimental techniques. Such multi-element comparisons do not appear routinely in the literature because the amount of work involved in sample preparation and testing using traditional "one at a time" methods is prohibitive. Thus this work also helps to demonstrate the usefulness of composition spread preparation and analysis techniques for fuel cell catalyst research. It should also be appreciated that the thin film vacuum coating methods used by 3M and Dalhousie are very amenable to

fabrication of multi-element materials, in contrast to wet chemical methods for forming conventional Pt catalysts supported on carbon blacks.

In the sections which follow we'll give a brief overview and highlight each of the four tasks, while a full account of the activities is given in the joint Dalhousie - 3M publications referenced at the end of this section and included in Appendix I. [1-3] These references should be considered an integral part of this section of the report. Emphasis will be given to both the new capabilities and the adaptation of preexisting hardware and testing methodology that were developed in fulfillment of the tasks listed above. These activities consumed a substantial part of the effort in this subcontract.

2.1.1.2 Materials Fabrication via the Compositional Spread Approach.

Due to their work developing new battery electrode materials, Dalhousie University had extensive expertise with combinatorial methods of materials science. In this collaboration, 3M's crucial contribution was in the choice of materials to be fabricated and the substrate – the 3M NSTF whisker supports - upon which the new materials were deposited. In order to achieve the desired compositional spreads, a sophisticated sputtering machine and coating procedures were used, the description of which follows.

Pt binary and ternary alloy compositional spreads were prepared via DC magnetron sputtering (Corona Vacuum Coaters sputtering system) in an argon plasma from pure metal targets (99.99% purity) onto a rotating, water-cooled, substrate table. Briefly, a range of substrates are loaded onto a 40 cm diameter table that is mounted on a bearing (allowing it to rotate) on the door of the sputtering chamber. A series of targets are located opposite the table (when the door is closed) such that, as the table rotates, the substrates pass by each target sequentially. Masks are placed over the sputtering targets to control the deposition profile. Typical masks are designed to give either constant deposition, or a radial linear gradient. The radial linear deposition gradient can go in either of two directions, with the thickest deposit closest to the outside of the table, referred to as a "linear out mask", or with the thickest deposit end closest to the inside of table, called a "linear in mask". Fig.1 illustrates how a combination of a "linear out" and a "linear in" mask can be used to prepare binary alloys covering the whole alloy range.

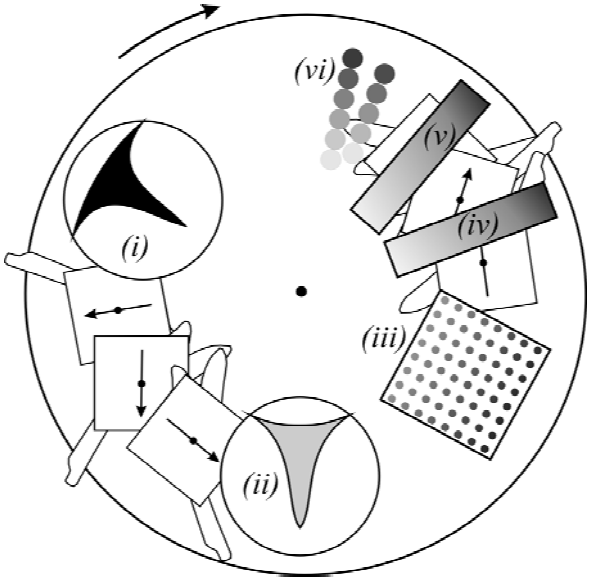

Fig. 1. Schematic diagram of the rotating substrate table used to prepare $Pt_{1-x}M_x$ binary composition spreads of fuel cell catalysts - (i) linear out mask over Pt target; (ii) linear in mask over M target; (iii) shadow mask over NSTF catalyst support film to produce sample for fuel cell testing; (iv) Si wafer for microprobe and XRD measurements; (v) other sample, e.g. glass slide for corrosion testing and (vi) aluminum foil disks for determining mass deposited. The table is approximately 40 cm in diameter.

The thickness of material deposited during a single rotation of the table past a masked target is controlled by changing

the rotation speed and target power. The total number of revolutions of the table controls the deposited film thickness. Fast rotation speeds and relatively low target powers were selected when intimate mixing between the deposited elements was desired. Under these conditions, less than a monolayer of a given element is deposited at the thick end of a mask over a target each time the table rotates past that target. The power settings for each of the sputtering targets were ramped down over the last few rotations to ensure that the surface composition was equivalent to the bulk.

The rotating table arrangement allows a number of different substrates to be mounted on the table for each sputtering run, with each substrate receiving the same deposition profile. Silicon wafer substrates were used to measure both x-ray diffraction (XRD) profiles and elemental compositions (through electron microprobe analysis). Nano-structured thin film (NSTF) support films were provided to Dalhouse by 3M. (See section 2.1.3 in this report for more information on the PR149 organic pigment coated whisker support film.) These support substrates were the identical roll-good substrates used by 3M to fabricate the NSTF catalysts. When preparing a compositional spread sample, the NSTF whisker coated substrates are taped onto the table and covered with an aluminum shadow mask plate containing an 8 x 8 grid of tapered holes, 2.36 mm in diameter. This can give 64 discrete catalyst compositions. During binary composition spread preparation, most of the composition variation occurs in one dimension of the rectangular catalyst grid – e.g. “vertically”. This means that many of the sputtered “dots” are actually quite close in composition, giving a good indication of repeatability.

More complex deposition schemes were applied for generating ternary libraries: $Pt_{1-x}[M_yM'_{1-y}]_x$ where a constant thickness Pt layer alternated with a wedge shaped layer of transition metals $M_yM'_{1-y}$ with y constant throughout the library; and $Pt_{1-x}[M_yM'_{1-y}]_x$ where constant thickness layers of Pt were modulated by mixed compositionally graded layers of $M_yM'_{1-y}$. [2]

During the duration of the project approximately20 libraries/year were produced and characterized.

2.1.1.3 Materials characterization

Materials characterization was done by rapid XRD for structural and electron microprobe analysis for composition determination. The composition of the films was determined quantitatively by a JEOL JXA-8200 Superprobe equipped with one energy dispersive (EDS) spectrometer and five wavelength dispersive (WDS) spectrometers. The metal content (Pt, transition metal and Si substrate), was measured by EDS and the oxygen content was analyzed by WDS. The real count time was about 1 minute for each measurement. The optical autofocus feature of the microprobe was used for the films deposited on the Si wafer. For the rougher NSTF substrate films, selected points were manually focused and the beam was operated in the scanning mode (covering an area of 150 μm x 110μm) to obtain accurate results. Measurements on libraries deposited on smooth Si wafers or on the NSTF substrates showed the same stoichiometry variation with position in the library. This is illustrated in Fig. 2 where composition of several libraries generated on NSTF substrate and on silicon substrates showing a good agreement are presented.

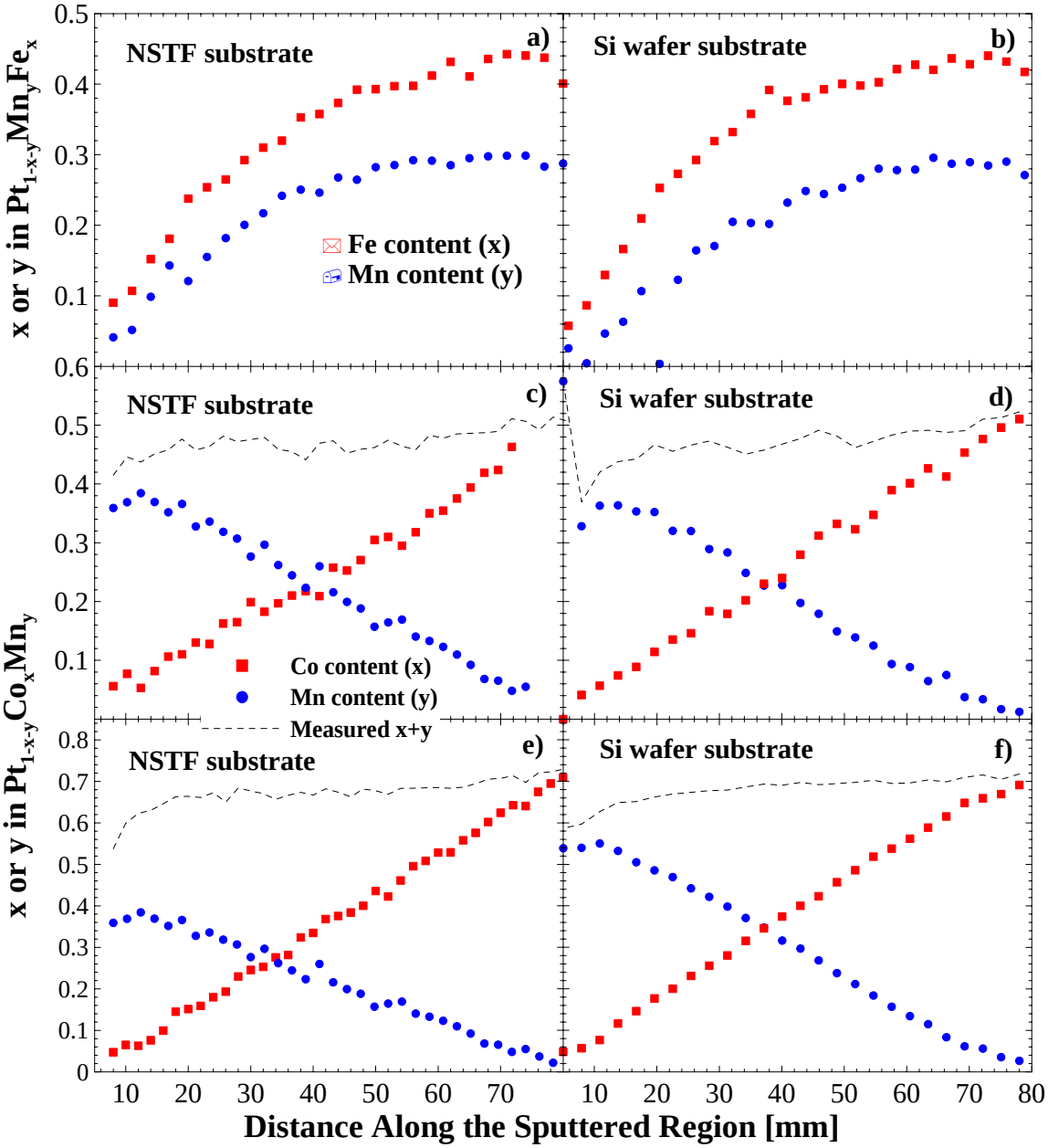

Fig. 2. Composition of several libraries as measured on NSTF (a, c, e) and Si wafer (b, d, f) substrates. The composition of the films deposited on the two different substrates are in good agreement.

Point by point x-ray diffraction patterns of the libraries were measured by an Inel curved position sensitive detector (CPS 120) and a PW-1720 Phillips X-ray generator using Cu Kα radiation. The size of the x-ray beam spot on the library was about 1 mm by 1 mm. A composition variation, $0 < x < 1$ or $0 < y < 1$ in $Pt_{1-x}[M_yM_{1-y}]_x$ occurred over a distance of 75 mm in our libraries. A typical presentation of the diffraction patterns Pt ternary spread is presented in Fig.3.

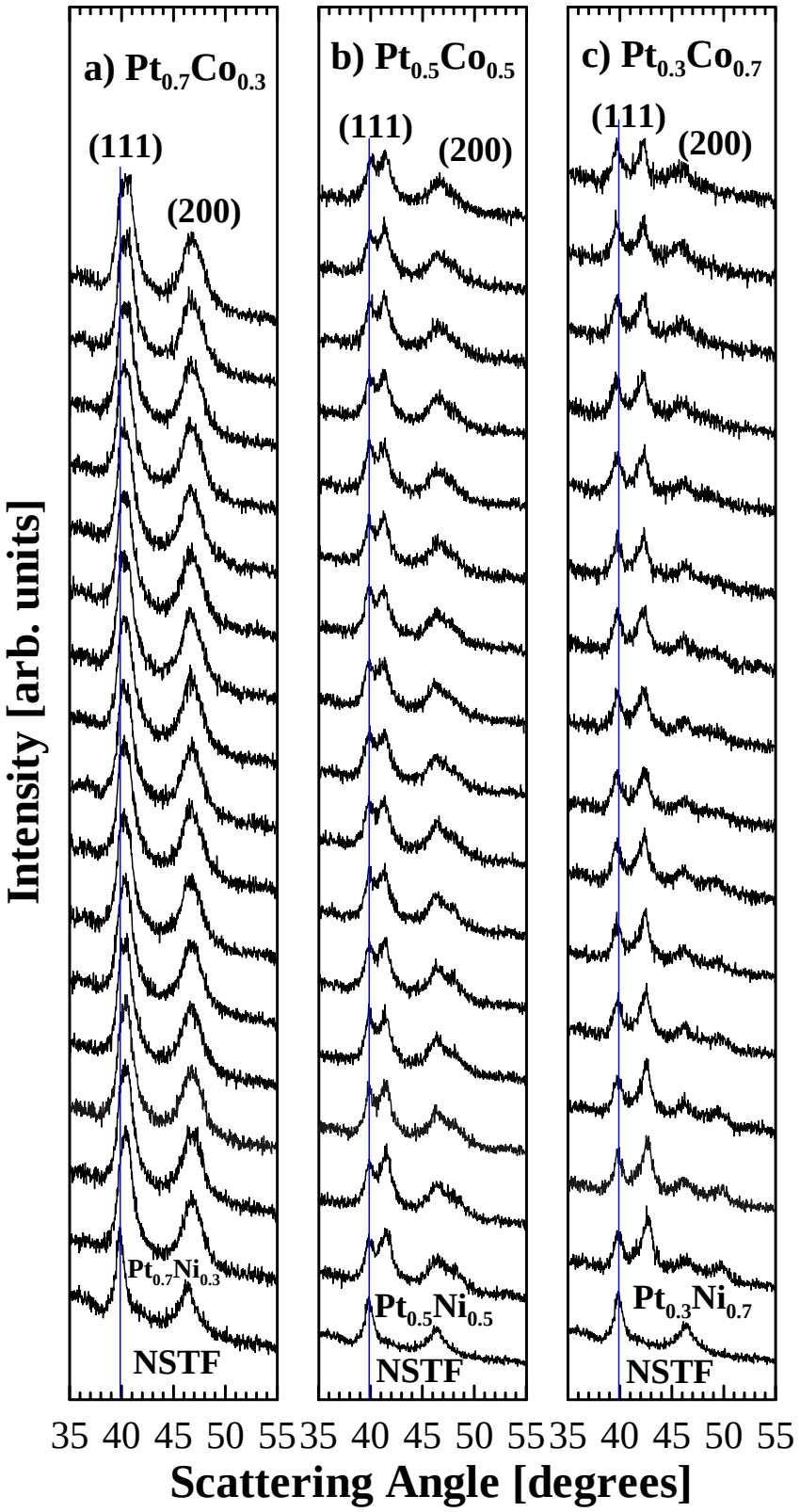

Fig. 3. Diffraction patterns of $Pt_{1-x}[Co_{1-y}Ni_{y\_x}]_x$ (x = 0.3,0.5,0.7; 0 < *y* <1); Libraries 7–9, showing a clear movement of thealloy fcc peaks to higher angles. The shift of the (111) peaks is greater for larger values of *x*.

2.1.1.4 Materials stability

Materials stability of the Dalhousie fabricated catalysts was evaluated both after fuel cell testing and in acid soak tests. All the acid treatments were performed on the electrocatalyst libraries on the NSTF supports. For a typical treatment, a 75 mm long x 6 mm wide NSTF strip containing the entire library was soaked in 25 ml of 1M H_2SO_4 (Reagent, analytical grade) acid and was kept in a sealed glass vial at 80°C for 10 days. After treatment, the samples were washed with de-ionized water and dried in air before further characterization by XRD and electron microprobe. Special care was always taken so as not to damage the nanometer-sized whiskers on the films during handling. In the case of Pt-Fe and Pt-Ni, atomic absorption measurements of the acid solution showed no detectable trace of dissolved Pt to within its detection limit.

For fuel cell measurements of the $Pt_{1-x-y}M_xM_y$' (M, M' = Co, Ni, Mn, Fe) libraries, catalyst coated membranes (CCM) were prepared using electrocatalysts from eight positions of each of the libraries and tested at 80^{o}C under humidified hydrogen and air. Typical tests lasted for several days and included cyclic voltammetry and polarizations. The methods to make the CCM's were the same as used by 3M to fabricate larger, 50 cm^2 CCMs for fuel testing and details of their fabrication are explained in more detail in section 2.1.3 fo this report. All the CCMs with the Dalhousie catalyst libraries were fabricated at the 3M St. Paul testing laboratories. After testing, the fuel cells were opened and the GDLs removed to expose the electrocatalysts adhering to the membrane. They were then characterized by electron microprobe to determine what changes in bulk stoichiometry had occurred due to the fuel cell testing, and compared to the acid soaked samples.

The compositional changes after the FC testing and the acid treatment are presented side by side in Fig. 4. The similarity in the composition for both libraries is obvious verifying that the acid soak treatment directly reflects the changes taking place during fuel cell testing.

2.1.1.5 Functional properties evaluation

Measuring catalytic activities of the combinatorial libraries with sufficient accuaracy and reliability to discriminate among the various compositions and structures within a given library has been and remains the main challenge for this high throughput method for discovering new ORR catalysts. Obtaining local properties of the catalyst requires that the surface area of the catalyst region under test be as small as possible. As such, the small surface area is more prone to impurity, short circuit and cross over effects which are common place in fuel cell testing. The approach we adopted for catalyst evaluation was based on the same principles developed in our previous 3M/DOE Cooperative Agreement (DE-FC02-99EE50582): viz. the catalyst evaluation should be performed under conditions that are as realistic to fuel cell testing as possible; and once promising candidates are identified, produce the identified composition on a sample large enough to be tested in a 50-cm^2 fuel cell or produce adeqate catalyst material for testing in a RRDE apparatus (see section 2.1.2.3 of this report). The most reliable catalyst surface property characterized in the compositional spread format was determination of the surface area. This was done by H_{upd}, by probing the catalytic active sites by CO adsorption/stripping, and by measuring the activity towards HOR, all of which could be related to the catalytic activity of the Pt sites towards ORR.

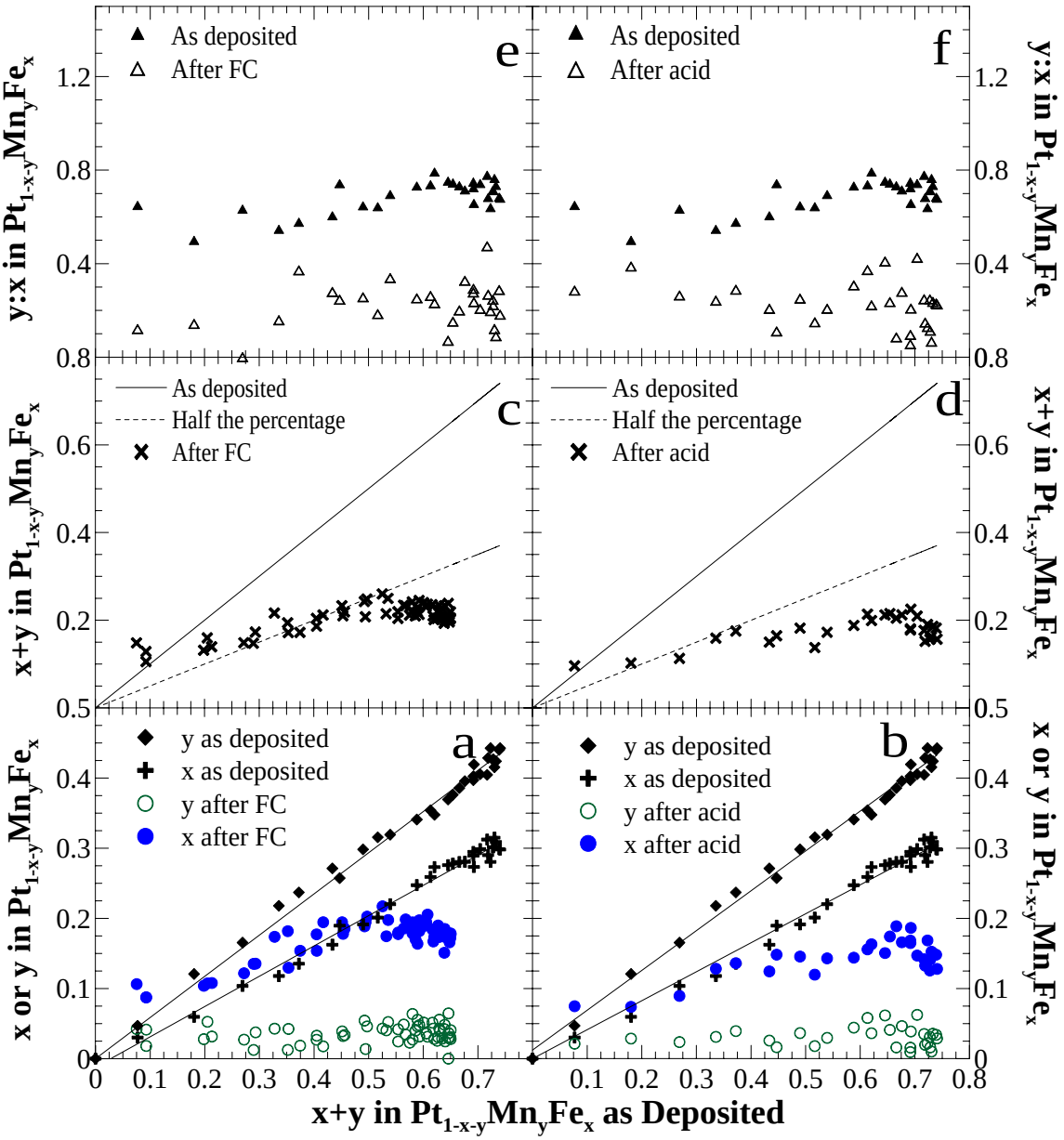

Fig. 4. Composition of the $Pt_{1-x-y}Mn_yFe_x$ with an initial Mn/Fe ratio = 0.65 after (a–c) fuel cell testing and (d–f) acid treatment vs the composition of the as-deposited film. Panels a and b show the individual metal contents (x and y), panels c and d show the total transition metal content (x + y), and panels e and f show the ratio of Mn toFe (y:x).

In early stage of the program an 8-segment cell was used which latter evolved into a 64-electrode fuel cell. The major drawback of the 8-segment cell was the fact that the segments were too large to be of a uniform composition.

The 64-electrode fuel cell test station design is based on the electrical design successfully used to test composition-spread arrays of lithium-ion battery electrode materials. 64 electrically isolated catalyst channels are connected through a parallel array of resistors to a Keithley Instruments 2440 current source. The potential of the cell is controlled by the current source and the current flowing to/from each channel is

determined by measuring the voltage drop across the in-line resistor (0.5 Ω for high currents, 30 Ω for low currents) with a Keithley Instruments 2700 scanning multimeter. This is shown schematically in Fig. 5.

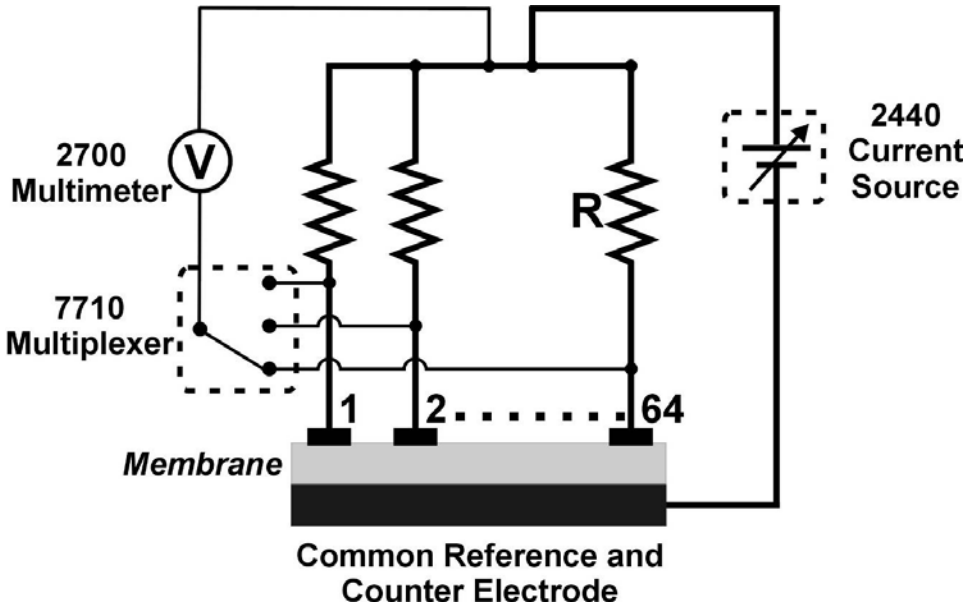

Fig. 5. Schematic diagram of the pseudo-potentiostat hardware used for the 64-electrode PEM fuel cells.

The individual resistor lines make electrical contact to each of the catalyst "dots" via spring loaded contact pins that press into the base of individual ¼" diameter Poco graphite rods embedded in an Ultem 1000 (polyetherimide) block (Fig. 6 (e))

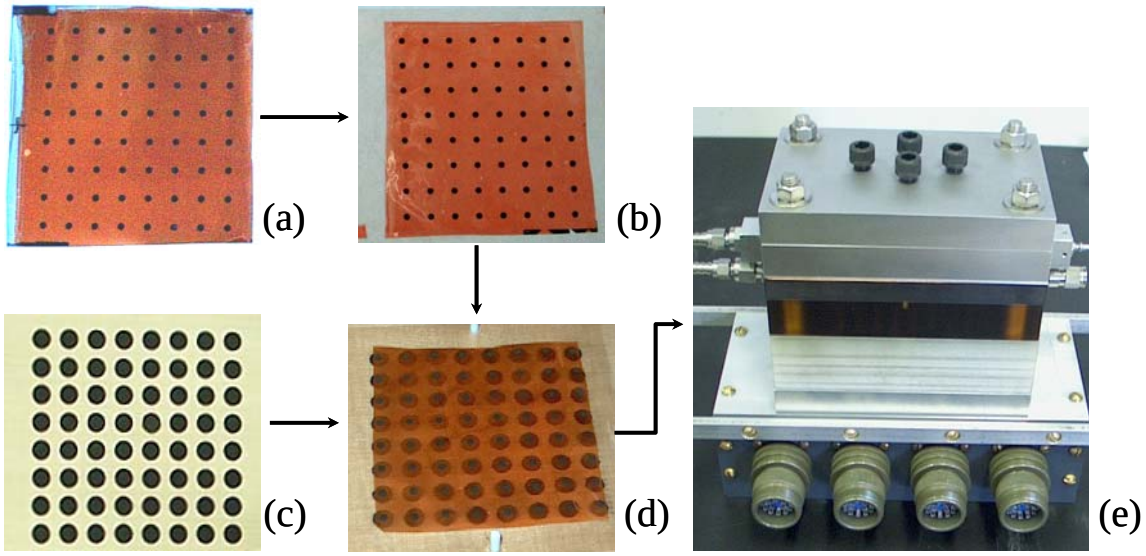

Fig. 6. Cell assembly procedure. (a): 64 catalyst compositions sputter deposited onto NSTF support through masks. (b): Catalyst array after lamination to polymer electrolyte membrane. (c): Gasket with 64 GDL disks. (d): Membrane with catalyst array placed on gasket. (e): Assembled 64-electrode fuel cell.

The “segmented electrode” block has a serpentine flow field milled into the top surface, with gas channels passing through each of the Poco graphite rods to supply humidified gases to the catalysts. The counter/reference electrode side of the cell comprises a continuous Poco graphite block with a serpentine flow field milled into one face. This block provides electrical contact for a common counter/reference electrode together with a path for humidified gas flow.

The cell itself is easy to assemble, with the whole process taking less than one hour. The steps involved are shown in Fig. 6. After sputter deposition, the NSTF support and catalyst coatings (Fig. 6 (a)) are transferred to a proton exchange membrane using hot-roll lamination (Fig. 6 (b)). The complete film is transferred in one pass through the laminator. The NSTF support is supplied on a polyimide backing that can be peeled away after lamination leaving the catalyst coated “whiskers” embedded into the membrane. For the reference/counter electrode, a NSTF support film with a continuous platinum coating (0.15 mg/cm^2) is laminated to a second membrane in the same way. A teflon-coated fiberglass gasket containing an 8 x 8 grid of holes 8 mm in diameter is place over the Ultem block. A gas diffusion layer (GDL) disk is placed in each of the holes (Fig. 6 (c)). The CCM with the catalyst compositions of interest is then placed on top of the gasket (Fig. 6 (d)), with the catalyst coated side facing the GDL disks. As the diameter of the sputtered “dot” is small relative to the GDL diameter, any lateral expansion or contraction of the membrane does not impact on channel performance. The counter electrode membrane is then placed on top of the segmented electrode membrane with the catalyst side facing the POCO Graphite flow field. A 75 x 75 mm piece of GDL is placed over the counter electrode catalyst within a rectangular hole cut in the center of another piece of teflon-coated fiberglass gasket. The counter electrode flow field plate, a copper current collector, a teflon spacer and two aluminum backing plates are added to the cell which is then sealed via external bolts (Fig. 6 (e)).

The whole cell is placed inside a mechanical convection oven (Yamato Scientific DKN600) to eliminate edge temperature effects. Ultra-high purity gases are supplied to the cell with either mass flow controllers or flowmeters, depending on the gas being used. Digital metering pumps (Lab Alliance Series I) are used to pump nanopure water (Barnstead Nanopure Diamond, > 18.2 MΩ) at a controlled rate into the gas streams. The humidified gas streams then pass through heated mixing chambers (to help evaporate any liquid water) before entering the fuel cell flow fields.

When first started, the cells were pre-conditioned through repeated cyclic voltammograms (CVs). The CVs were measured at room temperature with a scan rate of 50 mV/s. During this measurement, 5% hydrogen in argon (humidified) flowed across the counter/reference electrode and pure argon (humidified) flowed across the segmented electrode. The resolution of the sweep potential with the 2440 current source is 50 μV and thus the CVs were performed as a linear staircase with 50 μV steps. Electrochemical cycling was performed on all channels simultaneously. Current vs. potential data were collected on only two channels at a time, so a total of 32 CVs were needed before data was available for all channels. This process was continued until stable voltammograms were measured on each channel.

For CO stripping voltammetry measurements, the cell was operated at 80°C with humidified 5% H_2 in argon flowing across the counter electrode. The cell was held at 100 mV for 10 minutes with 2% CO in 40% H_2/balance N_2 flowing across the segmented electrode. This step was used to achieve steady-state CO coverage of the surface. To

remove residual (non-adsorbed) CO from the gas flow path, the cell was held at 100 mV with argon flowing across the segmented electrode for another 10 minutes. CO was then removed from the surface by measuring cyclic voltammograms. The potential was first swept up to 600 or 700 mV, to measure a CO stripping peak. Two more cyclic voltammograms were then recorded both to strip off any residual CO and to measure a baseline signal. As with the standard CV measurements, CO stripping voltammograms were recorded on two channels during each CO adsorption/desorption sequence.

Typical cyclic voltammograms for CO stripping on six $Pt_{1-x}M_x$ alloy catalyst arrays as a function of composition are presented in Fig. 7

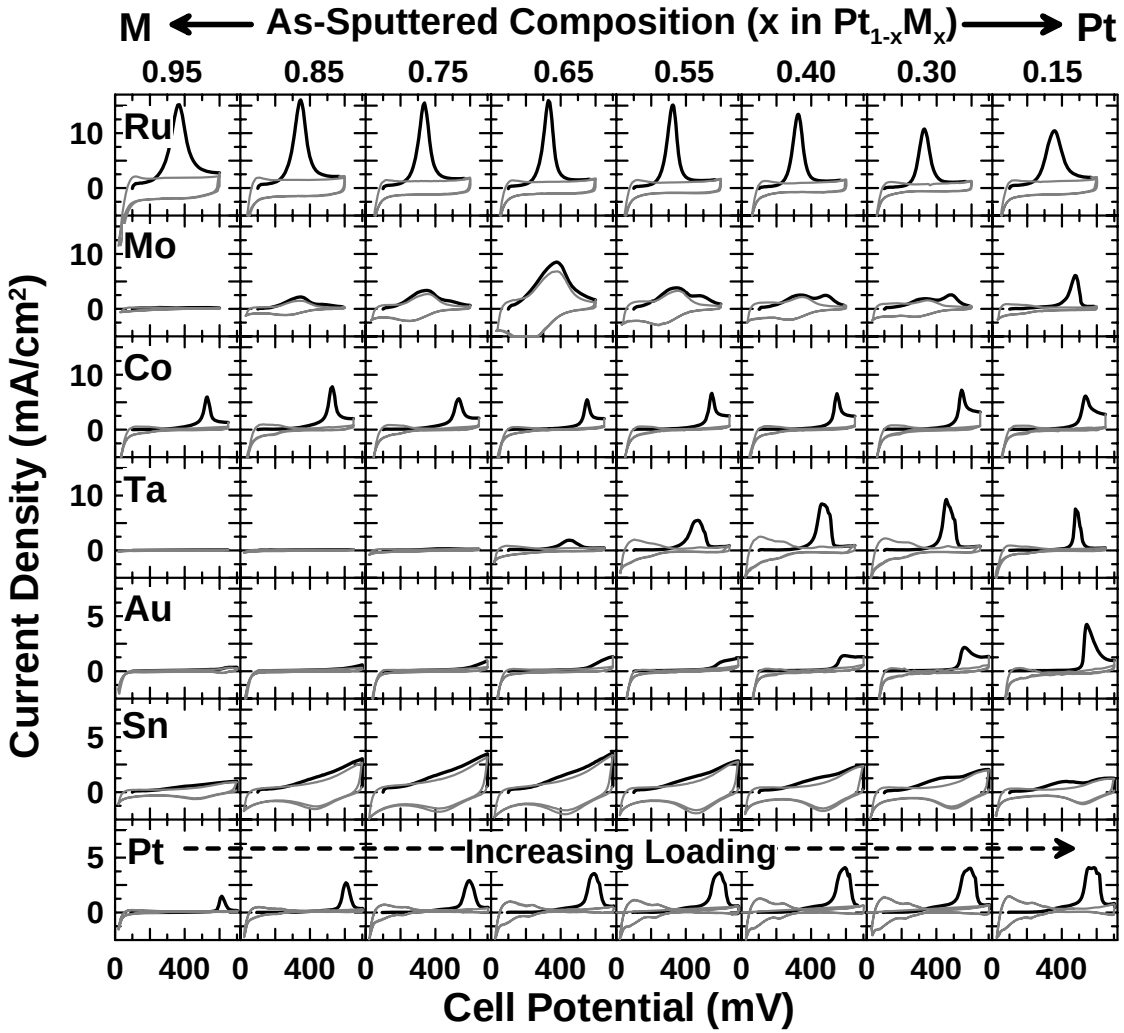

Fig. 7. CO stripping onset potentials as a function of composition for the six binary composition spreads and cyclic voltammograms after the removal of CO indicating Pt active sites through the H_{upd} region. Onset potentials for a cell with platinum only, ramping from ~ 0 to 0.5 mg/cm^2 is included on each panel for comparison. The platinum loading for a given x-position is equivalent to the platinum loading in the $Pt_{1-x}M_x$ alloy and is indicated along the top panels of the graph.

For comparison, the bottom row of panels shows CO stripping voltammograms measured on a sample containing only platinum. The platinum loading increases from left to right, to a maximum of 0.5 mg/cm^2. Each column in the graph has approximately

the same amount of deposited platinum. The currents measured during the first up sweep are shown in black on each panel of the figure. Clean CVs from subsequent sweeps are then shown in grey. For many of the compositions, a CO stripping peak can be seen centered around 300-500 mV during the first up sweep. This peak is not present during subsequent cycles implying the entire adsorbed CO has been removed. The six binary systems showed distinctly different trends in CO stripping. In addition to the CO stripping behavior, the cyclic voltammograms after the removal of CO provide a clear indication Pt active sites through the H_{upd} region (at potentials <400 mV).

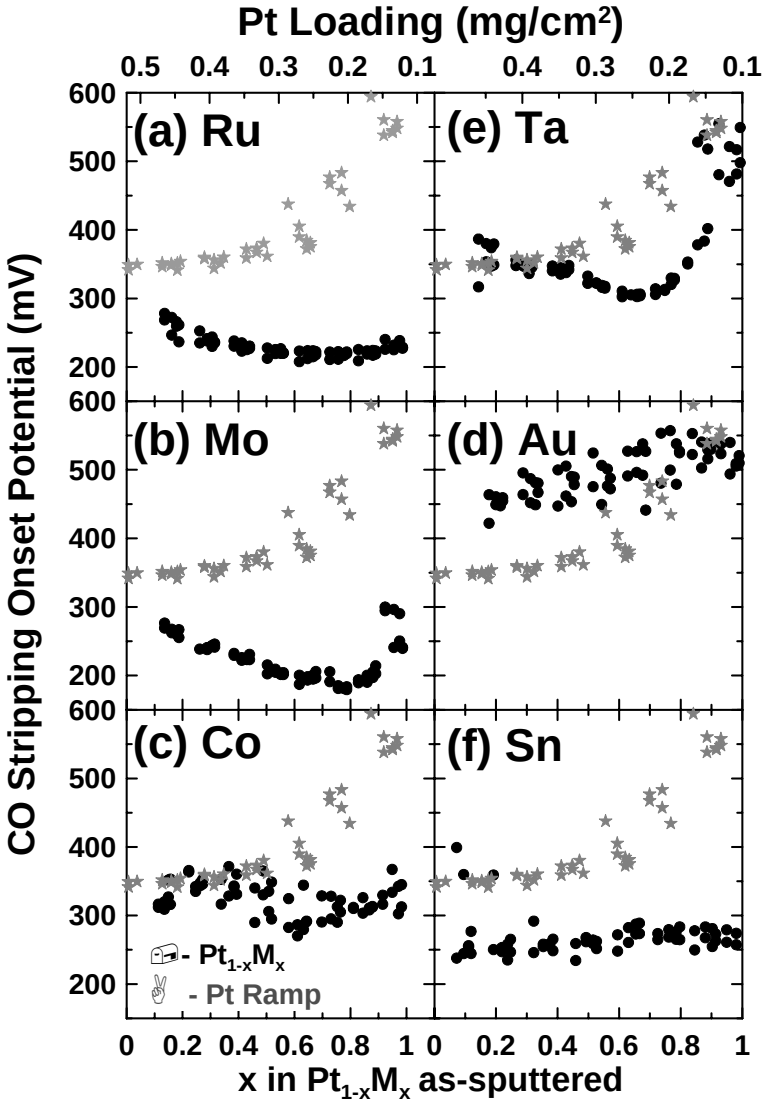

Fig. 8. "CO-tolerance" hydrogen oxidation polarisation curves as a function of composition for the 6 binary systems studied. Measurements made with 10 (grey lines) and 50 (black lines) ppm CO in (40 % H_2, 21 % CO_2, 39 % N_2) at 80°C, with humidified gas streams and no back-pressure regulation. The data have not been corrected for membrane resistances. The alloying element for each row is identified in the left-hand panel of the row; the approximate composition (as-sputtered) for each column is shown across the top of the figure. The bottom row of panels shows polarisation curves for a pure Pt sample with approximately the same Pt loading as the samples in the columns above.

Fig. 8 shows the CO stripping onset potentials as a function of composition determined from the CO stripping voltammograms for the catalyst arrays. This graph also shows onset potential data measured on the Pt ramp as a function of Pt loading. The axes for these plots have been scaled so that the platinum loadings are consistent with the platinum loadings present in the binary composition spread samples. For the pure Pt samples, the CO stripping onset potential increases at low platinum loadings, suggesting that the potential at which CO stripping occurs may depend on the primary Pt particle size, in agreement with the finding reported in section 2.1.2.3 of this report. At higher platinum loadings (0.3 mg/cm^2 and above), the onset for CO stripping occurs around 350 mV and is, to a first approximation, independent of loading.

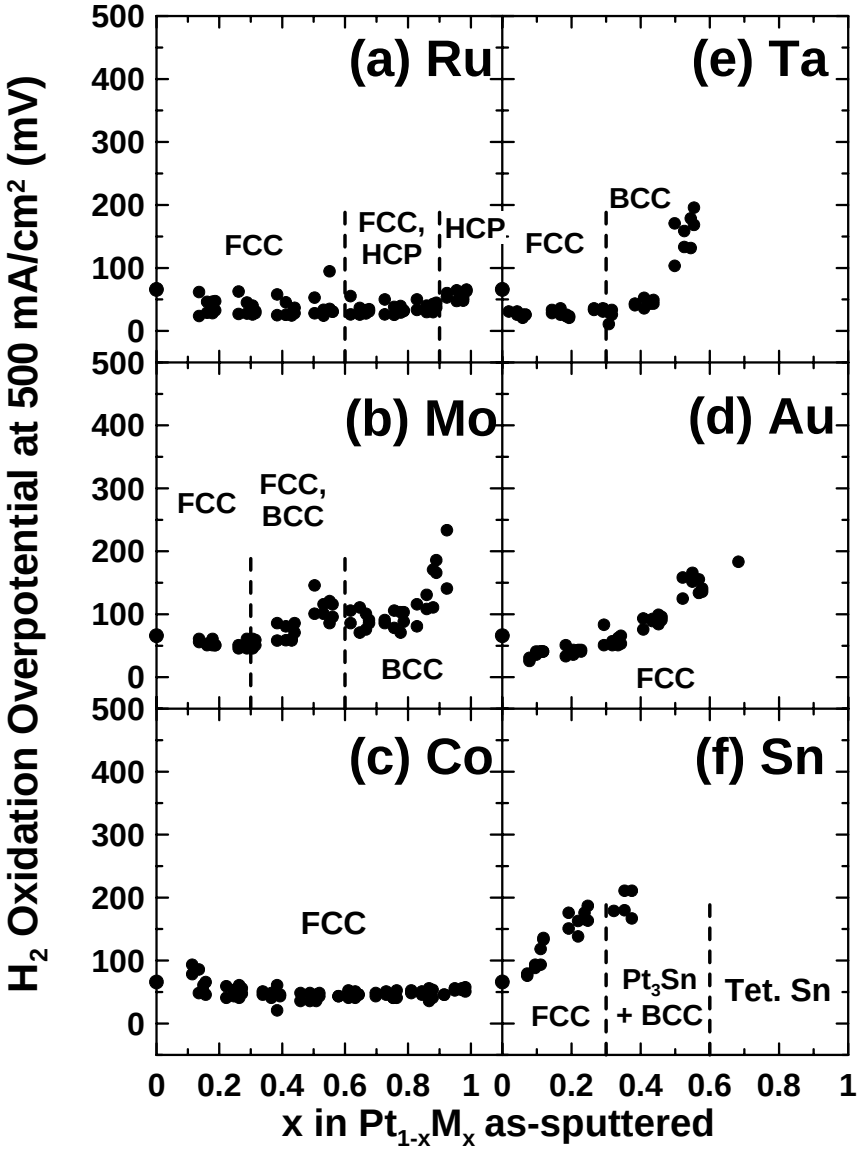

Fig. 9. Hydrogen oxidation overpotentials at a current density of 500 mA/cm^2 as a function of the as-sputtered composition for the 6 binary catalysts. Measurements were made at 80°C with humidified gas streams and no back-pressure regulation. The data have not been corrected for membrane resistances. The data at x = 0 were collected on a separate Pt-only cell.

To determine the activity of a given catalyst composition towards hydrogen oxidation, baseline performance was measured with pure hydrogen flowing across both sides of the cell. The electrodes were first cleaned electrochemically by holding the cell at 600 mV with H_2 at the counter/reference electrode and argon at the segmented electrode. The potential of the cell was then stepped from 5 to 250 mV then back to 5 mV in 5 mV steps, holding at each potential for 2 seconds. During this measurement, the cell was held at 80°C. This potential-time profile was repeated many times to ensure the current-potential curves measured were representative of performance.

Fig. 9 summarizes the HOR overpotentials for the six different binary samples, by showing the overpotential required to maintain a current density of 500 mA/cm^2 for each electrode. These overpotentials are plotted against the as-sputtered composition of each electrode. Data for any electrodes with an overpotential larger than 500 mV at 500 mA/cm^2 have not been included in the figure. Data from a pure Pt cell has been included on each panel at x = 0 for reference. Overall, smooth trends in overpotential vs. composition were observed. Based on these data, limits can be placed on the amount of alloying element that can be added to platinum without blocking its catalytic activity. Using an arbitrary cut-off potential of 150 mV at 500 mA/cm^2, the transition metal (TM) atomic % limits would be: Ru, Co – no limit, Mo – 80 %, Au, Ta – 50 %; and Sn 10 %.

2.1.1.6 Summary

The sample preparation and testing methodology at Dalhousie was designed to examine a wide range of compositions in a short period of time and to generate data of direct relevance to operating fuel cell electrocatalysts. Composition spreads have been deposited via DC magnetron sputtering through shadow masks onto 3M's nano-structured catalyst support. XRD and electron microprobe data confirmed the expected structural and composition gradients. It is important to note that testing binary composition ranges in the 64-channel fuel cell generates numerous repeat samples. But to fully utilize the 64-channel cell, we prepared and tested complete ternary alloy systems, many of which were later fabricated at 3M and tested in 50 cm^2 fuel cells as described in section 2.1.3 of this report. All 64 channels in these higher order libraries can have a different composition, greatly increasing the range of composition space examined. For each such experiment either the binary or ternary composition spreads could be prepared and tested over a two-week period. To prepare and test 64 different alloy compositions through standard alloying methods would certainly require a lot more time and effort than the methods utilized here. From this we conclude that the most efficient way to study complex alloy catalyst systems is to use composition spread methods similar to those discussed here.

A major effort was expended to determine the chemical stability, and by exention stability in the fuel cell environment, of various ternary alloys, using the acid soak tests described above. These results have been published and are attached in Appendix I of this report. There it is shown that in $Pt_{1-x-y}M_xM'_y$ alloys (M=Ni, Co, Mn, Fe) corrosion of the transition metal elements occurs when the electrocatalysts are subjected to 1M H_2SO_4 at 80°C, and also when they are utilized under the typical working conditions of a PEMFC. The composition changes that occur during the acid treatment mimic those that occur during fuel cell testing very closely. Regardless of the initial overall transition metal atomic fraction, the average transition metal atomic fraction is reduced to at most a value of about 0.3. This suggests that it is difficult for the transition metal atoms to diffuse from the cores of the grains when the atomic fraction becomes near 0.3. In all

cases, for all the libraries studied, we believe the composition of transition metals at the alloy surface has been reduced to zero. This explains why the average transition metal content is reduced even for alloys where the initial transition metal atomic fraction is less than 0.3.

References for Section 2.1.1

1. A. Bonakdarpour, J. Wenzel, D. A. Stevens, S. Sheng, T. L. Monchesky, R. Lobel, R. T. Atanasoski, A. K. Schmoeckel, G. D. Vernstrom, M. K. Debe, and J. R. Dahna, *J. Electrochem. Soc.*, **152**, A61, 2005.

2. A. Bonakdarpour, R. Lobel, R. T. Atanasoski, G. D. Vernstrom, A. K. Schmoeckel, M. K. Debe and J. R. Dahn, *J. Electrochem. Soc.*, **153**, A1835, 2006.

3. D. A. Stevens , J. M. Rouleau, R. E. Mar, A. Bonakdarpour, R. T. Atanasoski, A. K. Schmoeckel, M. K. Debe and J. R. Dahn, *J. Electrochem. Soc.*, **154**, B566, 2007.

2.1.2 Fundamental characterization and understanding

2.1.2.1 EC-IRAS Investigation of the NSTF Catalyst Surfaces

Introduction

In addition to the NSTF catalyst studies by high-resolution transmission electron microscopy (HRTEM) discussed in the following section 2.1.2.2, the morphological features were also probed by CO-stripping voltammetry and by electrochemical infrared reflection-absorption spectroscopy (EC-IRAS) measurements. The Urbana-Champaign group has advanced the use of a reflection mode infrared spectroelectrochemistry for studies of supported platinum nanoparticles. In particular, the group demonstrated high signal-to-noise data for CO chemisorption used as a probe of surface site properties. The link between such vibrational characteristics via the CO probe molecule and catalytic activity was clearly established. Infrared spectroscopy produced important qualitative information regarding bond strengths and binding arrangements of the CO probe, which was ideally suited for testing reactivity of the 3M catalytic materials. EC-IRAS data demonstrated that the NSTF catalyst samples exhibit basic voltammetric and surface vibrational properties similar to those of polycrystalline surfaces.

Experimental

Electrochemical experiments were performed in 0.1 M H_2SO_4 electrolyte, in a three-electrode electrochemical glass cell. Gold wire was used as the auxiliary electrode and the reference electrode was Ag/AgCl (3 M NaCl). The electrode potentials were calibrated vs. RHE, and all values below refer to the RHE scale. A shiny polycrystalline gold disk electrode (d = 0.9 cm) supporting the NSTF electrocatalyst was used as a the substrate for the working electrode. The working electrode was prepared in such a way to provide optimal electronic and optical properties for EC-IRAS experiments[1]. Prior to EC-IRAS, the working electrode was subject to a few electrode potential cycles between RHE and 1.3 V aiming at removal of impurities from the catalyst surface. Cyclic voltammetry and carbon monoxide stripping were conducted in Ar-saturated electrolyte while holding the electrode in a hanging meniscus position. CO was chemisorbed on the catalyst surface by bubbling CO in the electrolyte for at least 15 minutes, or by dosing with an aliquot of CO-saturated solution for a particular time to get sub-saturated CO adlayers.

The vibrational EC-IRAS spectroscopy was carried out with a Mattson Research Series 2 FTIR spectrometer. The spectrometer bench was connected to a custom-built external reflection chamber containing a narrow-band MCT detector.[2] A mirror-finished polycrystalline gold disk served as the highly reflective substrate while supporting partially IR-transparent thin film made of the electrocatalyst powders. The gold disk was mounted on a glass plunger, which was held either in the hanging meniscus position for electrochemistry (CV, CO-chemisorption) or pressed against the CaF_2 window to create an optical thin electrolyte layer for the spectroscopic measurements.[2] Finely dispersed sample powders were immobilized on gold by using chemical deposition or “wet” physical deposition, depending on the nature of the electrocatalyst. The deposition of the Pt samples involved surface modification by 3-aminopropyltrimethoxysilane (3-APTMS). In contrast, the procedure employing liquid-phase physical adsorption from a water-based electrocatalyst ink yielded EC-IRAS electrodes with better properties for testing the NSTF samples. Pure Pt, alloyed PtRu and PtNiFe NSTF samples were

analyzed in the form of a fine powder. For data comparison, Pt catalyst coated membranes (CCMs) were studied as well. In this case the CCM was wrapped around the gold disk and secured with a gold wire that also served as a current collector. In this case there was no electronic contact between the gold substrate and the electrocatalyst.

During infrared measurements of chemisorbed CO, the electrode potential-dependent spectra were recorded after averaging 100 interferometer scans at 4 cm^{-1} resolution. A single spectrum acquisition required ca. 35 seconds. The background spectrum was taken immediately after stepping to sufficiently high electrode potential where surface CO was electrooxidized to CO_2. Absolute absorbance spectra were obtained by ratioing the electrode potential-dependent CO spectra to the background (CO adsorption-free) single beam spectrum. A linear baseline-correction tool accessible in the WinFIRST software was applied to remove the effects of the electrode potential-dependent adsorption of dissolved ions on the absorbance spectra. The relative CO coverage (θ_{CO}) was estimated using the peak absorbance of CO_2, which remained trapped in a thin layer for a few minutes.

Results

Electrochemical and surface vibrational properties of the NSTF samples were analyzed by using basic electrochemical methods (Fig. 1) and infrared spectroscopy of chemisorbed carbon monoxide (Fig. 2). The cyclic voltametry and CO-stripping data for (i) Pt, (ii) PtRu, and (iii) PtNiFe are summarized in Figs. 1A and 1B, respectively. All three samples exhibit similar voltammetric behavior to the corresponding state-of-the-art nanoparticle systems.[3-5] For the pure Pt NSTF, the anodic sweep in the hydrogen UPD region exhibits Faraday currents resembling those of a polycrystalline surface that

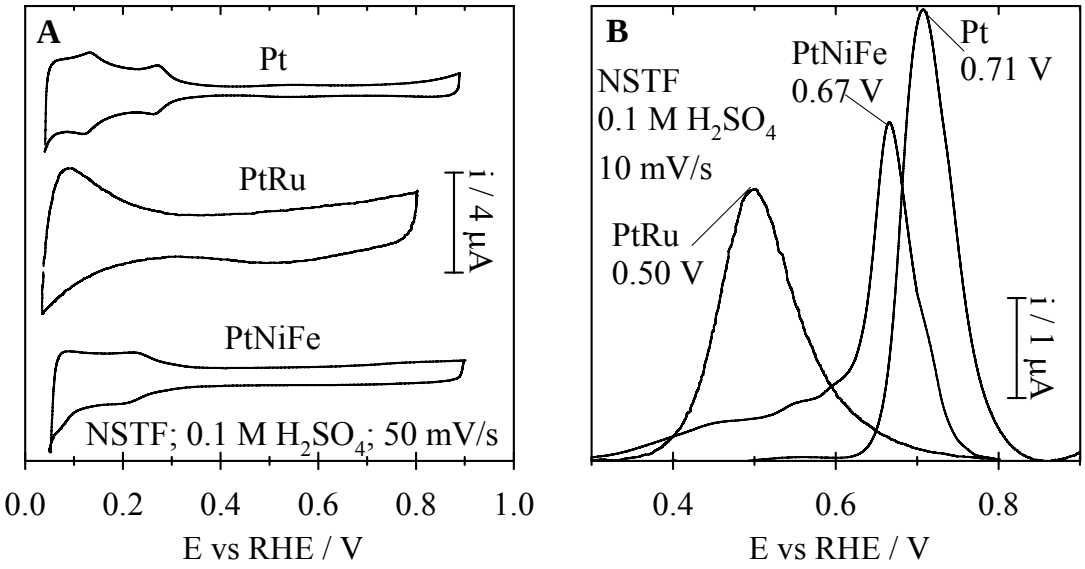

Fig. 1. (A) Cyclic voltammograms, and (B) baseline-corrected carbon monoxide (CO)-stripping lineshapes for thin-film electrochemical infrared reflection-absorption spectroscopy (EC-IRAS) for NSTFcatalysts. The areas under the CO-stripping curves are normalized to that obtained for the Pt NSTF. Data obtained in Ar-saturated 0.1 M H_2SO_4-electrolyte. A) CV at 50 mV/s; B) CO-stripping at 10 mV/s.

originate from the desorption of mobile as well as hydrogen atoms coordinated to surface sites of various morphology.[6]

For the PtRu NSTF, the hydrogen adsoption/desorption region is poorly defined and larger pseudocapacitive currents were measured. These both reflect a strong alteration by surface Ru. In case of the PtNiFe ternary, the hydrogen underpotential deposition (H_{UPD}) region is suppressed and less resolved compared to the pure Pt system since protons do not adsorb on the alloying elements in such conditions.[7] In concert with CV, CO-stripping voltammetry also reveals the alloyed nature of the surface of multi-metal NSTF systems (Fig. 1B). The CO electrooxidation peak potential is shifted towards lower electrode potentials for both alloy NSTF samples. On the PtRu NSTF, a value as low as 0.5 V is measured that is essentially identical with that determined for Johnson & Mathey PtRu HiSpec6000.[4] More importantly, the ignition potential is found at a lower (by ca. 300 mV compared to pure Pt) electrode potential for both alloys revealing their high CO-tolerance. On pure NSTF Pt, the CO electrooxidation curve peaks at 0.71 V, close to the value reported for (110) single crystal surfaces[8] and for larger (d < 5 nm) carbon-supported nanoparticles as well as nanoparticle blacks[9].

EC-IRAS of saturated CO adlayers on the NSTF electrocatalysts provides further support for the electrochemical data. Fig. 2 shows absolute absorbance spectra in the energy region where CO is linearly and two-fold coordinated on the particular metallic

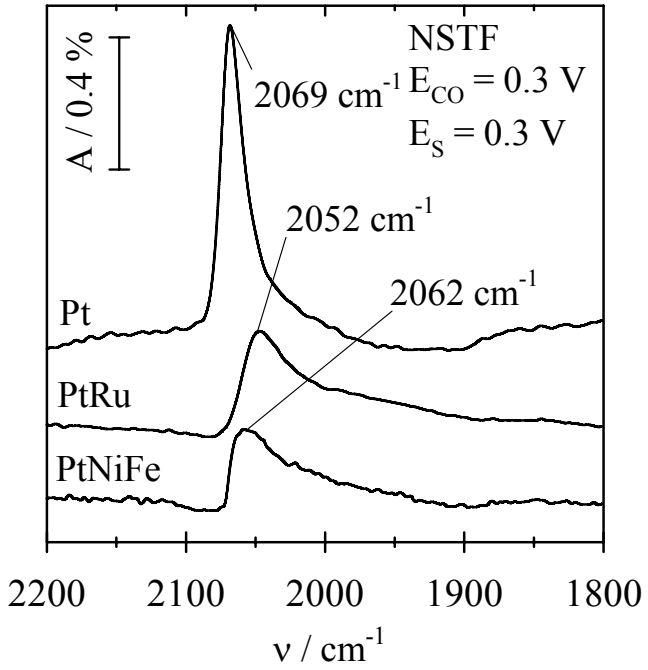

Fig. 2. EC-IRAS surface CO absorbance spectra for the Pt-, and Pt-alloy NSTFs in Ar-saturated 0.1 M H_2SO_4. The areas under the CO bands are normalized to that under the Pt NSTF CO peak. CO was chemisorbed at 0.3 V by bubbling for 15 minutes. Spectra obtained at 0.3 V are only shown. The reference (CO-free) spectrum was recorded at 0.9 V.

sites. It is evident that the three NSTF catalysts hold saturated CO adlayers with drastically different surface bonding structure. In addition to the considerably smaller absorbances and the significant redshifts in the wavenumbers of the Pt-CO_L peaks in the alloy spectra (see Table I below), new low intensity bands also emerge as long tails on the low-wavenumber side of the Pt-CO_L peak (between 2000 cm^{-1} and 1900 cm^{-1}). The band peaking at ca. 2000 cm^{-1} in the PtRu spectrum is assigned to Ru-CO_L,[2] whereas that at ca. 2040 cm^{-1} in the PtNiFe spectrum is assigned to Ni-CO_L.[10] According to Park et al.[2] such weak shoulders imply that some of the alloying elements segregated into islands, rather than all being perfectly intermixed with Pt on the surface. Although the lateral physical interactions between adjacent CO-adsorbates dramatically influence the surface vibrational spectrum, the presence of Ru as well as Ni on the surfaces of the alloy NSTF samples is clearly revealed.

In order to illuminate the morphological peculiarities of the NSTF electrocatalysts, we benchmarked some basic electrochemical and vibrational properties of the pure Pt NSTF system against those of various conventional Pt samples. Fig. 3 presents a collection of cyclic voltammograms for unsupported and supported Pt systems including a polycrystalline Pt disk, 60% Pt/C, and Pt black; all with which NSTF Pt bears some similarities. One of those is realized in the similar fine structure of the hydrogen adsorption/desorption region. Interestingly, the width of the hydrogen adsorption/desorption region and also the relative magnitude of Faraday currents at the lower (at ca. 0.14 V) and higher (at ca. 0.27 V) electrode potentials is the largest for the NSTF system followed by the 60% Pt/C sample. According to the general concept of the

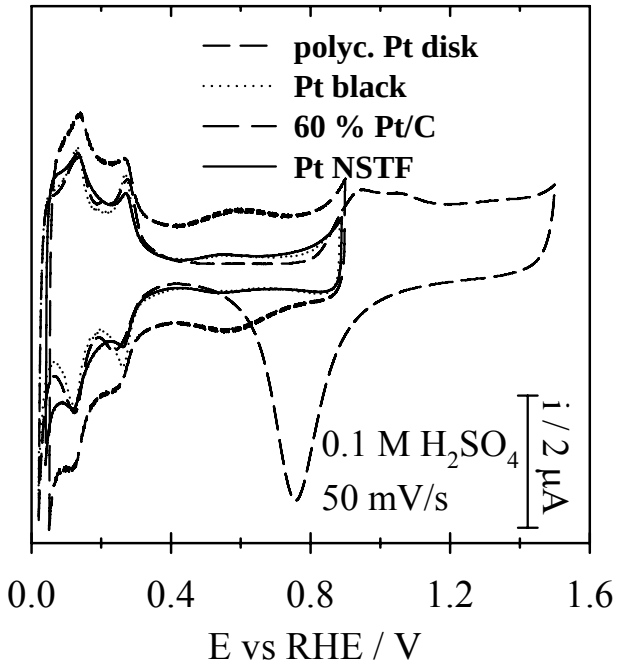

Fig. 3. Cyclic voltammetry curves for for polycrystalline Pt disk, unsupported Pt, 60% Pt/C, and Pt NSTF in Ar-saturated 0.1 M H_2SO_4-electrolyte solutions.

structure sensitivity of hydrogen adsorption[18], these observations imply the predominance of (111) surface sites and mainly those having low-coordination numbers over the (100) crystal planes, thus giving support to the HRTEM microscopy results in the following section and many XRD analyses.

Another striking feature of the NSTF voltammogram is that it exhibits a double layer charge as small as those for the unsupported samples. The measured small pseudocapacitive currents manifest that the support is essentially "invisible" for cyclic voltammetry in contrast to the conventional carbon support. This behavior is readily understood since the NSTF whisker support particle is largely masked by the deposited metal that essentially encapsulates it.

Typical morphological characteristics of the NSTF Pt electrocatalyst are further revealed by analyzing its absolute absorbance EC-IRAS CO spectrum in the light of those obtained for selected Pt samples. Fig. 4A compares absorbance-normalized Pt-CO_L bands recorded for saturated CO adlayers in identical experimental conditions. As Chang and Weaver have suggested[11], morphological variations alter surface vibrational properties predominantly via the physical interactions between neighboring adsorbates (via dynamic dipole effects) rather than through the static dipole or even more straightforwardly the chemical effect. Evidently, the effects of the lateral interactions are the most dominant for saturated adlayers. Given that the CO_L peak on low index single crystal Pt surfaces are expected to fall within a few wavenumbers for all the facets[2], as well as considering the apparent particle size-independent nature of the Pt-CO singleton frequency on carbon-supported nanoparticle systems, we use the dipole-dipole and short range interaction mechanisms to gain structural information.

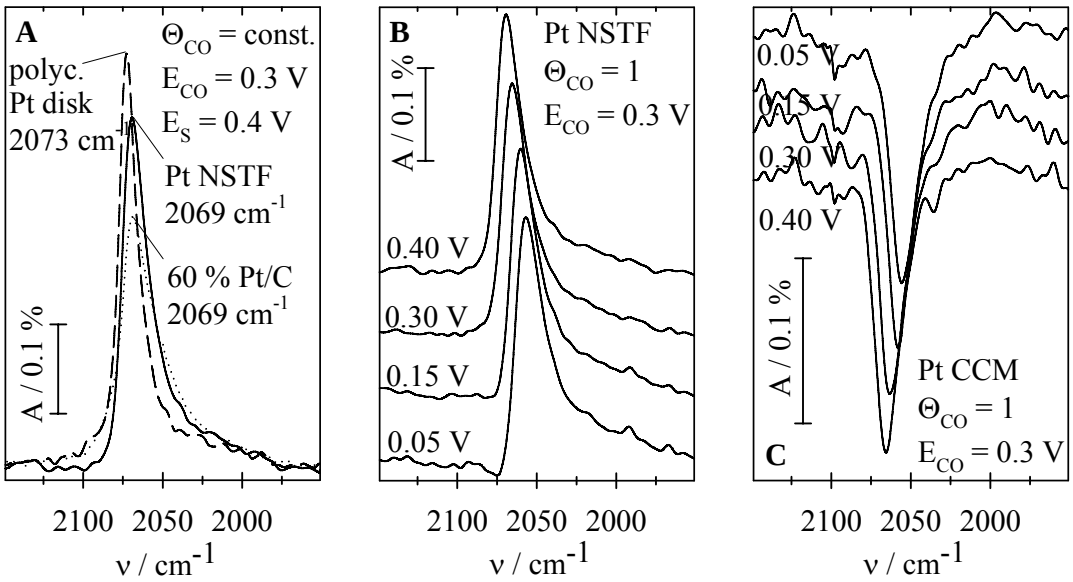

Fig. 4. EC-IRAS absorbance spectra for saturated CO adlayers formed on pure Pt electrodes in Ar-saturated 0.1 M H_2SO_4-electrolyte solutions. CO was chemisorbed at 0.3 V via bubbling. A) normalized spectra for polycrystalline Pt disk, 60% Pt/C, and PR-supported NSTF Pt. Each reference spectrum refers to 0.4 V, the background spectrum was recorded at 0.9 V. B) electrode potential-dependent CO spectra for a thin film EC-

IRAS working electrode with a thin layer of pure NSTF Pt particles; C): same for NSTF Pt catalyst coated membrane (CCM).

Firstly, close similarities are found between the wavenumber position and lineshape of CO_L bands formed on polycrystalline disk, carbon-supported nanoparticles and the NSTF Pt, i.e. between the respective CO adlayer structures. In comparison to nanoparticle systems constituted by distinct small clusters (corresponding data are presented in Ref.[13]), the blue-shifted and sharp CO_L peaks seem to be indicative of largely contiguous surfaces. Such extended adlayers can engender the screening effect of high frequency oscillations as well as the enhancement of surface electric fields by the low frequency oscillations, i.e. referred to as "intensity-transfer"[14-16]. Furthermore, there are "tails" observed on the CO_L peaks towards the lower wavenumbers. The "tail" carries implications to the morphology of the clusters as the magnitude of such asymmetric band broadening differs among the samples. This feature is noticeable for all samples including polycrystalline Pt suggesting that it has an origin other than the support or substrate material[17] or the heterogeneous distribution of nanoparticle size[18]. All samples were attached to the gold substrate by covering it with an organic monolayer through which Pt particles were anchored. Therefore, CO adsorption on Au as a possible origin for peak asymmetry[17] can be excluded. Park et al.[18] attributed the "tail" to CO binding on smaller nanoparticle segments. However, the NSTF sample exposes Pt clusters of various size distributions, i.e. the particle size distribution should be more heterogeneous than in the 60% Pt/C sample. Yet the CO_L peak for the NSTF is quite symmetric. We attribute this characteristic to the ability of CO molecules to arrange into more extended and uniformly dense adlayer structures than on Pt/C nanoparticles,

Fig. 4B shows that CO chemisorbed on a thin layer of NSTF Pt particles gives regular vibrational responses with the CO_L band gradually blue-shifting with increasing positive electrode polarization. The latter concurs with the trend obtained for all of the investigated Pt samples. However, when the NSTF Pt electrocatalyst is investigated as a part of a catalyst coated membrane (i.e. in an actual fuel cell electrode), its intensity direction appears inverted and the CO_L band shows larger FWHM values (Fig. 4C). Furthermore, the peak position is red-shifted in the EC-IRAS absorbance spectra (cf. Fig. 4B and Fig. 4C). Such characteristics are unambiguous signatures of the "abnormal infrared effects" (AIREs).[19] AIREs are described as operating via electron-hole damping between interacting nanoislands and the adsorbed CO molecules[20], and also reported as developing for agglomerated/thick nanostructured films via complex dielectric behavior of the nanoparticles therein[11]. Such structures are typically present in CCM fuel cell electrodes. While the above vibrational properties squarely follow those trends established for a series of "individually addressable arrays" of nanostructured Pt microelectrodes,[21] we found the Stark tuning rate (STR) behavior to be practically the same for the CCM and the powdered NSTF Pt. On both of them, a linear electrode potential dependence of the CO_L frequency is obtained with a slope of 33 cm^{-1} V^{-1} and 34 cm^{-1} V^{-1}, for the NSTF Pt CCM and powder, respectively (Table 1). While valuable information is accessible for actual fuel cell electrodes showing abnormal optical properties by means of potential-dependent FTIR emission spectroscopy[22] as well as simultaneously applied specular reflectance and online transmission FTIR spectroscopy[23, 24], our results strongly imply that changes in morphology and chemical composition can be monitored under fuel cell operation by a conventional EC-IRAS study as well.

Table I. Vibrational parameters of surface CO for the investigated electrocatalysts. The peak wavenumber positions and Stark tuning rates (STR) were determined for atop-CO in saturated adlayers.

Electrocatalyst type	*Metal*	$\nu_{CO(L)}$ (sat. CO, 0.4V) [cm^{-1}]	STR [cm^{-1} V^{-1}]
NSTF powder	*Pt*	**2069**	**34**
	PtRu	**2052**	**39**
	PtNiFe	**2062**	**36**
NSTF CCM	*Pt*	**2066**	**33**
Polycrystalline disk	*Pt*	**2073**	**30**
Carbon-supported nanoparticle	*Pt (60%)*	**2069**	**33**

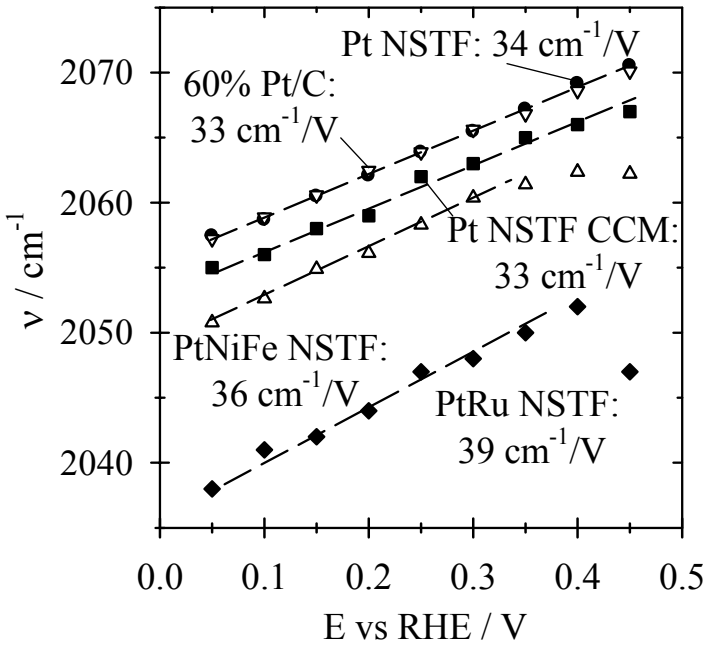

Fig. 5. Plot of linearly bonded CO peak center frequencies as a function of electrode potential for various NSTF systems and for the 60% Pt/C catalyst. Data were extracted from electrode potential-dependent EC-IRAS spectra for saturated CO-adlayers collected in Ar-saturated 0.1 M H_2SO_4 electrolyte.

Figure 5 shows $\nu_{CO_L}^{peak}$ vs. *E* plots for some of the investigated samples. As expected based on literature data[18, 25], a largely linear Stark behavior is observed for all Pt

samples, at least for spectra taken for saturated CO adlayers in the hydrogen adsorption/desorption region. Table 1 summarizes the important vibrational properties. Noteworthy that the CO_L stretching frequency at a selected electrode potential as well as the Stark tuning rate is the same for the NSTF as for the 60% Pt/C.. In the light of the markedly different surface morphology of the two samples this clearly indicates that the wavenumber position of CO_L provides chemical information for largely diluted CO adlayers only, wherein the effects of lateral interactions are eliminated. As discussed above, the Stark tuning rate for the NSTF Pt CCM electrode is indeed nearly the same as that for the powdered NSTF Pt sample. The $\nu_{PtC-O_L}^{peak}$ - *E* slopes are in fact expected to be insensitive to particle size,[18] and hence to the morphology of nanoparticles or continuous single and polycrystalline Pt electrodes as well.

As mentioned above, a linear Stark behavior with very similar tuning rate was found for all pure Pt samples when polarized in the hydrogen adsorption/desorption and double layer region. At the same time, the Stark effect is quite different for the binary PtRu and ternary PtNiFe NSTF.. First of all, the wavenumber of CO_L peak position drops if the alloy electrocatalysts are polarized to more positive potential than 0.4 V. In concert with our electrochemical data (Fig. 1B), this observation is directly related to a facile CO electrooxidation, i.e. high CO-tolerance, with the PtRu and PtNiFe alloy NSTF samples. EC-IRAS data collected for sub-saturated CO adlayers revealed the presence of the water-activating elements, Ru, Ni and Fe on the surface of the NSTF alloys. These elements further the formation of surface oxides, thereby the oxidative removal of CO, at low electrode potential. With a decrease in CO population in the adlayer, the lateral interactions become less dominant involving a concomitant red-shift in measured stretching frequency.

Furthermore, somewhat higher STR values were measured for the PtNiFe and PtRu NSTF samples, 36 and 39 cm^{-1} V^{-1}, respectively. A higher STR value reflects the electron backdonation from Pt to the 2□* orbital of CO_L becomes more sensitive to electrode polarization[26]. This can be explained straightforwardly by considering that Pt has a 5d electron vacancy for the alloys in comparison to pure Pt.[27] which translates to a more moderate electron backdonation mechanism for the former samples. Hence, any electrode polarization-induced change in surface electron density is more radically reflected in the CO_L stretching frequency as measured on the alloy NSTF surfaces.

Conclusions

The peak, and, most importantly, the onset of CO electrooxidation were observed at markedly lower electrode potentials (i.e. by ca. 300 mV lower for the onset potential) for the NSTF alloys. The presence of alloying elements at the surface was also attested to by the broadened and more asymmetric spectral lineshapes, and by the significant redshifts of the Pt-CO_L peaks in the EC-IRAS absorbance spectra taken for saturated CO adlayers. A comparative cyclic voltammetry and EC-IRAS study was performed on a series of Pt electrocatalyst systems in order to illuminate the surface characteristics. The NSTF has a polycrystalline surface, however, H_{UPD} revealed a shortfall in the number of (100) sites *versus* the low-coordination and the (111) sites.

The lineshape of the CO_L peak implies that the NSTF exposes an extended and well-ordered surface, where the lateral physical interactions in the adlayer enable an intense “intensity transfer” to the high frequency oscillations. The nanostructured layer of the

CCM exerted abnormal infrared effects, revealed by the inversion and blueshift of the CO_L bands of the vibrational spectra. Nevertheless, the wavenumber shift upon electrode polarization followed the same trend as the NSTF powder-based electrode which exhibited ideal optical properties. Our results indicate the capability of EC-IRAS to monitor surface elemental composition and/or morphology for actual CCMs used in fuel cells by exploiting the AIREs. For the NSTF alloys, the Stark-effect deviates from its linear trend at low electrode potentials suggesting their enhanced CO-tolerance by the presence of Ru and Ni (and Fe) on the surface. In the hydrogen adsorption/desorption region where the CO adlayer is stable and the measured CO_L wavenumber depends linearly on the electrode potential, systematically higher STR values were obtained for the alloy samples. This confirms the electronic interaction in between Pt and the alloying elements. Nevertheless, the presence of Ru, Ni, and Fe on the surface of the alloy NSTF samples was clearly demonstrated by EC-IRAS for sub-saturated CO adlayers.

References for section 2.1.2.1

1. Park, S.; Weaver, M. J., *J. Phys. Chem. B* **2002,** 106, (34), 8667-8670.
2. Park, S.; Wieckowski, A.; Weaver, M. J., *J. Am. Chem. Soc.* **2003,** 125, (8), 2282-2290.
3. Gasteiger, H. A.; Kocha, S. S.; Sompalli, B.; Wagner, F. T., *Applied Catalysis, B: Environmental* **2005,** 56, (1-2), 9-35.
4. McGovern, M. S.; Waszczuk, P.; Wieckowski, A., *Electrochim. Acta* **2006,** 51, (7), 1194-1198.
5. Paulus, U. A.; Wokaun, A.; Scherer, G. G.; Schmidt, T. J.; Stamenkovic, V.; Radmilovic, V.; Markovic, N. M.; Ross, P. N., *J. Phys. Chem. B* **2002,** 106, (16), 4181-4191.
6. Teliska, M.; O'Grady, W. E.; Ramaker, D. E., *J. Phys. Chem. B* **2004,** 108, (7), 2333-2344.
7. Paulus, U. A.; Wokaun, A.; Scherer, G. G.; Schmidt, T. J.; Stamenkovic, V.; Markovic, N. M.; Ross, P. N., *Electrochim. Acta* **2002,** 47, (22-23), 3787-3798.
8. Hayden, B. E., *Catalysis and Electrocatalysis at Nanoparticle Surfaces* **2003**, 171-210.
9. Guerin, S.; Hayden, B. E.; Lee, C. E.; Mormiche, C.; Owen, J. R.; Russell, A. E.; Theobald, B.; Thompsett, D., *J. Combinatorial Chemistry* **2004,** 6, (1), 149-158.
10. Cuesta, A.; Gutierrez, C., *Langmuir* **1998,** 14, (12), 3397-3404.
11. Chang, S. C.; Weaver, M. J., *J. Chemical Physics* **1990,** 92, (7), 4582-94.
12. Kim, C. S.; Tornquist, W. J.; Korzeniewski, C., *J. Chemical Physics* **1994,** 101, (10), 9113-21.
13. Park, S.; Tong, Y.; Wieckowski, A.; Weaver, M. J., *Electrochem. Communications* **2001,** 3, (9), 509-513.
14. Weaver, M. J.; Zou, S., *Advances in Spectroscopy (Chichester, United Kingdom)* **1998,** 26, (Spectroscopy for Surface Science), 219-272.
15. Iwasita, T.; Nart, F. C., *Progress in Surface Science* **1998,** 55, (4), 271-340.
16. Korzeniewski, C.; Severson, M. W., *Spectrochimica Acta, Part A: Molecular and Biomolecular Spectroscopy* **1995,** 51A, (4), 499-518.
17. Stamenkovic, V.; Arenz, M.; Ross, P. N.; Markovic, N. M., *J. Phys. Chem. B* **2004,** 108, (46), 17915-17920.
18. Park, S.; Wasileski, S. A.; Weaver, M. J., *J. Phys. Chem. B* **2001,** 105, (40), 9719-9725.
19. Sun, S.-G., *Catalysis and Electrocatalysis at Nanoparticle Surfaces* **2003**, 785-826.
20. Wu, C.-X.; Lin, H.; Chen, Y.-J.; Li, W.-X.; Sun, S.-G., *J. Chem. Phys.* **2004,** 121, (3), 1553-1556.

21. Gong, H.; Sun, S.-G.; Chen, Y.-J.; Chen, S.-P., *J. Phys. Chem. B* **2004,** 108, (31), 11575-11584.
22. Lu, X.; Faguy, P. W.; Liu, M., *J. Electrochem. Soc.* **2002,** 149, (10), A1293-A1298.
23. Sanicharane, S.; Bo, A.; Sompalli, B.; Gurau, B.; Smotkin, E. S., *J. Electrochem. Soc.* **2002,** 149, (5), A554-A557.
24. Tkach, I.; Panchenko, A.; Kaz, T.; Gogel, V.; Friedrich, K. A.; Roduner, E., *Physical Chemistry Chemical Physics* **2004,** 6, (23), 5419-5426.
25. Rice, C.; Tong, Y.; Oldfield, E.; Wieckowski, A.; Hahn, F.; Gloaguen, F.; Leger, J.-M.; Lamy, C., *J. Phys. Chem. B* **2000,** 104, (24), 5803-5807.
26. Park, S.; Wasileski, S. A.; Weaver, M. J., *Electrochim. Acta* **2002,** 47, (22-23), 3611-3620.
27. Igarashi, H.; Fujino, T.; Zhu, Y.; Uchida, H.; Watanabe, M., *Physical Chemistry Chemical Physics* **2001,** 3, (3), 306-314.

2.1.2.2. Crystallographic Characteristics of Nanostructured Thin Film Fuel Cell Electrocatalysts – A HRTEM Study

2.1.2.2.1. Introduction

Overview

This section reports the first in-depth study of thin film NSTF Pt and Pt-alloys by the use of High Resolution Transmission Electron Microscopy imaging. It was a collaboratoive study completed with the University of Illinois, Urbana. Dr. Lajos Gancs, as a post-doctoral fellow working with Prof. Andrzej Wieckowski, carried out the TEM work and developed most of the analsis. In this work, sputter-deposited thin catalyst films on the NSTF whiskers grow as polycrystalline layers that expose highly oriented fcc crystallites. Through this study, it has been found that the thin films comprise truncated pyramid-shaped crystallites which grow as acicular whiskerettes on the whisker sideplanes. The whiskerette shapes display a growth mechanism governed by a strong support-metal interaction and surface energy minimization. The surface structure of the crystalline whiskers facilitates metal nucleation sites that are spaced evenly along the whisker length by ca. 6-8 nm. The whiskerettes are the dominant structural form of the NSTF catalyst coatings at the loading levels investigated. Along just a few nanometers of a whisker's long axis, the whiskerettes can exhibit changes in aspect ratios up to a factor of five, and thus may increase the surface roughness by a factor of 6. Diffractogram indexing suggests that the truncated pyramids expose four (111) and one (100) planes which grow further into pillars by elongating their base along two of the (111) facets. Disregarding atomic scale roughness, the supported NSTF Pt-based electrocatalysts expose predominantly (111) facets.

Background

Various types of rough or graphitized carbon powders constitute the most common type of support materials for current fuel cell electrocatalyst applications. There are two main ways to prepare carbon-supported noble metal or metal alloy electrocatalysts[1]: (i) impregnation of the carbon powder with the precursor solution of the noble metal ions, and (ii) adsorption of metal-oxides or colloids onto the carbon surface, each followed by reduction to the pure metallic form. Such processes expose small metal nanoparticles, which possess dynamically varying physical properties with typical dimensions on the scale of a few nanometers.[2] Correlating such variations to electrocatalytic activity has been an important motivation of the fuel cell electrocatalysis research, as reviewed in Ref. [2-4]. In the case of nanoparticles in general, it is usually not the inadequacy of modern atomic-resolution microscopy and the spectroscopy techniques, but the propensity of nanoparticles to undergo diverse surface faceting and the atomic-scale roughness which make it difficult to draw reliable conclusions on how surface characteristics are related to activity. Although there are possibilities to tailor nanoparticle shapes and thereby surface faceting during preparation,[5] a high degree of uniformity in surface morphology and thus high reaction selectivity is not yet conveniently attainable.[1] The intrinsic instability of the nanoparticles, particularly in a fuel cell environment, also contributes to the complexity of the problem since the elemental composition, morphology and size might significantly change from that initially developed due to dissolution and agglomeration.[6,7] Furthermore, there have been concerns raised as to the cleanliness and corrosion resistance of carbon support materials in fuel cells, especially since those are exposed to the reaction environment to

a great extent. The stability of the catalyst support against corrosion at high electrode potentials experienced as a result of fuel starvation from water blockage, stop-start and other real dynamic phenomena is a critical durability issue.[8-11]

The long term durability and high performance are expected to be achieved with low precious metal content, i.e. using low metal loadings on a support material. In fuel cells for automotive applications, it has been suggested that the total Pt loading should be decreased by ca. four fold from that level currently used, down to 0.20 $mg_{Pt}\,cm^{-2}$ total, while at least the same activity should be maintained.[7] Given the sluggish kinetics of the cathodic oxygen reduction reaction (ORR), meeting such targets requires significant improvements in Pt mass-specific surface area [$m^2_{Pt}\ g_{Pt}^{-1}$] and Pt surface area-specific activity [$A\ cm^{-2}_{Pt}$].

The use of the crystallized form of an organic pigment, N,N-di(3,5-xylyl)perylene-3,4:9,10bis(dicarboximide), referred hereafter as perylene red (PR149), as the PEM fuel cell electrocatalyst support was introduced by Debe *et al.*[12-14] and such an electrocatalyst system is referred to as the nanostructured thin film (NSTF) catalyst[13]. The unique fabrication process and growth mechanism for generating this nanostructured thin film support structure have been described in detail.[14] Vacuum-annealing converts the initial as-deposited smooth organic film to an extremely dense and "random-like" array of discrete whiskers with areal number densities controlable in the range of 3 to about 10 billion cm^{-2}, that are uniformly oriented with their long axes normal to the substrate. The whiskers are crystalline, and subsequently have been shown to have high thermal, chemical, and electrochemical stability under the operation conditions relevant to PEM fuel cells.[13,15] (See also section 2.1.4 of this report). Structural characteristics of the PR149 support whiskers as determined by electron diffraction are presented elsewhere.[12] In brief, the whiskers' morphology comprises rectilinear lath-shaped crystalline elements with controlable lengths in the range of about 300 to over 1,500 nm depending on the thickness of the starting film used to grow them. The whiskers were determined to have mean cross-sectional dimensions of 52.5 ± 12.0 and 27.0 ± 7.5 nm that are fixed by the ratio of surface free energies of the whisker side-planes, and therefor less controlable by the process used to grow them. Such structural dimensions imply surface area enhancements by a factor of 5-15, depending on the areal number density and length of the whiskers.

In the NSTF electrocatalysts, another level of surface roughness is introduced when the layer of oriented mesostructured perylene red whiskers is conformally coated by a metal film, i.e. when the support organic whiskers are covered by a catalyst. The vacuum deposition method, process conditions and materials can all influence the roughness of the catalyst coating on the whiskers. Conventional electron microscopy imaging for the individual whiskers has shown already[13] that under some deposition conditions, the catalyst coating comprises a monolayer of closely packed but seemingly separated acicular-shaped metal grains (referred to as whiskerettes) that are uniformly oriented, off-normal to the side planes of the crystalline PR149 whisker. The individual nanoscopic metal whiskerettes are found to be highly crystalline.[13] It should be noted that this is a unique physical characteristic in contrast to the largely amorphous metal structures formed by their deposition onto carbon black by dual ion beam-assisted deposition (IBAD).[16] It has been shown that the PR149 support whisker's surface area as well as the metal loading affects the metal grain size,[13] just as in case of Pt dispersed on carbon-supported electrocatalyst systems (Pt/C). The coverage by the metal on the two supports however is quite different. First of all, except for ultra low loadings (for Pt

on appropriately sized whiskers, this means below 20 µg of Pt per cm^2), all of the PR149 surface area is coated, and the support material is encapsulated by a thin polycrystalline metal layer. Furthermore, while an increase in the weight percent Pt/C loading results in an increase in size and/or in areal number density of carbon-supported nanoparticles, the increase in Pt loading in the NSTF systems is manifested as an elongation of the PR149 whisker-supported metal whiskerettes. The dimensional aspect ratio of the whiskerettes varies along the long axis of the whisker particle. For example, for the PtRu NSTF sample discussed in Ref.13, the whiskerettes feature ca. 8 nm diameter cross-sectional dimensions and varying length up to 30 nm, depending on the position along the whisker's length. In general, the roughness of the metal coating on the sides of the whiskers can vary from very smooth to very rough. However, even when the catalyst coating on a single whisker particle exhibits a large roughness factor, the measured electrochemical surface area for NSTF-Pt is many times less than for conventional Pt/C layers of the same loading.[13] At the same time, the Pt surface area-specific oxygen reduction activity of the NSTF catalyst systems are found to be ca. 10 times higher compared to that obtained for high surface area Pt/C electrocatalysts.[30,31] (see also section 2.1.3 of this report). As a result, similar Pt mass-specific activities are obtained with NSTF Pt alloys as with the state-of-the-art PtCo/carbon electrocatalysts.[32]

The source of the activity gain with NSTF electrocatalysts is not completely understood. As proposed by Debe,[13] it might have contributions from the nature of metal/support interactions, the enhanced ionic transport at the interface of the catalyst surface and the membrane, or the differences in the type and degree of metal faceting, lattice strain or surface defects. Variations in surface morphology are considered as the primary origin of the so-called crystallite size effects in electrocatalysis.[17] Faceting and/or the formation of surface defects are known to have a large influence on ORR[17,18] as well as on the electrooxidation of chemisorbed carbon monoxide[18-20], and hence can alter electrocatalysis in hydrogen fuel cells on both the cathode and anode side, respectively. It is important to note that the Pt surface area-specific ORR activity with pure Pt NSTF matches those obtained with bulk polycrystalline Pt electrodes as determined using rotating ring disk electrode experiments and discussed at length in section 2.1.2.3 also.[30,31] This suggests the largely continuous nature of the thin film catalyst encapsulating each PR149 whisker particle is an important attribute leading to high surface area-specific activity, similar to the way in which the extended two dimensional nature of the bulk polycrystalline Pt is a key property for achieving high Pt surface area-specific activity.

While the mesoscopic physical and chemical characteristics of the PR149 material were previously discussed in great detail, [12-14] only a limited amount of work has concerned the morphology of the deposited metal (alloy) films. A preliminary EC-IRAS study has shown that the PR149-supported Pt NSTF exhibits voltammetric and surface vibrational properties similar to those of polycrystalline Pt.[21] (See also section 2.1.2.1 of this report.) The predominance of surface (111) facets was also suggested based on the preliminary data obtained by high resolution transmission microscopy (HRTEM) imaging.[21] The Berkeley group approximated the NSTF-Pt simply as a 30 nm sized particle electrocatalyst system with a large number of defect sites and irregularities in order to compare its electrochemical properties to conventional carbon-supported samples.[19,20] They also interpreted CO electrooxidation and ORR activity data by making that approximation.[17]

In this section, the equilibrium crystallographic characteristics of the crystalline whisker-supported Pt-based NSTF electrocatalysts are presented based on atomic-resolution electron microscopy images (via HRTEM) and surface energy considerations.[22] Fundamentals of the atomic-resolution real space HRTEM imaging, the image interpretation, and methodology for resolving structure of nanocrystals are available elsewhere.[22,23] We propose a model for metal crystal growth on the PR149 whisker support that explains the observed trends in equilibrium shapes and faceting.

2.1.2.2.2 Experimental

Preparation of the Nanostructured Thin Film Electrocatalysts

The NSTF electrocatalysts were prepared as described in section 2.1.3.1 of this report. In brief, the organic support consists of a monolayer of oriented crystalline whiskers of an organic pigment material, N,N-di(3,5-xylyl)perylene-3,4:9,10 bis(dicarboximide), (referred to hereafter as PR149). The NSTF catalyst coated whiskers are formed in a web coating process as a roll-good on a microstructured catalyst transfer substrate (MCTS).[13] The metals are sputter-coated on top of the PR149 whiskers so as to encapsulate each support whisker with a polycrystalline thin metallic film. The composition and structure of the metal coating were adjusted by the power levels and compositions of the sputtering targets. The loading of the pure Pt samples was adjusted in between 0.15 – 0.22 mg_{Pt} cm^{-2}. The PtRu binary alloy NSTF samples were prepared using two separate targets, pure Pt and pure Ru, to give a Pt loading of 0.22 mg cm^{-2} Pt and a Pt : Ru atomic ratio approximately one. The Pt-based ternary alloy NSTF was made using a Pt and a NiFe target consisting of Ni and Fe at the atomic ratio of 90:10. The total Pt loading of the PtNiFe NSTF was 0.1 mg cm^{-2}. The ratio of Pt to Ni + Fe was determined by controlling the relative thickness of the deposited layers. The total number of layers was determined by the desired loading of Pt. The catalyst coated whiskers were removed from the MCTS surface by brushing to obtain powders to form aqueous suspensions for TEM characterization.

Transmission Electron Microscopy

Conventional bright field (BF) and the dark field (DF) TEM images were obtained using a JEOL 2010 LaB6 microscope. High resolution transmission electron microscopy (HRTEM) and scanning transmission electron microscopy (STEM) measurements were carried out using a JEOL 2010F analytical electron microscope (AEM). The AEM was equipped with a Schottky field emission electron gun operating at 200 kV. The microscopes are computer-controlled through the JEOL FasTEM interface system. Micrographs were recorded digitally by a slow-scan charge-coupled device (CCD) and were processed using the DigitalMicrograph 3.6.5. software (Gatan Inc., USA). An ca. 10 µL drop of a water-based suspension of the NSTF catalyst coated whiskers was depostied onto a carbon film-coated copper mesh. The porous carbon grid specimen was then dried under a heat lamp at moderately high temperature and examined *ex situ* in a double-tilt TEM holder.

2.1.2.2.3 Results and Discussion

General structural characteristics

Physical and chemical properties of the PR149 organic pigment support have been discussed in great detail previously based on conventional TEM imaging and electron diffraction data.[12-14] The PR149 support layer is comprised of a densely-packed array of rectangular lath-shaped crystalline whisker-like particles, which have side dimensions in the range of a few tens of nanometers and for the samples used in this study, lengths on the order of 1 μm. In addition to the ca. 5 to 10 fold increase in roughness factor that the monolayer of whiskers enables, the fine structure of the metal film deposited onto the whiskers adds another level of surface roughness with respect to the geometric surface area. In the work reported here, the sputtered Pt and Pt alloy metals are found to form as distinct nanosized crystallites, referred to as whiskerettes[13], on the side planes of the PR149 whisker particles. The metal whiskerettes exhibit size dimensions in the range of a few nanometers with dimensional aspect ratios in the range of one to five. Such a morphology of the NSTFs yields surface areas multiple times higher than a smooth metal coating would provide on other support materials. In order to reveal the structural characteristics of the catalytic metal whiskerettes and also to find the reasons behind their growth habit, Pt, PtRu, and PtNiFe NSTF catalyst systems were subjected to a comprehensive analytical electron microscopy study. It was previously shown using electron diffraction[14] that the crystalline whisker has a body centered cubic (*bcc*) lattice structure, with [111] side facets, [01$\underline{1}$] edge facets and a [211] growth tip. The *bcc* lattice constant is 14.5(4) Angstroms and four PR149 molecules constitute a conventional unit cell (two molecules per each primitive lattice point).[14] Extensive XRD analyses of the Pt and Pt alloys suggested[25, 26] that the NSTF electrocatalysts are substitutional alloys having face centered cubic (*fcc*) structures, as should all of those studied in this work. Fig. 1(A-C) shows that all three metal whiskerette types (Pt, PtRu, PtNiFe) display very similar morphological characteristics to one another. As the micrographs demonstrate, the metal cluster morphology is indeed unique and quite different from those of any conventional nanoparticle catalyst. In the following, we will discuss the general structural characteristics of the PtNiFe ternary NSTF catalysts with various electron microscopy imaging strategies.

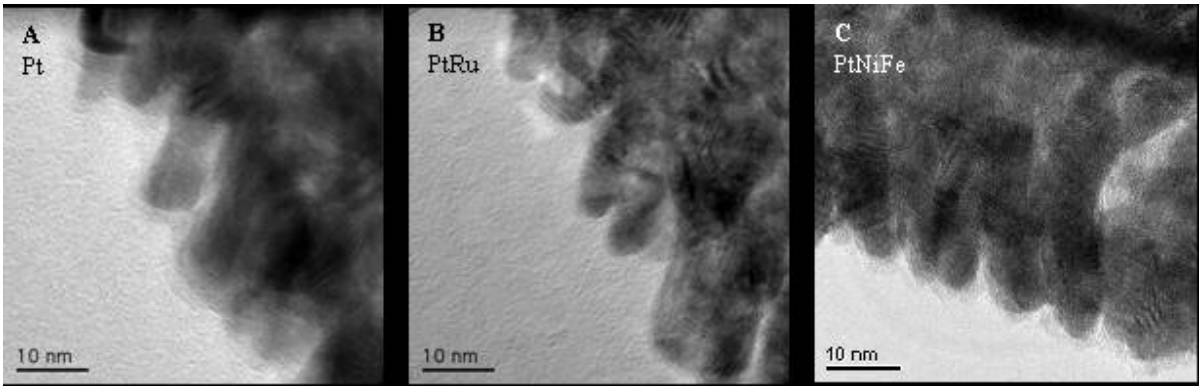

Fig. 1. HRTEM images of typical (A) Pt, (B) PtRu, and (C) PtNiFe metal crystallites supported on PR149 organic whisker particles. The magnification is 600,000.

Catalyst coating morphology

Distribution of the metal coating on the PR149 whisker particle was analyzed on the bright field (BF) images. Fig. 2 shows a BF TEM image of a cluster of the catalyst-coated, PR-149 whisker particles. Since growth of the PR149 whiskers follows a screw

dislocation growth mechanism,[14] the length of the whisker particles and, to some extent, their areal number density, can be controlled during sample preparation. The typical length of the whisker particles for all samples used in this study was ca. 0.8 μm. For the PtNiFe alloy at relatively heavy loading of 0.2 mg_{Pt} cm^{-2}, the alloy coverage is clearly not uniform along the longest axis of the lath or columnar-shaped support whiskers. Such a loading profile is due to self-shadowing effects during sputter deposition of the metal onto the densely packed whisker columns. The extent of the non-uniformity depends on the whisker length and spacing, as well as on the metal loading. For a typical whisker particle studied with a pure Pt loading (on the order of 0.1 mg_{Pt} cm^{-2}) the metal distribution is quite uniform, but is rather uneven at the higher loadings used for the PtNiFe system studied in this work.

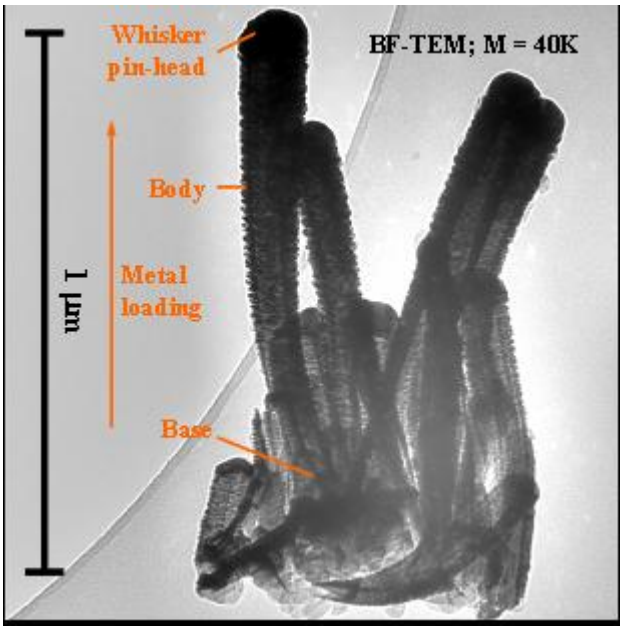

Fig. 2. Bright Field TEM image of a cluster of PR149 whisker particles carrying a typical Pt loading as used in this study.

Metal dispersion on a single PR149 support particle can be viewed by selecting an individual whisker (Fig. 3). Since the whiskers are distributed quite uniform, and are oriented with their long axes generally perpendicular to the substrate's surface, a heavily loaded whisker tip develops during metal coating, which generally faces the direction of the deposition. (There is not a fixed angle of deposition of the metals relative to the PR149 crystalline whiskers for two reasons. First, the whiskers are grown onto substrates that are roll-good webs of polyimide having a microstructured surface consisting of V-shaped grooves 6 microns tall and 12 microns peak-to-peak. The whiskers tend to grow perpendicular to their local substrate and hence point in generally orthogonal directions on alternate sides of each substrate V-groove. The V-grooves are parallel to the down-web direction. Secondly, the catalyst was sputter-deposited onto the whisker coated substrate as the web passed underneath planar magnetron targets, causing the line-of-sight angle of incidence to vary signifcantly over the time of passage under the targets.) It is important to mention that the tip of the crystalline whisker is a screw dislocation site.[14] Below the tip the metal coverage progressively decreases towards the whisker base down to where the whisker is attached to the MCTS substrate. While keeping the amount of the deposited metal the same, the dispersion can be

increased by increasing the length of the PR149 support particles. The equilibrium morphological characteristics of the metal coating on the PR149 support are discussed

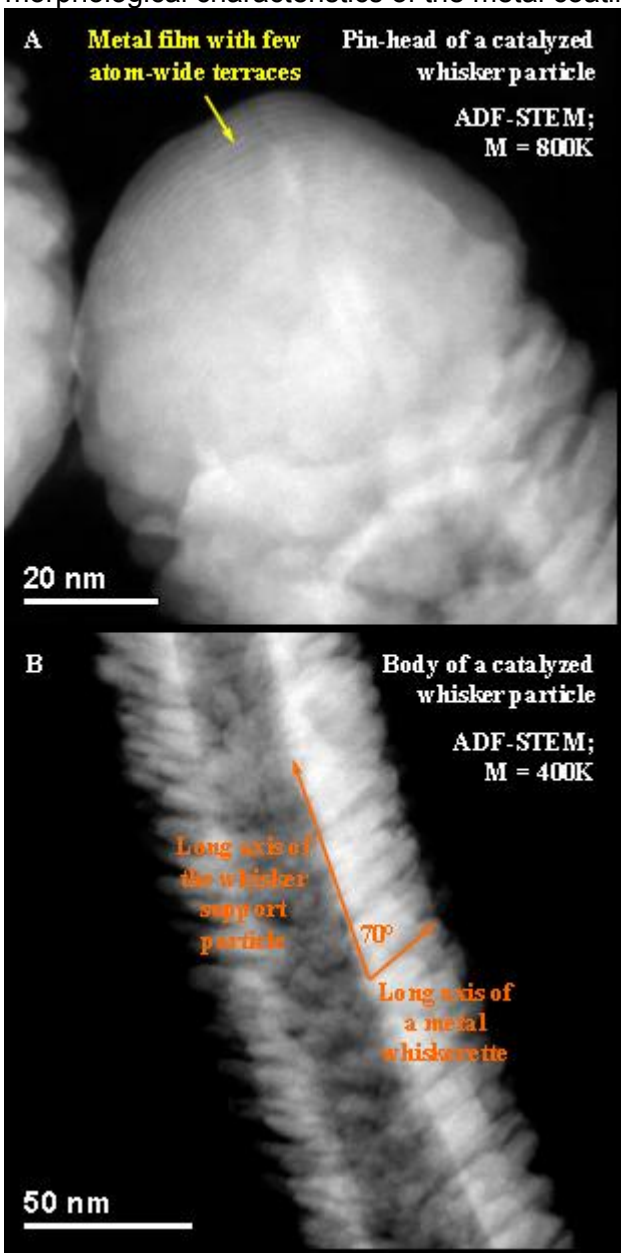

Fig. 3. ADF-STEM images (annular dark field scanning transmission electron microscopy) for the (A) "tip", and (B) "body" of a PtNiFe alloy-coated PR149 whisker particle.

based on the annular dark field (ADF) scanning transmission electron microscopy (STEM) images presented in Fig. 3. The images display strong mass-thickness contrast and thereby provide another picture of the metal dispersion on the organic whisker support particle. Basically, the deposited metals are incorporated in the three main differently structured domains on the PR149 whiskers. The metal atoms either become incorporated into the whisker tip (Fig. 3A), or form whiskerettes of similar shape but of varying lengths along the long axis of the whisker particle (Fig. 3B). Where the metal loading is low, the metal coating can appear as a finely grained film (low aspect ratio whiskerettes), as can readily be seen at the whiskers base (not shown in Fig. 3B). No other types of metal structures were observed in the metal coatings encapsulating the whisker. The surfaces of the metal-covered whisker tips consists of small terraces that

are evenly separated by steps of a few nanometers. This is apparent in Fig. 3A, where the dense and parallel lines on the tip of the whisker represent the edges of those terraces. Nevertheless, the surface of the tip is less structured compared to other parts of the whisker support. Although the tip of the rectangular prism-shaped PR149 whisker holds the highest metal mass per unit support surface area, only a fraction of the total mass of the deposited metal accumulates therein. It is important to note is that the tip is found to be the only part of the whisker particle where the metal crystallites are agglomerated (Fig. 3). Hence, the ultimate metallic surface area predominantly depends

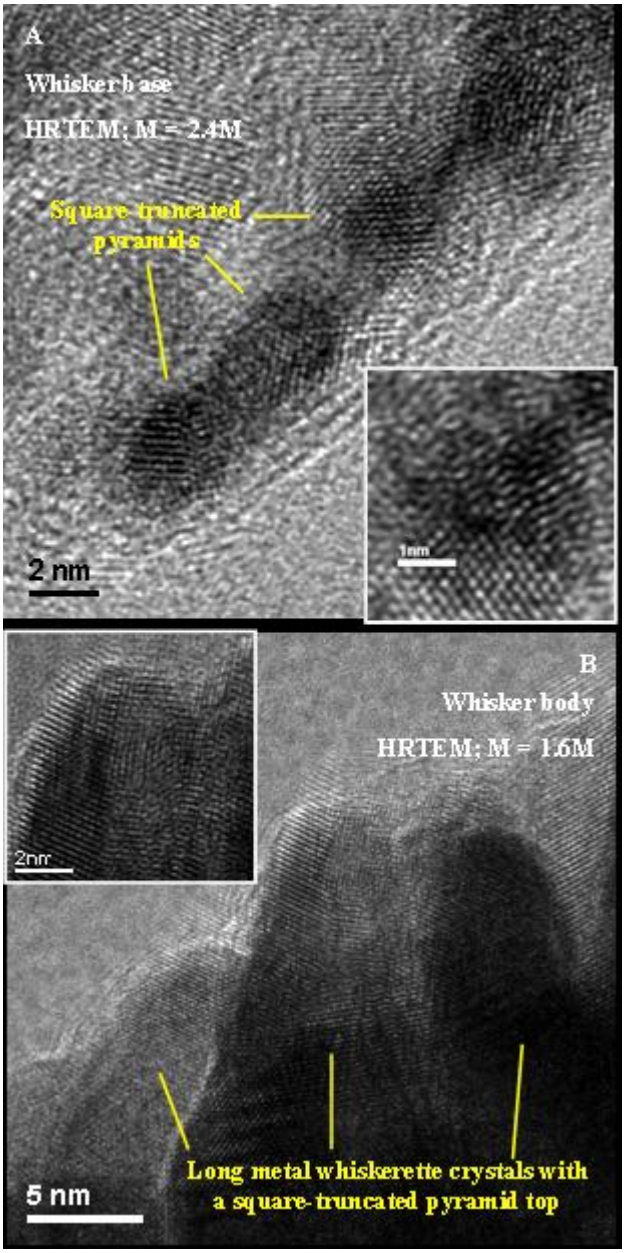

Fig. 4 HRTEM images for PtNiFe alloy crystallites located (A) at the "base", and (B) on the "body" of a PR149 whisker particle. The insets zoom onto selected crystallites having typical morphology.

on the areal number density and dimensions of the metal crystallites (whiskerettes, Fig. 3B).

It is now of importance to focus on the nanoscale morphology, as well as on the dimensions and faceting of the metal whiskerettes. Even though the deposited metal

film can encapsulate a PR149 support particle, it does not appear to be fully continuous in the vicinity of the whisker particle's base. Here, the population density, shape and dimensions of the metal whiskerettes are markedly different from those located on parts higher up the whisker particle. The HRTEM image in Fig. 4A taken of the base of a whisker particle shows the smallest metal crystallites that can be found in these examples. An extensive HRTEM study of such domains provided insights into the nucleation and growth mechanism of the metal whiskerettes on the PR149 whisker support particles. For instance, particularly low electron yields could be detected through the edges of the PR149 whisker particle, suggesting that the preferred surface sites to anchor metal atoms are located on the *bcc* [211] edges of the lath-shaped whisker crystals. In fact, TEM images of the small metal clusters nucleated along step edges (located parallel to the whisker long axis) provided the first evidence of the crystalline nature of the PR149 whisker supported element.[12] Also (not shown) metal crystallites nucleate on the wider [111] side planes of the whisker body as well, apparently associated with defects.[12] In general, in the present TEM study, the whiskerettes are observed to nucleate and grow on particular surface sites that are evenly separated from each other by ca. 6-8 nm. Under moderate and high metal loadings, a PR149 whisker surface becomes fully covered by the metal whiskerettes as their bases fuse together. However, the bodies of the whiskerettes remain distinct from their nearest neighbors, and project off the long axis of the rectangular lath-shaped whisker at an identical angle of 70° ± 1° (Fig. 3B). Note that the angle is the same as the angle between the (111) crystal planes in cubic lattices, *viz.* 70.53°. The alignment of the whiskerettes indicates the preferred direction of metal crystal growth thereby giving us a preliminary idea about the preferential surface faceting of the metal layers at the interface with the PR149 crystalline support whisker. Given the range of incidence angles seen during catalyst deposition, both spatially and temporally as described above, the existence of just one common and highly consistent angle of orientation of the whiskerette axes relative to the whisker axis suggests a materials driven mechanism rather than a process driven mechanism.

The highly ordered nature of the whiskerette postions is suggested here as due to the macromolecular crystalline structure of the PR149 whisker particle. Such a pattern of metal whiskerettes is also very different from the metal nanoparticles dispersed on conventional carbon particles, where the metal clusters are arranged largely randomly. On typical carbon support materials, the electron density varies according to the actual surface morphology at the nanoscale. In fact, our HRTEM and BET data (not shown) imply that the metal nanoparticles indeed tend to nucleate and grow at the edges of the carbon flakes of the micropores. The significant influence of the PR149 support material is suggested by the nucleation preferences of the metal whiskerettes on the whisker edges, and also by the unique shape, growth mechanism, and the highly ordered alignment of the whiskerettes. The additional growth mechanism and physical properties of the whiskerettes are discussed in the following sections of this communication.

The influential role of the PR149 support-metal interactions in developing the unique nanoscale morphological features of the NSTF catalysts is manifested by the morphology and the size distributions of the whiskerettes on a selected whisker particle. As seen in Fig. 1 and 3B, the great majority of the metal crystallites have a similar shape and well defined geometry, which is the representative form at the moderately and heavily loaded parts of the PR149 whisker. This observation is further supported using HRTEM in which phase modulation of the incident electron wave is the dominating

imaging mechanism (resulting in a fine contrast in the atomic distribution function). In other words, the high resolution electron micrographs can be analyzed and discussed also as thickness-projected images of the crystallites. In addition to the phase contrast, the diffraction (or amplitude) contrast contributes to the development of the HRTEM images. This contrast mechanism helps us to reveal the borders of the crystallites as well as the edges of the surface planes. By taking images of a selected metal crystallite at various orientations, the 3D geometry of the whiskerettes could be resolved.[23] Fig. 4 presents two characteristic whiskerette shapes, which could be found on a whisker particle. For the smallest metal crystallites, which are located at the base of the whisker particle (where the metal loading is low) the equilibrium morphology can be described using the square-truncated pyramid geometry. Such crystallites are pictured in Fig. 4A. In the inset, one selected metal particle is shown at higher resolution to facilitate resolving the geometry. The majority of the metal crystallites appear as acicular whiskerettes, which look like elongated columns with the square-truncated pyramids preserved on top. Fig. 4B and the inset therein provide evidence for such geometric structure of the typical whiskerettes that form the PR149-supported NSTF electrocatalysts.

Proposed mechanisms for whiskerette crystal growth and equilibrium surface faceting.

As discussed in the previous section, the sputtered metals develop into highly uniform crystalline whiskerettes rather than forming largely amorphous layers (like those on conventional carbon support materials). To explore their unique surface characteristics, which we propose originate from the molecular structure of the organic whisker support material, a pragmatic HRTEM imaging tactic was employed. Namely, the evolution of the whiskerette's equilibrium geometric shapes (Fig. 4) can be understood by imaging and resolving the morphology and surface structure of the metal crystallites as they develop along the longest axis of a PR149 whisker particle. Again, a typical whisker support particle demonstrates an increase in the metal loading from its base to its tip. In large part this is due to self-shadowing effects causing the rate of deposition to be lower at the base of the oriented whiskers than at the top. The analysis of the variations in the number density, shape and dimensions of the metal whiskerettes along the long axis of a whisker particle gives us some information on the crystal growth mechanism. A simple model can be set up for the growth mechanism of metal crystallites on the NSTF PR149 whisker support (see below).

The proposed whiskerette growth model is illustrated in Fig. 5. As is shown on the micrograph taken of the base of the PR149 whisker particle (also in Fig. 4A) the deposited metal atoms first take up some preferred sites on the support material, and arrange into small patches (islands). This tendency can clearly be seen in Fig. 1 of reference 12, where 2 nm sized clusters clearly decorate the linear step edges of the whisker's crystalline side planes. On the lightly metal-loaded parts, where the early stage of crystal growth can be examined, small pyramids develop. The peak of the pyramids was found to be truncated by a flat square. Such pyramids are imaged in Fig. 4A. The square-truncated pyramids' edge lengths have small dimensions, less than 8 nm and 3 nm for the base and the square-top edges, respectively. In the truncated pyramid crystallites, the aspect ratio of the base and the top-square edge lengths is found to be approximately three.

The truncated pyramid geometry can be anticipated by considering surface free energy for platinum-based crystallites. Simply put, the facets tend to be formed by truncating a

crystal in such a way that it will increase the proportion of the low Miller index planes. Generally, the following sequence is held for the magnitude of surface free energy of the basic crystallographic planes: (111) < (100) < (110).[23] It may therefore be expected that the small *fcc* crystallites will expose predominantly the (111) facets.

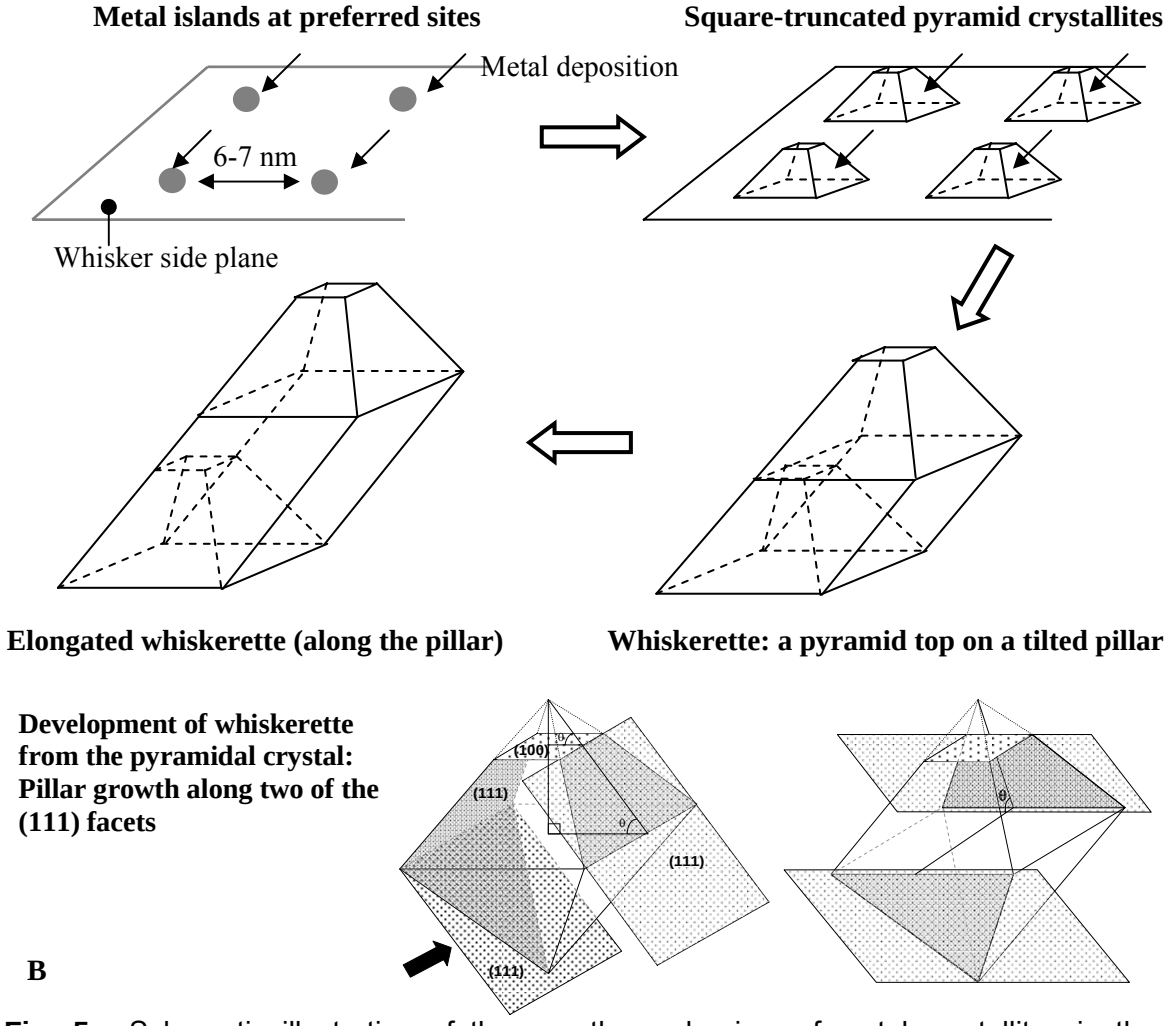

Fig. 5. Schematic illustration of the growth mechanism of metal crystallites in the PR149-supported NSTF electrocatalysts. Fig. (A) displays the typical metal structures at various stages of the crystallite growth process. Fig. (B) demonstrates the development of whiskerett pillars in terms of surface faceting.

From the spatial domain images of the metal crystallites, diffractograms were generated via fast Fourier transformation (FFT). By indexing the diffractograms based on the measured lengths of the two vectors and the contact angle in between them,[26] the surface faceting of the truncated pyramids could be revealed. In Fig. 6, a diffractogram is shown for a square-truncated pyramid metal crystallite facing the incident beam direction of [100]. The pattern indices were obtained based on the data in Ref.26 and were then correlated to the crystal planes after converting the diffractogram back to the spatial domain image using inverse FFT. As expected from surface energy minimalization, the smallest metal crystallites ideally expose four large (111) and one small (100) single crystal facets. Based on the geometric model, the edge and corner atoms make up less than 15 % of the total number of surface atoms for the crystallites

larger than a few nm. For the majority of the whiskerettes, the number of corner and edge atoms is negligibly small. Consequently, adsorption properties of the (111) single crystal planes in the NSTF electrocatalysts should play a dominant role in ORR reactions. As mentioned above, the small pyramids expose a (100) facet, which truncates the pyramid peak.

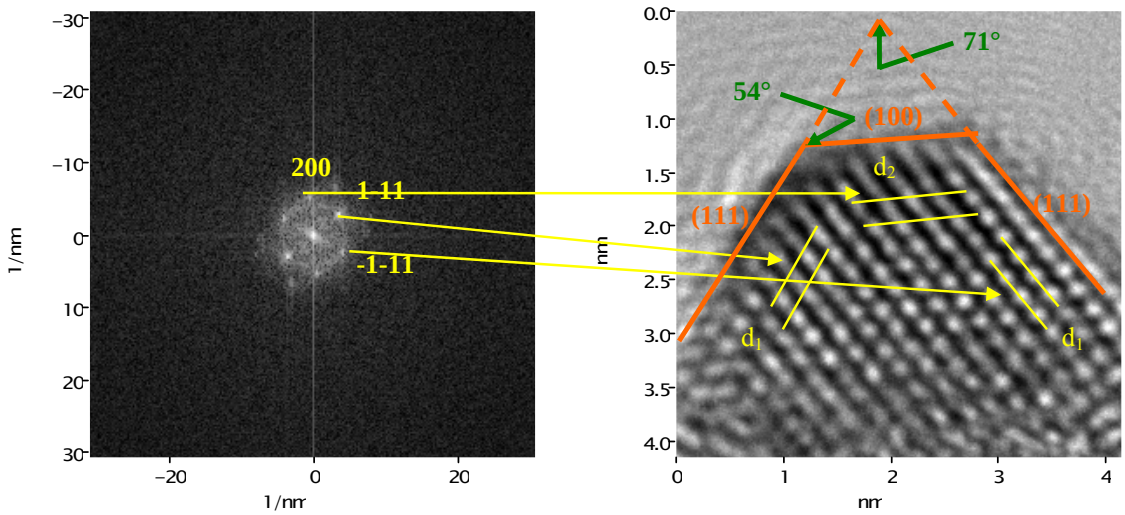

Fig. 6. Indexed diffractogram of a typical pyramid-shaped tip of a PtNiFe whiskerette particle, and the corresponding crystal planes and lattice parameters as shown on the reciprocal space image.

In order to further rationalize this faceting behavior, we calculated the geometric surface area as well as the surface free energy at various ratios of the top and base side edge lengths (*r*). When *r* approaches zero, the equilibrium shape approaches a perfect rather than a truncated pyramid. Data for the square-truncated pyramid of a 50 nm^3 volume, roughly representative of the small crystallites (see HRTEM images), are obtained by applying the embedded-atom-function calculation and using the parameters reported in Ref.[27] Fig. 7 summarizes the results. The plots indicate that the surface area as well as

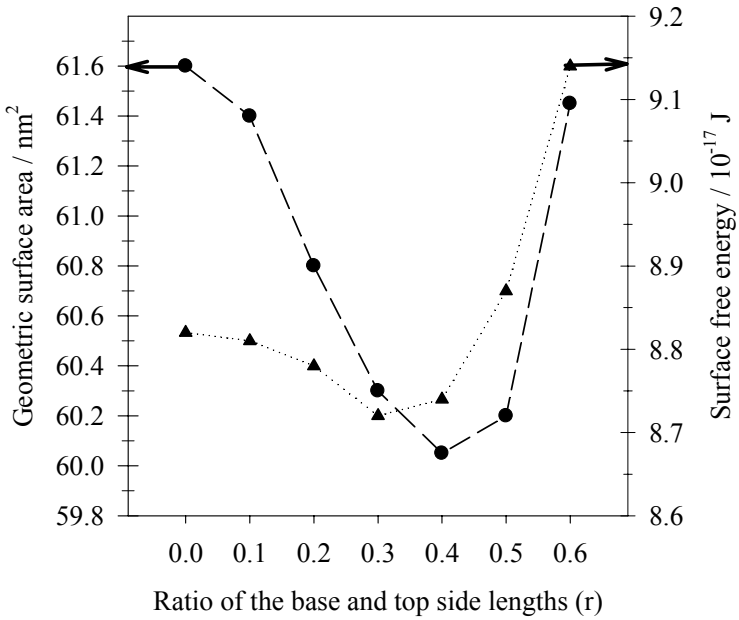

Fig. 7. Plot of the geometric surface area as well as the surface free energy as a function of the ratio of the lengths of top and base side edges for a 50 nm^2 square-truncated pyramid metal crystallite.

the surface free energy is minimal when *r* is approximately three. In other words, the surface free energy of a (100) plane-truncated pyramid crystallite is lower than that of a perfect pyramid for the same crystal volume. The calculated optimal value of three for *r* is in fact in a good agreement with the observed value of r~8/3 discussed above.

On the more typical acicular-shaped whiskerettes, formed higher up the whisker towards its tip (Fig. 4B), the truncated pyramid shape is still preserved and constitutes the top portion of the whiskerette. Such long metal whiskerette crystallites cannot be described by the truncated pyramid geometry, but appear much elongated. As depicted in Fig. 5A, the growth of whiskerettes takes place by keeping the initial pyramidal structure, while the metal crystallites grow further in one direction while developing into a long pillar. Again, the truncation of the whiskerette tip results from the tendency to reduce the surface energy. This also applies to the mechanism of the pillar growth as illustrated in Fig. 5B. The growth and elongation of the pillar can readily be understood based on the surface free energy order of the low index crystal planes.[23] As demonstrated in Fig. 5B, the pyramid, which is considered as the elementary shape of a cubo-octahedron, grows so as to extend two of its (111) facets. The elongated pillars exhibit gradually increasing length towards the whisker particle top. This results in a progressively higher metal loading towards the whisker tip. Interestingly, the pillars do not fuse together with each other while growing, but remain as distinct metal crystallites, featuring small dimensions along their short axes. While the whiskerette length may increase up to 25 nm, its width does not significantly deviate from ca. 6-7 nm, which is consistent with the maximum edge length of the pyramid's square base. The fact that the whiskerette cross-sectional dimensions do not change as their length changes is consistent with Wulff's theorem[33,34] for sub-micron sized crystals, the same reason the cross-sectional dimensions of the larger PR149 whiskers do not change as they grow longer, viz. the surface free energy per unit area of crystal face (*hkl*) is proportional to the distance of the crystal face from the center of the crystal.

Another remarkable characteristic of the whiskerette growth is that the whiskerettes become aligned so that they project off the side planes of the whiskers in a uniform direction tilting towards the whisker top. The whiskerette long axes and the whisker long axis display a uniform angle of ca. 70^{o}. We surmise this orientational angle results from the influence of the *bcc* (111) surface of the wider sides of the crystalline PR149 whiskers[12], resulting in an "epitaxial-like" Pt(111) nanoisland growth of the first few monolayers on the PR149(111) surface.

The question of why the whiskerettes are uniformly oriented in one direction, pointing towards the tips of the whiskers rather than their bases or any of four other possible directions for (111) symmetry, is of interest. This preference for one of the six possible directions is probably a result of the fact that the direction of the incidence of the incoming metal atoms is predominantly from the top of the whiskers during the sputter deposition process.

Based on the above proposed growth model, the structure of a typical whiskerette was constructed, and is outlined in Fig. 8. By showing the two-dimension projections, the analogy to the HRTEM micrographs (Fig. 3B) is apparent. Fig. 8 demonstrates a tilted alignment of the whiskerettes with respect to the side plane of the whisker support particle, as it is confirmed in the HRTEM micrographs (Figs. 1 and 3B). It is furthermore expected that the whiskerettes will show predominantly the (111) surface sites, although the ratio of the (111) to the (100) or other low-coordination (edge, vertex) sites should

decrease as the metal loading decreases. This will cause the lengths of the whiskerette pillars to decrease. Given different ORR activities of the different Pt(hkl) facets,[18] this effect might imply that the effective specific activity would also decrease with loading since the proportion of the surface area of the most active Pt(111) facets would decrease.

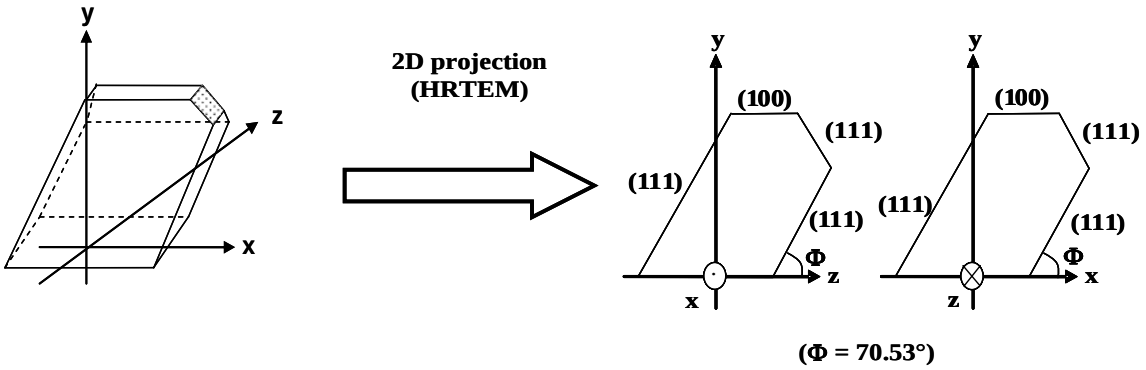

Fig. 8. Three dimensional sketch for a typical whiskerette particle that is tilted by 70.5° with respect to the whisker substrate's [111] plane, and the two dimensional projections.

Surface properties and implications for activity

Although the elemental composition of the catalyst surface is of crucial importance in electrocatalysis of typical fuel cell reactions, surface morphology also plays a significant role in product distribution and rate of such reactions[18] This is rationalized by examining the adsorption geometry and the reaction heat of adsorption involved in the reactions.[17,28,18,20]

As demonstrated above, surface properties of the PR149 crystalline whisker-supported NSTF catalysts are unique and can be tailored by the deposition practice. The Wulff construction of the whiskerettes[29] reveals that the typical PR149-supported metal crystallites expose six (111) and only one (100) plane. We have shown that a typical whiskerette exposes predominantly the (111) terrace sites, and only a few (100) terrace sites (see Fig. 5B, Fig. 6, and Fig. 8). Again, the long pillar base is bound by the (111) planes and the surface area of those planes provides the majority of the total metallic surface area at a typical metal loading. Essentially, the PR149-supported NSTF electrocatalysts can be considered as (111) single crystals with some surface defects. Nevertheless, the proportion of the (100) facets increases somewhat at ultra low metal loadings since the truncated pyramid structures do not develop further at long whiskerettes.

The equilibrium shape and faceting of the PR149-supported metal crystallites are demonstrated in Fig. 9A, that is, in the HRTEM image taken of a mid-sized metal whiskerette. By marking the edges of the facets guided by the phase thickness contrast, as well as after indexing the planes, the above proposed model for a typical whiskerette shape and faceting is self-consistent. Clearly, the predominance of the (111) sites in surface faceting is unique among all non-supported and supported electrocatalysts. For non-supported Pt and Pt-alloy crystallites, like those of a single Pt black particle in Fig.

9B, many small facets and other steps develop due to the tendency to minimize the cubo-octahedron surface energy [22]. At the same time, porous metal structures are formed on conventional carbon supports by ion-beam assisted deposition (IBAD). However, the structures formed by IBAD on carbon supports lack both a long-range-ordered crystallinity and the well-defined surface morphology.[16]

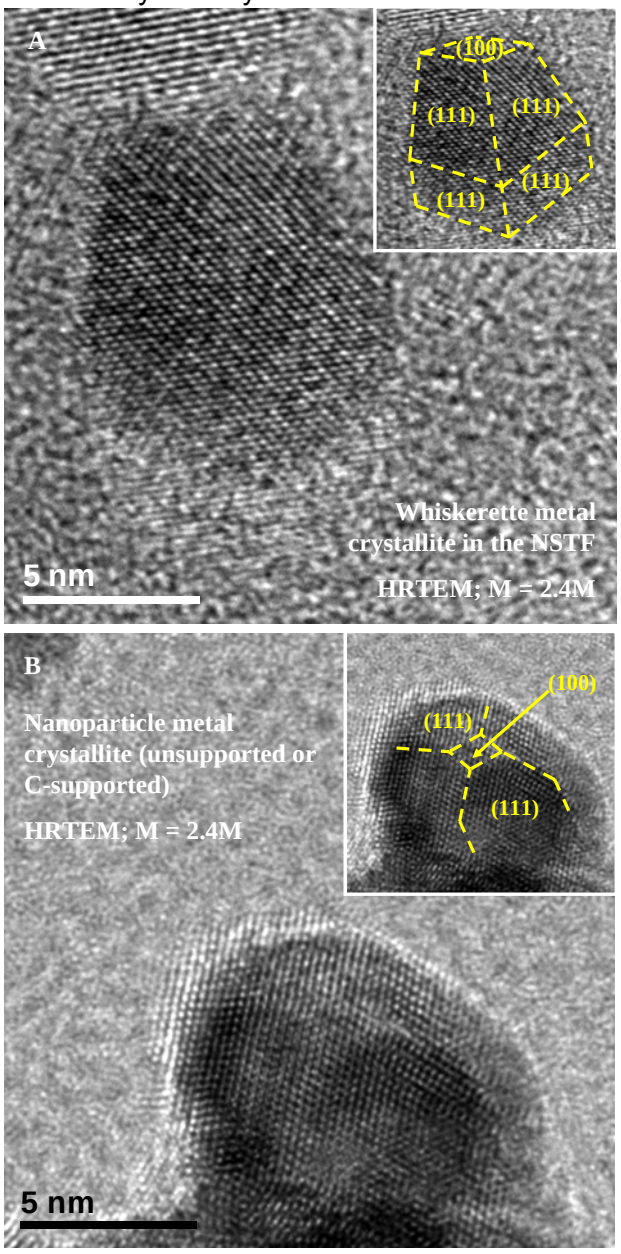

Fig. 9. HRTEM images for typical metal crystallites in (A) PR149 whisker-supported NSTF catalysts and (B) a nanoparticle system (Pt black). The insets highlight the faceting.

Parameters of the sputtering conditions used to prepare the NSTF samples are likely not to be responsible for the unique and uniform whiskerette morphology. During sputter deposition, the substrate is moving relative to the sputtering target while the angle of deposition is changing continuously, and the total metal deposition is achieved through multiple passes under the target. The uniaxial orientation of the whiskers presents the opportunity for self-shadowing, which is responsible for the higher loading on top parts of the whiskers compared to the bases. Consequently, the metal sputtering deposition

conditions applied to prepare the samples for this study are not expected to play any direct role in the development of the unique metal crystallography and uniform surface faceting, but may only be the determining factor specifying their uniform tilt towards the whisker tip. Rather, our experimental data imply that the metal whiskerette-crystalline organic whisker interfacial free energy is exceptionally low, or at the atomic level there is some epitaxial matching between the PR149 whiskers' crystal lattice structure (*bcc* (111)) and that of the whiskerett's bases (*fcc* (111)). Hence, the surface free energy of the metal crystallites as well as surface faceting seem to be strongly influenced by the nature of the PR149 material and the crystal structure. Based on previous electron diffraction study of the PR149 whiskers,[12] it is believed that the *bcc* face and the side planes are (111) and (011), respectively, with a 14.5(4) Å lattice constant. The whiskerettes, as discussed above, have the *fcc* lattice structure with a lattice constant of 3.92 Å for pure bulk Pt, and slightly less for the PtRu binary and PtNiFe ternary alloys.[24,35] The model in Fig. 8 suggests the *fcc* (111) planes are in a direct contact with the PR149 whisker *bcc* (111) side planes, resulting in the observed 70^{o} projection angle. The (111) truncation of the PR149 *bcc* Bravais lattice would present a hexagonal 2D surface net with surface lattice vectors of 14.5 × $(3)^{1/2}$ = 25.1 Å. This surface unit cell diameter of 5.01 nm could accommodate 7.4 of the 3.92 × $(3)^{1/2}$ = 6.8 Å Pt *fcc* (111) surface unit cells along the major dimensions of the cell. If lattice strain effects constrained this to an integral number of seven Pt unit cell dimensions per one PR149 unit cell dimension, then this could possibly be a mechanism for determining the absolute Pt whiskerette pillar diameter and spacing. The pillar diameter of ca. 5 nm calculated in this way comes close to the observed pillar diameter of ca. 6 nm. We must emphasize here that the same structural considerations apply for the PR149-supported PtRu and PtNiFe alloy NSTFs as for the pure NSTF Pt sample. It is furthermore important to note that no evidence for the segregation of the alloying elements was found through our high resolution energy dispersive spectroscopy studies (not shown).

HRTEM observations and the model proposed in Fig. 5A provide a basis to estimate the maximum possible geometric surface area. The roughness factor is estimated for whisker surfaces that carry metal loadings typical of the present work (for the average whisker length of 1 μm). As per Ref.[12], the rectangular lath-shaped whisker particles have the mean cross-sectional widths of 50 and 25 nm. Assuming that the whiskerettes are separated by ca. 6-7 nm from each other, at least 18 of the metal crystallites could be found around a whisker particle on the line perpendicular to the longest axis (3 and 6 on the wide and narrow side planes, respectively). Therefore, one whisker particle of 150,000 nm^2 area holds approximately 2250 whiskerettes in 125 of such zones along the whisker length. (The surface area of the less highly structured tip of the whisker is ignored for this estimate.) If each whiskerette shape is approximated by a square, and allowing their pillar axis to increase gradually from 0 to 25 nm from the bottom to the top of the PR149 whisker, a total of about 900,000 nm^2 of metal surface area can be calculated. This ca. six-fold increase in nanoscale roughness per whisker particle can be multiplied by the mesoscale roughness factor of 5-8 given by the typical areal number density of PR149 whiskers of 3-5 billion cm^{-2}.[13] We can then arrive at a nanoscale roughness factor (that is the ratio of total surface area compared to the planar or projected surface area) ranging between 27 and 45 for PR149-supported NSTF electrocatalysts. These values are higher by a factor of 2 to 3 compared to the electrochemical surface area measured by hydrogen adsorption/desorption at 70 ^{o}C on hundreds of membrane electrode assemblies using similarly prepared catalysts.

2.1.2.2.4 Conclusions

The structure of NSTF electrocatalysts supported on PR149-crystalline whiskers was investigated by high resolution transmission electron microscopy, and some general trends in the NSTF crystallography and surface characteristics were obtained. The Pt, PtRu, and PtNiFe samples display a *fcc* metal crystal structure and exhibit similar morphology to each other on the nanoscale. The catalyst coating on the PR149 whiskers produces small crystallites which encapsulate the whisker support particles, while appearing as distinct whiskerettes. Aside from the small tip of the PR149 support particle - where a less structured film is composed of fused and densely located whiskerettes - high metal surface area per unit of the support area is maintained along the entire whisker support particle.

Metal dispersion was found to increase progressively along a PR149 whisker from its base towards its top. We showed that the metal crystallites have different geometric shapes as well as gradually varying dimensions along the whisker length. The crystallographic features of the whiskerettes determine the surface area and surface faceting, thereby influencing the electrocatalytic performance. The whiskerettes exhibit unique equilibrium shapes in contrast to other nanostructured systems. A series of HRTEM images taken along the long axis of a whisker particle suggest the growth mechanism of the metal crystallites. Namely, in the early stage of the crystal growth, the metal atoms arrange into islands on preferential sites of the whisker side planes. With increasing loading, they take on a square-truncated pyramid structure. The nucleation sites are found on the edge and in the middle of the rectangular lath-shaped whisker's side planes, and are separated from each other by ca. 6-7 nm. Typically, the bases of the whiskerettes grow together. Yet, the metal crystallites appear as distinct, elongated pillar-based pyramids with cross-sectional dimensions of ca. 6 nm. The long axis of the whiskerette pillar is measured to project off the long axis of the support particle at an angle close to 70^{o}. Further, the size dimensions, uniform orientation, and possibly the natural spacing of the whiskerette pillars are directly related to the epitaxial-like growth on the whisker's *bcc* (111) surface. They are also related to the relative size of the whisker's *bcc* (111) surface unit cells as compared to the Pt or Pt alloy *fcc* (111) unit cell size. The length of the pillar reflects the distribution of the local metal loading along the long axis of the PR149 whisker particle. The whiskerettes are aligned uniformly on the support by being tilted towards to the top ends of the whiskers, in the general direction of incidence set by sputtering.

The crystal growth mechanism and morphology of the whiskerettes do not exactly follow the cubo-octahedron model of crystal growth. This is attributed to exceptionally strong support-metal interactions. The pyramid shape of the smallest (a few nanometers) metal crystallites is known to possess the lowest surface free energy because such crystallites possess (111) facets only. Assuming low interfacial free energy between the PR149 support and the Pt pyramid base, only the top side can be truncated by a (100) square plane unlike in case of round nanoparticles on a carbon support. The larger metal crystallites appear as acicular whiskerettes, which are uniformly tilted in two directions in order to maintain the thermodynamic trend. That is, the crystal growth occurs preferentially along the lowest Miller index single crystal facets. The observed 70^{o} angle between the whiskerette axes and the support whisker's axis is exteremly close to the angles between (111) planes in *fcc* or *bcc* lattices. A Wulff-construction of the whiskerettes reveals that a typical Pt-based metal crystallite exposes four extended (111) facets, appearing as a pillar with two smaller (111) facets as side faces of the

pyramid on the top, and one (100) plane. The latter typically has a negligible surface area compared to the (111) facets.

By determining the population density and some of the characteristic dimensions of the whiskerettes using HRTEM imaging, the ultimate surface area of the PR149-supported NSTF electrocatalysts could be estimated. Using the proposed equilibrium shape model to describe the surface area of a metal crystallite, we calculated that the surface area increases up to ca. 900,000 nm^2 in a typical PR149 whisker particle having 150,000 nm^2 surface area. If this roughly 6-fold enhancement on the nanoscale multiplies the mesoscale roughness factor of 5-8 provided by the PR149 substrate's whisker structures, an ultimate roughness factor of 27-45 can be estimated for the NSTF electrocatalysts studied here. This range is consistent with the H_{UPD} (Pt) surface area of the Pt NSTF MEA measured by cyclic voltammetry.

We conclude that the key difference found between the NSTF catalysts supported on PR149 and conventional carbon-supported electrocatalysts is due to the crystalline nature of the support material. While the PR149 support is not expected to play direct roles in electrocatalysis, its strong influence on the population density and the metal growth mechanism is evident, in contrast to conventional carbon supports.

References for Section 2.1.2.2

(1) Antolini, E., *J. Mat Sci.,* **2003**, *38*, 2995.
(2) Santra, A. K., Goodman, D. W., in Wieckowski, A., Savinova, E., Vayenas, C., eds., "*Catalysis and Electrocatalysis at Nanoparticle Surfaces"*, p. 281, Decker, New York, **2003.**
(3) Haruta, M., Tsubota, S., in Wieckowski, A., Savinova, E., Vayenas, C., eds., "*Catalysis and Electrocatalysis at Nanoparticle Surfaces"*, p. 645, Decker, New York, **2003.**
(4) Coq, B., Figueras, F., in Wieckowski, A., Savinova, E., Vayenas, C., eds., "*Catalysis and Electrocatalysis at Nanoparticle Surfaces"*, p. 847, Decker, New York, **2003.**
(5) Burda, C., Chen, X., Narayanan, R., El-Sayed, M. A., *Chem. Rev.* **2005**, *105*, 1025.
(6) Horky, A. *Fuel Cells Durability (1st Edition)* **2006**, 133. Editor ??Publisher??
(7) Gasteiger, H. A., Kocha, S. S., Sompalli, B., Wagner, F. T., *Applied Catalysis, B: Environmental* **2005**, *56*, 9.
(8) Tang, H., Qi, Z., Ramani, M., Elter, J. F., *J. Power Sources* **2006**, *158*, 1306.
(9) Roen, L. M., Paik, C. H., Jarvi, T. D., *Electrochem. Solid-State Letters* **2004**, *7*, A19.
(10) Ferreira, P. J., la O, G. J., Shao-Horn, Y., Morgan, D., Makharia, R., Kocha, S., Gasteiger, H. A. *J. Electrochem. Soc.* **2005**, *152*, A2256.
(11) Li, W. *Fuel Cells Durability (1st Edition)* **2006**, 101. Publisher??
(12) Debe, M. K., Drube, A. R., J. Vac. Sci. & Tech., B: Microelectronics and Nanometer Structures **1995**, 13, 1236.
(13) Debe, M. K., in "*Handbook of Fuel Cells – Fundamentals, Technology and Applications",* vol. 3, W. Vielstich, A. Lamm, H. A. Gasteiger, Eds., Chapter 45, Wiley, 2003.
(14) Debe, M. K., Poirier, R. J., J. Vac. Sci. & Tech., A: Vacuum, Surfaces, and Films, **1994**, 12, 2017.
(15) Debe, M. K., Schmoeckel, A. K., Vernstrom, G. D., Atanasoski, R., *J. Power Sources* **2006**, *161*, 1002.

(16) Saha, M. S., Gulla, A. F., Allen, R. J., Mukerjee, S., *Electrochim. Acta* **2006**, *51*, 4680.
(17) Mayrhofer, K. J. J., Blizanac, B. B., Arenz, M., Stamenkovic, V. R., Ross, P. N., Markovic, N. M., *J. Phys. Chem. B* **2005**, *109*, 14433.
(18) Markovic, N. M., Ross, P. N., *Surf. Sci. Reports* **2002**, *45*, 117.
(19) Arenz, M., Mayrhofer, K. J. J., Stamenkovic, V., Blizanac, B. B., Tomoyuki, T., Ross, P. N., Markovic, N. M., *J. Am. Chem. Soc.* **2005**, *127*, 6819.
(20) Mayrhofer, K. J. J., Arenz, M., Blizanac, B. B., Stamenkovic, V., Ross, P. N., Markovic, N. M., *Electrochim. Acta* **2005**, *50*, 5144.
(21) Wieckowski, A., Gancs, L., McGovern, M., Lu, G.-Q., Atanasoski, R., Debe, M. K., *227th ACS Meeting, Anaheim, CA,*March, **2004***,* Abs #.
(22) Markovic, N. M., Radmilovic, V., Ross, P. N., Jr., in Wieckowski, A., Savinova, E., Vayenas, C., eds., "*Catalysis and Electrocatalysis at Nanoparticle Surfaces"*, p. 311, Decker, New York, **2003.**
(23) Wang, Z. L., *J.Phys. Chem. B* **2000**, *104*, 1153.
(24) Bonakdarpour, A., Lobel, R., Atanasoski, R. T., Vernstrom, G. D., Schmoeckel, A. K., Debe, M. K., Dahn, J. R., *J. Electrochem. Soc.* **2006**, *153*, A1835.
(25) Bonakdarpour, A., Wenzel, J., Stevens, D. A., Sheng, S., Monchesky, T. L., Lobel, R., Atanasoski, R. T., Schmoeckel, A. K., Vernstrom, G. D., Debe, M. K., Dahn, J. R., *Journal of the Electrochem. Soc.* **2005**, *152*, A61.
(26) Williams, D. B., Carter, C. B., "*Transmission Electron Microscopy: A Textbook for Materials Science"*, Plenum Press, New York, **1996**.
(27) Foiles, S. M., Baskes, M. I., Daw, M. S., *Phys. Rev. B: Condensed Matter and Materials Physics* **1986**, *33*, 7983.
(28) Murthi, V. S., Urian, R. C., Mukerjee, S. *J. Phys. Chem. B* **2004**, *108*, 11011.
(29) Marks, L. D., *Reports on Progress in Physics* **1994**, *57*, 603.
(30) Mayrhofer, K.J.J., Blizanac, B.B., Stamenkovic, V.R., Ross, P.N., Markovic, N.M., Atanasoski, R.T., Schmoeckel, A.K., Vernstrom, G.D., Debe, M. K., "ORR activity on Pt and PtNiFe NSTF Catalysts: Comparative RRDE and Fuel Cell Evaluation," to be submitted.
(31) Bonakdarpour, A., Stevens, K., Vernstrom, G. D., Atanasoski, R. T., Schmoeckel, A. K., Debe, M. K., Dahn, J. R., *Electrochim. Acta*, **2007 (**in press**)**.
(32) Debe, M. K., "Status and Prospects of PEFC Electrocatalysts: Meeting the Requirements for Automotive Fuel Cells with Nanostructured Thin Film Electrodes," proceedings of 3rd International Hydrogen and Fuel Cell Expo Technical Conference, Tokyo Big Sight, Tokyo, Japan, Feb. 7-9, 2007, FC-8, p.5.
(33) Frank, F.C., in "*Growth and Perfection of Crystals",* Proceedings of the International Conference on Crystal Growth, Cooperstown, NY 1958, R. H. Doremus, B. W. Roberts, and D. Turnbull, Wiley, New York, **1958**.
(34) Burton, W. K., Cabrera, N. Frank, F. C., *Philos. Trans. R. Soc. London Ser. A* **243**, 299 (1951).
(35) Stevens, D. A., Rouleau, J. M., Mar, R. E., Bonakdarpour, A., Atanasoski, R. T., Schmoeckel, A. K., Debe, M. K., Dahn, J. R., *J. Electrochem. Soc.* **2007**, *154*, B566.

2.1.2.3. ORR activity on Pt and Pt ternary NSTF Catalysts: Comparative RRDE and Fuel Cell Evaluation

2.1.2.3.1 Introduction

This section describes the results of a collaborative effort with the catalyst group at Lawrence Berkeley National Laboratory, including K.J.J. Mayrhofer, B.B. Blizanac, V.R. Stamenkovic, P.N. Ross, and N.M. Markovic. The purpose of the study was to compare practical activity measurements made in 50-cm^2 fuel cells of NSTF catalysts with those obtained from rotating ring-disc electrode (RRDE) measurements, considered to be the most fundamental. For both methods, the samples measured for each catalyst composition came from the same NSTF catalyst lot. In this regard a detailed RRDE evaluation of the pure NSTF-Pt catalysts as well as Pt ternary catalysts was performed. One-to-one correspondence between the surface area and specific activity measurements in RRDE and the 50-cm^2 fuel cell was established. The major conclusion of this work was that the inherent catalytic activity of the Pt-NSTF catalyst is nearly as high as the activity of bulk platinum, which is consistent with the thin film nature of the catalyst. The ternary catalysts exhibited an increase in surface area as well as a higher specific activity. Consequently a higher mass activity in RRDE experiments was obtained, which explains the improved performance of these catalysts during fuel cell operation.

The NSTF catalyst performance has been documented in thousands of large area (50 cm^2) single cell measurements. Here we are reporting the first investigation comparing specific activities measured in 50-cm^2 fuel cells with those obtained at a more fundamental level with a rotating ring disc electrode (RRDE) using the technique developed at Lawrence Berkeley National Laboratory (LBNL). It is important to note that for each measurement method and catalyst composition, the catalysts were obtained from the same NSTF lot. In order to do this for the RRDE measurements, catalyst coated whiskers were removed from the substrate on which they were fabricated (before the normal transfer to the PEM surface), and applied to the disc of the rotator. A technique already used for dispersed carbon evaluation on RRDE was adopted for the use of the NSTF catalyst. Because of the large number of samples examined, this study also provides one of the most thorough comparisons of parallel RRDE and fuel cell evaluation of the same type and same batch of catalysts.

The study was conducted over a period of two years (2003 – 2005) during which a total of 21 NSTF catalysts were examined. LBNL reported the data in six reports. Results were discussed in direct communications between researchers at 3M and LBNL, form experimental details up to high level conclusions.
In addition, the RRDE results on pure platinum NSTF were used by LBNL in a comparative study on the effect of Pt particle size on the inherent catalytic activity for ORR.

2.1.2.3.2 Experimental

Specific activity

To determine catalyst oxygen reduction reaction (ORR) activity per unit of electrochemical surface area (ECSA), two independent measurements are required, viz. the activity and the ECSA. In the fuel cell testing, the approach of comparing the relative

"activities" per unit surface area of different catalyst types relied on a simple method based on potentiodynamic polarization scans (PDS) taken under ambient pressure H_2/air (75 ^oC, 800 sccm H_2/1800 sccm air). The scanning was initiated from high voltage (e.g. between OCV and 0.85V) to low voltages (~ 0.25 V) and back up again, in ~ 0.05 V increments with ~ 10 second dwell time at each voltage step. Between the PDS scans, the MEA is operated at a constant voltage, typically 0.4 volts, for 10 minutes. On the return scan (low to high voltage), hysteresis is typically observed in the kinetic region (high voltage), with the return scan always at higher current density than the initial down scan. Since holding the cell even briefly at low voltages polarizes the cathode sufficiently to remove any oxide, we attribute the higher return scan to less Pt oxide coverage on the surface, and hence higher current density. As a measure of the "relative ORR activity" of the clean surface we record the current density at 0.813 V (historical) on the return portion of the PDS H_2/air scan. This approach is referrred to as Method 1 in Section 2.1.3.1 and along with two other methods for measuring specific activities in 50 cm^2 cells were used to characterize approximately 100 different Pt alloy ternarys. The RRDE approach is method 4 in section 2.1.3.1.

RRDE testing

The electrochemical measurements were conducted in a temperature controlled, standard three-compartment electrochemical cell, using a ring-disc electrode setup with a bi-potentiostat and rotation control (*Pine*). A saturated calomel electrode (SCE), separated by an electrolytic bridge from the main cell compartment, was used for every experiment, however, all potentials are given with respect to the reversible hydrogen electrode (RHE). To minimize the error from the potential reading especially for the ORR, the hydrogen oxidation/evolution reaction was measured shortly before or after the ORR at 333 K to calibrate the RHE relative to the calomel electrode. A Pt mesh was used as a counter electrode. The electrolyte was prepared using pyrolitically triply distilled water and concentrated $HClO_4$ (*Aldrich*) [1].

In order to evaluate the NSTF catalysts on RRDE, the catalyst coated whiskers were carefully brushed off sections cut from the initial substrate roll. Precautions were taken to avoid contamination of the catalyst with impurities, physical or otherwise. The procedure for applying the NSTF onto a glassy carbon support for the RRDE measurements has been adopted from high-surface area catalysts, and described previously [2]. In short, the catalyst was dispersed ultrasonically in ultrapure water with concentrations of about 1 $mg_{Catalyst}$/ml. 40 µl of the suspension was pipetted onto a polished glassy carbon substrate (6 mm diameter, 0.283 cm^2 geometrical surface area) leading to a Pt metal loading of 42 µg cm^{-2} for all samples. No additional carbon was needed for the preparation, since the catalyst coated whiskers are excellent electronic conductors and remain in intimate contact with each other on the glass carbon substrate. After the evaporation of the water in an Argon stream, 20 µl of a diluted Nafion solution (5 wt.%, *Fluka*) was pipetted onto the glassy carbon to attach the catalyst particles to the substrate. The thus prepared electrode was then transferred to the electrochemical cell protected by a drop of ultra pure water, and immersed under potential control at 0.05 V in argon-saturated 0.1 M $HClO_4$ solution. The potential was then constantly cycled between 0.05 V and 1.0 V until a stable cyclic voltammogram was recorded. For ORR the electrolyte was purged with oxygen (*Airgas*) and the electrochemical cell was heated up to 333 K. The positive limit of 1.0 V was never exceeded in any experiment.

Electrochemical surface areas were measured by a similar protocol to that described above in the fuel cell testing section. Additionally, the CO-stripping behavior of every catalyst was studied in CO-free Ar purged solution, after adsorbing CO at a potential of 0.05 V until the electrode was completely covered. The active surface area was estimated using the peak area under the CO-stripping peak according to [3].

Table I lists the samples tested during this study:

Table I. Samples evaluated at LBNL by RRDE.

ID #	Sample Description	Pt loading, mg Pt cm^{-2}
PE4120	Pt, 0.15 mg/cm2	0.15
PE4121	PtNiFe, 0.15 mg Pt/cm2	0.15
ML030110-1	PtNiFe (90/10) [5,3,1], 0.1 mg Pt/cm2	0.1
ML030103-3	PtNiFe (90/10) [10,3,1], 0.1 mg Pt/cm2	0.1
ML030102-1	PtNiFe (90/10) [50,1,1], 0.1 mg Pt/cm2	0.1
ML030102-2	PtNiFe (90/10) [20,1,1], 0.1 mg Pt/cm2	0.1
ML030128-2	PtNiFe (90/10) [5,0.6,1], 0.1 mg Pt/cm2	0.1
ML021114-2	PtCoFe (80/20) [50,0.6,1], 0.1 mg Pt/cm2	0.1
ML030729-1	PtNiFe (95/5) [10,0.3,1], 0.1 mg Pt/cm2	0.1
ML030722-1	PtNiFe (95/5) [10,0.4,1], 0.1 mg Pt/cm2	0.1
ML030207-2	PtNiFe (95/5) [10,0.6,1], 0.1 mg Pt/cm2	0.1
ML030127-1	PtNiFe (90/10) [30,0.6,1], 0.1 mg Pt/cm2	0.1
ML030129-3	PtNiFe (90/10) [30,0.6,1], 0.05 mg Pt/cm2	0.05
ML030506-1	PtNiFe (90/10) [30,0.6,1], 0.025 mg Pt/cm2	0.025
ML040514-1	PtCoMn (90/10) [20,0.6,1], 0.1 mg Pt/cm2	0.1
ML040517-1	PtCoMn (90/10) [20,1.2,1], 0.1 mg Pt/cm2	0.1
ML040526-1	PtCoMn (90/10) [20,3,1], 0.1 mg Pt/cm2	0.1
ML040623-2	PtNiMn (90/10) [20,3,1], 0.1 mg Pt/cm2	0.1
ML040721-1	PtNiMn (90/10) [20,2.25,1], 0.1 mg Pt/cm2	0.1
ML040618-2	PtNiMn (50/50) [20,3,1], 0.1 mg Pt/cm2	0.1
ML040617-2	PtNiMn (90/10) [20,0.6,1], 0.1 mg Pt/cm2	0.1

In Table I the designation of the ternary catalysts is explained in detail in Section 2.1.3.1.

2.1.2.3.3 Results

RRDE on pure Pt NSTF

The measurements performed on *pure NSTF Pt* had two purposes. The first one was to explore how amenable the NSTF in a powder form would be as a particulate material for making a slurry and applying it as a thin layer on a RDE. The second purpose was to use the data for pure Pt as a model catalyst and to provide a baseline for the comparison with the performance of the ternary alloys.

The CV's in Ar saturated solution (Fig. 1a) are very similar to Pt high-surface area catalysts, with the typical features for Hupd below 0.4 V and oxygen adsorption/desorption above 0.7 V [4]. Somewhat striking however is the low pseudocapacity in the region between 0.4 and 0.7 V, which is due to the absence of a

carbon support. In CO-stripping a clear peak at about 0.7 V signals the oxidation of adsorbed CO (Fig. 1c). This occurs at much lower potentials than for high surface area catalysts (HSAC), for reasons that have been described in detail elsewhere [5]. In Fig. 1 (b) and (d) the roughness factor r_f, i.e. the ECSA divided by the geometric area of the electrode disc, is depicted against the Pt-loading of NSTF whiskers applied to the RDE disc. Both, the Hupd region of the cyclic voltammograms and the CO desorption measurement, show a strict proportionality between the Pt loading and the measured surface area with a slope of about 7 $m^2 g^{-1}$.

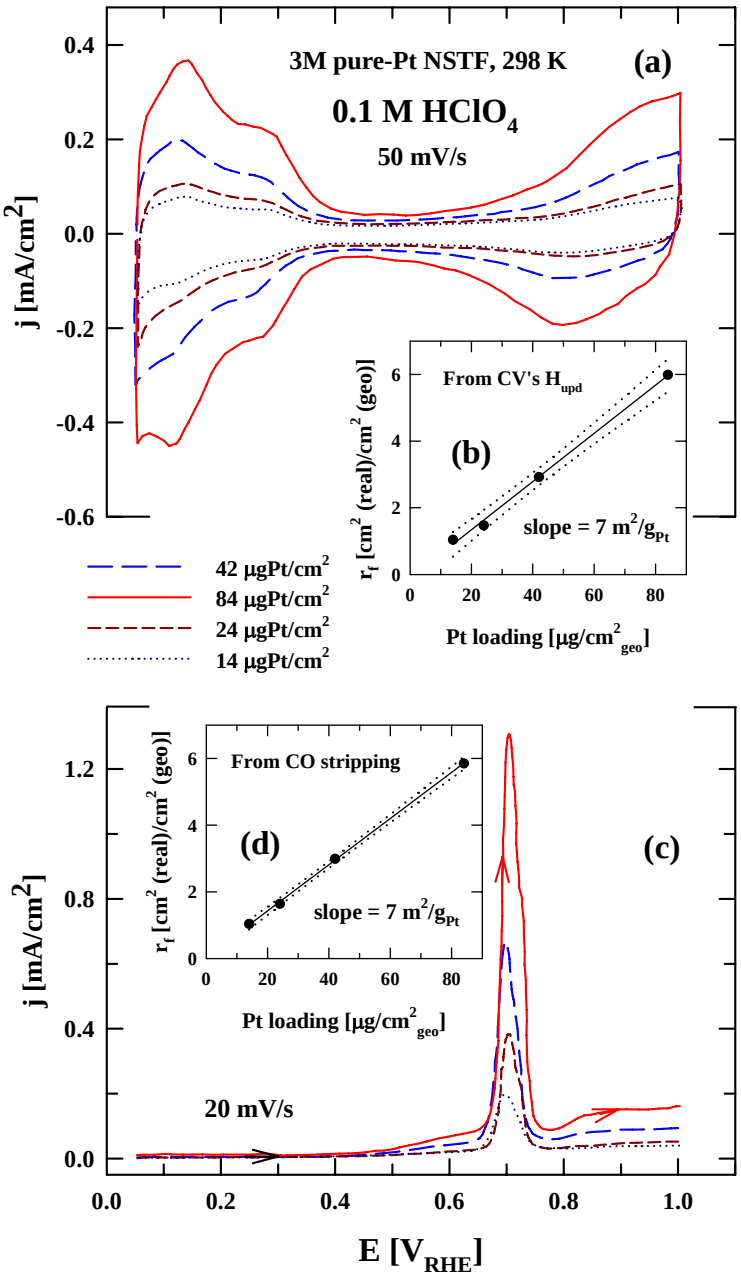

Fig. 1. Cyclic voltammetry (a) and CO stripping (c) on a pure Pt NSTF catalyst. In the insets (b) and (d) the roughness factor r_f is plotted against the Pt loading for the active surface area determined via H_{upd} and CO, respectively.

Having established that the kinetics for ORR are independent of the catalyst loading within a wide range, a Pt loading of 42 μg cm^{-2} was chosen for further studies on pure Pt NSTF catalyst. In Fig. 2a the polarization curves at different rotation rate show a strict proportionality of the diffusion limiting current with the square root of the rotation.

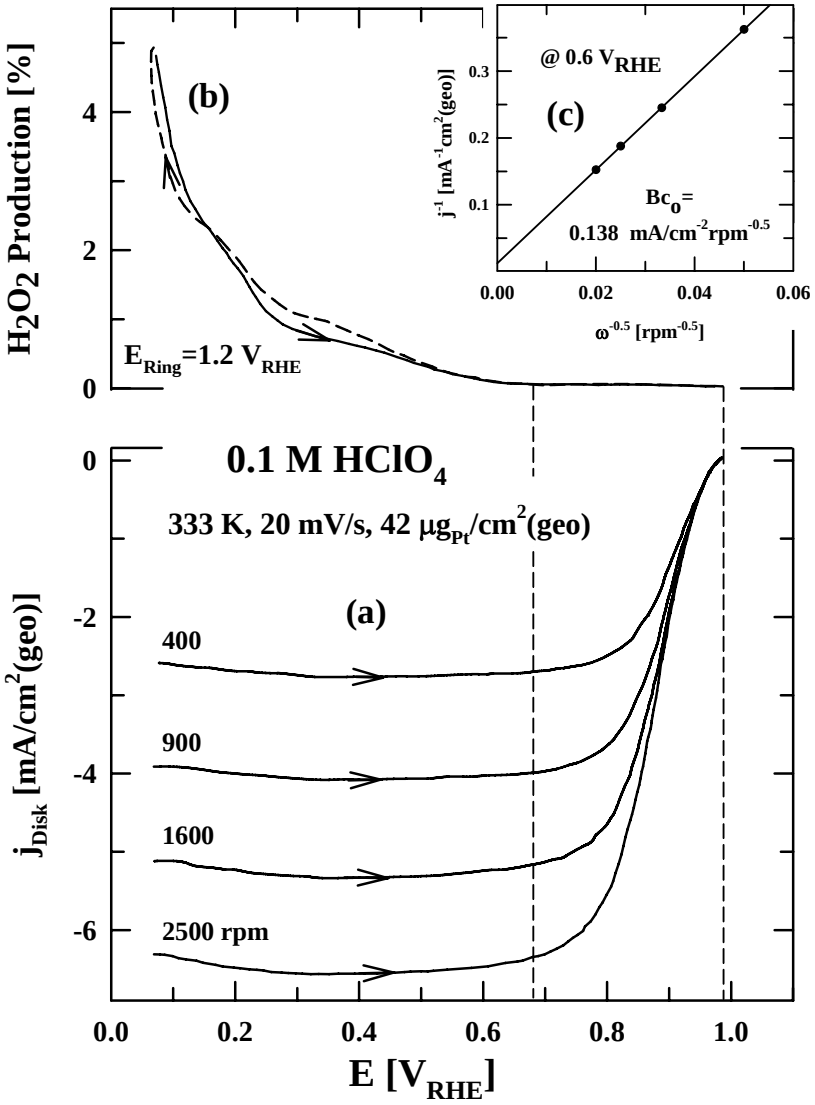

Fig. 2. Polarization curves for the ORR on a pure Pt NSTF (a) and the peroxide detected simultaneously on the ring at 1600 rpm (b). Data from the diffusion-limited region at 0.6 V_{RHE} in (a) is used for the Levich-Koutecky plot (c).

This is reflected in the Levich – Koutecky plot in Fig. 2c, from which additionally the value of 4 for the number of electrons exchanged in the ORR can be derived. The validity of the latest number was confirmed by the absence of any peroxide produced down to 0.6 V, as indicated by the lack of any current at the ring (Fig. 2b) for all rotation rates. Actually, the peroxide production is negligible in the potential region of FC

practical application, since it reaches measurable values only at much lower potentials with the maximum of 5% at 0.1 V. All these findings are in agreement with the behavior of bulk Pt as well as carbon supported catalyst tested under similar conditions [6,7]. The same is true for the temperature dependence of the polarization curves as presented in Fig. 3 against the oxygen overpotential. Note that the lower diffusion limited current recorded at 276 K is due to the lower solubility of oxygen [1]. A continuous change in the Tafel slopes (Fig. 3b) can be observed in the kinetic region, which disables the extraction of a single explicit value. Instead in Table II the change of the Tafel slopes with the temperature is presented for two different potential regions, for overvoltages around 0.3 V and higher than 0.3 V. Again, the observed decreases in the Tafel slopes with the temperature are in agreement with the values reported for bulk Pt and dispersed Pt on carbon, as is the apparent activation energy of ca. 22 kJ/mol for the ORR as derived from the Arrhenius plots (not shown). It is interesting to note that in FC measurements always a single Tafel slope of about 70 mV per decade is observed, and the slope does not change from the low current density (lcd) to the high current density (hcd) region. This disparity has to be analyzed still in more detail with the RDE technique.

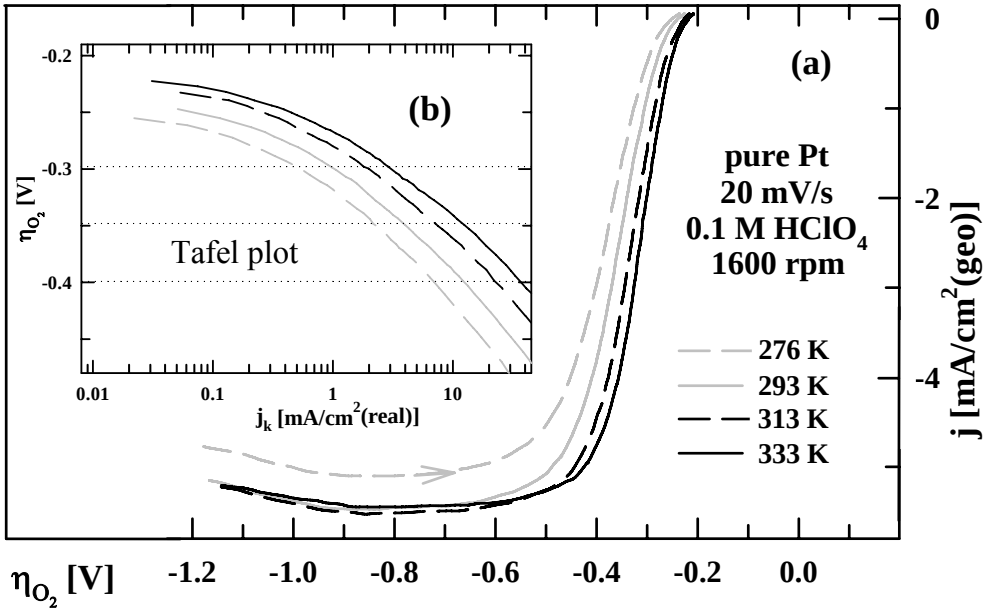

Fig. 3. ORR polarization curves at different temperatures vs. the overpotential against a (theoretical) reversible oxygen electrode (a). Inset (b): Tafel plot of the curves in (a).

Table II. Tafel slopes for the low current density (lcd) and high current density (hcd) region at different temperatures in RDE measurements.

T [K]	276 K	293 K	313 K	333 K
lcd [mV dec^{-1}] (for $\eta<0.3V_{RHE}$)	**-60**	**-57**	**-52**	**-45**
hcd [mV dec^{-1}] (for $\eta>0.3V_{RHE}$)	**-114**	**-113**	**-97**	**-93**

The data presented so far confirms that the technique for NSTF catalyst testing via the RRDE methodology was properly adopted and optimized. As a consequence the inherent activity of the Pt NSTF catalyst per its real surface area can be evaluated and directly compared to the activities of other Pt morphologies. Fig. 4 presents the specific activities for the ORR in the kinetic voltage region for a bulk polycrystalline platinum surface, prepared by flame annealing and UHV annealing, a typical dispersed carbon and Pt NSTF. Clearly the specific activity of Pt NSTF is comparable to the activity of bulk Pt, all of which are significantly higher than the activity of highly dispersed Pt on carbon. Further insights on the increased activity of Pt NSTF over dispersed catalyst is reported in the section below dealing with the effect of particle size on the catalytic activity [4].

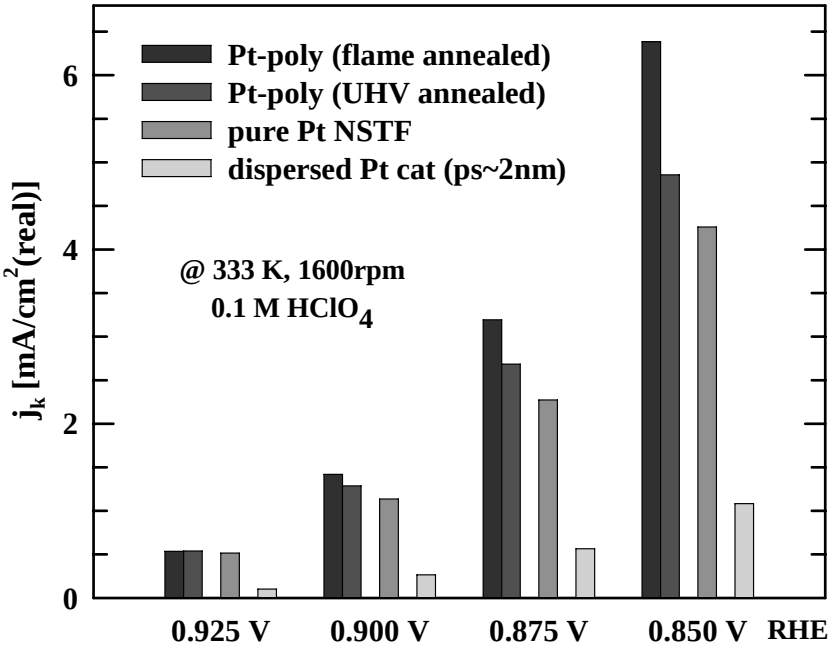

Fig. 4. Comparison of the specific activities for the ORR for different Pt samples in the RRDE using the same conditions.

ORR activity on Ternary Catalysts

The catalytic activity of the NSTF *ternary catalysts* will be illustrated with the first composition fabricated, PtNiFe. The fuel cell performance and some of the basic electrochemical characterization conducted in a fuel cell environment along with the ex-situ structural characterization of the catalysts we have already reported [8]. We present here the RRDE characterization of the effect of first row transition (non-precious) metals in the ternary Pt catalysts by comparing the properties on the samples containing 45% Pt (atomic) with the rest Ni and Fe in 4:1 ratio, to the behavior of pure Pt NSTF presented previously. These samples as the most numerous in this study allow a more credible correlation with the fuel cell data.

In comparison, there are two main differences in the behavior of the NSTF ternary Pt alloys vs. pure Pt NSTF: the stability of the alloys in the acid environment and the surface area. Both of these properties are illustrated in Fig. 5. In Fig. 5a, the cyclic

voltammograms for the ternary alloy at the beginning of the cycling and after three hours of cycling, when the steady state was reached, are presented. While the shape of the CV in (or under) steady state is very similar to the one recorded for pure Pt, the cyclic voltammogram shortly after the immersion (15 min.) clearly deviates in the anodic scan.

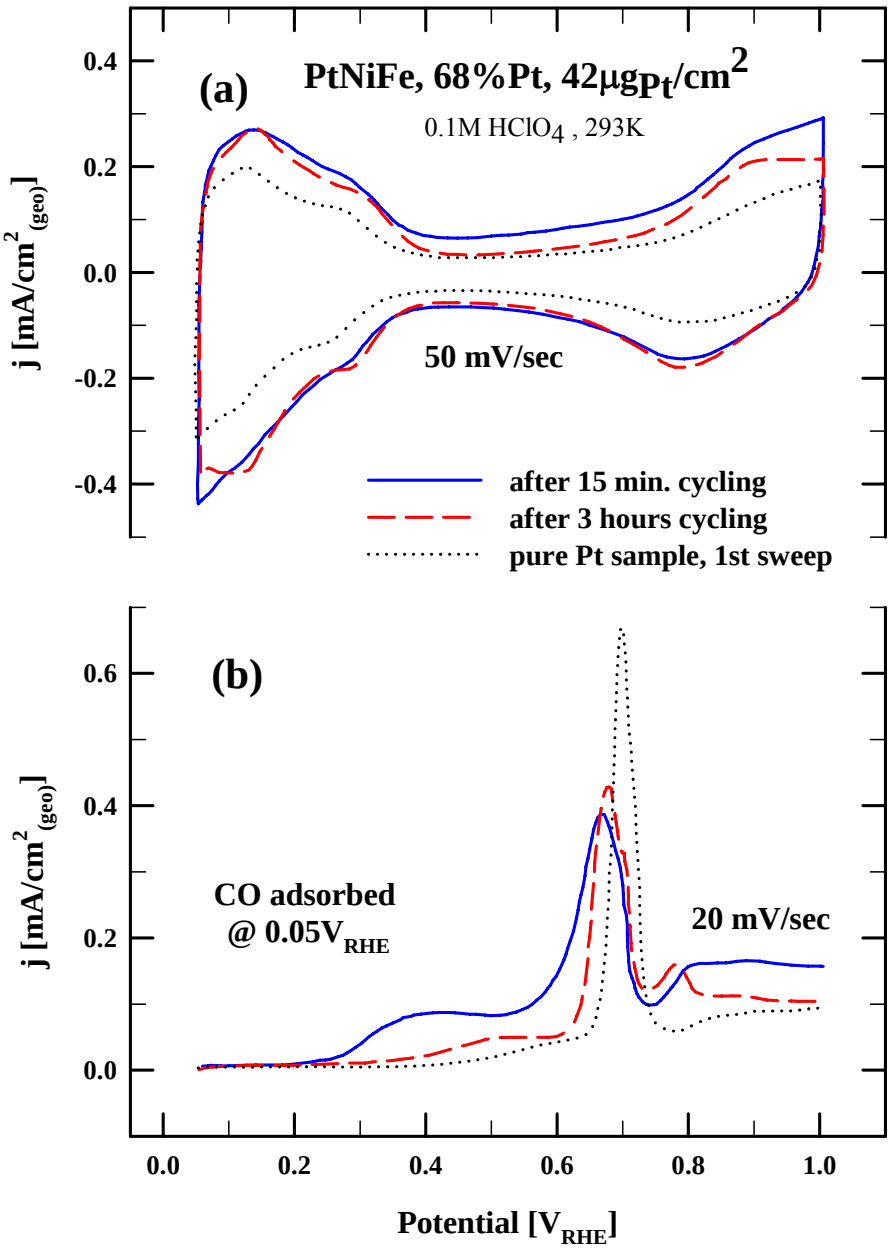

Fig. 5. V (a) and CO-stripping (b) on a ternary Pt NSTF catalyst electrode after cycling for 15 min. (solid) and 3 hours (dashed) in electrolyte, compared to the initial sweep (stable) on a pure-Pt NSTF sample (dotted).

A positive current signal is superimposed on the regular pseudocapacity and adsorption current for a Pt surface. The anodic deviation is strongest in the initial sweep after the immersion of the electrode (not shown), and becomes less until it reaches a steady

state. This behavior is obviously due to the presence of the other two transitional elements. As expected, at these positive potentials above 0.4 V_{RHE} in acid electrolyte they are leached out of the top surface layers. One model suggests that this leads to the formation of a "skeleton structure" in the NSTFC [9,10], with the ternary alloy film covered by a layer of Pt at steady state. The effect of the presence of the Ni and Fe (TM below) is even more noticeable on the CO stripping curves. A substantial pre-peak was recorded after only 15 min., reflecting the oxophilicity of the TM metals still at the surface at that time. The Ni and Fe atoms act as adsorption sites for OH at low potentials, which facilitates the oxidative removal of CO to CO_2 at lower potentials than if only Pt would be present on the surface [11-13]. Both the position of the pre-peak and its magnitude are getting closer to pure NSTF platinum with longer exposure time of the catalyst to the acid environment. This is again a sign for the leaching of the surface layers. Since the shape of the stripping peak is still slightly different even after three hours, it does not render itself as appropriate to the calculation of the active Pt surface area. For this particular reason the electrochemical surface area of the alloys was always calculated from the H_{upd} envelope only.

The phenomena of the dissolution of the TM elements from the NSTF catalyst were studied in detail both in acid and in a H_2/air FC environment and the extent of the dissolution of the TM after prolonged exposure were presented in this report and published elsewhere [14,15]. What we are reporting here is the fact that for the same amount of Pt, the ternary catalyst exhibits much larger surface area. In the case for the catalyst in Fig. 5, this increase is by a factor of 1.5. All other properties of the alloys remain almost the same as for pure NSTF platinum. The polarization curves exhibit slightly lower diffusion limiting currents, probably because of the incomplete dispersion of the catalysts on the GC electrode disc due to their unsupported structure. However, after the correction for this is factored in, the same kinetic information can be obtained. The Levich – Koutecky plot is a straight line with the number of electrons exchanged equal to 4, the production of the peroxide close to zero down to 0.65 V, the Tafel slopes continuously changing from ~ 50 mV/decade at low current densities to ~ 100 mV/decade in the high current density region, and the activation energy within the same, 20 - 24 kJ mol^{-1} range also.

Comparison of RRDE with FC data

Fig. 6. Surface area via H_{upd} on RRDE and 50-cm^2 fuel cell for a series of ternary PtNiFe catalysts with constant platinum loading (0.1 mg/cm^2) and varying amount of Ni/Fe (Ni/Fe = 90/10 % at.) relative to Pt. The surface area for pure Pt is presented for comparison.

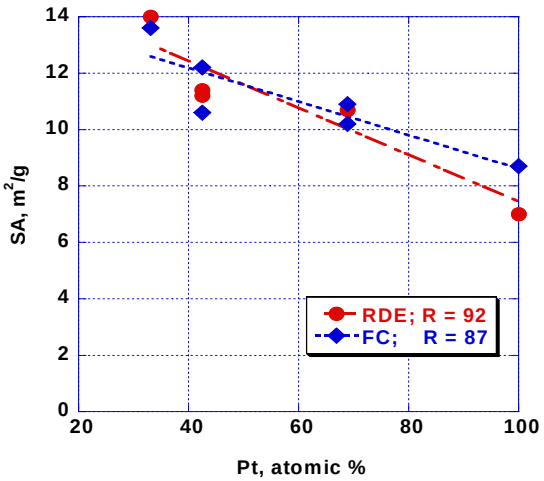

In spite of the differences of the FC and RRDE systems, the surface area and specific activity values for pure platinum and PtNiFe ternary catalysts obtained in 50-cm^2 fuel cells are highly equivalent to the values obtained in the RRDE environment. Fig. 6

compares the surface areas for the series of five PtNiFe catalysts with the same atomic ratio of Ni:Fe, 9:1, measured in the RRDE set up, with those obtained in the 50-cm^2 FC (loading 0.1 mg cm^{-2} Pt) measurements.

The agreement, within the experimental error of this type of H_{upd} measurements, is excellent. It is interesting to point out that within the compositional range explored in this series there is a well defined linear relationship between the TM content and the measured surface area. One can reasonably assume that with the corrosion of the Ni and Fe from the surface, the remaining Pt surface structure is more "developed". In accordance with our findings on bulk Pt alloys this can be described by a so-called "skeleton" structure, which is much rougher than the one of pure Pt [10].

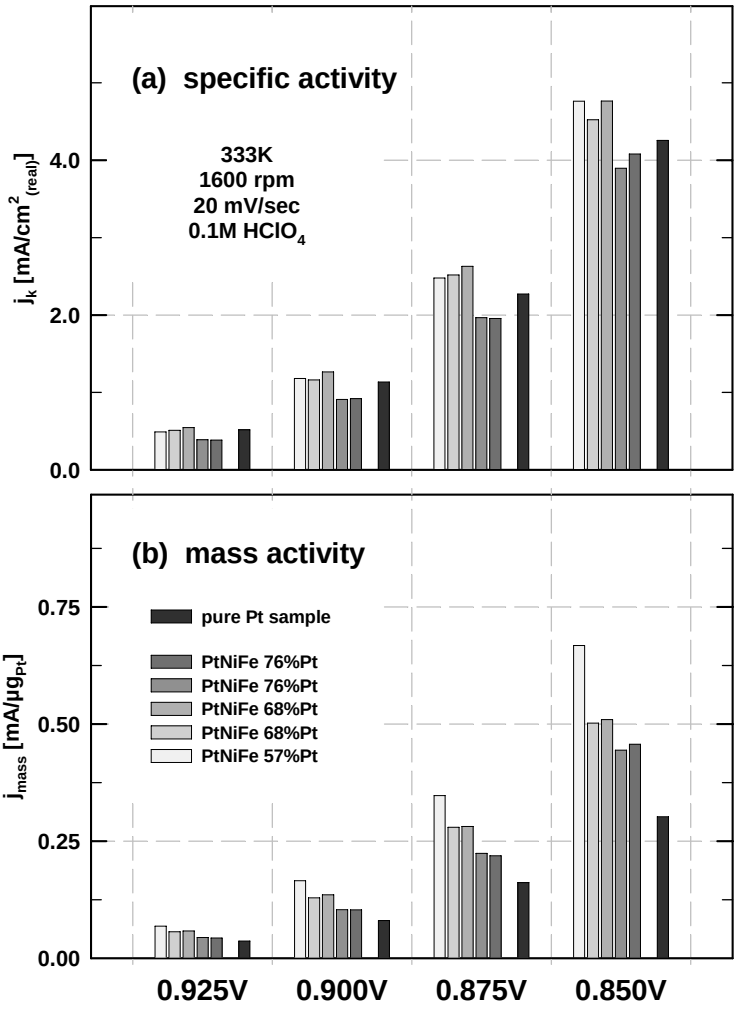

Fig. 7. RRDE specific activity (a) and mass activity (b) for a series of ternary PtNiFe catalysts with constant platinum loading (0.1 mg/cm^2) and varying amount of Ni/Fe (Ni/Fe = 90/10 % at.) relative to Pt. The activity for pure Pt is presented for comparison.

The RRDE specific and mass activity for this series of ternary catalyst is presented in Fig. 7 along with the activity for the pure Pt sample. It appears that the specific activity of the ternary catalysts fall within the error of the measurements for pure Pt, which is estimated to be about 10%. As a consequence, the enhancement observed for the mass

activity in Fig. 7b, as well as during fuel cell testing, is primarily due to the increase in surface area caused by the leaching of TM surface atoms. The catalyst with the highest initial amount of TM's, in this series the PtNiFe-57 % Pt, roughens the most and exhibits therefore the highest mass activity.

A different picture of the specific activity on the Pt content emerges when a wider range of catalyst compositions is considered. For this purpose, the specific activity of this catalyst series is added to the data for a series with higher Ni + Fe content, and for completeness and comparison purposes, by the data from FC measurements (Fig. 8).

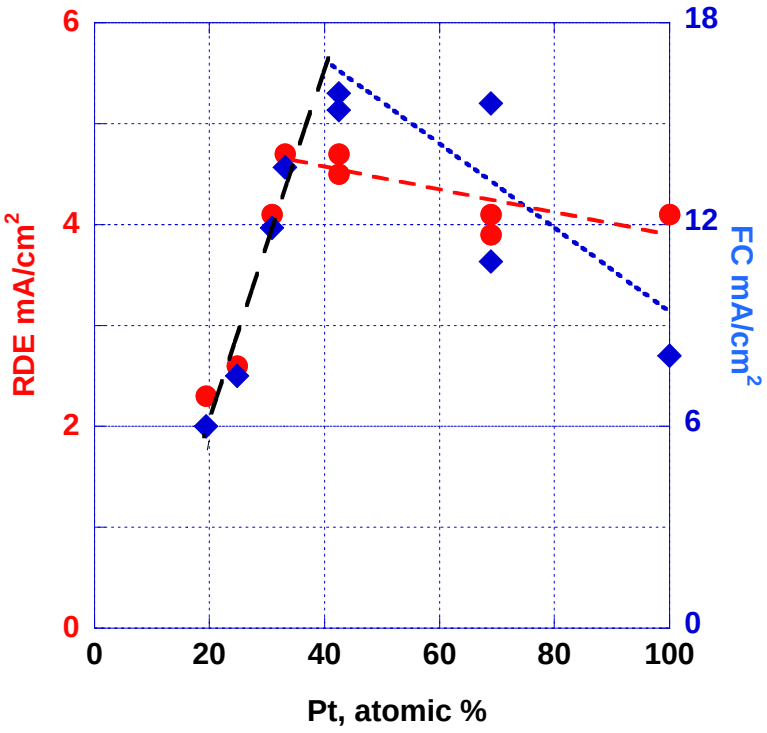

Fig. 8. Specific activity via RRDE (data from Fig. 7 at 0.85V_{RHE}, circles) and FC samples (performance measured at 0.813V on the up-scan of polarization curve at 75 ºC; see experimental for explanation, diamonds) of PtNiFe NSTF catalysts in a wide spectrum of Pt content. The Pt loading of 0.1 mg/cm^2 for all samples is constant.

Before analysis of the data presented in Fig. 8, one has to notice that in Fig. 8 the specific activity for the RDE measurements is given at 0.85 V while the activity for the FC measurements is given at 0.813 V (see experimental for explanation). Consequently, the Y axis for the measurements in the FC is scaled up by a factor of 3. This is reasonable if a correction is made for the activity of the catalysts in FC systems by taking into account that the Tafel slope in FC is always ~ 70 mV/decade (one has to bear in mind that an accurate correction is not possible due to differences in the testing conditions between the two systems, namely, not only the environment and the temperature but also the humidity, the activity of oxygen (air) etc. are different). The main point though is that in spite of the larger scatter of the data in comparison with the

surface area measurements, in both RRDE and FC systems the specific activity values for the ternary catalysts follow each other and in both systems the trend of the change in activity with Pt at. % is the same.

The plot in Fig. 8 consists of two distinctive parts. In the ascending part of the specific activity, from 20 - 40 % at. Pt, there is an extremely good agreement between the two types of activity measurements, FC and RRDE. Therefore, the line for the linear fit actually represents both sets of data. Up to the value of 40 % at. Pt, there is a sharp increase of the activity with the Pt content. From there on though, the specific activity is less dependent on the Ni + Fe content and, because of the scatter of the data in the RRDE measurements, one can argue that the activity is almost flat. However, combined with the data from the FC measurements, there appears to be an optimum at about 35 - 40% Pt. One possible explanation for the maximum in the activity could be an electronic effect from the remaining TM underneath the Pt surface layer after leaching. This effect has already been demonstrated for various alloy crystal surfaces [9,10,16]. As a consequence an increase in specific activity with a higher content of TM is expected. At a Pt content below 35 %, however, no stable Pt surface layer can be formed sufficient to inhibit the leaching process. Consequently the majority of TM atoms are leached out and the specific activity decreases again to that of pure Pt. If the thin film structure were degraded even more severely so that individual particles were formed, the catalyst would be expected to act similar to dispersed Pt, where the smaller particle size leads to lower specific activity [4].

While more experimental data are needed, one more observation could be made in Fig. 8. The specific activity curves obtained by the two methods, FC and RRDE, in the range above 40 % at. Pt are departing from each other more than the rest of the data presented in this section. One possible explanation for this discrepancy could be that the amount of TM in the surface layers between the two tests is different due to the fact that the time of the RRDE test is relatively short (hours) in comparison to the testing duration in real fuel cell (days). We have shown that after prolonged exposure in an acid environment the bulk ternary catalyst composition is the same, be it in fuel cell or in perchloric acid [14,15]. However, as discussed in the previous paragraph, the catalytic properties being a strictly surface phenomenon, and further studies of the surfaces are being pursued in order to get more insights into this observation as part of the suceeding 3M/DOE grant DE-FG36-07GO17007.

NSTF and Pt particle size effect

Further understanding of the increased specific activity of the NSTF catalyst can be obtained through comparison of the ORR catalytic activity, expressed per electrochemically measured surface area, on catalysts of different platinum particle size. It has been well established that the inherent ORR catalytic activity increases with the Pt particle size. The study conducted at LBNL produced insight into this phenomenon. In Fig. 9 the cyclic voltammograms for three different particle sizes are presented. While the detail experimental findings and discussion were published by LBNL group [2,5] , the main conclusion of this study, as illustrated if Fig. 9, was that a shift in the potential of zero total charge to more negative potentials with decreasing particle size, results in a similar potential shift for the adsorption of OH-species on the Pt surface. Since, however, OH_{ad} blocks the active surface sites, highly dispersed particles are less active for the ORR than a bulk Pt catalyst. For the extremely thin, yet continuous polycrystalline film structure of the NSTFC [17] the situation is quite different. While the surface of this film,

which is eventually responsible for the catalytic activity, can be much rougher than that of bulk Pt, this surface resembles bulk Pt much closer than does the dispersed Pt on carbon. On a fundamental level, this similarity of the Pt NSTF surface to bulk platinum is one of the most important distinctions of the NSTF catalyst vs. dispersed Pt catalysts.

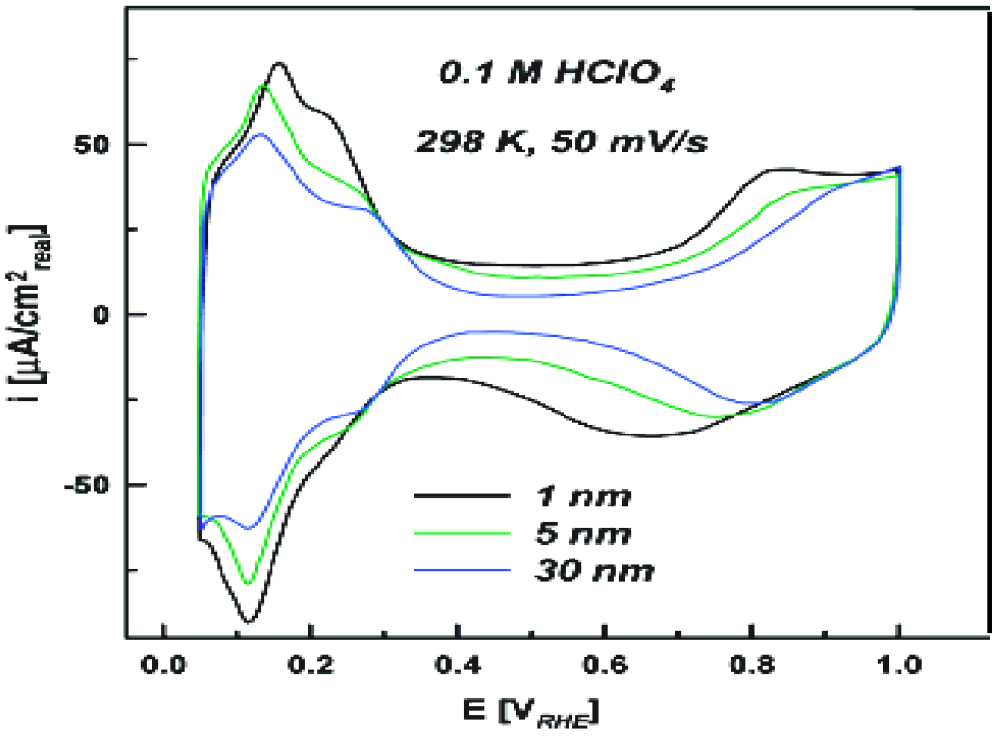

Fig. 9. Cyclic voltammograms of Pt catalyst samples of different particle size: 1 nm and 5 nm - Pt supported on carbon; 30 nm – Pt NSTF; recorded in 0.1M $HClO_4$; T=20 ^oC, scan rate 50 mV s^{-1}; currents are normalized to the measured Pt surface area.

2.1.2.3.4 Conclusion

We demonstrated that catalyst activity measurements in fuel cells can be directly compared with RRDE measurements qualitatively and even quantitatively under certain experimental conditions. In this context we confirmed the nature of the increased ORR activities of NSTF catalysts previously shown in fuel cells, now in a controlled electrochemical environment. The measurements of the surface area and specific activity by both methods were in excellent agreement. The inherent catalytic activity of the Pt-NSTF catalyst was close to the activity of bulk platinum, and therefore significantly higher than the carbon-supported, Pt high surface area catalysts. The ternary catalysts exhibited an increase in the electrochemical surface area, because of the leaching of Ni and Fe from the surface layers. As a consequence an improved mass activity in the RRDE was found, which is in agreement with the better kinetic performance of these catalysts during fuel cell operation.

References for Section 2.1.2.3

1. U. A. Paulus, T. J. Schmidt, H. A. Gasteiger, R. J. Behm, *J. Electroanal. Chem., **495***, 134 (2001).
2. K. J. J. Mayrhofer, M. Arenz, B. B. Blizanac, V. Stamenkovic, P. N. Ross, N. M. Markovic, *Electrochim. Acta, **50***, 5144 (2005).
3. K. Kinoshita, "*Electrochemical Oxygen Technology"*, Wiley, New York, 1990.
4. K. J. J. Mayrhofer, B. B. Blizanac, M. Arenz, V. R. Stamenkovic, P. N. Ross, N. M. Markovic, *J. Phys. Chem. B, **109***, 14433 (2005).
5. M. Arenz, K. J. J. Mayrhofer, V. R. Stamenkovic, B. B. Blizanac, T. Tomoyki, P. N. Ross, N. M. Markovic, *J. Am. Chem. Soc., **127***, 6819 (2005).
6. T. J. Schmidt, H. A. Gasteiger, W. Vielstich, H. A. Gasteiger, A. Lamm, in *Handbook of Fuel Cells - Fundamentals, Technology and Applications*, W. Vielstich, A. Lamm, H. A. Gasteiger, Eds.,Wiley, 2003.
7. N. M. Markovic, T. J. Schmidt, V. R. Stamenkovic, P. N. Ross, *Fuel Cells, **1***, 105 (2001).
8. J. McBreen, M. Balasubramanian, W.-S. Yoon, K. Y. Chung, H. S. Lee, X.-Q. Yang, R. Atanasoski, A. K. Schmoeckel, G. D. Vernstrom, M. K. Debe, *ECS Transactions, **1***, 149 (2006).
9. V. R. Stamenkovic, B. S. Mun, K. J. J. Mayrhofer, P. N. Ross, C. A. Lucas, N. M. Markovic, *Nature Materials, **(in press)*** (2007).
10. V. R. Stamenkovic, B. S. Mun, K. J. J. Mayrhofer, P. N. Ross, N. M. Markovic, *J. Am. Chem. Soc., **128***, 8813 (2006).
11. H. A. Gasteiger, N. M. Markovic, P. N. Ross, *J. Phys. Chem., **99***, 8290 (1995).
12. M. Arenz, V. R. Stamenkovic, B. B. Blizanac, K. J. J. Mayrhofer, N. M. Markovic, P. N. Ross, *J. Catalysis, **232*** 402 (2005).
13. V. Stamenkovic, M. Arenz, B. B. Blizanac, K. J. J. Mayrhofer, P. N. Ross, N. M. Markovic, *Surf. Sci., **576***, 145 (2005).
14. A. Bonakdarpour, J. Wenzel, D. A. Stevens, S. Sheng, T. L. Monchesky, R. Lobel, R. T. Atanasoski, A. K. Schmoeckel, G. D. Vernstrom, M. K. Debe, J. R. Dahn, *J. Electrochem. Soc., **152***, A61 (2005).
15. A. Bonakdarpour, R. Lobel, R. T. Atanasoski, G. D. Vernstrom, A. K. Schmoeckel, M. K. Debe, J. R. Dahn, *J. Electrochem. Soc., **153***, A1835 (2006).
16. V. Stamenkovic, B. S. Mun, K. J. J. Mayrhofer, P. N. Ross, N. M. Markovic, J. Rossmeisl, J. Greeley, J. K. Norskov, *Angewandte Chemie-International Edition, **45***, 2897 (2006).
17. M. K. Debe. In *Handbook of Fuel Cells - Fundamentals, Technology and Applications,* Ch. 45, W. Vielstich, A. Lamm, H. A. Gasteiger, Eds., Wiley, 2003.

2.1.3 50 cm^2 Fuel Cell Evaluation

2.1.3.0. Introduction

This subsection summarizes the results of a several year study of NSTF-PtM_1M_2 ternary alloy catalyst activity measurements, for which M_1M_2 are transition metals from the group NiFe, CoFe, MnFe, NiMn and CoMn. We used multiple measurement methods of relative specific activity to obtain the catalyst alloy composition and construction that gave the optimum specific activity in 50 cm^2 fuel cells. We found that the NSTF - PtNiMn and PtCoMn electrodes exhibited a maximum 250% gain in specific activity over pure NSTF – Pt. Because of the all-dry, vacuum coating nature of the NSTF catalyst and support fabrication processes, it is as cost effective to fabricate ternary and binary electrocatalysts using these methods as it is pure NSTF-Pt [1]. Following a summary of catalyst and MEA preparation and a description of single cell testing, the various types of catalyst evaluation measurements are described, including surface area, and four methods for specific activity. The NSTF catalyst whisker supports are then defined along with a complete listing of the NSTF ternary catalysts investigated. This is followed by an extensive summary of how mass specific area, mass activity, specific activity, and Tafel slope vary with the ternary catalyst composition and fabrication parameters such as bi-layer thickness, ratio of Pt to transition metal, and whisker support dimensions. The impact of these catalyst chararacteristics are then summarized in ambient and high pressure polarization curve performances. The effects of low catalyst loading levels are included to demonstrate record performances when better matched to the whisker support structure.

2.1.3.1. Experimental

2.1.3.1.1 Catalyst and MEA preparation

The NSTF catalysts and MEAs were prepared in general as described in reference [2][2]. The NSTF whisker support layer is a monolayer of oriented crystalline whiskers of an organic pigment material (CAS # PR149). [3,4] The support layer is deposited first onto a microstructured catalyst transfer substrate (MCTS) via a vacuum roll-good process. An in-line annealing process converts the pigment layer into a nanostructured monolayer of oriented crystalline whiskers. Catalysts sputter-coated on top of the whiskers encapsulates them as a polycrystalline thin film. Composition and structure of the catalyst coating is determined by the arrangement and composition of the sputtering targets. Primarily Pt ternary and baseline pure-Pt were used for the NSTF catalyst samples investigated. Although multiple lots of NSTF support whiskers were used, they were nominally identical in terms of whisker dimensions and areal number densities except when intentionally varied as described below. These nanostructured support whiskers were sputter coated with the Pt alloy composition using multiple passes over separate targets for the Pt and M_1M_2 transition metal (TM) combinations. For most ternary catalysts comparing specific activities, the Pt loading was held fixed at 0.1 mg/cm^2 and the TM component loadings were varied. The primary parameters of the ternary depositions were the M_1 / M_2 ratio, the bi-layer thickness of Pt and TM deposited per pass over the sputtering targets, and the Pt / [M_1+M_2] ratio. In some of the measurements, the Pt loading was varied below 0.1 mg/cm^2, for fixed Pt/TM ratio and in others, the Pt loading was varied while keeping the total as-made volume of the ternary catalyst constant.

NSTF catalyst coated membranes (CCM) were formed by embedding NSTF anode and cathode catalysts in the surfaces of 3M fabricated PFSA proton exchange membranes with 800 - 1000 EW, using a decal-transfer type roll-to-roll process. Both Nafion™ inonomer and the 3M ionomer were used to fabricate the membranes with thicknesses in the 30-40 micron range. The membranes were acid washed before use to remove impurities. Pure NSTF-Pt catalyst anodes at a loading of 0.15 mg/cm^2 were used for all the measurements except where intentionally varied. CCM's were placed between 3M-coated roll-good gas diffusion layer (GDL) media based on hydrophobically pretreated woven carbon cloth backings or carbon paper backings. GDL's were not bonded to the CCM's.

In deposition of the catalysts onto the whisker supports, several parameters were controlled; the transition metal types, M1and M2; the atomic ratio of M1/M2; the Pt and (M1+M2) bi-layer thickness, and the ratio of the Pt to (M1+M2) layer thicknesses. Regarding the whisker supports, the areal number density (number of whiskers per unit of planar area) and their lengths were varied over a limited range to investigate the impact of better matched whisker support surface area to the loading and volume of catalyst coating. A total of 113 different NSTF ternary catalyst constructions were evaluated including ten PtMnFe, twenty-eight PtNiFe, thirty PtCoFe, eight PtNiMn and sixteen PtCoMn.

2.1.3.1.2 Single cell testing

All the performance fuel cell tests were done in 50 cm^2 cells with quad-serpentine flow fields purchased from Fuel Cell Technology. Fuel cell performance was obtained on test stations purchased from Fuel Cell Technology, using 3M-developed test station control software. The MEA's were compressed between 25% and 30% of the original GDL thickness using hard-stop gaskets, and tested under a standard start-up protocol until the performance stabilized. This routinely involved a form of repetitive thermal cycling found to be necessary to remove residual MEA impurities and obtain maximum performance with the low surface area NSTF catalysts as described below. Cell bolts were uniformly torqued to 110 in-lbs.

Humidification was provided to the fuel cell by two LabAlliance HPLC pumps, one for each reactant stream. Each HPLC pump fed liquid water through PTFE tubing into a 316 stainless steel Swagelok tee, into which the gaseous reactants were also fed; the wet reactant streams were then fed to the fuel cell. The water was generally preheated prior to entering the cell, so the humidification water entered the cell primarily in the vapor phase. In our experience, this method of providing humidification works equivalently well as sparge bottle humidifiers.

Scripted software was used to break-in all MEAs with the same test protocol. The start-up protocol consisted of ambient pressure fast potentiodynamic scans (PDS) beween 0.85 V and 0.25 V in 0.05 V, 10 second steps; followed by 10 minute potentiostatic scans (PSS) at 0.4 V, repeated continuously over a 5 hour period, at 65^oC cell temperature and H_2/air inlet gases humidified at 70^oC dew points. The H_2/air were introduced to the cells in a counterflow mode with flow rates held constant at 800/1800 sccm.

Following the initial break-in period, the scripted protocol entered a thermal cycling stage in which the the same PDS/PSS scans were run with a 75^oC cell temperature and the

same 70°C dew points. Typically four sets of scans would be completed before an automatic shut-off and cool-down of the cell was completed sufficient for the cell to reach near ambient temperatures for a period of about one-half hour. During the shut-off period, the reactant gas flows were stopped but the HPLC water injection pumps continued to flush water through the cell. The cell was then restarted and the cycle repeated until the PDS current density values had stabilized. This thermal cycling procedure has been found necessary to remove residual impurities in the MEA which limit initial performance. More on conditioning an break-in is founn in section 2.1.5.4.

2.1.3.1.3 Catalyst evaluation measurements

The primary characterization of the catalyst ternary compositions and constructions was by measurement of their specific acitivty, A/cm^{2}-Pt. Three different protocols were used to measure the specific activity, as described below, all involved a common electrochemcial surface area measurement. In addition, catalyst characterization included fuel cell performance under various conditions of temperature, pressure, humidity, and flow rates; Tafel slopes; mass transport overpotential losses at 2A/cm^2 under hydrogen/air; and fluoride release rates.

Surface area measurements.

Cyclic voltammograms (CVs) for surface area determination and voltage cycling were measured using a Solartron 1470 potentiostat controlled by CorrWare software from Scribner Associates.

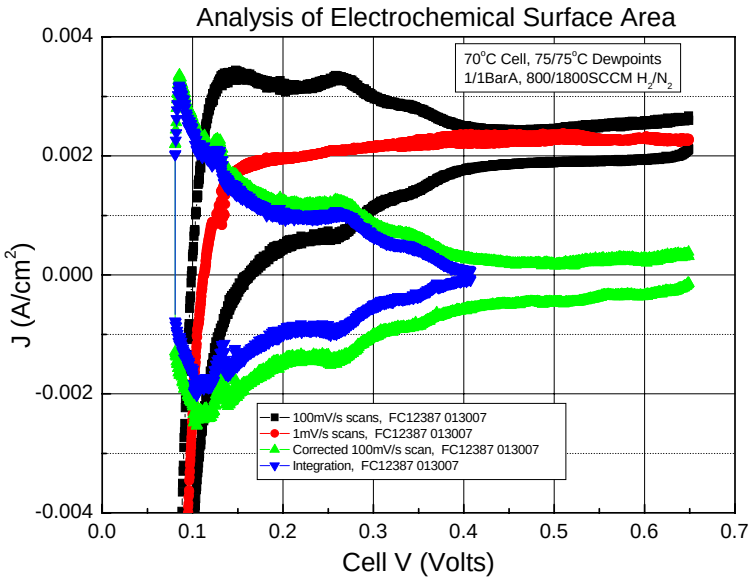

Fig. 1. Illustration of cyclic voltammograms used to measure the electrochemical surface area.

Electrochemical surface areas were generally measured at 70ºC with 75°C anode and cathode dewpoints, 800/1800SCCM H_2/N_2, and ambient cell outlet pressures. 50 to 100 cyclic voltammograms were taken, ranging from 0.09 to 0.65V versus the H_2 anode, with 100mV/s scan rates (Fig. 1).

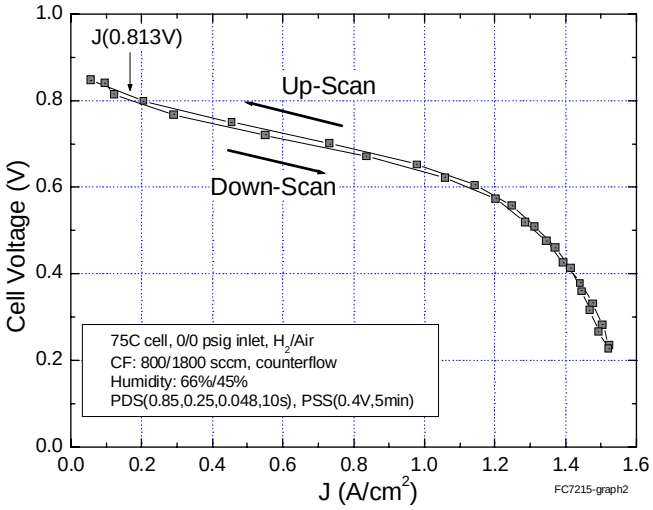

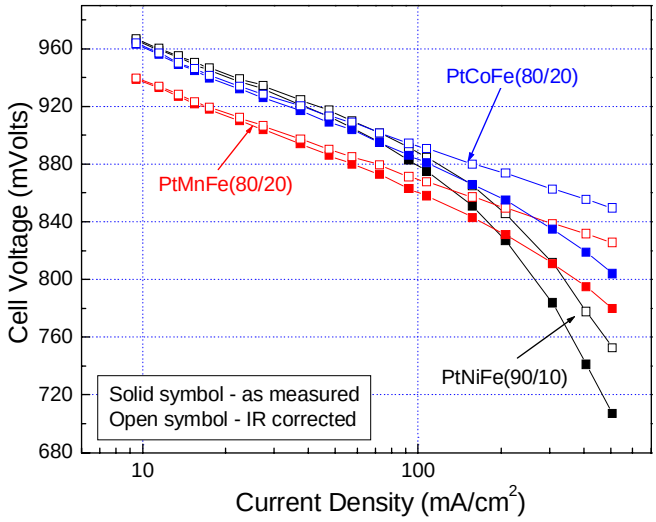

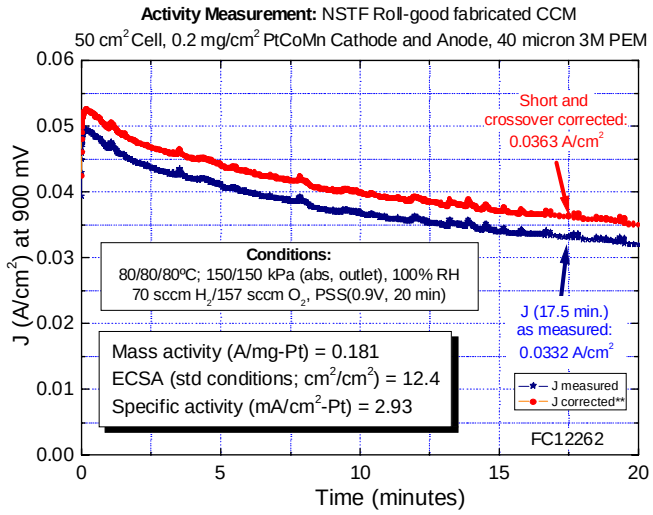

Following this, three slower scans were taken to aid in estimation of electronic shorting and crossover; scans were again taken between 0.09 V and 0.65 V versus the H_2 anode, at 2mV/s scan rates. Pt surface areas, electronic shorting, and hydrogen crossover were extracted from the CVs using custom software, which assumed 210 or 220 µC/cm^2-Pt. Fig. 1 illustrates the determination of surface area from the CVs before and after correcting for electronic shorting and hydrogen crossover currents, referenced to the RHE anode.

Fig. 2. Illustration of methods 1, 2 and 3 for determining specific activity as described below.

Catalyst specific activity measurements

Three different methods were used to obtain specific activity values for the various catalysts. In part this was due to adoption of different protocols over time and the need to compare with published literature values, but all were in good agreement.

Method 1.

In this method the activity (A/cm^2_{planar} at a given cell voltage) was determined from a fast potentiodynamic (PDS) polarization scan at ambient pressure and constant flow. The exact conditions used were a PDS scan from 0.85 V to 0.25 V and back to 0.85 V, in 48 mV steps at a rate of 10 seconds/step. The H_2/air pressure was ambient outlet, cell temperature 70 to 75 ^oC, and relative humidities generally around 70%RH, although this could vary. The current density at a cell voltage of 0.813 V, interpolating if necessary, on the back scan (0.25 to 0.85 V) was taken as the measure of activity, without IR-correcting the scan. Fig. 2 (top) illustrates this method 1. The value of 0.813 V is purely historical, since data was initially gathered from multiple MEA's, beginning in 1999, both with NSTF catalysts and conventional dispersed Pt on carbon, from the standard start-up polarization curves. The advantage of this method is that it is fast and convenient, and the Pt is presumeably free of oxides due to the reduction at the minimum cell voltage and fast back scan. Fig. 3 shows a comparison of the current density at 0.813 V from this method, plotted versus the electrochemical surface area for a series of 41 NSTF-Pt MEAs (cathode loadings 0.1 to 0.4 mg/cm^2) and 30 Pt/C MEAs (cathode loadings $\leq$ 0.63 mg/cm^2) in the 1999-2000 time period. (Fig. 3 is a modification of Fig. 3.15 in the final report for the preceeding 3M/DOE cooperative agreement DE-FC02-99EE50582). Both types of MEAs used multiple types and thicknesses of membranes and gas diffusion layers, and for the dispersed Pt/C MEAs, multiple catalyst loadings, Pt:C wt%, vendors and electrode ink ratios. The specific activity by Method 1 is this J(0.813 V) activity divided by the electrochemical surface area

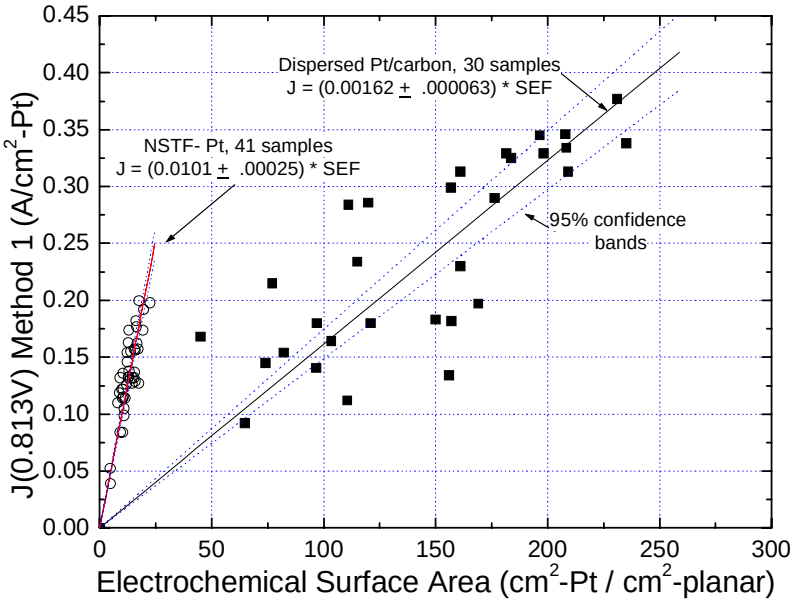

Fig. 3. Current density at 813 mV from Method 1 for determining the specific activity, as a function of electrochemical surface area, for multiple NSTF-Pt based MEAs and mulitple dispersed Pt/C MEAs. The specific activity by Method 1 is the slope of each data set.

and therefore the slope of the plotted data in Fig. 3. This was the first indication that the specific activities of the NSTF – Pt catalysts were multiples of the specific activity of the carbon supported dispersed catalysts, in this case over six.

Method 2.

In this method galvanodynamic polarization curves (GDS) were obtained under 300kPa H_2/O_2 at 75^{o}C, constant flow and supersaturated inlets, at a scan rate of 3 to 5 minutes per point. They were IR corrected using high frequency (8kHz) impedance values measured during the acquisition of the polarization curve, and the current density at 900mV obtained by interpolation from a least squares fit to a Tafel plot of the polarization curve. Fig. 2 (middle) illustrates the method for three of the ternary catalysts discussed below. The specific activity by Method 2 is this J(0.900V) activity divided by the electrochemical surface area. Tafel slopes were also measured for the different catalyst constructions discussed below.

Method 3.

In this method, suggested by GM researchers[5] and adopted by the Dept. of Energy fuel cell programs, the current density is averaged for 5 minutes starting 15 minutes after setting the cell voltage to 900mV, under 150kPa (abs) H_2/O_2, at 80^{o}C, with flow rates of 70/157 H_2/O_2, and 100% RH. At these conditions, the partial pressure of oxygen is one atmosphere. The cell current is corrected for shorting and hydrogen cross-over to obtain the activity value. Fig. 2(bottom) illustrates the measurement of the activity by this method. The specific activity by Method 3 is this current density, J(0.900V), divided by the electrochemical surface area.

Method 4.

This method refers to the values of specific activity obtained from rotating ring disc electrode measurements. Although no such measurements were conducted at 3M laboratories for this report, NSTF catalyst materials were provided to other laboratories, including LBNL, as discussed at length in section 2.1.2.3, and Dalhousie University, as shown in Appenidix II. We make comparisons of their results with those from Methods 1, 2 and 3 at the end of this section 2.1.3 in Fig. 25.

The results of these different measurement methods allow scatter plots of specific activities, mass specific areas, mass activities, Tafel slopes and surface areas to be obtained as a function of the as-made catalyst construction parameters. These parameters include the platinum to transition metal ratio (Pt/TM), transition metal types and their ratio (M1/M2), Pt+TM bi-layer thickness, and Pt catalyst loading. The measurements reported in this paper were obtained over a period of years, and not all the methods were practiced or used routinely at the same time. Hence, none of the catalyst constructions have activity measurements by all the methods.

2.1.3.1.4 NSTF whisker supports

For the majority of the catalyst compositions compared below, two nominally identical lots of the NSTF whisker supports were used, identified as PE652 and PE643 (shown in

Fig. 4). Portions of a third lot, PE628A, were also used. Each lot was fabricated as a roll-good with a high level of down-web control of the whisker support characteristics to minimize their impact on surface area and mass activity. For a subset of the measurements described below, the whisker support characteristics, areal number density and whisker lengths, were varied to determine the impact on mass specific area and to better optimize the activity of the ternary catalysts.

2.1.3.2 Results

Table I summarises the identity and primary results from the ninety-two NSTF PtM_1M_2 ternary catalysts investigated. The compositions are identified by the relative atomic fractions, Pt-loading and whisker support lot. However, the experimental parameters controlled during the catalyt depositions were the planar equivalent thicknesses of the Pt and TM (M_1 + M_2) layers and the atomic ratio M_1/M_2. From those the Pt + TM bi-layer thickness and layer-to-layer thickness ratios (designated Pt/TM) are determined. The mass specific surface areas, specific and mass activities and Tafel slopes determined by Methods 1 and 2 are given in Table I as a function of these parameters, and plotted in subsequent figures.

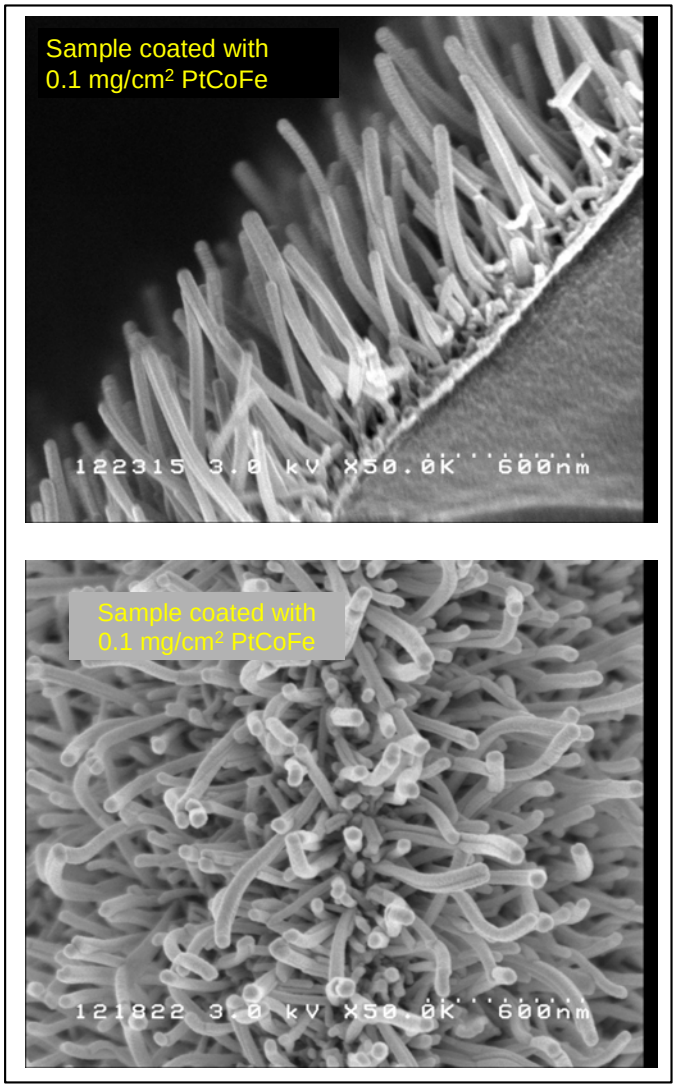

Fig. 4. Scanning electron micrographs at 50,000X (original magnification) of the NSTF whisker lot PE643 with a PtCoFe catalyst coating for which the Pt loading was 0.1 mg/cm^2.

Table I. Summary of the identities and characteristics of the ninety-two NSTF ternary catalysts investigated. The FC #### identifies a fuel cell test and 50 cm^2 MEA. The PtM1M2[#1,#2,#3](#4:#5) designation is defined at the end of this table.

Summary of PtM1M2 Ternarys Tested								
FC #	Cathode	x:y:z for $Pt_xM1_yM2_z$	Run Number	Pt Loading mg/cm^2	Whisker Lot	Cathode ECSA at 70°C (100% H2)	J (A/cm^2) at 0.813V on upscan	Specific Activity at 0.813V, Method 1
FC7119	Pt	Pt 0nly	ML021015-2			8.77	0.107	0.0122
FC6892	PtMnFe [10,1,1], 80:20	44.09:44.73:11.18	ML021008-1	0.1	PE652	7.94	0.071	0.0089
FC6914	PtMnFe [50,1,1], 80:20	44.09:44.73:11.18	ML021010-1	0.1	PE652	6.97	0.047	0.0067
FC6960	PtMnFe [10,2,1], 80:20	61.62:30.70:7.68	ML021011-1	0.1	PE652	10.37	0.099	0.0095
FC6971	PtMnFe [20,1.5,1], 80:20	55.02:35.98:9	ML021015-1	0.1	PE652	8.64	0.094	0.0109
FC6992	PtMnFe [50,3,1], 80:20	71.41:22.87:5.72	ML021016-1	0.1	PE652	10.54	0.108	0.0102
FC7023	PtMnFe [30,3,1], 80:20	71.41:22.87:5.72	ML021101-1	0.1	PE652	9.59	0.116	0.0121
FC7043	PtMnFe [30,1.5,1], 80:20	55.02:35.98:9	ML021024-1	0.1	PE652	9.29	0.132	0.0142
FC7427	PtMnFe [30,1.5,1], 80:20	55.02:35.98:9	ML021023-1	0.1	PE652	9.77	0.136	0.0139
FC7819	PtMnFe [30,1.5,1], 80:20	71.41:22.87:5.72	ML021105-1	0.1	PE652	9.74	0.135	0.0139
FC7799	PtMnFe [30,1.5,1], 80:20	71.41:22.87:5.72	ML021104-1	0.1	PE652	9.91	0.149	0.015
FC7400	PtNiFe [50,1,1], 90:10	45.39:49.15:5.46	ML030102-1	0.1	PE652	10.58	0.163	0.0154
FC7438	PtNiFe [50,1.5,1], 90:10	54.73:40.74:4.53	ML030103-1	0.1	PE652	10.27	0.163	0.0159
FC7497	PtNiFe [30,0.6,1], 90:10	33.14:60.18:6.69	ML030127-1	0.1	PE652	14.46	0.173	0.0120
FC7507	PtNiFe [10,0.6,1], 90:10	33.14:60.18:6.69	ML030128-1	0.1	PE652	12.75	0.214	0.0168
FC7550	PtNiFe [30,0.6,1], 90:10	33.14:60.18:6.69	ML030130-1	0.1	PE643	13.63	0.150	0.0110
FC7600	PtNiFe [5,0.6,1], 90:10	33.14:60.18:6.69	ML030128-2	0.1	PE652	13.61	0.187	0.0137
FC7659	PtNiFe [10,1.5,1], 90:10	54.73:40.74:4.53	ML030128-3	0.1	PE652	12.28	0.181	0.0147
FC7672	PtNiFe [10,3,1], 90:10	71.70:25.47:2.83	ML030103-3	0.1	PE652	10.12	0.158	0.0156
FC7673	PtNiFe [5,3,1], 90:10	71.70:25.47:2.83	ML030110-1	0.1	PE652	10.94	0.119	0.0109
FC7732	PtNiFe [30,3,1], 90:10	70.37:26.67:2.96	ML030205-1	0.1	PE643	11.73	0.143	0.0122
FC7733	PtNiFe [20,1,1], 90:10	45.39:49.15:5.46	ML030102-2	0.1	PE652	12.20	0.194	0.0159
FC7734	PtNiFe [20,2,1], 90:10	62.64:33.80:3.76	ML030129-2	0.1	PE643	11.42	0.151	0.0132
FC8000	PtNiFe [30,0.6,1], 90:10	33.84:59.54:6.62	ML030505-1	0.05	PE643	10.44	0.156	0.0149
FC8013	PtNiFe [30,0.6,1], 90:10	33.84:59.54:6.62	ML030506-1	0.025	PE643	6.09	0.084	0.0138
FC7613	PtNiFe [20,0.6,1], 95:5	30.88:65.66:3.46	ML030207-1	0.1	PE643	15.60	0.195	0.0125
FC7648	PtNiFe [10,0.6,1], 95:5	30.88:65.66:3.46	ML030207-2	0.1	PE643	16.23	0.160	0.0099
FC7761	PtNiFe [30,0.6,1], 95:5	30.88:65.66:3.46	ML030226-1	0.1	PE643	15.42	0.187	0.0121
FC7833	PtNiFe [50,1,1], 95:5	44.27:52.94:2.79	ML030317-1	0.1	PE643	12.24	0.141	0.0115
FC7844	PtNiFe [30,1,1], 95:5	44.27:52.94:2.79	ML030319-1	0.1	PE643	11.78	0.163	0.0138
FC7874	PtNiFe [10,1,1], 95:5	44.27:52.94:2.79	ML030325-1	0.1	PE643	12.27	0.158	0.0129
FC7891	PtNiFe [5,1,1], 95:5	44.27:52.94:2.79	ML030327-1	0.1	PE643	12.85	0.168	0.0131
FC7915	PtNiFe [30,3,1], 95:5	69.20:29.26:1.54	ML030407-1	0.1	PE643	11.81	0.161	0.0137
FC7940	PtNiFe [20,3,1], 95:5	71.02:27.53:1.45	ML030414-1	0.1	PE643	11.14	0.147	0.0132
FC7979	PtNiFe [50,3,1], 95:5	71.02:27.53:1.45	ML030423-1	0.1	PE643	10.56	0.151	0.0143
FC8201	PtNiFe [10,0.6,1], 95:5	35.48:61.29:3.23	ML030710-1	0.1	PE643	14.00	0.173	0.0124
FC8226	PtNiFe [10,0.5,1], 95:5	30.17:66.34:3.49	ML030721-1	0.1	PE643	18.08	0.164	0.0091
FC8239	PtNiFe [10,0.4,1], 95:5	24.78:71.46:3.76	ML030722-1	0.1	PE643	11.39	0.086	0.0076
FC8247	PtNiFe [10,0.3,1], 95:5	19.38:76.59:4.03	ML030729-1	0.1	PE643	14.00	0.084	0.0060
FC7146	PtCoFe [30,1.5,1], 80:20	54.11:36.71:9.18	ML021114-1	0.1	PE652	10.39	0.149	0.0143
FC7215	PtCoFe [30,3,1], 80:20	72.18:22.26:5.56	ML021119-2	0.1	PE652	9.02	0.159	0.0176
FC7244	PtCoFe [10,0.6,1], 80:20	33.28:53.37:13.34	ML021113-2	0.1	PE652	12.11	0.181	0.0149
FC7321	PtCoFe [50,0.6,1], 80:20	61.85:30.52:7.63	ML021114-4	0.1	PE652	9.52	0.147	0.0154
FC7351	PtCoFe [10,3,1], 80:20	72.18:22.26:5.56	ML021119-1	0.1	PE652	8.50	0.153	0.018
FC7451	PtCoFe [30,0.6,1], 80:20	33.28:53.37:13.34	ML021118-1	0.1	PE652	11.40	0.17	0.0149
FC7469	PtCoFe [10,1.5,1], 80:20			0.1	PE652			
FC7760	PtCoFe [50,1.5,1], 80:20	54.11:36.71:9.18	ML021114-3	0.1	PE652	9.70	0.141	0.0146
FC7769	PtCoFe [50,3,1], 80:20	72.18:22.26:5.56	ML021119-3	0.1	PE652	11.15	0.151	0.0135
FC7772	PtCoFe [50,2,1], 80:20	61.85:30.52:7.63	ML021114-2	0.1	PE652	9.98	0.194	0.0194
FC7777	PtCoFe [50,0.6,1], 80:20	33.28:53.37:13.34	ML021118-2	0.1	PE652	12.10	0.114	0.0094
FC7791	PtCoFe [5,1.5,1], 80:20	54.11:36.71:9.18	ML021119-4	0.1	PE652	8.50	0.134	0.0157

Table I. (Continued)

FC8362	PtCoFe [10,1,1], 90:10	39.78:54.2:6.02	ML030910-1	0.1	PE643	11.50	0.191	0.0166	76.3	111	9.65	1
FC8374	PtCoFe [50,0.6,1], 90:10	31.88:61.31:6.81	ML030911-1	0.1	PE643	12.80	0.149	0.0116	77.5	119	9.3	0.6
FC8377	PtCoFe [10,1,1], 90:10	42.81:51.47:5.72	ML030912-1	0.1	PE643	11.20	0.173	0.0154	78.6	145	13	1
FC8389	PtCoFe [50,3,1], 90:10	68.53:28.33:3.15	ML030915-1	0.1	PE643	9.20	0.134	0.0145	74.1	66.9	7.3	3
FC8396	PtCoFe [10,0.6,1], 90:10	31.88:61.31:6.81	ML030916-1	0.1	PE643	14.64	0.173	0.0118	69.1	145	9.9	0.6
FC8406	PtCoFe [10,3,1], 90:10	66.08:30.53:3.39	ML030917-1	0.1	PE643	10.00	0.152	0.0152	66.7	83.9	8.4	2.7
FC8405	PtCoFe [70,3,1], 90:10	68.41:28.43:3.16	ML030923-1	0.1	PE643	11.30	0.144	0.0127	64.5	82.3	7.3	3
FC8418	PtCoFe [30,0.6,1], 90:10	31.0:62.1:6.9	ML030919-1	0.1	PE643	14.40	0.15	0.0104	62.5	132	9.2	0.6
FC8421	PtCoFe [30,3,1], 90:10	69.44:27.5:3.06	ML030922-1	0.1	PE643	10.30	0.166	0.0161	62.3	93.5	9.1	3
FC8433	PtCoFe [70,1,1], 90:10	44.51:49.94:5.55	ML030924-1	0.1	PE643	9.90	0.172	0.0174	61.4	103	10.4	1
FC8448	PtCoFe [5,1,1], 90:10	31.0:62.1:6.9	ML030925-1	0.1	PE643	14.40	0.168	0.0117	63.4	158	11	0.6
FC8625	PtCoFe [30,1,1], 90:10	42.81:51.47:5.72	ML030918-1	0.1	PE643	9.70	0.159	0.0164	63.6	93.5	9.7	1
FC8603	PtCoFe [5,1,1], 90:10	31.0:62.1:6.9	ML031212-1	0.1	PE628A	12.50	0.183	0.0146	61.4	150	12	0.6
FC8482	PtCoFe [30,0.2,1], 90:10	14.67:76.8:8.53	ML030926-1	0.1	PE643	17.80	0.1	0.0056	75.4	113	6.35	0.25
FC8678	PtCoFe [5,CV], 90:10	23.96:68.43:7.6	ML031212-2	0.08	PE628A	12.33	0.192	0.0156	63.4	132	10.7	0.43
FC8650	PtCoFe [5,CV], 90:10	19.4:72.54:8.06	ML031215-1	0.06	PE628A	11.07	0.138	0.0125	70.8	82	7.4	0.33
FC8658	PtCoFe [5,CV], 90:10	12.73:78.54:8.73	ML031218-1	0.04	PE628A	8.37	0.107	0.0128	81.8	72	8.6	0.2
FC8666	PtCoFe [5,CV], 90:10	6.52:84.13:9.35	ML031219-1	0.022	PE628A	5.38	0.071	0.0133	82.7	29	5.4	0.1
FC9305	PtNiMn [20,3,1], 90:10	69.0:28.26:2.74	ML040618-1	0.1	PE675D	8.87	0.221	0.0249	66.7	136.5	15.39	3
FC9321	PtNiMn [20,1.2,1] 90:10	46.12:49.39:4.49	ML040617-1	0.1		10.2	0.179	0.0175	56.1	140.9	13.81	1.2
FC9322	PtNiMn [20,0.6,1] 90:10	30.64:63.57:5.79	ML040617-2	0.1		12.32	0.109	0.0088	74.1	98.7	8.01	0.6
FC9367	PtNiMn [20,0.6,1] 50:50	32.15:34.43:33.42	ML040621-1	0.1		14.46	0.129	0.0089	72.2	85.1	5.89	0.6
FC9364	PtNiMn [20,3,1] 50:50	70.13:15.16:14.71	ML040618-2	0.1		8.07	0.17	0.0211	73	103.2	12.79	3
FC9366	PtNiMn [20,1.2,1] 50:50	48.17:26.30:25.53	ML040621-2	0.1		9.4	0.172	0.0183	63.6	96.8	10.30	1.2
FC9420	PtNiMn [20,2.25,1] 90:10	?		0.1		8.64	0.192	0.0222				
FC9468	PtNiMn [,3,1] 90:10	?		0.1		6.9	0.172	0.0249				
FC8980	PtCoMn [20,0.6,1] 90:10	35.47:33.91:30.62	ML040329-1	0.1	PE671A	10.63	0.144	0.0135	80.6	63	5.93	0.6
FC8876	PtCoMn [20,1.2,1] 90:10	46.32:48.86:4.82	ML040312-1	0.1		11.06	0.202	0.0183	66.7	144	13.02	1.2
FC8940	PtCoMn [20,0.6,1] 90:10	35.47:33.91:30.62	ML040329-1	0.1	PE671A	10.86	0.134	0.0124	55.2	46.1	4.24	0.6
FC9176	PtCoMn [20,1.2,1] 90:10	46.32:48.86:4.82	ML040517-1	0.1	PE671A	11.47	0.203	0.0177				0.6
FC9180	PtCoMn [20,0.6,1] 90:10	30.86:62.93:6.21	ML040514-1	0.1	PE671A	11.67	0.148	0.0127				0.6
FC9208	PtCoMn [20,3,1] 90:10	69.05:28.16:2.78	ML040526-1	0.1	PE671A	8.6	0.202	0.0235				3
FC10056	PtCoMn [20,1.2,1] 50:50	48.05:26.93:25.03	ML050211-1	0.1		10.35	0.183	0.0177				1.2
FC10079	PtCoMn [20,2.1,1] 50:50	62.02:19.76:18.22	ML050214-1	0.1		9.12	0.197	0.0216				2
FC10098	PtCoMn [20,3,1] 50:50	69.82:15.70:14.48	ML050215-1	0.1		9.62	0.192	0.02				3
FC8942	PtCoMn [20,1.2,1] + [20,0.6,1] 90:10 Tandem	46.32:48.86:4.82	ML040330-1a	0.05	PE671A	11.27	0.164	0.0146	71.9	73.8	6.55	0.9
FC9032	PtCoMn [20,1.2,1] + [20,0.6,1] 90:10 Tandem,	32.25:61.66:6.09	ML040330-1b	0.05	PE671A	12.84	0.17	0.0133	68.7	76.7	5.97	0.6
FC9124	PtCoMn [20,1.2,1] + [20,0.6,1] 90:10 Tandem,		ML040330-1	0.1	PE671A	11.5			66.7	76.7	6.67	0.9
FC8890	PtCoMn [20,1.2,1] 70:30	48.10:35.76:16.14	ML040318-1	0.1		9.81	0.148	0.0151	63.6	83.9	8.55	1.2
FC8869	PtCoMn [10,1.2,1] 50:50	50.47:24.12:25.41	ML040311-1	0.1		10.22	0.146	0.0143	63	97.9	9.58	1.2
FC8954	PtCoMn [20,2.7,1] 50:50	67.08:16.03:16.89	ML040323-1	0.15		10.7	0.191	0.0179				2.6
FC8919	PtCoMn [20,2.7,1] 50:50	67.08:16.03:16.89	ML040323-1	0.15		11.5	0.146	0.0127				2.6

Each ternary catalyst is defined by a terminology that describes its composition and fabrication. In each designation of PtM1M2[#1,#2,#3](#4:#5), M1 and M2 are the two transition metals (TM). #1 is the bi-layer thickness in Angstroms of the combined Pt and M1+M2 deposition per pass over the sputtering targets. #2 is the ratio of the individual Pt/TM layer thicknesses per pass. #3 can be ignored. #4:#5 is the ratio of atomic fractions of the M1:M2 transition metals, with M2 = Fe or Mn.

2.1.3.2.1 Mass specific area versus whisker support lot

All the ternary catalysts in Table I were fabricated on nominally a single type of NSTF whisker support structure, for which the areal number density and average dimensions of the crystalline organic whiskers were the same and considered a “standard” by default. As discussed above the supports were fabricated in several lots over the time period of the measurements. The whisker dimensions determine the surface area of the support

and hence the degree of effective catalyst dispersion for a given catalyst loading and volume (which varies with transition metal type and amount).
To illustrate the degree to which the different whisker lots were similar, Fig. 5 shows the mass specific surface area, m^2/g, for the different lots as a function of Pt loading in various ternary constructions. For whisker support lot 628A, the Pt/TM ratio was varied as the Pt loading was reduced to maintain a constant overall volume of the coating applied to the whisker. The result is a linear dependence of mass specific surface area on Pt loading, as should be the case for loadings sufficiently low that the volume of the catalyst coating itself does not contribute significantly to the surface area. At higher loadings, the catalyst volume increases the effective dimensions of the whiskers and contributes to the catalyst surface area. For lot PE643, a similar linear dependence is seen for a different ternary that is parallel to and close to the values for the 628A lot. The other two data points in Fig.5 illustrate that as much difference is seen for different catalyst compositions as between whisker lots. The mass measurements of the catalyst depositions are all believed accurate to ± 5% or less, whereas the ECSA measurements are generally found to be reproducible to ±1 cm^2-Pt/cm^2-planar unit. These would suggest the mass specific area measurements to be no better than about ± 15%, consistent with the scatter seen in Fig. 5.

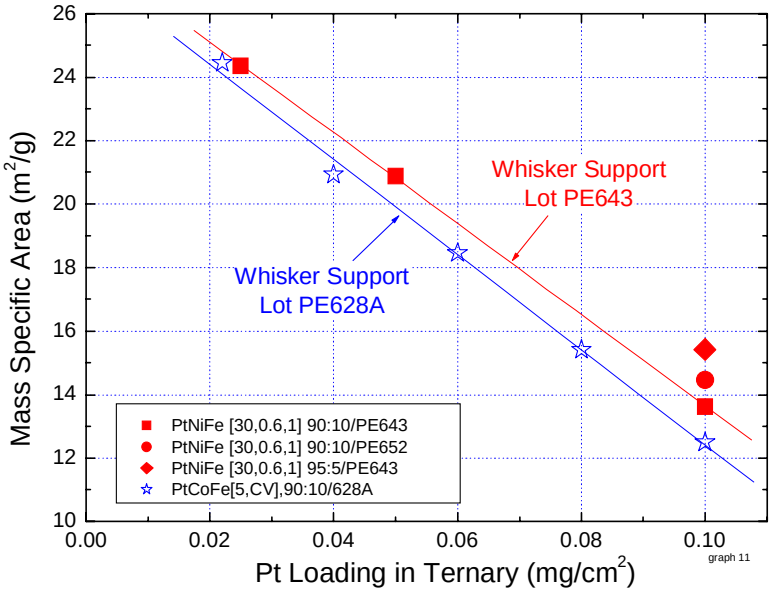

Fig. 5. Mass specific surface area for three whisker support lots, as a function of Pt loading and ternary type.

2.1.3.2.2 Activities and surface area comparisons for NSTF-ternary catalysts

Mass specific areas

In Fig. 6 the mass specific area is plotted as a function of Pt/TM layer ratio for the PtM_1Fe and PtM_2Mn ternaries. For both composition types there is a clear trend of an increase in mass specific area as the total TM component fraction increases. It has been previously established for $Pt_xM1_yM2_z$ ternary coated NSTF whisker supported

catalysts that the stable atomic ratio is x/(y+z) = 3. [6] Both acid soaked catalysts and fuel cell tested catalysts undergo the same degree of dissolution of the TM components

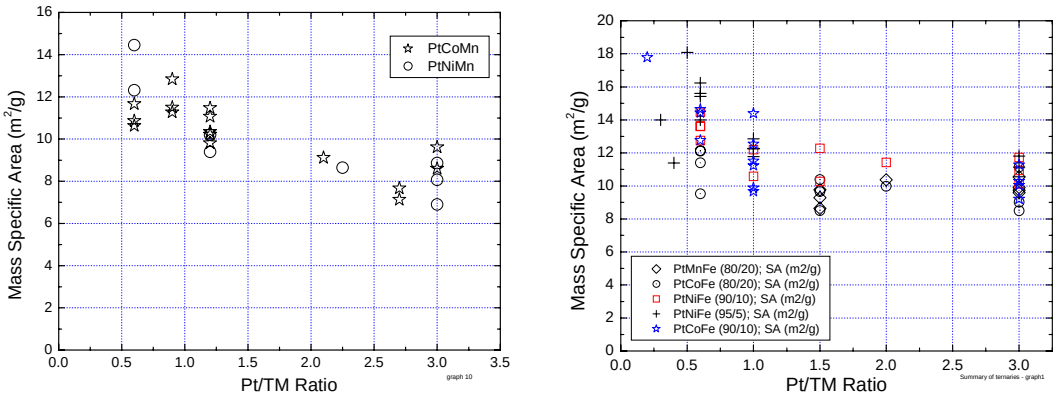

Fig. 6. Mass specific area as a function of Pt/TM layer ratio for the PtM_1Fe and PtM_2Mn ternaries.

in excess of this ratio. For very low ratios (high percentages of TM), the TM atoms in the bulk of the NSTF thin film coatings appear to be partially depleted. For initial x/(y+z) atomic ratios closer to three, only the surface appears to be depleted based on XRD and electron microprobe analyses. This would suggest that in Fig. 6, the TM fraction in excess of the equilibrium value of dissolves out from the alloy, possibly leaving a more porous Pt surface, and hence the higher mass specific surface area.

Specific and mass activities

Fig. 7 shows the specific and mass activity by method 1 plotted versus Pt/TM layer ratio for the PtMFe series. In these plots, for each Pt/TM value the data represent a range of

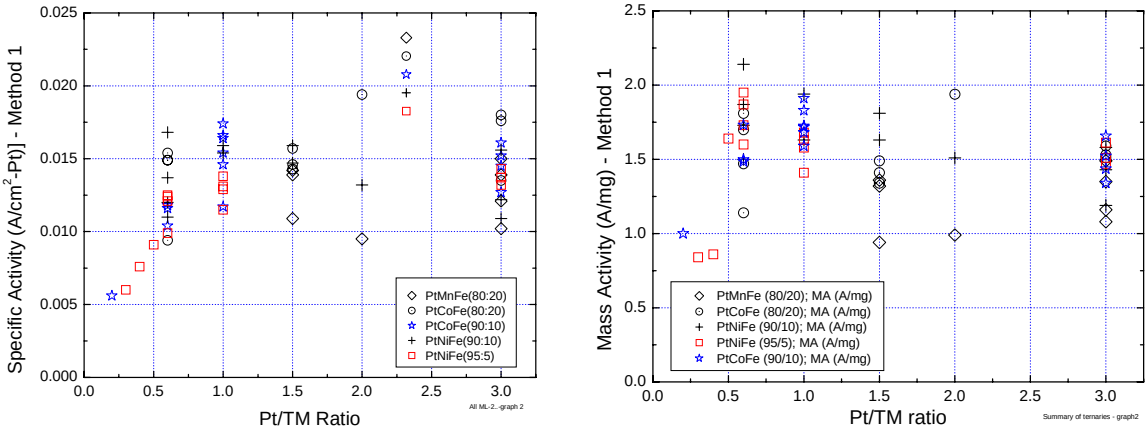

Fig. 7. Specific (left) and mass activity (right) by method 1 versus Pt/TM layer ratio for the PtMFe series.

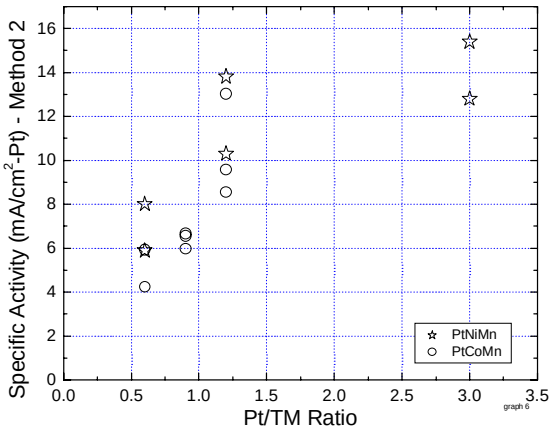

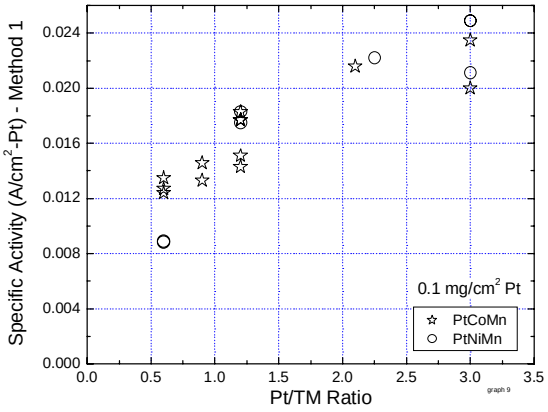

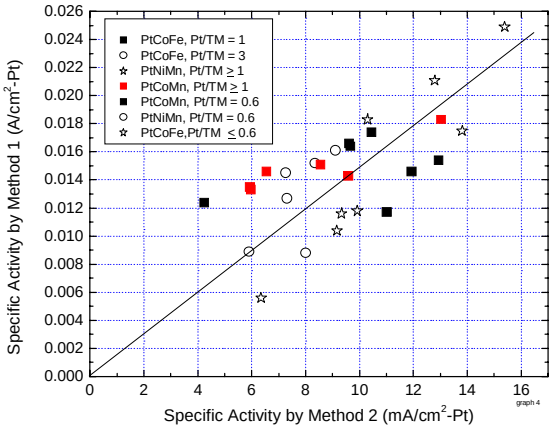

M1/M2 ratios as well as bi-layer thicknesses. There appears to be a trend to higher specific activity values at higher Pt/TM ratios, but the trend is confounded by the varying M1/Fe ratios and the varying types of M1 elements. If only the PtCoFe(90:10) values are considered, (star symbols in Fig. 7), then the trend is revealed to be stronger and suggesting a maximum specific activity by method 1 at Pt/(Co+Fe) layer ratio of 2.5.

Fig. 8 plots the specific activity of the PtCoMn and PtNiMn series by method 1(middle) and method 2 (top) versus Pt/TM layer thickness ratio. Several points are worth noting. Here there is a very consistent and clear trend that as the Pt/TM ratio increases to 3, the specific activity increases. Given the scatter in the data, the optimum specific activity values appear to be about the same for the PtCoMn and PtNiMn. Referring to Fig. 3 for which the specific activity by method 1 for pure NSTF - Pt is ~ 0.010 A/cm^2, the maximum obtained specific activity for these ternaries are ~ 2.4 times larger, for both 90:10 M1:Mn ratios, where M1 = Co or Ni. Since as the Pt/TM ratio increases to higher and higher values the ternary approaches pure Pt, this value probably represents the maximum value obtainable with these constructions. Also, as noted above and discussed further below, this Pt/TM layer ratio of ~ 3 is close to the equilibrium value expected after any excess TM has dissolved into the membrane. This ~ 250% increase of the NSTF - PtM1Mn ternary specific activity over that of pure NSTF – Pt, is similar to the increase seen in carbon supported, dispersed PtCo alloys over the pure Pt/C.[7]

Fig. 8. Specific activity by methods 1 (middle) and 2 (top) for the PtCoMn and PtNiMn series, and their comparison (bottom).

Finally, it is interesting to compare the specific activities by the two methods, 1 and 2. This is shown in Fig. 8 (bottom) for all the ternarys for which overlapping measurements are given in Table I. Qualitatively the two methods agree quite well despite the fact that the method 1 would not be considered a proper protocol to determine the specific activity for ORR.

Fig. 9. shows plots of mass specific area, mass activity (method 1) and specific activity (method 1) versus the Pt + TM bi-layer thickness for the PtM1Fe series. For any given bi-layer thickness, the data have a range of Pt/TM values. The scatter at each bi-layer thickness suggests the latter is a less sensitive parameter than the Pt/TM ratio.

There do not appear to be any statisitically significant trends apparent for the three variables, suggesting that the layer thickness during catalyst deposition is not a significant parameter. This might seem surprising over the range considered, from 5 to 70 Angstroms. However, if the geometric surface area of the NSTF whisker supports before coating with catalyst are on the order of 8 cm^2_{geo}/cm^2_{planar}, then even at the highest bi-layer thickness, for a Pt/TM layer ratio of 2, the thickness of each layer on the whisker is only on the order of 4 Angstroms, so good atomic mixing could be expected. Since bi-layer thickness was not found to be a significant experimental parameter for the PtMFe series, the subsequent PtMMn series were fabricated with predominanly one bi-layer thickness.

Fig. 10 (top, middle) shows the Tafel slopes, extracted from the method 2 protocol for measurement of specific activity, plotted versus this method 2 specific activity for the PtM_1Fe and PtM_1Mn catalysts. Fig. 9 (bottom) shows the Tafel slope plotted versus the Pt/TM layer thickness ratio. In general the Tafel slopes center around 70mV/decade, but only one solid trend is apparent for either of the two ternary types. Fig. 9(top) does suggest quite clearly that the specific activities by method 2 are generally higher for the PtCoFe goup than the PtMnFe or PtNiFe. There may be a weak apparent trend for lower Tafel slopes occuring at higher specific activities, which is a desirable scenario for fuel cell performance. Similarly, although the data set is limited, the Tafel slope does not appear to vary in any consistent manner with the Pt/TM layer ratio.

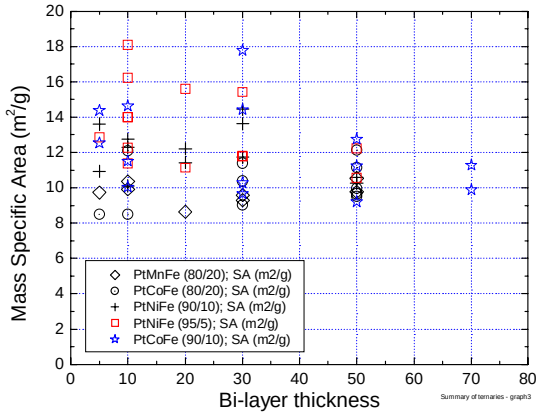

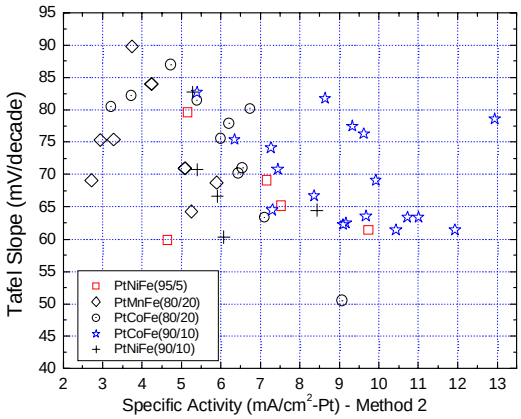

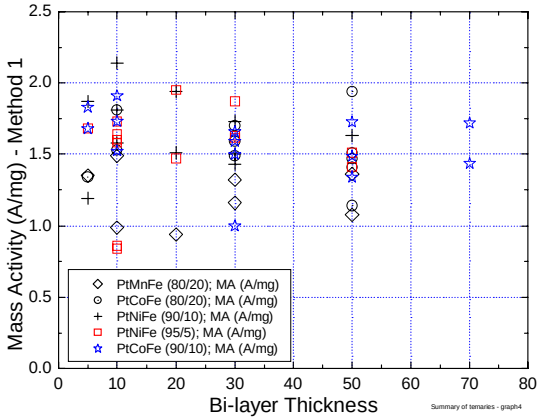

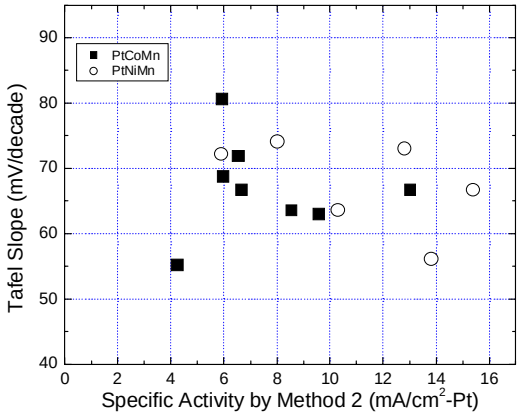

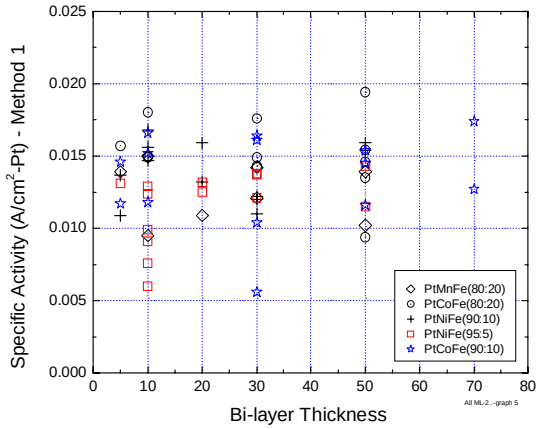

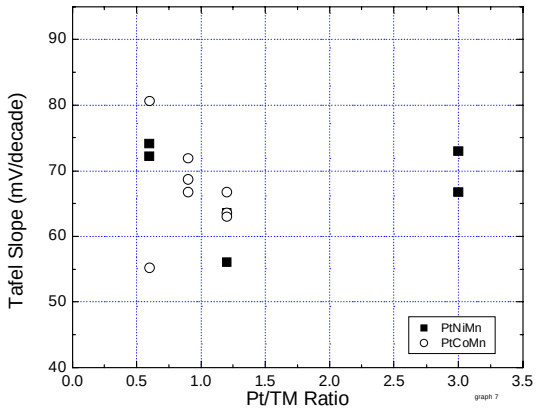

Fig. 9 (Left). Mass specific area (top), mass activity by method 1(middle) and specific activity by method 1 (bottom) versus the Pt + TM bi-layer thickness for the PtM1Fe series.

Fig. 10 (Right). Tafel slopes by method 2 plotted versus specific activity by method 2 for the PtM$_1$Fe and PtM$_2$Mn ternaries (top, middle) and versus the Pt/TM layer thickness ratio (bottom).

Specific and mass activities of down-selected catalysts by Method 3

We conclude this subsection on activities with examples of the measured specific and mass activities from what will be seen to be the down-selected catalysts (see section 2.1.5) viz. PtCoMn(90:10)[50,3,1]. MEA's were fabricated with this NSTF catalyst on both the anode and cathode at the same loadings of 0.2 mg-Pt/cm^2. All catalysts and CCM's were fabricated as roll-goods using the 3M 850EW membrane and tested with proprietary coated GDL paper backings in 50 cm^2 cellls with quad serpentine flow fields. The 150kPa saturated H_2/O_2 conditions are defined above in 2.1.3.1.3. Fig. 11 shows the raw data of current density at 900mV versus time from one such MEA, as well as the time trace after correcting for shorts and crossover. The short and cross-over currents are obtained from cyclic voltammograms used to determine the electrochemical surface area at the temperature and humidity of specific activity measurement (see Fig. 1). The activity value is obtained at the 17.5 minute mark after setting the cell potential to 900mV, or 44.0 mA/cm^2-planar. For the example in Fig. 11, the measured ECSA (or SEF = surface enhancement factor) was 14 cm^2-Pt/cm^2-planar. The resulting specific activity then is then 3.1 mA/cm^2-Pt.

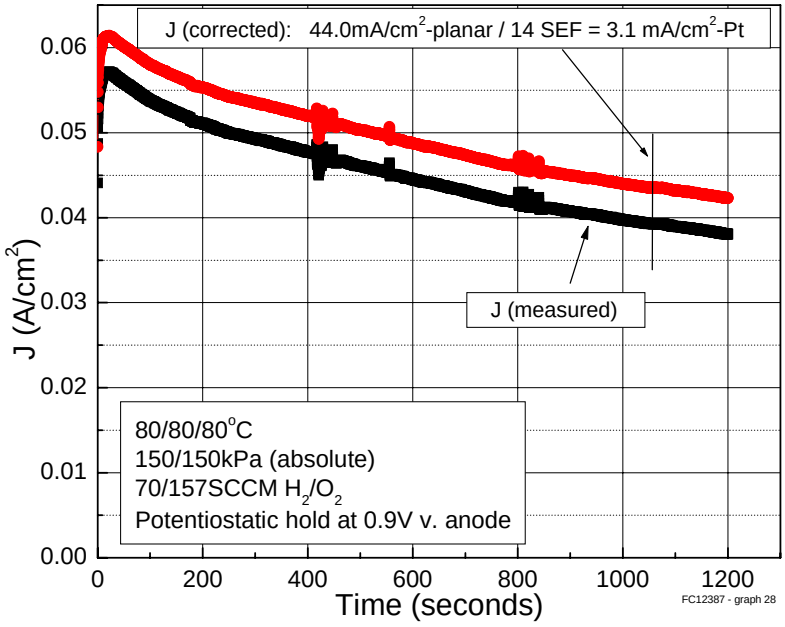

Fig. 11. Raw and corrected data for measurement of the specific and mass activities by method 3 for an MEA with the down-selected PtCoMn catalyst on the electrodes at a loading of 0.2 mg/cm^2.

The bottom panel in Fig. 2 gives another example for a similar MEA. For that sample, measured in the same way, the specific activity by method 3 was 2.93 mA/cm^2-Pt. The respective mass activities for these two samples are then 0.22 and 0.18 A/mg-Pt.

These can be compared to values for state-of-the-art dispersed Pt and Pt-alloy catalysts on corrosion resistant carbon supports. Under the same measurement conditions,

method 3, and same Pt loadings of 0.2 mg/cm^2 of Pt, the above NSTFC PtCoMn ternary electrodes show specific activity ~ 10x greater, and a mass activity 40% greater than that reported by GM for a typical Pt/C electrode (47% Pt/C fromTKK, 0.2 mg/cm^2-Pt cathode, anode)[8], or PtCo on corrosion resistant carbon [9]. For the Pt/Carbon the specific and mass activites were 0.247 mA/cm^2-Pt and 0.13 A/mg respectively. For the PtCo/Corrosion resistant carbon the respective values were 0.3 mA/cm^2-Pt and 0.10 A/mg.

2.1.3.2.3 Effect of whisker support dimensions and catalyst loadings

The surface area of the "standard" whisker support structure used for the catalyst depositions in Table I would not be optimum for all the different catalyst compositions since the volume of the catalyst coating depends on the amount of transition metal added to the fixed 0.1 mg/cm^2 of Pt. Both catalyst loading and its volume on a whisker would be expected to affect its mass specific area and hence mass activity, and also the effective electrode thickness and mass-transport of oxygen to the catalyst as shown in section 2.1.5.2. To investigate this a series of different catalyst loadings of the same $Pt_xCo_yMn_z$ construction were deposited onto four different types of NSTF whisker support films, having monotonically varying whisker densities and lengths as shown in Table II. The starting layer thickness of the perylene dicarboximide pigment from which the whiskers are grown was held constant in each case. Since the whisker growth process conserves mass, i.e. the PR149 material does not re-sublime, the total volume of the whiskers in each case is conserved. Hence, if the areal number density is low, e.g. 39 per square micron, then the whisker lengths are longer, 1.13 microns. At the other extreme, at 82 per square micron, then the whiskers are shorter at 0.49 microns. Fig. 12 shows SEM images from two of the four different whisker support types. Table II lists the specific and mass activities measured by Method 3. It suggests that both the mass and specific activity depend on the Pt loading and whisker support characteristics.

Table II. Specific and mass activities for $Pt_xCo_yMn_z$ deposited onto on four types of whisker supports with varying dimensions in a controlled loading experiment.

Sample	Catalyst Composition	Whisker Support, Type, Dimensions L(μm), N(#/$μm^2$)	Pt Loading (mg/cm^2)	Specific Activity Method 3 (mA/cm^2-Pt)	Mass Activity Method 3 (A/mg-Pt)
1	Pt	683C, 53, 0.75	0.15	2.0	0.09
2	$Pt_xCo_yMn_z$	683C, 53, 0.75	0.08	2.4	0.261
3	$Pt_xCo_yMn_z$	683A, 82, 0.49	0.06	2.18	0.24
4	$Pt_xCo_yMn_z$	683C, 53, 0.75	0.15	2.6	0.20
5	$Pt_xCo_yMn_z$	686A, 39, 1.13	0.06	1.9	0.195
6	$Pt_xCo_yMn_z$	686A, 39, 1.13	0.15	2.9	0.18

Although the statistics are poor, Table II is consistent in suggesting that shorter, higher number density whiskers are better suited to lower loadings, and taller, more sparse whiskers better suited to higher loadings. As will be seen below, this also translates to fuel cell performance.

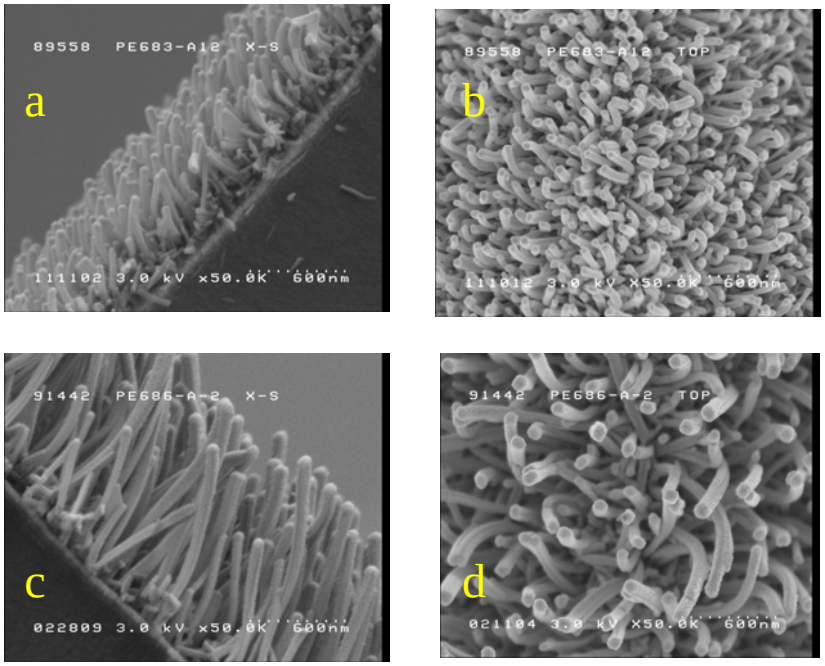

Fig. 12. SEM images of two of the four whisker support types used for the controlled loading experiment: (a,b) Type PE683A, short and high number density whiskers, (c,d) Type PE686A, long and low number density whiskers.

2.1.3.2.4 Effect of catalyst compositions and loading on polarization curves

Specific and mass activities for ORR are the usual parameters to characterise electrocatalysts with the understanding that the dominant impact of the catalyst is in the kinetic region of a polarization curve. However, the impedance and mass transport aspects of the polarization curves can also be affected by the catalyst, independent of the kinetics. One way this can happen is if alloy catalysts are applied with transition metal fractions in excess of the stable Pt alloy fractions as mentioned above. The excess TM will dissolve into the membrane and effectively increase its equivalent weight and reduce its water uptake potential. This will cause increases in the overpotential at high current densities. This effect can be seen in the polarization curves, discussed below, from the PtM1Mn and PtM1Fe series as the Pt/TM ratios decrease.

A complete study of the stability in acid solution of the as-made PtM1M2 ternary NSTF catalysts was completed at Dalhousie University [6]. This study is described in more detail in section 2.1.1. Briefly, for $Pt_zM_xM'_y$ (M = Ni, Co, Mn, Fe), it was shown that corrosion of the transition metal elements occurs when the electrocatalysts were subjected to 1 M H_2SO_4 at 80^{o}C, mimicing what was seen after fuel cell testing. Chracterization by electron microprobe and XRD before and after the acid soaking or fuel cell operation showed that, independent of the starting Pt/TM ratio, the equilibrium value of (x+y)/z atomic fraction of ~ 0.33 was found in each case after the testing. This suggests that the volume (layer) fractions of Pt/TM ~ 3 values listed in Table I would be close to the stable equilibrium values, but for layer ratios Pt/TM << 3, significant loss of TM to the membrane could occur.

Effect of ternary composition on polarization curves

Fig. 13 shows the impact of low Pt/TM ratios on both ambient pressure, constant flow, and pressurized constant stoichiometry H_2/air polarization curves for the PtNiMn series. In every case the polarization curves for the Pt/TM = 0.6 exhibit limiting currents that are significantly attenuated. The reduced performance of the Pt/TM = 1.2 versus 3 ratio is made clearer by the pressurized, GDS conditions.

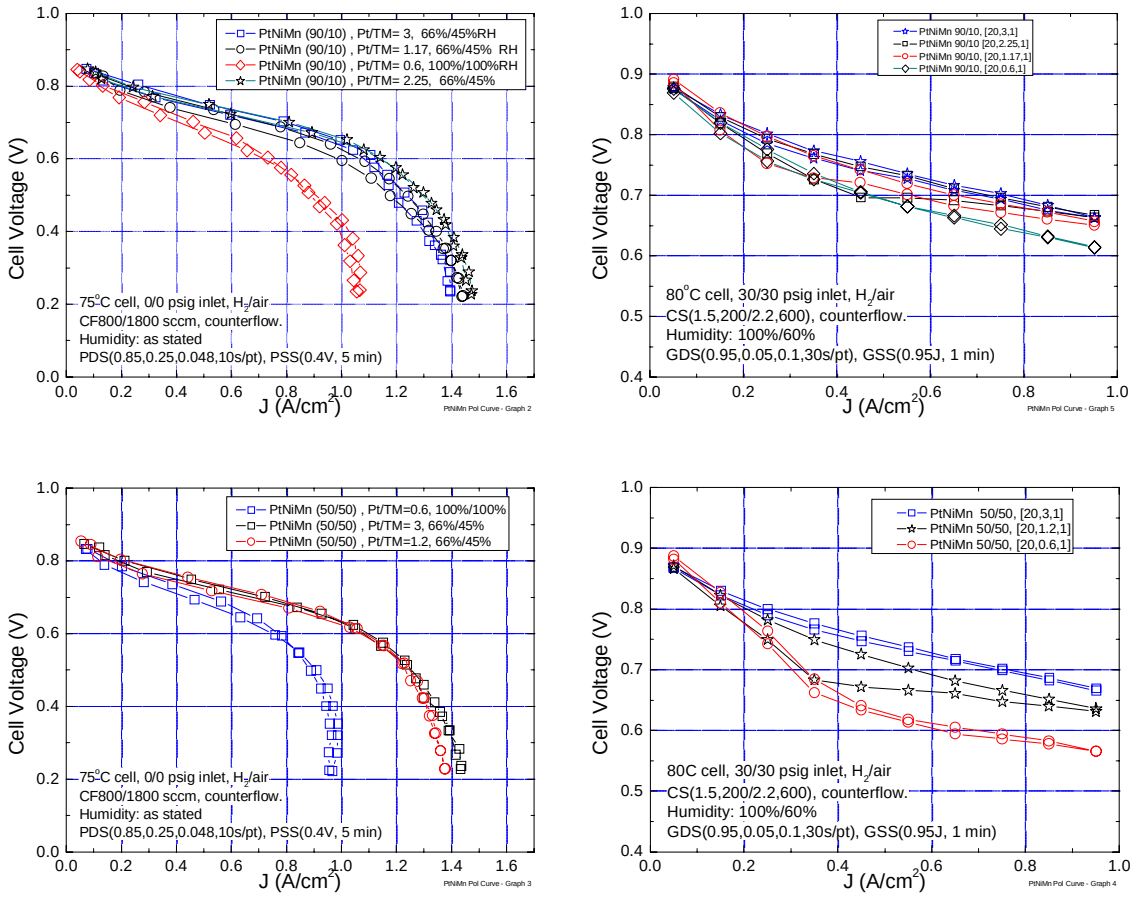

Fig. 13. Effect of ternary catalyst type on H_2/air polarization curves. Left: Ambient pressure, constant flow, potentiodynamic scans. Right: pressurized galvanodynamic, constant stoichiometry scans.

Since the Pt loading is fixed, the absolute amount of TM varies by a factor of five between Pt/TM = 3 and Pt/TM = 0.6. It should also be noted that the relative humidities for the polarization curves at the Pt/TM = 0.6 are saturated whereas those for the other curves are subsaturated. Normally, one might expect this to represent mass transport limitations due to flooding. However, that is not the case since operating the MEA's with Pt/TM = 0.6 at the reduced %RH only worsened the performance, while operating the MEA's with Pt/TM = 3 at 100% RH did not worsen performance. The conclusion is that the excess Co, Ni and Mn entered the membrane and reduced its effective equivalent weight, conductivity and water uptake potential, requiring operation at saturated conditions to even get the peak performance.

Fig. 14 makes a similar comparison of the ambient pressure H_2/air polarization curves from the preferred NSTF PtCoMn ternary, with 0.1 mg/cm^2 of Pt on the cathode, for four different Pt/TM ratios. There is essentially no impact of this parameter on this type of polarization curve for the 50:50 Co:Mn ratio and Pt/TM = 1.2, 2.1, 3 ratios. The Pt/TM = 3 for the 90:10 Co:Mn ratio does not appear to fit this trend and may have been an anomolous sample since it appears in Table I to have had an anomolously low surface area.

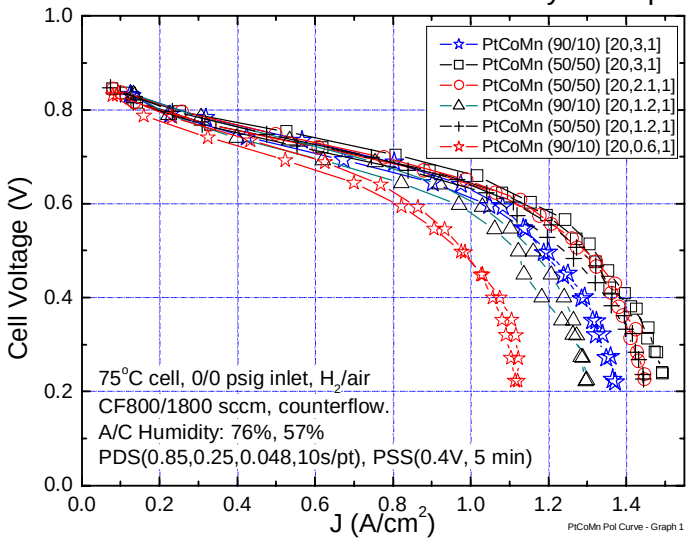

Fig. 14. Effect of Pt/TM ratio PtCoMn [50:50] ternary catalyst type on H_2/air polarization curves.

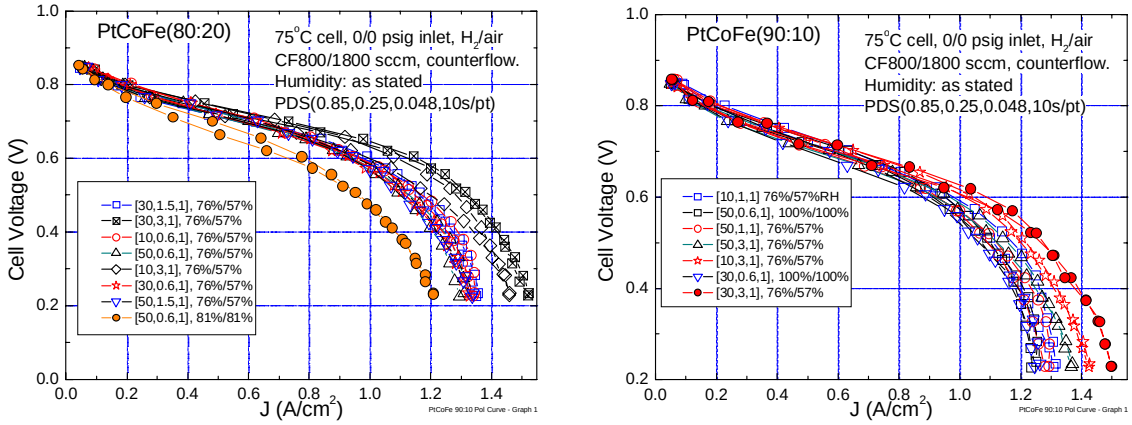

Fig. 15. Effect of PtCoFe catalyst construction on ambient pressure H_2/air polarization curves.

For the PtCoFe (Fig. 15) and PtNiFe (Fig. 16) series, a similar effect is also seen between the highest and lowest Pt/TM ratios. Careful inspection of the polarization curves in Figs. 15 and 16 suggests that depending on the bi-layer thickness, or just due to sample variability, the trend of lower performance is not monotonic with Pt/TM ratio, but still in general lower with lower ratios as for the Mn series. For the Fe series, more so than the Mn series, the sensitivity of the ambient pressure performances to %RH appeared to be stronger as well.

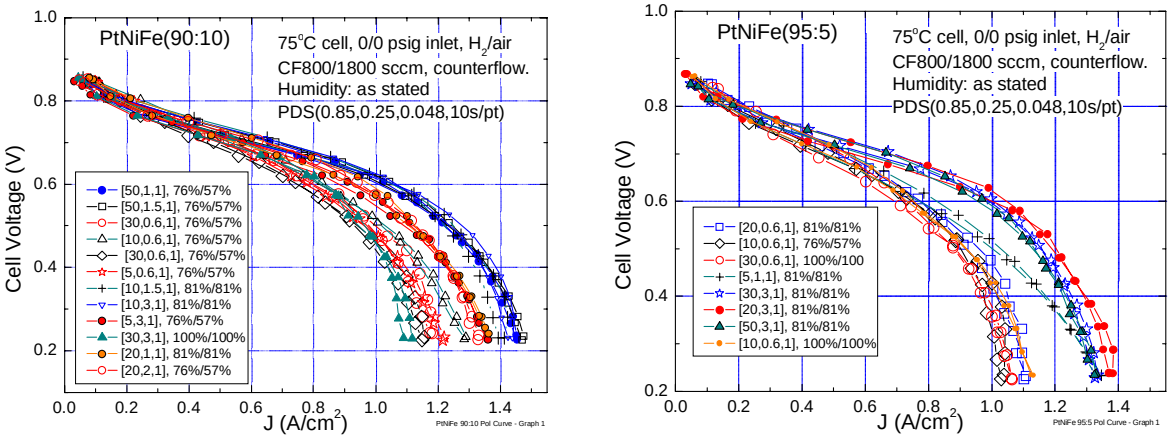

Fig. 16. Effect of PtNiFe catalyst construction on ambient pressure H_2/air polarization curves.

<u>Effect on polarization curves of whisker support and catalyst loading</u>

Fig. 12 and Table II illustrated the different whisker supports and their impact with catalyst loading on activity for one type of PtCoMn alloy construction (Pt/TM = 3, (90:10)). In this subsection we demonstrate how using whisker supports better matched to the catalyst loading (and volume) allow record performances with low loading levels of Pt in that ternary. Fig. 17 shows three such comparisons that also indicate the improvement of the ternary over pure Pt. In Fig. 17, the anode loadings are 0.15 mg/cm^2 of pure Pt, and the cathode loadings are 0.060mg/cm^2 of either Pt or Pt in PtCoMn.

The bottom row panel in Fig. 17 compares the ambient pressure PDS curves for the PtCoMn (90:10), Pt/TM = 3 catalyst, coated on the PE683A whiskers described in Table II, with plain NSTF-Pt coated onto the same whiskers, with both at Pt loadings of 0.060 mg/cm^2 . The ternary catalyst is clearly superior.

The top row, left panel of Fig. 17 compares the same PtCoMn ternary with pure Pt at the same loading of 0.060 mg-Pt/cm^2, coated this time onto the PE683C whiskers defined in Table II. There is a small but significant gain of the PtCoMn ternary by approximately 20mV over the pure Pt, which is consistent with the 2x gain in specific activity.

The top row, right panel of Fig. 17 compares the same PtCoMn ternary at the 0.060 mg-Pt/cm^2 loading on four types of whisker supports (see Table II). The ambient pressure polarization curves for this catalyst coating is clearly best on the PE683A whiskers having the highest number density and shortest lengths, and worst for the PE686A whiskers having the lowest number density and longest lengths. The performance is intermediate for the intermediate type of whiskers, PE683C.

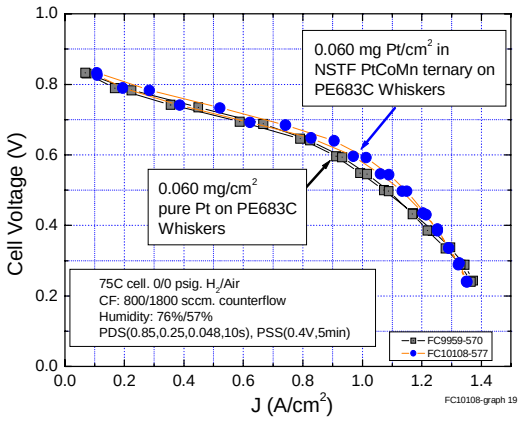

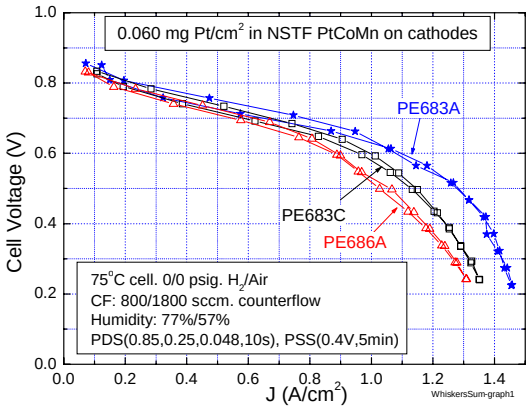

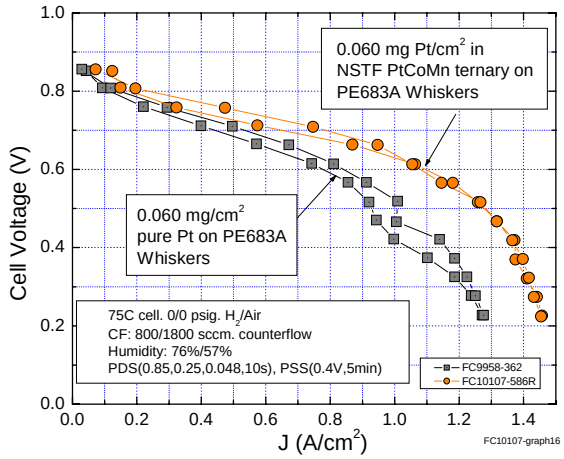

Fig. 17. Three examples of ambient pressure H_2/air polarization curve performances for low loadings of NSTF-PtCoMn and NSTF-Pt on various sized whisker supports, defined in Table II.

Two other examples of high performance with low loading are shown in Fig. 18. In Fig. 18 (left) the ambient pressure PDS performance curve is shown for an MEA having the 0.060mg-Pt/cm^2 PtCoMn ternary coated onto the best PE683A whiskers on both anode and cathode. Two polarization curves are shown, representing reversal of the test station flows and leads so that the side that was first a cathode became the anode for the second polarization curve. The peformance is extremely good for such a low total loading of only 0.12 mg-Pt/cm^2 total per MEA.

Fig. 18 (right) shows the effect of reversing the cell when the anode has the PtCoMn at the 0.15 mg-Pt/cm^2 loading initially, on the PE683C whiskers. There is an improvement in performance with the 0.15 mg-Pt/cm^2 PtCoMn on the cathode over the configuration in Fig. 16 (left), but surprisingly, the impact is not in the kinetics, but rather in the mass transfer loss region.

Fig. 19 shows the pressurized H_2/air GDS performance with the same MEA shown in Fig. 18 (right). It is notable that under the subsaturated inlet conditions, at the lowest pressures the membrane drying is substantial and in combination with electroosmotic drag causes the HFR impedance to increase substantially (not shown) at the higher current densities. By increasing the inlet humidification to saturation, substantial increases in the limiting current are obtained at the 7.5 psig conditions.

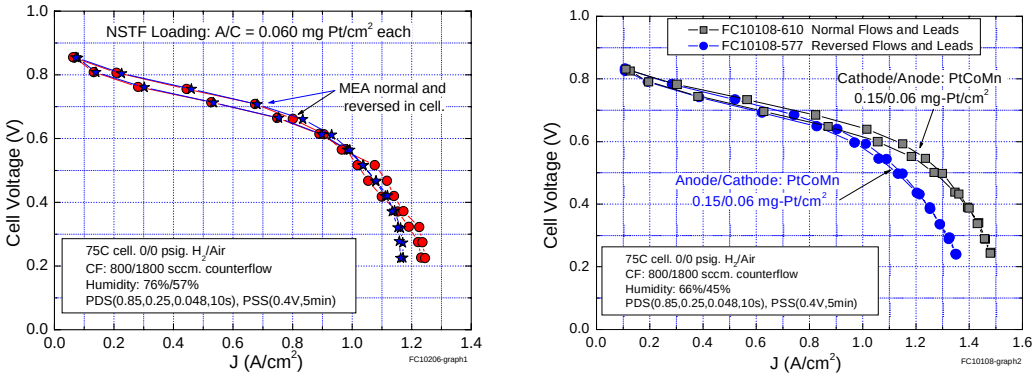

Fig. 18. (left). Ambient pressure H_2/air polarization curves with 0.060 mg-Pt/cm^2 on each electrode in the form of PtCoMn (90:10) [20,3,1], coated onto PE683A whiskers. (right) Same conditions but for MEA with same PtCoMn catalyst on the anode and cathode, but loadings of 0.15 mg/cm^2 and 0.06 mg/cm^2. Reversing the cell leads and reactant flows allows testing with either electrode as the cathode.

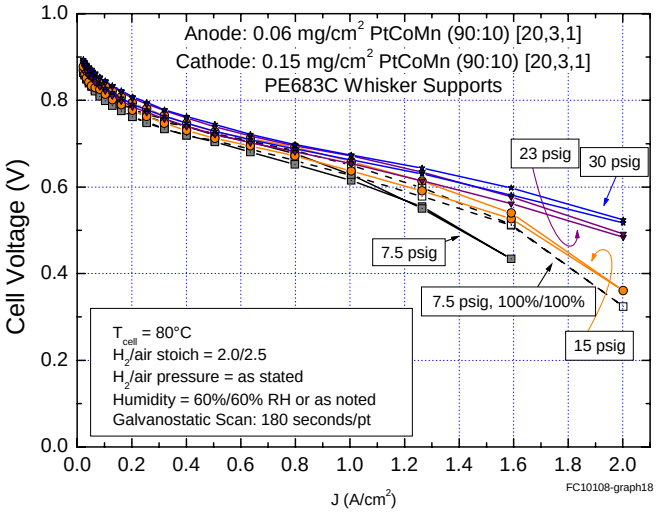

Fig. 19. H_2/air galvanodynamic polarization scans at various pressures for the MEA having the PtCoMn (90:10)[20,3,1] catalyst at loadings of 0.06 and 0.15 mg-Pt/cm^2 respectively on the anode and cathode, using PE683C whiskers.

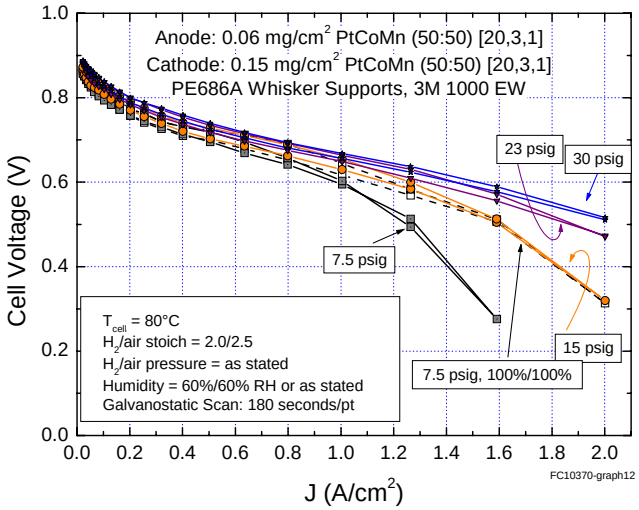

Fig. 20. H_2/air galvanodynamic polarization scans at various pressures for the MEA having the PtCoMn (50:50)[20,3,1] catalyst at loadings of 0.06 and 0.15 mg-Pt/cm^2 respectively on the anode and cathode, using PE686A whiskers.

This same effect is even more strongly seen in Fig.20 that shows the same pressurized H_2/air GDS performance conditions for a similarly l aded catalyst, but using the PtCoMn with a (50/50)[20,3,1] construction on the PE686A whiskers. The difference between the 90:10 and 50:50 Co:Mn ratios were not found to have any noticeable difference in activities.

To complete this section on low catalyst loading effects on performance, we first illustrate the performance effects of reduced cathode loadings for the PtCoFe series shown in Table I, in which the catalyst volume was kept constant (Pt/TM = CV in Table I). All catalysts were made with a 5 Angstrom bi-layer and a (90:10) Co:Fe ratio, but the Pt/TM ratio was varied as necessary to keep the total ternary catalyst volume constant. This was done as part of a study to determine the role of the catalyst volume impact on mass transport losses. A complicating factor, as noted above however, is the dissolution of excess transition metals into the membrane above TM/Pt atomic ratios of ~ 1/3. Fig. 21(right) shows the ambient pressure, constant flow PDS curves, and (left) the 30 psig H_2/air GDS, constant stoichiometry curves for this series, in which the Pt loading varies from 0.1 to 0.022 mg/cm^2. For both conditions, the performance is substantially compromised at cathode loadings of 0.06 mg/cm^2 and not nearly as good as that obtained with the PtCoMn preferred composition in Figs. 18-20.

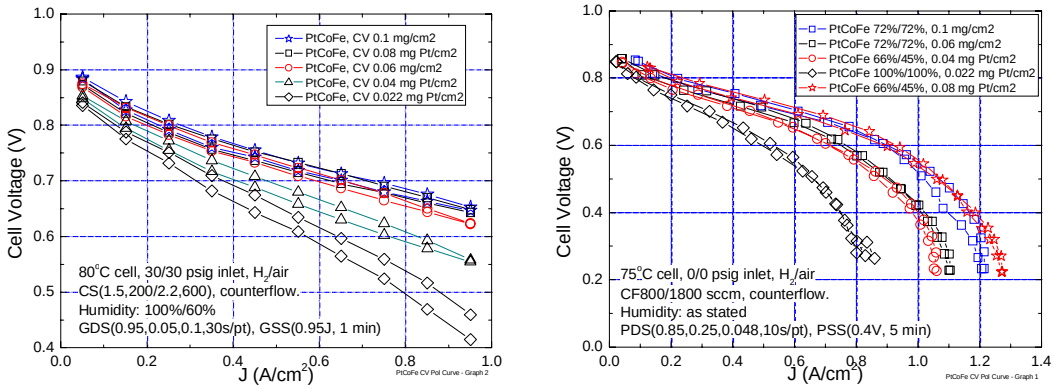

Fig. 21. Ambient pressure potentiodynamic (right) and pressurized galvanodynamic (left) polarization curves from the PtCoFe [90:10] constant volume (CV) series.

Finally, a series of MEA's were made with PtNiMn (90/10) [20,1.2,1], on the cathodes at a Pt loading of 0.1 mg Pt/cm^2 , and variable anode loadings of pure NSTF- Pt. The anode loadings are as indicated in Fig. 22, which shows the ambient pressure PDS, constant flow polarization curves. These would all have used a standardized whisker support analogous to PE 683C. The effect of reducing the anode loading to 0.05 mg/cm^2 appears minimal above 600mV and to have a primary effect in the mass transport region. Exactly why this is the case is not understood at this time. There are longer term effects that must be considered however as well for this level of anode loading to be viable. These relate to impurity adsorption, surface area loss mechanisms, and peroxide generation and scavenging at the anode that directly relate to membrane lifetime.

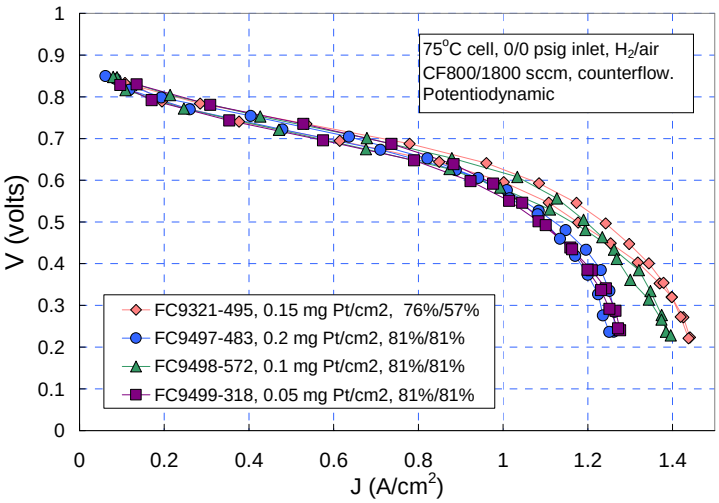

Fig. 22. Ambient pressure potentiodynamic constant flow polarization curves for a series of MEAs having reduced NSTF-Pt loadings on the anode given in the legend, but constant PtNiMn(90/10) [20,1.2,1] loadings on the cathode of 0.10 mg/cm^2.

2.1.3.2.5 Effect of acid soaking NSTF catalyst before forming CCM

The explanation for the reduced fuel cell performance at higher current densities with values of bi-layer ratios below Pt/TM ~ 1 discussed above, was that the excess transition metal cations, over and above the equilibrium atomic fraction of TM/Pt ~ 0.33, dissolve into the membrane resulting in membrane poisoning. This could be tested by acid leaching the excess TM from the NSTF catalyst before fabricating the catalyst coated membrane (CCM). This experiment was completed with the expected results.

The NSTF catalyst used was PtCoMn (50/50) [20,1.3,1], with a loading of 0.15 mg Pt/cm^2. A sheet of the catalyst was placed in 0.5M H_2SO_4 for 24 hours, then rinsed in DI water and dried in a 40ºC oven overnight. The CCM was fabricated in the standard fashion, using pure NSTF-Pt (0.15 mg/cm^2) on the anode and the etched sample transferred to the membrane as the cathode. The 3M membrane was acid washed and carbon cloth GDLs were used to make the full MEA. The MEA, identified as FC10533, was tested and compared to a control, FC10603, made with the identical cathode catalyst as cut from the production roll.

Fig. 23 below compares the ambient pressure constant flow polarization curves, and Fig. 24 the pressurized galvanodynamic, constant stoichiometry polarization curves with high frequency resistance (HFR) for the two samples. In both sets of conditions, the acid leaching of the TM metal has improved the performance. In the ambient pressure case the increase is a substantial, 25 mV in the kinetic region and more at higher current densities. Under higher pressure, the increase at higher current densities can be attributed to the reduced HFR. Both results are consistent with the explanation of the membrane poisoning by the excess TM.

Table III below summarizes the specific activity by method 1, and surface areas for the two sample types. The acid leached sample's surface area is a little smaller, but the specific activity is substantially increased.

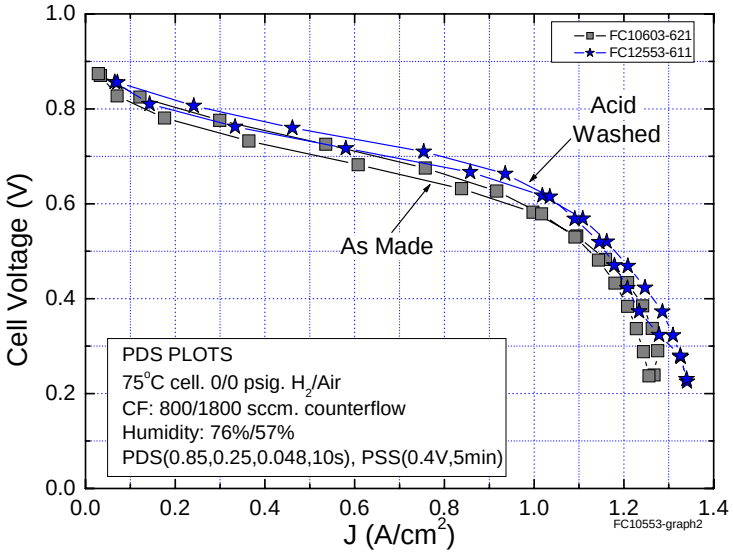

Fig. 23. Ambient pressure potentiodynamic polarization scans from MEAs with and without acid leached cathodes.

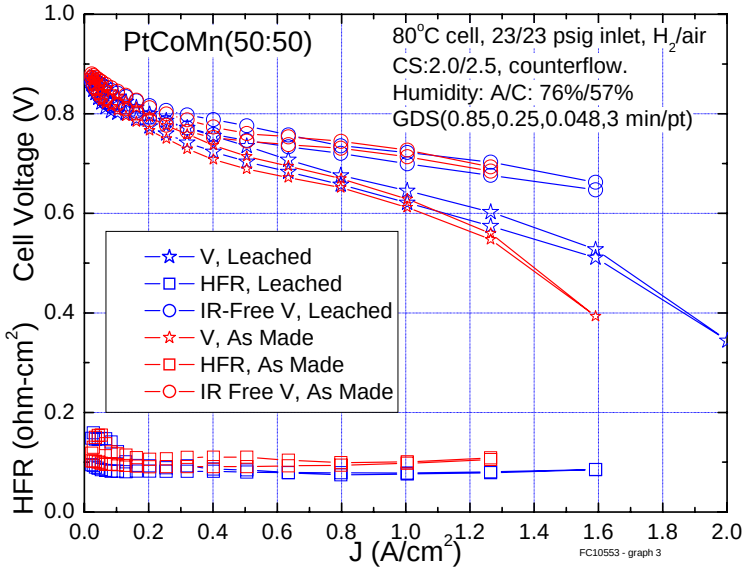

Fig. 24. High pressure galvanodynamic polarization scans from MEAs with and without acid leached cathodes.

Table III. Surface areas and specific activitity from acid leached versus as-made PtCoMn (50:50)[20,1,1] ternary catalyst.

	FC10603	**FC10553**
Treatment	None	Acid Leached
J(0.813V) A/cm^2$_{planar}$	0.164	0.220
ECSA (cm^2/cm^2)	13.5	10.8
Specific Activity A/cm^2-Pt)	0.012	0.020

2.1.3.3 Discussion and Conclusions

Specific activity (Amps/cm^2 of active Pt surface area) is a fundamental property defining the utility of an electrocatalyst for ORR. Section 2.1.3.2 above has summarized specific activity measurements of the NSTF catalysts by methods 1, 2 and 3, and section 2.1.2.3 has summarized these measurements by method 4, rotating ring disc electrode (RRDE), done at LBNL on NSTF – Pt and PtNiFe. It is very interesting to compare all these methods, as done in Fig. 25 below. First, Fig. 25 shows a remarkable level of agreement of the specific activities measured by all four methods. Whether by RRDE in liquid electrolytes using small area samples, or by fuel cell measurements using full size 50 cm^2 electrodes, the values agree quantitatively as well as qualitatively.

Fig. 25 clearly shows that the 5-10 fold enhancement of specific activity of the NSTF-Pt over Pt/C is seen in the RRDE measurements as well, as described in more detail in section 2.1.2.3. A possible inconsistency with the RRDE data is that the same specific activities were measured for the NSTF-Pt as for the NSTF-PtNiFe samples measured by LBNL, whereas for the particular ternary constructions sent, the fuel cell measurements would indicate higher values, possibly by as much as 200 %, should have been obtained based on Figs. 7 in section 2.1.3.2 above. It appears now, several years after those initial measurements at LBNL that an explanation for this inconsistency has been found. It has to do with the LBNL sample loading protocol, and when the PtNiFe measurements were recently repeated (under the DOE/3M contract following this one) with an upgraded protocol, the higher values were obtained, consistent with the fuel cell measurements.

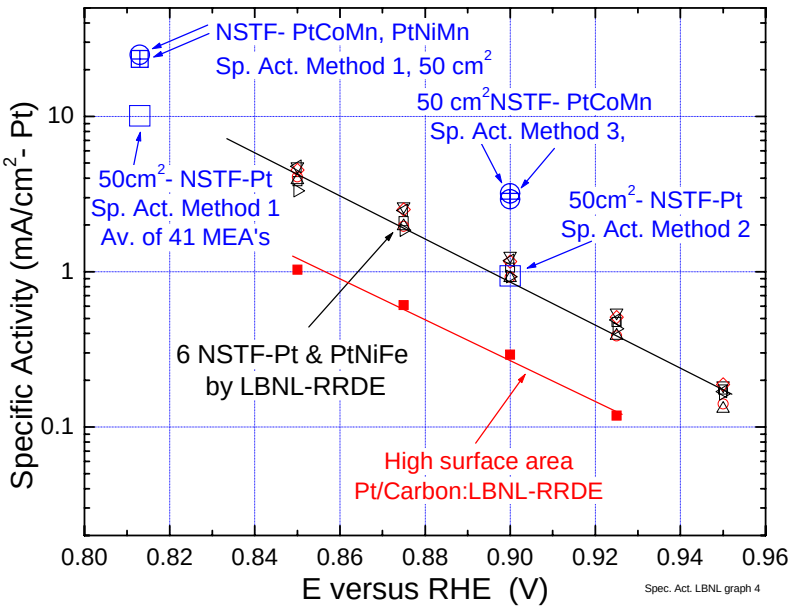

Fig. 25. Comparison of the specific activity measurements by methods 1, 2, 3 and NSTF-Pt (pure) and NSTF-ternary catalysts, with those by LBNL using method 4 for NSTF-Pt ,PtNiFe and high surface area dispersed Pt/Carbon.

Finally, Fig. 25 shows that the ~ 250% enhanced specific activity of the PtCoMn and PtNiMn ternaries over pure Pt are consistently measured by each method 1, 2 and 3. As

shown in Appendix II, Dalhousie University, using the same RRDE method 4 approach as LBNL, has also measured 200% enhancement factors of the NSTF-PtCoMn (90:10) (Pt/TM = 3) catalyst over pure NSTF-Pt. Finally, ANL, using the revised LBNL testing protocol, also clearly measure the ~ 250% gain of the same NSTF-PtCoMn catalysts over the NSTF pure Pt (not reported here, but a result of the subsequent 3M/DOE grant DE-FG36-07GO17007).

The measured RRDE specific activity of the NSTF-Pt agrees very well with that obtained on polycrystalline Pt, supporting the conclusion that the reason the specific activity of the NSTF thin film catalysts are 5-10 fold higher than finely dispersed Pt/C is because they have the same surface electronic properties as that of a polycrystalline bulk sample, and are in effect equivalent to a two dimensional “slab” of the bulk surface, but which is coated around the NSTF whisker supports.

Regarding the specific activities by the fuel cell measurements in section 2.1.3.2, and their dependency on the fabrication parameters, it appears that the bi-layer thickness is not a sensitive parameter, whereas the Pt/TM ratio is, for both activity and electrochemical surface area. There are likely different reasons for the sensitivity of these two characteristics. The specific activity dependence on the transition metal content is likely the same as for dispersed Pt alloys, since as in reference [7], the same 250% increase is obtained for dispersed PtCo alloys on carbon over Pt/C. These are electronic or lattice factor effects directly influencing the ORR. The surface area dependence of the NSTF-ternary catalysts on TM content is most likely related to the degree of TM dissolution and subsequent formation of a more porous Pt surface, as discussed in section 2.1.3.2.4 and 2.1.3.2.5.

We have shown that overall fuel cell performance however, is not predicted simply by the highest specific activity or surface area. The lowest Pt/TM ratios gave the highest kinetic activities and surface areas, but due to membrane poisoning from excess TM cations dissolved out of the ternary catalysts, above the equilibrium TM/Pt ~ 0.33 atomic ratio, both conductivity and water uptake potential of the membrane were degraded. The best performances, in general were obtained with Pt/TM ratios close to the equilibrium value, for which the specific activity was highest and the surface area essentially unchanged.

It was found that the specific activities and Tafel slopes of PtCoFe were in general superior to those from PtMnFe or PtNiFe, thus favoring Co for this series. The PtNiMn and PtCoMn produced the best overall activities at the Pt/TM ~ 3 ratios. The primary value of the Mn is its aid in reducing fluoride release rates from the membranes during fuel cell operation, as discussed in sections 2.1.4.3 and 2.1.5.2 below, whereas Fe contaminants in membranes is known to accelerate the degradation from peroxide radicals. These measurements also allowed differentiating between Ni and Co as discussed in 2.1.5.2.

It was shown that the NSTF whisker areal number density and lengths can clearly influence the mass activity for a given catalyst loading or volume. By tailoring the whisker support to better match the catalyst loading and TM fraction, the mass activitiy can be maximized and exceed current state-of-the art values published for dispersed alloys (PtCo) on more stable graphitized carbon supports. It was also demonstated that potentially record setting performances with 0.12 mg-Pt/cm^2 total per MEA could be obtained by this method.

There is still substantial opportunity to reach higher entitlement values of mass specific area (m^2/g) and further increases in specific activity and durability with the NSTF alloy or multi-element catalysts. This is being pursued under the subequent 3M/DOE grant DE-FG36-07GO17007.

References for Section 2.1.3

[1] M. Debe, A. Hester, G. Vernstrom, A. Steinbach, S. Hendricks, A. Schmoeckel, R. Atanasoski, D. McClure and P. Turner, "Nanostructured Thin Film Catalysts for PEM Fuel Cells by Vacuum Web Coating," in press, 50th Annual Technical Conference Proceedings of the Society of Vacuum Coaters, to be held Louisville, KY, April 30-May 3, 2007.

[2] M. K. Debe, in Handbook of Fuel Cells – Fundamentals, Technology and Applications, W. Vielstich, A. Lamm, H. A. Gasteiger, Editors, John Wiley & Sons, 2003, Ch. 45.

[3] M. K. Debe and R. J. Poirier, "Postdepostion growth of a uniquely nanostructured organic film by vacuum annealing," *J. Vac. Sci. Technol.* A **12**(4), 2017, 1994.

[4] M. K. Debe and A. R. Drube, "Structural characteristics of a uniquely nanostructured organic thin film," *J. Vac. Sci. Technol.* B **13**(3), 1236, 1995.

[5] Gasteiger et al. in Handbook of Fuel Cells – Fundamentals, Technology and Applications, W. Vielstich, A. Lamm, H. A. Gasteiger, Editors, John Wiley & Sons, 2003 chapter 46, pp 593-610.

[6] "Dissolution of Transition Metals in Combinatorially Sputtered, Pt1-x-y Mx M'y (M,M' = Co, Ni, Mn, Fe) PEMFC Electrocatalysts " A. Bonakdarpour, R. Lobel, R. T. Atanasoski, G. D. Vernstrom, A. K. Schmoeckel, M. K. Debe and J. R. Dahn, J. Electrochemical Society, Vol. **153 (10)**, 2006, A1835-A1846.

[7] T. R. Ralph and M. P. Hogarth, Platinum Metals Rev., 2002, **46**(1) 3-14.

[8] K. C. Neyerlin, W. Gu, J. Jorne and H. A. GAsteiger, J. Electrochem. Soc. **153**(10)A1955 (2006)

[9] F. T. Wagner, H. A. Gasteiger, R. Makharia, K. C. Neyerlin, E. L Thompson, S. G. Yan, ECS Trans. **3**(1) 19 (2006)

2.1.4 Catalyst Durability Testing

As PEM fuel cells move towards commercialization for various markets, needed improvements in performance, durability and cost are well documented, but generally different for different market segments. The fuel cell membrane electrode assemblies (MEAs) are key to achieving many of these targeted improvements for automotive applications [1]. Stability and durability in particular of PEM fuel cell membrane electrode assemblies are known to depend on all the MEA components. This includes the catalyst support resistance to corrosion; catalyst surface area stability against agglomeration, dissolution and poisoning; catalyst surface structure and composition stability; catalyst peroxide production rates; ion exchange membrane resistance to peroxide attack, loss of conductivity and mechanical failure; and stability of the gas diffusion layer against carbon oxidation or decomposition of hydrophobic binders causing impedance increases and loss of hydrophobicity. With respect to conventional electrocatalysts and their carbon supports, finely dispersed Pt/C catalysts rely on high surface area carbons and 2-3 nm sized catalyst particles for high levels of activity. However these same factors can contribute to reduce durability from oxidation of the carbon support by the Pt, and loss of electrochemical surface area (ECSA) due to Pt particle agglomeration and dissolution at high potentials [2,3].

In the following sub-sections, we summarize various types of accelerated durability tests conducted in 50cm^2 fuel cells during the period of this contract. These include CV cycling from 0.6 to 1.2 V to test the resistance of the catalyst against dissolution; holding at high potentials (1.5V) to test resistance of the catalyst support against corrosion; operation at 120^{o}C to test for MEA lifetime limits resulting from peroxide generation by the catalyst; stop/start cycling using an automotive recommended protocol to test for catalyst degradation; high current density operation under totally dry H_2/O_2; and lifetime load cycling. In nearly every case we are able to compare the test results using MEA's having the NSTF catalyst with those obtained using commercially obtained Pt/Carbon catalysts, but the same membrane and GDL. In every case, the durability and lifetime improvement with the down-selected NSTF PtCoMn ternary electrodes was significant.

2.1.4.1 NSTF Stability Under High Voltage Cycling

This section provides a comparative evaluation of electrocatalyst surface area stability in PEM fuel cells under accelerated durability testing. The two basic electrocatalyst types are conventional carbon-supported dispersed Pt catalysts (Pt/C), and nanostructured thin film (NSTF) catalysts. Both types of fuel cell electrocatalysts were exposed to continuous cycling between 0.6 to 1.2 volts, at various temperatures between 65^{o}C and 95^{o}C, with H_2/N_2 on the anode and cathode, while periodic measurements of electrochemical surface area were recorded as a function of the number of cycles. The NSTF electrocatalyst surface areas were observed to be significantly more stable than the Pt/C electrocatalysts. A first order rate kinetic model was applied to the normalized surface area changes as a function of number of cycles and temperature, and two parameters extracted, viz. the minimum stable surface area, S_{min}, and the activation energy, E_a, for surface area loss in this voltage range. S_{min} was found to be 10% versus 66%, and E_a 23 kJ/mole versus 52 kJ/mole, for Pt/C versus NSTF-Pt respectively. The loss of surface area in both cases is primarily the result of Pt grain size increases, but the Pt/C XRD grain sizes increase significantly more than the NSTF grain sizes. In addition, substantial peak shifts occur in the Pt/C CV's which ultimately end up aligning with the NSTF peak positions which do not change substantially due to the voltage

cycling. This result indicates that NSTF catalysts should be more robust against shut down/start-up, operation near OCV and local H_2 starvation effects.

2.1.4.1.1. Introduction

PEM fuel cells are moving steadily towards commercialization for various markets. Needed improvements in performance, durability and cost are becoming better defined, but are generally different for different market opportunities. Operation of PEM fuel cells in the field under real time conditions are expected to reveal further requirements for improvement. The fuel cell membrane electrode assemblies (MEAs) are key to achieving many of these targeted improvements for automotive applications [1], and durability is perhaps the most critical at this stage of technology development. Stability and durability in particular of PEM fuel cell membrane electrode assemblies are known to depend on all the MEA components. Considering just the catalyst electrodes, there are many properties that need to be met simultaneously before a successful system can be implemented. These include high catalyst mass activity, high catalyst utilization at all current densities, low mass transport losses, high tolerance to multiple surface area loss mechanisms, tolerance of a wide humidity and temperature operating window, cold start and freeze tolerance, and the ability to be fabricated by robust high volume-compatible, low cost processes. Specific durability and stability requirements include resistance to corrosion of the catalyst support; stability of surface area against agglomeration, dissolution, and poisoning (externally and internally generated); stability of catalyst surface structure and composition, and negligible peroxide/water (2 e^-/4e^-) production ratio. Also desirable for MEA durability are resistance of the ion exchange membrane to peroxide attack, low reactant permeability and high dimensional stability; and stability of the gas diffusion layer against carbon oxidation or decomposition that can cause impedance increases and loss of hydrophobicity.

Conventional carbon supported, finely dispersed electrocatalysts, rely on high surface area carbons and 2-3 nm sized catalyst particles on those carbon particles for electrical conductivity and high levels of catalyst activity respectively. However these same factors contribute to reduced durability from Pt catalyzed electrochemical corrosion of the carbon support itself, and loss of electrochemical surface area (ECSA) due to Pt particle agglomeration and dissolution at high potentials [2-6]. It is generally believed that carbon particle supports, whether carbon blacks, graphitized carbon or carbon nanotubes, are required for adequate electronic conductivity in low catalyst loading PEM fuel cell electrodes. For highly dispersed electrocatalysts on those supports that is true. For a different electrocatalyst structural paradigm however, carbon support particles are not required.

The 3M nanostructured thin film (NSTF) catalyst is such a non-conventional catalyst. Incorporated into an MEA, it contains neither carbon nor additional ionomer in the electrode layers that are 20-30 times thinner than conventional dispersed Pt/carbon based MEA's [7]. Fig. 1 shows SEM images of the NSTF catalyst coated whiskers, roll-good fabricated by an all-dry continuous process, prior to incorporation onto the surfaces of a PEM to form a catalyst coated membrane. Fig. 2 shows an SEM cross-section of one side of the catalyst-coated membrane, also fabricated by a dry roll-good process, illustrating the extreme thinness of the electrode layer. The NSTF catalysts comprise high aspect ratio elongated particles formed by vacuum coating catalyst thin films onto a monolayer of oriented crystalline organic (pigment) whiskers [7]. The organic whiskers are highly inert thermally, chemically, and electrochemically [8]. The thin film catalyst coating encapsulates the crystallized pigment whisker support particles, eliminating

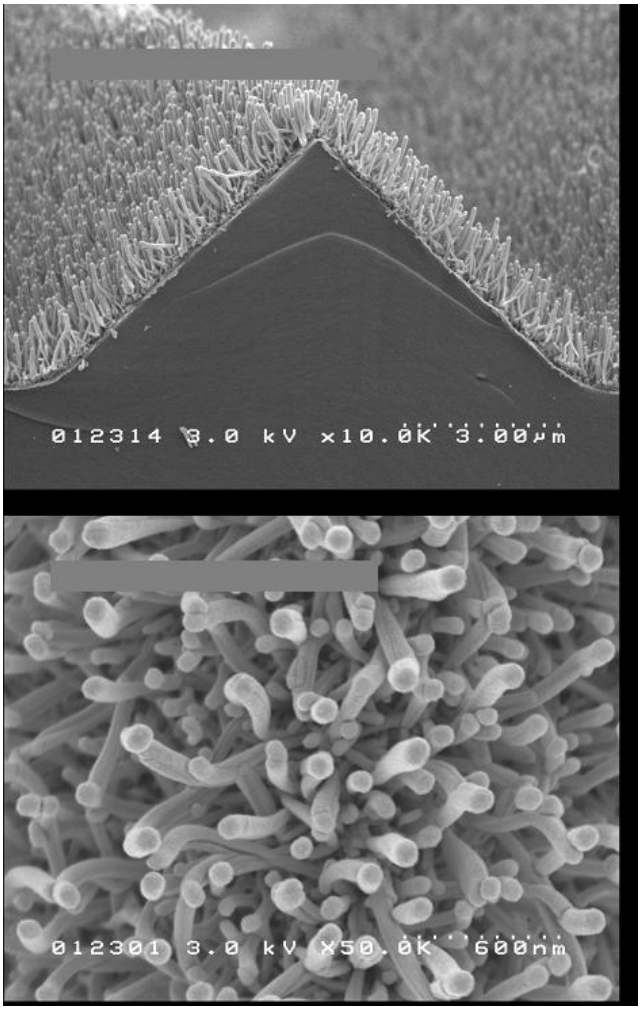

Fig. 1. (Left) Scanning electron micrographs of typical NSTF catalysts as fabricated on a microstructured catalyst transfer substrate, seen (top) in cross-section with original magnification of 10,000, and (bottom) in plan view with original magnification of 50,000. The dotted scale-bar is shown in each micrograph.

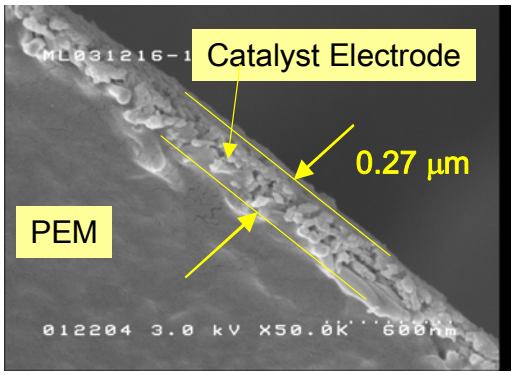

Fig. 2. (Above) SEM cross-section of NSTF CCM electrode.

issues with oxidatively unstable supports. The thin film catalyst coatings consist of relatively large crystallite domains or nanoscopic particles, which give to the NSTF catalysts both enhanced specific activity [9], and resistance to loss of surface area by Pt dissolution [8,10]. Most notable is the five-fold or greater gain in specific activity of the NSTF catalysts over high surface area dispersed Pt/Carbon [9,11,12], as discussed at length in section 2.1.3. We currently associate this fundamental gain in catalyst turn-over rate to be a consequence in some way of the thin film nature of the NSTF catalyst since the absolute values of the specific activity measured in rotating ring disc electrodes agree very well with those from bulk polycrystalline Pt surfaces [11,12]. This gain in specific activity compensates for the lower electrochemical surface area of the NSTF catalysts so that equivalent performances to high surface area carbon supported catalysts are achieved with reduced loadings. But a further critical aspect that enhances the performance of the NSTF electrodes is the extreme thinness of the electrode layer, particularly at high current densities. Because the bulk of the carbon support is eliminated, the NSTF electrode is some 10-30 times thinner than Pt/C based electrodes for the same mass loading of catalyst and this allows for 100% utilization of the catalyst thickness and reduction of the mass transport overpotential losses at high current densities. As discussed in section 2.1.5.3, for NSTF electrode thicknesses less than 0.3 microns, corresponding to Pt loadings of 0.10 mg cm^{-2} on the cathode, the mass transport losses under pressurized (303kPa) H_2/air at 2 A cm^{-2} are deduced to be

negligible since IR-corrected polarization curves have linear Tafel slopes of 70mV/decade from 0.02 to 2 A cm^{-2}.

The higher specific activity of the NSTF catalysts compared to nano-particle dispersed catalysts and the absence of exposed carbon also appear to contribute to another very important NSTF property critical for durability. Significantly reduced fluoride ion release rates in the water effluent from NSTF ternary catalyst-based MEA's operating at 120°C show fluoride ion release rates some seventy-five times lower than from MEA's made with nominally identical membranes and GDL's but with conventional Pt/C electrodes. The reduced F^- ion release rates correlated with significantly longer lifetimes, with the NSTF MEA's lasting over 1000 hours before catastrophic failure of the PEM versus only about 100 hours for the Pt/C based MEA's [11, 12] (see also section 2.1.5.2).

High voltage stability of the catalyst and its support particle is another key area recently found to uniquely differentiate the NSTF catalysts from conventional carbon-supported dispersed catalysts. The complete resistance of the NSTF to support corrosion at 1.5 volts is documented in reference [8] by showing no change in surface area or fuel cell performance occurring over periods as long as 3 hours. In sharp contrast, Pt/C catalyst based MEA's with identical membranes and GDL's exhibited large changes in surface area, performance and ac impedance in just 30 minutes [8]. The ability of the NSTF catalyst to withstand 1.5 volts under H_2/N_2 without corrosion of the support or loss of surface area or loss of catalyst activity, for either pure NSTF Pt or NSTF ternary catalysts, is a significant differentiating feature over carbon or graphitic carbon supported catalysts. In this report we compare in more detail the enhanced stability of the NSTF catalysts with respect to Pt dissolution and agglomeration. Surface area and fuel cell performance stability of NSTF-Pt and Pt/C electro-catalysts are compared under accelerated testing conditions of cyclic voltage scanning under H_2/N_2 from 0.6 to 1.2V at fast rates.

2.1.4.1.2. Experimental

Catalyst and MEA Preparation

The NSTF catalysts and MEAs were prepared as described in reference [7]. The NSTF whisker support layer is a monolayer of oriented crystalline whiskers of an organic pigment material. The support layer is deposited first onto a microstructured catalyst transfer substrate (MCTS) via a vacuum roll-good process. Then catalysts are sputter-coated on top of the whiskers so as to encapsulate them with a polycrystalline thin film. Composition and structure of the catalyst coating is determined by the arrangement and composition of the sputtering targets. Both Pt ternary and pure Pt were used for the NSTF catalysts samples used in this paper to compare with Pt/carbon catalysts for the CV scanning tests. For the first order kinetic rate model data, only pure Pt catalysts were used for both the NSTF and Pt/C MEA's. Typical NSTF Pt loadings were 0.1 and 0.15 mg cm^{-2}, while Pt/C loadings were 0.4 mg cm^{-2} per electrode. The specific surface areas of the NSTF-Pt catalysts were ~ 10 m^2 g^{-1}Pt. NSTF catalyst-coated membranes are formed by transfer of the catalysts from the initial substrate web (MCTS) to the proton exchange membrane.

For the voltage cycling measurements the dispersed Pt/C catalysts were commercially obtained and utilized 40-50 wt% Pt on Ketjen Black. The specific surface areas of the platinized carbon blacks were ~ 192 m^2 g^{-1}Pt. Conventional type ink of Pt/C catalysts in

Nafion™ were coated and decal-transferred to the surfaces of the membranes to form the dispersed catalyst-coated membranes.

In all cases the 3M fabricated membranes used were based on the 3M ionomer [14]. For the voltage cycling, the 3M membrane having a 1000 EW was used for both the NSTF and Pt/C type MEA's. The same 3M-fabricated GDL's were used for both types of MEA's and generally consisted of a carbon paper electrode backing coated with a microporous layer having a dispersed carbon chosen for its oxidative stability [15].

Accelerated electrochemical tests

Continuous CV cycling between 0.6 to 1.2 volts at 20 mV/s, with periodic measurements of electrochemical surface area were used to measure the surface area stability of various NSTF and Pt/Carbon supported catalysts. To further characterize the surface properties of the catalyst, full-scale CVs were recorded over the voltage range from 0 to 1.2 volts.

All the performance fuel cell tests were done in 50 cm^2 cells with quad-serpentine flow fields. Fuel cell performance was obtained on test stations purchased from Fuel Cell Technology, using 3M-developed test station control software. Cyclic voltammograms for surface area determination and voltage cycling were measured using a Solartron 1470 potentiostat controlled by CorrWare software from Scribner Associates.

The high voltage cycling conditions used were 20 mv/s with H_2/N_2 at RH:100%/100% on the anode/cathode respectively. The cell temperatures were controlled in the range of 65-95^oC, and a fresh MEA was used for each new temperature condition.

Electrochemical surface areas were measured at room temperature (~22 ^oC) from integrated hydrogen adsorption and desorption cyclic voltammograms, corrected for shorting and hydrogen crossover, and assuming 210 or 220 $\mu C/cm^2$ of Pt surface area at saturation coverage. For the NSTF catalyst, these CVs were performed at 100 mV/s, while the Pt/C CVs were at 50 mV/s.

X-ray diffraction characterization

X-ray diffraction was used for purposes of determining crystalline phase(s) present, apparent crystallite sizes with high voltage cycling, and semi-quantitative evaluation of the amount of Pt remaining in the MEAs after cycling. Data were collected using a Philips APD vertical diffractometer, copper K_α radiation, reflection geometry, and proportional detector registry of the scattered radiation. The apparent crystallite sizes and d-spacings/relative intensities for platinum were determined from observed diffraction peaks using a Pearson VII peak shape model, accounting for α_1/α_2 separation. The background, obtained from a reference "blank" of Nafion™, was subtracted prior to profile fitting.

2.1.4.1.3. Results

Each 50 cm^2 MEA was operated on ambient pressure hydrogen/air with saturated gases until performance had stabilized. The break-in protocol consisted of alternating potentiodynamic scans (PDS) and potentiostatic scans (PSS). Flow rates were held constant at 800 and 1800 sccm of H_2 / air and the cell temperature was held at 75^oC. The PDS ran between 0.85 and 0.25 volts in both directions with approximately 48 mV

steps and 10 sec dwell times at each potential. The PSS were held at 0.4 V for 10 minutes before another PDS was initiated. For the Pt/C based MEA's, this break-in protocol was continued for approximately 4 hours. For the NSTF MEA's, between 2 to 4 additional stop/starts of the fuel cell with cool-down of the cells to ambient temperature was implemented as well, while allowing water to continue to flow through the flow fields. These "thermal cycles" are found helpful to sweep away impurities and bring-up the fuel cell performance of the thin film electrodes more quickly.

For each MEA, after break-in, the initial surface area was measured and then repetitive cyclic voltammograms were acquired between 0.6 and 1.2 V as described above. Periodically the cycling was stopped and the surface area re-measured, after which the CV cycling was continued. This continued until the ECSA dropped below 10% of the initial value (Pt/C MEA's), or until the ECSA stabilized (NSTF MEA's). Since the surface areas of the Pt/C are much greater than that of the NSTF catalysts, to compare ECSA changes it is expedient to normalize the surface areas to the initial values. Fig. 3 illustrates the normalized surface area versus number of CV cycles from 0.6 to 1.2 V for four NSTF catalyst samples and three Pt/Carbon catalysts at 80°C. All MEA's used the same 3M ionomer PEM and GDL. This was a preliminary experiment to get a sense of the magnitude of change depending on the catalyst type and support. As seen, all the NSTF samples, with both pure Pt and PtCoMn catalysts lost about 30% of the initial surface area after about 3000 cycles, but then the surface area stabilized out to 14,000 cycles. In contrast, the Pt/Carbon supported catalysts lost 90% of their surface area in 2000 cycles, and even the Pt dispersed on graphitic carbon supports lost 90% or more of their surface areas in 5000 cycles.

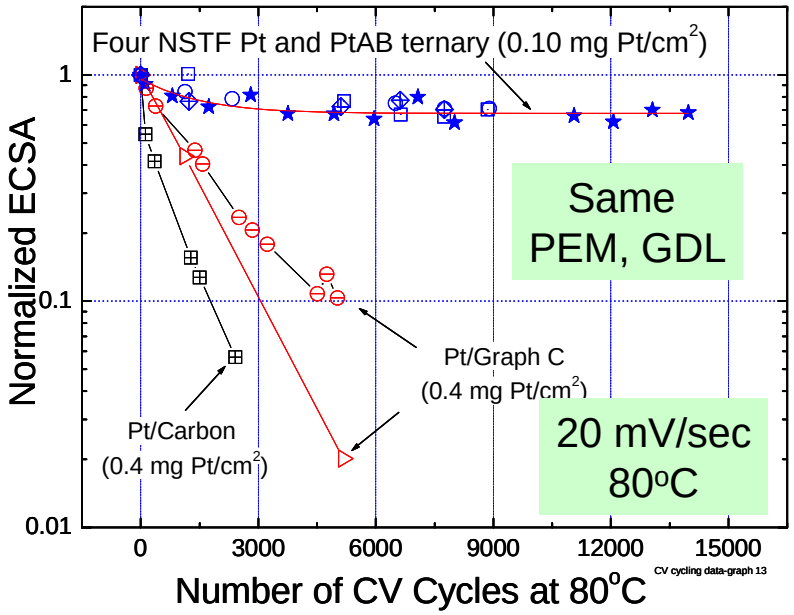

Fig. 3. Normalized surface area versus number of CV cycles from 0.6 to 1.2 volts for four NSTF catalyst samples and three Pt/Carbon catalysts at 80°C. For the NSTF samples, the solid star symbols were pure Pt at 0.15 mg/cm^2 loading, the open squares were pure Pt at 0.10mg/cm^2 loading, the open circles were $Pt_{49}Co_{26}Mn_{25}$ with 0.10 mg-Pt/cm^2, and the diamond-plus symbols were $Pt_{69}Co_{28}Mn_3$ also with 0.10 mg-Pt/cm^2. The initial mass specific surface areas for the Pt/Carbon, Pt-Graph-C and NSTF catalysts were 192, 147 and 10 m^2/g-Pt respectively.

To more carefully study the surface area loss processes for both types of catalysts, a new set of MEA's were evaluated with the same CV cycling protocol but varying cell temperatures. Also, only pure Pt based NSTF catalysts were tested for comparison to the Pt/Carbon (Ketjen black) supported catalysts. The NSTF MEA's were tested at 75, 85, 90 and 95°C while the Pt/C MEA's were tested at 65, 75, 80, 95 and 95°C.

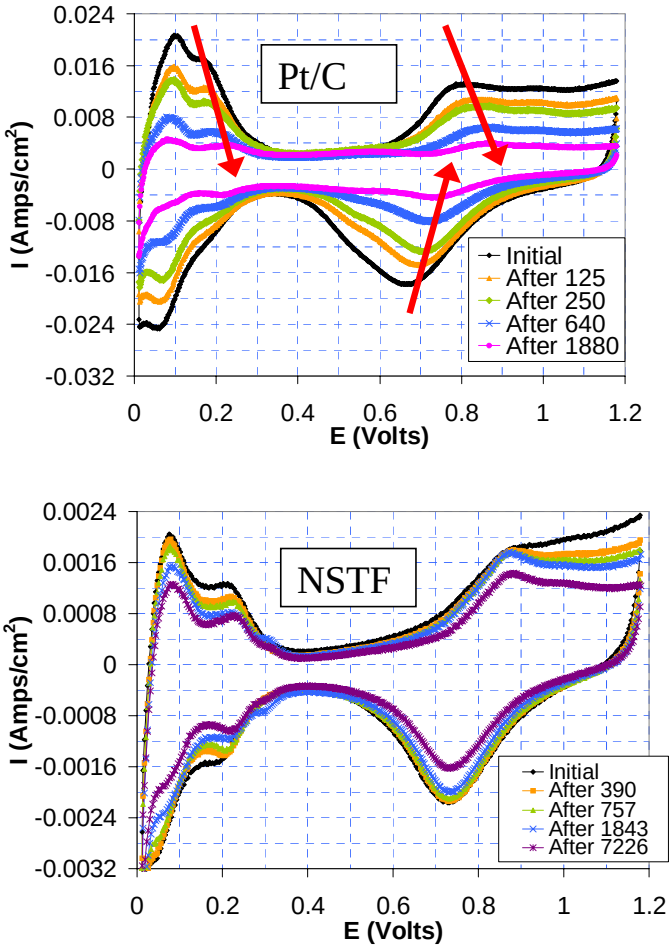

Fig. 4. Series of CV plots obtained at 75°C during 0.6 – 1.2 volt cycling at 20 mV/s under H_2/N_2 from (top) Pt/C MEA after 1880 cycles, and (bottom) NSTF MEA after 7226 cycles. CVs were obtained at room temperature (as part of the surface area routine) after CV cycling at 75°C. The arrows indicate shifts in the Pt/C CV peaks as the surface area is lost.

Fig. 4 shows a subset of the CV's obtained at room temperature after cycling at 75°C from the Pt/C MEA's during a total of 1880 cycles, and NSTF-Pt MEA's during a total of 7226 cycles. Whereas the Pt/C MEA CV's undergo significant changes, the NSTF MEA CV's are much more stable. Pt/Carbon peak positions shift dramatically as surface area is reduced by 95% over 1880 cycles at 75°C, while NSTF CV shape remains nearly unchanged, as surface area is reduced 32% over 7226 cycles. The former shows changes resulting from the considerable loss of surface area and also peak shifts indicated by the red arrows.

Fig. 5 shows a similar set of CV's after cycling at 90°C cell temperature that illustrates a similar behavior as seen at 75°C. There is again a significant shift in the peak positions for the Pt/C catalysts after 1890 cycles, and a measurable but much smaller shift for the NSTF-Pt CV's after 4235 cycles.

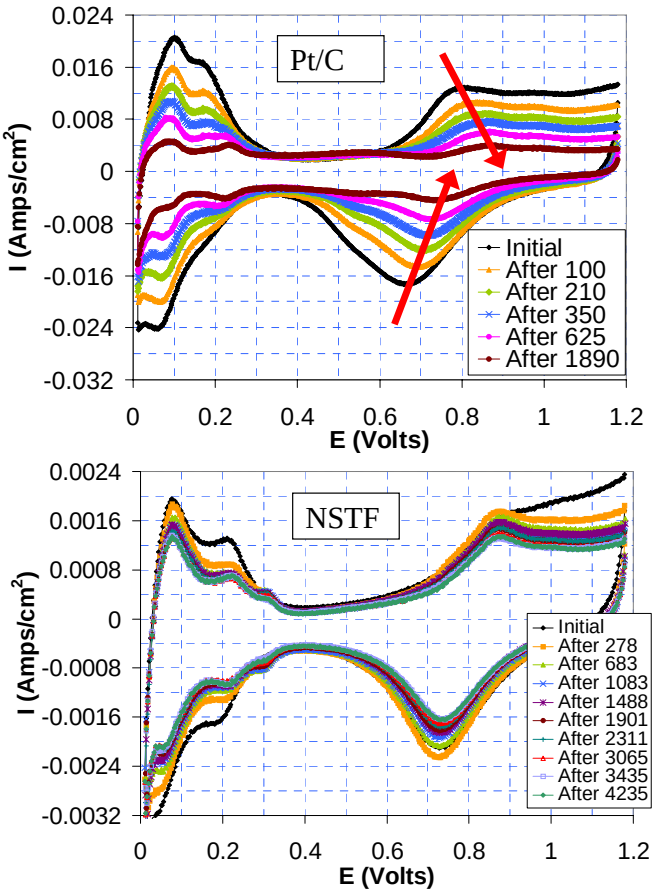

Fig. 5. Series of CV plots obtained at room temperature after 0.6 – 1.2 V cycling at 90°C and 20mV/ s under H_2/N_2 from (top) Pt/C MEA after 1890 cycles, and (bottom) NSTF MEA after 4235 cycles. The arrows indicate shifts in the Pt/C CV peaks as the surface area is lost.

Fig. 6 plots the normalized surface area versus number of cycles for the two catalyst types at all the temperatures measured. A similar response to that seen in the preliminary experiment of Fig. 3 was obtained. There appears to be a slight temperature dependence in that the higher the temperature the faster the loss-rate of surface area. Again the NSTF ECSA has stabilized at ~ 67% for all temperatures after 5000 cycles, while the Pt/C ECSA has decreased by ~ 90% in 2000 cycles.

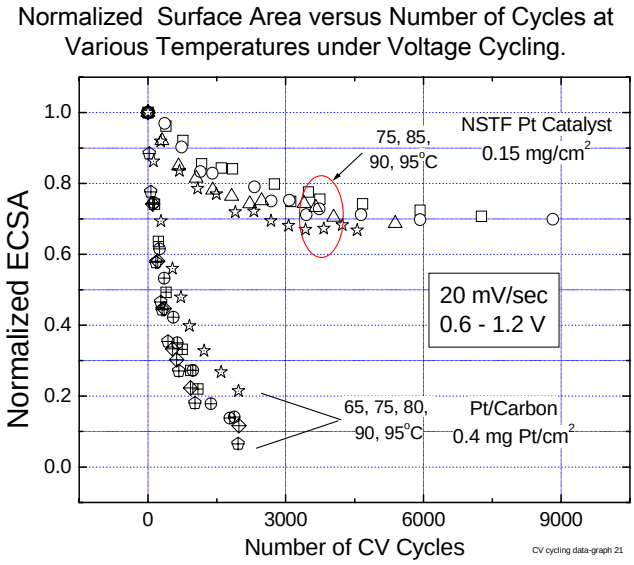

Fig. 6. Normalized catalyst surface area of the working electrode as a function of the number of CV cycles from the NSTF-Pt based MEA (0.15 mg/cm^2) at 75 (square), 85 (circle), 90 (star) and 95 °C (triangle), and from the Pt/C based MEA (0.4 mg/cm^2) at 65 (star), 75 (circle), 80 (square), 90 (diamond) and 95°C (pentagon).

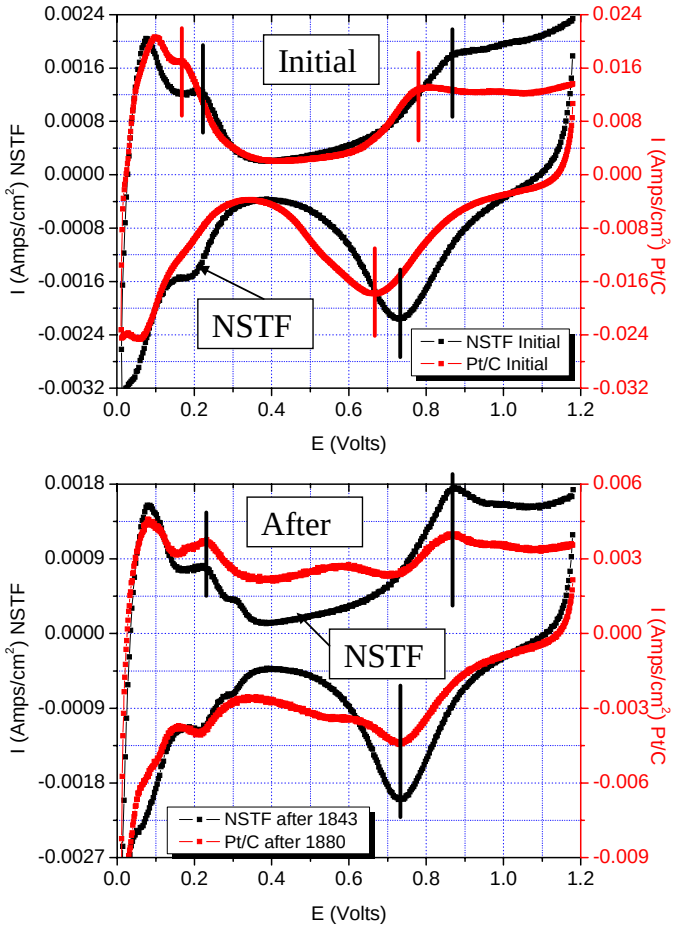

Fig. 7. Comparison of the initial (top) and final (bottom) full range cyclic voltammograms from the NSTF–Pt based MEA's and Pt/C based MEA's, showing shifts in peak positions and double layer capacitance occurring as surface area was lost. Note the change in the current density range for Pt/C between initial and final CVs.

Fig. 7 shows a comparison of the initial (top) and final (bottom) full range cyclic voltammograms from the NSTF–Pt based MEA's and Pt/C based MEA's, showing shifts in H_{upd} and Pt oxide formation and reduction peak positions and the shape of the double layer capacitance occurring as surface area was lost. What is remarkable is that on Pt/C the characteristic peak positions shift to become equal to those of the NSTF-Pt, which change very little or not at all. In conjunction with the XRD results discussed below, this suggests that the peak positions are closely tied to particle size, and the size of the Pt/C crystallites are approaching those of the NSTF catalysts. Also, with cycling the Pt/C CV's show a new peak in the double layer region consistent with additional carbon oxidation (quinone– hydroquinone redox peaks around 0.6 V.)

Fig. 8 shows a summary of the CV peak positions plotted as a function of the number of cycles for the Pt/C and NSTF-Pt based MEA's. The much larger relative change in CV peak positions of the Pt/C at 75 and 90^{o}C is clearly seen, and essentially complete after less than 1000 cycles.

Fig. 9 compares changes in the cathode and anode X-ray diffraction spectra from the Pt/C based MEA's (top), and the NSTF-Pt based MEA's (bottom). It is readily apparent that the XRD peak widths from the Pt/C electrodes, both anode and cathode, have changed significantly, whereas the NSTF-Pt peak widths have changed much less, and

the NSTF-Pt anode peak width hardly at all. The diffraction peak intensities can also be used to qualitatively if not quantitatively address the question of whether loss of ECSA is due to loss of Pt entirely. Table I compares the relative integrated peak intensities of the spectra shown in Fig. 9. The values suggest that to within 2%, the integrated peak intensities have not changed as a result of the CV cycling, and the Pt still remains within the CCM, if not within the electrode.

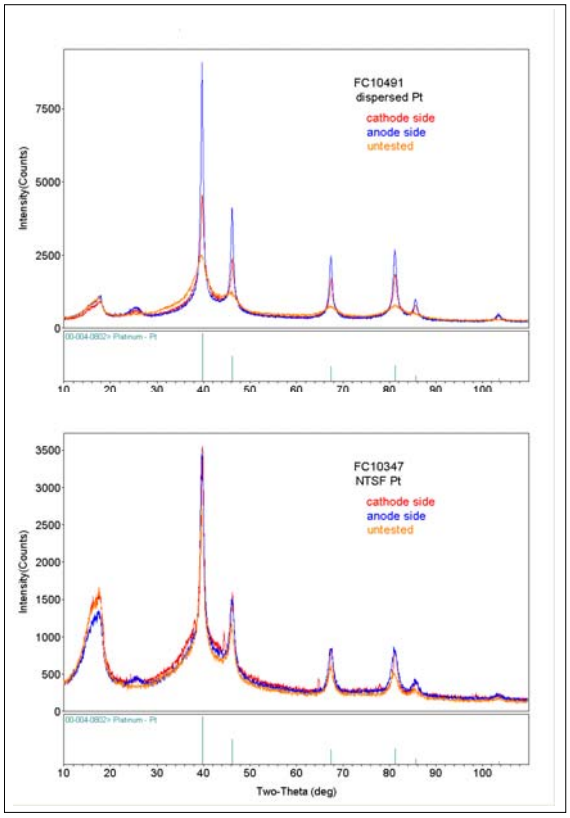

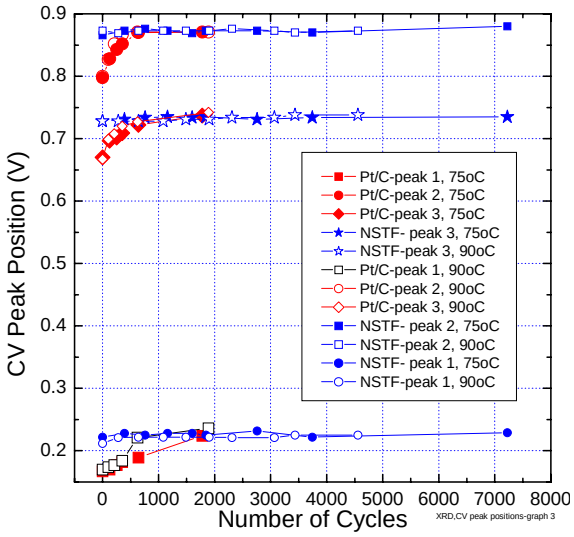

Fig. 8. Summary of the CV peak positions as a function of number of cycles for the Pt/C and NSTF-Pt based MEA's.

Fig. 9. Comparison of changes in the cathode and anode X-ray diffraction spectra from :(top) the Pt/C based MEA's, and (bottom) the NSTF-Pt based MEA's after 1880 and 7226 CV cycles respectively

Table I. Integrated peak intensities for the XRD spectra shown in Fig. 9.

Pt[hkl]	Pt/C Untested	Pt/C Cathode	Pt/C Anode	NSTF-Pt Untested	NSTF-Pt Cathode	NSTF-Pt Anode
(111)	100	100	100	100	100	100
(200)	35	46	42	31	38	33
(220)	18	37	28	18	23	23
(311)	22	45	29	15	6	22
(400)	5	13	8	3	2	6

Fig. 10 compares changes in the apparent crystallite sizes of the cathode and anode catalysts, extracted from the XRD spectra of Fig. 9, for the Pt/C based MEA and NSTF-Pt based MEA, after 1880 and 7226 CV cycles respectively. What is remarkable is that whereas the Pt/C anode crystallites' size increases even more than the cathode crystallites' size, the NSTF anode crystallites' size change very little while the NSTF cathode crystallites' size changes to become very similar to those of the Pt/C. The reason for this is not understood, but was experimentally verified multiple times.
Fig. 11 shows ambient pressure, constant flow PDS polarization curves from the Pt/C based MEA before and after 2429 cycles. The primary loss can probably be attributed to the 90% loss in electrochemically active catalyst surface area.

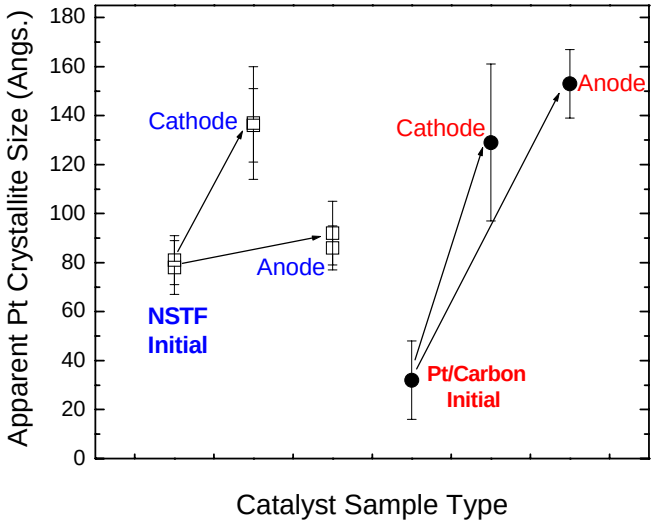

Fig. 10. Changes in the apparent crystallite sizes of the cathode and anode catalysts extracted from the XRD spectra of Fig. 9.

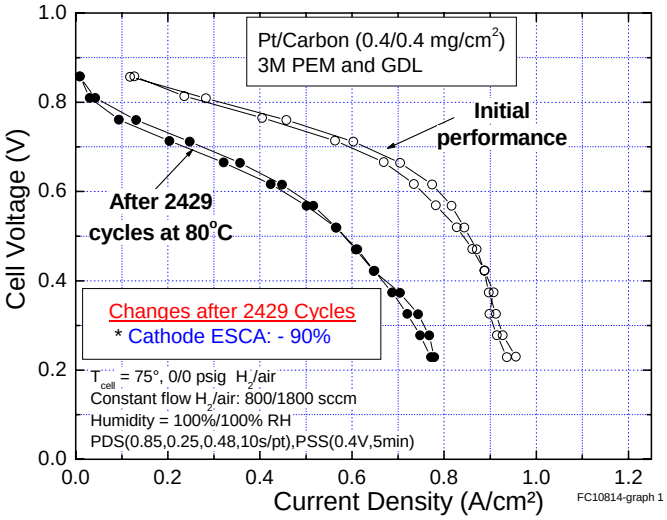

Fig. 11. Ambient pressure constant flow polarization curves from the Pt/C based MEA before and after 2429 cycles. The primary loss can probably be attributed to the 90% loss in electrochemically active catalyst surface area.

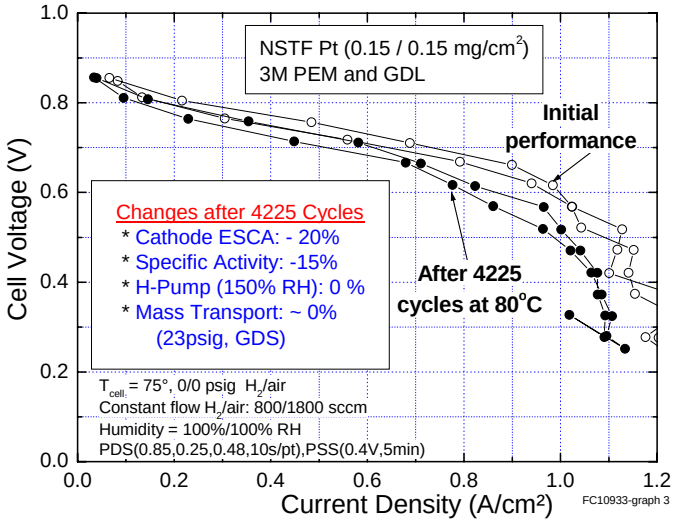

Fig. 12. Ambient pressure constant flow polarization curves from the NSTF-Pt based MEA before and after 4225 cycles. The insert indicates the contributions to the changes in fuel cell performance are due to ~ a 20% loss of surface area and an ~15% reduction in catalyst specific activity, measured at 900mV (after 15 minute hold) under 100kPa H_2/O_2 and 100% saturation.

Fig. 12 shows ambient pressure, constant flow PDS polarization curves from the NSTF-Pt based MEA before and after 4225 cycles. It is clear from Figs. 11 and 12 that the performance loss due to the CV cycling is much less for the NSTF-Pt MEA's. This performance loss can have contributions from changes in catalyst specific activity, catalyst surface area, overall MEA impedance and mass transport losses. The NSTF MEA impedance was characterized by H-pump measurements in which H^+ transport current across the MEA is measured as a function of applied potential under oversaturated (150% RH) H_2/H_2. The specific activity of the NSTF cathode for the MEA in Fig. 12 was also measured before and after the CV cycling. The measure of specific activity used in this instance was that proscribed by Gasteiger et al. [1] and described in more detail in section 2.1.3.1 of this report. It consisted of holding the cell at 900 mV under 100 kPa H_2/O_2 and 100% saturation (150 kPa total pressure) and recording the current level after a hold period of 17.5 minutes. This current density level, was then corrected for the measured shorting impedance and cross-over current density, and divided by the measured ECSA to obtain the specific activity. Table II summarizes the changes in surface area, specific activity and H-pump before and after 4225 CV cycles of the NSTF-Pt sample at 80°C producing the polarization curves in Fig. 10. No change in the H-pump value occurred before and after CV cycling for the sample, its specific activity was observed to decrease ~ 15% due to the 4225 cycles, while the surface area was reduced by ~ 20%. The combination of this loss of surface area and specific activity are sufficient to explain the performance change in Fig. 12.

Table II. Summary of ECSA, specific activity at 900mV under 150kPa H_2/O_2, and H-pump, measured before and after 4225 CV cycles for the NSTF-Pt MEA.

NSTF-Pt	ECSA (RT) (cm^2/cm^2) anode/cathode	Specific activity (mA/cm^2-Pt)	H-pump (ohm-cm^2) 150% RH
Before	15.2/13.1	1.72	0.065
After	15.9/10.4	1.44	0.067

For the Pt/C MEA performance loss in Fig. 11, no attempt was made to characterize changes in mass transport or specific activity due to the very high (~ 90%) loss of surface area. Qualitative X-ray fluorescence elemental analysis of the untested and tested MEA's of either type showed no statistically significant change in the kilocounts

/second due to the CV cycling. This is consistent with the XRD integrated peak intensities in suggesting Pt remains inside of but redistributed within the MEA.

2.1.4.1.4 First order kinetic rate model for surface area loss

Fig. 6 shows a significant difference in the overall behavior of the Pt/C and NSTF-Pt cathodes. The minimum value of normalized surface area reached after the CV cycling is dramatically different between the two catalyst types. Overall, an exponential type decay of the normalized ECSA is seen for both, which suggests the rate of surface area loss after N^{th} cycle is proportional to remaining surface area. Although less obvious, there is also a difference in the rates of surface area loss with temperature, suggesting the kinetics of the surface area loss may be different between the two catalysts types as well. To investigate this, a first order kinetic rate model was applied to the data in Fig. 6. It should be recognized that since the surface area loss can have contributions from multiple specific mechanisms, any activation energy derived from such a model is a composite for all contributing mechanisms to surface area loss from voltage cycling over the range of 0.6 to 1.2 V.

As a starting basis for the model, the normalized surface area, S(N), is considered to be a function of the number of cycles, N, and after any given number of cycles, N, the rate of surface area loss, dS/dN, is taken as directly proportional to the remaining losable-surface area, S, as in equation (1). The constant of proportionality, k, is a rate constant having the typical Arrhenius dependence on temperature and activation energy, E_a.

(1) $$dS/dN = -kS(N), \quad where \quad k \equiv G \cdot \exp^{-E_a/RT} \quad .$$

Integrating (1) between the expected limits of 0 < S(N) < 1 should give a plot of log[S(N)] that varies linearly with N. Fig. 13 shows, however, such a plot is definitely not linear. What is most apparent in Fig. 6 is that the NSTF-Pt electrodes have a minimum normalized surface area that is considerably larger than that of the Pt/C. In other words, there appears to be a minimum surface area, S_{min}, which is either stable or much less susceptible to loss by the voltage cycling, so that there is a maximum of normalized losable-surface area of 1-S_{min}. With that assumption, the integration limits of equation (1) are taken between 1-S_{min} and S(N)- S_{min} , giving:

(2) $$\ln\left[\frac{S - S_{min}}{1 - S_{min}}\right] = -k\,N = -G\,(\exp^{-E_a/RT})\,N$$

Fig. 14 is a plot of the left half of equation (2) with the value of S_{min} = 0.10 for the Pt/C data from Fig. 6. The lines are now substantially linear for all temperatures. A single value of 0.10 for S_{min} was found to give the observed fit for all the temperatures, although a value of 0.12 did improve the R^2 fit value for the T = 65°C case.

Fig. 15 shows the results of the left half of equation (2) for the NSTF-Pt data from Fig. 6. In this case a single value of S_{min} did not work satisfactorily for each temperature. The values of S_{min} which produced the best linear fits to the data in Fig. 6 for each temperature, as determined by the minimum value of R^2, were in the range shown of 0.64 < S_{min} < 0.69. Small differences in the value of S_{min} for the NSTF case have a greater impact on the curvature of the plotted lines in Fig. 15 compared to those in Fig 14 for the Pt/C case because the size of the signal (maximum loss of surface area) is less for the NSTF case (32% versus 90%). Also, the noise is increased since the

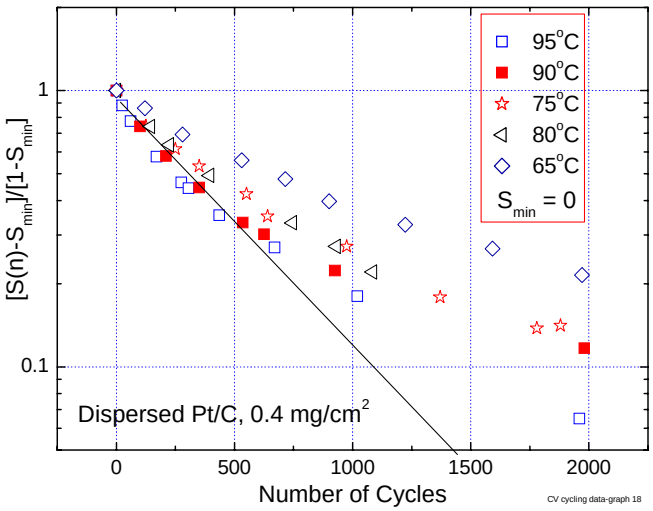

Fig. 13. Plot of the log of the normalized surface area, S(n), from the Pt/C based MEA data shown in Fig. 6 as a function of the number of CV cycles. S(n) = [(S(n) – S_{min})/(1-S_{min})] when S_{min} = 0.

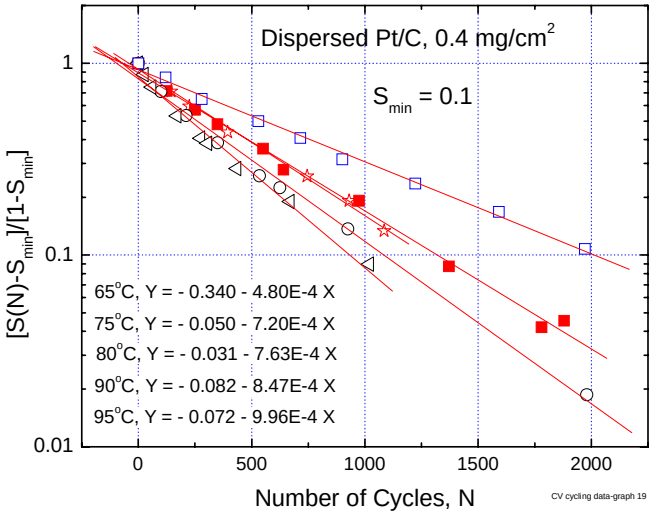

Fig. 14. Plot of the log of (normalized surface area - S_{min},) from the Pt/C based MEA data shown in Fig. 6 as a function of the number of cycles, when S_{min} = 0.1.

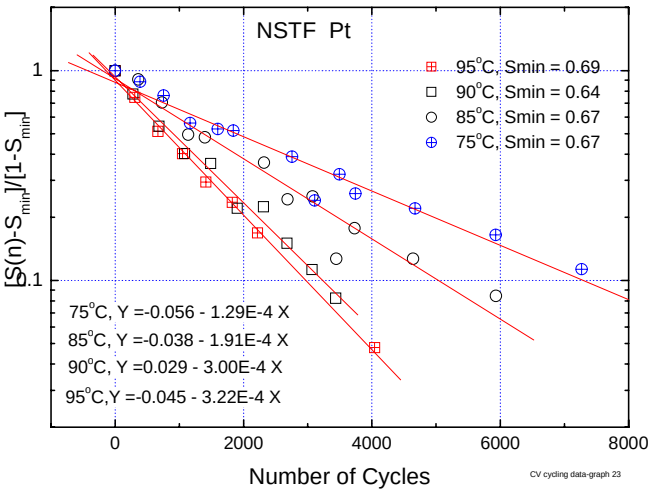

Fig. 15. Plot of the log of (normalized surface area - S_{min},) from the NSTF-Pt based MEA data shown in Fig. 6 as a function of the number of cycles, when 0.64 < S_{min} < 0.69 is selected for each temperature so as to give the straight line with the least R^2 fit.

absolute errors in S_{min} are counted twice in the plotted ordinate of Figs. 14 and 15. For example, if the absolute uncertainty in S_{min} is 3% and that of S(N) is 10%, then the fractional uncertainty in [S(N) - S_{min}] / [1- S_{min}] is 23%. With the model assumptions that a first order rate equation is applicable and the data plotted in Fig. 13 should be linear, the exact value of S_{min} was allowed to vary in the range of 0.64 to 0.69 for the NSTF-Pt case in order to obtain best-fit straight lines. Doing so generally gave R^2 values > 0.98, and p < 0.0001.

From the slopes of the linear fits to the data in Figs. 14 and 15, the values of the rate constants, k(T), are obtained at each temperature, T. By equation (3) plotting ln[k] vs 1/T should also produce a linear fit the slope of which the activation energy, E_a can be obtained:

(3) $$\ln[k] = \ln(G) - E_a/R\left(\frac{1}{T}\right)$$

Fig, 16 shows the resulting plots of equation (3) for the values of k(T) from Figs. 14 and 15. The overall activation energy, for all possible surface area loss mechanisms taken together, are E_a = 52.8 ± 8 kJ/mole for the NSTF-Pt electrodes, and E_a = 22.6 ± 3.6 kJ/moles for the Pt/C electrodes. The uncertainties in these values are the RMS deviation of the linear fits from the data shown in Fig. 16.

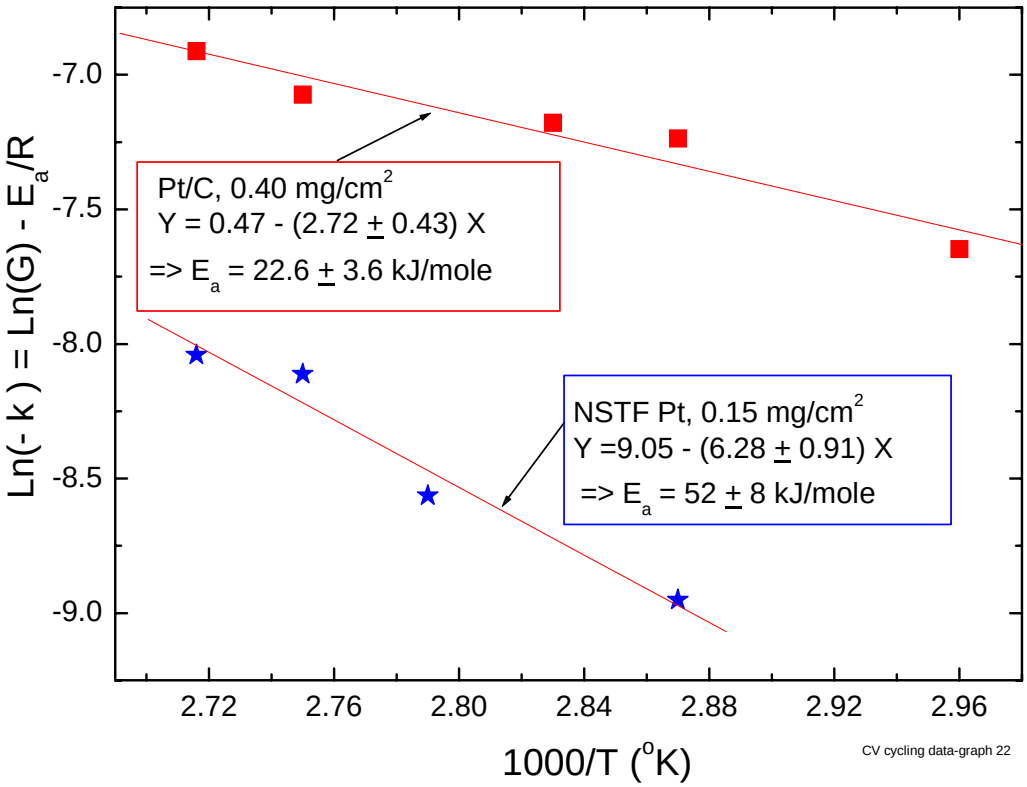

Fig. 16. Arrhenius plot of the linear slopes of the fitted lines from Figs. 8 and 9 as a function reciprocal temperature.

2.1.4.1.5. Conclusions

NSTF-Pt catalysts (0.15 mgPt cm^{-2}) are much more resistant to loss of surface area from high voltage cycling than are Pt/Carbon (Ketjen Black) with 0.4 mg Pt cm^{-2} loading. The NSTF-Pt asymptotically approaches a maximum of ~ 33% surface area loss in 9000 cycles, while the Pt/C loses ~ 90% of the initial surface area in 2000 cycles. The activation energy for surface area loss is twice as high for NSTF (52 vs 23 kJ/mole) reflecting a slower rate of surface area loss for NSTF. The NSTF surface area is therefore more stable due to two effects, the higher value of S_{min} and the slower rate of approach to that higher value with number of CV cycles. The surface area loss in both catalyst types appears to be primarily by agglomeration. Surface area loss of Pt/C is approximately 90%/2500 cycles, versus only ~20%/4225 cycles for the NSTF-Pt. Both anode and cathode Pt/C crystallite sizes increase 380% and 300% respectively, but the NSTF crystallite sizes increase only ~ 10% and 68% respectively. The thin film nature of the NSTF catalyst is very likely a key property enabling this enhanced stability, over and above that due to the initial larger Pt grain size. By this we mean the catalyst film's metal grains are contiguous and form a conformal layer enshrouding the NSTF whisker core. The NSTF-Pt grains are therefore already highly or even fully agglomerated. The CV cycling may still induce changes in the surface structure or roughness of the contiguous grains, changing the ratio of Pt[hkl] facets or defects such as steps and edges of single crystal planes. Such changes may be contributing to the measured changes in both surface area and specific activity of the NSTF catalysts.

The Pt/C dispersed catalyst particles are less stable both because the initial Pt nano-particle diameters are less stable than larger grain sizes, and because they are not contiguous so more Pt atoms can diffuse away from their parent Pt particle or the carbon support particle and become electrochemically inactive. Despite the increased Pt/C particle size, there does not appear to be any increase in catalyst specific activity or catalyst utilization to equal that of the NSTF since the Pt/C polarization curve performance is severely degraded, much more so than the NSTF-Pt.

Fuel cell stack cathodes can experience potentials between OCV under H_2/air (> 0.90V), and OCV under air/air (~ 1.23 V) during start-up and shut-down, and locally within the active area due to fuel starvation and oxygen cross-over effects. This is observed to lead to serious surface area loss by Pt dissolution and agglomeration [16-18]. Based on the accelerated tests reported above, NSTF catalysts should be more robust against shut down/start-up, operation near OCV and local H_2 starvation effects.

References for Section 2.1.4.1

1. H. A. Gasteiger, S. S. Kocha, B. Sompalli and F. T. Wagner, Applied Catalyssis B:Environmental **56** (2005) 9-35.
2. G. Haugen, David Stevens, Michael Hicks and Jeff Dahn, "Ex-situ and in-situ stability studies of PEM fuel cell catalysts: the effect of carbon type and humidification on the degradation of carbon supported catalysts," 2005 Fuel Cell Seminar, Palm Springs, CA, November 2005, poster No. 118.
3. D. Stevens, M. Hicks, G. Haugen and J. Dahn, "Ex situ and in situ stability studies of PEMFC catalysts: Effect of carbon type and humidification on degradation of the carbon," J. Electrochem. Soc., **152** (12), A2309 (2005).

4. Robert M. Darling and Jeremy P. Meyers, J. of Electrochem. Soc. **150**(11) (2003) A1523-A1527, J. of The Electrochemical Society **152**(1) (2005) A242-A247.
5. L. M. Roen, C. H. Paik and T. D. Jarvi, Electrochemical and Solid-State Lett., **7**(1) (2004) A19-A72.
6. S. D. Knights, K. M. Colbow, J. St-Pierre, and D. P. Wilkinson, J. of Power Sources **127**, (2004) 127-134.
7. M. K. Debe, in Handbook of Fuel Cells –Fundamentals, Technology and Applications, W. Vielstich, A. Lamm, H. A. Gasteiger, Editors, John Wiley & Sons, 2003, Ch. 45.
8. M. K. Debe, S. M. Hendricks, A. K. Schmoeckel, R. T. Atanasoski, G. D. Vernstrom, and G. M. Haugen, "Durability Aspects of Nanostructured Thin Film Catalysts for PEM Fuel Cells," in ECS Transactions-Durability and Reliability of Low-Temperature Fuel Cells Systems, 208th ECS meeting.
9. M. K. Debe, A. J. Steinbach, K. A. Lewinski, G. M. Haugen, G. D. Vernstrom, R. T. Atanasoski, A. E. Hester, P. L. Turner, R. J. Ziegler, J. M. Larson, M. T. Hicks and P. E. Serim, "Activities of Low Pt Loading, Carbon-Less, Ultra-Thin Nanostructured Film-Based Electrodes for PEM Fuel Cells, and Performances in Roll- Good Fabricated MEA's in Single Cells and Stacks," 2003 Fuel Cell Seminar, Nov. 3-6, 2003, Miami, FL.
10. M. K. Debe, A. K. Schmoeckel, R. Atanasoski, and G. D. Vernstrom , "High Voltage Stability of NanoStructured Thin Film Catalysts for PEM Fuel Cells," 2005 FC Seminar, Nov. 11-18, 2005, Palm Springs, CA.
11. M. K. Debe, "Advanced Catalyst and Membrane Technology with Enhanced Performance and Durability for Automotive Requirements," in proceedings, 4th International Fuel Cell Workshop 2005, Kofu, Japan, Sept. 22-24, 2005, page 62.
12. "VII.A.2 Advanced MEA's for Enhanced Operating Conditions," in DOE Hydrogen, Fuel Cells and Infrastructure Technologies Program FY 2005 Progress Report, page 672; and in DOE Hydrogen Program FY 2004 Progress Report, page 301.
13. Mark K. Debe, Susan M. Hendricks, Alison K. Schmoeckel, George D. Vernstrom, Radoslav T. Atanasoski, Paul J. Kadera, and Andrew J. Steinbach, "NanoStructured Thin Film, Thin Layer Electrodes Optimized for PEM Fuel Cell Peformance at High Current Density,", 2004 Fuel Cell Seminar, Nov.1-5, 2004, San Antonio, TX.
14. S. J. Hamrock, "The Development of New Membranes for PEM Fuel Cells," Advances in Materials for Proton Exchange Membrane Fuel Cell Systems, Asilomar Conference Grounds, Pacific Grove, CA, Feb. 21, 2005.
15. Joseph Frisk, Wayne Boand, Mike Hicks, Michael Kurkowski, Radoslav Atanasoski and Alison Schmoeckel , "MEA Component Durability,", 2004 Fuel Cell Seminar Nov. 1-5, 2004, San Antonio, TX.
16. Carl A. Reiser, Lawrence Bregoli, Timothy W. Patterson, Jung S. Yi, J. Deliang Yang, Mike L. Perry and Thomas D. Jarvi , Electrochemical and Solid-State Letters **8**(6) (2005) A273-A276.
17. Ping Yu, Marianne Pemberton, and Paul Plasse, J. of Power Sources **144** (2005) 11-20.
18. W. J. Plieth, J. Phys. Chem. **86**(16), (1982) 3166-3170.

2.1.4.2 NSTF Stability Under 1.5 V Hold

The next high voltage test involved holding the electrodes at 1.5 volts under saturated H_2/N_2 for 30 minute periods at 80°C. Under these conditions, the Pt catalysts might be expected to be passivated as oxides, while carbon support corrosion would be the significant instability mechanism. Fig. 17 compares a series of CVs from the NSTF-Pt catalysts obtained initially and then after 30, 60, 90, and 180 minutes at 1.5 volts. There is remarkably little change. In contrast, Fig. 18 shows the change in the CV from the Pt/C (50 wt% Ketjen Black) after just one 30 minute period. Except for the appreciable decrease in the H_{upd} envelope and low "quality" of the H_{upd} peaks, it is worth noticing the quinone– hydroquinone redox peaks around 0.6 V, indicating the outcome of the carbon oxidation that had taken place during the 1.5 V exposure.

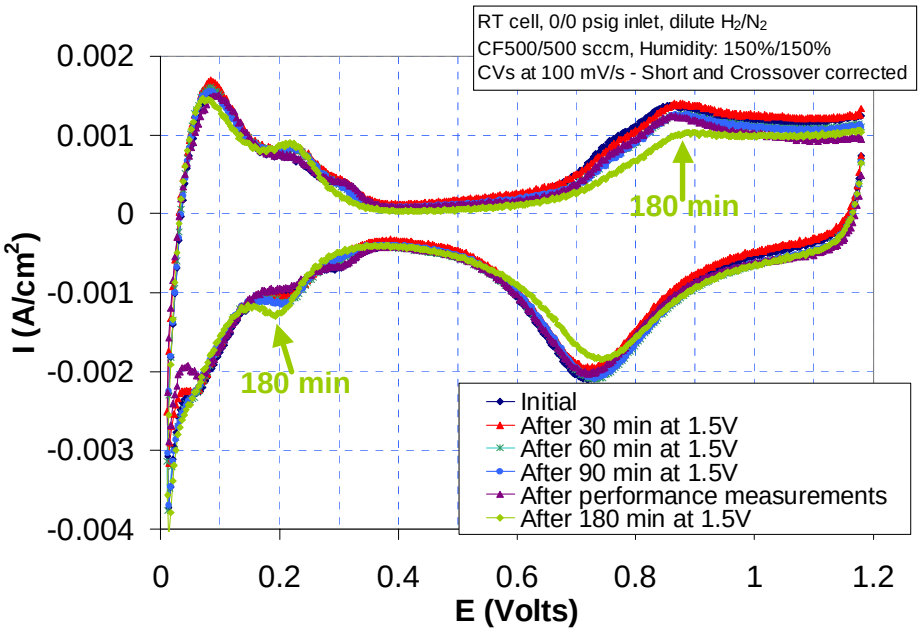

Fig. 17. Series of CV plots from the NSTF Pt MEA after 0, 30, 60, 90 and 180 minutes of constant potential at 1.5 volts under H_2/N_2.

Fig. 19 compares the surface area changes for the two types of catalysts after the same 30 minute increments. The ECSA of the NSTF catalysts are not changed to within experimental error even after a total of 3 hours at 1.5 volts, whereas the Pt/C has lost 64% of its surface area in 30 minutes.

The impact of the 1.5 volt hold on Pt/C catalyst kinetics is greater than just the surface area loss, however. In order to visualize these changes, AC impedance measurements were performed under diluted hydrogen (~1% in nitrogen) on the cathode side (working electrode) and 100% hydrogen on the anode side (counter and reference electrode). The AC impedances are equally dramatically different, as shown in Fig. 20. While at the beginning of the test the high frequency intercept is practically equal for both types of catalysts, indicating the same ohmic resistance, the semi-circle is much smaller for the dispersed catalysts, indicating the larger surface area of the "as received" dispersed platinum on carbon that is reflected in the total hydrogen kinetics. After testing, the NSTF electrodes show no change in the resistive component or in the hydrogen kinetics up to 90 minutes of exposure at 1.5 V and only a slight increment in the semi-circle after

180 minutes. However, the dispersed carbon-supported catalyst shows increases in both the high frequency impedance as well as in the hydrogen kinetics that go beyond what can be attributed to the decrease in Pt surface area. As pointed out in Fig. 19, even though substantially decreased, the Pt/C surface area after the 30 minutes at 1.5 V is still 8 times higher than that of NSTF platinum. Hence, the source of these additional AC impedance or charge transfer impedance changes can be attributed to other effects, such as corrosion of the carbon support, changes in the carbon – Pt bonding, or reconstruction of the platinum particles themselves (see Fig. 18).

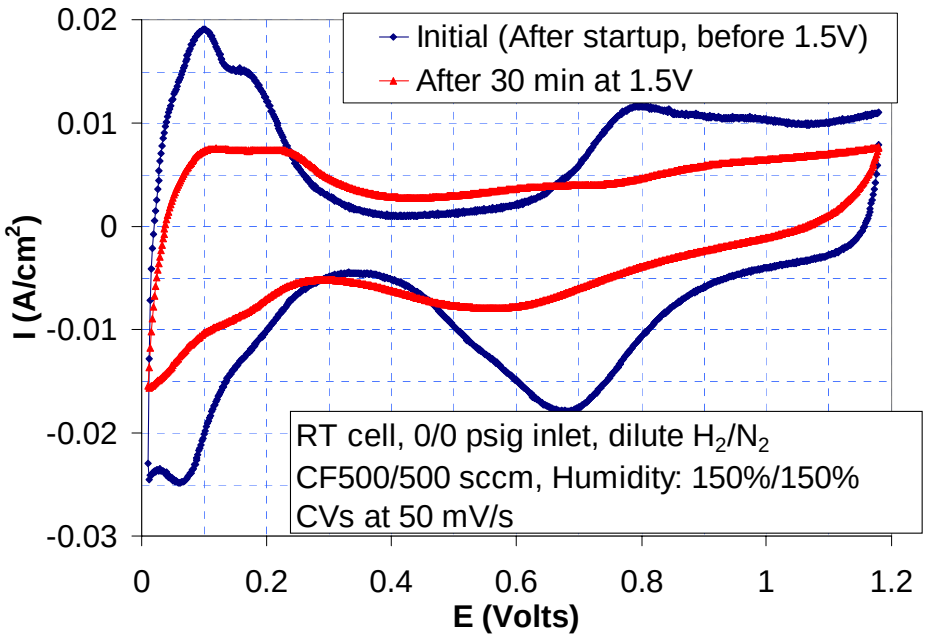

Fig. 18. CV plots from the MEA with Pt/C catalysts initially and after 30 minutes of constant potential at 1.5 volts under H_2/N_2.

The fuel cell performance changes are compared in Figs. 21 for the same 1.5 volt exposures of the Pt/C and NSTF-Pt catalyzed MEAs. Shown are the potentiodynamic (PDS), constant flow, polarization scans obtained at ambient pressure and 50% inlet RH. The PDS(0.85, 0.25, 0.048, 10 s/pt) means the potentiodynamic scans began at 0.85 volts, decreased to 0.25 volts in 48 mV steps at 10 seconds/pt, and then returned to 0.85 volts. Whereas there is no detectable change in the NSTF polarization curve after a total of three hours at 1.5 volts, the Pt/C MEA shows a dramatic loss in performance reflecting not only the significant loss in electrochemically active surface area but also the significant increase in charge transfer impedance suggested above.

Fig. 22 summarizes for an MEA having the NSTF-Pt ternary catalyst on the cathode and anode (0.20 mg/cm^2 loading per electrode), the impact of a 1.5 volt, 30 minute exposure on the CV curve, surface area and PDS polarization curve. As with the pure Pt NSTF catalyzed MEA, the NSTF ternary catalyst shows no loss of surface area, specific activity, conductivity, or mass transport overpotential due to the high voltage exposure.

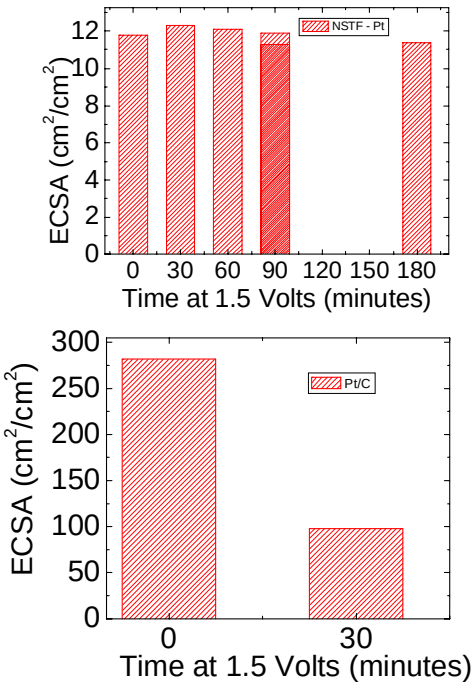

Fig. 19. Comparison of ECSA from: (top) the MEA with NSTF Pt catalysts before and after 30, 60, 90 (measured twice) and 180 minutes at 1.5 volts, and (bottom) the MEA with Pt/C catalysts before and after 30 minutes at 1.5 volts.

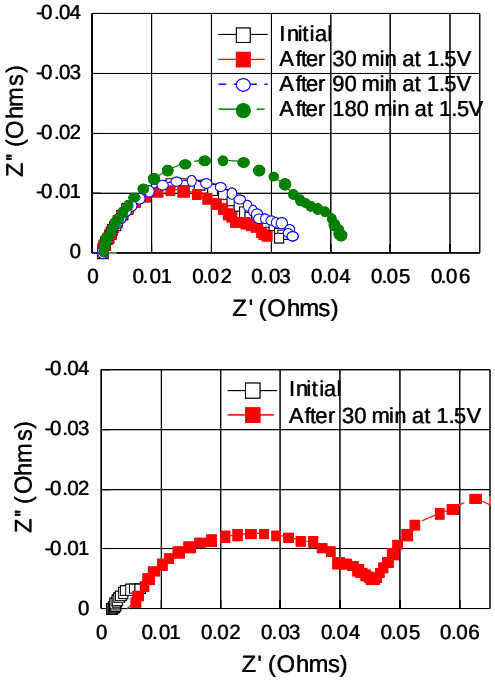

Fig. 20. Comparison of AC impedance plots from: (top) the MEA with NSTF Pt catalysts before and after 30, 90 and 180 minutes at 1.5 volts, and (bottom) the MEA with Pt/C catalysts before and after 30 minutes at 1.5 volts.

To conclude this section on electrochemical resistance to support corrosion, we show in Fig. 23 that even holding the MEA for 8 hours at 1.5 volts has also had not deleterious effect on the fuel cell perfomance. This particular MEA had what will be seen to be the down-selected catalysts (see section 2.1.5) viz. PtCoMn(90:10)[50,3,1]. MEA's were fabricated with this NSTF catalyst on both the anode and cathode at the same loadings of 0.2 mg-Pt/cm^2. The catalysts and CCM's were fabricated as roll-goods using the 3M 850EW membrane and tested with proprietary coated GDL paper backings in 50 cm^2 quad serpentine flow field cells.

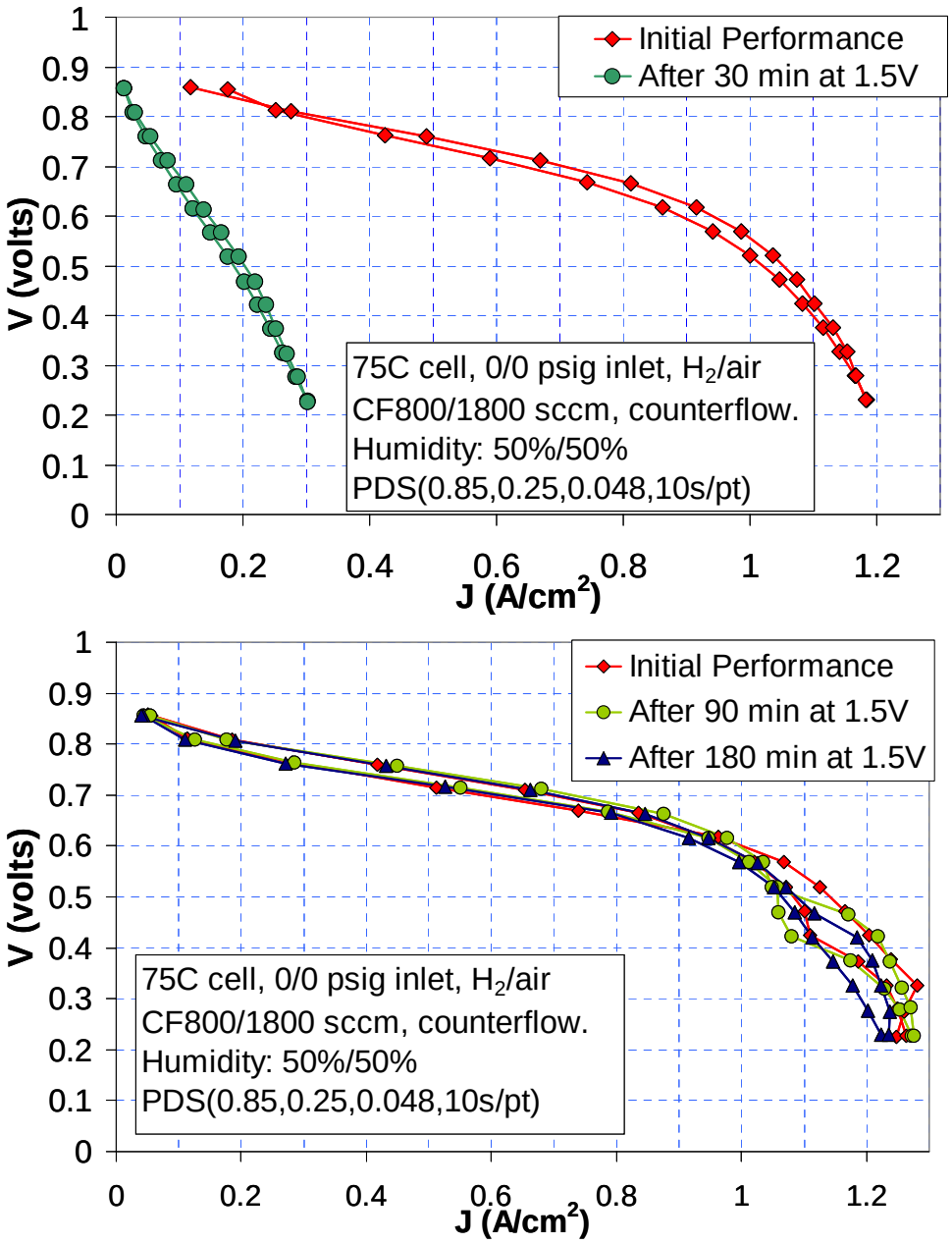

Fig. 21. Potentiodynamic, constant flow polarization curves at ambient pressure obtained from: (top) the MEA with Pt/C catalysts before and after 30 minutes at 1.5 volts; and (bottom), the MEA with NSTF Pt catalysts before and after 90 and 180 minutes at 1.5 volts. The Pt/C loadings were 0.4 mg/cm^2 on anode and cathode and had specific surface areas of 192 m^2/g-Pt. The NSTF-Pt loadings were 0.15 mg/cm^2 on anode and cathode and had mass specific area of ~ 10 m^2/g-Pt.

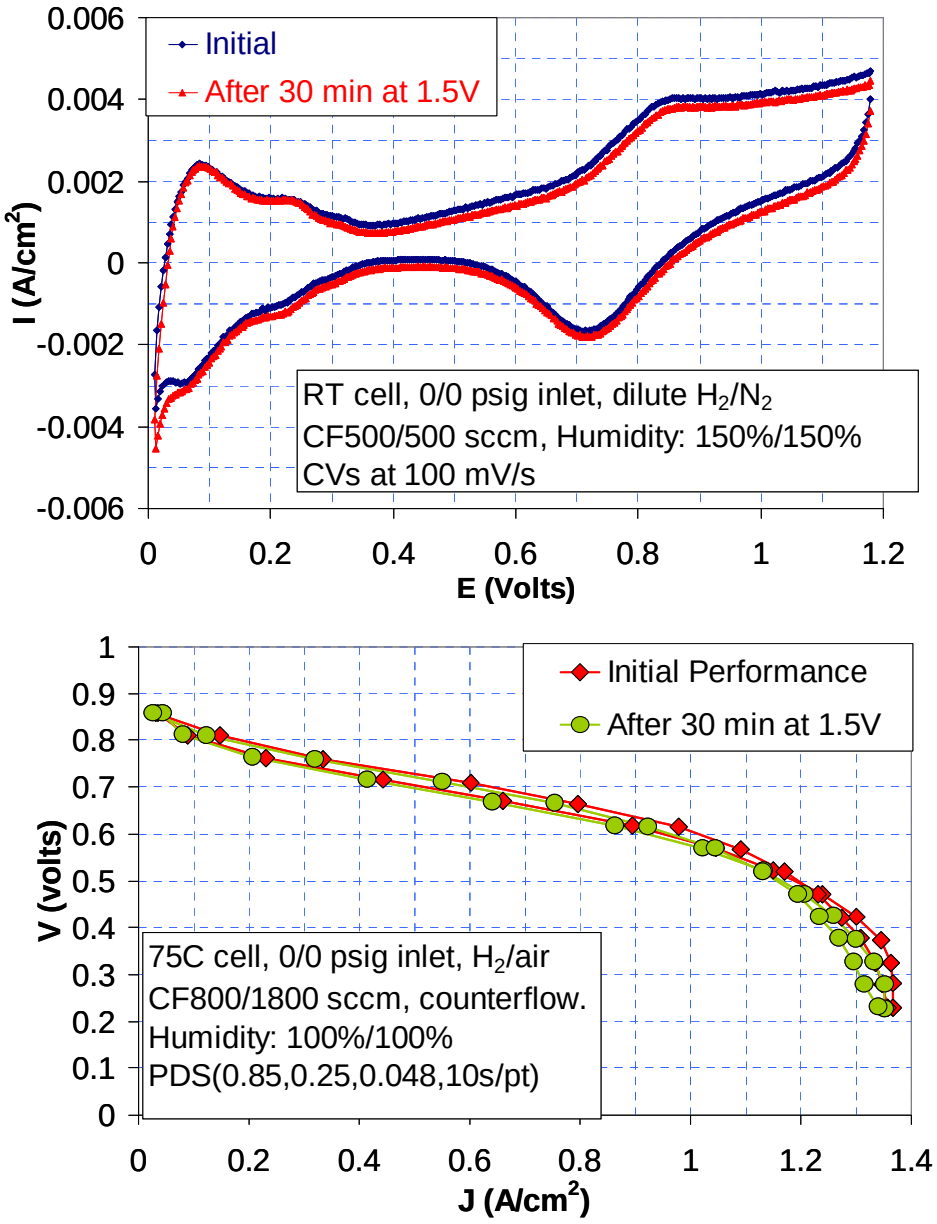

Fig. 22. Effect of 30 minute exposure at 1.5 volts under H_2/N_2 on an MEA having the NSTF Pt ternary cathode catalyst on: (top) CV scans for surface area - the surface area was 17.2 before exposure, and 17.9 cm^2/cm^2 after exposure; (bottom) potentiodynamic, constant flow polarization curves at ambient pressure and 100%RH. Pt content of the ternary catalyst was 0.20 mg/cm^2 on both anode and cathode.

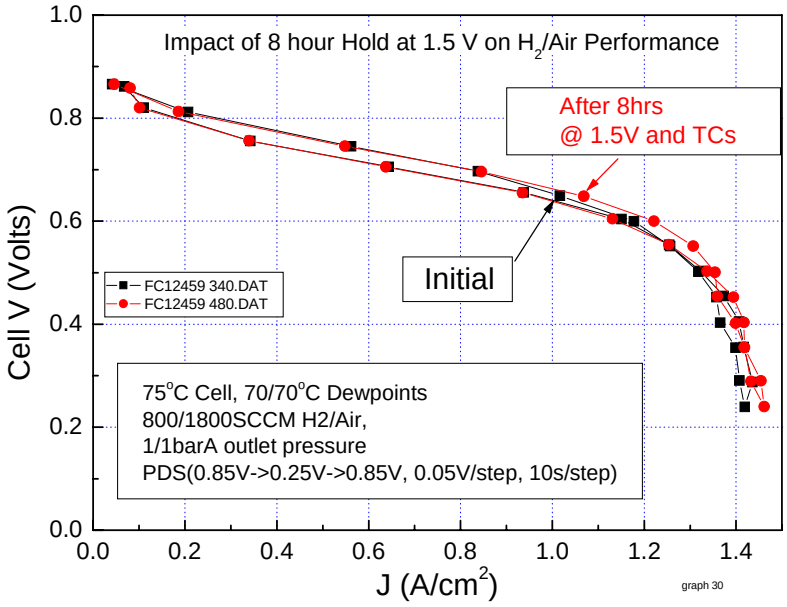

Fig. 23. Comparison of PDS polarization curves for an NSTF MEA with the down-selected PtCoMn catalysts on both anode and cathode, before and after 8 hours hold at 1.5 Volts under H_2/N_2.

2.1.4.3 NSTF Stability Under 120°C Stress Tests.

Introduction

This durability test focused on determining the lifetime to failure of the whole MEA when operated at 120°C. The original objective was to document the stability of the catalyst surface area over time, but it ultimately revealed that the very low flouride release rates characteristic of the NSTF catalyts also led to significantly enhanced lifetimes of the membranes at these temperatures. The 120°C temperature represented the maximum possible for the MEAs developed in Task 1.

These durability tests continued over a period of two years or more and involved a total of over two dozen MEA's. During that period the test protocol was developed and refined, a series of NSTF catalysts were screened and compared to Pt/C dispersed catalysts evaluated as controls, and several membrane options and four types of GDLs were explored. Initially, during development of the test protocol, the first few MEAs were evaluated in 50cm^2 cells on a test station in the St. Paul fuel cell laboratory. After that, the testing was conducted on larger production-control test stations at the 3M Menomonie, WI, fuel cell facilities. All these samples were 100 cm^2 MEAs, tested in cells with a 7 channel serpentine flow field. The summary of the results from these 120°C stress tests begins with these larger cell tests.

2.1.4.3.1 Experimental

The objective of the tests were to operate the cells continuously at 120°C under pressurized conditions, in a constant current mode, while monitoring the cell voltage for a period of time, followed by various diagnostics to characterize the state of the MEA components. The high temperature heating would then resume and the process repeated. Based on initial tests in smaller 50 cm^2 cells, and the daily production lab schedules where the cells would be tested, the period of time between diagnostics was chosen to be 20 hours, followed by four hours of diagnostics. This conveniently then allowed a script to be written for routine daily operation of the test stations. Some modifications to the test stations and cells had to be made to allow safe operation at 120°C, as well as some minor equipment changes found necessary to avoid contaminating the MEA from overheated components of the test station.

MEA definition

Table III summarizes the construction of the sequence of MEAs tested under the protocol described below. It does not include the samples used to develop the protocol. The 3M ionomer equivalent weight was ~ 1000 for all the 3M membranes used. Where indicated as pre-cleaned, the membranes were acid washed and rinsed in DI water, and dried before making into CCMs. Only neat ionomer was used; no additives for peroxide mitigation were used in the membranes. The 3M cast membranes were in the 1.2 to 1.5 mil thickness range. The type of catalyst, type of membrane and type of GDL all seemed to make a difference in the durability under this test. The second to the last column shows the total number of hours under test, including all the diagnostic testing at 70 – 80°C, until membrane failure occurred as evidenced by severe cross-over and loss of open circuit voltage. The last column shows the actual hours of operation at 120°C before MEA failure occurred, usually by a perforated membrane. Several of the NSTF MEAs were seen to exceed 1000 hours at 120°C, significantly longer than the Pt/C

controls. These lifetimes were found to correlate directly with the fluoride ion release rates from the different types of MEA's, as discussed below.

Table III. Summary of the 100 cm^2 MEAs tested using the 120°C stress test protocol.

8766	PtNiFe, 0.15	PtNiFe, 0.15	1.8 mil 3M cast Nafion	Paper Typer B	Station issue		
8859	PtNiFe, 0.15	PtNiFe, 0.15	1.8 mil 3M cast Nafion	Paper Typer B	Completed	119	73
8911	PtNiFe, 0.15	PtNiFe, 0.15	Nafion 112	Paper Typer B	Bad cell		
8950	PtNiFe, 0.15	PtNiFe, 0.15	Nafion 112	Paper Typer B	Station issue		
8957	PtNiFe, 0.15	PtNiFe, 0.15	Nafion 112	Paper Typer B	Bad cell		
8974	Pt, 0.15	PtCoFe, 0.10	1.1 mil 3M cast Nafion	Cloth	Completed	< 48 hours	21
9033	PtCoMn(90:10) [20,1.2,1], 0.10	PtCoMn(90:10) [20,1.2,1], 0.10	3M ionomer, pre-cleaned	Cloth	Cell T recalibrated, %RH	540	285
9168	PtCoMn(90:10) [20,1.2,1], 0.10	PtCoMn(90:10) [20,1.2,1], 0.10	3M ionomer, pre-cleaned	Paper Typer B	Completed	430	217
9320	PtCoMn(90:10) [20,3,1], 0.10	PtCoMn(90:10) [20,3,1], 0.10	3M ionomer, pre-cleaned	Paper Typer B	Completed	470	152
9449	PtCoMn(90:10) [20,3,1], 0.10	PtCoMn(90:10) [20,3,1], 0.10	3M ionomer, pre-cleaned	Paper Typer B	Completed	170	96.1
9486	PtNiMn(50:50) [20,1.2,1], 0.10	PtNiMn(50:50) [20,1.2,1], 0.10	3M ionomer, pre-cleaned	Paper Typer B	Completed	567	356
9585	PtNiMn(90:10) [20,3,1], 0.10	PtNiMn(90:10) [20,3,1], 0.10	3M ionomer, pre-cleaned	Paper Typer B	Completed	302	213
9708	PtNiMn(90:10) [20,3,1], 0.10	PtNiMn(90:10) [20,3,1], 0.10	3M 1000EW + 1% Mn	Paper Typer B	Completed	381	231
9824	PtCoMn(50:50) [10,1.2,1], 0.10	PtCoMn(50:50) [10,1.2,1], 0.10	3M ionomer, pre-cleaned	Paper Typer B	Completed	1825	**1082**
9917	Pt/C Dispersed, 0.2	Pt/C Dispersed, 0.2	3M ionomer, pre-cleaned	Paper Typer B	Completed	190	133
10066	PtCoMn(50:50) [10,1.2,1], 0.10	PtCoMn(50:50) [10,1.2,1], 0.10	3M ionomer, process M	Paper Typer B	Completed	1765	**1025**
10067	Pt/C Dispersed, 0.4	Pt/C Dispersed, 0.4	3M ionomer, pre-cleaned	Paper Typer B	Completed	157	110
10461	PtCoMn(50:50) [10,1.2,1], 0.10	PtCoMn(50:50) [10,1.2,1], 0.10	3M ionomer, process M, cleaned	Paper Typer F	Completed	1462	**1004**
11071	PtCoMn(50:50) [10,1.2,1], 0.10	PtCoMn(50:50) [10,1.2,1], 0.10	3M ionomer, process M, cleaned	Paper Type M	Completed	720	520
10837	PtCoMn(50:50) [10,1.2,1], 0.10	PtCoMn(50:50) [10,1.2,1], 0.10	3M ionomer, process M, cleaned	Paper Type M	Completed	669	514
10296	PtCoMn(50:50) [10,1.2,1], 0.10	PtCoMn(50:50) [10,1.2,1], 0.10	3M ionomer, , process M, cleaned	Paper Typer B	Tested at 120, 110,100, 90 °C	~ 750	N.A.
11225	PtCoMn(50:50) [10,1.2,1], 0.10	PtCoMn(50:50) [10,1.2,1], 0.10	3M ionomer, process M, cleaned	Paper Typer B	Completed	1350	**934**

Test protocol

Once the 100 cm^2 cells were loaded with the MEAs, they were conditoned on the test stations in St. Paul. Once broken-in, they were transferred to the production stations at Menomonie for the 120°C stress tests. The cells were operated in a galvanostatic mode, (GSS) at 0.4 A/cm^2, with 30/30 psig H_2/air inlet pressures, flow rates of 724/1326 sccm (equivalent to constant stoichs of 2.6/2.0) and inlet humidifications of 61%/84% on the anode and cathode respectively. This %RH and current density would in principle give a water balance of ~1.1, meaning the outlets would just be over saturation. Water was injected into the reactant inlet streams at controlled rates of 0.66/1.44 cc/min to achieve

these humidification levels. The cell was operated under these conditions for 18 hours (or longer over weekends), while monitoring the cell voltage. During the last ~ 2 hours of this period, water was collected from the anode and cathode effluents for measurement of the fluoride ion content, as described in section 2.1.5.2. After this the cell was cooled to 70°C to begin the diagnostics.

The first diagnostic was measurement of the anode and cathode electrochemical surface area, done at ambient pressure, 200%RH and 70°C. The method is described above in more detail in section 2.1.3. Following this, the cell was set at OCV for 5 seconds at 75°C cell and 70°C dewpoints. A potentiodynamic scan (PDS) from 0.85 volts to 0.25 volts in 50mV steps at 10 seconds per point was then acquired at the same 75/70/70 °C cell and dew point temperatures. (Again, see section 2.1.3 for more details). Once the diagnostics were completed, the cell temperature was elevated to 120°C and the cell operated in the GSS 0.4 A/cm^2 mode again for another ~ 18 hours. This cycle was repeated until MEA failure occurred.

2.1.4.3.2 Results

Cell voltage versus time behavior

Every cell that was tested exhibited the same overarching behavior of cell voltage at 0.4 A/cm^2 versus time illustrated in Fig. 24 for the NSTF MEA FC9824. During each ~ 18 hour period at 120°C, the cell voltage would decay at a rapid rate that was initially exponential (discussed below), until stopped for the diagnostics. After the diagnostics were completed and the cell returned to the 120°C stress portion of the next cycle, much of the cell potential was recovered. This behavior would repeat each cycle with the peak cell voltage recovered at the start of each cycle and reducing slowly over time. Although not readily apparent from Fig. 24 but discussed later, the exponential decay also became faster as the number of cycles continued. The reason for this decay is discussed below but believed to be due to the effects of catalyst activity or surface area loss from the effects of impurities generated by the degradation of the membrane.

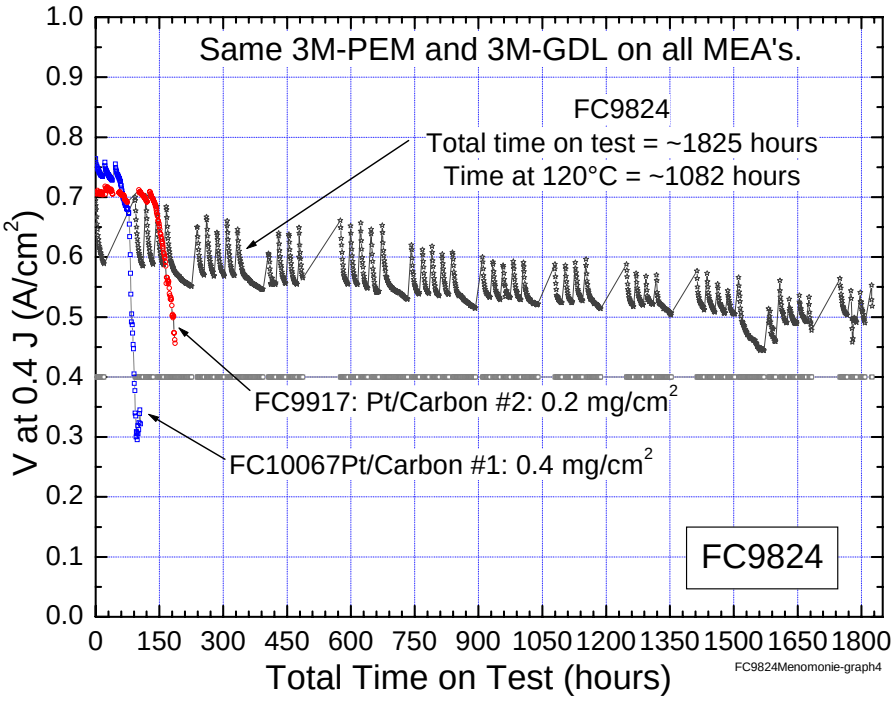

Fig. 24. Example behavior of the cell voltage at 0.4 A/cm^2 versus time observed for every sample tested.

In Fig. 24 the same behavior was seen for the two Pt/C dispersed MEA's, which as seen in Table II, had the identical 3M membrane and GDL types, but the time to failure was over an order of magnitude shorter. The cyclical variation in cell voltage is still seen with the dispersed catalysts, but with much reduced amplitude. A possible hypothesis to

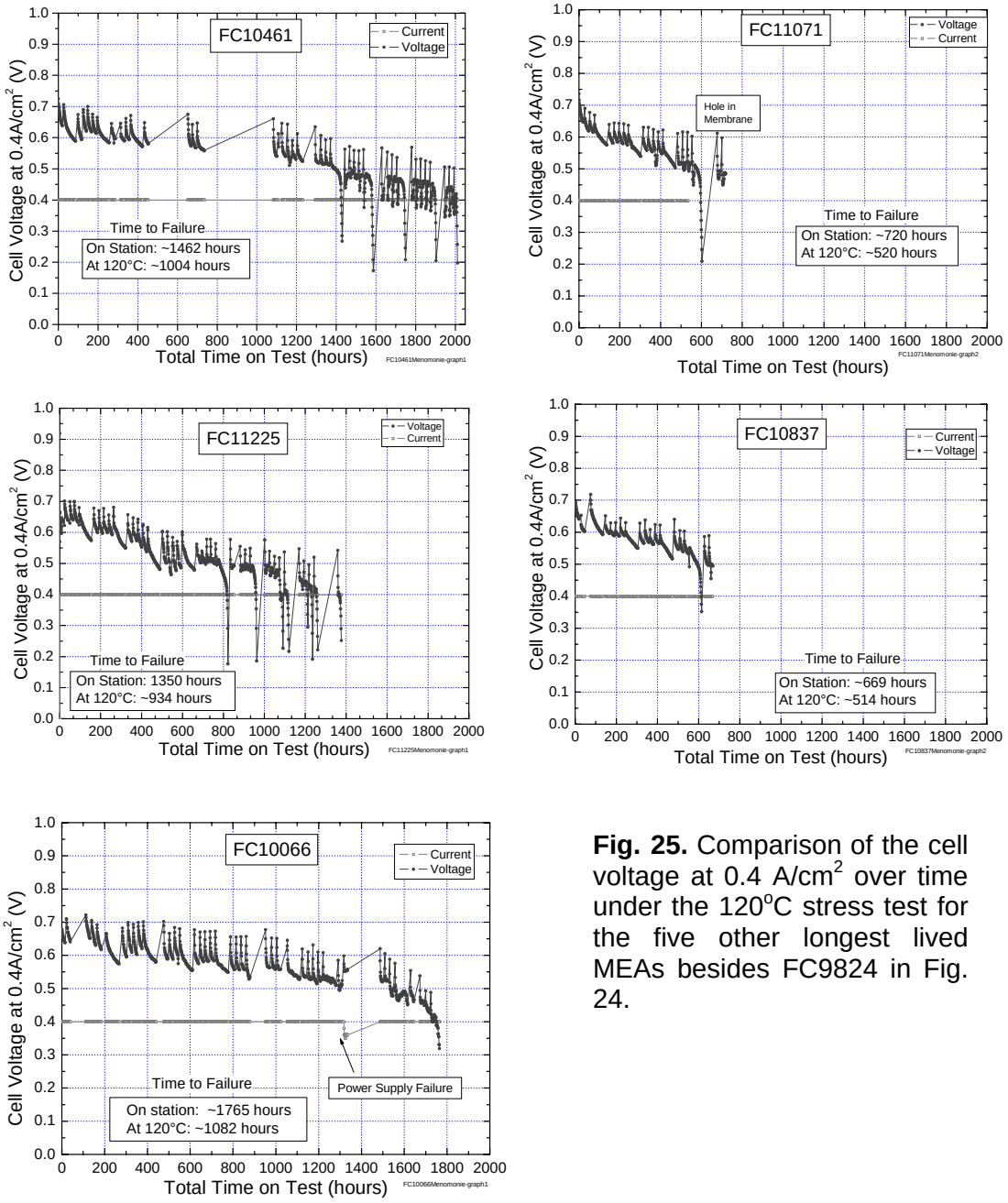

Fig. 25. Comparison of the cell voltage at 0.4 A/cm^2 over time under the 120°C stress test for the five other longest lived MEAs besides FC9824 in Fig. 24.

explain this at this time is that due to the orders of magnitude higher surface area of the dispersed catalysts compared to the NSTF catalysts, the percentage rate of loss of surface area due to poisoning is proportionately slower.

Fig. 25 summarizes the cell voltage versus time behavior for a subset of the samples in Table III that had lifetimes exceeding 500 hours. The primary difference of the four MEAs that survived at 120°C for ~ 1000 hours versus the two that failed at ~ 500 hours

was the type of GDL. The longer lived four had the type B carbon paper while the shorter lived two had the type M carbon paper.

Surface areas, cross-over, short resistance and F^- ion release rates

The diagnostic results were also very informative. The left panel in Fig. 26 plots for FC9824 (see Fig. 24), the peak voltage at the start of each daily cycle and also the measured total fluoride ion release levels versus the stress test cycle number. It is seen that the peak voltage at 0.4 A/cm^2 decayed gradually at a rate of - 3.1 mV per cycle or the equivalent of - 77microvolts/hr of testing time. The fluoride ion release rate remained extremely low at ~ .05 micrograms/min or < 24 nanograms/cm^2-hr over the whole period.

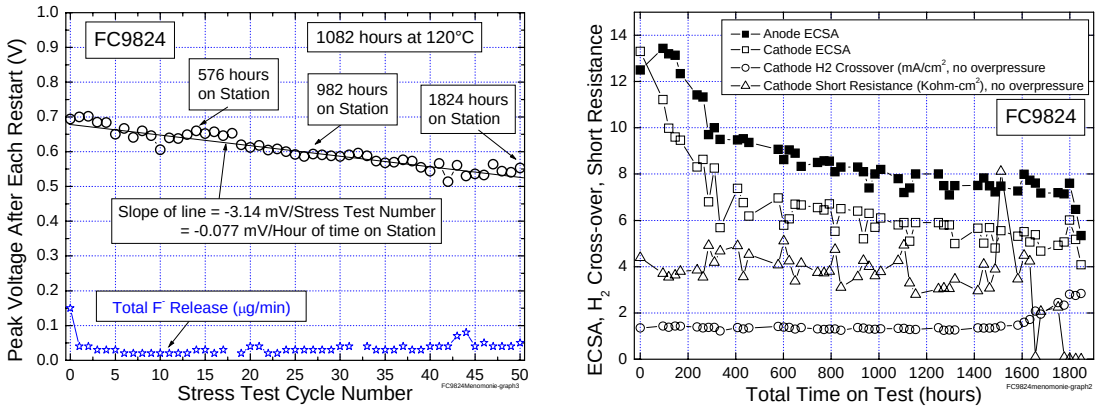

Fig. 26. Summary of the diagnostic results for FC9824 taken on each cycle thorughout the 120°C stress tests: (left) Variation of the peak cell voltage at the start of each cycle and the total fluoride ion release rates versus the cycle number, and (right) variation of the anode and cathode ECSAs, hydrogen cross-over and short resistance values versus total time on test.

In the right panel of Fig. 26, the anode and cathode surface areas, hydrogen cross-over and shorting resistance, as extracted from the ECSA measurements, are plotted versus the total time on test. The cathode and anode are seen to lose approximately half the Pt surface area over the test time, most of it in the first 500 hours. The H_2 cross-over is seen to remain constant until near the end, indicating greater permeation through the membrane due to the start of hole formation or significant membrane thinning. Post mortem inspection revealed no visible hole, but a general greying in the color the CCM. Likewise, the short resistance stayed fairly constant throughout the period, an indication that carbon fibers from the GDL had not penetrated the membrane nor had it thinned.

Figs. 27 and 28 summarize the diagnostic results for the other MEA's shown in Fig. 25 and compares them to FC9824. Fig. 27 plots the peak voltage at 0.4 A/cm^2 after each cycle restart and the total fluoride ion release rate measured at the end of each 120°C cycle period. All the peak voltage decay rates in are remarkably equivalent, at 0.20 $\pm$ 0.01mv/hr at 120°C, for FC11071, 10837, 11225 and 10461, but reduced to ~ 0.14$\pm$ 0.01mv/hr for FC9824 and FC10066. The Fluoride ion release rates remain at lower values for longer periods of time for the latter two MEAs before they start to increase.

Fig. 28 plots the variation of the anode and cathode ECSAs, hydrogen cross-over and short resistance values versus total time on test for these NSTF MEA's. The anode

surface areas all decay by about one-third to ~8 cm^2/cm^2, and the majority of the change occurs in the first 400 hours. The trend is not inconsistent with an exponential decay.

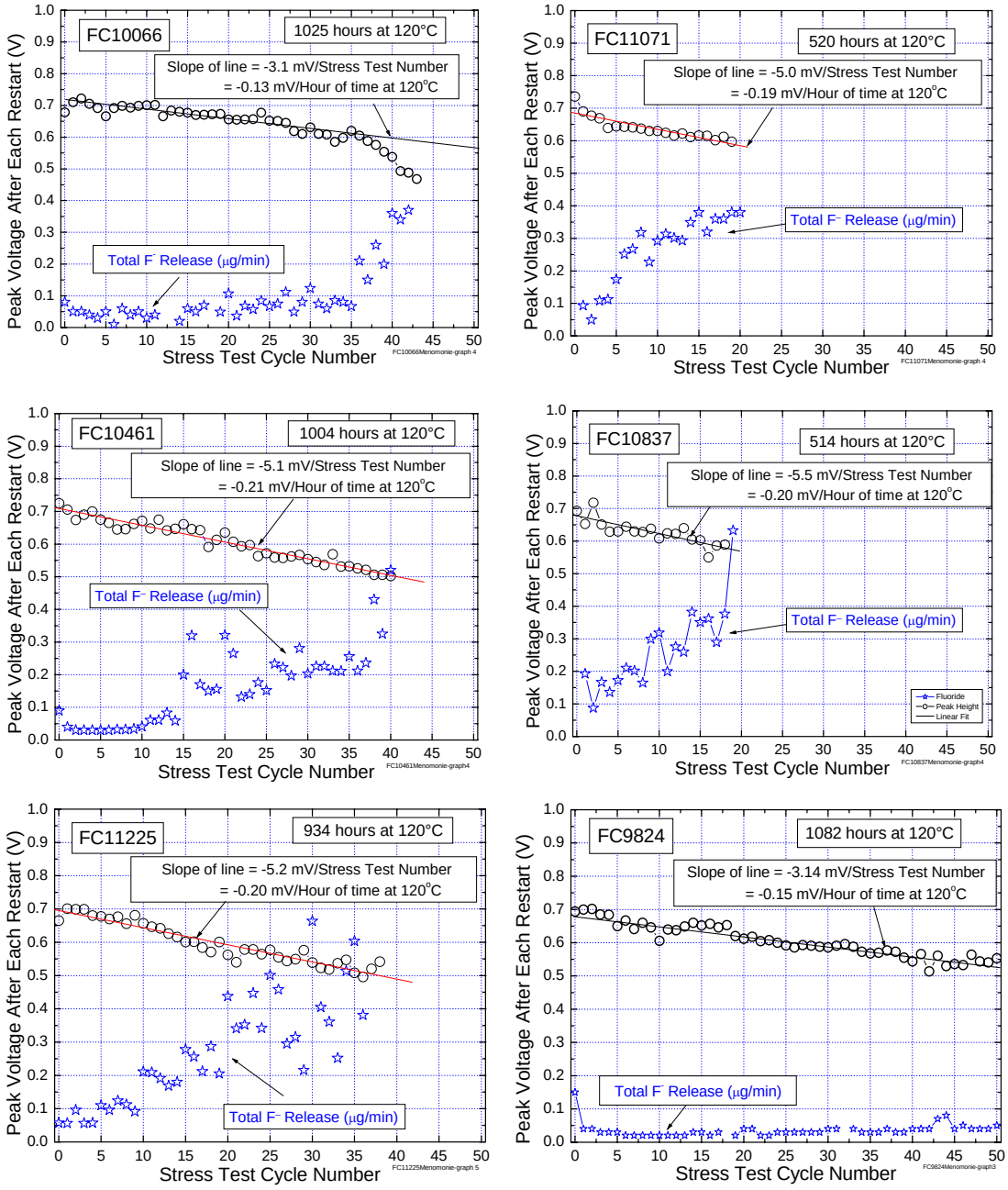

Fig. 27. Summary of the diagnostic results for all the NSTF MEA's that lived longer than 500 hours taken on each cycle thorughout the 120°C stress tests. Shown is variation of the peak cell voltage at the start of each cycle and the total fluoride ion release rates during the last two hours of each period at 120°C, versus the cycle number.

The cathode surface areas appear to decay about the same or slightly more than the anode in each case, and follows a similar trend with time. Roughly speaking, once the initial surface area loss occurs over the first ~400 hours, it then remains fairly constant

even though Fig. 27 shows that the cell voltage continues to decrease at a uniform rate. The hydrogen cross-over and shorting resistance values remain essentially unchanged throughout the testing time.

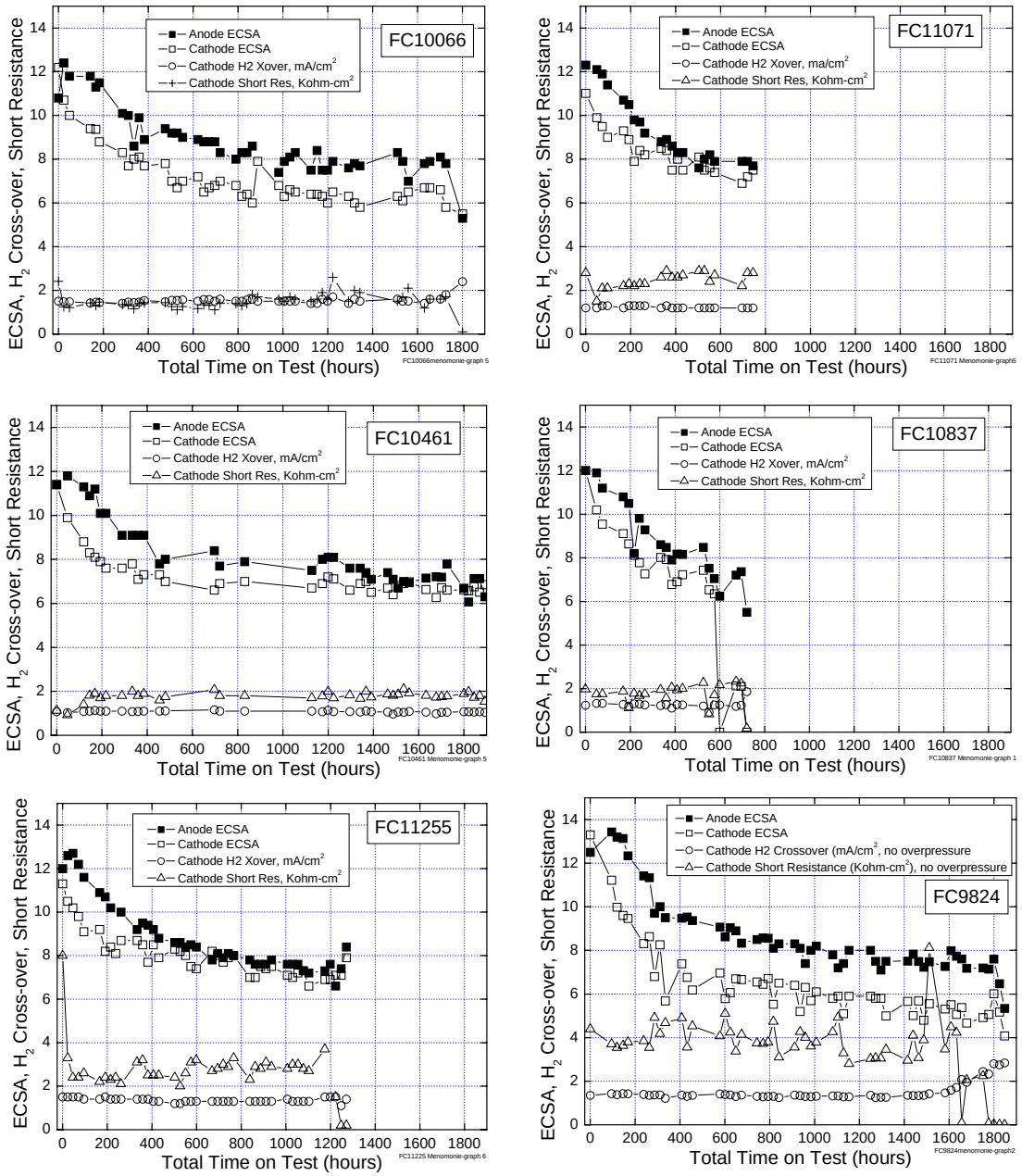

Fig. 28. Summary of the diagnostic results for all the NSTF MEA's that lived longer than 500 hours taken on each cycle thorughout the 120°C stress tests. Shown is variation of the anode and cathode ECSAs, hydrogen cross-over and short resistance values versus total time on test.

Pt/C Controls

The two control MEA's with Pt/Carbon electrodes had very short lifetimes at 120°C as shown in Fig. 24, so very few cycles were completed. Fig. 29 compares the measured ECSA for the two MEAs as a function of cycle number, as well as the short resistance

2.1.4.3 NSTF Stability Under 120°C Stress Tests

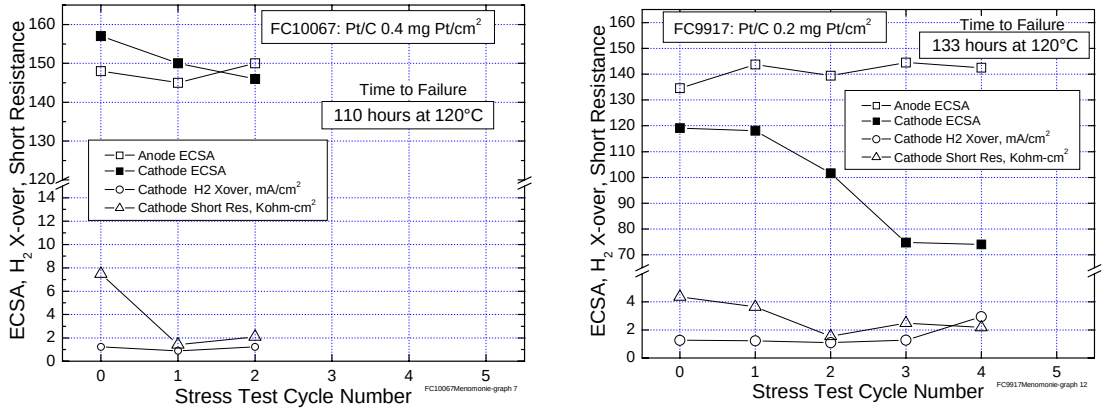

Fig. 29. Variation with cycle number of the anode and cathode surface areas, cross-over and short resistance values for the two controls with Pt/C electrodes.

and hydrogen cross-over values. There are both similarities and differences in the behavior of the two samples with different cathode loadings. For both MEA's the anode ECSA is seen to be fairly constant over the 110 hours of testing time at 120°C until the membrane failed. However the cathode ECSA decreases for both and most dramatically for FC9917 with the lower loading of Pt. In just two cycles, (~ 35 hours) at 120°C, its cathode lost about 40% of its surface area. This is ~ 1%/hr in contrast to the NSTF MEAs in Fig. 28 that lost about 30% of their surface area in 400 hours, or < 0.1%/hr. The NSTF anode ECSA values in Fig. 28 also increased for the first few cycles, so no long term comparison of the Pt/C is possible. The Pt/C in FC9917 is commerically available (TKK) type TEC10E20A, 20 wt% Pt dispersed on carbon having 800 m^2/g specific area and 1 nm Pt particle size. The Pt/C in FC10067 was NECC SA50BK with 3nm Pt dispersed onto carbon with 330 m^2/g BET surface area.

The most dramatic difference in the diagnostic measurements between the NSTF and Pt/C MEAs however was the fluoride ion release rates. These are plotted in Fig. 30 with the peak voltage values at the start of each cycle.

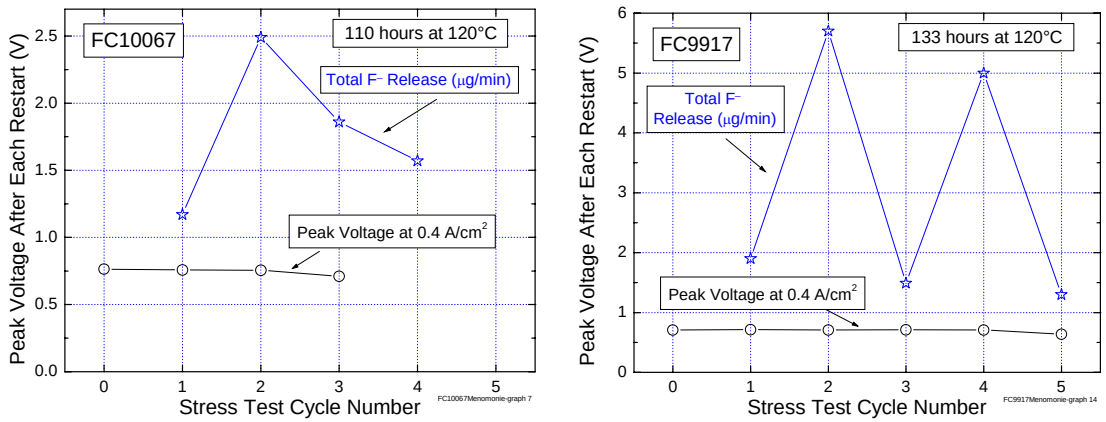

Fig. 30. Plots of the peak cell voltage at 0.4 A/cm^2 at the start of each cycle and the fluroide ion release rates measured at the end of each cycle for the two Pt/C dispersed control MEAs.

2.1.4.3 NSTF Stability Under 120°C Stress Tests

In contrast to the scale of the analogous plots for the NSTF MEAs in Fig. 27, the scale in Fig. 30 is significantly larger because the F^- ion release rates are nearly two orders of magnitude larger.

Table IV compares the average total F^- ion release rates, number of values used for computing that average, and lifetimes to failure for a number of the NSTF and Pt/C MEAs in Table III that had similar membranes and GDLs . The averaged F^- values are from the first ten cycles, usually the most stable period at the beginning of the test period, unless it was stable for more cycles in which case more were used to find the average, or fewer if there were less than 10 cycles total in the test.

Table IV. Summary of average total fluoride ion release rates and liftetimes to failure for the PtCoMn or PtNiMn and PtC electrode samples from Table III.

MEA FC ID	**Avg. Total F^- Ion Release Rate** µg/min | # Values Avrg'd		**Time at 120°C to MEA Failure (hrs)**
9917	2.99	6	87
10067	1.77	4	68
9824	0.034	47	1082
10066	0.043	15	1025
9486	0.06	15	356
9168	0.06	6	217
10461	0.042	10	1004
11225	0.086	10	934
10837	0.195	10	514
11071	0.22	10	520
9708	0.41	8	231
9033	0.13	8	285
9585	0.20	6	213
9320	0.21	6	152

Comparison with Table III indicates those MEAs that had the same PtCoMn(50:50)[10,1.2,1] ternary for the catalysts, viz: FC 9824, 10066, 10461, 11071, 10837, and 11225. The total lifetime hours at 120°C for these and the two Pt/C MEAs are plotted versus their average total F^- ion release rates in Fig. 31. A very consistent trend is apparent in Fig. 31 for the dependence of lifetime on the average initial fluoride ion release rate. We note again that for the two NSTF MEA's with lifetimes of approximately 500 hours, versus the four at ~1000 hours, the primary difference was the type of GDL carbon paper backing. Considering where the other MEAs in Table IV would be plotted on Fig. 31, it is apparent that those with the PtNiMn series of electrodes were not as robust as the PtCoMn series in Fig. 31. Similarly, the initial PtNiFe series of MEA's used at the very beginning of the test development period in Table II had even poorer lifetimes, some of which is probably due to the fact that Fe is known to facilitate peroxide radical formation.

In summary, the best NSTF MEA lifetimes under this 120°C stress test are 15 to 20 times longer than the dispersed Pt/Carbon MEAs, and the MEA lifetimes appear to scale logarithmically with the average F^- ion release rates. The loss of performance, cell voltage at 0.4 A/cm^2, degrades linearly with time at 120°C. Some of this is related to loss of catalyst surface area, which decays by approximately 1/3 over the first 400 to 500 hours, and then remains nearly stable, whereas the voltage performance continues to

degrade linearly over the entire lifetime. End of life occurs when permeation or perforation of the membrane occured to a sufficiently high degree that maintaining cell potential was no longer possible.

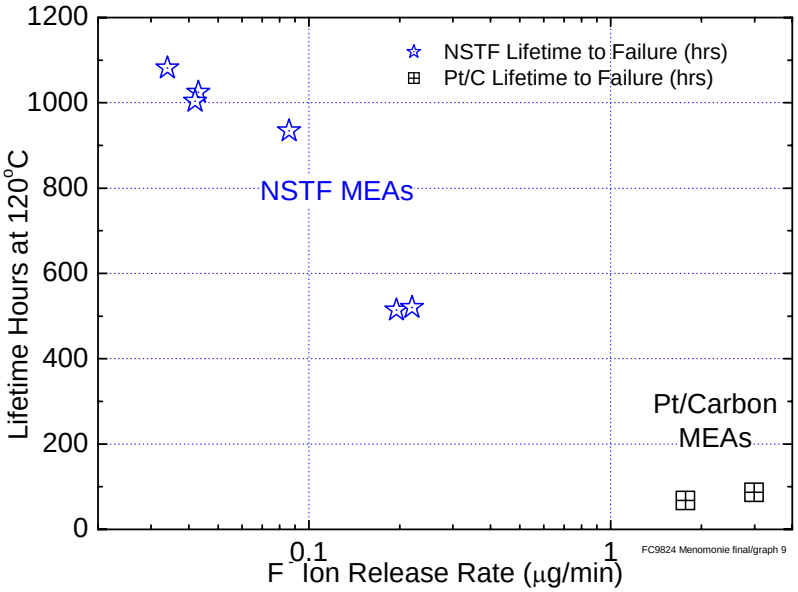

Fig. 31. Plot of the lifetime to failure at 120°C for the Pt/C controls and PtCoMn NSTF bearing MEA's from Table IV. All had the same additive free membranes and same GDLs.

Dependence of decay rates on temperature

A last experiment was done to assess the rate of parameter decay as a function of temperature. This was done with FC10296 in Table III. Due to the constraint of exiting the cell with a water balance of approximately 1.1, the inlet %RH also changed with the temperature. Fig. 32 shows the cell voltage at 0.4 A/cm^2 over time as the temperature was dropped from 120 to 110, 100, and then 90°C at two %RH conditions. The 2nd condition at 90°C was slightly wetter on the anode.

The same general behavior is seen at all the temperatures although a more detailed look at the exponential decay rates during each cycle would need to be done to determine if there was any dependence on temperature.

Fig. 33 is more revealing, showing how the anode and cathode ECSAs, hydrogen cross-over, shorting resistance and total fluoride ion release rates varied with temperature. All of the cathode surface area loss occurred in the first 200 hours of the tests, while at 120°C. The anode ECSA drops more slowly but continuously over the whole test period, as does the short resistance. Most noticeable, however, is the fluoride ion release rate, which starts at the values typical in Table IV but then drops continuously as the temperature drops to values of 5 $\pm$ 1nanogram/min at 90°C, which matches very well the values measured from the samples discussed in section 2.1.5.2 of this report from MEAs with similar catalysts at 0.4V and 90°C.

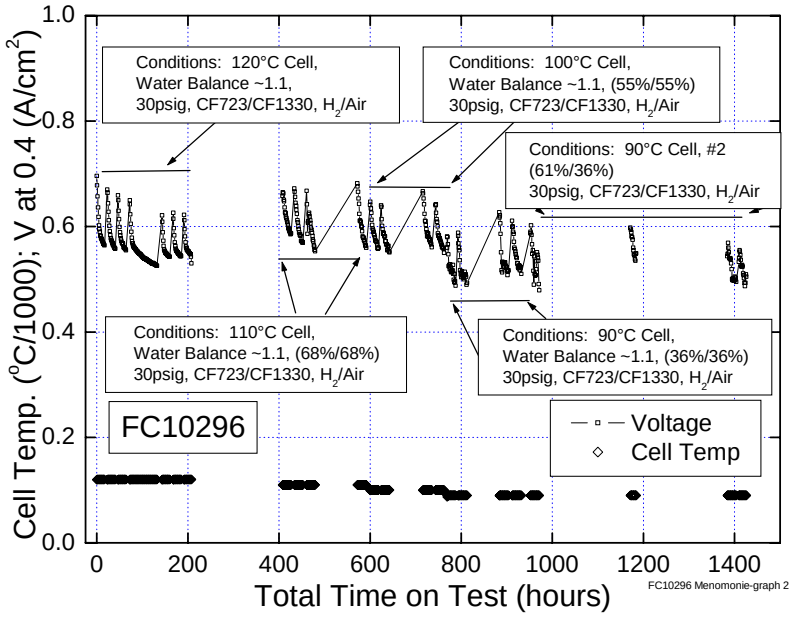

Fig. 32. Voltage at 0.4A/cm^2 over time during the same stress testing as above, but with the cell temperature changing from 120 to 110, 100, and 90°C, with two inlet %RH conditions for the 90°C case. Inlet RH was determined to make the outlet at a 1.1 x saturation.

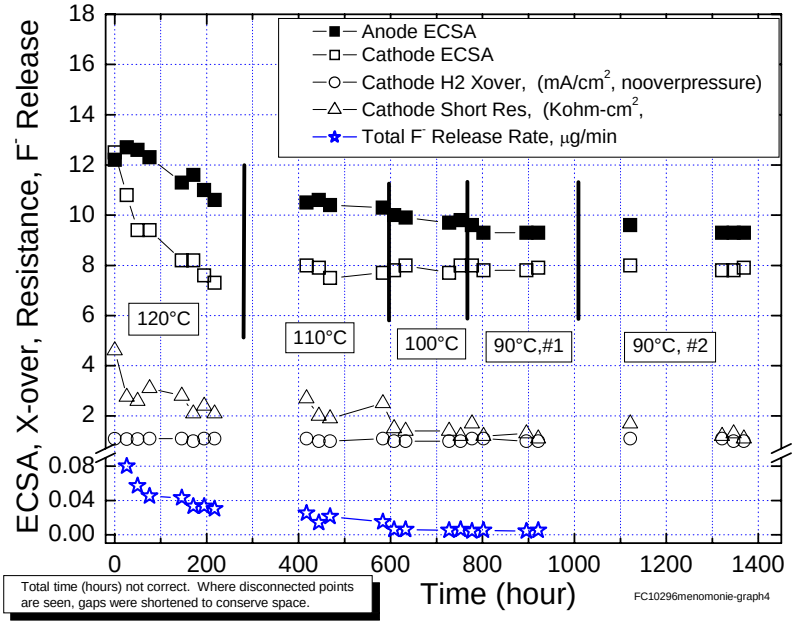

Fig. 33. Variation of the anode and cathode ECSAs, H_2 crossover, short resistance and F- ion release rate as the cell temperature changed from 120 to 110, 100, and 90°C, with two inlet %RH conditions for the 90°C case, for FC10296 identified in Table III.

2.1.4.3.3 Modeling the rate of voltage and surface area decay

As mentioned above, the cell voltage decay during each 120°C portion of the 24 hour (or longer if over a weekend) cycle of this stress test appeared to decay exponentially with time over most of the ~ 18 hour period at temperature. This could provide insight into the source of the decay, if e.g. the decay were due to reversible loss of surface area or catalyst specific activity due to adsorption of some type of impurities. To see how representative such exponential decay behavior was in general, the daily voltage decay curves were analyzed for several of the samples in Table III.

In Fig. 24 the time trace of the cell voltage over the entire 1800 hours of the test is shown for FC9824. There were 49 daily cycles. An expanded view of the individual daily (~ 18 hour) voltage versus time plots reveals a very exponential type decay. A useful way to display this dependence of voltage versus time that allows fitting parameters to be extracted is to plot for each day, the value of Vo - V(t) versus time, where Vo is the initial cell voltage at the start of the 120°C portion of the daily protocol.

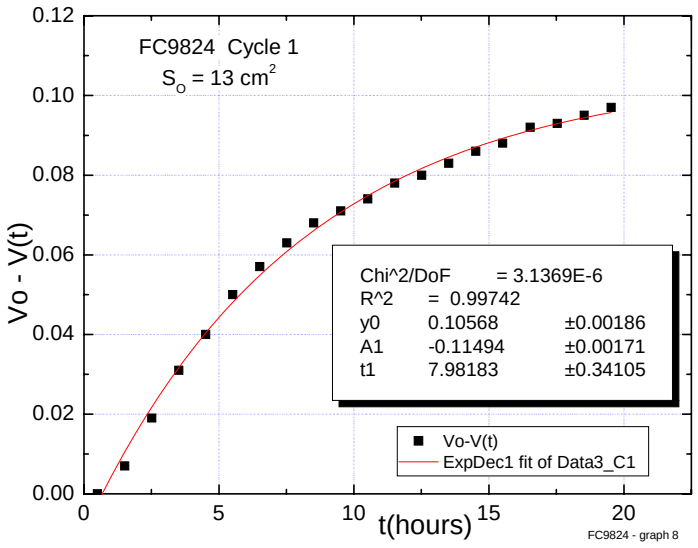

Fig. 34. Example of the exponential behavior of the cell voltage during each daily cycle at 120°C, and the fitting parameters extractable. The data points are for the 1st cycle in Fig. 24 for FC9824. The fit to Vo-V(t) = $y_o + A_1 e^{-t/t1}$ allows extracting a pre-exponential and the effective time constant, t_1, for the decay rate.

Fig. 34 shows this type of plot for the first cycle, *n*= 1, and the fitting parameters that can be extracted. The fitted curve is a fit to Vo-V(t) = $y_o + A_1 e^{-t/\tau}$ ($\tau = t_1$ in Fig. 34.)

Forty-two of these daily cycles were fit in this way. Fig. 35 shows a composite for twelve of the forty-two cycles, showing the high degree to which the cell voltage over each daily cycle had an excellent exponential decay profile.

Even for the longer cycle periods, over week-ends when the time at 120°C was near 36 hours, the exponential fit is quite good, as shown in Fig. 36.

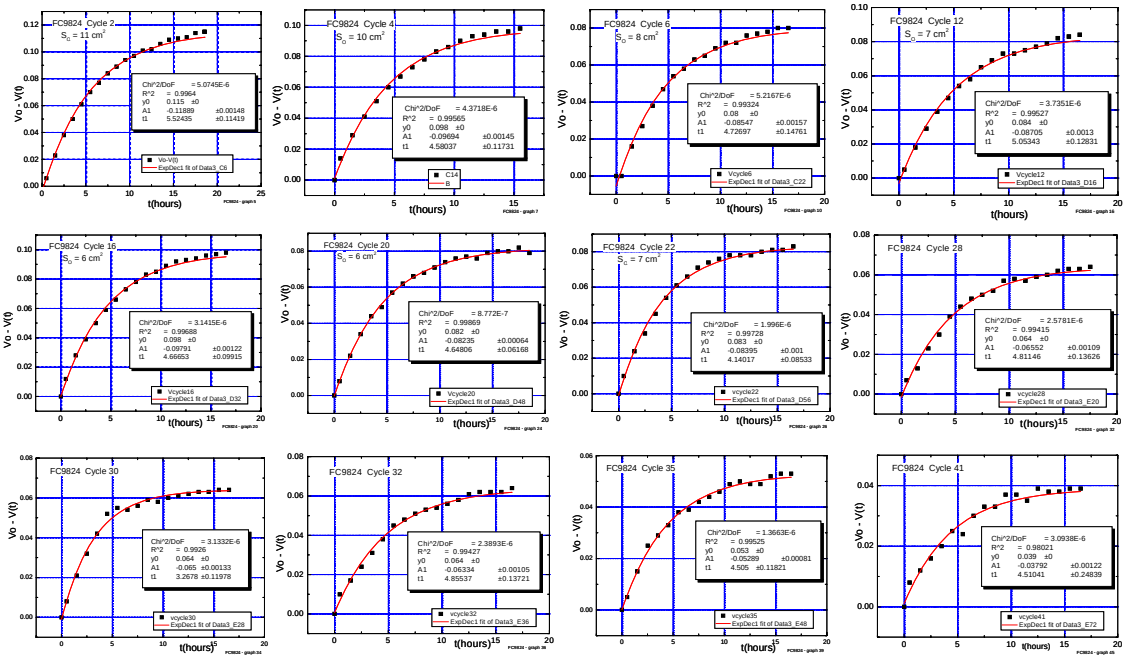

Fig. 35. Examples of the exponential behavior of the cell voltage during each daily cycle at 120°C, for 12 of the 42 daily cycles in Fig. 24 for FC9824.

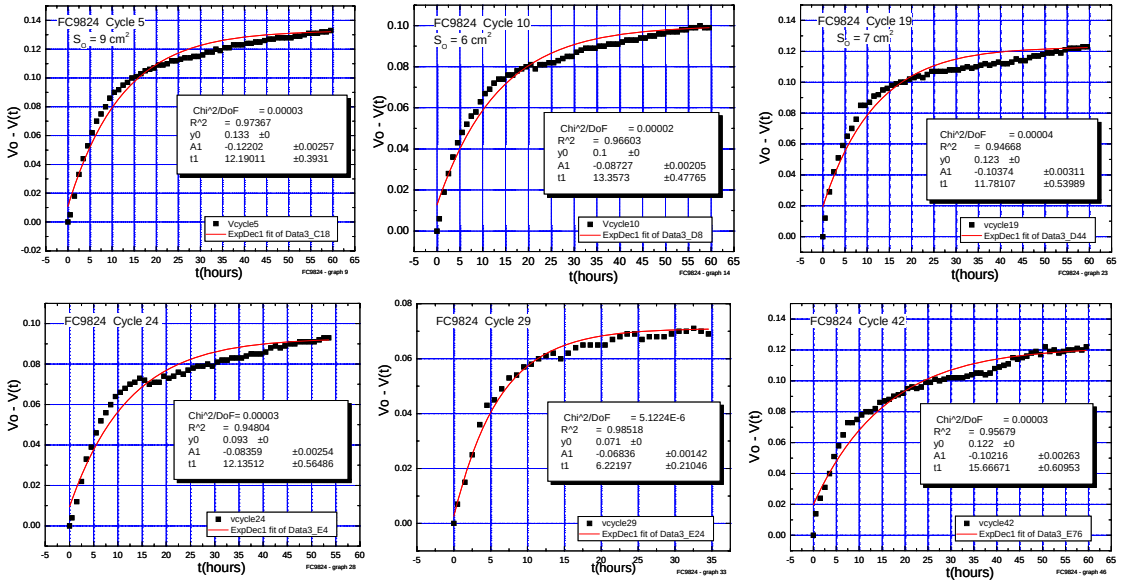

Fig. 36. Examples of the exponential behavior of the cell voltage during each week-end cycle at 120°C in Fig. 24 for FC9824.

As an initial approach to understand the data in Figs. 34 and 35, the daily voltage decay was first treated as resulting from adsorption of some type of impurity that gradually reduced the catalyst surface area available for ORR. Most of this loss would be recovereable. As seen in Fig. 28, over the whole test period the surface areas decrease more rapidly at first and then approach a minimum value that appears to remain stable. This surface area is not recoverable and represents the loss over the entire test period

not the daily period. However, we will assume in this analysis that during each daily period, the recoverable surface area loss due to impurity adsorption proceeds similarly towards a some minimum surface area. We define this minimum stable value during each cycle *n* as $S^{n}_{\min}$. If $S_n(t)$ is the actual remaining surface area at time *t* during the n^{th} cycle, then as for any adorption process, the rate of surface area loss would be proportional to the available surface area remaining available, or

(1) $$dS_n(t)\big/dt = -k[S(t) - S_{\min}]_n ,$$

Equation (1) can be integrated to:

(2) $$S_n(t) = S^{n}_{\min} + \left(S_o - S_{\min}\right)_n e^{-kt} .$$

We next make the assumption that the current density, *J*, at a given cell potential is proportional to the surface area by a constant that is a function of the surface area, or

(3) $J_o = a(J_o)S_n$, and so $\partial J / \partial S\big)_{J_o} = a(J_o)$, where for simplicity at this point we ignore any dependence of a on *n*.

Since the data was aquired in a constant current mode, to convert this to a voltage change we relate the time derivative of the voltage to the slope of the polarization curve and the current density derivative at a fixed current density J_o as in:

(4) $$\frac{dV_n(t)}{dt}\Big)_{J_o} = \frac{dV_n(t)}{dJ}\Big)_{J_o} \cdot \frac{dJ(t)}{dt}\Big)_{J_o} = \frac{dV_n(t)}{dJ}\Big)_{J_o} \cdot \frac{dJ(t)}{dS_n}\Big)_{J_o} \cdot \frac{dS_n(t)}{dt}\Big).$$

Defining $b(J_o)$ to be the slope of the polarization curve at J_o, with (3), (4) can be replaced with:

(5) $$\frac{dV_n(t)}{dt}\Big)_{J_o} = a(J_o)\cdot b(J_o)\cdot \frac{dS_n(t)}{dt}\Big).$$

Combining (1) and (5) gives:

(6) $$\frac{dV_n(t)}{dt}\Big)_{J_o} = a(J_o)\cdot b(J_o)\cdot k\cdot (S_o - S_{\min}\big)_n e^{-kt} .$$

Integrating (6) from V_o to V(t) gives:

(7) $$(V_o - V(t))_n = -a(J_o)\cdot b(J_o)\cdot (S_o - S_{\min}\big)(1 - e^{-kt}) .$$

This can be simpified as:

(8) $$V_{n,o} - V_n(t) = -C_n(J_o) + C_n(J_o)\cdot e^{-kt}$$ where,

(9) $$C_n(J_o) = a(J_o)\cdot b(J_o)(S_o - S_{\min})_n .$$

In the exponential fits to the voltage decay curves shown in Figs. 35 and 36, the fitting parameters are y^n_o and A^n_1 and $k = 1/t_1$ (below $t_1 = \tau$) where

(10) $$V_{n,o} - V_n(t) = y^n_o + A^n_1 e^{-x/t_1} .$$

Comparing (8) and (9) with (10) we see that

(11) $$y^n_o = -a(J_o)\cdot b(J_o)(S_o - S_{\min})_n$$ and $$A^n_1 = a(J_o)\cdot b(J_o)(S_o - S_{\min})_n .$$

From (11) it should follow that if we plot the fit parameters y_o^n and - A_1^n versus *n*, the cycle number, they should be equivalent. From all the fitting parameters extracted from the daily and weekend voltage decay curves for FC9824, this is indeed seen to be true as shown in Fig. 37.

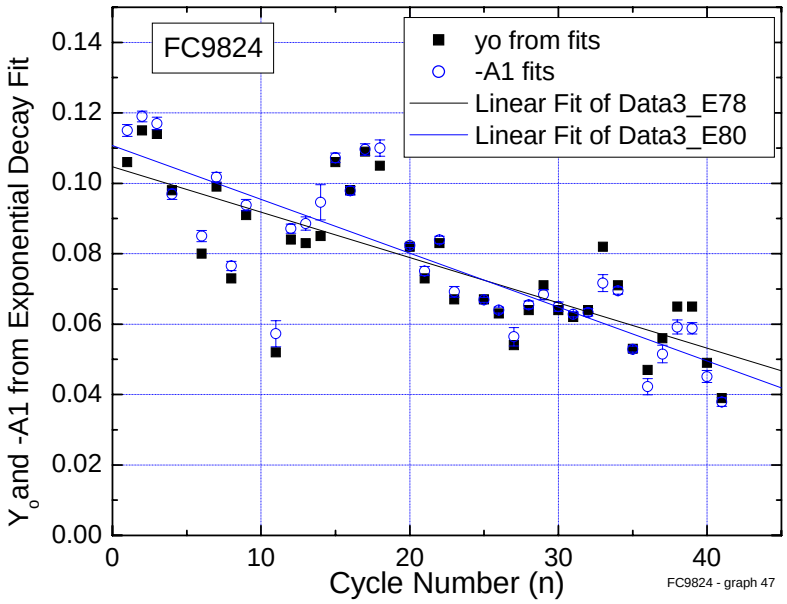

Fig. 37. Plot of the exponential fitting parameters y_o^n and - A_1^n versus *n* for all the daily and weekend cycles from FC9824 in Fig. 24 as illustrated in Figs. 35 and 36.

The y_o^n and - A_1^n parameters are seen to decrease with the number of cycles and assuming they are indeed equal, their linear fit parameters can be averaged to give mean estimates of $a(J_o)\cdot b(J_o)(S_o - S_{\min})_n$ by equation (11). This gives:

(12) $a(J_o)\cdot b(J_o)(S_o - S_{\min})_n$ = (0.1077±0.0043) - (0.0014 + 1.75x10^{-4})*n* .

The cathode surface area change with cycle number for FC9824 can also be fit by an exponential with fair representation, as shown in Fig. 38. This means we can write the surface area change as:

(13) $(S_o - S_{\min})_n = M_o + M_1 e^{-n/N}$ where *N* is the number of cycles for the surface area change to be 37% of it total possible change. From the fitting parameters in Fig. 38 this gives M_o = 5.48± 0.12, M_1 = 8.07 ± 0.54 and *N* = 6.52± 0.70. These are also parameters that could be compared among the various samples. We use M_1 and M_o to solve for $a(J_o)\cdot b(J_o)$ by letting *n* = 0 in (12) and (13) and obtain

(14) $a(J_o)\cdot b(J_o)$ = 7.95 x 10^{-3} ± 0.71 x 10^{-3}.

Using this value in (10) and (11) results finally in a general expression for the cell voltage at any time *t* within a cycle *n*, with V_o the initial voltage at *t* = 0 and *n*= 0.

(15) $V_n(t) = V_o - (7.95 \pm 0.71)\cdot 10^{-3}\cdot[(5.48 \pm 0.12) + (8.07 \pm 0.54)e^{-n/(6.52\pm 0.70)}(1 - e^{-t/\tau(n)})$

In (15) the time constant, $\tau(n)$ is a function of cycle number n in general. This can be obtained as well from the exponential fit plots in Figs. 35 and 36.

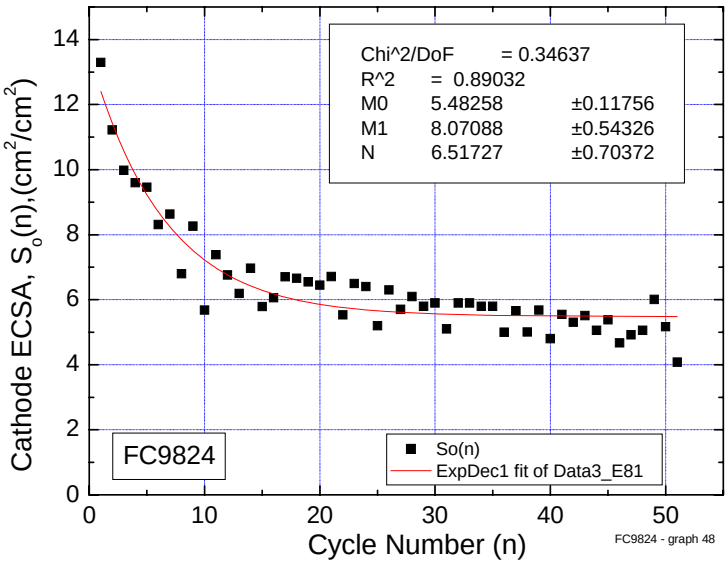

Fig. 38. Exponential fit of the cathode surface area change with cycle number for FC9824.

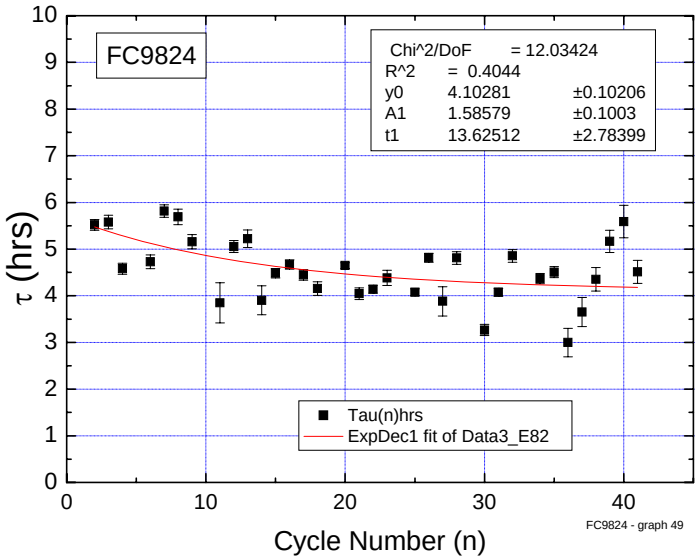

Fig. 39. Variation of the time constant fitting parameters extracted from the exponential fits to the daily and weekend cycles as in Figs. 35 and 36.

Fig. 39 shows the plot of $\tau(n)$ for FC9824. It begins with a value of 5.69 hours and slowly decreases with increasing cycle number to slightly over 4 hours. Since in this adsorbed impurity model, this is the time for 37% of the available surface area to become filled with a monolayer of adsorbate, the implication is that either the rate of impurity generation is increasing or surface area is decreasing, or both of these effects are occurring. Since we know that $S_o(n)$, the initial surface area at the start of any cycle,

is decreasing with *n* as per Fig. 38, plotting the ratio of $\tau(n)$ / $S_o(n)$ versus *n* should normalize out the change in surface area and leave the factor due to the change in rate of impurity adsorbate. This is easily done by ratioing the data in Figs. 39 and 38 and is shown in Fig. 40.

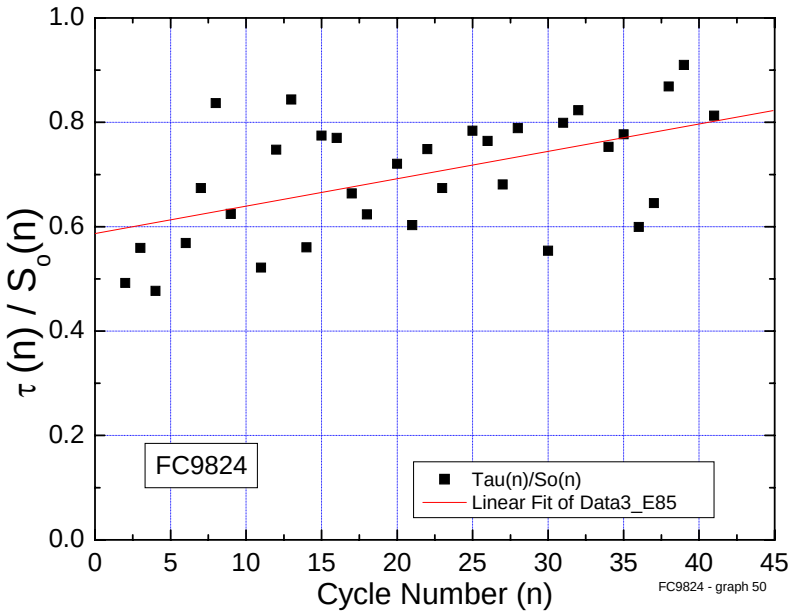

Fig. 40. Ratio of the change in time constant of the exponential voltage decay and the initial surface area decay as a function of cycle number for FC9824.

This ratio is seen to increase slightly with a slope of m = 0.57 $\pm$ 6.7x 10^{-3} *n*, suggesting the impurities are being depleted slowly or rather the rate of generation of the impurities is going down slightly over time. In Fig. 39, a monolayer is formed more quickly because the reduction in surface area occured at a faster rate than the reduction in the rate of impurity generation.

Summary of Model Analysis and Remaining Work

The above analysis is not complete, either with respect to its application to all the samples tested or its interpretation. At this point it has been found that the exponential decay fitting can be applied to all the samples' daily voltage decay curves, as it was here for FC9824. The time constant for FC10066 is on average 6.27 hours, slightly longer than for FC9824. Taking into account the rate of surface area decay for FC10066, the conclusion is that the rate of impurity generation for it is less than for FC9824. The y_o^n and - A_1^n fitting parameters for FC10066 are similar to those measured for FC9824, giving a value of $a(J_o)\cdot b(J_o)$ = 6.7 x 10^{-3}, close to that for FC9824 in (14).

The Pt/C dispersed MEAs, FC9917 and FC10067, have also been evaluated and the latter gives values of $a(J_o)\cdot b(J_o)$ that are a factor of 45 times lower than for FC9824. More significant, the voltage decay rate pre-exponential is only 3.4 times smaller than

that for FC9824, even though the surface area of FC10067 is 12.6 times larger. More analysis of these comparisons remains to be done as well.

The real value of this analysis when it is completed, however, will be any conclusions that can be reached about the nature of the hypothesized impurity this analysis is based upon. It is presumeably some decomposition product of the membrane, and something that is generated at least in proportion to the fluoride ion release rates. Although not yet completed, using the time constant values and straight forward estimates of the available surface site density for adorption on the Pt, some estimates can be easily calculated for the molar volume generation rate of thehypothesized impurity. These estimates are listed in Table V. Consistent with the higher F^- ion generation rates measured for the Pt/C dispersed electrode MEAs, these rates are also higher for the dispersed samples than the NSTF, by roughly an order of magnitude, similar to the ratio of observed liftimes. This would make sense if the generated impurity is a membrane decomposition product.

Table V. Preliminary estimates of the volumetric molar generation rate for impurities causing the daily reversible voltage decay by the model analysis above.

Sample FC Number	Impurity generation rate (moles/cm^3-sec)
9824 (NSTF)	5.53×10^{-11}
10066 (NSTF)	14.8×10^{-11}
10067 (Pt/C)	211×10^{-11}
9917(Pt/C)	$59.8\ 10^{-11}$

It may be possible to put upper bounds on the molecular weight of the adsorbed species given information derived from the model on the rate of surface area loss as a function of time during a daily cycle, and assumptions about the molar rate of impurity generation per unit volume of membrane from the measured F^- ion release rates for that cycle. This and other aspects of the analysis remain to be done.

2.1.4.4 NSTF Stability Under Stop Start Testing.

Stop/start cycling of PEM fuel cells can lead to high cathode potentials resulting in Pt dissolution and carbon corrosion. To simulate these conditions we conducted accelerated stop/start tests using an automotive start/stop (S/S) testing protocol that was provided through communication with Nissan. S/S cycling under H_2/air was conducted in single cells using 50 cm^2 MEA's with either NSTF PtCoMn alloy catalysts (12 samples) or Pt/C dispersed catalyzed MEA's (2 samples), both with 0.2 mg-Pt/cm^2 electrode loadings. Performance of the conventional Pt/C based MEA's seriously degrades after 100 cycles, whereas NSTF MEAs' performance loss was much less over 300 cycles and mostly recoverable by simply discontinuing and restarting the tests. Cyclic voltammograms, electrochemical surface areas, specific activities (900mV 150kPa H_2/O_2, saturated) and XRD crystallite sizes were measured before, periodically during, and after S/S testing. These are compared for both types of catalyzed MEA's, as well as S/S testing under H_2/air versus N_2/N_2.

2.1.4.4.1 Experimental

Catalyst and MEA Preparation

The NSTF catalysts and MEAs were prepared basically as described in reference [3]. The NSTF whisker support layer is a monolayer of oriented crystalline whiskers of an organic pigment material (CAS # PR149). Catalysts are sputter coated on top of the whiskers so as to encapsulate them with a polycrystalline thin film (Fig. 1). Composition and structure of the catalyst coating is determined by the arrangement and composition of the sputtering targets. NSTF PtCoMn ternary catalysts were used for the examples in this report to compare with Pt/carbon catalysts. The Pt loadings in the NSTF PtCoMn and Pt/C were 0.2 mg/cm^2 per electrode for the S/S durability tests, and 0.15 mg/cm^2 for the dry H_2/O_2 durability tests. NSTF catalyst coated membranes are formed by transfer of the catalysts from the initial substrate web to the proton exchange membrane. For all samples this was accomplished with hand-fabricated samples adequate for 50cm^2 active areas.

For the Stop-Start stress tests, the dispersed Pt/C catalysts were commercially obtained and utilized 40-50 wt% Pt on Ketjen Black. Conventional type inks with Nafion were coated and decal transferred to the surfaces of the membranes to form the dispersed catalyst coated membranes.

In all cases the 3M fabricated membranes used were based on the 3M ionomer [9]. For all the start-stop tests, the 3M polymer having a 980 EW was used for both the NSTF and Pt/C type MEA's. The membranes were acid washed (1 M HNO_3, 70^oC for 1 hour, followed by DI water rinse at 70^oC for 1 hour), and dried before catalyst transfer. For the dry H_2/O_2 high current polarization tests, the same type of membrane was used, however for a duplicate test done to characterize the fluoride ion release, the equivalent weight of the membrane was approximately 850.

The same 3M fabricated GDLs were used for both types of MEAs and generally consisted of a flexible non-woven carbon electrode backing, pretreated with a hydrophobic coating before application of a microporous layer having a carbon black chosen for its oxidative stability. The MEA's were installed in the test cells using Teflon impregnated fiberglass gaskets acting as hard-stops, with calipers carefully sized to the

GDL thicknesses for the desired in-cell compression. For the S/S tests, 30% and for the H_2/O_2 tests, 10% compression was used.

XRD and IC Analysis

X-ray diffraction was used for purposes of determining crystalline phase(s) present, apparent crystallite sizes, and d-spacing/relative intensity ratio calculations. Data were collected using a Philips APD vertical diffractometer, copper K_α radiation, reflection geometry, and proportional detector registry of the scattered radiation. The diffractometer is fitted with variable incident beam slits, fixed diffracted beam slits, and graphite diffracted beam monochromator. The survey scans were conducted from 10 to 110 degrees (2θ) using a 0.04 degree step size and 4 second dwell time. X-ray generator settings of 45 kV and 35 mA were employed. The apparent crystallite sizes and d-spacings/relative intensities for platinum only were determined from observed diffraction peaks using a Pearson VII peak shape model, accounting for α_1/α_2 separation. The background, obtained from a reference "blank" of Nafion™ membrane, was subtracted prior to profile fitting.

Ion chromatography was done using a Dionex® ICS-2000 Chromatography system. Periodically, fuel cell effluent water is collected during a specific time interval, and the average effluent flow rate determined. An aliquot of this effluent is then tested for fluoride ion content using the ICS-2000, and the average fluoride ion release rate (ng/min) determined as a function of time.

Fuel Cell and Electrochemical Testing

Start/stop testing was performed on a single Fuel Cell Technologies test station. The test station incorporated modifications to the electronic load, gas flow control, and humidification system which were necessary to perform the start-stop testing. The electronic load used for S/S was a TDI Dynaload MCL488, whose low input impedance allows for operation at the high currents and low cell voltages required by the test protocol without risk of cell reversal. The gas flow control sub-system used for S/S comprised four computer controlled thermal mass flow controllers. One of the controllers fed UHP hydrogen to the anode, the second fed air to the anode, the third fed air to the cathode, and the fourth fed nitrogen to the cathode. The air supply to the test station was polished using an air filter purchased from Donaldson Co. The humidification system for S/S testing consisted of calibrated Lab Alliance ISO-100 HPLC pumps fed by nominally 18 Mohm-cm deionized water; use of HPLC pumps allowed for automatic and immediate switching of humidification levels required by the test. H_2/O_2 durability testing was performed on a 3M-developed test station of similar capability to the station used for start/stop testing.

All fuel cell testing was performed in test cells comprising quad-serpentine flow fields with 50 cm^2 active areas; all but one result was obtained in the same physical cell. The test stations were controlled by 3M-developed software, which allowed for automation of a majority of the testing.

Electrochemical surface areas of the MEA electrodes were obtained by integration of hydrogen adsorption/desorption peaks from H_2/N_2 cyclic voltammograms. Voltammograms were measured using a Solartron 1470 potentiostat controlled by CorrWare software from Scribner Associates. During CVs, the MEA was held at 70°C, with 800/1800 SCCM H_2/N_2, 76/76°C dew points, and 100/100 kPa pressures. First, 20

CVs were measured between 0.09 V and 1.5 V at 100 mV/s; these CVs were used to visually observe changes in the Pt oxidation/reduction behavior of the electrode, as well as the presence of any electrochemically active contaminant species. These CVs were then followed by 50 to 100 CVs between 0.09 V and 0.65 V at 100 mV/s, finally followed by 3 CVs between 0.09V and 0.65V at 2 mV/s. Each set of CVs was averaged to reduce noise. The 2mV/s CVs were used to correct the 100 mV/s CVs for electronic shorting, H_2 crossover, and H_2 evolution currents. After removal of the capacitive currents and other small corrections, each half of the 100 mV/s scans were integrated, and the resultant up-scan and down-scan areas were averaged to obtain a mean hydrogen adsorption/desorption charge density (C/cm^2-geometric area). This charge density was converted to the electrochemical surface area (ECSA) by dividing by 220µC / cm^2-Pt.

O_2 Activity Metric for Calculating Specific Activity

To monitor changes in catalyst activity during the Stop-Start protocol, the cell was held at 80/80/80°C, 150/150 kPa, 70/160SCCM H_2/N_2, OCV for ~ 10-20 minutes to allow the system to equilibrate. Next, the cathode gas was switched to oxygen. After a short period of time, the OCV begins to rise, and rapidly reaches a peak value; at this moment, a potentiostat is used to polarize the cell at 0.900V and measure the current. The current density after 15 minutes is recorded as the "uncorrected current density".

Next, electronic short and hydrogen crossover are measured at temperature by measuring ECSA using a procedure similar to that noted above, except the cell is maintained at 150/150 kPa and 80/80/80°C. The "uncorrected current density" is corrected for the electronic short and hydrogen crossover to obtain the corrected current density. Specific activity at 80°C is then this corrected current density at 900 mV divided by the ECSA.

Stop/Start Testing Protocol

The following is an example of a typical sample testing chronology. First the MEA was conditioned using potentiodynamic scans (PDS) and thermal cycling until the PDS performance stabilized. Upon completion of conditioning, baseline H_2/air performance and H_2/O_2 activity at 900 mV were measured. CVs from 0.1 to 1.5V were taken from both anode and cathode to obtain initial ECSA values. Start/Stop protocol was then initiated, using cell temperature and anode/cathode dew points respectively of 80/59/71°C, under ambient pressure H_2/Air flowing at 522/2485 SCCM (1.5/3.0 stoich @ 1A/cm^2) during the operational portion of any S/S cycle (described below). Upon completion of nominally 300 cycles the test was terminated, or if after having been shutdown for a period of time (e.g. a mandated monthly week-end building emissions shutdown), the sample was restarted until all cycles were completed. After termination of the S/S testing, CVs to 1.5V, O_2 metric, PDS performance, and GDS performance were re-evaluated. The cell was then thermally cycled (on-off with continuous water flushing) until stable performance was achieved. Again, CVs to 1.5V, ECSA, GDS performance, and O_2 metric were re-evaluated.

Stop/Start Cycle Under H_2/air

Each start/stop cycle lasted 22.5 minutes. At t=0, the cell is at 80/59/71°C, 522/2485 SCCM H_2/air, and open circuit voltage. During the first minute, the current density is increased from 0A/cm^2 to 1A/cm^2 in 0.2A/cm^2 steps, and the cell is maintained in this

state for 10 minutes. The cell voltage obtained during the 10 minute 1A/cm^2 hold is used as a metric of cell performance during that particular cycle. After this period, the cathode, then anode gases are halted for a few minutes, then dry air is reintroduced into both electrodes. During this period of halted gases and air reintroduction, the electronic load holds the cell at ~0V (shorted). Over the next few minutes, the cell is held at open circuit voltage and the anode air flow rate is stepwise decreased while hydrogen flow is stepwise increased commensurately.

As an additional performance check, a polarization curve was taken every ~26th S/S cycle. For this measurement, the cell was operated at the same conditions as t=0 above, and polarization comprised of (1.0A/cm^2 for 5 minutes), (OCV for 3min), (0.1A/cm^2 for 3min), (0.2A/cm^2 for 3min), (0.4 A/cm^2 for 5min), (0.6 A/cm^2 for 5min), (0.8 A/cm^2 for 5min), (1.0 A/cm^2 for 5min). S/S cycling was immediately resumed, starting at the t=0 conditions.

Stop/Start Tests Under N_2/N_2

As a comparative case, S/S cycling was performed on an NSTF MEA where an identical protocol for S/S was used, but the reactant gases fed to the anode and cathode were N_2 for the duration of each cycle. Periodic H_2/air polarization curves were measured similar to the procedure outlined above. Upon completion of 396 cycles, S/S testing was halted and cyclic voltammetry and baseline polarization curves were measured. The cell was then thermally cycled until stable performance was achieved, and CVs, polarization curves, and O_2 metric were measured.

2.1.4.4.2 Stop/Start Results and Discussions

NSTF and Pt/C MEA Stop/Start Performance Effects

Throughout the course of this investigation of the S/S durability tests, a half-dozen MEA's were initially evaluated while developing and refining the test station capabilities to best match the desired S/S protocol. When the test station air filtering, humidification controls, and flow condition details were satisfactory, a total of eight more NSTF PtCoMn MEA's and two Pt/C based MEA's were tested using the same test station and test protocol. The S/S responses of all these NSTF catalyst based MEA's were very similar. A ninth NSTF PtCoMn MEA was tested under the N_2/N_2 protocol as described above. All of these samples except the first Pt/C MEA were also tested in the same 50 cm^2 test cell. The S/S performance responses of the two Pt/C MEA's in the two different test cells were very similar.

Fig. 41 compares the cell voltage at 1 A/cm^2 during the S/S protocol, as a function of the number of S/S cycles for the two MEA types. There are several notable features. First the Pt/C MEA performances began rapidly degrading after ~ 25 cycles, and were significantly degraded after about 75 cycles. In contrast, the NSTF catalyst MEAs' performances increased slightly during the first 30 cycles, before beginning a slow decay on the order of 0.8 mV/cycle. Most striking, however, is that when the testing was stopped and the cell shut down, upon restarting the tests the lost cell potential at 1 A/cm^2 was completely recovered. After that the voltage again began a similar or slightly faster decay, which again was substantially recoverable.

PDS and GDS polarization curves were taken every 26th S/S cycle, to monitor the full polarization curve progression.

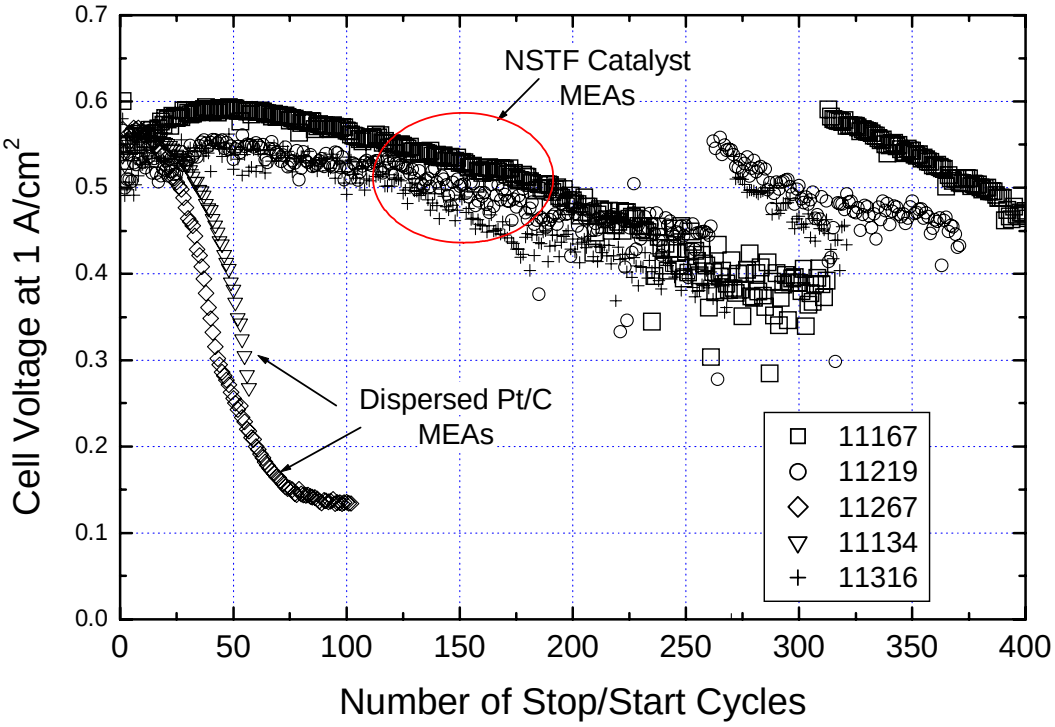

Fig. 41. Cell voltage at 1 A/cm^2 after each Stop/Start cycle, versus the number of cycles, for three NSTF catalyst MEA's and two Pt/C MEA's.

Fig. 42(top) shows the response from one of the Pt/C based MEA's over time. The performance degrades at all cell voltages. In contrast, Fig. 42 (bottom) shows a typical response from the NSTF catalyst MEA's. A much smaller change at both high and low current densities can be seen. This behavior is consistent with a small change in kinetic performance and a larger change in mass transport overpotential, much of which is recoverable, as shown in Fig. 41 by stopping the tests, cooling to ambient and then restarting the S/S tests. (Further polarization curve examples of the reversible recovery are discussed below.) When this mass-transport loss effect was observed for several of the NSTF catalyst MEA's, the effect of a higher cathode stoichiometric flow ratio was tested, viz CS =3 instead of CS=2, during the S/S protocol for both the NSTF and Pt/C MEA's. We could determine no statistically significant effect of cathode flow rate on the amount of reversible decay, and Fig. 41 includes results from both values of stoichiometric flow.

2.1.4.4 NSTF Stability Under Stop Start Testing

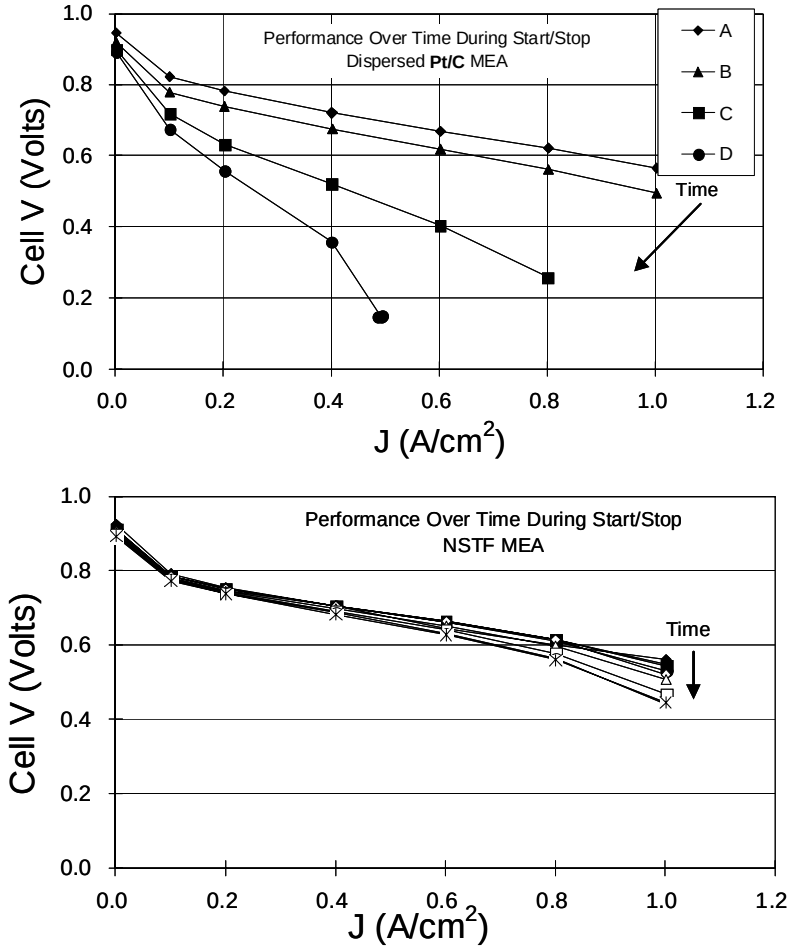

Fig. 42. Examples of how the GDS polarization curves progress over time, taken every 26th S/S cycle. The Pt/C based MEA's (top) lose performance at all cell voltages while the NSTF based MEA's (bottom) lose much less performance and primarily in the mass transport region of the polarization curve.

Cyclic Voltammograms and XRD

Stop/Start cycling effects could be affecting the anode and cathode catalysts' surface areas, specific activities, or more broadly the impedance and mass transport of the MEA. Insight into some of these factors can be gained first from H_2/N_2 cyclic voltammograms, taken from both the anodes and cathodes and compared before and after S/S cycling for both catalyst types.

Fig. 43. compares typical NSTF catalyst anode and cathode CVs taken after initial conditioning but before any H_2/air S/S testing. Fig. 43(left) shows the 1st, 2nd and 20th anode CVs out to a potential of 1.5 volts. The progressive changes in the pre-S/S anode CV's suggests that some oxidizable impurity species is being removed with each successive sweep. As indicated below, after S/S testing, only a very small change in successive CV sweeps was observed over the 0.1 to 1.5 volt range, implying the initial impurities once removed did not readsorb. Fig. 4(right) similarly suggests that some impurity is removed from the cathode by the first sweep past 1.4 volts, but thereafter little change occurs with further CV scans.

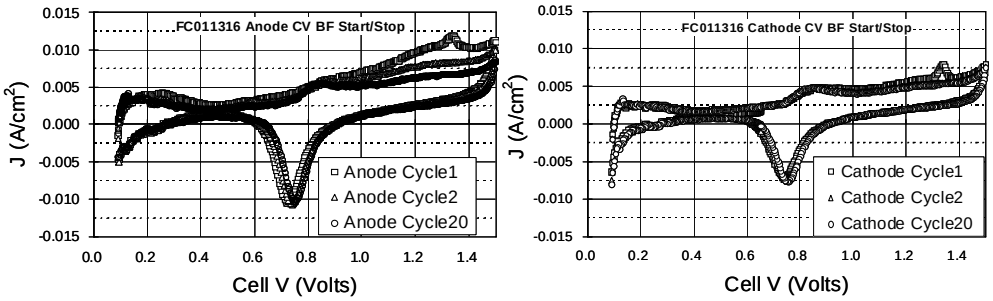

Fig. 43. Comparison of the 1st, 2nd and 20th CV scans before any S/S testing cycles, typical of the NSTF catalyst MEA's: (left) anode, (right) cathode.

Figs. 44 and 45 show typical CV changes from the NSTF anode and cathode respectively, comparing the 20th CV sweep before and after the S/S testing. The ECSA is determined from these short and cross-over corrected voltammograms. Fig. 44 illustrates typical changes after 300 cycles of the NSTF catalyst based MEA anodes. These changes were also observed to be non-reversible for the most part, i.e. thermal cycles to try and rejuvenate the MEA did not change the anode CVs. Some decrease in the hydrogen adsorption/desorption currents has occurred, from which an ~ 25% loss of anode catalyst surface area from 17.8 to 13.2 cm^2/cm^2 was determined. There is also an indication that S/S lead to removal of additional oxidizable species above 0.8 V, similar to that shown in Fig. 43. In Fig. 44 there is a noticeable reduction in the Pt oxidation and reduction peak areas, as well as a slight positive shift to higher potentials of the reduction peak. This shift upward of the Pt oxide reduction peak was previously shown to occur during CV cycling from 0.6 to 1.2 V, tests done to simulate the effects of S/S, as discussed in 2.1.4.1.3. There it was seen the dispersed Pt/C catalysts' Pt oxide reduction peak voltage increased substantially, commensurate with a large increase in the catalyst particle size, and much more than the NSTF Pt catalyst, which had a larger initial particle size.

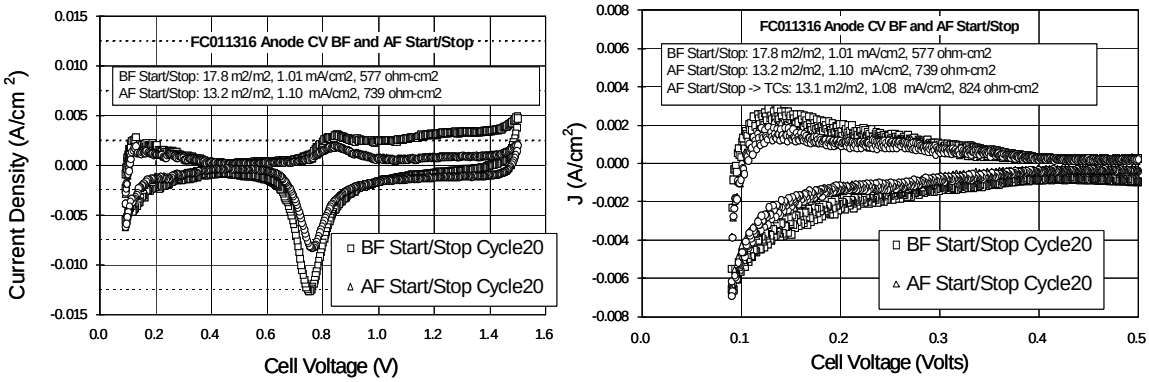

Fig. 44 Comparison of typical NSTF catalyst anode CVs (20th sweep) before and after 300 cycles of the H_2/air S/S test protocol: (left) sweep to 1.5 volts showing a reduction in the Pt oxide reduction peak and a slight shift upward by ~ 0.010 volts caused by the 300 S/S cycles. Subsequent thermal cycles had little effect on the post-S/S anode CVs. (right) expanded view of the CV sweeps used to determine the ECSA.

Fig. 45 similarly shows the changes occurring on the NSTF cathode catalysts due to 300 S/S cycles. The changes are similar to those seen on the anode, except there is a smaller degree of oxidative removal of some impurity species in the 0.8 to 1.5 volt region. The measured cathode ECSA decreased from 15.3 to 12.6 cm^2/cm^2, an ~ 20% decrease in this example. The initial ECSA should be expected to be identical on the anode and cathodes, and there is an ~ $\pm$ 10% uncertainty in the measured values. Among the six NSTF MEA's characterized in this way, the measured ECSA's before the S/S testing ranged from a low of 14.3 to a high of 18.1 cm^2/cm^2, with a mean value of 16.3 cm^2/cm^2. After the S/S testing the mean anode and cathode surface areas were measured to be 13.2 and 12.1 cm^2/cm^2 respectively. The average decreases in anode and cathode surface areas were 19% and 26% respectively.

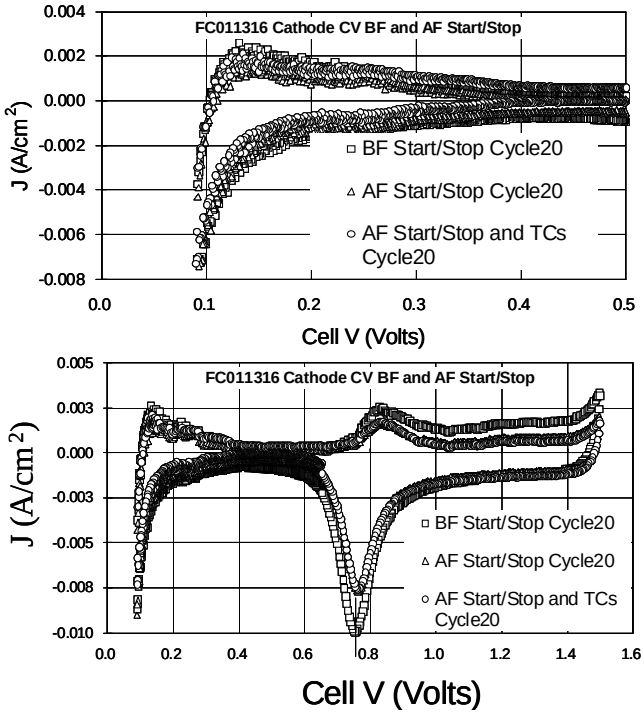

Fig. 45 Comparison of typical NSTF catalyst cathode CV's (20th sweep) before and after 300 cycles of the H_2/air S/S test protocol: (bottom) sweep to 1.5 volts showing a reduction in the Pt oxide reduction peak and a slight shift more positive by ~ 0.010 volts caused by the 300 S/S cycles. Subsequent thermal cycles had little effect on the post-S/S cathode CV's. (top) expanded view of the CV sweeps used to determine the ECSA.

Fig. 46 shows the changes occurring on the Pt/C MEA anode and cathode catalysts' 20th CV sweep due to 100 S/S cycles. These CV's are also short and cross-over corrected. The anode surface areas are reduced from 89.4 to 75.9 cm^2/cm^2, whereas the cathode surface areas have dropped from 95.7 to 18.4 cm^2/cm^2, 15% and 81% losses respectively. This large loss in cathode surface area is clearly responsible for most of the large loss in kinetic performance of the Pt/C catalysts. It is notable that although the S/S-produced surface area loss of the NSTF catalysts are much less than the dispersed Pt/C cathode, the NSTF anodes and cathode surface area changes are similar. In contrast, the Pt/C cathode loss is much greater than the Pt/C anode surface area loss.

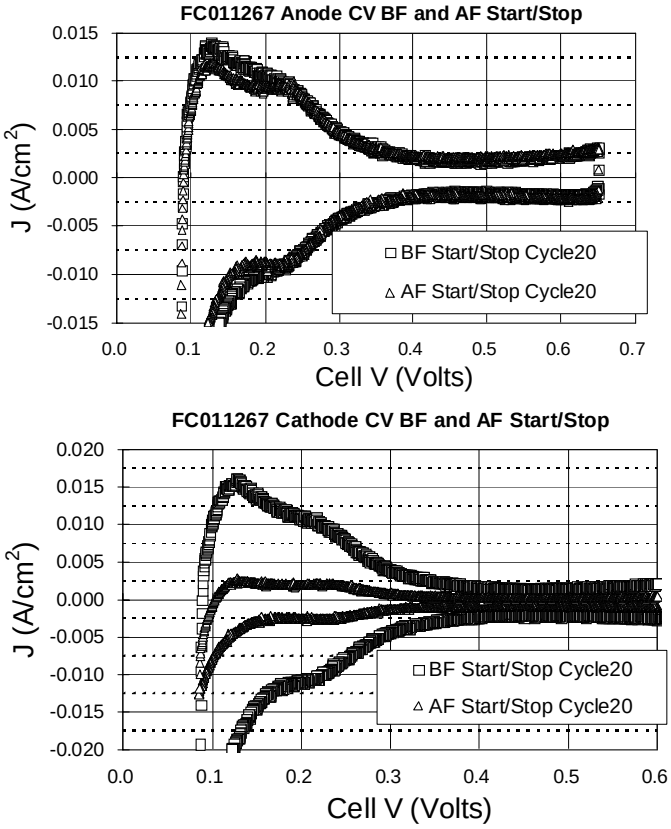

Fig. 46. Comparison of typical Pt/C catalyst CV's (20th sweep) before and after 100 cycles of the H_2/air S/S test protocol: (top) anode, (bottom) cathode.

A similar effect was also observed in the CV cycling experiments discussed in section 2.1.4.3]. In that study, the decreases in surface area were clearly determined from XRD to be associated with increases in the Pt particle size for the Pt/C catalyst, and the Pt grain size for the thin film NSTF catalyst. To investigate that possibility, XRD characterization was completed on two of the NSTF and both Pt/C catalyst coated electrodes after the S/S testing. Fig. 47 shows the observed diffraction spectra, revealing surprisingly similar peak shapes and widths for the two catalyst types, implying similar particle sizes. Table VI compares the measured Pt FCC lattice spacing and apparent Pt crystallite sizes determined from the diffraction spectra in Fig. 47. The alloy composition of the NSTF PtCoMn has caused the Pt lattice spacing to shift downward ~0.03 Angstroms from the pure Pt value of 3.92 Angstroms. This is consistent with previous measurements for a wide range of NSTF alloys [2,3]. (The anodes and cathodes for each MEA were not tracked through the XRD analysis, and are identified only as side 1 or 2.) The apparent crystallite sizes for the NSTF anodes and cathodes after S/S testing are similar to each other and to the as-made catalyst. Changes in crystallite size would not appear to be a source of the change in NSTF ECSA brought about by S/S cycling, but the uncertainty in particle size is large. The crystallite sizes of the dispersed Pt/C anodes and cathodes have changed significantly from the as-made Pt/C values, and so may partially contribute to the ECSA change of the Pt/C samples. However the anode and cathode crystallite sizes are similar to one another for each Pt/C

sample after S/S testing, and this is not consistent with the observed changes in ECSA discussed above in Fig. 46.

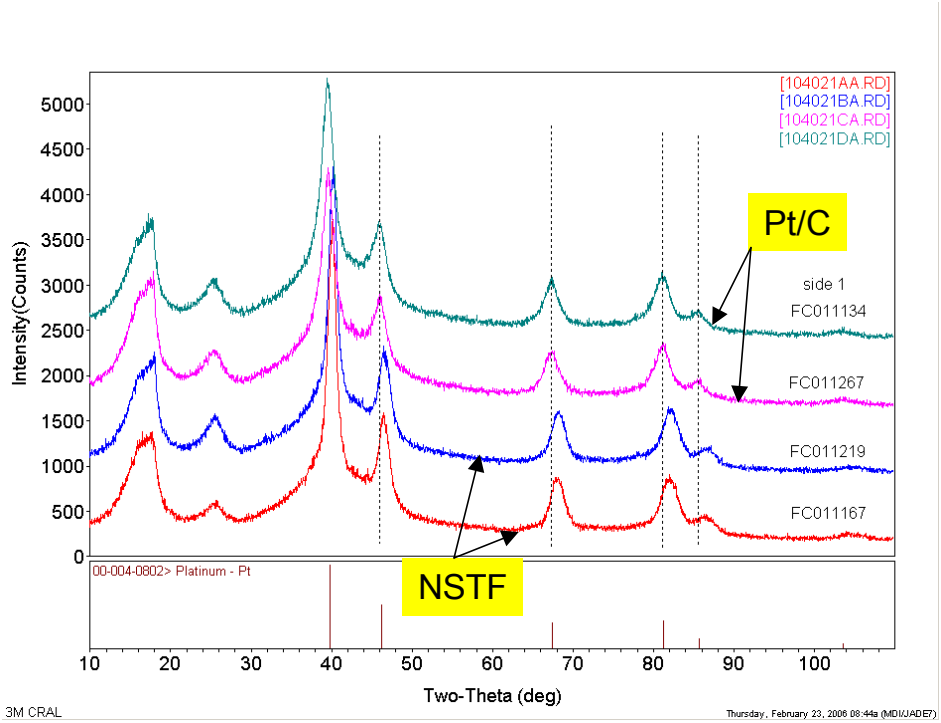

Fig. 47. XRD spectra from the anodes and cathodes of two NSTF catalyst MEA's and two Pt/C catalyst MEA's after the S/S testing.

Table VI. Summary of XRD Pt Crystallite Changes Produced by H_2/air S/S Tests

Sample Description	Number of S/S Cycles	Pt Lattice Parameter (Å)	Pt Apparent Crystallite Size (Å)
NSTF #11167, side 1	312	3.89	59 ± 12
NSTF #11167, side 2	312	3.89	60 ± 12
NSTF #11219, side 1	371	3.89	61 ± 12
NSTF #11219, side 2	371	3.89	57 ± 11
NSTF PtCoMn as made	0	3.88	59 ± 12
Pt/C #11267, side 1	100	3.92	62 ± 19
Pt/C #11267, side 2	100	3.92	63 ± 13
Pt/C #11134, side 1	55	3.92	55 ± 8
Pt/C #11134, side 2	55	3.92	55 ±11
Pt/C as made	0	3.92	32 ± 16

It is notable that the Pt/C sample #11134 exhibits apparent Pt crystallite sizes after 55 S/S cycles, which are intermediate between the as-made catalyst and that of sample # 11267 after 100 S/S cycles. For both Pt/C samples the crystallite sizes of the anode and cathode increased together as the number of S/S cycles increased, whereas the electrochemically determined surface area did not decrease to the same extent for both the anode and cathode of the Pt/C catalysts, as noted above. This could suggest that the much larger percentage loss of ECSA of the Pt/C cathodes is due to more than just an increase in particle size, such as loss of electrical contact of Pt with the cathode

electrode. This would occur, for example, if some of the cathode Pt migrated into the proton exchange membrane and/or carbon corrosion occurred, both effects causing Pt particles to become electrically isolated. Pt dissolution effects may also be contributing to the NSTF catalyst surface area decrease, without further agglomeration occurring.

Reversible and Non-reversible Losses

Fig. 41 illustrated that for the NSTF MEA's, the cell voltage at 1 A/cm^2 recorded during the S/S testing was recoverable simply by shutting down the cell and then restarting. After the S/S testing of each sample was completed, GDS and PDS polarization curves were acquired to compare with the initial curves. The samples were then also "thermally cycled" a number of times to recover as much performance as possible, and that also compared to the initial performance. Thermal cycling of the NSTF MEA's is generally used to improve the performance during initial break-in or start-up, and is known to remove impurities in the MEA that adversely affect the lower surface area of the catalyst. (The "thermal cycle" protocol means starting the cell under normal H_2/air operation for a few polarization scans, then shutting it off with water continuing to flow on the anode and cathode. The cell is then restarted and the cycle is repeated until stable performance is obtained.)

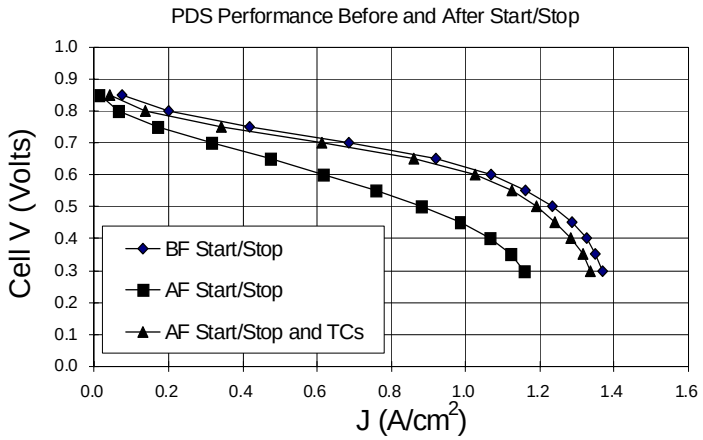

Fig. 48. Typical potentiodynamic polarization curve from the NSTF MEA's initially, after 300 S/S cycles, and after further thermal cycling to recover as much of the reversible performance loss as possible. Only a kinetic loss of ~10mV appears non-recoverable.

Fig. 48 shows a typical PDS, constant flow polarization curve from an NSTF MEA before and immediately after 300 or more S/S cycles, and then after it was further thermally cycled to recover as much reversible loss as possible. It is clear that the polarization curve is nearly completely recovered after the thermal cycling, and differs from the initial PDS curve by a fairly uniform vertical translation of the curve parallel to the voltage axis. This approximately -10 mV shift, due to a kinetic loss, is consistent with the ~ 25% loss of electrochemical surface area discussed above (70mV/dec => 9mV/25% loss of ECSA). There would appear to be no other substantial losses, due e.g. to increases in impedance or mass transport, required to explain the small change in fuel cell performance of the NSTF MEAs after 300 S/S cycles and thermal cycling. (Note, the test station used for these tests was not capable of measuring impedance during the S/S testing.)

Research to understand the mechanisms responsible for the reversible contribution of the S/S performance loss is on-going. While still preliminary, analysis of fuel cell feed and effluent water in separate experiments suggests accumulation of anions and cations within the MEA, which are at least partially removed from the MEA by condensed water when the cell is shut down and restarted. In addition, a linear correlation has been

identified between the reversible performance loss rate and concentration of chloride in the fuel cell humidification water supply.

Start/Stop Tests Under N_2/N_2

To verify that the losses observed were truly from cycling under oxygen and high potentials, and not some other effect, the same S/S protocol was applied to an NSTF MEA using N_2 on both the anode and cathode instead of H_2/air. As with the H_2/air S/S, the fuel cell performance was evaluated periodically. A total of 336 cycles under the N_2/N_2 S/S protocol were completed. Inadvertently, for this MEA, 59 cycles under H_2/air were also completed. Fig. 49 shows the PDS and GDS polarization curves obtained during the S/S testing.

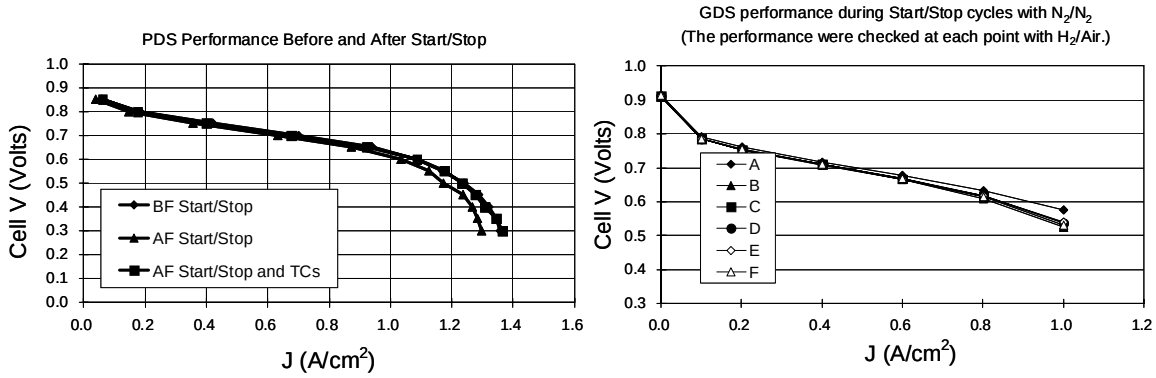

Fig. 49. (Left) Comparison of PDS performance before and after 336 S/S cycles under N_2/N_2. (Right) Comparison of H_2/Air GDS polarization curves taken at various intervals during N_2/N_2 S/S. Only a slight change in the mass transport region occurs from the testing and is fully recoverable by thermal cycling. The small reversible loss is believed to have occurred due to 59 inadvertent H_2/air S/S cycles.

Compared to NSTF MEA's exposed only to the full number of H_2/air S/S cycles, the N_2/N_2 S/S response showed even less change in the mass transport region. Again, the subsequent thermal cycling recovered even this small change. Furthermore, there does not appear to be any measurable irreversible loss at any current density (see Fig. 49, left). Consistent with this functional performance stability, after the 336 N_2/N_2 S/S (and 59 H_2/air S/S) cycles, there was less than 5% reduction in measured electrochemical surface area. It is highly likely that this was caused by the 59 H_2/air S/S cycles and in fact this amount of ECSA loss is quantitatively consistent with the ~ 25% average loss recorded for all the other NSTF MEAs after 300 or more H_2/air S/S cycles.

Fig. 50 compares the percentage change in measured ECSA for a number of NSTF MEA's under H_2/air with this MEA tested primarily under N_2/N_2.

Considerations of Specific Activity Changes from Stop/Start Cycling

To this point we have concluded that the non-reversible loss in the NSTF MEA's fuel cell performance after 300 or more S/S cycles under H_2/air occurs primarily in the catalyst kinetics. The preceding assessments of electrochemical surface area changes suggested that the ~ 25% change in cathode surface area was sufficient to explain the ~ 10mV drop in the kinetic contribution to the polarization curves (see Fig. 48). Another contribution could be a change in the specific activity of the catalysts. The method used

to measure the specific activity for five of the NSTF sample MEAs before and after S/S testing, and again after thermal cycling to recover the reversible performance loss,

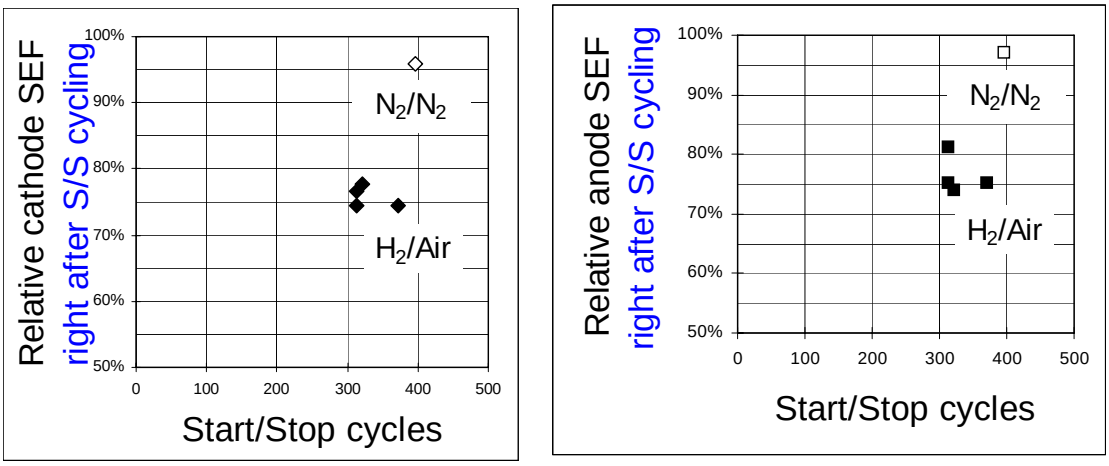

Fig. 50. Percentage of measured electrochemical surface area of the NSTF MEA's cathode (left) and anode (right), remaining after the S/S testing under both H_2/air and N_2/N_2.

was the 150 kPa O_2 metric at 900 mV as described in the experimental section. Excluding an outlier, the 900 mV metric for four of the five MEA's gave values lying in the range of 2.03 to 2.31 mA/cm^2-Pt after thermal cycling following the S/S testing. These values are very typical for this PtCoMn NSTF catalyst measured in fully conditioned MEA's we have tested in other experiments. The values immediately after the S/S testing, before thermal cycling to recover the reversible performance loss, ranged from 1.12 to 1.82 mA/cm^2-Pt. Since the specific activity was less immediately after S/S testing, but recovered with thermal cycling, it would appear by this metric there was some loss of specific activity associated with the reversible performance loss, but not with the non-reversible performance loss. Again the surface area loss appears to be the only significant factor contributing to the ~10 mV non-reversible kinetic loss.

2.1.4.4.3 Conclusions from Stop/Start Cycling

The NSTF PtCoMn catalyst-based MEAs all consistently exhibited substantially less performance loss under the Start/Stop test protocol than the dispersed Pt/Carbon catalyst-based MEAs. The Pt/Carbon catalysts lost 80% of the cathode surface area in less than 75 S/S cycles, versus approximately 25% after 300 cycles for the NSTF catalyst. This is similar to the behavior documented for the 0.6 to 1.2 V CV cycling tests in 2.1.4.1. Whereas the Pt/C performance loss appears irreversible, the performance loss of the NSTF MEA's under the S/S tests consists of a reversible contribution and an irreversible contribution. The reversible contribution shows up in both the "mass transport region" and kinetic portions of the polarization curve. This "mass transport region" reversible decay can be completely recovered by simply shutting down the cell and restarting the tests; no other activity was required to fully recover this reversible loss. Similarly, shutting down the cell and completing multiple thermal cycles with water flushing will nearly recover all the specific activity loss.

The irreversible loss appears to affect the performance primarily in the kinetic region of the polarization curve. This irreversible loss after the start/stop tests has contributions primarily from reduced electrochemical surface area. This ~25% loss in cathode

surface area measured after the S/S testing is not recoverable by thermal cycling and appears sufficient to explain the irreversible kinetic loss. X-ray diffraction characterization of the PtCoMn catalysts after the S/S tests indicate no change in the Pt alloy lattice spacing, which in turn suggests no change in the bulk alloy composition. If this result also applied to the crystallite surface composition, then that would be consistent with the lack of any change in specific activity. The apparent Pt crystallite size in the NSTF PtCoMn catalyst was not increased by the S/S testing, suggesting agglomeration is not occurring sufficient to explain all the ~ 25% surface area loss. In contrast, the Pt/C catalysts' crystallite size has roughly doubled after 100 S/S cycles, which is sufficient to explain a four-fold reduction in surface area, viz the 81% reduction of the cathode surface area. It is not consistent with the smaller ~ 20% loss of Pt/C anode surface area.

Doing the S/S tests under N_2/N_2 produces only a minimal detectable loss in surface area and no irreversible performance loss. This clearly suggests that the mechanism responsible for the ~25% loss in NSTF cathode surface area over the course of 300 S/S cycles requires oxygen and/or the high electrode potential it produces.

References for subsection 2.1.4.4

1. M. K. Debe, A. K. Schmoeckel, G. D. Vernstrom and R. Atanasoski, "High Voltage Stability of NanoStructured Thin Film Catalysts for PEM Fuel Cells," J. Power Sources **161**, 1002-1011 (2006).
2. A. Bonakdarpour, J. Wenzel, D. A. Stevens, S. Sheng, T. L. Monchesky, R. Lobel, R. T. Atanasoski, A. K. Schmoeckel, G. D. Vernstrom, M. K. Debe and J. R. Dahn, J. Electrochemical Society, Vol. **152 (1)**, 2005, A61-A72.
3. A. Bonakdarpour, R. Lobel, R. T. Atanasoski, G. D. Vernstrom, A. K. Schmoeckel, M. K. Debe and J. R. Dahn, "Dissolution of Transition Metals in Combinatorially Sputtered, Pt1-x-y Mx M'y (M,M' = Co, Ni, Mn, Fe) PEMFC Electrocatalysts "J. Electrochemical Society, Vol. **153 (10)**, 2006, A1835-A1846.

2.1.4.5 NSTF Stability under High Current Density H_2-O_2 Cycling.

Test Description

As another type of durability test, we have operated the same type of NSTF MEA as used for the S/S testing under highly oxidative, high power generation conditions. The 50 cm^2 MEA was mounted into a completely dry cell, and conditioned with totally dry H_2/O_2 reactant gases at 150 kPa and a constant potential of 0.5 V for the first hour, during which the cell self heated to 40°C. Conditioning continued for another 45 minutes during which the current density was increased to 0.7 A/cm^2 and the cell temperature to 60°C. This stage lasted for another two hours after which the reactant pressures were increased to 200 kPa, cell temperature to 65°C, and alternating galvanodynamic (GDS) and galvanostatic (GSS) polarization scans were initiated with constant stoichiometric anode and cathode flow ratios of 1.3 and 2.0 respectively. GDS and GSS repetitive scan cycles consisted of 10 minutes at 0.7 A/cm^2 followed by a ~ 50 minute GDS scans from 0.1 to 2.0 A/cm^2 and back to 0.1 A/cm^2 again. For a complete cycle, the effective mean current density was 0.99 A/cm^2. Approximately every 100 hours the cell was shut down for ~ 1.5 hours and restarted, after which it recovered any reversible cell voltage loss.

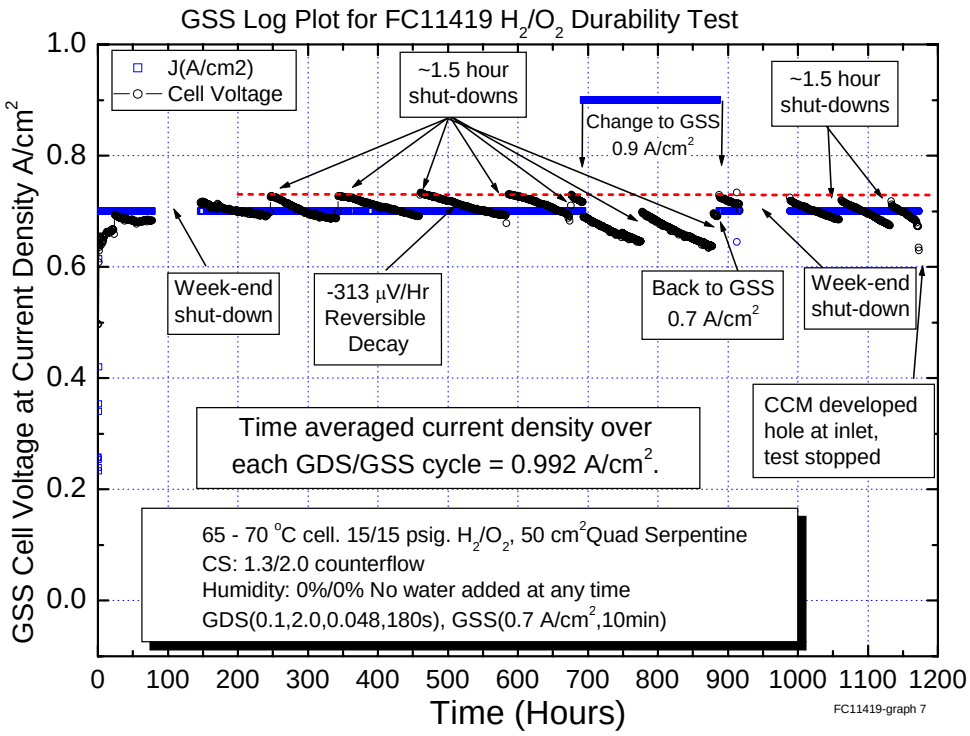

Fig. 51. Time-log plot of the cell voltage during the 10 minute, 0.7 A/cm^2 portion of the H_2/O_2 cycling, illustrating the recovery of reversible performance loss by shutting down the cell for 1.5 hours.

The MEA was operated under 200 kPa of totally dry, H_2/O_2 reactants. The reactants were introduced in a counterflow mode so that effective water backflow from the cathode to the anode occurred. The cell temperature was set at 65°C, but increased to ~ 70°C at the highest current densities. Ater an initial ~ 3 hour break-in period, also operating with

totally dry inlet gases, the cell was cycled slowly in a constant current mode between 0.1 and 2.0 A/cm^2, with 0.05 A/cm^2 steps, and constant stoichiometric flow rates of 1.3/2.0 anode/cathode. It would then sit at 0.7 A/cm^2 for 10 minutes before again starting the GDS polarization curve. Each cycle lasted approximately one hour, and the average current density over each cycle was 0.99 A/cm^2. However, it was observed that over a period of tens of hours, the GDS and GSS (0.7A/cm2, 10 min) voltages exhibited a small reversible decay on the order of 0.3 mV/hr that was completely recoverable by cooling the cell to room temperature for a total down time of 1.5 hours. Upon restarting the cell, the reversible performance loss was recovered. Fig. 51 illustrates the time-log of the cell voltage during the 10 minute 0.7 A/cm^2 portion of the cycle. It is seen that for multiple periods of ~ 100 hours, the reversible performance loss was fully recovered. Although impedance could not be measured during the durability testing, the changes in the GDS polarization curves were consistent with a slow membrane conductivity change (e.g from drying causing an increase in the impedance from 0.080 ohm-cm2 to 0.125 ohm-cm2. That is, using these values to IR correct the GDS polarization curves (shown below in Fig. 52) immediately after and before, respectively, the 1.5 hour shutdown periods, produced the same IR corrected GDS plots.

On top of this reversible decay, there was a slower, non-reversible performance loss which began to occur after 175 hours of operation and which continued to occur throughout the remainder of the test. The GDS polarization curves improved monotonically for the first ~ 175 hours, and then thereafter decreased at a slower rate. Fig. 52 shows a composite plot of the GDS curves taken near the re-start after each of the 1.5 hour shut-down periods. In total, between 175 and 815 hours, the cell voltage at 1 A/cm^2 in the GDS curves dropped only 7 mV (~ 11 microV/hour). After 815 hours the rate of performance loss increased, and substantially more after 960 hours.

In total, the test included 1000 hours of operation, consisting of over 1600 polarization cycles between ~0.87 V and ~0.5 V with minimal permanent performance loss, until the MEA finally failed due to formation of a hole.

A second, similar MEA was operated under the same protocol, this time with the test station enabled for water collection from the anode and cathode for measurement of the fluoride ion release rates. Since the only water in the system is that generated on the cathode, collecting the outlet water gave a quantitative measure of the water crossing over from the cathode to the anode. The ratio of water exiting the cathode to that exiting the anode was 2.0, so fully one-third of the generated water crossed over to the anode. The cathode and anode F^- ion levels were very low, close to the noise limits of the ion chromatograph, at ~ 3 $\pm$ 2.5 nanograms/min from each 50 cm^2 electrode (or 5 - 10 ng/cm^2 per hour). Low (24 ng/cm^2-hr) F^- ion release levels have been measured from NSTF MEA's operating under H_2/air at higher temperatures (120^{o}C) and correlated with lifetimes, in earlier studies as discussed in secton 2.1.5.2 of this report. The values measured here are below those values, despite the pure oxygen, probably because of the lower temperature. The low F^- ion release indicates low PFSA membrane decomposition, and in turn suggests that there are relatively low peroxide levels being produced on the NSTF catalyst surfaces. Both the higher specific activity and absence of exposed carbon surface area, which is a poor ORR catalyst, are believed to contribute to the improved 4-electron oxygen reduction process on the NSTF catalysts and lower peroxide generation rates observed in working fuel cells.

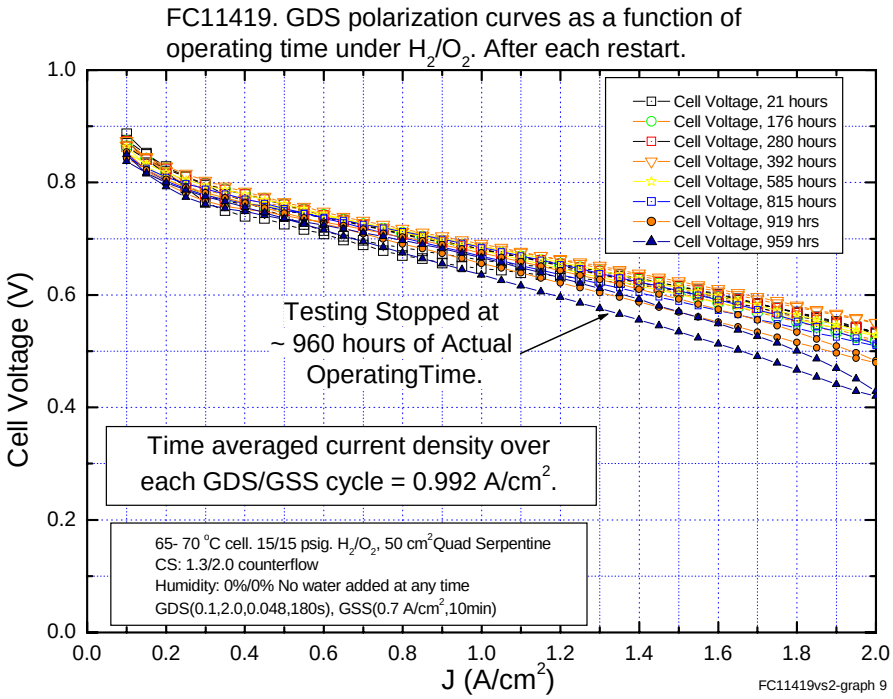

Fig. 52. Selected GDS polarization curves taken near the restart after each 1.5 hour shut-down illustrated in Fig. 12. The GDS polarization curves represent the performance with the reversible loss recovered by the 1.5 hour shut-downs.

Conclusions

The reversible performance loss observed under the H_2/O_2, high current density durability testing appears similar to the reversible performance losses at 1 A/cm^2 documented in the S/S testing in the preceeding subsection. In both cases a large fraction or all of the performance is recoverable by simply shutting down and restarting the cell. However, whereas the latter reversible losses manifest as mass transport losses, in the former the loss appears consistent with an impedance change. Fluoride ion release rates were measured to be less than 5 nanograms/min under the 200 kPa H_2/O_2 operation at an average current density of 1 A/cm^2. It is believed that such low rates contributed to the ~ 1000 hour lifetime of the MEA before the ~ 30 micron thick membrane developed a hole opposite a cell inlet. The low F^- ion release rates are believed to result from low peroxide generation rates on the NSTF catalyst surfaces.

This page left blank

2.1.4.6 NSTF MEA Stability under Load Cycling.

The next type of durability test used to characterize the down-selected NSTF catalyst based MEAs, with comparison to standard Pt/C MEAs, was a load cycling test. This was the same test used to demonstrate the enhanced durability of the 3M PEM with additives in section 2.2. The test station cycles ten 50 cm^2 cells through a nominally identical protocol consisting of eight test point conditions as shown in Table VII. The reactant flow rates were held constant, so that the stoichiometry varied at each test point. The cell temperatures and reactant dew points were held constant at 80/64/64^oC respectively. Periodically, the cycling through the eight test points was interrupted to set the cells at OCV. MEA lifetime was determined when the OCV fell below 800 mV.

Table VII. Load cycling test protocol.

Test Point	1	2	3	4	5	6	7	8
Stoichiometry	5	15	1.7	3	15	1.7	5	1.7
Duration (min.)	5	20	15	10	20	15	20	20
J (A/cm^2)	0.20	0.02	0.80	0.80	0.02	0.8	0.2	1.0

The NSTF CCMs had the PtCoMn (0.2 mg-Pt/cm^2) on each electrode, and used the 850 or 980 EW 3M PEM without additives. The CCM's were roll-good fabricated as described in section 4.1. They used the down-selected GDL discussed in sections 2.3 without bonding to the CCM. The NSTF MEAs did not have subgasket edge protection to mitigate mechanical failure.

The test results for the dispersed Pt/C MEA controls were available for comparison from work completed outside the contract. These used nominally the same type of 3M PEM, without lifetime enhancing additives, and Pt/C catalysts at loadings of 0.4 mg/cm^2 on the anode and cathode. Some of the control MEAs had edge protection and some did not.

MEA failure in this load cycling test can be due to both membrane failure from peroxide attack, and catalyst surface area loss due to surface area and activity degradation mechanisms. For generally short lifetimes, of a few hundred hours, when the OCV has dropped below 800 mV, it does so primarily due to enhanced cross-over and pinhole formation in the membrane. This in turn has occurred due to free radical attack of the membrane resulting from peroxides generated originally on the catalyst surface. This test, then, actually compares the relative amounts of peroxide generation and/or scavenging potential of the catalysts. As discussed in connection with section 2.1.5 (catalyst down-selection), MEAs with the NSTF-Pt catalysts generate significantly less F^- ion release rates compared to Pt/C catalysts, while the NSTF-PtCoMn catalysts reduce this by almost another factor of 5 to 10. These results are fully consistent with the load cycling test results shown below.

Fig. 53 below plots the lifetime versus MEA sample for seven of the Pt/C controls and four NSTF MEAs. It is clearly seen that the average lifetime to failure of the NSTF MEA's was consistently more than seven times that of the Pt/C control MEA's.

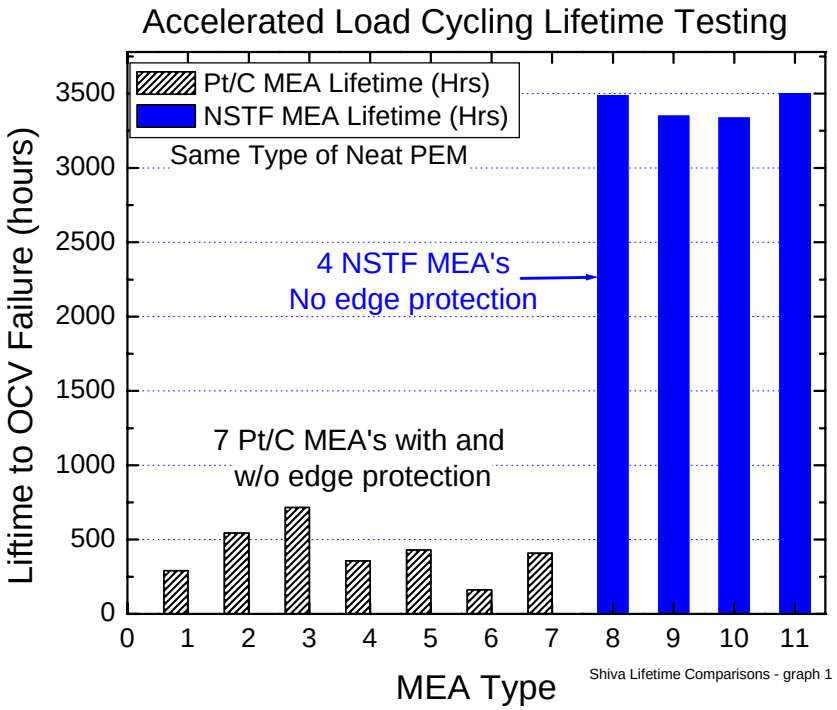

Fig. 53. Lifetime to failure, defined as when OCV drops below 800mV, for four NSTF PtCoMn MEAs and seven Pt/C control MEAs, undergoing a load cycling protocol.

This lifetime enhancement factor is consistent with the gain seen with the 120^{o}C stress tests discussed in section 2.1.4.3.

2.1.4.7 Conclusions on NSTF Catalyst Durability Evaluation.

Unlike dispersed catalysts consisting of nanometer sized isolated particles, which can dissolve and agglomerate resulting in loss of surface area, the NSTF catalysts are thin films comprised of contiguous, polycrystalline domains. They are, in effect, already highly agglomerated. X-ray diffraction measurements of the pure Pt NSTF crystallite sizes show very good stability of particle size with operational time in a fuel cell. Under CV cycling to high potentials, some further agglomeration or crystallite size increase of the NSTF is seen, but much less than observed with either the standard carbon or graphitic carbon supports.

The much superior ability of the NSTF catalyst to withstand thousands of fast voltage scans over the potential range most critical for Pt dissolution and Pt agglomeration demonstrates another significant differentiating feature over carbon supported catalysts. The much higher activation energy (52 vs 23 kJ/mole) and higher value of the minimum surface area, S_{min} , (67-70% versus 10%) means there are two ways in which the NSTF durability is enhanced, viz. the minimum stable surface area is higher, and it takes much longer (more cycles) to reach the minimum surface area.

The PR149 organic pigment used for the NSTF catalyst supports is much more stable against Pt catalyzed electrochemical corrosion than carbon. It is also highly thermally stable, and once the support whisker is encapsulated within the metal catalyst shroud, the support whisker is essentially not functioning in any manner critical for fuel cell operation. It is the catalyst coating itself which conducts electrons to and from the GDL.

The ability of the NSTF catalyst to withstand 1.5 V under H_2/N_2 without corrosion of the support or loss of surface area or loss of catalyst activity, for either pure NSTF Pt or NSTF ternary, is a significant differentiating feature over carbon or graphitic carbon supported catalysts. Furthermore, since the NSTF MEAs did not lose any performance due to the 1.5 volt exposure, the 3M GDL must be adequate as well to withstand these potentials with the protection provided by electrolysis of water by the NSTF catalyst.

These features of much greater stability under voltage cycling to 1.2 V and tolerance of even higher voltages for long periods of time, should offer significant robustness against loss of MEA performance due to start-stop, hydrogen starvation, or cell reversal events in real fuel cell stacks.

The enhanced durability of NSTF electrocatalysts should offer significant robustness against loss of performance due to start-stop, fuel starvation, or cell reversal events in real fuel cell stacks, and also enable new systems approaches to rejuvenating the MEA not possible with carbon based electrodes.

2.1.5 Catalyst Down-Selection

For the purposes of completing Task 3 of this contract, (scale-up and stack testing) it was necessary to down-select the MEA components. This section discusses the basis for the NSTF catalyst down-selection. The catalyst composition and loading had to be determined which would be used for scale-up to make the CCM roll-goods for evaluation in a 5kW short stack. Among the criteria used were catalyst activity, mass transport limitations or performance at high current densities, ease of start-up and reversible stability factors, and fluoride ion release since it relates to membrane lifetime.

2.1.5.1 Composition Selection – ORR activity and loading

On the basis of many specific activity measurements as discussed in section 2.1.3., and general fuel cell performance, the best NSTF ternary alloy composition was determined to be either PtNiMn or PtCoMn with a Pt/TM bi-layer ratio of 3. Although it was demonstrated there that optimizing the whisker support structure to better match the catalyst loading and volume could increase the mass activity, there was not the opportunity in this project to do so with the production process used for fabricating the roll-good NSTF support films. The "standard" whisker support films were therefore used with the belief that for higher loadings, ca. 0.2 mg/cm^2, they are probably close to the best.

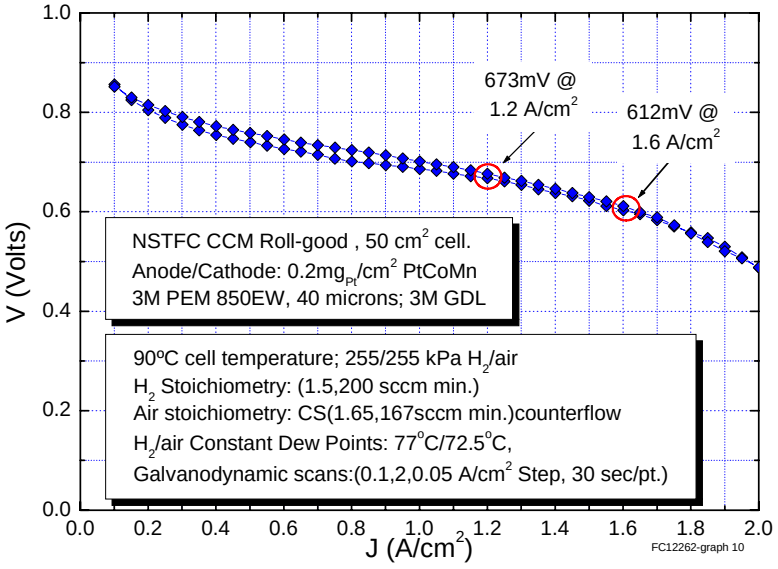

Fig. 1. GDS polarization curve from a roll-good CCM having the down-selected cathode catalyst and loading and 3M PEM, tested at automotive target conditions. The red circles indicate automotive performance targets.

Although most of the ternary catalyst development work had been conducted using 50cm^2 MEA's having 0.1 mg-Pt/cm^2 on the cathode, a higher value of 0.2 mg/cm^2 was chosen for various reasons. This value would still be sufficiently low to show a real improvement toward the project's overall DOE targets, yet be high enough to provide some "cushioning" against factors that might arise in stack testing due to impurities and break-in and start-up. Fig. 1 shows the GDS performance curve from a fully roll-good fabricated NSTF CCM having the down-selected PtCoMn catalyst {(90:10)[50,3,1] 0.2 mg-Pt/cm^2} on both the anode and cathode. It meets certain automotive performance targets under high temperature conditions. In the next section, the basis for selecting PtCoMn over PtNiMn is reviewed.

2.1.5.2 Fluoride Ion Release Rates

Introduction

It is well known that PEM fuel cell membrane degradation is primarily caused from free radical attack of the ionomeric polymer, where the radicals are generated from decomposition of peroxides that in turn are the result of incomplete 4-electron oxygen reduction. This can occur on the cathode or on the anode from oxygen cross-over. With dispersed catalysts, the carbon support is a very poor oxygen reduction catalyst, and as such can also be a source of peroxides and radicals.

Membrane degradation is a serious issue and multiple approaches have been practiced to minimize the effects of peroxides, such as protecting the fluoropolymer endgroups and adding materials to scavenge the peroxide radicals. In section 2.2, significant gains in lifetime were achieved by adding specific materials to the ionomer before membrane fabrication. The materials such as MnO_3, facilitate the rapid scavenging of the radicals before they can attack the polymer. The original source of the peroxides in the first place is the incomplete reduction of oxygen, the reaction stopping after a 2-electron transfer process instead of going all the way to a 4-electron reaction. So improving the catalyst to make it less of a source of the peroxides in the first place, is a key strategy.

It has been found during this contract, that it is an inherent property of the NSTF catalysts that lower fluoride release rates are produced compared to dispersed Pt/Carbon catalysts, and by significant amounts. NSTF-Pt produces about one-tenth as many fluoride ions per unit time as the equivalent loading of Pt/C under the same conditions. As shown below, the NSTF-PtCoMn ternary can reduce this by another factor of five to ten. In section 2.1.4.3 it is shown that at 120^{o}C, under identical conditions, Pt loadings, membrane and GDL, the NSTF PtCoMn based MEA's produced 75 times lower F^- ion release rates as Pt/C based MEAs, and had ten fold longer lifetimes-to-failure of the membrane.

This significantly lower membrane degradation rate is presumably due to both lower levels of peroxide production and better scavenging of the radicals that are produced. Since the NSTF does not contain carbon as a support, this source of incomplete oxygen reduction is eliminated. As shown in section 2.1.3, the specific activities of the NSTF ternaries are ten times higher than Pt/C, and to the extent that this means there is a larger fraction of 4-electron versus 2-electron reactions, less peroxide and more water would be produced. But probably the largest factor is from the transition metal scavenging that occurs from the transition metal excess, over the equilibrium Pt alloy fraction, that dissolves into the membrane from the catalyst. This is discussed in detail below.

Experimental

Fluoride ion release rates, in ng/min, from operating 50 cm^2 fuel cells were determined by collecting the water effluent from the anode and cathodes in carefully handled pristine polyethylene containers. The collection time was controlled and the F^- ion concentrations determined by ion chromatography. A series of experiments were first conducted to determine the best operating conditions for generation of the F^- ions, specifically operating voltage, temperature and pressure. This developed into the following test protocol.

The MEA's all used 3M membrane (1000 EW) precleaned by acid washing, and carbon cloth GDL's. (For more in-depth background on the fuel cell testing, see section 2.1.3.1.) Using NSTF MEA's that had been fully broken-in, the cells were operated at 15/15 psig H_2/air, 100%/100% RH and in a constant flow, constant voltage mode. With the temperature set at 70°C, hydrogen cross-over was measured first to make sure the MEA was good, i.e. had no pinholes. Then the cell was operated at a fixed voltage setpoint, e.g. 0.4 V, with a 20 minute initial equilibration time followed by water collection from both the anode and cathode each half hour for two hours (four samples), noting net water, time and date. This was repeated for other voltages (0.9 V to 0.4 V), and then the series repeated at 80°C and 90°C. The F^- level in the water samples was analyzed using a Dionex ICS-2000 system operated in isocratic mode and controlled by Dionex Chromoleon V6.60 software. Ion chromatography standards were prepared from verified single anion standards (Alltech 37035). The four sample values were then averaged. Overnight, the cell would be left at 0.8 V, and measurements continued the following day.

Results

This protocol was applied to an MEA having pure NSTF Pt on both the anode and cathode, and two series of MEAs having different PtNiMn and PtCoMn cathodes.

What was observed was that there was a definite voltage dependence of the amount of F^- release, with significant amounts starting to be produced below 0.7V, consistent with the nominal 0.68V for the equilibrium peroxide to water reaction potential. Also, and most interesting, for the catalyst samples tested, the lowest F^- production rates were obtained with the NSTF ternary catalysts containing Mn.

Fig. 2 below illustrates the measured F^- ion release rates as a function of cell voltage from the anode (left) and cathode (right) effluents of two NSTF MEAs. The cell temperatures were 90°C. FC9146 in Fig. 2 had pure Pt on both the anode and cathode. FC9305 had the same lot of pure Pt on its anode, but 0.1 mg/cm^2 of PtNiMn on its cathode. Values from multiple days are shown for FC9146 to illustrate the variability seen.

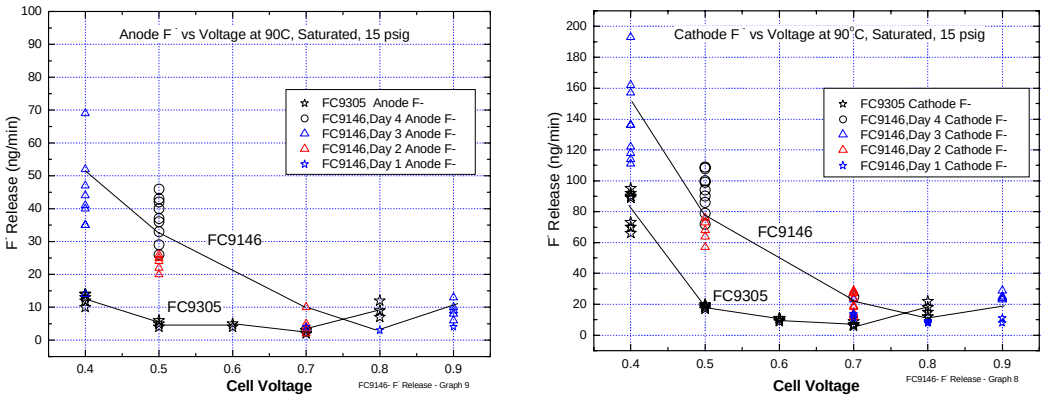

Fig. 2. F^- ion release rates from the anode (left) and cathode (right) effluents as a function of cell voltage for an MEA with pure Pt on the cathode and anode (FC9146) and an MEA with pure Pt on the anode and PtNiMn on the cathode.

Fig. 2 shows several important facts. First, FC9146 shows that cathode F^- rates are about three times larger than the anode rates at 0.4, 0.5, and 0.7 V. Second, F^- release rates for both anode and cathode increase as the cell voltage decreases (and current density increases). Third, the F^- release rates drop to near zero above 0.7 V.

Finally, the F^- release rates from the PtNiMn cathode are significantly lower than from the pure Pt cathode. Although not shown in Fig. 2, the cathode F^- release rates normalized to current density decreased approximately linearly with cell voltage, but current density-normalized anode F^- release rates did not appear to increase below 0.5V.

The fact that little F^- release occurs above about 0.7 volts is consistent with the RRDE measurements discussed in section 2.1.2.3, Fig. 2c, which showed negligible peroxide generation down to 0.6V. As explained in that section the Levich – Koutecky plot in Fig. 2c, from which additionally the value of 4 for the number of electrons exchanged in the ORR was derived, confirmed the absence of any peroxide produced down to 0.6 V, as indicated by the lack of any current at the ring (Fig. 2b) for all rotation rates. All these findings are in agreement with the behavior of bulk Pt as well as carbon supported catalyst tested under similar conditions.

The equilibrium potential for hydrogen peroxide co-evolution, $O_2 + 2e- + 2\ H^+ \Leftrightarrow H_2O_2$, is 0.67 – 0.68 V. So in a working H_2/air fuel cell, for cell voltages, V, above this value, $Eo(H_2O_2) < V < 1.23$ volts, there is no H_2O_2 generated due to incomplete ORR on the Pt catalyst from O_2 supplied to the cathode. Also, it is reported that H_2 is not oxidized on the oxide layer of platinum, implying H_2O_2 is not formed at the cathode under OCV due to H_2 cross-over from the anode (See M. Inaba paper, 4th Int. Conf. On Appl. of Cond. Polymers, 2004.) Taken together, these imply that on a Pt-only cathode (no carbon, etc.) there is no mechanism for peroxide formation on the cathode catalyst above $Eo(H_2O_2)$.

Since in Fig. 2 the most F^- ions are generated at 0.4 volts, this cell potential was chosen to compare a series of PtNiMn and PtCoMn cathodes.

F^- ion release rates from PtNiMn and PtCoMn cathodes

Fig. 3 shows the fluoride ion release rate as a function of cell voltage for the MEA's in Fig. 1 plus three additional ones, measured with the above protocol at 90°C, full saturation and 15 psig. The left panel shows the F^- ion release rate from the cathode and the right panel from the anode. FC9146, the only MEA with pure NSTF-Pt on both its anode and cathode, is seen to generate significantly more fluoride ions than any of the ternaries.

FC9305 had PtNiMn(90/10)[20,3,1] on its cathode, FC9367 had PtNiMn(50/50)[20,0.6,1] on its cathode, FC9366 had PtNiMn (50:50)[20,1.2,1], and FC9364 had PtNiMn (50/50)[20,3,1] on its cathode. Because the Pt/TM ratio is lower for FC9367 than FC9305, it has more Ni and Mn than FC9305, and similarly, because the Ni:Mn ratio is 50:50 for FC9364, it contains more Mn than FC9305, but less than FC9367.

The amount of Ni or Mn in the as-made catalyst can be determined from the fabrication designation. Table I in section 2.1.3 contains the various fabrication designations of the FC#### MEAs. We do not know a'priori which element, Ni or Mn, is most responsible

for the improvement in reduction of fluoride release, or if both are active or somehow synergistically working to reduce the effect of any generated peroxide radicals.

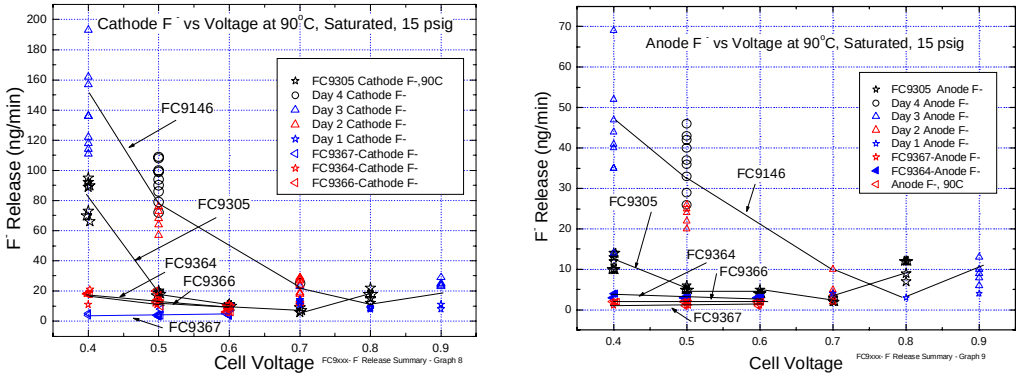

Fig. 3. Replot of Fig. 1 but with three additional MEAs with PtNiMn on the cathodes.

However, given the documentation in section 2.2 of this report how adding $MnNO_3$ to the ionomer before fabricating the membrane can reduce the F^- ion rates significantly, it is logical to assume that the Mn in the NSTF catalyst is helping. However, we will later show that between PtCoMn and PtNiMn, the former gives a further improvement. The following analysis focuses on the Mn as an example, but the same analysis could be done for the Ni.

FC9367 with the designation (50/50)[20.0.6,1] means 50% of the transition metal is Mn, by % atomic fraction. The 0.6 is the ratio of layer thicknesses, as made, and means the volume of Pt to TM total (Ni + Mn) is 0.6. For 0.1 mg/cm^2 Pt at a density of 21.45 g/cm^3, the equivalent volume thickness of Pt is 466 Angstroms. Hence the volume of total transition metal would be 466/0.6 = 777 Angstroms. Taking the density of Ni to be 8.90 g/cm^3 and that of Mn 7.32 g/cm^3, the mean density of the TM equivalent layer would be 8.1 g/cm^3. This implies that the 777 Angstrom thick TM "layer" contains 0.063 mg/cm^2 of the "mean" transition metal. The loading of Mn in this would be approximately 7.32/(7.32 +8.90)·0.063 = 0.028 mg/cm^2.

FC9366 with the designation (90/10)[20,1.2,1] means only 10% of the transition metal is Mn while the Pt/TM volume ratio is 1.2. Hence the same calculation implies the TM layer equivalent thickness was 388 Angstroms and the Mn loading would be 0.014 mg/cm^2, half of that in FC9367.

Similarly, FC9364 with a designation (50/50)[20,3,1] implies a Mn loading of ~ 0.0056mg/cm^2, intermediate between that of FC9305 and FC9367, and half that of FC9366.

FC9305 with the designation (90/10)[20,3,1] means only 10% of the transition metal is Mn while the Pt/TM volume ratio is 3. Hence the same calculation implies the Mn loading is only ~ 0.0011mg/cm^2, some 25 times less than in FC9367.

In Fig. 3 it is clearly seen that the pure Pt containing MEA's generated considerably higher F^- ion release rates than the PtNiMn containing samples, and that the higher the Mn loading in the original cathode, the lower the release rate at every voltage, viz., FC9305 > FC9364 ~ FC9366 > FC9367. This strongly suggests that the amount of

original transition metal in the as-made catalyst is influencing the fluoride release rate measured in the water exiting from both the anode and cathode sides. One hypothesis is that the excess Mn above the equilibrium alloy value, as discussed at length in section 2.1.3.2, dissolves into the membrane. The amount of Mn that might have leached into the PEM from each catalyst can be estimated, although there is no certain way to know if it would all stay in the membrane.

To estimate what fraction of the Mn in the as-catalyst could dissolve into the PEM, we utilize the results of the acid-soaking study completed under this contract by Dalhousie University and reported in Appendix II. From those Pt_{1-x-y} Ni_xMn_y composition-spread dissolution studies done in both acids and after fuel cell tests, for values of $x+y < 0.25$, the amount of Mn dissolved away was about 62%. For $x+y > 0.25$, about 84% of the initial Mn is dissolved away. Similar results were obtained from characterization of fuel cell tested MEA's made with the composition-spread libraries. Hence the FC9367 sample might have leached 0.028 x 0.84 = ~ 0.024 mg/cm^2 into the membrane, FC9366 might have leached 0.014 x 0.84 = ~ 0.012 mg/cm^2, while FC9305 would have leached 0.0011 x 0.62 = ~ 0.00068 mg/cm^2, or 35 times less than in FC9367. Finally, FC9364 would have leached 0.0056 x 0.84 = ~ 0.0047 mg/cm^2.

Subsequent to these samples, another MEA, designated FC9674 (90:10)[20,1.2,1] was tested similarly. It contained 0.0285 mg/cm^2 of Mn as made and could potentially dissolve 2.39 μg/cm^2 into the PEM.

Fig. 4 shows the cathode F^- release at 0.4 volts from these samples plotted versus the as-made Mn content (bottom) and versus this possible leached amount of Mn (top). A clear monotonic dependence is seen on the amount of Mn in both cases. Furthermore, at the highest values, the fluoride release rates have been reduced to nearly that of the DI water control value. We emphasize that similar plots would be obtained for the Ni content, since its fraction in the as-made catalysts and potential amount dissolved would be proportional to the Mn. However, given the clear advantages discussed in section 2.2 of this report on the role of Mn additives to the membrane ionomer as a means to reduce the effect of peroxides and fluoride release rates with dispersed catalysts, it is logical to assume that it is the Mn more than the Ni that is the key additive in the NSTF ternary alloys enabling the reduced release rates. That this is not the whole story is shown below where a PtCoMn series provides even lower fluoride release rates than PtNiMn.

Since excess transition metal dissolved into the membrane can cause the membrane conductivity to decrease and its water uptake potential to decrease, too much dissolved Mn or Ni can have negative consequences. This was discussed at length in section 2.1.3.2.4 of this report as the reason for seriously degraded fuel cell performance for Pt/TM < 1. As a catalyst down-select criterion, this metric was used to determine the range of Pt/TM values.

The same series of measurements were completed for the PtCoMn series as for the PtNiMn series, and Fig. 5 shows the resulting plot of F^- ion release rates as a function of the initial Mn content.

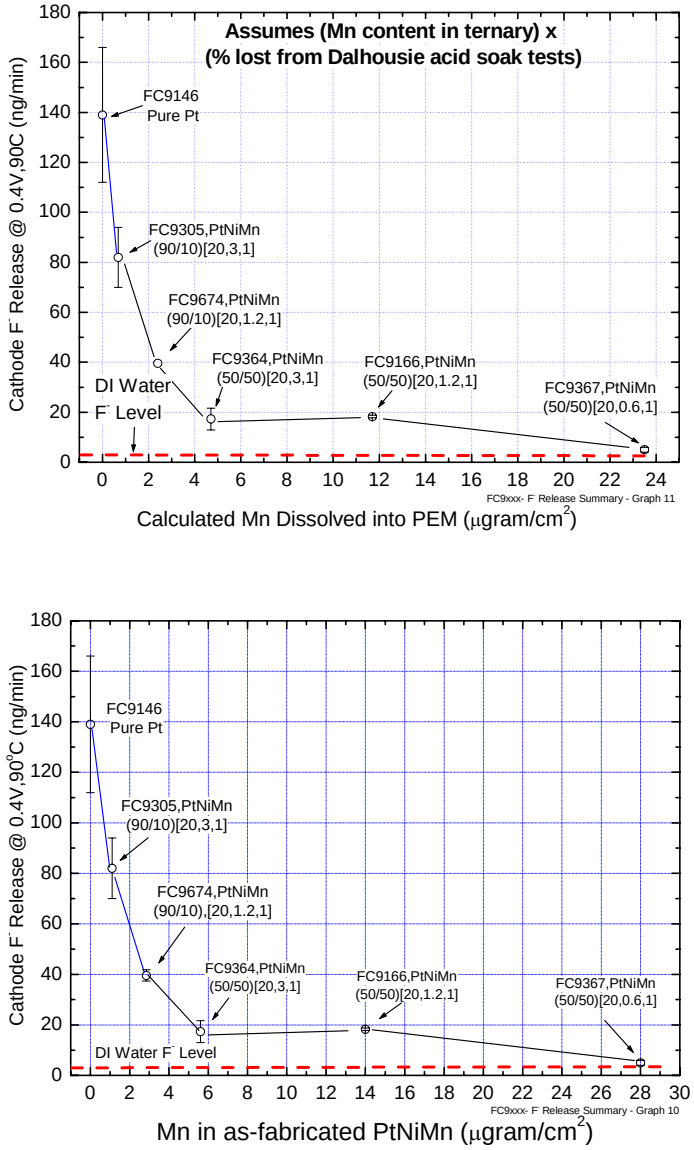

Fig. 4. Variation of the cathode F^- ion release rate as a function of the Mn in the as-fabricated PtNiMn cathodes (bottom), and as a function of the calculated amount of Mn that could have dissolved into the membrane, in excess of the Mn/Pt ~ 0.33 equilibrium alloy fraction.

It is clear from Fig. 5 that the PtCoMn ternary is giving a further improvement in reduction of fluoride release rate over PtNiMn. Even the relatively high value of Pt/TM = 3 for FC9550, with the designation (90:10)[20,3,1], has F^- ion release levels within a factor of two of those MEAs having TM values at much higher levels which would cause fuel cell performance loss and reduced specific activity as shown in section 2.1.3.2.

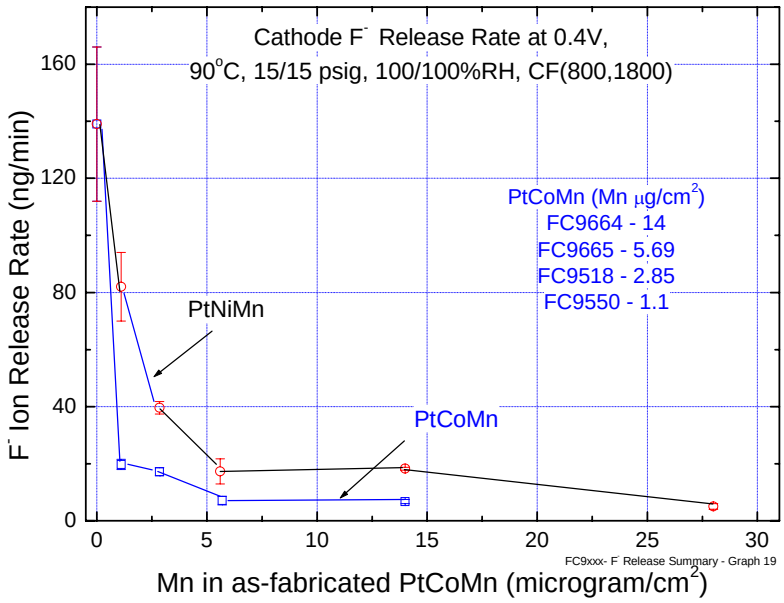

Fig. 5. Comparison of the F^- ion release rates for MEAs having the PtNiMn series and PtCoMn series on the cathodes, as a function of the Mn in the as-fabricated ternary.

Conclusion

Since all the results above were obtained with Pt loadings of 0.1 mg/cm^2 on the cathode, it must be recognized that if the loadings were higher, then there would be a proportionate increase in the absolute amount of dissolved transition metal. Since even at the equilibrium Pt/(CoMn) = 3 ratio for the MEA in Fig. 5 (FC9550, Mn = 1.1 µg/cm^2) the F^- ion release rates were within a factor of two of the minimum, this composition would clearly be adequate at higher loading values. In the preceding section, the down-selected loading was 0.2 mg-Pt/cm^2. From this metric then, the preferred ternary catalyst for down-selection for scale-up and short stack testing would be PtCoMn (90:10)[L,3,1], where the bilayer thickness, L, is arbitrary, at the 0.2 mg-Pt/cm^2 loading.

2.1.5.3 Minimizing Mass Transfer Losses

Introduction

The performance of a PEM fuel cell is represented by its polarization curve, under any given set of operating conditions. The polarization curve is a plot of the cell voltage versus current density, usually expressed as A/cm^2 of active area of the MEA. Traditionally, the polarization curve is described as having three basic loss contributions, each manifested as the dominant loss mechanism in different current density domains. In the lower current density range, e.g. < ~ 0.2 A/cm^2, the loss is primarily kinetic, due to catalyst activation and concentration overpotential losses. In the mid-range of current

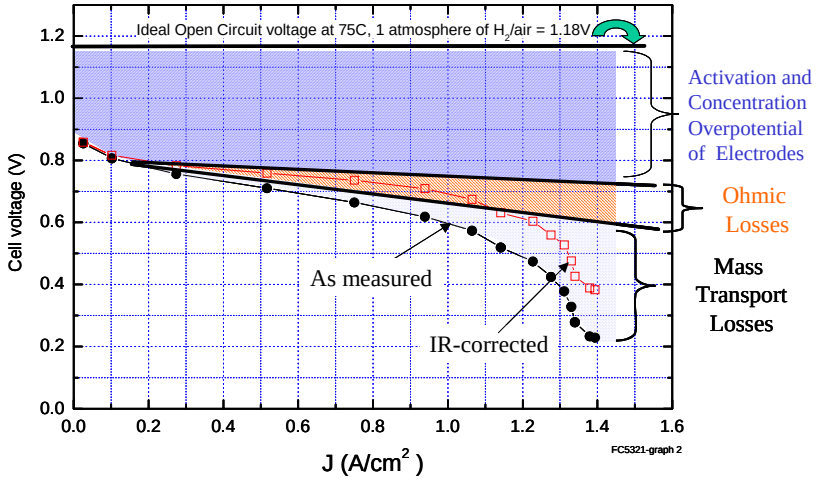

Fig. 6. Illustration of the three major contributions to the cell voltage loss as the current density increases.

density, e.g. 0.2 < j < ~ 1 A/cm^2, the loss of cell voltage is dominated by electrical impedances of the MEA components and interfaces. In the highest current density range, the loss of cell voltage is predominantly due to increasing difficulty of reactants to reach the catalyst sites, referred to as mass transport overpotential. Both the gas diffusion layer and the catalyst layer can contribute to the mass transport overpotential losses. Fig. 6 illustrates this.

In this section we demonstrate how a physical property of the catalyst layer electrode structure can be controlled to obtain increased cell voltage at the highest current densities, at which in conventional membrane electrode assemblies, mass transport limitations of the reactants can limit the maximum current density obtainable. What we discovered is that if the NSTF catalyst electrode layer thickness can be kept below approximately 0.25 microns, then there is no mass transport overpotential at current densities as high as 2 A/cm^2 under pressurized hydrogen/air operation. Furthermore, we demonstrate for one type of catalyst support particle and constant Pt mass loading of 0.1 mg/cm^2, a linear relationship exists between the catalyst layer thickness and the amount of mass transport overpotential at 2 A/cm^2 for pure Pt and Pt ternary catalysts.

Experimental

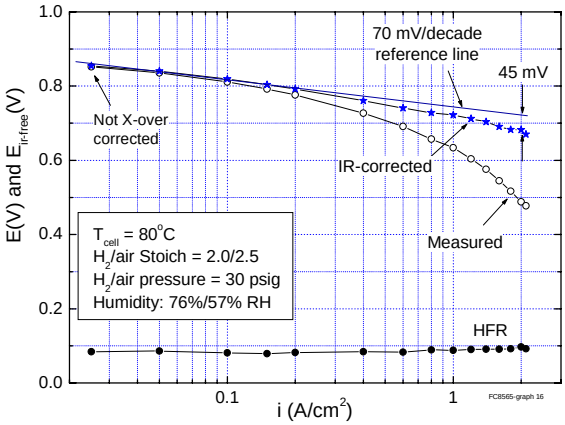

Fig. 7. Representation of the fuel cell polarization curve logarithmically to extract the amount of mass transport overpotential loss: The gap between the IR-corrected cell voltage curve and the kinetic loss line (70mV/decade assumed) is attributed to mass transport loss. At 2 A/cm^2, this MTL = 45 mV.

The kinetic loss contribution is well known by theory and experiment to obey an exponentially decreasing function, whereas the resistance loss is a strictly linear function of current density. The mass transport loss contribution (MTL) is a more complicated function, and most easily separated from the kinetic and IR losses in a logarithmic representation of the polarization curve, as illustrated in Fig. 7. The slope of the kinetic contribution is usually taken as approximately 70 mV/decade of increase in current density. For the NSTF electrodes, this Tafel slope is very close to 70 mV/decade as discussed in section 2.1.3.2. If a high frequency impedance measurement is taken at the same time as the cell voltage versus current density, then the cell voltage can be corrected for the IR loss by adding the product of the current density and cell resistance to the measured cell voltage, indicated in Fig. 7 as the IR-corrected cell potential. The remaining gap between the 70mV/decade kinetic loss line and the IR-corrected curve represents the cell voltage loss due to mass transport loss (MTL), seen in Fig. 7 as 45 mV.

A series of MEA's were fabricated having different NSTF ternary catalysts on the electrode. The different constructions had different volumes of catalyst in the electrode layers and hence presented different degrees of thickness and porosity in the ultra-thin electrode layer once the catalyst was transferred to the membrane to form the CCM. The gas diffusion layers placed on either side of the CCM to form the MEA were fabricated by coating a gas diffusion micro-layer on one side of a carbon cloth electrode backing layer. The MEA was installed in a 50 cm^2 cell, having quad-serpentine flow fields, at about 30 % compression, and tested under various conditions until the performance stabilized. For each of these example MEAs the fuel cell tests were conducted with the same protocol, consisting of the standard break-in and conditioning of the MEA followed by a series of PDS and GDS polarization curves to characterize the performance. Testing continued under multiple sets of operating conditions, including galvanostatic scanning at 80°C, 30 psig (3 atmospheres absolute = ~ 303kPa), 70% relative humidity on anode (hydrogen) and 57% cathode (air), and constant stoichiometric flow rates of 2.0 on the anode and 2.5 on the cathode. The high frequency resistance (HFR) was measured at the same time as the current density to allow obtaining the IR-corrected polarization curve. For each such example, the MTL was obtained as illustrated in Fig. 7. For a subset of the examples, scanning electron micrographs (SEM) were obtained of the CCM's to determine the thickness of the cathode layers. Since the catalyst loading and composition was known, as well as the

volume of the NSTF PR149 support whisker, the total volume of catalyst per unit planar area, equivalent to an effective thickness, could be calculated. The MTL could thus be plotted as a function of either the SEM determined thickness or the calculated thickness. Fig. 8 below shows the SEM cross-sections and resultant thickness of the electrodes for the four examples measured.

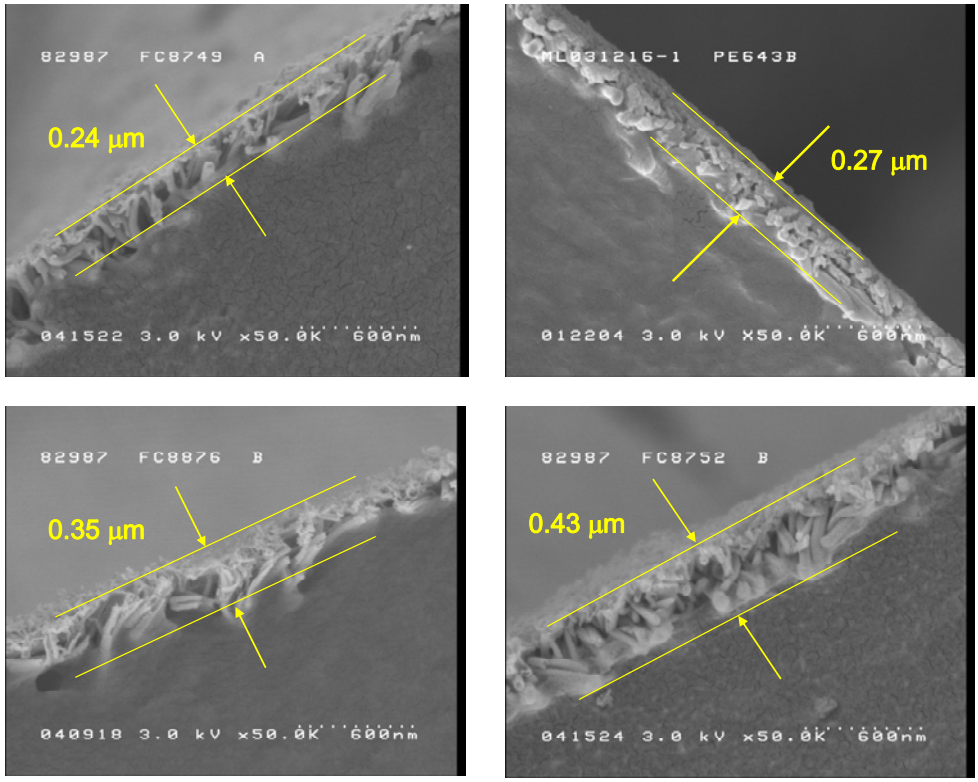

Fig. 8. SEM cross-sections of the CCM's in examples 1-4. Example 1 (top-right); Example 4 (top-left); Example 3 (bottom left); Example 2 (bottom right).

Results

Example 1: In this example an MEA identified as FC8565, was assembled with a pure Pt NSTF anode catalyst (0.15 mg/cm^2), and a PtCoFe ternary cathode (with 0.1 mg-Pt/cm^2), onto a 1.36 micron thick cast Nafion^{TM} PEM with equivalent weight of about 1000. The cathode ternary catalyst had a Pt/CoFe volume ratio of 3, Co:Fe atomic ratio was 90:10 and a Pt and CoFe bi-layer thickness of 70 Angstroms (see section 2.1.3 for more information on the catalyst designation and method of fabrication.) Fig. 9 shows the measured cell potential, IR-corrected cell potential, and the 70mV/decade kinetic loss line. Assuming negligible mass transport losses at 0.2 A/cm^2, (where the 70 mV/decade dashed line is made to osculate the data) then the conclusion is that there is also negligible mass transport loss at 2 A/cm^2, since the IR-corrected polarization curve is co-linear with the dashed kinetic loss line. A scanning electron micrograph of the catalyst coated membrane is shown in Fig. 8 (top-right) and the cathode catalyst layer is seen to be only about 0.27 microns thick.

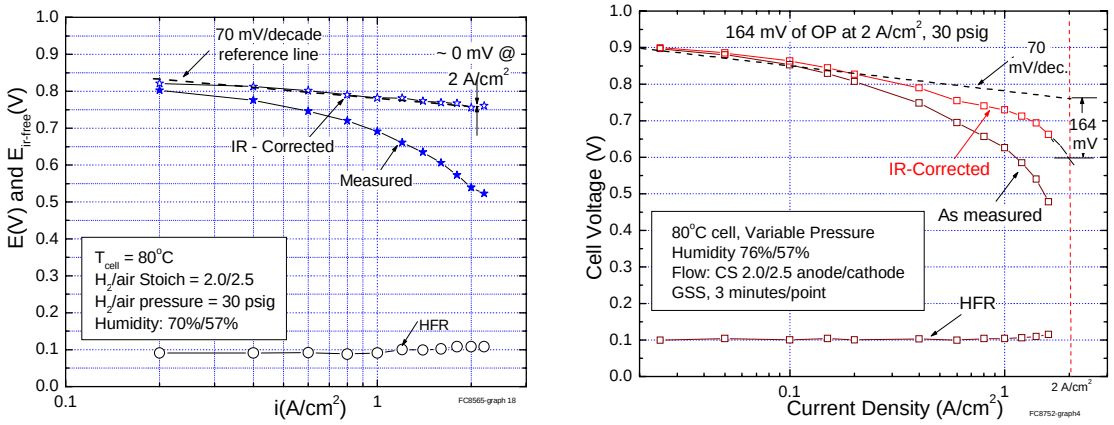

Fig. 9. GDS polarization curves of examples 1 and 2 tested under the fuel cell conditions shown, to obtain the mass transfer overpotential. An indicated ~0mV of MTL at 2 A/cm^2 is shown for example 1 (left), but 165mV for example 2 (right).

Example 2. This MEA, identified as FC8752, had a Pt/NiFe catalyst with Pt/TM ratio of 0.6. The Ni:Fe atomic ratio was 95/5 and 30 Angstrom thick bi-layers. From the fuel cell polarization curve the mass transport loss at 2 A/cm^2 was measured to be 164 mV (see Fig. 9). The SEM cross-sectional thickness of the cathode layer was measured to be 0.43 microns, as shown in the bottom right panel of Fig. 8.

Example 3. This MEA, identified as FC8876, had a PtCoMn NSTF ternary catalyst with a Pt/TM layer thickness ratio of 1.35 and bi-layer thickness ~ 17 Angstroms. From the fuel cell polarization curve the mass transport loss at 2 A/cm^2 was measured to be 107 mV. The SEM cross-sectional thickness of the cathode layer was measured to be 0.35 microns, as shown in the bottom left panel of Fig. 8.

Example 4. This MEA, identified as FC8749, had a pure Pt NSTF catalyst having a Pt loading of 0.15 mg/cm^2. The fuel cell polarization curve gave a mass transport loss at 2 A/cm^2 of 23 mV. The SEM cross-sectional thickness of the cathode layer was measured to be 0.24 microns as shown in the top left panel of Fig. 8.

Fig. 10 shows a plot of the mass transfer overpotential loss, in mV, from examples 1-4, plotted as a function of the measured SEM thickness in those same examples. The straight line is a linear fit to the data points. A linear dependence of the mass transport loss on the electrode thickness is indicated.

Three other MEA examples were tested as well, for which the thickness was not measured by SEM, but determined by calculation as shown below. The mass transfer overpotential or loss was determined in the same way for these three examples as for examples 1-4.

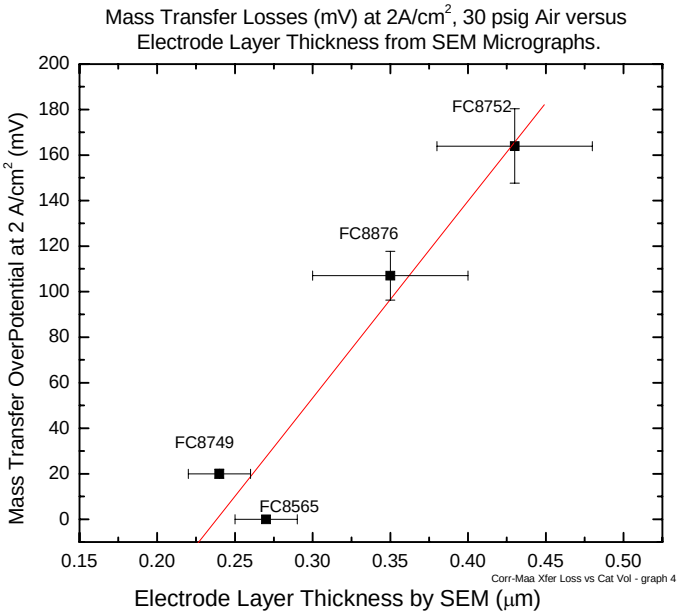

Fig.10. Mass transfer loss, in mV, from examples 1-4, plotted as a function of the measured SEM thickness

Example 5. An MEA , identified as FC8676, was fabricated as in Example 1, except the cathode catalyst was a PtCoFe NSTF ternary catalyst having a Pt loading of 0.15 mg/cm^2, Pt/CoFe volume ratio of 3. The Co:Fe atomic ratio was 90/10 and the multi-element NSTF ternary catalyst was made by alternating layers of Pt and CoFe with 70 Angstrom thick bi-layers. The fuel cell polarization curve was measured under the same conditions as in Example 1, and the mass transport loss at 2 A/cm^2 was measured to be 45 mV (see Fig. 7). This catalyst had the same composition as that of Example 1, but had 50% more Pt and CoFe. The volume of the catalyst layer was thus 50% larger than that in Example 1, for which the MTL was ~ 0mV versus the 45mV of this example.

Example 6. This MEA, identified as FC8772, was fabricated with a PtNiFe ternary catalyst having a Pt loading of 0.10 mg/cm^2, Pt/NiFe volume ratio of 0.6, Ni:Fe atomic ratio was 95/5 and 30 Angstrom thick bi-layers. The mass transport loss at 2 A/cm^2 was measured to be 175 mV, as shown in Fig. 11.

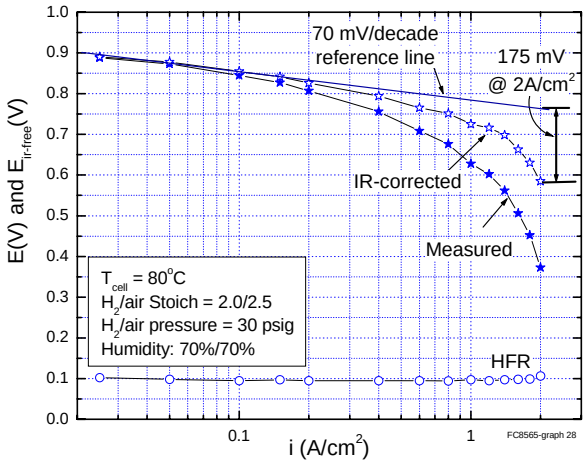

Fig. 11. GDS polarization curves of example 6 tested under the fuel cell conditions shown, to obtain the mass transfer overpotential. A mass transfer loss of 175 mV of MTL at 2 A/cm^2 is shown.

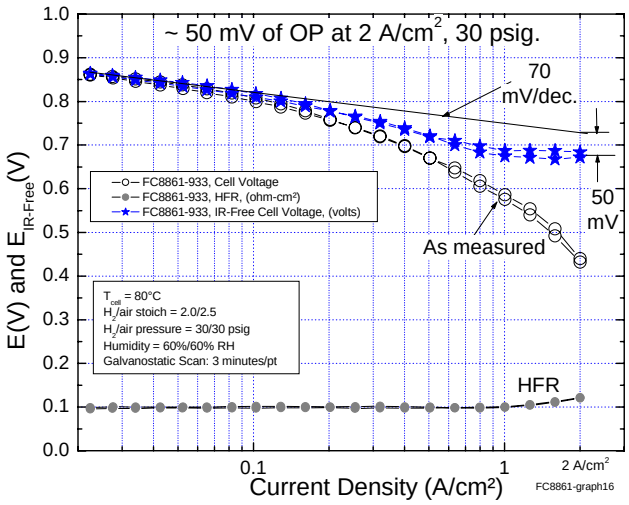

Fig. 12. GDS polarization curves of example 7 tested under the fuel cell conditions shown, to obtain the mass transfer overpotential. A mass transfer loss of 50 mV of MTL at 2 A/cm^2 is shown.

Example 7. This MEA, identified as FC8861, was fabricated with a cathode catalyst of pure Pt with a Pt loading of 0.15 mg/cm^2. The fuel cell polarization curve, shown in Fig. 12, indicated a mass transport loss at 2 A/cm^2 of 50 mV.

In each of the examples 1-7, the total cathode catalyst layer volume per unit area (as it was deposited) is known. E.g. for a ternary catalyst having a Pt loading of 0.1mg/cm^2 and Pt/TM (transition metal) ratio of 3, the planar equivalent thickness of the Pt is 466 Angstroms and that of the TM is 1/3 of 466 Angstroms, making the total layer equivalent thickness equal to 620 Angstroms. This is effectively the total thickness of the Pt and transition metal components as it was deposited. Fig. 13 shows a plot of the mass

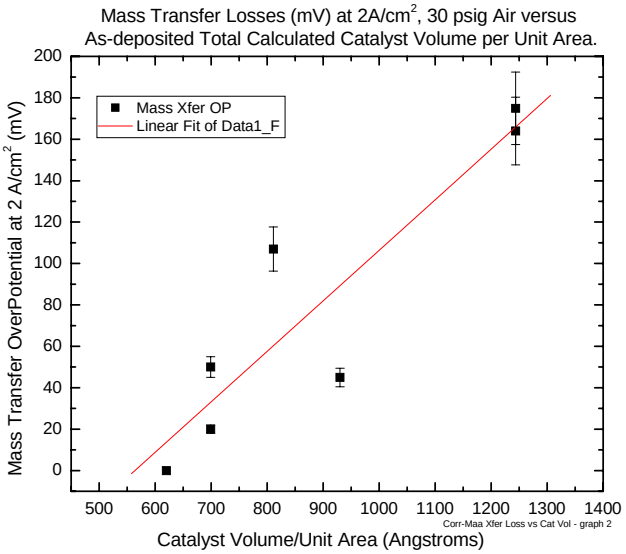

Fig. 13. Mass transfer loss, in mV, from all examples plotted as a function of the calculated thickness of the electrode layer, which is equivalent to the catalyst volume per unit planar area.

transport overpotential loss as a function of the catalyst volume/unit area for all the examples and again a linear relationship is statistically suggested. Because the NSTF thin film catalysts are deposited onto the nanostructured PR149 support whiskers, the catalyst film is distributed over a thicker volume than the simple planar equivalent layer

thickness. This gives the electrode layers a certain degree of porosity that in principal should be a function of the surface area of the PR149 whisker support film. All the examples above were deposited onto nominally identical whisker support films. It is clear that for this specific type of PR149 support whisker, defined by the number of whiskers per unit area of substrate, the length of the whiskers and their cross-sectional dimensions, for a desirable mass transport loss of less than about 40mV at 2 A/cm^2, it is preferable to have a catalyst volume/unit area of less than about 700 Angstroms.

Estimating electrode porosity

For examples 1-4, for which the CCM electrode layer thickness was measured from SEM micrographs, the effective porosity of the layers can be simply estimated from the ratio of the total planar equivalent thickness to the measured SEM electrode thickness. Table 1 below shows the calculated porosity of the four cases in Exs. 1-4. The volume of the PR149 support whisker is known from the PR149 layer thickness of ~ 0.015 microns. For examples 1-3 that had ternary catalysts, it would appear preferable to have an electrode porosity of at least 75%. The porosity of the electrode layer is filled to varying degrees by ionomer, depending to what degree the catalyst coated whiskers are pressed into the surface of the PEM during catalyst transfer and lamination. Since this may be varying among the samples and is difficult to characterize or measure, the examples in Table 1 may not be expected to be completely consistent given the small sample number.

Another complicating factor is that the PtTM ternary composition as-made is not the composition of the catalyst layer in the fuel cell. It is known that for the ternary catalyst containing transition metals Ni, Fe, Co and Mn, that a portion of the TM dissolves into the PEM soon after starting the fuel cell testing, and reaches an equilibrium value. This was discussed at length in the preceding sections 2.1.5.2 and 2.1.3.2. An estimate of the layer porosity assuming that the known fraction, > 60%, of the TM is removed does not appear to show any correlation in the percentage porosity and the mass transport loss. Note, even though TM is lost by dissolution, the lattice constant of the solid metal solution increases (back towards pure Pt) since the TM atoms are smaller than the Pt, and the volume actually expands, however not by enough to fully compensate for the loss of TM presumably.

Table I. Estimate of the cathode layer porosity from the as-deposited catalyst planar equivalent thickness and the observed SEM electrode layer thickness.

	Ex. 1	Ex. 2	Ex. 3	Ex. 4
Catalyst volume thickness + 0.015 for PR149 = t	0.077 microns	0.139 microns	0.096 microns	0.085 microns
SEM electrode layer thickness = L	0.27 microns	0.43 microns	0.35 microns	0.24 microns
% Porosity = 100%(1 – t/L)	71.5%	68%	73%	65%
MTL (mV)	0 mV	164 mV	107 mV	23 mV

Conclusions

This effective (non-catalyst) porosity of the electrode layer is certainly filled or nearly filled by ionomer and water, depending to what degree the catalyst coated whiskers are pressed into the surface of the PEM during catalyst transfer and lamination, and the local operating conditions (relative humidity, water generation rates and water removal rates). It is this effective thickness and tortuosity of ionomer and water then through which reactants must diffuse to reach the catalyst surface.

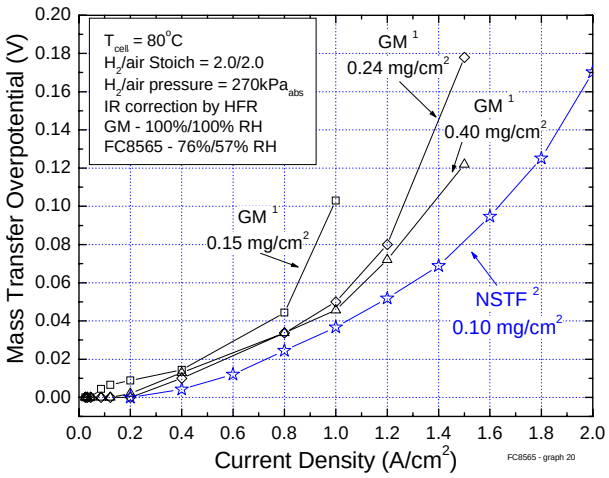

Fig. 14. Comparison of mass transfer losses as a function of loading, measured from Pt/C cathodes (extracted from Ref. 1) and the NSTF MEA in example 1, but assuming Tafel slopes of 65 mV/decade as done in Ref. 1 below.

Gastieger et al.[1] published a study of the efficiency loss contributions for beginning of life MEA performances for conventional carbon supported Pt catalysts, and specifically looked at the dependence on catalyst loadings. Fig. 14 reproduces a portion of Fig. 7(c) from Ref. 1, showing the mass transfer loss for Pt/C cathode loadings ranging from 0.15 to 0.4mg/cm^2. The example 1 MEA in Fig. 1, with 0.1 mg-Pt/cm^2 was also tested under the conditions used in Fig. 14. The mass transfer extracted as a function of current density, assuming now 65mV/decade as used in Ref. 1, is plotted as shown in Fig. 14 for an NSTF loading of 0.10 mg/cm^2. Surprisingly, the trend in the Ref. 1 data is for the mass transfer loss to increase with decreasing loadings, yet the lower NSTF-loading produces lower losses than any of the Pt/C loading values. The difference in humidification conditions (100% versus 70%) of the inlet gases should not be responsible as this NSTF catalyst performance is not sensitive to RH in this range.

In conclusion, the mass transfer loss is a very sensitive function of the NSTF electrode thickness, but can be much smaller than in conventional dispersed catalysts due to the extreme thinness possible with low volume NSTF catalysts. The implications are that the ternary catalyst volume should be as low as possible, commensurate with obtaining the best overall performance, specific activity and fluoride release rates. The down-selected PtCoMn(90:10)[50,3,1] construction was consistent with this metric.

Ref. 1: *H. A. Gasteiger, et al., "Beginning-of-life MEA performance – Efficiency loss contributions," Handbook of Fuel Cells – Fundamentals, Technology and Applications, Eds. W. Vielstich, H. A. Gasteiger and A. Lamm, Vol. 3, 2003 John Wiley & Sons, Ltd., Chapter 46, pp 593 – 610.*

2.1.5.4 Conditioning and break-in

The relatively low surface area NSTF MEAs appear more susceptible than highly dispersed catalysts to poisoning from initial contaminants in the as-made CCMs, most of which appear to come from organic decomposition products of residual solvents in the as-made membrane resulting from its highly acidic nature. The effects of these impurities manifest themselves in the ultimate MEA performance and also the time to condition or break-in the MEA. These impurities can be minimized by improving the processing methods for fabrication of the membranes, and that is briefly discussed in section 2.3.1 of this report. As discussed in this section, the impurities can also be removed *in-situ* during initial conditioning of the MEA in the fuel cell by a special start-up protocol. Finally, we show how the impact on the time for this break-in conditioning of the MEA is a strong function of the NSTF catalyst construction and surface area.

As described in section 2.1.3.1, humidification was provided to all the 50cm^2 fuel cells tested by two LabAlliance HPLC pumps, one for each reactant stream. Each HPLC pump fed liquid water through PTFE tubing into a 316 stainless steel Swagelok tee, into which the gaseous reactants were also fed; the wet reactant streams were then fed to the fuel cell. The water was generally preheated prior to entering the cell, so the humidification water entered the cell primarily in the vapor phase. In our experience, this method of providing humidification works equivalently well as sparge bottle humidifiers. The use of these HPLC water pumps facilitated the conditioning protocol we call "Thermal Cycling," developed specifically to accelerate the conditioning and clean-up of the MEA's. For some catalyst and membranes, this break-in period can take as long as 20 hours. Much of the understanding of the method was developed in the preceding contract to the present one, and the final report for that contract (DE –FC02-99EE50582) contains a discussion as well in its section 3C. In that previous contract we showed that certain pretreatment processes of the membrane ionomer could significantly reduce this time to a few hours.

Scripted software was always used to break-in all MEAs with the same test protocol. The start-up protocol consisted of ambient pressure fast potentiodynamic scans (PDS) between 0.85V and 0.25V in 0.05V, 10 second steps; followed by 10 minute potentiostatic scans (PSS) at 0.4V, repeated continuously over a 5 hour period, at 70^{o}C cell temperature and H_2/air inlet gases humidified at 70^{o}C dew points. The H_2/air were introduced to the cells in a counterflow mode with flow rates held constant at 800/1800 sccm.

Following the initial break-in period, the scripted protocol entered a thermal cycling stage in which the same PDS/PSS scans were run with a 75^{o}C cell temperature and the same 70^{o}C dew points. Typically four sets of scans would be completed before an automatic shut-off and cool-down of the cell was completed sufficient for the cell to reach near ambient temperatures for a period of about 45 minutes. Reaching ambient temperature was also found to be very important. During the shut-off period, the reactant gas flows were stopped but the HPLC water injection pumps continued to flush water through the cell. The cell was then restarted and the cycle repeated until the PDS current density values had stabilized. This thermal cycling procedure has been found necessary to remove residual impurities in the MEA which limit initial performance. A key fact of the thermal cycling protocol is that only the electrode side used as the cathode, i.e. exposed to air, is "cleaned-up" by the thermal cycling. The cell leads and reactants have to be switched around to fully clean-up both electrodes.

Fig. 15 illustrates a typical log-plot of the start-up of a cell. The plot shows the current density at 0.8V, 0.7V, 0.6 V, 0.5V and 0.3 V extracted from the PDS polarization curves, and plotted versus the number of the data file used to store the polarization curve. In this example, the cell had pure Pt NSTF catalyst on the "anode" of the CCM as-made, and a Pt ternary on the cathode. The cell was started with the air introduced to the

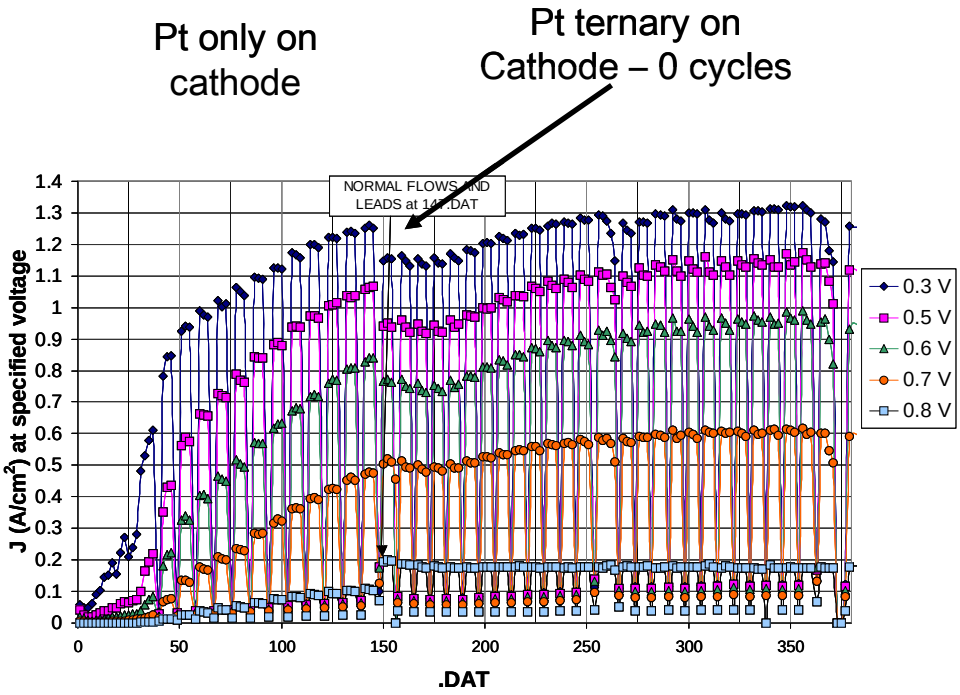

Fig. 15. Example of a log-plot of the conditioning break-in period for an MEA. The current densities at 0.3V, 0.4V, 0.5V, 0.6V, 0.7V and 0.8V are plotted versus the data file number of the ambient pressure polarization curve from which the values were extracted.

original anode (pure Pt) side first and the conditioning protocol started. At data file record 150, the current leads and reactant tubing were switched on the cell to make the original ternary cathode the working cathode. It is seen that the number of thermal cycles to break-in the pure Pt side was over a dozen just for the kinetic region (0.8V) to stabilize. In contrast, with the ternary as the cathode, the kinetic performance was as its maximum immediately, without requiring any further thermal cycles. The higher current density performances did benefit from further thermal cycles however.

The impact of pre-cleaning the membranes by acid washing on the start-up log-plots is shown in section 2.3.1 of this report. However, pre-cleaning the membranes is not an option for scaling up. A significant amount of progress has been made at understanding the dependence on PEM processing and post fabrication factors on thermal cycling start-up requirements, and the most critical of those have been implemented. However in this section we focus on the effects of the catalyst on the number of thermal cycles required to bring the MEA to full performance, although the synergistic effect of combining the best ternary catalyst for rapid start-up with the best membrane processes is also demonstrated.

PtMFe Catalyst Series

Table II lists a series of PtNiFe (top) and PtCoFe (bottom) MEAs used to investigate the impact of the catalyst composition and construction on the number of thermal cycles to achieve full performance at 0.8 volts, as measured from log-plots as in Fig. 15. The CCMs were made with membrane made by casting Nafion™ ionomer 1.2 mil thick. Cathode catalysts were PtNiFe or PtCoFe, each containing 0.10 mg/cm^2 Pt. The anode catalyst was Pt at loadings between 0.15 mg/cm^2 and 0.2 mg/cm^2. The GDLs were all the same type of carbon cloth based backing with the same microporous layer, installed in the cell with 30% compression.

Table II. Summary of the PtNiFe (top) and PtCoFe (bottom) MEAs used to investigate the impact of the catalyst composition and construction on the number of thermal cycles to achieve full performance at 0.8 volts for the Fe series.

FC# - 90/10NiFe	Pt/TM Ratio	Bi-layer thickness (A)	# TC's		FC#- 95/5 NiFe	Pt/TM Ratio	Bi-layer thickness (A)	# TC's
7550	0.61	30	2.		7613	0.61	20	1
7600	0.59	5	2		7648	0.6	10	1-2
7659	1.5	10	9		7761	0.6	30	1
7672	3	10	11		7833	1	50	1
7673	3	5	12-13		7844	1	30	3
7734	2	20	14-15		7874	1	10	1
7507	0.6	10	2		7891	1	5	3
					7915	3	30	14
					7940	3	20	13
					7979	3	50	16

FC # - 90/10CoFe	Pt/TM Ratio	Bi-layer thickness (A)	# TC's		FC # - 80/20CoFe	Pt/TM	Bi-layer thickness (A)	# TC's
8362	1	10	15-16		7469	1.5	10	8
8374	0.6	50	1		7760	1.5	50	12
8377	1	50	14		7769	3	50	15
8389	3	50	17		7772	2	50	8
8396	0.61	10	1		7777	0.6	50	1
8406	3	10	14		7791	1.5	5	7
8418	0.59	30	1					
8421	3	30	15					
8405	3	70	19					

The designation in Table II of the NSTF ternary catalyst composition and construction parameters such as bi-layer thickness, Pt/TM ratio and M1/M2 ratio are described in detail in section 2.1.3.2 of this report.

From the Pt/TM ratio and bi-layer thickness for a given MEA, the individual Pt or TM layer thickness per pass during the deposition can be calculated. These are not shown in Table II, but are plotted as the abscissas in Fig. 16 to see if there is any dependence on those parameters of the number of thermal cycles to reach the peak current density at 0.8 V. Fig. 16 would appear to indicate that there is a lot of scatter in the plots and no consistent trend of the number of thermal cycles to reach full kinetic performance on individual layer thicknesses.

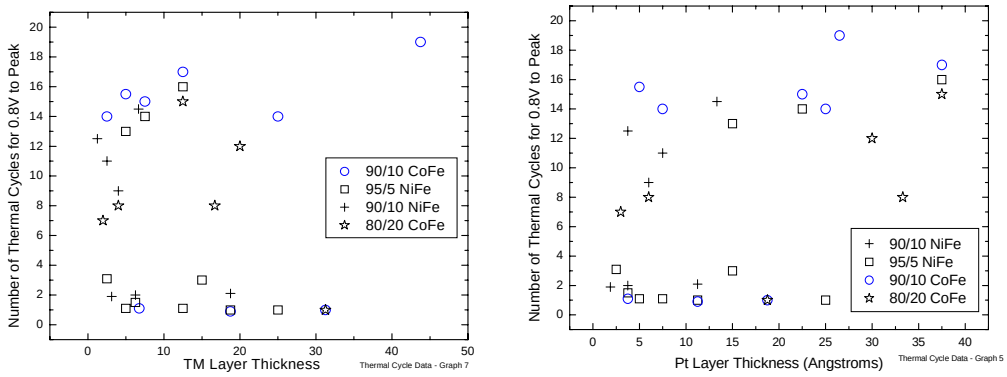

Fig. 16. Plot of the number of thermal cycles required to bring the current density at 0.8 volts to its peak value during break-in conditioning versus the transition metal layer thickness (left) and Pt layer thickness (right).

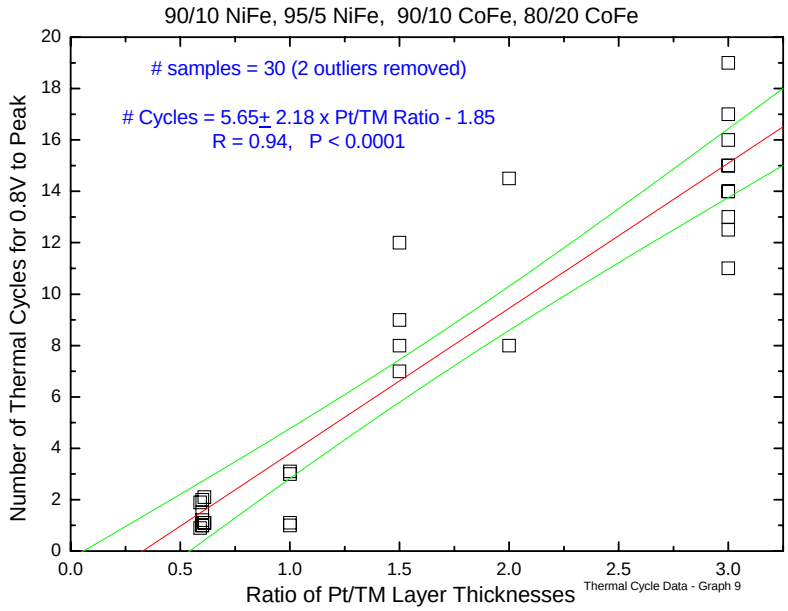

Fig. 17. Number of thermal cycles as a function of the ratio of the Pt/TM layer thicknesses. The higher the amount of transition metal, Co or Ni, the faster full kinetic performance was achieved.

When plotted as a function of the Pt/TM ratio however, as shown in Fig. 17, the number of thermal cycles to reach full kinetics is clearly indicated to be linearly dependent on this parameter with good statistics ($p << 0.05$).

The question of why the electrodes with high amounts of Co or Ni and Fe relative to the amount of Pt condition more quickly is immediately relevant. It has been further observed that the surface area of the catalyst is also a strong function of this Pt/TM ratio. Fig. 6 in section 2.1.3.2.2 illustrates this for the mass specific area for many of these same PtMFe ternary catalysts. As the Pt/TM ratio decreases from 3 to 0.6, the mass specific area increases from about 8 to about 13 m^2/g. This suggests a strong dependence of the number of thermal cycles on surface area would also be seen. As discussed at some length in section 2.1.3.2.4, the transition metals in excess of the Pt/TM ~ 3 ratio, dissolve into the membrane and can negatively impact the polarization curves at values of Pt/TM < 1. At the lowest value, 0.6, the transition metal is even extracted from the bulk of the NSTF catalyst crystallites, as discussed at length in section 2.1.1 and Appendix II.

Hence it is not clear if the strong reduction in the number of thermal cycles to condition the PtMFe MEA's and achieve full kinetic performance is a function of the surface area or the excess transition metals that go into the membrane and possibly help break down the organic species under the electrochemical environment of the cathode. But the impact of combining the most appropriate catalyst with the improved membrane processing is clearly illustrated in Fig. 18.

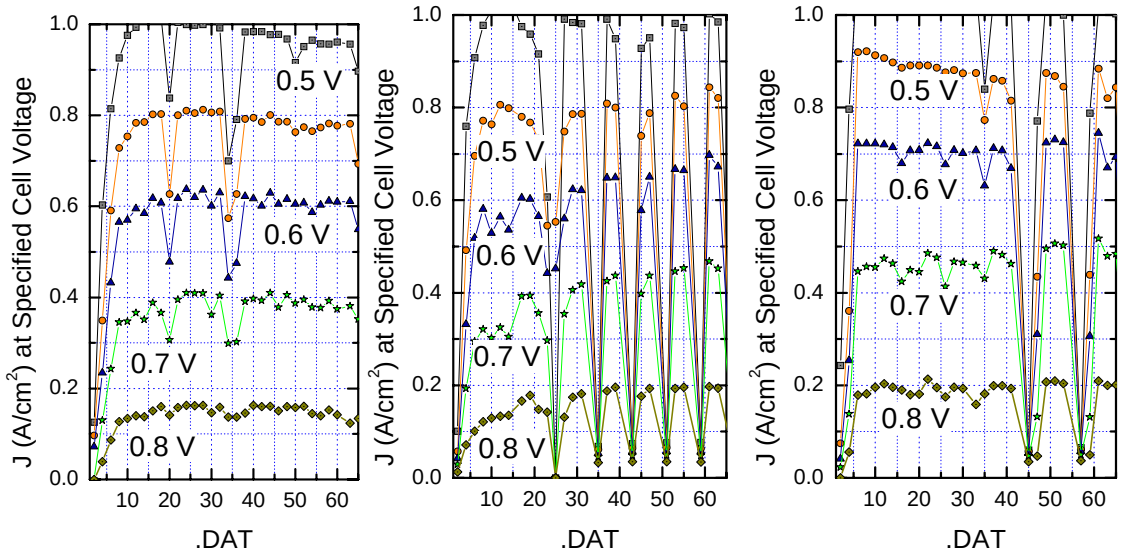

Fig. 18. Comparison of the start-up log plots for three CCMs using the best PtNiFe ternary catalyst for quick-start, with three different 3M-ionomer based membranes made with different post-process treatments: (left panel) membrane cleaned by acid washing; (middle panel) membrane process improvement A; (right panel) membrane process improvements B and C.

The left panel in Fig. 18 shows the start-up log plot for a CCM made with the PtNiFe ternary catalyst (90:10)[30,0.6,1] on the cathode at a loading of 0.1 mg-Pt/cm^2 , and an acid-washed 3M ionomer membrane. Nearly full kinetic performance was achieved

during the preliminary conditioning phase in about one hour, before any thermal cycling. (The drop-down data points are outliers, not thermal cycles.) The right panel in Fig. 18 shows the start-up of a CCM with 0.2 mg-Pt/cm^2 of the PtNiFe catalyst on the cathode, but with the 3M membrane fabricated with two process improvements. The start-up performances were higher at all potentials, and the full kinetic performance was achieved after just the third PDS scan, in approximately 20 minutes.

PtMMn Catalyst Series

The PtCoMn and PtNiMn catalysts were later found to have the same effect on start-up. Fig. 19 shows the number of thermal cycles required to reach full performance at both the 0.8 V level and 0.6 V level, as a function of the Pt/TM ratio, for the PtMMn series, M = Ni or Co. There is a clear functional dependence of the number of thermal cycles for start-up on the amount of TM again, as seen for the PtMFe series, suggesting the minor Fe and Mn components are not the critical factors.

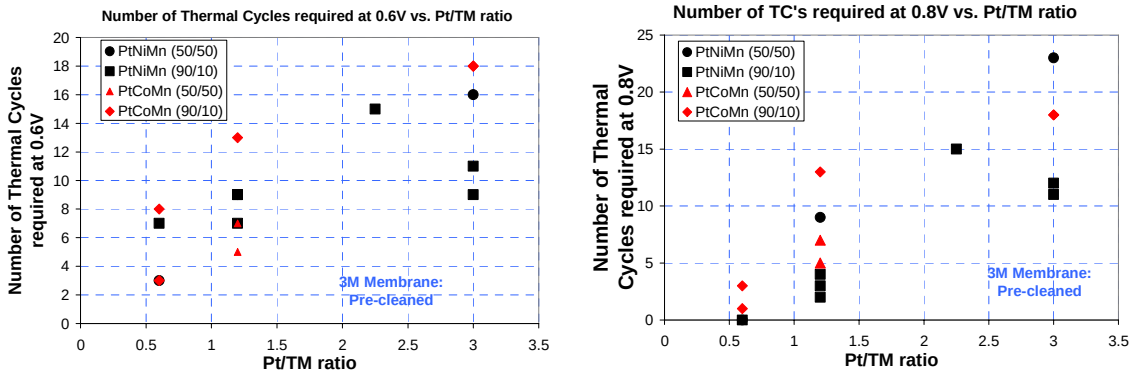

Fig. 19. Plots of the number of thermal cycles required to reach full performance at 0.6 and 0.8 volts as a function of the Pt/TM ratio for the PtMMn series of cathode catalysts.

Fig. 20 shows the number of thermal cycles required to reach full performance at both the 0.8 V level and 0.6 V level, as a function of the cathode catalyst surface area, for this PtMMn series. There is a very strong functional dependence of start-up time on surface area.

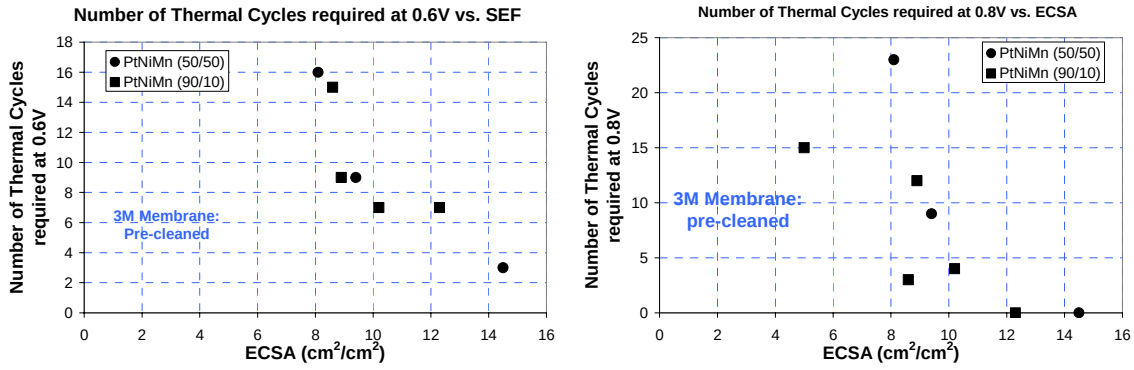

Fig. 20. Plots of the number of thermal cycles required to reach full performance at 0.6 and 0.8 volts as a function of the cathode ECSA for the PtMMn series of catalysts.

Conclusions

In conclusion, it was discovered that the catalyst composition and structure has a significant effect on the conditioning and break-in times, as does the membrane processing parameters. For fast conditioning, the preferred catalysts were the ones with very high amounts of transition metals relative to the Pt amount. This however, was not the optimum ternary catalyst which maximized the specific activity, durability and high current density performance, as described in sections 2.1.3 or 2.1.4. For this reason, then, the latter catalysts were ultimately down-selected for the scale-up and subsequent stack testing, rather than the ones that minimized the time for break-in conditioning of the MEA. Instead, the improvements in the membrane processing were adopted, and the ternary catalyst loading was increased to 0.2 mg-Pt/cm^2, which would increase the absolute amount of transition metal and help reduce the start-up conditioning time.

Section 2.2 Membrane Development for 85 ≤ T ≤ 120°C

This section reviews the work done under the second major subtask of Task 1 discussed in section 1.2, to develop durable MEAs for operation in the temperature range of 85 ≤ T ≤ ~ 120°C while operating on low humidification with PFSA based ionomers and lower cost catalysts. The focus of this section is on the membrane development.

Table of Contents for Section 2.2

2.2.1 Introduction

The development and commercialization of affordable hydrogen fuel cells are necessary for the realization of a hydrogen-based economy. Proton exchange membrane fuel cells (PEMFC's) represent a promising technology for automotive, small stationary and portable power applications. PEMFC's are energy conversion devices that process a fuel gas (e.g., hydrogen) and an oxidant gas (e.g., air) and generate electricity. Half cell reactions on the anode and cathode electrodes are separated by a polymeric membrane that serves to isolate the reactant gases and to transport protons from the anode to the cathode. While many breakthroughs have been made over the last few years in the area of PEMFC's, technical and economic barriers to their commercialization still exist[1]. In order to maximize power output from the cell, the cell internal resistance must be minimized. Electrolyte resistance is typically the major contributor to overall cell resistance. Therefore, it is desirable to design the cell with very thin, and highly proton-conductive membrane. For membranes that rely on moisture to maintain their proton conductivity, thin membrane approaches also help with exploiting the water that is generated by the cell for membrane hydration. Fig. 1 gives the chemical structures of Nafion™ and 3M's perfluorosulfonic acid (PFSA) ionomer. At odds with the use of very thin membranes (e.g,. < 50 microns) to achieve high power density is the need for the membrane to be a reliable and long-lived physical barrier for the reactant gases. The development of tears or pinholes in the membrane is the most common source of cell failure, and these events are certainly more frequent for cells that include thin membranes. To be sure, state of the art PEMFC constructions in terms of power density performance are always running on the edge of not meeting system durability requirements. Thus, interestingly, advances in what could be considered one or the other of these attributes can actually be distributed over both to some extent, at the discretion of the cell designer.

2.2.1.1 Durability needs for PEMFC's operating under hot and dry conditions

The lifetime of PEMFC's is largely determined by the chemical and mechanical stability of its material components and its operating conditions. One of the primary factors limiting fuel cell lifetimes is the stability of the membrane. In fact, lifetime can vary over orders of magnitude for operating conditions that might at first seem remarkably similar. For example, the same fuel cell design might survive for 10,000's of hrs while operating at 70°C and with saturated gas streams, but fail in only 100's of hours while operating at 80°C and with 70°C dew point gas streams. At the same time, there is significant motivation from a system design standpoint to raise the temperature of operation and reduce the humidity requirements for the cell. Raising the operating temperature and reducing the humidity requirements of the cell pays off dramatically in the form of simpler and cheaper thermal management, fuel generation, and humidification strategies, and also higher overall system efficiency. At the inception of the currently reported program under DE-FC36-02AL67621, lifetime targets and operating conditions for the most demanding application (automotive) were still being developed, but 1000's of hours of operation and cell temperatures in the range of 120-150°C were being considered. Such high temperatures would allow the use of onboard-reformed hydrocarbon fuel gases, with their relatively high levels of CO. At present, if there is a consensus in the automotive field, it is that 5000hrs of load-cycle operation at 90-120°C with 60-80°C dew point gas streams, including more pure hydrogen fuel gas, is a legitimate "first node" in the widespread commercialization of fuel cell powered automobiles. With respect to stationary powder applications, the operating conditions are milder and the timeframes are longer. Specifically, a reasonable target would be 40,000hrs of operation at 70°C with saturated gas streams.

There are several contributors to the declining performance of PEMFC's over time. While the gradual decay in performance largely derives from changes that occur in the catalytic electrode layers, the source of catastrophic failure is generally the membrane. Essentially, chemical erosion and/or mechanical stress eventually lead to the development of a tear or pinhole in the membrane.

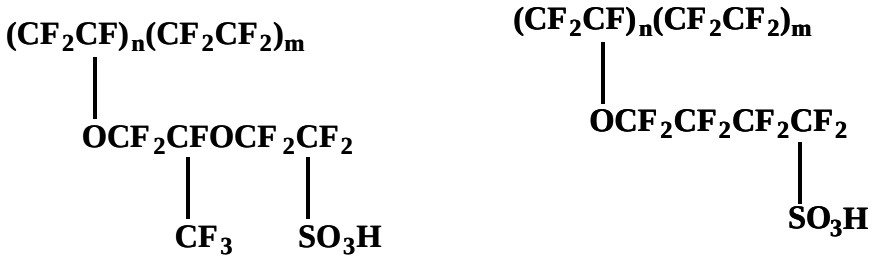

a) b)

Fig. 1. PFSA ionomers a) Dupont Nafion™ and b) 3M ionomer (m/n = 3-7).

$$(CF_2)_n\text{-}CO_2H + H_2O_2 \longrightarrow (CF_2)_n\text{-}CO_2\bullet + \bullet OH + H_2O$$

$$(CF_2)_n\text{-}CO_2\bullet + \bullet OH \longrightarrow (CF_2)_{n-1}\text{-}CF_2\bullet \ \bullet OH + CO_2\uparrow$$

$$(CF_2)_{n-1}\text{-}CF_2OH \longrightarrow (CF_2)_{n-1}\text{-}COF + HF$$

$$(CF_2)_{n-1}\text{-}COF + H_2O \longrightarrow (CF_2)_{n-1}\text{-}CO_2H + HF$$

Fig. 2. Proposed peroxide induced fluoropolymer decomposition pathway.

The primary source of chemical degradation of perfluorosulfonic acid (PFSA) membrane in an operating fuel cell is thought to be attack by hydrogen peroxide or related species generated at the electrodes, but the exact mechanism of chemical degradation remains an area of continued uncertainty and investigation[2,3]. In one generally accepted degradation mechanism, the primary pathway involves hydroxyl radicals, generated by the decomposition of hydrogen peroxide, attacking the carboxlate end groups of the polymer, generating carbon dioxide, and "unzipping" the polymer chain one carbon atom at a time. This mechanism is shown in Fig. 2. Recent work has suggested that there may be other, perhaps secondary, pathways by which hydrogen peroxide generated radicals may attack the ionomer[4].

In an attempt to avoid oxidative degradation of membrane polymers, it has been suggested that peroxide decomposition agents could be helpful[5]. The rationale for their addition includes the idea that they provide a decomposition pathway for hydrogen peroxide that would reduce the overall concentration in the cell. Perhaps more importantly, a benign hydrogen peroxide decomposition pathway could reduce the formation of other more reactive species (e.g., radicals). Along this line of reasoning, many classes of candidate additives have been proposed [5,6] Addition of transition metals or metal oxides to PFSA membranes has been shown to stabilize the membrane towards the attack of radicals generated in Fenton's reagent. These additives also increase the lifetime of MEA's made from these membranes in accelerated durability tests [7].

The work undertaken in this subtask involved the use of a low EW PFSA ionomer developed at 3M which has improved mechanical properties, and combining it with additives to stabilize the membrane towards decomposition by hydrogen peroxide and its by-products.

2.2.1.2 Power performance needs for PEMFC's operating under hot and dry conditions

The power performance of a PEMFC is determined by numerous design and materials property factors. Indeed, the PEMFC is a very complex system, with its governing phenomena including gas diffusion, catalysis, proton transport, electronic conduction, and water transport, to name just the primary factors. Among these phenomena, the key contributors to power performance are found. Thermodynamically, there is a definite chemical potential difference associated with the reactant gas streams and their reaction products. Of course, in a real system, that chemical potential difference is never realized fully, in the form of the voltage given by the Nernst equation. Impediments to the flow of reactant gases to the electrodes, the energetic cost imposed by the electrode catalysts, and the non-zero resistance to current flow for electronic and protonic conductors all contribute to shortfalls in voltage for operating fuel cells, and hence power. Fig. 3 is a hydrogen-oxygen fuel cell polarization curve, annotated with the sources of voltage loss that come into play with increasing current density. As illustrated, the ohmic losses, which are heavily influenced by electrolyte membrane resistance, are of key importance to overall cell power performance. The slope of the polarization curve in the linear region is largely determined by the membrane's proton conductivity and its thickness.

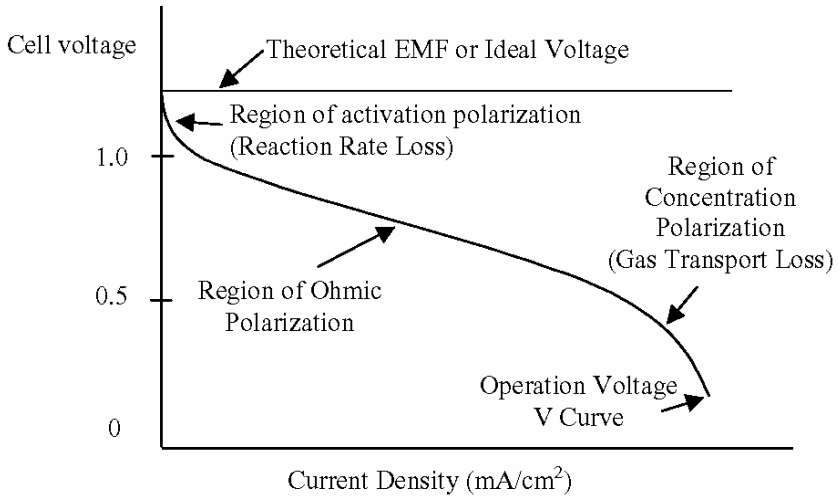

Fig. 3. Annotated fuel cell polarization curve, giving the sources of loss in different current density regimes.

Fig. 4 is a plot of measured proton conductivity vs. temperature (at a fixed dew point) for 3M's perfluorosulfonic acid membrane (Fig. 1b) with one thousand equivalent weight (1000EW; EW is the polymer molecular weight per mol of acid groups). The curve in Fig. 4 defines the membrane materials challenge facing the PEMFC community. Mainly, the curve reflects the dependence of proton conductivity on hydration for PFSA ionomers.

Fig. 5 illustrates the impact of higher temperature/lower %RH on fuel cell performance, due in large part to membrane resistance, as well as the negative effects of low humidity on electrode performance. This issue is discussed further in section 2.2.0. The overarching goal in

membrane development, in addition to increasing durability, is to flatten the humidity dependence of proton conductivity at a level near 100mS/cm, while preserving the favorable interactions that PFSA materials have with electrode catalysts.

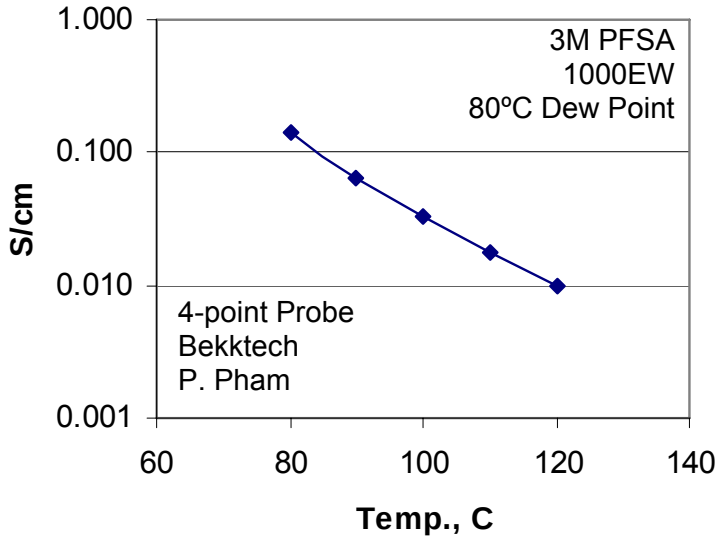

Fig. 4. Proton conductivity of 3M's PFSA ionomer membrane.

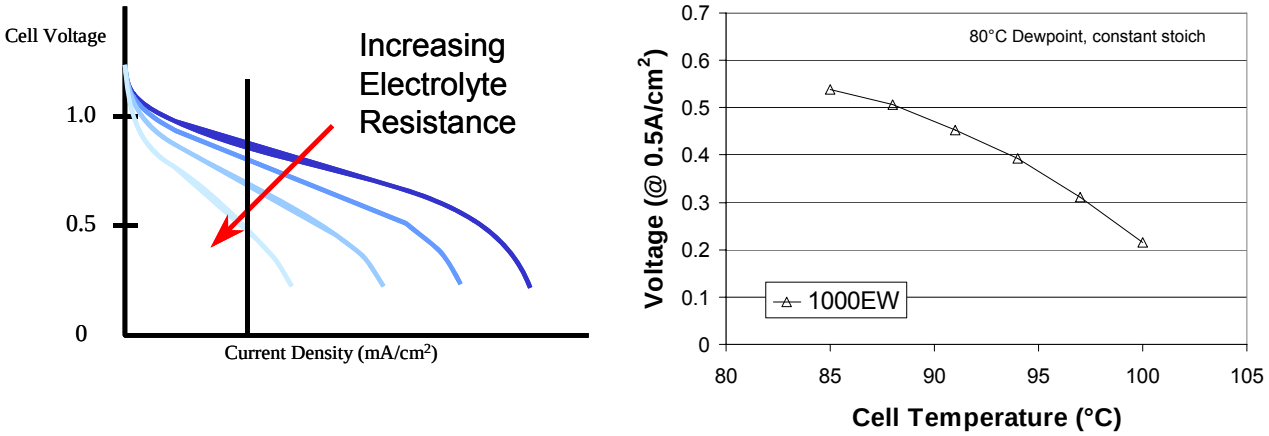

Fig. 5. Effect of operating temperature on fuel cell power performance at a fixed dew point and 1atm pressure; left) schematic description of effect of decreasing membrane conductivity, as shown in Fig. 4, on the polarization curve; right) measured data for voltage change with T°C.

2.2.2 Electrode Refinement

In order to gain an understanding of the potential benefits of membrane modifications and additives, efforts were made to define fuel cell test protocols and MEA constructs that would best measure and quantify those benefits. The fuel cell screening protocol that was developed had to also be one where potentially water soluble additives were not washed away before their effect on PEM conductivity could be determined. The thought guiding this screening protocol was that it is important to screen additives to understand their advantage before investing the

time to develop the chemistries to stabilize them. Efforts were made to optimize the electrodes so that differences in PEM performance were not masked by poor conducting electrodes.

Two factors were important in designing a fuel cell test to minimize any potential of liquid water in the cell. The first factor was determining the outlet RH at each test condition giving the gas consumption and water produced at different currents. Test conditions were then adjusted to make sure the outlet gas stream never approached saturation at each phase of the test script. The second factor came in the design of the humidifier. The test station humidification system was modified to insure complete vaporization of the inlet gas streams. This was accomplished by metering the 18MΩ DI water using an HPLC pump with the water being pumped into a former sparge bottle filled with 916 SS wool along with the inlet gas. The bottle was heated to 10°C above the dewpoint setpoint and the humidified gas steam exited the top of the bottle precluding any chance of liquid water leaving the bottle.

The test script had three phases to the test – incubation, temperature challenge, and an aging test where effluent water is collected for Fluoride release rate determination. For all testing the outlet gas steams were at ambient pressure. The test cell used was a 50cm^2 active area Fuel Cell Technologies cell with quad serpentine flow fields operating in co-flow mode. Operation in counter-flow would have given better more homogeneous results (see section 2.3.3.1 in this report for example) but could have led to conditions where liquid water was present in the cell.

Before cell incubation, the cell was raised to 80°C with dry H_2/air flows of 348/833sccm. Cell incubation was carried out at 80°C cell temperature with H_2/air flows of 800/1800sccm and with 70°C inlet gas streams. Polarization scans were taken every ten minutes with the cell sitting at 0.5 volts between scans. Polarization scans were taken by changing the cell potential from 0.9 to 0.3 volts and back in 50mV steps and 10 second dwell times while recording the current. The incubation period lasted for approximately six hours, always a sufficient time to reach a stable level of performance. This level of performance was consistent but less than the level of performance seen if the MEA had first been incubated at full humidified test conditions and then run at the dry incubation conditions.

After incubation the testing script took the cell to the challenge phase of testing. The flows were set to 348 and 833sccm, hydrogen and air respectfully. That equates to a stoichiometry of 2/2 at the 0.5 Amps/cm^2 setpoint. The cell was first heated to 85°C. For the rest of the challenge phase only the cell temperature was varied from 85 to 100°C in 3°C intervals. At each temperature, the cell was held at condition and current for twenty minutes before the final voltage was recorded in another ten minute scan. In that last ten minute scan, full spectrum impedance measurements were taken three to four times during the last scan. The impedance measurement was carried out under load and made use of a square wave of potential >10mV that was sent across the cell and a known shunt resistor in the circuit. Fast Fourier transforms were used to derive the impedance as a function of frequency (see section 2.3.2.2.2).

The last stage in the testing was the aging step that would loop until the operator shut down the cell. It was during this phase of the testing that the effluent water collections were made. At least eight pairs of collections were made unless the cell was not holding current or the OCV was dropping precipitously. For the aging step the cell temperature was held at 90°C with the hydrogen/air flows at 348/833 sccm and the inlet gas steams held at 70°C dewpoints. The cell cycle between 30 minutes at 0.5 Amps/cm^2 and then a 2 minute measurement was taken at OCV before returning to the constant 0.5 Amps/cm^2 scanning. Effluent water was collected from both the anode and the cathode outlet steams recording both time of collections and the mass of water collected. Water samples where later analyzed for F^- ion concentration using a Dionex

Ion Chromatography setup (see section 2.1.5.2-*Experimental* for more information on the IC measurement.)

Nearly a third of the high frequency resistance of an MEA with Pt catalysts dispersed on carbon supports can be attributable to the electrodes at the best conditions of full gas saturation. Given that the concentration of water tends to be lower at the outside of an MEA then in the middle under dry conditions it stands to reason that the contribution of the electrode resistance could be even larger under dry test conditions. In order then to make sure that the high frequency resistance of the MEA was not governed by the electrode resistance instead of the bulk resistance of the PEMs under test, two series of MEAs were made with four different equivalent weight ionomers in the electrode ink (697, 779, 990 and 1100 EW). The difference between the two series was the equivalent weight of the 1.2 mil thick PEMs – 719 and 990EW. The anode and cathode electrodes in each MEA were identical. The electrode inks were made with a dispersed carbon catalyst 50% Pt loading (NECC- SA50BK). The ionomer to carbon weight ratio was fixed at 0.8. All inks were hand brushed onto a carbon paper with a target loading of 0.4 mg/cm^2 platinum. The results of this study using the temperature challenge portion of the screening test can be seen in Fig. 6, **Fig. 7** and Fig. 8 showing respectively the performance, HFR and IR-free voltage as a function of cell temperature at a fixed dewpoint. In the legend of the plots, the 719/990/719 denotes anode/PEM/cathode ionomer equivalent weights.

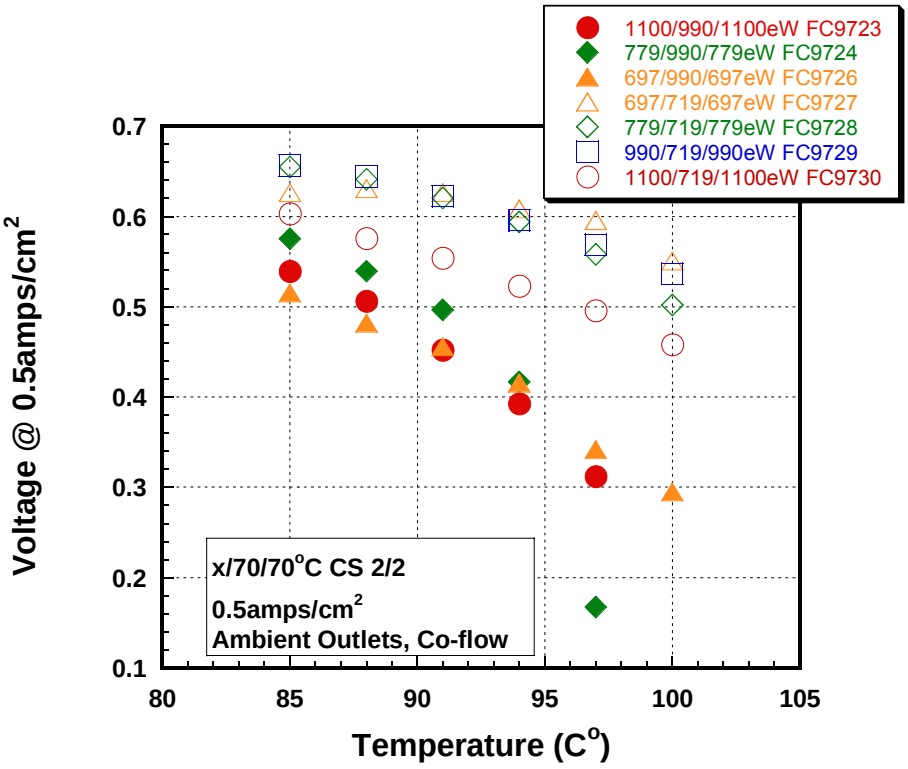

Fig. 6. Performance as a function of cell temperature for different equivalent weight electrodes paired with two different equivalent weight membranes.

The best performance is for the lowest equivalent weight. It is interesting to note that the IR-free plot shows such differences. If the differences in performances were just IR then all the data would fall on a single line. The difference is most likely attributable to importance of water in the ORR reaction and that lower EW ionomers hold provide more accessible water. It is

important to note that the lowest EW electrodes did show a dip in performance at the least dry test condition. Testing of the hydrogen pump of these same MEAs over a set of cell temperatures at a fixed dewpoint (**Fig. 9**) shows an increase in the hydrogen pump resistance at the wettest conditions. This is most likely an effect of the increased swelling for the lowest equivalent weight ionomers at the wetter conditions resulting in mass transport and/or physical gaps in the conductivity pathways. Decreasing the ionomer to carbon ratio in the electrode ink minimized this. The low equivalent weight electrode was used for the bulk of materials screening testing due to its increased performance at hot and dry conditions.

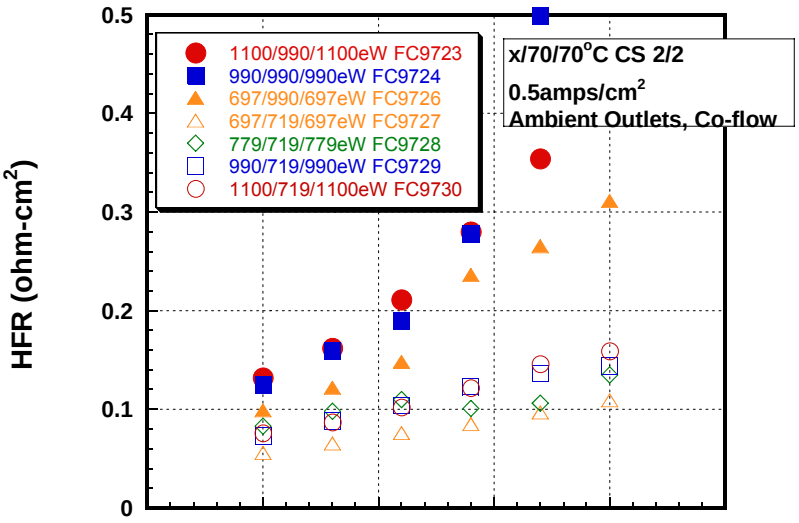

Fig. 7. High frequency resistance as a function of cell temperature for different equivalent weight electrodes paired with two different equivalent weight membranes.

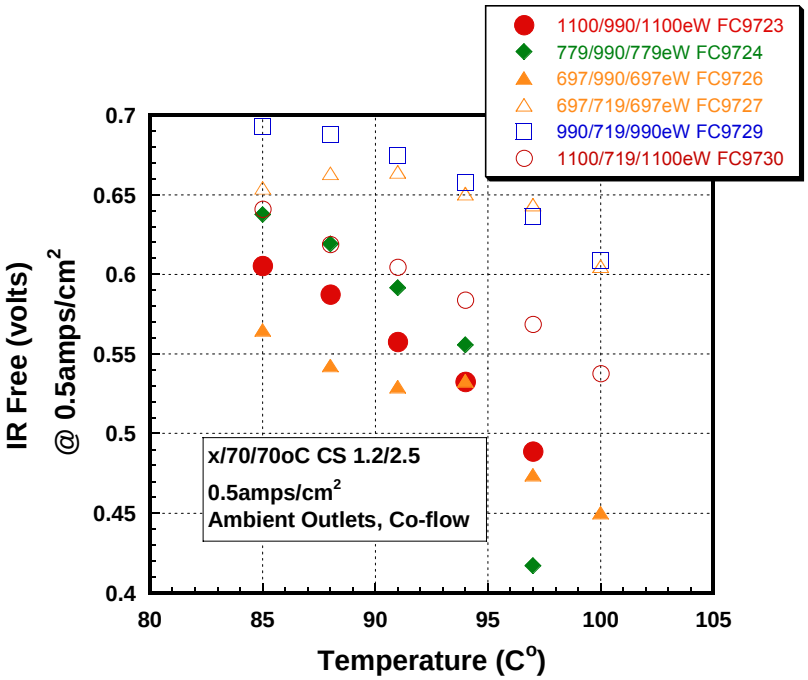

Fig. 8. IR free performance as a function of cell temperature for different equivalent weight electrodes paired with two different equivalent weight membranes.

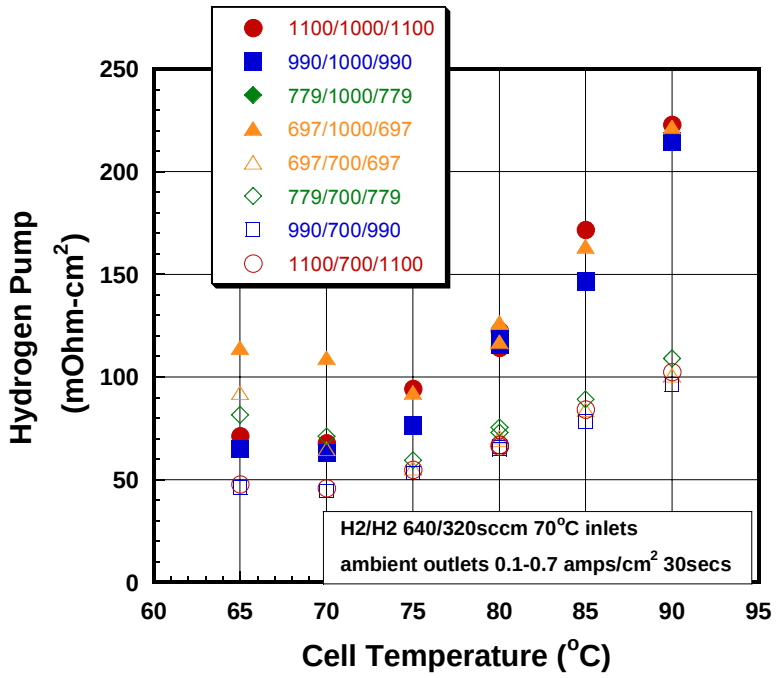

Fig. 9. Hydrogen pump resistance as a function of cell temperature for different equivalent weight electrodes paired with two different equivalent weight membranes.

2.2.3 Properties of the 3M Ionomer

2.2.3.1 Synthesis and Structures of the 3M Ionomer

Fig. 10 shows the process used to synthesize the MV4S monomer basic to the 3M ionomer. This process avoids the more common method of starting with tetrafluoroethylene (TFE) and instead uses the electrochemical fluorination of an organic feed to get the perfluorinated sulfonyl fluoride-acid fluoride precursor. This compound is then coupled with hexafluoropropene oxide and decarboxylated to give the perfluorinated monomer which is copolymerized with TFE to give the sulfonyl fluoride form of the polymer. This polymer is then hydrolyzed, acidified and processed into an ionomer membrane.

The structure of the ionomer is shown again in Fig. 11. The polymer side chain is a lower MW than other ionomers often used, such as DuPont's Nafion™ ionomer. The mechanical integrity of PFSA membranes rely heavily on crystallinity formed by short TFE segments along the polymer backbone[8]. Since a minimum amount of TFE in the backbone is required for crystallization, for a given MW side chain, there is a minimum equivalent weight (EW) or ion exchange capacity at which crystals can form, and below this threshold the polymer will be quite weak. At any given EW, polymers with a lower MW side chain will have more TFE in the backbone, leading to a higher level of crystallinity and improved mechanical properties. We have found that these new polymers have adequate crystallinity to maintain good mechanical properties when hydrated with EW's down to *ca.* 800 g/mole. At EW's above 800, the membranes can be boiled for extended periods and still remain good, strong films. At EW's approaching 700, the boiled membranes become quite weak and tear easily, although they do not dissolve.

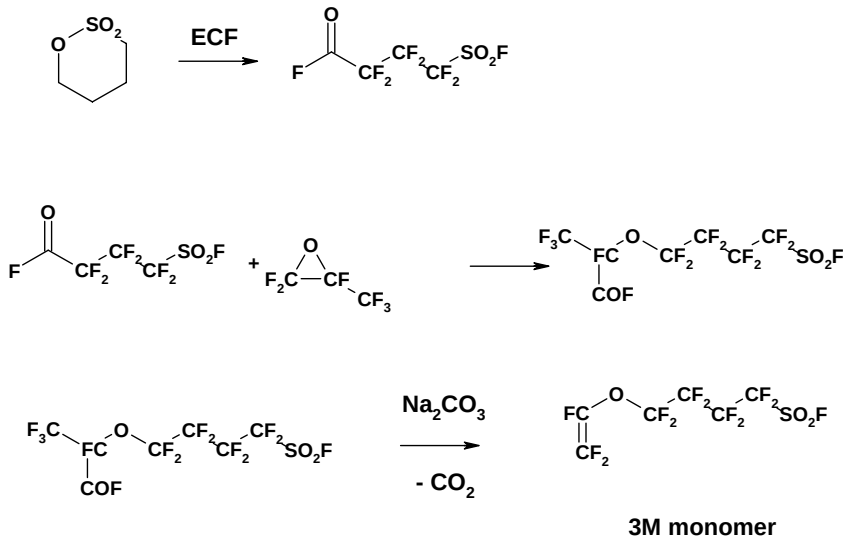

Fig. 10. Synthetic procedure for the MV4S monomer

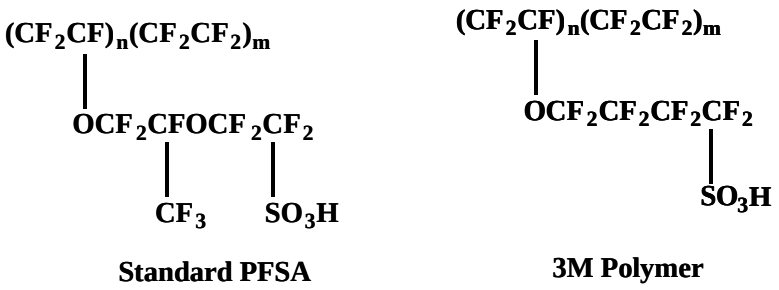

Fig. 11. Structure of a commercially available ionomer and the new 3M ionomer.

2.2.3.2 Physical Properties of the 3M Membrane

Fig. 12 shows DMA (differential mechanical analysis) of two 30 micron cast membranes, a membrane made from the 3M ionomer and a Nafion™ membrane as a control. Both are nominally 1,000 EW. The tan delta peak indicates the position of the alpha (Tα) transition of the ionomer, the transition associated with weakening of the electrostatic interactions within the ionic aggregates[9]. The position of this transition is about 125ºC for the 3M ionomer, about 25ºC higher than for the Nafion™ membrane. In addition, the storage modulus for the 3M membrane is higher both above and below the Tα. The increased Tα of this polymer should allow higher use temperatures, and the increase modulus may also prevent membrane deformation or creep and possibly increase MEA lifetime during fuel cell operation.

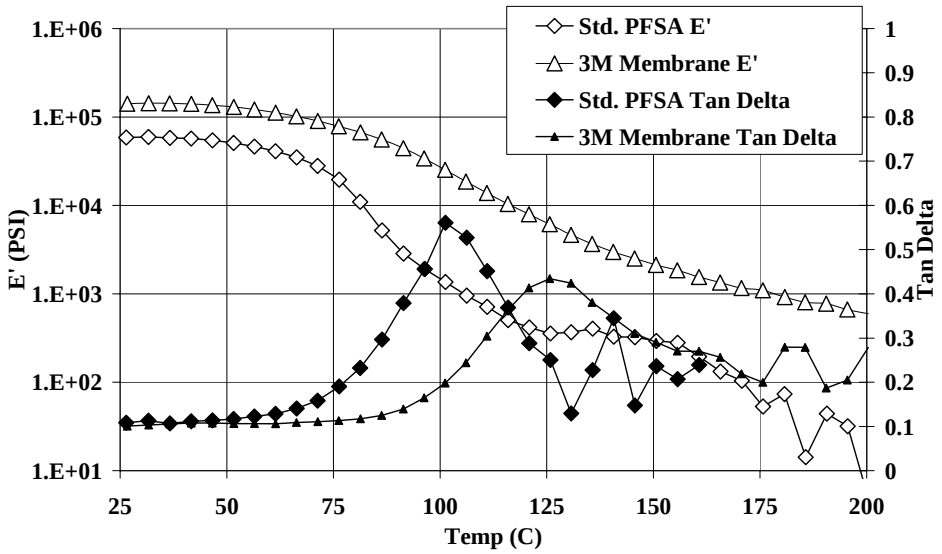

Fig. 12. Dynamic Mechanical Analysis shows higher Tα and storage modulus than cast standard PFSA membrane at 1,000 EW.

2.2.3.3 Conductivity, Fuel Cell Performance and Durability of the 3M Membrane

It is often suggested that reducing the equivalent weight of the fuel cell polymer has some effect on MEA durability. Most common is the idea that lower equivalent polymers expand more from water and therefore create mechanical problems within a constrained fuel cell system. Others subscribe to the theory that lower equivalent weight is a weaker material that is more susceptible to chemical attack.

In contrast, some possible benefits that could occur from lower equivalent weight include higher conductivity (which leads to better performance), and lower dependency on water for hydration (meaning the fuel cell can be run at lower humidification and still maintain performance).

The result of conductivity measurements on a range of EW's is shown in Fig. 13. In this 4 point probe experiment, the dew point of the incoming gas is kept at 80ºC and the cell temperature is increased from 80ºC to 120ºC in increments of 10ºC. At 120ºC the conditions have become quite aggressive, with the dew point of the gas having dropped below 25% RH. The conductivity increases with decreasing EW, as expected, and at 120ºC the conductivity of the 730 EW sample is about 25 mS/cm, about 2.5 times higher than that of the 1,000 EW sample. While these conductivity differences between the different EW samples appear somewhat uniform over this temperature range, the potential impact on fuel cell performance may not be.

In Fig. 14, the same data shown in **Fig. 13** is presented to show the calculated performance loss of a fuel cell operating at 0.6 A/cm^2 which is due only to the ohmic losses caused by the increasing cell temperature. At 80ºC, the voltage loss due to the membrane resistance is small, about 10 mV, and the difference between the different EW's is small, about 4 mV. As the temperature rises the impact of the resistance increase grows and at 120ºC, the resistance of the 1,000 EW ionomer accounts for a performance loss of about 160 mV compared to the fully humidified samples at 70ºC. The 730 EW sample fairs better, but still looses about 80 mV.

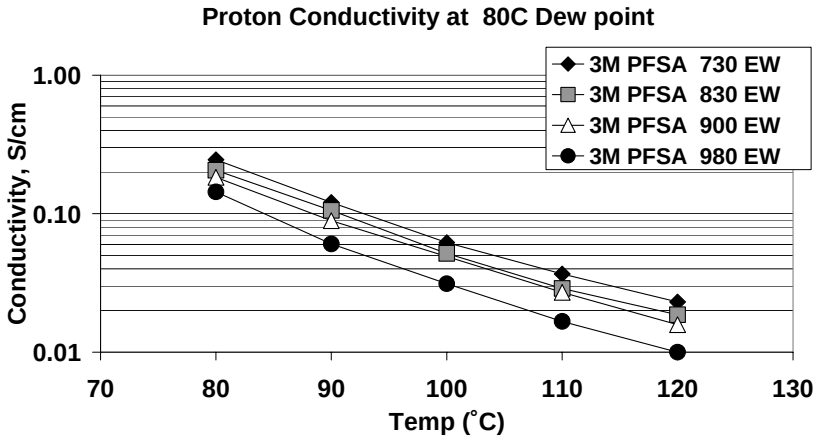

Fig. 13. Conductivity of the new 3M membrane with an 80ºC dew point as a function of temperature.

Membrane electrode assemblies made using these membranes have been tested for both fuel cell performance and durability. This experiment investigates the effect of accelerated testing at hot and dry conditions on various equivalent weight polymers to look for trends in durability or performance. MEAs were tested on single stations and on a multi-cell durability station to evaluate performance, fluoride release and lifetime results.

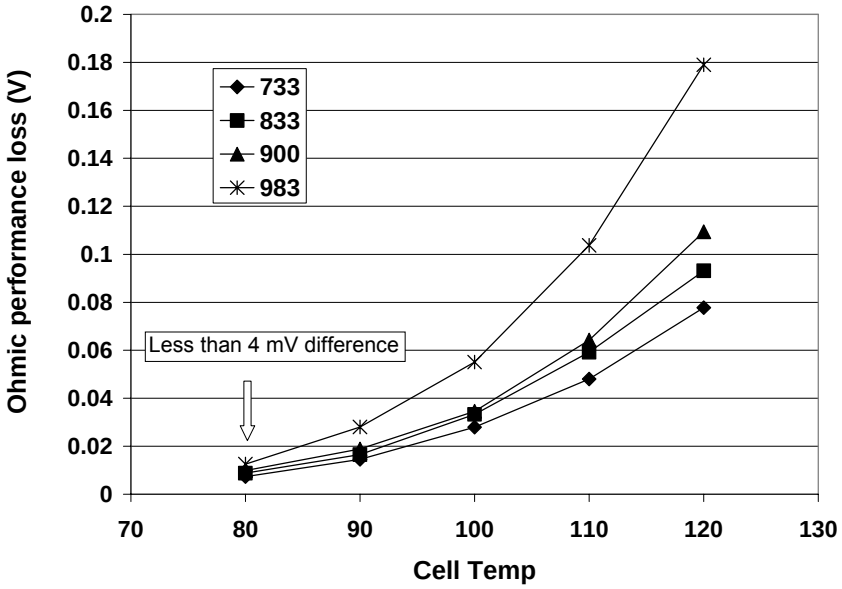

Fig. 14. Calculated performance loss (using data from Figure 6) due to membrane ohmic losses at 0.6 A/cm^2 for different EW membranes.

Fig. 15 shows the voltage at 0.6 A/cm^2 of MEA's run with H_2/air at 70ºC with full humidified inlet gasses. These MEA's, made with membranes ranging from 700 to 1,000 EW, show little difference in performance. As expected, the trend for impedance with respect to EW showed lower cell resistance with lower EW, but this is not reflected in improved performace. Fig. 16 shows the same MEA's running at 0.5 A/cm^2, 90ºC cell temperature and 30% RH. The trend for impedance with respect to EW also showed improved cell resistance with lower EW. Now the membrane EW has a pronounced effect on performance, with a 75 mV difference in

performance between 700 and 1,000 EW samples. It should be noted that these samples were made with electrodes prepared with 1,100 EW ionomer and were not optimized for higher temperature operation.

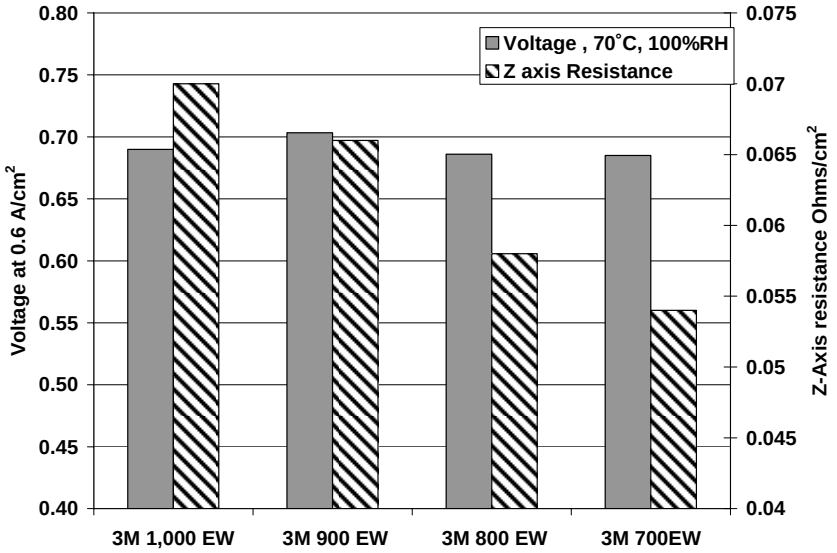

Fig. 15. Cell voltage and high frequency resistance measured at 0.6 A/cm2 for 50 cm2 fuel cells operating at 70ºC with fully humidified H2 and air.

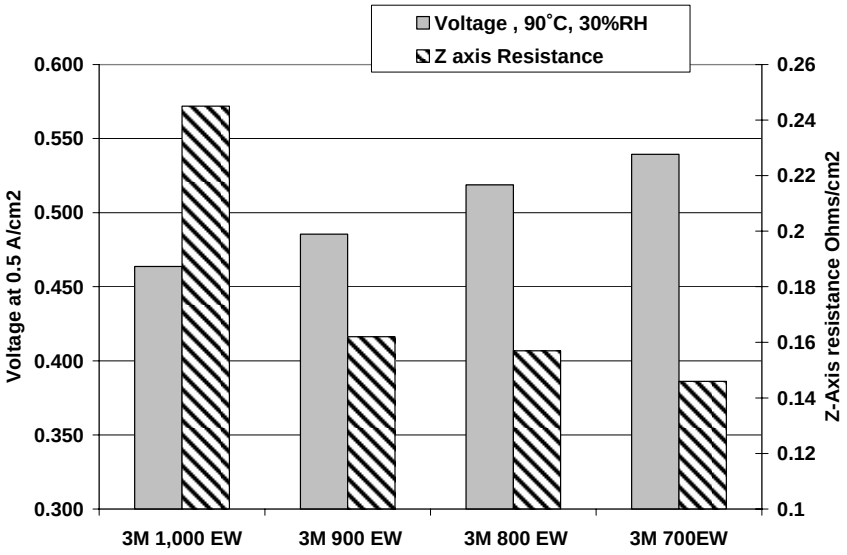

Fig. 16. Cell voltage and high frequency resistance measured at 0.5 A/cm^2 for 50 cm^2 fuel cells operating at 90ºC with 30% RH H_2 and air.

The durability of the different equivalent weight samples does not show an apparent trend. Fig. 17 shows normalized lifetimes and fluoride release rates for the different EW membranes. The durability data certainly suggests that going to lower EW membrane does not compromise durability under these conditions and in fact the 800 EW membrane shows the best durability. Since lower EW weight can remain humidified at dryer conditions it is possible that phenomena

had some effect on lifetime. However since there was not a clear trend it is probably not the only characteristic that affected durability in the study.

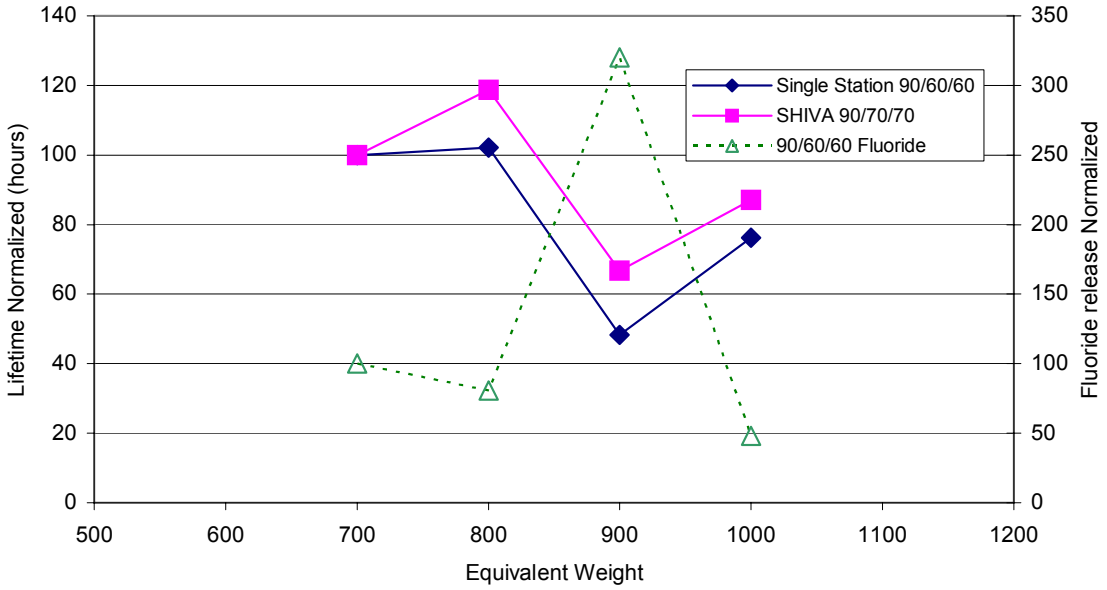

Fig. 17. Lifetime and fluoride release for different equivalent weight samples tested under accelerated testing conditions

2.2.4 Improved durability of PFSA PEM's with inorganic additives

There are a limited number of strategies available for improving the chemical durability of PFSA membranes. Two of the approaches focus on modifying the polymer in order to make it less susceptible to attack. Of course, the migration from hydrocarbon membranes to fluorinated membranes was the first major step in this direction. To further improve the stability of fluorinated membranes, past researchers have focused on the most susceptible sites for oxidative attack. One such approach is end-group fluorination, which refers to the conversion of standard carboxylic acid termini to trifluoromethane termini, done most conveniently by exposure of the polymer to fluorine gas.[10] Although end-group fluorination has been shown in work done at 3M (M. Yandrasits, et al., unpublished) to improve durability, the improvements are generally on the order of a doubling of membrane electrode assembly (MEA) lifetime. The limited extent of this improvement may be the result of i) a tendency for the termini to convert back to susceptible carboxylic acid groups, ii) incomplete fluorination, or iii) continued presence of other susceptible sites of attack on the polymer. With regard to the latter, other researchers have focused on elimination of the ether linkages like those contained in the polymers of U.S. Patent Application No. 2005/0004335. In the currently reported work, the 3M PFSA ionomer, with its ether linkages and carboxylic acid termini, was stabilized through addition of inorganic additives.

2.2.4.1 Initial Studies of Inorganic Oxides

Early in the contract the focus of the membrane efforts was on the addition of inorganic additives, both acid functionalized and not functionalized, to the PFSA PEM. At least four different additives were tested by themselves at various concentrations, also acid functionalized versions, and various different methods of incorporating the additive. The additives could be

imbibed into already cast membranes, added to the casting solution prior to casting or precipitated in the PEM coating process. The concept behind this approach was that the additives would impede the water loss of the PEM in sub saturated gas streams. This approach is often referred to as the "sand" approach as silica is the most commonly tested inorganic additive. The approach was for the most part not successful, though it was illustrative, and did point us to expanded testing of HPA additives. Further work on HPA's is described later in the section 3.0 of this report, "Membrane Materials and Approaches for T> 120ºC".

The test method used predominately to study the effect of the addition of inorganic additives was hydrogen pump and impedance spectroscopy on 5cm^2 active area MEAs. A hydrogen pump consists of a polarization curve taken with both electrodes in a hydrogen atmosphere. There is usually very little anode overpotential so the slope of the current voltage curve represents the ionic resistance of the PEM in series with the electronic resistance of the gas diffusion layer. Hydrogen pump can be very illustrative in showing water management properties of the membrane as observed in the limiting current of the hydrogen pump. Under current in a hydrogen pump, water is pulled from the anode by a combination of electro-osmotic drag and the increased gas volume due to hydrogen evolution on the cathode. This is counter balanced by water back diffusion, but the hydrogen pump will reach a limiting current if there is not enough water at the anode to supply the current. The high frequency resistance as measured in the impedance spectroscopy agreed well with the resistance of the hydrogen pump at low currents. A test station was built to test PEMs four at a time by doing hydrogen pumps and impedance spectroscopy using a multi-potentiostat. The testing was carried out using a fixed dewpoint of 70 or 80°C and ambient pressure outlets as the cell temperature was changed from 80 to 120°C in ten degree increments. Impedance measurements were made prior to each polarization scan at OCV with a 10mV oscillation voltage over a frequency range of 20kHz to 10Hz. Polarization scans were carried out in a galvanodynamic mode over the range of 2 amperes to -2 amperes with the current reversing if the voltage was above 0.8 volts. In addition some measurements were carried out on a single cell station at 120°C, 30psig, as a function of RH.

In all the permutations tested, the addition of an inorganic additive either increased the cell resistance or decreased the limiting current of the hydrogen pump. With a number of inorganic additives the HFR at zero current could be comparable to the control but the real difference was in the hydrogen pump limiting current. Also, acid functionalized inorganic additives tended to give even higher cell resistances and lower limiting currents. Fig. 18 shows one such example evaluated using NSTF electrodes. The only additive that showed some promise was the use of heteropoly acids (HPA) such as phosphotungstic acid. However, when this HPA was combined with inorganic additives to stabilize the water soluable HPA the resistance increased again. This can be seen in Fig. 19. In addition some PEMs were made using a porous reinforcing media that was filled with combinations of PTA and inorganic additives for the purposes of hydrogen pump measurements and conductivity testing.

It is not clear why the addition of inorganic additives and especially acid functionalized ones could increase the resistance or at least decrease the limiting current. In part, it could be just a volumetric matter with the volume of ionic conducting PFSA being reduced being responsible for the changes in resistance. It could be also that the addition of additives that retain water inhibits conductivity based on water movement with the protons.

Puncture testing was carried out to examine the effect of the additives on the mechanical properties of the PEMs. Puncture tests were done in an oven with a controllable relative humidity but the majority of measurements for the additives were carried out at room

temperature. Only a subset of all the inorganic additive PEMs made were tested for puncture resistance. In all cases, the addition of an inorganic additive tended to weaken the PEMs puncture resistance. There were some differences in the degree to which they were weakened but no attempt was made to correlate that to particle size as there was no easy method to determine the average particulate size with any confidence in a cost effective manner. Fig. 20 shows the effect of the addition of one inorganic additive added in one method.

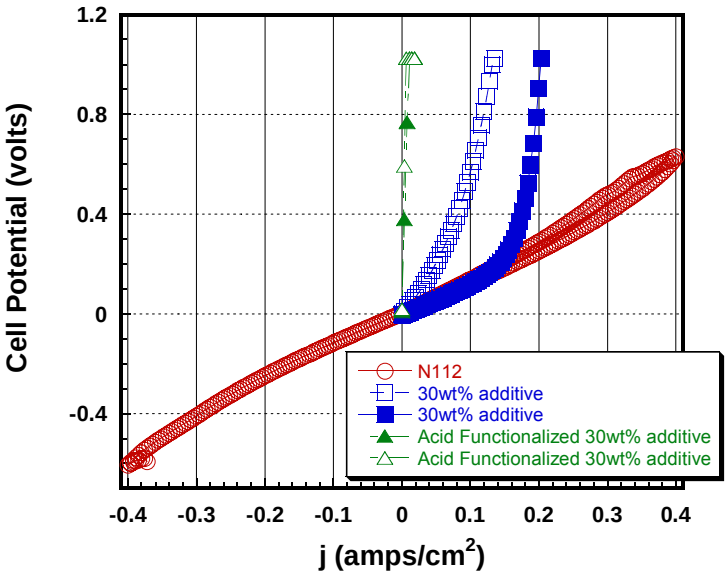

Fig. 18. Hydrogen pumps carried out at 120oC, 80oC dewpoint hydrogen at ambient outlet pressure, for an inorganic acid both acid functionalized and as is.

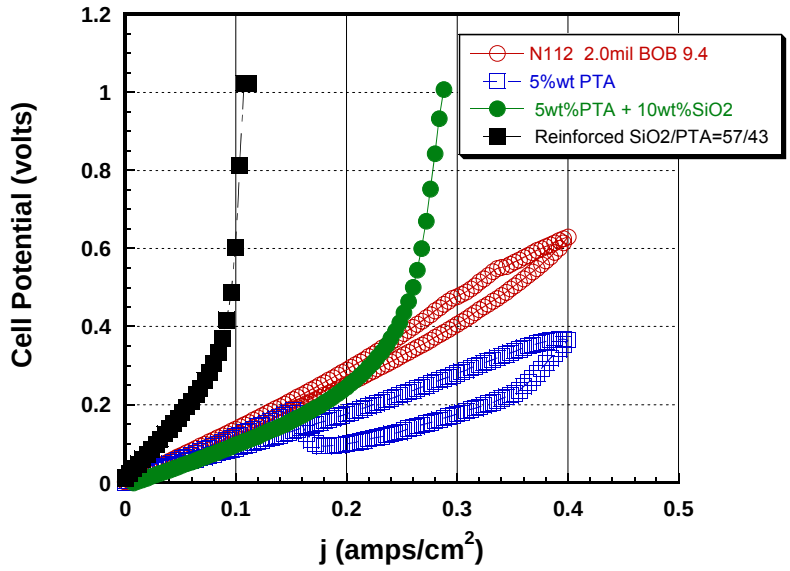

Fig. 19. Hydrogen pump polarization of PEMs with various permutations of PTA and SiO_2 additives measured at 120°C, 80°C dewpoint hydrogen at ambient outlet pressures.

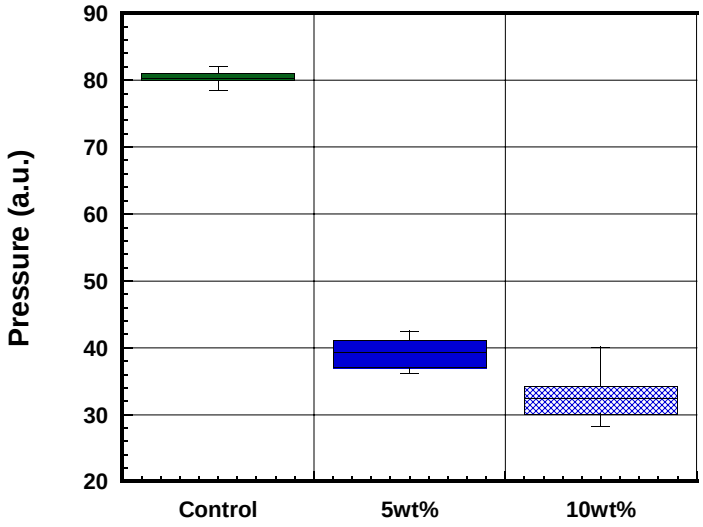

Fig. 20. This figure shows the effect of the addition of one inorganic additive added by one method on puncture resistance.

2.2.4.2 Screening of stabilizers with ex situ peroxide soak testing

In order to evaluate a large number of candidate additives with respect to their stabilizing effect on PFSA membranes, a soak test was developed wherein the weight loss of membranes as a result of exposure to a peroxide solution was monitored. The test was adapted from a procedure laid out in U. S. Patent No. 6,335,112 on hydrocarbon-based membranes.[11] The chemical degradation of these easily hydrated polymers is characterized by release of the decomposition products into the hydrogen peroxide solution, and hence weight loss for the film. After attempting such procedures over a range of temperatures, times, and starting H_2O_2 concentrations, it was determined that a reproducible weight loss "signal" for PFSA membranes could be detected after soaking for five days at 90°C in a H_2O_2 solution of starting concentration 1M. Furthermore, membranes lacking stabilizers exhibited increasing weight loss as iron was added to them at increasing concentration (in the form of ferric nitrate dissolved in the polymer dispersion before membrane casting), consistent with degradation models based on hydroxyl radical attack.

Fig. 21 gives measured weight loss vs. iron doping level for 1000EW 3M PFSA membranes. The membranes were cast from a dispersion of the polymer in 70/30 by weight mixed n-propanol/water solvent. They were cast with a 20mil gap bar coater on glass, followed by 15min of air drying, 10min of drying in air at 80-90°C, and 15min of annealing in air at 200°C. The inclusion of 100-500ppm (0.01wt%) iron by way of ferric nitrate addition to the casting dispersion was used frequently throughout the screening studies for additives. For reference, 3M's PFSA ionomer is prepared with iron content generally less than 5ppm. The additives that were investigated for potential stabilizing activity for PFSA ionomers are listed in
Table **I**. In all cases, the compounds were added to the ionomer dispersion before membrane casting. Many of the salts dissolved readily in the dispersion, yielding clear films after casting and annealing. Exceptions included the palladium, platinum, and silver salts, which yielded films that had a slightly hazy gray or tan appearance. The oxide additives generally seemed insoluble in the casting dispersion.

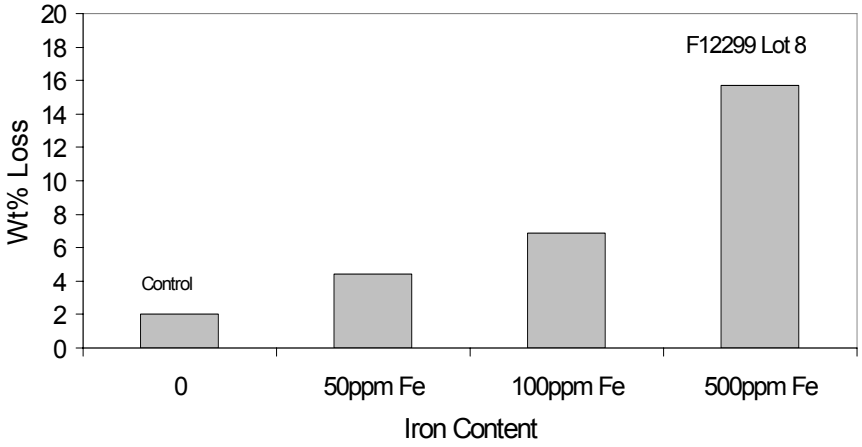

Fig. 21. Peroxide soak test screening results for 1000EW 3M PFSA ionomer membranes with controlled additions of ferric nitrate (5days - 90°C - 1M H_2O_2 starting concentration).

Table I. Candidate additives to PFSA membranes screened using the *ex situ* soak test.

$VOSO_4$	$Er(NO_3)_3$-$5H_2O$	Tm_2O_3
$Cr((NO_3)_3$-$9H_2O$	$Tm(NO_3)_3$-$5H_2O$	Yb_2O_3
$Mn(NO_3)_2$	$Yb(NO_3)_3$-$5H_2O$	ThO_2
$Fe(NO_3)_2$-$9H_2O$	$Th(NO_3)_4$	RuO_2
$Co(NO_3)_2$-$6H_2O$	$AgNO_3$	ZrO_2:AuPd
$Ni(OOCCH_3)_2$-$4H_2O$	$RuCl_3$	TiO_2:AuPd
$CuSO_4$-$5H_2O$	$PtCl_4$	C
$Zn(NO_3)_2$-$6H_2O$	$PdCl_2$	C-SO_3H
$Cd(NO_3)_2$-$4H_2O$	Co_3O_4	C:Pt
$Y(NO_3)_3$-$4H_2O$	TiO_2	C:Pd
$Ce(SO_4)_2$	ZrO_2	C:Ru
$Ce(OOCCH_3)_3$	PbO	C:PtRu
$(NH_4)_2Ce(NO_3)_6$	PbO_2	H-phthalocyanine
$Ce(NO_3)_3$-$6H_2O$	SnO_2	Mn-phthalocyanine
$Ce_2(CO_3)_3$-$1.56H_2O$	Sb_2O_5	Perylene red (PR)
$Ce(OH)_4$	MnO_2	PR:Pt
$Pr(NO_3)_3$-$2H_2O$	Mn_2O_3	PR:PtRu
$Sm(NO_3)_3$-$6H_2O$	CeO_2	PR: PtNiFe
$Eu(NO_3)_3$-$6.2H_2O$	Pr_6O_{11}	Ruthenium Red
$Tb(NO_3)_3$-$6H_2O$	Eu_2O_3	
$Dy(NO_3)_3$-$5H_2O$	Tb_4O_7	

One exception to the latter observation was the behavior of manganese dioxide, discussed later. In general, the candidate additives were stirred into casting dispersions for at least 12 hrs. In the case of some experiments on powder additives, the powder was first ball-milled overnight

in a 70/30 mixture by weight of n-propanol/water, before stirring the milled suspension into the polymer casting dispersion. Fig. 22 gives example weight loss data recorded for 1000EW 3M PFSA ionomer films with various salts added, after soaking in capped jars for five days at 90°C in aqueous solution with starting concentration of 1M H_2O_2. The film size was generally between 0.03g and 0.07g, and the amount of solution was 50g. It is worth noting that the spontaneous decomposition of commercial hydrogen peroxide solutions is fairly rapid at 90°C, and potassium permanganate titrations showed that after only one day, over 90% of the starting H_2O_2 decomposes. Notwithstanding the rapid decomposition of H_2O_2, membranes were shown in targeted experiments to lose mass progressively over the remainder of the five-day test.

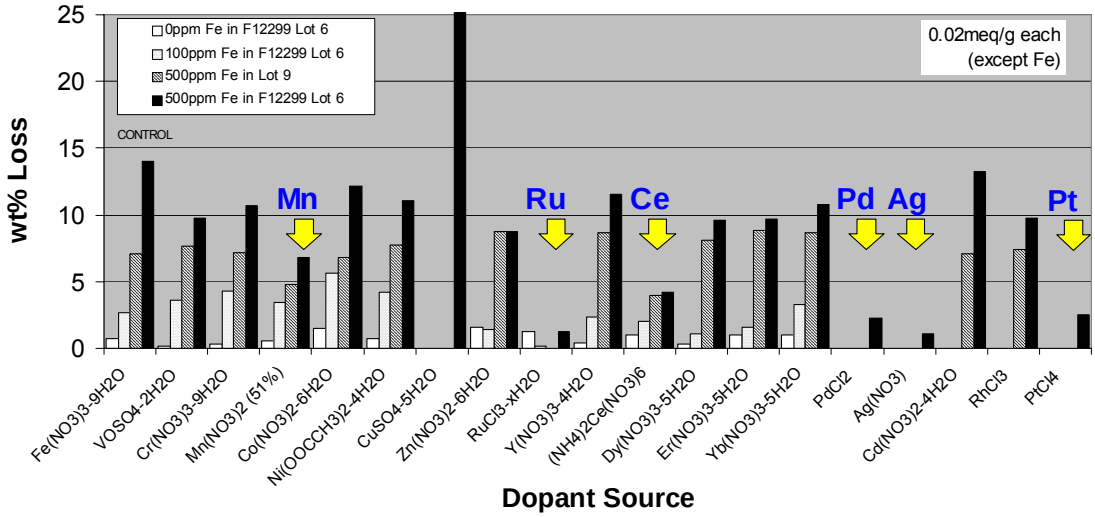

Fig. 22. Example peroxide soak test screening data for 3M PFSA ionomer membranes loaded with inorganic salts (5days - 90°C - 1M H2O2 starting concentration).

2.2.4.2.1Ruthenium, platinum, palladium, and silver

Fig. 23 gives weight loss data for membranes co-doped with ferric nitrate and ruthenium chloride salts (soluble in the casting dispersion). Ruthenium-based additives were among the most effective for limiting weight loss in the peroxide test, as were additives based on platinum, palladium, and silver. Metals, oxides, and salts of these elements reproducibly limited weight loss readings to near zero. In general, they also catalyzed vigorous decomposition of hydrogen peroxide when added to H_2O_2 solutions. When membranes doped with these species were placed in H_2O_2 solutions, gas bubbles were often observed to form on the membrane surface.

2.2.4.2.2 Copper, lead, and carbon

Copper sulfate and lead(IV) oxide emerged from the study as generating the most negative effects on weight loss in the peroxide soak test, with weight loss values reaching 30-50%. The result for copper is not entirely surprising, given the known similarity of Cu(I) to Fe(II) with respect to Fenton's reaction.[12] Measurements of weight loss were also made for membranes containing lead(II) oxide. The results for the latter were mixed, but did range up over 30%. Carbon additions increased the weight loss, but not nearly as dramatically as copper- or lead-

based additives. For example, 3.6wt% and 8.4wt% additions of XC-72 to cast Nafion™ membranes yielded weight loss values of 6.0wt% and 8.4wt%, respectively, after 90hrs in the 1M H_2O_2 solution at 90°C.

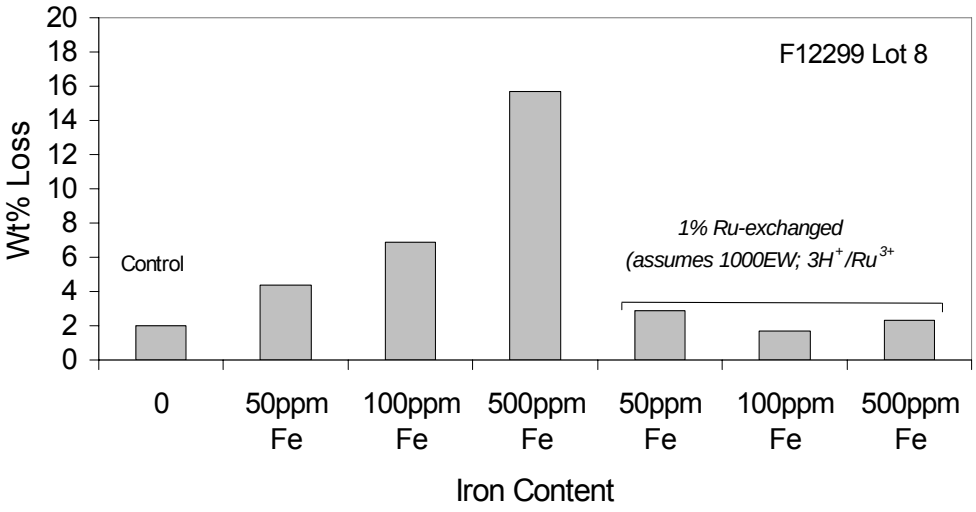

Fig. 23. Peroxide soak test screening results for 1000EW 3M PFSA ionomer membranes with controlled additions of ferric nitrate and ruthenium chloride (5days - 90°C - 1M H_2O_2 starting concentration).

2.2.4.2.3 Manganese and cerium

Manganese and cerium were elements which proved to be less dramatic in their suppression of weight loss than ruthenium, platinum, palladium, and silver, but were equally reproducible. Salts and oxides of the former elements, added first to the polymer dispersion before film-casting, both resulted in reduced weight loss in the peroxide soak test. Generally, weight loss readings were reduced to 1/4-3/4 of control values. For manganese, the screening was limited to $Mn(NO_3)_2$, Mn_2O_3, MnO_2, and Mn-phthalocyanine. For cerium, experiments were performed with CeO_2 powder, CeO_2 colloid, $Ce(SO_4)_2$, $Ce(OOCCH_3)_3$, $(NH_4)_2Ce(NO_3)_6$, $Ce(NO_3)_3$-$6H_2O$, $Ce_2(CO_3)_3$-$1.56H_2O$, and $Ce(OH)_4$. Fig. 24 gives weight loss results for the cerium-based additives (two replicates per sample type).

In addition to the peroxide soak weight loss studies, Mn- and Ce-based additives were investigated for their impact on ion-exchange capacity (IEC) and proton conductivity. IEC was determined by titration. Although a number of procedures were used throughout the research program, most of the titrations were carried out by stirring a 0.1-0.2g piece of membrane in 100g of 0.1M NaCl solution and adding 0.05M NaOH until equivalence was reached. For selected samples, an alternative approach was taken, wherein pH measurements of the NaCl solution before and after film addition were combined with the mass values for the film and solution, to allow calculation of the starting acid content of the film (assuming that the film released all of its protons as it ion-exchanged with the dramatic excess of sodium cations in solution). IEC determined by this latter procedure is reported for CeO_2-containing membranes below, for example. As expected, every ionic and particulate additive that was studied by titration reduced the IEC of the PFSA ionomer. For example, the addition of $Mn(NO_3)_3$ in Fig. 25 resulted in the loss of 2 equivalents of acid groups per equivalent of Mn(II) added. Fig. 26 reports the reduction of IEC that resulted from addition of cerium oxide powder (Rhodia Polishing Opaline).

With reference to the gray dashed lines in the figure, the reduction in IEC was intermediate between that which would be predicted for simple mass dilution by the CeO_2 and that which would be predicted for full dissolution of the CeO_2 and ion-exchange of acid groups by Ce(IV).

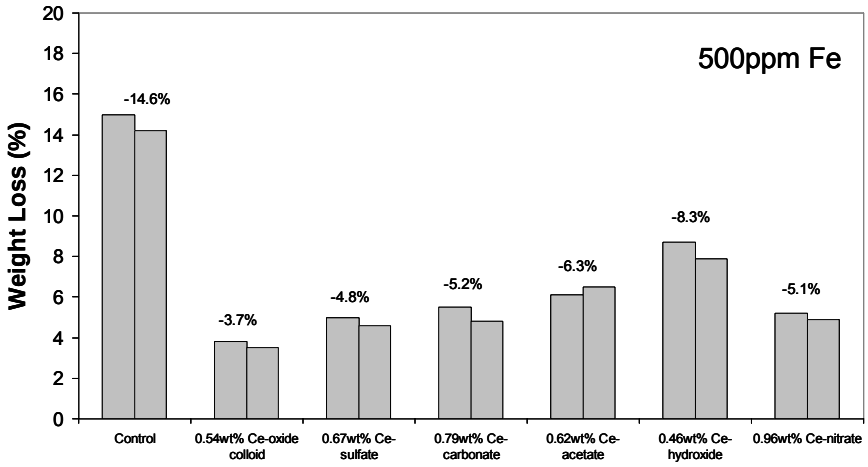

Fig. 24. Peroxide soak test screening results for 1000EW 3M PFSA ionomer membranes with controlled additions of cerium-based compounds (5days - 90°C - 1M H_2O_2 starting concentration).

Fig. 27 reports the dependence of proton conductivity for the 1000EW 3M PFSA on loading for additions of MnO_2. Clearly, there are larger reductions in conductivity that can be explained only on the basis of volume dilution of the conductive polymer phase. Consistent with this finding, MnO_2 powder additions to the PFSA casting dispersion appeared to dissolve at least partially on stirring for several days. Initially dark gray turbid dispersions became turbid white. Although the MnO_2 powder was confirmed not to be soluble in strong mineral acid solutions (e.g,. HNO_3), the work carried out in this research program revealed that the PFSA dispersion apparently can dissolve some quantity of the MnO_2. As a general strategy, the loss in proton conductivity that accompanies stabilizer addition can be offset by reduction of EW (Fig. 28).

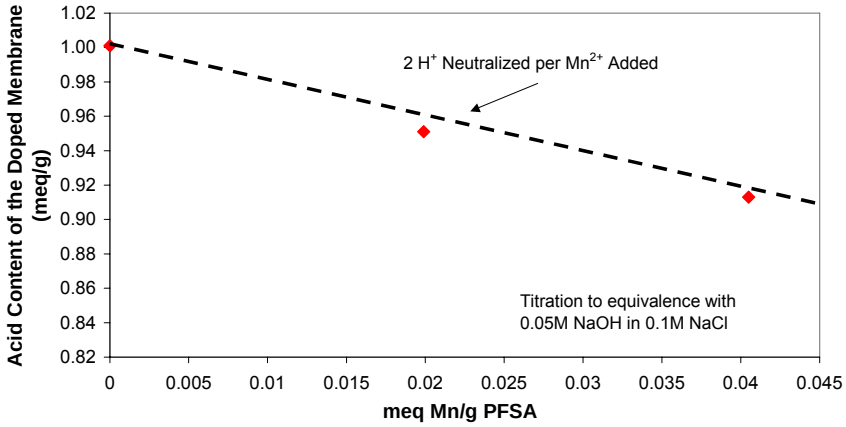

Fig. 25. Effect of manganese nitrate addition on measured acid content of 1000EW 3M PFSA ionomer membrane.

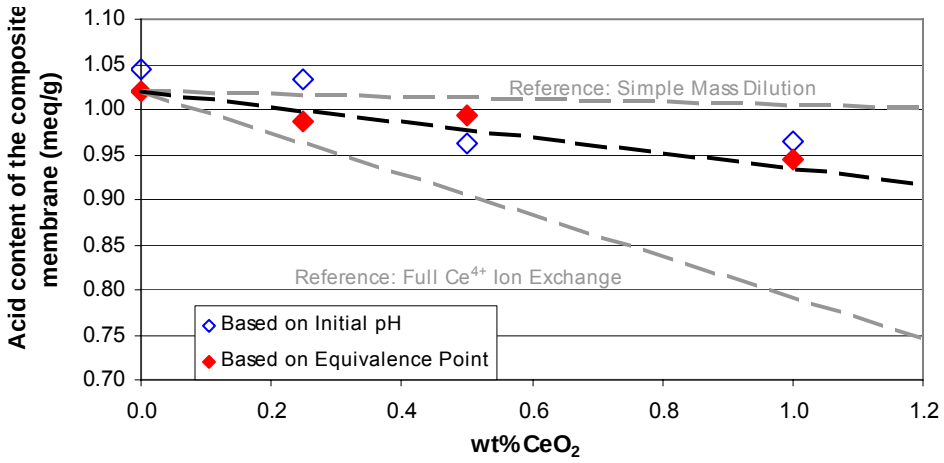

Fig. 26. Effect of cerium oxide addition on measured acid content of 1000EW 3M PFSA ionomer membrane.

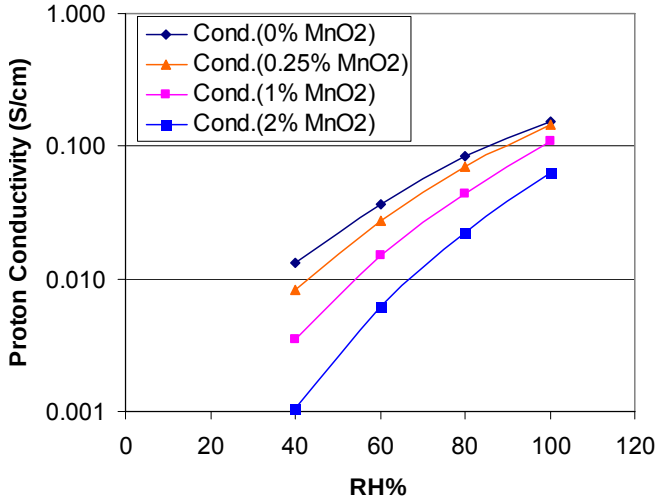

Fig. 27. Effect of manganese(IV) oxide addition on measured proton conductivity of 1000EW 3M PFSA ionomer membrane (70°C).

1.1.1. *2.2.4.2.4 Remaining elements from Table* I

Compounds comprising the remaining elements from Table **I** (V, Cr, Co, Ni, Zn, Cd, Y, Pr, Sm, Eu, Tb, Dy, Er, Tm, Yb, Th, Ti, Zr, Sb) were mixed and marginal in their screening soak test results and/or reproducibly ineffective. Pr_6O_{11}, Tb_4O_7, and ThO_2 were interesting in that they seemed to reduce weight loss for 3M PFSA membranes

where ferric nitrate was not added, but offered no advantage when 100ppm Fe was added as the salt. Therefore, these oxide additives were advanced for fuel cell evaluation.

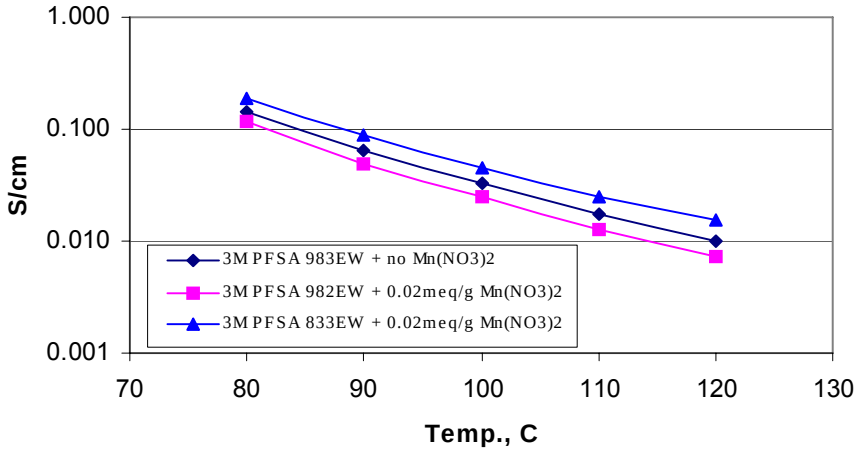

Fig. 28. Effects of $Mn(NO_3)_2$ addition and EW reduction on proton conductivity for 3M PFSA ionomer.

2.2.4.3 MEA load-cycle testing : F^- ion evolution and lifetime

As additives exhibiting efficacy in the screening H_2O_2 soak test were identified, they were advanced for evaluation in fuel cell operation. MEA's were fabricated and tested under various load cycle conditions for fluoride ion evolution and lifetime. Fuel cell MEA's having 50 cm^2 of active area were prepared as follows. An electrocatalyst layer was applied to one side of the membrane by handbrushing an ink, described below for each example. The final Pt loading was 0.4mg/cm^2. The ink was dried at 100°C at a pressure of less than 1 torr for 20 min. To assemble the MEA, two pieces of CCM were sandwiched together with PTFE-treated carbon paper gas diffusion layers and polytetrafluoroethylene/glass composite gaskets. This assembly was pressed in a Carver Press (Fred Carver Co., Wabash, IN) with 13.4 kN of force at 132 °C for 10 min. The MEA's were tested in a test station with independent controls of gas flow, pressure, relative humidity, and current or voltage (Fuel Cell Technologies, Albuquerque, NM). The test fixture included graphite current collector plates with quad-serpentine flow fields. MEA's were operated under various load cycle (and sometimes humidity cycle) conditions. The content of fluoride in the effluent water was measured using an ion chromatography system (Dionex ICS-2000, Sunyvale, California). Accounting for the duration over which the water was collected, a fluoride release rate was calculated, in units of micrograms per minute, and taken as an indication of membrane degradation rate. In addition to the fluoride release rate determination, some MEA's were operated until failure (membrane breach).

Table II summarizes the fluoride ion evolution behavior of MEA's based on 3M PFSA ionomer membranes, w/ or w/o various inorganic additives. Illustrative of the principle positive findings in these studies, MEA's incorporating manganese- or cerium-based additives exhibited dramatically reduced fluoride ion evolution rates. Although not reported in the table, particularly negative results were obtained for RuO_3, $RuCl_3$, Pt/C, and $AgNO_3$ additions (high F^- ion evolution rate and short lifetime). These distinctly negative findings for Ru, Pt, and Ag, (as compared with those for Mn and Ce) taken in combination with the H_2O_2 soak test data, clearly indicate that fuel cell MEA stabilization requires chemical activity that is not exactly probed using the soak test. In an operating fuel cell, it is reasonable to conclude that the oxidative challenge,

in terms of concentrations and species of oxidants, is different from that generated in the soak test, raising significant questions regarding the mechanism of stabilization (see next section).

Table II. Fluoride ion evolution rates for fuel cells operating at 90°C/60°C/60°C temp/DP-anode/DP-cathode under load cycle, using stations 5, 17, and 19.

		Average Fluoride Ion Release (µg/min)		
Sample Identification	**Number of Samples**	**21 hours**	**29 Hours**	**50 Hours**
Nafion™ PEM TAM04337-07	4	0.054	0.084	0.103
24-4030-5000A; 3M PEM w/o $Mn(NO_3)_2$	2	0.049	0.093	0.191
AGL05208-01 3M PEM w/ $Mn(NO_3)_2$	5	0.018	0.011	0.009
AGL05126-01 3M PEM with 0.25 wt% CeO_2	3	0.006	0.006	0.006
24-4030-5001A; ECL 4030 + 0.5 wt % CeO_2	3	0.007	0.010	0.014
24-4030-5004A; ECL 4030 + 0.5 wt % ThO_2	3	0.070	0.136	0.260
24-4030-5003A; ECL 4030 + 0.5 wt % Pr_6O_{11}	2	0.045	0.099	0.222
24-4030-5002A; ECL 4030 + 0.5 wt % Tb_4O_7	2	0.044	0.090	0.289

An important aspect of the approach taken in the presently reported work is the use of reduced-EW polymers in combination with the inorganic additives. As first mentioned with respect to Fig. 28 above, MEA's being developed (and already sampled to automotive customers as of time of this report) importantly include polymers of EW less than traditionally used in the fuel cell community. The work done in the presently reported program determined that equivalent power-performance to traditional MEA constructions (e.g,. based on 1000EW membranes) could be achieved for inorganically stabilized membranes when the EW was reduced to values less than 900.

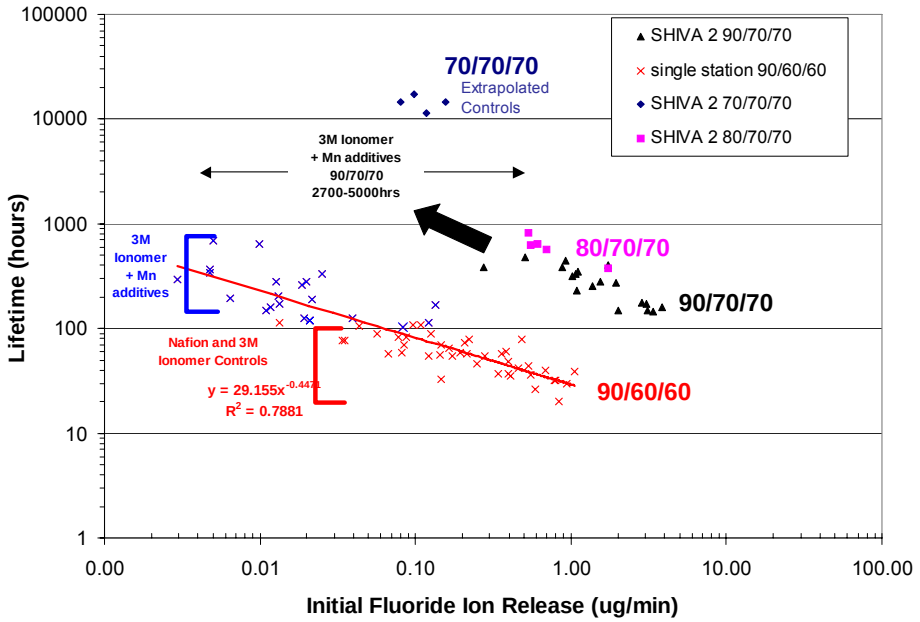

Fig. 29. Fluoride ion evolution rate and lifetime for fuel cell MEA's based on 3M's PFSA ionomer membrane (with $Mn(NO_3)_3$ where noted; usually 0.02mmols Mn / gram polymer).

Fig. 29 gives the dependence of lifetime on initial fluoride ion release rate for a number of operating conditions. The data for manganese-containing MEA's indicates that an order-of-magnitude improvement in lifetime (commensurate with an order of magnitude reduction in fluoride release rate) was realized, as compared with control MEA's. Using the 3M manganese-stabilized MEA's, similarly impressive results have already been obtained by a large automotive partner to 3M. MEA's incorporating Pr_6O_{11}, Tb_4O_7, or ThO_2 exhibit behavior that was essentially no different from that of control MEA's.

2.2.4.4 EPR study - transition metal and radical species

In order to establish the proton exchange membrane PEM fuel cell (FC) as an economical power source for residential and automotive applications the system must provide stable performance for over 5000 hours. Perfluorinated sulfonic acid (PFSA) membranes used in commercial PEM fuel cells have a tendency to develop pinholes in the time frame range from a few hundred to a few thousand hours depending on the operating conditions. These defects result in high rates of hydrogen crossover, which, in turn causes rapid performance decay or catastrophic failure of the whole system. The formation of reactive oxygen species during catalytic processes in FC operation has been amply demonstrated: H_2O_2 and $HO^{\cdot}$ are the most commonly reported species and their presence is implicated in membrane deterioration.[13] Oxidative degradation of the PFSA ionomer via oxygen free radicals (OFR) is believed to be the main cause for this type of failure. Certain functional groups in the ionomer are unstable towards OFR attack. Specifically, polymer end groups with residual H-containing terminal bonds are generally identified to be the initial degradation sites. In the case of 3M ionomer which lacks H-containing terminal bonds the oxidative degradation is believed to initiate at the –COOH terminated end groups.

H_2O_2 by itself, under highly acidic conditions in the fuel cell membrane (proton conducting electrolyte) is rather benign. However, in the presence of metal ions, such as Fe^{3+} (often present as an impurity) can undergo Fenton type reaction to generate $HO^{\cdot}$ radicals.[14]

$$H_2O_2 + Fe^{2+} \rightarrow Fe^{3+} + HO^{\cdot} + HO^{-}$$

Metal ions and several other organic phenolic compounds are known to decompose peroxides and act as antioxidants. A large number of these additives have been screened in a systematic manner for their antioxidant efficacy in a fuel cell environment. Two of these additives in particular, manganese and cerium, when added to the polymer electrolyte membrane have been shown to improve the oxidative stability of the ionomer to a great degree. A pertinent question is to understand what role these additives actually play inside the ionomer in peroxide mitigation? What is the state of these additives inside the ionomer? An understanding of the mechanism of peroxide mitigation may enable us to develop better and possibly discover new additives for use in the membrane. Since manganese and cerium are both multivalent ions and in this study we are focusing on their reactivity with free radicals Electron Paramagnetic resonance (EPR) would be the method of choice. We have carried out an extensive background literature search and carried out some preliminary EPR experiments in order to understand the state of the additive in the ionomer membrane. In this section, we report on some of the initial results from this study.

2.2.4.5 Experimental

2.2.4.5.1 Sample Preparation

We prepared different PFSA solutions containing varying amounts of $Mn(NO_3)_2.6H_2O$ or $Ce(NO_3)_3.6H_2O$. The films were prepared on a glass plate using a coater. We carried out a series of EPR experiments on the undoped control film and Mn-doped films.

2.2.4.5.2 EPR Data Acquisition

Spectra were acquired using a Bruker EleXsys 500 spectrometer equipped with the SHQ cavity. Spectra were acquired over a range of 2000 G at varying microwave powers. For all spectra, field modulation was at a frequency of 100 kHz with a modulation amplitude of 5.0 G. Sample temperature was maintained at appropriate temperature by using the Bruker temperature controller, with the sample cell inside a quartz dewar. Samples for saturation experiments were flushed with N_2 gas to remove oxygen. Typically, samples containing small strips of films were suspended in the 0.4 mm inside diameter EPR tubes. The sample was centered in the active part of the cavity. The temperature was controlled within $\pm$1 K. All samples were allowed to equilibrate for at least 10 min after reaching the desired temperature.

2.2.4.6 Results and Discussion

In Fig. 30 we show the EPR spectra for the undoped control film at 293K and 200K. As expected the EPR signal is broad at RT whereas it sharpens as the temperature is lowered to 200K. The g value calculated from the spectra is 1.999 indicative of S=1/2, a free electron.

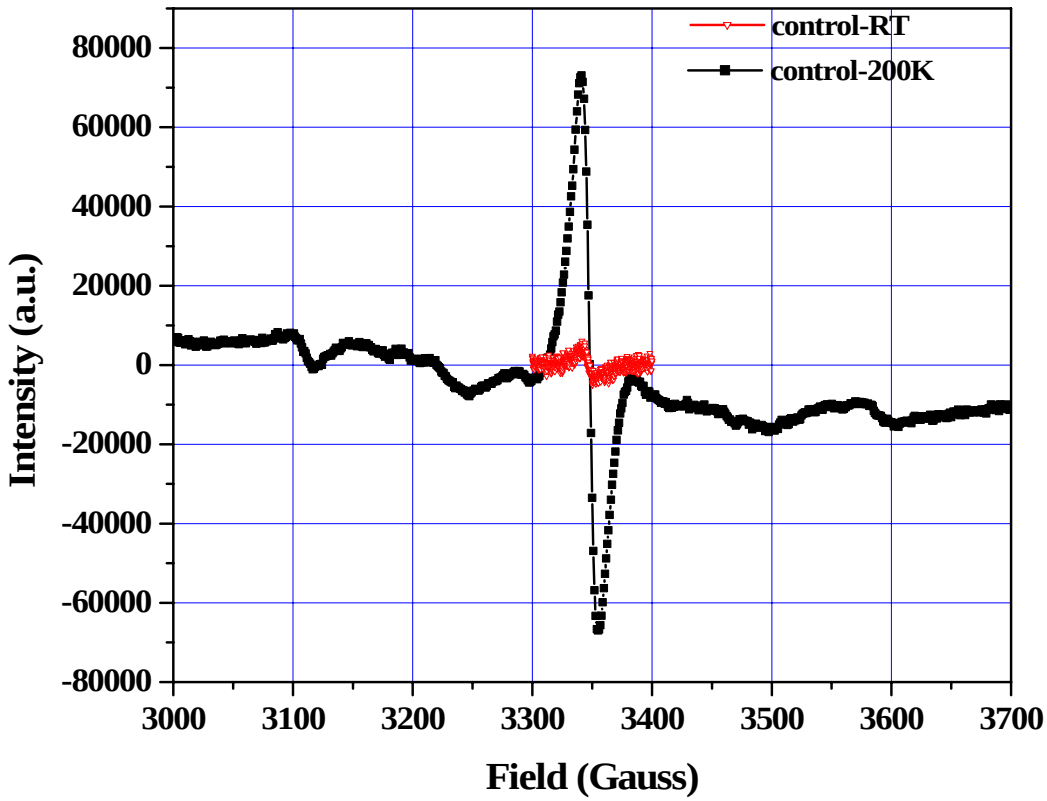

Fig. 30. EPR spectra for a control 3M ionomer membrane

Iron present as an impurity can be low spin Fe^{3+} $d^{5/2}$ (S=1/2) or high spin Fe^{3+} (S=5/2). This signal points to the presence of iron oxide clusters, iron oxyhydroxides and several other Fe^{3+} species present in the membrane.

Fig. 31 shows the EPR spectra for manganese containing films at 200K in the presence and absence of H_2O_2. After addition of H_2O_2 the temperature was raised to 90˚C (363K) and the spectra was recorded again.

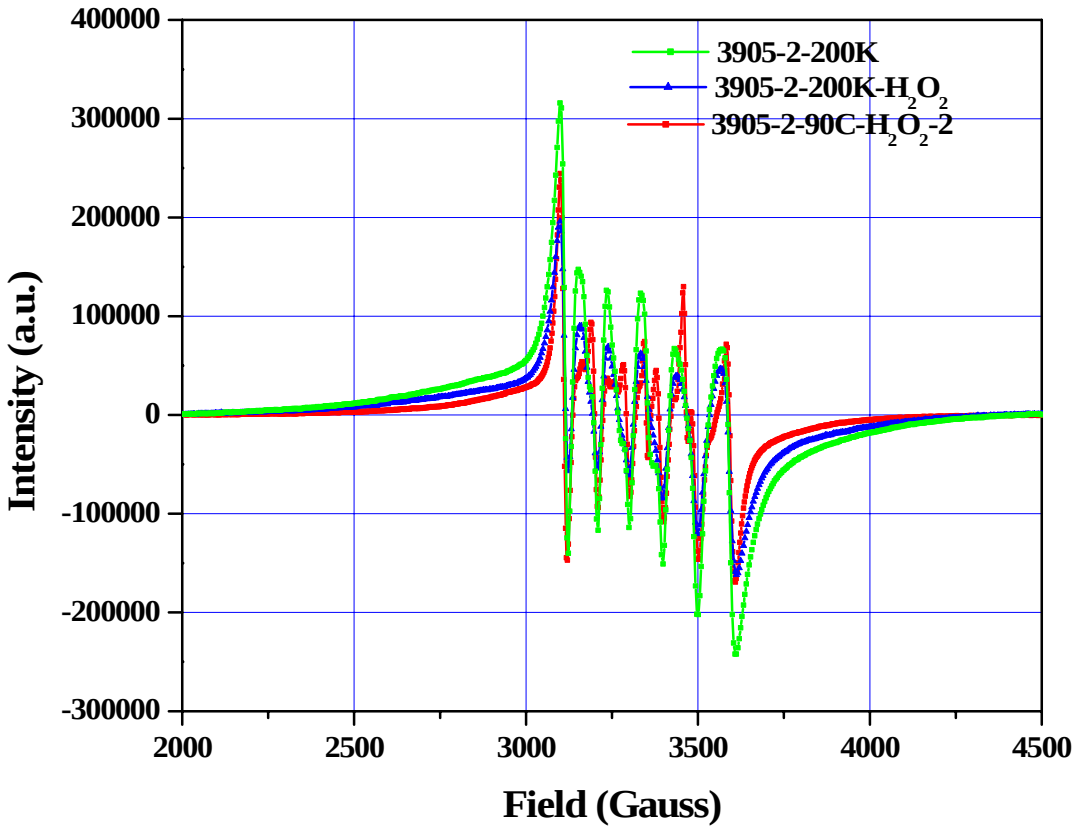

Fig. 31. EPR spectra for a partially exchanged Mn^{2+} containing 3M ionomer membrane

The spectra at 200K reveals the six line EPR signal due to Mn^{2+} (S=5/2 2S+1 = 6). The Mn^{2+} is present primarily as a hexaqua ion $Mn(H_2O)_6^{2+}$ and not bound to sulfonate or carboxylate group in the polymer or else the EPR signal would be dampened or completely absent. Addition of H_2O_2 results in the narrowing of the lines, thereby indicating further dilution and hydration of manganese. On raising the temperature to 90˚C, the six line signal splits, which might indicate both dehydration of the Mn^{2+} environment as well as bonding of manganese to other sites in the membrane (see Fig. 32). It is unclear if this is accompanied by a change in oxidation state of manganese or not. Since electron transfer processes when the temperature is raised, the signal splits. At present it is hard to conclude if this represents a change in the oxidation state of Mn^{2+} or evolution of some other species.

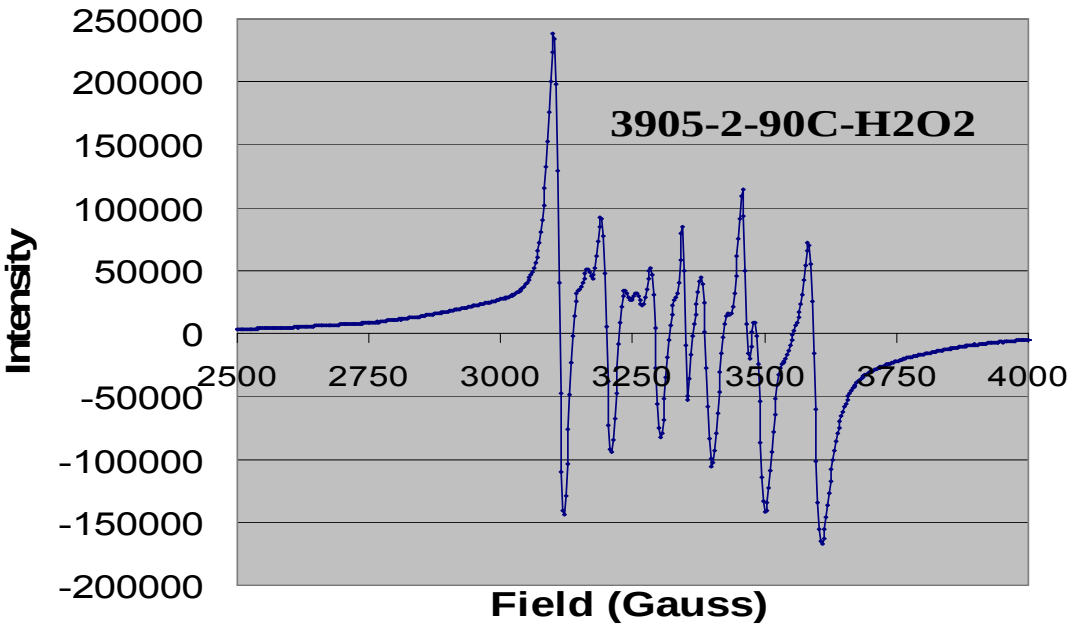

Fig. 32. EPR spectra for a Mn^{2+} containing 3M ionomer membrane at 90˚C in presence of H_2O_2.

In order to study the a possible change in manganese oxidation state/environment a time dependent study was carried out in the presence of H_2O_2 at room temperature. The spectra at various times are shown in Fig. 33, Fig. 34 and Fig. 35.

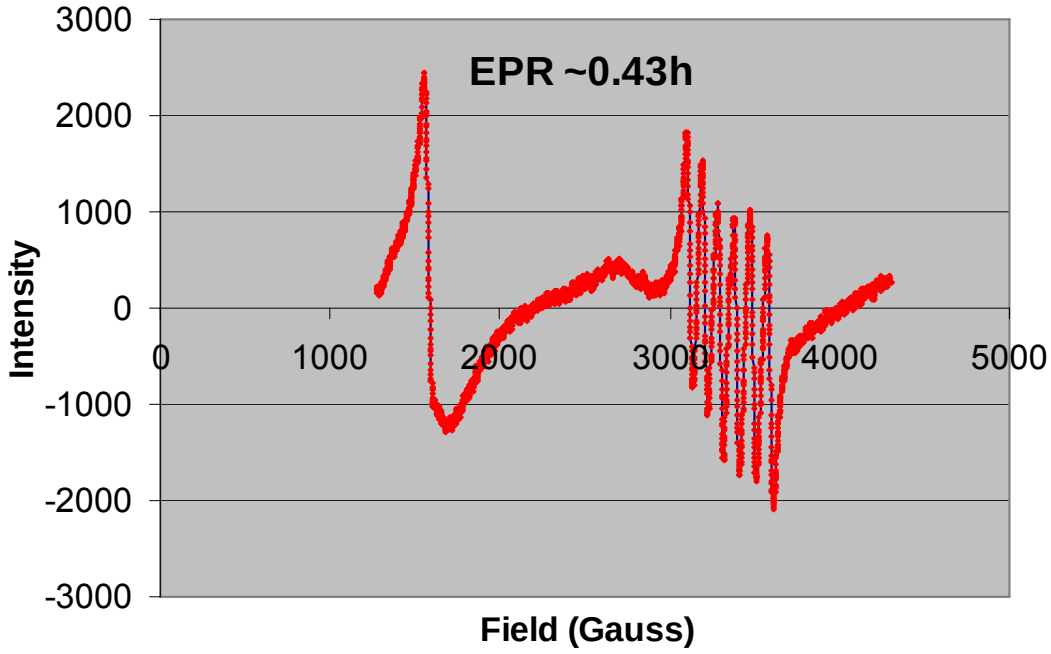

Fig. 33. Time Dependent EPR spectra for Mn^{2+} containing 3M ionomer membrane at RT in presence of H_2O_2.

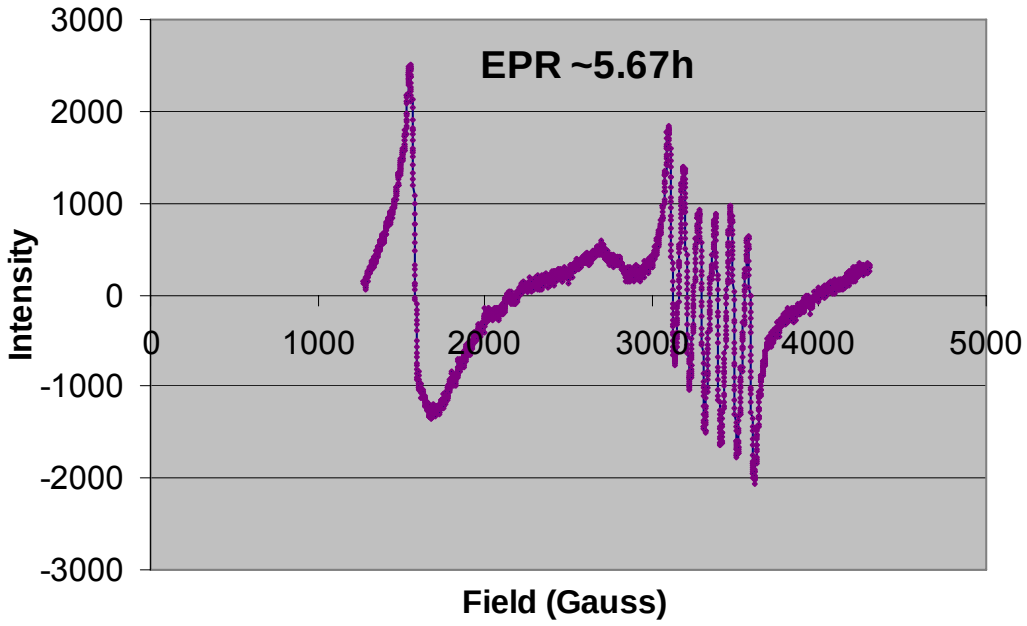

Fig. 34. Time Dependent EPR spectra for Mn^{2+} containing 3M ionomer membrane at RT in presence of H_2O_2.

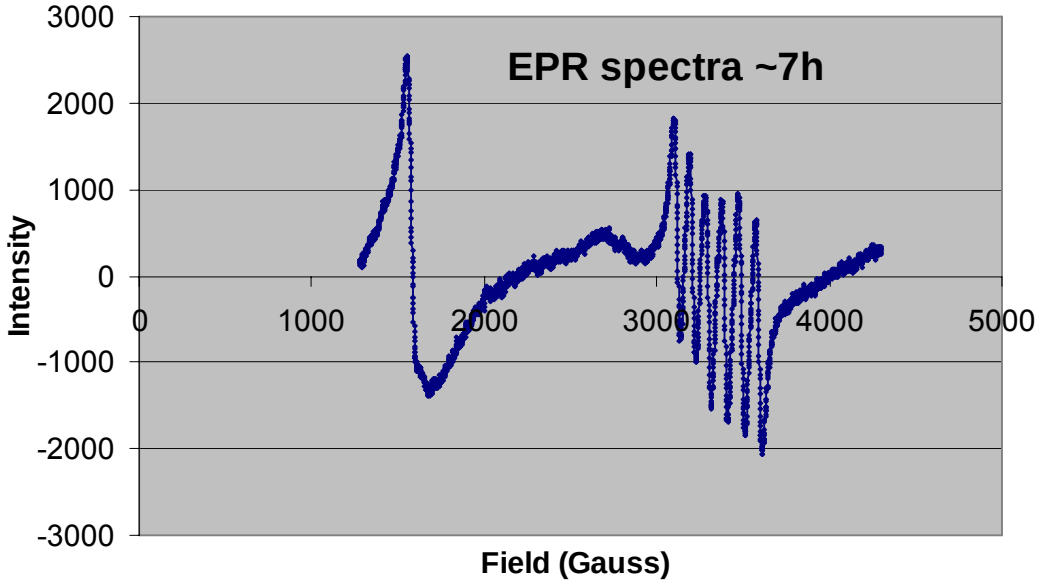

Fig. 35. Time Dependent EPR spectra for Mn^{2+} containing 3M ionomer membrane at RT in presence of H_2O_2.

No appreciable change is noticed even after 7hr, either in the shape or intensity of the signals. This indicates that there is no change in oxidation state of manganese under the given conditions. This has also been witnessed when manganese (II) nitrate was added to H_2O_2 solution. Another point worth mentioning is that the actual fuel cell operation occurs at higher temperature and drier conditions, where manganese may not be present in the fully hydrated form. Further experiments need to be carried out at higher temperatures. In addition, spin trapping / radical scavenging experiments need to be carried out.

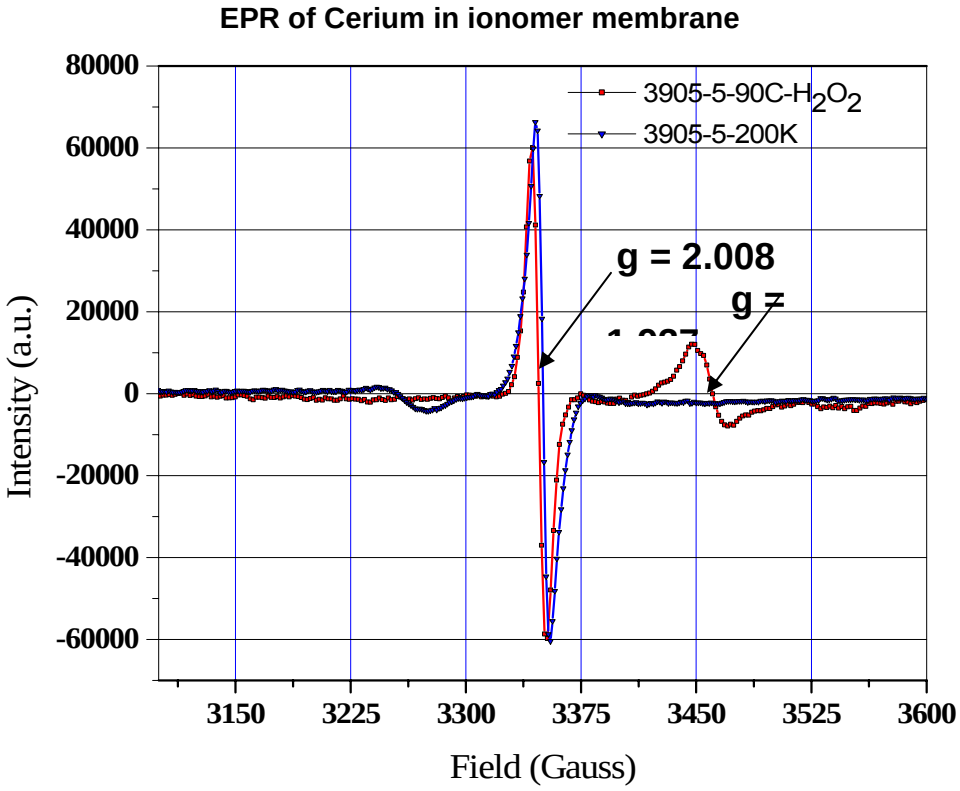

Fig. 36. Time Dependent EPR spectra for Ce3+ containing 3M ionomer membrane in different environments.

The EPR spectra of cerium containing samples at 90˚C, on adding H_2O_2, shows evolution of a new signal which in some cases in the literature has been assigned to defects present in bulk CeO_2 (Fig. 36).

Further EPR experiments need to be carried out in order to ascertain that these additives are indeed scavenging the free radical species generated by Fenton type reaction in the fuel cell.

2.2.4.7 Role of additives in oxidative stability

A close survey of the literature shows that, akin to the PEM fuel cell, reactive oxygen species (ROS), including superoxide ($O2^{\bullet-}$), hydrogen peroxide (H_2O_2), and hydroxyl radicals ($^{\bullet}OH$), are generated in biological systems as well by a number of pathways, some remarkably similar to that existing in PEM fuel cell.[15] Accumulation of these active oxygen species in aerobic organisms may cause DNA strand breakage, peroxidation of membrane lipids, and inactivation of enzymes. Defense systems derived from enzymatic and nonenzymatic antioxidants in living organisms can minimize the deleterious effects of active oxygen free radicals. Superoxide dismutases (SOD), catalase, and peroxidase are among these important antioxidant enzymes. SODs are a group of metal-containing enzymes that catalyze the dismutation of superoxide radical to oxygen and hydrogen peroxide.[16] These enzymes may be classified into three types according to their metal cofactor requirements: manganese (MnSOD), copper/zinc (CuZnSOD), and iron (FeSOD) forms. Superoxide dismutases (SODs) are a family of metalloenzymes that provide a defense against the toxicity of superoxide. SODs catalyze the removal of superoxide

radicals providing a major protective effect in our bodies. They catalyze the conversion of $O2^{\bullet-}$ to hydrogen peroxide (H_2O_2) and dioxygen (O_2), seen in the reaction below.

$$2O_2^{\bullet-} + 2H^+ \longrightarrow H_2O_2 + O_2$$

Studies showed MnSOD is widespread in bacteria, plants and animals. In most animals, MnSOD is largely located in the mitochondria [3]. The reaction mechanism of MnSOD catalysis can be written as:

$$Mn^{3+} + O_2^{\bullet-} \Leftrightarrow [Mn^{3+} - O_2^{\bullet-}] \longrightarrow Mn^{2+} + O_2$$

$$Mn^{2+} + O_2^{\bullet-} \Leftrightarrow [Mn^{2+} - O_2^{\bullet-}] + 2H^+ \longrightarrow Mn^{3+} + H_2O_2$$

SOD mimics catalyze the dismutation of $O_2\bullet-$ to hydrogen peroxide (H_2O_2) and dioxygen (O_2) as illustrated in reactions (1) and (2). M represents a metalloenzyme, that is, a metal containing complex that acts to catalyze reactions. Mn+ is this complex in the oxidized state and M(n-1)+ is in the reduced state.

$$M^{n+} + O_2^{\bullet-} \longrightarrow M^{(n-1)+} + O_2 \qquad \textbf{(1)}$$

$$M^{(n-1)+} + O_2^{\bullet-} + 2H^+ \longrightarrow M^{n+} + H_2O_2 \qquad \textbf{(2)}$$

But metals have such problems as that they can react with H_2O_2 to make the more reactive oxygen species, the hydroxyl radical (•OH). This product is very reactive and reacts very quickly. Thus, it enhances cell toxicity rather than protecting against $O2^{\bullet-}$ induced damage. The general redox process of molecules containing metals is illustrated in reactions (3) and (4).[17]

$$M^{n+} + O_2^{\bullet-} \longrightarrow M^{(n-1)+} + O_2 \qquad \textbf{(3)}$$

$$M^{(n-1)+} + H_2O_2 \longrightarrow M^{(n-1)+} + OH^- + \bullet OH \qquad \textbf{(4)}$$

For a metal containing mimic to be deemed protective the rate of reaction **(2)** must be greater than the rate of reaction **(4)**.[18]

The reactions in biological systems occur at near neutral pH whereas in a PEM fuel cell the environment is highly acidic. Based on the literature we believe a similar mechanism operates in the PEM fuel cell, wherein manganese and cerium ions play an important role in peroxide mitigation. The possible reactions occurring may be:

$$Mn^{2+} + O_2^{\bullet-} + 2H^+ \rightarrow Mn^{3+} + H_2O_2$$

$$2Mn^{3+} + H_2O_2 \rightarrow 2Mn^{2+} + 2H^+ + O_2$$

For Cerium ions the reaction can be written as

$$Ce(III) + O_2^{\bullet-} + 2H^+ \rightarrow Ce^{4+} + H_2O_2$$

$$Ce^{4+} + O_2^{\bullet-} \rightarrow Ce^{3+} + O_2 \ .$$

References for Section 2.2

1. S. J. Hamrock and M. A. Yandrasits, *Journal of Macromolecular Science, Part C: Polymer Reviews,* **46**, 219 (2006)
2. A) A.B. LaConti, M. Hamdan, R. C. McDonald, in *Handbook of Fuel Cells: Fundamentals, Technology and Applications,* Vol 3, pp 647, W. Vielstien, H. A. Gasteiger, A. Lamm, Editors,; John Wiley & Sons: West Sussex, UK, (2003). B) D.E. Curtian, R.D. Lousenberg, T.J. Henery, P.C. Tangeman, M.E. Tisack, *J. Power Sources,* **131,** 41 (2004).
3 . V. O. Mittal, H. R. Kunz, and J. M. Fenton, *J. Electrochem. Soc.,* **154** B652-56 (2007),
4. D.S. Schiraldi, *Journal of Macromolecular Science, Part C: Polymer Reviews,* **46,** 315, (2006).
5 M. Asukabe and G. Xie, U.S. Patent No. 6,335,112 (2002).
6. H. Wessel, M. Bender, K. Harth, A. Fischer, and M. Holzle, U. S. Patent Application 2003/0008196 A1 (2003).
7. M.T. Frey, S.J. Hamrock, G.M. Haugen, P.T. Pham, U. S. Patent Application 2006/0063055 (2003).
8. K.A. Maritz, R.B. Moore, R. B. *Chem. Rev.* **104,** 4535 (2004).
9. K. A. Page, F. A. Landis, A. K. Phillips, and R. B. Moore, *Macromolecules,* **39,** 3939 (2006).
10. R. A. Morgan, W. H. Tuminello, and M. E. Wagman, U.S. Patent No. 5,397,829, 1995.
11. M. Asukabe and G. Xie, U. S. Patent No. 6,335,112, 2002.
12. M. A. Al-Omar, C. Beedham, and I. A. Alsarra, *Saudi Pharmaceutical Jourmal* 2004, **12** [1] 1-18.
13. Schmidt, T. J.; Paulus, U. A.; Gasteiger, H. A.; Behm, R. J. *J.Electroanal. Chem.* 2001, **508,** 41-47 and references therein.
14. H. J. H. Fenton, *J. Chem. Soc*. 1894, **65**, 899-910.
15. Fridovich I. *Annu Rev Biochem*. 1995, **64,** 97-112.
16. McCord JM, Fridovich I. *J Biol Chem.* 1969, **244**, 6049-6055.
17. Koppenol WH, Levine F, Hatmaker TL, Epp J, Rush JD. *Arch Biochem Biophys.* 1986, **251,** 594-599.
18. Czapski G, Goldstein S. *Free Radic Res Commun.* 1991, **12,** 167-171.

Section 2.3 MEA Integration

This section reviews the work done under the first major subtask of **Task 1** discussed in section 1.2, to develop durable MEAs for operation in the temperature range of 85 $\leq$ T $\leq$ ~ 120^{o}C while operating on low humidification with PFSA based ionomers and lower cost catalysts. The focus of this section is on the integration of the catalyst, membrane and GDL for effective MEA operation.

Table of Contents for Section 2.3

2.3 MEA Integration

2.3.0 Introduction

This section summarizes the work done related to integration of the down-selected MEA components. This includes the membrane, its integration with the NSTF down-selected catalysts, and the GDL, for best overall performance and durability. It is divided into four sections. The first addresses work done to down-select the membrane to be used with the down-selected NSTF catalyst for scale-up and final short stack testing, as discussed in section 4.0 of this report. The second subsection addresses similar work done to select the GDL, and the third subsection addresses aspects of water management issues intrinsic to the ultra-thin NSTF electrode layers.

Good progress was made in optimizing the membrane and GDL components for their intended purposes, and choice of cell operating conditions for best performance. The difficulty of the modeling problem, however, prevented its full objective from being realized.

2.3.1 Membrane down-selection for NSTF catalyst

The membrane and catalyst can only be developed independent of one another up to a point. Together they comprise a system in which they can influence one another in multiple ways. The catalyst can contain transition metals that may contaminate the membrane as discussed in section 2.1.3.2.4 of this report. The membrane can contain residual impurities, both inorganic and organic cations and anions that seriously compromise low loading or low surface area catalysts. These residual membrane impurities can result from decomposition in the highly acidic environment of the PFSA membrane, of residual solvents and/or dispersion aids used during the membrane fabrication. The membrane processing method, e.g. solvent casting versus extrusion, drying temperatures and post-process annealing temperatures can affect the degree to which those residual impurities are formed or remain in the membrane. These residual impurities can affect the catalyst's electrochemically active surface area directly or the kinetics through the charge transfer impedance. A thin layer electrode, like the NSTF catalyst, can impact the degree to which water, like the reactants, can permeate into or out of the membrane, affecting its conductivity, as discussed in section 2.1.5.3 of this report. The catalyst on the other hand is the source of the original peroxides that can lead to free radicals that attack the PFSA membrane end groups, side chains etc., producing fluoride ions detectable in the fuel cell effluent water as discussed in section 2.1.5.2.

In this section we discuss some of the data and factors evaluated to down-select the membrane type to best match the NSTF ternary catalyst down-selected for its catalytic properties as described in section 2.1.5 of this report.

2.3.1.1 Nafion™ versus 3M ionomer and effects of post fabrication cleaning

At the start of this contract, the membrane used exclusively for evaluation with the NSTF catalyst was Nafion™ (Nafion™ is a registerd trademark of DuPont) film, available as either Nafion 112 or as fabricated at 3M by solvent casting with thicknesses on the order of 30 microns. As the PFSA membrane using the 3M ionomer developed as described in section 2.2 of this report became available, the NSTF catalyst was increasingly transitioned to testing with it until the 3M ionomer based membrane was exclusively used for catalyst coated membrane (CCM) development. The performances with the 3M membrane were

quickly found to be superior to those obtained with Nafion, even with nearly the same equivalent weights.

A very important factor for membrane use, known generally in the literature as well, is that pre-cleaning the membranes, such as by acid washing to remove residual cations, is important to achieve the full conductivity and water uptake properties of the membrane. This was clearly the case for the membrane development for the NSTF catalysts, and was found to impact not only performance but the speed of initial break-in conditioning as well as discussed in section 2.1.5.4 of this report. Standard protocols for acid washing and rinsing in deionized water were implemented to prepare the membranes in as standard initial state as possible. Fig. 1 below compares the effect of cleaning versus not-cleaning a 3M membrane lot, on the standard ambient pressure PDS curve. (See section 2.1.3.1.2 for details on single cell testing.) There is an impact on kinetics, mass transport and possibly impedance seen in the polarization curves.

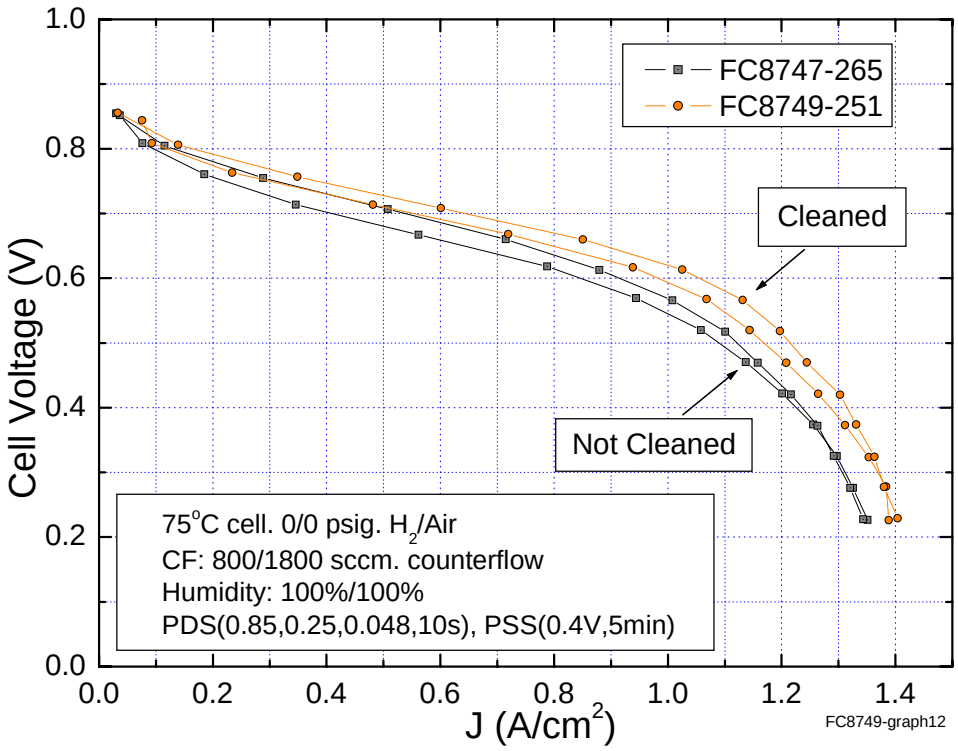

Fig. 1. Effect of pre-cleaning the membrane by acid washing on the ambient pressure PDS polarization curve.

More dramatic is the impact of removing residual impurities from the membrane on the time for conditioning the MEA. Fig. 2 compares the log plots of the break-in conditioning for the same two MEAs shown in Fig. 1. The cleaned MEA shows initial performance significantly higher in the first 75 data files than for the non-cleaned membrane, even before the start of the thermal cycling. Also, the number of thermal cycles (T.C.) required to reach full performance is nearly half those for the cleaned membrane. (see section 2.1.5.4 for discussion of the log plots and break-in conditioning.)

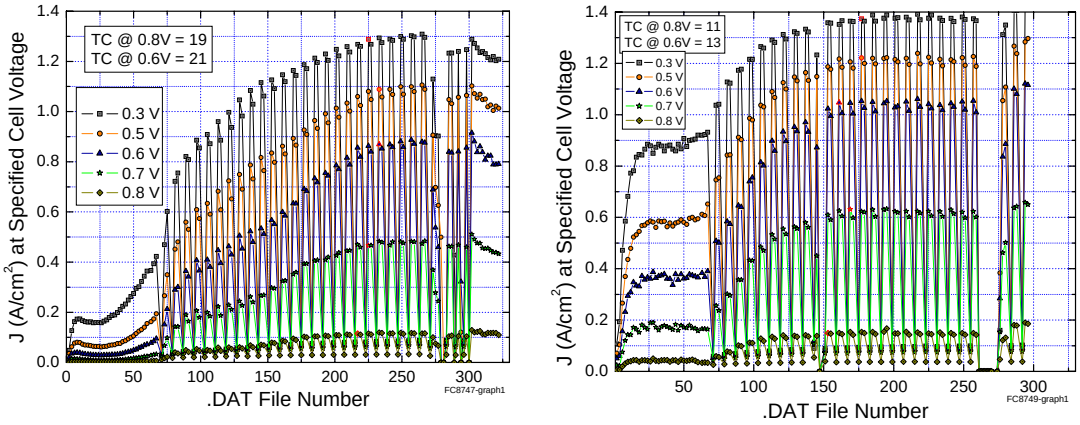

Fig. 2. Effect of cleaning the membrane on the time for break-in conditioning of the MEA: cleaned membrane (right), and non-cleaned membrane (left).

Fig. 3 below shows an example of the standard potentiodynamic polarization curve (PDS) at ambient pressure from two CCMs containing the identical NSTF pure Pt catalysts on the anode and cathodes (0.15 mg-Pt/cm^2), same GDLs, but membrane made with the 3M ionomer (EW ~ 1000) versus Nafion 112, both of which were precleaned. This plot is used here to just exempify that that better performance was obtained with the 3M ionomer based membranes, since certainly many processing factors could also cause such differences as well.

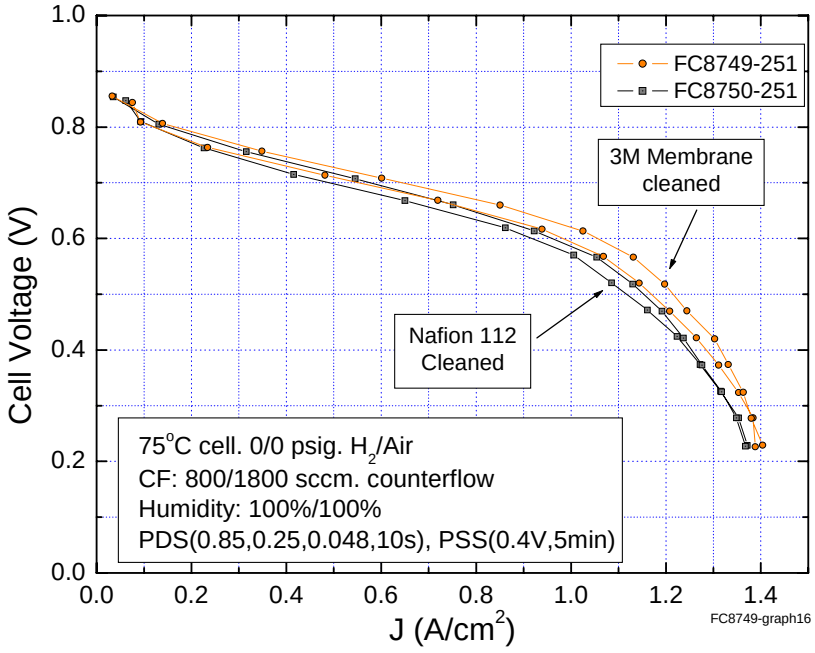

Fig. 3 Comparison of ambient pressure polarization curves from MEAs containing identical NSTF catalysts and GDL, but different PFSA membranes made with the 3M ionomer and commerically obtained Nafion 112.

2.3.1.2 Evaluation of membrane additives and equivalent weights

In section 2.2 of this report, the development of an advanced 3M membrane is discussed. A specific and important advance was the improvement of its durability under load cycling tests by an order of magnitude and commensurate reduction in fluoride ion release levels, through the use of additives to the ionomer. Often these additives are effectively cations that can function to reduce the conductivity of the membrane if added at too high a concentration. They might also impact the catalyst activity directly if they adsorb on the Pt surface. This also has implications in that once the membrane is made with the additives, acid washing to remove other impurities is not possible as it would likely remove the additive materials as well. Although acid washing is not desireable from a process and scale-up perspective, for the purposes of laboratory development and understanding of how the catalyst integrates with it, cleaning the membrane is useful in order to get membrane properties that are reasonably close to the intended pure membrane response and also more standardized from membrane lot to lot.

At the time this membrane down-select work with the NSTF catalyst was completed, the primary 3M ionomer equivalent weight being utilized for the NSTF CCM development was 1000EW. Work with the nominal 800EW was just starting then, so at the time the work with the additives was being done, the best results were obtained with the higher EW 3M membrane. Later, the full advantage of the 800EW in a neat form using different process methods was realized, but without the use of additives.

Table I. Compilation of membranes and catalyst combinations used to investigate impact of additives to the ionomer on performance.

Test Cell ID	A/C Catalyst	A/C Loading	3M PEM EW	Additive	PEM Lot ID	Post treatment
8860	Pt/Pt	.15/.15	1000	0%Mn	A	Case Cleaned
8861	Pt/Pt	.15/.15	1000	2% Mn	A	
8943	Pt/Pt	.15/.15	1000	2% Mn	A	
8946	Pt/PtNiFe	.15/.1	1000	3% Mn	A	
8752	Pt/PtNiFe	.15/.1	1000	0%Mn	A	Case Cleaned
9162	Pt/PtNiFe	.15/.1	1000	3% Mn	B	
9455	Pt/PtNiMn	.15/.1	1000	?%Mn	C	
9461	Pt/Pt	.15/.15	1000	~ 2%Mn	C	
8747	Pt/Pt	.15/.15	1000	0%Mn	D	Not Cleaned
8749	Pt/Pt	.15/.15	1000	0%Mn	D	Case Cleaned
8751	Pt/Pt	.15/.15	1000	0%Mn		Not Cleaned
8860	Pt/Pt	.15/.15	1000	0%Mn		Case Cleaned
9880	Pt/Pt	.15/.15	1000	0.3% Mn	E	
9881	Pt/Pt	.15/.15	1000	1.0% Mn	F	
9935	Pt/Pt	.15/.15	1000	1.0% Mn	F	
9936	Pt/PtCoMn	.15/0.1	1000	1.0% Mn	F	
10038	Pt/PtCoMn	.15/0.1	1000	0.3% Mn	E	
9785	Pt/Pt	.15/.15	800	0%Mn	G	Case Cleaned
9851	Pt/Pt	.15/.15	800	0.3% Mn	H	
9912	Pt/Pt	.15/.15	800	1.0% Mn		

The primary point of these investigations was to assess the impact of the additives on the MEA performance, rather than durability, as that would come later if a suitable combination

were found. Table I summarizes the MEA membrane and NSTF catalyst combinations used to screen for the impact of $MnNO_3$ additives on the fuel cell performance. The %Mn is the molar ratio to the number of sulfonate groups in the ionomer, Mn^{o} / SO_3^{-1}.

The MEAs in Table I were generally tested for the impact of start-up, e.g. the number of thermal cycles required to reach full performance, the ambient air PDS performance, catalyst surface area, GDS polarization curve performance at 7.5, 15, 23 and 30 psig H_2/air pressures, and for a few of them, the fluoride ion release rates at 0.4 V and 90°C (see section 2.1.5.2 for a discussion of the selection of these conditions). We summarize below the most relevant performance comparisons for the various MEA's in Table I.

Fig. 4 shows the ambient pressure PDS curves at two levels of humidification, for FCs 9912, 9935 and 9936, comparing the 1000EW and 800EW with 1%Mn levels, and also the impact of 0.10 mg-Pt/cm^2 in PtCoMn on the cathode versus 0.15 mg-Pt/cm^2 pure Pt. Considering the saturated conditions first, left panel, the PtCoMn ternary (9936) shows slightly better performance in the kinetic and mid-range than the pure Pt, consistent with the higher specific activity discussed at length in section 2.1.3.2 of this report. Both the 1000EW examples are signficantly better than the 800EW MEA performance. This was unexected at the time and latter believed to be due to deficiencies with these early 800EW lots, as ultimately the 800EW ionomer was the down-selected membrane. Fig. 6 addresses this issue further

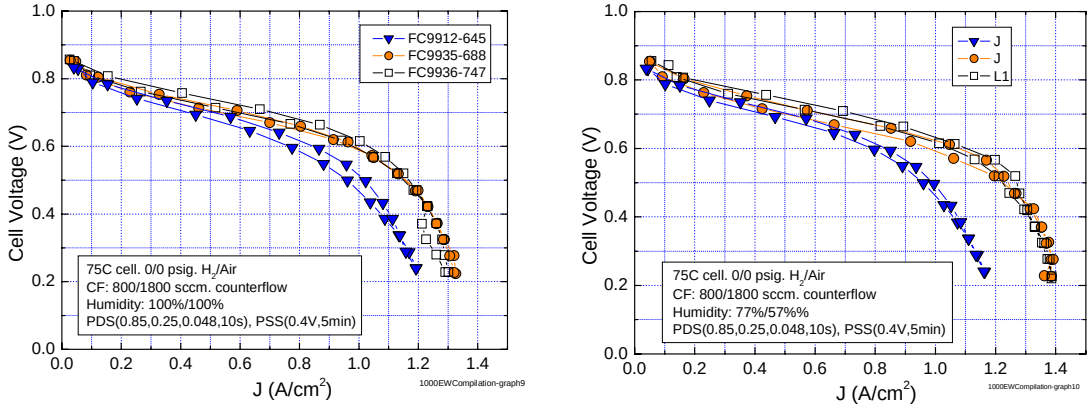

Fig. 4. Comparison of the ambient pressure H_2/air polarization curves for FCs 9912, 9935 and 9936 identified in Table I at two levels of humidification: left panel – 100%/100% %RH; right panel – 77%/57% anode/cathode %RH.

Under the drier conditions, (right panel in Fig. 4) the 1000EW samples are little affected, but slightly improved if anything in all regions of the polarization curve compared to the saturated conditions. The 800 EW case is slightly worse by about the same small amount. The behavior of the 800EW sample is indicative that in reality it did not have an equivalent weight lower than the 1000EW samples, as though it was poisoned by cations or some other contaminants. The measured H-pump values however were all very similar among the three, viz. 0.076, 0.075 and 0.078 ohm-cm^2 for FC9936, 9936 and 9912 respectively.

Fig. 5 (left panel) compares the PDS polarization curves for just the 1000EW membrane samples, FCs 8751, 9880, 9935 and 9936 in Table I at varying %Mn levels, and at saturated inlet humidification levels. For FC8751, the control with 0%Mn, the membrane was not precleaned in order to compare it better with the additive containing samples. It is clear that

all the pure Pt based cathodes have indistinguishable performance, suggesting in this membrane at these conditions, the 0%, 0.3% and 1% Mn levels are not adversely affecting membrane conductivity. The PtCoMn cathode kinetics are still substantially better.

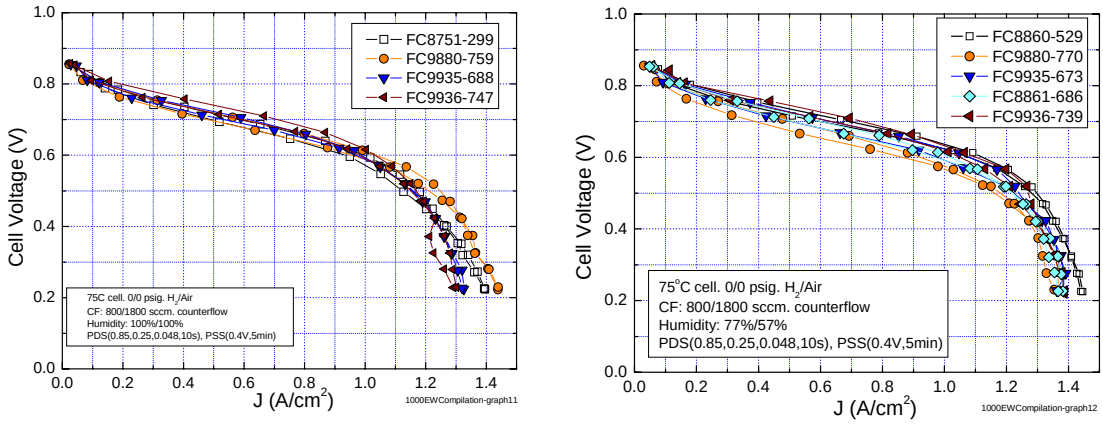

Fig. 5. Comparison of the ambient pressure H_2/air polarization curves for: (left panel) FCs 8751, 9880, 9935 and 9936 identified in Table I at saturated inlet humidification; (right panel) FCs 8860, 9880, 9935, 9936 and 8861 at 77%/57% anode/cathode %RH inlets

Under drier inlet conditions, (right panel in Fig. 5) the performances are again little changed, except for the 0.3% Mn sample which may be affected by some other factor. Added in the right panel is FC8861, with 2%Mn, and again the performance is not substantially different from the 1%Mn case. In this graph, the pre-cleaned membrane control sample, FC8860, was substituted for the FC 8751 shown at saturated conditions. FC8860's performance is higher than the Mn-PEM samples, but still not as high as that from the PtCoMn cathode sample with the 1%Mn in it.

Returning to the comparison of the 800 and 1000EW samples, and the question of some other type of impurity in the 800EW membrane, Fig. 6 compares the ambient pressure PDS performance from the 1000 and 800EW samples FC 8860 and 9785, for which the membranes were precleaned by acid washing, with no additive. Acid washing the 800EW membrane was not adequate to recover the expected performance. The reason for the two different %RH conditions, is that the 800EW membrane required saturated inlet conditions for its best performance, whereas the 1000EW's performance was slightly better at drier conditions, as noted above. The H-pump impedance for FC9785 was 0.071 ohm-cm^2 versus 0.082 ohm-cm^2 for FC8860, so impedance was not the issue. The measured electrochemical surface areas were 12.5 cm^2/cm^2 for FC8860 but only 8.9 cm^2/cm^2 for FC9785, a 25% reduction. In Fig. 6, the kinetic region is depressed at least 20 mV for the 800EW sample relative to the 1000EW sample, which would be equivalent to a loss of about half the available surface area assuming 70mV/decade Tafel slope. This might suggest that the specific activity of the catalyst surface area remaining is also reduced. The mass transport region is clearly affected by whatever the additional impurities may be.

These results above were encouraging that with %Mn additive levels as high as 1 to 2%, the performances with the NSTF electrodes, and the PtCoMn ternary in particular, were not significantly adversely affected. This suggested that if additional additives were needed for gaining further membrane lifetime, that it could be implemented. In section 2.1.5.2 of this report it is shown in some detail that the NSTF Mn containing ternaries possess excellent, extremely low fluoride ion release rates with neat or acid-washed membranes. However,

because there could still be unforseen effects due to interaction of the additives with the low surface area NSTF catalysts, and there were more issues to be understood with respect to the membrane processing and catalyst/membrane integration, further work with the additives was discontinued in the membrane down-selection process. Since there were good reasons to expect that the 800EW membrane should provide not only better conductivities than the 1000EW, but improved water management, efforts were spent instead on optimizing the CCM's using the NSTF PtCoMn ternary with new lots of membranes made from new lots of the 3M 800EW ionomer. As work proceeded, improved performances, under all conditions, were realized with the 800EW membranes, exceeding those obtained with the 1000EW membranes, and development of the CCMs transitioned completely to testing with the new 800EW membranes. As shown in section 4.1, the roll-good fabricated CCM's using the downselected 800EW membrane roll-good materials and

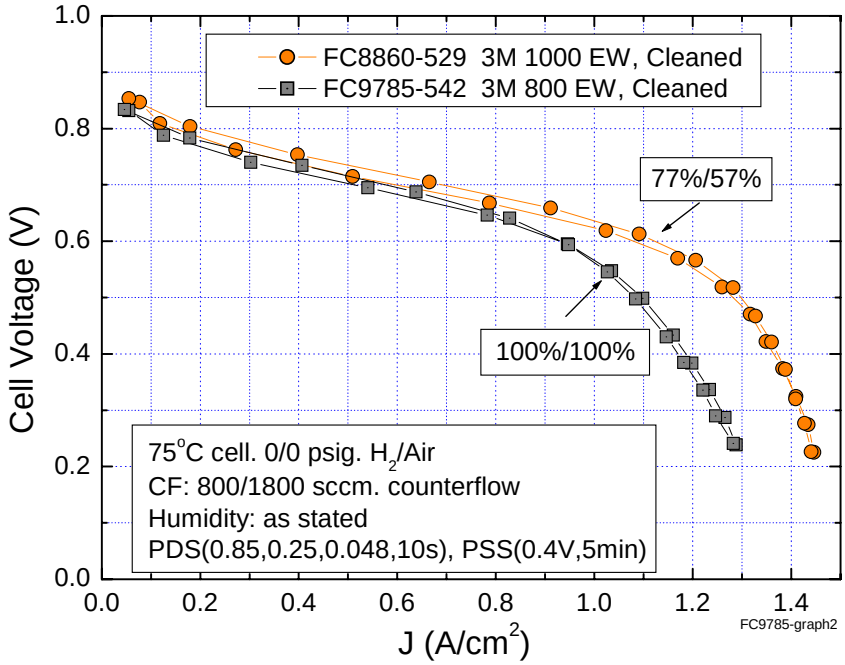

the PtCoMn NSTF electrodes gave the best performances to date.

Fig. 6. Comparison of the 800 and 1000EW membranes made into MEAs after pre-cleaning by acid washing.

2.3.1.3 Membrane processing effects and final down-selected membrane

As indicated above, work continued to understand how to better process the 800EW membrane. Alongside the performance issue, the effect of the contaminated membranes was also revealed in the time required for the initial break-in conditioning of an MEA. The metric for this was the number of thermal cycles required to reach peak performance. It appeared many of the same factors were involved in both reducing the peak performance and the difficulty to reach that performance. In section 2.1.5.4 of this report we discuss the importance of the cathode catalyst surface area in reducing the time for break-in conditioning of an MEA, presumably because of its impact on oxidizing residual organic impurities in the membrane that poisoned the catalyst. To a lesser degree, there were also important membrane factors that affected both peak performance and break-in times,

starting with the state of the 3M ionomer as it was received for membrane processing, through a number of post-membrane fabrication treatments. Many of these were explored in some depth and found to be effective. Perhaps the most signficant was the solvent used to cast the membrane, followed by how the membrane was then dried, annealing conditions, the conditions for laminating the NSTF catalysts to the membrane surface, and finally the actual start-up test protocols.

Many of these process improvements are proprietary. The net result of implementing them was that the performances improved with the 800EW membranes to the point that they exceeded those with the 1000EW membranes, it was no longer necessary to pre-clean the membranes to obtain peak performances, roll-good processing the CCMs gave better performances than the hand-made laboratory CCMs, and the full kinetic performances were achieved immediately without the need for more than one thermal cycle. The remaining issue was that to achieve the full performance at high current densities, fairly extensive thermal cycling was still required to improve the mass transport region of the polarization curves, which diagnostics still indicated were due in some way to residual impurities that had to be washed out before full performance was achieved.

In conclusion, the final down-selected membrane for the scale-up and stack testing discussed in section 4.0, was the nominal 3M 800EW membrane, used without additives, and processed with many of the advantages referred to in preceeding paragraphs.

2.3.2 GDL screening and down-selection

2.3.2.1 Introduction

One of the subtasks within Task 3 was down-selection of a gas diffusion layer (GDL) for use with the CCMs in the 5kW stack testing, as discussed in section 4.2 of this report.

Thirteen experimental GDLs comprising two experimental series were evaluated in 50cm^2 single cells under a range of test conditions. One series evaluated the impact of different GDL backing hydrophobization agents and the level of said agent, all using the same carbon backing layer and same microporous layer (MPL). A second series evaluated a range of GDLs with different backings, MPLs, and backing hydrophobization treatments.

The metrics used for GDL evaluation included cathode stoichiometry sensitivity, polarization curve performance at different pressures under hot-and-dry operating conditions, temperature sensitivity, and high temperature humidification sensitivity.

The performance of the experimental GDLs was rated against a baseline GDL, which was previously down-selected and used in the 1kW 3M NSTF stacks under 3M/DOE Cooperative Agreement DE-FC02-99EE50582. This baseline GDL, based on a woven carbon cloth, demonstrated excellent performance under a range of test conditions, but one issue was its relatively low in-plane flexural stiffness and resultant potential for tenting into the reactant flow channel. The basic guidelines for GDL down-selection were performance comparable or better than the baseline GDL with higher flexural stiffness to reduce potential tenting into the flow channel.

2.3.2.2 Experimental

2.3.2.2.1 Sample Description

3M 1000 equivalent weight (EW) membranes were pretreated to remove organic and cationic contaminants. The PEMs were first boiled in DI water, heated in 70ºC 3% H_2O_2, boiled a second time in DI water, heated in 70ºC 1M HNO_3, rinsed with DI until the rinse water was neutral, boiled in DI a third time, and then dried for at least 24 hours between clean TexWipe cloths in a 30ºC oven.

NSTF PtCoMn ternary catalyst, containing 0.15mg/cm^2 Pt, was prepared as a roll-good on continuous vacuum deposition equipment, as described in section 4.1 of this report.

Catalyst coated membranes (CCMs) were then prepared. 50cm^2 catalyst substrates of the same catalyst type were cut from the uniform roll-good catalyst prepared above. The substrates were placed on either side of the PEM and passed through a heated, pressurized laminator, after which the substrates were removed.

50cm^2 gas diffusion layers (GDLs) were cut from laboratory-prepared sheet goods. The same GDL was used on both anode and cathode electrodes. CCMs, GDLs, and gaskets were assembled into a typical 50cm^2 quad serpentine test cell obtained from Fuel Cell Technologies. Further information on general testing is found in section 2.1.3.

Table II lists the GDL samples evaluated in this study. All variables other than the GDL were nominally fixed. The GDL variables include 6 types of backing, backing hydrophobization level and type, and 3 types of microporous layer. Due to the large number of samples, the data reported in the Results section are divided into two sets, one based on GDL backing type "A", and the other encompassing the remainder of the samples.

Table II. GDL samples evaluated for down-selection for stack testing.

Cell ID	Backing Type	Backing Hydrophobization Level, Type	MPL Type	Final GDL Thickness (mils)	Graph Set
FC10130 (Baseline)	C	1% B	B	12.6	1,2
FC10093	A	5% A	A	8.4	1
FC10096	A	3% A	A	5.5	1
FC10110	A	1% A	A	7.7	1
FC10099	A	7% A	A	7.9	1
FC10116	A	1% A	A	5.5	1
FC10174	A	1% A	A	6	1
FC10168	A	0.25% A	A	6.7	1
FC10197	D	Vendor	Vendor	10.5	2
FC10207	B	10% B (Vendor)	A	6.9	2
FC10264	B	10% B (Vendor)	D	6.6	2
FC10281	E	10% B (Vendor)	D	9.4	2
FC10376	F	5% A	A	9.5	2
FC10423	B	10% B (Vendor)	D	8.8	2

Sample FC10130 was the baseline sample for the test. This sample was comprised of a carbon cloth based GDL, and was the GDL used for the 1kW stack used in the previous 3M/DOE contract identified above. The results from this sample are shown in both graph sets of each figure below for comparison purposes.

Samples FC10093, FC10096, FC10110, FC10099, FC10116, FC10174, and FC10168 all comprised the same backing and MPL type. The primary variable for these samples was the level of hydrophobization. 3M applied the backing hydrophobization and MPL to these samples. The results from these samples are reported in graph set 1 of each figure.

Sample FC10197 was a purchased, fully finished GDL. The details of backing hydrophobization and MPL were not available.

Samples FC10207, FC10264, and FC10423 were comprised of a purchased non-woven hydrophobized backing, to which 3M applied a MPL. The MPL type varied among these samples.

Sample FC10281 was comprised of a purchased non-woven hydrophobized backing, to which 3M applied a MPL.

Sample FC10376 was comprised of a purchased non-woven backing, which 3M hydrophobized and then applied a MPL.

2.3.2.2.2 Test Plan

Table III provides an overview of the testing.

Table III. GDL down-select test plan.

Test	Test Description
1	Initial Conditioning
2	Cathode Stoich Sensitivity
3	Galvanodynamic (GDS) Performance at 50kPag with Fixed Stoichiometry
4	Galvanodynamic (GDS) Performance at 100kPag with Fixed Stoichiometry
5	Galvanodynamic (GDS) Performance at 150kPag with Fixed Stoichiometry
6	Temperature Sensitivity
7	Humidity Sensitivity

The MEAs were initially conditioned using a process we refer to as “thermal cycling”. The thermal cycling process consists of two sub-processes, “operational” and “cooldown”. In the “operational” sub-process, cells were operated for a period of 40 minutes at 75ºC cell temperature, ambient reactant pressure, 800/1800SCCM H_2/Air, and 70ºC anode and cathode dewpoints. Every 5 minutes, the cells were scanned between 0.85V and 0.25V with 0.05V, 10 second steps; between scans, cells were held at 0.40V. For the “cooldown” sub-process, gas flows were halted, the load was disconnected, and the cells were cooled to room temperature over a 45 minute time period. During this time, DI water was fed into the anode and cathode flow fields using the HPLC pumps, at flow rates of 0.26 and 0.40mL/min, respectively. The thermal cycling “operational” and “cooldown” processes were repeated until stable performance was achieved, typically within 40-60 hours.

Under Test 2, the cell’s cathode stoichiometry sensitivity was measured. Here, the cells were held at 90ºC cell temperature, 100kPag anode and cathode reactant inlet pressures, with an anode stoichiometry of 2.0. For each cathode stoichiometry (2.5, 2.25, 2.0, 1.9, 1.8, 1.7, 1.6, 1.5), the cell was first held at 0.4A/cm^2 for two hours to allow the cell to stabilize, and then the cell was held at 0.8A/cm^2 for 15 minutes. As the cathode stoichiometry decreased, the anode and cathode dewpoints were decreased from 83ºC to 76ºC; these adjustments were made to keep the calculated cell outlet at 110% RH. During the holds, AC impedance spectra were measured on the cells, between 10kHz and 1kHz with 15 logrithmically spaced steps. The high frequency resistance (HFR) was estimated by fitting the spectra to a Randle’s cell model. The cell voltage and HFR from the final 5 minutes of the 15 minute 0.8A/cm^2 hold were averaged and these averaged values were reported.

Under Tests 3-5, polarization curves were measured at 50, 100, and 150kPag anode and cathode reactant pressures. For each pressure, the cell was held at 90ºC, with reactant stoichiometries of 2.0 on anode and cathode, and the reactant dewpoints were adjusted to attain a calculated outlet %RH of approximately 110%. For each pressure, the cell was held at 0.4A/cm^2 for two hours to stabilize the cell, and then two galvanodynamic polarization curves were taken. The polarization curve current density started at 0.1A/cm^2, and was stepwise increased until the cell voltage reached 0.4V, at which time the scan direction automatically reversed and the current was stepwise returned to 0.1A/cm^2. The dwell time and step size of the polarization curves was 30

seconds and 0.05A/cm^2, respectively. HFR was determined as in Test 2. The current density, cell voltage, and HFR from the second polarization curves were reported. In addition, the current density at 0.45V and 0.75V and the HFR at 0.2A/cm^2 were reported.

Under Test 6, the cell's performance under cool and wet conditions was evaluated with cell temperatures of 30, 40, 50, and 60ºC and fully saturated gases. For each cell temperature, the cell was operated with fixed reactant flows of 800/1800SCCM H_2/Air and fixed humidification of 100/100% RH for the anode and cathode. Under each condition set, two polarization curves were taken. The polarization curve current density started at 0.02A/cm^2, and was stepwise increased logrithmically until the cell voltage reached 0.4V, at which time the scan direction automatically reversed and the current was stepwise returned to 0.1A/cm^2. The dwell time and step size of the polarization curves was 30 seconds and 15steps/decade of current density, respectively. The current density at 0.50 V from the second polarization curve was reported.

Under Test 7, the cell's humidification sensitivity was evaluated. In this test, the cell was held at fixed cell temperature of 90ºC, 100kPag reactant pressures, 2/2 reactant stoichiometry, and a current density of 0.4A/cm^2. The anode and cathode dewpoints were stepwise decreased from 90ºC to 46ºC, with the cell held at each humidification level for 2 hours. The humidity steps were determined to correspond to calculated cell outlet %RH of 165, 110, 100, 90, 80, 70, 60, and 50% RH. HFR was determined as in Test 2. The cell voltage and HFR from the final 5 minutes of the 120 minute 0.4A/cm^2 hold were averaged and these averaged values were reported. Note that not all cells were evaluated under Test 7.

2.3.2.2 Results

2.3.2.2.1 Test 2 – Cathode Stoich Sensitivity

In this test, cells were operated with variable cathode stoichiometry with the cell held at 90ºC, subsaturated humidification, 100kPag constant reactant pressure, and fixed current density of 0.8A/cm^2. Figs. 7 and 8 show the voltage and HFR response of the cells as a function of cathode stoichiometry. Tables IV and V report the numeric results of this test for graph sets 1 and 2 in these figures.

In graph set 1, sample FC10116 yielded performance in excess of the baseline, and samples FC10110 and FC10168 were just slightly lower. These samples contained the lowest levels of backing hydrophobization. It was observed that in general, as the backing hydrophobization level increased, the performance decreased and the impedance increased. For graph set 2, all samples performed comparably or better than the baseline, and all samples but FC10376 had impedance lower than the baseline. Note that the sample with the lowest impedance value of the 2nd set, FC10281, also had the lowest measured performance, so other unknown factors influenced the performance.

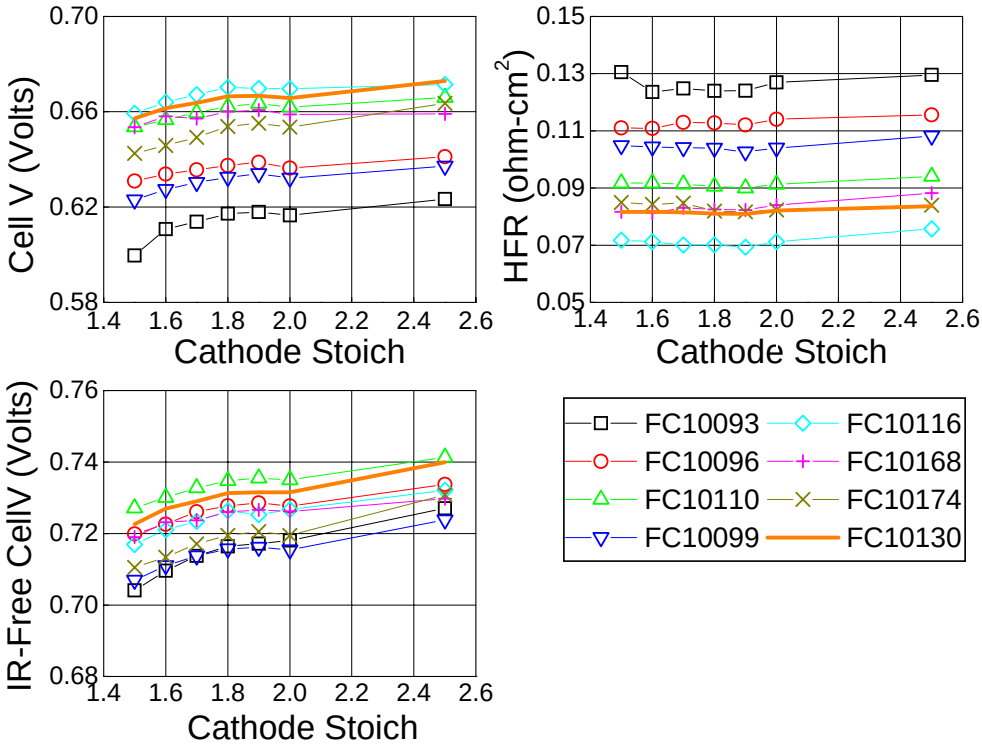

Fig. 7. Test 2, 1st graph set. Cell voltage, HFR, and IR-Free cell voltage versus cathode stoichiometry.

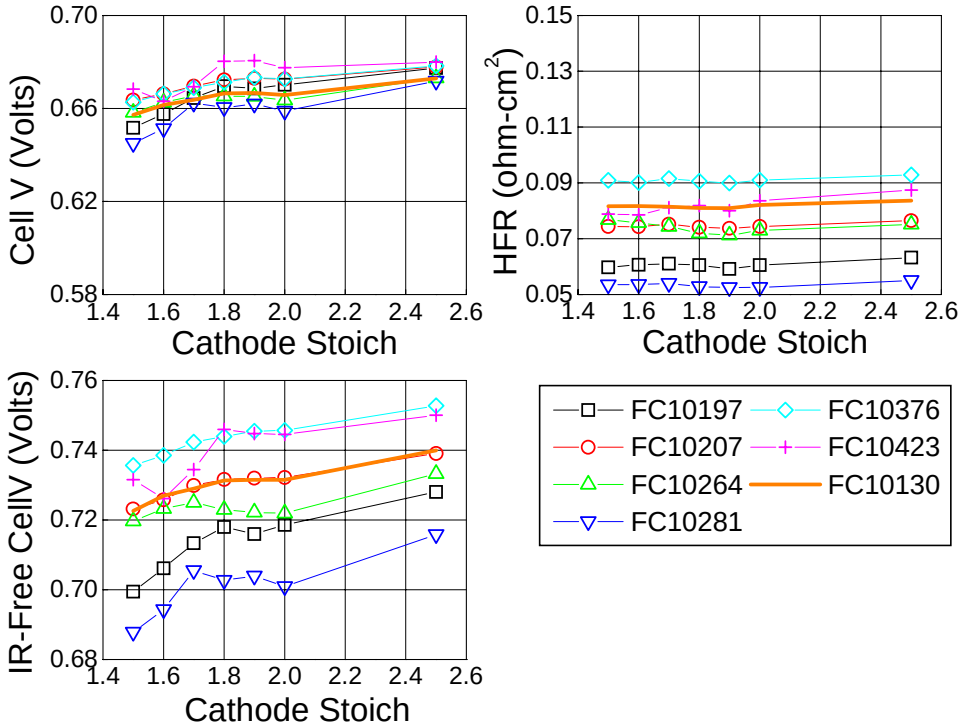

Fig. 8. Test 2, 2nd graph set. Cell voltage, HFR, and IR-Free cell voltage versus cathode stoichiometry.

Table IV Test 2, Set 1 measured cell voltage and HFR v. cathode stoichiometry at 0.80A/cm^2. Cell voltage reported in volts, HFR in ohm-cm^2.

	FC10130	FC10093	FC10096	FC10110	FC10099	FC10116	FC10168	FC10174
V, 2.5	0.673	0.623	0.641	0.666	0.637	0.671	0.664	0.659
V, 2.0	0.666	0.617	0.636	0.662	0.632	0.670	0.654	0.659
V, 1.9	0.667	0.618	0.639	0.663	0.634	0.670	0.655	0.661
V, 1.8	0.666	0.617	0.637	0.662	0.632	0.670	0.654	0.660
V, 1.7	0.664	0.614	0.636	0.660	0.630	0.667	0.649	0.657
V, 1.6	0.662	0.611	0.634	0.657	0.627	0.664	0.646	0.658
V, 1.5	0.657	0.600	0.631	0.654	0.623	0.659	0.643	0.654
HFR, 2.5	0.088	0.13	0.12	0.11	0.094	0.076	0.063	0.084
HFR, 2.0	0.084	0.13	0.11	0.10	0.091	0.071	0.060	0.082
HFR, 1.9	0.082	0.12	0.11	0.10	0.090	0.069	0.059	0.081
HFR, 1.8	0.082	0.12	0.11	0.10	0.091	0.070	0.061	0.081
HFR, 1.7	0.083	0.13	0.11	0.10	0.091	0.070	0.061	0.082
HFR, 1.6	0.081	0.12	0.11	0.10	0.092	0.071	0.061	0.082
HFR, 1.5	0.082	0.13	0.11	0.11	0.092	0.072	0.060	0.082

Table V. Test 2, Set 2 measured cell voltage and HFR v. cathode stoichiometry. Cell voltage reported in volts, HFR in ohm-cm^2.

	FC10130	FC10197	FC10207	FC10264	FC10281	FC10376	FC10423
V, 2.5	0.673	0.677	0.678	0.673	0.672	0.678	0.680
V, 2.0	0.666	0.670	0.673	0.664	0.659	0.673	0.678
V, 1.9	0.667	0.669	0.673	0.665	0.662	0.673	0.681
V, 1.8	0.666	0.670	0.672	0.665	0.660	0.671	0.680
V, 1.7	0.664	0.664	0.670	0.665	0.662	0.669	0.669
V, 1.6	0.662	0.658	0.666	0.663	0.651	0.666	0.663
V, 1.5	0.657	0.652	0.664	0.658	0.645	0.663	0.668
HFR, 2.5	0.088	0.084	0.076	0.075	0.055	0.093	0.087
HFR, 2.0	0.084	0.082	0.074	0.073	0.053	0.091	0.084
HFR, 1.9	0.082	0.082	0.074	0.071	0.052	0.090	0.080
HFR, 1.8	0.082	0.082	0.074	0.072	0.053	0.091	0.082
HFR, 1.7	0.083	0.085	0.075	0.074	0.054	0.092	0.081
HFR, 1.6	0.081	0.084	0.074	0.076	0.054	0.090	0.079
HFR, 1.5	0.082	0.085	0.074	0.077	0.053	0.091	0.079

2.3.2.2.2 Test 3 – Galvanodynamic Peformance at 50kPag.

In this test, polarization curves were taken with the cell at 90ºC, subsaturated humidification, and constant stoichiometry with fixed reactant pressure of 50kPag (inlet). Fig. 9 shows the resultant polarization curves and HFR. Tables VI and VII report the numeric results for graph sets 1 and 2 for Tests 3-5.

For graph set 1, samples FC10116, FC10110, and FC10168 yielded performance similar or slightly lower than the baseline. The three samples with the lowest performance in set 1 had the highest impedance. For graph set 2, all samples yielded similar kinetic performance, but FC10281, FC10197, and FC10423 had lower limiting currents. All samples in set 2 had similar or lower HFR than the baseline.

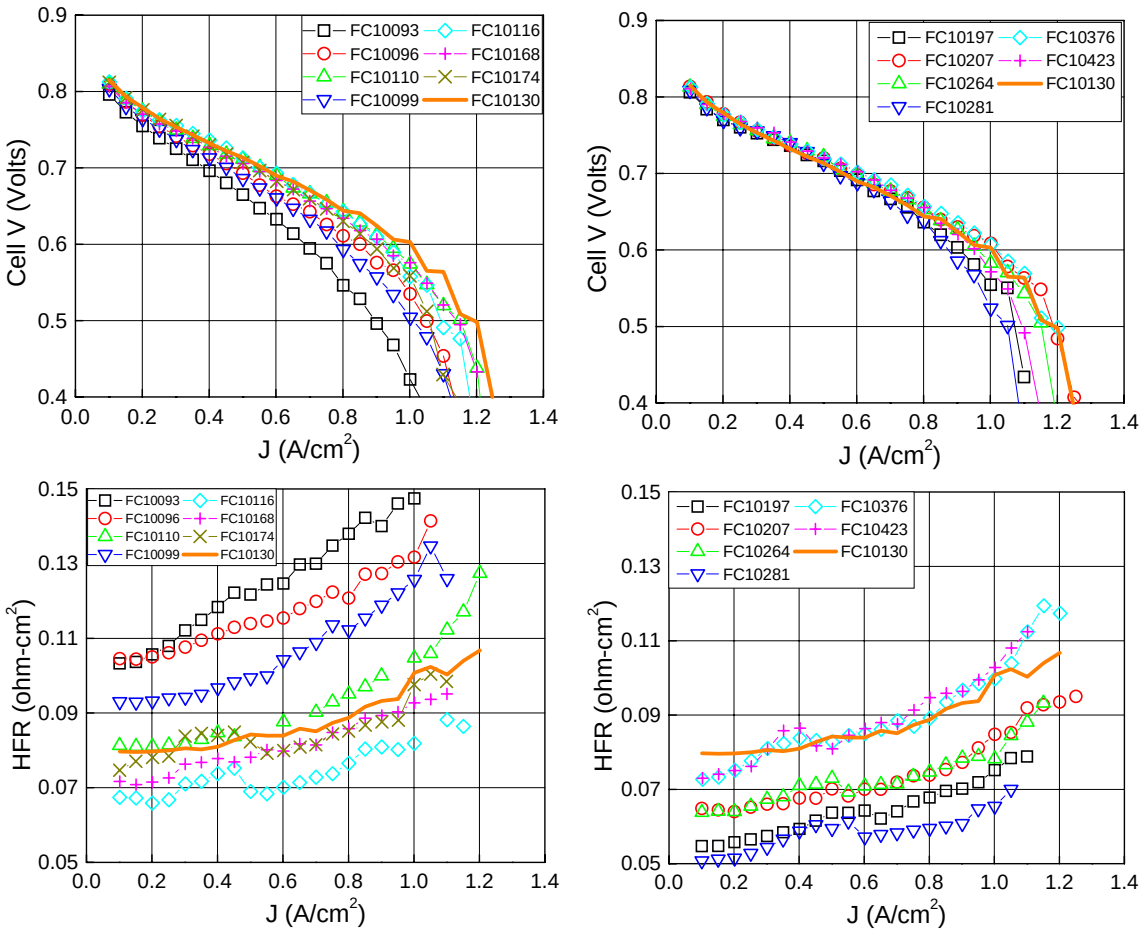

Fig. 9. Test 3, 50kPag galvanodynamic polarization performance. Left column: Set 1. Right column: Set 2. Top row: Cell voltage response v. current density. Bottom row: HFR response v. current density.

2.3.2.2.3 Test 4 – Galvanodynamic Performance at 100kPag.

In this test, polarization curves were taken with the cell at 90ºC, subsaturated humidification, and constant stoich with fixed reactant pressure of 100kPag (inlet). Fig. 10 shows the resultant polarization curves and HFR. Tables VI and VII report the numeric results for graph sets 1 and 2 for Tests 3-5.

For graph set 1, sample FC10116 peformed similarly or better than the baseline. Samples FC10110 and FC10168 had kinetic performance similar to the baseline, but lower limiting currents. Samples FC10099, FC10096, and FC10093 had performance lower than the baseline for a majority of the polarization curve. As was the case in Test 3, the three samples with the lowest performance had the highest impedance values.

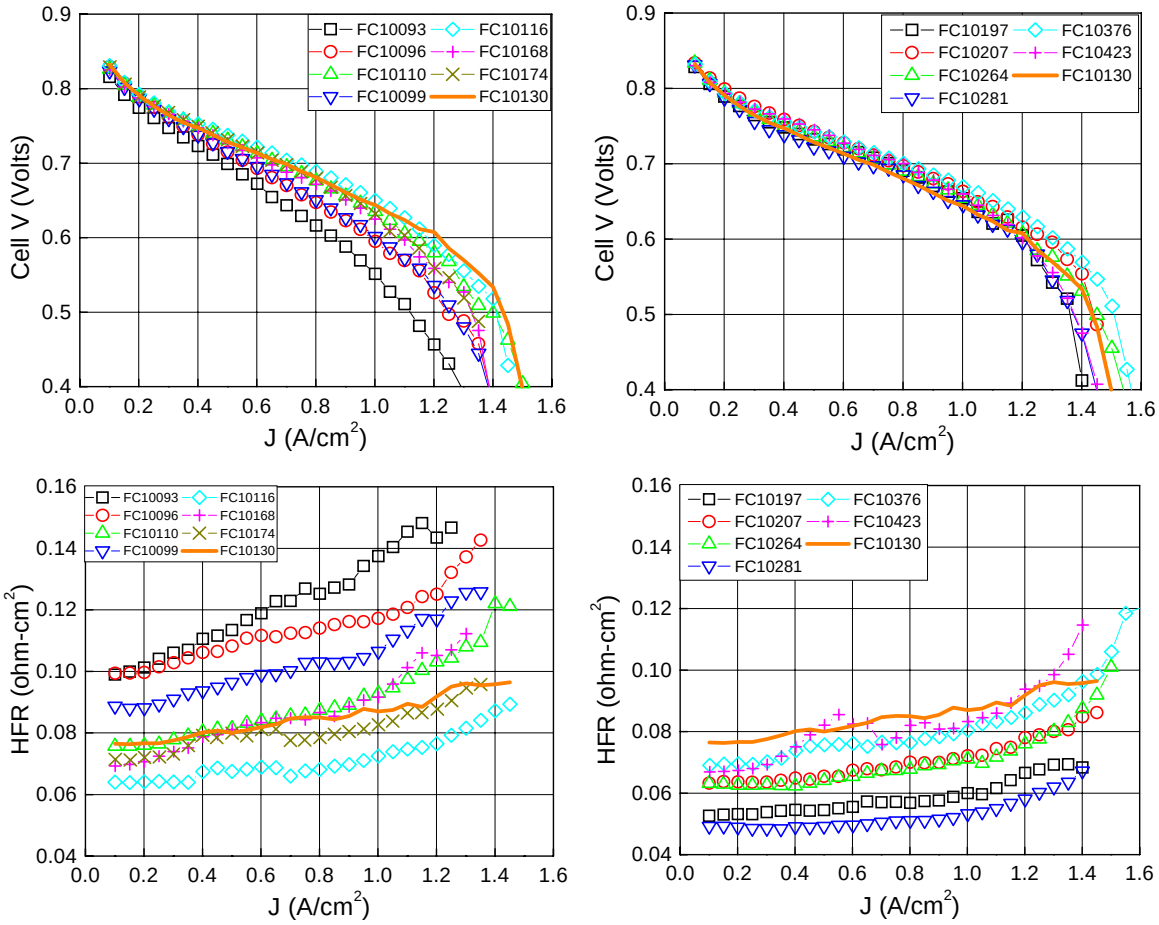

Fig. 10. Test 4, 100kPag galvanodynamic polarization performance. Left column: Set 1. Right column: Set 2. Top row: Cell voltage response v. current density. Bottom row: HFR response v. current density.

For graph set 2, most samples demonstrated kinetic performance which was similar or better than the baseline. Sample FC10376 had a slightly higher limiting current, FC10264 and FC10207 had similar limiting currents, and FC10197, FC10281, and FC10423 had slightly lower limiting currents. The impedance of most samples was better than the baseline; FC10423 had similar impedance as the baseline.

2.3.2.2.4 Test 5 – Galvanodynamic Performance at 150kPag.

In this test, polarization curves were taken with the cell at 90ºC, subsaturated humidification, and constant stoich with fixed reactant pressure of 150kPag (inlet). Fig. 11 shows the resultant polarization curves and HFR. Tables VI and VII report the numeric results for graph sets 1 and 2 for Tests 3-5.

For graph set 1, samples FC10110, FC10116, and FC10174 had similar kinetic performance as the baseline, and slightly lower limiting currents. Sample FC10168 had lower kinetic performance and slightly lower limiting currents than the baseline. Samples FC10093, FC10096, and FC10099 had markedly lower kinetics and limiting currents. Again, the three samples with the lowest performance had the highest impedance.

For graph set 2, most samples demonstrated kinetic performance which was similar or better than the baseline; only FC10281 had markedly lower kinetic performance. Sample FC10376 had the highest performance at currents just below the limiting current. Limiting currents for all samples in set 2 were similar to the baseline, and all samples in set 2 had impedances similar or lower than the baseline.

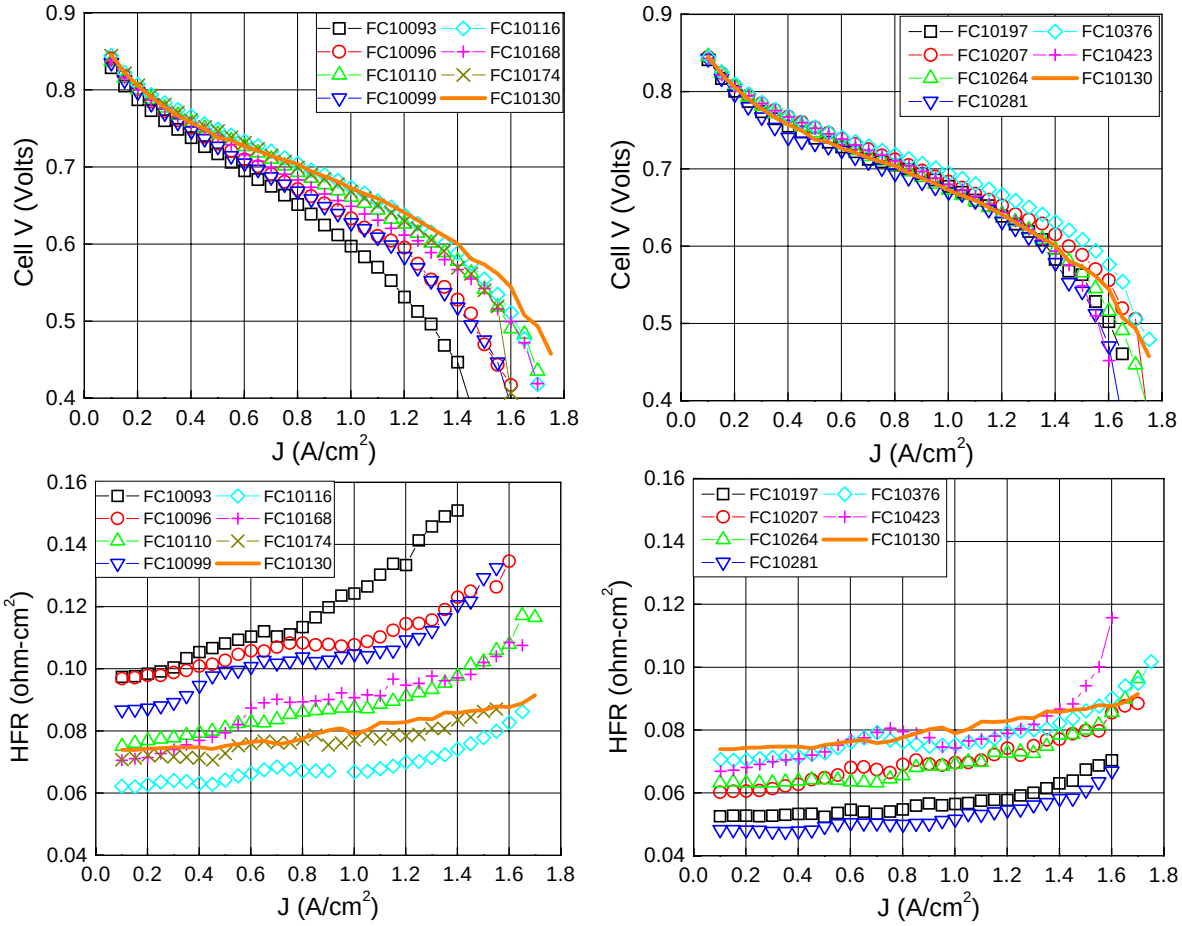

Fig. 11. Test 5, 150kPag galvanodynamic polarization performance. Left column: Set 1. Right column: Set 2. Top row: Cell voltage response v. current density. Bottom row: HFR response v. current density.

Table VI. Tests 3-5, Set 1. Measured current density at 0.75V and 0.45V, and measured HFR at 0.2A/cm^2. Current densities reported in A/cm^2, HFR in ohm-cm^2. Test 3: 50kPag. Test 4: 100kPag. Test 5: 150kPag.

FC#	10130	10093	10096	10110	10099	10116	10168	10174
Test 3 J @ 0.75V	0.32	0.22	0.27	0.30	0.25	0.33	0.32	0.29
Test 4 J @ 0.75V	0.38	0.29	0.35	0.39	0.35	0.42	0.40	0.39
Test 5 J @ 0.75V	0.45	0.35	0.4	0.45	0.39	0.49	0.47	0.44
Test 3 J @ 0.45V	1.23	0.97	1.12	1.19	1.08	1.15	1.10	1.20
Test 4 J @ 0.45V	1.48	1.21	1.36	1.45	1.34	1.43	1.40	1.38
Test 5 J @ 0.45V	1.75	1.39	1.54	1.68	1.55	1.68	1.58	1.66
Test 3 HFR @ 0.2A/cm^2	0.071	0.11	0.105	0.093	0.081	0.066	0.056	0.080
Test 4 HFR @ 0.2A/cm^2	0.070	0.10	0.10	0.088	0.076	0.064	0.053	0.077
Test 5 HFR @ 0.2A/cm^2	0.071	0.098	0.098	0.087	0.077	0.063	0.053	0.074

Table VII. Tests 3-5, Set 2. Measured current density at 0.75V and 0.45V, and measured HFR at 0.2A/cm^2. Current densities reported in A/cm^2, HFR in ohm-cm^2. Test 3: 50kPag. Test 4: 100kPag. Test 5: 150kPag.

FC #	10130	10197	10207	10264	10281	10376	10423
Test 3 J @ 0.75V	0.32	0.32	0.33	0.33	0.34	0.34	0.37
Test 4 J @ 0.75V	0.38	0.39	0.46	0.40	0.33	0.44	0.47
Test 5 J @ 0.75V	0.45	0.44	0.53	0.48	0.36	0.53	0.52
Test 3 J @ 0.45V	1.23	1.08	1.22	1.17	1.07	1.20	1.12
Test 4 J @ 0.45V	1.48	1.38	1.46	1.50	1.42	1.54	1.42
Test 5 J @ 0.45V	1.75	1.65	1.72	1.70	1.61	1.75	1.60
Test 3 HFR @ 0.2A/cm^2	0.071	0.078	0.064	0.064	0.051	0.075	0.075
Test 4 HFR @ 0.2A/cm^2	0.070	0.072	0.064	0.063	0.049	0.070	0.067
Test 5 HFR @ 0.2A/cm^2	0.071	0.072	0.061	0.063	0.048	0.070	0.068

2.3.2.2.5 Test 6 – Temperature Sensitivity.

In this test, polarization curves were taken with the cell at temperatures of 30 to 60ºC, with fixed relatively high constant reactant flows, fully saturated reactants, and ambient reactant pressure. The approximate limiting current (at 0.50V) is reported as a function of temperature. Fig. 12 shows the resultant current density versus cell temperature, and Tables VIII and IX show the resultant numerical data.

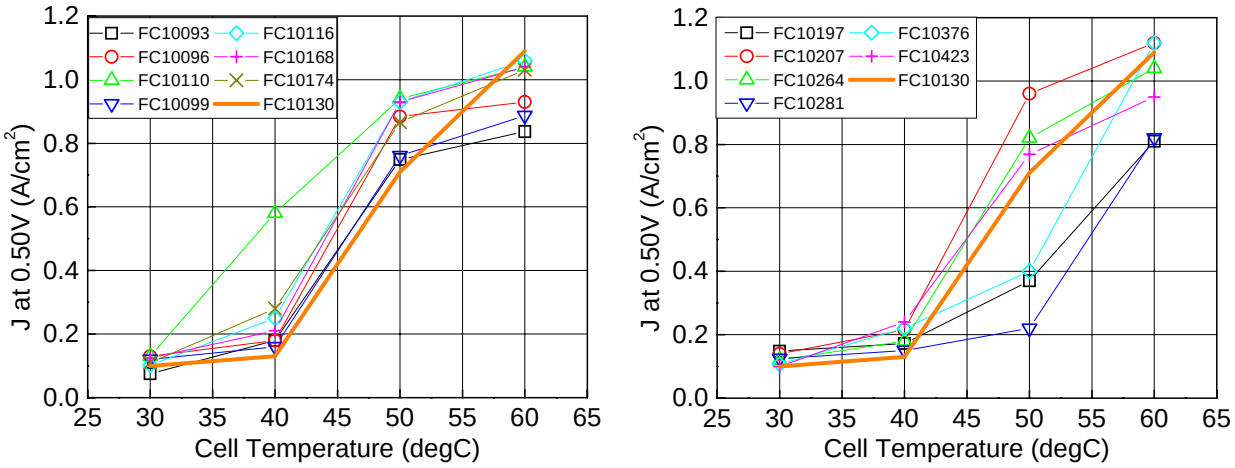

Fig. 12. Test 6, approximate limiting current v. cell temperature. Left: Set 1. Right: Set 2.

In Fig. 12 for graph set 1, all samples showed similar performance at 30ºC. At 40ºC, sample FC10110 performed markedly better and samples FC10174 and FC10116 performed moderately better than the baseline. At 50ºC, all samples but F10093 and FC10099 had performance markedly higher than the baseline. At 60ºC, the performance followed the order primarily observed for the higher temperature tests 3-5, with samples FC10093, FC10096, and FC10099 having markedly lower performance than the baseline. It is not known why FC10110 had markedly higher performance than the rest only at 40ºC

For graph set 2, all samples demonstrated performance similar to the baseline at 30ºC. At 40ºC, all samples performed similar to or slightly higher than the baseline. At 50ºC, samples FC10376, FC10197, and FC10281 underperformed considerably relative to the baseline, and FC10207, FC10264, and FC10423 outperformed the baseline; these outperforming samples all had electrode backing B. At 60 ºC, the performance generally followed the order observed for Tests 3-5.

2.3.2.2.6 Test 7 – Reactant Humidity Sensitivity.

In this test, the performance of the cell v. reactant humidity was measured, with the cell at 90ºC, 150kPag reactant pressures, and constant reactant stoichiometries of 2.0. Fig. 13 shows the resultant cell voltage and HFR v. humidification. Tables X and XI report the numeric results of this test for sets 1 and 2. Note that not all cells were evaluated under Test 7.

Table VIII. Test 6, Set 1. Measured current density at 0.80V and 0.50V v. cell temperature. Current densities reported in A/cm^2.

FC #	10130	10093	10096	10110	10099	10116	10168	10174
30°C J @ 0.80V	0.04	0.04	0.06	0.05	0.05	0.05	0.05	0.04
40°C J @ 0.80V	0.05	0.05	0.07	0.06	0.06	0.07	0.09	0.06
50°C J @ 0.80V	0.08	0.07	0.11	0.09	0.08	0.11	0.10	0.09
60°C J @ 0.80V	0.12	0.08	0.14	0.10	0.09	0.13	0.12	0.10
30°C J @ 0.50V	0.10	0.08	0.13	0.13	0.12	0.10	0.11	0.13
40°C J @ 0.50V	0.13	0.18	0.18	0.58	0.16	0.25	0.28	0.21
50°C J @ 0.50V	0.71	0.75	0.88	0.94	0.76	0.93	0.87	0.93
60°C J @ 0.50V	1.09	0.84	0.93	1.04	0.89	1.06	1.03	1.04

Table IX. Test 6, Set 1. Measured current density at 0.80V and 0.50V v. cell temperature. Current densities reported in A/cm^2.

FC #	10130	10197	10207	10264	10281	10376	10423
30°C J @ 0.80V	0.04	0.06	0.06	0.05	0.04	0.07	0.05
40°C J @ 0.80V	0.05	0.07	0.07	0.07	0.07	0.09	0.07
50°C J @ 0.80V	0.08	0.10	0.10	0.09	0.08	0.10	0.10
60°C J @ 0.80V	0.12	0.11	0.13	0.11	0.12	0.13	0.13
30°C J @ 0.50V	0.10	0.15	0.14	0.12	0.13	0.11	0.10
40°C J @ 0.50V	0.13	0.17	0.22	0.18	0.15	0.22	0.24
50°C J @ 0.50V	0.71	0.37	0.96	0.82	0.22	0.40	0.77
60°C J @ 0.50V	1.09	0.81	1.12	1.04	0.82	1.12	0.95

For graph set 1, all cells yielded relatively similar performance at the highest humidity level. At drier conditions, sample FC10116 outperformed the baseline, FC10099 underperformed, and the remainder of the cells performed similar to the baseline. FC10099 had markedly higher impedance than the other cells at drier conditions.

For graph set 2, all samples demonstrated performance similar to the baseline for outlet humidity greater than 60%. At 60% outlet RH, cells FC10197 and FC10423 had slightly higher performance than the baseline, and samples FC10376, FC10207, and FC10264

had lower performance. FC10376, the sample with the lowest performance at the driest condition, had the highest HFR at the driest condition.

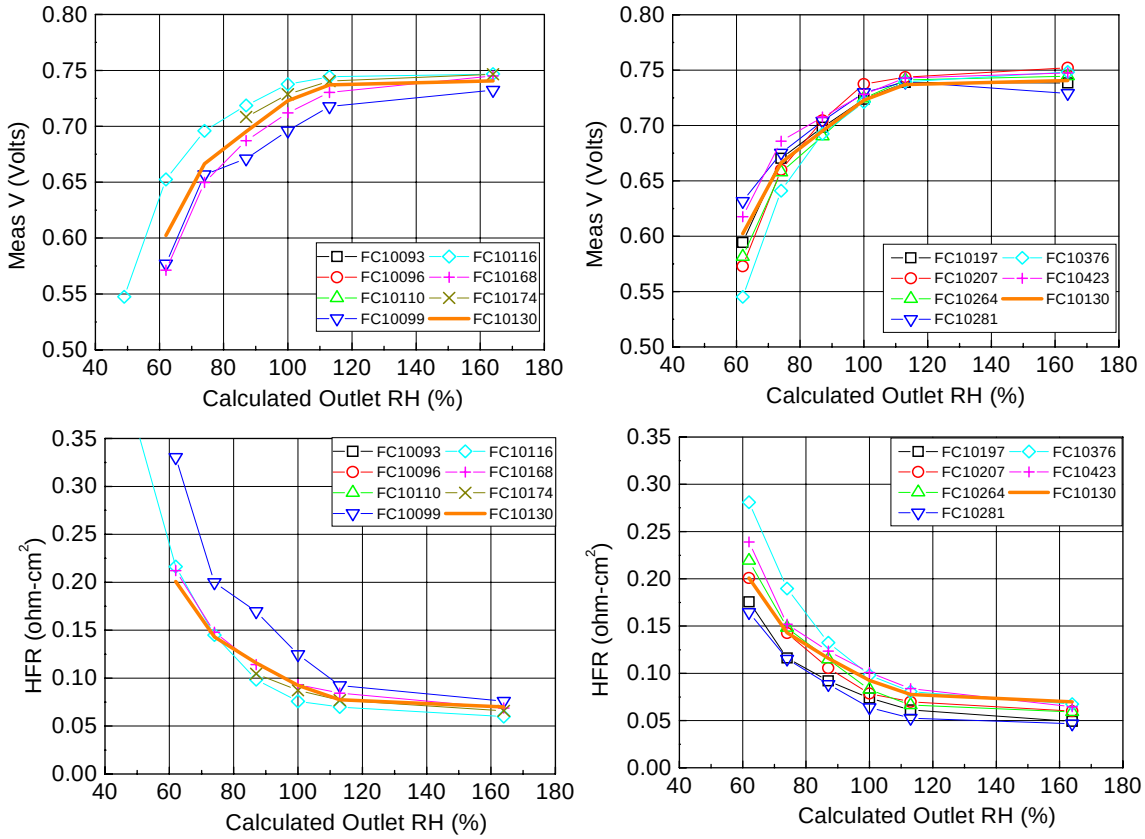

Fig. 13. Test 7, cell voltage and HFR v. humidification. Left column: Set 1. Right column: Set 2. Top row: Cell voltage response v. calculated outlet %RH. Bottom row: HFR response v. calculated outlet %RH.

Table X. Test 7, Set 1. Measured cell voltage and HFR at 0.40A/cm^2 v. inlet anode and cathode dewpoint. Cell voltage reported in volts, HFR in ohm-cm^2.

FC #	10130	10093	10096	10110	10099	10116	10168	10174
V, 90°C	0.741	Not run	Not run	Not run	0.732	0.747	0.746	0.745
V, 77°C	0.737	Not run	Not run	Not run	0.718	0.744	0.740	0.730
V, 73°C	0.723	Not run	Not run	Not run	0.696	0.738	0.729	0.712
V, 67°C	0.695	Not run	Not run	Not run	0.671	0.719	0.708	0.687
V, 61°C	0.667	Not run	Not run	Not run	0.657	0.696	NA	0.650
V, 52°C	0.602	Not run	Not run	Not run	0.577	0.652	NA	0.571
HFR, 90°C	0.070	Not run	Not run	Not run	0.076	0.060	0.066	0.069
HFR, 77°C	0.078	Not run	Not run	Not run	0.092	0.070	0.077	0.084
HFR, 73°C	0.093	Not run	Not run	Not run	0.125	0.076	0.087	0.093
HFR, 67°C	0.116	Not run	Not run	Not run	0.170	0.098	0.105	0.114
HFR, 61°C	0.143	Not run	Not run	Not run	0.200	0.145	NA	0.148
HFR, 52°C	0.201	Not run	Not run	Not run	0.330	0.216	NA	0.212

Table XI. Test 7, Set 2. Measured cell voltage and HFR at 0.40A/cm^2 v. inlet anode and cathode dewpoint. Cell voltage reported in volts, HFR in ohm-cm^2.

FC #	10130	10197	10207	10264	10281	10376	10423
V, 90°C	0.741	0.739	0.752	0.745	0.729	0.748	0.748
V, 77°C	0.737	0.739	0.744	0.741	0.739	0.739	0.743
V, 73°C	0.723	0.724	0.737	0.725	0.730	0.721	0.728
V, 67°C	0.695	0.698	0.705	0.690	0.704	0.693	0.708
V, 61°C	0.667	0.670	0.660	0.658	0.675	0.641	0.686
V, 52°C	0.602	0.594	0.573	0.581	0.632	0.545	0.618
HFR, 90°C	0.070	0.049	0.060	0.059	0.047	0.067	0.065
HFR, 77°C	0.078	0.061	0.070	0.066	0.053	0.081	0.084
HFR, 73°C	0.093	0.074	0.079	0.083	0.064	0.098	0.100
HFR, 67°C	0.116	0.092	0.106	0.115	0.088	0.132	0.124
HFR, 61°C	0.143	0.116	0.143	0.148	0.115	0.190	0.152
HFR, 52°C	0.201	0.176	0.201	0.219	0.164	0.281	0.239

2.3.2.4 GDL down-selection

Using the data from Tables IV-XI, the performance of each sample was compared relative to the baseline. For test 2 and test 7, performance was evaluated by determining the average voltage difference from the baseline cell's voltage. For tests 3-5, performance was evaluated by determining the average current density % change from the baseline performance at 0.80V and separately at 0.45V. For test 6, performance was evaluated by determining the average current density % change from the baseline performance at 0.80V and separately at 0.50V. Tables XII and XIII show the results of this analysis. For example, under Test 2, sample FC10093 performed 51mV less than the baseline and sample FC10432 outperformed the baseline by 9mV.

Table XII. Performance difference from baseline, Set 1. dV refers to voltage difference from baseline (millivolts), and %J refers to % current density change from baseline.

FC #	10093	10096	10110	10099	10116	10168	10174
Test 2 dV @ 0.80A/cm^2	-51	-29	-4	-34	2	-13	-7
Test 3-5 %J @ 0.80V	-26	-11	-1	-14	7	3	-3
Test 3-5 %J @ 0.50V	-20	-9	-3	-11	-4	-9	-5
Test 6 %J @ 0.80V	-10	29	4	-2	24	25	0
Test 6 %J @ 0.50V	-1	20	101	8	31	35	28
Test 7 dV @ 0.40A/cm^2	NA	NA	NA	-19	22	NA	-11

Next, for each test's metrics, the data was sorted in numerical order, and a rank was assigned to each sample. For example, for Test 2, sample FC10093 showed the lowest

performance relative to the baseline, so it was ranked 13, and sample FC10423 had the highest performance, and was assigned a rank of 1. Next, the per-test rank average and standard deviation were calculated for each sample, and again these average per-test ranks were sorted to achieve an overall rank. Table XIV shows the results of this analysis.

Table XIII. Performance difference from baseline, Set 2. dV refers to voltage difference from baseline (millivolts), and %J refers to % current density change from baseline.

FC #	10197	10207	10264	10281	10376	10423
Test 2 dV @ 0.80A/cm^2	1	6	0	-6	6	9
Test 3-5 %J @ 0.80V	0	13	5	-8	14	18
Test 3-5 %J @ 0.50V	-8	-1	-2	-8	1	-7
Test 6 %J @ 0.80V	18	25	12	2	39	17
Test 6 %J @ 0.50V	2	36	17	-13	9	20
Test 7 dV @ 0.40A/cm^2	0	1	-4	7	-13	11

Table XIV. Per-test rankings, average per-test ranking, and overall rank. dV refers to voltage difference from baseline (millivolts), and %J refers to % current density change from baseline.

	Test 2 dV	Tes t 3-5 J @ 0.80V	Test 3-5 J @ 0.45V	Test 6 J @ 0.80V	Test 6 J @ 0.50V	Test 7 dV	Average rank	Overall rank
FC10093	13	13	13	13	12		12.8±0.4	13
FC10096	11	11	11	11	7		10.2±1.8	11
FC10110	7	7	7	7	1		5.8±2.7	5
FC10099	12	12	12	12	10	9	11.2±1.3	12
FC10116	4	4	4	4	4	1	3.5±1.2	3
FC10168	10	10	10	10	3		8.6±3.1	10
FC10174	9	9	9	9	5	7	8.0±1.7	8
FC10197	5	5	5	5	11	5	6.0±2.4	6
FC10207	2	2	2	2	2	4	2.3±0.8	2
FC10264	6	6	6	6	8	6	6.3±0.8	7
FC10281	8	8	8	8	13	3	8.0±3.1	9
FC10376	3	3	3	3	9	8	4.8±2.9	4
FC10423	1	1	1	1	6	2	2.0±2	1

Samples FC10423, FC10207, FC10116, and FC10376 were ranked 1-4, respectively. Samples FC10423 and FC10207 were comprised of the same backing and hydrophobization level, but had different MPLs.

Based on these rankings, the GDL with backing type “B” and 10% B hydrophobization, and MPL type D was the best overall performing GDL. However, one metric which

wasn't included numerically was the GDL in-plane or flexural stiffness. The GDL from samples FC10423 and FC10207 were much, much less stiff than the GDL from FC10376. Qualitatively, the GDLs from FC10423 and FC10207 had stiffness less than or similar to the baseline, whereas the GDL from FC10376 was much stiffer than the baseline. Since one of the overall criteria in this study was finding a stiffer replacement to the highly-flexible cloth baseline GDL, the GDL used in FC10376 was ultimately down-selected.

2.3.2.5 Summary

Thirteen experimental GDLs were evaluated in 50cm^2 single cells. The evaluations included cathode reactant stoichiometry sensitivity, temperature sensitivity, humidification sensitivity, and polarization performance at three reactant pressures under hot-and-dry operating conditions. The results of these evaluations were rated against a baseline GDL, which had been used as the down-selected GDL from 3M/DOE Cooperative Agreement DE-FC02-99EE50582. A single GDL design was down-selected which had simultaneously equivalent or better performance and higher flexural stiffness than the baseline GDL.

2.3.3 Water management issues

One of the primary distinguishing features of the NSTF electrode is its 20 to 30 fold reduction in thickness compared to conventional dispersed Pt/C electrodes. This has advantages with respect to higher temperature and drier operating conditions, enabling lower mass transport losses as discussed in section 2.1.5.3 of this report, but it also introduces new requirements for water management at lower temperatures. Although developing the MEA for low temperature operation was not a specific goal or requirement of this contract, this is a requirement for any commercializable MEA approach. In this subsection we indicate a number of interesting behaviors that help to define the extent of the water management characteristics for the NSTF MEA system.

2.3.3.1 Reactant flow directions for operation under dry conditions

Fig. 14 below clearly illustrates the advantages of operating a 50 cm^2 cell in what is referred to as a counter-flow mode, for dry operation. In this mode the anode reactants flow through the serpentine flow field in the opposite direction to the air flow direction. The cell's anode outlet is directly across the MEA from the cathode inlet.

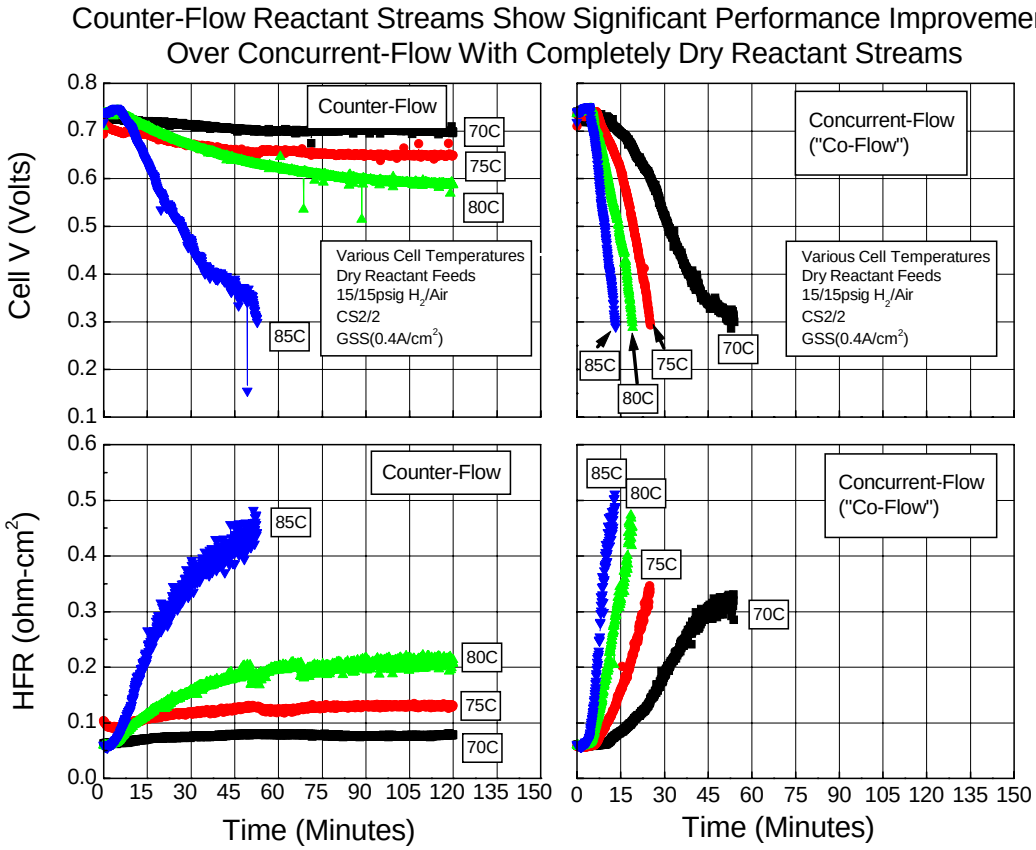

Fig. 14. Illustration of the advantages of operating a 50 cm^2 cell in a counter-flow mode when using dry reactants.

This can be easily understood since as the cathode product water builds up to saturated or even oversaturated (condensed) levels at the outlet, there is a driving force for that excess water to diffuse across the membrane to the anode where the inlet is driest. On the other end, at the dry cathode inlets, the anode region directly across the MEA from the cathode is humidified by picking up moisture from the cathode outlet as described in the previous sentence. This humidified anode can supply the cathode with water and the intervening membrane, to keep it active. The net effect is that the internally generated water is circulating within the MEA. As seen in Fig. 14, the NSTF MEA's can operate quite stably in a counter-flow mode with totally dry reactants under 200kPa H_2/air, at 70^{o}C and stoichiometric ratios of 2. Even at 75 and 80^{o}C the performance is fairly stable but reduced due to the increased HFR from some dryout of the membrane. In sharp contrast, however, in a co-flow mode, where both the dry hydrogen and air enter on the same side of the MEA, the membrane and electrodes dry out very quickly.

Although the exact flow field design cannot always be implemented in larger area MEAs for full operating stacks, many of the aspects of the counter-flow concept can be and should be preserved. The flow field design used in the 5kW stack used for the short stack testing discussed in section 4.2 did preserve this feature, as can be seen in the photographs of the plates. Even though the total active area is 312 cm^2, the flow field is segmented into four 78 cm^2 areas, each with a serpentine flow field analogous to the smaller 50 cm^2 single cells. The stack manifolds were designed to enable counter flow.

This effect also has implications for the water management properties of the GDL so that it can best facilitate the counter-flow water circulation mechanism described above.

2.3.3.2 Observation of a novel effect when operating under dry conditions

Operating with totally dry inlet gases, at different pressures, temperatures and constant stoich to obtain constant outlet humidification at each (J,V) operating point, has revealed a remarkable effect illustrated in Fig. 15.

The implication is that performance loss, observed as the MEA dries out to varying degrees, is equivalent to a macroscopic fraction of the active area becoming totally inactive while the remaining fraction maintains full ORR kinetics and low impedance.

In Fig. 15, the top left panel shows the measured GDS polarization curves obtained with totally dry H_2/air inlet gases, in counter-flow, at 23 psig inlet pressure and stoichiometries of 2. At 70^{o}C, the cathode outlet is fully saturated since the water of generation can exceed the rate of water removal by vapor phase transport out of the cell at that temperature and stoichiometry. At higher temperatures, however, the fraction of water in the exit gas increases and begins to exceed the rate of water generation, resulting in a cathode outlet that is undersaturated. The result is that the MEA dries out, the performance drops, and as shown in the top right panel of Fig. 15, the high frequency resistance (HFR) increases dramatically.

Normally, it might be expected that if one corrected the polarization curves by simply IR-correcting them in the normal manner, the IR-corrected curves would be nearly identical. Normal IR-correction means adding to the measured potential at any given current density, the value of the product of the current density and the measured HFR at that

current density. As seen in the bottom left panel of Fig. 15 however, this normal IR correction fails significantly to make the corrected polarization curves overlap.

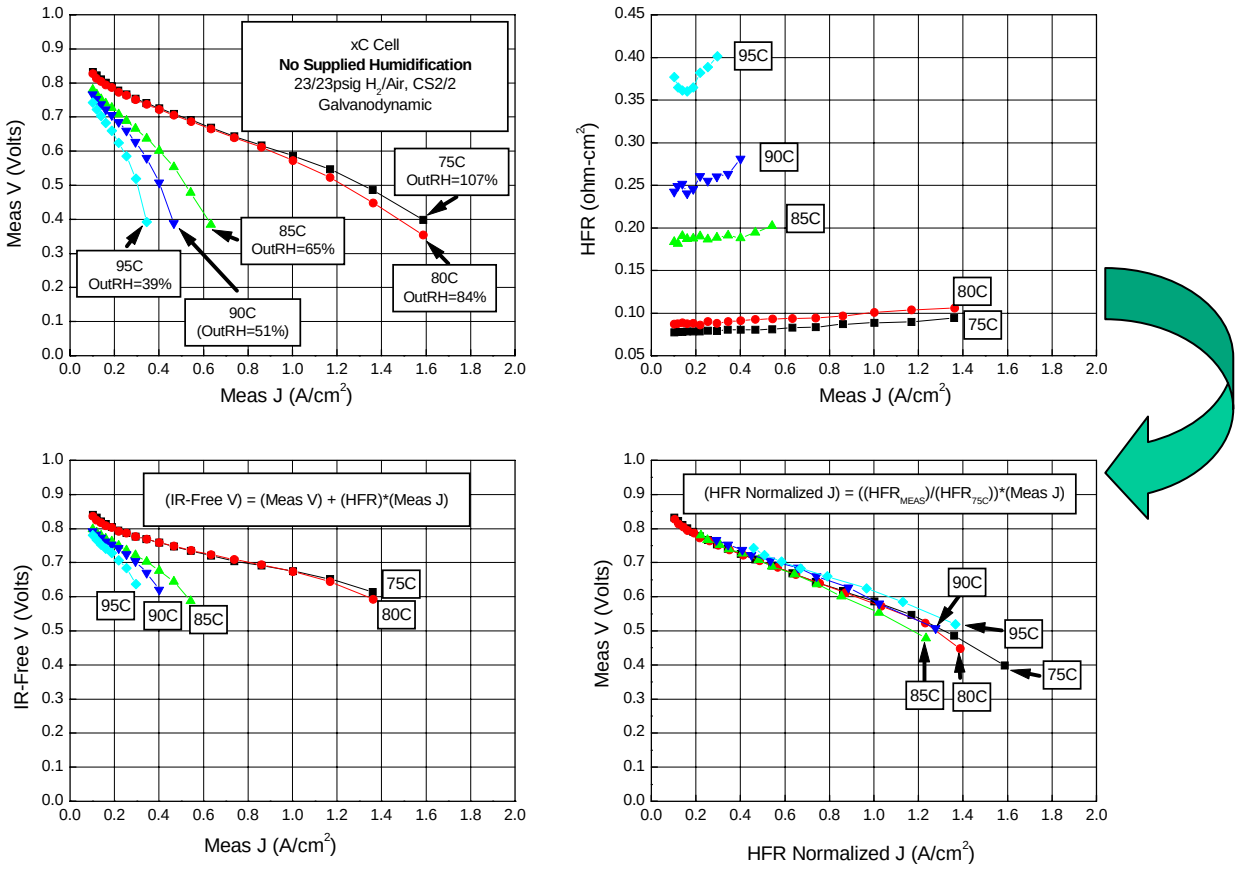

Fig. 15. Illustration of the unique effect when operating MEA's under dry-out conditions that scaling the polarization curve current density by the ratio of the HFR change induced by the drying, can exactly account for all the performance loss upon dry out.

Instead, as shown in the bottom right panel of Fig. 15 if the current densities of the polarization curve as measured are scaled by the ratio of the measured HFR to the minimum HFR (at 75°C in this case), a near perfect correlation is obtained at all temperatures.

Since the normal IR-free corrrection corrects the potential of a polarization curve to reveal just the kinetic overpotential at each current density (neglecting mass transport losses which would still be there), and intrinsically assumes the active area has not changed, that the IR-free curves do not overlap implies these basic assumptions are not true.

On the other hand, that correcting the current density, not the cell potential, by a scaling factor does result in a near perfect normalization of the dried-out polarization curves at all potentials, is consistent with the basic concept that as the MEA dries out, those

sections or fractional areas affected stop working almost completely, and this fraction can be predicted by the simple ratio of the change in HFR.

2.3.3.3 Water management related to cool-start issues

Although as indicated in the introduction, developing the MEA for cold start was not an objective or goal of this contract (rather it was for hotter and drier conditions as discussed in section 1.0), a successful MEA must be able to start from cold conditons.

This subsection gives some indication of the water management issues observed with the ultra-thin NSTF MEAs at low temperatures. It is found that for cool start, meaning from room temperature, in a single 50 cm^2 cell with its typical high heat capacity relative to the heat generation rate of a single MEA, NSTF MEAs cannot self-start until the cell temperature is in the ~45 ^oC range. In contrast, with dispersed electrodes this was not the case. This is illustrated in Fig. 16, where the Pt/C dispersed MEA is shown on the left and the NSTF MEA is shown on the right. The sequence of 50cm^2 cell polarization curves were taken at increasing cell temperatures, heated by an external heating source.

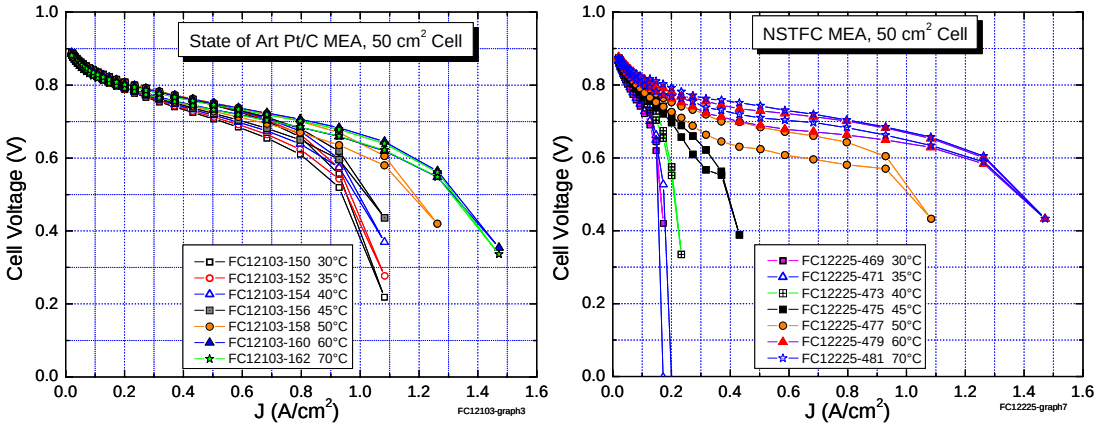

Fig.16. Comparison of "cool-start" protocol applied to a state-of-the-art MEA with dispersed catalyst electrodes (left) with an NSTF catalyst based MEA (right). Conditions were: ambient pressure H_2/air GDS polarization curves (30 seconds/point), constant flow (800/1800 sccm), 100%RH on anode and cathode, and counterflow.

This comparison will have some dependencies on the exact protocol used, and the shut down procedures between the experiments. In this case the cells are shut down fully humidified as a worst case. The 20 to 30 fold reduction in thickness of the NSTF electrode layer means the water generation rate per unit volume is proportionately higher, implying the rate of water removal per unit volume must be increased to reduce the effect of flooding. The GDL has been found to be important here, as well as the properties of the catalyst layers for facilitating water transport out of the cathode. These effects are already studied under the DOE/3M contract subsequent to the present one.

A second very important fact to note is that cool start or cold start in a 50 cm^2 cell is very different than in a well designed fuel cell stack where thermal masses are minimized and self heating by the MEAs can quickly bring local tempertures above those required to

prevent water condensation. As a first indication of this, the short stack used for the stack tests reported in section 4.2 of this report, was briefly tested for cool start during the 8-cell build version of it preceeding the final stack testing. By optimizing the shut down conditions prior to a cool start, such as briefly drying out the stack, and introducing coolant from the test station after the stack had self-heated to a preset point, it was possible to bring the stack to full performance at the ¼-power point in less than a minute. This could never be done with a single cell and suggests that with optimized sytem operating protocols, stack design features, and MEA improvements, the targeted full stack start-up times of less than 15 seconds will be achievable.

Section 2.4 Investigation of Air Management Strategy

This section reviews the work done under Tasks 1 and 3 related to investigation of an air supply pressure versus flow rate profile more advantageous for operation of the MEA.

Table of Contents for Section 2.4

2.4.1 Introduction

The objective of the air management (Subtask 1.1) task of this contract was to investigate the air-supply conditions which optimize the ability of the 3M MEA's to operate under hotter, drier conditions. Fuel cell cathode kinetics improve in direct proportion to the partial pressure of oxygen, so using a compressor to pressurize the incoming air can be advantageous. Obviously, the benefits must exceed the compressor parasitic power losses. Water management is also closely tied to operating pressure, since pressurized air carries less water per unit mass of air than ambient pressure air. So the reactant pressures can strongly affect the conditions for either MEA drying or flooding.

A common type of compressor used for supplying compressed air in commercial automotive applications is a turbocompressor (TC). The pressure versus flow rate characteristic of a TC is one in which pressure increases as flow rate increases. This is not necessarily the best operating characteristic, however, for a PEM fuel cell. In an operating fuel cell system, particularly for automotive applications, most of the operating time is spent at low power conditions, and fuel efficiency (stack voltage) is a key performance parameter. As noted above, higher pressures at low stack power conditions would engender better reaction kinetics and higher stack voltages at a given current density, and therefor higher operating efficiency. Therefor, high pressures at low current densities would be best as long as water removal rates were not an issue.

At higher current densities or stack powers, higher pressures can improve mass transport losses for better performance and efficiency at high stack power conditions. Since water generation rates are highest at high current densities, and can lead to flooding if the water removal rates are not sufficient, it can be advantageous to reduce the stack outlet pressure at high current densities to take advantage of the higher water vapor fractions contained in lower pressure air. At high operating current densities, a low air pressure or one decreasing as current density increases would be desireable.

So although the operating temperature can strongly influence the state of MEA drying or flooding for either of the above two conditons of low or high stack power, a preferred air pressure versus flow rate characteristic from the MEA standpoint would generally appear to be one in which the stack inlet pressure is either constant or slowly varying with total air mass flow rate, or at least decreasing with mass flow rate – just the opposite of a turbocompressor output. It is well known as well that almost universally, when single cell fuel cell performances are reported in the literature, they are shown at constant inlet or back pressure. Compressors that would have such a characteristic are positive displacement machines, such as piston or rotary vane compressors.

2.4.2 VAIREX Corp. and Compressor Design and Development

The above concepts were discussed with VAIREX, Corp., of Boulder, CO, with potential requirements for short stack power levels and stoichiometries. A set of tasks and milestones were established to investigate development of suitable compressor technology and ultimately fabrication and delivery of a unit to 3M for evaluation. The first subtask included preparation of a written report on the quantitative considerations of air systems as they apply to pressure ratio vs flow rate profiles. It also included consideration of the effect of basic gas laws on energy consumption as a function of

pressure, and the resulting compressor efficiencies, discharge temperatures and relative humidity. A survey of compressor types was completed and their various pressure profiles, motor torque curves, and overall efficiencies identified. A MatLab simulation modeling tool was also developed to allow a system designer to predict air system performance and power consumption as a function of fuel cell stack pressure profile requirements. This tool was delivered to 3M and a workshop was conducted on its use.

The second subtask was focused on defining and characterizing the compressor hardware required for assembly of a brass-board air supply system. This was followed by fabrication and delivery to 3M of the final compressor technology for evaluation.

2.4.2.1 Compressor design

VAIREX had significant experience with positive displacement compressor technology in the form of piston and fixed vane type compressors. The basic fixed vane models were the VAIREX vane (VV) 520 and VV1020 series. A critical design parameter required before compressor modeling/simulation could begin was the pressure profile required for the fuel cell operation. 3M provided a prelimary one to VAIREX based on the best performing NSTF MEAs available at the time. The MatLab simulation tool was then applied to the VV1020 series to explore pressures up to a pressure ratio of 2.0. Fig. 1 shows an example of the input and Figs. 2 and 3 the output from the compressor modeling tool for a pressure profile varying between 1.8 at minimal power to 1.4 at maximum power.

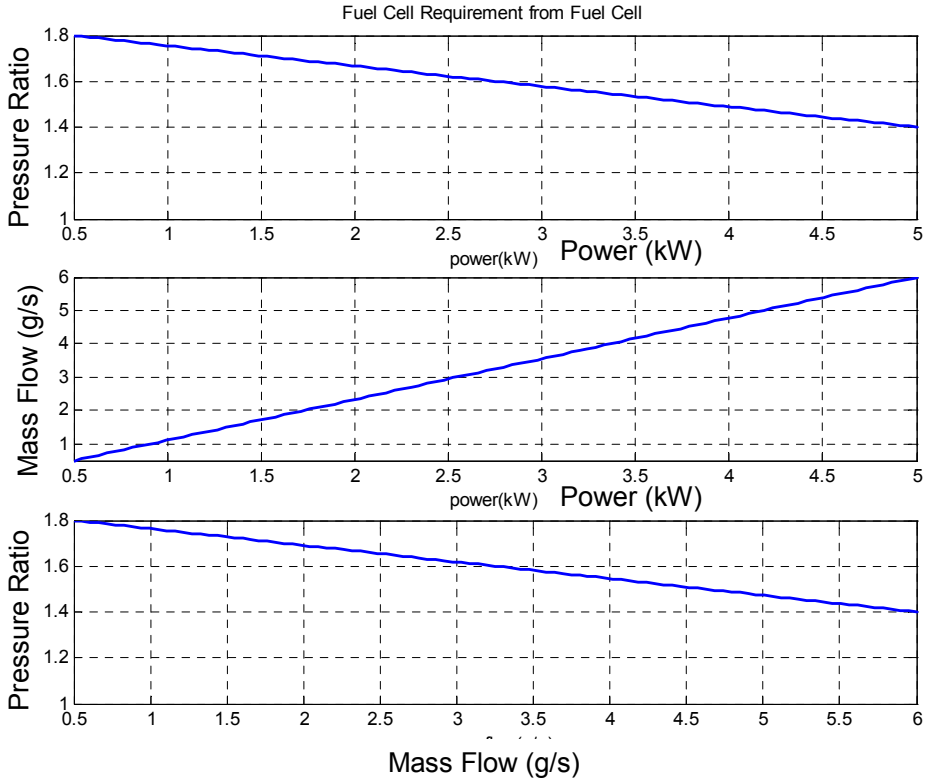

Fig. 1. Specification of pressure ratio versus stack power, and mass flow rate versus stack power, used as initial inputs for the initial simulation modeling of the VAIREX fixed vane compressor.

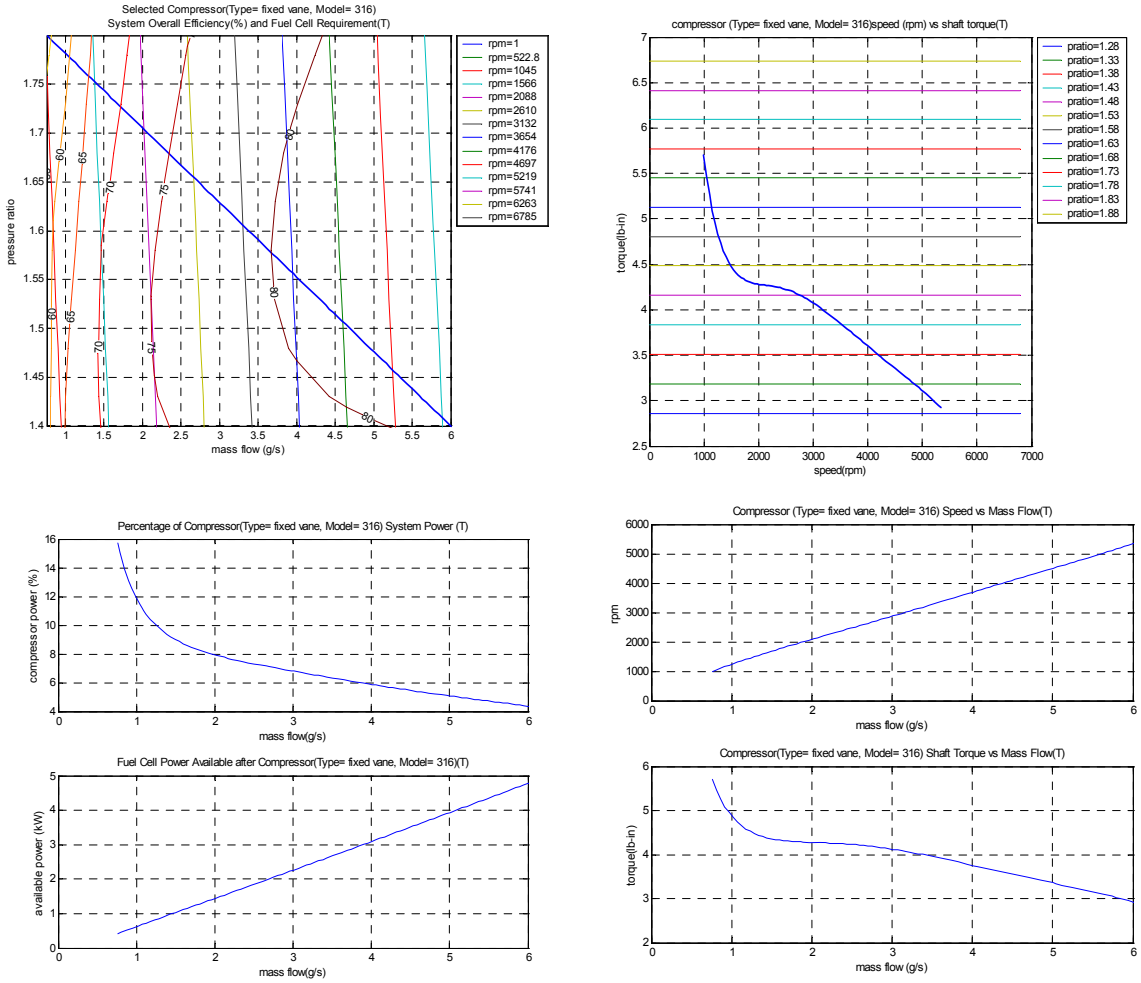

Fig. 2. Output from the MatLab simulation tool for the VAIREX fixed vane compressor with input data from Fig. 1.

Maximum pressures cited by various automotive fuel cell companies were as high as 23 psig (250kPa) and the NSTF MEA best performances were always obtained at constant pressures this high. This would equate to a maximum compressor pressure ratio of 2.6.

Although VAIREX had extensive experience developing zero clearance piston compressors that could reach pressure ratios as high as 4.0, the VAIREX vain (VV) clearance compressor series was not rated for operation above 2.0. This difference would have substantial implications for the compressor power, thermal and structural loads. VAIREX completed additional testing on the VV1020 air compressor at constant pressure ratios up to 2.25 and extrapolated performance at higher pressure ratios up to 2.6 for incorporation into their MatLab simulation model. VAIREX then carried out MatLab simulations for constant pressure operation for 5 pressure ratios between 1.8 to 2.6 in steps of 0.2. These pressures were run for four different compressors, including the VV520 andVV1020 and proposed VV215 model vane compressor types, as well as a proposed piston compressor (G7). Mass flow rates and fuel cell power levels were selected to be compatible with each vane compressor. For the piston simulation, mass

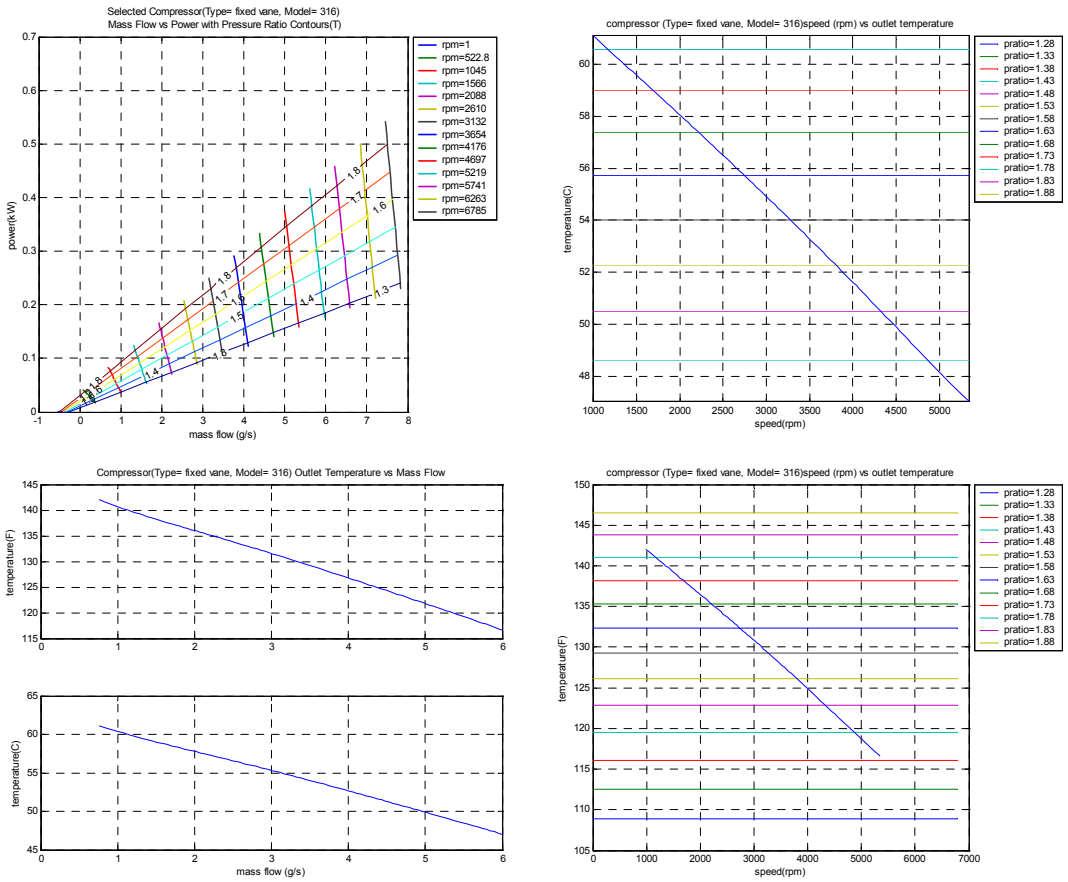

Fig. 3. Additonal output from the MatLab simulation tool for the VAIREX fixed vane compressor with input data from Fig. 1.

flow and fuel cell power were set at the same values used for the VV520. This resulted in a total of 20 output files, and some useful conclusions resulting from these models were as follows. Zero clearance compressors (piston machines) operate better at higher pressures than clearance compressors (vane machines) and this effect is particularly pronounced at low flow rates. Although this behavior is rooted in compressor physics and well known, the magnitude of the effect was greater than expected. For example, a piston compressor running at constant pressure ratio of 1.8 starts at under 50 watts but rises to just under 600 W at full load, which represents a higher than desirable parasitic load at full power. For the same pressure ratio and output, the vane compressor had a parasitic power of 350 watts already at the low power condition that rose to 650 watts at maximum power. The 350 watts at low power exceeds the 300 watt output of the fuel cell it would be powering at those conditions.

Now turning to a pressure ratio of 2.6, the piston compressor still required about 700 watts at maximum mass flow, not much of a change for the 1.8 pressure ratio. But the vane compressor at constant 2.6 pressure ratio requires 650 W at low flow, over twice the fuel cell output, and at full load the power is 1050 W, almost twice that of the piston.

So based on this initial modeling, and design constraints provided by 3M of sufficient air supply for a 3kW stack and turn-down ratio of at least 10:1, VAIREX suggested that a zero clearance, postive displacement compressor (e.g. a piston machine) would be the only type able to meet such a performance envelope. There are no commercially

available compressors able to meet this performance window. Unfortunately, all their own existing piston designs and hardware were for much higher flow rates, and the budget limits of the subcontract did not allow redesigning into a smaller unit. The proposal that was accepted was to modify a commercially available oil-free industrial compressor. Thomas Pumps and Compressors (Sheboygan, WI) manufactures a number of candidates that are close to the desired specifications, but are designed for constant speed and powered by AC induction motors. VAIREX chose the Reitschele Thomas VX-100 dry piston compressor and proposed replacing the constant speed AC induction motor with a higher efficiency brushless DC variable speed motor.

In addition, VAIREX also looked at the design of their vane machines, specifically the VV1020, to see if they could be modified to improve the high pressure performance, especially at low flow rates, e.g. by increasing the number of vanes from three to four, changing to ceramic coated stainless steel vanes to cope with higher temperatures and tighter clearances, and higher operating speed.

Further MatLab simulations were carried out for both the modified VX-100 piston and the redesigned VV1020 vane approaches. Additional lab tests with available versions of the machines were carried out first to provide data for the simulations on the power drawn as a function of mass flow for a power ratio of 2.6 and 1.6. The simulations are shown in Fig. 4 below for the two compressors (RT Piston = Thomas HP-1000). The power drawn by the air management system (AMS) is expressed as a % of the hypothetical fuel cell output. In these graphs, the RT Piston model includes the effect of a brushless DC motor only, and none of the other possible improvements. In all cases motor-controller efficiency was set at a constant 80%.

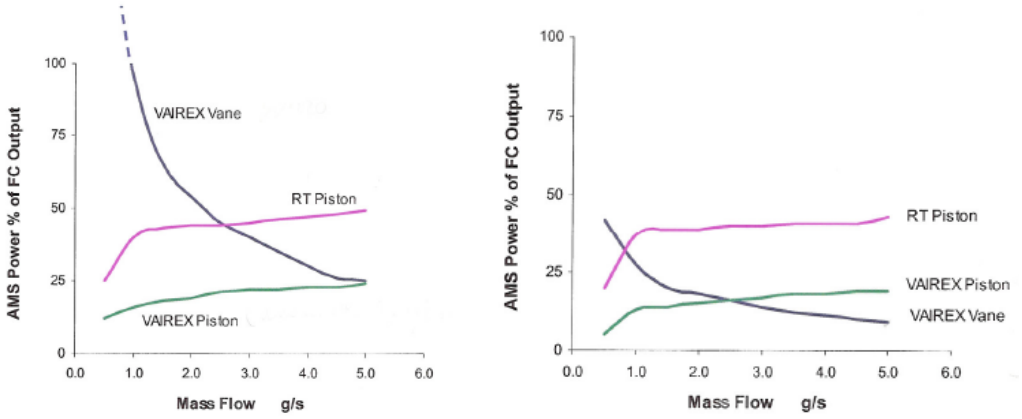

Pressure Ratio = 2.6 Pressure Ratio = 1.6

Fig. 4. Comparison of compressor power draw versus mass flow rate at two pressure ratio extremes for three compressor types.

At a pressure ratio of 2.6, the piston compressor is clearly necessary because the vane compressor consumes considerably more power than the stack produces at the minimum flow rate, even assuming that the “high-pressure” modifications would work as expected. The RT piston compressor will operate over the entire operating range up to a 2.6 pressure ratio, but still draw much too high a power for practical use. For comparison, in Fig. 4, the power consumption of the VAIREX piston machine, assuming it was down-sized to meet the target size, would draw half as much power, but still be

higher than the 10-15% AMS parasitic loss budget typical of most fuel cell system designs.

As the other extreme, a pressure ratio of 1.6, the power consumption of all three compressors falls significantly as expected. The VAIREX Vane outperforms the RT piston at every operating point above 1.0 g/sec of air, which is equivalent to roughtly a 5:1 turndaown ratio. The Vane machine is still unacceptable at low flows, but has significantly lower power consumption than either of the piston machines at maximum flow. The general pattern shown in Fig. 4 remained true at pressure ratios between 1.6 and 2.6.

In conclusion, for high pressures at low flow rates, positive displacement, zero clearance compressors are a natural fit, of which the piston machine is the classic type. Diaphram pumps and free vane machines also belong in this category but for this application are not likely choices. In VAIREX experience, diaphragm pumps suffer from low efficiency and do not scale well above design air flow rates of 1-2 g/s. Free vane machines with high vane counts can be considered “semi-zero clearance” and perform well at high pressures and low flows, but generally suffer from high friction losses at high flows that limit their effective operating range. The VAIREX Vane is a restrained vane, postive displacement, clearance machine that can offer excellent efficiency at moderate to high flow rates, but is clearly challenged at low flows. Other machines in this class have the same general charateristics, and include classical compressors such as the Scroll, Lyscholm (Twin Screw), and Roots, as well as a number of more exotic designs such as the DyneEco Univane and Mechanology’s Toiroidal Intersecting Vane Machine which are being considered for fuel cell applications. Dynamic compressors such as regenerative (or side channel) blowers and turbocompressors offer excellent packaging and good efficiency, but have flow-pressure characteristics unsuitable for the desired operating strategy discussed in the introduction. Multi-stage systems have been successfully employed by Ballard in fuel cell busses, but probably would not be a solution below 200kW sizes.

It might be possible to conceive of a “best of both worlds” machine that would operate as a zero clearance machine at low flow rates and high pressures, but as a clearance machine at high flow rates for low friction.

2.4.2.2 Compressor Development and Delivery

Based on the compressor design work discussed above, VAIREX proposed supplying both a piston and a vane compressor, each modified from existing machines, the RT VX-100HA and the VAIREX VV1020. At a minimum each delivered compressor would operate at the published specifications, attached at the end of this section in subsection 2.4.5.

An early step in the plan was to procure the Reitschle-Thomas model VX100HA air compressor and test it prior to replacing the constant-speed AC induction motors with higher efficiency, variable speed BLDC motors. This was accomplished and the MatLab simulation was updated with a module based on the data to include this unit. Subsequent modeling predicted a maximum operating speed (~3,000 rpm) that was higher than expected based on the product literature. This raised operating friction and raised questions about the critical frequency of the reed valves.

VAIREX then procured two larger Reitschle-Thomas units, model (VX150HA), and tested and modeled them in the same manner. Predicted maximum operating speed dropped to 1,400 rpm, which lowered friction and valve losses. Efficiency is higher, and more in line with earlier simulations. On the other hand, motor torque is almost double at any given mass flow, and the minimum speed of ~200 rpm is quite low. Their decision was to concentrate on development of the larger unit (VX150HA).

To meet the requirements of the R-T piston compressor, and the high-pressure *VAIREX* vane compressor, *VAIREX* selected a semi-custom rotor-stator set sourced from a major motor manufacturer and incorporated into a hybrid air-cooled core and liquid-cooled housing designed by *VAIREX*. This reduced the motor to less than half the size of the stock AC induction motor and made it commensurately lighter.
Figs. 5 and 6 show pictures of the protoype compressors as delivered. In Fig. 5 the brushless DC motor is roughly half the size of the initial AC induction motor.

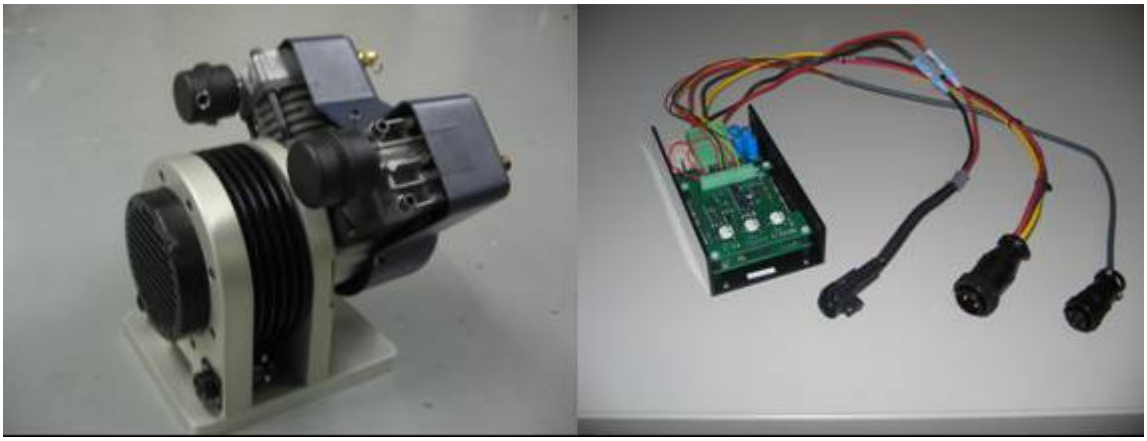

Fig. 5. VAIREX VP – 526 piston prototype compressor (left) and its motor controler (right), as delivered, based on a modified RT-VX150HA.

Fig. 6. VAIREX VV-1020 modified vane compressor as delivered.

2.4.3 Compressor evaluation at 3M

This section is divided into two sub-sections. The first is a description of the equipment and process used to characterize the two prototype compressors and the performance results measured from them. The second section deals with the evaluation of the modified VAIREX VV- 1020 HT vane while supplying a 1.4 kW fuel cell stack.

2.4.3.1 Compressor Characteristic Tests

2.4.3.1.1 Experimental

A test bed was assembled to evaluate the compressors. The goal was to reproduce the theoretical curves supplied by VAIREX for back pressure versus air flow rate through the system in grams/second (g/s) for various power levels ranging from 200 Watts to about 1200 Watts. Back pressure is defined as the ratio to room pressure plus intrinsic back pressure. The two compressors evaluated were designated as models VP – 526, a twin piston compressor, and the model VV-1020 HT restricted vane based compressor.

The first step was to obtain appropriate power supplies that could provide the needed voltage (up to 60 Volts) at high currents up to 35 Amps. Two power supplies were purchased, each a Lambda model Gen 60-25, that were then connected in parallel to provide up to 60 Volts at up to 50 Amps.

For interconnecting a compressor to pressure control valves, pressure gauges, ballast tanks, flow meters and various types of tubing were tried. For the VP-526 compressor it was found that 0.5 inch diameter plastic tubing with Swagelok^{TM} connectors worked best. From the compressor output the tubing led to a Swagelok-cross with a needle type pressure gauge in the top arm, a ballast tank opposite the gauge, and a back pressure valve in the lower arm followed by a Bronkhurst mass flow meter with a 350 SLM full scale transducer to measure gas flow. It was found a large ballast tank was needed because of the pressure fluctuations from the two pistons interfered with the needle type pressure measurement gauge. The analysis of the VV-1020 HT rotary vane based compressor was in some ways easier as it did not require the ballast to damp out the pressure fluctuations and it was less noisy as well.

2.4.3.1.2 Assessment of the VP-526 (Piston) Compressor

This compressor worked fairly well but was very noisy even with a muffler on its inlet, and it also was subject to intense vibrations. Figure 7 shows a graph of absolute pressure ratio (P/P_o) vs. flow rate in g/s, where $P = P_{gauge} + 1$ atm, and $P_o = 1$ atm. As shown the flow rate was not very large and there was a large intrinsic back pressure which could have been reduced further if larger diameter tubing had been used. The curves do reproduce the predicted curves quite well over the range we were able to test.

The VP-526 compressor's maximum flow rate is only appropriate for small stacks, probably much less than one kW. The controller was difficult to use as several parameters had to be adjusted and balanced for optimum operation.

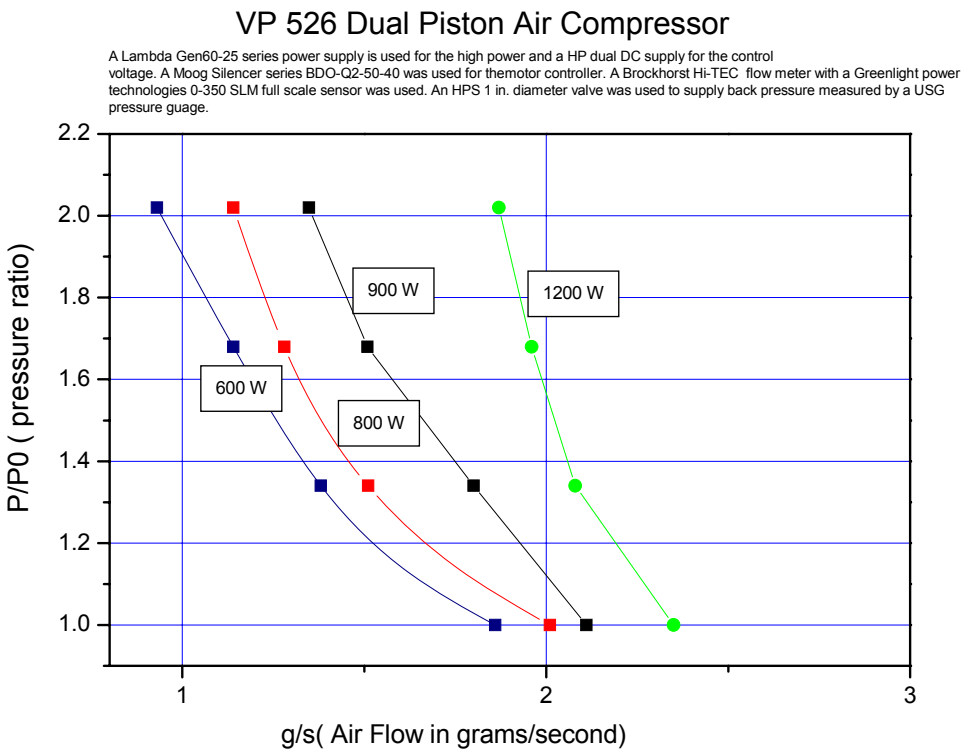

Fig. 7. Measured performance of the Vairex VP 526 compressor, absolute pressure ratio versus flow rate in grams/second, compared to the theoretical performance.

2.4.3.1.3 VV-1020 HT (Restrained Vane) Compressor

The VV-1020 compressor had a theoretical flow rate over 20 g/s, but the flow meters available could only handle up to about 8 g/s. Consequently, only a portion of the available rated range of this unit was evaluated. However, the conclusion was that this would be adequate for supplying up to a 2 kW stack operating at a pressure ratio of 2.0, and according to the compressor specifications this could easily be obtained.

The controller was much easier to use with this unit compared to the VP 526. A five volt control signal was externally supplied which increased motor speed in RPMs as measured by a Tektronix oscilloscope. The motor output current was also monitored.

The initial evaluation of the VV-1020, with an input voltage to the controllers of 48 volts, is shown in Fig. 8. Difficulty achieving some of the high power conditions was believed to be due to the motor casing getting too hot, causing the unit to kick off and require a reset. For this data, a temperature sensor on the case of the unit was not operational.

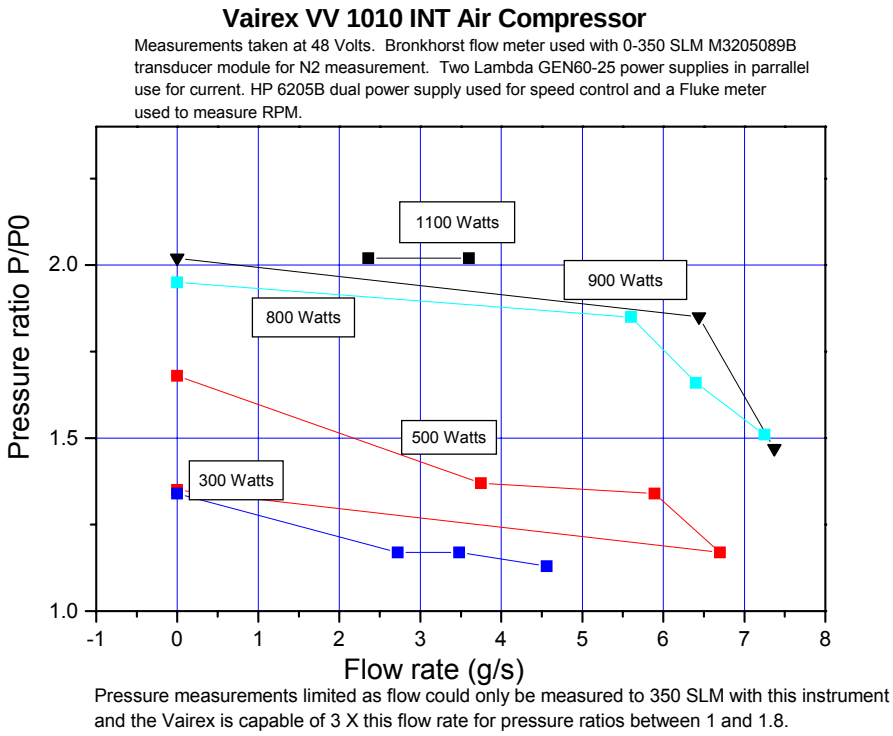

Fig. 8. Measured performance of the modified VV 1020 HT compressor, absolute pressure ratio versus flow rate in grams/second, at various fixed compressor power levels.

Comparing Figs. 7 and 8 shows a significant difference in air flow range between the two compressors. The rotary vane compressor's range is several times larger than the piston's at similar presure ratio and power, and its turn-down curve also appears flatter over a much larger range of flow rate. This indicates a much larger range of flow can be obtained with a given back pressure. Fewer static points were achieved at higher powers because of the overheating and shut off problems. Heat would build up very quickly and as shown in section 2.4.3.2 below, could not be adequately dissipated. As predicted by the VAIREX MatLab simulations, the piston compressor in Fig. 7 had no difficulty hitting higher presure ratios

After the experiments with the stack described in section 2.4.2.2 below, another set of measurements were made using a larger 1300 SLM flow meter. In contrast to the 48 V supply voltage used in the theoretical performance curves and for the data in Fig. 8, the input voltage for this post-stack test data was 60 volts, on the assumption that the compressor would generate and dissipate less heat because of the lower currents needed. The results are summarized in Table I and plotted in Fig. 9 as flow rate in grams/sec vs. supplied power at several different pressure ratios ranging from 1.0 to over 2.0. It shows that the vane compressor was able to deliver fairly uniform pressure ratios over a 500% or greater range of flow rate.

Table I – Compressor data operating at 60 V supply voltage without a stack.

Supply Voltage	Current (A)	Power (W)	Motor Signal Voltage	Pressure (kPa)	Pressure Ratio	% of Flow Range	Total Flow (SLM)	Flow Rate (g/s)
60	2.14	128.4	0.022	3.2	1.03	9	117	2.2425
60	2.5	150	0.031	4.8	1.05	11.6	150.8	2.890333
60	3.28	196.8	0.038	6.78	1.07	15.3	198.9	3.81225
60	4.48	268.8	0.086	10.4	1.10	20	260	4.983333
60	6.2	372	0.137	14.6	1.14	25	325	6.229167
60	7.5	450	0.176	17.9	1.18	28.9	375.7	7.200917
60	8.9	534	0.224	21.5	1.21	32.5	422.5	8.097917
60	11	660	0.289	24.6	1.24	36.2	470.6	9.019833
60	12	720	0.328	28.1	1.28	38.7	503.1	9.64275
60	11.76	705.6	0.315	32	1.32	36.2	470.6	9.019833
60	12.6	756	0.345	38.5	1.38	36.1	469.3	8.994917
60	13.8	828	0.381	45.5	1.45	35.7	464.1	8.89525
60	14.3	858	0.397	50.4	1.50	35	455	8.720833
60	16	960	0.456	61	1.60	34.5	448.5	8.59625
60	18	1080	0.523	73.5	1.73	33	429	8.2225
60	20	1200	0.59	85	1.84	32.5	422.5	8.097917
60	23.7	1422	0.65	101.5	2.00	30.7	399.1	7.649417
60	5	300	0.1	13.8	1.14	22	286	5.481667
60	5.7	342	0.127	22	1.22	20.7	269.1	5.15775
60	6.8	408	0.109	32	1.32	19.4	252.2	4.833833
60	5	300	0.099	13.7	1.14	20.8	270.4	5.182667
60	3.5	210	0.063	9	1.09	16.4	213.2	4.086333
60	3.8	228	0.071	12.8	1.13	15.9	206.7	3.96175
60	4.26	255.6	0.081	17.2	1.17	15.8	205.4	3.936833
60	4.86	291.6	0.096	23.4	1.23	15.2	197.6	3.787333
60	5.6	336	0.115	31	1.31	14.5	188.5	3.612917
60	6.8	408	0.15	42	1.42	13.4	174.2	3.338833
60	8.42	505.2	0.2	50	1.50	15.3	198.9	3.81225
60	9.8	588	0.24	60	1.59	14.6	189.8	3.637833
60	11.45	687	0.29	71.4	1.71	13.6	176.8	3.388667
60	13.25	795	0.347	85	1.84	12.5	162.5	3.114583
60	14.8	888	0.396	93	1.92	11.4	148.2	2.8405
60	19.8	1188	0.55	121	2.20	8.7	113.1	2.16775
60	5.9	354	0.12	39	1.39	10.8	140.4	2.691
60	6.58	394.8	0.139	44	1.44	11.5	149.5	2.865417
60	7.1	426	0.156	47	1.47	12	156	2.99
60	10.6	636	0.267	66	1.65	14.8	192.4	3.687667
60	12.1	726	0.314	73.7	1.73	16	208	3.986667
60	13.9	834	0.374	81	1.80	17.4	226.2	4.3355
60	17.4	1044	0.489	93	1.92	19.4	252.2	4.833833
60	20.5	1230	0.59	104	2.03	21.1	274.3	5.257417
60	19.6	1176	0.576	46	1.46	60	780	14.95
60	22.7	1362	0.688	51	1.50	51.6	670.8	12.857

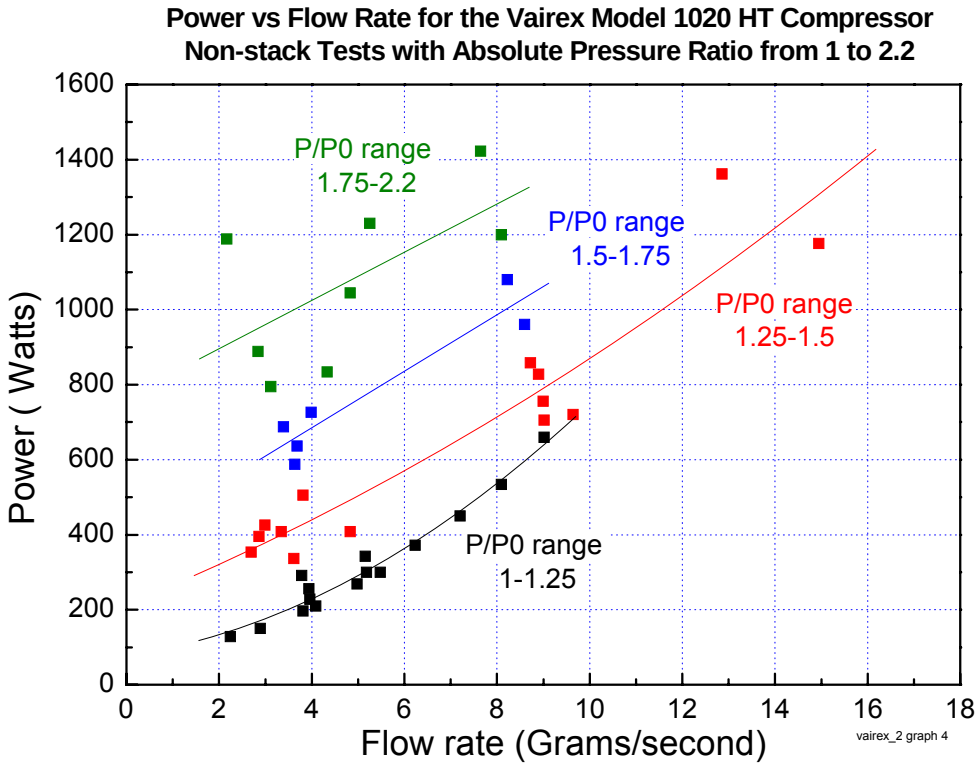

Fig. 9. Applied power vs flow rate for four ranges of back pressure ratios, measured with the VV 1020 HT compressor with 60V input power as summarized in Table I.

The VV 1020 HT compressor had more salient features than the VP 526, including being smaller, lighter and much quieter. The working flow rate range for a near constant pressure ratio was also much larger. However it had some operational issues. It was suspected, but not verified, that the unit contained a surge protector of some type to measure the amount of applied torque at a given pressure ratio, which shut the unit off if the torque was too great over a short period of time in order to protect the unit. Cooling is a major issue since the motor's own cooling air is determined by the rpm's it generates at the desired flow rate it is supplying. At higher powers there was very poor heat transfer and cooling since for the conditions tested, the flow rates were quite low and far off the maximum efficiency curve supplied. This could be corrected by improved air flow and a larger cooling fan. The unit is designed for higher flows at high power but this was in a range too high for our test bed or the short stack tests. Re-evaluating this unit with a larger stack would be more successful after changes to the air flow cooling strategy and cut off issues are answered.

2.4.3.2: Testing of 3M 8-cell stack with Vairex VV 1020 HT compressor

This section summarises test results obtained by using the modified VAIREX VV 1020 HT compressor to supply air to a 3M 8-cell stack built with MEAs based on nanostructured thin film (NSTF) catalyst.

2.4.3.2.1 The stack

The short stack used was the same stack design (designated as DOE3_091506) described in section 4.2. It used MEAs with active electrode areas of 312.5 cm^2 and 8 cells for a nominal power of 1.4 kW. Nominal power for this stack is defined as the average power at 0.7 V/cell under H_2/Air at 3.5 Bar pressure (absolute), 80 ºC temperature, stoichiometry of 2.0 on the anode and 2.5 on the cathode and full humidification. Since for these tests, the catalyst system was different (NSTF), operating pressures were chosen to be much lower and some other operating conditions and parameters (such as cathode humidity for example) were not precisely controlled.

The stack used stainless steel bipolar plates, along with current collectors and compression hardware all covered with protective layer of electrolytically deposited Au. This was done to prevent contaminating of MEAs by byproducts of stainless steel corrosion, to which fuel cell catalysts are rather sensitive. The stack was operated in a horizontal mode, in which the plane of the plates are parallel to the ground, with cell #1 as the lowest one. In the S1 design, such an orientation facilitates product water drainage, however it also has a tendency to cause cell #1 to flood under wet operating conditions. Since our compressor testing was performed under excessively dry conditions (totally dry cathode) this was was found not to be a concern.

2.4.3.2.2 Test station

The S1 8-cell stack was mounted on the 3M Hydrogenics (LAA) test station. The test station is manufactured by GreenLight (subsidiary of Hydrogenics) and is equipped with control of all parameters necessary to safely operate the fuel cell stack. This includes coolant flow and temperature control; fuel composition and flow rates, temperature, pressure, %RH control; and air flow rates, temperature, pressure and %RH control. The stack's output is measured by an electronic variable load capable of applying up to 1 kA of current and voltage monitoring circuitry. For the purpose of this experiment the air side of the LAA test station was modified to accommodate the air supply from the VAIREX compressor. In order to supply air from the compressor, the house air supply was disabled, and the compressor outlet was plumbed into the LAA directly past the humidifier valve. This way, pressure losses associated with two layers of control from the mass flow control and steam delivery systems were bypassed, leaving only minor pressure overhead associated with the gas lines connected directly to the stack under test. The test station retained control of the back pressure. Unfortunately, bypass of the steam valve rendered the humidification subsystem ineffective, and also the flow control was moved to the compressor control loop. This meant the stack had to be fed dry cathode gas only with the flow controlled by the compressor. This imposed limitations on further testing, particularly with respect to choice of operating conditions, as shown below.

2.4.3.2.3 Experimental

Two operating modes of the LAA with the Vairex compressor were enabled, differing by the method of mass flow control employed. One of the modes involved operating the compressor in a constant speed/constant flow mode coinciding with the maximum demand point and then controlling the air delivered to the fuel cell stack by bleeding-off the excess air through a needle valve. A second mode of operation involved true direct flow control via the control of the speed of the compressor's motor. That last mode mimics very well expected real life operating conditions during deployment. In both cases, the back pressure control was performed by the LAA test station.

It is important to note that the stack tested with the Vairex compressor was substantially undersized relative to the compressor's flow capabilities. The stack, as tested under the achievable operating conditions, was in the 1 kW size range while the compressor was sized for larger sized stacks in the 3- 5 kW range. This meant that the flow range required by the stack would fall on the very inefficient extremes of the operational range of the compressor. This created the propensity of the compressor to stall, with associated noise and vibration, and led to a tendency of the compressor head to heat up excessively because there was insufficient cooling air drawn into the reconfigured motor. The replacement of the AC induction motor with the brushless DC motor led to a very compact compressor but resulted in a tendency of the drive motor to overheat (due to the limits of heat dissipation). These overheating tendencies of the compressor's motor limited the maximum power that could be reliably applied to the compressor head before its thermal protection would activate, and therefore limited achievable back-pressures to about 150 kPa(P/P0=1.5) at maximum. Pursuing pressures above that level resulted in the compressor either shutting down by tripping its thermal overload switch (too much power required), or going into a surge (not enough torque delivered for the pressure level attempted) and stopping, reversing, or ultimately also overheating the motor.

2.4.3.2.4 Mode 1 Operation:

In this first mode, the stack's air flow was controlled by bleeding off a portion of the total flow generated by the compressor running at a constant speed with the remainder fed to the stack. The experimental setup involved connecting the compressor outlet to a tee, with one end of the tee allowing diversion of a portion of the flow to the atmosphere via a control valve (manual control with flow meter), and the other end of the tee connected to the fuel cell stack via a mass flow meter (MFM). A section of tubing was added between the tee and MFM to prevent high temperatures of compressed gas from reaching (and possibly affecting) the MFM. The motor speed (RPM) was controlled by the supplied voltage. In our case, two stack inlet pressures were explored; near-ambient and 150 kPa, both at a maximum constant flow of 80 SLM to the stack. Initially, the control valve was closed and the compressor revved up to achieve flow above the targeted maximum flow of air to the stack at given pressure. Once this was achieved, the bleed valve was cracked open to divert the excess flow generated by the compressor to the atmosphere until the targeted 80 SLM of flow through the stack was reached. The system was configured such that the majority of the flow generated by the compressor was directed towards the stack and only a minor amount was vented.

The opposite experiment where only a small portion of the compressor-generated flow would be allowed through the stack with the majority being vented was envisioned. It targeted more efficient flow regimes of the compressor head, but the power required for

such operation exceeded the motor's heat removal rates (even despite substantial increases in compressor efficiency). Constant flows through the stack were therefore employed in this experiment with 60 SLM of hydrogen and 80 SLM of air being used for the anode and cathode respectively. Anode flow and pressure were entirely controlled by the test station. Cell temperatures were 70 ºC for near-ambient operation, and 75 ºC and 80 ºC for 150 kPa pressure. Data from these experiments are plotted below in Figs. 10, 11 and 12.

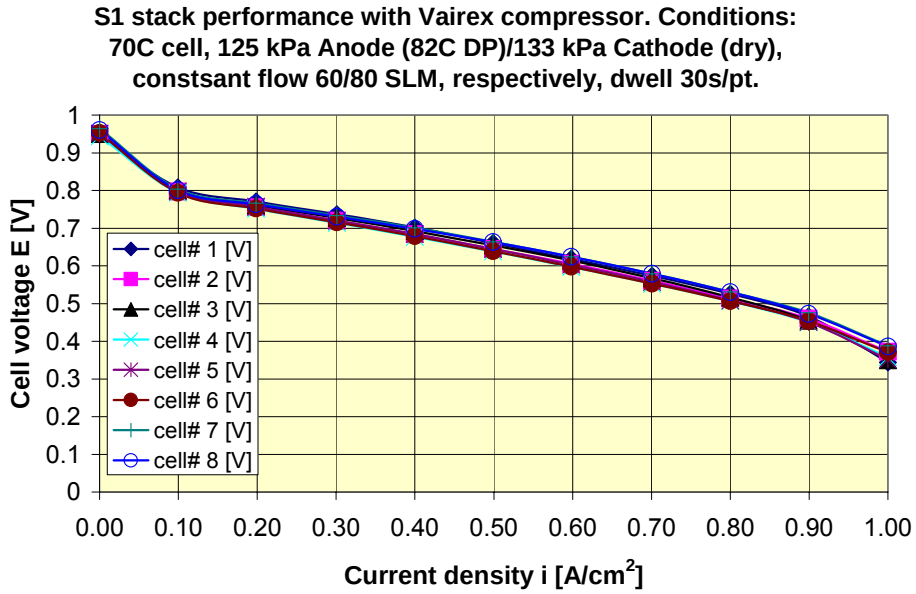

Fig. 10. Stack cell performance with compressor supplied air by mode 1 at conditons shown: 70°C cell, 150kPa pressures, dry cathode, saturated anode, constant flow.

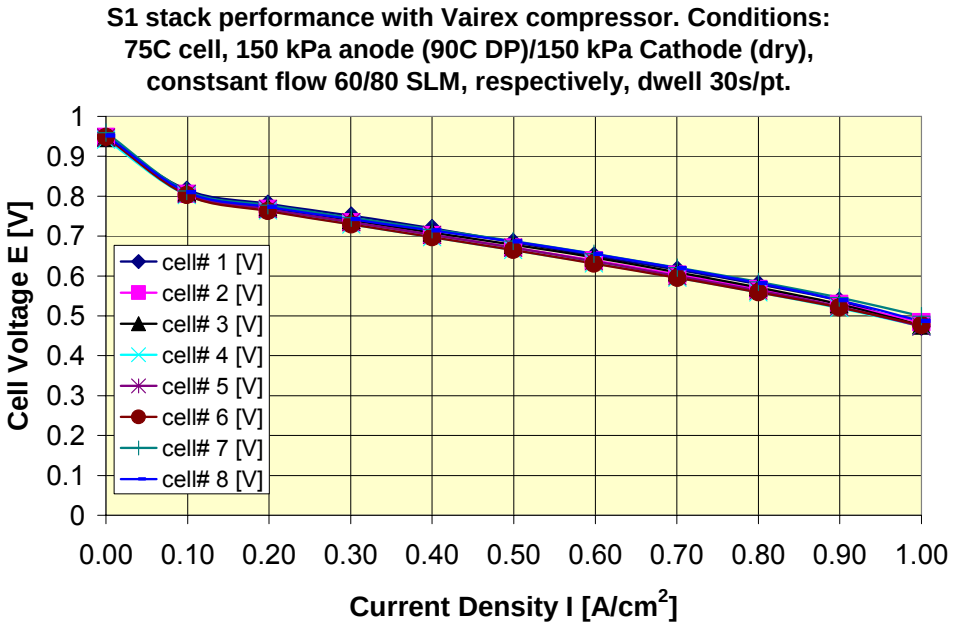

Fig. 11. Stack cell -performance with compressor supplied air by mode 1 at conditons shown: 75°C cell, 150kPa pressures, dry cathode, saturated anode, constant flow.

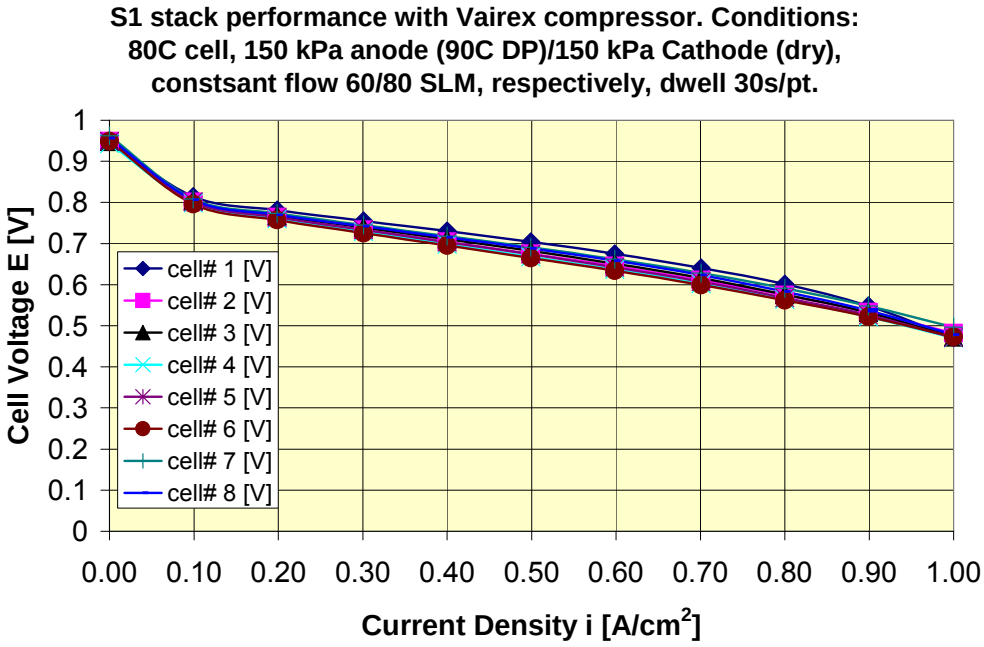

Fig. 12. Stack cell performance with compressor supplied air by mode 1 at conditions shown: 80°C cell, 150kPa pressures, dry cathode, saturated anode, constant flow.

As can be seen from the above figures, the performance of the stack with compressor air supply was stable with minimal cell-to-cell spread under the conditions used.

2.4.3.2.5 Mode 2 Operation

In this mode, the stack flow was controlled by varying the speed of the compressor. All flow generated by the compressor was directed toward the stack and monitored with a mass flow meter. As previously, a section of tubing was added between the compressor and mass flow meter (MFM) to prevent high temperatures of compressed gas from reaching (and possibly affecting) the MFM. The only flow control mechanism employed was altering the air pump motor speed via an increase in supply current to the pump's motor controller. The resultant airflow was monitored by the MFM, and the motor RPMs could be manually adjusted to compensate for changing back-pressure to maintain constant flow rate for a given flow point. Such small adjustments were necessary due to the change in the stack's internal pressure drops resulting from changes in rate of water production and elimination at different points along the polarization curve and transitions associated with moving between those points on the polarization curve. All measurements were performed at 150 kPa stack inlet, both anode and cathode back-pressure settings being controlled by the test station back pressure control circuitry. Flows for individual points on a polarization curve were calculated before hand and arrived at via RPM control as mentioned above. Anode flow was controlled by the test station and set at the constant stoichiometry of 2.0. The cathode flow was compressor controlled and targeted stoichiometries of 1.8 and 2.0 for the two experiments plotted below. Cell temperatures were kept at 70 ºC. Data from these experiments are plotted in Figs. 13 and 14.

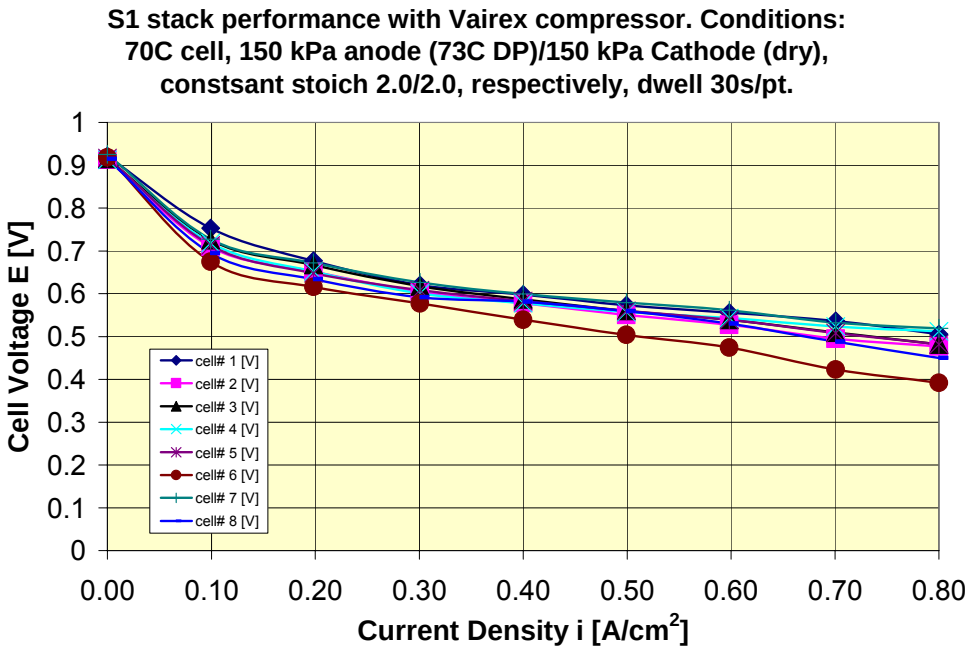

Fig. 13. Stack cell performance with compressor supplied air by mode 2 at conditons shown: 70°C cell, 150kPa pressures, dry cathode, saturated anode, constant stoich.

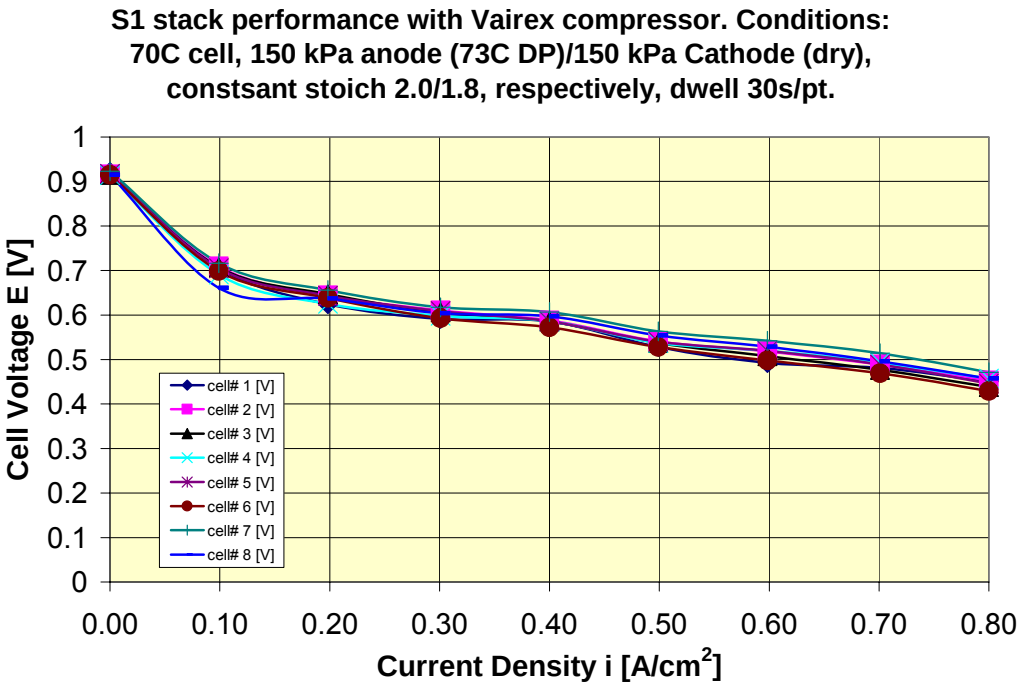

Fig. 14. Stack cell performance with compressor supplied air by mode 2 at conditons shown: 70°C cell, 150kPa pressures, dry cathode, saturated anode, constant stoich.

2.4.3.2.6 Control experiment

In order to verify the correct operation of the stack, control experiments were conducted during a few stages of the experiment. This was done to monitor the health of the stack, and to ensure that only changes related to operating mode and conditions were reflected in the data and not any superimposed changes of the stack's condition itself. To that end, a set of operating conditions were chosen as close to where we would expect to run the compressor, and yet remain within the realm of typical operating conditions for our NSTF catalyst system. The control experiment involved a short pre-conditioning of the stack to equilibrate it with the operating conditions followed by recording of the polarization curve. The operating conditions were as follows: Stack temperature was set at 75 °C, both Anode and Cathode RHs were set to 70°C dew point, inlet pressures were 108 kPa (Anode) and 140 kPa (Cathode), constant flow of fuel and oxidant was employed at 30 SLM and 80 SLM, for Anode and Cathode respectively, and the dwell time was 30 seconds per point. The initial polarization curve (recorded immediately after stack was first built and conditioned) and the one recorded following the completion of compressor experiments can be seen in Fig. 15.

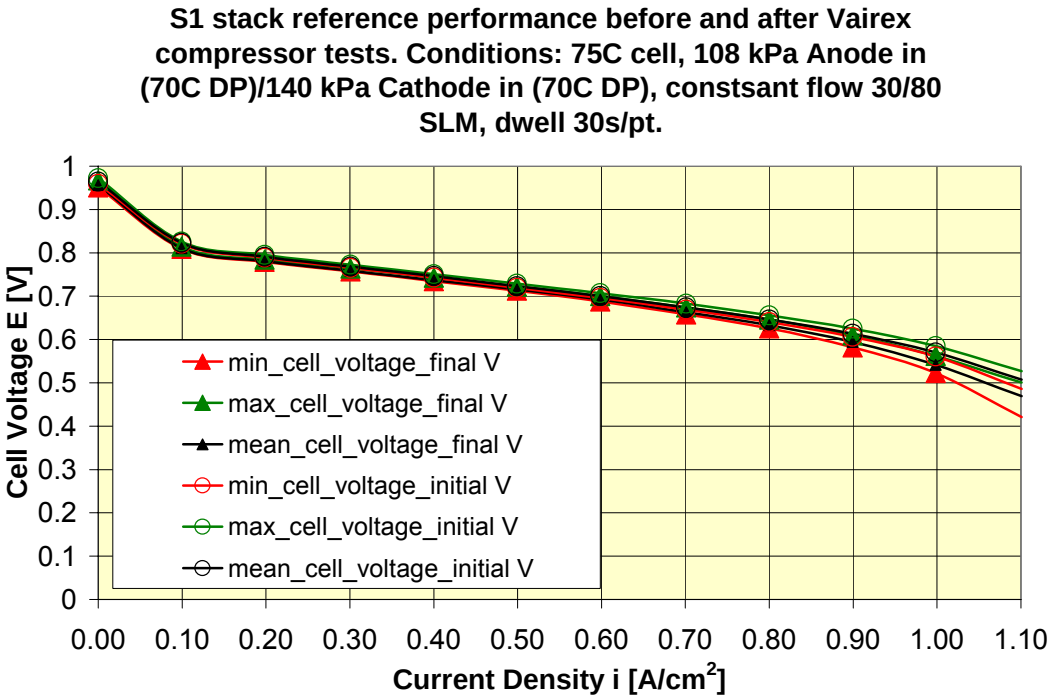

Fig. 15. Comparison of the initial stack performance with that after testing with the compressor, to verify not damage occurred to the stack.

As can be seen, in the current density ranges of interest for this work, virtually no performance changes were observed.

2.4.3.2.7 Conclusions

The main goal of this exercise was to demonstrate the capability to operate an NSTF MEA based fuel cell stack with the VAIREX air compressor providing the air supply. As such the goal of the exercise was achieved and such operation is clearly feasible. It should be however noted that the performance of the stack was sub-optimal. The observed under-performance is related to the operating conditions we were able to operate at while using a compressor, with the compressor clearly limiting available choices. Operating NSTF catalyst based MEA in a dry cathode environment is feasible at higher operating pressures with virtually no loss in performance. Such higher pressures were not achievable with the modified fixed vane compressor, so sub-optimal pressure/operating temperature choices had to be made, and these clearly were reflected in the recorded performance. What would have been possible if humidity control was available for the cathode side was demonstrated in control experiments, where the stack produced 1.4 kW at or near 1.0 A/cm^2. This figure was limited to 1.2 kW at about the same current density for the Mode 1 experiments, where air flow in excess of the cathode flow requirements was allowed (constant flow experiment), but only about 1 kW for the controlled stoichiometry experiment (Mode 2). Such tradeoffs may be practical if one takes into account that the system is considerably simpler with the compressor being the only device to control.

As for the larger objective, of determining the net advantages of operating a stack with a pressure ratio profile more conducive to the MEAs optimum performance, we are not able to draw any firm conclusions from the above tests, due to the limitations of the match between the compressor's operating conditions and the stack's operating conditions and size. Also, the optimum compressor design as discussed in the preceeding section 2.4.2, would have to be developed for a definitive test. There are of course other system components, other than the MEA, whose performance and efficiencies have their own dependencies on pressure, and the actual pressure profiles and turndown ratios would have to be defined with the objective of optimizing the whole fuel cell system performance and efficiency. An attempt to look at this approach with the 3M NSTF MEA developed under this contract was inititated by the DOE fuel cell system modeling group at Argonne National Laboratory, led by Dr. Rajesh Ahluwalia, and is discussed in the final subsection below.

2.4.4 Optimized system polarization curve

2.4.4.1 Introduction

Complete system modeling of fuel cell performances and efficiencies for automotive applications are conducted by the modeling group at Argonne National Laboratory, led by Dr. Rajesh Ahluwalia. Their objective is to incorporate the latest component characteristics developed for MEA, stack and balance of plant components under into their whole-system fuel cell model to judge the gaps between the state-of-the-art performances and DOE targets for 2010.

The ANL group was directed by DOE to utilize the 3M MEA characteristics developed under this contract, into their system models. At the request of ANL, considerable data was provided on the 3M NSTF catalysts and 3M membrane, the development of which is primarily concentrated in sections 2.1 and 2.2 of this report. The following is a summary of the data provided to ANL and a brief review of their conclusions that were

documented in their power point presentation in Appendix VIII and their presentation at the 2007 DOE Annual HFCIT Program Review.

Two system designs were considered, identified as S1 and S2. S1 used a high pressure compressor/expander air management module capable of operating up to 2.5 bar, while the S2 used a VAIREX restricted vane blower capable of 1.5 bar operation and turn-down ratio of 10.

The overall conclusion of the system model using the NSTF/3M PEM MEA is that it enabled the S1 FC system to meet 2010 targets for power densities and come within 2% of target efficiencies at 25% load. These benefits accrued because of lower Pt loadings and higher performance under hotter, drier conditions of the 3M MEA.

2.4.4.2 Data provided to ANL for system modeling

MEA component characteristics were provided to ANL to the extent possible, per their request for the items listed below.

Catalyst (Data for overpotential modeling (preferably with optimized Pt alloy and whisker structure)

- ECSA (m^2-Pt/g-Pt) vs. Pt content
- RRDE or equivalent data for ORR and HOR showing effect of T, $P(O_2)$, $P(H_2)$
- Any data or estimates for electronic and ionic conductivity of catalyst layers?

Polarization curves for stack model development

- Single cell data
- 8-cell data
- 22-cell data
- VI data showing effects of T, P, RH and H_2 and O_2 stoichiometry
- Limiting current data

Fig. 16 below illustrates the single cell data provided for model calibration.

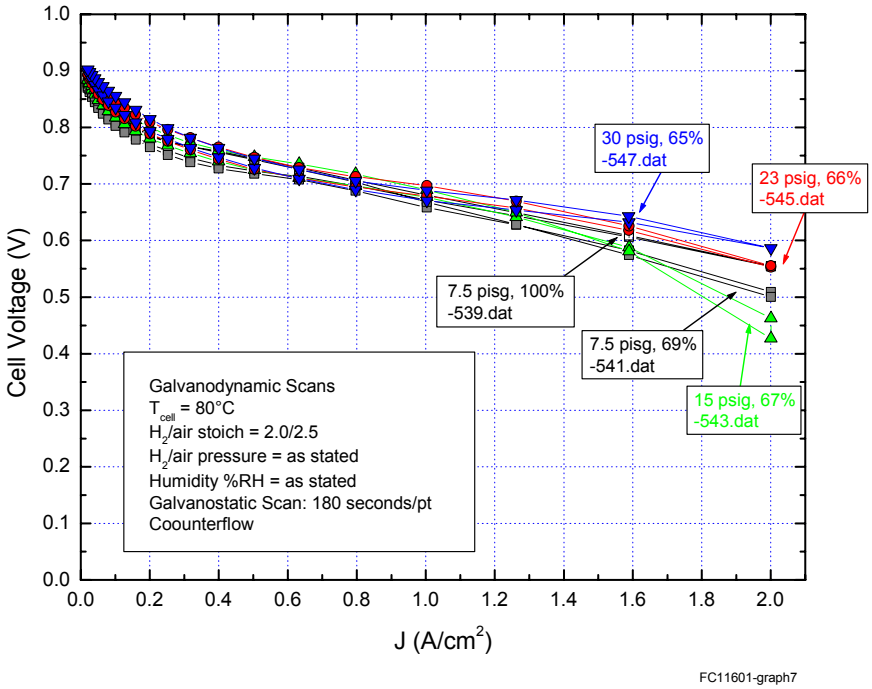

Fig. 16. Example of performance data for the 3M NSTF/PEM MEA provided to ANL for model development.

GDL data (with compression, if available) for water transport model development

- Thickness
- Porosity
- Pore size distribution PSD
- Permeability (k)
- Relative Permeability as function of saturation s: kr (s)
- Hydrophilic / Hydrophobic content and PSD
- PTFE contents
- Micro-porous layer details

Membrane data provided to extent possible

- Thickness (δm)
- Equivalent weight (EW)
- Density (ρm) and membrane swelling (s)
- Water content: λ (RH, T)
- Ionic Conductivity: σ (λ, T)
- Water diffusion coefficient: Dw(λ, T)
- Electro-osmotic drag: ξ (λ)
- H_2 and O_2 cross-over as function of λ and T

With the above information, ANL projected the MEA performance for various system conditions to find the best overall operating conditions. The specific pressure, humidity, and stoichiometry operating maps are given in their summary presentation in Appemdix VIII. The specific pressures and flow rates as a function of current density were provided to 3M and the opportunity was taken to briefly operate the final 22 cell short stack under those conditions, once all the other, required performance tests had been completed, but before the final durability stress testing was completed. The stack tests are described at length in section 4.2 and Appendix VII. Fig. 17 below shows the final stack averaged cell performance under the ANL conditions, and its comparison with the ANL model prediction performance. There is a significant discrepancy in the measured and modeled curves. However, as described at some length in section 4.2 of this report, the final stack build was the second build of the stack, and by the time the testing had been completed, there was substantial plate corrosion and performance degradation, below the initial performance of the MEAs shown in Fig. 16 and on which the modeling was based. So it is expected that without the plate corrosion, the 22 cell stack result would more closely approach that of the ANL model.

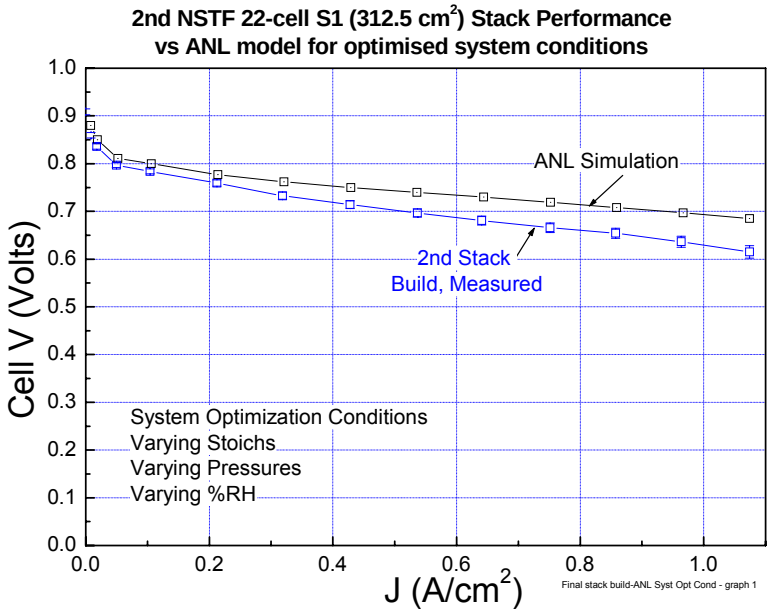

Fig. 17. Comparison of the 22-cell stack test results, operating under the ANL system optimized conditions, with the ANL simulated performance based on the 3M NSTF/PEM MEA. The 2nd stack build performance was below the intial build performance due to plate deterioration.

2.4.5. Specifications for the RT VS100 piston and VV-1020 restrained vane compressors from VAIREX.

VX OIL-LESS RECIPROCATING PISTON

Compressors
3/4 & 1 HP

MODELS:

Standard models available:

VX075HA (184013), VX075HC (184015), VX100HA(184012), VX100HC (184014), VX075HD (184021), VX100HD (184020)

Other models based on availability and minimum purchase.

FEATURES:

- Oil-less design
- High capacity, permanently lubricated and sealed bearings
- All aluminum design
- Enclosed crankcase
- Low operating sound level
- Long, service free life
- Increased field service capability
- High volumetric efficiency
- 90° V-design - low vibration, high efficiency rating, & full rated pressure restart capability

Consult factory for custom applications

DIMENSIONS: Millimeters are in ( )

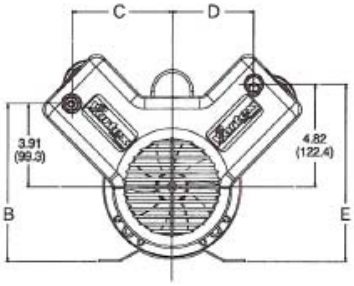

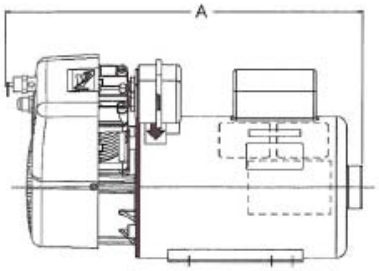

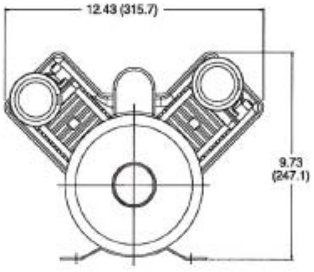

PART NO.	MODEL NO.	A IN. (MM)	B IN. (MM)	C IN. (MM)	D IN. (MM)	E IN. (MM)
184013	VX075HA	15.47 (393.0)	7.44 (189.0)	4.84 (123.0)	3.93 (99.9)	8.35 (212.1)
184015	VX075HC	15.72 (399.0)	7.44 (189.0)	4.84 (123.0)	3.93 (99.9)	8.35 (212.1)
184021	VX075HD	16.72 (424.7)	7.44 (189.0)	4.84 (123.0)	3.93 (99.9)	8.35 (212.1)
184049	VX075HG	17.09 (434.1)	7.41 (188.3)	4.82 (122.5)	3.91 (99.4)	8.32 (211.4)
184012	VX100HA	16.22 (412.0)	7.42 (188.5)	4.82 (122.5)	3.91 (99.4)	8.33 (211.6)
184014	VX100HC	16.22 (412.0)	7.42 (188.5)	4.82 (122.5)	3.91 (99.4)	8.33 (211.6)
184020	VX100HD	17.22 (437.4)	7.42 (188.5)	4.82 (122.5)	3.91 (99.4)	8.33 (211.6)
184050	VX100HG	17.59 (446.8)	7.41 (188.3)	4.82 (122.5)	3.91 (99.4)	8.33 (211.6)

ISO 9001 CERTIFIED

THOMAS®
PUMPS & COMPRESSORS

3/4 & 1 HP PERFORMANCE DATA:

		STANDARD		STANDARD		STANDARD			STANDARD		STANDARD		STANDARD		
MODEL NUMBER:		VX075HA		VX075HC		VX075HD		VX075HG	VX100HA		VX100HC		VX100HD		VX100HG
MANUFACTURING CODE:		184013		184015		184021		184049	184012		184014		184020		184050
HEAD CONFIGURATION:		Pressure Only		Pressure Only		Pressure Only		Pressure Only	Pressure Only		Pressure Only		Pressure Only		Pressure Only
PRESSURE:		Flow @ 115V/60/1 Hz		Flow @ 230V/60/3		Flow @ 230V/50/1		Flow @ 200V/50/3	Flow @ 115V/60/1 Hz		Flow @ 230V/60/3		Flow @ 230V/50/1		Flow @ 200V/50/3
CFM @ PSI	LPM @ bar														
PSI	bar	CFM	LPM	CFM	LPM	CFM	LPM	CFM LPM	CFM	LPM	CFM	LPM	CFM	LPM	CFM LPM
0	0.0	5.94	152.9	5.94	152.9	5.10	144.4	5.10 144.4	6.20	175.6	6.20	175.6	5.17	146.4	5.17 146.4
5	0.5	5.70	144.7	5.70	144.7	4.86	134.4	4.86 134.4	6.03	168.5	6.03	168.5	4.96	137.8	4.96 137.8
10	1.0	5.46	135.4	5.46	135.4	4.61	124.4	4.61 124.4	5.85	161.3	5.85	161.3	4.75	129.2	4.75 129.2
15	1.5	5.22	127.3	5.22	127.3	4.37	115.3	4.37 115.3	5.68	154.1	5.68	154.1	4.54	121.4	4.54 121.4
20	2.0	4.98	122.3	4.98	122.3	4.12	109.3	4.12 109.3	5.50	146.9	5.50	146.9	4.33	116.7	4.33 116.7
25	3.0	4.81	109.8	4.81	109.8	3.98	98.3	3.98 98.3	5.33	133.8	5.33	133.8	4.21	107.7	4.21 107.7
30	5.0	4.64	84.6	4.64	84.6	3.83	80.8	3.83 80.8	5.15	116.4	5.15	116.4	4.10	92.4	4.10 92.4
35	7.0	4.47	69.9	4.47	69.9	3.69	64.6	3.69 64.6	4.98	98.5	4.98	98.5	3.98	76.4	3.98 76.4
40		4.29		4.29		3.54		3.54	4.80		4.80		3.86		3.86
50		4.01		4.01		3.34		3.34	4.59		4.59		3.70		3.70
60		3.72		3.72		3.14		3.14	4.38		4.38		3.54		3.54
80		3.18		3.18		2.68		2.68	3.95		3.95		3.10		3.10
100		2.72		2.72		2.31		2.31	3.51		3.51		2.71		2.71
125		2.16		2.16		1.81		1.81	3.02		3.02		2.43		2.43
145		1.70		1.70		1.44		1.44	2.70		2.70		1.95		1.95
MAX. CONTINUOUS PRESSURE:		125 PSI		125 PSI		125 PSI		125 PSI	125 PSI		125 PSI		125 PSI		125 PSI
MAX. INTERMITTENT PRESSURE:		145 PSI		145 PSI		145 PSI		145 PSI	145 PSI		145 PSI		145 PSI		145 PSI
MAX. AMBIENT AIR TEMP.:		40°C		40°C		40°C		40°C	40°C		40°C		40°C		40°C
MIN. AMBIENT START TEMP.:		0°C		0°C		0°C		0°C	0°C		0°C		0°C		0°C
MAX. RESTART PRESSURE:		125 PSI		125 PSI		125 PSI		125 PSI	125 PSI		125 PSI		125 PSI		125 PSI
MOTOR VOLTAGE/FREQUENCY:		115/230/60/1		230/460/60/3		230/50/1		200/400/50/3	115/230/60/1		230/460/60/3		230/50/1		200/400/50/3
HORSEPOWER:		3/4		3/4		3/4		3/4	1		1		1		1
MOTOR TYPE:		Capacitor Start		Polyphase		Capacitor Start		Polyphase	Capacitor Start		Polyphase		Capacitor Start		Polyphase
CURRENT AT RATED LOAD (AMPS):		13/6.5		4.0/2.0		6.4		3.0/1.5	15.8/7.9		5.4/2.7		7.8		4.4/2.2
POWER AT RATED LOAD (WATTS):		850		850		800		800	1250		1250		1200		1200
STARTING CURRENT (LOCKED ROTOR, AMPS):		65/32.5		20/10		32		15/7.5	79/39.5		27/13.5		39		22/11
INSULATION CLASS:		B		B		B		B	B		B		B		B
MIN. FULL LOAD SPEED (RPM):		1725		1725		1425		1425	1725		1725		1425		1425
THERMAL PROTECTOR:		Yes		No		Yes		No	Yes		No		Yes		No
NET WEIGHT:		43.0 lbs.	19.5 Kg	43.0 lbs.	19.5 Kg	43.0 lbs.	19.5 Kg	43.0 lbs. 19.5 Kg	45.0 lbs.	20.4 Kg	45.0 lbs.	20.4 Kg	45.0 lbs.	20.4 Kg	45.0 lbs. 20.4 Kg
SHIP WEIGHT:		48.0 lbs.	21.8 Kg	48.0 lbs.	21.8 Kg	48.0 lbs.	21.8 Kg	48.0 lbs. 21.8 Kg	50.0 lbs.	22.7 Kg	50.0 lbs.	22.7 Kg	50.0 lbs.	22.7 Kg	50.0 lbs. 22.7 Kg

The information presented in this material is based on technical data and test results of nominal units. It is believed to be accurate and reliable and is offered as an aid to help in the selection of Thomas products. It is the responsibility of the user to determine the suitability of the product for his intended use and the user assumes all risk and liability whatsoever in connection therewith. Thomas Industries does not warrant, guarantee or assume any obligation or liability in connection with this information.

Note: Models pictured are representative of the series and do not represent a specific model number. Consult factory for detailed physical description.

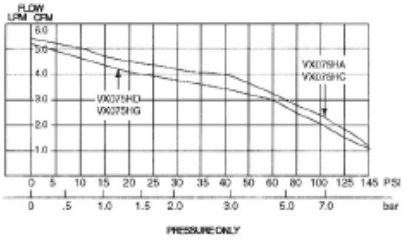

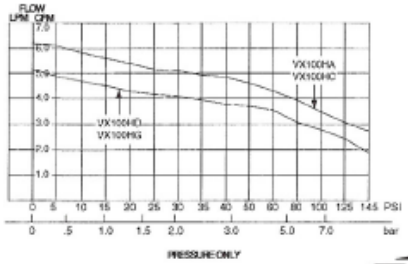

THOMAS®
PUMPS & COMPRESSORS

1419 Illinois Avenue, P.O. Box 29
Sheboygan, WI 53082-0029 USA
(920) 457-4891 Fax (920) 451-4276
Internet: http://www.thomaspumps.com

Printed in U.S.A. Form No. 850-2584 5/03

VV-1020 HT

VAIREX corporation

SPECIFICATION

Description:

The Model VV-1020 Air Delivery System incorporates *VAIREX* proprietary dry-vane technology. The Air Delivery System consists of a VAIREX vane pump, integrated brushless dc motor, motor speed controller.

Specifications

System type: *VAIREX* model VV-1020 HT, dry, fixed vane

Outputs: 1) pressurized air.

Output ratings	Min	Max	Peak [1]	Units
Output 1, Pressure [2]	1.1	2.0 (@10g/s)	2.2	ratio
Output 1 Mass Flow [3]	2	20 (@1.1 P/p)	22	grams/sec
Noise, Acoustic		<75		dB A
Output temperature delta	0	120		°C
Compressor Speed	0	2500	2700	RPM
Motor Speed [4]	0	2500	2700	RPM
Inputs				
Control voltage [5]	0	5		Volts DC
Atmospheric Air [6]				
Inlet pressure range	10.3	15.1		psia
Inlet temperature	-20	40		°C
Inlet humidity [7]	0	100		% R.H.
Voltage range	46	50		Volts DC
Current range [8]	0	40		Amps
Precision				
Speed control precision	2.5	2.5		+/- %
System Parameters				
Total power consumption	0	1600		watts
Total volume (Pump/Motor)		6.0		liters
Total volume (Controller)		0.7		liters
Total weight (Pump/Motor)		19.0		kg
Total weight (Controller)		0.4		kg
Maintenance interval	500	1000		Hours [9]

Notes:

1) Air Delivery System is limited in peak parameters for 30 seconds operation, not more than once per hour.
2) The output shall be capable of achieving a pressure ratio of the specified value. Pressure from the air delivery system shall be controlled by the downstream backpressure provided by the customer's device. Peak output pressure shall be limited to 110% of maximum operating pressure.
3) Flows at output 1 are standardized for 25 °C inlet temperature, 14.7-psia inlet pressure.
4) Motor speed may be limited by max compressor speed.
5) 0.5 – 5.0 volts for pulse-width-modulation control, 5.0 – 10.0 volts for simple commutation control.
6) Ambient supply of air shall be free of particulate matter greater than 20 microns in size.
7) Non-condensing
8) Max operational line amperage is contingent on applied voltage (i.e. @ 48 volts Imax ~35amps)
9) Duration at 100% Duty Cycle (2500 rpm, 2.0 pressure ratio).

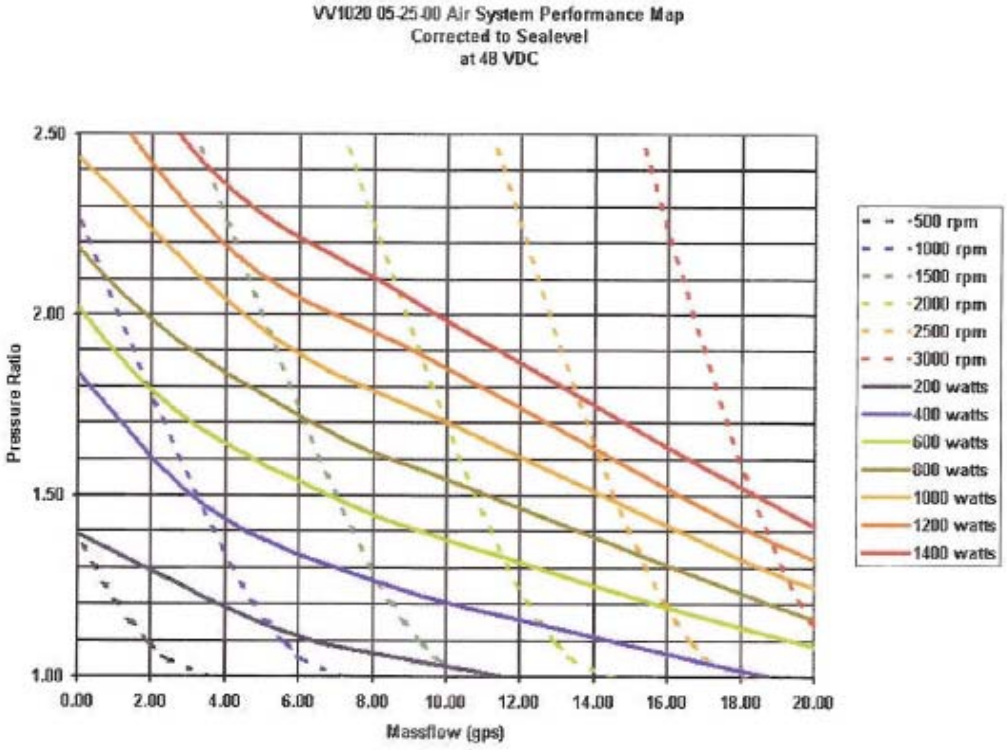

Section 2.5 Advanced MEA Modeling

This section summarizes the work done under Task 1.2 with the U. of Miami, directed at adapting a 3D MEA model to work with the ultra-thin 3M nanostructured thin film (NSTF) electrode structures and extending it to properly account for aspects of two phase humidified gases.

Table of Contents for Section 2.5

2.5 Advanced MEA modeling

2.5.0 Introduction

Understanding the steady state environment within an operating PEM fuel cell, either locally or globally, is a signficant challenge. The interplay of the dynamic physical, chemical and electrochemical processes taking place within the principal PEM, GDL and electrode components, or at their interfaces, presents mulitple levels of complexity. The spatial non-uniformity of the reactants (H_2 and air) and reaction products (water) as a function of current generation present another level of complexity. The strong dependence of the physical state of the water on local temperature, pressure and humidity, and their variability with the operating load state of the fuel cell system is still another level. Attempts to measure the local conditions internal to the fuel cell, or worse, internal to the MEA, are fundamentally limited by the difficulty of access to components that are extremely thin without disturbing the process parameters of interest, or the existence of suitable probes to measure those parameters.

These experimental needs and difficulties are the drivers for the use of mathematical modeling tools to try and simulate the processes and reactant states at any point within the fuel cell, its flow fields or most important, it's MEAs. Today's computational fluid dynamic codes are highly reliable predictors of the steady state three dimensional (3D) environment within the fuel cell manifolds and flow fields.[1] Predicting the electrochemical states of the components, electric and reactant current distributions under load conditions within those components is quite another matter. Mathematical fuel cell MEA models have become increasingly sophisticated since their first development as one-dimensional problems[2], or analytical solutions[3], and more focused on trying to develop a full 3D capability that can address two-phase flow.[4] Two-phase flow refers to the vapor and liquid states of water, the relative degrees of which can dictate whether a fuel cell is running too dry or too wet. It is assumed that if one had an accurate, fast and verifiable mathematical model of an MEA, it would lead to a more comprehensive understanding of how to design the components for optimized performance and durability.

The University of Miami has had a dedicated effort since about 1995 to develop a comprehensive computer model of a PEM fuel cell using their unified domain approach.[4] 3M supported research and development of the modeling work at U. of Miami for two years prior to the start of work on this contract. The work continued under this contract beginning formally 3rd quarter, 2003, with the goal of extending the model capabilities to include various different fuel cell designs and materials, including the ultra-thin NSTF electrodes, and improving the model's capability to handle two-phase flow within the various components.

2.5.1 Task objectives

The model development work with the U. of Miami was done under Task 1.2 of this cooperative agreement. A key objective of the work was to develop the model sufficient to provide insight into the effects of operating conditions and internal MEA properties on fuel cell performance. Under the previous work (solely funded by 3M) with Prof. Hongtan Liu, the U. of Miami 3D modeling capability was adapted for simulating the local reactant, temperature and flow conditions within the fuel cell active area and within the catalyst electrode areas and membrane of 3M's GEN 1 commercial MEA, based on conventional

Pt/C catalyst technology and membrane ionomer. For the current cooperative agreement, three subtasks were originally proposed.

2.5.1.1 Subtask 1

The first subtask was the model's extension and improvements. This included extending it to handle specifically new membrane materials and the ultra-thin 3M nanostructured thin film (NSTF) electrode structures. It was also originally planned to extend the model from a single 3D channel to a serpentine flow field design, if computation times could be made practical. Extending it to more completely account for measurable component property parameters and properly accounting for aspects of two phase humidified gases were other milestones. This would require coupling the energy equation with two-phase flow to account for evaporation and condensation. If it could be achieved, then the water and temperature distributions within the cell could be predicted, and that would in principle help determine key GDL and flow field requirements for stable operation of the NSTF MEA under dry, high temperature conditions, or cool start conditions. Incorporating these extensions would force a balance between complexity and practical usability. Near the end of this subtask, a version of the code was supplied to 3M and collaborative work continued at both 3M and the U. of Miami to meet the objectives of subtask 2.

2.5.1.2 Subtask 2

The second subtask was model verification. This work required collaboration with 3M experimentalists to provide fuel cell performance data and MEA component properties for calibration and verification of the model. It also involved close collaboration with the 3M modeler to develop tools around the U. of Miami codes for multi-processor execution, automated parameter sweeps, iterative execution to obtain results for desired voltages, and post–processing; additionally, the 3M modeler performed detailed model verification and made suggestions for ways to obtain faster convergence.

2.5.1.3 Subtask 3

The final subtask focussed on design optimization. Once verified by direct comparison to experimental data, the model was used to perform various studies to find the impact of various operational and material parameters on the steady state conditions within the cell flow field and MEA itself.

2.5.2 U. of Miami 3D model

The U. of Miami 3D model[4] solves the equations of continuity, momentum, energy, and species concentrations in different elements (membrane, channel, microporous layer, electrode backing layer, catalyst layer) of the fuel cell MEA and flow-field. It includes as well the equations for phase potential in the membrane and the catalyst layer. This set of governing equations, coupled with the electrochemical reaction kinetics, can be solved simultaneously in coupled domains without prescribing any arbitrary boundary conditions at the various interfaces between the different MEA/Cell elements. The output from the 3D model includes detailed distributions of oxygen, hydrogen, and water concentrations within the fuel cell, as well as distributions of local current density, temperature and of course, polarization curves.

Fig. 1 illustrates the geometry of the basic 3D model cell. It consists of a single, long channel from inlet to outlet. The model assumptions are: a) the gas mixtures act as perfect gases and are incompressible, b) in the GDL and gas channel the volume of liquid water is negligible, c) flow is laminar everywhere and only the steady state case is considered, and d) the GDL, catalyst layers and PEM are considered as isotropic porous media. The cell temperature is taken as the boundary condition imposed on the collector plates.

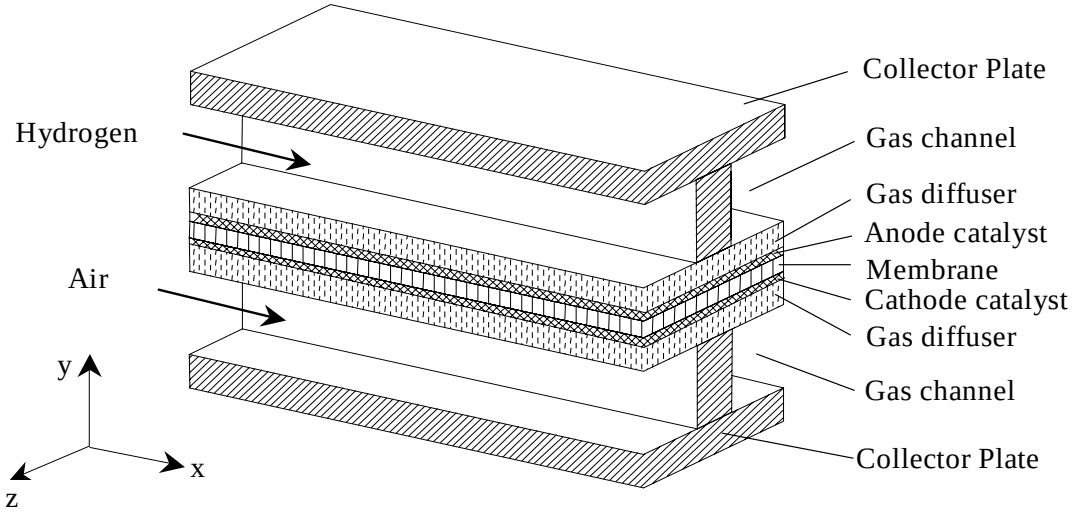

Fig. 1. Geometry of the University of Miami model.

Such a model allows looking in detail in three dimensions, within the MEA, to understand local conditions at any point within the catalyst layers, membrane, gas channels, under the lands to predict: a) polarization curves under varying conditions, b) local current density distributions, c) local oxygen and hydrogen mole fractions, d) water vapor concentrations, e) local temperature distributions.

For all the model work done several other assumptions were made as well: any overpotential from the anode could be ignored assuming the flow and and reaction rates were sufficient; density of the gases and viscosity are not functions of temperature; cross-over through the membrane was ignored; and a linear H_2O profile across the membrane was assumed, as opposed to a more complex shape.

A full 3D model can be reduced or simplified by using a simple parabolic flow profile in the channel and GDL together, with a slip condition introduced at the inerface of the GDL and the gas channel. The velocity field is found to be little different for the two cases. Of course other simplifications that may be useful are a reduction to two-dimensions (pseudo 3D) in which there is no GDL/land interface, and assuming only single phase reactants. These simplifications can be necessary as other complexities are incorporated, such as the ultra-thin electrodes, which affect mathematical convergence and computation time. For a straight mono-channel model, the in-plane permeability or conductivity of the GDL is not opperative since there is no diffusion over the land between channels. This is also true for the 2D version of the model, since only the active area over the channel is considered. As shown below, most of the information to improve and extend the model were done in 2D because it was much faster and did not compromise the factors being improved upon.

2.5.3 Baseline Model inputs

The baseline model was the version available at the start of the contract that had been adapted to the 3M conventional MEA in the prior two years. Variables in the input files of the baseline version of the model included the channel dimensions (length, width and depth), the MEA layer thicknesses (PEM, catalyst, GDL), porosities (GDL and catalyst layer), tortuosities(GDL and catalyst layer), ionomer content of the catalyst layer, thermal properties (κ, c_p) of the gases and materials, inlet conditions (pressure, temperature, flow rates, reactant percentage, and relative humidity), ionomer conductivity, exchange current density and active area of the catalyst, cell temperature and the overpotential.

2.5.4 Model improvements and extensions

Several improvements and extensions to the baseline model were identified as desirable or necessary for applicability to the intended needs of this contract. These included:

- Adding 2-phase effects in the GDL
  - Energetics of condensation/evaporation (Energy coupling with partial saturation humidification model)
  - Blockage from liquid water (reduction in effective porosity)
- Adding thermal effects of water evaporation and condensation
- Adding electrical resistance of both anode and cathode catalyst layers
- Adding electrical resistance of both anode and cathode GDL layers
- Account for heat generated by IR loss in the catalyst and GDL layers
- Account for ionic resistance of ionomer in the catalyst layers
- Improve the algorithm relating membrane conductivity and humdification
- Extending the model to handle extremely thin electrode layers, with the constraint that the model geometric domain-cell size is fixed.
  - Use effective porosity and tortuosity for proper gas diffusion rate
  - Use Henry's law to determine oxygen concentration in liquid water and hydrated membrane material
  - Calibrate with specific NSTF data

Most of these changes were successfully incorporated, as illustrated in the subsections below, and some features had a greater impact than others. Most of the iterative changes were made to the baseline model for the thick electrode (conventional dispersed Pt/C type electrodes) MEA, while the challenges with the ultra-thin model could be addressed separately.

Table I lists chronologically the code versions delivered to 3M and their differentiation according to the type of catalyst electrode, 2-D or 3-D, and whether they were set up for constant flow or constant stoichiometry.

The extension of the code to treat the ultra-thin NSTF electrode was the most difficult aspect, due to both data calibration and software issues relating to convergence, particularly with regard to energy dissipation in the catalyst layer. After much study of the results and codes, it was determined by U. of Miami that the simulations for the temperature profiles in the electrodes could not be made to converge or converge to physically correct values. This had its origins in the combination of an extremely large positive source term in the energy equation and very large aspect ratios of the domain grid, both a consequence of the NSTF layer thinness. Together these effects prevented the energy equation from converging. In

the end, it was necessary to constrain the catalyst layer to be isothermal to get the required model convergence, which is the meaning of the isothermal versions at the end of Table I. This necessitated in turn ignoring evaporation.

Another difference in the way the model had to be changed when adapting from the thick layer (Pt/C) case to the thin layer (NSTF) case had to do with the way the diffusivity changes at the interface of the electrode and GDL in order to obtain smoothly varying reactant concentrations across the interface. The extreme thinness of the catalyst layer relative to the GDL thickness led to a disproportion of the boundary finite volume belonging to the GDL and that to the catalyst layer. More specifically, for thicker catalyst layers, one can assume the diffusivity changes linearly from a (catalyst) value within the catalyst layer grid cell to the (GDL) value within the adjacent GDL grid cell at the catalyst/GDL interface boundary. For the thin NSTF layer, this approximation could not be used, and another effective medium approximation had to be used.

Table I. MEA modeling code versions received from U. of Miami.

Year	Month	Day	Disp Constant Stoichiometry	Dispersed Constant Flow	NSTF Constant Stoichiometry
2003	11	25		2D, 3D	
2003	12	10	2D, 3D	2D, 3D, GUI	
2003	12	19	2D, 3D	2D, 3D	
2004	01	07	2D	2D	
2004	01	16	3D	3D	
2004	01	27	2D	2D	
2004	04	14		2D	
2004	06	25	2D	2D, 3D	
2004	07	21	2D	2D, 3D	
2004	12	16	2D	2D, 3D	
2005	02	09	2D	2D	
2005	03	17	2D, 3D	2D, 3D	
2005	04	04			2D, 3D
2005	05	16	3D	3D	
2006	01	11		2D	
2006	02	03		3D, GUI	2D, 3D
2006	07	11			3D isothermal
2007	01	10			2D 3D, isothermal

It was also found necessary to adjust the exchange current density and charge transfer coefficient, α = 1, in the Butler-Volmer equation to match the data and the 70mV/decade Tafel slope. This value of unity for the charge tranfer coefficient, α, has also been recently reported in the literature as most appropriate for fuel cell electrodes demonstrating only one Tafel slope.[5]

2.5.5 Experimental data provided for NSTF thin layer model calibration

The initial data provided to U. of Miami for calibration of the NSTF-code versions, was constant stoichiometric data, at CS = 2 and 2.5. This is discussed in 2.5.5.1. This range of stoichiometry however was eventually found to be too large for good calibration, and a series of constant flow data had to be provided later to complete the calibration. This data set are the four samples discussed in section 2.5.5.2.

2.5.5.1 FC8565 and FC8676

The key data used for initially calibrating the ultra-thin U. of Miami model was that summarized in Figs. 2 and 3 below, for FC8565, and FC8676. FC8565 was previously discussed in section 2.1.5.3 of this report as an example of the thinnest NSTF electrode

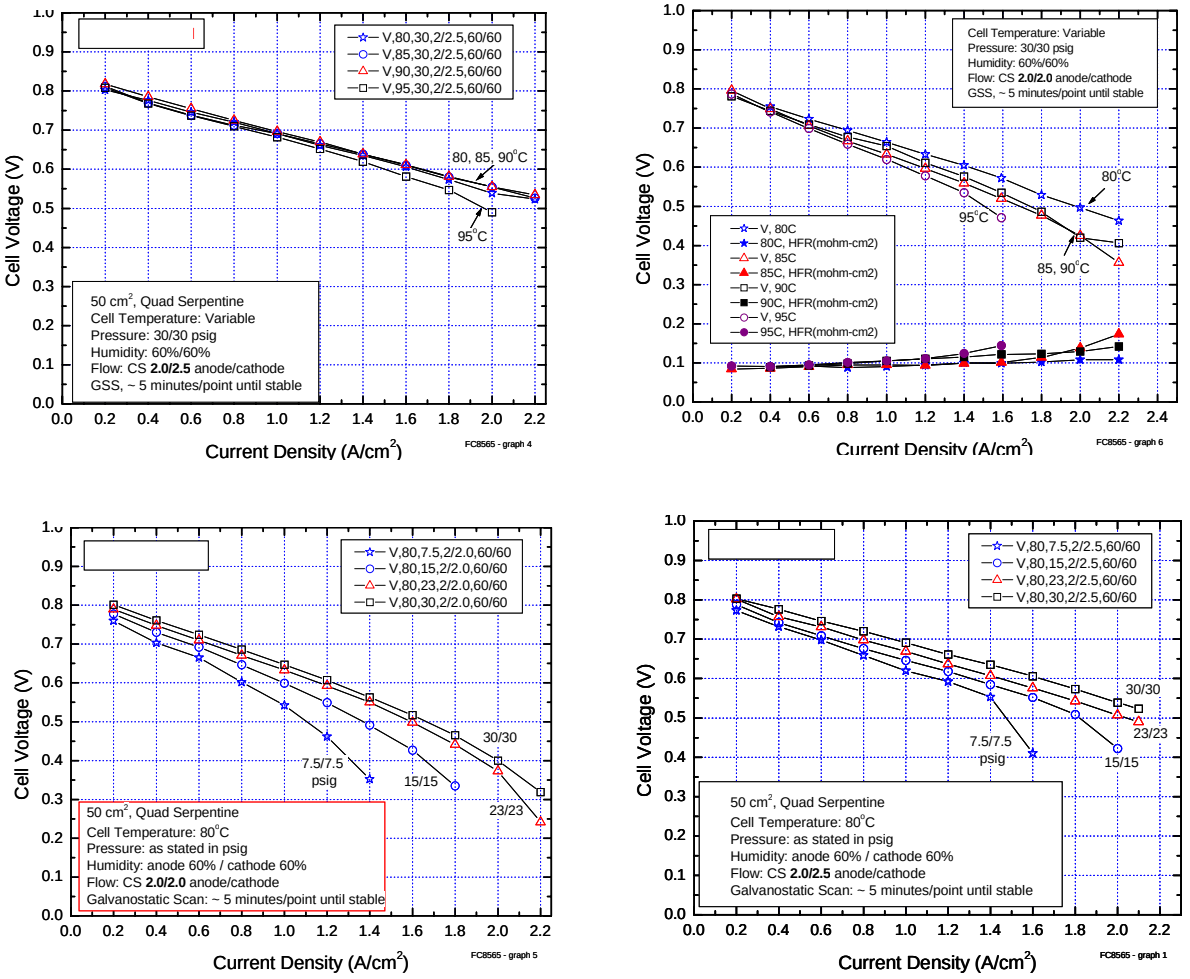

Fig. 2. FC8565 data used to calibrate the NSTF ultra-thin layer electrode version of the U. of Miami model.

layer made, 0.27 microns, which exhibited negligible mass transport losses at 2 A/cm^2 under pressurized air. FC8676 on the other hand was one of the thickest, at 0.67 microns, and would exhibit a different degree of mass transport losses in the electrode layer. Fig. 3 shows just one comparative set of data from FC8676, which when compared to FC8565, is clearly seen to be performing at a lower level. This MEA had a PtCoFe ternary instead of the PtCoMn, which also would contribute to its lower performance, as discussed at length in section 2.1.3.

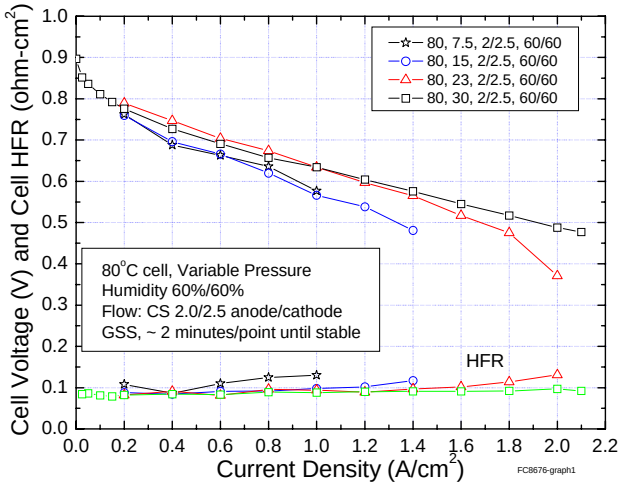

Fig. 3. Part of the FC8676 data used to calibrate the NSTF ultra-thin layer electrode version of the U. of Miami model. The same complete data set as taken as for FC8565.

2.5.5.2 FC10062, FC10073, FC1062, FC10095

For the new calibration data set, specific measurements were done with four types of NSTF MEAs. They used two types PtCoMn ternary catalyst on the cathode (see section 2.1.3 in this report for identification) at a loading of 0.1 mg/cm^2, the acid-washed 3M membrane (see section 2.3.1 in this report) and two types of GDL- a carbon paper and a carbon cloth. The conditions for all four included fixed anode flows at 800 sccm; cathode flows of 500, 1000, 1500 and 2000 sccm; and H_2/air inlet humidities of 60%RH and saturation. Fig. 4 shows a the data set from one of the MEAs, FC10095, comparing the effects of cathode flow rate at ambient and 15 psig pressure and 60% and 100% RH, for the MEA with the carbon paper GDL.

In Fig. 4 there clearly is a strong tendency for flooding with this particular paper GDL, and it was chosen as much for this impact. In constrast, the MEAs with the carbon cloth type GDL performed much better at all conditions, but most notibly at the saturated 15 psig condition for which the water removal rate is lease effective. This comparison is made in Fig. 5 between two MEAs each with a different GDL type. Whereas at the highest constant flow rate, the limiting current of the cathode of the MEA with the carbon paper GDL can barely exceed 1 A/cm^2 , that with the cloth GDL can reach 1.6 A/cm^2. This is not an intrinsic property of cloth versus carbon paper, since some carbon papers can perform even better then the carbon cloth used in this example. It also depends strongly on the type of hydrophoization treatment of the electrode backings. The intent was to provide as wide a range of performance as possible for calibration purposes of the model.

Since the primary issues were related to the effective diffusivity and porosity of the GDL and catalyst layers, generating data with GDLs having two widely varying permeabilities was the startegy.

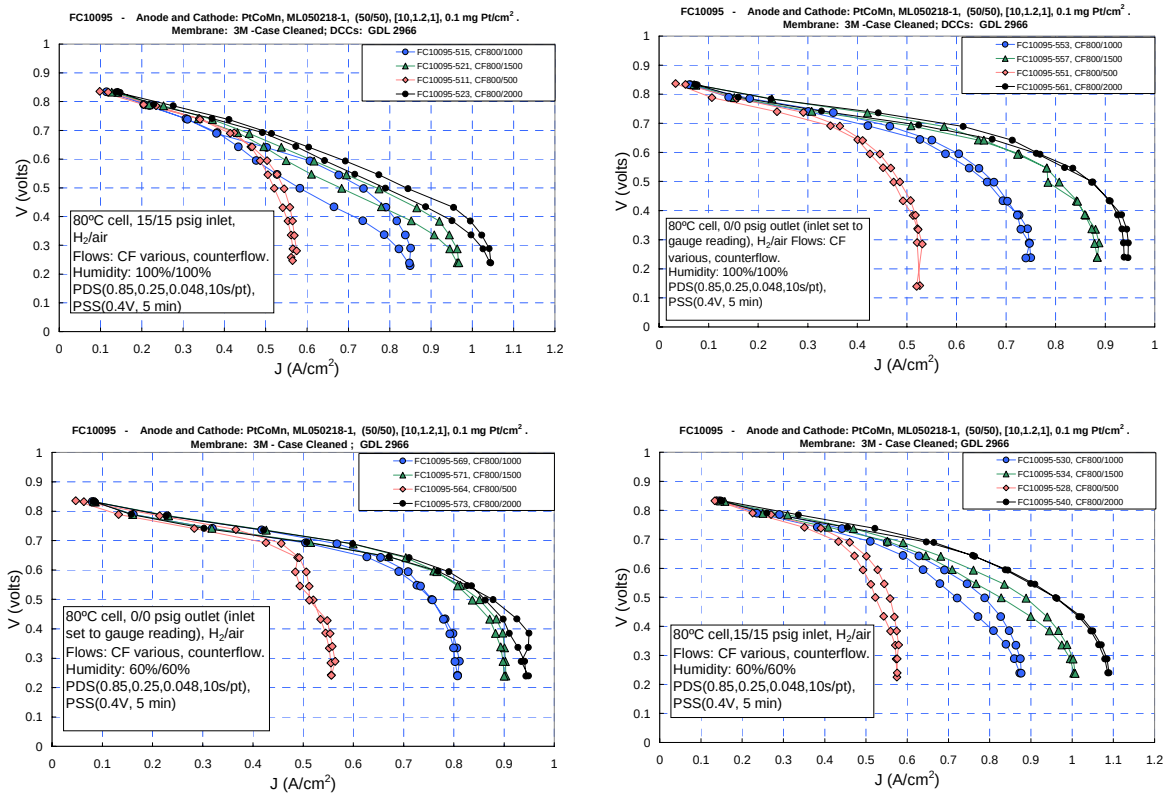

Fig. 4 Constant flow data set for calibration of the ultra-thin layer electrode model, from one of four MEAs tested with the carbon paper type GDL.

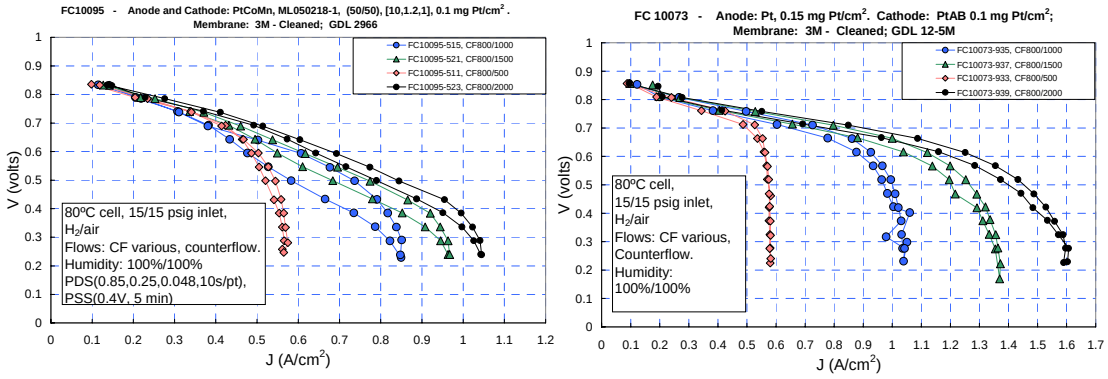

Fig. 5 Comparison of the effect of the GDL type on the constant flow potentiodynamic polarization curves at 15 psig pressure and saturated inlets, used as calibration data for the NSTF thin layer model: (left) carbon paper type GDL; (right) carbon cloth type GDL.

2.5.6 Example simulations of model extensions by U. of Miami

Over the course of the project, Dr. Tianhong (Amy) Zhou and Prof. Hongtan Liu, Department of Mechanical Engineering, University of Miami, carried out various studies with their model after incorporating the the various extensions discussed above. These included comparisons of interdigitated flow field versus channel; justification of using a 2D versus a 3D model; co-flow versus counter-flow; effects of electrical resistance of the catalyst and GDL layers; single phase versus two-phase flow; and a model calibration study comparing results for the ultra-thin catalyst layer with those from the baseline dispersed MEA results.

Since many of these were developmental studies on the path to incorporating the model extensions, many of the results were preliminary studies. The following is a sampling of the of some of the results from a few key reports which relate most closely to the project objectives. Again, all the model extensions were done with the thick catalyst layer type of MEA.

2.5.6.1 Co-flow versus counter-flow

As discussed in section 2.3.3.1, the direction of reactant flow can be very important when operating with dry or subsaturated inlet gases. Counter-flow, in which the hydrogen and air flow in opposite directions in channels across the MEA from each other, allows significantly better operation for either an NSTF MEA or an MEA with dispersed catalyst electrodes. One of the model extensions was to allow for counter-flow conditions. U. of Miami incorporated this feature in a dispersed MEA code version (prio to those in Table I) and demonstrated the effects with eight comparative cases, viz. four for co-flow and four for counter-flow. For each configuration, the four subcases were a) anode saturated, cathode saturated, b) anode saturated, cathode dry, c) anode dry, cathode saturated, and d) anode dry, cathode dry.

Again there are too many figures to include to illustrate all eight of the configurations, but Fig. 6 compares a set of polarization curves for each of the four conditions for counter-flow (top) and co-flow (bottom). The counter flow cases are better whenever one of the inlets is dry.

Fig. 7 compares the local current density distribution at ~ 0.65V when the anode is dry and the cathode saturated, for counter-flow (left) and co-flow (right). Here it is very clear there is a different current distribution along the channel for the two flow configurations, with the counter-flows averaged current density of nearly 0.59 A/cm^2 significantly exceeding that of the 0.47 A/cm^2 from the co-flow case.

Fig. 8 and 9 compare the water vapor concentration at the cathode, anode and liquid water content within the membrane when the anode is dry and cathode saturated for counter-flow (Fig. 8) and co-flow (Fig. 9). The higher water content in both the cathode and the membrane are predicted for the counter-flow case.

The conclusions from considering all eight configurations were:
1) when the anode is dry, counter-flow will improve performance as the water diffuses from the cathode to the anode,
2) when the anode is fully saturated, counter-flow will not have much infuence on the fuel cell performance, for either state of the cathode, and
3) in both co-flow and counter-flow cases, while a dry cathode reduces the fuel cell performance, the dry anode inlet will lead to the worst performance.

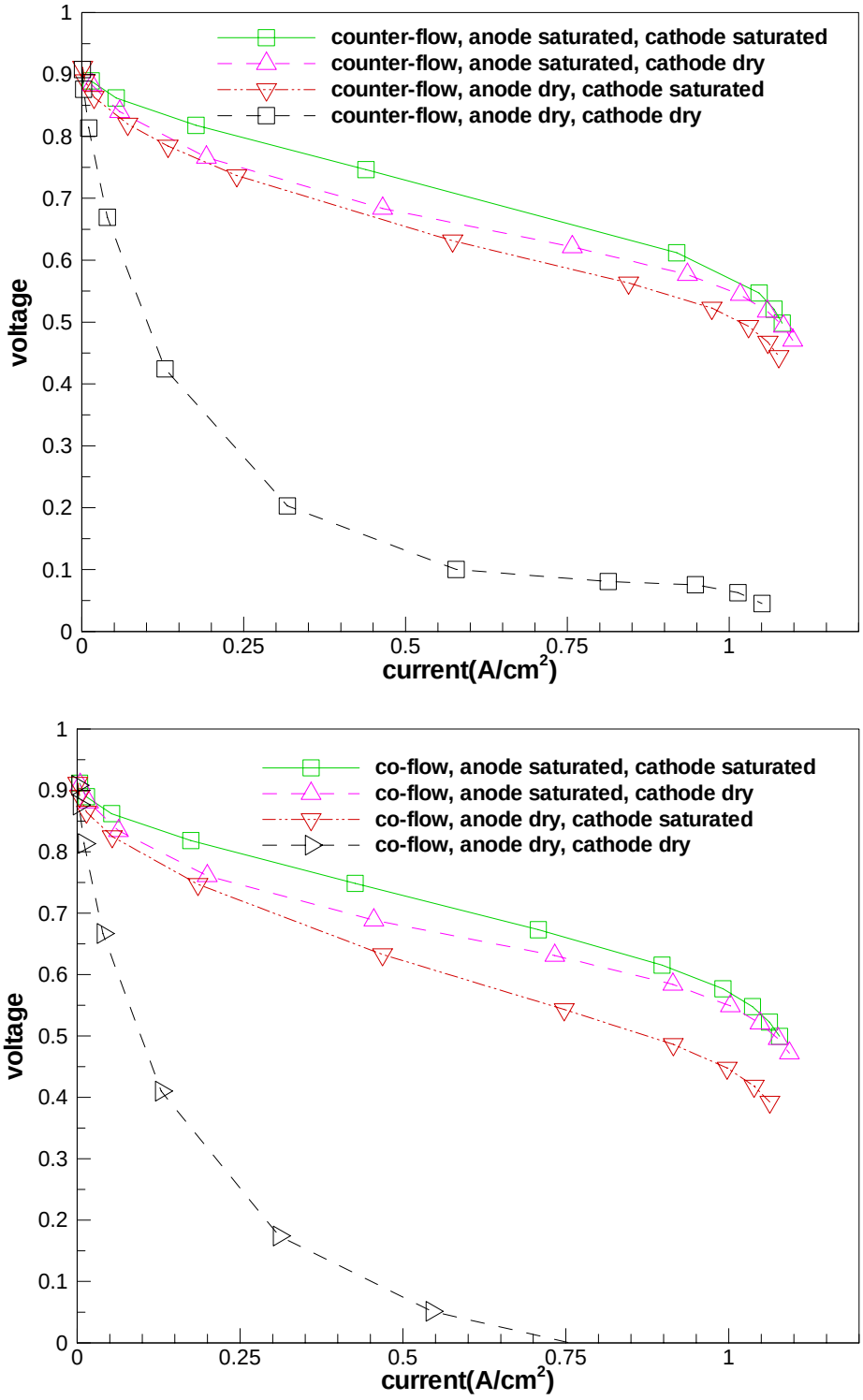

Fig. 6. Comparison of simulated polarization curves for each of the four conditions for counter-flow (top) and co-flow (bottom).

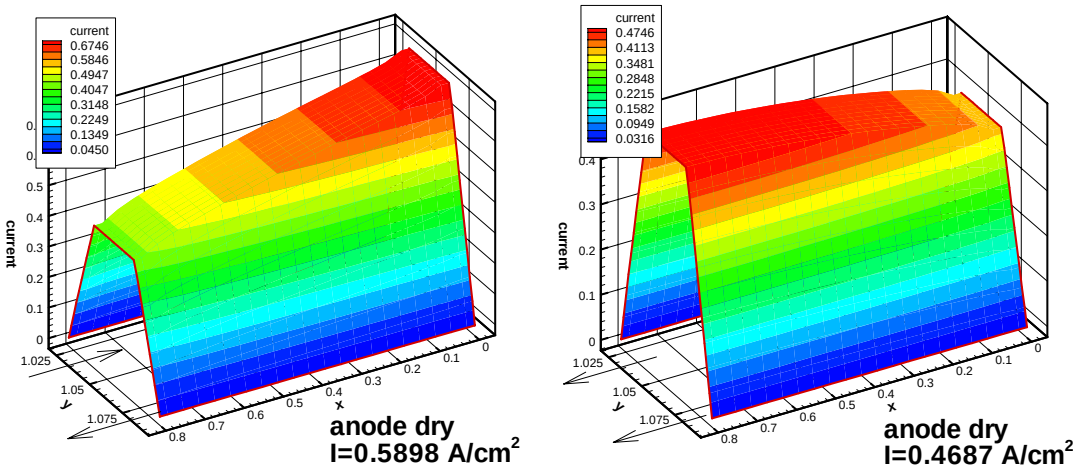

Fig. 7. comparison of the current density distribution at ~ 0.65 volts for counter-flow (left) and co-flow (right) when the anode is dry and the cathode saturated.

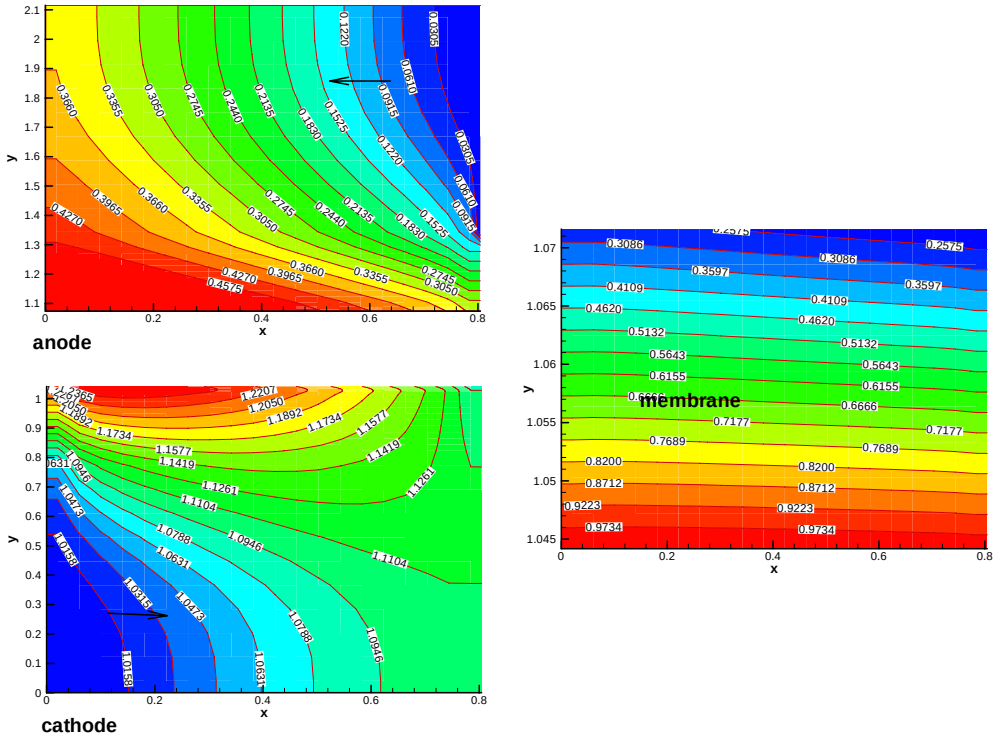

Fig. 8 The water vapor concentration at cathode, anode and liquid water content within the membrane, for counter-flow, I=0.5898 A/cm^2 **Anode dry, cathode saturated**

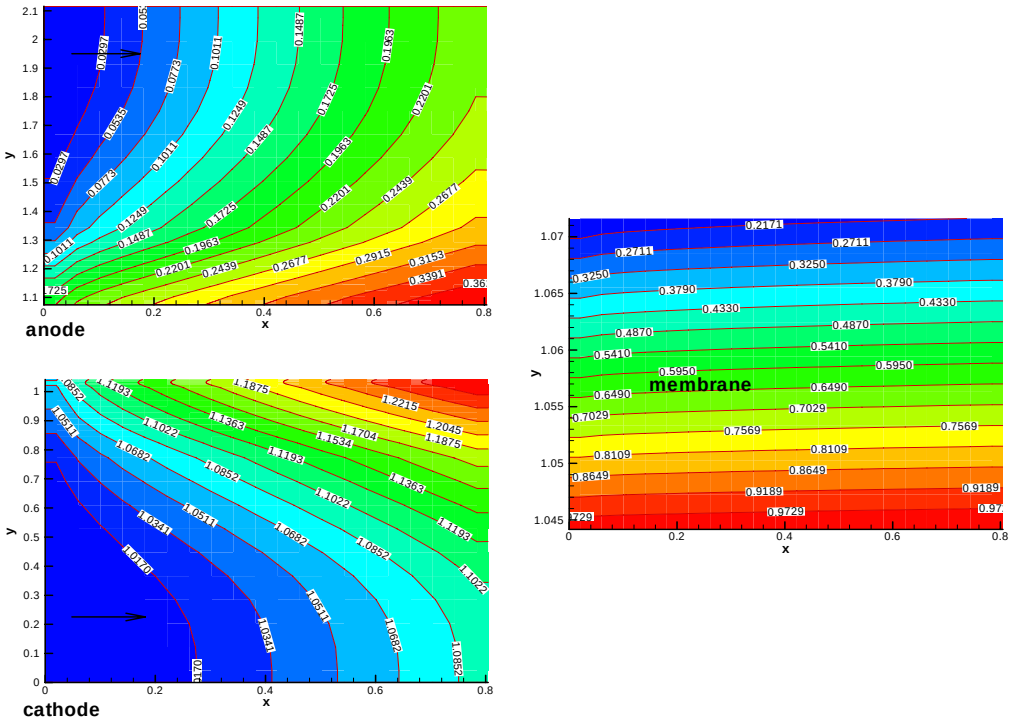

Fig. 9 The water vapor concentration at cathode, anode and liquid water content within the membrane for co-flow, I = 0.4687 A/cm^2. **Anode dry, cathode saturated.**

2.5.6.2 Effects of electrical resistance of the GDL and catalyst layer

The effects of electrical resistance of the GDL and catalyst layers were also studied. At the time this extension was done, direct measured data on the effective electric conductivities (or electric resistances) of the GDL and catalyst layers were not available, so the values used in the model calculations below are either from the GDL manufacturer or estimated from a simple model for the catalyst layer.

For the GDL, the value used was from Toray Industries, Inc. and should be very reasonable. Note that the electric conductivity values provided by the manufactures are assumed to be measured before compression, thus the true electric conductivities under compression must be higher. Therefore the effects of electrical resistance predicted by the model and conductivity should be an over-estimation. Even so, the effects are extremely small and negligible.

For the catalyst layers, the effective electrical conductivity was estimated from a simple mixture model based on the electrical conductivity of the Black Pearl carbon black (220 S/m). The preliminary results based on this value of effective electrical conductivity show that the effects are negligible. Since the effective electrical conductivity is not directly measured, the estimated value could have a large uncertainty. Another factor to consider is that the electrical conductivity could decrease if the catalyst layers swell due to hydration.

The electric conductance of the GDL and catalyst layer depends on many factors, such as particle size, composition, structure, and specific area, etc. The value used for the GDL was the lowest one provided by Toray Industries, Inc. of 1250 S/m for through plane conductivity.

An effective conductivity was computed based on a Black Pearl carbon black electrical conductivity of 220 S/m, and an appropriate mixture algorithm. The effective value was 63.6 S/m. With these typical values, their voltage loss impact on the polarization curves was found to be negligible, and it was not until the catalyst layer conductivity dropped significantly, to 10% or less, that there was a noticeable loss. The catalyst layer resistance and IR loss only becomes comparable to the ionic loss in the catalyst layer, when the electrical conductivity drops by a factor of 50. This is illustrated in Fig. 10 for the case in which the catalyst layer conductivity is only 1.4 S/m.

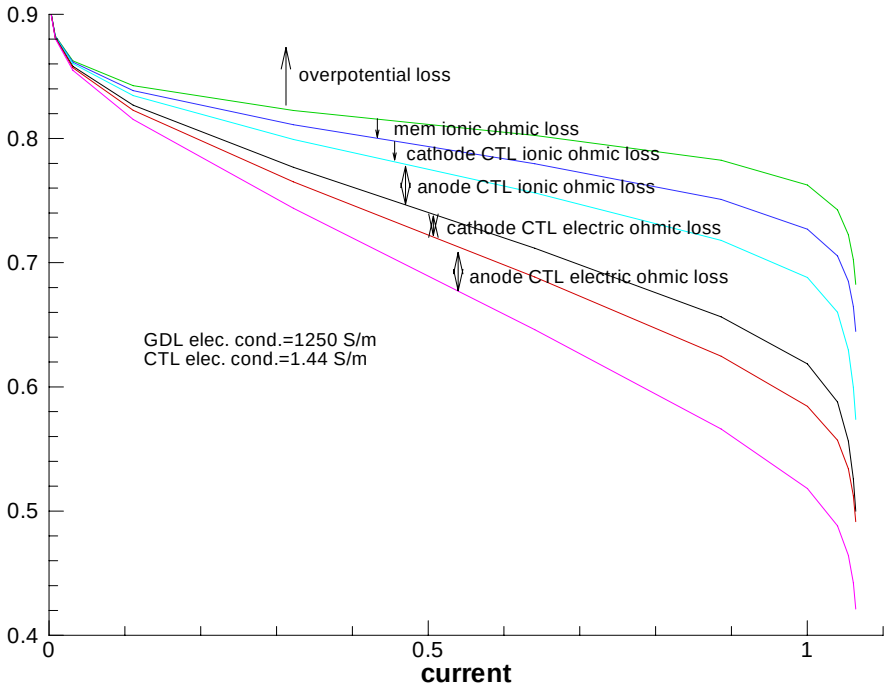

Fig. 10. Various ohmic losses in the membrane and catalyst layer (CTL) for the case in which the catalyst layer's electrical conductivity is reduced a factor of about 50 below the nominal value.

2.5.6.3 Comparison of single- and two-phase models (U. of Miami)

This U. of Miami study, on extending the model from single-phase to two-phase capability, is included here in total. The results reported here are still considered to be preliminary. The primary model modifications for this extension involved adding thermal changes due to evaporation/condensation. To study the effects of latent heat of evaporation/condensation, the following 4 cases were simulated using both the single-phase and two-phase models:

- Anode inlet dry, cathode inlet dry
- Anode inlet dry, cathode inlet fully saturated
- Anode inlet fully saturated, cathode inlet dry

- Anode fully saturated, cathode inlet fully saturated

Figure 11 is the comparison of the temperature contours when both inlets are dry and the current density = 1.0 A/cm^2. Figure 12 is the comparison of the corresponding temperature profiles. As both inlets are dry, there is evaporation occurring from the membrane. As a result, the modeled temperature in the MEA is not as high as the modeling result when this thermal change is omitted. At even low current density, this phenomenon is more obvious. Figure 13 is the temperature contour when the current density is about 0.27A/cm^2. Figure 14 is the corresponding temperature profiles. At this low current density, the heat generated within the MEA is quite small. The heat lost to the evaporation of water from the MEA will be so big that the core temperature of the MEA will be even lower than the bath temperature.

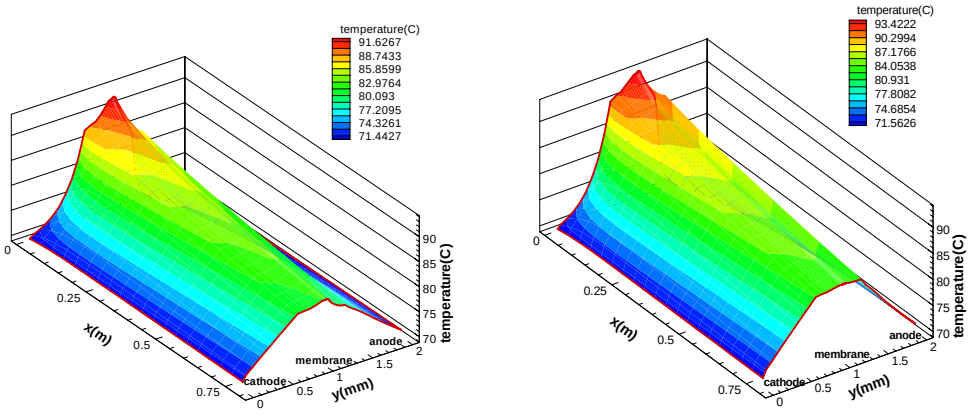

(a) two phase model (b) single phase model

Fig. 11 Temperature contours when both inlets are dry, current density = 1.0 A/cm^2.

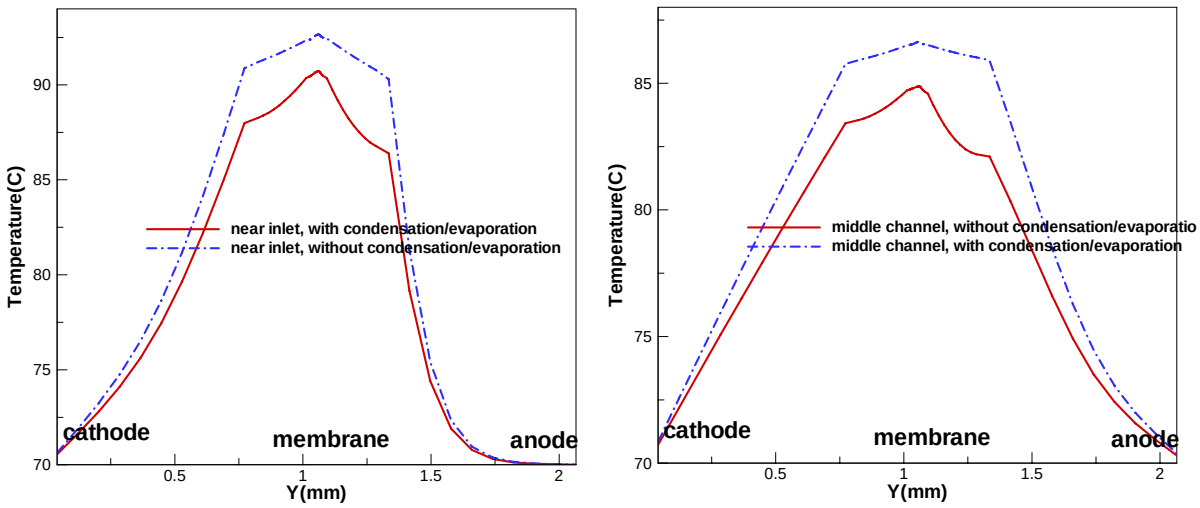

(a) near inlet (b) middle channel

Fig. 12 Temperature profiles when both inlets are dry, current density = 1.0 A/cm^2.

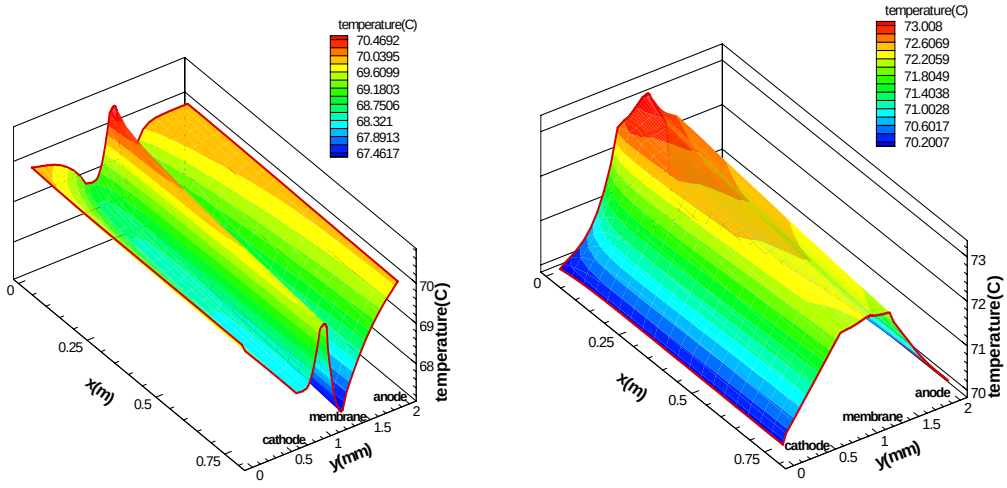

(a) two phase model (b) single phase model

Fig. 13 Temperature profiles when both inlets are dry, current density = 0.27 A/cm^2.

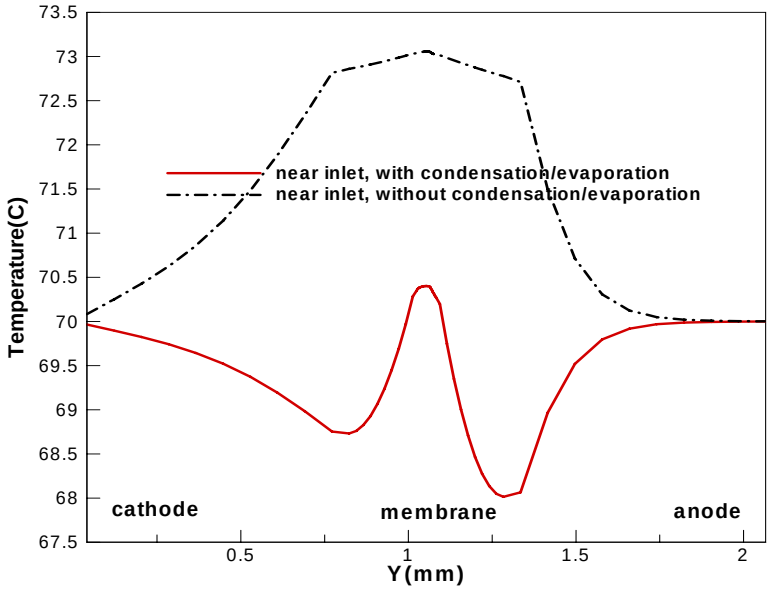

Fig. 14 Temperature profile when both inlets are dry, current density = 0.27 A/cm^2.

Fig. 15 is the comparison of the temperature contours when anode inlet is dry while cathode inlet is fully saturated. The current density is about 1.0 A/cm^2. Fig. 16 is the comparison of the corresponding temperature profiles. As anode inlet is dry and cathode inlet is fully saturated, evaporation occurs at the anode and condensation occurs at the cathode. As a result, when this thermal change is considered, evaporation at the anode leads to lower temperature and condensation leads to higher temperature at cathode. Fig. 17 is the temperature contour when the current density is about 0.39A/cm^2. Fig. 18 is the temperature profile when the current density is about 0.39A/cm^2. At this low current density, the heat generated within the MEA is quite small. The heat lost to the evaporation of water at the anode causes he temperature at the anode is greatly reduced.

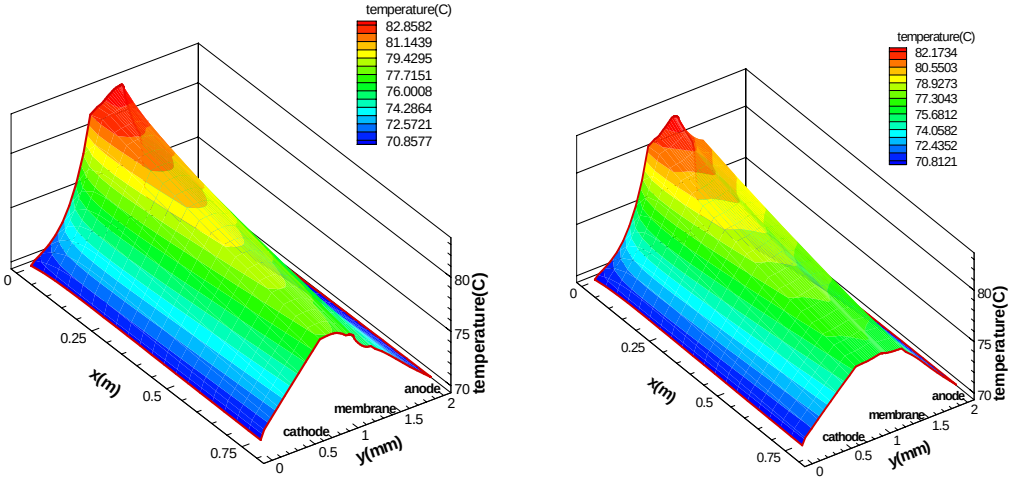

(a) two phase model (b) single phase model

Fig. 15 Temperature profiles when anode inlet is dry while cathode inlet is fully saturated. current density = 1.0 A/cm^2.

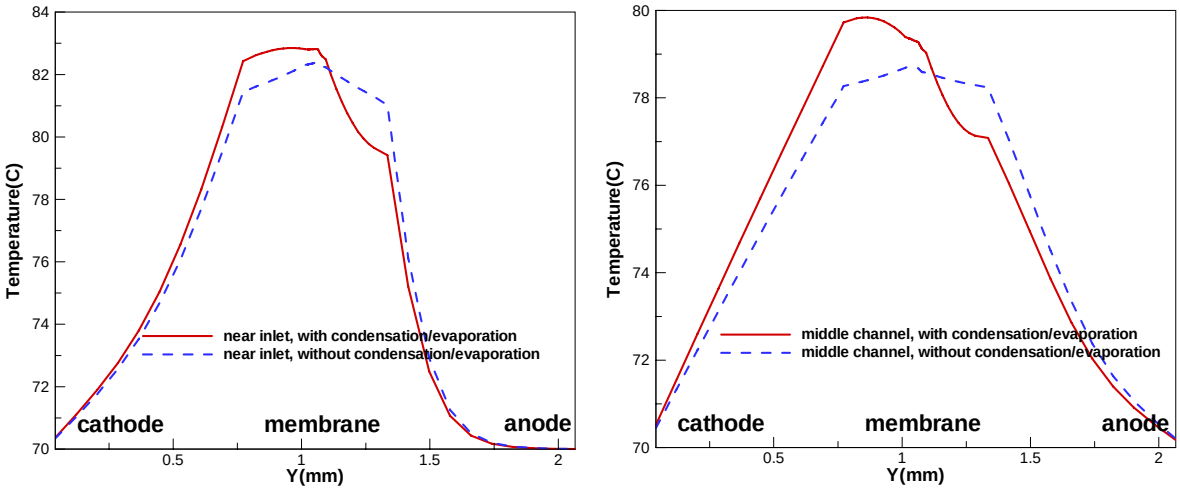

(a) near inlet (b) middle channel

Fig. 16 Temperature profiles when anode inlet is dry while cathode inlet is fully saturated. current density = 1.0 A/cm^2.

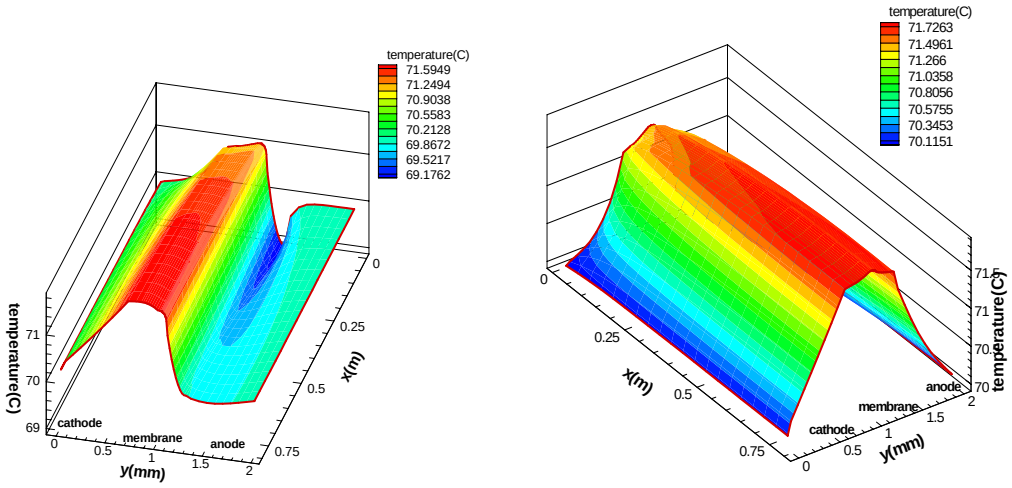

(a) two phase model (b) single phase model

Fig. 17 Temperature profiles when anode inlet is dry while cathode inlet is fully saturated. current density = 0.39 A/cm^2.

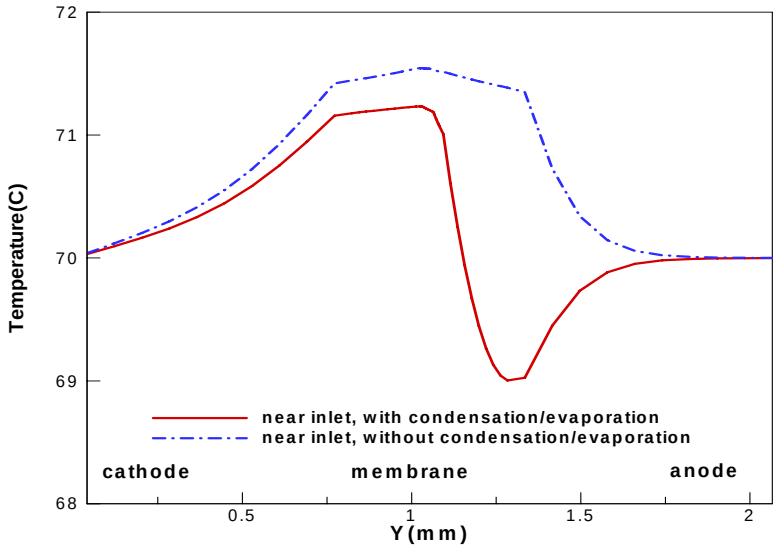

Fig. 18 Temperature profiles when anode inlet is dry while cathode inlet is fully saturated, current density = 0.39 A/cm^2.

Fig. 19 is the comparison of the temperature contours when anode inlet is fully saturated while cathode inlet is dry. The current density is about 1.08 A/cm^2. Fig. 20 is the comparison of the corresponding temperature profiles. As anode inlet is fully saturated and cathode inlet is dry, evaporation occurs at the cathode and condensation occurs at the anode. As a result, when this thermal change is considered, evaporation at the cathode leads to lower temperature at the cathode. Fig. 21 is the temperature profile when the current density is about 0.66 A/cm^2.

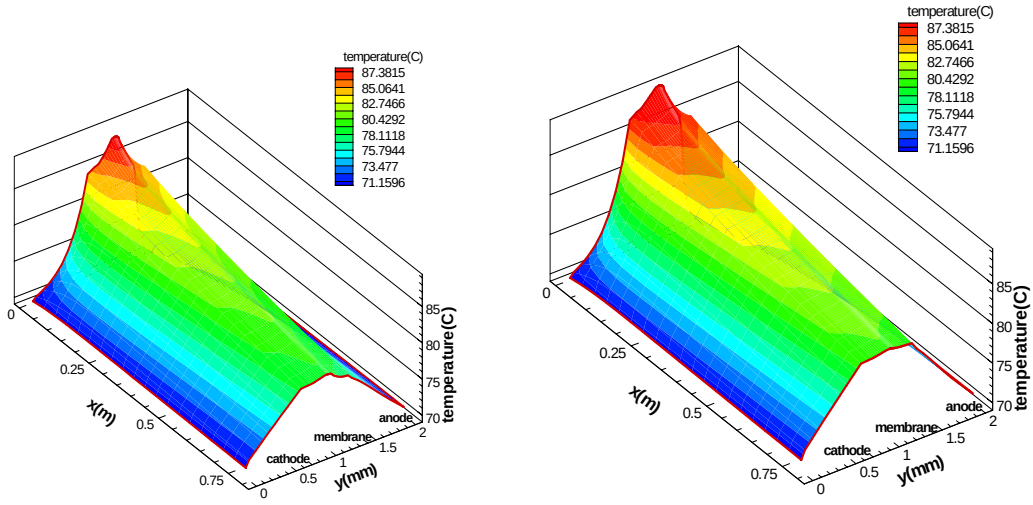

(a) two phase model (b) single phase model

Fig. 19 Temperature profiles when anode inlet is fully saturated while cathode inlet is dry. current density = 1.08 A/cm^2.

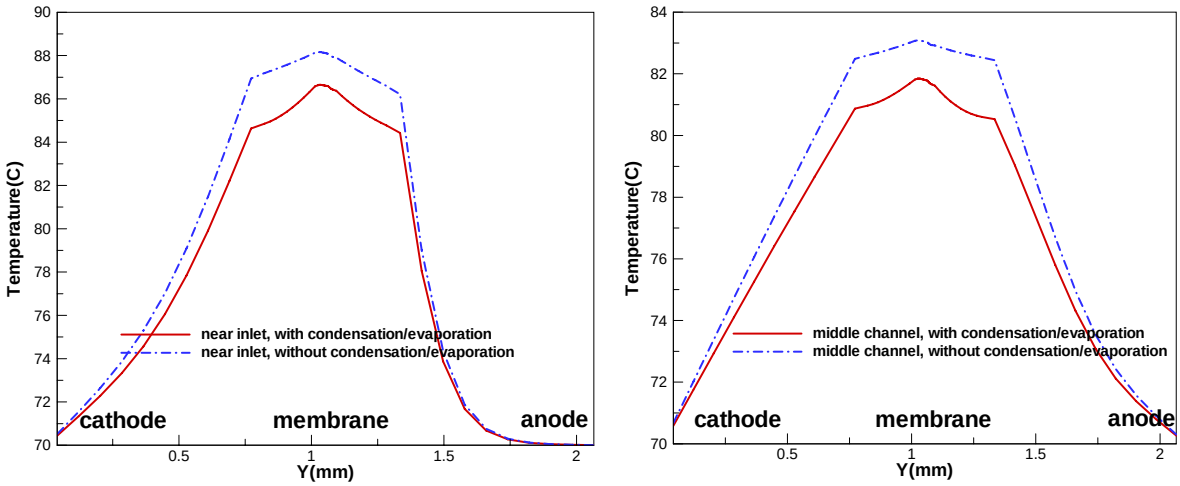

(a) near inlet (b) middle channel

Fig. 20 Temperature profiles when the anode is fully saturated while cathode inlet is dry current density = 1.08 A/cm^2.

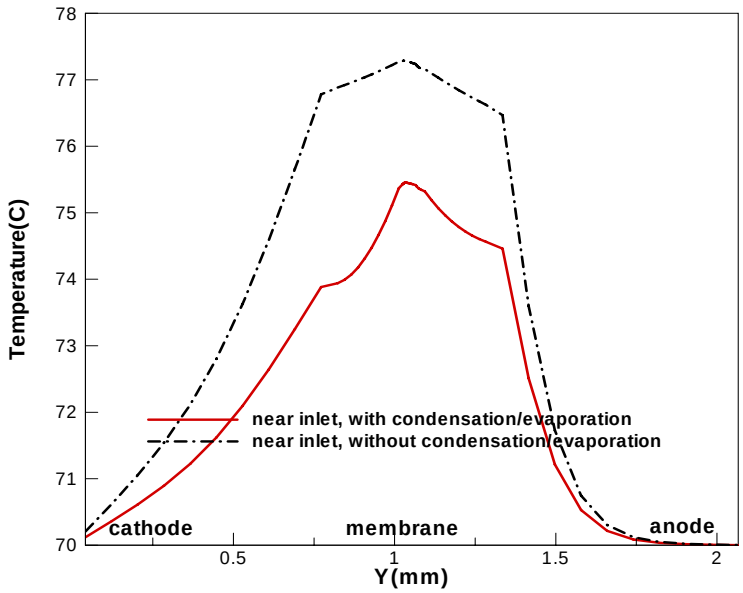

Fig. 21 Temperature profiles when the anode is fully saturated while cathode inlet is dry, current density = 0.66 A/cm^2.

Fig. 22 is the comparison of the temperature contours when both anode and cathode inlets are fully saturated. The current density is about 1.05 A/cm^2. Fig. 23 is the comparison of the corresponding temperature profiles. Fig. 24 is the temperature profile when the current density is about 0.63 A/cm^2.

In conclusion, thermal changes will cause lower or higher temperature within the MEA, depending on the inlet humidification conditions. However, as the differences of the modeled temperatures are not very large, the influences on the polarization curves may not be large either for the conditions of these models.

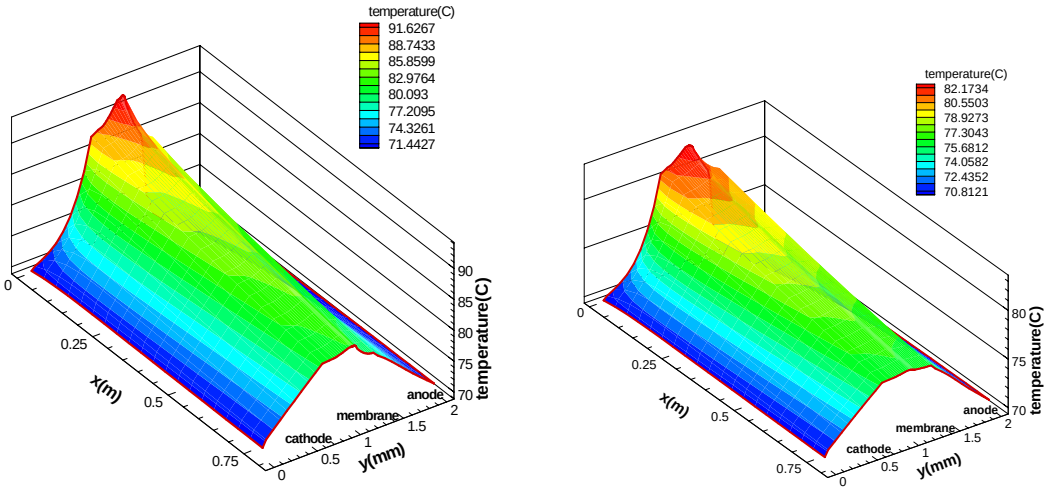

(a) two phase model (b) single phase model

Fig. 22 Temperature profiles when both anode inlet and cathode inlet are fully saturated. Current density = 1.05 A/cm^2.

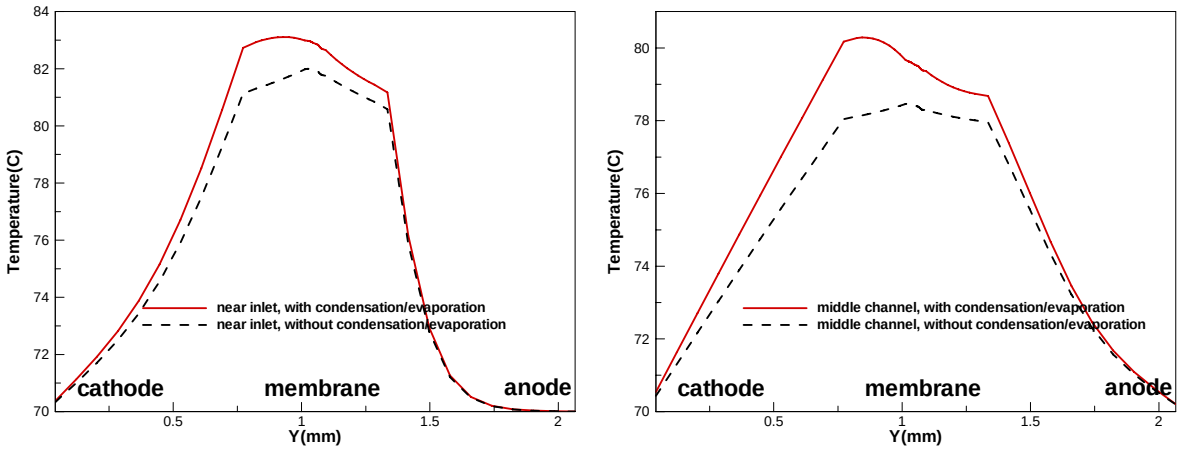

(a) near inlet (b) middle channel

Fig. 23 Temperature profiles when both inlets are saturated, current density = 1.05 A/cm^2.

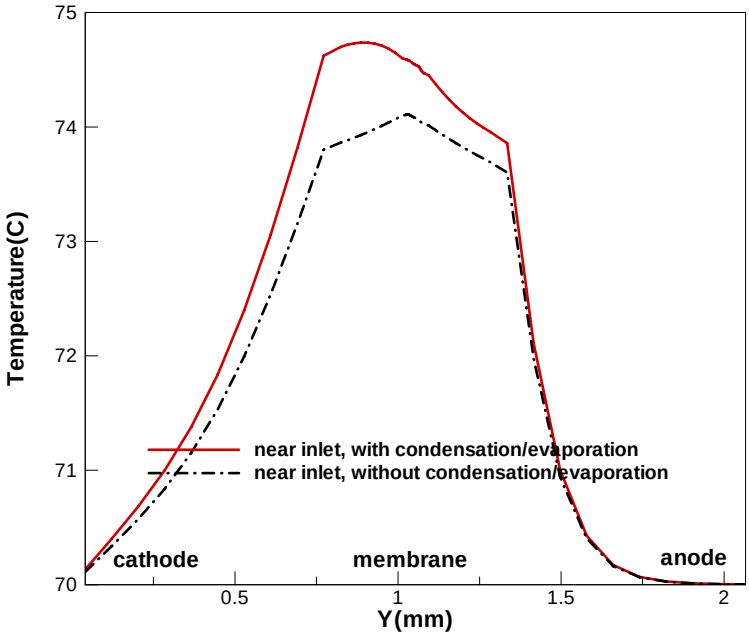

Fig. 24 Temperature profiles when both inlets are fully saturated, current density = 0.63 A/cm^2.

2.5.6.4 Model calibration results for the ultra-thin catalyst layer and comparison of Baseline dispersed and NSTF model calcualtions.

This study represented the final report from U. of Miami on the model extensions for application to the ultra-thin NSTF electrode layer. It is included in its entirety in Appendix III. We extract here a few examples of the results because of the signficant differences in certain calculated MEA parameters between the thick electrode (baseline dispersed) and thin (NSTF) electrode cases. The data from FC8565 and FC8676 discussed above were the primary basis for the calibration of the thin catalyst model. It must be strongly noted, however, that U. of Miami considered these preliminary results as well, and the conclusions about the significant (relative) temperature differences in the two types of electrode layers are no longer considered valid due to the convergence issues discussed above in section 2.5.4 above. It represents results, then from the first ultra-thin layer model version and not the isothermal version used at 3M for the results discussed below in section 2.5.7.

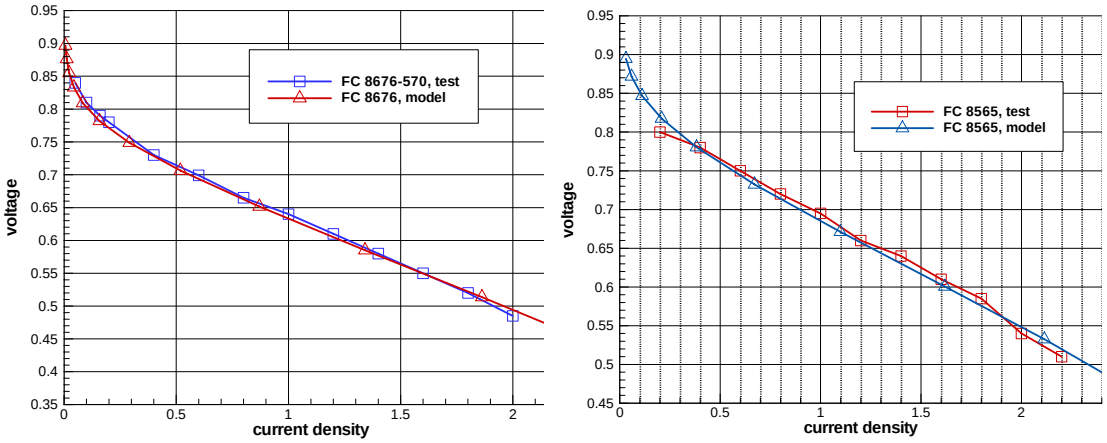

NSTF MEA FC 8676, 0.1 mg/cm^2 ternary NSTF MEA FC 8565, 0.1 mg/cm^2 ternary

Calibration of Model with Measured Polarization and HFR Data

Fig. 25. Example of agreement of the measured and calcuated polarization curves with the first ultra-thin model version.

The first sampling of results is shown in Fig. 25. It compares the level of agreement between the measured and calculated polarization curves for the two MEAs used for calibration. The agreement is very good.

The second example shows the current density distribution down-channel at approximately 1 A/cm^2 for one of the MEAs in Fig. 26 (left). It would be similar for the other MEA. In Fig. 26 (right) an example of the temperture distribution as calcuated is shown. This is representative of data that may not have been correct at the time it was generated due to the convergence issues, but shows again the potential when the issues are resolved.

The next example compaes the overpotential, ionic and electronic losses in the membrane, GDL and catalyst layers for the two MEAs for the polarization curves shown in Fig. 25.

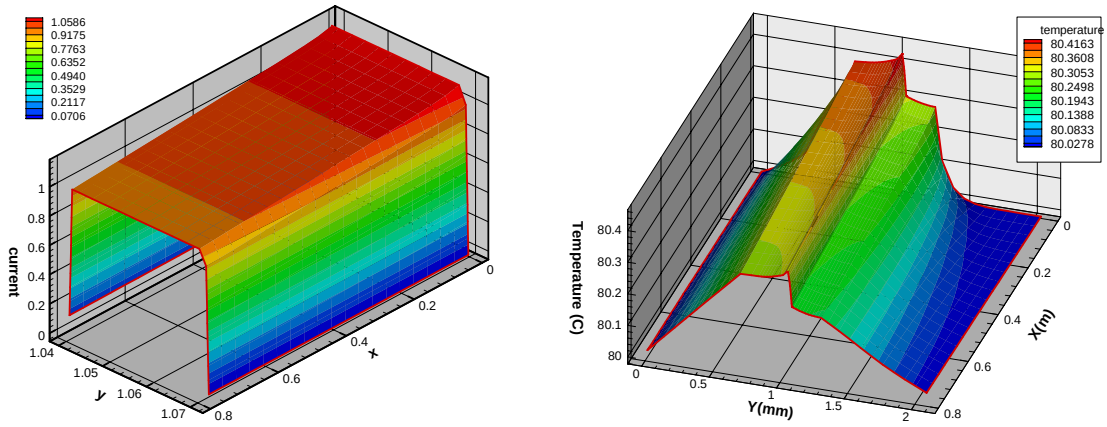

Current Density Distribution for FC8676 At 1.04 A/cm^2

Temperature Distribution for FC8565 At 1.07 A/cm^2

Fig. 26 Example of the current density distribution for the MEAs (left) and the associated temperature distribution within the MEA as calcuated. Both MEAs would be expected to hae similar looking distributions.

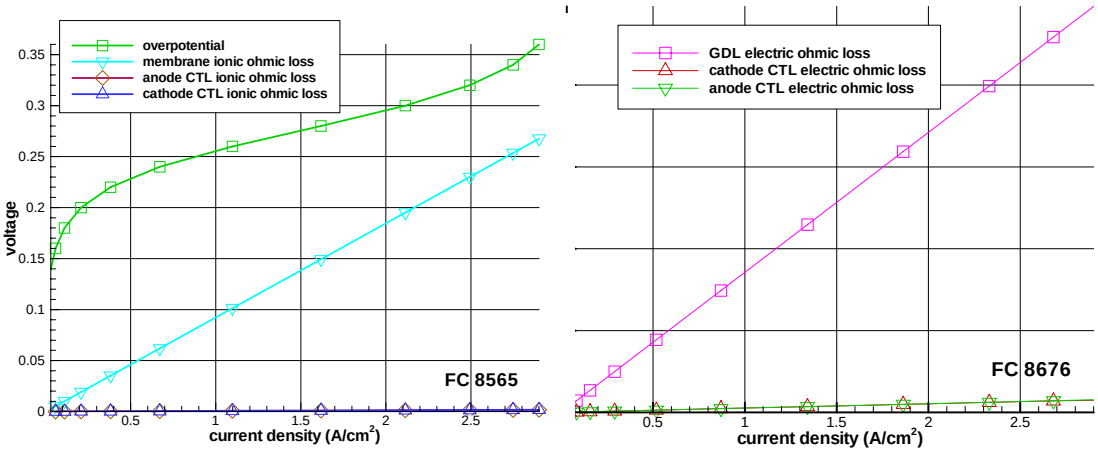

Fig. 27. Comparison of the overpotential, ionic and electronic losses in the two MEAs for the polarization curves shown in Fig. 25.

As expected, the kinetic overpotential dominates, but membrane ionic loss dominates the other electronic and ionic contributions The electrode electronic and ionic ohmic losses are negligible compared to the GDL electronic contribution which is much larger than the catalyst layer electronic losses. The interface impedances were not modeled.

Fig. 28 compares the ionic and electronic ohmic losses of the dispersed MEA with the NSTF MEAs. The much larger ionic ohmic loss in the dispersed case is due to its much thicker catalyst layer and lower ionic conductivity (due to lower Nafion fraction). The

catalyst layer in the dispersed case has Nafion fraction of 16%, while this value in the two NSTF cases is estimated at about 70% from the percent void volume determined in Table I of section 2.1.5.3 of this report. The larger electric ohmic loss in the dispersed case is because of the thicker layer.

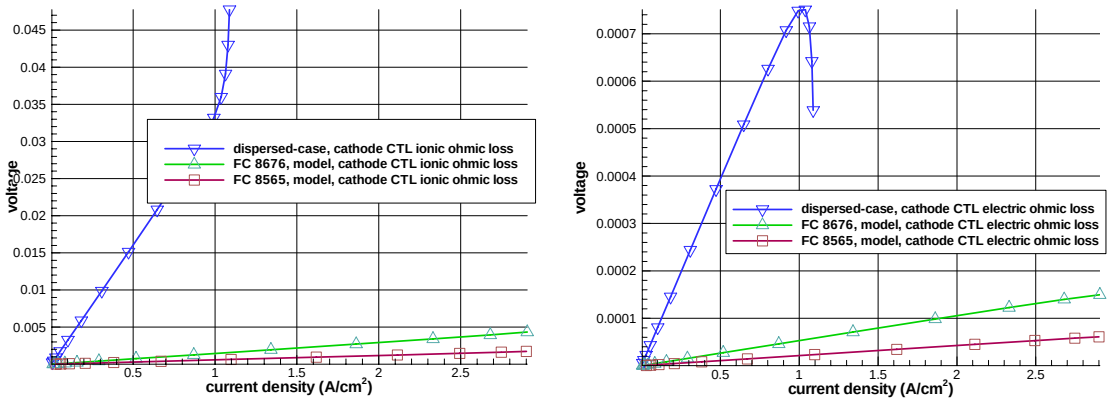

Fig. 28. (left) Comparison of the ionic ohmic loss in the dispersed electrode versus the two NSTF electrodes, and (right) comparison of cathode catalyst layer electric ohmic losses for the two types of MEA.s

Although the heat generation curves and temperture distributions were calcuated, the caveats discussed above with respect to convergence issues do not allow full confidence in their accuracy. These results are included in the full report in Appendix III. However there is good reason to believe that qualitatively the NSTF catalyst layers may operate somewhat cooler due to several aspects identified in the modeling. These points are:

1) The thermal resistance is greatly reduced with the NSTF cases since the thermal resistance is proportional to (layer thickness/ thermal conductance). So a much lower thermal impedance would be expected due to the extreme thinness, and heat transfer out of the electrode would be proportionately more efficient.
2) The thermal conductivity would be higher as well due to less void space in the porosity of electrode, i.e. higher % ionomer in the electrode layer.
3) Lower ionic and ohmic Joule heating in the NSTF electrodes (< ~ 1% of total due to Joule and Kinetics). Thus less heat is generated in the electrodes from IR losses.

2.5.7 Example simulations of model applications by 3M - Comparison of 2D isothermal-NSTF with non-isothermal-NSTF

As seen in Table 1, two basic NSTF code versions were received from U. of Miami, 4/4/05 and 7/11/06. They were compared using MEA property information characteristic of a recent roll-good NSTF CCM and MEA discussed in section 4.0. The model simulation curves for the two versions (isothermal and previous) are compared in Fig. 29 for three different pressures, three different %RH and two different stoichiometries. The effect of forcing the MEA temperature to be uniform (isothermal –solid lines) has increased performance at each pressure and stoichiometry. This is somewhat surprising that it has not had more of an effect, but the difference does increase as current density increases and therefore internal heat generation.

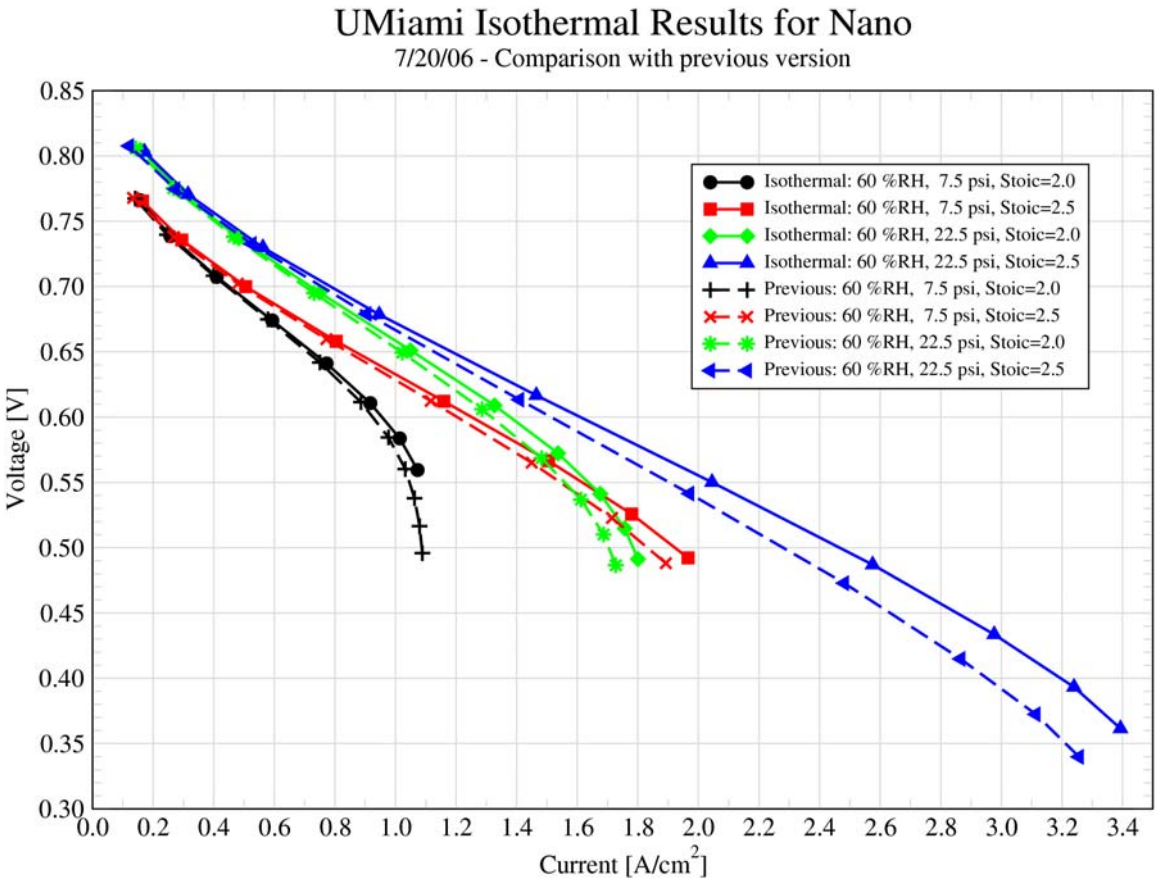

Fig. 29. Comparison of the NSTF model results for the initial thin layer NSTF (or Nano) version and the later isothermal version. MEA properties and conditions are the same as in the following Fig. 30, for FC12225.

Experimental data from a representative MEA, FC12225, are shown in Fig. 30 (bottom), taken at the same conditions used for the isothermal model (Fig. 30 top) comparison. Comparing the model curves with the experimental curves, plotted with the same scale axes, shows a fairly good match. Both show 550 mV at 2 A/cm^2 under 23 psig and a stoich of 2.5 on the cathode.

Of perhaps more interest than the polarization curve, are the reactant concentrations within the MEA and flow field of a working fuel cell. For the model calculations above, those parameters are known. Fig. 31 shows an example of the current density, water vapor concentration, and oxygen concentration distributions along the channel from inlet to outlet, for the conditions of 23psig, 60% RH and 0.68 V, for which the average cell current density is 0.95 A/cm^2. In these figures, the position units are domain cell units, not real spatial units, and furthermore, each component has the same number of cells, e.g. the half-channel is 10 unit cells wide, the GDL is 10 unit cells wide, the catalyst and half-membrane are each 10 unit cells wide. The channel length is 20 cells long, but the cell's aspect ratio is much longer than one since the channel is much longer than it is wide. The water activity in Fig. 31 is seen to exceed unity, which is not incorrect but a consequence of the definitions of water concentration in the channel vapor phase and in the membrane.

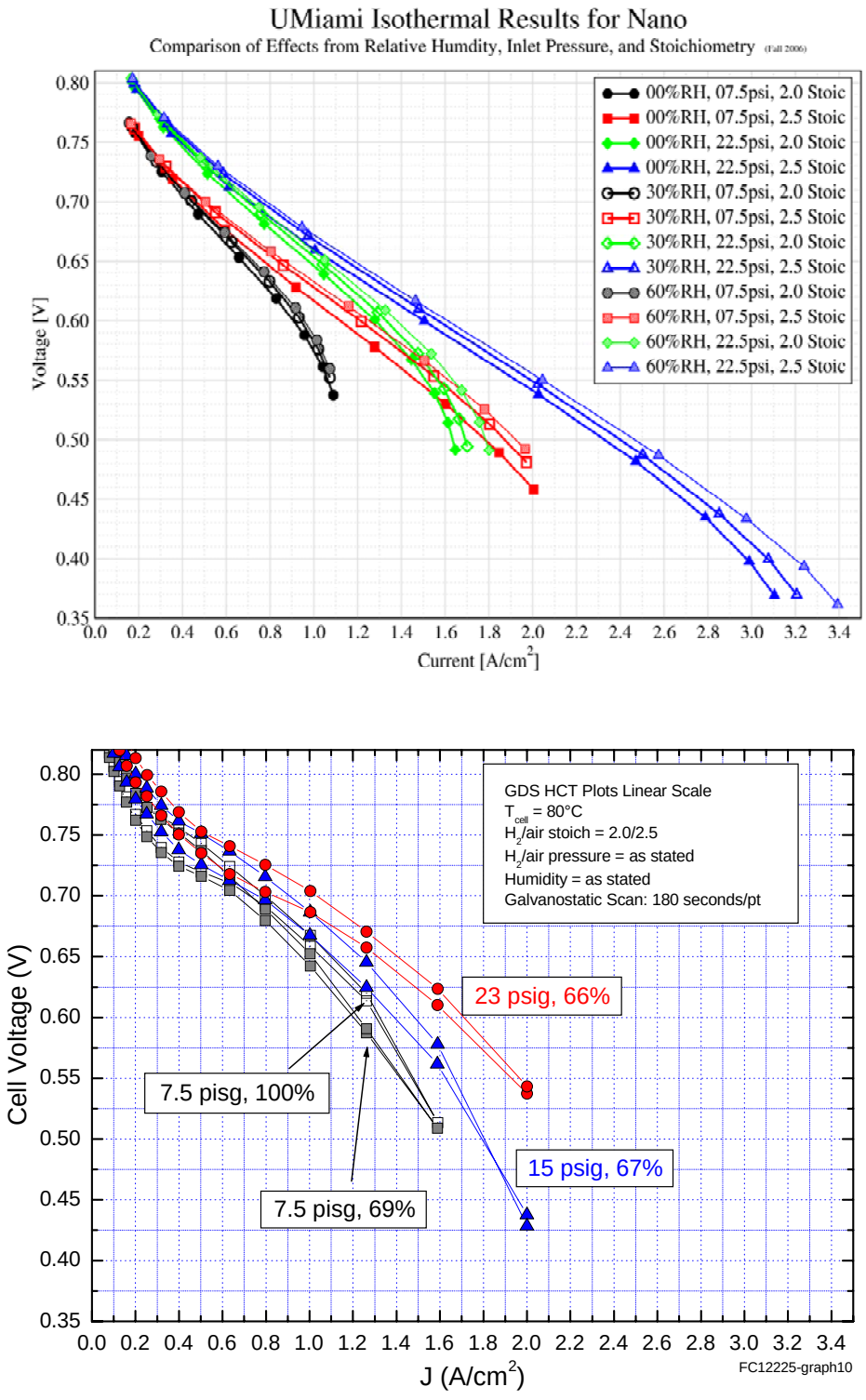

Fig. 30. Measured polarization curves for FC12225 (bottom), and model simulation comparisons of 2D NSTF isothermal models for MEA similar to that in Fig. 29.

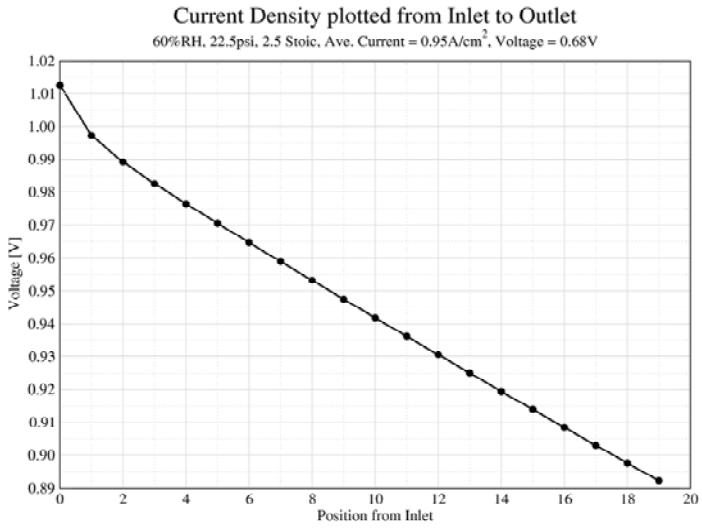
Current Density plotted from Inlet to Outlet
60%RH, 22.5psi, 2.5 Stoic, Ave. Current = 0.95A/cm^2, Voltage = 0.68V
Voltage [V]
Position from Inlet

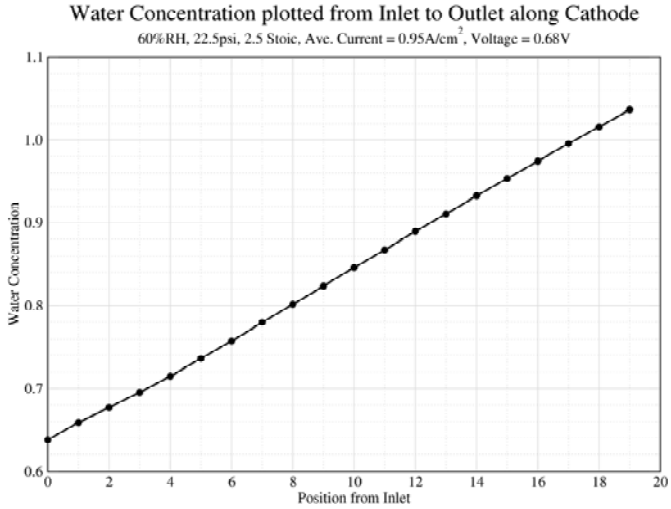
Water Concentration plotted from Inlet to Outlet along Cathode
60%RH, 22.5psi, 2.5 Stoic, Ave. Current = 0.95A/cm^2, Voltage = 0.68V
Water Concentration
Position from Inlet

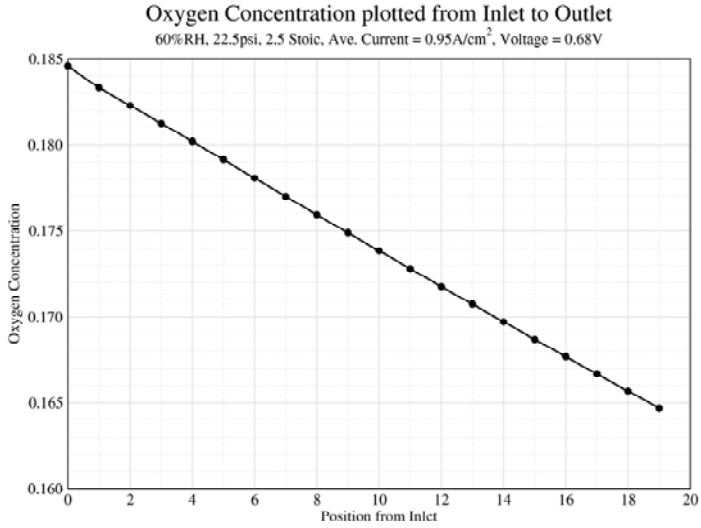
Oxygen Concentration plotted from Inlet to Outlet
60%RH, 22.5psi, 2.5 Stoic, Ave. Current = 0.95A/cm^2, Voltage = 0.68V
Oxygen Concentration
Position from Inlet

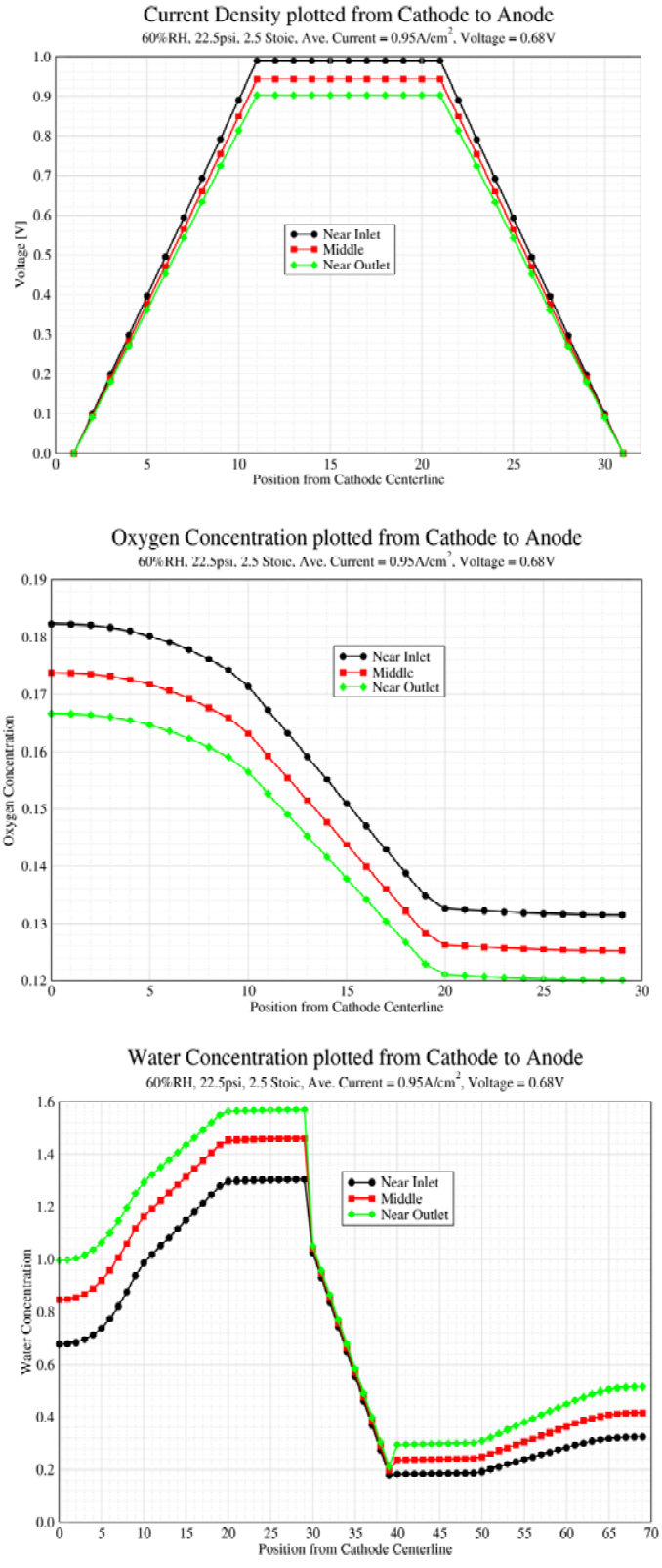

Fig. 32. Plots of current density, oxygen concentration and water concentration versus position in the direction perpendicular to the plane of the MEA. Conditions are for the case of 23psig, 60% RH and 0.7vol in Fig. 30 above. The position units are not real spatial dimensions, but the domain cell units used for the calculation.

Finally, Fig. 32 plots the same three variables across the MEA, beginning in the middle of the cathode center line and extending towards the anode either 30 or 70 cell units. Considering the oxygen plot first, what is noticeable is that there is essentially no oxygen gradient in the catalyst layer (cell units 20 to 30) implying little mass transport overpotential. Instead it all occurs in the GDL and to a lesser extent the channel. This is a consequence of the extreme thinnes of the catalyst layer. Considering the current density distribution (top plot), the current desnity builds linearly through the cathode catalyst layer (cells 1 to 11) and anode catalyst laye (cells 31 to 21), implying all the catalyst thickness is used uniformly. It is seen to not vary much down channel either, as there is sufficiently high flow stoichiometry. Finally, the water concentration (bottom plot) is shown across the entire model, from the middle of the cathode channel (cells 0 to 10), through the cathode GDL (cells 10 to 20), across the cathode catalyst (cells 20 to 30), the membrane (cells 30 to 40) where there is a very steep gradient, and then from the membrane out through the anode catalyst, GDL and anode channel. The steepness and direction of the water gradient through the membrane indicates that water is flowing back through the membrane from the cathode to the anode as a means for removing water from the cathode.

2.5.8 Summary and Conclusions

The majority of the original goals of this advanced modeling task were accomplished. All facets of the original plans were investigated and most of the intended model improvements and extensions were implemented, although some were much easier than others to implement. A modeling simulation code capable of treating an ultra-thin electrode layer was successfully developed for the first time, and as a tool can provide useful insight into the internal environment of the NSTF MEA fuel cell. The model was not able to be developed in time to impact the GDL down-selection (discussed in section 2.3) as originally intended, due to the unforseen complexities of adapting the model to the ultra-thin electrode structure. Compromises were also forced by the difficulties of achieving proper energy convergence, requiring an isothermal version to be implemented. This could be overcome in future versions by using a smaller domain cell size near to and encompassing the ultra-thin electrode layer. For the present code and time available, this was not possible, but would be a desirable next model extension. The executable code was successfully transferred to 3M, and will enable further understanding to be achieved on the subtleties of water management for such electrodes even in its present form.

References for Section 2.5

1. Mark K. Debe and Thomas Herdtle, “Design and Development of a Novel Flow Field for Pem Fuel Cells to Obtain Uniform Flow Distribution,” ECS Transactions **1**(6), 581-604 (2005).
2. D. M. Bernardi, and M. W. Verbrugge, “Mathematical Model of a Gas Diffusion Electrode Bonded to a Polymer Electrolyte,” AIChE Journal **37**, 1151-1163 (1991).
3. V. Gurau, F. Barbir and H. Liu, “An Analytical Solution of a Half-cell Model for PEM Fuel Cells,” J. Electrochem. Soc. **147**, 2468-2477 (2000).
4. T. Zhou, T. and H. T. Liu, “A General Three-Dimensional Model for Proton Exchange Membrane Fuel Cells,” Int. J. Transport Phenomena **3**, pp 177-198, (2001).
5. K. C. Neyerlin, Wenbiin Gu, Jacob Jorne and Hubert A. Gasteiger, J. Electrochem. Soc. **153** (10) A1955-A1963 (2006).

Section 3

Membrane Materials and Approaches for T > 120ºC

Section 3 Membrane materials and approaches for T > 120°C.

This section reviews all the work completed under Task 2.1, directed at developing membrane materials and approaches for operation at temperatures above 120°C.

Section 3 Table of Contents

3.0 Membrane Materials and approaches for T> 120ºC

3.1. Introduction for Subtask 2.1

The work proposed for this subtask is described below.

3.1.1. Technical Concept (Subtask 2.1)
Numerous examples of ionomer replacements for Nafion exist in the literature.[1] Most are based on either other perfluorinated ionomers with structures very similar to Nafion or sulfonation of aromatic polymers known to have good oxidative stability. All of these require water for ionic conductivity, and none have been shown to have significantly improved thermal stability at higher temperatures. Sulfonated aromatics are known to be prone to de-sulfonation and crosslinking at higher temperatures, and, while the mechanism of Nafion degradation at higher temperatures is not fully understood, it also involves loss of sulfonic acid groups.

Replacement of water with other higher boiling liquids has also been explored.[2] The most extensively studied high temperature PEMFC membrane to date is phosphoric acid imbibed polybenzimidazole (PBI).[2a] While these membranes show good conductivity at higher temperatures, fuel cell performance is limited by the strong interaction of the phosphoric acid electrolyte with the cathode catalyst and low oxygen reduction kinetics. These membranes also suffer from loss of phosphoric acid when exposed to liquid water.

The objective of the task proposed here is to develop a new membrane for PEMFC's to address the requirements of Subtopic 1.A.2. The new membrane would be based on new technology that would allow the fuel cell to operate at 120°C to 150°C. These new membrane materials would have to maintain conductivity at these higher temperatures by providing a mechanism for proton transport across the membrane that requires little or no water. In addition, these materials would have to be thermally and oxidatively stable under the conditions of operation, be non-volatile and insoluble in water, be a good barrier to reactant gasses and shorting, and form a stable interface with electrode catalyst materials. Durability is another key requirement. These membranes and interfaces would have to be able to maintain these characteristics for the lifetime of the device (5,000 to 20,000 hours of operation).

We are proposing a three-pronged technical path to achieving these goals.
i) Development of inorganic materials capable of assisting in proton conduction.
ii) Development of new fluorinated proton conducting liquids.
iii) Development or identification of a host polymer matrix for one or both of these materials with the requisite properties.

A variety of electrochemical techniques, described in detail in Task 2.3, would be used to screen and characterize both the bulk properties of new materials and their interfaces with the catalysts. Electrochemical impedance spectroscopy (EIS) would be one workhorse for evaluating conductivities and changes in conductivities as a function of pressure, temperature and degree of humidity, as well as monitoring material changes over time. Thermal analysis techniques, such as DSC and TGA, can tell us about the thermal properties (Tg, Tm) as well as stability of new materials. When done as a

function of pressure, temperature, and degree of humidity, they can tell us about the affinity of new materials for water and other liquid membrane components under high temperature operating conditions. Mechanical properties such as tear strength, puncture strength, tensile strength, and modulus would also be important for selection of the new membrane and can also be monitored as a function of pressure, temperature and degree of humidity.

Innovative microstructures: A great deal has been reported concerning inorganic proton-conducting phases. Some of those materials are described below. Notwithstanding their transport properties, most inorganics are not viable electrolyte materials "on their own." Their synthetic characteristics and physical properties make them impractical for direct utilization in real fuel cells. In some manner, the inorganic material must be supported. More so than the challenge of identifying inorganic materials with sufficiently high property values, the major obstacle here is engineering a total material system that allows the inorganic component to contribute conductivity while not losing the processability and handling characteristics of a solid polymer film.

It is a key characteristic of the 3M approach that novel synthetic pathways and resultant composite morphologies be developed for polymer-matrix electrolytes. Most attempts to-date to incorporate inorganic phases into polymer matrices fall into one of the following categories:

i) physical dispersion of an inorganic filler into a polymer melt or pre-polymer solution
ii) solution impregnation of a soluble additive into a preformed polymer[3]

The proposed research here differs in the following way. We propose a focus on exploring new pre-polymer and inorganic precursor chemistries designed for the co-synthesis of multiphase materials with novel microstructures. Central to the achievement of useful inorganically modified polymers or hybrid organic/inorganic materials, will be the ability to control the dimensionality and connectivity of new microstructures. The utility of a high-conductivity inorganic constituent within a polymer matrix will hinge on an ability to establish a high degree of "connectedness" for that constituent. At the same time, it would not be desirable for the inorganic component to dominate the other physical properties (modulus, strain-to-failure, toughness, etc.). Literature reports detailing attempts to combine solid inorganic filler particles with polymer matrices underscore this issue. To illustrate, Boysen *et al.* incorporated $CsHSO_4$ particles into a matrix of PVDF.[4] The measured composite conductivity values fell short of that for pure $CsHSO_4$ by at least one order of magnitude until the inorganic particle loading was raised to the point that the samples were "brittle and easily broken." The authors clearly appreciated the value of retaining the physical properties of a polymer. To avoid this problem for polymer systems filled with discrete inorganic particles, it is foreseen that wholly new synthetic approaches and microstructures are needed.

In our view, fulfilling the promise of inorganic electrolyte materials in elevated temperature (>120ºC) PEM fuel cells depends on developing new routes to incorporate the inorganic constituent within thermally and oxidatively stable polymer support matrices. Although not yet fully applied in the proton exchange membrane area, the concept of hybrid organic/inorganic composites with very small scale interpenetrating microstructures is well developed. Owing to an abundance of available and readily synthesized molecules, silicate-modified polymers have received the most attention.

Numerous polymers have been modified with an internal molecular-scale interpenetrating silicate network.[5,6]

Silicate-modified polymers ranging from acrylates to epoxies to polyethers have been investigated. For most polymer systems, property values like modulus and hardness can be increased continuously upon such modification. Through careful precursor development, it has been shown that inorganic functionality can be gracefully rendered to polymer systems. Proton exchange membranes for elevated temperature operation may be an ideal application for such an approach. *The key goal of the proposed research will be arriving at a precursor chemistry that incorporates a desired inorganic constituent with the necessary degree of connectivity for high conduction, with the necessary control over scale and loading of that constituent not to compromise the polymer's physical properties.*

The proposed research will go beyond the silicate and polymer chemistries already reported. Considering the families of inorganic proton conductors below as starting points, hybrid materials will be synthesized that incorporate key inorganic structural elements for enhanced conductivity and durability. For the polymer, the focus will also be on thermal and oxidative stability as well as mechanical properties. The most suitable candidates are expected to be drawn from the fluorinated and aromatic compounds.

Inorganic ion conducting phases: The following families of inorganic proton conductors suggest the types of structural elements that may be usefully incorporated in a polymer system. The variety of materials represented below is an indication of the varied environments in which protons can find themselves mobile. Of course, water still plays a role in the conduction mechanism for some of the materials. By and large however, the hydration state is more stable for these inorganics than for perfluorinated ionomers like Nafion.

- acid salts (e.g., $CsHSO_4$)
- heteropolyoxometallates (e.g., 12-phosphotungstic acid)
- layered metal phosphates and phosphonates (e.g., $Zr(HPO_4)2H_2O$)
- bulk-conductive perovskites (e.g., $BaCeO_3$)
- surface-conductive high surface area oxides (e.g., SiO_2)

For microporous, low-temperature-synthesized oxides like SiO_2 or TiO_2, surface chemical factors like acidity and extent of protonation influence conductivity. For such oxides formed with surface area values of 100's of m^2/g, Anderson and coworkers have reported conductivity values that reach 4 mS/cm at 92ºC-81% RH.[7] On an even smaller scale, a mechanism not unlike surface conduction operates in the case of layered metal phosphates and phosphonates. In the case of zirconium phosphates for example, it is along the surface of separated hydroxylated zirconium phosphate planes that protons are mobile.[8] When organic, protogenic functional groups are attached in place of hydoxyls on the planes, the hydrated compounds have increased proton conductivity.[8]

Other inorganics of interest include a family of proton-conductive metal acid salts that exhibit a unique range in structural dimensionality. Specifically, in the $CsHSO_4$-CsH_2PO_4 system, phases with various symmetry characteristics and proton conduction behavior exist.[4] Phases containing hydrogen-bonded sulfate and phosphate groups with 1-, 2-, or 3-dimensional connectivity have been shown to undergo structural transitions between

room temperature and 150ºC that lead to proton conductivity values in excess of 10 mS/cm. Acid salts such as these are not very useful directly, owing to their water-solubility and poor mechanical characteristics. However, the hydrogen-bonded sulfate and phosphate groups themselves, if connected and bound in a polymer matrix, may provide the conductive functionality without the undesirable solubility and mechanical properties of the salts.

Clearly, the proton conductivities and other properties of these bulk inorganic materials are not suitable for use in PEM fuel cells. The present section is intended to communicate the breadth of options that exists for using known inorganic materials as the starting point for contemplating polymer-matrix systems modified with inorganic functionality. In the proposed research, it is anticipated that new inorganic-organic microstructures with heretofore unreported, improved properties will be prepared. A key aspect of the effort will be the rational synthesis of new precursors. Through optimization of the microstructure, and possibly incorporation of other conductivity enhancing components such as the fluorinated liquids described below, we hope to develop a composite membrane having an optimized morphology and area specific resistance of less than 0.1 ohm-cm^2, as required in Subtopic 1.A.2.

Fluorinated liquids: As stated above, perfluorinated sulfonic acid containing polymers such as Nafion are the basis for most current PEM's. Polymers based on other similar "super acid" anions such as bis sulfonyl imides and bis sulfones have been proposed as Nafion replacements with increased thermal stability, although these materials still suffer from loss of conductivity due to drying at high temperatures.[9] Liquid fluorinated acids and their salts, such as trifluoromethane sulfonic acid,[10, 11] tetrafluoroethane-1,2-disulfonic acid,[12] and bis(trifluoromethanesulfonyl) methane[13] have been studied as potential liquid fuel cell electrolyte materials. These materials show good oxygen solubility and oxygen reduction kinetics. The larger, highly non-coordinating anions, such as the bis sulfonyl imides and bis(trifluoromethanesulfonyl) methane in particular, should be less likely to adsorb on the catalyst surface. Addition of fluorinated sulfonic acid salts to phosphoric acid based electrolytes has also been shown to improve oxygen reduction kinetics.[14] As with the inorganic materials described above, these liquids must be isolated in a polymer membrane for use in a PEM fuel cell. Some examples of incorporation of fluorinated liquids into a polymer film have been reported.[10] These films have shown good ionic conductivity at ambient[10a] and elevated[10b] temperatures.

Several technical challenges still remain to allow membranes of this type to be used in high temperature fuel cells. While the "ionic liquid" based proton conducting films described by Doyle et. al. [10b] have good conductivity at high temperatures, the stability of this system has not been demonstrated. The salts used are water-soluble and the organic cations would not be expected to have the oxidative stability required. While less polar, non-water soluble ionic liquids of this type are known[15], the protonated form of these anions, which should exist in equilibrium with the salt, are still quite volatile. Slow loss of these acids would lower the number of charge carriers in the electrolyte and limit the lifetime of these membranes. The thermal and oxidative stability of the Nafion matrix could also pose a problem at higher temperatures. An additional problem exists in using a non-polar liquid such as these in an MEA. In MEA's using a dispersed, particulate catalyst system, the porous catalyst layer can absorb the fluorinated liquid from the membrane, causing loss of electrolyte conductivity and mass transport problems in the catalyst. This would be particularly true for Teflon™ containing dispersed catalyst systems.

High boiling liquid ion conductors based on 3M's fluorinated sulfonic acid/sulfonyl imide technology could be an effective "water replacement" in these membranes and, used in conjunction with 3M's nanostructured thin layer catalyst technology, could provide MEA's capable of operating for extended periods at elevated temperature. 3M has a great deal of experience in developing partially and completely fluorinated anions based on bis sulfonyl imides, bis and tris sulfonyl methanes[16]. In particular, partially fluorinated perfluoroalkyl-aromatic mixed bis sulfonyl imides developed here have been shown to have similar acidity and oxidative stability to their perfluorinated counterparts and have boiling points much higher (≥100°C). These molecules have substantially higher thermal stability than the corresponding aromatic sulfonic acids, which de-sulfonate at elevated temperatures. Bis or poly-acids based on these molecules are essentially non-volatile when protonated, and some remain liquid at room temperature. Salts of some of these fluorinated compounds with aromatic or aliphatic, quaternary or protonated nitrogen containing cations are also liquids at room temperature, some of which are insoluble in water. Incorporation of these acids, either in the acid or salt form, into a stable polymer or nanocomposite matrix can give a PEM suitable for use in high temperature MEA's.

The ratio of cations to anions and the identity of R and Rf groups should be such to provide non-volatile water insoluble liquids with good proton conduction. Proton conduction in materials of this type is not fully understood. Varying the chemical structure, and in some cases the cation/anion ratio, and then measuring conductivity, proton conductivity and performance in model fuel cell systems (i.e. with Nafion or PBI under dry hot conditions) will allow us to develop some understanding of factors affecting proton transport. Theoretical modeling, as described in Subtask 2.3, will also give insight here.

These fluorinated materials can be evaluated as neat liquids or solutions, but ultimately must be incorporated as part of a membrane. Careful consideration needs to be given to selection of the polymer matrix. Existing acid containing, base containing, or neutral polymer matrices could be suitable, or the fluorinated liquids could be added to the organic/inorganic composite materials outlined above. A PBI type polymer could be a good matrix for some of these liquid acids. The surface of an inorganic component could also serve as an acid or base in conjunction with one of the structures shown above. *Particular attention will be given to "matching" the properties of the fluorinated material and the inorganic material in such three phase composites.*

New polymers may be required. Polymer morphology, stability, thermal properties and cost would be important factors here. Synthesis of a two or three phase composite including one or both of the materials described above would have to be done carefully to give a membrane with the proper morphology to give performance and durability. While Nafion could be used as a matrix polymer for some initial testing of approaches, thermal stability, mechanical properties, and price issues could make another polymer more desirable.

Work Plan (Subtask 2.1)

a) Synthesis of inorganic conducting phase materials, both in bulk form, in standard polymer matrices such as Nafion and PBI, and in composite microstructures. Do electrochemical evaluation of these materials using EIS with 4-probe cell at different temperatures, pressures and humidity levels.

b) Develop methods of formation of novel microstructures, and understand relationships between morphology and proton conductivity. Do electrochemical evaluation as in (a). Identify catalyst system for initial fuel cell screening tests.
c) Synthesize fluorinated liquids with low volatility and freezing point below room temperature.
d) Test liquid phase conductivity, oxygen reduction kinetics at Pt, and the thermal and electrochemical stability of fluorinated liquids.
e) Test fluorinated liquids in standard polymer matrix, using EIS and fuel cell testing with nanostructured catalyst. Develop understanding of relationship between matrix functionality (acid, base, neutral) and physical and electrochemical properties of blend.
f) Identify polymer or nanocomposite matrix for fluorinated liquid that gives best performance, mechanical properties and durability.
g) Select optimized membrane from above materials.
h) Develop coating or membrane forming technique and optimize membrane thickness.

3.2. Addition of Inorganic Components To PFSA's For Improved Performance

As described in the previous sections, there is a significant need to improve the power performance of PEMFC's operating under hot and dry conditions. A primary contributor to the drop in performance with increasing temperature and decreasing relative humidity is the steep drop in PFSA membrane proton conductivity. Accordingly, there has been a substantial effort underway in the materials science and electrochemistry communities to develop membrane materials with a flat humidity dependence of high proton conductivity, and the review article by Li *et al.* provides an excellent introduction.[17] No attempt will be made here to generate an exhaustive review of the literature, as the volume of reported work in this area has exploded in recent years and it can be searched readily. As part of the presently reported program, a number of inorganic materials were investigated for their potential as additives to improve the performance of PFSA membranes.

In the open literature, there are an immense number of articles now published on the use of inorganic materials in PEMFC membranes. Table I presents a sampling of the materials that have been reported. To be sure, the increasing breadth of the materials systems addressed has dramatically outpaced the characterization that is needed to fully assess them. Compared with what is now known and understood about PFSA membranes, the vast majority of research that has been done on PEMFC's with inorganic materials in the membrane cannot be described as much more than proof of concept. Combined with this shortage of actual fuel cell measurement results is the considerable challenge of reproducibility that accompanies these complex electrochemical devices. Thus, the 3M research that is reported herein includes a fair amount of work that can be considered a reproducing of past studies, except now with the use of 3M's PFSA, instead of Nafion™. That being said, this report includes new work on certain organosulfonic acid-functionalized silica materials, certain heteropolyacids, including attempts to immobilize Lacunary heteropolyacids using sol-gel chemistry, and modified sol-gel zirconium alkoxide additions to PFSA's.

Most strategies for exploiting inorganic materials in PEMFC electrolytes can be broken down into the following categories:

1. Addition of hygroscopic oxides to PFSA's to improve water retention

2. Addition of bulk or surface proton-conducting phases (e.g., heteropolyacids (HPA)) to PFSA's or other polymers to enhance overall conductivity
3. Combination of phosphoric acid with basic polymers (e.g. polybenzimidazole)
4. Polymer binder support of superprotonic conductors (e.g., $CsHSO_4$)
5. Incorporation of phosphoric acid or HPA with polysiloxanes

After reviewing the literature and testing some initial materials in Category 1 above, it was decided that any improvements that the approach could yield would be marginal at best, compared with the need. The superprotonic conductors of Category 4 suffer from a strong temperature dependence of conductivity and water solubility. Also, in formulating composites with these brittle materials, it has proven very difficult for other researchers to balance the need for inter-particle conductivity (and hence connectivity) and composite material flexibility. The superprotonic conductors were avoided in the presently reported work. Materials akin to those of Category 3 were investigated under DOE DE-FC04-02AL67621, using 3M fluorinated acids instead of phosphoric acid, together with metal oxide powders and polymeric binder. The latter work is reported in section.

Polysiloxane materials with phosphoric acid (Category 5) were investigated briefly in the current program. However, they tended to exude the acid and were physically very much inferior to PFSA materials. Future work could be reasonably directed at the polysiloxanes. Finally, the materials that were studied most extensively, reported in the following three sections, fall within Category 2. They are PFSA-matrix membranes with heteropolyacids, organosulfonic acid-functionalized silica, or zirconium oxide-based additions.

Table I. Sampling of inorganic materials that have been studied as potential proton electrolyte membrane materials for fuel cells (alone or in combination with a proton-conducting polymer like PFSA).

SiO_2 particles (Bocarsly)	Polysiloxane - H_3PO_4 (Honma)
TiO_2 particles (Bocarsly)	Polysiloxane - H_3PO_4•12(WO_3)•xH_2O (Honma)
ZrO_2 (alkoxide-impregnated) (Mauritz)	B_2O_3-SiO_2 gel (sulfonated) (Fujinami)
SiO_2 (mesoporous particles) (Peled)	$Mg_4Si_6O_{15}(OH)_2$•6H_2O - SO_3H (Acosta)
SiO_2 (alkoxide co-synthesis) (Kim)	$Sn_{3.6}Si_{40}Al_8O_{128}H_{56}$ (Knudsen)
TiO_2 (alkoxide co-synthesis) (Nunes)	$CsHSO_4$ (Haile)
Pt-SiO_2 (Watanabe)	H_3PO_4•12(WO_3)•xH_2O (Chandra, McGrath, etc.)
Pt-TiO_2 (Watanabe)	H_3PO_4•12(MoO_3)•xH_2O (Chandra)
SiO_2-P_2O_5 gel (Matsuda)	H_4SiO_4•12(WO_3)•xH_2O (Savagado)
CaO-P_2O_5 gel (Kasuga)	SiO_2 - H_4SiO_4•12(WO_3)•xH_2O (Staiti)
TiO_2-P_2O_5 (Tsuru)	SiO_2 - H_4GeO_4•12(WO_3)•xH_2O (Yu)
SiO_2-B_2O_3-P_2O_5 gel (Morin)	□-Zr(O_3POH)•H_2O (Alberti, Bocarsly, Grot)
SiO_2-P_2O_5-ZrO_2 gel (Klein)	□ -Zr(O_3PR^1)$_x$(O_3PR^2)$_{2-x}$•xH_2O (Alberti)
ZrO_2-H_3PO_4 (Boilot)	□ -Zr(O_3POH)•H_2O (intercalated) (Calevi)
SiO_2-H_3PO_4 (Matsuda)	□ -Zr(O_3POH)•H_2O (exfoliated) (Mallouk)
Siloxane - peroxopolytungstic acid (Orel)	

3.2.1. Heteropolyacids (HPA's)

Heteropolyacids are a class of inorganic compounds characterized by a well-defined proton-charge-balanced oxo-anion cluster comprising multiple cations of a primary transition metal and at least one heteroatom cation. At present there are hundreds of known heteropolyacid compounds. In their pure form, they exist as hydrated crystals comprising a hydrogen-bonded assembly of the oxo clusters. As an example Fig. 1, illustrates some aspects of the structure of silicotungstic acid. The exceptional proton conductivity of heteropolyacids was first reported in the 1970's by Nakamura, and their potential as proton-conducting electrolytes for fuel cells was noted immediately.[18] Notwithstanding 30 years of attention, these materials still are not being used in fuel cell applications. The primary limitations of HPA's are:

- Water solubility
- Brittleness
- Hydration dependence of proton conductivity
- Interfacial contact to electrode catalyst

Among all inorganic solids, with the exception of superprotonic conductors, the heteropolyacids exhibit the highest proton conductivity. The reason that HPA's were chosen for investigation over superprotonic conductors in the currently reported program is that the latter rely on a particular long-range crystalline structure (and associated vibrational dynamics) for their properties. Accordingly, in contrast to the behavior that might be expected for disordered or nanostructured materials comprising HPA's with their fast proton transport that occurs between and amongst clusters, assemblies of superprotonic conductor crystals are expected to be limited more substantially by interparticle barriers. Individual HPA clusters and the surfaces of HPA particles, with their property of transporting protons along or outside the clusters, were expected to interact more favorably with sulfonic acid groups in the PFSA ionomer than bulk conductors like cesium sulfate. Of course, future work might reasonably be directed at exploring this assumption.

Fig. 2 gives the dependencies of hydration on relative humidity and proton conductivity on hydration for a number of HPA's. Like the PFSA's, HPA's exhibit a sharp dependence of proton conductivity on extent of hydration. Taken on their own, the properties depicted in **Fig.** 2 would not give much hope for HPA's to positively impact the properties of PFSA membranes. However, research by others has shown that HPA's can boost the properties of materials whose properties on their own are superior to those of HPA's. These examples of benefits from HPA's highlight a current perception in the fuel cell membrane community that there are favorable, but not well understood, interactions between HPA's and polymeric electrolytes.

In the three sections that follow, research is presented that was aimed at determining the potential of HPA's to improve the performance of MEA's based on 3M's PFSA ionomer. In addition to determining performance improvements, work was started to overcome the problem of water solubility. Results are presented from experiments aimed at determining whether interactions between HPA and silica could lead to improved HPA retention. The experiments reported herein are limited to those performed at 3M. It is important to note that most of the work aimed at HPA retention was carried out as a collaboration with the Colorado School of Mines (subcontractor on DOE DE-FC04-

02AL67621), Prof. Andrew Herring, Professor. Specifically, although there was work initiated and carried out at 3M on combinations of HPA with TEOS or colloidal SiO_2 in the PFSA membranes, a great deal of work on using more reactive Lacunary HPA's with sol-gel silica chemistries was initiated and carried out at CSM. 3M consulted on the latter work, and received samples for evaluation. No further information on the CSM-initiated work will be reported herein, but is included in a final report from CSM (Appendix A).

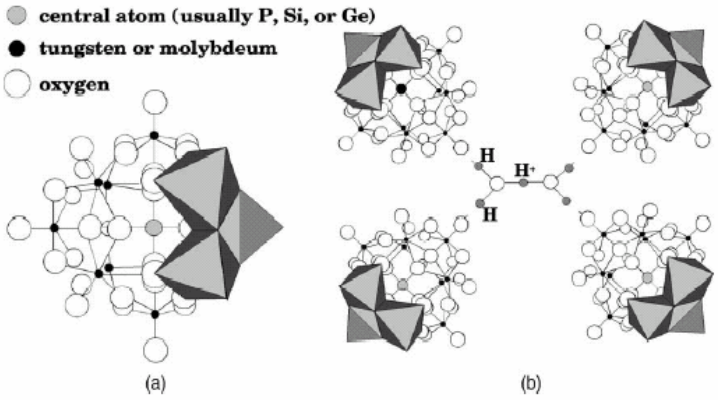

Fig. 1. Structure of Keggin family of heteropolyacids**.** [19]

TABLE 1. Composition of Crystal Hydrates $HPC \cdot nH_2O$ as a Function of the Humidity (p/p_0) at T = 20°C

Sample No.	HPC	Degree of hydration n at p/p_0:			
		0.4	0.6	0.8	0.9
1	$Cs_2HPMo_{12}O_{40}$	4.0	4.6	5.8	6.1
2	$(NH_4)_4SiW_{12}O_{40}$	4.8	6.5	6.9	7.3
3	$H_3PW_{12}O_{40}$	11.0	13.7	21.1	30.0
4	$H_3PMo_{12}O_{40}$	11.8	14.0	29.0	32.0
5	$H_4SiW_{12}O_{40}$	18.0	25.1	32.8	Deliquesces
6	$H_5PW_{10}V_2O_{40}$	22.0	22.0	33.0	–
7	$H_6P_2W_{18}O_{62}$	29.7	40.0	–	–

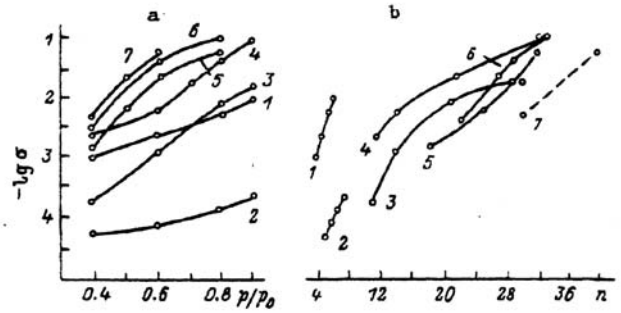

Fig. 1. Conductivity σ $(\Omega \cdot cm)^{-1}$ of heteropoly compounds as a function of the relative humidity p/p_0 (a) and the degree of hydration n (b). The numbering of the curves corresponds to the data in Table 1.

Fig. 2. Published property data for HPA's. [20]

3.2.1.1. Measured Properties For Starting Compounds

A number of HPA compounds were synthesized at the Colorado School of Mines (CSM) and delivered to 3M for investigation. The experimental approach was to measure conductivity of the HPA powders first on their own, because properties for many of the compounds are not reported in the literature. Next, the compounds were loaded into 3M's ionomer to give composite electrolyte films, and those films were characterized for proton conductivity and fuel cell performance. Finally, various experiments were carried out to immobilize one of the compounds (silicotungstic acid, STA) on silica. This section reports the measured properties for HPA compounds on their own.

Table II lists the HPA compounds that were received from CSM. Proton conductivity for each of the powders was measured by impedance spectroscopy, using a specially fabricated conductance cell. Fig. 3 gives a schematic drawing of the cell, which included small cross bores so that the sample slugs could be exposed to different atmospheres during measurement. For each measurement, 0.1g of HPA powder was loaded into the sample volume and compressed to the following dimensions: 8.2mm dia and 1mm thickness. The cell was placed in an oven with humidity control. Impedance complex plane plots were analyzed, with the high-frequency real-axis intercept taken as the sample resistance. A total sample conductivity was calculated, based on the cell dimensions. Therefore, the properties reported should be regarded as including contributions from the HPA crystals, any void space among crystals, and interfaces between crystals. Accordingly, each of the HPA compounds can be regarded as possessing bulk conductivity that is at least as high as the values reported. Fig. 4 gives conductivity curves for eleven of the HPA's in Table II. Although substantial differences between compounds was observed, it became apparent in carrying out the study that different conductivity ranges were strongly associated with certain physical properties for the powder. Specifically, some of the HPA powders exhibited a plastic quality during pressing, while others were notably hard and brittle. The former led to sample slugs in the cell that were quite strong and apparently characterized by intimate particle-to-particle interfaces. The latter led to sample slugs in the cell that crumbled more easily. The compounds that formed slugs with strong interparticle bonding were measured to have the highest conductivity values, while the hard and brittle powders were measured to have lower conductivity values. Therefore, in the interpretation of the data in Fig. 4, there is an open question as to the influence of interparticle conductivity on the measured values. That is, the higher measured values may be the result of truly higher bulk conductivity or they may be the result only of higher interfacial conductivity. It may be reasonable to speculate that the two explanations are indeed both applicable, given that the bulk conductivity and the compressibility into strong pellets would both be expected to be maximized for the same compounds, those with the greatest capacity to retain large amounts of water of hydration. The data presented in Fig. 4 represents all of the effort applied to characterizing the HPA compounds on their own.

Table II. Heteropolyacid compounds received from Colorado School of Mines**.**

Sample Description	Shorthand
$H_3PW_{12}O_{40}$-x H_2O	**PTA**
$H_4SiW_{12}O_{40}$-x H_2O	**STA**
$H_6ZnW_{12}O_{40}$-x H_2O	**ZTA**
$H_7AlCoW_{11}O_{39}$-x H_2O	**ACTA**
$H_6CoW_{12}O_{40}$-x H_2O	**CTA**
$H_5SiAlW_{11}O_{39}$-x H_2O	**SATA**
$H_{21}B_3W_{39}O_{162}$-x H_2O	**BTA**
$H_6P_2W_{21}O_{71}$-x H_2O	**$PT_{21}A$**
$H_8SiW_{11}O_{39}$-x H_2O	**$ST_{11}A$**
$H_6As_2W_{21}O_{69}$-x H_2O	**ATA**
α-$H_3P_2W_{18}O_{62}$-x H_2O	**α-PTA**
$H_{12}Fe_4W_{30}O_{112}$-x H_2O	**IPTA**

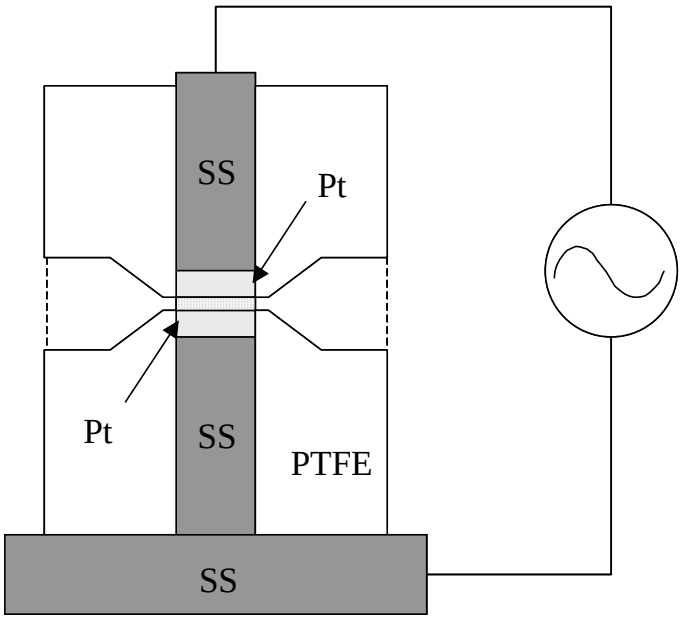

Fig. 3. Schematic representation of the powder conductivity test cell; powder sample area = 0.52cm2, thickness = 0.1cm.

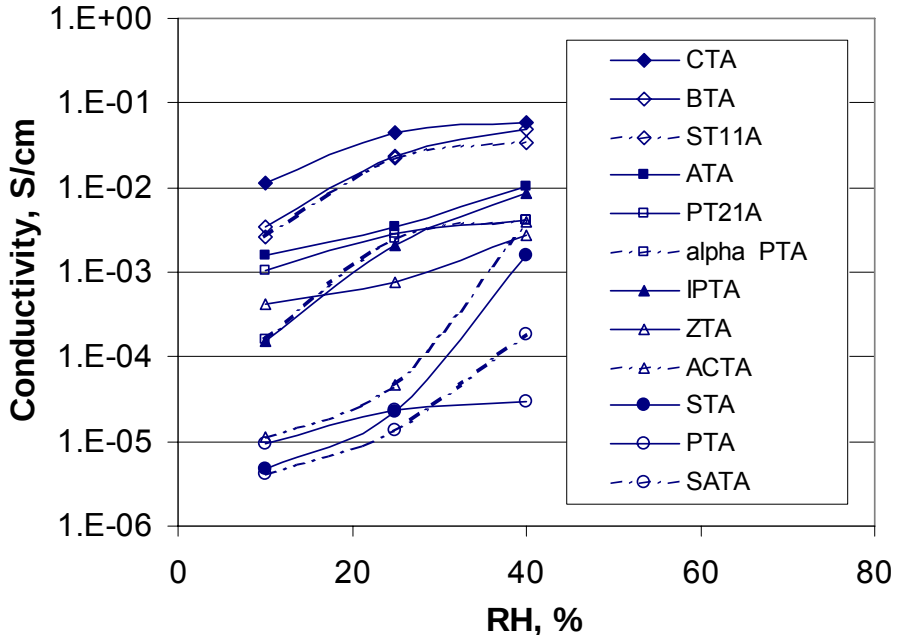

Fig. 4. Measured powder conductivity for the HPA compounds in Table II**.**

3.2.1.2. Addition Of HPA's To The 3M PFSA Ionomer

Numerous other researchers have added HPA compounds to proton-conducting polymer films, including PFSA films.[10] Consistent with the general observation for inorganic materials in polymeric electrolytes, the reported data are very inconsistent. Thus, it was reasonable in carrying out the presently reported program to pursue fairly simple approaches to evaluating this class of compounds in 3M's PFSA, and to determine independently what improvements could be realized for 3M's MEA constructions and operating conditions of interest.

Each of the HPA compounds in Table II was added to the 70/30 by weight mixed-solvent n-propanol/water dispersion of 1000EW 3M PFSA ionomer, with stirring. Table III gives the observations of the HPA-added dispersions. In many cases, the HPA dissolved to give a clear dispersion. In other cases, addition of the crystals yielded turbid dispersions. In the latter case, the turbid dispersions did not seem to be simply suspensions of the original, fairly large crystals, but rather a stable finer-scale suspension of particles. Nothing more was done to study the state of the HPA clusters and/or particles in the ionomer casting dispersions. Membrane films were cast from the dispersions using a 20mil-gap bar coater on glass, with 15min drying in air, 10min drying in air at 80-90°C, and 15min annealing in air at 200°C.

Fig. 5 through Fig. 7 give measured proton conductivity for 3M PFSA ionomer membranes with 5 or 10wt% loadings of different HPA's. As indicated in the Figures, silicotungstic acid and phosphotungstic acid both resulted in progressively higher proton conductivity with increasing wt% loading, particularly under higher relative humidity conditions. The data for STA and PTA in Fig. 5 and Fig. 6 represent the most significant and consistent improvements in proton conductivity that were realized for PFSA/HPA composites in the study. Fig. 7 is a collection of proton conductivity curves for a variety

of PFSA/HPA composite membranes with 10wt% HPA added, illustrating the range of data that was observed.

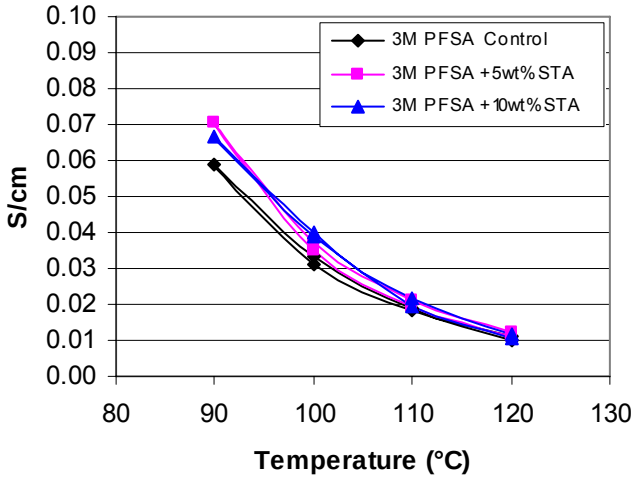

Fig. 5. Proton conductivity vs. temperature at fixed dew point of 80°C for ca. 1000EW 3M ionomer membranes loaded with 0, 5, and 10wt% silicotungstic acid.

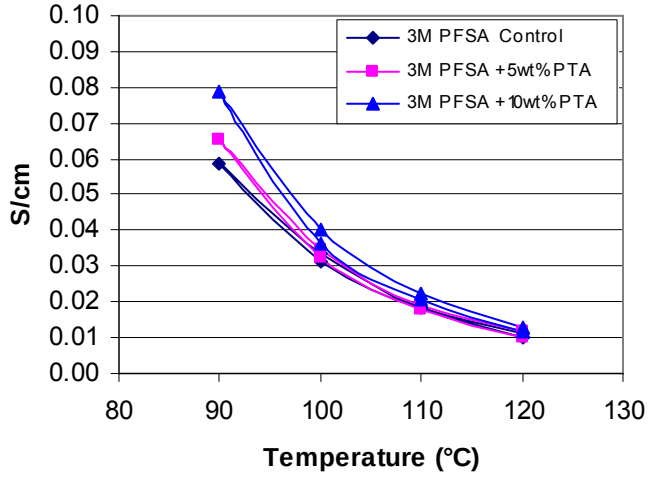

Fig. 6. Proton conductivity vs. temperature at fixed dew point of 80°C for ca. 1000EW 3M ionomer membranes loaded with 0, 5, and 10wt% phosphotungstic acid.

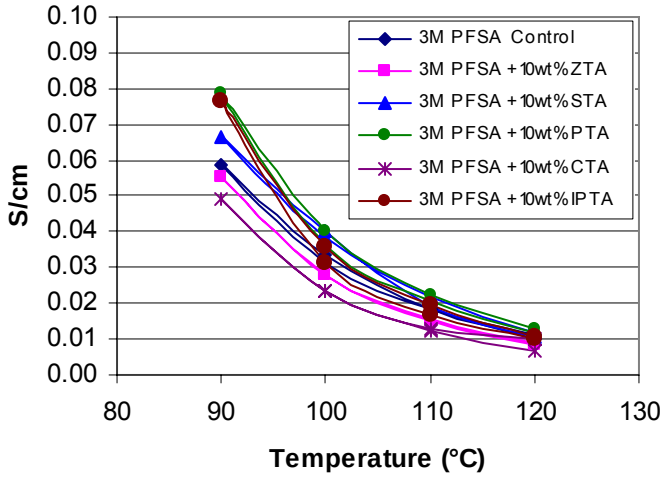

Fig. 7. Proton conductivity vs. temperature at fixed dew point of 80°C for ca. 1000EW 3M ionomer membranes loaded with 0 or 10wt% various HPA's (see Table II).

Table III. Observations of HPA-loaded PFSA casting dispersions and films.

Sample Description	Shorthand	Casting Dispersion	Cast Films
1000EW 3M Ionomer Control		Clear and nearly colorless	Clear light amber
10wt% $H_3PW_{12}O_{40}$-*x* H_2O	PTA	Clear and nearly colorless	Clear light amber
10wt% $H_4SiW_{12}O_{40}$-*x* H_2O	STA	Clear and nearly colorless	Clear light amber
10wt% $H_6ZnW_{12}O40$-*x* H_2O	ZTA	Turbid and yellow-green	Clear dark brown
10wt% $H_7AlCoW_{11}O_{39}$-*x* H_2O	ACTA	Slightly turbid blue-green	Clear brown-orange
10wt% $H_6CoW_{12}O_{40}$-*x* H_2O	CTA	Slightly turbid darker blue-green	Clear brown-orange
10wt% $H_5SiAlW_{11}O_{39}$-*x* H_2O	SATA	Turbid yellow	Clear amber with **blister-like bubbles**
10wt% $H_{21}B_3W_{39}O_{162}$-*x* H_2O	BTA	Turbid colorless	Clear amber
10wt% $H_6P_2W_{21}O_{71}$-*x* H_2O	$PT_{21}A$	Turbid colorless	Clear light amber
10wt% $H_8SiW_{11}O_{39}$-*x* H_2O	$ST_{11}A$	Slightly turbid colorless	Clear light amber with **many small bubbles**
10wt% $H_6As_2W_{21}O_{69}$-*x* H_2O	ATA	Clear and slightly yellow	Clear brown-orange (**bubbles in some samples**)
10wt% α-$H_3P_2W_{18}O_{62}$-*x* H_2O	α-PTA	Clear and nearly colorless	Clear light amber

Many of the HPA-loaded membranes were further tested for fuel cell power performance and fluoride ion evolution. MEA's were fabricated with dispersed catalyst electrodes. Results were quite varied for MEA's that included 3M ionomer membranes with HPA's added, ranging from substantially reduced power performance for ZTA additions to

modest improvements for STA additions. STA proved to have the greatest positive impact on both power performance and fluoride ion evolution.
Fig. **8** gives measured voltage at 0.5A/cm^2 current density for MEA's with and without 10wt% STA added to the membrane. In addition to the modest power performance improvement, the evolution rate of fluoride ion was reduced from 0.092 to 0.055 micrograms/min. To the authors' knowledge, prior to the currently reported work, HPA's had not been observed to contribute a stabilizing effect on the degradation of PFSA ionomers.

As opposed to results for most other inorganic additions to PFSA membranes, it was established in the currently reported research, with replication of samples and measurements, that STA at least can improve the power performance of PFSA PEMFC's, under some conditions. At the time of the close of the DOE DE-FC04-02AL67621 contract, the improvements are considered interesting and worthy of further development, but not yet extremely significant.

3.2.1.3. Addition of HPA's to 3M PFSA ionomer, together with SiO_2

Recognizing that the benefits of HPA addition to PFSA membranes are somewhat impractical if the HPA can be washed out by water, and knowing that water generation and transport by diffusion and electroosmotic drag are constantly occurring in a PEMFC, attempts were made to immobilize various HPA's in 3M's PFSA ionomer. The approaches can be categorized as follows:
Combination of HPA with tetraethylorthosilane (TEOS) in the PFSA dispersion
Combination of HPA with colloidal SiO_2 in the PFSA dispersion
Combination of Lacunary HPA with TEOS and/or other silanes in the PFSA dispersion

As stated above, this report is limited to the first two immobilization approaches above. In large part, this work was exploratory and empirical in nature. Specifically, characterization in several cases was limited to measurements of weight loss on exposure of composite membranes to water, and thus upper limits on the amount of HPA that was washed out were determined. Given the volume of other research pursued under the program, there was not time to follow up with more extensive investigations.

Using the 70/30 by weight n-propanol/water mixed-solvent casting dispersion for 1000EW 3M PFSA ionomer, controlled additions of phosphotungstic acid (PTA) and TEOS allowed for the preparation of a matrix of composite membrane samples, with PTA levels ranging from 0 to 30wt% and SiO_2 levels of 0 or 10wt% (assuming full conversion of the TEOS to SiO_2). Films were cast using a 20min gap bar coater on glass, with 15min drying air at room temperature, 10min drying in air at 80°C, and 15min annealing in air at 160°C. Weighed pieces of the films were then boiled in water for 1hr. Mass readings after boiling were used to calculate weight loss for each sample. Table IV gives the results of this study. The primary finding was that TEOS additions had helped to retain PTA, but only when the HPA addition reached fairly high levels. A potential mechanism of such retention might be one of physical entrapment of the HPA clusters. Physical entrapment would be regarded as the least desirable of retention mechanisms, because encapsulation of the HPA would most likely render it useless in aiding proton conduction, if its interaction with the hydrated sulfonic acid groups of the polymer is required. A useful conclusion from the experiment was that TEOS-derived

silica alone does not offer a substantial chemical interaction that leads to HPA retention (at least not PTA) in PFSA membranes.

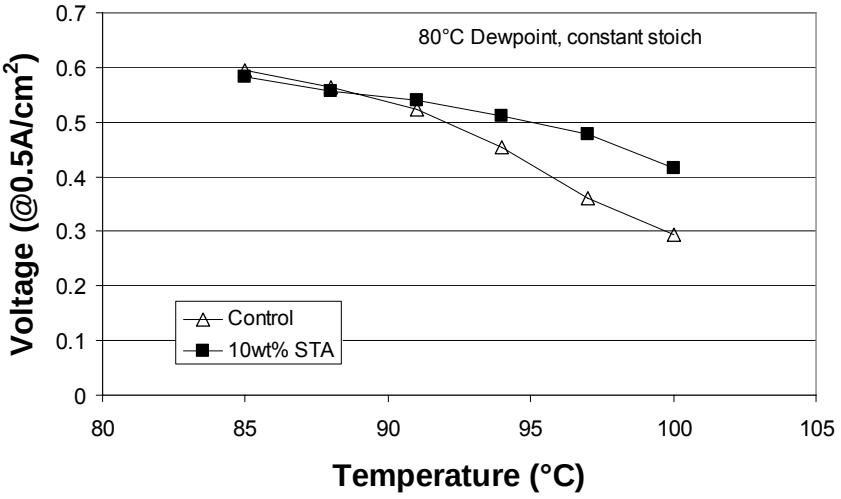

Fig. 8. Fuel cell power performance improvement under progressively drier conditions for ca. 1000EW 3M PFSA ionomer membrane with 10wt% silicotungstic acid.

Combination of HPA with TEOS in PFSA casting dispersions

Table IV. Weight loss for PFSA/SiO2/PTA composite membranes on boiling; figures are taken to be the amounts of HPA that were washed out.

wt% PTA	wt% SiO_2 = 0	wt% SiO_2 = 10
5	5.1	5.4
15	13.9	9.4
30	26	9.2

Combination of HPA with colloidal SiO_2 in PFSA casting dispersions

Based on i) the finding above that TEOS aided in HPA retention only when the HPA was added at high levels, ii) the expectation that the limited amount of HPA that was retained was probably physically encapsulated, and iii) the desire for HPA to remain exposed to the PFSA matrix, work was done to investigate HPA interactions with various silica colloids. In this experiment, commercial silica colloids were added, together with PTA or STA, to the 70/30 by weight n-propanol/water mixed-solvent casting dispersion for 1000EW 3M PFSA ionomer, with stirring. Films were cast using a 20min gap bar coater on glass, with 15min drying air at room temperature, 10min drying in air at 80°C, and 15min annealing in air at 200°C. In all cases, the wt% levels of SiO_2 and HPA in the cast membranes were both 10%. The samples were investigated for the ability to retain the HPA in two stages. First, each film sample was stirred in water at room temperature for 1hr, and its weight change determined. Next, each sample was further stirred in boiling water for 1hr, and its final weight change (relative to its initial weight) was determined. Fig. 9 gives results for the HPA retention experiment. Nalco 2326 is a

basic colloidal silica sol with excess ammonia and a particle size of 5nm. Nalco 2327 is a basic colloidal silica sol with excess ammonia and a particle size of 20nm. Nalco 1042 is an acidic silica sol comprising essentially only the negatively charged 5nm silica particles and free protons. Two key findings revealed in Fig. 9 were i) that the basic silica sols caused PTA to be preferentially retained, while a negative effect was realized for STA, and ii) the acidic silica sol had no effect on either HPA.

Because it was known that the addition of a basic silica sol, with its excess ammonia, would i) reduce the acid content of the PFSA membrane, and ii) possibly yield the ammonium salt of the HPA's, and those might have very different solubility properties in each case to their acid forms, follow-on experiments were carried out. First, the acid contents of colloidal silica-loaded PFSA films were measured by titration. Fig. 10 gives titration results for the films. The data in Fig. 10 illustrate that the loss in IEC that would be predicted for simple mass dilution of the PFSA by SiO_2 is realized after reacidification with H_2SO_4, for PFSA/SiO_2 (basic colloid) composites. Next, membranes comprising the PFSA matrix, SiO_2 added in the form of the basic silica sol, and PTA were determined for their HPA retention behavior *after reacidification*. Interestingly, even after reacidification, PFSA composites comprising PTA and silica added as a basic silica sol, exhibit low weight loss values on boiling, suggesting that some lasting retention feature exists for that combination. No further work was done to investigate or exploit this interaction.

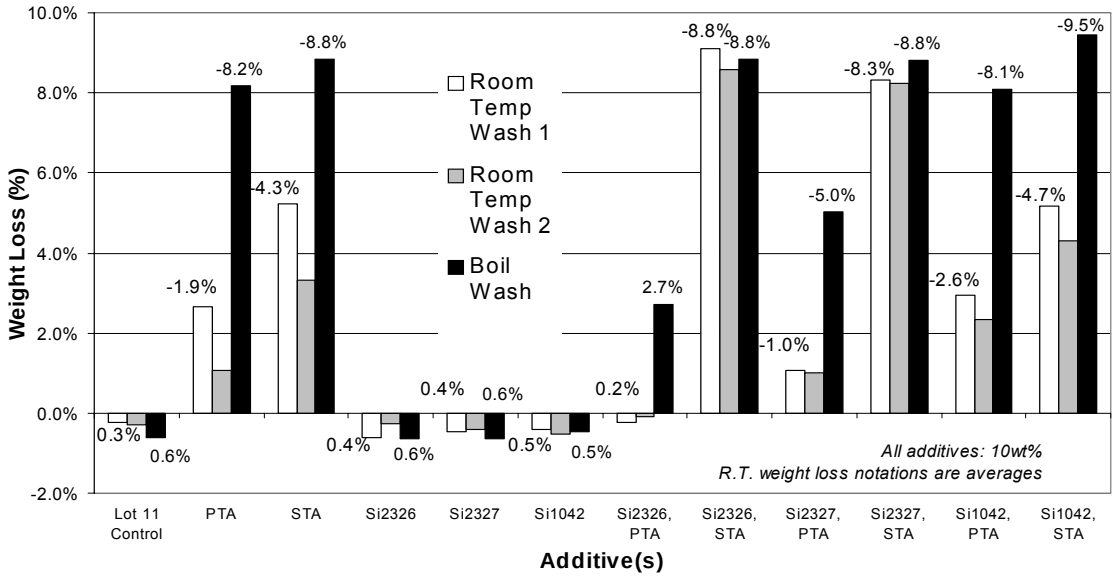

Fig. 9. Mass loss for PFSA membrane films with and without additions of PTA or STA and/or colloidal silica.

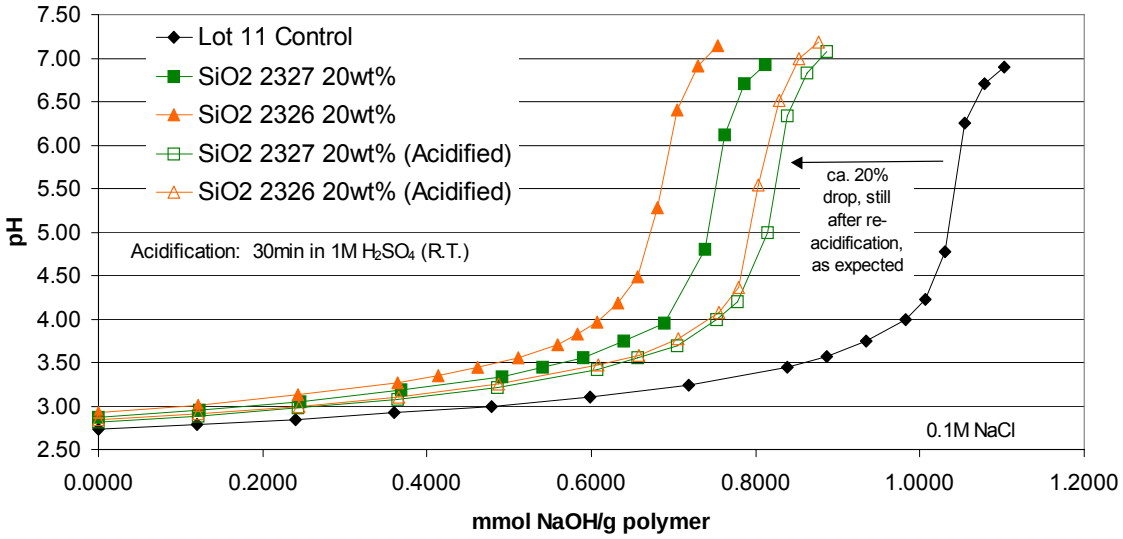

Fig. 10. Titration curves for PFSA membranes with increasing addition of basic colloidal silica, before and after reacidification with H_2SO_2.

3.2.2. Organosulfonic Acid-Functionalized Silica (SiO_2-RSO_3H)

A strategy that has proven very effective for boosting the proton conductivity of PFSA membranes, and hence the power performance of MEA's that include them, is to lower their equivalent weight. Fig. 11 gives fuel cell performance data for MEA's made from 1000EW and 700EW 3M PFSA ionomer membranes. Clearly, under challenging conditions of high temperature and low relative humidity, non-linear increases in performance, relative to the content of acid groups per unit volume in the membrane, are realized. This finding prompted a series of studies aimed at furthering these benefits by adding inorganically supported sulfonic acid groups to the PFSA membranes, hence further lowering the EW. Fortunately, a significant amount of sol-gel chemistry, including sulfonic acid functionalization and nanoscale structural templating by self-assembly, had been reported in the literature and could serve as a starting point for the work.

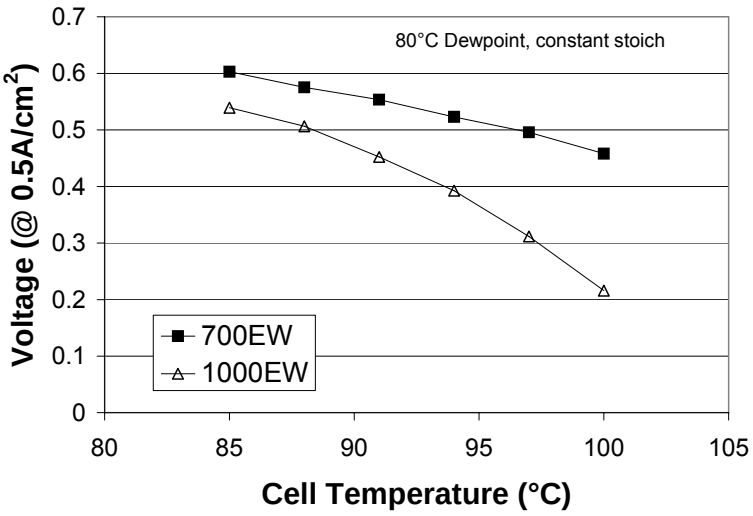

Fig. 11. Fuel cell power performance for PEMFC's with 1000EW and 700EW 3M PFSA ionomer membranes.

3.2.2.1. Proton Conductivity for Mesoporous SiO_2-RSO_3H Powders

Surfactant-templated silica (STS) with ordered mesoporous structures were first reported by researchers at Mobil in 1992.[21] Since that time, a large amount of work has been done to expand the variety of templating chemistries and integrate surface functionalization.[22] Among the functional groups explored has been propylsulfonic acid.[23] STS with phenyl surface functionality has also been reported.[24] These materials are claimed to be potentially useful for catalysis and sorption, respectively. As a complement to the phenyl STS reports, there has been work done to sulfonate other phenyl-modified silicas.[25] Thus, the work reported here included the sulfonation of phenyl-functionalized STS. Further, a study was carried out to determine potential advantages for proton conduction that might result from surfactant-templating. That is, it was believed that the introduction of a nanoscale pore structure, together with sulfonic acid functionality, might yield proton conductive properties superior to unstructured sulfonic acid-functionalized silica. The authors are aware of no reports in the literature on the proton conductive properties of sulfopropyl- or sulfophenyl-functionalized silica materials, including STS materials.

The study on powder proton conductivity began with the preparation of an array of samples, including various combinations of templating agent and functional group. Specifically, cetyltrimethyammonium bromide (CTAB) was used to template 2-3nm pores and BASF Pluronic P123 EO20—PO70—EO20 triblock copolymer surfactant was used to template 5-6nm pores. CTAB surfactant was removed by acid extraction. P123 was removed after synthesis by refluxing the powder samples in ethanol for at least 24hrs (>100X excess ethanol, on a weight basis). Some powder samples were also prepared with no templating agent. To prepare materials with propylsulfonic acid groups, the syntheses were carried out with mixtures of TEOS, mercaptopropyltrimethoxysilane (MPTMS), and hydrogen peroxide. To prepare materials with phenylsulfonic acid

groups, syntheses were carried out with mixtures of TEOS and phenyltrimethoxysilane (PTMOS) , followed by sulfonation with fuming sulfuric acid.

SiO_2-prop-SO_3H

Stucky and coworkers have reported the detailed synthesis of P123-templated mesoporous SiO_2-prop-SO_3H, and their procedure was followed in the presently reported work.[18] Fig. 12 below gives a pore size distribution for such material, measured using nitrogen adsorption. The distribution highlights a feature of our materials that was not addressed in the report by Stucky. Specifically, Fig. 12 suggests that a distinct bimodality in pore size exists in these co-condensed organo-STS materials. Such data calls into question expectations in the literature that such materials are likely homogeneous in their distribution of organic groups. SiO_2-prop-SO_3H powders without templated pore structure were also prepared in the current study, in identical fashion, except without the surfactant present. Finally, smaller-pored, CTAB-templated SiO_2-prop-SO_3H was prepared by combining TEOS and MPTMS in basic solution of CTAB, followed by extraction.

SiO_2-phenyl-SO_3H

Mann and coworkers reported the detailed synthesis of CTAB-templated mesoporous phenyl-SiO_2.[19] Their procedure was repeated in the currently reported study. Phenyl SiO_2 powders with templated pore structure were prepared in identical fashion, except without the surfactant present. Finally, larger-pored, P123-templated phenyl-SiO_2 was prepared by combining TEOS and phenyltrimethoxysilane (PTMOS) in 1.9M HCl solutions of P123 surfactant, similarly to the report by Stucky.[19] Sulfonation of the phenyl silicas was carried out by combining 2g of powder with 50g of fuming sulfuric acid (20% SO_3) and stirring at 90°C for two hours. The mixture of powder and fuming sulfuric acid was quenched by very slow addition (highly exothermic!) of excess ethanol and then water. The powder was recovered by repeated decanting and then vacuum filtration with water washing. Early in the work on phenyl-SiO_2, it was noted that as-dried (e.g., 100°C) TEOS/PTMOS-derived powders degraded on exposure to the fuming sulfuric acid, yielding somewhat gelatinous suspensions that could not be filtered. Accordingly, all of the SiO_2-phenyl-SO_3H powders reported herein were calcined for 2hrs at 350°C before sulfonation

Fig. 13 gives titration results for powders that were later characterized for proton conductivity. For each type of functionalized sample, syntheses were carried out iteratively to determine relative amounts of reagents necessary to yield a set of approximately equal-IEC powders for the study. At the outset of the study, the intention was to prepare 0.5meq/g and 1.0meq/g examples for each type of functionalized sample. In the end, difficulties in achieving powder precipitation under both acidic (for the P123-templated materials) and basic (for the CTAB-templated materials) surfactant micelle-loaded media, with two types of mixed-silane silica sources, limited the study to the single, approximately reproduced IEC level reported. All of the ion-exchange capacity values for the silica-based powders were within about 15% of their mean.

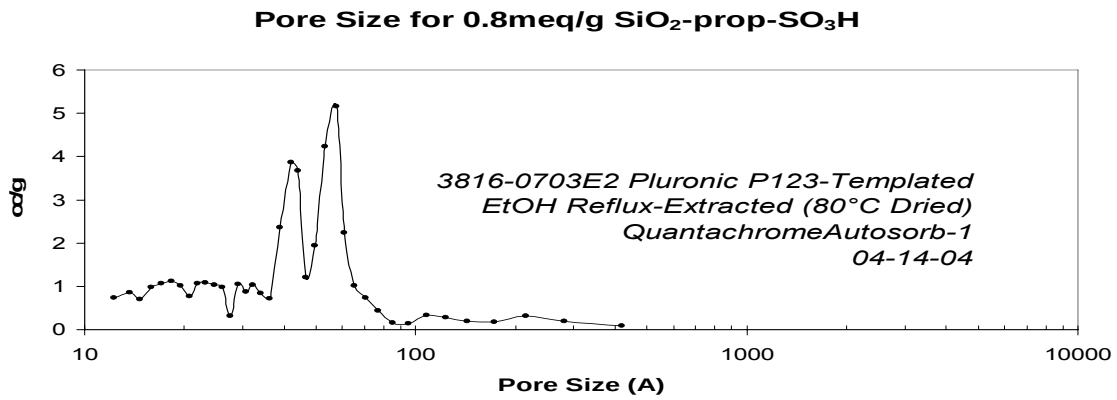

Fig. 12. Pore size distribution for solvent-extracted mesoporous surfactant-templated silica co-condensed from TEOS and MPTMS, with in situ H2O2 oxidation of the thiol.

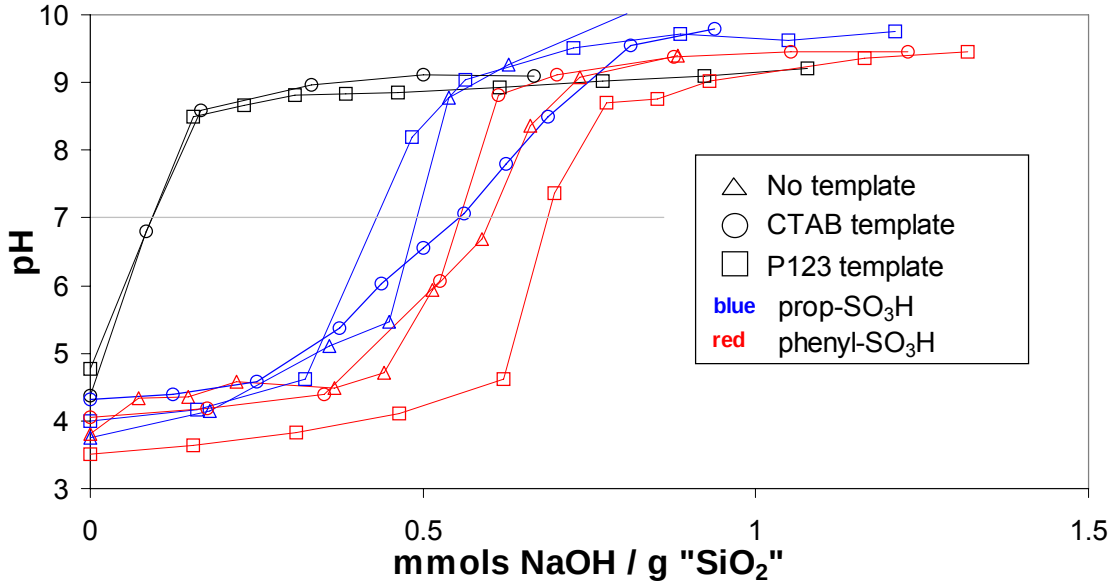

Fig. 13. Titrations carried out on various functionalized and non-functionalized silica powders.

Proton Conductivity

The powder cell described in Fig. 3 was used to characterize the proton conductivity of the powders described in Fig. 13. Fig. 14 gives the conductivity results for the powders. Consistent trends in the data were:

- higher conductivity values for the acid-functionalized powders, vs. non-functionalized powders
- sulfophenyl silicas exhibited higher conductivity values than sulfopropyl silicas for the templated materials

- conductivity for sulfophenyl and sulfopropyl silicas were nominally equivalent when not templated with surfactant
- smaller-pored CTAB-derived silicas exhibited higher conductivity than P-123-derived silicas

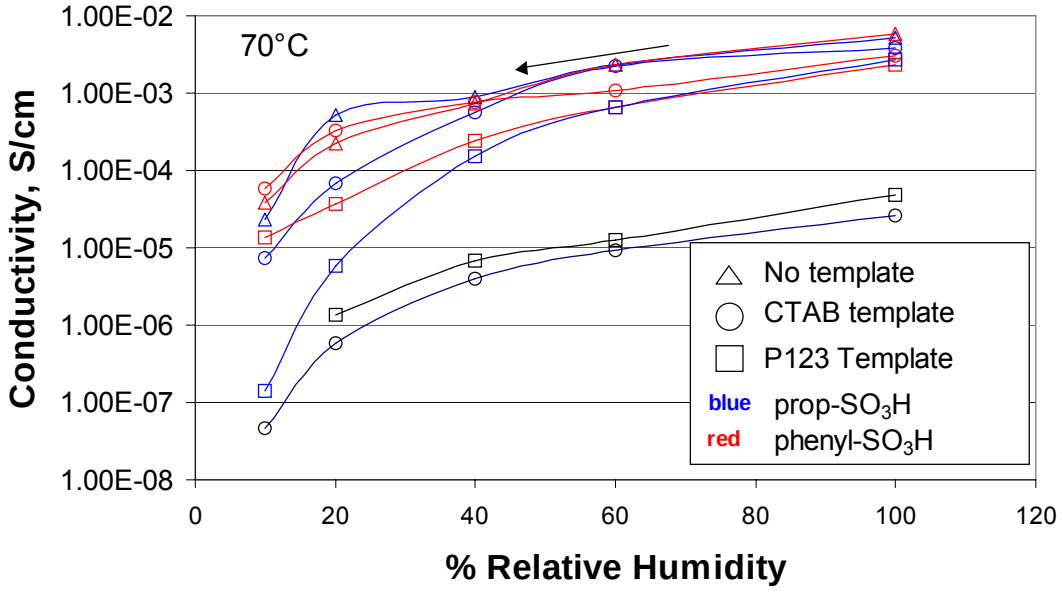

Fig. 14. Measured powder cell proton conductivity for silica powders, with or without acidic surface functionality and with or without surfactant templating.

3.2.2.2. Reduction Of Equivalent Weight With SiO_2-RSO_3H Additions

Based on the neutral-to-negative results for surfactant-tempated, functionalized silica materials, relative to functionalized silica material made more easily without surfactants present, the next phase of research in this area focused on maximizing the impact of the hybrid organic-inorganic additives on net IEC (and hence effective EW) for PFSA-based membranes. Three series of powder samples were synthesized, using the following combinations of reagents:

S-SiO_2-1: TEOS + MPTMS; in situ oxidation by H_2O_2
S-SiO_2-2: TEOS + PTMOS; w/ post-sulfonation by fuming sulfuric acid
S-SiO_2-3: TEOS + chlorosulfophenylethyltrimethoxysilane (CSPETMS); in-situ hydrolysis

The series of powder samples were prepared with increasing proportions of the eventual acid-supporting organosilane, relative to TEOS. Essentially, the work was aimed at preparing each class of hybrid filler with the highest IEC possible.

Because the powder of type S-SiO_2-1 was prepared with high enough IEC (>2meq/g) to be expected to reduce the EW of 3M's PFSA ionomer, much more easily than S-SiO_2-2

is prepared (and S-SiO_2-3 was not prepared until late in the program), S-SiO_2-1 was added to the PFSA first. Interestingly, the IEC of the composite film comprising 10wt% 2.39meq/g S-SiO_2-1 powder and 90wt% 1.10meq/g PFSA measured only 1.13meq/g by titration, compared with the expected weighted average of 1.23meq/g. That is, the composite film had substantially less IEC than was predicted based on a simple mixture of the components, with their known starting IEC's. This result was observed repeatedly for fillers of type S-SiO_2-1, when added to PFSA films. Based on these results, expounded upon in the next section on thermal stability, it was decided to pursue more stable organic groups.

The powder of type S-SiO_2-3 was developed in response to the aforementioned results for S-SiO_2-1. S-SiO_2-2 was considered most likely to be stable, but the successful synthesis high-IEC powders of this type could not be confirmed during the program. S-SiO_2-3 powder with IEC of 3.65meq/g was added at 10wt% to the 1.10meq/g 3M PFSA. When titrated, the IEC of the film was 1.29meq/g. The expected IEC, based on a weighted average of the starting components for the composite was 1.36meq/g. Although an appreciable increase in IEC had been achieved, there was again a shortfall for the S-SiO_2-3-added composite, as compared with the expected value. The thermal stability of the CSPETMS-derived functional group, as well as the proton conductivity of PFSA composites incorporating the powders of type S-SiO_2-3, are reported upon in the following sections.

Direct addition of chlorosulfophenylethyltrimethoxysilane to PFSA casting dispersion

In a different approach from adding functionalized powders to the PFSA dispersion, work was also done on the direct addition of chlorosulfophenylethyltrimethoxysilane to the the 70/30 by weight n-propanol/water mixed-solvent casting dispersion for the 3M PFSA ionomer. CSPETMS was added at levels intended to yield 500EW and 600EW films (assuming full conversion to $SiO_{3/2}(CH_2CH_2C_6H_4)SO_3H$ upon hydrolysis of the sulfonyl chloride and hydrolysis and condensation of the alkoxy groups). PFSA films with CSPETMS added yielded higher IECs by titration than the control value (1.88meq/g for the 500EW target film and 1.85meq/g for the 600EW target film, compared to 1.06meq/g for the control). However, after boiling the films, which was done to investigate practical utility of this approach for real fuel cell membranes, IECs similar to, if not lower than, the control value were measured (0.93meq/g for the 500EW film and 1.05meq/g for the 600EW film; again, compared with 1.06meq/g for the control).

To summarize the work on equivalent weight reduction using organosulfonic acid-functionalized silica, propylsulfonic acid-functionalized materials were easy to synthesize with high IEC, but proved ineffective for lowering EW. Phenylsulfonic acid-functionalized materials proved challenging to make with high IEC. Sulfophenylethyl-functionalized materials proved easy to synthesize, and were the most effective for reducing EW, and thus were studied further for their impact on proton conductivity, reported in section Measured Proton Conductivity For PFSA:SiO2-RSO3H Composites.

3.2.2.3. Thermal Stability Of The SiO_2-RSO_3H Additives

Due to the shortfalls in measured IEC for PFSA-matrix composite membranes that included silicate powder fillers (vs. predicted values, based on IEC measurements for the matrix PFSA and for the filler powders, before composite film formation), a study of heat-treatment effects on the organosulfonic acid-functionalized silicate powders and their composites with PFSA was carried out.

Annealing Temperature during Film Formation

To prepare the PFSA-based composite films with organosulfonic acid-functionalized silica powders, the fillers were added and stirred overnight into the ionomer casting dispersion (at 10wt%, based on the final weight of the composite film). To study the potential role of high annealing temperature (200°C) on reducing the expected impact on IEC for the S-SiO_2-1 (2.39meq/g), powders, films were cast and annealed at 160°C, 180°C, and 200°C. Based on titration, the IEC values for the films were 1.11, 1.11, and 1.08meq/g respectively, vs. a value of 1.10meq/g for the PFSA alone and a value of 1.23meq/g that was calculated as the weighted average of the two composite film components. Thus, even for lower annealing temperatures (<200°C, fillers of type S-SiO_2-1 proved ineffective for lowering EW.

Extended heat-treatment of the powders

Sample powders of type S-SiO_2-1 (2.39meq/g) and type S-SiO_2-3 (3.65meq/g) were both heated for 10min, 20min, and 1hr at 200°C and titrated. IEC versus time at 200°C is plotted for the heat-treated powders in Fig. 14. The IEC dropped from 2.39meq/g to 1.43meq/g after 10min and to 1.30meq/g and 1.21meq/g after 20min and 60min, respectively for S-SiO_2-1. The IEC increased from 3.65meq/g to 3.86meq/g after 10min and dropped to 3.69meq/g and 3.27meq/g after 20min and 60min, respectively for S-SiO_2-3.

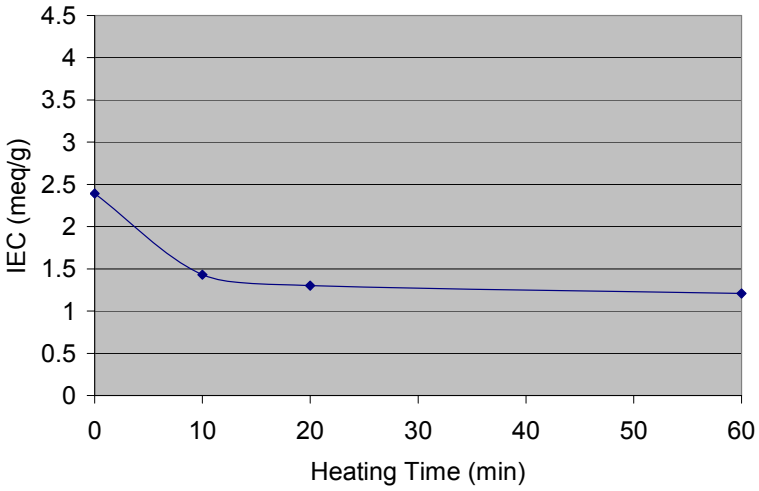

a)

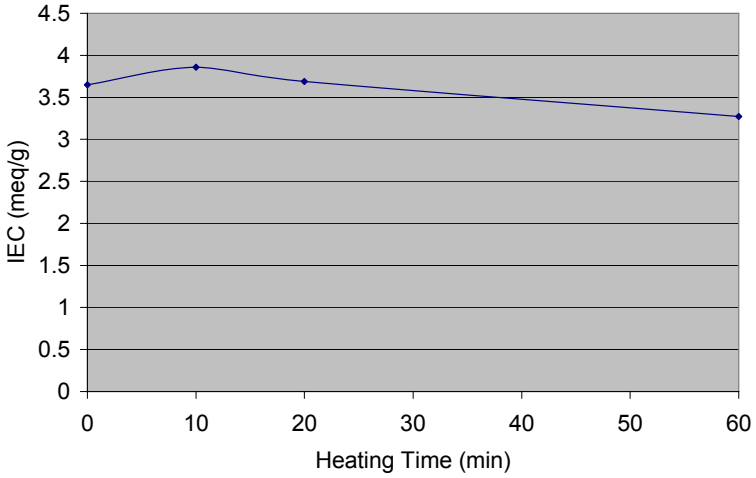

b)

Fig. 15. Effect of heat-treatment at 200°C on measured IEC for organosulfonic acid-functionalized silica powders; a) S-SiO2-1; b) S-SiO2-3

3.2.2.4. Measured Proton Conductivity For PFSA:SiO_2-RSO_3H Composites

PFSA membranes incorporating filler powders of type S-SiO_2-3, as well as PFSA membranes prepared with direct additions of CSPETMS, were characterized further to determine impact of the additions on proton conductivity. Also, the stability of these additives against boiling in water was further investigated. Recall that when S-SiO_2-3 was added at 10wt% to the 3M PFSA film as a powder, the measured IEC was raised from 1.10meq/g to 1.29meq/g. However, after boiling, the measured IEC dropped to 1.13meq/g. Therefore, similar to the behavior for direct CSPETMS additions, the benefits to EW are not entirely stable to boiling.

Addition of the S-SiO_2-3 powder (3.65meq/g) to 909EW 3M PFSA ionomer led to a marginal improvement in conductivity, as shown in Fig. 16**.** In further work, where the powder was added to ca. 800EW 3M PFSA ionomer, there was no improvement in proton conductivity observed, as shown in Fig. 17**.** Direct addition of CSPETMS raised the IEC of the PFSA films before boiling (1.88meq/g for the 500EW target film and 1.85meq/g for the 600EW target film, compared to 1.06meq/g for the control), but did not significantly improve conductivity, as shown in Fig. 18. In general, the improvements in proton conductivity with addition of organosulfonic-acid-functionlized silicas were somewhat disappointing, as were the observations related to thermal and boiling water stability. However, it would be justifiable to do some fuel cell evaluation of these new electrolyte films.

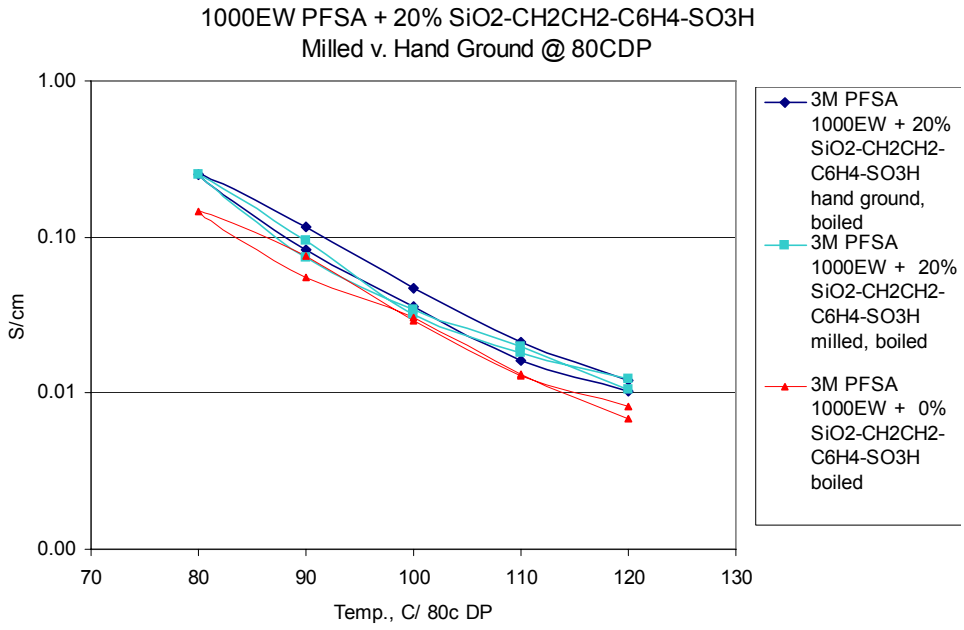

Fig. 16. Measured proton conductivity for 909EW-PFSA composite membranes with 20wt% addition of SiO2-CH2CH2C6H4SO3H powder.

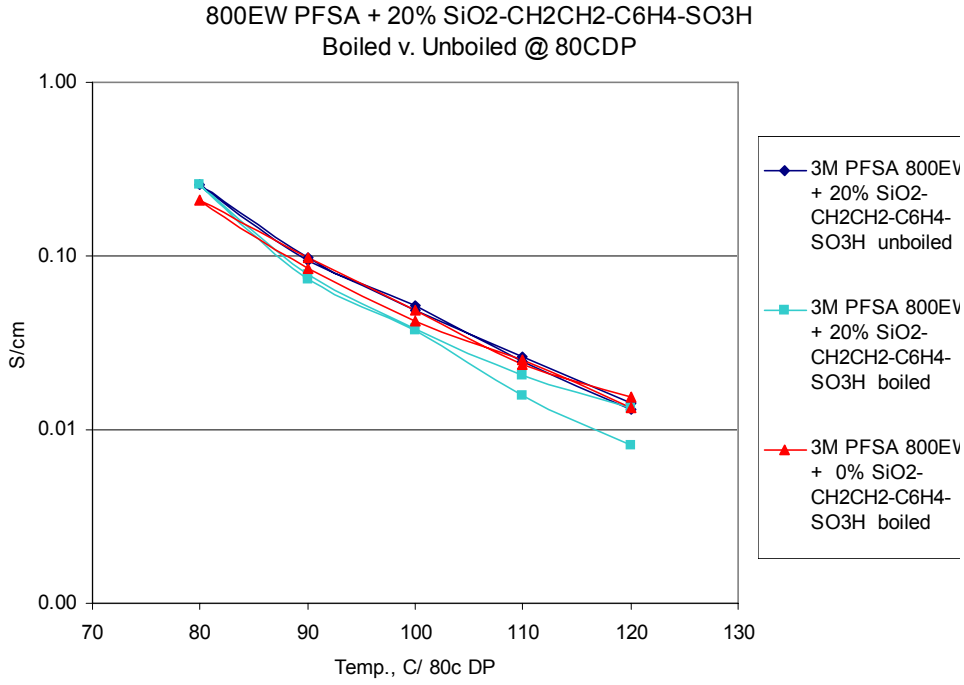

Fig. 17. Measured proton conductivity for ca. 800EW-PFSA composite membranes with 20wt% addition of SiO2-CH2CH2C6H4SO3H powder.

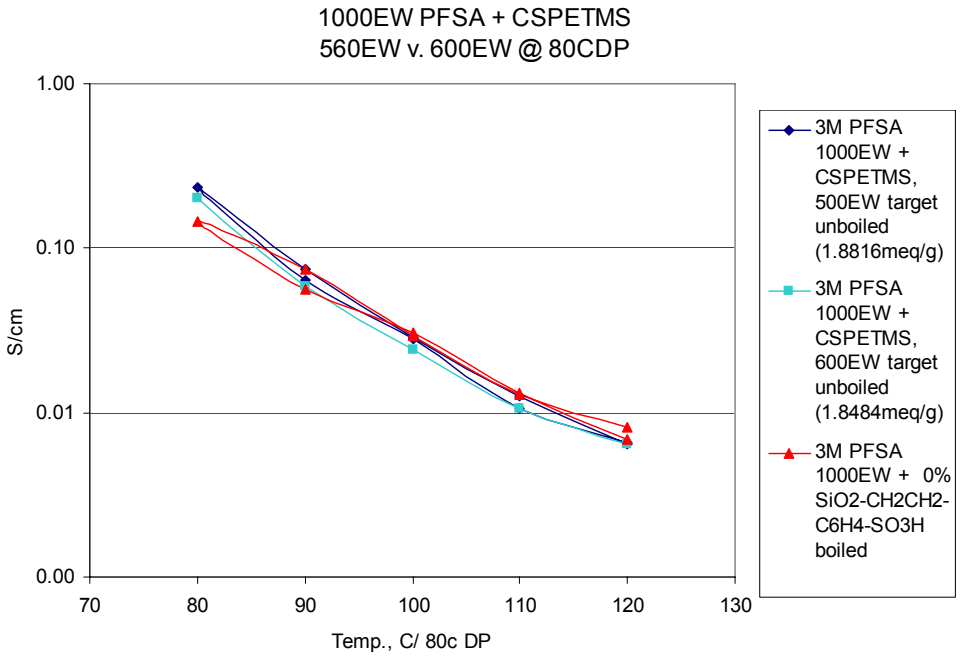

Fig. 18. Measured proton conductivity for ca. 800EW PFSA membrane with direct additions of CSPETMS.

3.2.3. Zirconium Oxide-Based Materials

Another metal oxide with sufficient chemical stability to be considered for development as an additive to PFSA membranes is zirconium oxide. And, while there isn't the substantial metal-carbon-bonded organic functionalization chemistry through zirconium that one can access for silicon, there is a very rich inorganic chemistry involving phosphates, sulfates and the like. Specifically, there are strong interactions between zirconia surfaces and those inorganic anions, leading to the superacid, sulfated zirconia for example, an important catalyst. Additionally, there are many zirconium phosphonates with very high reported proton conductivity values. Therefore, early stage exploration of zirconium oxide and more extensive work on zirconium phosponates were done in the currently reported program.

3.2.3.1. Incorporation Of Modified Zirconium Alkoxides To PFSA Membranes

Because of the convenience with which n-propanol/water mixed solvent PFSA dispersions are obtained and routinely cast, some scouting work was done to compatibilize zirconium alkoxides, an important and flexible zirconia precursor family, with that membrane processing system. Specifically, different chelating agents for zirconium n-propoxide (Zr-(*n*-OPr)$_4$) were explored for their ability to suppress premature hydrolysis and condensation of the alkoxide in Du Pont's Nafion™ SE 20092 casting dispersion, which is similar to 3M's standard 70/30 mixed solvent casting dispersions.

The basic procedure in this work was to combine the chelating agent with the alkoxide at various molar ratios, and then combine that modified alkoxide with the PFSA casting dispersion. The final mixtures were observed for possible precipitation. The chelating agents studied were acetic acid, acetylacetone, and triethanolamine (TEA). For all proportions of all three of the three chelating agents, immediate precipitation was observed. That is, none of the modifiers proved useful for slowing the hydrolysis and condensation kinetics for Zr-(*n*-OPr)$_4$ to the extent necessary to carry out controlled sol-gel chemistry in the casting dispersion. In a second round of work, the PFSA dispersion was first neutralized with lithium hydroxide, yielding a dispersion "in lithium form." Dispersions neutralized with sodium hydroxide behaved similarly. The same modifications to Zr-(*n*-OPr)$_4$ were carried out, and the modified alkoxides were added to the lithium form dispersion. For all levels of acetic acid and acetylacetone, the alkoxide addition again led to immediate precipitation. Only modification with triethanolamine, with its potential for tridentate coordination, led to an alkoxide-derived zirconia precursor that could be added to the lithium form dispersion. The TEA was required to be added at a 1:1 molar ratio with the Zr-(*n*-OPr)$_2$.

Lithium form films, with TEA-modified Zr-(*n*-OPr)$_4$ added to the SE 20092 dispersion, were cast on glass and annealed at 160°C. Loadings for ZrO_2 (assuming full conversion of the modified alkoxide) of 5 and 10wt% were investigated. The films were very clear, essentially identical in appearance to the unmodified PFSA membrane films. An indication that an extended zirconia structure was forming in the clear films, they were found to become very brittle as more modified alkoxide was added. 5 and 10wt% sol-gel zirconia-added Nafion™ films were noticeably more brittle than control films. The 10wt% zirconia-added films were brittle enough that they had to be handled carefully. ZrO_2-added PFSA membranes prepared in this way were used as the starting materials for the following brief study on phosphate immobilization in PFSA.

3.2.3.2. Treatment Of PFSA:Zirconia Composites With Phosphoric Acid

PFSA membranes with and without sol-gel-derived zirconia at 5wt% or at 10wt%, as described above, were treated with phosphoric acid, in order to reacidify (exchange out the lithium). In addition to the acidification of sulfonate groups, the immobilization of phosphate groups was investigated. Specifically, the films were investigated using x-ray fluorescence (XRF) to detect for phosphorous. The measurement was not quantitative, but the sol-gel zirconia-added PFSA membranes yielded a strong phosphorous signal after H_3PO_4-reacidification, while the non-zirconia-added film showed near zero signal for phosphorous after the same H_3PO_4-reacidificaiton. For the 5wt% and 10wt% zirconia additions, the [P,Zr] signals (in kilocounts per second] were [38,165] and [41,283], respectively (CRAL analytical request no. G72076). For any future inorganic/organic electrolyte strategies based on zirconium phosphates or phosphonates, it would be very interesting to use this modified zirconium alkoxide approach.

3.2.3.3. Synthesis And Incorporation Of Zirconium Sulfophenylphosphonates

Numerous types of the PEMFCs (polymer electrolyte membrane fuel cells) are presently under investigation for use in automobiles and stationary power applications. In recent years, the necessity of decreasing greenhouse emission and dependability on fossil fuels, has led to considerable effort to develop this technology. However, their still remain major obstacles to large scale commercialization, prominent being high cost of the known proton-conducting membranes, low-proton conductivity at low relative humidity, poor mechanical properties above about 130±°C. The increased temperature raises the evaporation rate of water from the membrane and the vapor pressure required to keep a given amount of water in the membrane; thereby increasing the likelihood that water loss will occur and significantly reduce proton conductivity. The conductivity of a dry membrane is orders of magnitude lower than a fully saturated membrane. A number of alternative strategies have been investigated to maintain membrane conductivity in a dehydrating environment (i.e. elevated temperature and reduced relative humidity). The addition of an inorganic material into a polymer membrane can alter and improve physical and chemical polymer properties of interest (such as elastic modulus, proton conductivity, solvent permeation rate, tensile strength, hydrophilicity, and glass transition temperature) while retaining its important polymer properties to enable operation in the fuel cell.

To attempt to overcome the problems of low conductivity associated with high temperature operation a large number of research groups have focused on nanocomposite membranes. Some of the key inorganic and composite high temperature proton conductors are listed in the Table V. All the nanocomposite membranes considered here consist of an ionomer (usually containing acid or superacid -SO_3H groups) in which inorganic or inorgano-organic solid particles are dispersed. The properties of these composite membranes not only depend on the nature of the ionomer and the solid used but also on the amount, homogeneous dispersion, size, and orientation of the solid particles dispersed in the polymeric matrix. In ionomers such as Nafion™, where well-separated hydrophilic and hydrophobic domains are present (see below), the distribution of the dispersed particles in the different domains is also important.

Layered metal phosphonates are one of the promising inorganic additives studied for this application. Layered metal(IV) phosphonates are good proton conductors. Organic moieties (R) which are contained in the $\alpha(M^{IV}(O_3P–R)_2 \cdot nH_2O)$ and γ $(M^{IV}PO_4(O_2P(OH)R)_2 \cdot nH_2O)$ structure are bridged through phosphorus atoms to an inorganic two dimensional matrix. These species act as protonic conductors when the R contains a protogenic function (e.g. –COOH, $–PO_3H$, $–SO_3H$, $–NH_3^+$). [26] The most extensively studied groups of metal^{IV} phosphates in terms of proton conductivity is zirconium phosphate. Zirconium hydrogen phosphate, α-$Zr(HPO_4)_2 \cdot H_2O$ (henceforth α-ZrP), was first synthesised by Clearfield and Stynes in 1964[27] by reflux, and then Alberti and Torracca[28] produced this material by complexing with hydrofluoric acid (See Fig 1). Nonetheless, extensive investigations into its use as a proton conductor did not commence until the 1990's. There are two predominate structures of zirconium hydrogen phosphate α- and γ- as illustrated in Fig. 19 and Fig. 20. Recent investigation has led to the discovery of new structures synthesized via hydrothermal routes, designated as τ-ZrP[29] and ψ-ZrP.[30] The structure of α-ZrP lends itself best to proton transport because it has a pendant –OH group which extends into the interlayer region and forms hydrogen

bonded network with water. That said, the *γ*-ZrP does have the advantage of having an extra water molecule per formula unit and is more acidic than the *α*-ZrP.[31] The transport mechanism in *α*-ZrP at room temperature is dominated by surface transport; four orders of magnitude greater than the bulk transport, however the crystallinity also plays an important role.[32] In addition, conductivity in *α*-ZrP is highly dependant on the hydration, varying by two orders of magnitude as the relative humidity is increased form 5 to 90%.[33] Recent research has confirmed the dominance of the surface transport and demonstrated enhancements that can be made through modification of the P–OH groups.[34] Based on this understanding of *α*-ZrP, attempts to enhance the proton conductivity have been made in the following directions

(i) Intercalation of functional groups.
(ii) Composites *α*-ZrP membranes.
(iii) External surface area maximization (mechanical and colloidal synthesis).
(iv) Internal surface area maximization (sol–gel synthesis and pillaring).

Attempts to improve the conductivity of solid acid membranes have included the synthesis of new layered compounds, where Brønsted bases are intercalated in the interlayer region or functionalized organic radicals replace the hydroxyl of the phosphate group.[25] Significant improvement was achieved with the intercalation of strong acidic functional groups of $–SO_3H$ (there was little improvement for the weak –COOH) into the interlayer region. $Metal^{IV}$ sulfophosphonates and zirconium alkyl sulfophenylphosphonates or the variety $(Zr(O_3PC_6H_4SO_3H)_{0.85}(O_3PC_2H_5)_{1.15}\cdot nH_2O)$ and $(Zr(O_3PC_6H_4SO_3H)_x(O_3PCH_2OH)_{2-x}\cdot nH_2O)$ have been investigated for their conductivity under different temperature and relative humidity regimes.[35,36] In this section we focus on our efforts to understand the proton conductivity and fuel cell performance characteristics of Zirconium sulfophenylphosphonates composites prepared with 3M ionomer. Since pure zirconium sulfophenylphosphonates $(Zr(O_3PC_6H_4SO_3H)_2.nH_2O)$ are highly soluble we prepared zirconium sulfophenylphosphonates phosphates $(Zr(O_3PC_6H_4SO_3H)_x(O_3P(OH))_{2-x}\cdot nH_2O)$ as well.

Table V. Reported proton conductivity for selected metal phosphates and metal phosphonates.

Table 1
Benchmark high temperature conductors

Compound	σ (S cm^{-1})	Conditions
Composites		
Nafion/α-ZrP	0.1	373 K,100%RH
SPEEK/α-ZrP	0.01	298 K,100%RH
STA/α-ZrP polymer compound	1.9×10^{-2}	373 K,100%RH
Imidazole/Nafion (transverse)	0.1	433 K,100%RH
Zirconium		
α-$Zr(O_3POH)_2 \cdot H_2O$	10^{-5} to 10^{-6}	293 K, 90%RH
α-$Zr(O_3POH)_2$	1×10^{-7}	453 K, 00%RH
pellicular α-$Zr(O_3POH)_2 \cdot nH_2O$	1×10^{-4}	293 K, 90%RH
α-$Zr(O_3PCH_2OH)_{1.27}(O_3PC_6H_4SO_3H)_{0.73} \cdot nH_2O$	1.6×10^{-2}	293 K, 90%RH
	8×10^{-3}	373 K, 60%RH
α-$Zr(O_3PCH_2OH)_{1.15}(O_3PC_6H_4SO_3H)_{0.85}$	1.2×10^{-4}	453 K, 00%RH
α-$Zr(O_3PC_6H_4SO_3H)_2 \cdot 3.6H_2O$	2.1×10^{-2}	378 K, 85%RH
γ-$Zr(PO_4)(H_2PO_4) \cdot 2H_2O$	2×10^{-5}	293 K, 90%RH
γ-$Zr(PO_4)(H_2PO_4)_{0.54}(HO_3PC_6H_4SO_3H)_{0.46} \cdot nH_2O$	1×10^{-2}	293 K,90%RH
Zirconium phosphate (sol–gel)	3×10^{-2}	293 K, 50%RH
Zirconium phosphate pyrophosphate	1.3×10^{-3}	293 K, 90%RH
	2×10^{-6}	373 K, 02%RH
Titanium		
$Ti(HPO_4)_{0.25}(O_3PC_6H_5)_{0.12}(O_3PC_6H_4SO_3H)_{1.63}$	1.3×10^{-1}	278 K, 85%RH
Cesium		
β-$Cs(HSO_4)_2(H_x(PS)O_4)$	3×10^{-5}	363 K, 00%RH
	1.6×10^{-2}	473 K, 00%RH
α-$Cs(HSO_4)_2(H_2(PO)_4)$	2.5×10^{-3}	313 K, 00%RH
Other		
Fullerene	7×10^{-7}	293 K, 00%RH

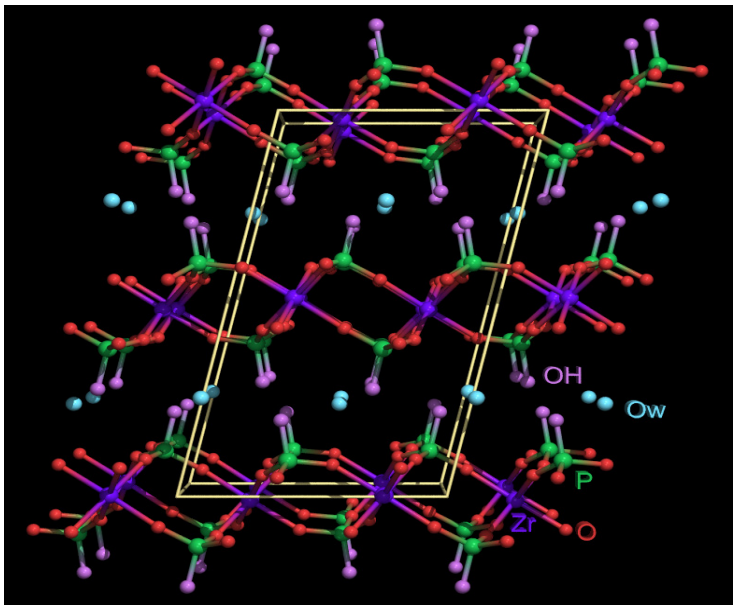

Fig. 19. Layered structure of α-Zr(HPO4)2•H2O.

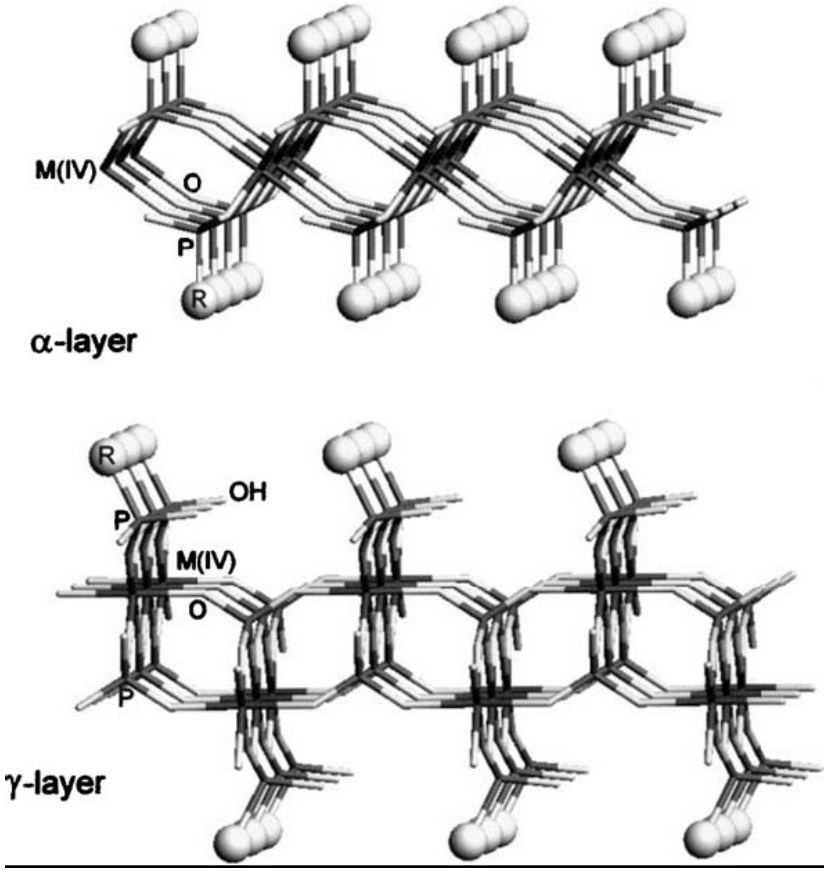

Fig. 20. Single layer showing differences in connectivity in α-Zr(HPO4)2•H2O and γ-Zr(H2PO4)(PO4)•2H2O.

3.2.4. Experimental

Materials Synthesis

Synthesis of Zirconium sulfophenylphosphonates

The synthesis was carried out in two steps

1) Preparation of zirconium phosphite phenylphosphonates
2) Sulfonation of the solids prepared in step above.

Preparation of zirconium phosphite phosphonates

$ZrOCl_2.8H_2O$ was dissolved in water and HF. To it stoichiometric amounts of H_3PO_3 (phosphorus acid) and Phenylphosphonic ($C_6H_5PO_3H_2$) was added and the mixture was stirred. The composition of the reaction mixture was $ZrOCl_2.8H_2O$:15-20HF: (2-x)H_3PO_3 : (x)Phenylphosphonic acid : 300H_2O. The mixture was heated in an open polypropylene bottle in an oil bath at 80˚C over a period of 2 days. The final solid is filtered and washed with copious amounts of water to remove any excess fluoride ions. The solid is then dried in hot air oven at 80˚C.

Sulfonation of zirconium phosphite phenylphosphonate

1. 12 gm of the sample to be sulfonated was taken in a pestle and mortar and ground well. The powder is then transferred to a round bottom flask.
2. 90 gm of fuming sulfuric acid (20% free SO_3) is added to it.
3. The flask is heated at 80˚C in a preheated oil bath under reflux condenser for 1 hour.
4. The flask is removed from the oil bath and cooled in an ice bath.
5. Deionized water is added dropwise to convert the unreacted SO_3 to H_2SO_4 (care should be taken as this is extremely exothermic)
6. Addition of slight excess of water forms a gel.
7. Methanol ~150ml is added to the mixture to recover the solid.
8. The mixture is centrifuged in a polypropylene bottle at ~1800-2000rpm.
9. The recovered solid is suspended in methanol and recentrifuged to wash out the excess sulfuric acid.
10. The above process is repeated until the supernatant liquid on post centrifugation is clear.
11. The solid is now ready for dialysis to remove any excess sulfuric acid /sulfate ions.

Dialysis of sulfonated material

1. Deionized water is added to the recovered gel after centrifugation after sulfonation.
2. The mixture is then poured into a 1000/3500 MWCO (molecular weight cut off) dialysis tube and suspended in a beaker containing deionized water under constant stirring.
3. The water in the beaker is replaced by fresh deionized water every hour until the pH of the water is ~5.
4. The dialysis tube is opened and the mixture is poured into a beaker and dried at 80˚C to recover the dialyzed material.

Characterization

The product obtained before and after sulfonation was characterized by powder XRD, Infrared spectroscopy and ICP elemental analysis. Fig. 21 shows the XRD pattern for the zirconium phosphite phenylphosphonate (3876-16) and zirconium phenylphosphonate (3876-18). The layered topology is evident from the XRD pattern. Sulfonation is believed to occur at *meta* position (with respect to $-PO_3H_2$ group), accompanied by increase in d-spacing. Sulfonation also leads to inclusion of water in the interlayer space which also contributes to the increased interlayer spacing. For a fully hydrated zirconium sulfophenylphosphonate the d-spacing observed is close to 19.6Å. The XRD pattern for the sulfonated material is shown in Fig. 22. The phosphite $-HPO_3$ group is oxidized to $-HPO_4$ during sulfonation process.

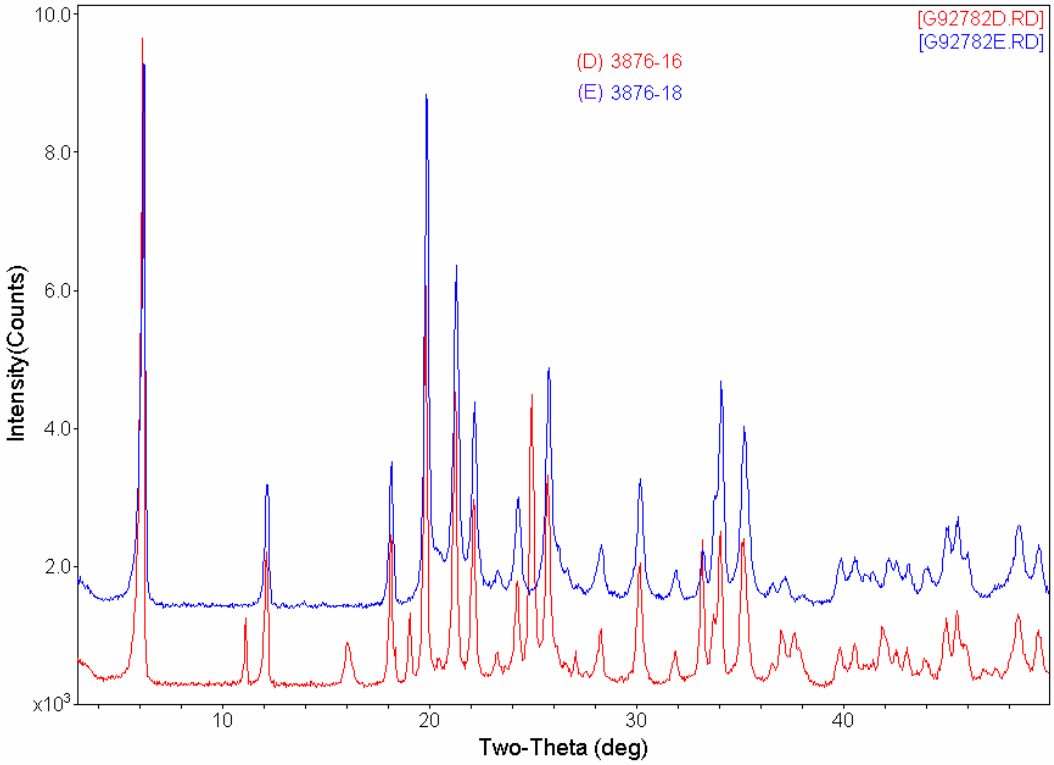

Fig. 21. XRD patterns for Zr(HPO3)(O3PC6H5) (red) and Zr(O3PC6H5)2 (blue).

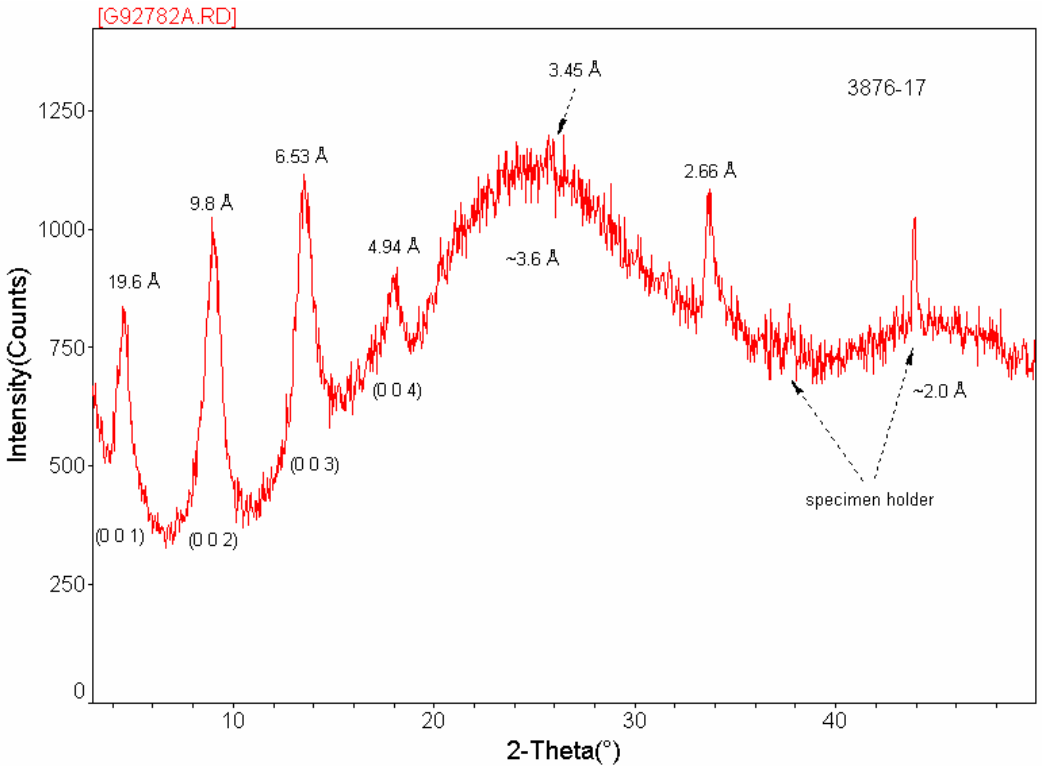

Fig. 22. XRD pattern of sulfonated sample of composition Zr(HPO4)(O3PC6H4SO3H)**.**

The successful sulfonation is also evident from the Infrared spectra recorded for the unsulfonated 3876-18 (Fig. 23**)** and sulfonated 3876-23 samples (Fig. 24). The sulfonated material shows a broad -OH band ~3400-3500cm^{-1} due to -SO_3H group and water in the sulfonated material. The stretch at 1715cm^{-1} due to water is much strong in sulfonated material. These bands are completely absent in the unsulfonated materials. The bands at 688 & 808 cm^{-1} are indicative of *meta*-disubstituted aromatic ring. The 808cm^{-1} band is absent in unsulfonated material. Also seen in the spectra are shoulder peaks on 900-1300cm^{-1} due to S-O stretches overlapping with P-O stretches (1072, 1140 and 1180cm^{-1}. The bands at 2920-2960 cm^{-1} are due to aromatic C-H stretch, and band at 1439cm^{-1} is due to C-C stretch. These bands are present in both the materials.

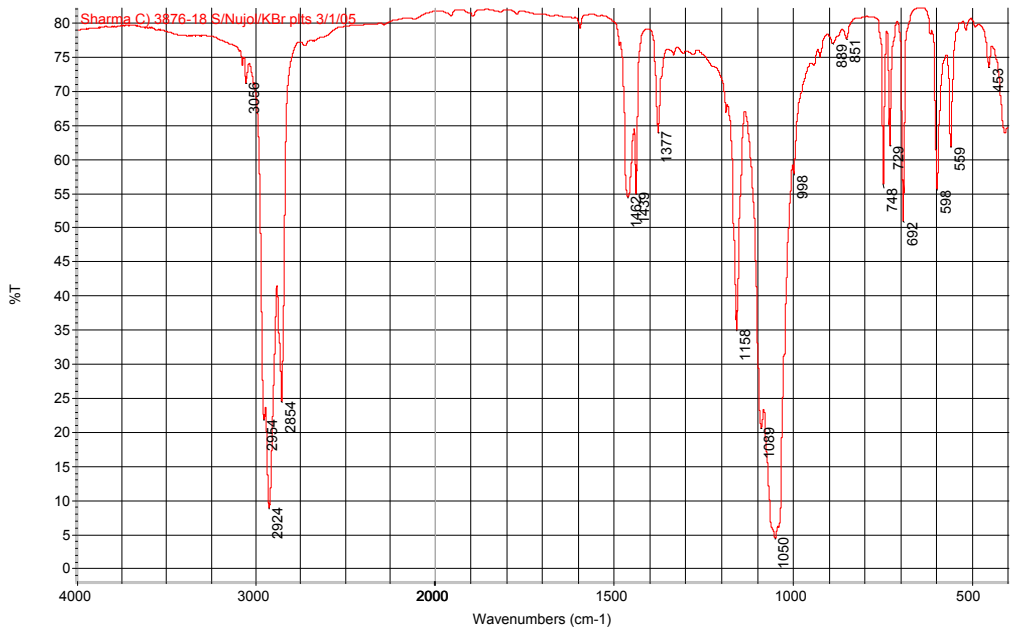

Fig. 23. FT-IR spectra of Zr(O3PC6H5)2 in Nujol mull.

Fig. 24. FT-IR spectra of Sulfonated Zr(O3PC6H5)2 of composition Zr(O3PC6H4SO3H)2 in Nujol mull.

The TGA-IR spectra shows that the sulfonated material loses SO_2 above 300˚C evident from stretch at 1300cm^{-1}, indicative of sulfonation (Fig. 25**)**.

(b)

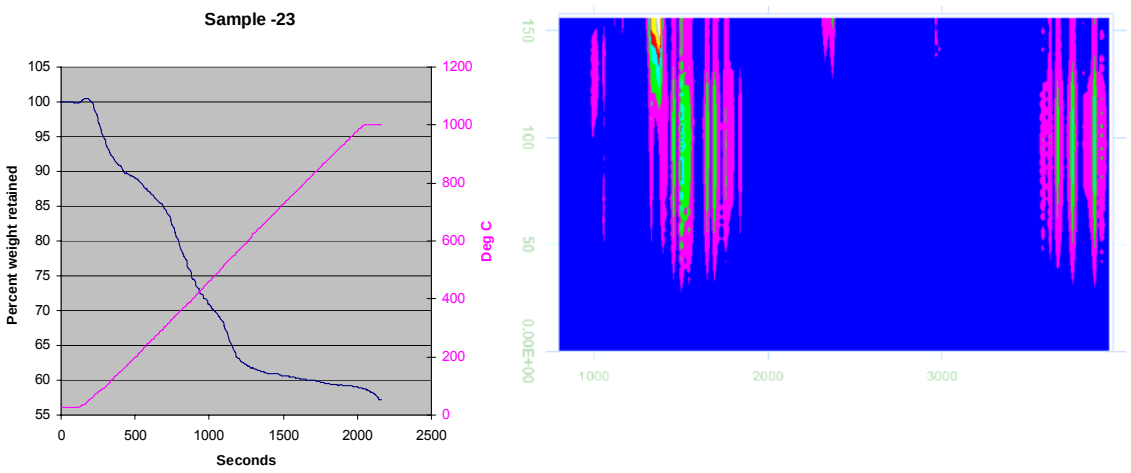

Fig. 25. TGA IR for sulfonated sample Zr(O3PC6H4SO3H)2.

Table VI shows the elemental analysis for some of the sulfonated material obtained before and after dialysis. Please note the change in elemental composition on prolonged sulfonation.

Table VI. Elemental composition of some of the sulfonated materials obtained by ICP.

		Theoretical	Measured	Difference
3876-22 $Zr(HPO4)(O_3PC_6H_4SO_3H)_2$	**Phosphorus**	**12.6**	**11.4 ± 0.3**	**-22**
	Sulfur	**7.6**	**8.9 ± 0.2**	**17**
	Zirconium	**21.5**	**18.9 ± 0.5**	**-12**
3876-23 $Zr(O_3PC_6H_4SO_3H)_2$	**Phosphorus**	**11.0**	**8.1 ± 0.1**	**-26**
	Sulfur	**11.4**	**11.5 ± 0.2**	**1**
	Zirconium	**16.2**	**13.0 ± 0.2**	**-20**
3876-31 $Zr(O_3PC_6H_4SO_3H)_2$ (Sulfonated 1hr) (Dialyzed sample using 1000 MWCO membrane)	**Phosphorus**	**11.0**	**8.2 ± 0.2**	**-25**
	Sulfur	**11.4**	**10.3 ± 0.2**	**-10**
	Zirconium	**16.2**	**13.7 ± 0.2**	**-15**
3876-32 $Zr(O_3PC_6H_4SO_3H)_2$ (Sulfonated 3.5 hr) Dialyzed (White Zirconia powder)	**Phosphorus**	**11.0**	**8.8 ± 0.3**	**-20**
	Sulfur	**11.4**	**8.6 ± 0.2**	**-25**
	Zirconium	**16.2**	**21.4 ± 0.8**	**32**

The final product was further mixed with 3M ionomer to prepare coating solution in order to prepare handspreads. The scheme (Fig. 24) and procedure are shown below.

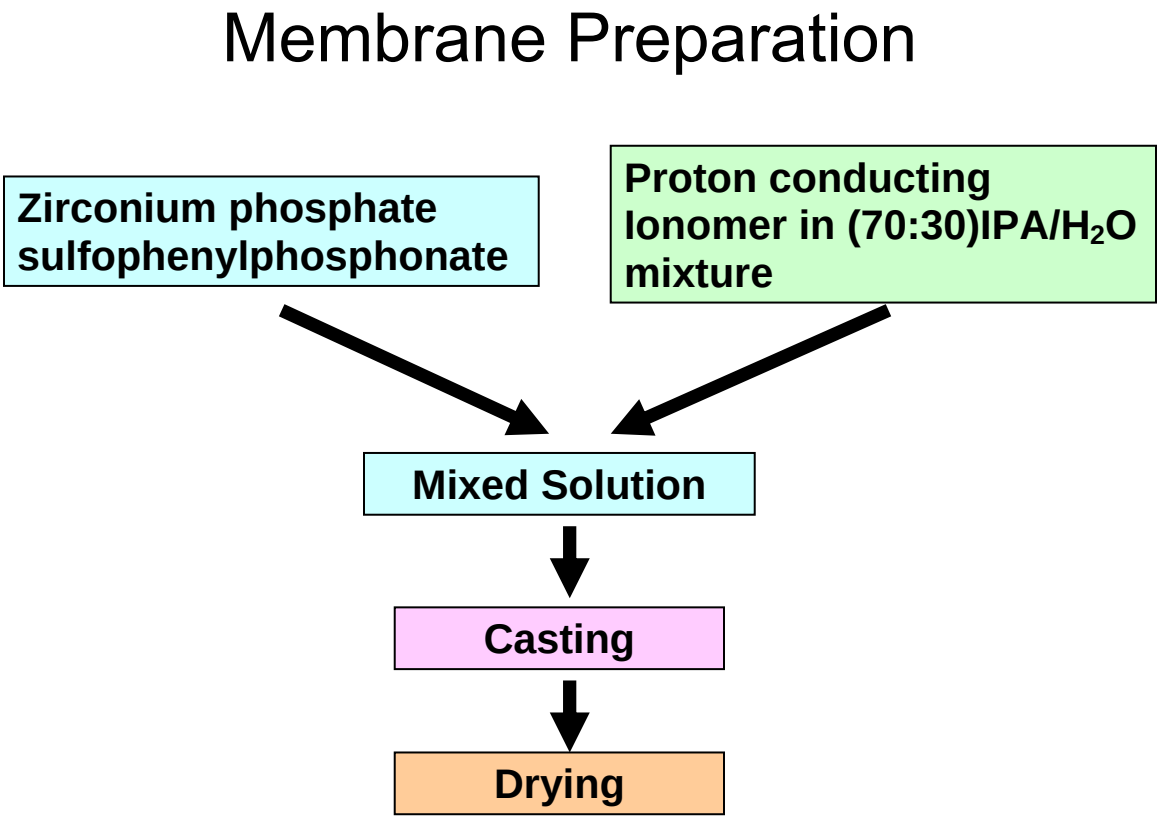

Fig. 26. Schematic for preparing composite membranes.

Coating procedure for Handspreads

1. Clean surface of glass plate with isopropanol and a Kimwipe. Inspect to assure that there are no visible particles.
2. Use spirit level to assure that the glass plate is level.
3. Place "multi-gap" coating bar on the glass surface with 20 mil gap facing down and along left-hand side edge of the glass.
4. Pour polymer casting solution on glass, inside the area of the square-shaped coating bar. Try to avoid the formation of air bubbles.
5. Steadily, but quickly, draw the bar to the right (keeping it in contact with the glass), generating the wet polymer layer.
6. Allow the film to dry at room temperature for 15 min.
7. Transfer the film-coated glass to the 80˚C oven for 20 min.
8. Transfer the film-coated glass to the 200˚C oven for 15 minutes. **Handle with leather gloves / heat protective gloves**
9. Remove the film-coated glass from the 200˚C oven and place it on porous ceramic refractory block, and allow cooling to room temperature.
10. After the glass plate has cooled to room temperature, peel an edge of the film from the glass and then continue the removal by peeling slowly.
11. Let the film dry overnight

Proton conductivity and Fuel cell Testing

The proton conductivity date for the samples with varying -SO_3H content dialysed using 1000MWCO membranes is shown in Fig. 27. The % of SO_3H groups is based on amount of phenylphosphonate in the initial material prior to sulfonation. 50% SO_3H here means $Zr(HPO_4)(O_3PC_6H_4SO_3H)$, whereas 100% SO_3H material has a composition of $Zr(O_3PC_6H_4SO_3H)$. Only the sample containing 10 wt% ZrSPP(50%SO_3H) shows improved or comparable proton conductivity to that of the control sample. All the other samples show lower proton conductivity than the control. The reason for this behaviour may be attributed to the leaching of smaller sulfonated particles out of the composite membrane. In order to decrease the leaching of smaller particles higher 3500 MWCO dialysis membranes were used. Both the boiled and unboiled 10 wt% ZrSPP(75%SO_3H) samples dialyzed with 3500 MWCO membranes show proton conductivity comparable to that of control, but higher loading of inorganic results in a drop in proton conductivity (Fig. 28). This may be due to leaching of materials at higher loadings or other factors. The increasing -SO_3H content renders the zirconium sulfophenylphosphonate materials highly soluble in water. The fuel cell performances for these samples are shown in Fig. 29. Only 10 wt% ZrSPP(50%SO_3H) performs similar to the control. All the other samples exhibit poor fuel cell performance. The leaching of the zirconium sulfophenylphosphonate materials from the composite membrane has also been confirmed by titrating the membranes soaked in water (Fig. 30).

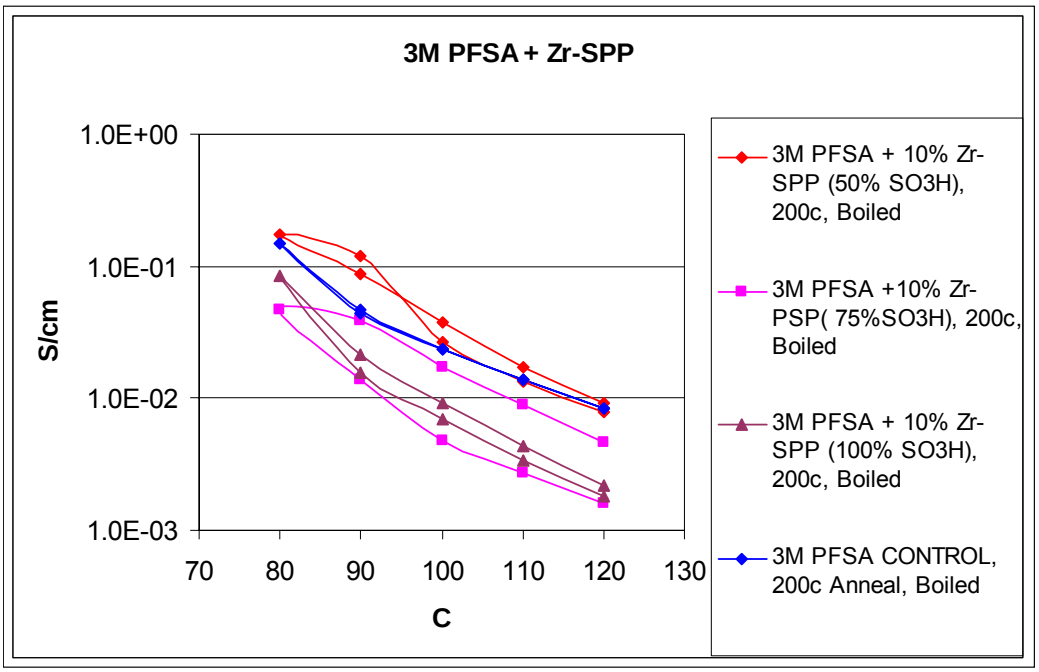

Fig. 27. Ionic conductivity data for composite membranes. The inorganic ZrSPP additives use to prepare the composite membranes were dialyzed with 1000MWCO filter.

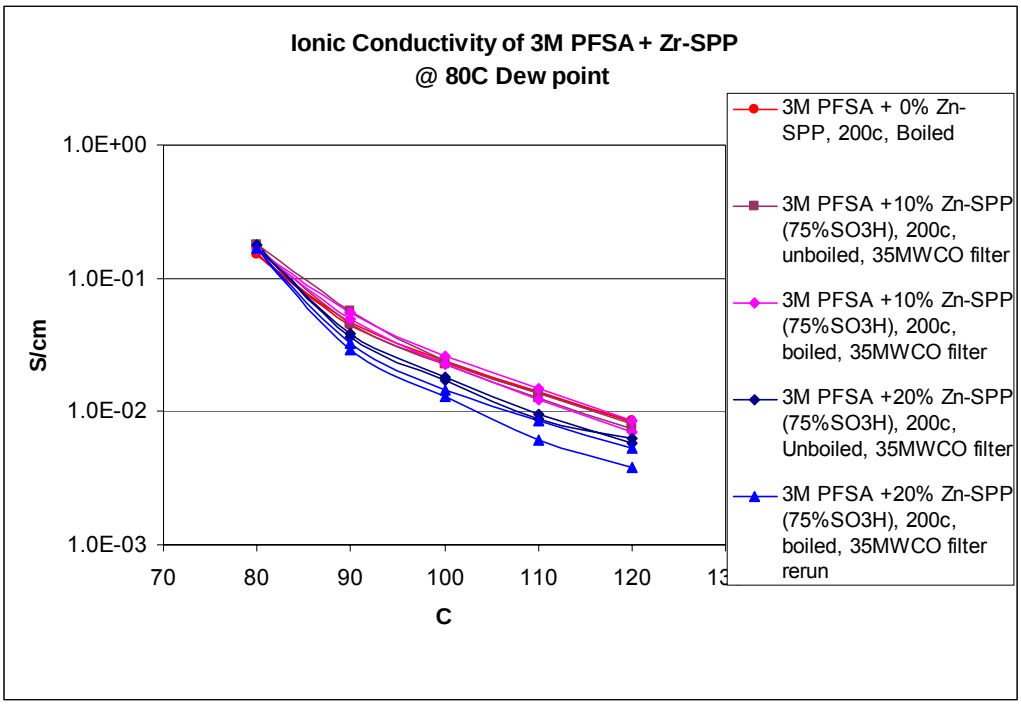

Fig. 28. Ionic conductivity data for composite membranes. The inorganic ZrSPP additives use to prepare the composite membranes were dialyzed with 3500MWCO filter.

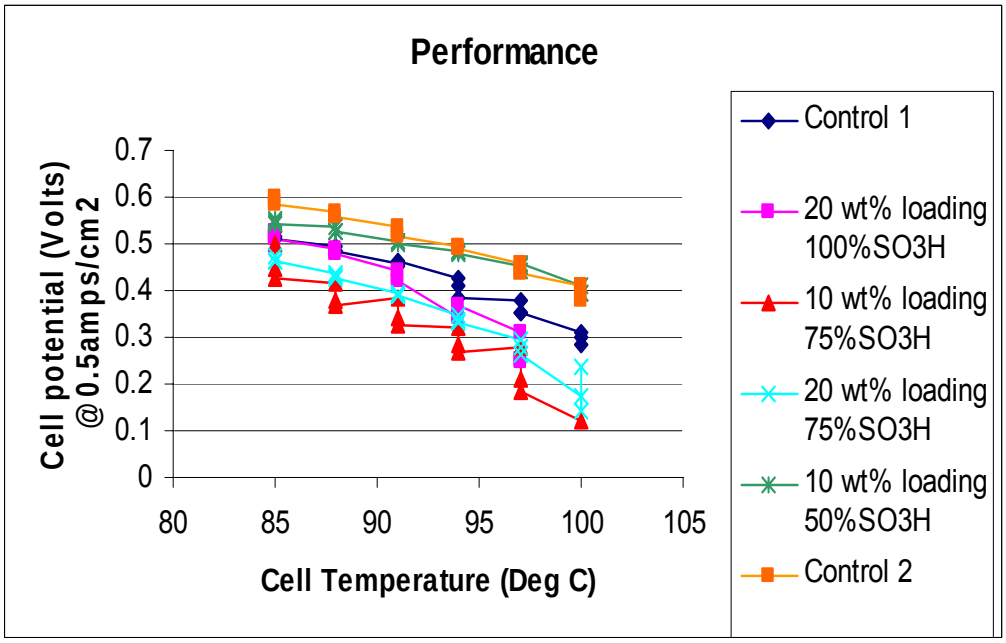

Fig. 29. Fuel Cell testing data for composite membranes. The inorganic ZrSPP additives use to prepare the composite membranes were dialyzed with 1000MWCO filter.

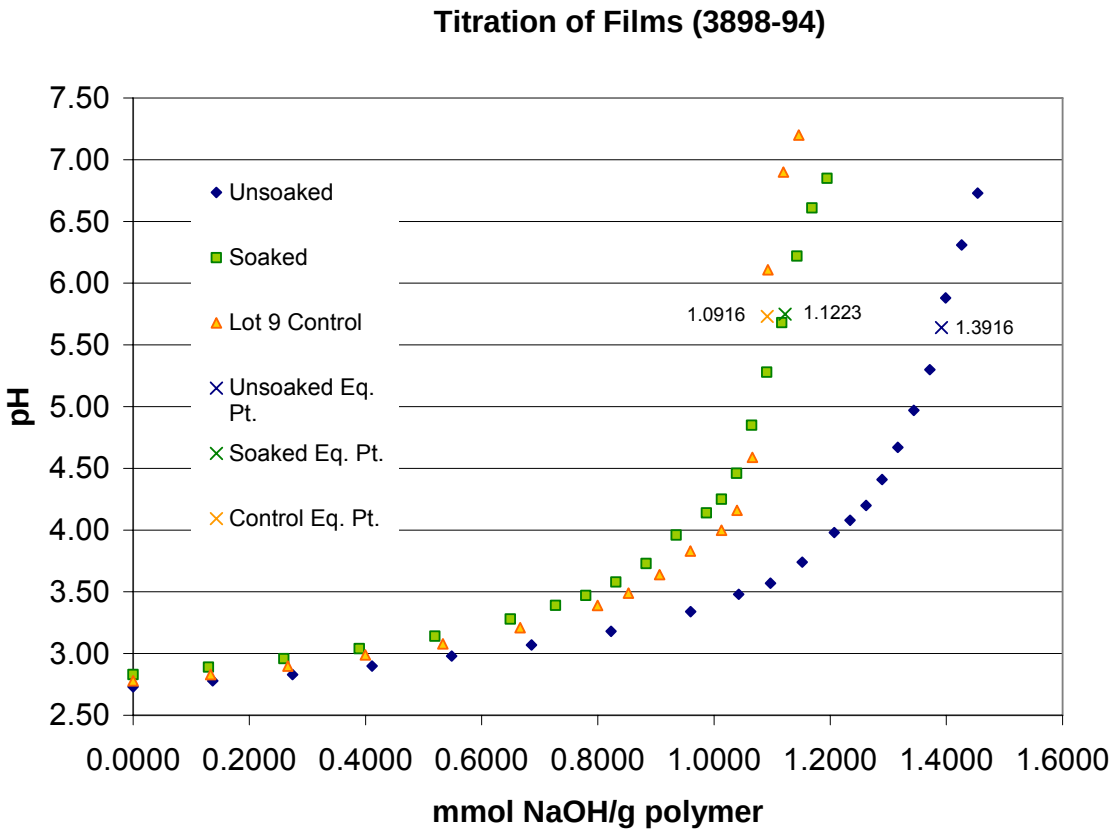

Fig. 30. Titration curves for the control, unsoaked and soaked composite membranes. The inorganic ZrSPP additives use to prepare the composite membranes were dialyzed with 3500MWCO filter.

3.2.5. Summary- Addition of inorganic components to PFSA's for improved hot and dry performance

Results were reported for studies aimed at improving the power performance of PFSA PEMFC's under hot (T ≥ 90°C) and dry (dew point ≤ 70°C) conditions. In studies on heteropolyacids, organosulfonic acid-functionalized silica, and zirconia-based materials like zirconium sulfophenylphosphonate, proton conductivity or fuel cell performance was usually reduced by the additives, and any improvements were limited to about 30% increases in voltage at 0.5A/cm2, 80°C dew point, 100°C cell temperature for fuel cells (milder than target conditions of 120-150°C), and about 10% increases in membrane proton conductivity. Previously unreported, anion-immobilizing interactions in PFSA medium between heteropolyacid anions and colloidal silica and between phosphate anion and sol-gel zirconia, were unconvered. More work will be required to develop an understanding of these interactions and exploit them.

3.3. Polymer Matrices Swollen with Liquid Acids

Elements included in membrane development approaches were:

1. Development and identification of inorganic materials capable of assisting in proton conduction;
2. Development of fluorinated ionic liquids as electrolytes for proton conduction;
3. Development of low molecular weight (MW) fluorinated proton conducting materials; and
4. Development or identification of a host polymer matrix for one or both of the above types of materials.

Three major approaches that encompassed these development elements were:

- *Approach A:* Expanded polytetrafluoroethylene matrices were filled using mesoporous silica precursor solutions. After processing to form mesoporous silica, the silica-filled porous composite was filled with electrolyte using either fluorinated ionic liquids or fluorinated acids. The objective was to retain these low molecular weight electrolytes by strong capillary forces resulting from the small pores in the mesoporous silica.
- *Approach B:* Polymer matrices were formed from mixtures of polymer and inorganic oxides by solvent induced phase separation. The pores were filled with electrolytes as in Approach A. The objective was to retain these low molecular weight electrolytes by strong capillary forces resulting from the small pores in the mesoporous silica.
- *Approach C:* Membranes were formed from solutions of polybenzimidazole polymers (PBI or PBIO) that included perfluorinated acids, inorganic oxides, or heteropolyacids. In this case, swelling of the polymer by the perfluorinated acid was the mechanism for retention of the perfluorinated acids.

Some measure of success was achieved with each approach for conductivity under 80°C inlet humidification conditions:

- *Approach A:* A 0.5 mil membrane that was filled with ionic liquid electrolyte provided an AC conductivity of 70 mS/cm at 120°C (18 mohm-cm^2), but was too flimsy to be practical. The more robust 1 mil thick membrane had a conductivity of 10 mS/cm at 120°C (80°C inlet dew point) with corresponding area resistance of 254 ohm-cm^2. This membrane achieved 40 % of the contract target based on AC conductivity results. Useful conductivity results, however, were not obtained under fuel cell conditions. Possible causes were interference of the ionic liquid with the electrode, especially for the cathode, or loss of the acid through evaporation. The silica-filled matrix was not evaluated with other electrolytes, so this type of matrix might be useful with other electrolytes such as the bis-perfluorinated acids.
- *Approach B:* A PVDF-silica matrix that was filled with a perfluorinated bis-imide acid had an AC conductivity of 20 mS/cm at 120°C (2.4 mil thick), which achieved about 30 % of the contract target at this thickness. The major draw back of this approach was inadequate retention of the acid under fuel cell operating conditions. While much of the pore volume may have been in the nanometer size range, the inadequate retention of electrolyte was likely due to

the presence of too many large pores for retention of the acid by strong capillary forces.

- *Approach C:* This approach was determined to have the best potential for retention of the low molecular weight fluorinated acid electrolytes. The best AC conductivity at 120° was 9.3 mS/cm for a 1.1 mil thick for a PBIO-based membrane that had 3 equivalents of a perfluorinated disulfonate acid, 22 wt. % of an amorphous fumed silica, and reinforcement with a polymeric nonwoven. This membrane achieved 33 % of the contract target for conductivity at 120°C under dry conditions. At 90°C, the conductivity of this membrane was 63 mS/cm at 90°C, which exceeded the contract target by 225 %. It met the contract objective of 100 mohm-cm^2 at 100°C (with 80°C inlet dew point). A major problem that had to be overcome for this approach was exudation of acid under pressure for membranes that contained either a disulfonic acid by itself or in combination with bis-imide acids. This problem was minimized through composition optimization. Compositions that had added metal oxides and/or heteropolyacids were found for which there was no exudation under pressure within experimental error.

The best fuel cell results were for a poly-(phenyleneoxide benzimidazole) (PBIO)-based membrane that had 2 equivalents of a perfluorinated disulfonate, two equivalents of a perfluorinated bis-imide acid, and 15 wt. % amorphous fumed silica. At 100°C, the voltage at 0.3 amps/cm^2 was about 0.46 V with this membrane as compared to about 0.28 amps/cm^2 for a conventional PBI-phosphoric acid membrane. On the other hand, the AC conductivity for the PBI-phosphoric acid membrane was much greater, about 90 mS/cm (34 mohm-cm^2) for the latter as compared to 5.3 mS/cm (960 mohm-cm^2) for the PBIO-based membrane. This showed that AC conductivity measurements did not correlate with fuel cell performance if some other factor were involved. The difference was believed to be due to catalyst poisoning in the case of the PBI-phosphoric acid membrane. IR-corrected results showed that very little polarization over potential loss for the PBI-phosphoric acid membrane was due to membrane resistance, whereas much of the over potential loss for the Approach C PBIO membrane was due to membrane resistance rather than due to poisoning. The implication is that fuel cell results could be improved through reductions in Approach C membrane resistance through thickness reduction and/or composition changes.

The major challenge for Approach C would be to improve retention of the fluorinated acids under fuel cell operating conditions and to reduce area resistance. Fuel cell operating times for these membranes covered only from 24 to 100 hours. Given the generation of water at the cathode, wash out by water would be a likely issue. Approaches for increasing resistance to wash out include increasing the molecular weight of the acids, inclusion of sites for cross linking after membrane formation, and covalent attachment to inorganic particulates. Attachment of these fluorinated acids to a polymeric backbone would be the same as the conventional Nafion™ ionomer approach. Thinner reinforced membranes were prepared that had higher conductivity but were not evaluated under fuel cell conditions. An advantage of the Approach C membranes would be that no special processing equipment such as that required for handling perfluorinated monomers, though development would be needed to more efficiently remove the solvents used than the 4 hr. at 140°C used for laboratory preparations.

In addition, new reinforcement matrices were developed to enable use of PFSA ionomers at higher temperatures due to excessive softening of PFSA ionomers at higher

temperatures. Novel matrices filled with sulfated zirconium oxide were prepared by solvent induced phase separation methods. Conductivity of 20 mS/cm at 80°C/20 % RH was achieved for this type of matrix that was filled with PFSA ionomer. Issues with this approach included skin formation on the air side per film casting, macro pores near the air surface, and the fact that the zirconium oxide particles filled the pore space. All of these impeded achieving complete filling using Nafion™ ionomer solution. A novel method was found for elimination of the air surface skin, which enabled filling, and compression after filling removed the macro voids near the air surface. Removal of the air surface skin, however, reduced matrix strength considerably. Additional work would be needed to determine viability of this approach.

In addition to decreasing conductivity with increasing temperature, there is also a decrease in strength at temperatures above the glass transition (T_g) for conventional perfluorinated sulfonic acid (PFSA) membranes. Development described in this report addressed both conductivity and strength at higher temperatures using the following general approaches for proton conduction under drier conditions:

1. Development and identification of inorganic materials capable of assisting in proton conduction;
2. Development of fluorinated ionic liquids as electrolytes for proton conduction;
3. Development of low molecular weight (MW) fluorinated proton conducting materials; and
4. Development or identification of a host polymer matrix for one or both of the above types of materials.

The contract objective was to achieve an area resistance of 100 mohm-cm^2. For a 1 mil thick membrane, this corresponded to a conductivity of 25 mS/cm.

Most of the specific approaches described in this report involved a combination of all of the above general approaches. Development of mesoporous materials for retention of low MW acids through strong capillary forces was the focus of two approaches. Swelling of polymers was another major approach for retention of acids.

The approach that was down selected for more intensive development was based on mixture of basic polymers such as polybenzimidazoles and bis-perfluorinated acids. This was seen as the best approach for retention of the acids. The majority of the conductivity evaluations were for membranes of this type and a summary is given below. For the other membrane approaches, conductivity results are given along with general discussion of the approach and results.

A glossary of materials and abbreviations is provided in the experimental section.

3.3.1. Reinforcement Matrices

Reinforcement matrices were an integral element of many membrane development approaches. As noted above, conventional PFSA ionomers soften considerably above 100°C and PFSA ionomer was softened further by addition of fluorinated ionic liquids, which necessitated mechanical reinforcement. Basic polymers were also swollen due to addition of fluorinated acids in some cases and also required mechanical reinforcement.

In addition to use of off the shelf porous matrices for reinforcement, new matrices containing inorganic additives were prepared and then used in similar approaches as those given above.

Commercial nonwoven or woven webs were used for reinforcement of electrolytes that contained inorganic particulates that were too large for filling into ePTFE or other matrices having pores ~ 1 micron or less.

3.3.1.1. Membranes Reinforced with Commercial or 3M Matrices

Off-the-shelf membranes used for reinforcement included:

- Commercial expanded polytetrafluoroethylene (ePTFE);
- 3M porous poly(vinylidene difluoride) (PVDF) membranes made by a thermally induced phase separation process (TIPS); and
- 3M membranes made by solvent phase inversion (SIPS) under laboratory scale conditions, such as those formed from solutions of (p-phenylene ether-sulfone) (PES) in N-methylpyrrolidinone (NMP) through immersion of cast films into water.

The types of materials that were reinforced with the above types of matrices included:

- PFSA ionomers combined with ionic liquid electrolytes, which plasticized the ionomer and necessitated the use of a reinforcement matrix; and
- Inorganic acids that were deposited into the matrix followed by filling with either PFSA ionomer and/or mesoporous silica precursors.

3.3.1.2. Reinforcement of PFSA Ionomers

As determined in other work done under this contract, stability at 120°C was found to be the critical issue for PFSA ionomers rather than conductivity. Thus, reinforcement of PFSA ionomers was of interest for evaluations at higher temperatures. Development of laboratory procedures for filling off-the-shelf polymeric matrices was also needed as a guide to development of procedures for filling them with mixtures of PFSA ionomer and ionic liquid electrolytes.

Complete and uniform filling of 3M PVDF TIPS matrix with commercial Nafion™ coating solution (SE20042) was difficult to do consistently, whereas complete filling of ePTFE was easier to do consistently. Completeness of filling was judged by transparency after drying. In both cases, however, pre-filling the matrix with a solvent was essential for achieving complete filling consistently, especially for PVDF TIPS.

While good filling of ePTFE with Nafion™ solutions could be achieved by laying a piece that was pre-filled with 1-propanol into a layer of Nafion™ solution, this tended to leave a matte surface on the air side. The thickness of the wet Nafion™ solution was selected based on calculation of the amount needed for complete filling of the pores with ionomer and for skins on both surfaces. A matte surface was an indication of insufficient ionomer for complete coverage of the surface, whereas a glossy surface was an indication of sufficient or excess ionomer on the surface. Matte surfaces were undesirable since direct contact with ePTFE rather than with PFSA ionomer would create high interfacial resistance. Application of Nafion™ solution to both sides of the composite, was more involved but ensured complete filling and provided for the presence of a thin layer of Nafion™ of both sides of the ePTFE.

3.3.1.3. Reinforcement of PFSA/Ionic Liquid Membranes

The six-step procedure given below was used as a starting point for filling porous matrices with solutions containing Nafion™ ionomer and ionic liquids. 1-Ethyl-3-methyl-imidazole bis-(trifluoromethane sulfonimide) (EMI TFSI) was the ionic liquid that was used. Ionic liquids were of interest based on their potential for proton conduction without water. Addition of ionic liquids to Nafion™ was suggested in the literature to have the potential for increasing the operating temperature of Nafion™ membranes.[37] As liquids, however, some method for containment in a membrane was needed. While addition to Nafion™ provided one method for containment, EMI TFSI plasticized Nafion™. Thus, mechanical reinforcement was needed.

Solutions of Nafion™ containing 20 wt. % EMI TFSI relative to Nafion™ were prepared through addition of a 10 wt. % solution of EMI TFSI in 1-propanol to Nafion™ SE20092, which lowered the viscosity of the Nafion™ solution[38]. Direct addition of EMI TFSI to Nafion™ solutions resulted in immediate gellation. While there were no special problems for casting films of Nafion™/EMI TFSI on glass plates, filling of either ePTFE or PVDF TIPS turned out to be problematic. The problem was determined to be due to the early onset of gellation during drying. Premature gellation prevented imbibing additional solution into the pores of the microporous porous matrix. Dilution of the Nafion™ solution with the propanol/EMI TFSI solution also created filling problems since the wet thickness required to fill a microporous membrane such as 1.4 mil thick ePTFE (% porosity of about 78 %) was such that it was difficult to prevent the coating from running even when dried on a level surface. A knife coater gap of $\geq$ 30 mil knife coater gap was required. While filling was achieved over parts of samples as indicated by transparency, the resulting total caliper was very non-uniform with a difference of several mils over a few inches due to running of the low viscosity coating layer. Multiple thinner coatings gave even less penetration or lack of penetration to the back side of the ePTFE (side facing the glass plate), uniformly opaque film, and total caliper that was consistent with the first thinner coating sealing off the pores from penetration by subsequent coatings.

Attempts to increase solution viscosity by stripping excess 1-propanol using a rotary evaporator resulted in massive gellation after removal of about 70 % of the n-PrOH that had been added as part of preparation of the Nafion™/EMI TFSI solution. Gellation around the top of the flask had been noted before this point was reached. This result provided strong evidence that the problem for filling porous matrices with Nafion™/EMI TFSI was due to premature gellation The normal mechanism for complete filling of the pores of a microporous membrane through coating with a solution containing a polymeric material is continual imbibition of more polymer solution as solvent evaporates. This mechanism becomes inoperable obviously once gellation prevents further mass transport of the polymer.

A two-step filling method was developed that got around the above problem with premature gellation. The method was to:

1. Fill the porous matrix with a solution of EMI TFSI in 1-propanol followed by removing excess using a rubber roller and drying to remove solvent;
2. Optionally fill the membrane pores with another solvent to aid imbibing of ionomer solution;
3. Optionally remove surface excess of solvent for step (4); and

4. Apply a layer of ionomer solution followed by drying and annealing.

An example of this method is provided by the following example:

1. ePTFE from Tetratec, 1.4 mil thick, was coated with 1-propanol/EMI TFSI = 90/10 using a 5.5 mil knife coater gap and dried to remove the 1-propanol. The amount of EMI TFSI added was obtained by difference in area weight before and after coating (1.83 mg/cm^2 for ePTFE, 2.51 mg/cm^2 after drying, 0.68 mg/cm^2 EMI TFSI by difference).
2. The coated ePTFE from (1) was coated with 1-propanol using a 4 mil knife coated gap and the excess removed quickly using a rubber roller. The removal of excess 1-propanol from the surface was found to remove about 25 % of the EMI TFSI that was deposited in step (1). Coating methods that would apply only the amount of 1-propanol needed for filling the pores would avoid this loss.
3. A bead of Nafion™ SE20092 was then applied and spread using a knife coater.
4. The resultant composite was dried for 10 min. in an exhaust hood, then for 10 min. in a circulating air oven, and then annealed for 10 min. at 160°C.

After annealing, the composite was completely transparent. The composition of the composite was obtained from area weight determinations:

- ePTFE (1.83 mg/cm^2), 18.5 wt. %
- EMI TFSI (0.68 mg/cm^2 * 0.75 = 0.51 mg/cm^2), 5.1 wt. % (6.3 % relative to Nafion™).
- Nafion™ (9.91 mg/cm^2 total – 1.83 – 0.51 = 7.57 mg/cm^2), 76.4 wt. %

While the present example is based on Nafion™ and ionic liquid compositions, the method is applicable in general to any composition that cannot be imbibed into the pores of a microporous membrane due to gellation during drying, due to crosslinking due to acid-base interactions, or due to any other physical interaction between the ionomer and additives that increases the viscosity to the point at which filling ceases.

While AC conductivity was observed for ePTFE-Nafion™/EMI TFSI composites, work on this approach was discontinued after fuel cell experiments showed lack of proton conductivity. The difference in conductivity results was thought to be due to poisoning of the catalyst by the EMI TFSI.

3.3.1.4. Matrices Filled with Inorganics and Electrolytes

Rather than filling the pores of a matrix such as ePTFE with a Nafion™/ionic liquid mixture, another approach was to first coat or fill the matrix with inorganic materials followed by filling with an electrolytes. An expectation for this approach was that nano-size pores would be useful for retention of low MW electrolytes. Shale oil was seen as an example of strong retention of a liquid by a porous matrix.

An advantage of pre-coating a matrix with solutions of dissolved inorganic materials, inorganic sols, or finely dispersed inorganic particles was avoidance of removal of particles by the matrix functioning as a filter. For solutions that included inorganic particles, well dispersed particles that were at least ten times smaller than the smallest membrane pore were needed. For a matrix having 0.1 – 1 micron pores, this required

that the particles be ≤ 10 nm. The most useful type of inorganic solution for this purpose was inorganic sols in organic solvent.

For electrolytes that contained larger particles, nonwoven or woven matrices having larger pores were useful for reinforcement either by filling with solution and drying or by pressing a dried film into the matrix for compositions that were thermoplastic. Results in Table XVII below for membrane C-10 showed that it was possible to fill ePTFE with a mixture that contained dispersed amorphous fumed silica particles.

3.3.1.4.1. ePTFE Filled with STS Silica and Electrolyte

This membrane formation approach involved filling ePTFE with mesoporous silica precursor solution, heating to condense the silica precursors, removing surfactant used for pore formation, and filling the pores with fluorinated acids. Pores in the silica formed by this method would be expected to all be of the same size and to be about 5 - 7 nm. Any cracks in the material would, of course, create very large pores.

Membranes were prepared by first filling the pores of ePTFE with isopropyl alcohol (IPA), coating with a solution that contained precursors for formation of mesoporous surfactant-templated-silica (STS), drying to remove solvent, heating to condense the silica precursors and/or to remove surfactant, and filling the pores with an electrolyte such as EMI TFSI or perfluorobutane disulfonic acid (DS, $HO_3S(CF_2)_4SO_3H$).

One challenge for this approach was that the stability of the resultant silica was limited by the temperature to which the polymeric matrix could be heated. For ePTFE, the upper use temperature was 320°C. Stability of the silica was evaluated by boiling in deionized water (pH 6). Stability, as expected, was directly related to the temperature used for heat treatment. For material processed at 80°C:

- There was no significant loss of translucency after boiling in water for one hour.
- There was significant loss of silica after boiling in water for 8 hr. as indicated by turning white.
- Conductivity for the membrane itself without added electrolyte was 0.01 S/cm at 70°C and 80 % relative humidity (RH) before boiling.

For membrane that was processed at 200°C, there was a slight increase in haze after boiling for 4 hr. For membrane that was processed at 300°C, there was just a slight loss of translucency after boiling for 7 hr.

Removal of the surfactant used for formation of the STS silica was done initially by boiling in water, but it was later found to be possible to remove it by heat treatment at 200 - 300°C. While heat treatment at 200 - 300°C removed surfactant, liquids did not penetrate membrane that was heat treated at 300°C, though liquids did penetrate membrane that was heat treated at 200°C. For membrane that was heat treated at 300°C, liquids did penetrate after boiling the membrane for several hours.

Initial attempts to fill some thicker grades of ePTFE with STS silica were not successful, though filling of a 0.2 mil thick grade (Tetratex #1311) was successful. The thickness of the composite was about 0.5 mil. To prepare thicker composites, a technique was developed for layering two pieces of 0.2 mil ePTFE while they were wet, which gave an inseparable composite. Some thicker grades were found later that could be completely filled in a single coating pass with the STS precursor silica solution. For Tetratex #1316,

the ePTFE thickness was about 0.5 mil and the thickness after filling was about 1 mil. For Tetratex #1307, the ePTFE thickness was about 1 mil and the thickness after filling was about 2 mil. Filling the #1307 ePTFE in a single coating pass required a more concentrated STS precursor solution.

SEM images for the surface of ePTFE filled with mesoporous STS silica before and after heat treatment at 300°C and boiling are given below in Figures 31-33.

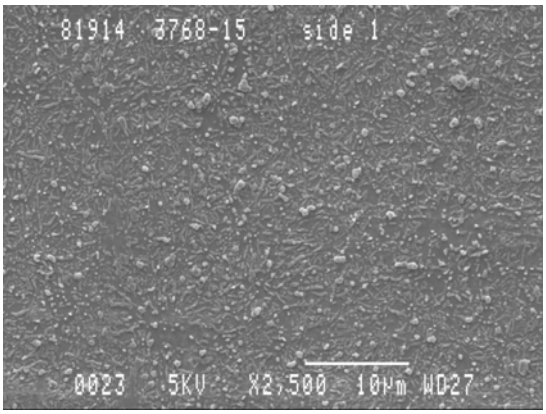

Fig. 32. SEM for surface of ePTFE/SiO2 after heat treatment at 300°C.

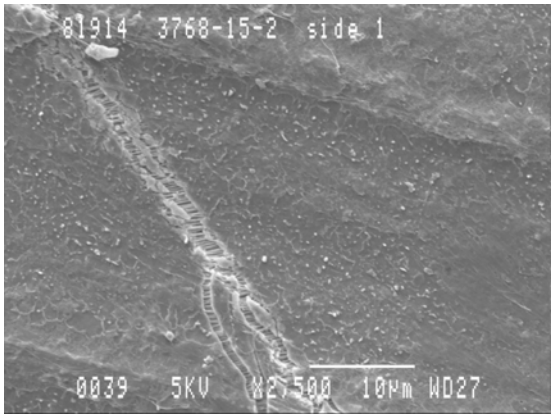

Fig. 31. SEM for surface of ePTFE/SiO2 after heat treatment at 300°C and boiling.

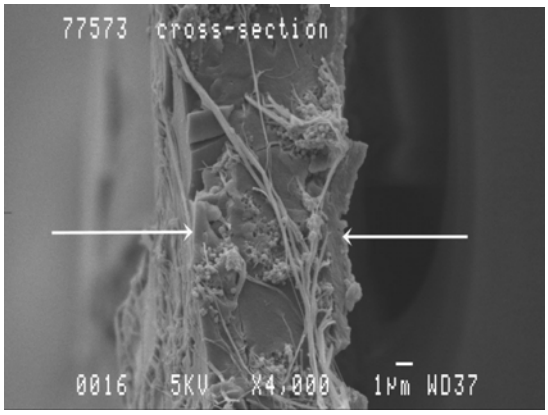

Fig. 33. SEM for cross section of ePTFE/SiO2 after heat treatment at 300°C and boiling.

The fissures seen in the surface for Figure 31 after boiling were not seen in the surface in Figure 32. for membrane after heat treatment at 300°C. The development of fissures after boiling explained why electrolyte did not penetrate the composite before boiling but did penetrate after boiling. Figure 33 showed monolithic blocks of SiO_2 in the cross section. While such membranes were flexible and translucent, flexing the membrane would induce cracking of monolithic blocks of silica.

Retention of electrolyte would likely be much better if a way were found to infiltrate electrolyte into ePTFE/STS silica composites without boiling after heat treating at 300°C

given the lack of cracks/fissures for the former. Perhaps one way to do this would be to incorporate the electrolyte into the STS silica solution rather than adding it later. This would require stability of the electrolyte at 300°C, which would be a bit higher than what 3M fluorinated acids could withstand. Heteropolyacids might be more suitable due to their greater heat stability. The silica-filled ePTFE composites described above would also not be able to retain low MW fluorinated proton conductors based on retention by fine capillaries due to the large pores between the silica platelets, though filling with higher MW materials might be useful.

AC conductivity results for ePTFE/STS silica membranes that were filled using a 90/10 mixture of EMI TFSI/HTFSI are given in Fig. 34. The 90/10 mixture of EMI TFSI/HTFSI was shown in other work to provide optimal conductivity (HTFSI is the acid form of TFSI). The AC conductivity results were determined under dry oven conditions from 50 to 120°C. The membranes were of different thickness but were all prepared using single coating passes of STS silica precursor solution using ePTFE of different thicknesses: Tetratex #1311 for the 0.5 mil composite, Tetratex #1316 for the 1 mil composite, and Tetratex #1307 for the 2 mil composite. As noted above, a more concentrated STS silica precursor had to be used for filling the #1307 ePTFE. Before filling with electrolyte, the ePTFE/STS silica composites were heat treated at 300°C for 1 hr. and then boiled in water for 1 hr.

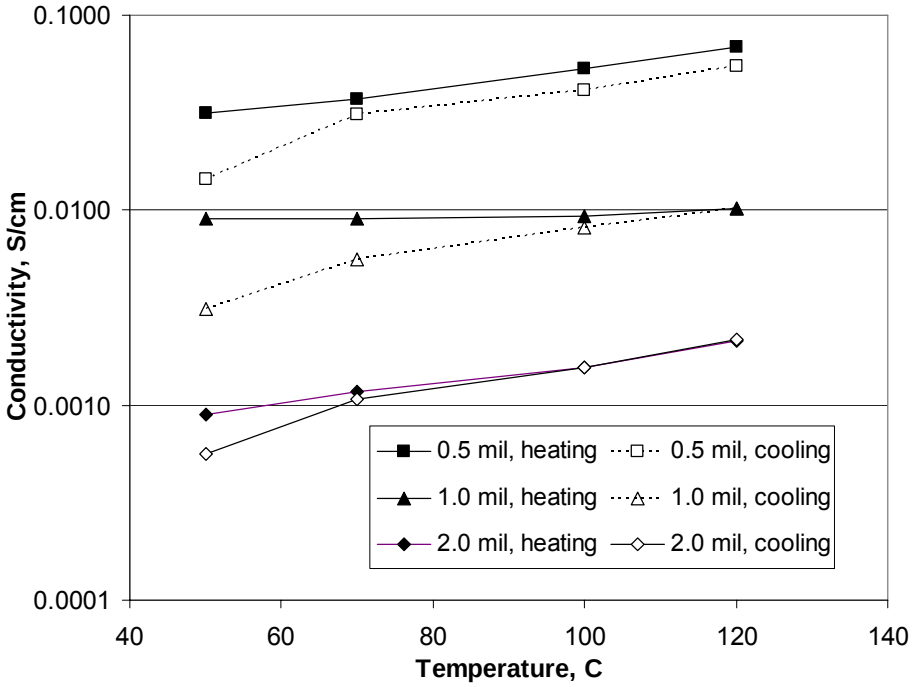

Fig. 34. Conductivity for different thickness ePTFE/STS silica composites filled with EMI TFSI/HTFSI = 90/10 electrolyte under dry oven conditions.

Conductivity increased as temperature increased for the above composites. Upon cooling, conductivity decreased but there was significant hysteresis for the two thinner membranes. If the membranes had the same material properties, then conductivity would not have changed as a function of thickness. The results in Fig. 34, however,

showed substantial conductivity differences for the different membranes. Differences other than thickness for these membranes may have been differences in tortuosity for the different PTFE grades or differences in the effect of the heat treatment/boiling conditions. The boiling process might have had more of an effect on surface layers of silica than the bulk, so the effect would be greatest for the thinnest membrane. While the highest AC conductivity was for the 0.5 mil membrane, it was fragile and difficult to handle. Its AC conductivity of 70 mS/cm at 120°C corresponded to an area resistance of 18 mohm-cm^2, which was much lower than the target of 100 mohm-cm^2. The more robust 1 mil thick membrane had a conductivity of 10 mS/cm at 120°C with corresponding area resistance of 254-ohm-cm^2 (a conductivity of 25 mS/cm would have corresponded to the target area resistance of 100 ohm-cm^2), so about 40 % of the target was met for the 1-mil thick composite.

AC conductivity results under dry oven conditions are given in Fig. 35 for three STS silica filled membranes that were filled with EMI TFS/HTFSI = 90/10 electrolyte. All three membranes were about 1 mil thick. Preparation conditions for the three membranes according to methods described above were:

- A: Single layer of Tetratex #1316 that was filled with 3M STS silica solution using a single coating pass, heat treatment at 300°C for 1 hr., and boiling in water for 7 hr.
- B: Wet lamination of two layers of Tetratex #1311 that were filled with 3M STS silica solution, heat treatment at 300°C for 1 hr., and boiling in water for 7 hr.
- C: Single layer of Tetratex #1316 that was filled with 3M STS silica solution using a single coating pass, heat treatment at 200°C for 1 hr., but not boiled.

The results showed significantly greater conductivity for the two membranes (membranes A and B) that were boiled than for the membrane that was just heat treated at 200°C (membrane C). Conductivity was about 0.01 S/cm at 120°C for membranes A and C as compared to about 0.003 S/cm for membrane B that was heated at 200°C but not boiled. The difference in conductivity was apparently related to whether the membrane was boiled or not, though the heat treatment temperatures were also different. Recall that electrolyte did not readily penetrate membrane that was heat treated at 300°C but not boiled, whereas electrolyte did readily penetrate membrane that was just heat treated at 200°C. The similar conductivity results for membranes showed that conductivity for a given thickness was the same regardless of whether the membrane was formed from a single layer of ePTFE (membrane A) or from wet lamination of two thinner layers of ePTFE (membrane B).

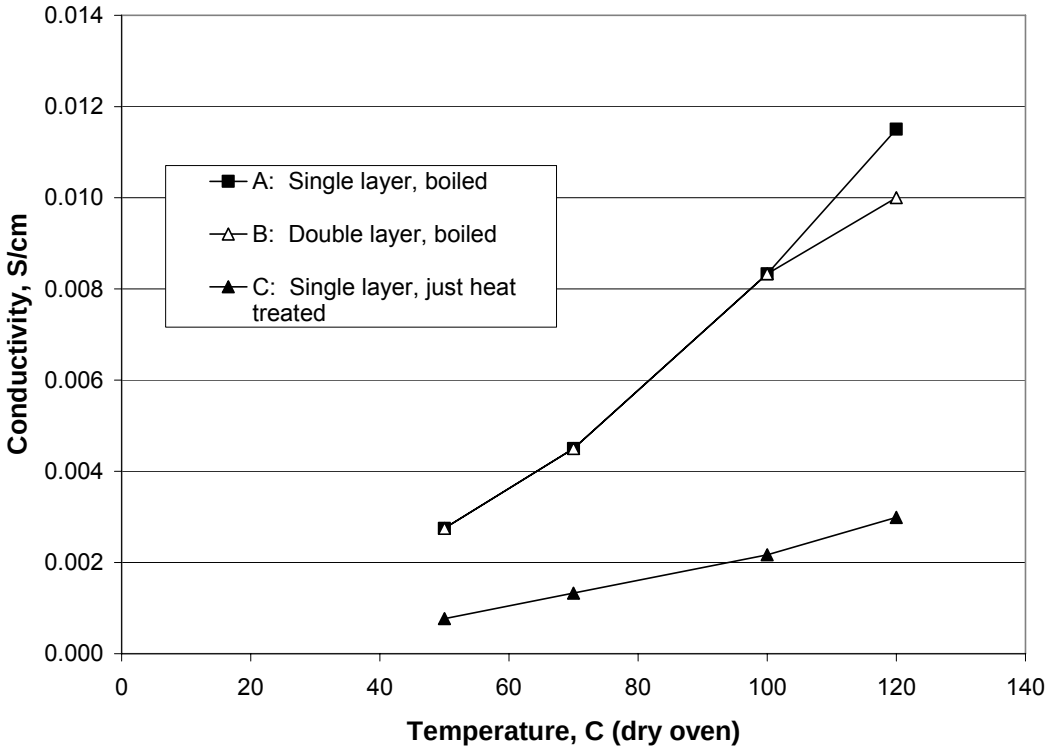

Fig. 35. Conductivity for ePTFE filled with STS silica precursor and EMI TFSI/HTFSI under dry oven conditions as function of process conditions.

While the AC conductivity results for ePTFE filled with STS silica and EMI TFS/HTFSI = 90/10 were encouraging, electrochemical impedance and hydrogen pump conductivity from fuel cell evaluations were flat between 100° - 120°C at about 0.001 S/cm and, even more significantly, were the same using either hydrogen or nitrogen. Area resistance measurements at 15 % and 30 % compression were done on just the matrix itself without added electrolyte in a fuel cell configuration to determine whether electrical shorting was a problem. The results did show an increase in electrical conductivity in going from 15 % to 30 % compression, but even at 30 % compression, the electrical conductivity was low compared to AC conductivity for the matrix filled with electrolyte as determined using a BekkTech cell (120°C, 80°C inlet dew point).

Table VII. Electrical and Total Conductivity for ePTFE filled with STS silica and EMI TFSI/HTFSI = 90/10.

Thickness mils	**Electrical Conductivity for Matrix - S/cm**		**Total AC Conductivity with Electrolyte at 120°C** S/cm
	15 % Comp.	30 % Comp.	
0.5	3.18E-05	8.47E-05	0.070
1	2.54E-06	2.54E-05	0.010
1.8	3.05E-07	4.57E-07	0.0022

While the specific cause for the above fuel cell results was not determined, wetting of the electrodes by the EMI TFSI/HTFSI electrolyte was thought to be a likely cause. This would more likely to be an issue for oxygen reduction. The bis-perfluorinated acids used for the swollen polymer approach were not evaluated with this silica-filled matrix approach, so results for evaluation with ionic liquid electrolytes did not preclude utility for this type of silica-filled ePTFE matrix with other electrolytes. Another possible cause was evaporation of the acid from the electrolyte given the 180°C boiling point for HTFSI.

While electrical shorting was not thought to be the issue for the above fuel cell problems, shorting under fuel cell compression conditions would not be surprising given the brittle nature of monolithic blocks of silica. This would be a general challenge for all monolithic inorganic proton conducting membranes. Monolithic sheets of inorganic oxides have been evaluated as membranes for proton conduction.[39] A solution would likely require alternative types of MEAs and flow fields to avoid cracking the materials due to non-uniform stresses.

The conductivity of ePTFE filled with just mesoporous STS silica was evaluated at 70°C as a function of percent relative humidity (RH) using x-y conductivity cell in a humidity chamber. As shown in Fig. 36, there was a rapid increase in conductivity above 60 % RH from 10^{-6} S/cm to about 10^{-2} S/cm at 80 % RH. It was interesting that conductivity as high as 0.01 S/cm could be attained with just mesoporous silica. It would be expected that functionalizing the mesoporous silica with acidic groups might provide significantly higher conductivity at both higher and lower humidification. Acid functionalized silica was prepared and evaluated as an additive for PFSA membranes but were not evaluated in this type of composite.

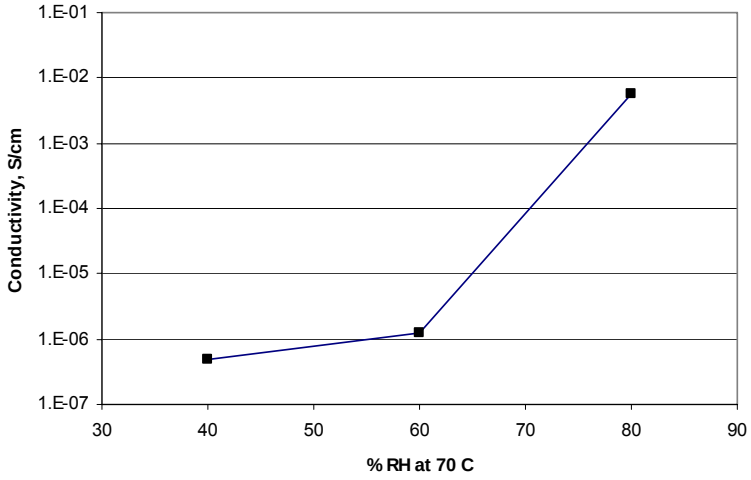

Fig. 36. Conductivity for silica-filled ePTFE without any additional electrolyte added.

3.3.1.4.2. ePTFE Filled with Inorganic Acid and Electrolyte

Another embodiment of the general approach of this section was to first partially fill the pores of ePTFE with an inorganic proton conductor such as a heteropolyacid and a silica precursor such as tetraethylorthosilicate (TEOS) followed by filling with PFSA ionomer solution having optional additional inorganic additives. Two compositions were evaluated:

- Nafion™/SiO_2/phophotungstic acid = 81/11/8 (after drying)
- Nafion™/SiO_2/phophotungstic acid = 60/10/30 (after drying)

The amount of SiO_2 was calculated assuming complete conversion of TEOS to SiO_2. The PFSA was from Nafion™ SE20092 solution. These compositions by themselves did not form good films due to the high amounts of inorganic additives. Solutions containing components calculated to provide the above compositions were aged for 1 day to allow for hydrolysis of TEOS and condensation. These compositions were then either filled into 1.4 mil virgin ePTFE or into ePTFE that had been first coated with a methanol solution having 4 % phosphotungstic acid (PWA) and 10 % TEOS. For filling of ePTFE that was not pre-treated with the latter, the ePTFE was first filled with 1-propanol before application of the modified Nafion™ solutions.

Conductivity results at 80°C/40% RH for a cast Nafion™ control membrane, ePTFE that was pre-coated with TEOS/PTA per above and then filled using Nafion™ SE20092 solution, and ePTFE that was pre-coated with TEOS/PTA per above and then filled with a solution calculated to provide Nafion™/SiO_2/PTA = 60/10/30 composition are given in Table VIII. The AC conductivity cell was placed inside a humidity controlled oven. Hydrogen pump slope values were obtained using a fuel cell at 120°C with 80°C inlet dew point.

Table VIII. Conductivity for ePTFE with TEOS/PTA Pre-Coat and with TEOS/PTA added to Nafion™ Coating Solution.

Membrane	AC Conductivity 80°C/40% RH	H-Pump Slope 120°C/80°C Dew Point
	mS/cm	ohm-cm^2
Cast Nafion™	17	200
ePTFE-TEOS-PWA filled with Nafion™ solution	11.6	750, then sharp increase at 0.5 amps/cm^2
ePTFE-TEOS-PWA filled with Nafion™-TEOS-PWA solution	5.9	750, then sharp increase at 0.1 amps/cm^2

The results in Table VIII showed that addition of PWA/SiO_2 to the ePTFE matrix before filling with Nafion™ decreased AC conductivity and that including additional TEOS/PWA in the Nafion™ filling solution decreased the conductivity even further. The fuel cell hydrogen-pump measurements also indicated introduction of a current density limitation due to pre-coating the ePTFE matrix and an even stronger current density limitation due to inclusion of additional TEOS/PWA in the Nafion™ solution used for filling. Note that

temperature and humidification conditions for AC conductivity and hydrogen pump slope were different. One explanation for the decreased AC conductivity and increased hydrogen-pump slope with increased amounts of TEOS/PWA would simply be replacement of the more conductive PFSA ionomer with less conductive inorganic materials. Another explanation would be that decreased conductivity was due to poor connectivity in these compositions. As noted above, these compositions did not have good film forming characteristics due to the high amounts of inorganic additives. While filling into ePTFE provided mechanical support, there could have been loss of conductivity due to loss of connectivity within the material due to low cohesive strength. An important lesson may be that good film formation properties might still be important even for reinforced materials. Assuming this were the case, decreasing the amount of added inorganic additives to the point where film formation were better might have provided better conductivity results.

3.3.1.4.3. Glass Cloth and Inorganic Oxide Fillers

Reinforcement of polybenzimidazole (PBI)/$CF_3SO_2NHSO_2(CF_2)_4SO_2NHSO_2CF_3$ (C1-bis-imide or C1BI) membranes was looked at after it was discovered that compositions that had more than one equivalent of C1BI flowed away from the electrodes of the BekkTech conductivity cell under the test conditions used. This was a case for which reinforcement was necessary just to be able to measure conductivity. Two approaches were used: filling with various types of silica and/or pressing into glass cloth, Thonex PW106 (see Glossary). An advantage of glass cloth was that the openings were large enough so that there weren't any problems filling with particle-filled compositions. Compositions containing dispersed amorphous fumed silica were coated, dried, and then pressed into the glass cloth, as described in and V.M. As discovered later, it was possible to reinforce a PBIO/fumed silica/DS composition using ePTFE without apparent segregation of the silica due to filtration by the ePTFE.

The resistance of C1BI/PBI compositions to flow was evaluated by first laminating the membrane to Teflon film and then placing in a 120°C oven at a tilt of 10° from horizontal. Lamination to Teflon film was done as a way to remove from the glass plate after drying. This was done by placing a piece of Teflon film on top and laminating by hand. Under the above test conditions, C1BI/PBI compositions without silica would flow, whereas C1BI/PBI = 2:1 with $\geq$ 7 % AF-100 or 3M STS silica did not flow. Manifestations of flow included movement beyond the initial membrane area or formation of voids due to dewetting. Similarly, C1BI/PBI = 2:1 without any added silica that was pressed into Thonex PW06 glass cloth did not flow under these conditions. C1BI/PBI = 3:1 with ~ 13 wt. % AF-100 silica showed some signs of dewetting. For conductivity evaluations, a combination of filling with silica and pressing into glass cloth was used to ensure complete lack of flow during conductivity measurements. Conductivity results for all PBI and PBIO-based membranes are given in Section AC Conductivity for PBI/Fluorinated Acid Membranes

3.3.1.4.4. Polymeric Nonwoven

As for glass cloth, the large pores of polymeric nonwovens were advantageous for ease of filling, especially for filling with compositions having dispersed inorganic particulates. An advantage for polymeric nonwovens compared to available woven glass cloths was that ionic contamination from glasses was not a concern for polymeric nonwovens. Another advantage was large volume commercial availability and reasonable cost. Thermal oxidative stability was a concern for a polymeric nonwoven. The nonwoven selected was made from a 100 % liquid crystalline polymer available under the trade designation "HM090" from Crane & Co., Inc (~ 2 mil thick, 8.9 g/square meter).

Filling of this nonwoven was done using a method that was similar to that for ePTFE. For conductivity results, see Tables 11 and 12. Membranes C-11 and C-41 per Tables 11 and 12 were prepared by the solution coating method and C-18 per Table XVII was prepared by the press method.

3.3.1.4.5. ePTFE Filled with PBIO, Silica, and Fluorinated Acid Electrolyte

Initially, ePTFE was not thought likely to be useful for compositions that contained dispersed inorganic particulates given that filling even just with PFSA ionomer solutions was a challenge. An expectation was that the ePTFE would filter out the inorganic particles. Conductivity results for a DS:PBIO = 3:1 with 28 wt. % of dispersed AF-100 amorphous fumed silica that was filled into Tetratex #1316 ePTFE were similar to the same composition filled into Crane HM090 nonwoven (see C-11 in Table XV). The filling procedure was the same as that given for filling with PFSA ionomer solutions except that at 50/50 mixture of isopropyl alcohol/NMP was used for pre-filling the ePTFE. Analysis was not done to look for segregation of particle at the ePTFE surface, but visual inspection and the similarity in conductivity results were consistent with no segregation since conductivity for this composition without dispersed silica was much lower.

3.3.1.5. Development of New Polymer Matrices

Rather than taking a pre-made polymeric matrix and filling with some combination of inorganic materials and/or other electrolytes, another approach was to make polymeric matrices that contained inorganic materials and to then imbibe electrolyte into them. Membranes formed from PVDF and inorganic oxides with dominant pore volume comprised by pores smaller than 2 nm have been described in the literature.[40] Membranes having pores of this size were thought to be useful for retention of low MW electrolytes through capillary forces.

Two types of inorganic-filled matrix based on solvent induced phase separation (SIPS) methodology were evaluated:

- Polyether sulfone (PES) matrices that were filled with sulfated zirconia; and
- Polyvinylidene fluoride matrices that were filled with a variety of types of silica.

3.3.1.5.1. Development of S-ZrO_2-Filled Matrices

PES porous membranes containing sulfated-zirconia oxide (S-ZrO_2) were prepared using a SIPS method for membrane formation. As known from the literature, the proton conductivity of S-ZrO_2 was a strong function of preparation conditions but capability for evaluation of conductivity of powders wasn't developed until later in the contract. Thus, the conductivity of the S-ZrO_2 used was not known. The highest ratio S-ZrO_2/PES used was 86/14 w/w (or about 56/44 on a volume basis). Increasing the S-ZrO_2/PES ratio was found to decrease skin formation and to increase pore size.

A problem with formation of membrane matrices by the above method was that there was a tight skin layer on the air side surface that impeded filling with PFSA ionomer solutions and conductivity. A solution to this problem was achieved through application of a layer of NMP on top of the first layer coated that contained the mixture of PES and ZrO_2 in NMP. SEM images for the air and glass sides and cross section of a membrane made using PES/NMP = 80/20 and PES/S-ZrO_2 = 14/86 are given in Fig. 37, a, b, and c respectively. The matrix before filling was about 1.9 mil thick and had a pore volume of about 75 %. A striking observation from these SEM images was that the particles were in the pores of the matrix rather than contained in or on the polymer fibrils as is typical for particle-filled membranes made using thermally induced phase separation. This provided an explanation for the difficulty encountered in obtaining complete filling or the void space with PFSA ionomer solutions.

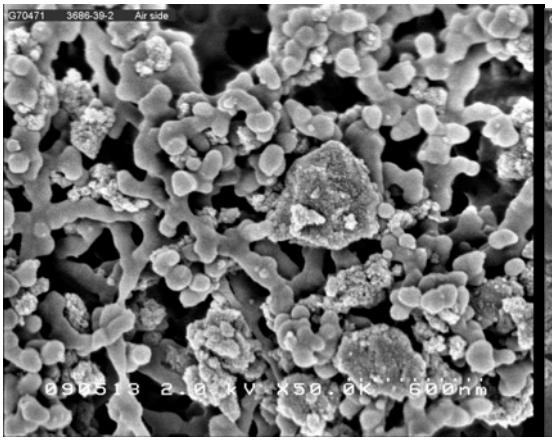

Fig. 37a. Air side for PES/S-ZrO_2.

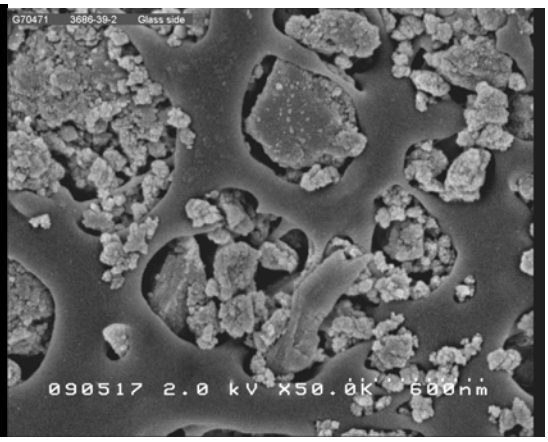

Fig. 37b. Glass side for PES/S-ZrO_2

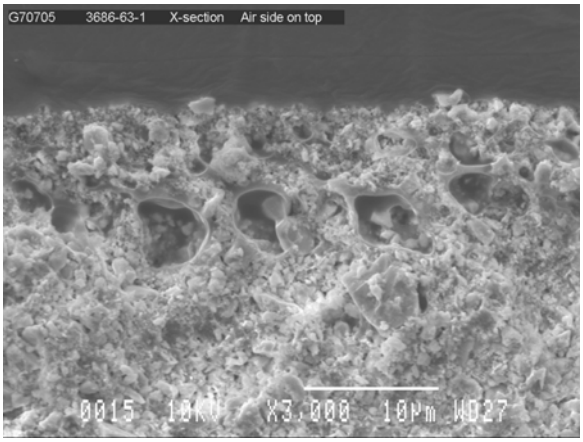

Fig. 37c. Cross section near air side for PES/ZrO_2

Fig. 37. SEM Images for Surfaces and Cross Section of PES/ZrO2 Matrix

One draw back to elimination of the air surface skin was that the resultant matrices were significantly weaker. Increasing the PES/NMP ratio in the casting mixture increased matrix strength but also increased skin formation and skin elimination was found to be more difficult for higher PES/NMP ratios. Coating with a multi-layer extrusion die would likely provide much greater control and consistency than lab coating methods.

Elimination of the skin on the air surface increased penetration by ionomer solution greatly for PES/S-ZrO_2 matrices, such as those depicted in Fig. 37. Filling with ionomer did increase strength. Fluorine x-ray material analysis (F-XRMA) results in Fig. 38 were for a composite that had about a 25 micron layer of Nafion™ on the air side, a filled-matrix layer of 50 microns, and a Nafion™ skin on the glass side of about 2 microns. The F-XRMA results in Fig. 38 were consistent with a thick layer of Nafion™ ionomer on the air side, a thin layer on the glass side, and a lower but consistent amount of Nafion™ throughout the cross section of the composite. The F-XRMA images themselves, however, showed incomplete filling of some large macro-pores near the air surface (see Fig. 37c) that were the result of the phase immersion conditions used. Reducing the amount of Nafion™ solution applied resulted in decreased filling of the macro pores near the air surface and decreased conductivity. The macro-pores resulted from the fast rate of mixing demixing of NMP and into water upon immersion of the coated membrane composition into water. Application of an NMP over-coat layer decreased macro-pores. Use of a thicker NMP over-coat layer and/or more work on composition and phase immersion conditions might eliminate macro-pores.

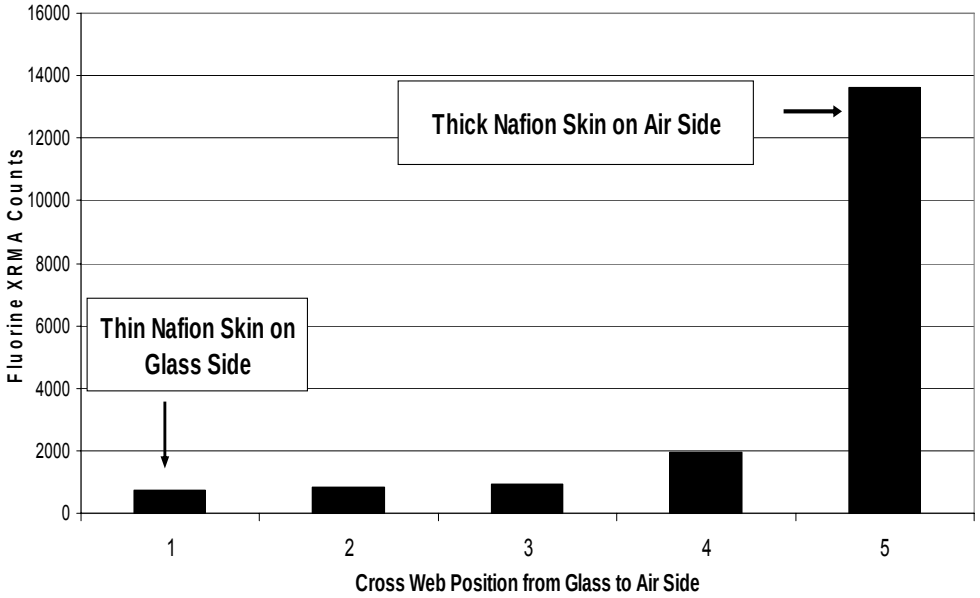

Fig. 38. Fluorine distribution for cross section of S-ZrO2/PES matrix that was filled using Nafion™ coating solution.

Compression of PES-ZrO_2 matrices was looked at as a way to eliminate macro-pores near the air side surface. For unfilled PES- ZrO_2, application of 4000 psi at 130°C did reduce the thickness of a PES-ZrO_2 matrix by as much as 40 % but did not remove the macro-pores or change the surface porosity significantly. Surprisingly, compression of a Nafion™-filled composite did appear to remove the macro-pores but did not improve conductivity. The composite was compressed at 160°C for 5 min. at 5000 psi. The initial thickness was 3.1 mil and thickness after compression was about 2.3 mil. This treatment did result in darkening of the membrane color.

AC conductivity results for a Nafion™-filled PES-ZrO_2 = 86/14 matrix (skin free per Fig. 36) was 0.02 S/cm at 80°C and 20 % RH as determined by AC impedance. Hydrogen pump conductivity results were 10-times lower than for Nafion™, whereas AC conductivity results were 5-times lower than for Nafion™ (0.10 S/cm). Some possible causes for the lower than expected conductivity for this composite could have been low conductivity of the S-ZrO_2, low surface area for proton conduction due to the relatively large S-ZrO_2 particle size (1 -2 microns), incomplete filling (as indicated for macro-pores above), possible lack of interconnection of pores, or membrane tortuosity. A 25 % reduction in conductivity would be expected if the volume occupied by the S-ZrO_2 filled matrix contributed nothing to the conductivity. Since the observed reduction in conductivity was much greater, some other factor would more likely be responsible. Tortuosity factors of 2 to 3 would be typical for this type of matrix, so tortuosity could perhaps account for a 2- to 3-fold reduction in conductivity by effectively increasing the path for proton conduction 2- to 3-fold. The location of particles in the pores could increase the tortuosity factor for proton conduction even more. The presence of some macro-pores near the air side surface could have also been a significant factor, though F-XRMA showed that they were lined with a layer of Nafion™.

A goal for the above type of composite was to derive higher proton conductivity under drier conditions form inorganic proton conducting particles. A problem for this approach was that it still depended upon some other electrolyte to provide a conductivity between particles. If only a small amount of bridging electrolyte were needed, reasonable overall conductivity would still be possible even for a bridging electrolyte that had lower conductivity under hotter/drier conditions.

3.3.1.5.2. Development of Inorganic-Filled PVDF-HFP Matrices

Given the problems with brittleness and large cracks in ePTFE-silica composites, flexible polymeric matrices having nano-size pores for retention of low MW electrolytes were of interest. Matrices were prepared using poly(vinylidene difluoride-hexafluoropropylene) copolymers, PVDF-HFP. Literature claims for good retention of triflic acid by PVFD-HFP/metal oxide matrices made using SIPS type preparation methods were attributed to most of the porosity being comprised by pores < 10 nm.[41] Preparation procedures did not provide specific information on mixing procedures. Membranes prepared following procedures given in the literature were too weak to be handled. Thus, alternative preparation methods had to be developed to evaluate the usefulness of this type of matrix for retention of 3M electrolytes. The general method involved use of the following:

- High surface area particulates having nano-size primary particles
- Polymer
- A solvent for the polymer having a low boiling point
- A solvent for the polymer having a high boiling point
- Casting a layer of the above composition onto a supporting substrate
- Evaporation of at least some of the low boiling point solvent
- Immersion into water to induce phase separation and to remove the higher boiling point solvent to provide a porous matrix that was filled with nano-porous particulate.

The primary differences between this method of preparation and that given in Section II.B.1 was the primary particle size of the inorganic particulate, the type of polymer, use of two types of solvent versus a single solvent, and membrane formation conditions. An advantage of the above procedure was that it allowed dispersion of a high amount of high surface area particulate through use of a volatile solvent that was evaporated before phase inversion, which provided a mixture suitable for membrane formation by the SIPS method. Attempts to prepare membranes using just a single solvent failed (e.g., dimethylformamide (DMF), PVDF, and high surface area silica at 30 – 40 vol. percent relative to PVDF).

A typical solvent system used in literature examples was a 97/3 (w/w) mixture of cyclopentanone (CP), propylene carbonate (PC), and Kynar Flex 2801-01 (battery grade poly(vinylidene difluoride-hexafluoropropylene) (PVDF-HFP) [42]. For the present report, Kynar Flex 2750-01 PVDF-HFP was also used. The melting point for PVDF-HFP copolymer is ~ 140°C as compared to ~ 168°C for PVDF. Types of silica and titania that were evaluated and internal acronyms assigned to them for reference were:

- Amorphous fumed silica, 100 m^2/g (#89376 from Alfa) – AF-100
- Amorphous fumed silica, 200 m^2/g (#42740 from Alfa) – AF-200
- Amorphous fumed silica, 400 m^2/g (#42737 from Alfa) – AF-400
- Silica gel (large pore size), 300 m^2/g (#41502 from Alfa) – SG-300

- Silica gel, 600 m^2/g (#42729 from Alfa) – SG-600
- STS silica prepared by 3M, 800 m^2/g (higher surface area due to internal pores), 3 nm pore size.
- Amorphous synthetic titanium dioxide, 50 m^2/g (P25 from Degussa)

Since mixing methods weren't specified in the literature, initial mixture preparation was done by adding the PVDF to the CP/PC mixture in a vial, placing on a bottle roller to dissolve the polymer, and then mixing in the silica using a mortar and pestle. For casting on either Teflon film or glass plates, cracks and holes developed upon drying in an exhaust hood at RT in less than four hours. From the rough film surface it was evident that the silica was not adequately dispersed.

Dissolving PVDF in CP/PC as indicated above gave cloudy solutions, which indicated incomplete dissolution of the polymer. NMP, DMF, and dimethylacetamide (DMAc) were evaluated as solvents since they were known to be good solvents for PVDF at RT. Methyl ethyl ketone (MEK) was used as the more volatile solvent in combination with either NMP or DMF. PC/CP = 20/80 (w/w) and NMP/DMF were also found to be useful solvent pairs.

Factors that affected membrane strength and other properties were:

- The type of solvent used for dissolving the PVDF and the order of dissolving had a large effect on membrane strength. Dissolving the PVDF completely in a good solvent before addition of the second solvent was found to result in stronger membranes. Membrane strength was much lower if it were dissolved in a dispersion of the inorganic particulate in a mixture of the two solvents.
- The surface area and the type of silica had a large effect on membrane strength. Strength was better for lower surface area amorphous fumed silica. Strength was also better for 3M STS silica. While surface area for the latter as determined by nitrogen adsorption experiments was high, 800 m^2/g, the particles were relatively large. Thus, most of the surface area was internal and so would not affect the amount of polymer needed to wet its surface. The better strength for membranes with 19/36 (w/w) mixtures of SiO_2 and TiO_2 (50/50 on v/v basis) was thought to be due to the much lower surface area of the latter.
- Use of a high shear mixer was important both for membrane strength as well as for membranes that were free of holes and that had smooth surfaces. Longer high shear mixing times were needed for TiO_2 as compared to SiO_2.
- Use of DMF/MEK = 35/65 gave stronger membrane than NMP/MEK = 35/65.
- Some of the strongest membranes resulted from initial dissolving of the PVDF in a smaller amount of NMP/DMF = 50/50 (w/w) followed by addition of more DMF before dispersion of the inorganic material. For NMP/DMF co solvents, some of the DMF was evaporated at 100°C in a circulating air oven. The drying time at 100°C for removal of some of the DMF was found to be significant and had to be limited to no more than 5 min.
- Use of PC/CP = 20/80 as compared to literature precedent for use of PC/CP = 3/97 provided the strongest membrane. The higher strength was likely due to greater shrinkage during drying, as indicated by a percent porosity of 50 % as compared to about 70 - 77 % for other membranes.
- Use of PC/CP = 20/80 resulted in greater surface roughness. The greater roughness was thought to be due agglomeration of silica, an indication of lower dispersion stability upon standing. The difference in dispersion stability made

sense given the greater hydrocarbon character for CP as compared to NMP or DMF.

- Use of a mixture of SiO_2 and TiO_2 gave stronger membrane than for just SiO_2, consistent with results reported in the literature. Also, shrinkage upon drying after water immersion and extraction of solvent was much lower for a mixture of TiO_2/SiO_2 than for just SiO_2.

Factors that did not make a difference for membrane strength were:

- The grade of PVDF used didn't make a difference. Similar results were obtained using either Kynar Flex 2750-01 or 2801-01 (battery grade).
- Use of either an electric or air driven rotor-stator mixer did not make a difference. It had been thought that greater dispersion of the inorganic materials might have been achieved due to the higher rpm that was accessible for the air driven mixer.

Strong and stretchy PVDF (2750-01 grade) membranes were obtained for 44 wt. % (40 vol. %) of the following types of silica using DMF/MEK = 35/65 in their preparation:

- 100 m^2/g amorphous fumed silica
- 300 m^2/g silica gel
- 800 m^2/g STS silica prepared by 3M

Porosity was typically about 70 %.

For PVDF membrane made using only 400 m^2/g of amorphous fumed silica at 44 wt. %, a moderately strong membrane was obtained by dissolving the PVDF at 18 wt. % in a 50/50 w/w mixture of NMP/DMF followed by dilution with DMF to 4.15 wt. % PVDF before dispersion of the silica. The cast film was heated for 5 min. (longer time gave poorer results) at 100°C in a circulating air oven, cooled under ambient conditions, and then immersed in water. Unlike the above three examples, this membrane was not stretchy (strength was reasonable but elongation was low).

For PVDF membrane made using a 50/50 v/v mixture of 400 m^2/g of amorphous fumed silica and 50 m^2/g of titania, a moderately strong membrane was obtained using NMP/DMF = 35/65, partial removal of the DMF by heating for 5 min. at 100°C in a circulating air oven, cooling under ambient conditions, and then immersing into water. The resultant membrane could be bent 180° without breaking. A stronger but less flexible membrane (150° bend before breaking) was obtained for the same composition using PC/CP = 20/80 w/w for solvents. After casting, the CP was allowed to evaporate slowly at RT in an exhaust hood for 16 to 22 hr. before immersion into water. Many other preparation conditions gave much weaker membranes which showed that formation of the PVDF matrix was very sensitive to conditions.

PVDF-HFP/STS silica matrix filled with C1BI acid was evaluated for conductivity and for functioning in a fuel cell. Conductivity was evaluated using a BekkTech cell over 80 to 120°C with inlet humidification kept constant at an 80°C dew point. See Fig. 39 for conductivity results. The matrix was prepared using Kynar Flex 2750-01, 3M STS silica at 44 wt. % relative to PVDF-HFP, and DMF/MEK = 35/65 per procedures given above. SEM images of this matrix showed silica particles present on both surfaces, 10 micron diameter pores on the air side and 5 microns in diameter on glass side. Images of a cross section showed a cellular structure having elongated pores that were 5 to 10 microns in the elongated direction. The pores were mostly filled with silica particle

agglomerates made up of primary particles that were of about 0.5 micron diameter. The membrane was ~ 2.4 mil thick.

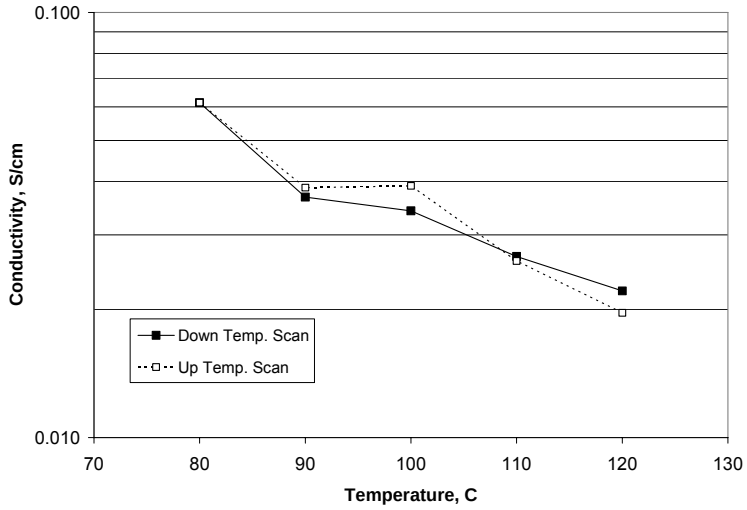

Fig. 39. Conductivity from AC Impedance for PVDF/STS Silica Matrix filled with C1BI acid for constant 80°C inlet dew point.

Given the encouraging AC conductivity results using the BekkTech cell, a sample was evaluated in a fuel cell using the hydrogen pump method for measurement of conductivity. The initial conductivity was 10^{-4} S/cm after conditioning at 120°C with 80°C inlet dew point but slopes for polarization with hydrogen and nitrogen were the same between 100 to 120°C. Conductivity did increase to 10^{-3} at 80°C. Inspection of the membrane after the test showed that the membrane had turned white in the active area, which was a clear indication that the acid had been washed out of the pores. These results indicated that much smaller matrix pores would be needed for retention of this type of electrolyte. A matrix with STS silica was chosen because it was strong and stretchy and had known porosity and pore size. A matrix filled with 300 m^2/g silica gel or 400 m^2/g amorphous fumed silica might have been better choices for retention of the acid, though for hydrogen/oxygen polarization, water produced at the cathode might wash low MW acid out of even low nm size pores.

3.3.1.5.3. PBI Matrix

Given the problem with preparing PBI membranes that contained DS by solution methods, preparation of porous PBI membranes by solvent induced phase separation was investigated to see whether a PBI-fluorinated acid membrane could be prepared by filling the pores of a porous PBI membrane with the acid.

PBI was cast from DMAc. A 24 wt. % solution was prepared by dissolving PBI at 260°C in a pressure vessel, filtering and concentrating the solution, coating onto a glass plate, and immersing into water to induce phase separation. The water-filled membrane was about 11 – 12 mil thick after extraction of the DMAc through three soak cycles in water. After drying, the resultant film was found to not be porous as indicated by density calculations and by lack of penetration by solvents. The membrane was shown to be porous before drying, however, by exchanging the water first with 10 M phosphoric acid and then with 15 M (85 %) phosphoric acid. The membrane thickness increased from

11 – 12 mils to 14 – 16 mils after exchanging the water with phosphoric acid. The amount of water displaced was calculated from the gain in mass due to phosphoric acid, which indicated 75 % porosity for the water-filled PBI. Attempts to displace the water in the PBI matrix by bathing with an 50 % solution of C1BI in water having enough C1BI to fill the calculated pore volume, however, led to severe distortion, shrinkage, and loss of porosity. Bathing with additional C1BI-water solution resulted in increased curling. Heating first at 80°C and then at 120°C did not remove the curl, though heating to 160°C did relax the curl and the surface was observed to be sticky upon removal. Upon cooling, however, the membrane became hard, which would not have been the case had the C1BI been mixed molecularly with the PBI since that would have plasticized the PBI. C1BI was used for these experiments since it was known to plasticize PBI, so the chances for replacing water in the PBI SIPS membrane were thought to be better than for the DS. Finding a way to combine PBI with DS was the original goal.

Phosphoric acid filled PBI SIPS membrane was prepared for AC conductivity evaluation by exchanging the water from the water immersion process with 11 M phosphoric acid. This concentration was chosen by analogy for what would be typically used to swell PBI film to provide a reasonable balance of conductivity and mechanical properties. Three soaks spanning 24 hr. were done by covering the membrane with excess phosphoric acid solution. Based on literature reports, this amount of time should have also been enough for the phosphoric acid to swell the PBI. It was thought that this might provide an alternative useful method for making PBI-phosphoric acid membranes. Conductivity results were poor. A reason might have been reduction of the volume of acid in the pores due to evaporation of water, which might have reduced the volume of without fully collapsing the pores. This would have resulted in a deficiency of phosphoric acid in the surface layer pores.

3.3.1.5.4. PBI-PES Matrix

Given the problems with PBI SIPS membranes collapsing upon drying, membranes made from blends of PBI and PES by the SIPS process were looked at to see whether the PES would prevent collapse of the porous structure on itself during drying. A 40/60 PBI/PES mixture at 23 wt. % in DMAc was cast on a glass plate, immersed in water to induce phase separation, soaked in excess DI water three times to remove DMAc, and dried. The resultant membrane had a porosity of about 70 % and was fairly strong. Water wetted and penetrated the membrane, which was surprising given that PES is hydrophobic though PBI is hydrophilic. If the void volume of this membrane were filled with C1BI, the calculated ratio of equivalents of C1BI:PBI would be 2:1. The membrane thickness was about 2 mils. SEM photomicrographs in Fig. 40a-c showed very different morphologies for the air-side and glass-side surfaces (as defined per membrane casting). For the glass side, there were large islands on the order of 50 microns surrounded by matrix polymer. For the air side, SEM showed pores in the range of about 1 micron diameter that contained spheres of about 0.3 micron diameter. Smaller spheres of about 0.05 micron diameter were scattered throughout the surrounding matrix polymer. The cross section morphology was quiet complex with regions having large scale pores on the order of 3 – 15 microns, medium scale pores of about 1 micron, and regions having a much finer pore structure.

A piece of the above porous PBI/PES membrane was filled with an aqueous solution of C1-bis-imide (50 %) and dried at 120°C. The resultant material was transparent at

120°C and was very soft, gooey and stretchy. It became hazy and then turbid upon cooling and turned to light brown color. Since PES was present at higher weight percent than PBI, PES would have been thought to have been the continuous phase. Filling PES and PES/43 % silica membranes that were prepared by the SIPS process with C1BI aqueous solution (application of excess solution followed by drying), however, showed that C1BI did not swell PES. The conclusion from these results was that PBI had to have been the continuous phase for the above 40/60 PBI/PES membranes matrix since the membrane would not have been swelled by C1-bis-imide had PES been the continuous phase.

Filling of the PBI/PES matrix with DS did not result in swelling, which was consistent with what was known about incompatibility of the DS and PBI. This provided a way to fill a porous PBI/PES matrix with DS. As for other SIPS matrices, however, retention of the acid was not good.

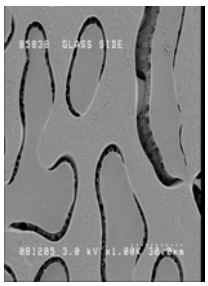

Fig. 40a. Glass Side per Solution Casting

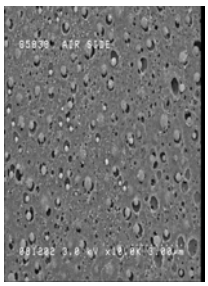

Fig. 40b. Air Side per Solution Casting

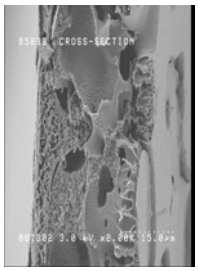

Fig. 40c. Cross Section

Fig. 40. SEM photomicrographs

3.3.1.5.5. Silica-Filled PES Matrices

Inorganic-filled PES matrices were prepared by the SIPS method for evaluation using methods that were somewhat different than those for PVDF. Membranes were moderately strong and flexible, though there was a skin on the air side. The membranes would likely be significantly weaker as for S-ZrO_2 filled membranes if procedures for skin minimization were used. PES is an amorphous polymer with a T_g at 229°C and has high oxidative stablity since all hydrogens on the phenylene groups are deactivated by a sulfone group. Thus, PES might provide have higher temperature resistance than PVDF-HFP copolymers that melt at about 140°C.

3.3.1.5.6. Sulfonation of Polymer Matrix

PES was sulfonated to see whether sulfonation would improve conductivity for composites made using a porous matrix made using sulfonated PES and to improve its interface with conductive materials filled into its pores. Proton NMR showed that treatment of PES with chlorosulfonic acid resulted in sulfonation of only about 1 % of the phenylene groups. Sulfonation with liquid sulfur trioxide gave about 17 % sulfonation as indicated by proton NMR. While this was lower than the targeted percent sulfonation, the latter was evaluated for formation of a porous matrix by dissolving in NMP, coating on a glass plate, and immersing in water. The resultant water-filled matrix collapsed on itself due to coalescence during drying. The same happened for attempts to prepare porous polybenzimidazole (PBI) membranes by immersing coatings of PBI in DMAc into water. The addition of attractive hydrogen-bonding forces to those exerted by removal of water from the pores of these phase separated membranes was sufficient to collapse the pores.

3.3.2. Electrolyte Swollen Polymers

In this section, membranes prepared from solutions of polymer and fluorinated acids are described. The intent of this approach was to retain acids in polymers swollen by them. Inorganic additives were also incorporated both for conductivity and for mechanical reinforcement. An unanticipated result for mixtures of disulfonate and imide acids was swelling of the polymer by the imide and phase separation induced by the disulfonate. The types of polymers evaluated were basic polymers such as polybenzimidazoles.

Fluorinated acids have long been the subject of evaluation as electrolytes. Fundamental electrochemical studies were reported in 1985.[43] Fluorinated acids were added to phosphoric acid fuel cells to decrease poisoning of the Pt catalyst.[44] Perfluorinated monomeric to polymeric sulfonimides were evaluated as additives for phosphoric acid fuel cells.[45]

This section describes membranes formed from mixtures of PBI or PBIO with bis-fluorinated acids, metal oxides, and inorganic acids. Compositions, membrane strength, and characterization by differential scanning calorimetry (DSC), dynamic mechanical analysis (DMA), x-ray diffraction (XRD), polarized light microscopy, and thermal gravimetric analysis (TGA) are provided in sections below. Other sections describe results from washing experiments and morphological inferences from the results, resistance of acids to wash out by liquid water.

3.3.2.1. Membrane Formation

Three types of polymers were evaluated for membrane formation with bis-fluorinated acids:

- poly(2,5-benzimidazole) (ABPBI)
- poly[2,2'-(m-phenylene)-5,5'-bibenzimidazole] (PBI from Celanese); and
- PBIO (trade name for a phenylene oxide benzimidazole from Fumatech).

The following fluorinated acids were prepared by William Lamanna at the 3M Company. For the C4-bis-imide, the C_4F_9- groups were linear. The DS and C1BI were tetrahydrates.

Disulfonate (DS): $HO_3S(CF_2)_4SO_3H$

C1-bis-imide (C1BI): $CF_3SO_2NHSO_2(CF_2)_4SO_2NHSO_2CF_3$

C4-bis-imide (C4BI): $C_4F_9SO_2NHSO_2(CF_2)_4SO_2NHSO_2C_4F_9$

Addition of solutions of PBIO in NMP to solutions of either imide or sulfonate acids or mixtures thereof provided homogeneous solutions after simple mixing without precipitation. Addition of solutions of PBI in DMAc to solutions of imide acids in DMAc also gave homogeneous solutions, but addition of even very dilute PBI/DMAc solutions to solutions of the DS acid resulted in immediate precipitation. Addition of solutions of DS to solutions of PBI also resulted in precipitation even for very dilute solutions. Blending salts of the acids with the polymers followed by re-acidification after membrane formation, as typically done for blending acidic and basic polymers, was not possible since that procedure would have washed the acids out of the membrane.

The ratio of acid to basic polymer used for membrane formation was designated in terms of equivalents of acid to equivalents of base. Note that PBI has two basic nitrogens per repeat unit, whereas PBIO has only one. Thus, a membrane composition resulting from addition of one equivalent of PBIO to two equivalents of DS and two equivalents of C1BI was designated as DS:C1BI:PBIO = 2:2:1.

For reasonable mechanical strength, the total equivalents of acid per equivalent of basic polymer were about ≤ 4, though self supporting membranes having up to a total of 8.5 equivalents of acid were prepared for DS:C1BI:PBIO compositions. For DS:PBIO $\geq$ 4:1, the surface became increasingly rougher and scalier as the amount of DS increased. Polarized light microscopy revealed a close packed cone surface topology for DS:PBIO = 4:1. For DS:C1BI:PBIO compositions, addition of as little as 0.1 equivalent of C1BI completely eliminated rough surface topology.

A summary of qualitative estimates of membrane strength as a function of added acid(s), different types and surface area silicas, and combinations of silicas and heteropolyacids (HPAs) is given in Table IX. For a membrane rated as strong, a palpable amount of stress could be applied by hand without tensile failure. A membrane rated as strong might have sufficient strength for use as a self-supported membrane. For a membrane rated as weak, the smallest amount of stress that could be applied by hand was sufficient for tensile failure. A membrane rated as weak would likely need reinforcement. The results in Table IX were grouped by type of inorganic additive for analysis of the impact of their addition on strength.

For PBIO with added C1BI, membranes were weak for C1BI:PBIO > 1:1. Preparation of PBIO membranes with added C4BI was complicated by dewetting from either glass or Teflon during drying. Addition of inorganic additives provided the ability to dry without dewetting and reduced stickiness and stretchiness. Inclusion of AF-100 silica in a C4BI:PBIO = 4:1 composition provided a strong membrane that stretched 2-fold during removal from glass with no recovery (not rubbery). On the other hand, DS: PBIO membranes were strong for DS:PBIO $\leq$ 4:1. Addition of AF-100 silica decreased membrane strength for DS:PBIO $\geq$ 3:1. A 2:1 membrane with added silica was strong.

In the absence of inorganic additive, DS:C1BI:PBIO membranes at 3:1:1, 2:2:1, and 1:3:1 ratios were all strong membranes. Addition of AF-100 reduced strength to the moderate range in general and reduced strength greatly for DS:C1BI:PBIO = 1:3:1. On the other hand, the effects were opposite for addition of high surface area amorphous fumed silica, AF-400, for DS:C1BI:PBIO compositions. For these compositions, the 3:1:1 composition was the weakest and membrane strength increased moving to the 1:3:1 composition. Changing to DS:C4BI:PBIO with AF-400, changed the strength relationships again: the 3:1:1 composition with AF-400 was strong and the 1:3:1 composition was weak.

In general, compositions with SG-300 silica gel were strong, both for C1BI:PBIO and DS:C1BI:PBIO compositions. On the other hand, compositions with SG-600 were weak for C1BI:PBIO but were strong for DS:PBIO and DS:C1BI:PBIO compositions. Turning to the C4BI, C4BI:PBIO compositions with SG-600 were strong for C4BI:PBIO = 3:1 and moderately strong at 4:1.

For membranes containing SiWA at 50 %, strong membranes were obtained for DS:C1BI:PBIO = 3:1:1 and 2:2:1; at 1:3:1, the membrane was weak. For C4BI, strong membranes with SiWA were obtained for DS:PBIO = 3:1 and for DS:C4BI:PBIO = 3:1:1. For compositions that also contained AF-100, DS:C1BI:PBIO membranes were weak for AF-100 in combination with $\geq$ 50 % SiWA, though stronger with lower percent SiWA.

The above results demonstrated that membrane formation and resultant strength was the result of subtle interplay between the type of acid, mixtures of acids, ratios of acids, type of silica and silica surface area, and presence and percent SiWA alone and in combination with silica.

For C1BI:PBIO membranes and PBI-phosphoric acid membranes, the liquid droplets that formed on the surface upon exposure to ambient air and the liquid was acidic. Since this could result in loss of acid from the membrane, all handling and operation would have to be under dry conditions. In contrast, no droplets developed on the surface of DS:PBIO or DS:C1BI:PBIO membranes upon exposure to humid air. While the reason for this difference in behavior was not understood, the lack of water condensation in humid air would be a practical advantage for the present membranes.

Table IX. Summary of Membrane Strength for PBIO with Added Acids and Inorganic Additives.

Acid(s)	Ratio to PBIO	MOx	Other Additive	Strength
DS/C1BI	1:3:1	none	-	strong
DS/C1BI	2:2:1	none	-	strong
DS/C1BI	3:1:1	none	-	strong
DS	4:1	AF-100	-	weak
DS	3:1	AF-100	-	weak
DS	2:1	AF-100	-	strong
C1BI	4:1	none	-	weak
C1BI	3:1	none	-	weak
C1BI	3:1	AF-100	-	weak
C4BI	4:1	AF-100	-	strong, stretchy
DS/C1BI	4:1:1	AF-100	-	moderate
DS/C1BI	3:1:1	AF-100	-	moderate
DS/C1BI	2:2:1	AF-100	-	moderate
DS/C1BI	1:3:1	AF-100	-	weak
DS/C1BI	3:1:1	AF-400	-	very weak, brittle
DS/C1BI	2:2:1	AF-400	-	weak
DS/C1BI	1:3:1	AF-400	-	moderate
C1BI	3:1	SG-300	-	strong
DS/C1BI	1:3:1	SG-300	-	strong
DS/C1BI	2:2:1	SG-300	-	strong
DS/C1BI	3:1:1	SG-300	-	strong
DS	3:1	SG-600	-	strong
C1BI	3:1	SG-600	-	weak
C1BI	4:1	SG-600	-	very weak
C4BI	4:1	SG-600	-	moderate
C4BI	3:1	SG-600	-	strong
C4BI	3:1	none	SiWA (50)	moderate
DS/C1BI	3:1:1	SG-600	-	strong
DS/C1BI	2:2:1	SG-600	-	strong
DS/C1BI	1:3:1	SG-600	-	strong
DS/C1BI	1:3:1	AF-100	SiWA (30)	weak
DS:C1BI	1:3:1	none	SiWA (50)	moderate
DS/C1BI	1:3:1	AF-100	SiWA (50)	very weak
DS/C1BI	1:3:1	AF-100	SiWA (60)	very weak
DS/C1BI	2:2:1	none	SiWA (30)	strong
DS/C1BI	2:2:1	AF-100	SiWA (30)	strong
DS/C1BI	2:2:1	AF-100	SiWA (50)	weak
DS/C1BI	2:2:1	AF-100	SiWA (60)	weak
DS/C1BI	2:2:1	AF-100	ST11A (30)	moderate
DS:C1BI	3:1:1	none	SiWA (50)	strong
DS/C1BI	3:1:1	AF-100	SiWA (30)	strong

3.3.2.2. Membrane Characterization by DSC

Addition of either C1BI or C4BI to PBI or PBIO resulted in significant plasticization of the polymer as shown by DSC results in Fig. 41 and Fig. 42 below. Water also plasticized PBI and PBIO without or with added fluorinated acids. DSC results for hydrated C1BI:PBI membranes are given in Fig. 42. For clarity, the curves were spread apart on the heat flow axis. The relative intensities are correct but the absolute position on the heat flow axis has no meaning. These results showed a large decrease in T_g for addition of even one equivalent of C1BI and additional decreases for each additional equivalent. For C1BI:PBI = 4:1, the Tg was -56°C. Addition of silica for C1BI:PBI = 2:1 further decreased the T_g. The T_g for dry PBI membrane was 420°C and 355°C for PBI membrane that was hydrated (about 16 wt. % water). The C1BI:PBI membranes were hydrated merely by exposing to ambient air (~22°C and 30 to 40 % RH). The initial DSC evaluations were done using sealed pans to look for changes between first and second heats that were not related to loss of water. Results showed no change in T_g for six heat and cool cycles for scans up to 150°C. Exceeding 150°C resulted in rupture of the lids and contamination of the instrument cell with acid, so subsequent experiments were done using punctured lids and limited upper temperature for the first scan to 150°C to ensure removal of water before scanning to a higher temperature on the second scan. For evaluation using a punctured lid, the Tg for the second heat was then about 20 C° higher for all C1BI:PBI samples, which showed that water also plasticized these materials.

First heat results were done on membranes that had been conditioned under ambient temperature and humidity to determine the effect of absorbed water on morphology. Second heat results were more indicative of membrane morphology with minimal water present as would be the case under hotter/drier fuel cell operating conditions, though the dynamics of fuel cell operation include possible absorption of product water from the cathode with back diffusion to the anode.

For PBIO, a broad endotherm was seen in the first heat but was absent in the second heat, which was consistent with removal of water, as shown in Fig. 42. The T_g for dry PBIO was 238°C and 81°C for humidified PBIO. As for PBI membranes above, conditioning and DSC analyses were similar to the second procedure used for PBI:C1BI membranes.

Addition of one equivalent of C1BI to PBIO introduced some crystalline order as indicated by an endotherm at 65°C in the first heat. This endotherm was absent in the second heat and a T_g at 76°C was observed. For addition of four equivalents of C1BI to PBIO, there was only a T_g at -61°C for the first heat. For the second heat, the T_g moved to -48°C, there were two broad endotherms between 50-200°C with maximum for one at 90°C and the other at 163°C, and there was an exotherm at 19°C. For addition of one equivalent of DS, a T_g at 69°C and a broad endotherm with maximum at 113°C was observed in the first heat. For the second heat, however, there was no endotherm and the T_g moved up to 197°C. Thus, the main effect for addition of one equivalent of DS to PBIO was just to depress the T_g. For addition of four equivalents of DS, however, there was no T_g in the first heat, a strong endotherm at 82°C and a broad endotherm at about 120°C. For the second heat, a T_g at -20°C , an exotherm at 80°C, and endotherm at 121°C were observed. These results showed that morphology changed as a function of

the equivalents of DS added and that the morphology changes were substantial. Addition of either DS or C1BI acids to PBIO introduced order that was not present for the amorphous PBIO polymer itself.

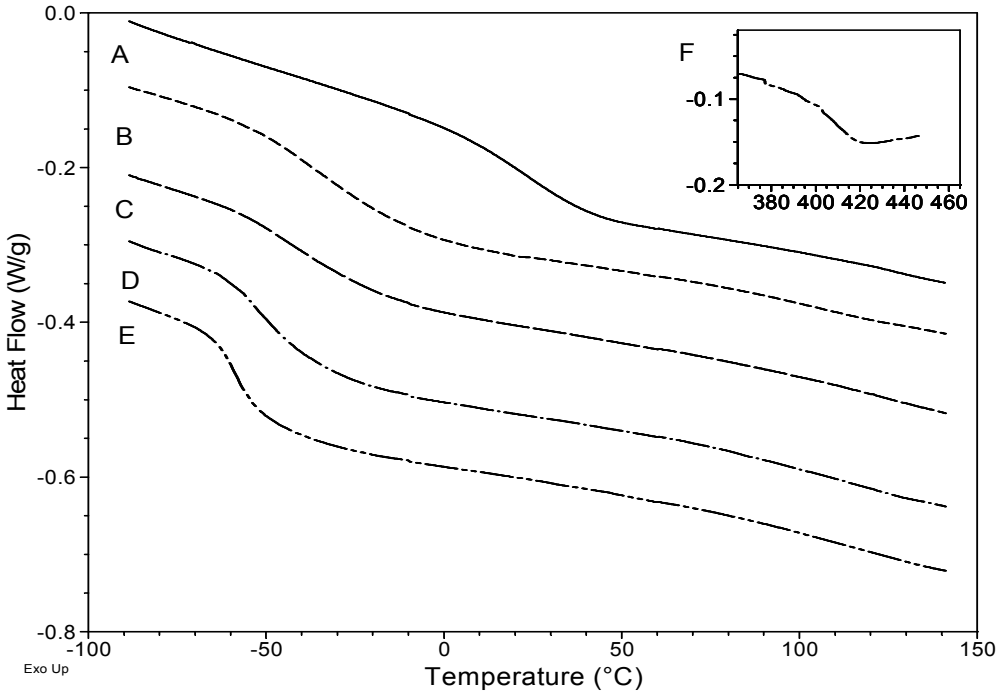

Fig. 41. DSC results after six scans at £ 150°C in sealed pans. A: C1BI:PBI = 1:1. B: C1BI:PBI = 2:1. C: C1BI:PBI = 2:1 + silica. D: C1BI:PBI = 3:1. E: C1BI:PBI = 4:1. F: PBI (insert frame).

DSC results in Fig. 41 for DS:C1BI:PBIO = 2:2:1 membrane were different from those for either the DS:PBIO or C1BI:PBIO membranes. For the first heat, there was a T_g at -59°C and endotherms at 61°C and 72°C. For the second heat, the T_g moved to -42°C and there was only a broad endotherm at 149°C. These results suggested that a much lower degree of ordering for the DS:C1BI:PBIO = 2:2:1 membrane than for membranes with either just DS or just C1BI. The degree of ordering was much greater for DS:PBIO than for C1BI:PBIO.

The occurrence of exotherms followed by endotherms (recrystallization followed by melting) in the second heats for C1BI:PBIO = 4:1 and DS:PBIO = 4:1 membranes showed that reordering processes in these membranes after heating/cooling were either slow or that absorption of water was needed for the reordering to occur. Similarly for the DS:C1BI:PBIO = 2:2:1 membrane, movement of sharp endotherms in the first heat to a broader endotherm in the second heat at a higher temperature indicated that reordering to the original morphology was slow or that water was needed for the reordering to occur. Subsequent DSC results for similar membranes with added silica showed 3rd heat results that were similar to 1st heat results for samples that were exposed to humid

air after the 2nd heat, which implied that absorption of water was necessary to return to the initial morphology.

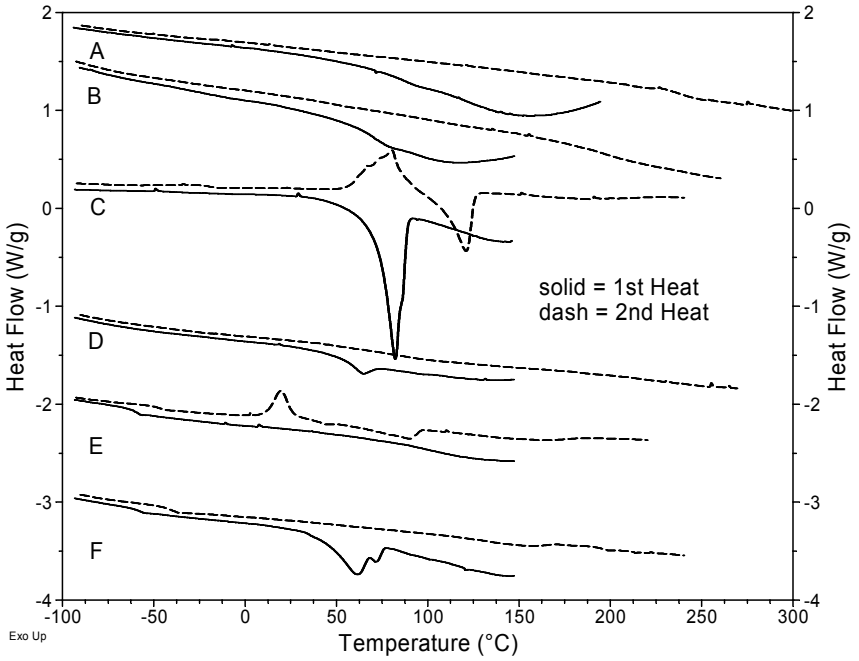

Fig. 42. DSC results for first heat and second heat for PBIO and PBIO with fluorinated acids. A: PBIO. B: DS:PBIO = 1:1. C: DS:PBIO = 4:1. D: C1BI:PBIO = 1:1. E: C1BI:PBIO = 4:1. F: DS:C1BI:PBIO = 2:2:1.

Given the large increase in AC conductivity for PBIO/fluorinated acid membranes due to addition of silica, selected membranes of this type were evaluated by DSC to look for relationships between morphology and conductivity. See Table X for modulated DSC results for first heats for humidified membranes and Table XI for second heat results for DS:PBIO and DS:C1BI:PBIO membranes with and without AF-100 silica. Abbreviations and conventions for results in these tables are:

- HF: signal related to net heat flow
- R: signal related to reversible heat flow (heat capacity)
- NR: signal related to non-reversible heat flow
- (+) peak area: exothermic heat flow
- (-) peak area: endothermic heat flow

Results are also provided in Table XI for the effect of quench rate after drying as part of membrane preparation.

For first heat results in Table XI, there was a strong endothermic peak in the first heat for all compositions and most of the heat flow was due to the non-reversing component of the total heat flow. The non-reversing heat flow was related to loss of water and/or loss of order in the structure related to water. For both DS:PBIO and DS:C1BI:PBIO membranes, the addition of silica decreased the onset temperature and peak temperature significantly for all three types of modulated DSC signals. The endotherms with silica were broader and more shallow (lower J/g) and the peak minimum were at a lower temperature, which was indicative of a more disordered structure or imperfect

packing. While no glass transitions were seen in first heats, glass transitions were observed in the cooling curve and were similar to values for T_g observed in the second heat per Table XI.

For DS:C1BI:PBIO = 2:2:1 compositions with and without added AF-100 silica, the magnitude of endothermic heat flows for the first heat was 50 to 70 % less than for DS:PBIO compositions. The heat flow was larger for the 2:2:1 membrane with AF-100 (-133 J/g) than for the 2:2:1 membrane without AF-100 (-76 J/g) with most of the flow being non-reversing in both cases. This was opposite to the relative values of heat flows for the endothermic transitions for the DS:PBIO membranes with and without AF-100 silica. These differences indicated a difference in morphology and difference in contribution of water to the morphology between DS:PBIO and DS:C1BI:PBIO compositions.

For second heat results in Table XI for DS:PBIO compositions, there were exotherms followed by endotherms at temperature above the glass transition in some cases, though the net peak area was exothermic in all cases. The reversing heat flows were endothermic and the non-reversing heat flows were exothermic. For the second heat, the magnitude of the total heat flow was smaller by about an order of magnitude than those for the first heat. The endotherm magnitudes were much smaller for the DS:C1BI:PBIO = 2:2:1 compositions with our without silica, $\leq$ -1 J/g for the most part, than for DS:PBIO compositions. Interestingly, there were no reversing exothermic of endothermic transitions for the DS:C1BI:PBIO = 2:2:1 membrane without added silica in the second heat, though there was a small non-reversing endotherm that was identical to the total heat flow. For the first heat, most of the heat flow was related to changes in the morphology that were related to removal of water; whereas for the second heat, the smaller heat flows can be attributed to changes in the polymer-acid structure itself in the absence of absorbed water. Unlike first heat results for which total heat flow transition energies were all strongly endothermic for all components of modulated heat flow, heat flows for second heats for DS:PBIO compositions were mildly exothermic with the reversing component being endothermic and the non-reversing component being exothermic. The exothermic transitions, which had a substantial non-reversing component, would likely be indicative of recrystallization to a different morphology.

Difference in the above results between DS:PBIO and DS:C1BI:PBIO membranes could simply have reflected absorption of different amounts of water but more likely reflect differences in morphology between these two different types of compositions. While XRD indicated some crystallinity for both humidified and for dried membranes, the second heat results for the DS:C1BI:PBIO = 2:2:1 compositions implied that the heat of fusion for any structure was quite low. Relative to consideration of impact on use as fuel cell membranes under hotter/drier conditions, the differences in morphology might correspond to differences in the ability to retain water given the differences in energy required to remove water from the two types of composition. On the other hand, fuel cell use temperatures of 90° to 120°C would be well above any the exo- or endothermic transitions for any of these PBIO membranes, though morphology at lower temperatures could be important relative to proton conductivity at lower temperatures during start up and membrane morphology as affected by absorption of water during cool down.

Another indication of a difference in morphology between DS:C1BI:PBIO and DS:PBIO membranes was that the former were porous after extraction of the acids by water,

whereas the latter were not. This difference might relate to the fact that DS:C1BI:PBIO membranes were characteristically stronger than DS:PBIO membranes.

For DS:C1BI:PBIO = 2:2:1 membranes with and without added AF-100 silica, the effect of quench rate after drying during membrane fabrication was evaluated by modulated DSC for its impact on morphology. See **Table** X and Table XI. Faster quench rate was found to decrease loss of acid under pressure. For first heat results, T_g was higher for the faster quench rate (-63°C as compared to -72°C) and the onset of melting was lower (17°C as compared to 29°C). These results would be consistent with a slightly more disordered structure for the faster rate of quenching, which would be expected. There was no effect of quench rate on second heat results, which indicated that any difference in morphology due to quench rate was removed by re-heating. Thus, the reduction in exudation with increased quench rate would more likely be related to a reduction of pore size for the polymeric matrix rather than to a change in polymer-acid morphology.

DSC results for scrupulously dry acids showed that they themselves were crystalline solids. Melting points were: DS at 174°C, C1BI at 189°C, and C4BI at 175°C. After exposure to humid atmosphere, however, the DSC results were much more complex with multiple melting points, T_g transitions in some cases, and recrystallization followed by melting transitions.

Table X. Effect of Added Silica on Modulated DSC First Heat Results for PBIO Membrane Compositions.

Sample Description		Signal Type	Glass Transition	Endotherms/Exotherm Transitions				
				Peak Onset	Shoulder Peak	Peak Minimum/ Maximum	Shoulder Peak	Net Peak Area
			°C	°C	°C	°C	°C	J/g
DS:PBIO = 3:1	slow	**HF**	none	70		79		-226
DS:PBIO = 4:1	slow	**HF**	none	72	53, 70	77	110, 126	-241
DS:PBIO = 3:1 + 22 % AF-100	slow	**HF**	none	47		66		-162
DS:PBIO = 3:1	slow	**R**	none	36		62	80	-42
DS:PBIO = 4:1	slow	**R**	none	47		68	80, 127	-46
DS:PBIO = 3:1 + 22 % AF-100	slow	**R**	none	41		61		-22
DS:PBIO = 3:1	slow	**NR**	none	71		78		-184
DS:PBIO = 4:1	slow	**NR**	none	71	53	77	108, 124	-195
DS:PBIO = 3:1 + 22 % AF-100	slow	**NR**	none	48		67		-141
DS:C1BI:PBIO = 2:2:1	slow	**HF**	NA	42	NA	61	NA	-76
DS:C1BI:PBIO = 2:2:1 + AF-100	slow	**HF**	NA	29	NA	61	NA	-133
DS:C1BI:PBIO = 2:2:1 + AF-100	fast	**HF**	NA	17	NA	62	NA	-115
DS:C1BI:PBIO = 2:2:1	slow	**R**	-55	39	NA	61	NA	-61
DS:C1BI:PBIO = 2:2:1 + AF-100	slow	**R**	-72	-5	NA	62	NA	-11
DS:C1BI:PBIO = 2:2:1 + AF-100	fast	**R**	-63	-7	NA	59	NA	-10
DS:C1BI:PBIO = 2:2:1	slow	**NR**	NA	43	NA	61	NA	-15
DS:C1BI:PBIO = 2:2:1 + AF-100	slow	**NR**	NA	29	NA	61	NA	-122
DS:C1BI:PBIO = 2:2:1 + AF-100	fast	**NR**	NA	18	NA	62	NA	-105

Table XI. Effect of Added Silica on Modulated DSC Second Heat Results for PBIO Compositions.

Sample Description	Quench Rate	Signal Type	Glass Transition	Endotherms/Exotherm Transitions				
				Peak Onset	Peak Minimum/ Maximum	Shoulder Peak	Peak Area	Net Peak Area
			°C	°C	°C	°C	°C	J/g
DS:PBIO = 3:1	slow	HF	NA	33	60	NA	23	23
DS:PBIO = 4:1	slow	HF	NA	25	43	-3	22	9
				78	104	114	-13	
DS:PBIO = 3:1 + 22 % AF-100	slow	HF	NA	17	51	NA	21	10
				76	98		-11	
DS:PBIO = 3:1	slow	R	-23	72	99	114	-11	-11
DS:PBIO = 4:1	slow	R	-22	67	102	NA	-28	-28
DS:PBIO = 3:1 + 22 % AF-100	slow	R	-26	62	97	NA	-15	-15
DS:PBIO = 3:1	slow	NR	NA	33	60	NA	33	32
				112	115	NA	0	
DS:PBIO = 4:1	slow	NR	NA	25	43	-3	21	21
				109	114	NA	-2	-2
DS:PBIO = 3:1 + 22 % AF-100	slow	NR	NA	14	51	NA	28	25
				95	112	NA	-2	
DS:C1BI:PBIO = 2:2:1	slow	HF	NA	-5	2	NA	NA	-1
DS:C1BI:PBIO = 2:2:1 + AF-100	slow	HF	NA	-6	2	NA	NA	-1
					71	NA	NA	-1
				72	73			
DS:C1BI:PBIO = 2:2:1 + AF-100	fast	HF	NA	59	81	NA	NA	-3
DS:C1BI:PBIO = 2:2:1	slow	R	-41	none	none	NA	NA	NA
DS:C1BI:PBIO = 2:2:1 + AF-100	slow	R	-25	65	82	NA	NA	-1
DS:C1BI:PBIO = 2:2:1 + AF-100	fast	R	-25	63	81	NA	NA	-1
DS:C1BI:PBIO = 2:2:1	slow	NR	NA	-5	2	NA	NA	-1
DS:C1BI:PBIO = 2:2:1 + AF-100				-5	2			-1
	slow	NR	NA	38	41	NA	NA	-0.04
				69	72			-0.02
DS:C1BI:PBIO = 2:2:1 + AF-100	fast	NR	NA	61	81	NA	NA	-2

3.3.2.3. Membrane Characterization by XRD and Polarized Light

XRD results for PBIO showed that it was perfectly amorphous, which was consistent with DSC results. For PBIO-acid membranes, XRD patterns were found to be differ as a function of the type of acid(s), the ratio of acid to polymer, the presence of inorganic oxides such as silica, and whether hydrated or dry. For both DS:PBIO = 4:1 and DS:C1BI:PBIO = 2:2:1 membranes, crystallite size was too large to estimate by XRD other than to say that the size was > 150 nm. Crystallite size was about 600 Å for DS:PBIO = 4:1 with 19 wt. % silica and for DS:C1BI:PBIO = 2:2:1 with 16 wt. % silica. For DS:PBIO = 4:1, the crystallinity index was about 0.5 with or without added silica. For DS:C1BI:PBIO = 2:2:1, the crystallinity index was about 0.3 without added silica and about 0.2 for membrane having about 20 wt. % silica.

Selected membranes were also evaluated by optical microscopy using polarized light (10X objective, red compensator, and crossed polarizers using transmitted light.) This method is capable of revealing crystals that are larger than ~ 1000 nm provided that the crystals are anisotropic and are sufficiently different in refractive index from the surrounding medium . DSC and XRD results were also useful for determination of the presence of crystallinity as well as some indication of crystallite size for XRD. Observations with crossed polarizers provided additional qualitative information on crystal size. The membranes were evaluated under ambient conditions, and so the results reflected effects due to absorbed water.

A summary of observations for images obtained using polarized light microscopy is given in Table XII. Crystallites were observed for both C1BI:PBIO and DS:PBIO compositions. For DS:C1BI:PBIO compositions, crystallites were observed for :

- 3:1:1 compositions with added ZrO_2 or AF-100 silica. For SG-300 silica gel, the membrane was too opaque for observation of transmitted light.
- 2:2:1 compositions with added ZrO_2, AF-100 silica, or SG-300 silica gel but not for 2:2:1 without inorganic additive.
- 1:3:1 with added SG-300 silica gel but not for other metal oxides or for 1:3:1 membrane itself.

Polarized light images for PBIO with single acids and silica are shown in Fig. 43.
For C1BI:PBIO = 3:1, many small crystallites were observed. In comparison, crystallinity was much less pronounced for C1BI:PBIO = 3:1 with added SG-300 silica gel. For DS:PBIO = 4:1, the polarized light images revealed an array of close packed cones. Addition of AF-100 silica to DS:PBIO = 4:1 eliminated this conical surface texture and resulted in formation of very large crystals (larger than field of view). For PBIO with a mixture of DS and C1BI acids/silica, polarized light images in Fig. 44 showed a progression from pronounced crystallinity for DS:C1BI:PBIO = 3:1:1 + AF-100 silica to no crystallinity for 1:3:1 membranes.

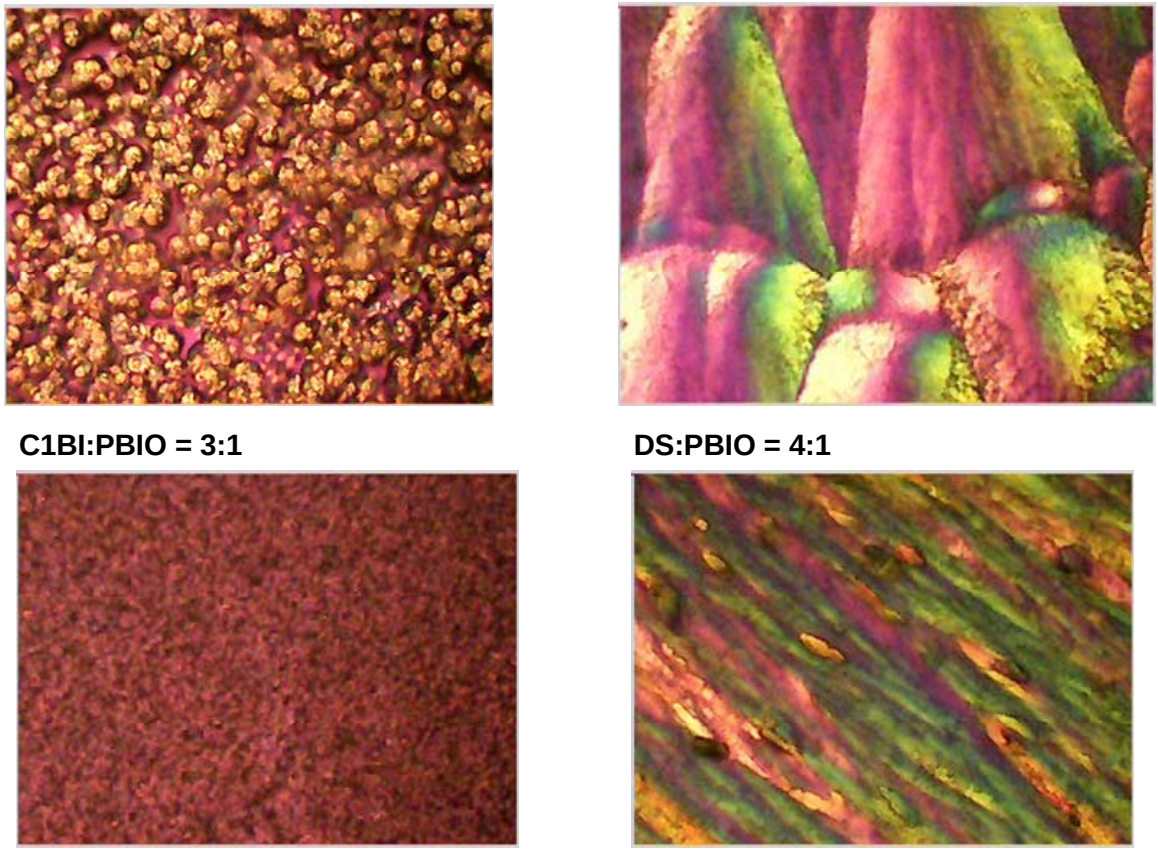

Fig. 43. Polarized light images at 10X for PBIO membranes having a single fluorinated acid and/or added silica.

DS:C1BI:PBIO = 3:1:1 + AF-100

DS:C1BI:PBIO = 2:1:1 + AF-100

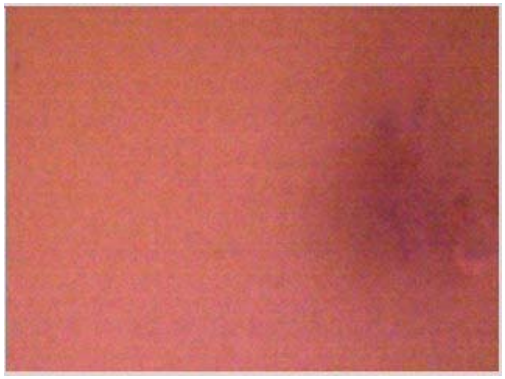

DS:C1BI:PBIO = 1:3:1 + AF-100

Fig. 44. Polarized light images at 10X for DS:C1BI:PBIO membranes with added amorphous fumed silica.

Table XII. Summary of Characterization of PBIO Membranes using Polarized Light.

Acid(s)	Mole Ratio to PBIO	MOx	Crystallinity
none	na	none	No
C1BI	3:1	none	Yes. Many small crystal and some regions with no crystals large enough to be seen.
C1BI	3:1	none	Yes. Large crystallites
DS	4:1	none	Yes
DS:C1BI	1:3:1	none	No
DS:C1BI	2:2:1	none	No
DS	4:1	ZrO_2	Large and small crystals
DS:C1BI	1:3:1	ZrO_2	No
DS:C1BI	2:2:1	ZrO_2	Some large crystals and some regions with random small spots of different color
DS:C1BI	3:1:1	ZrO_2	Some small crystals and regions with random small spots of different color
DS	4:1	AF-100	Yes. Very large crystals
C4BI	4:1	AF-100	?
DS:C1BI	1:3:1	AF-100	No
DS:C1BI	2:2:1	AF-100	Yes. Some regions with many small crystals and some regions with none.
DS:C1BI	3:1:1	AF-100	Yes. Large crystals
C1BI	3:1	SG-300	No.
C1BI	3:1	SG-300	No.
DS:C1BI	1:3:1	SG-300	Yes. Large crystallites and many small colored spots.
DS:C1BI	2:2:1	SG-300	Yes. Large crystals
DS:C1BI	3:1:1	SG-300	Sample too opaque for room light source

3.3.2.4. Membrane Characterization by TGA

Results for TGA analysis for the first major mass loss not related to loosely bound water are given in **Table** XIII. While more TGA results were obtained that could be the subject of much more extensive discussion, the results in **Table** XIII are sufficient to determine the limiting thermal stability of these materials relative to their intended use temperature.

While PBIO was somewhat less stable than PBI as indicated by a mass loss of 12 % at 288-292°C as compared to 4 % at 418-491°C, the thermal stability for PBIO as indicated by TGA was still very good. Thermal stability for the three acids was also good with clean loss of most of their mass at 300- 320°C. Thermal stability of polymer-acid membranes, however, was of more interest. For the most part, there was only minor loss of mass at temperatures similar to those for which the acids themselves disappeared. For these cases, the stability of the polymer-acid membrane was actually better than for the acid itself and not that much poorer than for PBIO or PBI. While a mixed comparison, mass losses for DS:PBIO =4:1 and for DS:C1BI:PBIO = 2:2:1 was significantly higher than for C1BI:PBI = 4:1. Also curious was that the 10 % mass loss for DS:PBIO = 1:1 began at a lower temperature than for the other polymer-acid membranes. In any case, these strong fluorinated acids did not appear to significantly degrade the thermal stability of the polymer.

Table XIII. TGA results for first mass loss not associated with loss of loosely bound water for polymers and polymer-acid membranes.

Material	Range (C),	% Mass Loss
PBI	418 – 491	4
PBIO	288 – 392	12
DS	305 - 307	89
C1BI	299 - 306	89
C4BI	313 - 322	93
C1BI:PBI = 1:1	266 - 313	10
C1BI:PBI = 4:1	274 - 306	12
DS:PBIO = 1:1	196 - 278	10
DS:PBIO = 4:1	302 - 316	57
DS:C1BI:PBIO = 2:2:1	257 - 274	67

3.3.2.5. Membrane Characterization by DMA

Results for DMA tan delta maxima for PBIO and PBIO with added acids are given in Table XIV. The relative magnitude of the tan delta maxima were indicated qualitatively as either strong (s) or weak (w) in Table VIII. The elastic modulus (E') for PBIO and for PBIO with added acids was about 10^{10} dyne/cm^2. For PBIO, there was a shallow minimum for E' at about 110°C in the first heat, but E' remained about 10^{10} dyne/cm^2 for the first heat. For the second heat, however, there was a rapid decrease in E' to a minimum of 10^6 dyne/cm^2 at about 100°C followed by an increase to 10^9 dyne/cm^2 at 160°C. During three additional heats, the E' curves moved somewhat closer to that for the first heat. Similar trends were observed for the loss modulus (E"). There were similar differences between first and second heats for PBIO with added acids. For addition of DS to PBIO, the number of tan delta maxima seen in the first heat increased for each added equivalent of acid. For the second heat, there was only one tan delta maximum except for the DS:PBIO = 3:1 case. Differences between first and second heats were most likely due to removal of water during the first heat, which showed that absorbed water had significant effects on E' and E". For the DS:C1BI:PBIO = 2:2:1 membrane, however, there was only one T_g for the first heat and for the second heat, which indicated that its mechanical properties were less affected by the loss of water than for the other membrane types. While a minimum was still observed for E' and E" in the first heat at 155°C, the results for the second heat were uncomplicated and were similar to what would be seen for a normal viscoelastic polymer.

Table XIV. DMA Tan Delta Maxima for DS:PBIO and DS:C1BI:PBIO Membranes.

Membrane	**DMA Tan Delta Maxima**	
	1st Heat °C	**2nd Heat °C**
PBIO	~ 110 (weak)	100 (strong)
DS:PBIO = 1:1	100 (w), 185 (s)	125
DS:PBIO = 3:1	60 (w), 110 (w), 175 (s)	110 (w), 185 (s)
DS:PBIO = 4:1	30, 65, 100, 125, 180 (s)	185
DS:C1BI :PBIO = 2:2:1	155	~ 130

DSC results also showed significant differences between first heats and subsequent heats if water were allowed to escape. The differences were ascribed in part to the loss of water, slowness of reordering and/or the need for absorbed water for reordering. The same could be said for the DMA results. Both DSC and DMA results suggested that the morphology and mechanical properties of DS:C1BI:PBIO = 2:2:1 membrane compositions would be more robust to temperature and humidity changes than compositions containing just a single fluorinated acid.

3.3.2.6. Resistance of Acids to Wash Out

Results of qualitative experiments to compare the resistance to wash out of perfluorinated acids from PBIO membranes as compared to phosphoric acid from PBI are given in Fig. 45. The results showed that the rate of wash out increased as equivalents of DS to PBIO increased. For DS:PBIO = 4:1, the rate of pH change was similar to PBI with 3 equivalents of phosphoric acid (600 mole % as described by Savinell[46]). For the DS:C1BI:PBIO = 2:2:1 membrane, however, the first part of the curve was similar to that for just 2 equivalents of DS and the subsequent rate was slower. While these membranes would be subject to the same issues for loss of acid due to liquid water as commercial PBI-phosphoric acid membranes, they would be at least as good or better in this respect.

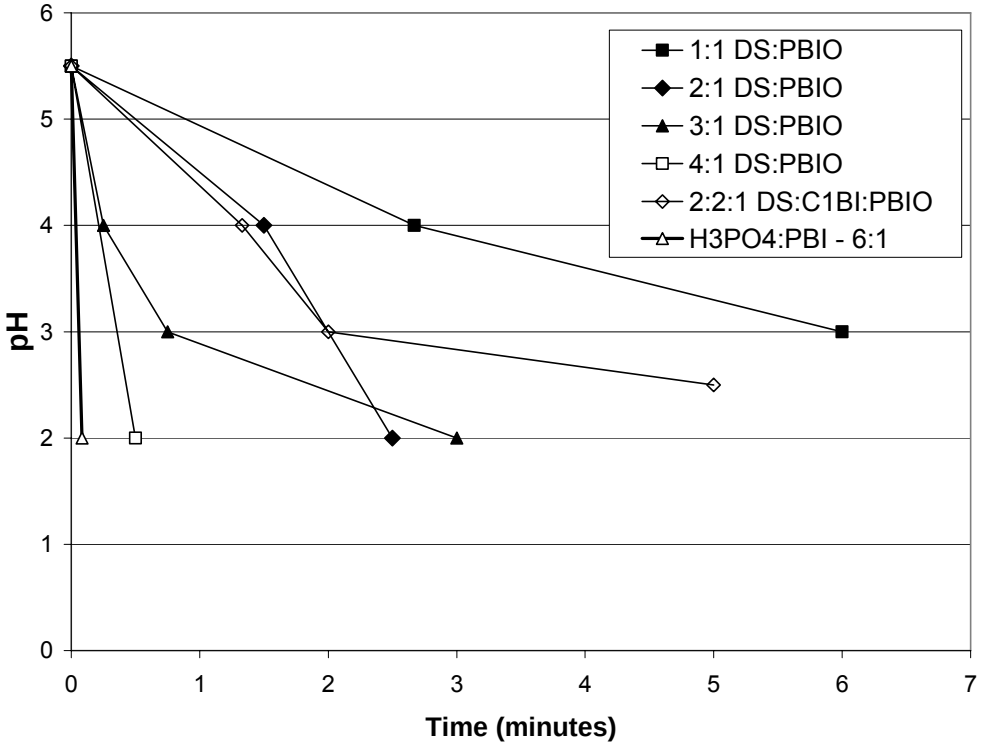

Fig. 45. pH versus time for PBI/phosphoric acid and for PBIO with perfluorinated acids for samples immersed in deionized water.

3.3.2.7. Membrane Morphology after Washing

Membranes made using PBI with added imide acids remained transparent after extraction of acid by soaking in water and drying. This was also the case for PBIO membranes having just a single type of acid, either DS or imide. PBIO membranes containing a mixture of imide and sulfonate acids, however, were opaque after extraction of acid following soaking in water and drying. Solvents such as isopropanol penetrated the resultant membranes readily and a porous structure was observed by scanning electron microscopy. These results showed that there was a fundamental difference in morphology for membranes that contained just a single type of acid and those that contained more than one type. While it is possible that the phase separated structure for the washed DS:C1BI:PBIO = 2:2:1 membrane did not develop until immersion in water, the good mechanical properties as indicated by hand and by DMA would be consistent with a phase separated morphology with PBIO as the continuous phase.

3.3.2.8. Exudation of Acid under Pressure

In initial attempts to evaluate conductivity of DS:PBIO = 4:1 membranes in fuel cells, the conductivity was found to be low, about 0.001 S/cm, and independent of temperature. Follow up compression experiments were done to determine whether shorting was the cause. In the course of these experiments, formation of strongly acidic crystalline material was indicated by etching along the edges of the aluminum press plates. Mass losses for DS:PBIO = 4:1 membrane were found to increase with press temperature for

compression at 4000 psi between two pieces of 3M microstructured catalyst transfer substrate:

- Negligible mass loss at room temperature;
- 30 % mass loss at 90°C; and
- 53 % mass loss at 132°C

While the melting point of the anhydrous DS was 174°C, exposure to water resulted in multiple lower melting points and no melting point in some DSC experiments. Mass loss did not occur for PBI-phosphoric acid membranes as a result of compression. Exudation occurred only for compositions having a mixture of sulfonated and imide acids or just sulfonated acid. Compositions having just imide acids flowed as a whole as for a thermoplastic polymer.

A method for measurement of mass loss was developed The percent mass that was lost through exudation was found to depend on many factors, including whether the membrane was evaluated after drying or after exposure to ambient humidity. In all cases, the membrane was dried before and after testing to compare masses under similar degrees of dryness. The ambient humidity for membrane conditioning was recorded but not controlled. This needs to be taken into account in comparing results since it did have an effect on the mass loss at least in some cases.

The exudation test results in Table XV for PBIO membranes having a single fluorinated acid/inorganic additives and in Table XVI for PBIO membranes having a mixture of fluorinated acids/inorganic additives. For reference purposes, the results were labeled as **EXU-xx**. Results were for 10 min. at 130°C and 1300 psi. The press pressure was calculated from the applied force and total sample area since the actual area of contact with the tips of the 3M MSCT film was not known. The variability ranged from as low as 5 % to as high as 30 % of the mean. Part of this variability was likely due to sample variability. About 10 % relative error was thought to be representative of the method. There was a good visual correlation between the area of the 3M MSCT film that was clarified by wetting with exudate and the percent mass loss results.

Percent mass loss – exudation - was found to depend on the following factors:

- For humidified membranes, exudation tended to be higher the higher the percent RH under which the membrane was humidified, as illustrated by EXU-1 and -2. There were some cases, however, for which the mass loss was similar regardless of percent RH, EXU- 27, or higher under lower percent RH for membrane humidification, as for EXU-49. Given the expectation that mass loss would be higher for humidified membranes, the majority of evaluations were done on humidified membranes.
- Mass loss increased linearly as a function of pressure (percent mass loss = 0.15*pressure (psi) + 6.96, R^2 = 0.95).
- The lower the ratio of acid to polymer, the lower the % exudation, as exemplified by EXU-2, -5, and -15 for DS:PBIO membranes
- Addition of metal oxides reduced mass loss considerably and there was an interaction between addition of metal oxides and ratio of acid to PBIO. The magnitude of reduction was a function of type of metal oxide (silica or zirconia), metal oxide surface area, and the percent metal oxide.
    - For DS = 3:1 compositions, mass loss for compositions with zirconia was lower than for those with silica. Mass loss with added zirconia was negligible within experimental error for 43 wt. % zirconia. The wt. %

zirconia was higher than for the silica additives but that was due to the much greater density for zirconia (~ 6 g/cc as compared to ~ 2 g/cc). For DS:C1BI:PBIO membranes, higher percent zirconia also reduced mass loss considerably more than for silica. For DS:C1BI:PBIO = 1.6:1.6:1 membranes, results with either silica or zirconia were about the same.
    - For Nalco 1042 silica, mass loss was about half that for the control until the percent added increased to 34 wt. %, for which mass loss was 3 %, as compared to 22 % for the control.
    - The effects of silica surface area were mixed: in some cases, mass loss for a given type was less for the higher surface silica (e.g., EXU-17 and-18); in other cases, it mass loss was greater was greater for higher surface area silica (e.g., EXU-3 and -4).
    - Mass loss was much lower for DS:PBIO = 2:1 with added AF-100 and for DS:CIBI:PBIO = 1.6:1.6:1.
- For addition of heteropolyacids (HPAs) to DS:C1BI:PBIO membranes, the type of HPA, the percent HPA, and combination with metal oxide additive affected mass loss.
    - For DS:C1BI:PBIO = 2:2:1 with about 30 % HPA, mass loss was 9 % for PWA as compared to 21 % for SiWA.
    - For DS:C1BI:PBIO = 2:2:1 with 11 wt. % AF-100, addition of 50 wt. % SiWA reduced mass loss to 3 % as compared to 21 % for 30 wt. % SiWA.
- Mass loss for DS:C4BI:PBIO membranes with inorganic additives was not significantly different than for DS:C1BI:PBIO membranes in most cases, though results between DS:C4BI:PBIO and DS:C1BI:PBIO were different for the former for :
    - EXU-60: 25 % ZrO_2 did not have much effect on mass loss compared to EXU-33
    - EXU-61: 10 % AF-100/30 % SiWA did reduce mass loss compared to EXU-36
- Mass loss was reduced by increasing the cooling quench rate upon removal from the drying oven by 1.) coating onto a thinner glass plate and 2.) placing the glass plate with dried membrane onto a cooled aluminum plate upon removal from the oven. For a DS:C1BI:PBIO = 2:2:1 membrane having 15 wt. % AF-100 silica, the mass losses for the following three quench conditions were:
    - Coating on thick glass plate (6 mm) placed on cork ring: 18.3 ± 0.1 % mass loss.
    - Coating on thin glass plate (2 mm) place on 6 mm thick aluminum plate that was at room temperature: 14.4 ± 0.1 mass loss.
    - Coating on thin glass plate (2 mm) place on 6 mm thick aluminum plate that was chilled to -9°C: 11.8 ± 0.3 mass loss.

Mass loss was ≤ 5 % for the following humidified membranes:

- DS:PBIO = 3:1 with the following inorganic additives:
    - 22 wt. % SG-300, 2 % mass loss
    - 34 % Nalco 1042, 3 % mass loss
    - 32 % ZrO_2, 4 % mass loss
    - 43 % ZrO_2, 0 % mass loss
- DS:PBIO = 2:1 + 28 wt. % AF-100, -1 % mass loss
- DS:C1BI:PBIO = 2:2:1 + 16 wt. % silica from Nalco 1042, 3 %
- DS:C1BI:PBIO = 1:3:1 + 14 wt. % SG-300, 3 % mass loss

- DS:C1BI:PBIO = 1.6:1.6:1 with following inorganic additives:
  - AF-100 (18 wt. %), 5 %
  - Silica from Nalco 1042 at 18 and at 25 wt. %, -1 and +2 mass loss, respectively
  - ZrO_2 (37 wt. %), 2 % mass loss
- DS:C4BI:PBIO = 1.6:1.6:1 + 10 wt. % AF-100 and 30 wt. % SiWA, 5 % mass loss.

Membrane Designation	Acid(s)	Ratio to PBIO	Inorganic Add., (wt.%)	Inorganic Add., (wt. %)	Percent Mass Transferred		
					Membrane Conditioning		
					Dry	Humidified	Ambient RH
EXU-1	DS	4:1	-	-	-	30	53-59
EXU-2	DS	4:1	-	-	15 (3, 5) *	22 (3, 1) *	20 -24
EXU-3	DS	4:1	AF-100 (19)	-	-	8	45-59
EXU-4	DS	4:1	AF-400 (19)	-	-	19	45-59
EXU-5	DS	3:1	-	-	-	22	53-59
EXU-6	DS	3:1	AF-100 (22)	-	-	12	36-53
EXU-7	DS	3:1	AF-400 (22)	-	-	22	36-53
EXU-8	DS	3:1	SG-300 (22)	-	-	2	50 - 59
EXU-9	DS	3:1	Nalco 1042 (15)	-	-	14	53 - 59
EXU-10	DS	3:1	Nalco 1042 (22)	-	-	10	53 - 59
EXU-11	DS	3:1	Nalco 1042 (28)	-	-	11	53 - 59
EXU-12	DS	3:1	Nalco 1042 (34)	-	-	3	53 - 59
EXU-13	DS	3:1	ZrO_2 (32)	-	-	4	55 - 60
EXU-14	DS	3:1	ZrO_2 (43)	-	-	0	55 - 60
EXU-15	DS	2:1	-	-	-	11	50 - 59
EXU-16	DS	2:1	AF-100 (28)	-	-	-1	55-60
EXU-17	C1BI	3:1	SG-300 (17)	-	2	24	20 - 24
EXU-18	C1BI	3:1	SG-600 (17)	-	7	6	20 - 24
EXU-19	C4BI	3:1	-	SiWA (50)	-	1	24 - 27

Table XV. Exudation under Pressure for PBIO with Single Added Acid and Additives.

Table XVI. Exudation under Pressure for PBIO with Mixed Acids and Additives.

Membrane Designation	Acid(s)	Ratio to PBIO	Inorganic Additive (%)	Inorganic Additive (%)	Percent Mass Transferred		
					Membrane Conditioning		
					Dry	Humidified	Ambient RH
EXU-20	DS:C1BI	3:1:1	-	-	11	30	20 - 24
EXU-21	DS:C1BI	3:1:1	AF-100 (17)	-	4	12	20 -24
EXU-22	DS:C1BI	3:1:1	SG-300 (17)	-	1	7	20 - 24
EXU-23	DS:C1BI	3:1:1	SG-300 (17)	-	1	-	-
EXU-24	DS:C1BI	3:1:1	SG-600 (17)	-	5	14	20 - 24
EXU-25	DS:C1BI	3:1:1	ZrO_2 (36)	-	-	20	24 - 27
EXU-26	DS:C1BI	3:1:1	-	SiWA (50)	-	20	24 - 27
EXU-27	DS:C1BI	2:2:1	-	-	35	33	20 - 24
EXU-28	DS:C1BI	2:2:1	-	-	-	35	20 - 24
EXU-29	DS:C1BI	2:2:1	-	-	-	18	47 - 54
EXU-30	DS:C1BI	2:2:1	AF-100 (15)	-	-	16 (6, 3)	
EXU-31	DS:C1BI	2:2:1	SG-300 ((15)	-	13	-	20
EXU-32	DS:C1BI	2:2:1	ZrO_2 (33)	-	-	19	24 - 27
EXU-33	DS:C1BI	2:2:1	ZrO_2 (29)	-	-	19	47 - 54
EXU-34	DS:C1BI	2:2:1	ZrO_2 (44)	-	-	9	47 - 54
EXU-35	DS:C1BI	2:2:1	ZrO_2 (52)	-	-	7	47 - 54
EXU-36	DS:C1BI	2:2:1	AF-100 (11)	SiWA (30)	13	21	20 - 24
EXU-37	DS:C1BI	2:2:1	AF-100 (11)	SiWA (50)	-	3	24 - 27
EXU-38	DS:C1BI	2:2:1	AF-100 (10)	PWA (32)	-	9	45 - 59
EXU-39	DS:C1BI	2:2:1	Nalco 1042 (16)	-	-	3	55 - 60
EXU-40	DS:C1BI	2:2:1	ZrO_2 (23)	SiWA (30)	-	16	45 - 59
EXU-41	DS:C1BI	1.6:1.6:1	AF-100 (18)	-	-	5	55 - 60
EXU-42	DS:C1BI	1.6:1.6:1	Nalco 1042 (18)	-	-	-1	55 - 60
EXU-43	DS:C1BI	1.6:1.6:1	Nalco 1042 (25)	-	-	2	55 - 60
EXU-44	DS:C1BI	1.6:1.6:1	ZrO_2 (37)	-	-	2	55 - 60
EXU-45	DS:C1BI	1:3:1	-	-	27	35	20 - 24
EXU-46	DS:C1BI	1:3:1	AF-100 (14)	-	11	23	20 - 24
EXU-47	DS:C1BI	1:3:1	AF-100 (14)	-	15	18	20 - 24
EXU-48	DS:C1BI	1:3:1	AF-100 (14)	-	-	11 (4, 1)	24 - 33
EXU-49	DS:C1BI	1:3:1	SG-300 (14)	-	12	3	20 - 24
EXU-50	DS:C1BI	1:3:1	SG-300 (14)	-	-	10	54-59
EXU-51	DS:C1BI	1:3:1	SG-600 (14)	-	18	23	20 - 24
EXU-52	DS:C1BI	1:3:1	ZrO_2 (22)	-	11	13	20 - 24
EXU-53	DS:C1BI	1:3:1	-	SiWA (50)	-	14	24 - 27
EXU-54	DS:C4BI	2:2:1	AF-100 (13)	-	-	23	45 - 59
EXU-55	DS:C4BI	2:2:1	AF-400 (13)	-	-	17	45 - 49
EXU-56	DS:C4BI	2:2:1	AF-400 (18)	SiWA (30)	-	10	43 - 46
EXU-57	DS:C4BI	2:2:1	SG-300 (19)	SiWA (30)	-	7	43 - 46
EXU-58	DS:C4BI	2:2:1	SG-600 (9)	SiWA (30)	-	12	43 - 46
EXU-59	DS:C4BI	2:2:1	-	SiWA (50)	-	24	47 - 54
EXU-60	DS:C4BI	2:2:1	ZrO_2 (25)	-	-	23	45 - 49
EXU-61	DS:C4BI	1.6:1.6:1	AF-100 (10)	SiWA (30)	-	5	45 - 49

3.3.2.9. AC Conductivity

All results in this section were determined using a BekkTech conductivity cell. A summary of conductivity results is provided in Table XVII for membranes having a single fluorinated acid and in Table XVIII for membranes having a mixture of fluorinated acids. These summary tables provide conductivity results at 90°C and at 120°C (down temperature scan and up temperature scan). Full results for scans from 90° - 120°C are given in graphical form for selected results in the sections below. The inlet humidification was at an 80°C dew point at all temperatures, so the reason for decreased conductivity at increased temperatures was the lower humidification. The percent relative humidities (RH) for temperatures used were:

- 90°C, 67 % RH
- 100°C, 46 % RH
- 110°C, 33 % RH
- 120°C, 24 % RH

The contract objective was to achieve an area resistance of 100 mohm-cm^2. For a 1 mil thick membrane, this corresponded to a conductivity of 25 mS/cm.

3.3.2.10. AC Conductivity for PBI/Fluorinated Acid Membranes

In the course of attempts to evaluate conductivity for PBI/C1BI membranes, the need for reinforcement became apparent. With the exception of C1BI:PBI = 1:1, there was too much flow of the material away from the electrodes to measure conductivity using a BekkTech cell. Even with just two equivalents of C1BI, there was some flow away from the electrodes. Reinforcement using silica and glass cloth provided membranes that did not flow under the test conditions. Conductivity results were similar for three different types of silica: about 10 mS/cm at 90°C and about 3 – 4 mS/cm at 120°C for both the up and down temperature scan points.

3.3.2.11. Conductivity for PBIO Membranes with Single Fluorinated Acid

Conductivity results were obtained only for DS:PBIO membranes since C1BI:PBIO membranes were too weak to evaluate. While fabrication of C4BI:PBIO membranes was complicated by dewetting during drying, it was possible to prepare a 3:1 C4BI:PBIO membranes having reasonable physical properties through addition of inorganic additives and reinforcement. See Table XVII below for conductivity results for PBIO membranes with a single fluorinated acid.

For DS:PBIO membranes, conductivity generally decreased as the ratio of DS to PBIO decreased. Some results did not fit a smooth monotonic decrease with decrease of DS to PBIO. An explanation for this discrepancy might be variability in conductivity results due to the unusual surface topology and surface scale that was observed for membranes that had ≥ 4 equivalents of DS.

PBIO membranes having only C1BI were fairly weak, so most of the development focus was placed on membranes formed using DS or DS/imide mixtures. An interesting result for C1BI:PBIO = 4:1 and DS:PBIO = 4:1 membranes was that temperature dependence for conductivity was much less for the C1BI membrane than that for the DS membrane, as shown in Fig. 46 (90° - 120°C at constant 80°C inlet dew point).

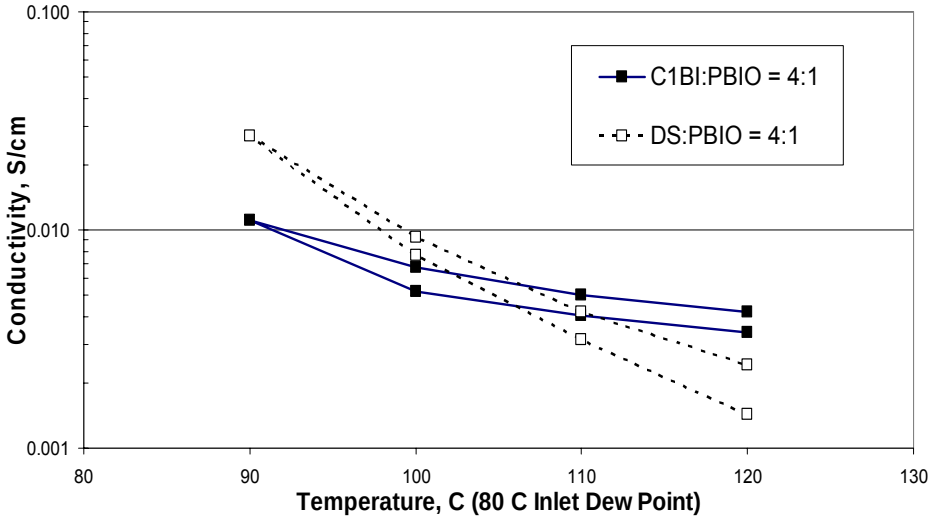

Fig. 46. Temperature/Humidity Dependence for C1-Bis-Imide and Disulfonate PBIO Membranes.

Conductivity results for DS:PBIO 3:1 and 2:1 membranes with and without silica are given in Fig. 47 (membranes C-6, C-7, C-9, and C-18). As expected, conductivity was greater for the 3:1 than for the 2:1 membrane. Addition of silica increased conductivity substantially for both 3:1 (22 % by weight silica) and 2:1 DS:PBIO (28 % by weight silica) ratios. For the DS:PBIO = 3:1 with silica membrane, the conductivity at 90°C was as high as typical values reported for perfluorosulfonic acid polymers such as Nafion™, about 100 mS/cm, though only about 10 mS/cm at 120°C. The thickness of this membrane (C-10) was about 2 mils (50 microns). The contract target was for an area resistance of 100 mohm-cm^2, which translated to a conductivity of 50 mS/cm at 2 mil thick. Thus, 10 S/cm at 120°C met only about 20 % of the contract objective (500 mohm-cm^2 versus target of 100 mohm-cm^2).

To decrease area resistance, the composition of C-10 was reinforced with a nonwoven, Crane HM090 per membrane C-11. The thickness of C-11 was only 1.1 mil, almost 50 % less than for C-10. As shown in Fig. 47, conductivity was only somewhat lower than for C-10. Membrane C-11 achieved 33 % of the contract target for conductivity at 120°C under dry conditions due to its lower thickness. At 90°C, the conductivity of C-11 membrane was 63 mS/cm at 90°C.

DS:PBIO =3:1 membranes were not very strong, so reducing thickness to reduce resistance was not practical without reinforcement. Reinforced membranes using both a nonwoven (Crane HM090) and ePTFE (Tetratex #1316) were prepared by filling from solution. Thicknesses were 1.1 and 1.9 mil, respectively. Conductivity results for both C-10 and C-11 were about 60 mS/cm at 90°C, as compared to 100 mS/cm without reinforcement, but conductivity at 120°C for the up temperature scan was about 9 mS/cm in both cases. For the non-woven reinforced membrane at 1.1 mil (C-11), 9.3 mS/cm was 34 % of the contract target.

There was greater hysteresis between the down temperature scan and the up temperature scan for membranes with silica, which suggested that the silica helped to retain more of the water absorbed during the down temperature scan during the subsequent up temperature scan. The difference in conductivity between the down temperature scan and the up temperature scan increased with temperature. This difference indicated that the membrane did not revert quickly to the lower humidified state and conductivity observed during the down temperature scan given that the membrane was conditioned for 90 min. at each temperature. Experiments were not done to determine the time required to return to the original conductivity for the down temperature scan.

DS:PBIO = 2:1 membranes were quite strong. Conductivity with added silica (membrane C-17) was reasonably good at 120°C, about 5.7 mS/cm for the up temperature scan for a sample having caliper that ranged from 1.4 to 1.9 mil. Given the strength of this membrane, it probably would have adequate strength without reinforcement at 1 mil thick.

Conductivity results for the two C4BI:PBIO membranes (C-18 and C-19) with inorganic additives were quite poor and significantly lower than for the C1BI:PBI membranes (C1-C3). The higher acid equivalent weight for the C4BI as compared to C1BI would be one explanation but not enough to account for the relative difference in conductivity.

Table XVII. AC Conductivity for PBI(O) with Single Acid and/or Inorganic Additives.

								Conductivity mS/cm		
Membrane Designation	Polymer	Acid(s)	Ratio to Polymer	Inorganic Add. (wt. %)	Inorganic Add. (wt. %)	Reinforcement Matrix	Thickness mils	mS/cm at 90 C	mS/cm at 120 C, 0.3 % RH	
								40 % RH	Dn Scan	Up Scan
C-1	PBI	C1BI	3:1	AF-100 (11)	none	Thonex PW106	10.0 - 10.6	9	3.3	3.3
C-2	PBI	C1BI	3:1	SG-300 (14)	none	Thonex PW106	4.1 - 5.0	9.6	3.7	4.1
C-3	PBI	C1BI	3:1	SG-600 (13)	none	Thonex PW106	4.7 - 5.2	11.6	3.7	4.3
C-4	PBIO	DS	4.5:1	none	none			48	2.8	5
C-5	PBIO	DS	4:1	none	none		2.4 - 2.5	30	1.4	2.4
C-6	PBIO	DS	3:1	none	none		1.8 - 2.4	43	2.3	5.7
C-7	PBIO	DS	2:1	none	none		0.8 - 1.1	6.2	0.5	0.6
C-8	PBIO	DS	4:1	AF-100 (19)	none		1.7 - 2.0	-	-	-
C-9	PBIO	DS	3:1	AF-100 (19)	none		1.9 - 2.1	100	3.2	10.4
C-10	PBIO	DS	3:1	AF-100 (28)	none	ePTFE	1.9	55	3	8.4
C-11	PBIO	DS	3:1	AF-100 (28)	none	Crane HM090	1.1	63	3.2	9.3
C-12	PBIO	DS	3:1	SG-300 (22)	none		1.6 - 1.8	17	0.5	3.6
C-13	PBIO	DS	3:1	SG-300 (22)	none	Thoenex PW06		10	3.4	4.2
C-14	PBIO	DS	3:1	Nalco 1042 (40)	none			36	2.1	7.8
C-15	PBIO	DS	3:1	ZrO2 (32)	none		1.5 - 1.9	38	1.6	2.9
C-16	PBIO	DS	3:1	ZrO2 (32)	none		1.5 - 1.9	38	1.6	2.9
C-17	PBIO	DS	2:1	AF-100 (28)	none		1.4 - 1.9	20.4	1.3	5.7
C-18	PBIO	C4BI	3:1	AF-100 (8)	SiWA (33)	Crane HM090	3.3 - 3.6	3.3	0.8	0.9
C-19	PBIO	C4BI	3:1	SG-600 (13)	none		2.5 - 2.7	2.3	1.1	1.4

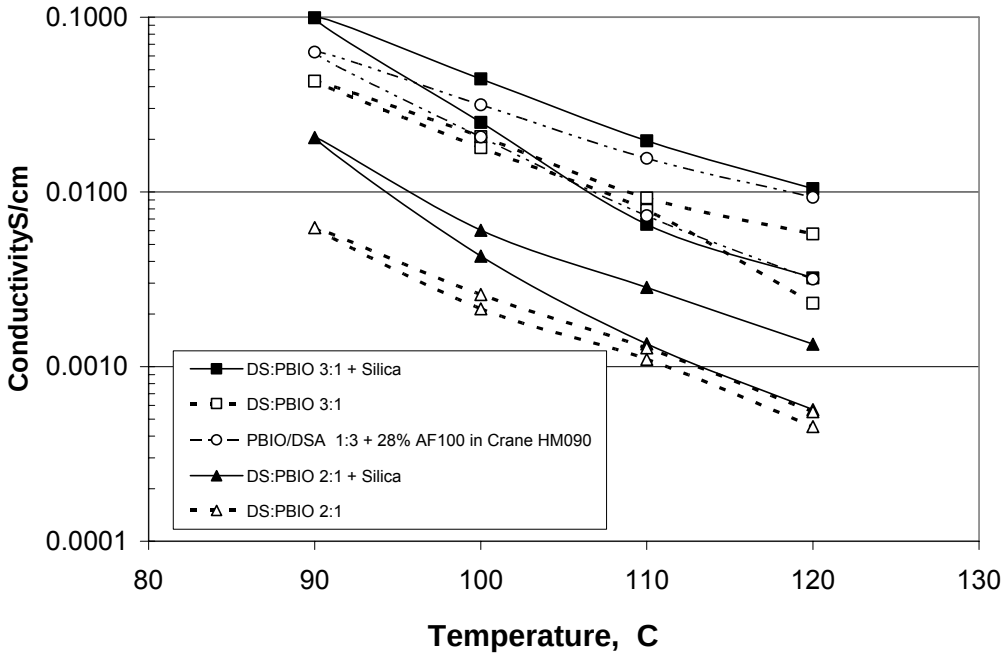

Fig. 47. Conductivity for DS:PBIO membranes with and without added silica at two ratios of acid to polymer for constant 80°C inlet dew point.

3.3.2.12. Conductivity for PBIO Membranes with Mixed Fluorinated Acids

Table XVII gives conductivity results for PBIO membranes that were made using mixtures of fluorinated acids and/or inorganic additives. Only a few of the results at 90°C and 120°C approached those for DS:PBIO membranes. An advantage for the mixed acid membranes, however, was that they had greater strength in general.

Conductivity results for membranes without inorganic additives were about the same for DS:C1BI:PBIO = 3:1:1, 2:2:1 or 1:3:1 membranes (C-20, C-21, and C-32). For 2:2:1 DS:C1BI:PBIO membranes with added metal oxides, conductivity with 15 wt. % AF-100 silica (membrane C-22) was significantly greater than for the base membrane with no added silica. For 29 wt. % ZrO_2 (membrane C-30), conductivity was significantly greater than for AF-100 at 90°C but significantly lower at 120°C. For 25 wt. % zirconium sulfophenyl phosphate (Zr-SPP) (membrane C-31), conductivity was about the same as for ZrO_2 at 90°C but greater at 120°C (closer to conductivity for added AF-100 at 120°C). For addition of silica and SiWA, addition of even 50 wt. % SiWA by itself (C-23) did not increase conductivity relative to the baseline 2:2:1 membrane (C-21). Addition of both AF-100 and SiWA (C-24, C-25) increased conductivity but not much more so than for just AF-100. Results for SG-300/SiWA (C-27) were about the same as for AF-100/SiWA (C-24, C-25), though results for SG-600/SiWA (C-28) were considerably lower. Conductivity for a 2:2:1 composition made using DS, C4BI, AF-100, SiWA and PBIO (membrane C-29) was not much better than for just a DS:C1BI:PBIO =2:2:1 membrane with no additives. The best conductivity results for this series were for a

mixture of AF-100 and PWA (membrane C-26): 60 mS/cm at 90°C and 6 mS/cm for the up scan at 120°C.

A comparison of conductivity results for PBI having 3 equivalents of phosphoric acid (600 mole percent), DS:C1BI:PBIO = 2:2:1 with 15 wt. % silica (C-22), and DS:C1BI:PBIO without added silica (C-21) is provided in Fig. 48. As expected, the conductivity for the PBI-phosphoric acid membrane was high and did not decrease very much as temperature increased with concomitant decrease in relative humidity (inlet dew point was held constant at 80°C). Conductivity for the 2:2:1 membrane with 16 wt. % silica was about the same as for the DS:PBIO = 2:1 membrane with 28 wt. % silica. Similarly, conductivity for the 2:2:1 membrane without added silica was similar to that for the 2:1 membrane without silica. While these results might have been coincidental, the similarity in conductivity between 2:2:1 and 2:1 membranes suggested that the DS was the primary source of proton conductivity. As noted above, the pH versus time curve for the 2:2:1 membrane was coincident with that for the 2:1 membrane for the first part of the curve. While conductivity for the DS:PBIO = 3:1 membrane with added silica was considerably greater, it was notably weaker. On the other hand, the 2:1 membranes and 2:2:1 membranes with or without silica were reasonably strong.

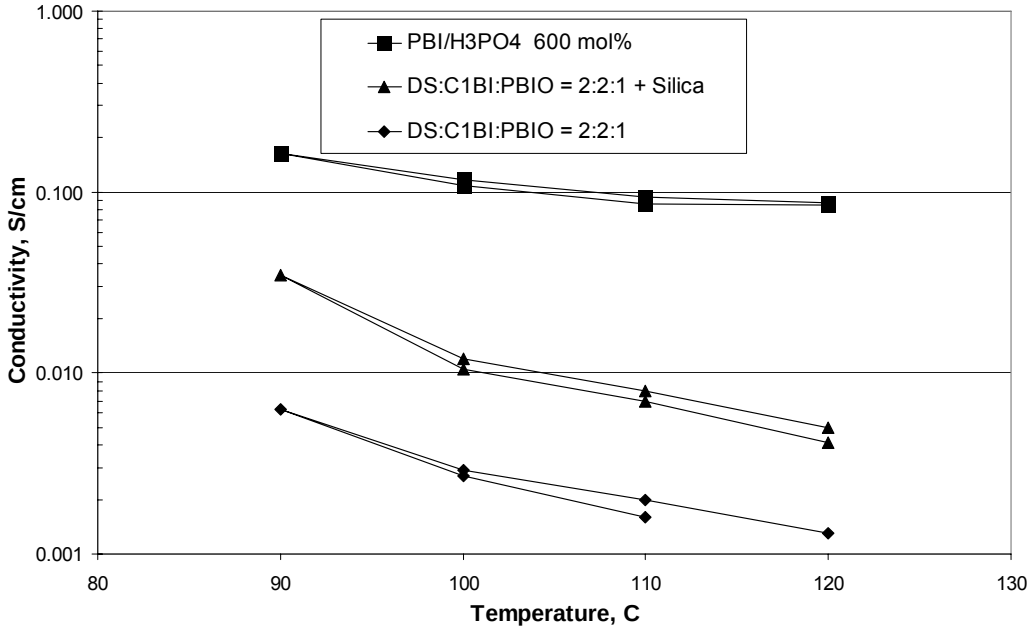

Fig. 48. Conductivity for DS:C1BI:PBIO = 2:2:1 membrane without added silica (Membrane C-21), with added AF-100 silica (Membrane C-22) and for PBI with 3 equivalents of phosphoric acid (600 mole percent).

For purposes of increasing membrane strength and reducing exudation, DS:C1BI:PBIO 1.6:1.6:1 and 1.5:1.5:1 compositions with inorganic additives were evaluated. As expected, conductivity for DS:C1BI:PBIO = 1.5:1.5:1 (membrane C-38) was significantly lower than for the analogous 2:2:1 membrane (C-21). See Table XVIII. Conductivity for DS:C1BI:PBIO = 1.5:1.5:1 with 16 wt. % added AF-100 silica (C-39) was about as high as for the analogous 2:2:1 membrane (C-22) but its strength was greater and acid

exudation under pressure were lower. Addition of more silica (C-42 and C-42) did not help to increase conductivity. Surprisingly, increasing the mole ratio of DS and C1BI slightly to 1.6:1.6:1 and adding AF-100 silica (C-34) increased conductivity considerably at 90°C and somewhat at 120°C. Membrane C-34 also had much lower mass loss under pressure than the analogous 2:2:1 membrane (C-22), 5 % versus 16 %. Mass loss under pressure was even lower, about -1 to +2 %, for Nalco 1042 silica (EXU-42 and-43), though conductivity was somewhat lower (C-35). Addition of other types of silica such as Nalco 1042 (C-35), ZrO_2 (C-36), or AF-100/SiWA (C-37) weren't as effective as just AF-100. See Fig. 49 for conductivity comparisons for 1.5:1.5:1 and 1:6:1.6:1 compositions with and without AF-100.

Table XVIII. Conductivity for PBIO with Mixed Fluorinated Acids and/or Inorganic Additives.

								Conductivity mS/cm		
Membrane Designation	Polymer	Acid(s)	Ratio to Polymer	Inorganic Add. (wt. %)	Inorganic Add. (wt. %)	Reinforcement Matrix	Thickness mils	mS/cm at 90 C	mS/cm at 120 C, 0.3 % RH	
								40 % RH	Dn Scan	Up Scan
C-20	PBIO	DS:C1BI	3:1:1	none	none		0.5 - 1.0	12	1.6	1.6
C-21	PBIO	DS:C1BI	2:2:1	none	none		2.0 - 2.3	7.5	0.7	1.4
C-22	PBIO	DS:C1BI	2:2:1	AF-100 (15)	none		1.8 - 2.0	30	4.2	5.3
C-23	PBIO	DS:C1BI	2:2:1	none	SiWA (50)		2.2 - 2.3	12	1.1	1.4
C-24	PBIO	DS:C1BI	2:2:1	AF-100 (8)	SiWA (50)		1.5 - 2.0	30	3	6
C-25	PBIO	DS:C1BI	2:2:1	AF-100 (11)	SiWA (30)		2.4 - 2.5	30	1.6	3
C-26	PBIO	DS:C1BI	2:2:1	AF-100 (10)	PWA (30)		2.2 - 2.7	60	2.5	6
C-27	PBIO	DS:C1BI	2:2:1	SG-300 (10)	SiWA (30)		2.0 - 2.7	30	3	4
C-28	PBIO	DS:C1BI	2:2:1	SG-600 (11)	SiWA (30)		1.4 - 1.7	12	1.4	2.3
C-29	PBIO	DS:C4BI	2:2:1	AF-100 (9)	SiWA (30)		2	16	1.7	2.3
C-30	PBIO	DS:C1BI	2:2:1	ZrO_2 (29)	none		1.2	40	1.4	2.9
C-31	PBIO	DS:C1BI	2:2:1	Zr-SPP (25)	none		1.6	39	3.4	4.8
C-32	PBIO	DS:C1BI	1:3:1		none		1.3 - 1.6	10	4.3	4.3
C-33	PBIO	DS:C1BI	1:3:1	ZrO_2 (20)	none		1.4 - 1.6	10	2.8	3.8
C-34	PBIO	DS:C1BI	1.6:1.6:1	AF-100 (18)	none		2.4	57	3.6	7.5
C-35	PBIO	DS:C1BI	1.6:1.6:1	Nalco 1042 (17)	none		0.9	40	2.1	5
C-36	PBIO	DS:C1BI	1.6:1.6:1	ZrO_2 (37)	none		1.1	11	1.4	2
C-37	PBIO	DS:C4BI	1.6:1.6:1	AF-100 (10)	SiWA (30)		1.7	44	1.3	1
C-38	PBIO	DS:C1BI	1.5:1.5:1	none	none		1.6	3.1	0.3	0.7
C-39	PBIO	DS:C1BI	1.5:1.5:1	AF-100 (16)	none		1.1	27	3.7	5.9
C-40	PBIO	DS:C1BI	1.5:1.5:1	AF-100 (19)	none		1.3	11	1.5	2.4
C-41	PBIO	DS:C1BI	1.5:1.5:1	AF-100 (19)	none	Crane HM090	2.9	6.9	1.3	1.6
C-42	PBIO	DS:C1BI	1.5:1.5:1	AF-100 (28)	none		1.4	19	1.9	3.2
C-43	PBIO	DS:C1BI	1.5:1.5:1	Nalco 1042 (22)	none		0.8	7.4	0.8	1.3

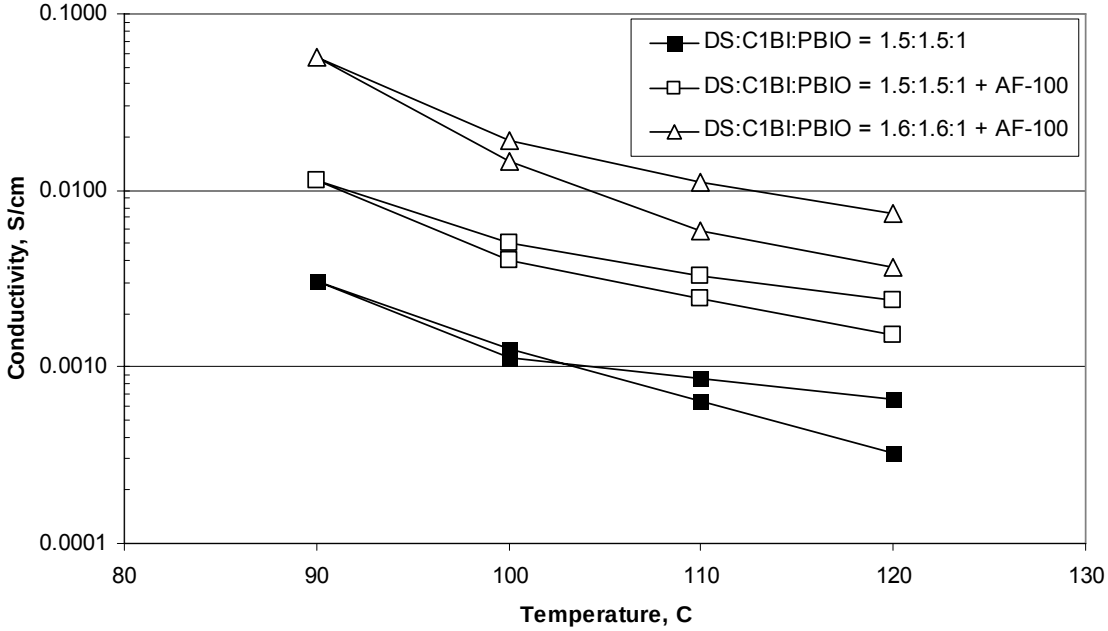

Fig. 49. Conductivity for DS:C1BI:PBIO Membrane with AF-100 Silica.

3.3.2.13. Fuel Cell Evaluations

Ambient pressure hydrogen/air fuel cell polarization results at 100°C and 110°C (constant 80°C dew point for inlet gases) are given in Fig. 49 for the following two types of membranes:

- DS:C1BI:PBIO = 2:2:1 with added silica (C-22 per Fig. 50, ~ 2 mil thick)
- PBI-phosphoric acid membrane (1.2 mil thick) that had 3 equivalents of strong acid (600 mole percent).

Conventional dispersed platinum electrodes having 0.4 mg/cm^2 of platinum were used. Given that AC conductivity was significantly lower for the PBIO membrane than for the PBI membrane (see Fig. 48), it was surprising that fuel cell performance was significantly better for the former than for the latter. Conductivity for the DS:C1BI:PBIO membrane was 5.3 mS/cm at 120°C (increasing temperature scan),which corresponded to an area resistance of 960 mohm-cm^2, as compared to a conductivity of about 90 mS/cm with corresponding area resistance of 34 mohm-cm^2 for the PBI-phosphoric acid membrane. Given that the area resistance for the DS:C1BI:PBIO membrane was 28 times greater than for the PBI-phosphoric acid membrane, it was amazing that fuel cell performance for the DS:C1BI:PBIO membrane was significantly better than for the PBI-phosphoric acid membrane. This mismatch in AC conductivity and fuel cell performance was most likely due to the well known poisoning of platinum due to phosphate adsorption as compared to minimal poisoning by fluorinated acids.

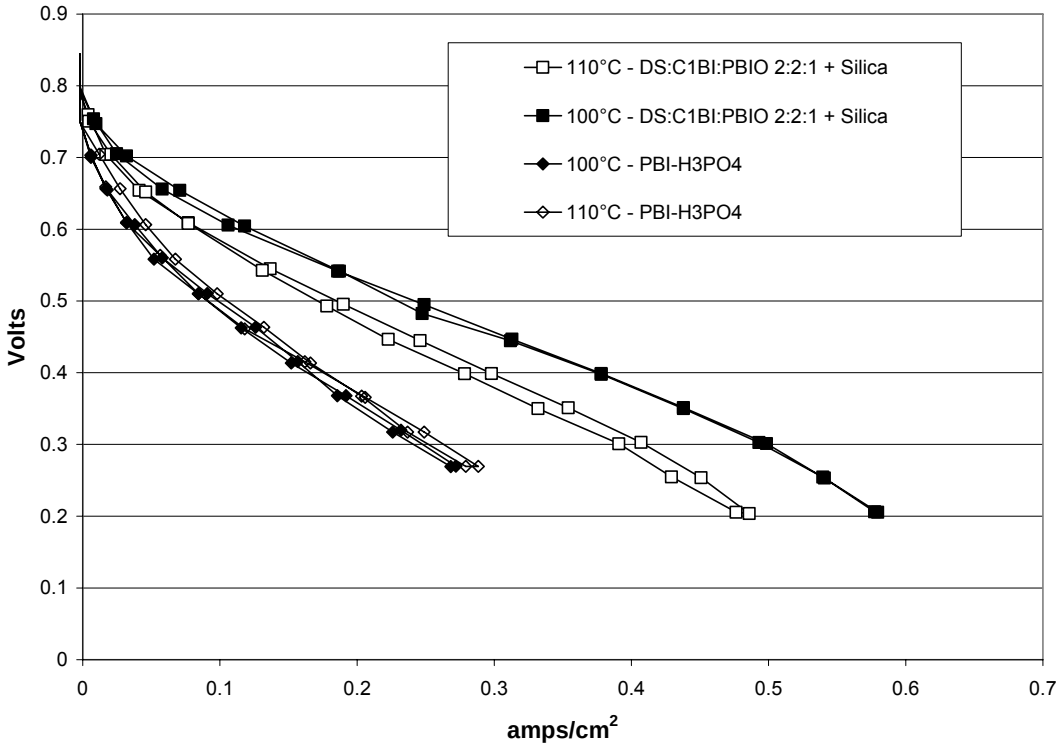

Fig. 50. Hydrogen/air fuel cell polarization for DS:C1BI:PBIO = 2:2:1 membrane as compared to PBI with 3 equivalents of phosphoric acid (600 mole percent).

A comparison of quasi IR-corrected performance for the membranes of Fig. 50 is given in Fig. 51 for results at 110°C (80°C inlet dew point). The IR correction calculation was based on membrane thickness and AC conductivity under the same conditions rather than on high frequency resistance measurements under total membrane electrode assembly polarization conditions. The quasi IR-corrected results in Fig. 51 do not take into account IR drop for the electrode or IR gain due to greater water back diffusion for thinner membranes. For the PBI-phosphoric acid membrane, the IR-corrected polarization curve was only slightly greater than the experimental polarization curve. The increase due to IR correction was small due to the thinness of the membrane and due to its high conductivity. For the DS:C1BI:PBIO = 2:2:1/silica membrane, the IR correction was much greater due to the greater membrane thickness and due to its much lower conductivity. The slope of the IR-corrected performance for this membrane was fairly shallow out to about 0.5 amps/cm^2, which indicated much room for improvement for this type of membrane through reduction of thickness or through increases in conductivity. The much higher performance of this MEA vs. the PBI-phosphoric acid containing MEA is presumably due to lower electrode over potentials, due in turn to the lower propensity of the fluoroalkyl sulfonic acid or imide groups to absorb to the catalyst surface compared to phosphoric acid.

The open circuit voltage (OCV) is one indicator of electrode over potential. For PFSA membranes, OCV is typically > 0.92 V. For the above DS:C1BI:PBIO = 2:2:1/silica membrane, the OCV was 0.79 V at 110°C and 0.76 V at 110°C. OCV for the PBI-phosphoric acid membrane was 0.70 at 100-110°C. The relative order of OCV was consistent with the known strong adsorption of phosphate anion on platinum as

compared to adsorption by fluorinated acids on platinum. The low OCV for the present PBIO membrane with relatively free fluorinated acids is due to greater anion adsorption for free fluorinated acid as compared to fluorinated acid that is bound to a polymer, as for Nafion™, since there is no restriction on adsorption of free acid other than platinum surface area, whereas adsorption by polymer bound acid is limited by the amount of acid per unit volume of ionomer that can adsorb.

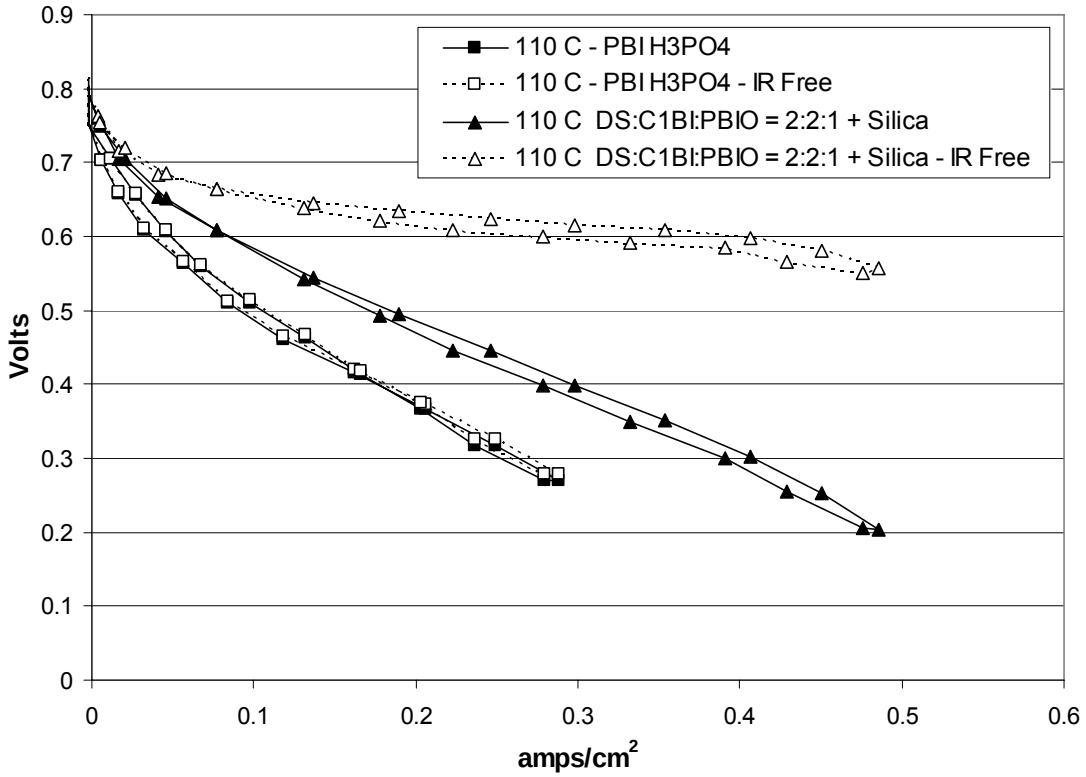

Fig. 51. IR Corrected Hydrogen/air fuel cell polarization for DS:C1BI:PBIO = 2:2:1 membrane as compared to PBI with 3 equivalents of phosphoric acid (600 mole percent) at 110°C with 80°C Inlet Dew Point.

3.3.3. Conclusions

Of three major approaches for development of membranes for hotter/drier proton exchange membrane fuel cell operation, membranes formed from polybenzimidazoles and bis-fluorinated acids was down selected as the best approach for retention of low molecular weight bis-fluorinated acids. The best AC conductivity (80°C inlet dew point humidification/ambient pressure) and major problems for each approach were:

- ePTFE/STS silica filled with EMI TFSI/HTFSI ionic liquid:
  - 10 mS/cm for a 1-mil thick membrane at 120°C, which corresponded to 254 mohm-cm^2 or about 40 % of the target for area resistance.
  - Interference of the ionic liquid with the electrode was thought to have been the cause for problems with obtaining proton conductivity under fuel cell conditions.

- Polymeric/inorganic oxide matrix formed by solvent induced phase separation filled with C1-bis-imide acid:
  - 20 mS/cm for a 2.4 mil thick membrane at 120°C corresponding to 305 mohm-cm^2 or about 30 % of the target area resistance target.
  - Retention of acid under fuel cell conditions was the major problem. The reason was thought to be the failure to have achieved a strictly nanoporous matrix for retention of the acid through strong capillary forces.
- A DS:PBIO = 3:1 + 28 wt. % AF-100 silica composition that was reinforced with a polymeric nonwoven provided 9.3 mS/cm for a 1.1 mil thick membrane at 120°C, which corresponded to 300 mohm-cm^2 or about 30 % of the target for area resistance. While the emphasis for Task 2 membrane development was performance at 120°C, this reinforced membrane had a conductivity of about 30 mS/cm at 100°C, which corresponded to 93 mohm-cm^2 as compared to target of 100 mohm-cm^2.
- A DS:C1BI:PBIO = 2:2:1 + AF-100 silica membrane provided 5.3 mS/cm at 120°C for a 2 mil thick membrane (corresponding area resistance of 960 mohm-cm^2), as compared to a conductivity of about 90 mS/cm for the 1.2 mil thick PBI-phosphoric acid membrane (corresponding to an area resistance of 34 mohm-cm^2). Given that the area resistance for the DS:C1BI:PBIO membrane was 28 times greater than for the PBI-phosphoric acid membrane, it was amazing that fuel cell performance for the DS:C1BI:PBIO membrane was significantly greater than for the PBI-phosphoric acid membrane. IR-corrected polarization for the 1.2 mil PBI-phosphoric acid membrane was only slightly better than for the observed polarization, which showed that catalyst poisoning rather than conductivity or thickness was responsible for the large polarization losses. For the 2 mil DS:C1BI:PBIO membrane, however, IR-corrected polarization was substantially better than the observed polarization, which showed that conductivity and, to a lesser extent, thickness, were responsible for polarization losses in the mass transport region. A DS:C1BI:PBIO = 1.6:1.6:1 + AF-100 silica composition (membrane C-34 per Table XVII) was found to provide an optimal balance of conductivity, mechanical strength, and minimization of exudation. Conductivity on the up temperature scan for 120°C was 7.5 mS/cm, which corresponded to an area resistance of 800 mohm-cm^2 at 2.4 mil thick. Reinforcement would allow reduction membrane thickness to about 1 mil, which would further reduce area resistance.

While similar or better conductivity at 120°C was achieved for the first two approaches, the swollen polymer approach was the only approach for which it was possible to obtain fuel cell performance. In addition, it was possible to obtain membranes having good mechanical properties with or without reinforcement depending upon the compositions.

A DS:PBIO = 2:1 membrane (C17 in Table XIV) was quite strong and had conductivity that was as good as a DS:C1BI:PBIO =2:2:1 membrane with added silica (C22 in Table XVII) despite the fact that the former had only two equivalents of acid as compared to 4 equivalents of acid for the latter. Proton conduction was also similar for DS:PBIO = 2:1 and for DS:C1BI:PBIO = 2:2:1 membranes without silica, though conduction was lower of course in both cases without silica than with silica. These results suggested that the DS acid was responsible for most of the proton conduction for the 2:2:1 membrane,

perhaps related to its phase separated structure, as discussed below. This point was also supported by rates of wash out of acid that were also similar for DS:PBIO = 2:1 and DS:C1BI:PBIO = 2:2:1 membranes. Resistance to wash out of acid upon immersion into liquid water was shown to be at least as good as or better than for PBI-phosphoric acid membrane.

In general, metal oxides improved mechanical properties and conductivity. Differences between first heats and subsequent heats for DSC and DMA results were thought to be due in part to loss of water during the first heat, slowness of reordering, and/or the need for absorbed water for reordering. One set of DSC results showed that re-absorption of water restored the membrane to its original morphology, which showed that loss of water and lack of re-humidification before the second heat was responsible for the differences seen between the first and second heats. In DMA experiments, multiple transitions were observed in the first heat for DS:PBIO compositions, though only a single transition for a DS:C1BI:PBIO =2:2:1 membrane for both first and second heats. These results showed that mechanical properties for DS:PBIO compositions were strongly affected by absorbed water and that the mechanical properties of the DS:C1BI:PBIO = 2:2:1 membrane were much less affected by water. DMA results for the DS:C1BI:PBIO = 2:2:1 composition were most like those of a typical viscoelastic material and were least affected by absorbed water, whereas those for DS:PBIO compositions were quite unusual.

DSC results showed that PBI was plasticized by perfluorinated bis-imide acids (C1BI or C4BI). Attempts to solution blend PBI and DS led to precipitation. PBIO could be solution blended with either DS or the imide acids without precipitation. Membranes formed from PBIO and either DS or imide acids were semicrystalline. For both DS:PBIO and DS:C1BI:PBIO membranes, crystal size was greater than could be determined by XRD, > 150 nm. For both types of membranes, addition of silica decreased crystallite size to about 60 nm from XRD results. The crystallinity index from XRD, however, was unchanged by addition of silica to DS:PBIO = 4:1, though did decrease it from 0.3 to 0.2 in the case of DS:C1BI:PBIO = 2:2:1 membrane. Addition of silica significantly decreased the onset of melting, peak temperature, and transition energy (J/g) for the melting endotherm for both DS:PBIO = 3:1 and DS:C1BI:PBIO = 2:2:1 membranes. This indicated that the addition of silica resulted in a more disordered structure/less perfect packing. As noted above, XRD showed that silica also reduced crystal size but did not decrease crystallinity index except for the DS:C1BI:PBIO = 2:2:1 case. While speculative, these results suggest that the significant increases in conductivity due to addition of silica were due to creation of a more disordered structure. This more disordered structure may have been related to water absorbed on silica and the interaction of this silica bound water with the fluorinated acids. For other types of membranes, an increase in amorphous character is related to an increase in proton conduction since proton conduction typically occurs only in the amorphous phase.

TGA analysis showed that the acids and membranes formed with them were stable for the most part up to about 300°C.

Polarized light microscopy showed presence of very large crystals (> 1000 nm detection limit) for C1BI:PBIO, DS:PBIO, and DS:C1BI:PBIO. For DS:C1BI:PBIO, crystallinity decreased in going from 3:1:1 to 2:2:1 to 1:3:1. No crystallinity was evident for the 1:3:1 compositions by polarized light microscopy.

For PBIO, a mixture of imide and sulfonate acids was shown to result in a phase separated morphology. A phase separated morphology was consistent with the reasonable tensile strength of DS:C1BI:PBIO membranes. These membranes did not require reinforcement. DS:PBIO membranes, on the other hand, were relatively weak at ≥ 3:1 and did benefit from reinforcement. DS:PBIO membranes were transparent after washing with water, whereas DS:C1BI:PBIO compositions were white and porous, which was consistent with a phase separated morphology for the latter before washing, though transparency for the former after washing did not necessarily imply lack of phase separation before washing.

A challenge for PBIO compositions containing DS was exudation of acid under pressure. Exudation was shown to be a function of pressure, percent relative humidity under which the membrane was humidified, ratio of acid:PBIO, type and percent of metal oxide, type and percent of HPA, combinations of HPAs with metal oxides, and quench rate upon removal from drying oven. Compositions were identified for which mass loss at after 10 min. at 130°C and 1250 psi between 3M microstructured film was negligible within experimental measurement error as well as visual indication. The pressure used in these exudation screening experiments was much higher than for fuel cell compression especially since it was based on total sample area rather than contact area with the microstructured film.

Substantial work on reinforcement approaches was done in conjunction with development of the above three type of new proton conducting membrane development for operation under hotter and drier conditions. Addition of ionic liquid electrolytes strongly plasticized PFSA ionomers, which necessitated reinforcement. Reinforcement was also needed for PFSA ionomers themselves due to excessive softening at higher temperatures. Reinforcement with ePTFE was problematic. The problem was shown to be due to premature gellation of the ionomer by the ionic liquid during drying. Glass cloths were found to be useful for reinforcement, especially for compositions having larger inorganic particulates, though purer grades of glass would be needed. A nonwoven made from a liquid crystalline polymer was also shown to be useful. Both glass cloth and nonwovens could be filled either by solution coating or by pressing dried membrane compositions that were thermoplastic. Given general problems with filling ePTFE, it was surprising that good filling appeared to have been obtained for filling ePTFE with a solution of DS, PBIO, and amorphous fumed silica composition using a 50/50 mixture of isopropyl alcohol and NMP to pre-fill the ePTFE. AC conductivity results were about the same for this composition filled into either a nonwoven or into ePTFE (membranes C-10 and C-11 per Table XIV).

A novel porous matrix was formed from polyether sulfone and sulfated zirconium oxide for use either for reinforcement of electrolytes or for serving as a reservoir for electrolytes. Conductivity of 20 mS/cm at 80°C/20 % RH was achieved. A novel method was found for elimination of skins on the air surface per solution casting and phase inversion. This improved the ability to fill with ionomer greatly. Removal of the air surface skin, however, reduced matrix strength considerably. Compression after filling was found to remove macro voids near the air surface, though this did not improve the conductivity. The large sulfated-zirconium oxide particles were found to reside in the pores of the matrix, which was thought to impede filling with PFSA ionomer solution. Better results might have been obtained using smaller size particulate.

3.3.4. Experimental

Unless otherwise noted, all percentages and ratios were by mass.

Glossary of Materials

Abbreviation	Description
Inorganic Additives	
AF-100	Amorphous fumed silica having 100 m^2/g surface area available from Alfa Aesar, catalog #42737, Ward Hill, MA
AF-400	Amorphous fumed silica having 400 m^2/g surface area available under the trade designation "CAB-O-SIL EH-5" from Cabot Corp., Tuscola, IL
SG-300	Silica gel having 300 m^2/g surface area available from Alfa Aesar, catalog #41502, Ward Hill, MA
SG-600	Silica gel having 600 m^2/g surface area available from Alfa Aesar, catalog #42729, Ward Hill, MA
SiWA	Silicotungstic acid available from Alfa Inorganics, catalog #87372, Beverly, MA
PWA	Phosphotungstic acid available from Matheson Coleman & Bell, catalog # CB 582 PX1055, Cincinnati, OH
Nalco 1042	Silica sol available under the trade designation "NALCO 1042" from Nalco, Naperville, IL (acid-stabilized and nominally free of anions)
ZrO_2 sol	A zirconia sol having 20 nm particles that were stabilized by acetic acid was prepared by 3M per filed patent application
Polymers	
ABPBI	Poly(2,5-benzimidazole) available under the trade designation **ABPBI-Powder** from FuMA-Tech GmbH, Postfach 13 27 .D66363 St. Ingbert, Germany.
Nafion™	"Nafion™" is a registered trademark from Dupont and refers to PFSA ionomers. Nafion™ coating solutions such as SE20042, which contained 1000 EW sulfonic acid ionomer.
PBI	Poly[2,2'-(m-phenylene)-5,5'-bibenzimidazole] powder available under the trade designation Celazole™ from Celanese Corp., Dallas, TX.
PBIO	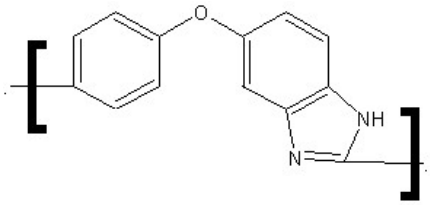 available under the trade designation **PBIO-Powder** from FuMA-Tech GmbH, Postfach 13 27 .D66363 St. Ingbert, Germany.
PES	Poly(p-Phenylene ether-sulfone) was purchased from Scientific Polymer Products (melt flow index of 3.9 g/10 min. at 320°C).
PVDF	Poly(vinylidene difluoride)
PVDF-HFP	Poly(vinylidene difluoride -hexafluoropropylene) copolymer

	(PVDF-HFP). Two grades were evaluated, Kynar Flex 2750-01 and Kynar Flex 2801-01 (battery grade).
PFSA	Perfluorinated sulfonic acid ionomer
SE20042	Nafion™ coating solution having 1000 EW PFSA ionomer.
Acids	
DS	$HO_3S(CF2)_4SO_3H$, from 3M Company
C1BI	$CF_3SO_2NHSO_2(CF_2)_4SO_2NHSO_2CF_3$, from 3M Company
C4BI	$C_4F_9SO_2NHSO_2(CF_2)_4SO_2NHSO_2C_4F_9$, 3M Company
Solvents	
NMP	1-methyl-2-pyrrolidinone
DMAc	dimethylacetamide
MeOH	methanol
MSA	methane sulfonic acid
Reinforcement Matrices	
Thonex PW106	A plain weave glass cloth made from E-glass available under the trade designation **PW106** from Thonex Corp, Cross River, NY (1.5 mil thick, 0.73 oz/sq. yard, 24 x 23 threads/cm).
Crane HM090	A nonwoven made from a 100 % liquid crystalline polymer available under the trade designation **HM090** from Crane & Co., Inc (2 mil thick, 8.9 g/square meter).
PVDF TIPS	Porous membrane made internally by 3M by TIPS process using PVDF polymer.
PTFE	Several Tetratex® grades of ePTFE were obtained from the Donaldson Company (Ivyland, PA). A summary of grades and properties is given in Table XIX.
Miscellaneous	
TEOS	tetraethylorthosilicate
TMOS	tetramethylorthosilicate
Pluronic 123	poly(ethylene oxide-propylene oxide-ethylene oxide) tri-block copolymer surfactant from BASF having average MW = 5750
CTAB	cetyltrimethylammonium bromide (Aldrich)

Table XIX. Properties for ePTFE Grades from Tetratec.

Grade	BW (g/m^2)	Caliper (mils)	Density g/cc	% Porosity	Gurley - sec./50 cc			
					5 oz. 1" dia.	5 oz. 0.1" dia.	20 oz. 1" dia.	20 oz. 0.1" dia.
T-1311	2.3	0.2	0.46	80	<1	2	-	
T-1316	7.4	0.4 - 0.5	0.65	72	20	-	-	13
T-3101	19	1.5	0.49	79	40	-	-	12
T-3107	14	1.0 - 1.2	0.46	80	28	-	< 1	5.3
T-3109	3.5	0.2 - 0.3	0.57	75	<< 1	2	-	

Preparation of Polymer Solutions

Before dissolving, all polymers except PVDF-HFP were dried at 138°C in a vacuum oven overnight at 5 – 10 mm Hg using a nitrogen purge stream.

For PBI, the higher MW fraction was obtained by refluxing a mixture of about 20 wt. % PBI in dry DMAc (< 0.005 wt. % water) for at least 5 hr. followed by filtration to remove the undissolved higher MW polymer. The insoluble fraction was about 25 % of the total initial mass. The high MW fraction had an inherent viscosity of 1.35 dL/g in 96 % sulfuric acid at 30°C as compared to 1.08 dL/g for PBI before fractionation using an Ubbelohde viscometer (type 1B, obtained through VWR Scientific Products, Minneapolis, MN). This insoluble fraction was then dissolved at about 5 wt. % in DMAc at 260°C using a Parr pressure vessel (model 4563, 600 mL). Pressure generated was about 100 psi. This solution was then concentrated to about 10 wt. % using a rotary evaporator.

PBIO was dissolved in dry NMP (< 0.005 % water) at about 5 wt. % at 260°C using the Parr pressure vessel. Pressure generated was about 40 psi. Solutions were subsequently concentrated to about 10 wt. % using a rotary evaporator.

ABPBI was dissolved in dry methane sulfonic acid (> 99 % MSA) at about 4.5 wt. % at reflux. It was subsequently diluted with MSA to 3.00 wt. % ABPBI to lower the viscosity.

PES was dissolved in NMP by mixing with a mechanical stirrer under a dry nitrogen atmosphere.

PVDF-HFP was dissolved at RT at RT using either a bottle roller or a magnetic stirrer.

Filling Procedures for PVDF TIPS, ePTFE, and Nonwovens

The following procedure provided good filling for both PVDF TIPS[47] and ePTFE[48] using Nafion™ SE20092 solution:

1. A piece of porous polymer matrix was taped to a glass plate. The tape was used to hold one edge of the matrix in place and to serve as a hinge for laying the matrix into a layer of ionomer solution in subsequent steps. Excess 1-propanol was applied to the matrix using a hand-held knife coater.

2. A layer of Nafion™ solution was applied to the glass plate in the direction opposite to orientation of the matrix after filling with propanol. The knife gap was set to apply about half the amount of Nafion™ needed to fill the pores of the membrane.
3. The excess 1-propanol in step (1) was removed using a rubber roller.
4. The propanol-filled matrix was then laid into the layer of Nafion™ solution by holding the two loose corners of the membrane and the tape hinge to apply tension to control laying down of the matrix into the pool of Nafion™ solution.
5. A bead of Nafion™ solution was then applied to the surface of the matrix on the edge next to the tape hinge and spread using a knife coater gap that was calculated to apply sufficient Nafion™ after drying to provide about 0.25 mil excess dried Nafion™ on either side of the reinforcement matrix.
6. The coated matrix was left attached to the glass plate and placed in a 90°C circulating air oven to dry for 90°C. The membrane was annealed at a later time, typically at 160°C for 10 min. Note that annealing conditions were not optimized at the time that work in this section of the report was done.

For filling ePTFE with STS silica solutions, a similar procedure was used except that 2-propanol was used instead of 1-propanol for pre-filling the ePTFE and the coating was done on top of a piece of Teflon film that was taped to a glass plate to avoid bonding of the STS silica with the glass plate. After drying for 15 min. in the exhaust hood, the composite was dried at 80°C for 10 min. As indicated in the text, additional heating and/or boiling procedures were used to complete the membrane preparation before filling with electrolytes.

For filling grades of ePTFE that were thicker than 0.5 mil, STS silica coating solutions of about 10 wt. % solids after drying were needed to decrease the volume of the low viscosity solutions needed for filling the pore volume of the ePTFE. Also, use of 1 % CTAB in IPA in the pre-fill solution helped to improve filling. For filling ePTFE with PBIO formulations in NMP, a 50/50 mixture of IPA/NMP was used.

For filling polymeric nonwovens by coating, the same method as for filling ePTFE or PVDF TIPS with Nafion™ ionomer solution was used except that PBIO-based solutions were used in place of Nafion™ solutions. As for ePTFE, the nonwoven was taped to a glass plate to form a hinge and a pool of the filling solution was applied to the glass plate on the side of the hinge not covered by the nonwoven. Whereas ePTFE filling also required pre-filling with solvent(s), filling of nonwovens did not require this step. For thermoplastic compositions, glass cloth or nonwovens could also filled by pressing material that was obtained by coating and drying into these matrices.

Preparation of Matrices by SIPS Method using PES and S-ZrO2

The powder was milled into NMP using a vibratory mill and ceramic cylinders. The highest workable solution contained about 60 wt. % S-ZrO_2. PES pellets were added to the S-ZrO_2/NMP dispersion in a 3-neck round bottom flask that was equipped with mechanical stirrer and dry nitrogen purge and stirred under dry nitrogen to dissolve the PES. The resultant mixture was applied to a glass plate, spread using a hand-held knife coater, and immersed in deionized water to induce phase separation. The NMP was removed using three soak cycles in DI water. Soak cycles were typically 30 min. per cycle. The membrane typically separated from the glass plate and floated to the

surface. Membranes were dried slowly by sandwiching between two cotton TexWipes and drying under ambient conditions.

Application of an overcoat layer of NMP after coating the membrane precursor mixture and before immersion into water to induce phase separation was found to eliminate skin formation on the air surface.

Preparation of Inorganic-Filled PVDF-HFP SIPS Matrices

The following general procedure was found to provide reasonably strong membranes in some cases:

1. PVDF was dissolved first at RT in the better solvent (PC, NMP, or DMF) in a capped glass bottle using a magnetic stirrer.
1. The more volatile but poorer solvent for the PVDF was then mixed in using the magnetic stirrer.
2. The inorganic particulates were then dispersed into the mixture from (2) using a Silverson rotor-stator mixer.
3. The mixture from (3) was spread on a glass plate using a hand-held knife coater.
4. For cases for which MEK was used, the resultant coating was dried in an exhaust hood to the point at which the edges became white, about 30 min., and then immersed in water. The resultant membrane spontaneously released from the glass plate during soaking in water. Three 60-min. soaks in deionized water were done to extract the solvent.
5. The resultant membrane was then dried between cotton TexWipes that were wetted with deionized water.

Preparation of Matrices by SIPS Method using PES and Silica

Porous PES membrane containing 43 wt. % of 400 m^2/g of amorphous fumed silica was prepared by jar milling the silica into NMP followed by dissolving the PES polymer into this dispersion to provide PES/silica =57/43. The resultant viscosity was too high for coating, so it was diluted with DMF to provide NMP/DMF = 65/35. The solution was cast onto a glass plate, placed in a 100°C oven for 10 min. to remove some of the DMF, cooled at RT with a glass plate on top to limit intrusion of moisture during cooling, and then immersed into water to induce phase separation. The NMP was removed using three, 30 min. soaks in excess DI water. The washed membrane was sandwiched between two cotton TexWipes that were wetted with DI water and dried under ambient conditions.

Blending Acid-Base Solutions without Additives

For PBI or PBIO, the polymer concentration of solutions used for blending was typically about 10 wt. %. The acid(s) were dissolved in a small amount of solvent (same solvent as for the polymer) that was calculated to provide about 20 wt. % or greater total solids after blending, which was suitable for knife coating. The calculated mass of dry acid was transferred into a small vial inside a nitrogen purged dry box. For a typical membrane preparation, a total of 0.25 g of acid was used. The calculated amount of solvent was added to the acid inside the dry box. A magnetic stir bar was used for mixing. Dissolution typically occurred within about 30 min. The calculated amount of polymer solution was then added to the acid solution inside the dry box and mixed with a magnetic stirrer for 30 min. to 1 hr. before coating.

Blending Acid-Base Solutions with Additive Dispersed in Polymer Solution

Blending and membrane preparation were the same as described above. except that the inorganic powder was first dispersed in the polymer solution by adding the dry inorganic powder, about 14 ceramic milling cylinders (type BRUNHP050 from U.S. Stoneware Corporation, East Palestine, Ohio), and 25 – 30 g of ~ 10 wt. % polymer solution to a screw-cap 4 oz. glass bottle. The sealed bottle was rolled on a bottle roller at ≤ 100 rpm. A double layer of 2-mil Teflon film was inserted between the bottle and the bottle cap. The number of milling cylinders and/or rpm were adjusted if needed in order to get the cylinders to tumble. In addition, if necessary, the solution viscosity was adjusted by adding more solvent. To determine the maximum amount of solid that could be dispersed by this method, small increments were added up to the point where the viscosity became too high for the cylinders to move upon rolling of the bottle. For all types of silica that were evaluated, it was possible to prepare mixtures having silica/polymer at a ratio of at least 113/100 parts by weight starting with polymer solutions that were about 10 wt. % polymer. After the final addition of inorganic powder, the mixture was typically rolled for at least 24 hr. In all cases, membranes prepared by this method were free of any particles that could be seen by eye. SEM analysis of the cross section of the membrane of Example 1 showed that the particles were uniformly dispersed and ≤ 2 micron diameter. SEM analysis of the surfaces of the membrane of for C-22 per Table XV after extraction of the acids with water showed that both surfaces were uniform and that there were no large particles seen on the surfaces and that the pores were filled uniformly with agglomerates of primary silica particles. For small-scale laboratory preparations, this method has the advantage that it does not require any expensive equipment and that it prevents adsorption of water by the components. Other types of high shear mixing equipment could be used provided that a dry atmosphere is maintained to prevent absorption of water from the atmosphere.

Blending Acid-Base Solutions with Additives Dispersed in Both Solutions

Inorganic additives were added to either the acid or the polymer solution depending on compatibility with other components in the solution and precipitation of the polymer. Dispersion of inorganic oxides in the polymer solution was advantageous since the polymer and inorganic additives were more plentiful and less expensive than the acids and since larger volumes of material were needed for dispersion by bottle rolling.

Sols of inorganic oxides could be added to either the solution of acids or solution of polymer before blending or added to the blended acid/polymer solutions.

Heteropolyacids were combined with the dry acids in glove box that was purged with dry nitrogen, NMP was added, and the resultant mixture was mixed using a magnetic stirrer overnight. Silica, if used in combination with the heteropolyacid, was dispersed in the polymer solution.

Blending Acid-Base Solutions with Inorganic Sol in Organic Solvent

Silica or zirconia sols were transferred from their native aqueous solvent to NMP using the following procedure. For silica, Nalco 1042 was used. Information from Nalco for this sol indicated a particle size of 20 nm, 34 % solids, acid stabilization and that the sol was nominally free of anions. The zirconia sol was prepared by 3M per pending patent applications and was stabilized using acetic acid. The total percent solids were 46.24 %

and the total percent zirconia was 41.52 % with the difference due to acetic acid. The nominal particle size was 20 nm.
NMP and 1-propanol were added to the sol. The amount of NMP was chosen to provide the desired final weight percent of the inorganic material in NMP. The amount of 1-propanol was in excess of what was needed for azeotropic removal of the water in the sol (28.3 % water in azeotrope, 87.7°C boiling point for azeotrope at STP as compared to 97.2°C for 1-propanol at STP). Distillation was continued until the distillate boiling point reached a plateau value for 1-propanol. More 1-propanol was added if necessary and distillation continued until this was achieved. Residual 1-propanol was then removed using a rotary evaporator with an initial bath temperature of 40°C and –26 inches of Hg vacuum. The bath temperature was increased to 65°C as 1-propanol was removed and removal continued until mass loss versus time became asymptotic. Complete removal of the 1-propanol at higher vacuum tended to induce some precipitation, so leaving $\leq$ 5 wt. residual 1-propanol was preferred. This amount of residual 1-propanol did not induce polymer precipitation during blending. The only critical requirements for the azeotroping agent was that it not precipitate or induce agglomeration of the sol and that small residual amounts remaining after stripping did not precipitate the polymer or interfere with other additives. 1-propanol was used because of its large capacity for removal of water and since it was compatible with inorganic sols and residual amounts (typically $\leq$ 3 wt. %) did not precipitate the polymer.
For addition of inorganic sols in organic solvent to compositions that also included an acidic inorganic material such as a heteropolyacid, addition of a portion of the total solvent for the coating formulation to the acids (fluorinated and heteropolyacid) and dissolving the fluorinated acids before adding the inorganic sol to the acid solution was done to avoid direct interaction of the solid heteropolyacid particles with the sol particles. The total amount of solvent used in the formulation was adjusted so that the total percent solids was at least 20 wt. %.

Membrane Formation from Coatings

In general, coating solutions were applied to a glass plate using a plastic pipette and spread using a hand-held, 6-inch wide Gardner-Neotec knife coater from Pacific Scientific. The knife gap used was calculated to provide a dry thickness of about 2 – 3 mil based on the solution percent solids and the general rule that the wet thickness provided by a knife coater is about half the knife coater gap. The actual thickness varied depending on viscosity. The solvent was then removed using an explosion proof circulating air oven.

For DMAc and NMP, coatings of mixtures containing polymers and other additives, the following temperature ramp was used: 10 min. at 80°C, 10 min. at 100°C, 10 min. at 120°C, and 4 hr. at 140°C. For methane sulfonic acid (MSA), 2 hr. at 200°C was used. After removal from the oven, the membranes were cooled under various conditions. After cooling, membranes were left exposed under ambient conditions to absorb water loosen their bond to the glass plate. Even at 20 % RH, the membranes absorbed sufficient water after several hours to allow them to be peeled from the glass plate.

Quench Conditions after Drying

For slow rate of cooling after drying of coatings, solutions were coated onto thick glass plates (6 mm). Upon removal from the oven after heating to remove solvent, samples

were placed on cork rings to cool under ambient conditions. Unless noted otherwise, the slow rate of cooling method was used.

For faster rates of cooling, solutions were applied to a thin glass plate (2 mm). Upon removal from the drying oven, they were placed on either a 6 mm thick aluminum plate at room temperature or on a 6 mm thick aluminum plate that was cooled to -9°C and removed from the freezer immediately before placing the coated glass plate on it.

Membrane Reinforcement by Pressing into Matrix

For reinforcement matrices such as woven cloths and nonwovens that had large pores (e.g. greater than about 10 microns), dried membrane compositions having imide acids could be pressed into the matrix at elevated pressure, though these matrices could also be filled using coating solutions. Preparation of compositions for subsequent pressing was done by solution coating and drying as usual. Before pressing, the material was dried over night in a glove box that was purged with nitrogen. The dried material was then pressed into the reinforcement matrix by placing some of the composition on one or both sides of the matrix, sandwiching between two pieces of 2-mil Teflon film, placing between two press plates, pre-heating in the press without pressure for about 2 min., and then pressing for about 10 min. For compositions that flowed easily, gaskets were used to control the thickness after pressing. The press temperature needed depended on the composition.
For membranes C1-C3 per Table XVII, the press temperature was 132°C, the sample area was about 26 cm^2 and the press force was 1000 lb-force. Thonex PW106 glass cloth was used for C1-C3. For C-13 in Table XVII, the press temperature was 350°C, the sample area was about 26 cm^2, and the press force was about 2000 lb-force. For C-18 per Table XVII, for which Crane HM090 nonwoven was used, the press temperature was 400°C for 4 min.

Measurement of Exudation under Pressure

Membranes were evaluated for exudation of acid under pressure by:

1. Cutting a 5-cm^2 piece of the membrane using a die and placing in a nitrogen flushed dry box overnight to dry. The dry mass was then recorded.
2. 2 in. x 2 in. pieces of a microstructured film prepared as described in US 6,136, 412 were dried at 140°C for at least 30 min., cooled in the dry box, and the dry mass recorded. This film had a 90/12 microstructured pattern consisting of repeating peaks and valleys in which the included angle of the valley side walls was 90°C and the distance between valleys was 12 microns. The peaks heights were nominally 6 microns tall, with a 9 micron peak repeated every thirtieth groove. The grooves were formed by microreplication using a UV-cured acrylate composition. An advantage of this type of film was that it provided an open space for exudate.
3. For the dry test condition, the membrane was then evaluated in its dry condition as indicated below shortly after removal from the dry box. For the humidified test condition, the membrane was exposed to ambient humidity for 24 hr. before testing (room temperature was typically 22°C).
4. The membrane was placed between two pieces of 3M microstructured film with the grooves facing the membrane and then pressed for 10 min. at the pressure

indicated. The pressure was calculated from the initial sample area, not the actual contact area, and the applied press force.

5. The microstructured film was separated from the membrane after cooling, dried at 140°C for at least 30 min., cooled in the dry box, and the dried mass determined. The percent by weight of the initial membrane mass that was transferred to the microstructured film was calculated by dividing the difference between the initial and final masses for the microstructured film by the initial membrane mass and multiplying by 100.

Results showed that exudation increased with pressure, temperature, and with the ambient humidity under which the membranes were conditioned before testing. The pressure and temperature for results in **Table**s 10 – 11 were 1250 psi and 132°C. For membranes comprising a mixture of imide and sulfonic acids, the membrane area did not change as a result of pressing, at least up to a test temperature of 190°C.

Resistance of Acid to Wash Out

Relative resistance to washing out of the acids was determined by adding 5-cm^2 pieces to a 50 ml beaker containing 25 ml water while stirring with a micro magnetic stir bar and observing pH change versus time using multi range pH paper.

Thickness measurement

For easily compressed materials such as reinforcement matrices, a spring-loaded gauge from Mitutoyo, No. 7326 was used. For solid polymer membranes, a Sylvac Ultra Digit Mark IV gauge having an 8 mm foot diameter was used. To prevent direct contact of the gauge with the membrane, the membrane was sandwiched between two pieces of 2-mil Teflon film and the thickness due to the Teflon film was zeroed out.

Morphological Characterizations

Differential scanning calorimetry (DSC) was done using a TA Instruments Q1000 Modulated Differential Scanning Calorimeter equipped with #130, Cell RC-296 in either modulated or in standard DSC mode using standard Q1000 TA aluminum pan using a scan rate of 20°C/min. for standard heat flow measurements. For initial experiments, evaluation with retention of water was of interest, so sealed pans were used and the upper temperature was limited to 150°C. Heating above 150°C was found to rupture the cells and to contaminate the measurement cell with acid, so subsequent evaluations were done with punctured lids, the upper temperature limited to 150°C for the first scan to remove water without splattering, and only then going to higher temperatures for the second scan.

Modulated DSC was also done using the TA Q1000 using a linear heating rate of 4°C/min. and a perturbation amplitude of ± 0.636°C every 60 seconds. The heat/cool conditions were from -120°C to 165°C. Peak integrations were evaluated using the total heat flow (HF) curve, the reversing (R) heat flow curve (heat capacity changes), and the non-reversing (NR)/kinetic heat flow curve. Peak integration results were normalized for sample mass and reported in J/g.

Elastic moduli were evaluated from 25°C to 200°C in tension (dynamic mechanical analysis) using a Rheometric's Solid Analyzer (RSA II) at 1 Hz (6.28 rad./sec.) with heating at 3°C/min. and cooling to 25°C under dry nitrogen. A 6.5 mm by 23.4 mm by 0.030 mm strip was mounted in the clamps and tightened. Pre-determined amplitude and frequency were applied and the stress response was measured.

X-ray diffraction was done using a Phillips vertical diffractometer, copper K_α radiation, and proportional detector registry of the scattered radiation. The unit was fitted with variable incident slits, fixed receiving slits, and graphite monochrometer. Scans were conducted from 3° to 45° (2θ) using a 0.05 degree step size and 6 or 32 second dwell time. X-ray generator settings of 45 kV and 35 mA were employed. Scans were conducted under ambient conditions on materials that had been conditioned under either ambient humidity or under flowing dry nitrogen.

Thermal gravimetric analysis was done using a TA Instruments 2950 HI-Resolution Thermogravimetric Analyzer. An initial heating rate of 50°C/min. was applied with a resolution setting of 4.0. Under these conditions, the instrument heated until weight loss was detected, the temperature stabilized until weight loss diminished, and then heating recommenced.

Evaluation of conductivity using BekkTech cell

Conductivity evaluations were done by measurement of AC impedance using a four-point probe conductivity cell from BekkTech (Loveland, Colorado) on a 1 cm x 3cm piece of membrane. The conductivity cell was electrically connected to a potentiostat (Model 273, Princeton Applied Research) and an Impedance /Gain Phase Analyzer (SI 1260, Schlumberger). The sample was first conditioned in the cell for 5 hr. at 120°C with 80°C dew point (<0.3 % RH) followed by AC impedance measurements using Zplot and Zview software (Scribner Associates). AC impedance measurements were then done at each of the following temperatures after conditioning for one hour at each temperature (all at constant 80°C dew point) with: 110°C (< 1 % RH), 100°C (< 3 % RH), 80°C(100RH), 90°C(39 % RH), 110°C (< 1% RH), and 120°C (<0.3 % RH). The conductivity was calculated from the average AC impedance at high frequency by following the formula: Conductivity = (1/R) l/A, where l/A is the cell constant.

Fuel Cell Evaluation

Fuel cell electrodes having 0.4 mg/cm^2 of Pt were prepared by coating a catalyst ink onto a carbon paper gas diffusion layer. Membrane electrode assemblies (MEAs) were tested in a Fuel Cell Technologies single serpentine 5-cm^2 cell. Gas flow rates for H_2 and air were fixed at 100 and 500 sccm respectively. Inlet humidification was kept constant at an 80°C dew point at all temperatures.

Preparation of Surfactant Templated Silica and STS Coating Solutions

To prepare solid STS silica, cetyltrimethylammonium bromide (CTAB, Pluoronic 123) (147.5 g) was combined with 576 g methanol, 1154.7 g DI water, 579.3 g concentrated ammonium hydroxide (27.5-29 wt% aqueous) in a 4-liter beaker. This solution was agitated with an overhead stirrer; and 152 g tetramethoxysilane (TMOS) was rapidly added. The resulting opaque white gel (which formed in approx. 3-5 sec.) was stirred for

~10 min. and allowed to sit quiescent for ~2 hr. The final molar ratios were 1.00 TMOS : 0.13 CTAB : 87 water : 18 methanol : 4.8 ammonium hydroxide. The gel was filtered with a 9 cm Buchner funnel. The following day the wet cake was loaded into a 6 cm wide x 50 cm long x 2 cm deep hemispherical fused silica boat. The material was calcined in a large tube furnace at 550 °C for 6 h in air. The ramp from room temperature was over 1 h; the cool down was with the power to the furnace off.

To prepare STS coating solutions, a TEOS stock solution was first prepared by combining 892 mL absolute ethanol, 892 mL TEOS, 72.0 mL deionized water (18MΩ), and 0.0210 mL concentrated HCl (29 % aqueous) in a 9 liter flask. The solution was stirred with an overhead air-drive stirrer and heated on a programmable hot plate with temperature probe for 90 min. at 60°C. After cooling, this stock solution was stored at 0°C in polypropylene bottles.

For preparation of a 10 wt. % coating solution, the following were combined in a polypropylene bottle in the order indicated with swirling to mix after each addition: 34.5 mL of 2.16 M TEOS stock solution, 4.14 mL of 0.07 N HCl, 1.38 mL deionized water, and 80 mL of ethanol. The bottle was placed in a 50°C bath for 15 min. After cooling to room temperature, 5.26 g Pluronic 123 surfactant (BASF) were then added, and the bottle was inverted periodically over about one hour to dissolve this surfactant. The percent solids of the resultant solution was found to be 10.3 wt. %. The pore size in STS silica made using Pluronic 123 is about expected to be 5 – 7 nm. XRD results were not suitable for estimation of pore size and TEM images were not available.

Preparation of Zirconium Sulfophenylphosphate

($Zr(O_3PC_6H_5)_2$) was prepared by dissolving about 10 g of $ZrOCl_2.8H_2O$ (Aldrich) in 200 g of deionized water in a polypropylene bottle. About 20 g of HF (50 wt. %) was added to this solution. Then 9.6 g of phenylphosphonic acid $C_6H_5PO(OH)_2$ (Aldrich) was added to the mixture under vigorous stirring. The mixture was heated under stirring at 75°C for 2 days until all the water evaporated. The resulting solid was filtered and washed with copious amounts of water and dried at 75°C.

($Zr(O_3PC_6H_5)_2$) from above, 10.1 g, was ground into a powder using a mortar and pestle. The powder was placed in a round bottom flask and 82 gm of fuming sulfuric acid (20% free SO_3) were added to it. The flask was heated at 75 ± 5°C in a preheated oil bath under reflux for 1 hour and then cooled in an ice bath. Deionized water was then added drop wise to convert the unreacted SO_3 to H_2SO_4 (extremely exothermic). Subsequent addition of slight excess of water forms a gel. Methanol, 150 mL, was then added and the mixture was centrifuged in a polypropylene bottle at about1800-2000 rpm to recover the solid. The recovered solid was suspended in methanol and centrifuged to remove the excess sulfuric acid. The above process was repeated 6 times until the supernatant liquid on post centrifugation was clear.

Dialysis was then done to remove any excess sulfuric acid /sulfate ions. Deionized water was added to the recovered gel/solid after centrifugation from the procedure outlined above. The mixture was then poured into a 1000 or 3500 MW cut off dialysis tube and suspended in a beaker containing deionized water under constant stirring. The water in the beaker was replaced by fresh deionized water every hour until the pH of the

water was about 5. The dialysis tube was then opened and the mixture was poured into a beaker and dried at 80˚C to recover the dialyzed material.

Preparation of Sulfated Zirconium Oxide

Preparation of sulfated zirconium oxide involved three steps: precipitation, acid-treatment, and heat treatment.

Precipitation: Using a plastic beaker and a pneumatic mixer, 50g of 30% ammonium hydroxide was poured with vigorous stirring into 200g of 35wt% zirconyl nitrate (aqueous, Aldrich 39,182-4). This reaction produced a suspension of gelatinous hydrous zirconia precipitate. The gel solid was washed by hand-stirring into about a liter of DI water, followed by vacuum filtration with the Buchner funnel. This washing procedure was carried out twice. The wet, washed gel powder weighed 173.50g. The washed gel powder was dried overnight at 110°C. The dried powder weighed 50.62g. The powder was lightly ground with a mortar and pestle.

Acid-Treatment: The dried powder was stirred into an aqueous sulfuric acid solution for 30min. The acid solution was prepared by combining concentrated sulfuric acid with water. The mass proportions of components for acid treatment were powder : H_2SO_4 (conc., 96%): DI water = 1 : 0.167 : 5.92. The acid-treated powder was separated by vacuum filtration and washed with DI water, yielding 73.86g of wet powder. The powder was dried overnight at 110°C, yielding 48.17g of dried "sulfated" powder.

Heat-Treatment: The sulfated powder was calcined in air by heating at 10°C/min to 500°C and holding at 500°C for 1hr, followed by furnace-cooling.

3.4. High Temperature Membranes Based on Ionic Liquids

3.5. Ionic Liquid And Super Acid Model

Since 3M is capable of making anhydrous perfluorinated super acids and highly stable fluorinated ionic liquids, EMI-TFSI and perfluorobutanesulfonic were therefore chosen for this liquid Nafion™ model study. The ionic liquid EMI-TFSI provides low viscosity at room temperature, a low m.p. (–18°C) and thermal stability up to at least 350°C whereas the perfluorobutanesulfonic acid is a liquid at room temperature and is relatively nonvolatile (b.p. ~ 200°C at 760 Torr).

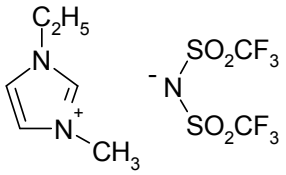

(EMI-TFSI)

$CF_3CF_2CF_2CF_2SO_3H$

(Perfluorobutanesulfonic acid)

3.5.1. Proton conductivity of ionic liquid/ super-acid systems

For PEMs made of polyperfluorosulfonic acids, such as Nafion™, proton conductivities are generally determined by AC impedance techniques. In the presence of water the proton (H^+) from the sulfonic acid group is solvated to form a hydronium ion (H_3O^+). Hydronium ion is the only ion that has the ability to move and carry charges. The remaining polymer bounded SO_3^- group is the immobilized counter-anion. In PEMFC, high proton conductivity from the membrane is required for a high current density. However, when an additive is added, especially when it is small molecule and is a salt such as an ionic liquid, the ionic conductivity measured by AC impedances might not be the only source of conductivity. But it probably includes the conductivity from ions other than protons. Therefore, a liquid cell was developed for ionic liquid and super-acid systems to determine their proton conductivities using Hydrogen pump (H pump) method with DC measurement technique, where the resistance was calculated from a voltage-current curve under H_2.

3.5.2. Experimental

Conductivity measurement procedures for PEMs with different conductivity cells

Two point probe

Two-point probe (2pp) is often used for measuring the ionic conductivity of a thin membrane under high relative humidity conditions. It consisted of, from bottom up: a stainless steel base, a non- conductive Teflon layer, two flat platinum electrodes (for holding testing sample, PEM in this case), Teflon separating layer and another stainless steel cover on top. All components with the external dimensions of 3 cm x 4 cm and internal dimensions of 1.3 cm x 2 cm (created a hole for water absorption) are tightened together by four stainless steel bolts. The final thickness of the complete cell is about 2.5 cm. The distance between two electrodes is 2 cm. Two pictures on the top of the Fig. 52showed the actual 2pp cell. The first is the bottom half with a membrane lying on two electrodes. The second is the complete and ready-to-test 2pp cell. Fig. 53 is a three-dimension enlarged complete 2pp cell.

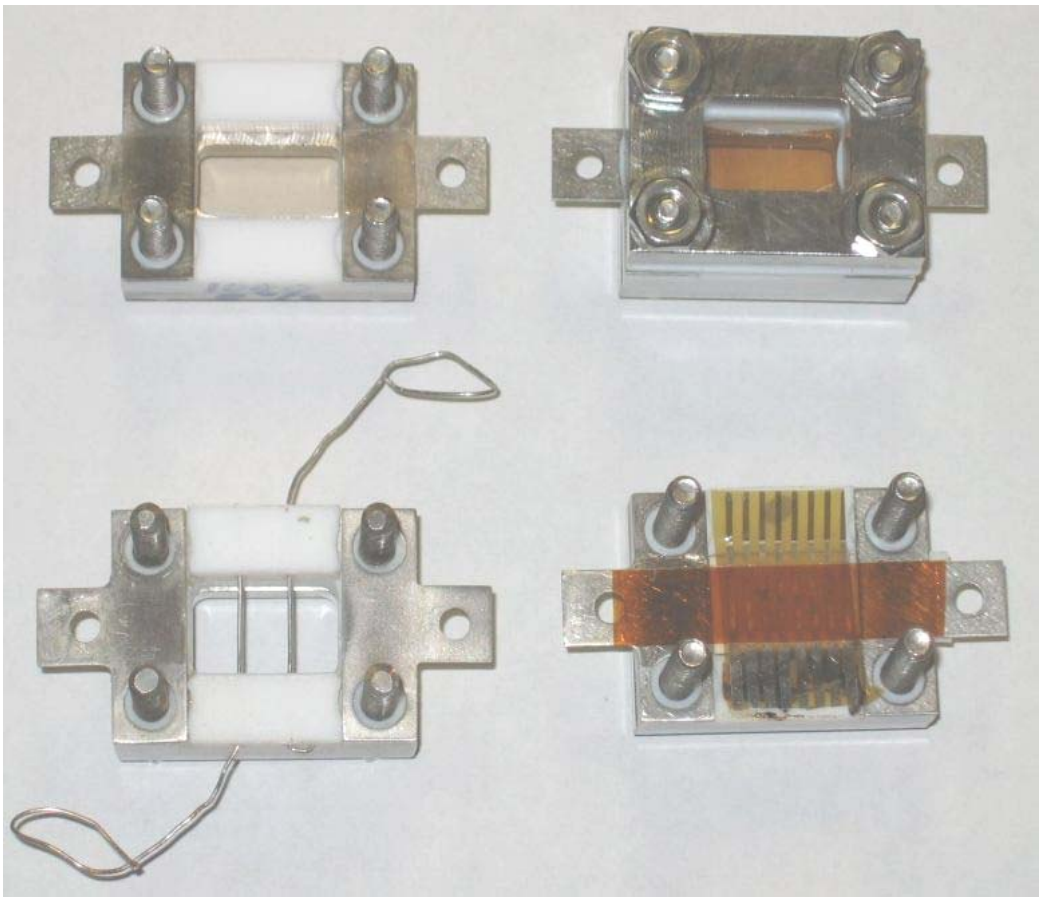

Fig. 52. Conductivity cells

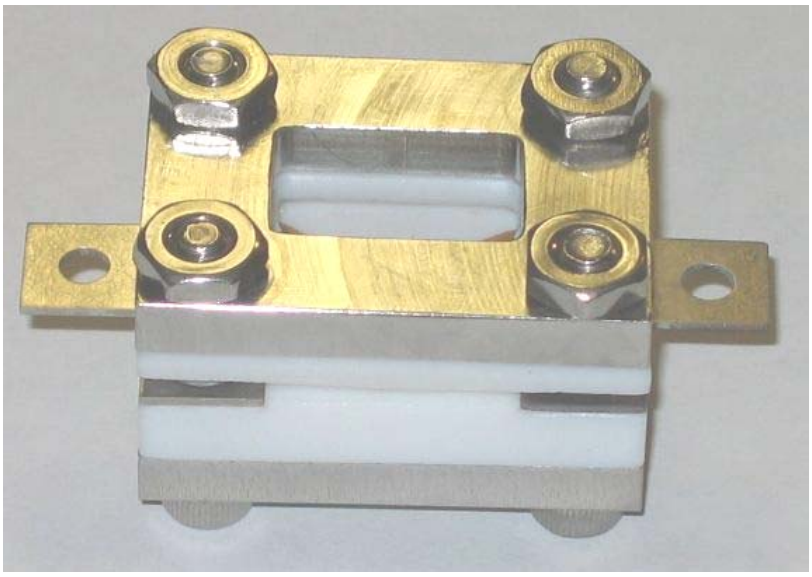

Fig. 53. Two-point-probe

Four-point-probe with two circular wire inter-electrodes

Four- point probe (4pp) is constructed similarly to the two-point probe except for the two additional circular platinum wires inserted into the non conductive Teflon base. These two new wires function as inter-electrodes and are laid in the same plane with the other two external electrodes. The distance between two inter-electrodes is 0.6 cm. The bottom left picture in Fig. 52 is the bottom half of 4pp cell.

Four-point-probe with multiple flat inter-electrodes

A new four- point probe was developed using a four–point probe concept except replacing the two inter-electrodes with flat multiple thin platinum strips (0.8mm wide and 1.2mm apart) which were deposited on a Polytetrafluoroethylene (PTFE) film or polyimide (PI) film (see Fig. 52). The intention of the Pt/ PTFE or Pt/PI cell design was to overcome the concerns of contact resistance, melting at high temperatures and the reliability of single data point generated from the first 4-point probe cell, when at high temperatures and in dry conditions.

The cell made by Pt strips /PI was the best performer because it gave a smooth surface for good contact with test samples and also was stable physically and electrochemically under high temperatures and acidic environments. Fig. 54 showed the Pt strips on PI film which was used as the base for 4pp cell. The bottom right picture in the Fig. 52 demonstrated how the multiple electrode film was used.

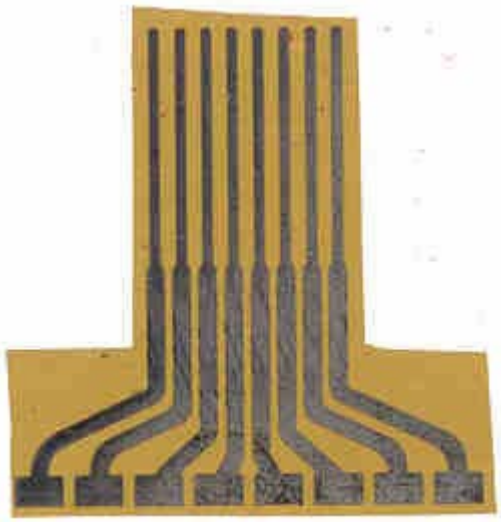

Fig. 54. Pt/PI film image

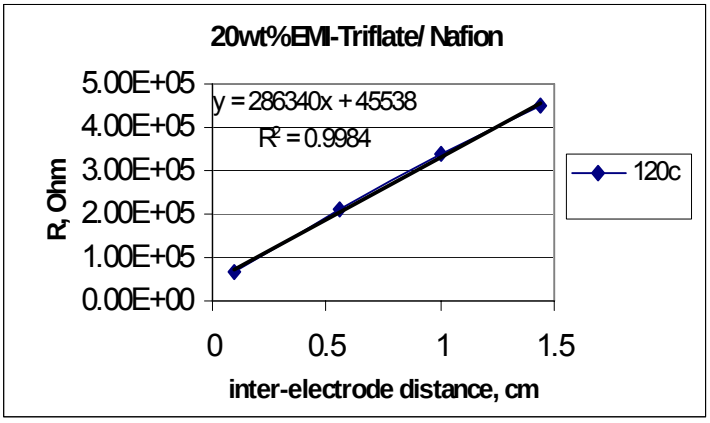

Fig. 55. A typical slope of a Resistance/distance curve

Membrane sample preparation

After casting and removing solvents by heating, the proton exchange membrane was cut into a 1 cm x 4 cm size under the room condition. There was no boiling or drying prior to cutting. In some cases (if specified) the membrane was boiled in de-ionized water for 30 min and then air-dried prior to testing. The thickness of membrane was measured by taking the average from at least three different areas. Typically membrane thickness was from 25 to 50 micrometers.

Connection procedure between cell and measuring instruments

For the two-point probe: The working and sense electrode from the electrochemical instruments were connected to one platinum electrode of the cell. The counter and reference electrode were connected to another platinum electrode of the cell.

For the four-point probe: The four electrodes of the cell were connected to the electrochemical instruments in the following order: Working/Sense/Reference/Counter to outer/inter/ inter/outer electrodes of the cell.

AC impedance measurement procedure for membranes:

The AC impedance was measured using Zplot software over the frequency range of 100 kHz -1 Hz with a potentiostat (PAR, 273A) and a frequency response analyzer (Solatron, 1260). DC potential of 0 V and 10 to 100 mV for AC amplitude was applied. The conductivity cell with membrane is placed into the humidity and temperature chamber (TAIBAI, Platinous Rainbow PR1G) or in the high temperature chamber purged with nitrogen gas. At each testing condition two or three measurements were repeated. The equilibrium time for each condition was 30 minutes. The AC impedance was measured using the Z real axis at zero-phase angle by circle or linear fitting technique. The conductivity was then calculated from AC impedance by following the formula: Conductivity = (1/R) L/A, where R is membrane impedance and L/A is cell constant. The cell constant is based on L which is the distance between two electrodes (for two-point probe) or the distance between inter-electrodes (for four-point probe) and A which is the surface area in cm^2 of the edge where membrane and electrode contacted. The unit of conductivity was in S/cm. For the multiple 4pp method, the AC impedances were collected at different inter-electrode distances and then a slope of the curve was plotted

from the data. That slope was then used to calculate the correct ionic conductivity.

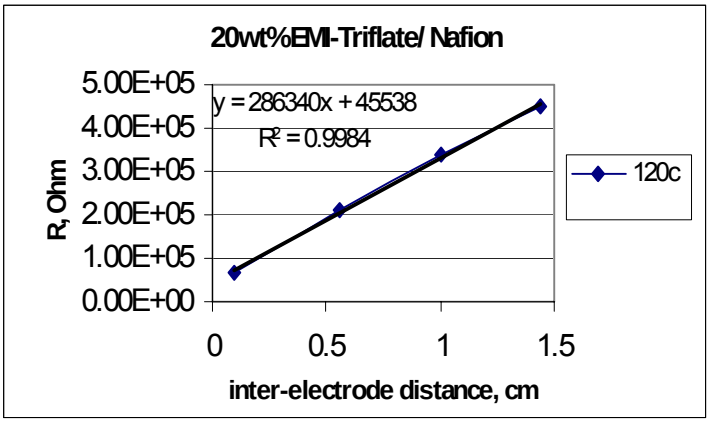

Fig. 55 is an example of this calculation.

Conductivity measurement procedures for liquid electrolytes with different cells:

Standard conductivity cell (for ionic conductivity)

A standard commercially available conductivity cell was purchased from YSI Incorporated (Model# 3403). It is used to measure the resistance of liquid electrolytes. The cell body is made of Pyrex. The electrodes are a platinum–iridium alloy coated with platinum black. The cell constant (K) is 1.

Conductivities of the liquid solutions were measured in a threaded glass tube equipped with the YSI conductivity cell (Model 3403). They were performed initially in a N_2-filled dry-box. Connection of the conductivity cell to an external a frequency response analyzer (Solatron, 1260) and a potentiostat (PAR, 273A) were made via electrical feed-through in the sidewall of the dry-box. For the experiments involved with water, the measurements were performed outside of the dry-box.

3.5.3. New liquid cell (for proton conductivity measurements)

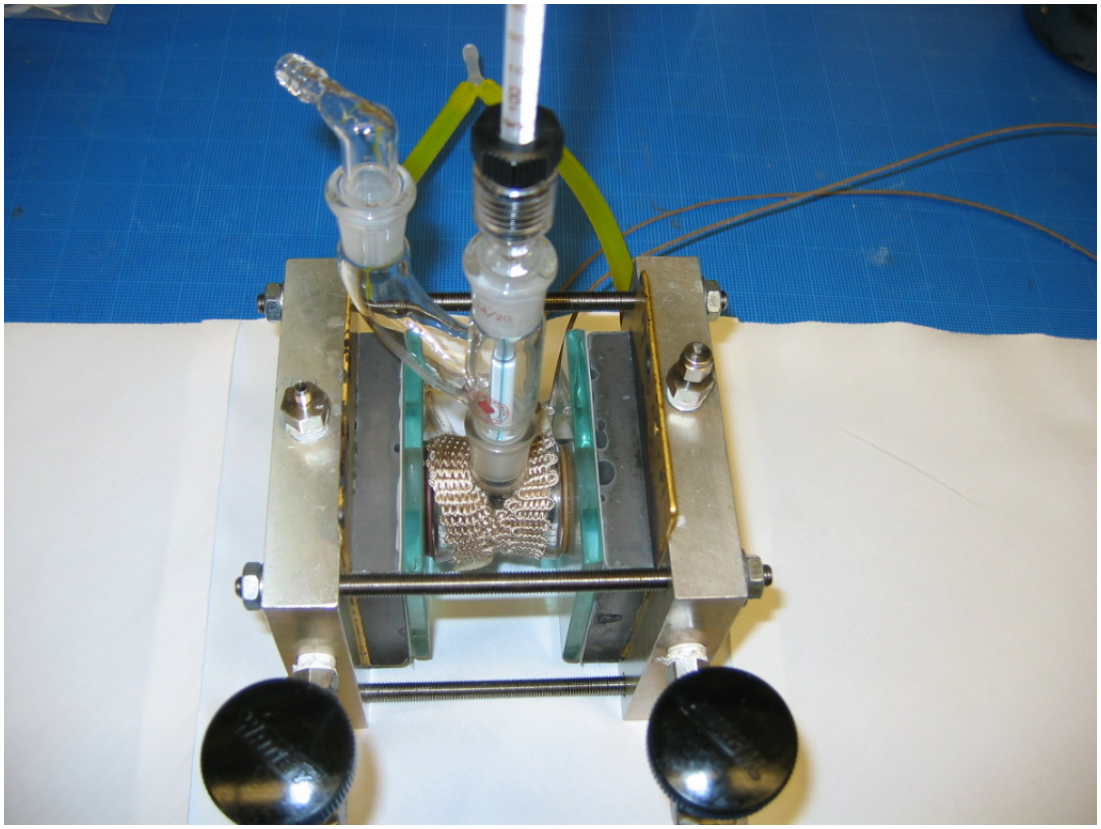

Fig. 56. Liquid conductivity cell

Three symmetrical components from a 50 cm^2 fuel cell were used to build a new liquid conductivity cell, which contains a three-way glass cell with a volume of about 25 ml for liquid electrolyte testing. Two bottom sides of the glass tube with the surface area of 18 cm^2 were connected to circular dispersed catalyst/gas diffusion layers. Gaskets, glass plates and Teflon layers with holes served as leakage protection. A flexible electric heating tape was wrapped around the glass cell for heating. A thermometer and pressure release adapter was connected from the top of glass cell (See Fig. 56).

Every component of the liquid cell was cleaned and dried before assembling and then placed in a glove box, which was continuously pursed with N_2. The ionic liquid and acid were charged through the top outlet. For each experiment, above 20 ml of ionic liquid was started without acid addition and then incremental additions of designed acid based on mole ratio. A thermometer was inserted into the liquid for measuring the electrolyte temperature. The ultra pure hydrogen gas was charged to the cell through the flow-fields and catalyst layers of both sides.

The DC resistances (H pump) were measured from the slopes of the current-voltage curves (from –1.0 to 1.0 V). The current-voltage curves were scanned from Z-Corrware software using a potentiostat (PAR, 273A) and a frequency response analyzer (Solatron, 1260). Each concentration was measured several times over a period of up to 60min

until a stable result was obtained The conductivity was then calculated from the average DC resistance by following the formula: Conductivity = (1/R) l/A, where l/A is the cell constant.

Ionic liquids and super-acids preparations

The materials were prepared in anhydrous form and were then stored and handled in a dry-box to prevent the re-absorption of water. The ionic liquids were prepared according to the procedures described in patent US 6372829. The imide acids were prepared according to the procedures described in patent US 5874616. The methide acids were prepared according to the procedures described in patent US 5554664.

Viscosity measurement procedure

The effects of viscosity on proton conductivity of ionic-liquids and super-acids were studied. Their viscosities as a function of temperature were measured using a Dynamic Stress Rheometer (model# DSR 200) at the shear rate of 1 rad/sec and temperature between 20 and 90°C under nitrogen. The dried samples were places between 40 mm parallel plates with 1 mm distance. The unit of viscosity was in centipoises (Cp).

3.5.4. Results and Discussion

3.5.4.1. Testing procedure comparison

A number of published papers related to the methodology of AC impedance measurements on Nafion™-based membranes have been reviewed. To confirm the accuracy of 3M testing methodologies Table XX provides a list of proton conductivities of membranes measured at 3M using four-point probe cell and other data selected from some relevant papers. Most the data on conductivity as a function of relative humidity (RH) from Simonsson[50] and Doyle[37] agreed with our data.

Table XX. Conductivity as a function of relative humidity at 80ºC

MEMBRANE	DESCRIPTION	20%RH S/CM	40%RH S/CM	60%RH S/CM	80%RH S/CM	100%RH S/CM
Cast Nafion™	3M -4-Point Probe	0.006	0.013	0.046	0.075	0.112
N117	Zawodzinski- 4-Point Probe[49]	0.005	0.018	0.036	0.063	0.108
N117	Simonsson-4-Point Probe[50]	0.002	0.008	0.020	0.030	0.080

3.5.4.2. Standard Ionic Liquid with Nafion™

The first (standard) ionic liquid, EMI-TFSI, was blended with Nafion™ using 25.75 wt % ratios. The conductivity of this new membrane and a standard extruded Nafion™ N112 were measured by 4pp cell under two major different conditions. At 80°C from 20 to 100% relative humidity in a humidity chamber all the conductivities of EMI-TFSI/Nafion™ were below that of Nafion™ with the same testing conditions (Fig. 57). Interestingly, that behavior was dramatically changed when the samples were tested under dry conditions

in a nitrogen purged oven. The conductivity of ionic liquid doped Nafion™ increased from 10^{-6} S/cm at RT to near 10^{-4} S/cm at 160°C, while Nafion™ stayed around 10^{-6} S/cm during the same temperatures without water (Fig. 58). The results indicated that EMI-TFSI and other ionic liquids might be good water replacement candidates in PEMs for high temperature applications.

Sample #	*Membrane*
1.	N112 DuPont extruded membrane
2.	EMI-TFSI /Nafion™ blend (25/75 by wt.).

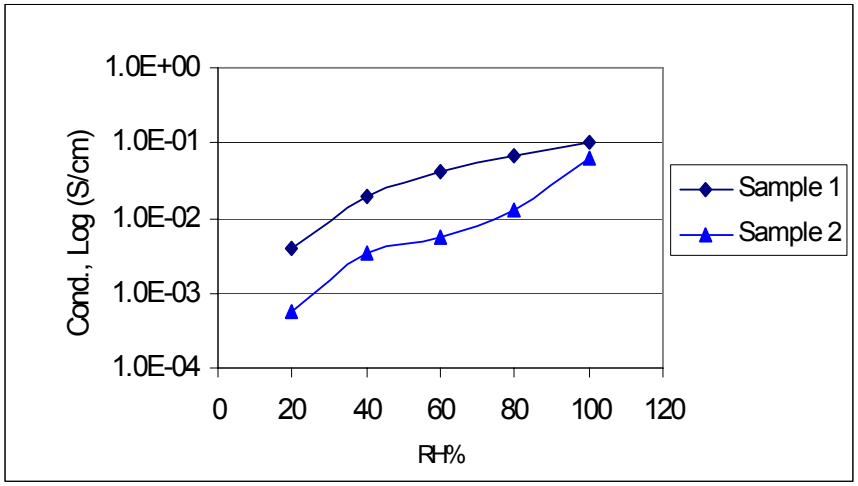

Fig. 57. Conductivity As a Function of Relative Humidity at 80°C

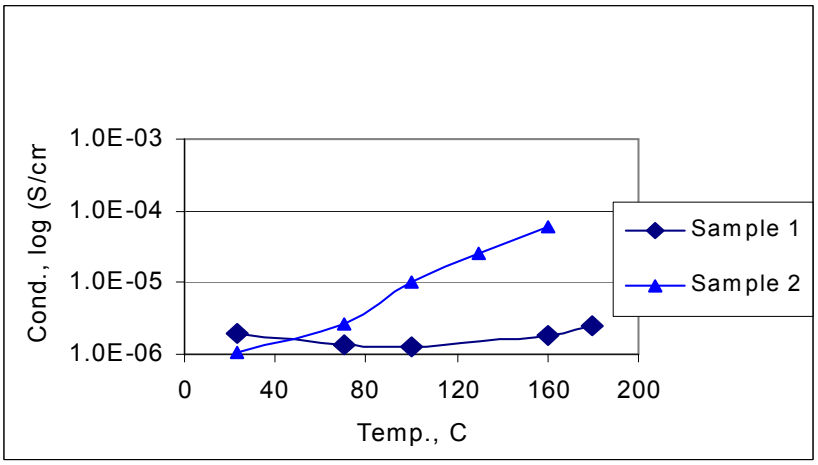

Fig. 58. Conductivity As a Function of Temperature under Nitrogen

3.5.4.3. Conductivity stability of ionic liquid/ Nafion™ under high humidity

Several new membranes were tested using a four-point probe with a newly developed protocol. Below are conductivities of cast Nafion™ and 20% EMI-Triflate /Nafion™. The conductivity of cast Nafion™ was very stable with 2 cycles, but the 20% EMI-Triflate was not, may be due to the loss of IL additive under humidified condition.

3.5.4.4. Conductivities of 20% ionic liquids in Nafion™

Six new hand cast membranes were tested which consisted of 20 % of additives in Nafion™ solutions. The ionic liquids were:

EMI-TFSI	Liquid
EMI- Triflate	Liquid
EMI- $N(SO_2C_4F_9)_2$	Liquid
Guanidine $N(SO_2C_4F_9)_2$	Solid
Guanidine TFSI	Solid
Melamine $N(SO_2C_4F_9)_2$	Solid

All additives, except melamine $N(SO_2C_4F_9)_2$, were soluble in 1-propanol. At 20 wt % level, these additives formed good cast membranes with smooth surfaces and defects free using the same casting conditions as of Nafion™. However, melamine $N(SO_2C_4F_9)_2$ was only soluble in hot methanol/water solution, but formed a very brittle film after casting with Nafion™. Therefore, only five new handleable membranes together with a standard 3M cast membrane were tested on their conductivities following the established protocol with 2 testing cycles for each sample. Used the standard 4-point probe configuration for all samples. The results of cast Nafion™ showed the comparable data to the literature on the relative humidity measurements.

3.5.4.4.1. Conductivity as a function of relative humidity at 80C

Table XXI. Conductivities of additives in Nafion™

MEMBRANE	DESCRIPTION	Cycle # Average	20%RH S/CM	40%RH S/CM	60%RH S/CM	80%RH S/CM	100%RH S/CM
Cast Nafion™	Nafion™ only	1st cycle	0.0055	0.0132	0.0458	0.0750	0.1121
		2nd cycle	0.0057	0.0135	0.0448	0.0759	0.1126
EMI-Triflate	20% in Nafion	1st cycle	0.0043	0.0134	0.0415	0.0863	0.1639
		2nd cycle	0.0022	0.0071	0.0199	0.0492	0.1113
EMI-TFSI	20% in Nafion	1st cycle	0.0005	0.0022	0.0079	0.0262	0.0737
		2nd cycle	0.0007	0.0023	0.0076	0.0249	0.0708
EMI- $N(SO_2C_4F_9)_2$	20% in Nafion	1st cycle	0.0026	0.0096	0.0267	0.0620	0.1167
		2nd cycle	0.0053	0.0100	0.0259	0.0606	0.1162
Guanidine-TFSI	20% in Nafion	1st cycle	0.0008	0.0037	0.0129	0.0376	0.0897
		2nd cycle	0.0013	0.0034	0.0118	0.0339	0.0844
Guanidine-$N(SO_2C_4F_9)_2$	20% in Nafion	1st cycle	0.0017	0.0070	0.0225	0.0513	0.0979
		2nd cycle	0.0034	0.0085	0.0223	0.0496	0.0919

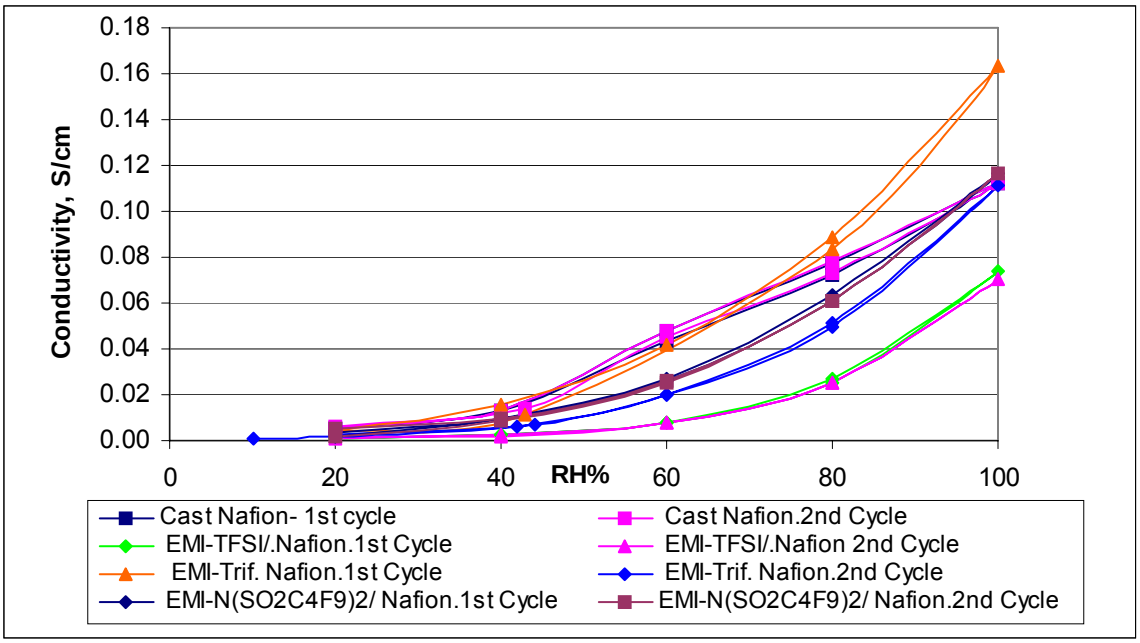

Fig. 59. Conductivities of additives in Nafion™

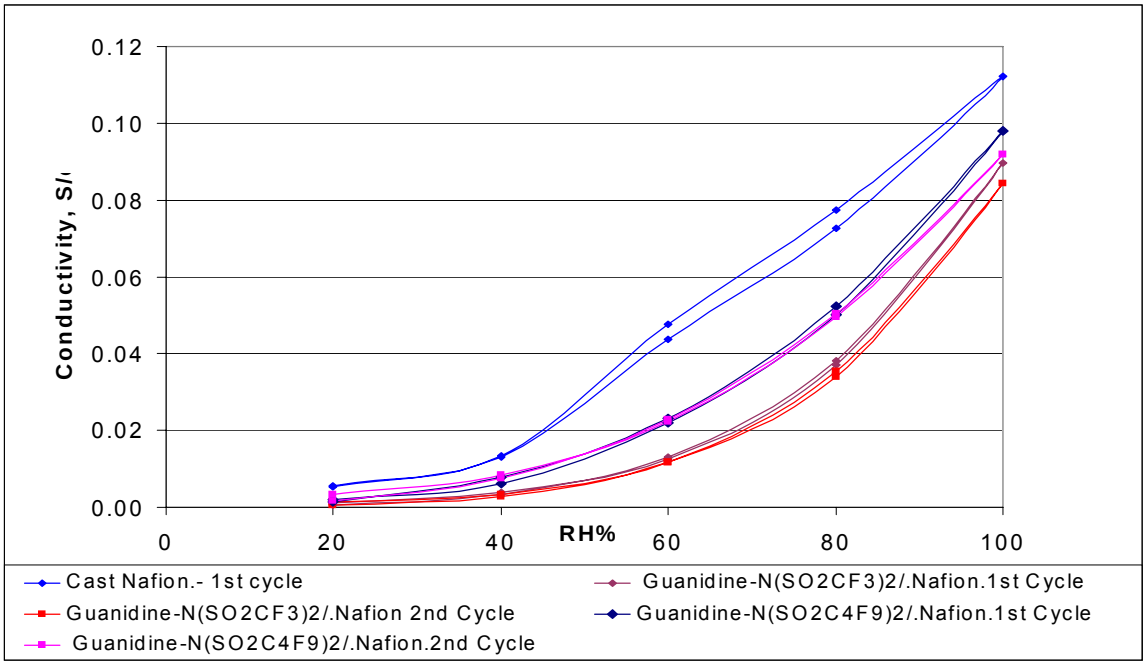

Fig. 60. Conductivities of additives in Nafion™

Together with a standard Nafion™ cast membrane, their conductivities were measured following the established protocol with two testing cycles for each sample to learn about their performance stabilities. A four-point probe configuration was used for all samples. The temperature and humidity chamber was set at a constant 80°C and from 20 to 100% RH. The conductivity results were listed on Table XXI. The data of control cast Nafion™ shows comparable results to the literature on the similar testing conditions.

No improvements on conductivity were found on these membranes at 80°C when 20% of additives were added to the Nafion™. All show an equal or lower conductivities compared with control Nafion™, except with the case of EMI-Triflate which gives a higher number than that of Nafion™ at 100%RH on the 1st cycle but looses all the gain on the 2nd cycle (Fig. 59). This short life improvement of EMI-Triflate is possibly due to its high solubility in water. Other membrane conductivities do not change with two cycles, suggesting that the leaching out of additives under 80°C and humidified condition must be negligible or very small. The conductivity of the Guanidine–$N(SO_2C_4F_9)_2$/Nafion™ was higher than of the Guanidine-$N(SO_2CF_3)_2$/Nafion™ but still lower than of Nafion™ alone.

The study results suggest that at the temperature of 80°C or below, adding an ionic liquid to an ionomer could not boost the conductivities in the presence of water. The decreasing of SO_3H group from Nafion™ by replacing with ionic liquids may explain for lowering their conductivities under humidified conditions. At higher temperatures and dry environments the performances of these additives were investigated and reported below.

3.5.4.4.2. Conductivities as Function of Temperature

Membrane samples (1 cm x 4 cm) were laminated on the Pt/PI electrode film and then annealed at 160°C for 20 minutes to give a good bonding before tests. The membranes were heated from 70 to 180°C (called heating curve) and then cooled down to 70°C (called cooling curve) in a nitrogen purged oven. Each measuring temperature was equilibrated for 30 minutes. Three data sets were collected for each condition and the slopes were plotted from the data of the resistances vs. electrode distances. The slopes were then used as resistances for conductivity calculations. Most the slopes of measured samples were linear that suggested that the conductivity data were reliable. Therefore, the concerns of contact resistance and data interpretation consistency were solved.

A membrane of Polybenzimidazole (PBI)/Phosphoric acid (PA) with 1:6 mole ratios was also prepared for comparison with ionic liquid/ Nafion™ membranes. The Fig. 61 showed the similarity of conductivity between literature (Savinell, CWRU) and tested results at 3M under dry condition on PBI/PA membrane. The conductivity from 1st heating curve of 3M made PBI/PA was comparable but the cooling curve was far lower than the literature values. This behavior might relate to the losing of water by 1st heating.

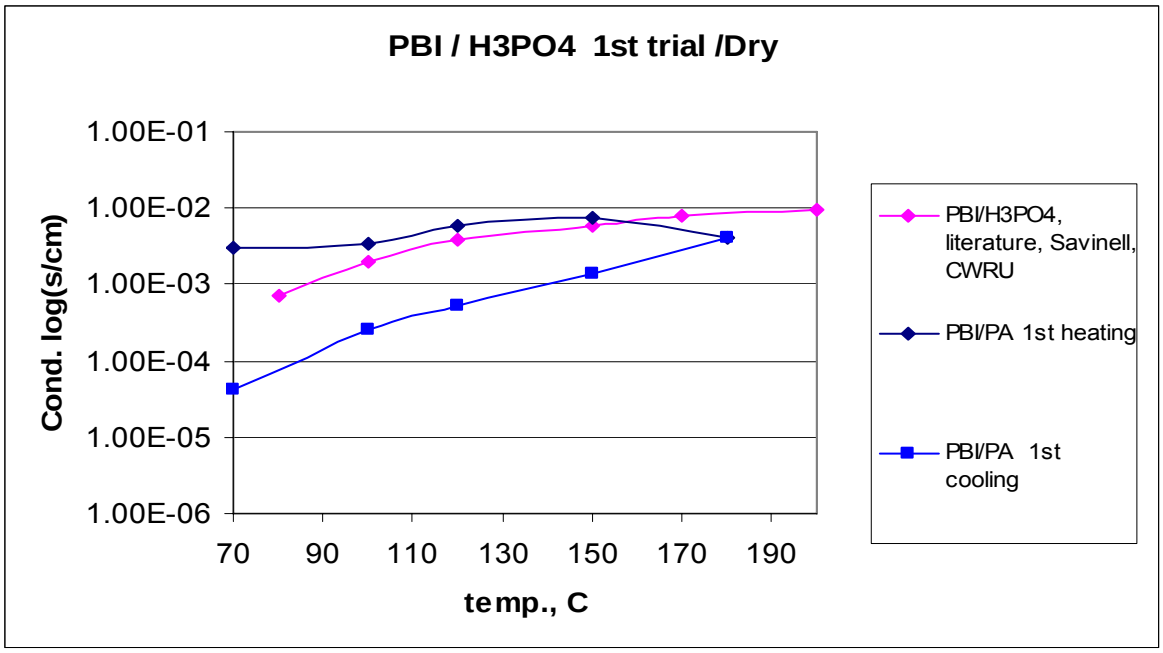

Fig. 61. Conductivity of PBI Membranes

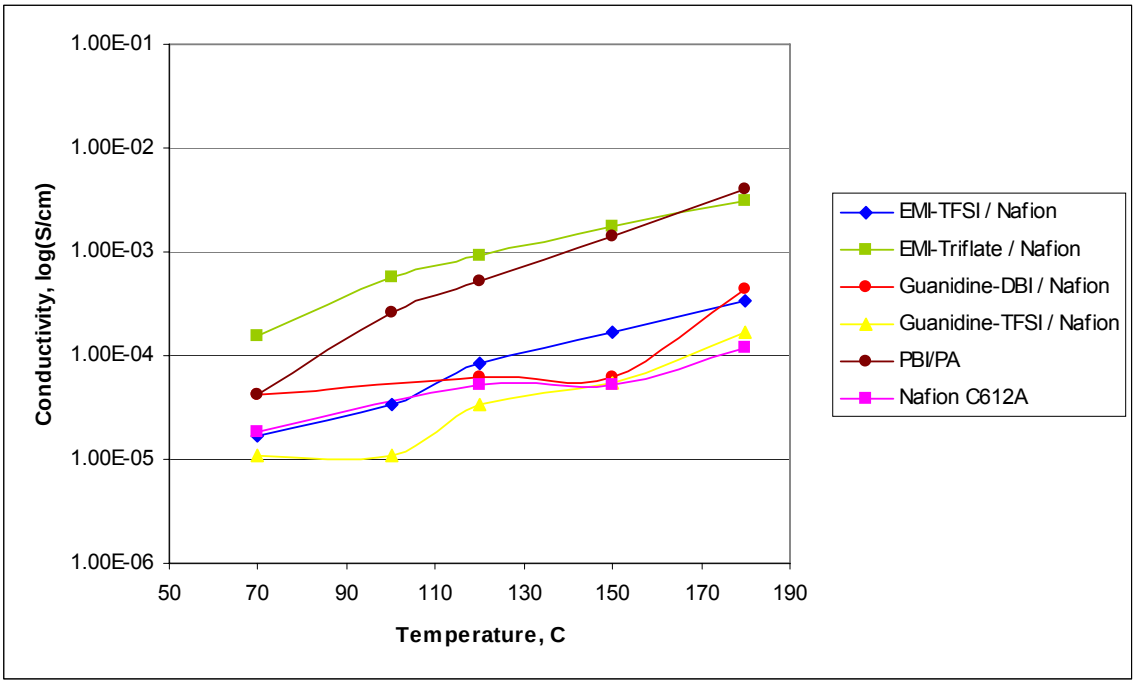

Fig. 62. Ionic Conductivity As a Function of Temperature /N_2

The conductivities of the cooling curves of ionic liquid/Nafion™, Nafion™ and PBI/PA membranes from 180°C down to 70°C under N_2 are compared in Fig. 62. EMI-Ttriflate/Nafion™ gave the highest and similar performance to PBI/PA in the range of 10^{-4} to 10^{-3}S/cm, while the other four remaining membranes generated about one order of magnitude lower on conductivities. EMI-TFSI/Nafion™ did better than Gaunidine – TFSI/Nafion™ and Nafion™ alone. Leaching of ionic liquids under high temperature

testing compression especially at the electrode areas seemed to be the main reason why the conductivity was not that high for Nafion™ with ionic liquids. And without the presence of water or ionic liquid additives, the actual Nafion™ conductivity might be different due to the lacking of wetting on electrodes when too high of a temperature was applied.

The higher level of EMI-TFSI in Nafion™ (50/50 wt %) was prepared and tested. Fig. 63 showed a significant improvement of this new membrane over the 20/80 wt % membrane. The conductivity of 50/50 wt % jumped from 10^{-5} to 10^{-3} S/cm at 70°C and from 10^{-4} to 10^{-2} S/cm at 150°C, and more importantly, they were repeatable with two complete cycles. The evidence indicated that more ionic liquid concentrations were needed to boost the conductivity of membranes under dry and hot conditions. This phenomenon consistently correlated to the results found in the liquid cell when ionic liquids were added to the non-polymeric acids which are also reported in this paper.

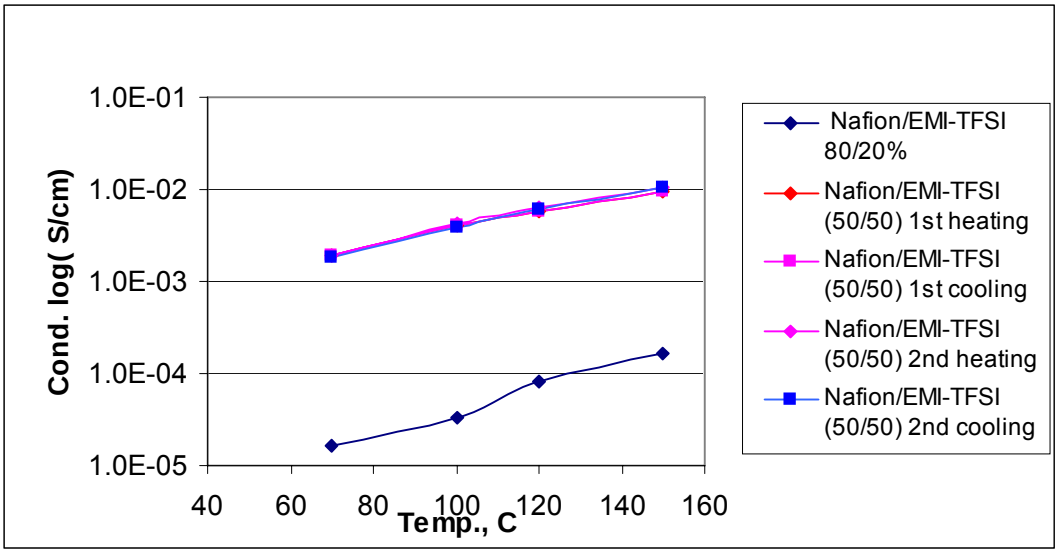

Fig. 63. Conductivities of Nafion™/EMI-TFSI

Based on the good results of Nafion™ /EMI-TFSI above, one formulation of Nafion™/EMI-TFSI/Imidazole with 45/45/10 wt% was chosen to make a membrane for conductivity test. The reasons for having 10% of imidazole were: 1) To reduce the high level of EMI-TFSI which created a weak membrane and leaching problem; 2) Imidazole is a base which could interact with Nafion™ and ionic liquid to boost the conductivity. Fig. 64 proved just that expectation. The conductivity as a function of temperature under N_2 purged environment of this Nafion™/EMI-TFSI/Imidazole (45/45/10 wt %) membrane was dramatically higher than that of the membrane of Nafion™/EMI-TFSI (50/50 wt %). However, the cooling curve (after heating to 150°C) was lower than the heating curve may be the result of leaching of imidazole which is melted at 90°C.

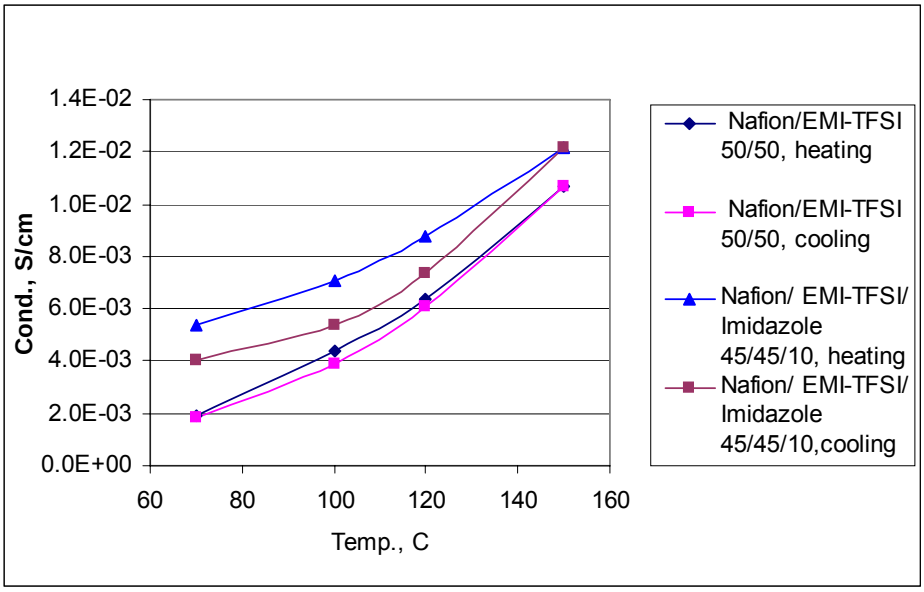

Fig. 64. Conductivity of Nafion™/ EMI-TFSI (50/50 wt%).

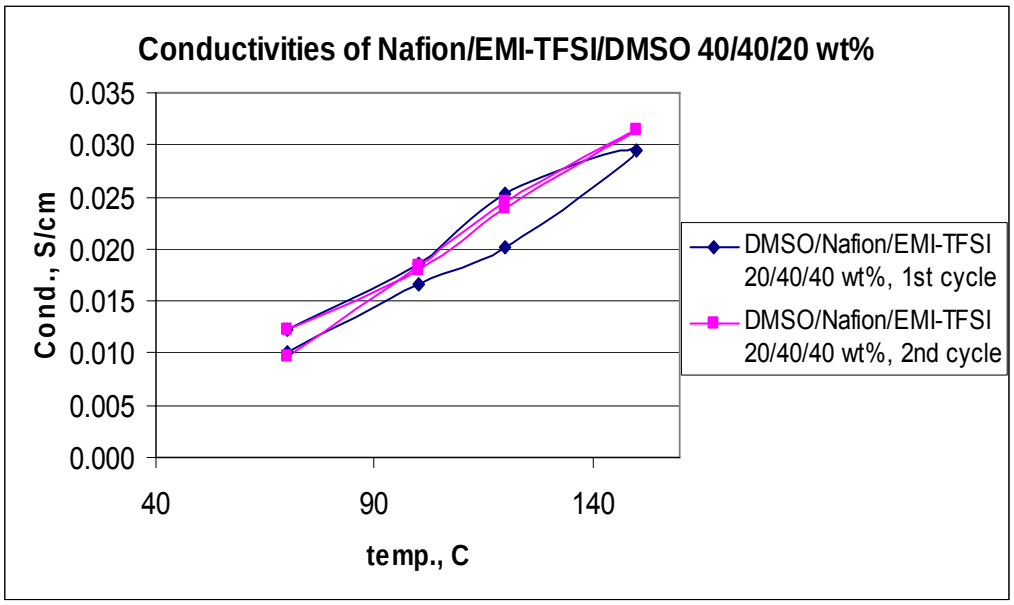

Fig. 65. Conductivities of Nafion™/EMI-TFSI/DMSO 40/40/20 wt%.

Interestingly, a membrane made by Nafion™/EMI-TFSI/dimethylsulfoxide (DMSO) with 40/40/20 wt % provided high conductivity from 0.01 S/cm at 80°C to 0.03 S/cm at 150°C (Fig. 65). That suggested the importance of having a second liquid beyond ionic liquid such as DMSO, imidazole which have high dielectric constants (47) to boost the dissociation of proton from Nafion™ for improving the conductivity. The drawback of using DMSO or other high dieclectric constant organic materials is their water solubility and therefore it is not practical to utilize such additives in fuel cell applications.

Another class of conducting material based on polybenzimidazole (PBI), super-acid and ionic liquid was prepared and evaluated. The PBI was blended with H-TFSI and EMI-TFSI with different mole ratios to form standstill membranes. They were then tested in the same way with Nafion™ using 4pp cell under nitrogen. The conductivities as a function of temperature were showed in figure 15 suggested that a base polymer when blended to an ionic liquid and a fluorinated acid with the right molar ratio could generate a high conducting membrane. Without the fluorinated acid the conductivities of PBI/EMI-TFSI were in the unacceptable ranges. The first heating curve of PBI/ EMI-TFSI/H-TFSI (1/2/4) gave the highest performance – from 0.01 S/cm at RT to 0.08 S/cm at 140°C. But its cooling curve after reaching 160°C was lowered substantially. However, the loss is probably related to the evaporation of water when the testing sample was not completely dried. Importantly, the actual high conductivities of the dried samples in Fig. 66 indicated that ionic liquid was a good candidate for replacing water. A lesson learned from this experiment was that some humidification at medium temperature might be needed to obtain a conductivity of about 10^{-1} S/cm, if required.

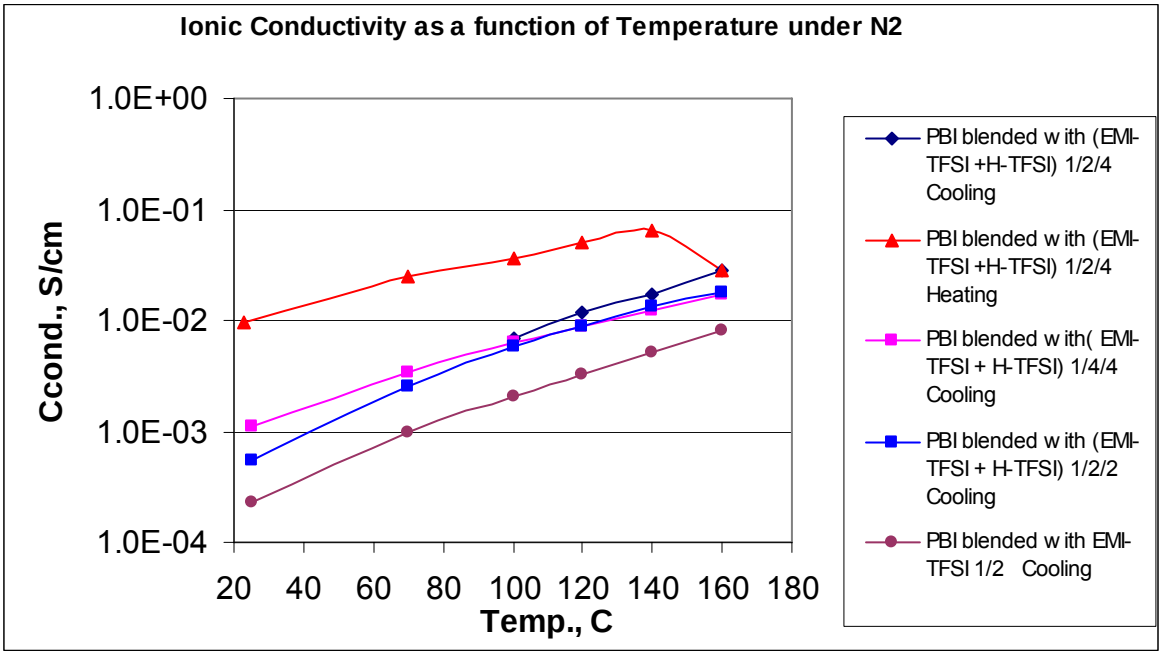

Fig. 66. Ionic Conductivity as a function of Temperature under N_2

3.5.5. Liquid Nafion™ Model

3.5.5.1. Ionic Conductivities of Ionic Liquid And Acid Model With And Without Water

Initial measurements were conducted using a standard commercially available conductivity cell on a neat sample of the EMI-TFSI ionic liquid in a dry box. The material was found to have moderate ionic conductivity (about 10^{-2} S/cm) from room temperature to 110°C (Fig. 67). Since no proton source was present, the moderate ionic conductivity was not due to proton conductivity. Next, incremental amounts of pure, anhydrous $C_4F_9SO_3H$ were added to the ionic liquid up to a total of 180 mole% based on the

number of moles of ionic liquid initially present. With each addition of acid, the components were thoroughly mixed to give a homogeneous solution, and the temperature was allowed to re-equilibrate to RT before the conductivity was re-measured. The resulting plot of conductivity as a function of mole % $C_4F_9SO_3H$ is shown in Fig. 68.

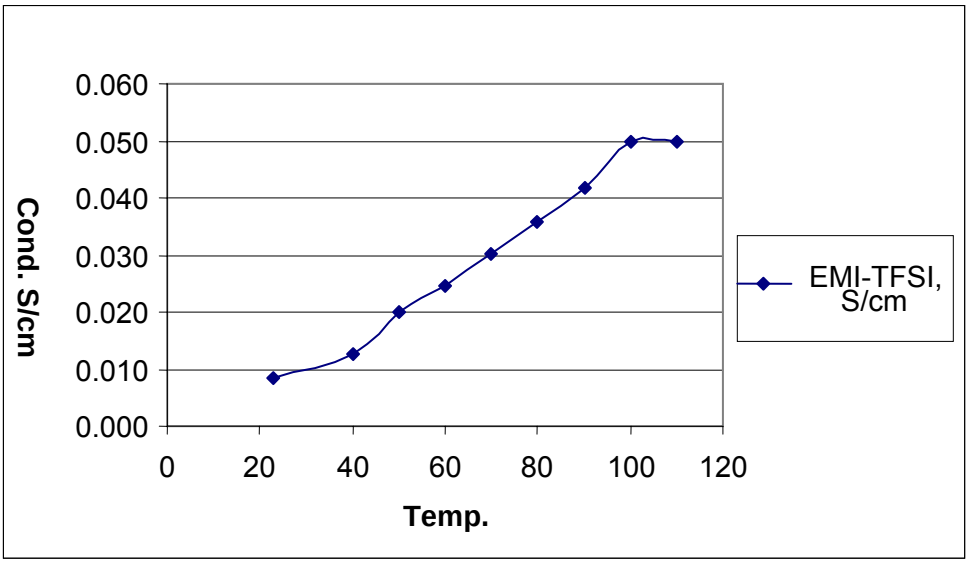

Fig. 67. Conductivity of EMI/TFSI

Surprisingly, the addition of liquid super acid to the ionic liquid causes the conductivity to decrease rather than increase. This suggests that there is little proton conductivity contributed by the acid or any possible adducts formation from the ionic liquid. Essentially, the acid appears to act as nonconductive diluents to the ionic liquid. This is similar to the situation with Nafion™ under dry conditions where the proton conductivity is negligible. The final liquid mixture containing 180 mole % $C_4F_9SO_3H$ in EMI-TFSI was taken out of the dry box and begin adding incremental amounts of water to determine how the mole ratio of water to $C_4F_9SO_3H$ affects the conductivity. The results of this study are shown on Fig. 69 and Fig. 70 (red line).

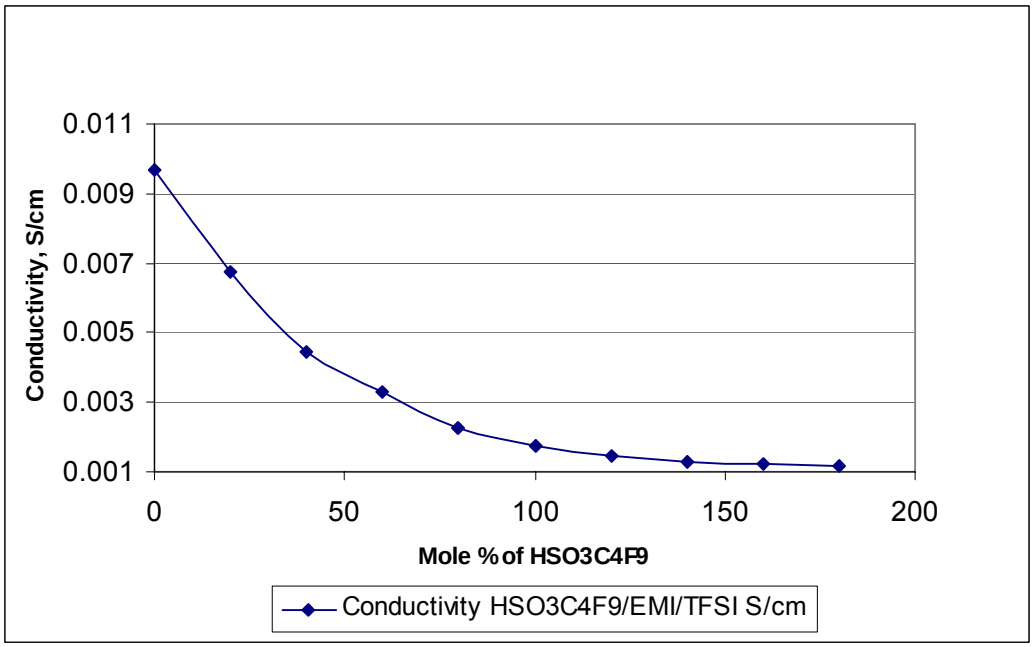

Fig. 68. Conductivity of HSO3C4F9/EMI/TFSI

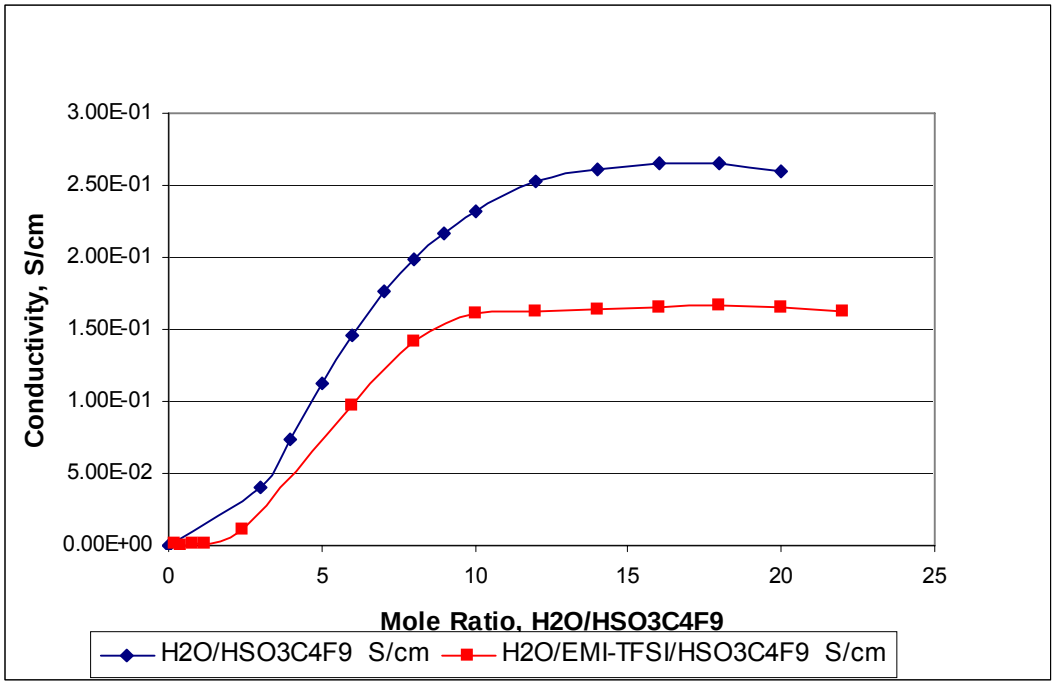

Fig. 69. Conductivity of H2O/EMI-TFSI/HSO3C4F9

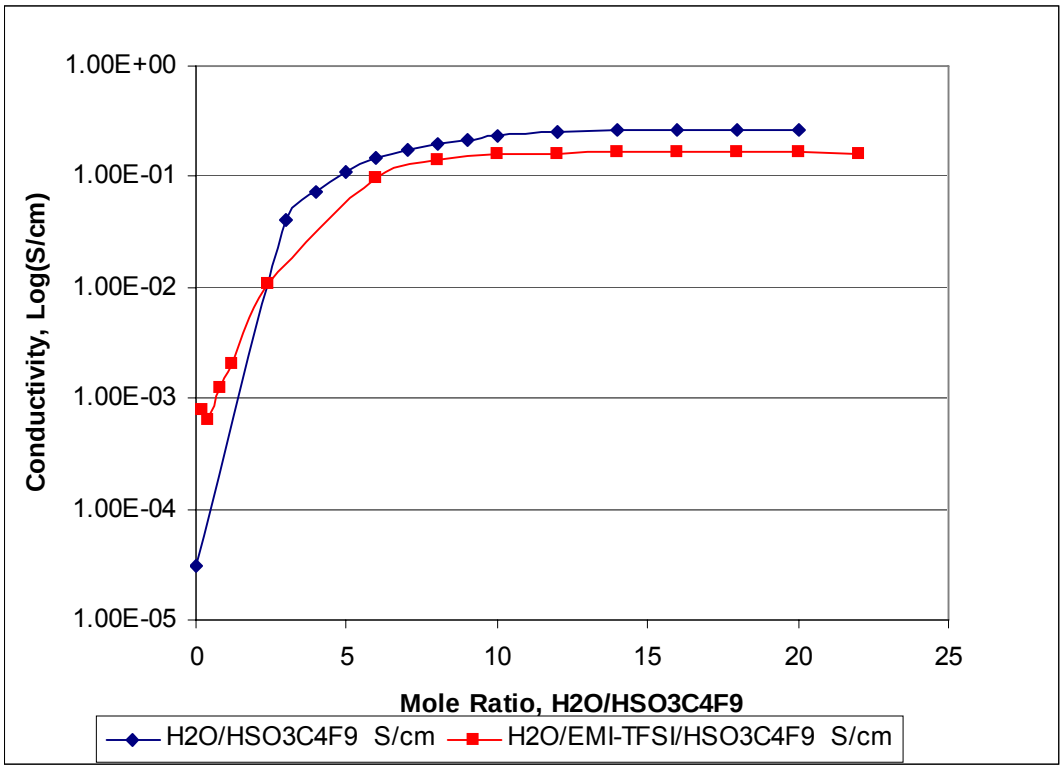

Fig. 70. Conductivity of H2O/EMI-TFSI/HSO3C4F9

Interestingly, minor additions of water were relatively ineffective at raising the conductivity. Only when the mole ratio of water to acid exceeds 2.0 does the conductivity start to increase dramatically and move into a potentially useful range (>/= 10^{-2} S/cm). Similar behavior has been observed at low water levels in Nafion™. At a mole ratio of 6.0, the conductivity of the liquid mixture is 10^{-1}S/cm, close to the value for fully hydrated Nafion™. Further additions of water to the $C_4F_9SO_3H$ / EMI-TFSI mixture resulted in a further increase in conductivity until a maximum conductivity of $1.7x10^{-1}$ S/cm was reached at a mole ratio of about 16. The conductivity of Nafion™ reportedly peaks at a mole ratio of approximately 20 waters per acid site. The dependence of conductivity of this liquid mixture on the mole ratio of water to acid was similar to the reported behavior of Nafion™, strongly suggesting that the liquid mixture may be a useful model system for determining the effect of other conductivity additives (besides water) on Nafion™ conductivity. In this model system, the liquid sulfonic acid, $C_4F_9SO_3H$, mimics the behavior of the perfluorinated sulfonic acid sites of Nafion™ and the ionic liquid serves as an inert liquid matrix to keep the entire composition liquid and homogeneous.

A parallel study was conducted by starting with pure anhydrous $C_4F_9SO_3H$ and measuring the conductivity initially in the dry state and then with incremental additions of water. The results are summarized in Fig. 69 and Fig. 70 (blue line). The general behavior was similar to that observed with the ionic liquid present. In the dry state, conductivity was negligible (around 10^{-5} S/cm). At high water levels (>2:1 water: acid mole ratio) conductivity increased rapidly with increasing water, reaching a maximum of $2.7x10^{-1}$ S/cm at a mole ratio of about 16. At intermediate water levels (mole ratio between 0 and 2) it was not possible to measure liquid conductivity at RT due to

formation of a crystalline solid hydrate. Thus, in this case, one advantage of the ionic liquid containing system is that it enables one to maintain homogeneity and a liquid state throughout a broad composition range. Otherwise the two systems provide similar results and both have potential utility as liquid Nafion™ models. The next step is to use the liquid Nafion™ models to screen the performance of other potential conductivity additives (organic and inorganic) that might have the capability to take the place of water.

3.5.5.2. Ionic Conductivities Of Acid Model With Different Additives

With the same liquid–Nafion™ model, the conductivities of new liquid electrolyte formulations have been measured using the combination of perfluorobutansulfonic acid ($HSO_3C_4F_9$), ionic liquid (EMI-TFSI) and an additive. Chosen high boiling point additives might have potential taking place of water in Nafion™-like membranes. The studies were done in the dry box purged with N_2. EMI-TFSI alone has its own ionic conductivity of $1x10^{-2}$S/cm at RT and $5x10^{-2}$S/cm at 100°C.

Based on the conductivities and solubility from previous studies, one or two different mole ratios were prepared for each additive candidate.

List of additives:

Formamide	$HCONH_2$
Imidazole,	$C_3H_4N_2$
Tetramethylene Sulfone	$C_4H_8SO_2$
Sulfamide	$H_2NSO_2NH_2$
Phenyl ether	$(C_6H_5)_2O$
12-crown-4	$C_{12}O_4$
Guanidine–TFSI	$HNC(NH_2)_2$-$N(SO_2CF_3)_2$
DMSO	CH_3SOCH_3
Nitrobenzene	$C_6H_5NO_2$
p-Nitrobenzenesulfonic acid	$NO_2C_6H_4SO_3H$
1,3-Phenylenediamine	$C_6H_4(NH_2)_2$
Trihydroxybenzene (pyrogallol)	$C_6H_3(OH)_3$
Phenyl sulfone	$(C_6H_4)SO_2$
Sulfanilic acid	$NH_2C_6H_4SO_3H$
4-Hydroxybenzenesulfonic acid	$HOC_6H_4SO_3H$
3-Pyrinesulfonic acid	$NC_5H_4SO_3H$

Although pervious experiments suggested that there was little proton conductivity generated by the liquid acid or any adducts which may form with the addition of ionic liquid, ionic liquid is still considered a good component for high temperature membrane when water is not available. With good thermal and oxidative stabilities as well as low volatility and low water solubility of EMI-TFSI, the utilization of ionic liquid in the membrane may act like a medium for proton transport and help the solubility of

additives. For these specific qualities, EMI-TFSI was chosen to be used in these experiments

Unless an additive was not soluble in $HSO_3C_4F_9$/ EMI-TFSI, both RT and 100°C measurements were carried out. See Fig. 71 and Fig. 72 below for detail results:

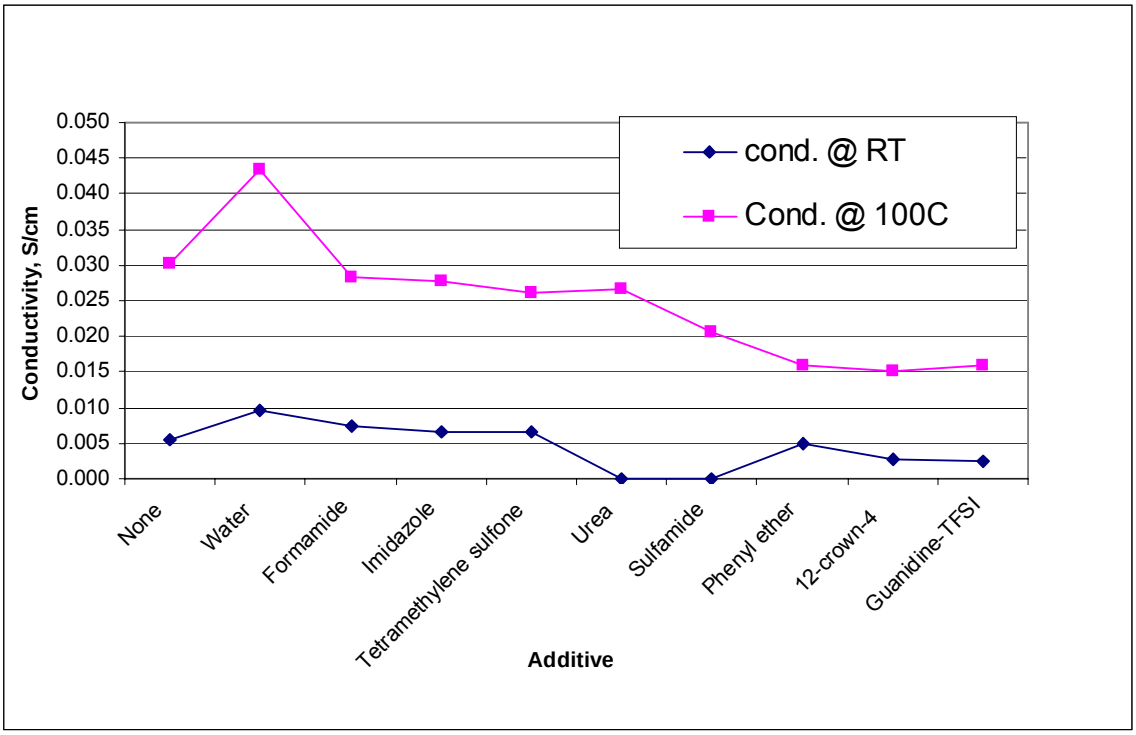

Fig. 71. HSO3C4F9 +EMI-TFSI + Additive (1: 5: 5 mole ratio)

The conductivities of these liquid Nafion™ models with the mole ratios of 1:5:5 (acid/ionic liquid/additive) indicated that only few candidates provided higher ionic conduction at RT but all additives gave lower conduction at 100°C relative to that without additive (Fig. 20). And again, water was still the best additive. Based on the high mole ratio of the EMI-TFSI, its high conductivity probably dominated any effects from other additives. Therefore, the second mole ratios of 1:2.5:5 were prepared to reduce that effect of ionic liquid and to get closer to the practicable wt% for membrane coating when Nafion™/Ionic liquid/Additive formulations are chosen.

Interestingly, the conductivities of the 1:2.5:5 mole ratios showed that at RT and 100°C several additives generated better performance than the control with no additive (Fig. 72). All three good additives (formamide, imidazole and DMSO) have small structures and low MW, which might have kept the viscosity of mixtures low and thus enhanced the conductivity.

A membrane with a reasonable mechanical strength contains 50/50 wt% of Nafion™ / EMI-TFSI has been tested. The conductivities as a function of temperature under dry conditions were measured by using a newly developed technique 4-point probe based on Pt strips polyimide mask. The very linear slopes from the resistances vs. distances of inter-electrodes gave highly reliable converted conductivity data. The good results were

probably due to better contacts between membrane and electrodes created by high ionic liquid wt% and to good design testing technique.

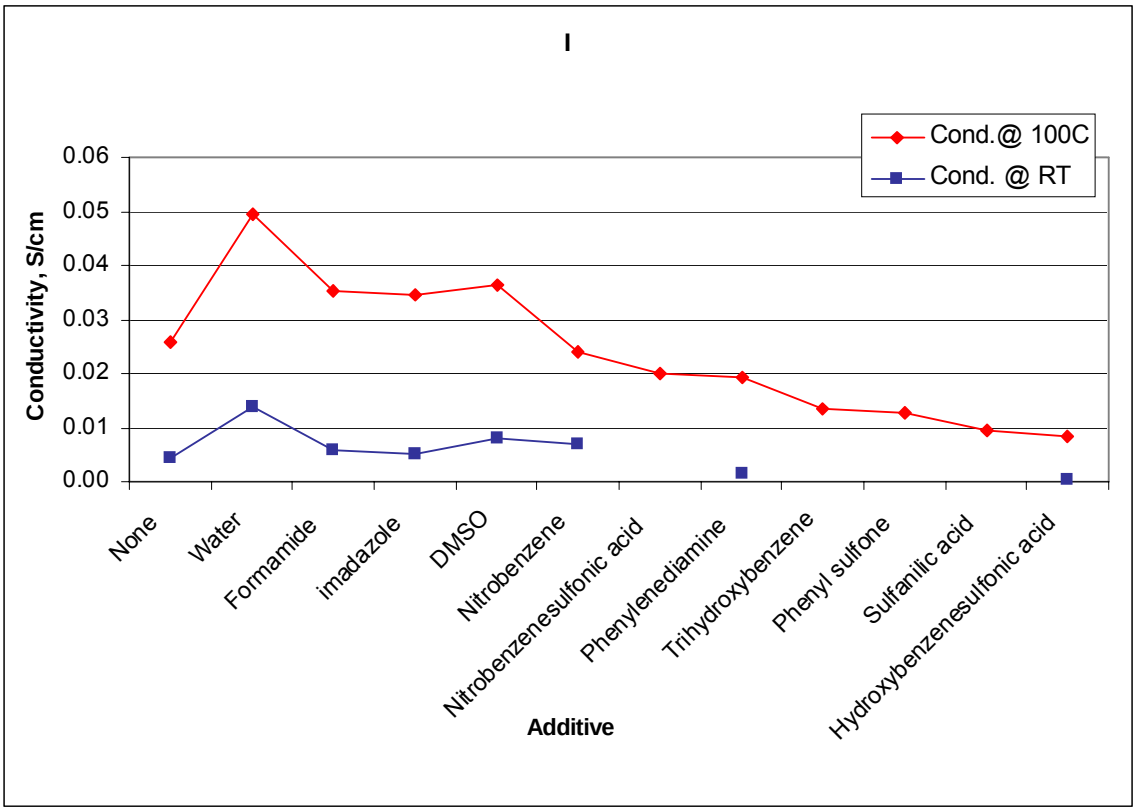

Fig. 72. Ionic Conductivities of HSO3C4F9 + EMI-TFSI + Additive (1:2.5:5 mole ratio)

3.5.6. New Liquid Cell

3.5.6.1. List of Test Electrolytes

As discussed above, the conductivities were measured on the electrolytes with ionic liquids using a standard conductivity cell were ionic conductivities. In order to determine accurately the proton conductivities, the only useful ones in the hydrogen fuel cells, the new liquid cell was designed for these measurements.

A number of ionic liquids (salts) and super acids were chosen for proton conductivity measurements using DC (H pump) technique via the described liquid cell. Some of these salts and acids are solid at RT, but become liquid when a salt is combined with an acid at 85ºC or above.

Ionic liquid
EMI-TFSI
EMI-$N(SO_2C_2F_5)_2$
EMI-$N(SO_2C_4F_9)2$
EMI-$SO_3C_4F_9$

EMI-$C(SO_2CF_3)_3$
ImH-TFSI
Quanidinium-TFSI
Bu_3NMe-TFSI
Bu_4N-TFSI
Bu_4P-TFSI
Bu_4N-O_3SC4F_9
Bu_4P-SO_3C4F_9
Et_3NMe-TFSI
Et_3NMe-$O_3SC_4F_9$

Acid
H-$SO_3C_4F_9$
H-$N(SO_2CF_3)_2$
H-$N(SO_2C_2F_5)_2$
H-$C(SO_2CF_3)_3$
H-$SO_3(CF_2)_2SO_3$-H

3.5.6.2. Proton Conductivity Data

To study how the proton conductivity is correlated to each type of ionic liquid and acid regarding the size, and other physical and chemical properties when they are combined three separate sets of electrolytes were prepared and tested in a dry box. The proton conductivities were plotted as a function of mole percentages of ionic liquid all at 85°C. The first set included EMI-TFSI with different acids such as H-TFSI, H-$N(SO_2C_2F_5)_2$ and H-$C(SO_2CF_3)_3$. Fig. 73 illustrated that H-TFSI acid gave the best proton conductivity at most mole percentages of ionic liquid (in this case it was EMI-TFSI). So the smallest size of H-TFSI acid may contribute to the observed performance. The second set involving H-TFSI acid with different ionic liquids. Fig. 74 showed that EMI-TFSI, when interacted with H-TFSI, was giving the highest proton conductivity among the other ionic liquids such as EMI-BETI, ImH-TFSI, Bu_3N Me-TFSI, Bu_4P-TFSI and Quanidine-TFSI. Note that the only major differences on these ionic liquids were their cations and they all had the same TFSI anion (except EMI-BETI). That suggested that EMI^+ played an important role in this proton conduction mechanism. The third set of tested electrolytes were having the same anion pairs, namely, EMI-TFSI + H-TFSI, EMI-$SO_3C_4F_9$ + H-$SO_3C_4F_9$ and EMI-$C(SO_2CF_3)_3$ + H-$C(SO_2CF_3)_3$. Again, the EMI-TFSI and H-TFSI with TFSI pair was the highest proton conducting system. The low conductivities of the other anion pairs also suggested that having the same anion was not necessary to enhance the proton conductivity, which primarily depends on the type of ionic liquid and acid used.

Some of the above data were combined in the Fig. 77 for comparison. This figure strongly indicated that EMI-TFSI + H-TFSI is the best conducting mixture, followed by EMI-TFSI + H-$N(SO_2C_2F_5)_2$ and EMI-TFSI + H-$C(SO_2CF_3)_3$. Most combinations suggested that very high levels of ionic liquid are needed to achieve highest possible proton conductivity (between 80 to 90 mole %). Only one exception is ImH-TFSI + H-TFSI which peaked at 50 mole %. The study results showed that EMI-TFSI ionic liquid, which is chemically stable with a high boiling point, has a good potential of replacing water. The proton conductivity is up to $10x^{-2}$ S/cm range when 90 mole % of EMI-TFSI is added to 10 mol% of H-TFSI. That is a significant improvement when compared to

presumably no or very low proton conductivity of H-TFSI without additive. The proton transport mechanism for these ionic-liquid/ acid systems was specifically studied by 3M Case Western Reserve University using Pulsed-Field Gradient Spin-Echo NMR as described in Appendix B and Modeled by the University of Minnesota as described in Appendix C.

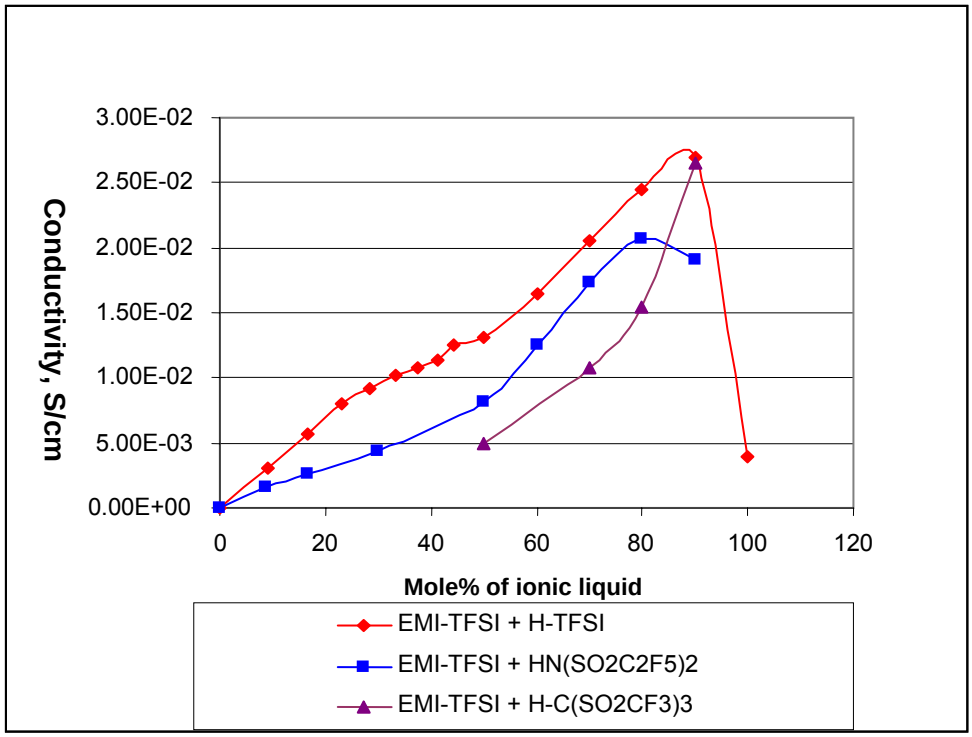

Fig. 73. Proton conductivities of EMI-TFSI with different acids at 85ºc

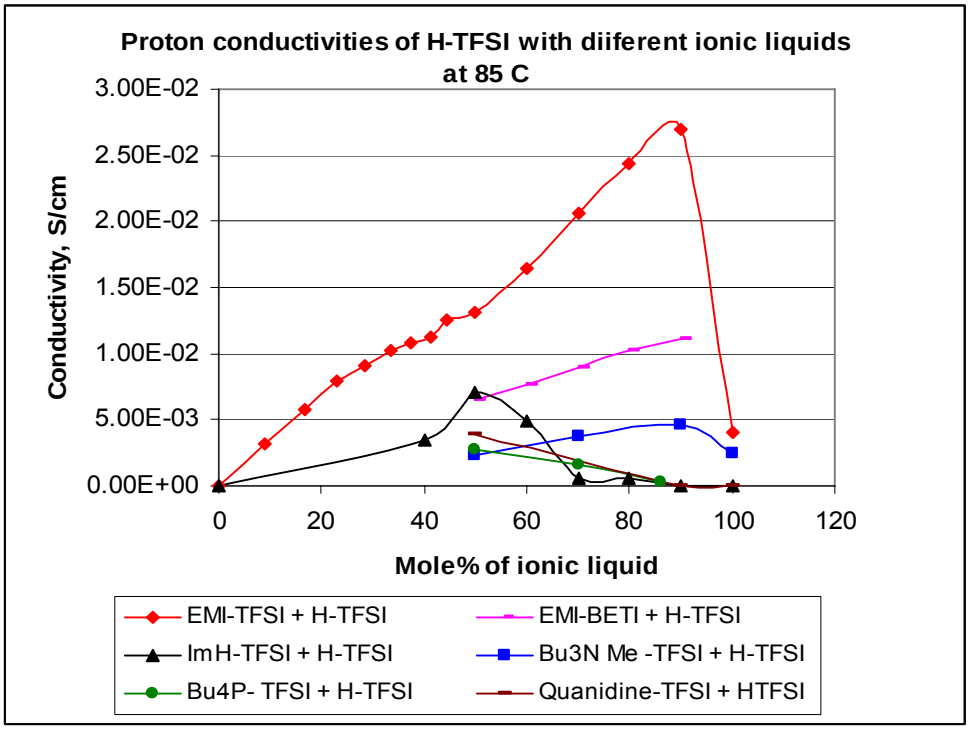

Fig. 74. Proton conductivities of H-TFSI with different ionic liquids at 85ºC.

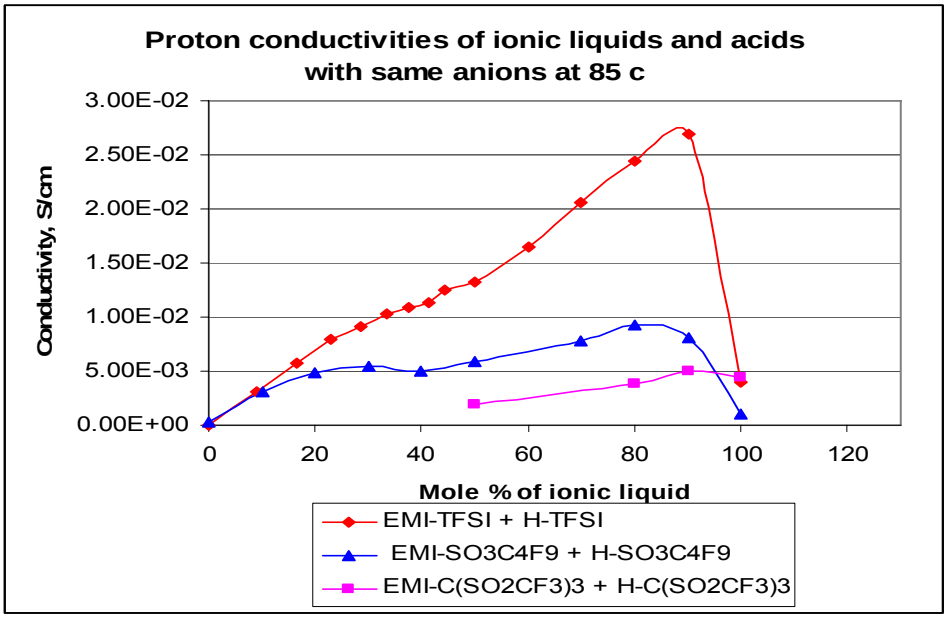

Fig. 75. Proton conductivities of ionic liquids and acids at 85ºC

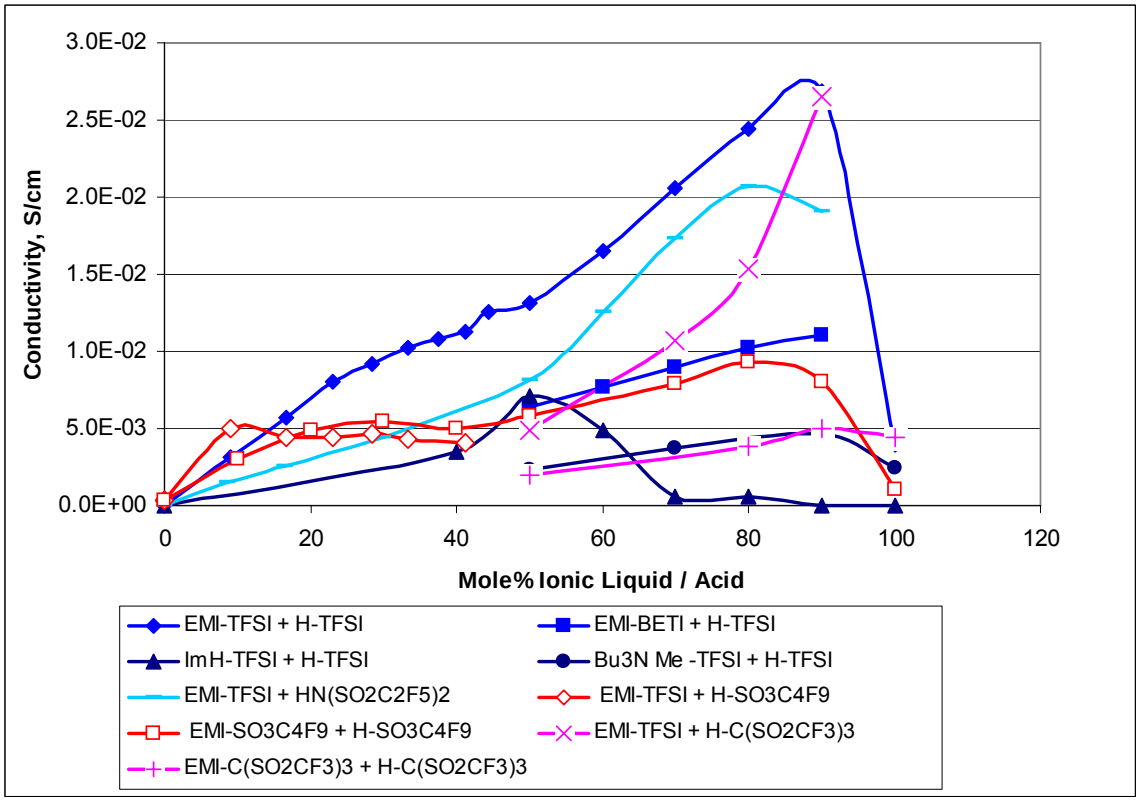

Fig. 76. Conductivity vs. Mole% Ionic Liquid

3.5.6.3. Proton conductivity of Ionic liquid /Acid vs. temperature

To learn the effects of temperature on proton conductivity of ionic liquid/acid, the liquid cell was heated from standard testing temperature of 85 to 120°C. The DC impedances were measured from the voltage-current curves using the same method for 85°C (under H_2). The results from Fig. 74 show that the proton conductivity increased linearly with higher temperatures but the degree of increasing depended on the level of ionic liquid added. The mixture with less ionic liquid yielded a smaller increase on conductivity at higher temperature. A double conductivity was observed with the H-TFSI/EMI-TFSI (10/90 mole %) mixture from 23 mS/cm at 85°C to 40 mS/cm at120°C.

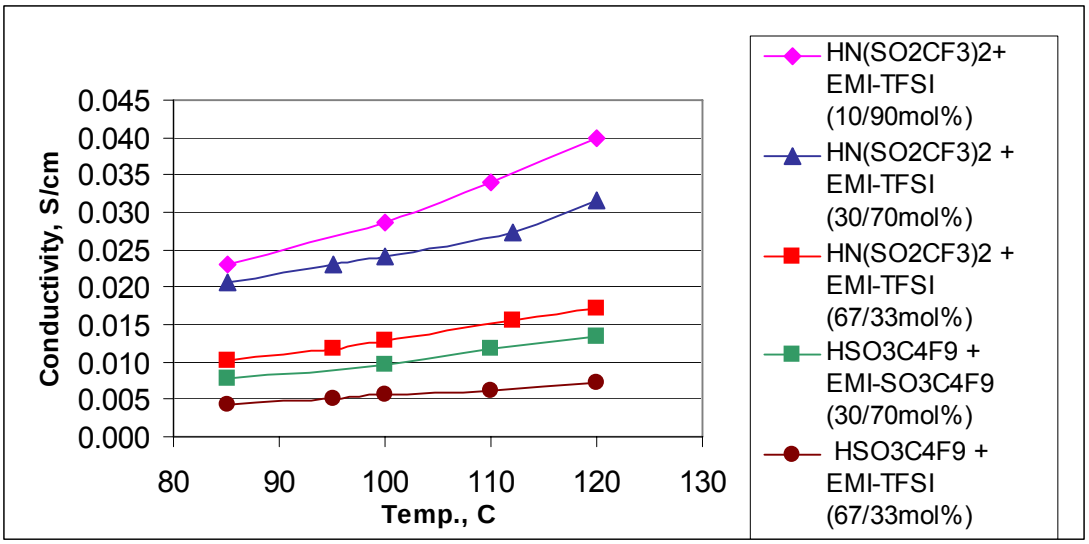

Fig. 77. Proton Conductivity of dry Acid / Ionic liquid as a Function of Temperature under H_2.

3.5.6.4. Proton conductivity of Ionic liquid /Acid as a function of water

The effects of water on proton conductivity was also studied using the best conducting mixture by adding water to the EMI-TFSI/ H-TFSI (90:10 mole ratio) from 0 to 20 mol ratio (of water /acid). However, up to 5 mole ratio of water, its conductivity did not change (Fig. 75). Surprisingly, much higher amount of water (15 mole ratio) was needed for the conductivity to peak at 33 mS/cm, about a 40% increase. The incompatibility between ionic liquid and water as well as the dominant amount of ionic liquid in the mixture may contribute to the poor effect of water on conductivity.

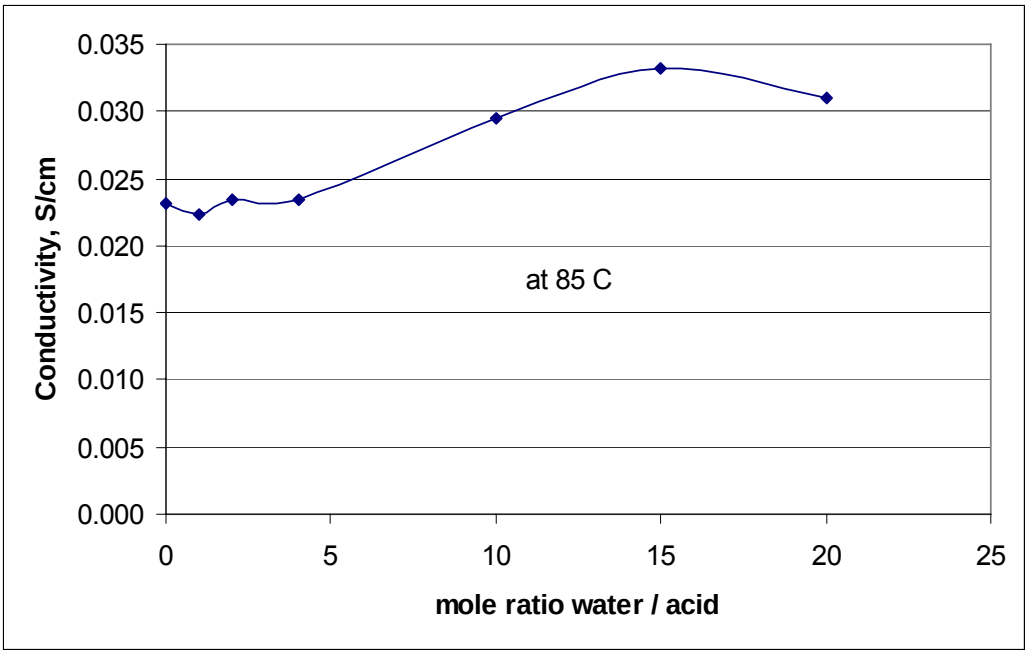

Fig. 78. Proton Conductivity of EMI-TFSI/ HTFSI (90:10 mole ratio) as a function of water/acid ratio

3.5.7. Relationship Between Conductivity, Viscosity and Temperature

The results from Fig. 76 suggest that EMI-TFSI has the lowest viscosities compared to the other ionic liquids at all tested temperature. For example, the viscosities of EMI-TFSI, EMI-$SO_3C_4F_9$ and EMI-$C(SO_2CF_3)_3$ are 25, 237, 2769 Cp at 20°C and 5, 20, 211 Cp at 85°C, respectively (note: 85°C was the temperature used for proton conductivity measurements in the liquid cell). The low viscosity of EMI-TFSI may partly explain for the highest ionic and proton conductivity when tested alone or with super-acids.

The viscosities of ionic liquids and acids with different mole ratios were also measured using the same technique as described above for ionic liquids. Interestingly, at low temperatures for the EMI-TFSI / H-TFSI and EMI-$C(SO_2CF_3)_3$ / H-$C(SO_2CF_3)_3$, the higher the ionic liquid level the lower the viscosity, but there is almost no differences on viscosity at high temperatures (Fig. 78 and Fig. 79).
The relationship between conductivity and viscosity is even more profound when the comparison is made for three sets of mixtures (Fig. 79). With different mole ratios of the most interesting ionic liquid/acid system (EMI-TFSI/ H-TFSI) their viscosities revealed that at low temperature the higher mole ratio of ionic liquid created the lower viscosity. It was mainly due to the liquid form of ionic liquid and the solid state of acid at ambient temperature. However, when the mixtures of ionic liquid/acid were heated to above 60°C they became clear liquid solutions and their viscosities were very similar.

The viscosity of three sets of ionic-liquids and super-acids with different mole ratios were also selectively measured at 85°C. They were EMI-TFSI/ H-TFSI, EMI-$SO_3C_4F_9$/ H-$SO_3C_4F_9$ and Bu_3NMe-TFSI/ H-TFSI. The

Fig. **81** (where the conductivity and viscosity as a function of mole ratio were plotted) revealed two interesting behaviors:
a) There were no significant changes on viscosity with different mole ratios of the same ionic-liquid/acid system; b) The smaller molecules like EMI-TFSI and H-TFSI gave the lower viscosity, and the lower viscosity system gave the higher proton conductivity

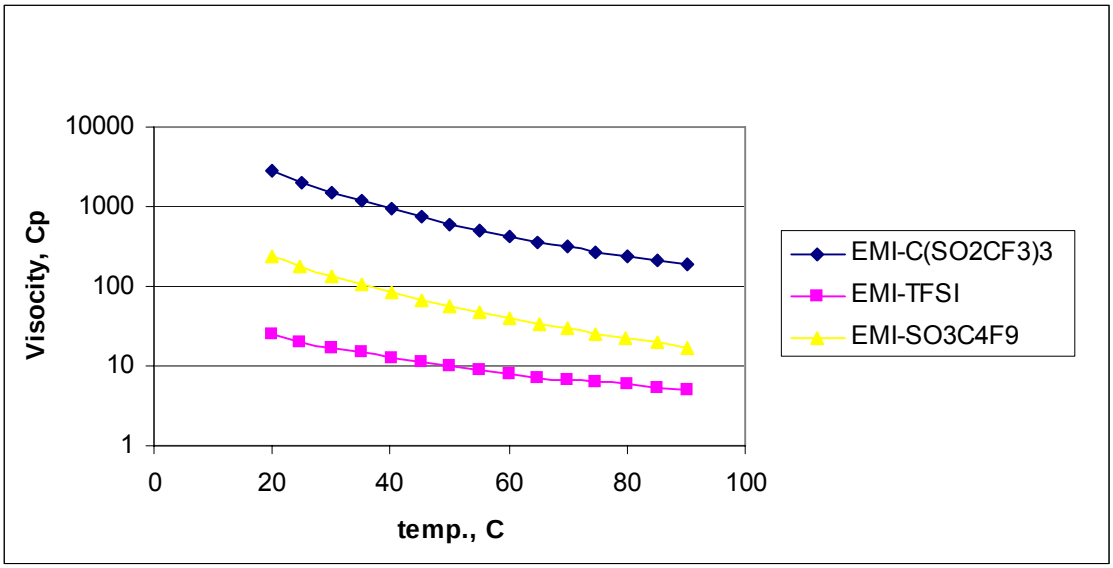

Fig. 79. Viscosity of ionic liquid vs. temperature

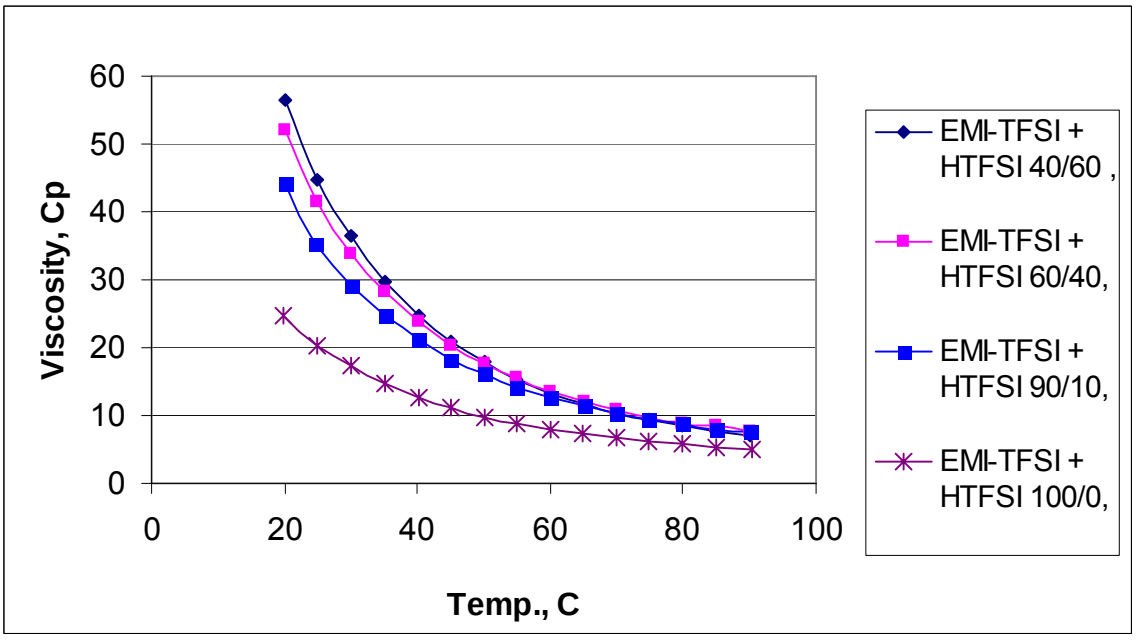

Fig. 80. Viscosity of EMI-TFSI/H-TFSI

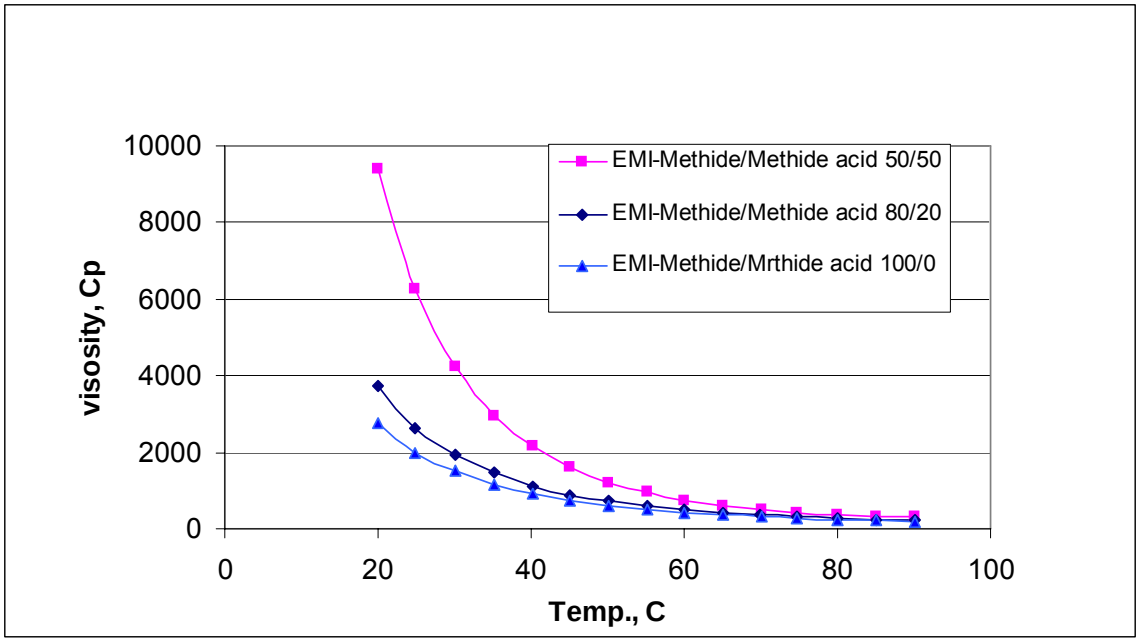

Fig. 81. Viscosity of EMI-$C(SO_2CF_3)_3$ /$HC(SO_2CF_3)_3$

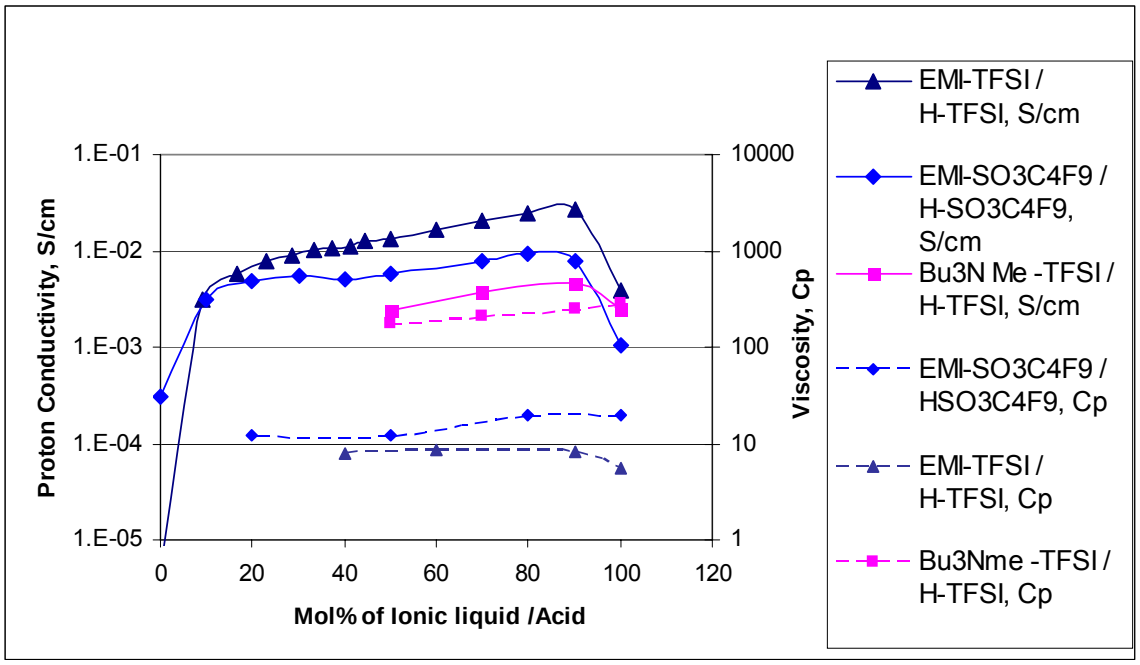

Fig. 82. Relationship between viscosity and proton conductivity at 85ºC

[1] Savadogo, S., *J. New Materials for Electrochemical Systems*, ***1***, 47-66 (1998).
[2] a) J. J. Fontanella, M. C. Wintersgill, J. S. Wainright, R. F. Savinell and M. Litt, *Electrochimica Acta*, ***43***, 1289-1294 (1998). b) K. D. Kreuer, A. Fuchs, M. Ise, M. Spaeth and J. Maier *Electrochimica Acta*, ***43***, 1281-1288 (2000). c) M. Bhamidipati, E. Lazaro, F. Lyons and R. S. Morris, *Mat. Res. Symp. Proc., **496,*** 217-222 (1998).
[3] K. A. Maritz, *Materials Science and Engineering, **C6,*** 121-133 (1998).

[4] D. A. Boysen, C. R. I. Chisholm, S. M. Haile, and S. R. Narayanan, *J. Electrochem. Soc.*, ***147*** 3610-3613 (2000).
[5] *Materials Research Society Proc. 435*, "Better Ceramics Through Chemistry VII: Organic/Inorganic Hybrid Materials," Ed. B. K. Coltrain, C. Sanchez, D. W. Schaefer, and G. L. Wilkes (1996).
[6] M. W. Ellsworth and B. M. Novak, *J. Am. Chem. Soc.* ***113,*** 2756-2758, (1991).
[7] F. M. Vichi, M. T. Colomer, and M. A. Anderson, *Electrochem. and Solid State Lett.*, **2** [7] 313-316 (1999).
[8] G. Alberti and M. Casciola, *Solid State Ionics*, **97** 177-186 (1997).
[9] A. J. Appleby, O. A. Velev, J-G. LeHelloco, A. Parthasarthy, S. Srinivansan, D. D. DesMarteau, M. S. Gillette and J. K. Ghosh, *J. Electrochem. Soc.,* ***140,*** 109-111 (1993).
[10] a) E. Peled, T. Duvdevani and A. Melman, *Electrochemical and Solid State Letters,* ***1,*** 210-211, (1998). b) M. Doyle, S. K. Choi and G Proulx, *J. Electrochem. Soc.,* ***147,*** 34-37 (2000).
[11] a) A. J. Appelby and B. S. Baker, *J. Electrochem. Soc.,* ***125,*** 404- (1978). b)R. T. Atanasoski, W. E. O'Grady and C. E. Shea, *J. Electroanal. Chem.,* ***219,*** 347-353 (1987).
[12] K. A. Stiebel, P. C. Andricacos, E. J. Cairns, P. N. Ross and F. R. McLaron, *J. Electrochem. Soc.,* ***132,*** 2381-2384 (1985).
[13] H. Saffarian, P. Ross, F. E. Behr, G. L. Gard, *J. Electrochem. Soc.,* ***137,*** 1345-1348 (1990).
[14] L. Qingfeng, H. A. Hjuler and N. J. Bjerrum, *Electrochimica Acta*, ***45***, 4219-4226 (2000).
[15] V. R. Koch, C. Nanjundiah and R. T. Carlin, U. S. Patent 5,827,602..
[16] a) J. E. Wadell, W. M. Lamanna, G. G. I. Moore and S. J. Hamrock, US Patent 5,514,493. b) R. D. Howels, W. M. Lamanna, A. D. Fanta and J. E. Waddell, U. S. Patent 5,874,616. c) S. J. Hamrock and P. Pham, U. S. Patent 6, 063,522. d) S. S. Mao, S. J. Hamrock and D. Ylitalo, U. S. Patent 6,090,895.
[17] Q. Li, R. He, J. O. Jensen, and N. J. Bjerrum, *Chem. Mater.* ***15*** 4896-4915 (2003).
[18] O. Nakamura, T. Kodama, I. Ogino, and Y. Miyake, *Chemistry Letters*, pp. 17-18 (1979).
[19] Y. S. Kim, et al., *J. Membrane Sci*, ***212*** 263-282 (2003).
[20] L. A. Fisun and V. N. Pak, *Russ. J. Appl. Chem.* 65 [2] 213-216 (1992).
[21] J. S. Beck, *et al.*, *J. Am. Chem. Soc.* ***114*** 10834-10843 (1992).
[22] A. Stein, B. J. Melde, and R. C. Schroden, *Adv. Mater.* ***12*** [19] 1403-1419 (2000).
[23] D. Margolese, J. A. Melero, S. C. Christiansen, B. F. Chmelka, and G. D. Stucky, *Chem. Mater.* ***12*** 2448-2459 (2000).
[24] S. L. Burkett, S. D. Sims, and S. Mann, *Chem. Commun.* 1367-1368 (1996).
[25] R. K. Iler, *The chemistry of silica,* New York: Wiley, 1979.
[26] G. Alberti, M. Casciola, *Solid State Ionics* ***97***, 177–186 (1997).
[27] A. Clearfield, J. Stynes, *J. Inorg. Nucl. Chem.* ***26***, 117–129 (1964).
[28] G. Alberti, E. Torracca, *J. Inorg. Nucl. Chem*. ***30***, 317–318 (1968).
[29] A. Clearfield, A.I. Bortun, L.N. Bortun, J.R. Garcia, *Inorg. Chem. Commun*. ***1***, 206–208 (1998).
[30] A. Anderson, P. Norby, J. Hanson, T. Vogt, *Inorg. Chem*. ***37***, 876–881 (1998).
[31] G. Alberti, M. Casciola, U. Constantino, R. Vivani, *Adv. Mater*. ***8***, 291–303 (1996).
[32] G. Alberti, M. Casciola, U. Costantino, M. Leonardi, *Solid State Ionics* ***14*** 289–295 (1984).
[33] M. Casciola, D. Bianchi, *Solid State Ionics* 1985, **17**, 287–293.
[34] D. Carriere, M. Moreau, K. Lhalil, P. Barboux, J.P. Boilot, *Solid State Ionics*, ***162***, 185–190 (2003).
[35] G. Alberti, M. Casciola, U. Costantino, A. Peraio, E. Montoneri, *Solid State Ionics*, ***50***, 315–322 (1992).
[36] E.W. Stein Sr., A. Clearfield, M.A. Subramanian, *Solid State Ionics* ***83***, 113–124 (1996).
[37] Doyle, et. al., *J. Electrochem. Soc.*, ***147*** 34-37 (2000).

[38] A solution of 1.40 g of EMI TFSI in 14.00 g of n-PrOH was added incrementally with mixing after each addition to 20.00 g of Nafion™ SE20042 (about 21 % ionomer).
[39] F. M. Vichi, M. Teresa, and M. A. Anderson, Electrochemical and Solid-State Letters, ***2*** 313-316 (1999).
[40] E. Peled, T. Duvdevani, A. Melman, Electrochemical and Solid-State Letters, ***1,*** 210-211 (1998).
[41] E. Peled, T. Duvdevani, H. Melman, US patent 6,811,911.
[42] Ibid.
[43] W. E. O'Grady, NTIS Publication PB86201084 (U.S. Department of Commerce), 1986.
[44] M. Razaq, A. Razaq, E. Yeager, NTIS Publication PB89178768 (U.S. Department of Commerce), 1989.
[45] A. J. Appleby, D. DesMarteau, V. Jalan, S. Srinivasan, M. S. Gillette, J. K. Gosh, A. Parthasarathy, E. R. Gonzalez, D. Deshai, NTIS Publication DE95015701 (U.S. Department of Commerce), 1992.
[46] R. F. Savinell, M. H. Litt, US patent 6,099,988
[47] 3M Porous Film Department RR #1580, 0.9 mil thick measured at 7.3 psi, 4.3 sec/50 cc Gurley number using a 28 oz. cylinder, 0.804 micron mean pore size, and bubble point pore size of 1.3 micron
[48] For initial experiments, ePTFE of about 5 mil thick measured at 7.3 psi. A roll of this material was provided by 3M Porous Film Department. The origin was not known. For later experiments, thinner ePTFE of about 1.5 mil from Tetratec was used.
[49] T, Zawodzinski et al, *Solid State Ionics* ***60*** 199-221 (1993).
[50] D Simonsson et al, *J. Electrochem. Soc*, ***143***, (1996).

3.5.8. Conclusion

Reliable testing methodologies were successfully developed for conductivity measurements on both solid (membrane) and liquid (electrolyte) forms. Many ionic liquids were added to small acid molecules as liquid Nafion™ models or to polymers with and without other second additives. The liquid electrolytes were measured in the liquid cells and the cast solid membranes were tested in the two or four-point probes. Good ionic conductivities from membranes and proton conductivities from new liquid electrolytes were obtained. The highest level was 0.04 S/cm given by EMI-TFSI/ H-TFSI (90/10 mole ratio) mixture and in the range of 10^{-2} S/cm on some ionic liquid containing membranes without water, which was sufficient for high temperature fuel cell operation requirements. The achieved conductivities in this study were also in the target range of DOE 3 contract. The big drawback, however, of using these ionic liquids-- mainly due to their liquid properties--might be their leaching from the membranes which will cause them to end up in the catalyst or gas diffusion layers of membrane catalyst assemblies. If the leaching of ionic liquids is significant, the conductivities of membranes will be decreased over time and the surface areas of active catalysts will be reduced as well which lead to lower fuel cell performances. This suspected behavior and how to control it in fuel cell need to be studied carefully before a meaningful conclusion can be made on their utilization for high temperature fuel cell applications.

Section 4

MEA Scale-up and Stack Testing

Section 4 - MEA Scale-up and Stack Testing

This section reviews the work done under Task 3 on scale-up and fabrication of the MEAs for operation in the temperature range of 85 ≤ T ≤ ~ 120°C for stack testing in a 5kW rated short stack.

Section 4 Table of Contents

4.0 Introduction

This section has two major parts. The first summarizes the work done on scale-up activities for fabricating the down-selected NSTF catalysts and membranes discussed in section 2.3 of this report. The catalysts, the membranes and the CCMs formed from them were all processed as roll-goods, consistent with high volume manufacturing processes.

The second and larger part of this section reviews all the results from the short stack testing of 7-layer MEAs with integrated gaskets made from those roll-good fabricated CCMs and down-selected GDLs discussed in section 2.3.

Performance and durability evaluation of the delivered 5kW stack occurred at a 3M test facility in Menomonie, WI between May 21st and June 30th, 2007. Testing occurred under the supervision of Dr. Ira Bloom, Mr. Lee Walker, and Mr. John Basco, members of the Fuel Cell Test group at Argonne National Laboratory. The resultsfrom the 5kW and smaller stack builds leading up to the final stackt tests are reviewed in detail.

Under a durability stress test lasting over 554 hours, the average per-cell stack performance decreased 8 $\pm$ 4mV at 0.1A/cm^2 and 17$\pm$ 22 mV at 1.2 A/cm^2 under reference conditions. During the experiment, the stack unipolar plates corroded significantly; after semi-quantitative removal of the estimated ohmic loss contribution induced by this corrosion, the per-cell stack performance decreased by just 6$\pm$3 mV and 0.1$\pm$15 mV at 0.1 and 1.2 A/cm^2, respectively, over the 554 hours.

Post mortem analysis of the MEAs and stack separator plates were completed after the closing date of the contract, but are included here for completeness. These results indicated that the primary sources of performance loss were due to contamination of the MEAs with high levels of Ni from failure of the stack unipolar plate corrosion-resistant coating. This contamination resulted in a 30% decrease of the specific activity for the test MEAs, and an approximate 20% and 50% reduction in limiting current for the typical and most degraded MEAs, respectively. No significant loss of Pt catalyst surface area was noted for either MEA.

The stack plate technology and flow field design used for these tests were developed outside this contract and were not a developmental task under this contract.

Section 4.1 Scale-up and Process Optimization

4.1.0 Introduction

The processes for fabricating the NSTF catalyst coated membranes are signficantly different from those required to fabricate dispersed ink coated membranes or catalyst coated GDL's. At the most basic level the same three components are required to synthesize, disperse and coat a layer of catalyst, viz. a source of Pt, some type of powdered material to support the catalyst, and a substrate on which to coat a layer of the dispersed or supported catalyst. Fig. 1 illustrates these differences in a simple process flow diagram for the conventional carbon supported wet-chemical dispersed Pt catalysts, on the left, and the NSTF catalyst on the right. The number of major process steps for the NSTF are significantly fewer due to the fundamental nature of vacuum coating and growth of the NSTF support whisker that is made from the organic pigment compound PR149 (CAS 4948-15-6). Similarly the vacuum sputtering process preferred for application of the catalyst to the whiskers is fully consistent with the process for coating the support whiskers such that they can both be done in a single process step. Other advantages of the thin film approach have been discussed in reference [1] of section 2.1.3.

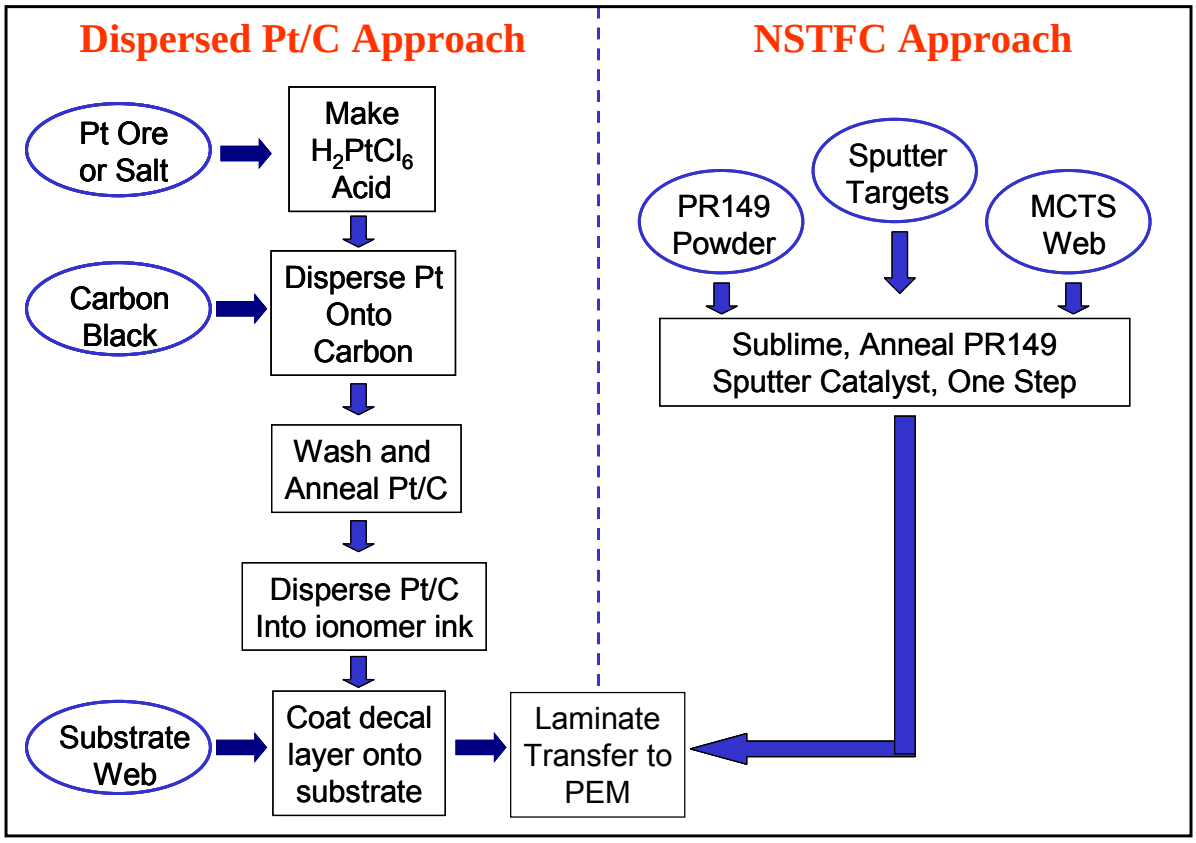

Fig.1. Comparison of basic process flow steps to make NSTF and conventional catalysts.

The MCTS web (microstructured catalyst transfer substrate) is the substrate that the whiskers are deposited on and represents the first article requiring scale-up in the fabrication process of an NSTF coated membrane. The whisker support coating on the MCTS and catalyst coating on the whiskers are the next fabrication processes, which although they occur at the same time, require separate process scale-up development. Finally, the bringing the anode and cathode

catalyst coated MCTS webs together with a membrane to form the final CCM (catalyst coated membrane) is the final process step for scale-up development. The following subsections summarize the work completed in part under this contract, to scale-up the down-selected NSTF catalysts and membrane described in sections 2.1.3 and 2.3.

4.1.1 NSTF Process Steps

Scale-up of the NSTF CCM roll-good using the down-selected catalysts and membrane required development and optimization of five separate process steps. The process by which NSTFCCM is made starts with the fabrication of a microstructured catalyst transfer substrate, or MCTS, roll good. The MCTS is coated with the organic pigment (PR149-perylene red) which gets converted into nanostructured catalyst support whiskers by a thermal process and then coated with a ternary catalyst in the next two steps. A proton exchange membrane is made by casting a dispersion of the 3M ionomer using 3M proprietary coating equipment to form a 1.4-mil thick membrane. Roll-to-roll transfer of the catalyst coated NSTF support whiskers onto either side of a proton exchange membrane occurs in the final step to produce the NSTFCCM roll-good. These basic steps are shown in Fig. 2.

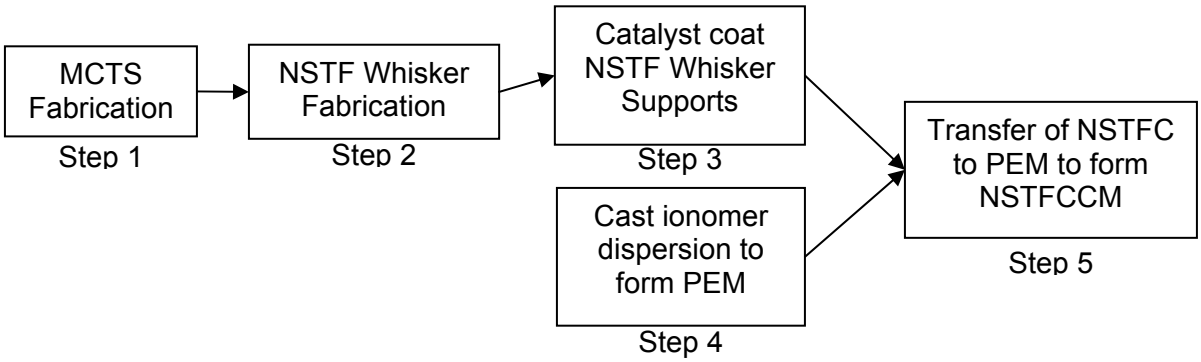

Fig. 2. Process steps in fabricating the NSTF CCM.

4.1.1 Microstructured Catalyst Transfer Substrate (MCTS)

The MCTS roll good is a film comprising a microstructured cured acrylate coating which supports and protects nanostructured catalyst support whiskers prior to their transfer to a proton exchange membrane and provides increased catalyst surface area. At the onset of this contract, this product required both formulation and process changes to reliably produce roll good substrate that complied with TSCA standards, was within specification, and producible at high yield rates. After over a dozen experiments and process runs, the product is fully TSCA compliant, and the process has produced over 16,000 sq. ft. (3.1 miles) of MCTS roll good with yield rates moving from an average of 35% at DOE3 start to over 96% for the last half of the quantity produced.

4.1.2 NSTF Catalyst Support Whiskers

Scale-up of the process for fabricating NSTF catalyst support whiskers began under the preceding contract to the present one, with an end result of a single pass coating and annealing process to produce what is now known as standard NSTF catalyst support substrate. Under the current contract, over 50 process runs and experiments were conducted. Utilizing the protocol previously established under the predecessor contract, over 6300 sq ft of standard material was

produced. Additionally, new protocols have been established to vary NSTF whisker attributes such as length and number density, producing the longest whiskers to date, and setting the stage for customized whisker geometries suited to various NSTF catalyst compositions for optimized fuel cell performance (see section 2.1.3.1.4)

4.1.3 NSTF Catalyst

The ability to reliably coat long lengths of NSTF whiskers with a variety of metal catalysts is well established. Over the course of this contract a total of 66 process runs and experiments were performed, producing 5400 linear feet of NSTF catalyst with 7 different compositions involving different binary and ternary catalysts and various overall catalyst loadings. This work provided NSTF catalyst for several laboratory research activities done under the contract, as well as the process scale up of NSTFCCM and generation of materials for the short stack testing in section 4.2.

4.1.4 Proton Exchange Membrane

A number of improvements were made to the process for making proton exchange membrane that is best suited for use with NSTF catalyst. Several trials of various dispersions were explored to identify a formulation that eliminated the need for specialized cleaning of the membrane prior to use with NSTFC and reduced thermal cycling (see section 2.3). The casting process also evolved over the course of the contract, arriving at a protocol for producing membrane of uniform caliper and good mechanical strength on pilot equipment capable of batch sizes of hundreds of lineal feet, and of the same type as manufacturing equipment capable of batch sizes of thousands of lineal feet.

4.1.5 NSTF CCM

The process by which NSTF catalyst is transferred to the membrane underwent the greatest amount of development under this contract. At the start of the contract, NSTF CCM fabrication was done using a pilot line owned by another organization within 3M. The pilot line had limited control over key process parameters and web handling. Transfer of this process to a Fuel Cell owned manufacturing line was a key milestone. To achieve this transition, five designed experiments were conducted to explore, define, and optimize the NSTF catalyst transfer process on the Fuel Cell Program pilot line. Using protocol defined in the experimental runs, 13 additional qualification runs were conducted to demonstrate repeatability of the process. Approximately 1300 lnft of NSTF CCM was made, including NSTF CCM used in the final fuel cell stack builds described in the following section. Further, NSTF CCM of sufficient width has been made which allows for 100% utilization of the NSTF catalyst roll good width. Throughput improvements of as much as 300% have also been demonstrated. Table I summarizes the process scale-up activities.

Fig. 3 illustrates the performance of a typical roll-good fabricated CCM in a 50 cm^2 cell.

Table I. NSTF Process Scale Up and Optimization – AT-A-GLANCE

Process Step	Number Exper/Runs	Footage Produced	Greatest Advancement in Contract Period
MCTS	13	16,000	▪ Reformulated product for TSCA compliance ▪ Defined protocol for reliable production, increasing yields from less that 40% to greater than 96%.
NSTF Whiskers	50	6,300	▪ Demonstrated repeatability of process for making standard NSTF whisker substrate ▪ Gained deeper understanding of process to arrive at NSTF whiskers of specific geometries.
NSTF Catalyst	66	5,400	▪ Produced all “rev 1” NSTF catalyst roll-good in support of all contract sub-tasks, with high repeatability (see Fig. 4).
PEM	23 (est)	2,400 (est)	▪ Defined dispersion for optimized performance with NSTF catalyst ▪ Defined casting process on pilot line of same form as manufacturing lines used for other fuel cell membrane casting.
NSTFCCM	18	1,300	▪ Qualified process on manufacturing equipment producing high performing NSTF CCM, including material used in final fuel cell stack builds and testing.

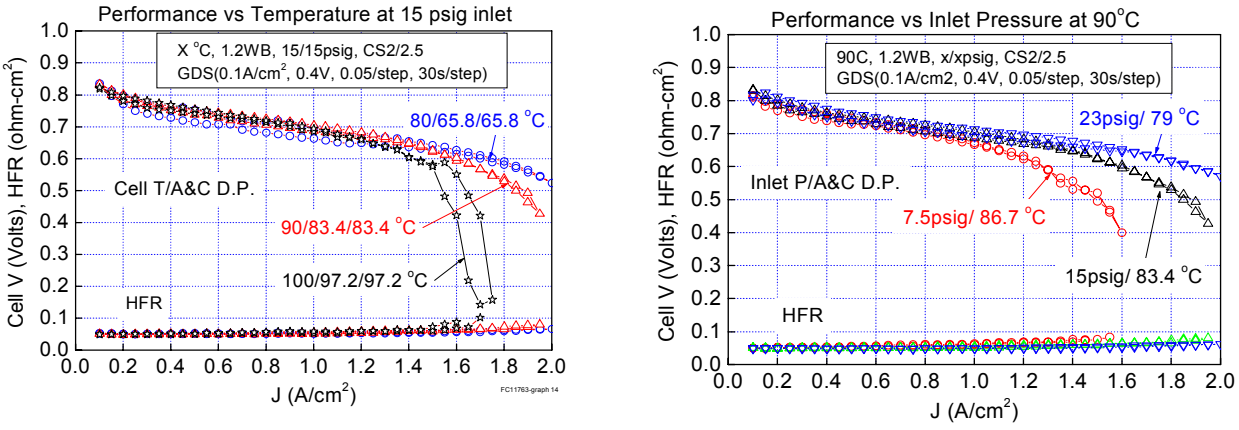

Fig. 3. Performance examples of a typical roll-good fabricated CCM, as tested in a 50 cm^2 cell, at various temperatures and inlet humidifications.

Fig. 4 shows an example of the overall process capability for the combined steps of fabricating and coating catalyst and transferring it to the membrane. The loading is very tight over the length of a 50 ft section of CCM web. For a targeted loading of 0.2 mg/cm^2 of Pt on each electrode, or 0.40 mg/cm^2 total, the mean cross-web loading (5-values averaged cross-web) averaged down-web was 0.419 $\pm$ 0.017 mg/cm^2, a 5% overage that can be corrected with calibration of the sputtering rates. The down-web average of the standard deviation of the cross-web loading values was $\pm$ 0.011 mg/cm^2. This $\pm$ 4% standard deviation represents the cumulative errors in the catalyst sputter deposition, catalyst transfer to the membrane, catalyst removal and analysis of the Pt loading by the UV/IC analytical technique. Process qualification would be expected to improve this further.

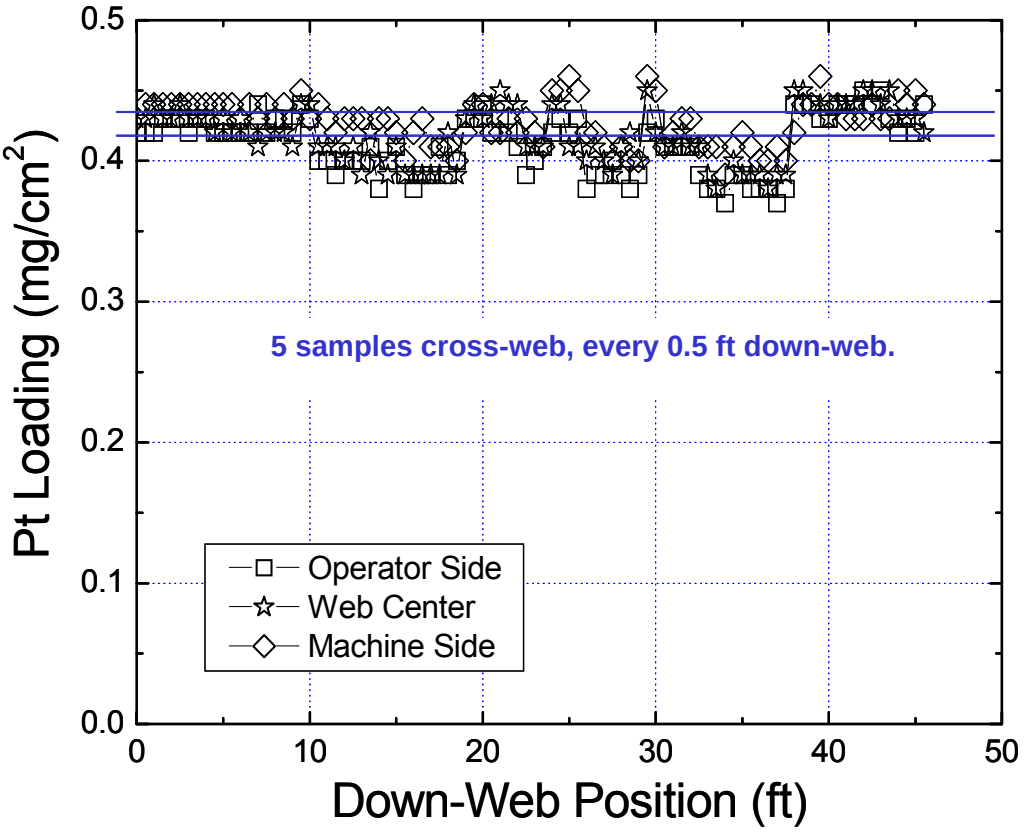

Fig. 4. Example of the cross-web and down-web uniformity of the PtCoMn catalyst loading as measured by removal of the Pt from the CCM at 5 postitions cross-web and every 0.5 ft down-web.

Section 4.2 5kW Short Stack Testing

4.2.1 Introduction

Under Task 3, 3M demonstrated the performance and durability of 3M NSTF MEAs developed under 3M/DOE Contract No. DE-FC36-02AL67621 in a 5kW (rated) short stack. Over the course of this task, 3M built and evaluated 5 stacks of various sizes, including two 22-cell stacks capable of producing in excess of 5kW.

Performance and durability evaluation of the final 5kW stack occurred at a 3M test facility in Menomonie, WI, between May 21st and June 30th, 2007. Testing occurred under the supervision of Dr. Ira Bloom, Mr. Lee Walker, and Mr. John Basco, members of the Fuel Cell Test group at Argonne National Laboratory.

Performance evaluations consisted of polarization curves measured at a variety of stack coolant temperatures ranging from 80 to 100°C and a range of reactant stoichiometries, subsaturated humidities, and pressures. The stack demonstrated a rated power of 5.15kW at 0.60V/cell, and a peak power of 5.5kW at 0.50V/cell.

Durability was evaluated via a dynamic stress test protocol provided by Dr. Bloom, in which the stack load was cycled repeatedly, with current densities ranging from OCV to 1.27A/cm^2, and with a fixed 90°C stack coolant temperature. Over 554 hours, the average per-cell stack performance decreased 8±4mV at 0.1A/cm^2 and 17±22mV at 1.2A/cm^2 under reference conditions. During the experiment, the stack unipolar plates corroded significantly; after semi-quantitative removal of the estimated ohmic loss contribution induced by this corrosion, the per-cell stack performance decreased 6±3mV and 0.1±15mV at 0.1 and 1.2A/cm^2, respectively, over the 554 hours.

Diagnostic tests were performed on the most significantly degraded stack MEA as well as an MEA which had degraded a typical degree. These results indicated that the primary sources of performance loss were a 30% decrease of the specific activity for both MEAs, and an approximate 20% and 50% reduction in limiting current for the typical and most degraded MEAs, respectively. No significant loss of Pt catalyst surface area was noted for either MEA. The reductions of limiting current and specific activity are consistent with failure of the stack unipolar plate corrosion-resistant coating, resulting in contamination of the MEAs with high levels of Ni.

4.2.2 Experimental

4.2.2.1 Timeline of Task 4.2

Work under Task 4.2 began in earnest in early 2006 with down-selection of stack hardware. NSTF MEAs were evaluated in two different 3M-designed stacks to determine suitability for demonstration of NSTF MEA technology. Note that these stacks were designed and fabricated by 3M outside of this 3M/DOE contract. During this work, a new method of integrating NSTF CCMs with gaskets and GDLs was also validated and incorporated into the final evaluated stack.

After selection of stack hardware, a single 8-cell stack (stack ID “DOE3_091506”) was built and evaluated. The objectives of this work included learning of general stack performance characteristics, determination of operating conditions for use in the final contract-evaluated stack, and obtaining baseline data under a range of test conditions. This work occurred in September-October 2006.

Upon completion of the 8-cell stack evaluation, a first 22-cell stack was built ("DOE3_103006"), using the same material set and stack hardware as the 8-cell stack. The intention was this stack would be the one evaluated at Argonne National Laboratories (ANL) under the terms of the contract. The stack was conditioned, baselined, and ready for shipment to ANL as of Nov. 2nd, 2006.

The stack arrived at ANL on Nov. 27th, 2006. Due to difficulties with experiment setup, initiation of testing was delayed until Nov. 30th. On Nov. 30th, after approximately 20 minutes of station operation, testing was halted due to a CO gas sensor false alarm. Testing in the ANL fuel cell laboratory was suspended indefinitely while the cause of the false alarm was investigated. The stack was prepared for long-term storage by draining the coolant from the stack and flowing approximately 100SLM of dry nitrogen to the anode and cathode with the stack at room temperature for approximately 5 minutes. The procedure used for this preparation was not the 3M-specified protocol for long-term storage, but was a necessary compromise with the limitations imposed by the shutdown.

Testing was delayed until mid-March, 2007, and the DOE3_103006 stack was stored at ANL during that time. One concern which arose due to the long-term storage was potential corrosion of the stack's gold-coated 316SS unipolar plates. The stack was transported back to 3M for evaluation, and it was determined that the performance of the stack was significantly degraded relative to the initial performance. All cells demonstrated some performance loss, but a few cells demonstrated significant performance loss coupled with large increases in estimated cell resistance, which dictated that the stack MEAs be replaced.

Upon disassembly of DOE3_103006, significant discoloration of several of the stack unipolar plates and manifolds was observed. This discoloration was suspected to be corrosion of the unipolar plates. Experiments showed that the deposit was visually diminished upon exposure of the plates to 0.1M HNO_3, although the discoloration was still present. Analysis of the acid after exposure to the plate determined that nickel was a major component of the discoloration.

In light of the apparent corrosion of the Au-coated unipolar plates, the preferred course of action was to recoat the unipolar plates. However, due to the short time frame available for stack rebuilding to allow completion of stack testing by the end of the contract (June 30th, 2007), recoating of the unipolar plates was not determined to be feasible. As the next best option, 3M decided to reuse the existing plates and remove as much of the deposit from the unipolar plates and stack hardware as possible, to minimize possible MEA contamination and development of an electrically-insulating passivation layer on the plates. The unipolar plates and stack hardware were processed by soaking in room temperature 0.1N HNO_3 for 10 minutes, rinsing very thoroughly with deionized water, then drying the plates between clean TexWipe cloths. This process resulted in visible reduction but considerably incomplete removal of the discoloration.

After the stack hardware was processed, the 2nd 22-cell stack (DOE3_042607) was built with new MEAs and gaskets, conditioned, baselined, and was ready for shipment to ANL as of May 4th, 2007. Note that the unipolar plates used for each cell of DOE3_103006 were reused in the same cells as DOE3_042607, except that the cell 0 anode and cathode plates were replaced with an unused plate and the cathode plate from cell 0 of DOE3_091506, respectively.

Due to the considerable performance degradation of the DOE3_103006 stack, contamination of the stack by external sources was also considered. 3M requested that ANL evaluate a single

cell on ANL's stack test station under a specific test protocol which was sensitive to external impurities, such as Cl- in the humidification water. The results of this test suggested that considerable levels of one or more unknown impurities were present; ANL later reported to 3M that one contaminant was a sulfur species present in the hydrogen supply.

Due to the results of the contaminant test, representatives from 3M, ANL, and DOE agreed to conduct the stack evaluation at the 3M facility in Menomonie, WI, under the supervision of ANL personnel. Testing under the test plan was initiated on May 21st, 2007. Initial performance Tests 7.1a(a-j), 7.1d(a,b), 7.2, and 7.3 were completed by May 29th, at which point durability testing under Test 7.4 was commenced.

Evaluation under Test 7.4 was conducted between May 29th and June 25th, after completion of 554 hours of testing. After reconditioning, the final reference performance of Test 7.4 was measured on June 30th, 2007.

Upon completion of Test 7.4, the stack was prepared for long-term storage by flowing dry nitrogen into the stack for 4 minutes at 95/225SLM for the anode and cathode, with the stack at 80°C. The coolant was also then removed. The stack remained idle for a period of 1 month.

In August 2007 some additional, unrelated testing was periodically performed for an additional month. A final RPT and H_2 pump was recorded on August 28th, 2007, after which the stack was prepared for long-term storage as above.

In early September 2007, the stack was disassembled to allow for diagnostics, which included performance characterization of stack MEAs in 50cm^2 single cells, photographs of select unipolar plates and MEA components, ICP-AES of portions of several stack CCMs to analyze for cationic content, and Auger electron spectroscopy of a unipolar plate section to analyze the nature of the unipolar plate discoloration.

4.2.2.2 Stack Description

MEAs consisted of 800 equivalent weight (EW) 3M polymer electrolyte membrane, gas diffusion layers, NSTFC PtCoMn ternary catalyst containing 0.2mg/cm^2 of Pt, and integrated gaskets; see section 2.3 for descriptions of the down-selected MEA components. All components were made on 3M production equipment. The MEA active area was 312.5cm^2.

The NSTF PtCoMn ternary catalyst, containing 0.2mg/cm^2 Pt, was prepared as a roll-good on continuous vacuum deposition equipment, as referenced in the previous section, 4.1. Catalyst coated membrane (CCM) was formed via a continuous process, where a web comprised of the PEM and catalyst substrates on either side was passed through a heated nip, after which the substrates where removed . Gas diffusion layers (GDLs) consisted of the Task 2.3.2 down-selected GDL.

The components were then assembled into 7-layer, fully integrated MEAs. The GDLs were integrated into the gaskets, forming gasket integrated GDLs (GIGs) which had a pressure sensitive adhesive on the active (toward CCM) side. Two such GIGs were placed on either side of a precut CCM, which was then die-cut to form the final 7-layer MEA. The GIG concept and technology for its fabrication were developed outside of this contract.

The stack hardware comprised the unipolar plates, current collectors, insulating layers, compression plates, manifolds, seals and gaskets, compression tie-rods, washers, and nuts,

and a voltage probe assembly. The stack hardware was designed by 3M outside of this contract.

The unipolar plates consisted of 0.050" thick 316SS, which were chemically etched to form pertinent features and then were coated with gold to minimize corrosion. Plates were formed through chemical etching of 0.050" thick 316SS sheets to form the reactant and coolant flow fields and passages, features for alignment and sealing, and ports for compression bolts. The plates were then vibratory and vapor honed to reduce sharpness of the features and to nominally improve adhesion of the gold. A nickel "strike" layer was electrodeposited onto the plates, followed by 8 alternating 15micro-inch layers of Ty 3 "soft" gold and Ty 2 "hard" gold. Two identical unipolar plates were used for each cell.

The compression plates and manifolds consisted of ¾" thick 304SS, the current collectors consisted of 1/8" thick oxygen-free copper, and the insulators consisted of a G-11 epoxy composite; all were machined to form various ports for reactant, coolant, seals, and compression hardware. The compression plates, manifolds, and current collectors were coated with gold, in a manner similar to the unipolar plates, to minimize corrosion.

The stack was formed by first stacking the MEAs and various stack hardware elements, and then compression was applied to the stack by tightening the compression nuts. The stack was constrained perpendicularly to the compression direction during compression to minimize twisting and shifting of the components. The stack compression nuts were tightened stepwise, and the stack thickness was measured at multiple positions after each step to ensure compression uniformity. The stack compression continued until a pre-determined thickness was reached, corresponding to 10% compression of each GDL.

Evaluation of the stack primarily occurred on a stack test station at the 3M facility in Menomonie, WI. The test station allowed for control of stack coolant temperature, reactant humidification, reactant flow rate, reactant pressure, and current load. The test station also had capability to pressurize the coolant, which was required for high temperature (> 90°C) stack evaluation. The station regulated the coolant temperature via measurement at the stack's coolant outlet; any reference to stack temperature should be understood to reference the stack coolant outlet.

Reactants consisted of 99.95% industrial grade hydrogen from Praxair and filtered ambient air. The primary impurity of the hydrogen was specified as water vapor. The water used for humidification was generated on-site by passage of water through deionization beds, which yielded typical water resistivity of 18.0-18.1Mohm-cm.

Prior to initiation of the test plan, the test station was calibrated for reactant flow, pressure, temperature, and humidity, load current, stack and cell voltage, and coolant temperature.

4.2.2.3 Test Plan

The test plan consisted of five primary stages: initial conditioning, beginning-of-life performance characterization, constant load hold, cycling durability testing, and post-stack testing diagnostics.

The stack was conditioned using a process we refer to as "thermal cycling". The thermal cycling process consists of two sub-processes, "operational" and "cooldown". In the "operational" sub-process, the stack was operated for a period of approximately 30 minutes at 75ºC coolant temperature, ambient reactant pressure, 95/225SLM H_2/Air, and 70ºC anode and cathode dewpoints. Approximately every 5 minutes, polarization curves were taken, with scan limits of

0A and the maximum current which the stack could tolerate with all cell voltages above 0.40V; between scans, the stack was held at this maximum current. For the "cooldown" sub-process, gas flows were halted, the load was disconnected, the reactant inlet lines were disconnected from the stack, and the stack was cooled to room temperature over a 45 minute time period. During this time, DI water was fed into the anode and cathode outlet manifolds using a pressurized DI source which was regulated to 3psig. The DI water passed through the anode and cathode reactant flow fields and then passed out of the stack via the reactant inlet ports. The thermal cycling "operational" and "cooldown" processes were repeated until stable performance was achieved.

Beginning-of-life performance characterization consisted primarily of polarization curves at various stack temperatures, reactant pressure, reactant humidity, and cathode stoichiometry, with hydrogen as the fuel and air as the oxidant. Table I lists the major parameters of each beginning-of-life test.

Table I: Beginning-of-Life Performance Characterization Tests

Test ID	Stack Temp (°C)	Anode, Cathode Dewpoint (°C)	Anode, Cathode Reactant Inlet Pressure (kPag)	Anode, Cathode Stoichiometry
7.1a(a)	80	77/77	0 (outlet)	2.0/2.5
7.1a(b)	80	76/76	0 (outlet)	2.0/2.0
7.1a(c)	85	80/80	50/50	2.0/2.5
7.1a(d)	85	78/78	50/50	2.0/2.0
7.1a(e)	90	83/83	100/100	2.0/2.5
7.1a(f)	90	81/81	100/100	2.0/2.0
7.1a(g)	90	78/78	100/100	2.0/1.7
7.1a(h)	90	79/79	150/150	2.0/2.5
7.1a(i)	90	75/75	150/150	2.0/2.0
7.1a(j)	90	70/70	150/150	2.0/1.7
7.1d(a)	95	87/87	150/150	2.0/2.5
7.1d(b)	100	95/95	150/150	2.0/2.5
7.2	90	75/75	150/150	2.0/2.0
ANL Sys. Model	85-90	71-88/71-88	10-150/10-150	1.4-14/2-22

Polarization curve scan limits were between 0A and either the maximum current the stack could generate with all cell voltages above 0.50V, or the maximum current density with the cathode reactant pressure drop less than 35kPag. For all Tests except 7.2, polarization curves started at the maximum current and stepped towards 0A in 0.1A/cm^2 steps with 240s dwell time at each step; for Test 7.2, the current was varied randomly.

At the highest currents for each test, the cathode pressure drops approached 30-35kPag. To minimize anode-to-cathode pressure differential, the anode inlet pressure was adjusted at each current density of the polarization curve such that it was approximately mid-way between the cathode inlet and cathode outlet reactant pressure.

For all experiments, test station limitations required a minimum reactant flow rate of 30SLM of hydrogen and air. The consequence of this limitation was the anode stoichiometry was higher than the specified 2.0 for any current densities smaller than 0.313A/cm^2, and the cathode stoichiometry was higher than specified for any current densities smaller than 0.105, 0.132, and 0.155A/cm^2 for tests where the targeted cathode stoichiometry was 2.5, 2.0, and 1.7,

respectively. In addition, a fixed coolant flowrate of 20L/min was used for all tests; under Test 7.1a(h) where the maximum thermal load was produced, the 20L/min flow rate yielded a coolant temperature rise of 7°C.

3M chose the operating conditions for all tests in Table I except the "ANL Sys. Model" test. Several aspects were considered in selection of these conditions. First, the range and values of reactant pressures were selected. Cathode stoichiometry was then selected, based on considerations of performance, demonstration of low stoichiometry capability, and resultant stack pressure drops at the peak load at each reactant pressure. Next, for each reactant pressure and stoichiometry set, the stack temperature was selected to attain relatively high temperatures and moderate degrees of reactant subsaturation. Particular values of humidification were selected to approximately attain a theoretical water balance, where the total humidification water fed to the stack and the total water produced would be just sufficient to saturate the reactant outlet streams at the reactant outlet pressures and coolant outlet temperatures.

The "ANL Sys. Model" conditions were provided by Rajesh Ahluwalia from Argonne National Laboratory (see Appendix VIII). During this test, the stack operating conditions were varied as a function of load. The variation of reactant pressure with load was based on a modeled compressor turn-down curve, and the variation in reactant dewpoints accounted for the change of waterbalance-demanded humidification change as the reactant pressures and stoichiometries changed. One of the model's constraints was constant MEA temperature of 90°C; to account for increased thermal gradients between the MEA and the coolant as the current density increased, the coolant temperature was reduced to compensate. Due to test station limitations, the minimum reactant flow rates were 30SLM, so the actual anode stoichiometry used was higher than the model specification for current densities of 0.42A/cm^2 and less. The model also specified variable coolant flow rate with load, which was not able to be incorporated in this test.

Upon completion of the tests in Table I, Test 7.3, the constant load hold test, was conducted. The objective of this test was to measure the stability of the stack performance over a 50 hour period at 25% rated power. Due to test station limitations, a slightly higher load was used, corresponding to 31% power. Table II lists the conditions for the constant load hold test. To measure the extent of the performance change, a reference performance test (RPT) was performed before and after the constant load hold. The RPT consisted of a polarization curve taken in the same fashion as Test 7.1a(i) in Table I above. Note that prior to measurement of the RPT after Test 7.3, a single "thermal-cycle" was performed akin to the process used during initial conditioning to recover the stack from any reversible losses which may have occurred during Test 7.3.

Table II: Constant Load Hold Test Operating Conditions.

Test ID	Stack Temp (°C)	Anode, Cathode Dewpoint (°C)	Anode, Cathode Reactant Inlet Pressure (kPag)	Anode, Cathode Stoichiometry	Load (A/cm^2)
7.3	90	75/75	150/150	2.0/2.0	0.352

Upon completion of the constant load hold test, Test 7.4, cycling durability testing, was initiated. The cycling durability testing consisted of repeatedly performing, in order, a dynamic stress test (DST) protocol, one or more stack shutdowns and restarts, a DC H_2/H_2 polarization curve (H_2 pump), and a RPT. During the course of the contract testing, 554 hours of DST were conducted; an additional 64 hours were conducted after the contract.

The details of the DST protocol can be found in Appendix VII, the ANL report to DOE on the 3M stack testing. In summary, the stack was held at fixed stack temperature of 90°C, fixed humidification of 100% RH, fixed inlet pressures of 135/150kPag, and fixed coolant flow of 20 L/min. Over an approximately 465 second cycle, the stack current was held at 0, 0.040, 0.171, 0.408, 1.040, and 1.267A/cm^2 (non-sequentially and one-or-more times) for periods of 8 to 40 seconds each. The current values correspond to the load obtained at specific stack voltages during the initial RPT measured prior to initiation of the cycling durability test. The 465 second cycle was repeated throughout the duration of the DST. DST was performed for periods of approximately 60 to 90 hours at a time.

Next, the stack was shutdown and restarted one or more times, using the protocol used for initial conditioning. The primary objective of the stack shutdown and restart was to remove accumulated catalytic poisons (e.g. Cl^-) from the stack MEAs.

After the shutdown and restart process, a DC H_2/H_2 polarization (H_2 pump) was performed. For this test, humidified hydrogen is fed to both anode and cathode, and current is forced through the stack using an external DC power supply. Hydrogen gas is oxidized on the anode and evolved on the cathode. Since the electrode overpotential associated with these reactions is assumed to be relatively small, the remaining voltage loss can be ascribed to primarily ohmic (electronic and ionic) resistances. Later analysis suggests that the assumption of relatively small overpotential losses may not be accurate here, and the results of the H_2 pumps are semi-quantitative only.

During the H_2 pump, hydrogen was fed to the typical stack anode reactant inlet and was provided to the cathode by connecting tubing between the stack anode reactant outlet and the stack cathode reactant inlet. In this configuration, current will not spontaneously be produced by the stack, so a high current DC power supply is connected in series with the stack and electronic load. The operating conditions used were 70°C coolant outlet, 95SLM H_2 at 70°C dewpoint, and ambient stack outlet pressure (at the cathode outlet). A polarization curve between 1.0A/cm^2 and 0A/cm^2 was taken, with 30 second, 0.033A/cm^2 steps. The resistance of each cell was then estimated by linear regression fitting of the current density v. cell voltage.

After the hydrogen pump test, an RPT was measured, using the conditions of 7.1a(i) in Table I. The RPT was used as the gauge of stack performance over the cycling durability test.

4.2.2.4 Stack-Tested MEA Single Cell Performance Evaluation

Upon completion of stack testing, MEAs were removed from the stack and individual 4x4" sections of the MEA were cut-out. The GDLs were pealed from the CCM, and were further cut-down to 50cm^2. Gaskets suitable for the single cell were selected to provide 10% compression of the GDL. The GDLs, gaskets, and CCM were installed into a single cell test cell such that the anode-to-cathode and spatial orientations were identical as in the stack. The test cell was a standard 50cm^2 quad-serpentine flow-field cell obtained from Fuel Cell Technologies.

The cells were connected to a single cell test station, and were then re-conditioned by thermal cycles in a manner analogous to that used in the stack until stable performance was achieved, typically for 12-30 hours.

The cell performance was then measured under Test 7.1a(i) (RPT) polarization conditions. During the RPT polarization, the cell's impedance was measured using a 3M-developed frequency response analyzer. The AC impedance spectrum was measured between 10kHz and

1kHz with 15 logarithmically-spaced steps. These spectra were then fit to a Randle's cell model to obtain the high frequency resistance.

Next, electrochemical surface area was measured by cyclic voltammetry. The cell was held at 70°C cell temperature, anode reactant conditions of 0psig, 800SCCM, 100% RH H_2, and cathode conditions of 0psig, 1800SCCM, 100% RH N_2. The cell anode served as the reference electrode, and the cell cathode was the working electrode. A potentiostat was employed to measure 50 cyclic voltammograms between 0.65 and 0.09V at 100mV/s scan rate, followed by measurement of 3 scans at 2mV/s scan rate. The 2mV/s scans were used to correct the 100mV/s scans for electronic short, hydrogen crossover, and hydrogen evolution. These corrected 100mV/s scans were integrated to estimate the charge associated with adsorption and desorption of hydrogen, and this charge was converted to Pt surface area by dividing by 220μC/cm^2-Pt. These measurements were performed three times in succession, and the average Pt-surface area, in terms of cm^2-Pt/cm^2 geometric area, is reported as the surface enhancement factor (SEF).

The cell's H_2 pump slope was then measured in the same method as used for the stack. The cell was held at 70°C cell temperature with 800SCCM, 0psig, 75°C dewpoint H_2 fed to the anode. The anode effluent gas was then fed to the cathode. A polarization curve was then measured between 0 and 1A/cm^2, and the current density v. cell voltage data was fit by linear regression to obtain the hydrogen pump slope.

Lastly, catalyst absolute and specific activity were measured. The cells were held at 80°C cell temperature, anode reactant of 696SCCM, 100% RH, 50kPag H_2, and cathode reactant of 1657SCCM, 100% RH, 50kPag O_2. A potentiostat was used to hold the cell at 0.900V (0.904V actual) for 20 minutes. This was followed by measurement of several potentiostatic holds at 0.15, 0.20, 0.25, 0.3, 0.35, and 0.40V, using the same conditions as above except N_2 was used on the cathode. The final stabilized current and voltage values from the multiple H_2/N_2 potentiostatic holds were used to estimate the electronic shorting and hydrogen crossover currents. Three trials of this were performed in succession. The reported absolute activity is the three-trial average current density after 15 minutes from the 0.904V hold under O_2, after correcting for the electronic short and hydrogen crossover currents. The reported specific activity is the reported absolute activity divided by the reported SEF (surface area enhancement factor).

This process was conducted once with the stack MEA's cathode as the cathode in the single cell, and then the cell's electrical leads and reactant connections were modified such that the stack MEA's anode was operated as the single cell's cathode.

4.2.2.5 Analysis of Stack-Tested CCMs by Inductively Coupled Plasma – Atomic Emission Spectroscopy (ICP-AES)

Pre-weighed catalyst coated membranes were carefully transferred to acid-washed quartz beakers. The beakers were covered with acid-washed quartz watch glasses and heated overnight in a muffle furnace at 700ºC. Two empty control beakers were heated in the same manner. After cooling the beakers to room temperature, 4 mL of concentrated aqua regia (3:1 HCl:HNO_3) were added, and the covered beakers were heated on a hot plate. Another 4 mL of aqua regia were added once most of the hydrochloric acid had been driven off. The beakers were heated until the sample volumes were each reduced to approximately 1 mL. 4 mL of concentrated hydrochloric acid and 2 mL of deionized water were then added, and the samples were heated until the remaining solid had completely dissolved. The solutions were

then quantitatively transferred to polypropylene centrifuge tubes and diluted to 50 mL with 18-MΩ deionized water. Prior to analysis, the samples were diluted an additional 10-fold with water.

The instrument used for elemental analysis was a Perkin Elmer Optima 3300DV ICP optical emission spectrophotometer. The samples were analyzed against external calibration curves generated using acid-matched solution standards containing 0, 0.2, 0.5, and 1 ppm of each analyte. A 0.5 ppm quality-control standard was used to monitor the accuracy of the calibration curves during the analysis. A 1 ppm solution of Sc was run in-line with the samples and standards to serve as an internal standard.

4.2.3 Results

4.2.3.1 Performance Comparisons of 3M 8-Cell and 22-Cell Stacks to 50cm^2 Single Cells

Fig. 1 shows the performance of the 3M 8-cell stack, two 22-cell stacks, and comparative data from 50cm^2 reference single cells, under Test 7.1a(h) conditions. Sample DOE3_091506 was an 8-cell stack, DOE3_103006 was the initial 22-cell stack, and DOE3_042607 was the second 22-cell stack which was evaluated under the full test protocol and whose results are primarily reported in this document. Sample FC12060 was a reference 50cm^2 single cell which comprised the same CCM and GDL components lots as DOE3_091506 and DOE3_103006. Sample FC12645 was a reference 50cm^2 single cell for DOE3_042607.

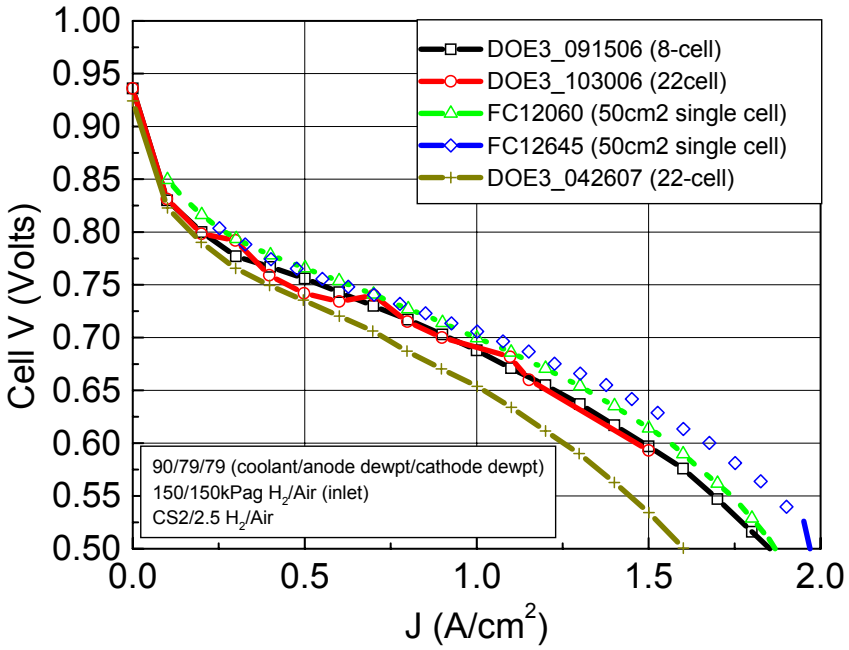

Fig. 1. Comparison of initial performances obtained with a 3M 8-cell stack, two 22-cell stacks, and comparative 50cm^2 single cells. Tests were conducted under conditions of Test 7.1a(h).

Reasonably good agreement was obtained between the 8-cell stack and the initial 22-cell stack. The reference 50cm^2 cell, FC12060, yielded approximately 10-15mV higher performance than the initial 8-cell and 22-cell stacks over the entire polarization curve.

The second 22-cell stack, DOE3_042607, yielded markedly lower performance than the 8-cell stack and the initial 22-cell stack over a majority of the polarization curve; the 2nd stack also underperformed considerably relative to its reference cell, FC12645. The two reference cell's performed similarly.

Fig. 2 compares the estimated cell resistance of DOE3_091506, DOE3_042607, and their respective 50cm^2 reference cells soon after initial conditioning was performed. In addition, the estimated cell resistance of DOE3_103006, after returning from ANL in March 2007, is also shown. Estimated impedance data was not available for DOE3_103006 immediately after conditioning. For the stacks, impedance was estimated by hydrogen pump, whereas AC impedance was used for the single cells. The estimated resistance of DOE3_091506 and DOE3_042607 are quite similar, so cell resistance is not likely the source of the lower-than-expected performance of DOE3_042607. Fig. 2 also clearly shows the large increase in resistance noted for cells 0, 18, and 19 of DOE3_103006 after returning from ANL.

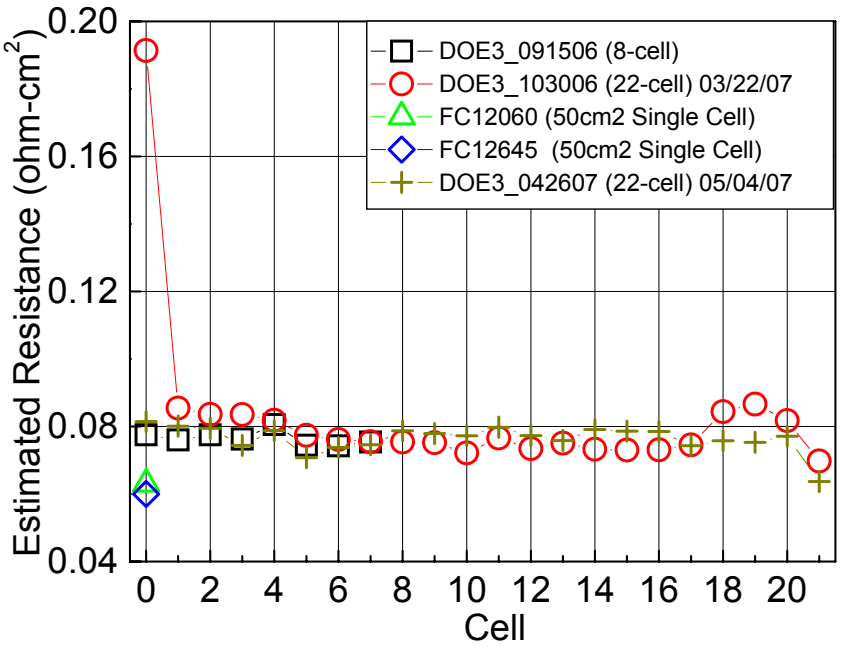

Fig. 2. Comparison of estimated cell resistances. Squares: 8-cell DOE stack (DOE3_091506), after approximately 2 weeks of operation. Circles: First 22-cell stack (DOE3_103006), after returning from Argonne National Laboratories in March 2007. Triangle: Reference single cell for DOE3_091506 and DOE3_103006. Diamond: Reference single cell for DOE3_042607. Cross: Second 22-cell stack (DOE3_042607), immediately after initial conditioning and baselining.

The cause for the lower-than-expected initial performance of DOE3_042607 is not known. Since the reference cell performed at expected levels, the component MEA materials are not likely the issue. The cell resistance of DOE3_042607 also appears to not be an issue, since its estimated cell impedances were similar to the DOE3_091506 stack, which performed well. Certainly, the apparent corrosion of the unipolar plates noted after DOE3_103006 was disassembled is a possible contributing factor, although the exact mechanism for the reduced initial performance of DOE3_042607 is not understood at this time.

Fig. 3 compares the performance of the DOE3_103006 stack, immediately after initial conditioning to after it was returned from ANL in March 2007. The figure shows individual cell

voltages at 0.6A/cm^2 under Test 7.1a(h) conditions. All cells demonstrated considerable performance loss after the idle period from late November 2006 to March 2007. Excluding cell 0, the stack average performance decreased from 733 ± 6mV to 701 ± 6mV, cell 0 lost approximately 300mV, and cell 19 lost 54mV.

The specific reasons for the performance loss of the DOE3_103006 stack between the idle period of November 2006 and March 2007 are not known with certainty. The primary suspected source is corrosion of the unipolar plates, which affected all cells but to varying degrees. Cell 0 was located at the gravitational bottom of the stack, and it is reasonable to posit that due to the modified long-term storage procedure used at ANL in November 2006, considerable amounts of liquid water were still present in the reactant manifolds of the stack, and this water eventually drained into cell 0's reactant flow fields. Any corrosion products produced in the stack would have had direct contact, via the water, with the cell 0 MEA. Rationale specific for the other cells is not known.

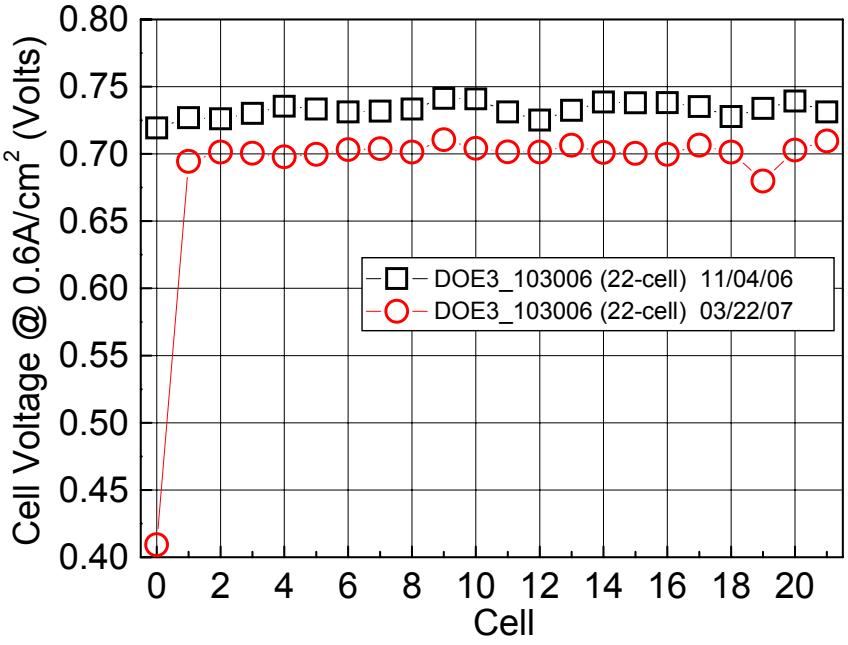

Fig. 3. Comparison of performance of DOE3_103006 stack before and after degradation. Squares: Immediately after initial conditioning in Nov. 2006. Circles: After returning from ANL in March 2007.

4.2.3.2 Initial Performance Tests 7.1a(a-j), 7.1d(a,b), 7.2, ANL System Model

In Tests 7.1a(a-j), stack performance was measured as a function of cathode stoichiometry, stack temperature, and reactant pressure (with minor adjustments to humidity to attain a theoretical water balance state). Since some commonality exists for the various conditions, the data can be compared as a function of stoichiometry (with fixed stack temperature and reactant pressure) or as a function of pressure and stack temperature (with fixed stoichiometry).

Figs. 4 and 5 show a summary of the polarization curve data from Tests 7.1a(a-j), grouped by stack temperature and reactant pressure. The mean cell voltage v. current density is plotted in Fig. 4, and the cell voltage range v. current density is plotted in Fig. 5. Each subgraph within

Figs. 4 and 5 show the impact of cathode stoichiometry for a particular stack temperature and reactant pressure group.

Referring to Fig. 4, the stack performance was found to generally increase moderately with increased stoichiometry, most notably at higher current densities where mass transport limitations have larger influence. At 100 and 150kPag, each stepwise increase in stoichiometry resulted in an approximate 0.1A/cm^2 increase in stack limiting current; at 0kPag, the maximum current density was limited to the values shown to avoid excessive cathode pressure drop.

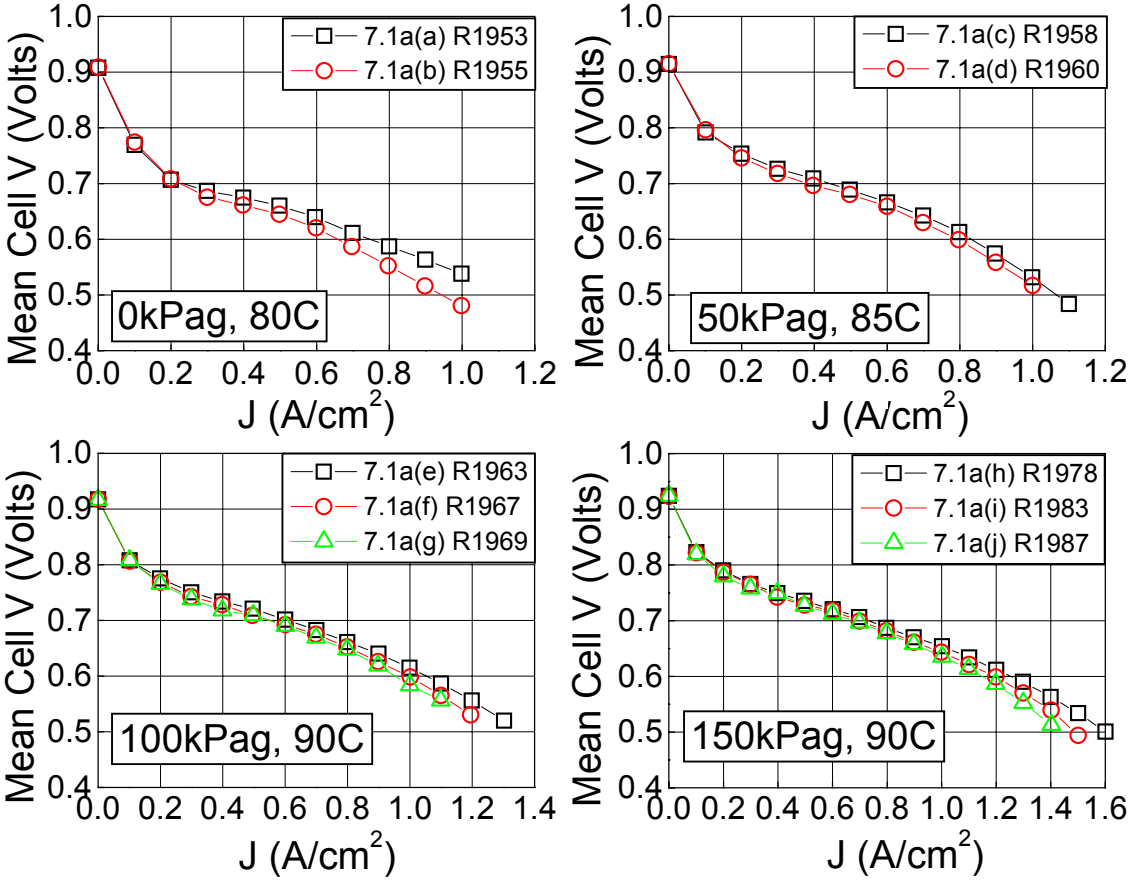

Fig. 4. Stack mean cell voltage for Tests 7.1a(a-j). Upper left: 0kPag anode and cathode reactant pressure, 80°C coolant temperature. Upper right: 50kPag, 85°C. Lower left: 100kPag, 90°C. Lower right: 150kPag, 90°C. Squares: 2.5 cathode stoichiometry. Circles: 2.0 cathode stoichiometry. Triangles: 1.7 cathode stoichiometry.

Fig. 5 shows the cell voltage range for the same tests as Fig. 4. For each pressure and stack temperature set, the cell voltage range at each current generally decreased as the cathode stoichiometry increased.

In general, as the current density was decreased from the maximum current density to moderate current densities, the cell voltage range decreased, which indicates increased voltage uniformity. However, as the current density was further decreased, the cell voltage range generally began to increase again, peaking at 0.3-0.5A/cm^2. As the current density decreased further, the uniformity again improved, and was typically 10mV at zero load, regardless of stoichiometry, pressure, or stack temperature. The cause(s) of the cell voltage range peak in the 0.3-0.5A/cm^2 region is not known; one observation is the cell voltage range in the peak

region was generally smaller with higher stoichiometry, suggestive that cathode reactant mass transport is playing a role.

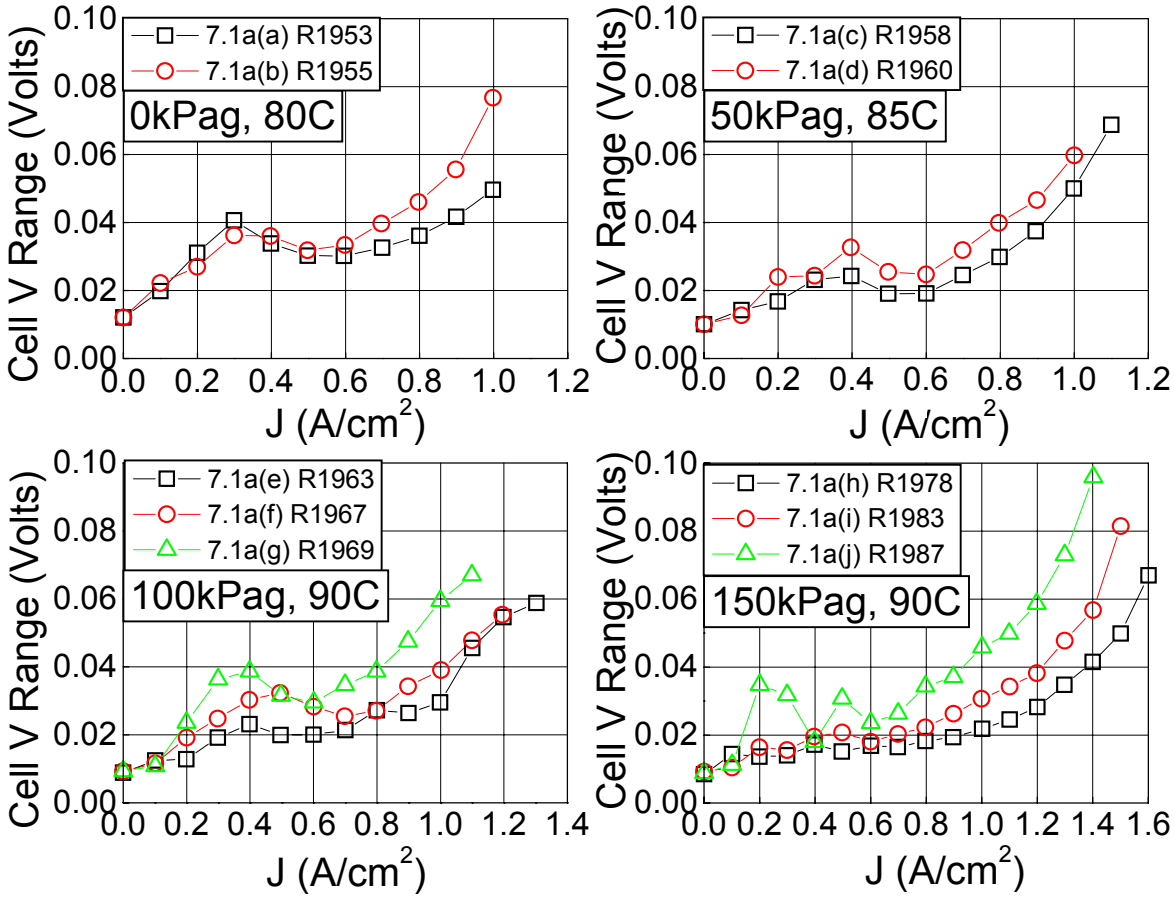

Fig. 5. Stack cell voltage range for Tests 7.1a(a-j). Upper left: 0kPag reactant pressure, 80°C coolant temperature. Upper right: 50kPag, 85°C. Lower left: 100kPag, 90°C. Lower right: 150kPag, 90°C. Squares: 2.5 cathode stoichiometry. Circles: 2.0 cathode stoichiometry. Triangles: 1.7 cathode stoichiometry.

Fig. 6 plots the same data as Figs. 4 and 5, but grouped such that each sub-graph shows the effect of stack temperature and reactant pressure at fixed cathode stoichiometry. As the pressure and temperature are increased, stack kinetic performance, limiting current density, and cell voltage uniformity generally improve, as expected. Curiously, in the 2.5 cathode stoichiometry sub-graph, the mean cell voltage for the 0kPag (outlet) and 50kPag (inlet) overlap at the highest current densities; this is due to the fact that for the 0kPag (outlet) case, the reactant inlet pressure approaches 50kPag.

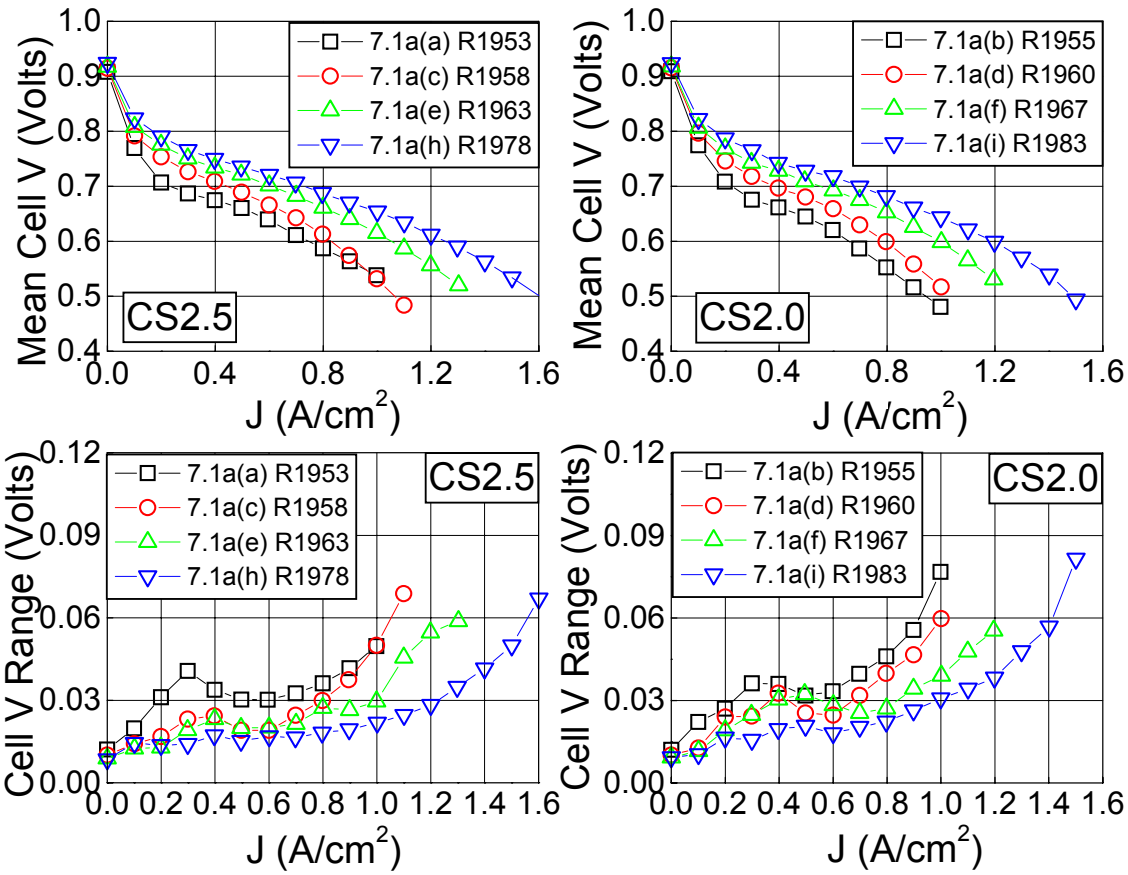

Fig. 6. Stack mean cell voltage for Tests 7.1a(a-j). Left: Cathode stoichiometry of 2.5. Right: Cathode stoichiometry 2.0. Squares: 0kPag reactant pressure, 80°C coolant temperature. Circles: 50kPag, 85°C. Triangles: 100kPag, 90°C. Diamonds: 150kPag, 90°C.

Fig. 7 compares the impact of stack coolant temperatures between 90 and 100°C on performance at 150kPag reactant pressure and cathode stoichiometry of 2.5. Fig. 8 shows the cell voltage range and cathode pressure drop which occurred during these tests. As the coolant temperature was increased, virtually no change in stack performance was observed. The cell voltage range increased only slightly as the temperature increased from 90 to 95°C, and slightly more so as the temperature was further increased to 100°C (Fig. 8, right). As the coolant temperature was increased from 90 to 100°C, the maximum current density decreased from 1.6A/cm^2 to 1.1A/cm^2. This decrease in the maximum current was not due to any observed limitation of the MEAs, but rather the current density was reduced by test operator choice to prevent large anode-to-cathode pressure differentials caused by increased cathode pressure drop at the higher temperatures (Fig. 8, left). The increased pressure drop was likely primarily caused by the increased vapor content of the reactant stream as the cathode dewpoint was increased to maintain water balance as the stack temperature was increased.

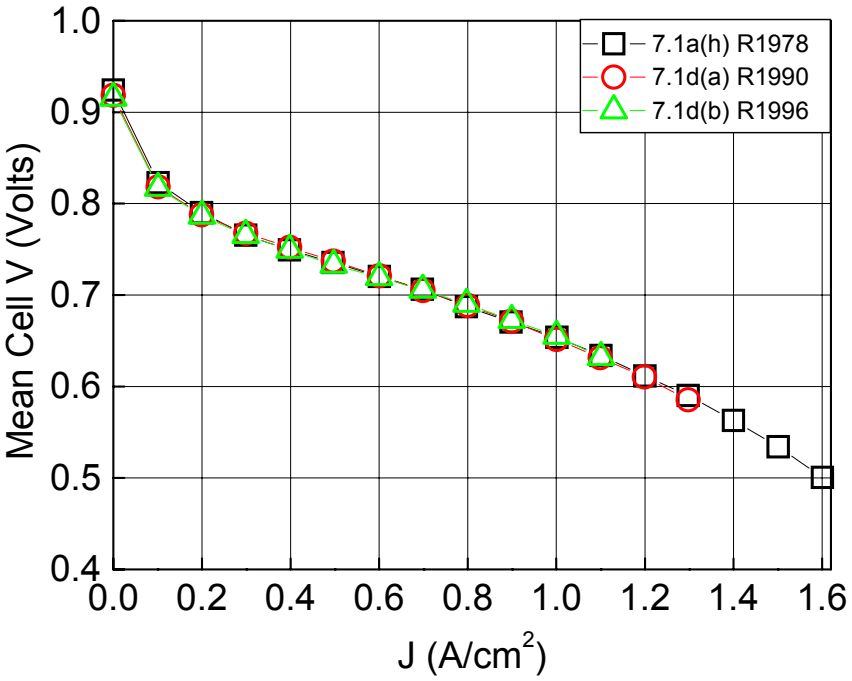

Fig. 7. Stack mean cell voltage for Tests 7.1a(h), 7.1d(a,b). Squares: 90°C coolant temperature. Circles: 95°C. Triangles: 100°C.

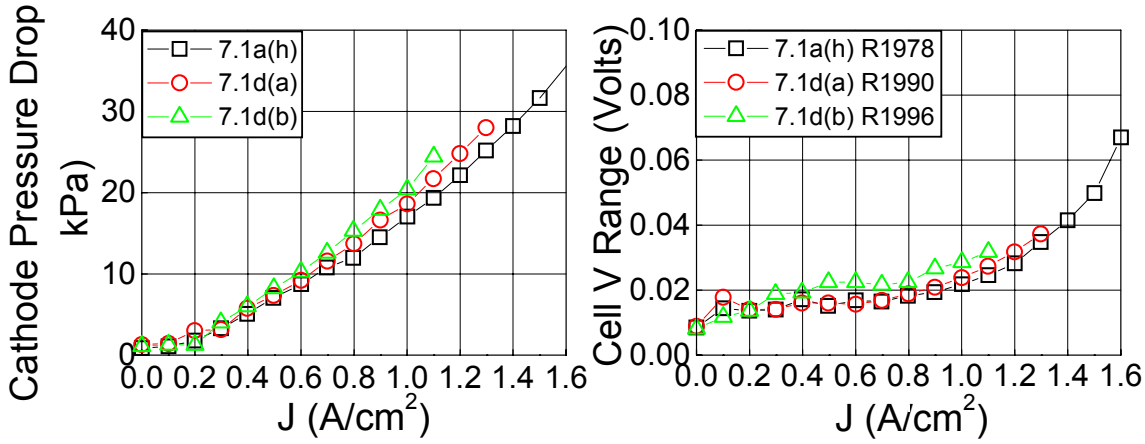

Fig. 8. Cathode pressure drop and cell voltage range for Tests 7.1a(h), 7.1d(a,b). Squares: 90°C coolant temperature. Circles: 95°C. Triangles: 100°C.

Fig. 9 shows the results from the ANL System Model Test. In this test, the anode and cathode reactant pressure, dewpoint, stoichiometry, and coolant temperature were varied as a function of current density. In general, as the current density increased, the reactant pressures increased and the stack coolant temperature, anode dewpoint, and cathode dewpoint decreased.

For current densities of 0.05A/cm^2 and higher, the combination of operating conditions resulted in nearly linear dependence of mean cell voltage and total stack power with current density, and a peak power of 4.53kW at 0.614V/cell.

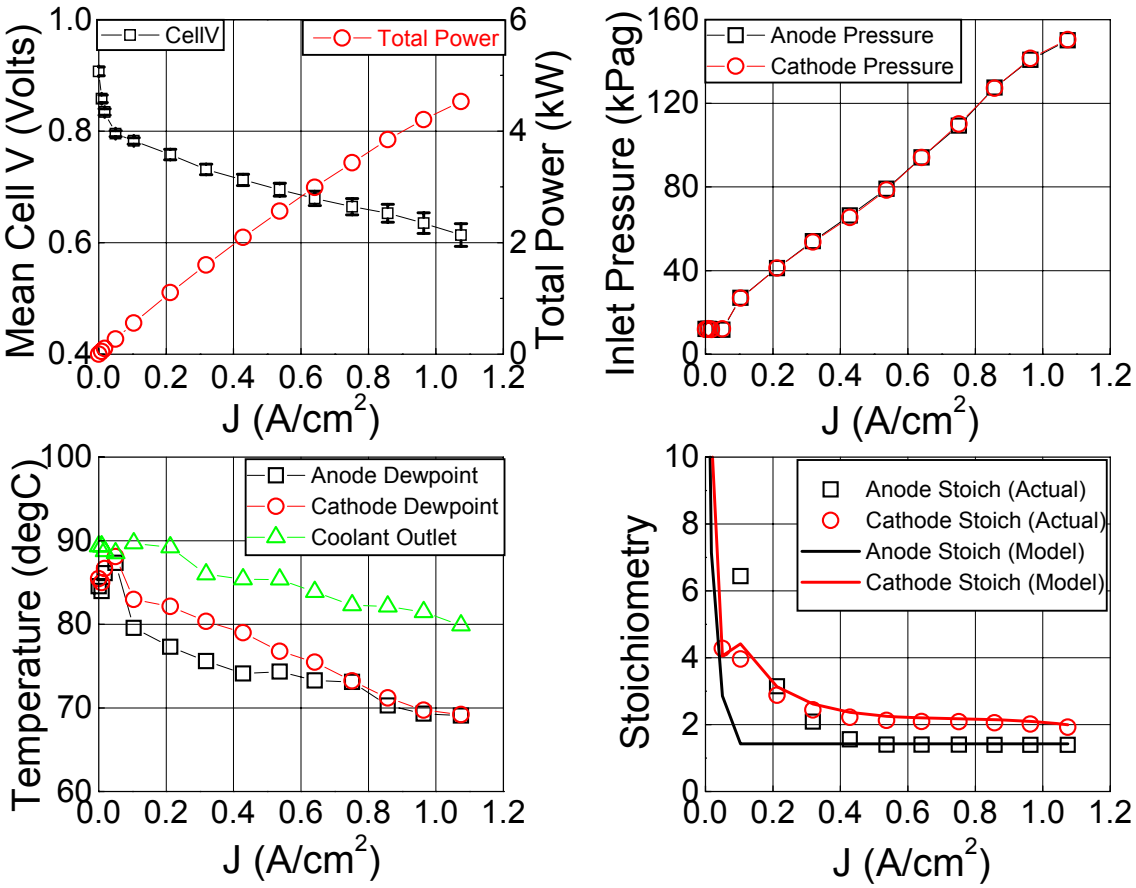

Fig. 9. Performance and current-dependent operating conditions for ANL System Model Test. Upper left: Mean cell voltage and total stack power v. current density; error bars denote cell voltage range. Upper right: reactant inlet pressure. Lower left: coolant outlet temperature and reactant dewpoints. Lower right: Reactant stoichiometry, model-specified and actual.

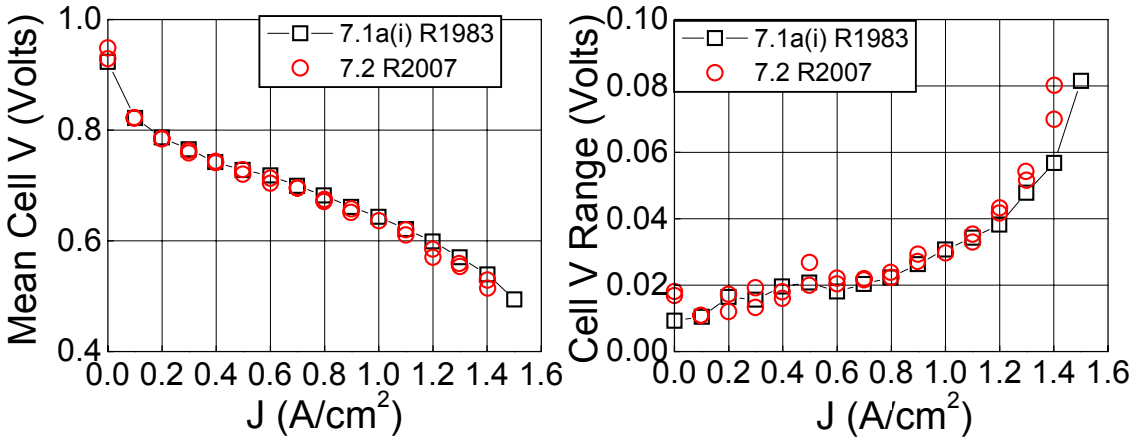

Fig. 10. Comparison of sequential and random polarization curve (7.1a(i) v. 7.2). Left: Mean cell voltage v. current density. Right: Cell voltage range v. current density. Squares: Sequential polarization curve (1.5 -> 0A/cm^2). Circles: Polarization curve in random sequence.

Fig. 10 compares the results of Test 7.2 to Test 7.1a(i). The primary difference between these tests is the order of the current densities at which the stack was held during the polarization curves. For Test 7.1a(i), the current was stepped in order from 1.5A/cm^2 to 0A/cm^2, while for Test 7.2, the order of the current steps was random; in addition, for Test 7.2, each current value was applied twice.

Very little difference in performance was noted between the two tests. Under some current densities, the cell voltage range was perhaps 5mV larger for the random polarization curve than the sequential curve. It is not known if this represents a real difference, or is within the normal testing variability range.

DOE3_042607 Constant Load Hold Stability, Test 7.3

Fig. 11 shows a summary of the performance before, during, and after Test 7.3. Under Test 7.3, the stack was held at 0.352A/cm^2 for 50 hours. Prior to and after Test 7.3, reference polarization curves were taken to gauge the performance change.

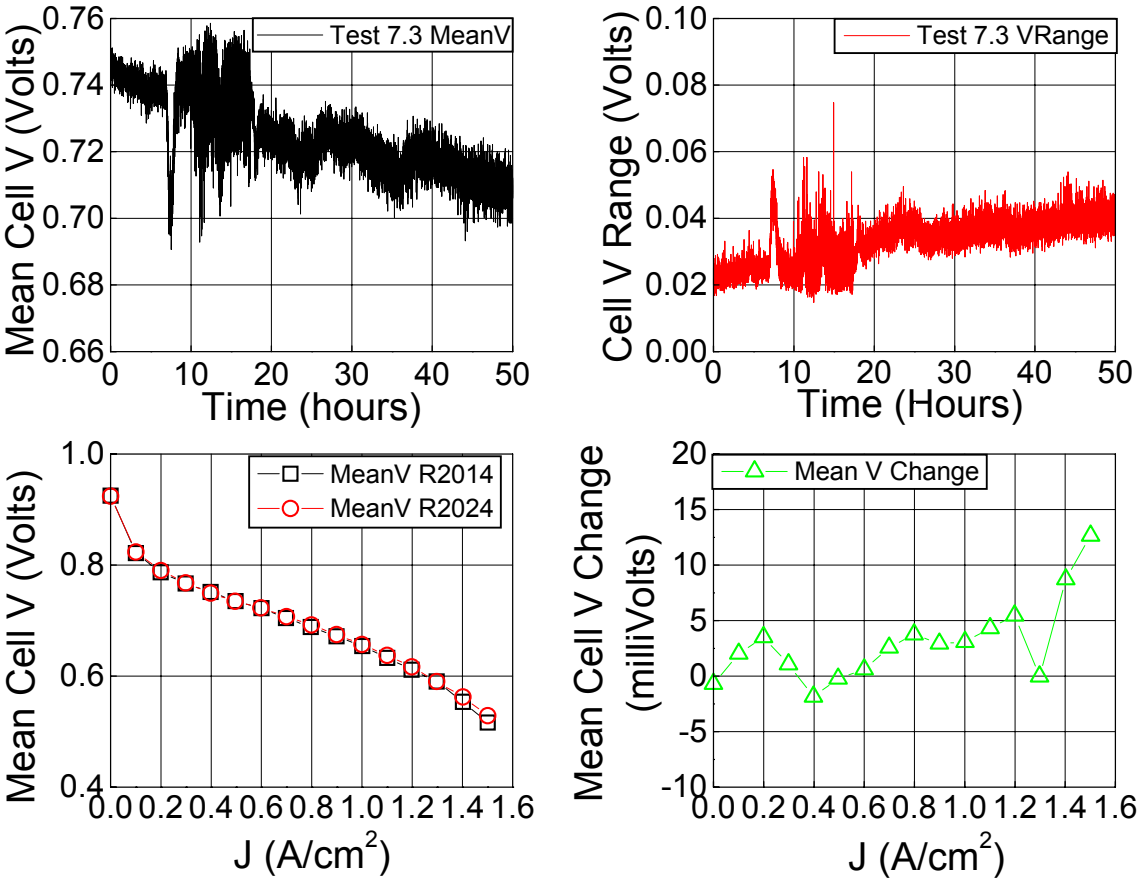

Fig. 11. Performance before, during, and after Test 7.3. Upper left: Mean cell voltage during Test 7.3. Upper right: Cell voltage range during Test 7.3. Bottom left: Reference performance tests before (Squares) and after (Circles) Test 7.3. Bottom right: Average cell voltage change after Test 7.3, based on reference performance tests.

During Test 7.3, the mean cell voltage showed an overall decrease from approximately 0.746V to 0.709V in 50 hours, with a resultant average decay rate of 0.74mV/hr/cell. The mean cell

voltage displayed shorter-term and longer term oscillations, with periods of a few minutes and approximately 10 hours. The source of these oscillations in mean cell voltage is not known. In addition to the decrease in mean cell voltage, the cell voltage range increased from approximately 25mV to 40mV.

The bottom of Fig. 11 compares the results of the reference performance tests taken before Test 7.3 and after a thermal cycle performed after Test 7.3. These results show that no performance was lost due to Test 7.3, and if anything, performance improved slightly. These seemingly contradictory results are consistent with reversible adsorption of impurities onto the MEAs' electrocatalyst during Test 7.3. During the 50 hour hold, performance decreased as impurities adsorbed onto the catalyst, leading to a reduction in available sites for reaction. During the thermal cycle cooldown, these impurities desorbed from the catalyst and were carried out of the stack with the DI water fed through the stack during the cooldown. One likely impurity is chloride ion, which we have found to be a common, considerable reversible MEA poison in other experiments.

4.2.3.3 Test 7.4, Durability Stress Test

Upon completion of Test 7.3 (50 hour stability), Test 7.4, the durability stress test, was commenced. 554 hours of durability testing was completed during the course of the contract, comprised of typically 60-90 hour sessions. After each session, the stack was thermal cycled one or more times, followed by a DC H_2/H_2 polarization curve and a H_2/Air reference performance test (RPT).

Fig. 12 shows the J-V and coolant temperature response during a typical dynamic stress test (DST) cycle. This cycle is continually repeated during each 60-90 hour session. Under the DST test, all parameters other than load are nominally fixed with time. During the DST, the coolant outlet temperature varies from approximately 88 to 94°C, and the coolant inlet temperature varies from 87 to 89°C. The variation in coolant outlet temperature is due to the variation in stack heat generation with load, and the variation in coolant inlet temperature is due to the test station's response in attempting to maintain a fixed 90°C coolant outlet temperature. Other operational parameters, such as pressure and flow, did not appear to vary significantly during the DST testing.

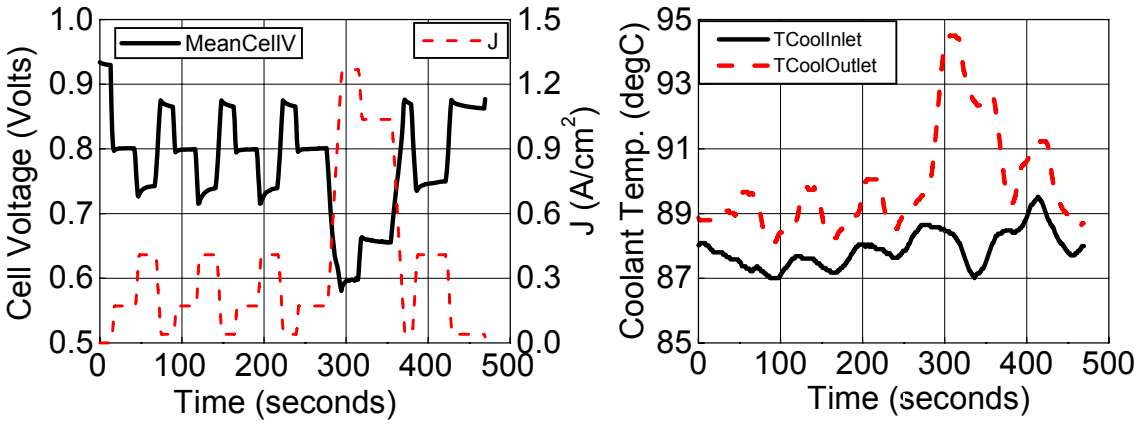

Fig. 12. Example DST profile under Test 7.4. Left: Mean cell voltage and current density. Right: Coolant inlet and outlet temperature.

Table III lists when RPTs were taken in terms of hours of operation under the DST protocol, as well as provides comments about any modifications to the test protocol.

Table III. Overview of RPTs taken during Test 7.4.

RPT #	Hours of DST	Comments
0	0	
1	65	No H_2 pump data. 1TC
2	133	1TC
3	224	1TC
4	241	After loss of hydrogen event. 5TCs
5	328	1TC
6	397	1TC
7	488	2TCs
8	554	1TC
9	554	5TCs over 4 days.

One such modification occurred prior to RPT4. The test facility experienced an inadvertent loss of H_2 supply coincident with DST evaluation of the stack. Instead of immediately aborting testing, the test stand held the stack at conditions similar to the DST conditions, except that the stack was held at OCV, the hydrogen flow was off, and the reactant outlet pressures were ambient. The stack was held under these conditions for approximately 6 hours, at which time the station was shutdown completely and the stack was allowed to remain idle for approximately 40 hours. After this event, stack performance was markedly degraded. 5 thermal cycles were performed, and the performance of the stack recovered to pre-event levels. Another modification was that after RPT8, the stack was thermal cycled an additional 5 times over a period of 4 days, after which RPT9 was measured.

Fig. 13 summarizes the mean cell voltage performance and cell voltage range for 5 select RPTs, and also shows relative changes based on voltage loss at several fixed current densities and percent current density loss at several fixed mean cell voltages. These RPTs represent the initial performance (RPT0), performance after 328 hours (RPT5), performance after 554 hours (RPT8), and the performance after 554 hours with 5 additional thermal cycles (RPT9). Note that RPT10 is included for reference for discussion purposes; RPT10 was taken 1 month after RPT9, during which the stack was not operated. The voltage loss data was obtained through simple subtraction of the mean cell voltage at a given current from the initial RPT0 data. The percent current density loss data was obtained by linearly interpolating the polarization curves to obtain the specific current densities at the specified voltages, and comparing these values to those obtained from RPT0.

After the first 328 hours of testing, RPT5 shows some performance loss occurred and the cell voltage range increased, relative to RPT0. The cell voltage loss, relative to the initial performance, varied between 9-31mV as the current density increased from 0 to 1.4A/cm^2. The % current density loss varied between 7 to 21% as the cell voltage increased from ~0.55V to 0.80V. The cell voltage range increased 0-30mV, relative to the initial RPT cell voltage range, as the current density increased from 0 to 1.4A/cm^2.

After 554 hours of testing (RPT8), additional performance loss was observed. The cell voltage loss, relative to RPT0, varied between 13 and 41mV, and the % current density loss varied between 11 and 28%. The cell voltage range also increased an additional 10-20mV.

After RPT8, the stack was thermal cycled 5 additional times over a period of 4 days, and RPT9 was measured. RPT9 showed marked improvement over RPT8. The cell voltage loss, relative to RPT0, varied between 3 to 21mV, and the % current density loss varied between 5 and 19%. The cell voltage range also generally improved at low-moderate current densities, relative to RPTs 5 and 8; at higher current densities, the cell voltage range was larger than the other tests. The large performance increase observed during RPT9 was not an experimental artifact, as RPT10, taken a month after RPT9, also shows significantly improved performance compared to RPT8.

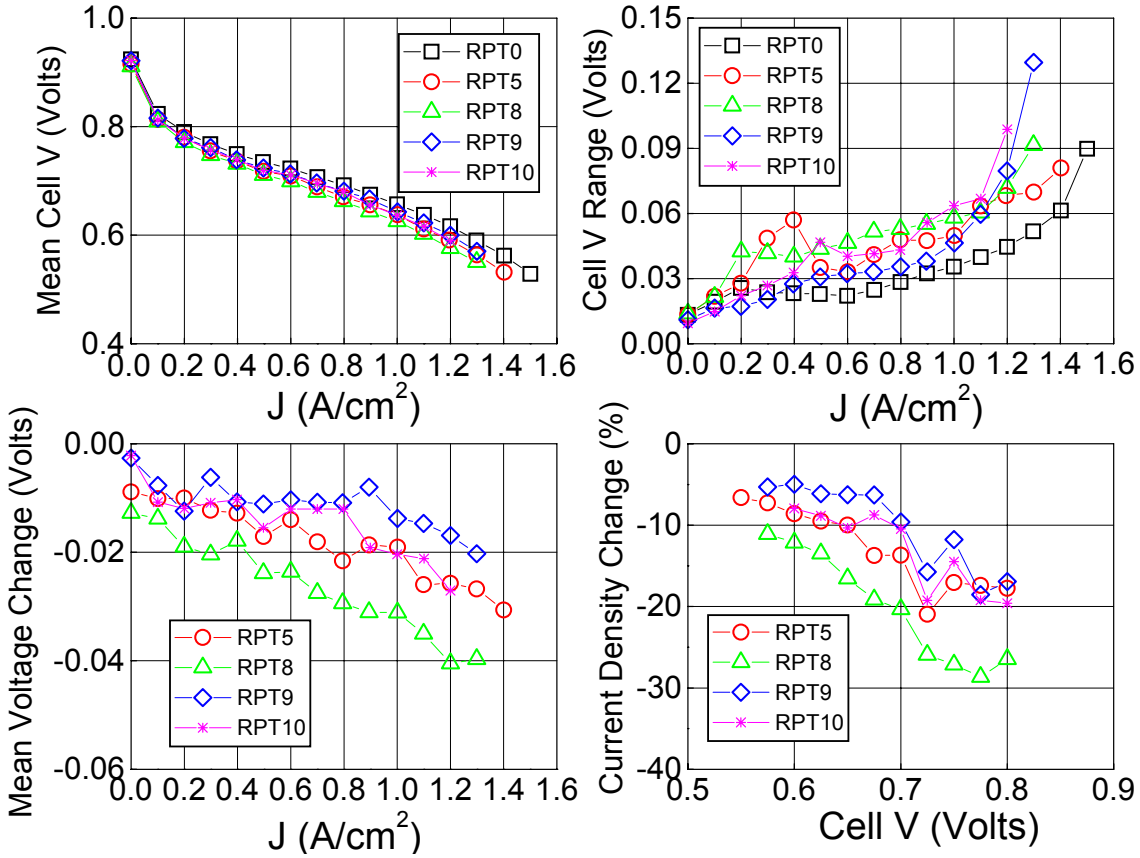

Fig. 13. Select reference performance tests during Test 7.4. Upper Left: Mean cell voltage. Upper Right: Cell voltage range. Lower left: Mean cell voltage loss. Lower Right: Percent current density loss. Squares: Initial (RPT0). Circles: After 328 hours (RPT5). Triangles: After 554 hours (RPT8). Diamonds: After 554 hours and 5 additional thermal cycles (RPT9). Stars: After 1 month stack idle period, immediately following RPT9.

The considerable performance recovery observed after performing the additional 5 thermal cycles prior to RPT9 indicates both reversible and irreversible components of the overall performance loss which occurred during DST testing. Irreversible performance losses can occur due to permanent change of the MEA and/or stack components. One form of reversible loss can occur due to adsorption of impurities on the electrocatalyst, which are largely removed by thermal cycling (internal 3M research.) These results also suggest that the one or two thermal cycles performed throughout Test 7.4 were insufficient to completely recover the performance such that only irreversible losses remained. As such, it is worthwhile to separate the truly irreversible losses (as measured by the performance loss between RPT0 and RPT9)

from the total losses (irreversible and some reversible) which are measured by the other RPTs with only one or two thermal cycles.

Fig. 14 shows a summary of all RPT tests taken during Test 7.4. In Fig. 14, the mean cell voltage at specific current densities is plotted versus the DST run time. Linear regression fits were performed to estimate the rate of performance loss with time. The data from RPT9 ("irreversible only") was separated from the other RPT data in this analysis.

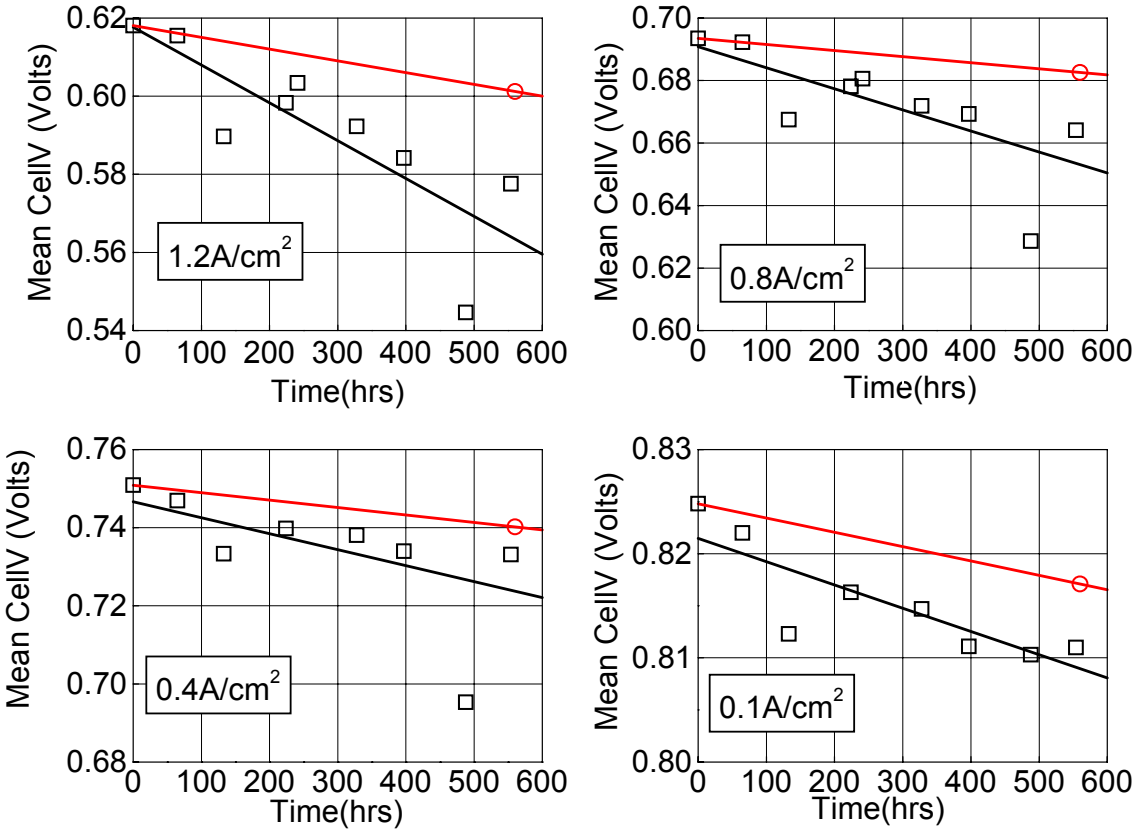

Fig. 14. Mean cell voltages at selected current densities from RPTs taken during Test 7.4, as a function of total DST operational hours. Black squares: Mean cell voltage from RPT with "irreversible + some reversible" losses. Red circle: Mean cell voltage from RPT9 ("irreversible only").

Considerable scatter is present in the "irreversible and some reversible" data. Data points at 133 and 488 hours appear markedly lower than the linear regression line. The data point at 133 hours may have been compromised, due to moderate overheating of the stack prior to acquisition of the RPT. There is no known cause for the depressed performance at 488 hours and the subsequent performance recovery at 554 hours.

Table IV: RPT Decay Rates v. Decay Mode from Fig. 14

RPT Current Density (A/cm^2)	Voltage Decay Rate **"Irreversible + Some Reversible"** (microvolt/hr)	Voltage Decay Rate **"Irreversible Only"** (microvolt/hr)
1.2	-97 +- 25	-30

0.8	-67 +- 21	-19
0.4	-41 +- 22	-19
0.1	-22 +- 4.7	-14

Table IV lists the linear regression fits of the data in Fig. 14. Since only one data point was available for the irreversible-only loss, it is not known how the irreversible-only component of the loss varied over time. In general, as the current density decreased, both "irreversible + some reversible" and "irreversible only" decay rates decrease. The "irreversible-only" decay rates were 26-59% lower than the "irreversible + some reversible" decay rates.

One factor which contributed to the irreversible decay rate was an increase in cell resistance over time, as estimated by hydrogen/hydrogen DC polarization ("H_2 Pump"). Fig. 15 (upper left) shows how the stack average H_2 pump slopes varied over the course Test 7.4; note the error bars denote the range of values for all cells.

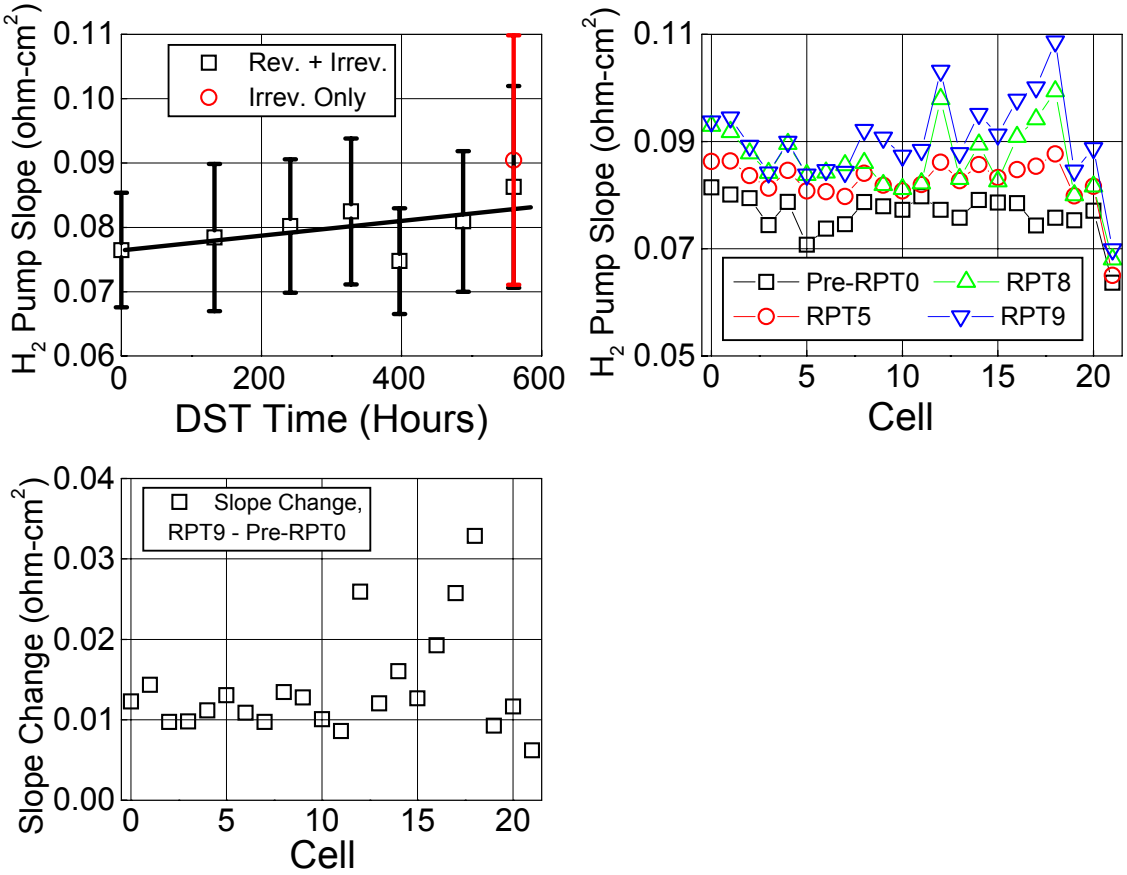

Fig. 15. Mean H_2/H_2 DC polarization (H_2 Pump) slopes and slope changes as a function of total DST operational hours. Upper left: Mean slope during DST testing. Upper right: Individual cell's slopes initially (Pre-RPT0), after 328 hours of DST (RPT5), after 554 hours (RPT8), and after 554 hours of DST with 5 thermal cycles (RPT9). Lower left: Individual cell's slope change between RPT9 and pre-RPT0.

The H_2 pump-estimated cell resistance in general increased with operational time. The value at 397 hours was markedly lower than the overall trend would suggest; the cause is not known. In addition, the range of H_2 pump slopes also increased with time, indicative that the slopes of one or more cells increased faster than the mean. It is worth noting that on average, the additional 5

thermal cycles prior to RPT9 did not improve the H_2 pump slope relative to RPT8, but in fact the slope increased slightly. As such, the significant improvement in performance noted in Fig. 13 after the 5 thermal cycles prior to RPT9 was not due to a reduction in estimated cell impedance.

Fig. 15 (upper right) shows a select set of H_2 pump slopes of individual cells, taken at different times during Test 7.4. These data were taken at similar times as the RPT data in Fig. 13, except for the initial value, which was taken immediately after the stack was initially conditions (pre-RPT0). The pre-RPT0 slope values ranged from 64-82mohm-cm^2, and the RPT9 slope values ranged from 70-108mohm-cm^2. Some cells showed marked increases in H_2 pump slopes, whereas others increased only slightly. Cell 21 had markedly lower H_2 pump slopes than any other cell; the cause is not known.

Fig. 15 (lower left) shows the change in individual cell H_2 pump slopes between when the stack was initially conditioned and after RPT9. Most impedance changes were between 8-15 milliohm-cm^2, but cells 12, 16, 17, and 18 experienced markedly higher changes of 19-34milliohm-cm^2. For reference, 10 milliohm-cm^2 increase in resistance results in 10mV of cell voltage loss at 1A/cm^2, which is a significant loss.

The H_2 pump slopes can be used to approximately correct the RPTs and decay rate data for performance loss due to increases in ionic and electronic resistance; the remaining voltage losses are due to kinetic overpotential and mass transport losses. This correction must be considered approximate because the H_2 pumps and RPTs were taken at different stack temperature and reactant humidification conditions. The H_2 pumps were taken with 70°C stack temperature and fully saturated reactant, whereas the RPTs were taken at 90°C stack temperature and 75°C dewpoint reactants. At fully saturated conditions the PEM resistance would be expected to decrease slightly as the temperature increased, whereas at fixed stack temperature, the PEM resistance would increase considerably as the reactant humidification is decreased. The PEM resistance increase due to the subsaturated reactants during the RPT is moderated somewhat by the water produced from the H_2/Air reaction; in fact, water balance calculations and single cell data suggest that the impedance increase is rather minor. It is the author's estimation that the temperature and humidification differences between the H_2 pump and RPT would result in at most 5milliohm-cm^2 error in estimation of impedance.

In addition to the temperature and humidification impact on H_2 pump estimated-impedance errors, any excessive electrode polarization of the HER and HOR during H_2 pump would result in errors in the estimated electronic and ionic resistance. Single cell data comparing the H_2 pump estimated resistance and AC impedance measured resistance usually agree to within ~15milliohm-cm^2.

Finally, AC impedance data of single cells operated on H_2/Air often shows increasing impedance as the limiting current is approached, especially at subsaturated conditions. The H_2 pump slopes do not account for this error, which can be as large as 30-40milliohm-cm^2.

It is important to note that in the 50cm^2 single cell diagnostic testing of stack-tested MEAs reported in section 4.2.4, the actual discrepancy between H_2 pump and the AC impedance-estimated HFR was larger than expected for the stack-tested MEAs. Cell 10's 50cm^2 cell H_2 pump-estimated HFR was 18mohm-cm^2 larger than the AC impedance-estimated HFR, 33mohm-cm^2 larger for cell 18's, and 13 mohm-cm^2 larger for the reference MEA. The % overestimation was 31%, 47%, and 18% for the cell 10, cell 18, and reference MEAs. Since the deviation in estimated HFR between H_2 pump and AC impedance was larger than expected,

and may vary from cell to cell, the following discussion of the correction of polarization data by H_2 pump-estimated impedance should be considered semi-quantitative.

Figs. 16 and 17 compare the stack performances during the select RPTs taken during Test 7.4, with and without correction for estimated impedance.

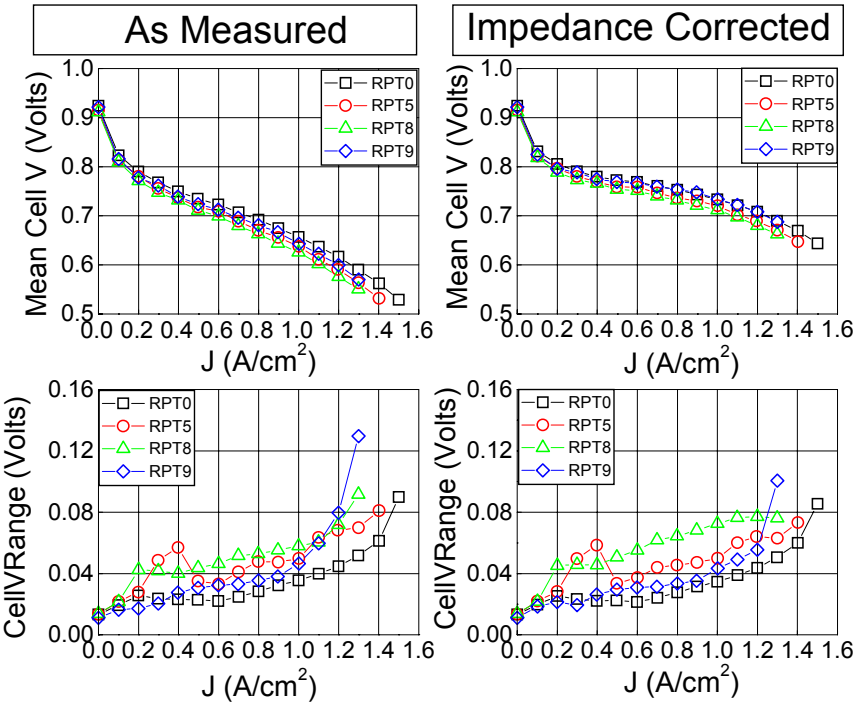

Fig. 16. Select reference performance tests during Test 7.4, *with and without correction for estimated impedance by H_2 pump*. Squares: Initial (RPT0). Circles: After 328 hours (RPT5). Triangles: After 554 hours (RPT8). Diamonds: After 554 hours and 5 additional thermal cycles (RPT9).

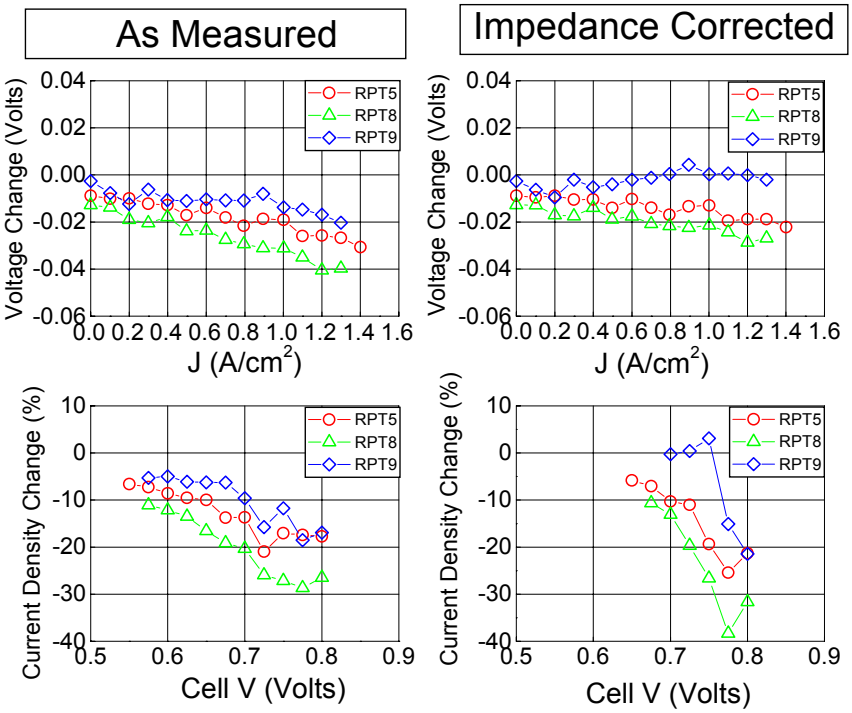

Fig. 17. Change in select reference performance tests during Test 7.4, relative to initial, *with and without correction for estimated impedance by H_2 pump*. Circles: After 328 hours (RPT5). Triangles: After 554 hours (RPT8). Diamonds: After 554 hours and 5 additional thermal cycles (RPT9).

Comparison of RPT9 to RPT0 shows that at current densities larger than 0.7A/cm^2, no performance loss was observed when the estimated impedance increase is taken into account. At lower current densities, where the influence of the catalyst kinetics is largest, the impedance-corrected performance loss is 6mV at 0.1A/cm^2 and 21% at 0.80V.

Fig. 18 compares the RPT performance at several current densities as a function of DST operation time, with or without correction for estimated impedance, and Table V lists the regression-fit-determined performance decay rates. As in Fig. 14, the data is separated to account for irreversible-only and “irreversible + some reversible” losses.

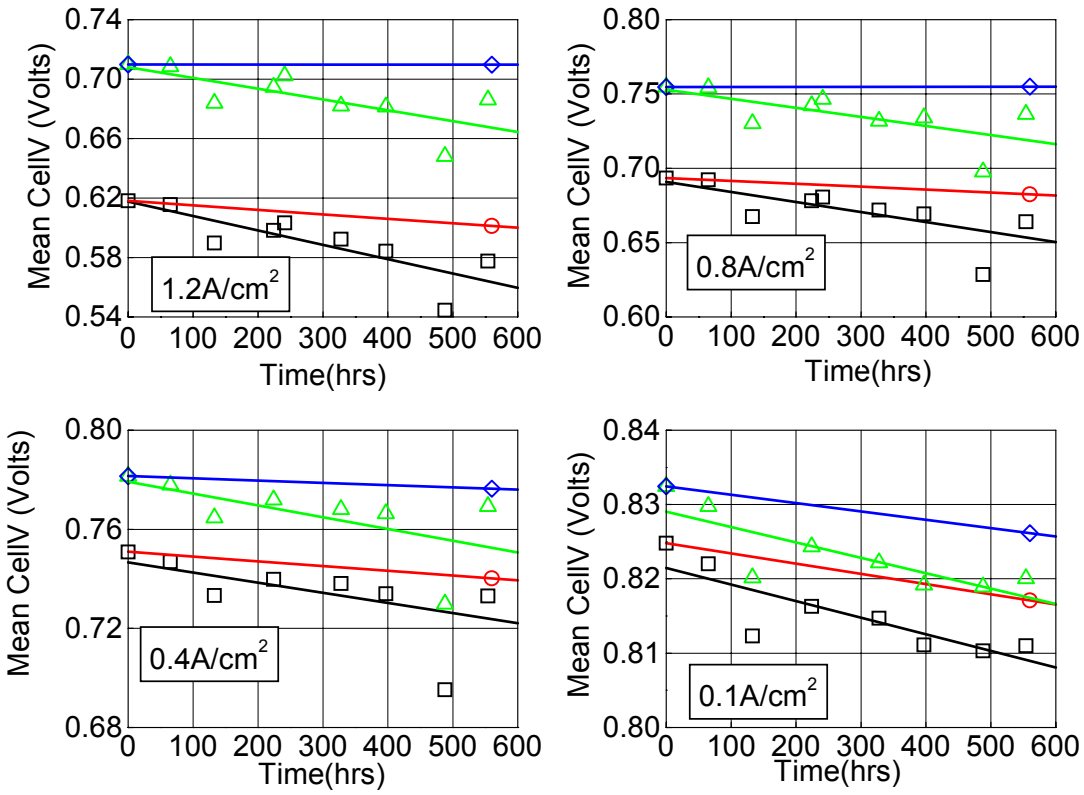

Fig. 18. Mean cell voltages at selected current densities from RPTs taken during Test 7.4 as a function of total DST operational hours, with and without estimated impedance correction. Squares: Mean cell voltage from RPT with "irreversible + some reversible" losses, as measured. Circles: Mean cell voltage from RPT9 with "irreversible-only" losses, as measured. Triangles: Same as squares, but with estimated impedance correction. Diamonds: Same as circles, but with estimated impedance correction.

Table V: Measured v. IR-Free RPT Voltage Decay Rates v. # of Thermal Cycles

RPT Current Density (A/cm^2)	Decay Rate **"Irreversible + Some Reversible"** (microvolt/hr)		"Decay Rate" **"Irreversible Only"** (microvolt/hr)	
	Measured	IR-Free (est.)	Measured	IR-Free (est.)
1.2	-97±25	-72±26	-30	-0.2
0.8	-67±21	-61±26	-19	-0.5
0.4	-41±22	-48±25	-19	-9
0.1	-22±4.7	-21±6	-14	-11

With both "irreversible + some reversible" losses present, correction for estimated impedance resulted in an improvement of 25 microvolt/hr at $1.2A/cm^2$, but had little impact at lower current densities. However, when only considering the irreversible loss (RPT9), the decay rate decreased from 30microvolt/hr to 0.2microvolt/hr at $1.2A/cm^2$, and was found to improve moderately at lower current densities.

Fig. 19 compares the change in individual cell voltages between the initial RPT and RPT9, with and without correction for H_2 pump-estimated impedance. Table VI lists the mean and standard deviations of the data in Fig. 19.

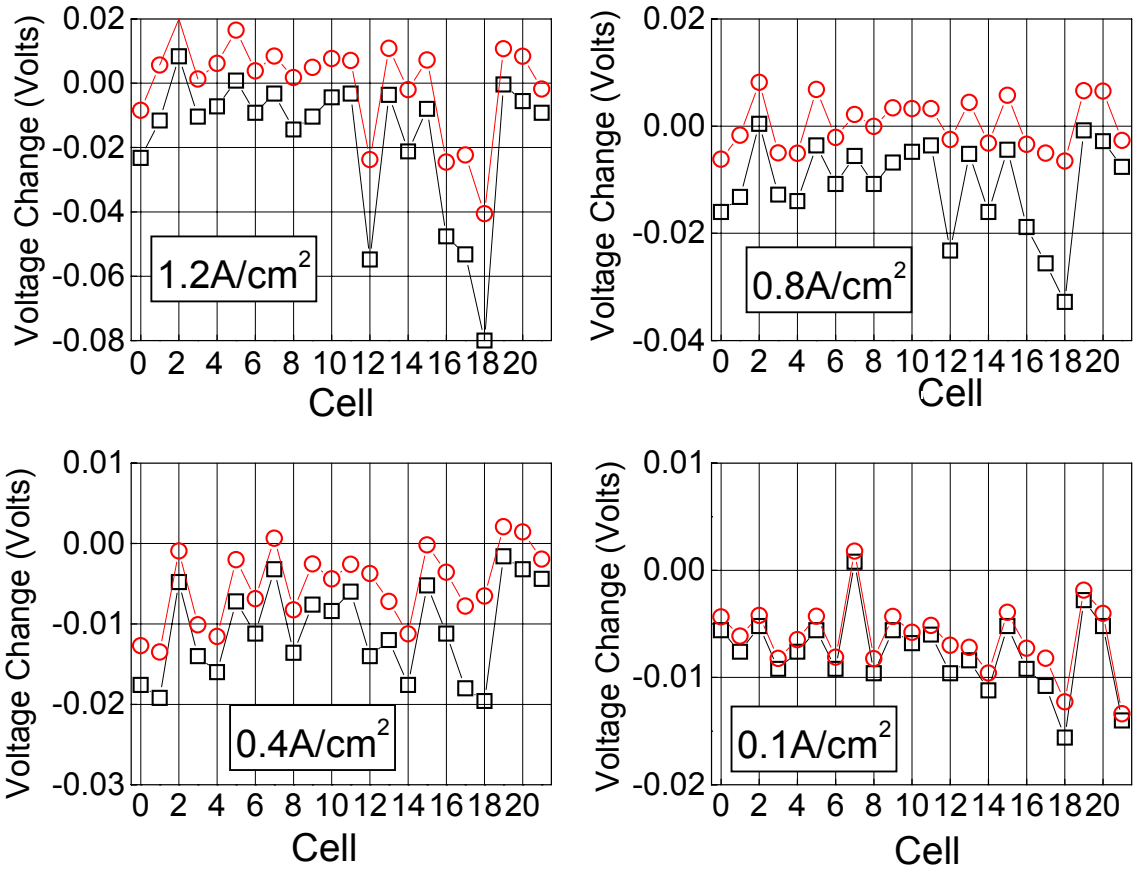

Fig. 19. Comparison of individual cell voltage changes between RPT0 and RPT9, with or without impedance correction, at various stack current densities. Squares: As measured. Circles: Estimated-impedance corrected.

Table VI: Mean Cell Voltage Change Between RPT0 and RPT9, as measured v. impedance corrected. Errors denote standard deviation.

RPT Current Density (A/cm^2)	Mean Cell Voltage Change, As Measured (milliVolts)	Mean Cell Voltage Change, Impedance Corrected (milliVolts)
1.2	-17±22	-0.1±15
0.8	-11±9	0.3±5
0.4	-11±6	-5±5
0.1	-8±4	-6±3

At 1.2A/cm^2, the mean as-measured cell voltage change was -17±22mV. However, cells 12, 16, 17, and 18 showed significantly larger voltage losses of 48-80mV. Estimated-impedance correction resulted in -0.1 ± 15mV voltage loss on average, but cells 12, 16, 17, 18 appeared to lose 20-40mV, again statistically different than the average cell.

At 0.8A/cm^2, the average as-measured cell voltage change was -11±9 mV. Cells 12, 16, 17, and 18 again had voltage losses considerably larger than the mean (19-33mV). Impedance correction resulted in 0.3±5mV average voltage loss. In this case, however, cells 12, 16, 17, and 18 had voltage losses of 3-7mV, which was nearly within one standard deviation of the average voltage loss.

At 0.4A/cm^2 and 0.1A/cm^2, where performance is largely influenced by ORR kinetics, the as-measured mean cell voltage changes were -11±6 and -8±4mV, respectively; impedance correction decreased the mean cell voltage changes to -5±5 and -6±3mV. Only cell 18 yielded voltage losses larger than one standard deviation, albeit just slightly.

In the absence of cell failure, the dominant mode of fuel cell performance loss at low current densities with this type of durability cycling is typically loss of cathode Pt surface area and/or loss of specific activity. Unless unusually severe, changes in mass transport or purely ohmic behaviors impact the performance only subtly in the kinetic-dominated regime. Under this protocol, the loss of ORR kinetics resulted in 8mV of performance loss per cell, or 6mV after estimated impedance changes are considered.

At high current densities (e.g. 1.2A/cm^2), the stack performance is dominated by mass transport and ohmic losses. Performance at high current densities is only subtly impacted due to kinetic change, unless the kinetic losses are severe (which was not the case here). Ohmic losses can usually largely be accounted for by correcting the polarization curves for impedance, leaving primarily mass transport losses as the dominant loss mode. The above analysis suggests that at 1.2A/cm^2, none of the cells other than cells 12, 16, 17, and 18 showed an increase in mass transport loss over the duration of the DST experiments, within the uncertainty of this semi-quantitative method. As such, the primary source of the average 17mV loss at 1.2A/cm^2 for most cells was increased ohmic resistance, while cells 12, 16, 17, and 18 demonstrated both increased ohmic and mass transport losses.

4.2.4 Diagnostic Evaluation of Tested Components

Upon conclusion of stack evaluation, the stack was disassembled to allow for detailed diagnostic evaluation. These diagnostics included performance characterization of stack MEAs in 50cm^2 single cells, photographs of select unipolar plates and MEA components, Auger analysis of the cell 17 cathode unipolar plate, and Inductively Coupled Plasma – Atomic Emission Spectroscopy (ICP-AES) analysis of stack CCMs for cationic content.

4.2.4.1 Discussion

During the durability testing in the stack, performance losses can be due to one or more potential performance degradation modes. These degradation modes include irreversible contamination or degradation of the electrocatalyst, PEM, and GDLs, and development of electrically-insulating passivation layers on the stack unipolar plates.

As observed in Fig. 15, all cells in DOE3_042607 showed some degree of increase in estimated ohmic resistance. Some cells, notably cells 12, 16, 17, and 18, showed markedly larger increases in ohmic resistance and also increased mass transport loss. In addition, as shown in Table VI, the stack MEAs' performance decreased on average 8±4mV at 0.1A/cm^2 during the 554 hour durability test, a clear indicator of kinetic performance loss.

The electrocatalyst can be degraded in several ways, which can lead to loss of electrochemical surface area and/or specific activity for the hydrogen oxidation reaction and the oxygen reduction reaction. Known degradation mechanisms include accumulation of catalytic poisons and agglomeration and/or dissolution of Pt catalyst particles.

One mechanism of PEM degradation, in the absence of breach failure, is accumulation of metallic cations, which leads to reduced conductivity and detrimental changes in MEA water management, such as the water uptake capacity of the PEM.

GDL degradation can occur as a result of carbon oxidation of the microporous layer, loss of desired hydrophobicity due to changes or loss in the typically-applied hydrophobic coatings, blockage of pores from particulates resulting in reduced reactant and water transport, and breakage of carbon fibers in the GDL backing resulting in reduced mechanical support and reduced GDL-to-CCM contact.

Degradation of the relatively thick, Au-coated stainless steel stack unipolar plates can occur due to failure of the gold coating resulting in corrosion of the underlying stainless steel, or due to accumulation of contaminants at its surface. Depending upon the extent of these phenomena, the unipolar plates can become more resistive.

4.2.4.2 Photographs of Stack-Tested Unipolar Plates and MEA Components

Upon disassembly of the stack, considerable discoloration was visible on several of the unipolar plates and MEAs. Fig. 20 shows photographs of matched sections of the anode and cathode GDLs and reactant flow fields from cells 10, 18, and 21. From Fig. 15, cell 10 had a typical impedance increase, cell 18 had the highest impedance increase, and cell 21 had the lowest impedance increase (and lowest impedance overall). Due to variable lighting, differences in color from one photograph to the next should not be considered significant. The orientation is such that the top of each photo corresponds to the reactant inlets. To aid in visualization, the GDLs have been mirror image flipped left-to-right such that any matching features between the GDL and flow field can be more readily discerned. Fig. 21 shows higher-resolution images of the cell 18 GDL, and fig. 22 shows high resolution images of a unipolar plate removed from the DOE3_103006 stack.

The discoloration of the unipolar plates only occurred in the regions corresponding to the reactant flow fields and lands. No or minimal discoloration was present in the gasket or coolant flow field regions. The extent of discoloration varied considerably from plate to plate. There did not appear to be a consistent pattern as to where the discoloration occurred within the active area. In general, the cathode plates showed larger degrees and areal extents of discoloration than the anode plates.

The MEAs also showed discoloration on the face of the GDL facing the unipolar plates. In general, the patterns and darkness of the GDL discoloration matched the patterns and darkness of the unipolar plates. On the GDLs, however, the discoloration appeared to occur primarily in areas corresponding to the flow field channels.

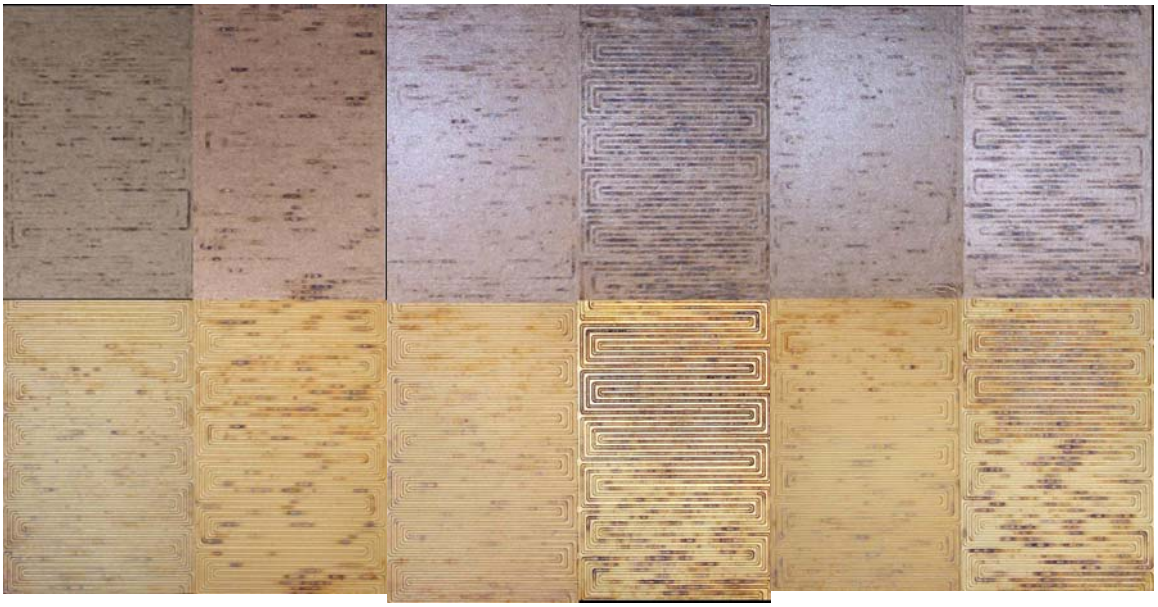

Fig. 20. Photographs of sections of stack cells 10 (left pair), 18 (middle pair), and 21 (right pair). Top row: GDL. Bottom row: Flow fields. Left column of each pair: Anode. Right column of each pair: Cathode. Note GDL images have been flipped horizontally such that positions at (x,y) on the GDL and flow field were areas directly in contact in the stack.

Qualitatively, the discoloration did not correspond with the estimated impedance increase observed in the stack. Cell 18's H_2 pump slopes were markedly higher than cell 10's, consistent with the markedly larger degree of discoloration of the cell 18 cathode. However, the cell 21 cathode GDL and plate had markedly greater extent of discolored area than cell 10, but cell 21 had the lowest overall impedance and lowest overall impedance increase during the Test 7.4 experiments.

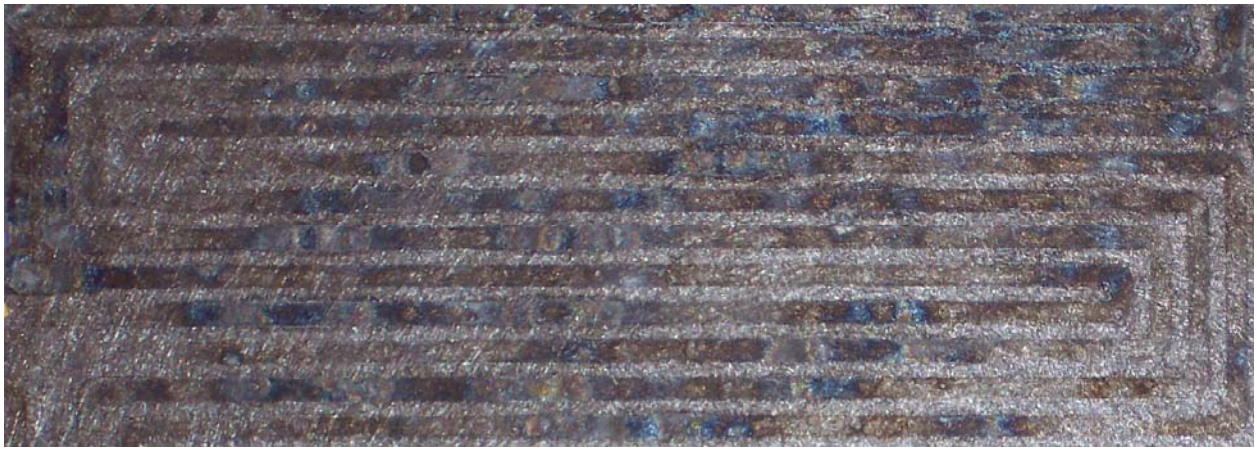

Fig. 21. Photograph of cell 18 cathode GDL, flow field side.

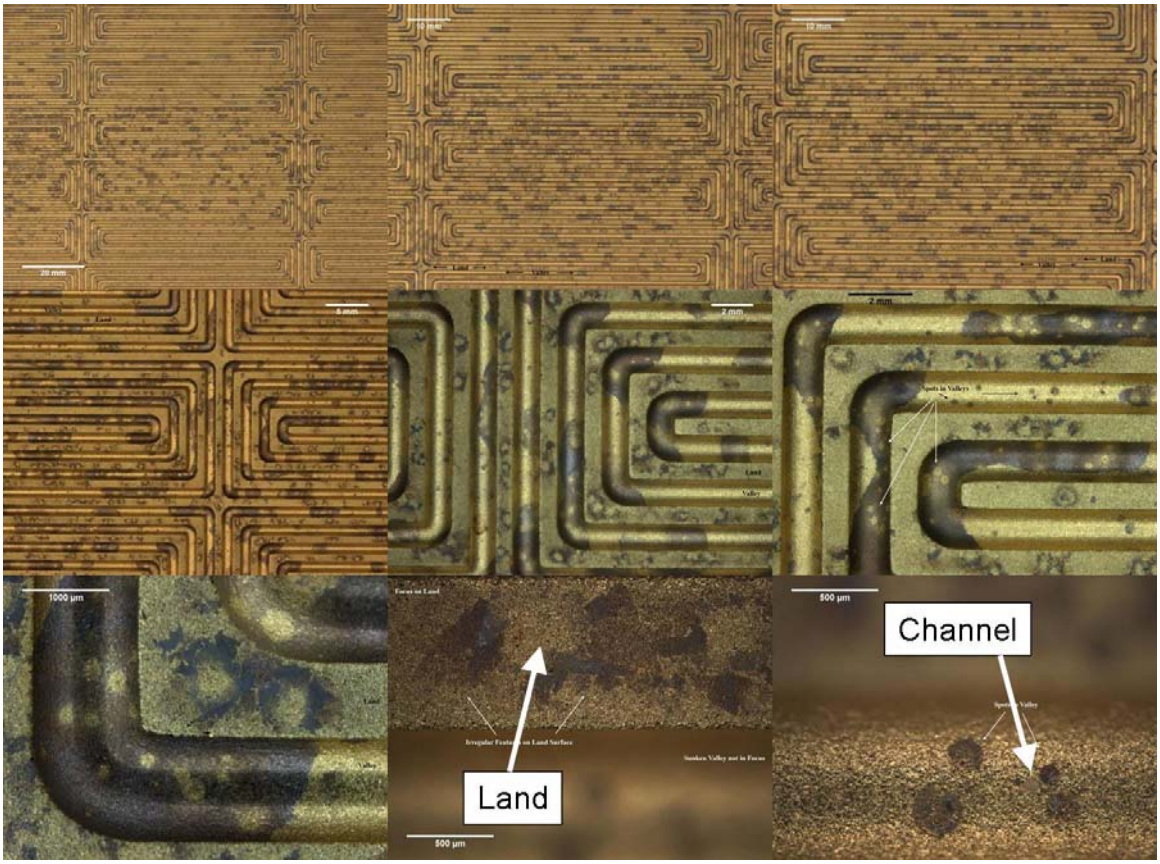

Fig. 22. Optical micrographs at various magnifications of reactant side of a degraded unipolar plate.

Fig. 23 shows photographs of the anode and cathode electrodes of the CCM and the CCM-side of the anode and cathode GDLs from a portion of cell 18. For the CCM anode and cathode, the pattern of the flow field is evident, especially so on the cathode. The anode GDL is essentially featureless, while the cathode GDL is patterned with the flow field. The darkness of the features on the cathode CCM is due to transfer of a portion of the microporous layer (MPL) of the GDL to the CCM. Of 8 stack MEAs examined in this fashion, all showed similar MPL characteristics as cell 18; any differences in performance between MEAs likely cannot be attributed to this MPL transfer. The type of flow field pattern impression observed on the anode CCM is typical for operated CCMs; typically both anode and cathode have similar patterns. The transfer of MPL to the CCMs' cathode electrodes observed on the stack-operated MEAs is not typically observed, although the high temperature, duration, and scanning protocol of the stack experiments are also not typically used. Since both the anode and cathode MPLs are exposed to the same heat and pressure, it is suggestive that this transfer of the cathode MPL to the cathode electrode requires the presence of oxygen and/or relatively higher potentials.

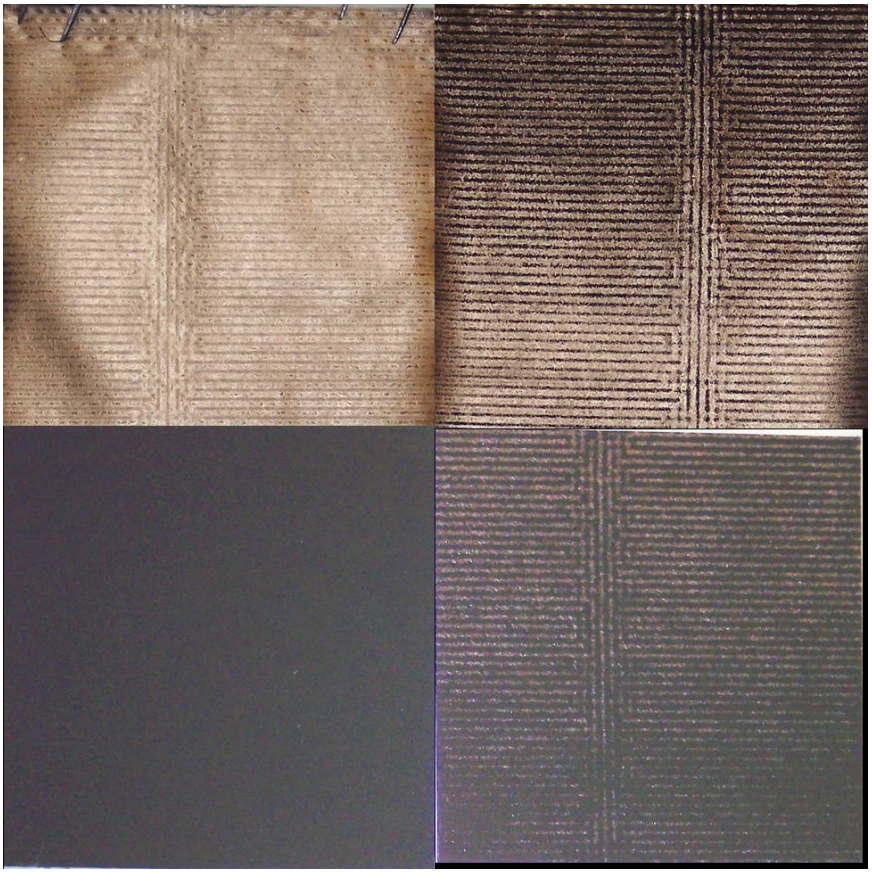

Fig. 23. Photographs of cell 18 anode and cathode MEA components. Upper row: CCM. Lower row: GDL, CCM side. Left column: Anode. Right column: Cathode. Note GDL images' brightness and contrast were increased identically on anode and cathode to enhance visibility of patterning on the cathode GDL.

As noted in section 4.2.2.1, the stack unipolar plates used in this stack were reused from a previous stack build (DOE3_103006). The unipolar plates after use in DOE3_103006 demonstrated some degree of discoloration, similar to that shown in Fig 22. To aid in determination of the nature of the discoloration, various spots of one unipolar plate from DOE3_103006 were exposed to 5mL aliquots of 2% nitric acid. After 10 minutes, a majority of each aliquot was removed and analyzed by inductively coupled plasma – atomic emission spectroscopy. Ni was found in 180ppm concentration in the nitric acid, while all other screened elements were generally less than 1ppm.

4.2.4.3 Single Cell Evaluation of Stack-Tested MEAs

Upon disassembly of the stack, portions of two stack MEAs were cut out to provide samples for testing in 50cm^2 single cells, a typical test vehicle in our laboratory. During sample cutout, the anode v. cathode orientation of the GDLs and CCM were recorded. The samples were mounted in typical 50cm^2 cells with quad serpentine flow fields. The cells were thermal cycled for 12-30 hours, and then performance at RPT conditions was measured. Finally, electrochemical surface area (ECSA) and specific activity were measured three times. The cells were evaluated first with the original stack cathode of the CCM as the cathode, then the reactant gas flows and electrical leads were reconfigured and the original stack anode of the CCM was evaluated as the cathode in the single cell.

The following discussion which follows compares the 50cm^2 single cell performance to the final RPT (RPT12) taken on August 28th, 2007. To simplify discussion, a convention will be used such that the "C" electrode is the electrode operated as the cathode in the stack, and the "A" electrode is the electrode which was operated as the anode in the stack.

The two stack MEAs evaluated were from DOE3_042607 cells 10 and 18. Cell 10 was selected to represent the typical stack MEA, and cell 18 was chosen as it was the cell which degraded most (Fig. 19). An MEA made from the same components but not stack tested was also evaluated and provides a reference performance.

Fig. 24 compares the performances of MEAs from cell 10 and cell 18 initially in the stack (RPT0), at the end of stack testing (RPT12), in 50cm^2 testing with either electrode "C" or "A" as cathode, and to a non-stack tested reference MEA.

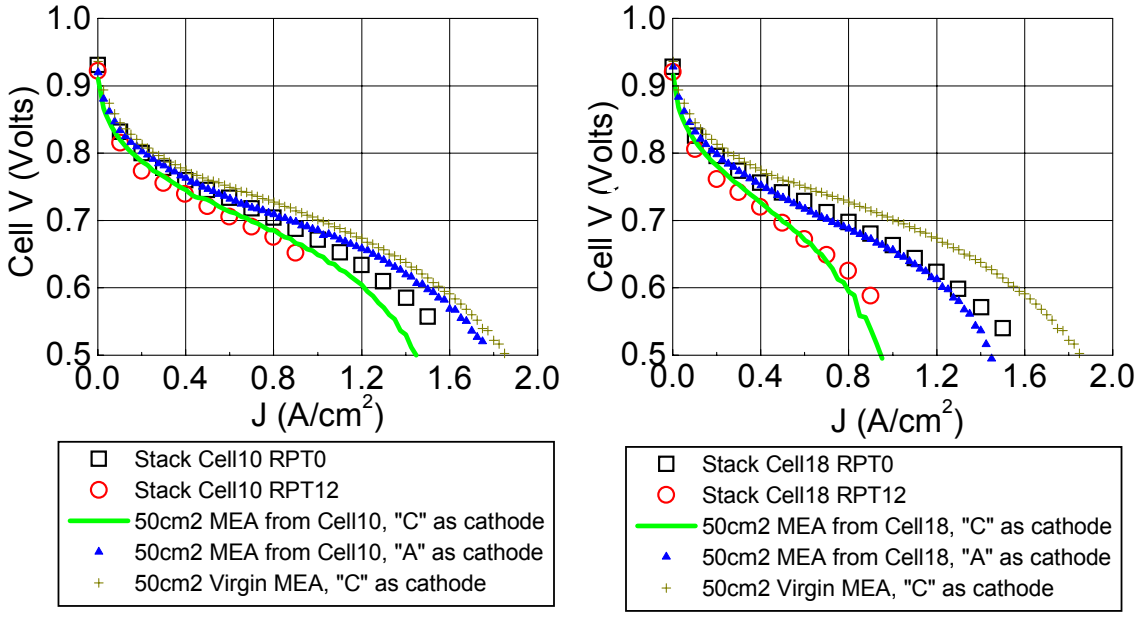

Fig. 24. Comparison of performance of cells 10 and 18 in stack initially (squares) and at end of stack testing (circles), in 50cm^2 MEAs with "C" as cathode (line) and "A" as cathode (triangle), as compared to a stack-untested MEA (cross).

For both the cell 10 and cell 18 MEA, reasonably good agreement is observed between the final stack performance and the performance in 50cm^2 cells with "C" as cathode, indicating that the single cell hardware is a reasonable test bed for evaluation of the performance changes which occurred in the stack.

In the 50cm^2 cell, with "C" as cathode, both the cell 10 and cell 18 MEA yielded lower performance than the reference MEA, although the cell 18 MEA was much lower. With "A" as cathode, the cell 10 MEA yielded performance much improved relative to "C" as cathode, but still slightly lower than the reference MEA. The cell 18 MEA with "A" as cathode yielded performance which was also improved relative to "C" as cathode, but this performance was still lower than the reference.

Fig. 25 shows the estimated HFR for cells 10 and 18 in the stack initially (RPT0) and at the end of stack testing (RPT12) by H_2 pump, in 50cm^2 single cells with "C" and "A" as cathode

estimated by AC impedance, in 50cm^2 with "C" as cathode estimated by H_2 pump, and the reference MEA by AC impedance and H_2 pump.

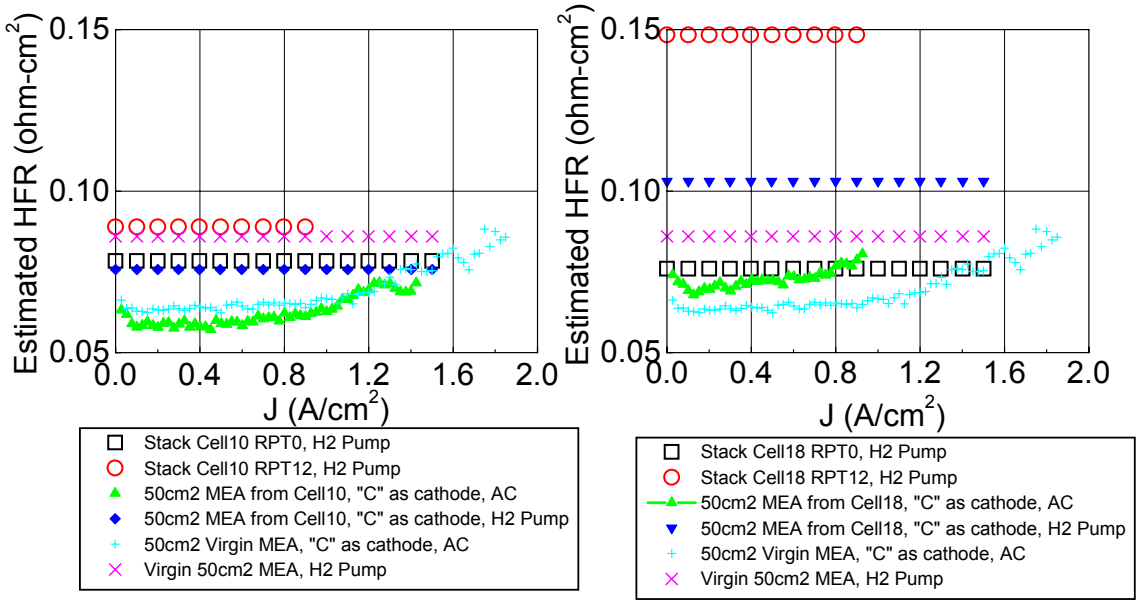

Fig. 25. Estimated high frequency resistance for MEAs from stack cells 10 (left) and 18 (right), measured in the stack at RPT0 or RPT12 with H_2 pump, or in 50cm^2 cells with "C" or "A" as cathode with AC impedance and H_2 pump. The comparative reference MEA data is also shown.

For cell 10 and 18, the H_2 pump-estimated HFR were initially similar to each other at RPT0. As noted previously, the in-stack HFR increased dramatically by RPT12, especially so for cell 18. However, when evaluated in 50cm^2 cells, both cell 10's and 18's AC impedance-estimated HFRs were markedly lower than the values obtained in the stack, with cell 18's impedance being just slightly higher than cell 10's. When measured by H_2 pump, both 50cm^2 cells' HFRs were lower than those measured in the stack during RPT12, but still moderately higher than the HFR values estimated by AC impedance, especially so for cell 18. Both cell 10's and cell 18's AC impedance-estimated HFRs were similar to the reference cell's AC impedance-estimated HFR, with cell 18's being slightly higher and cell 10's slightly lower. The reference cell's H_2 pump-estimated HFR was higher than the cell 10 50cm^2 cell's H_2 pump-estimated HFR, but lower than cell 18's.

Upon discovery of this larger-than-expected discrepancy between the single cells' AC impedance and H_2 pump-estimated HFRs, the individual AC impedance spectra for the 50cm^2 were re-examined and validated to be correct. Since the measured performances of both cells in the stack at RPT12 was similar to the performance measured in the single cells, and the performance differences between cell 10 and cell 18 were still present, it is likely that the H_2 pump-estimated HFR was considerably higher than the "true" AC impedance HFR. These data suggest that the assumption of negligible anode and cathode electrode polarization during H_2 pump is not strictly valid here.

Fig. 26 compares cyclic voltammograms of the both orientations of the stack-tested MEAs to the reference MEA. Table 7 lists the calculated Pt catalyst surface enhancement factor (SEF) from these voltammograms, the H_2/O_2 absolute activity and specific activity, and and also

summarizes the RPT performance and AC-impedance HFR data for the various stack-tested and reference 50cm^2 cells.

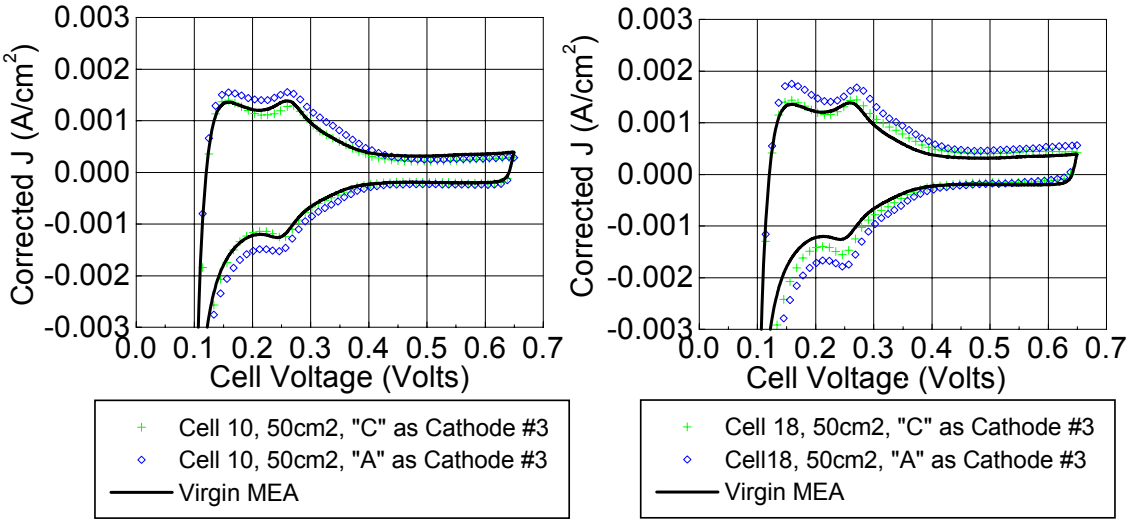

Fig. 26. Cyclic voltammograms of stack-tested and reference MEAs. Left: Cell 10. Right: Cell 18. Current densities corrected for electronic short and hydrogen crossover.

Table VII. Summary of Surface Area, Specific Activity, and RPT Performance of Stack-Tested and Reference MEAs in 50cm^2 single cell. SEF, 0.904V Activity and Specific Activity values are the average of 3 measurements. Electronic short and hydrogen crossover corrections were applied to 0.904V Activity and Specific Activity values. Errors noted below are standard deviations of the three trials for the electrochemical measurements. Typical sample-to-sample SEF, specific activity, and HFR values are within ± 10%.

	Cell 10, "C" as cathode	Cell 10, "A" as cathode	Cell 18, "C" as cathode	Cell 18, "A" as cathode	Reference MEA
SEF (m^2-Pt/m^2-geo)	10.49±0.07	13.1±0.6	11.9±0.2	14.38±0.09	10.5±0.3
0.904V Activity (mA/cm^2-geo)	18.2±0.8	30.9±0.4	20±2	27±1	24.7±0.5
0.904V Specific Activity (mA/cm^2-Pt)	1.73±0.08	2.3±0.1	1.7±0.2	1.88±0.07	2.35±0.08
0.800V J (RPT) (A/cm^2-geo)	0.16	0.21	0.15	0.19	0.26
0.700V J (RPT) (A/cm^2-geo)	0.69	0.87	0.50	0.71	1.00
0.600V J (RPT) (A/cm^2-geo)	1.21	1.49	0.79	1.23	1.56
0.20A/cm^2 RPT AC Impedance HFR (milliohm-cm^2)	58	56	70	64	63

When evaluated with "C" as cathode, the SEFs of both cell 10 and 18 were as large or larger than the reference cell's, indicating no loss of Pt surface area of the cathode electrocatalyst during the duration of stack testing. Interestingly, cell 10's and 18's "A" as cathode electrode had SEFs higher than the "C" as cathode electrodes or the reference. These numeric comparisons are validated qualitatively by the area of the hydrogen adsorption and desorption

peaks in the Fig. 26 voltammograms.The absolute and specific activities with "C" as cathode decreased 28% relative to the reference cell for both the cell 10 and cell 18 MEAs. The cell 10 "A" as cathode electrode's specific activity was the same as the reference MEA, but cell 18's "A" as cathode specific activity was lower than the reference.

For the stack-tested MEAs, the RPT current density at 0.80V followed trends similar to those predicted by the absolute activity. However, the reference cell's RPT 0.80V current density was markedly higher than all of the stack-tested MEAs', even though the absolute activity was lower than for the stack-tested MEAs' "A" as cathode electrodes. It is clear that while the absolute activity and surface area has influence, it is not sufficiently explanatory of the differences in RPT performance of these cells.

After analysis of cell 18 in the 50cm^2 cell was complete, the GDLs (from the stack MEA) were replaced with fresh GDLs of the same lot. Fig. 27 shows the RPT performances of the cell 18 CCM with the original and new GDLs and the reference MEA. With the new GDLs, the MEA yielded a considerable degree of performance improvement relative to the MEA with the stack-used GDLs, primarily in the mass transport regime. The HFR improved slightly with the new GDLs, but not enough to explain the improved performance. These results suggest that at least for cell 18, part of the mass transport performance loss is due to changes in the stack-tested GDLs which caused increased mass transport loss. While not proven, it is possible that cell 18's GDL-induced performance loss may be related to the large degree of discoloration of the cathode GDL, nominally caused by corrosion of the unipolar plate (Fig. 21). It is not certain if and to what extent this type of GDL degradation occurred in other cells of the stack.

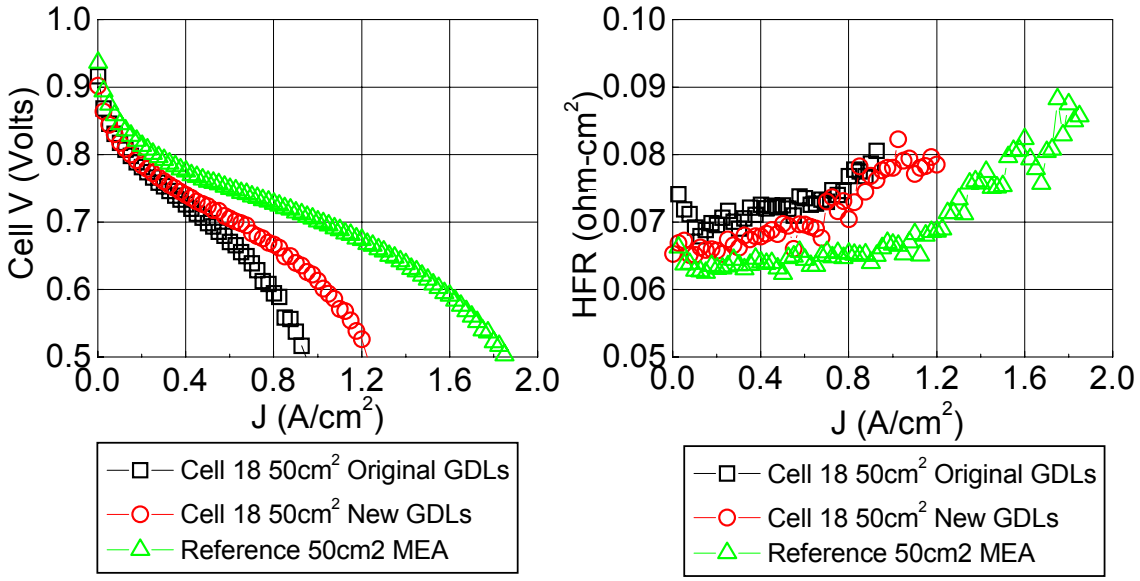

Fig. 27. Comparison of RPT performance of the cell 18 CCM with original stack GDL (squares) or with new GDLs (circles) to the reference MEA (triangles).

4.2.4.4 Analysis of Stack-Tested CCMs by Inductively Coupled Plasma – Atomic Emission Spectroscopy (ICP-AES)

Table 8 lists the results of the ICP-AES analysis of stack CCMs from cells 0, 10, 12, 16, 18, and 21, as well as 3 untested CCMs. For cell 12, analysis was performed in 3 different areas of the

CCM. For comparison purposes, cells 0, 12, 16, and 18 had higher than average measured voltage losses during durability Test 7.4, and cells 10 and 21 had lower than average voltage loss (Fig. 19). Note also that approximately 550ppm of Pb was found in the cell 0 CCM, but could not be accurately quantified by this method.

Table VIII. Analysis for cations in untested and stack-tested CCMs by ICP-AES. Concentrations reported in microgram-cation per gram of CCM (ppm). dV refers to total cell voltage loss during Test 7.4 (durability) at 1.2A/cm^2 (see Fig. 19).

	Al	Ca	Co	Fe	K	Mn	Na	Ni	Zn	dV (mV)
Untested CCM	34±5	15±2	5503±25	22±4	36±25	490±0	48±3	6±6	9±1	
Cell0	46	510	5400	27	130	480	51	2960	54	-23
Cell10	36	460	5620	24	61	500	70	3570	20	-4
Cell12 EndA	82	610	5860	88	250	530	110	8380	69	-55
Cell12 Middle	51	420	6450	65	150	620	56	6270	13	-55
Cell12 EndB	60	590	5970	36	100	540	47	5170	28	-55
Cell16	70	750	5860	45	84	550	65	5850	67	-48
Cell18	53	480	6100	37	28	560	43	5650	17	-80
Cell21	89	730	5820	24	62	530	58	2800	53	-9

The stack tested CCMs showed an approximate thousand-fold increase in Ni content, hundred-fold increase in Ca, and relatively moderate increases in Al, Fe, K, Na, and Zn. Co and Mn levels, present in the original PtCoMn electrocatalyst, were relatively unchanged in the tested CCMs as compared to the untested CCMs, indicating that these materials were not significantly lost during testing. Qualitatively, the MEAs which showed the largest performance loss tended to have higher levels of cation contamination.

The most likely source of the Ni contamination is the Ni present as an underlayer for the gold-coated unipolar plates. Although Ni is also present in the system as an element of stainless steel, Fe content only increased slightly, so corrosion of stainless steel is likely not a significant source of Ni. Ca, K, and Na are common environmental cations, and it is certainly feasible that residual levels in the deionized humidification water or reactant air could cause a slow accumulation of these species with time.

Separate studies in single 50cm^2 cells provide guidance in terms of the impact of cation contamination on fuel cell performance. Fig. 28 shows performance and characterization data for CCMs with either a PEM which had been contaminated with Ca or an uncontaminated PEM. These CCMs were identical to the stack CCMs, except that they used 1000EW 3M PEM instead of the 800EW PEM. Note that the operating conditions used for the analysis in Fig. 28 differ somewhat from those used in the analysis of stack CCMs above (Figs. 24-26), most notably the activity measurement which used ambient reactant pressures here and 50kPag for stack CCM analysis.

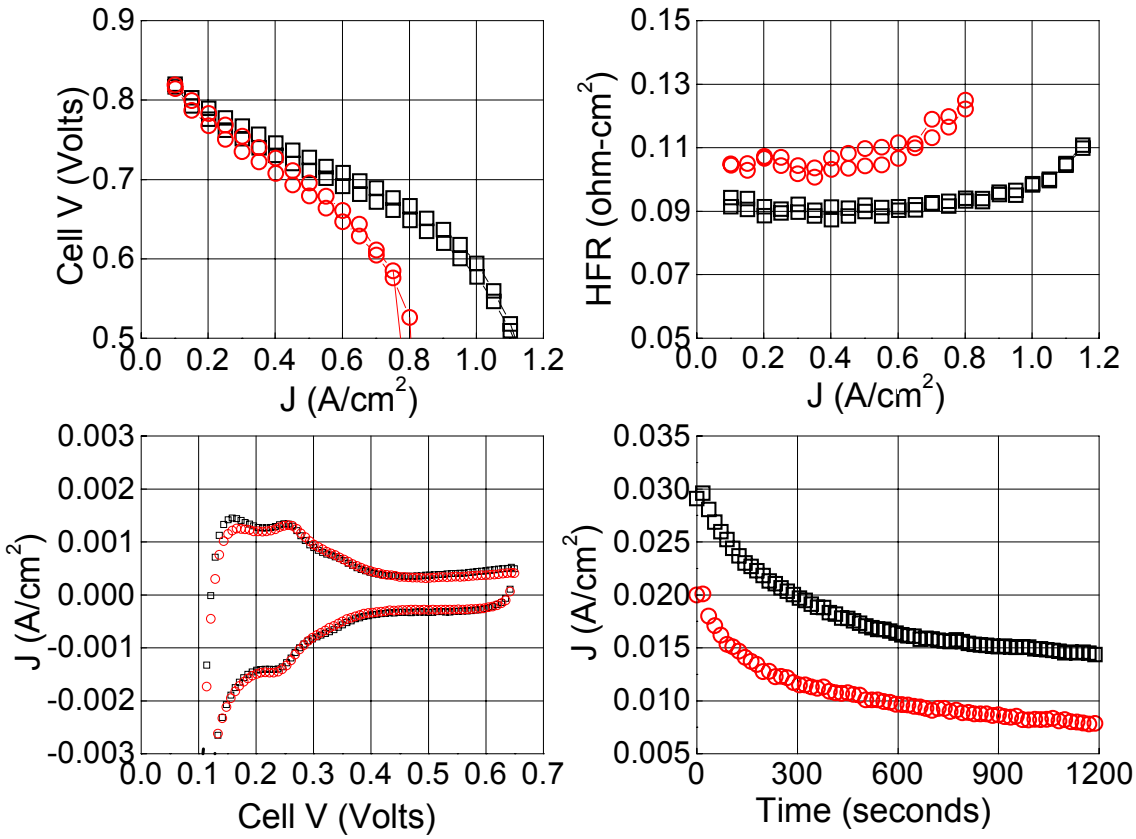

Fig. 28. Characterization of a Ca-contaminated NSTF MEA of similar type as the stack MEAs. Upper left: Galvanodynamic performance at 80°C cell, 100% RH, ambient pressure, 696/1657SCCM H_2/Air. Upper right: HFR taken during galvanodynamic performance test. Lower left: H_2/N_2 cyclic voltammetry at 80°C cell, 100% RH, ambient pressure, 696/1657SCCM H_2/N_2. Lower right: Current density over time during absolute activity measurement at 80°C cell, 100% RH, ambient pressure, 696/1657SCCM H_2/O_2. Squares: Uncontaminated CCM. Circles: Ca-contaminated CCM.

Fig. 28 shows that the Ca-contaminated PEM MEA has a significantly reduced limiting current relative to the uncontaminated PEM sample. In this case, the limiting current was reduced from approximately 1.2 to 0.8A/cm^2. The HFR for the Ca-contaminated sample was moderately higher than the uncontaminated sample. One of the key characteristics of PEM cation poisoning is that the HFR increase largely does not compensate for the performance loss purely by ohmic considerations. The cyclic voltammograms in Fig. 28 show that the measured Pt surface area does not appreciably change with Ca contamination. Lastly, Ca contamination resulted in a decrease of approximately 40% of the absolute activity (Fig. 28, lower right, at 900s); since the Pt surface area did not change, the specific activity decreased by 40% also.

Other results from this separate study show that the limiting current decreases strongly as the cation concentration in the PEM increases; a 13,000ppm Na-contaminated PEM showed a limiting current decrease from 1.2 to 0.45A/cm^2 under the same conditions as shown in Fig. 28. In addition, performance at currents considerably less than the limiting current is also moderately degraded. Our current hypothesis is the dominant mode of performance loss due to moderate levels of Ca, Fe, Na, and Al contamination is primarily due to deleterious changes in PEM water transport properties, resulting in decreased oxygen mass transport in the cathode

catalyst layer and/or GDL. Lastly, it was determined that these H_2/air performance changes with cation-contamination of the PEM impacts Pt/C (dispersed) electrode based MEAs almost identically as NSTF MEAs.

While data is not directly available for Ni in controlled studies, the data from the Na and Ca-contaminated PEM studies noted above suggests that the levels of Ni present in the stack CCMs are qualitatively consistent with the observed decreases in limiting current and specific activity.

4.2.4.5 Analysis of a Stack-Tested Unipolar Plate by Auger Electron Spectroscopy

Figs. 29-32 show Auger analysis of the cell 17 cathode unipolar plate, after testing in the DOE3_042607 stack.

Fig. 29 shows optical images of a relatively lightly-discolored section of the cell 17 cathode unipolar plate reactant flow field. In the channel areas, several regions showed cracks and deformation of the gold coating.

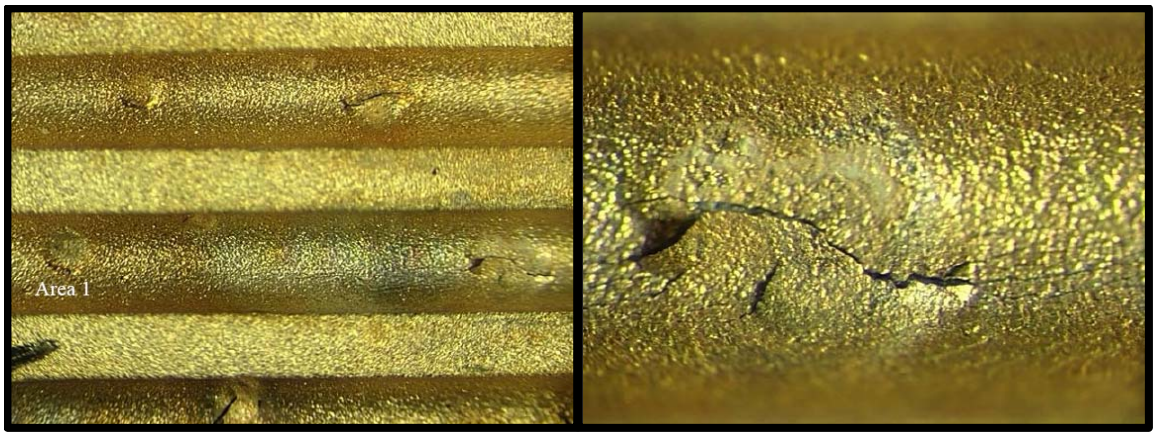

Fig. 29. Optical images of corrosion of cell 17 cathode unipolar plate reactant lands and channels.

Fig. 30 shows SEM and Auger images of a particular channel defect site. C, O, and Ni were present at the surface of this area, but Fe was not. This suggests that the Ni "tie-layer" between the Au and 316SS was the source of Ni and not corrosion of stainless steel, since one would have also expected to have found Fe. Examination of 4 different channel areas showed considerable Ni content but < 5-10% Au at the surface. One examined land area showed 20% Au at the surface, but nickel oxide was still the primary species at the surface.

Fig. 31 shows the results of an Auger depth profile. At this location of the surface (t=0), there was approximately 4 times more Ni than Au present. As the surface was sputtered away, the Ni content initially increased then decreased while the Au content increased continually with time. This suggests that in this area there was nearly complete contamination of the original Au surface by Ni.

Fig. 32 shows Auger spectra from two regions of the unipolar plate. One region was an area from the reactant flow field and the other was from a region which wasn't exposed to reactants. The region of the unipolar plate exposed to reactant shows peaks corresponding to the

presence of surface Ni, while the unexposed region shows no evidence of Ni within detection limits. These results indicate the requirement of humidified air for the corrosion to occur.

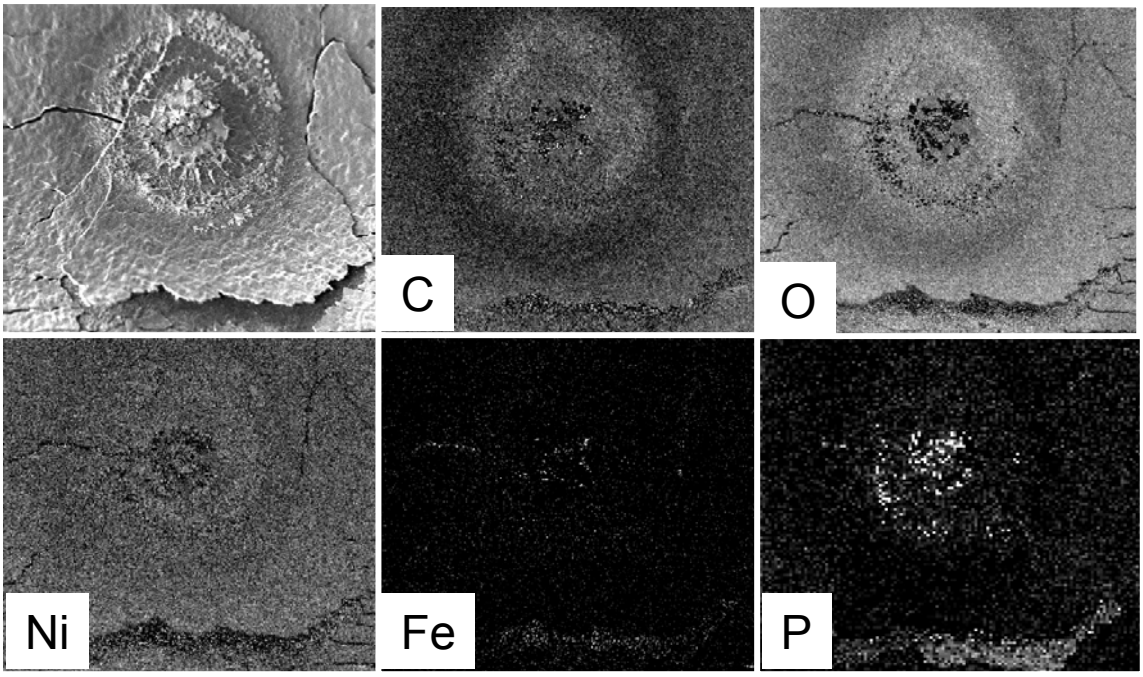

Fig. 30. Auger images of corrosion spot. Upper left: SEM, 725micron field of view. Other images show maps of surface content of the noted elements.

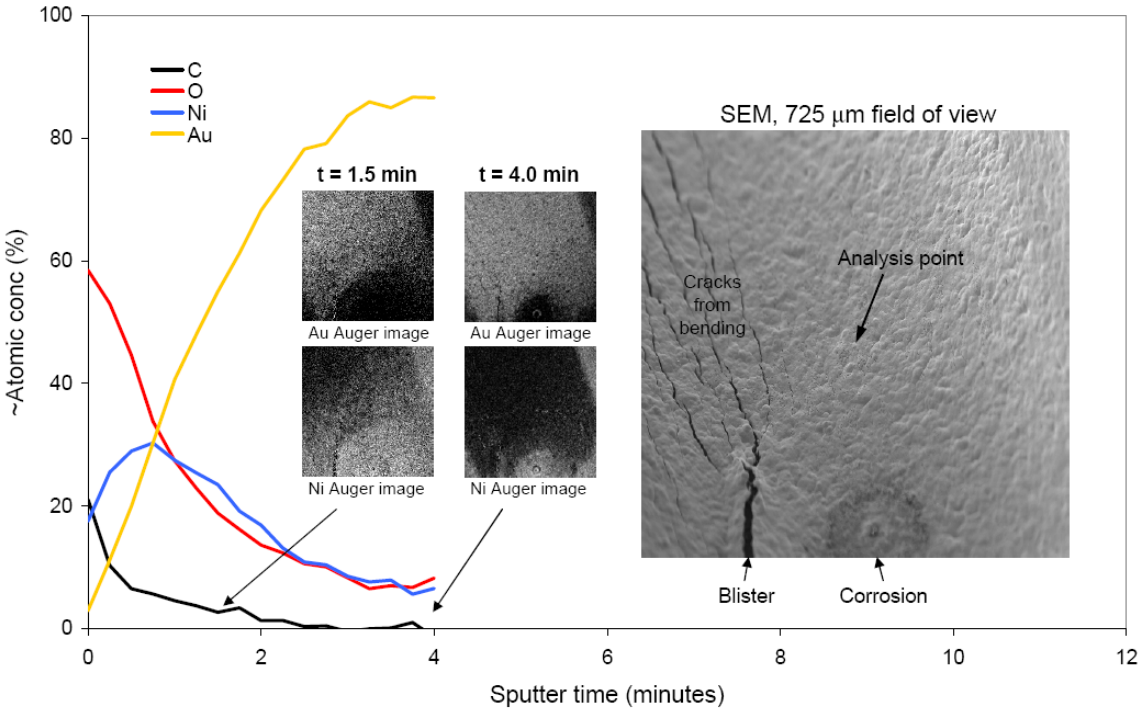

Fig. 31. Auger depth profile of area near corrosion.

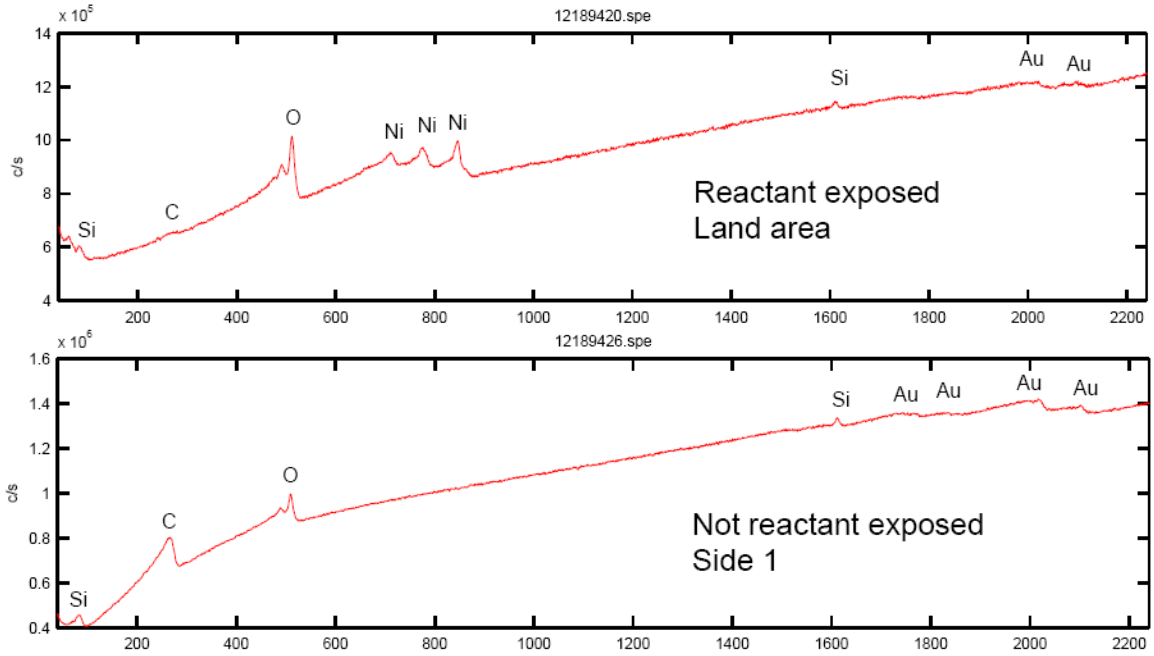

Fig. 32. Auger spectra from various positions on cell 17 cathode unipolar plate. Upper: Land area of reactant flow field. Lower: Area of same unipolar plate not exposed to reactants.

4.2.5 Summary

Under Task 3, 3M evaluated the performance and durability of a 22-cell, 312.5cm^2 active area 5kW short stack with MEAs containing 3M PtCoMn NSTF catalyst with 0.2mg/cm^2-Pt per electrode and 3M 800EW PEM, both developed under the auspices of this contract.

Performance characterizations encompassed polarization curve measurements under a variety of hot-and-dry operating conditions. The stack was evaluated with reactant pressures ranging from near ambient to 150kPag, stack coolant temperatures ranging from 80 to 100°C, reactant humidification ranging from 45 to 85%RH, and cathode stoichiometry ranging from 2.5 to 1.7. The stack performance variation with these parameters was mainly as expected. The stack delivered a peak (rated) power of 5.15kW at 0.600V/cell, and a peak power of 5.50kW at 0.500V/cell, at 90°C coolant temperature, 150kPag reactant pressures, reactant stoichimetries of 2.0/2.5, and 66% RH reactant humidification. The overall initial performance obtained with this stack was considerably less then expected, based on the results of single 50cm^2 cells and a predecessor stack. The predecessor stack, which used the same physical stack hardware and was the same total size, produced 6.19kW at 0.600V/cell under identical conditions as above. It is believed, but not proven, that degradation of the unipolar plates' corrosion resistant coating compromised the initial performance of the stack reported here. It is posited that Ni at the surface of the unipolar plates migrated to the stack MEAs during the initial conditioning phase, but only ex-situ analysis of the MEAs at that point in time would confirm this hypothesis.

Durability evaluation consisted of a protocol where the stack was held at 90°C coolant temperature while the stack current was varied between 0 and 1.27A/cm^2 over a 465 second cycle. A total of 554 hours of durability testing were completed by the end of the contract. Over the 554 hours of durability testing, the average per-cell irreversible performance loss at reference conditions was 8±4mV and 17±22mV at 0.1 and 1.2A/cm^2, respectively. During the

experiment, the stack unipolar plates corroded significantly; after semi-quantitative removal of the estimated ohmic loss contribution induced by this corrosion, the per-cell stack performance decreased 6±3mV and 0.1±15mV at 0.1 and 1.2A/cm^2, respectively.

Single cell diagnostic tests were performed on the most significantly degraded stack MEA as well as an MEA which had degraded a typical degree. These results indicated that the primary sources of performance loss were an approximate 30% decrease of the specific activity for both MEAs, and an approximate 20% and 50% reduction in limiting current for the typical and most degraded MEAs, respectively. No significant loss of Pt catalyst surface area was noted for either MEA.

Evaluation of the stack unipolar plates after stack testing indicated that the protective gold layer on the unipolar plates had failed, which exposed Ni to the reactant streams. Analysis for cationic contamination of some stack CCMs indicated that each of these CCMs was grossly contaminated with Ni. Results from an unrelated study, which evaluated the impact of common metallic cations on fuel cell performance, catalyst surface area and catalyst specific activity, suggested that the Ni contamination of the stack CCMs was the likely primary source of the decrease in limiting current and specific activity observed in the stack.

Section 5

Technology Transfer Activities

Section 5 - Technology Transfer Activities

Significant efforts were expended to disseminate the results of the research and development findings from this contract to the wider fuel cell community. In total approximately 36 presentations were made over the period of 2003 to 2007 at national and international meetings and conferences, fourteen of these invited. Twenty-six publications were prepared for journal publications or conference proceedings, and four annual DOE progress reports. Ten patent applications were generated from this work and all have published. Finally, close interactions with six Universities and three National Laboratories during the contract have also enabled transfer of the technology and concepts in both directions as a result of the interactions. As a result of this interaction, one PhD. Thesis was completed. MEA's containing the NSTF PtCoMn catalyst and 3M PFSA based membrane, and the 3M membrane with enhanced durability, as developed in part under this Contract, are being sold and sampled to customers for evaluation.

5.1 Publications and Presentations 2003-2007

1. M. K. Debe, A. K. Schmoeckel, G. D. Vernstrom, R. T. Atanasoski, S. M. Hendricks, and A. J. Steinbach, "Oxygen reduction activities of nanostructured thin film alloy electrocatalysts," to be sumitted, Oct., 2007.

2. Lajos Gancs, Takeshi Kobayashi, Mark K. Debe, Radoslav Atanasoski, and Andrzej Wieckowski*, "Crystallographic Characteristics of Nanostructured Thin Film Fuel Cell Electrocatalysts – A HRTEM Study," to be submitted, Sept., 2007.

3. "LOW PLATINUM AND NON-PRECIOUS METAL CATALYSTS FOR PEM FUEL CELL APPLICATION", R. Atanasoski, invited talk at Nanoscale Inorganic Catalysis Symposium – American Chemical Soc., Chicago, March, 2007.

4. R. Atanasoski: "RECENT ADVANCES IN THE 3M TECHNOLOGY FOR PEMFC: LOW PLATINUM AND NON-PRECIOUS METAL CATALYSTS", Key-note lecture at the International Conference on "New Proton Conducting Membranes and Electrodes for PEM FCs" In honour of Professor Giulio Alberti, Assisi, Italy, October 26, 2005.

5. K.J.J. Mayrhofer, B.B. Blizanac, V.R. Stamenkovic, P.N. Ross, N.M. Markovic, R.T. Atanasoski, A.K. Schmoeckel, G.D. Vernstrom, M.K. Debe, "ORR activity on Pt and PtNiFe NSTF Catalysts: Comparative RRDE and Fuel Cell Evaluation," to be submitted, J. Power Sources, 2007.

6. L. Jia, D. Nguyen, J. W. Halley , P. Pham, W. Lamanna, S. Hamrock, " Modeling Proton Transport in HTFSI-TFSI-EMI Mixtures" J. Chem. Physics, Submitted for publication.

7. M. Emery, M. Frey , M. Guerra, G. Haugen, K. Hintzer, K. H. Lochhaas, P. Pham, D. Pierpont, M. Schaberg, A. Thaler, M. Yandrasits, and S. Hamrock, " New Membranes for PEM Fuel Cells", prepared for presentation at the 212th ECS meeting, Washington, DC, October 7-12, 2007, and submitted to ECS Transactions.

8. Arman Bonakdarpour, Krystal Stevens, George D. Vernstrom, Radsolav Atanasoski, Alison K. Schmoeckel, Mark K. Debe, and Jeff R. Dahn, "Oxygen Reduction Activity of

Pt and Pt-Mn-Co Electrocatalysts Sputtered on Nano-structured Thin Film Support ," in press, Electrochimica Acta, 2007.

9. Arman Bonakdarpour: "A Combinatorial Study of Pt-Based Oxygen Reduction Electrocatalysts for Hydrogen Fuel Cells," PhD Thesis, Dept of Physics and Atmospheric Science, Dalhousie University, Halifax, Canada, 2007.

10. J.M. Larson, S.J. Hamrock, G.M. Haugen, P. Pham, W.M. Lamanna, A. Butenhoff Moss, "Membranes based on basic polymers and perfluorinated acids for hotter and drier fuel cell operating conditions," Journal of Power Sources, in press

11. Haugen, G. M.; Meng, F.; Aieta, N. V.; Horan, J. L .; Kuo, M.-C.; Frey, M. H.;. Hamrock, S. J; Herring, A. M., "The Effect of Heteropoly Acids on Stability of PFSA PEMs under Fuel Cell Operation" Electrochem. Solid-State Lett., 10, B51-B55, 2007

12. T. Kalapos, D.R. Lebzelter, R. Subbaraman, S. Hamrock, M. Yandrasits, P. Pham, H. Ghassemi, "Properties of New Perfluorinated Acid Membranes", the International Conference on Batteries-Fuel Cells, Rome, Italy, June 11, 2007.

13. M. Debe, A. Hester, G. Vernstrom, A. Steinbach, S. Hendricks, A. Schmoeckel, R. Atanasoski, D. McClure and P. Turner, "Nanostructured Thin Film Catalysts for PEM Fuel Cells by Vacuum Web Coating," in press, 50th Annual Technical Conference Proceedings of the Society of Vacuum Coaters, Louisville, KY, April 30-May 3, 2007.

14. M. K. Debe, "Status and Prospects of PEFC Electrocatalysts: Meeting the Requirements for Automotive Fuel Cells with Nanostructured Thin Film Electrodes," presented at and in proceedings of 3rd International Hydrogen and Fuel Cell Expo Technical Conference, Tokyo Big Sight, Tokyo, Japan, Feb. 7-9, 2007.

15. A. K. Schmoeckel, G. D. Vernstrom, A. J. Steinbach, S. M. Hendricks, R. T. Atanasoski and M. K. Debe, "Nanostructured Thin Film Ternary Catalyst Activities for Oxygen Reduction," presented at the 2006 Fuel Cell Seminar, Honolulu, Hawaii, Nov. 13-17, 2006.

16. K. Noda, A. Steinbach and M. Debe, " Start-stop durability testing of 3M's Nanostructured Thin Film Catalysts for PEM Fuel Cells, presented at the 210th ECS meeting, Oct. 29-Nov. 3, 2006, Cancun, Mexico, and published in ECS Transactions, Volume 3(1), 835 (2006).

17. D. A. Stevens, J. M. Rouleau, R. E. Mar, J. R. Dahn, R. T. Atanasoski, A. K. Schmoeckel and M. K. Debe, "64-Electrode PEM Fuel Cell Studies of CO-Tolerant Hydrogen Oxidation Catalysts, presented at the 210th ECS meeting, Oct. 29-Nov. 3, 2006, Cancun, Mexico, and published in ECS Transactions, Volume 3(1), 355 (2006).

18. A. Bonakdarpour, R. Lobel, R. T. Atanasoski, G. D. Vernstrom, A. K. Schmoeckel, M. K. Debe and J. R. Dahn, "Dissolution of Transition Metals in Combinatorially Sputtered, Pt1-x-y Mx M'y (M,M' = Co, Ni, Mn, Fe) PEMFC Electrocatalysts "J. Electrochemical Society, Vol. **153 (10)**, 2006, A1835-A1846.

19. Haugen, G. M.; Meng, F.; Aieta, N. V.; Pham, P.; Horan, J. L .; Frey, M. H.;. Hamrock, S. J; Herring, A. M., "Increased Stability of PFSA Proton Exchange Membranes Under Fuel Cell Operation by the Decomposition of Peroxide Catalyzed by Heteropoly Acids" presented at the 2006 Fuel Cell Seminar, Honolulu, Hawaii, Nov. 13-17, 2006.

20. Haugen, G. M.; Meng, F.; Aieta, N. V.; Horan, J. L .; Kuo, M.-C.; Frey, M. H.;. Hamrock, S. J; Herring, A. M., "Increased Stability of PFSA Proton Exchange Membranes Under Fuel Cell Operation by the Decomposition of Peroxide Catalyzed by Heteropoly Acids" presented at the 210th ECS meeting, Oct. 29-Nov. 3, 2006, Cancun, Mexico, and published in ECS Transactions, Volume 3(1), 355 (2006).

21. N.V. Aieta, M.A. Yandrasits, S. J. Hamrock, R. J. Stanis, D.J. Cookson, A. M. Herring, "SAXS measurements of hydration processes in Nafion® and Nafion- like membranes", presented at the 210th ECS meeting, Oct. 29-Nov. 3, 2006, Cancun, Mexico.

22. J. M. Larson, S. J. Hamrock, G. M. Haugen, P. Pham,, W. M. Lamanna, A. Butenhoff Moss, "Proton Exchange Membranes With Bis-Fluorinated Acids For Fuel Cell Operation Under Hotter And Drier Conditions", presented at the Symposium on Fuel Cell Chemistry and Operation at the American Chemical Society National Meeting, San Francisco, CA September 10-14, 2006.

23. M.A. Yandrasits, N. Aieta, R.J. Stanis, S.J. Hamrock , D.J. Cookson, A.M. Herring, "Dynamics of PFSA polymer hydration measured in-situ by SAXS", presented at the Symposium on Fuel Cell Chemistry and Operation at the American Chemical Society National Meeting, San Francisco, CA September 10-14, 2006.

24. N.V. Aieta, M.A. Yandrasits, S. J. Hamrock, R. J. Stanis, A. M. Herring, "In-situ synchrotron SAXS studies of hydration processes in Nation® and other perfluorosulfonate membranes for high temperature / low relative humidity PEM fuel cell applications" presented at the Symposium on Fuel Cell Chemistry and Operation at the American Chemical Society National Meeting, San Francisco, CA September 10-14, 2006.

25. A.M. Herring, F. Meng, S.F. Dec, S. J. Hamrock, M.H. Frey, J.A. Turner, N. Aieta, J Horan, "Understanding the Implications of Doping PFSA Ionomers with Heteropoly Acids", presented at the Annual International Society of Electrochemistry Meeting, Edinburgh, UK, August 23, 2006.

26. M. K. Debe, 2006 DOE Hydrogen Program Review, Washington, DC, May 17, 2006.

27. M. K. Debe, A. K. Schmoeckel, G. D. Vernstrom and R. Atanasoski, "High Voltage Stability of NanoStructured Thin Film Catalysts for PEM Fuel Cells," J. Power Sources **161**, 1002-1011 (2006).

28. J.R. Dahn, D.A. Stevens, A. Bonakdarpour, E.B. Easton, M.T. Hicks, G.M. Haugen, R.T. Atanasoski and M.K. Debe, "Development of Durable and High-Performance Electrocatalysts and Electrocatalyst Support Materials," Symposium on Durability and Reliability of Low-Temperature Fuel Cell Systems, ECSTransactions, Vol.1, No. 8, 2006.

29. M. K. Debe, A. K. Schmoeckel, S. M. Hendricks, G. D. Vernstrom, G. M. Haugen and R. T. Atanasoski, “Durability Aspects of Nanostructured Thin Film Catalysts for PEM Fuel Cells,” presented at Symposium on Durability and Reliability of Low-Temperature Fuel Cell Systems, 208th ECS meeting, Oct. 16 - 21, 2005, Los Angeles, CA and published in ECSTransactions, Vol.1, No. 8, 2006, pages 51-66.

30. F. Meng, S. Dec, M. Frey, S. Hamrock, J. Turner, and A. Herring, "Spectroscopic Studies of Heteropoly Acid Doped 3M Perfluorinated Sulfonic Acid Polymer Membranes," Proton Exchange Membrane Fuel Cells V, in Honor of Supramaniam Srinivasan, ECS Transactions, Vol.1, No. 6, 255-262, 2006.

31. M. K. Debe, S. J. Hamrock, and R. T. Atanasoski, DOE Hydrogen Program FY2006 Annual Progress Report, 2006.

32. J. McBreen, M. Balasubramanian, W.-S. Yoon, K. Y. Chung, H. S. Lee, and X. Q. Yang, R.T.Atanasoski, A.K. Schmoeckel, G.D. Vernstrom, and M.K. Debe, “PEM Fuel Cells: Materials Issues,” Fifth International Symposium on Proton Exchange Membrane Fuel Cells, In Honor of Dr. Subramanian Srinivasan, 208th ECS Meeting, Los Angeles, CA, Oct. 16 - 21, 2005.

33. J.R. Dahn, D.A. Stevens, A. Bonakdarpour, E.B. Easton, M.T. Hicks, G.M. Haugen, R.T. Atanasoski and M.K. Debe, “Development of Durable and High-Performance Electrocatalysts and Electrocatalyst Support Materials,” Symposium on Durability and Reliability of Low-Temperature Fuel Cell Systems, 208th ECS meeting, Oct. 16 - 21, 2005, Los Angeles, CA.

34. Mark K. Debe, Alison K. Schmoeckel, Radoslav Atanasoski and George D. Vernstrom, “High Voltage Stability of NanoStructured Thin Film Catalysts for PEM Fuel Cells,” 2005 Fuel Cell Seminar, Palm Springs, California, Nov. 14 - 18, 2005.

35. F. Meng, S. Dec, M. Frey, S. Hamrock, J. Turner, and A. Herring, "Spectroscopic Studies of Heteropoly Acid doped 3M Perfluorinated Sulfonic Acid Polymer Membranes," 208th Meeting of the Electrochemical Society, Los Angeles, CA, Oct. 18, 2005.

36. S. Hamrock, "The Development of New PEM Fuel Cell Membranes at 3M," Golden Gate Polymer Forum, 25th Anniversary Symposium, Oct. 23, 2005, San Francisco, CA.

37. A. M. Herring, J. A. Turner, S. F. Dec, F. Meng, J. Horan, N. Aieta, and R. J. Stanis, "The Use of Heteropoly Acids in the Production of High Performance PEM Fuel Cell Components," 2005 Fuel Cell Seminar, Nov. 15, Palm Springs, CA.

38. S. Hamrock, "New PFSA membranes with Improved Durability," Pacific Polymer Conference IX, Maui, Hawaii, Dec. 12, 2005.

39. “Advanced MEA’s for Enhanced Operating Conditions, Amenable to High Volume Manufacture,” 13th Quarterly Review, 2005 DOE FreedomCAR Tech Team Annual Review, USCAR, Detroit, MI, July 20, 2005.

40. M. K. Debe, "Advanced Catalyst and Membrane Technology with Enhanced Performance and Durability for Automotive Requirements," invited presentation at 4th International Fuel Cell Workshop 2005, Kofu, Yamanashi, Japan, Sept. 23-24, 2005.

41. "Studies of Transition Metal Dissolution from Combinatorially Sputtered, Nano-Structured Pt1-x Mx (M=Fe, Ni; 0<x<1) Electrocatalysts for PEM Fuel Cells," A. Bonakdarpour, J. Wenzel, D. A. Stevens, S. Sheng, T. L. Monchesky, R. Lobel, R. T. Atanasoski, A. K. Schmoeckel, G. D. Vernstrom, M. K. Debe and J. R. Dahn, J. Electrochemical Society, Vol. 152 (1), 2005, A61-A72.

42. 2005 DOE Hydrogen, Fuel Cells, and Infrastructure Technologies Program Review Meeting, May 23 - 26, 2005, Arlington, VA, Presentation FC-3.

43. "The Use of Heteropoly Acids in Composite Membranes for Elevated Temperature or Low Humidity PEM Fuel Cell Operation," A. Herring, J. Turner, S. Dec, J. Malers, F. Meng, J. Horan and N. Aieta, 2nd International Conference on Polymer Batteries and Fuel Cells, Las Vegas, NV, June 13, 2005.

44. "Mechanical Property Measurements of PFSA Membranes at Elevated Temperatures and Humidities," M. A. Yandrasits, 2nd International Conference on Polymer Batteries and Fuel Cells, Las Vegas, NV, June 14th 2005.

45. "Prospects and Challenges for PEM Fuel Cells with a Focus on MEA Development for Automotive Applications," M. K. Debe, Invited Plenary Lecture, 2005 Annual Meeting of the North American Membrane Society, Providence, RI, June 15, 2005.

46. "3M MEA Technology for PEMFC: The Catalysts," Radoslav Atanasoski, presented at the Dept. of Chemical Engineering, USC, Columbia, 21 April 2005

47. "The development of new membranes for PEM Fuel Cells," Steve Hamrock, Advances in Materials for Proton Exchange Membrane Fuel Cell Systems, Asilomar Conference Grounds, Pacific Grove, CA, Feb. 21, 2005.

48. "NanoStructured Thin Film, Thin Layer Electrodes Optimized for PEM Fuel Cell Performance at High Current Density," Mark. K. Debe, Susan M. Hendricks, Alison K. Schmoeckel, George D. Vernstrom, Radoslav T. Atanasoski, Paul J. Kadera, and Andrew J. Steinbach, 2004 Fuel Cell Seminar, San Antonio, TX, Nov. 1-5, 2004.

49. "Corrosion of Transition Metals in $Pt_{1-x}M_x$ (M = Fe, Ni, Mn) Proton Exchange Membrane Fuel Cell (PEMFC) Electrocatalysts," A. Bonakdarpour, R.Löbel, J. Wenzel, D.A. Stevens, R.T. Atanasoski[a], A.K. Schmoeckel[a], G.D. Vernstrom[a], M.K. Debe[a], and J. R. Dahn, 206th Electrochemical Society Meeting, Hawaii, USA (2004).

50. **"**Multi-channel fuel cell for testing of sputtered combinatorial arrays of oxygen reduction catalysts," D.A. Stevens, R.E. Domaratzki and J. R. Dahn, 206th Electrochemical Society Meeting, Hawaii, USA (2004).

51. "Combinatorial PEM fuel cell studies of binary platinum alloy," D.A. Stevens, R.E. Domaratzki, A. Bonakdarpour , R. Lobel and J. R. Dahn, 206th Electrochemical Society Meeting, Hawaii, USA (2004).

52. “The Search for Higher Temperature Proton Conductors for the PEM Fuel Cell,” J. Woods Halley, Symposium on Fuel Cells, MRS Meeting, Boston, MA, December 1, 2004.

53. “Recent Advances on 3M MEA Technology for PEMFC”, Radoslav Atanasoski, Invited talk, International Conference on Conducting Electrolites-4 Como, Italy, 18- 20 February 2004.

54. “Nanostructured Thin Film (NSTF), Thin Layer Catalyst Electrodes for PEM Fuel Cells,” M. K. Debe, 2004 Gordon Research Conference on Fuel Cells, July 25-30, Roger Williams University, Bristol, RI.

55. 2004 DOE Hydrogen Fuel Cells and Infrastructure Technologies Annual Review, Philadelphia, PA, May 24-27, 2004.

56. Annual Report in Hydrogen, Fuel Cells, and Infrastructure Technologies FY2004 Progress Report.

57. “Dissolution of Fe and Ni in Combinatorially Sputtered $Pt_{1-x}Fe_x$ and $Pt_{1-x}Ni_x(0<x<1)$ Electrocatalysts,” A. Bonakdarpour, J. Wenzel, D. A. Stevens, S. Sheng, T. L. Monchesky, R. T. Atanasoski, A. K. Schmoeckel, G. D. Vernstrom, M. K. Debe and J. R. Dahn, presented at the First International Conference on Fuel Cell development and Deployment, March 7-10, 2004, Connecticut Global Fuel Cell Center, Stores, CT.

58. “In-situ Vibrational Spectroscopy with Fuel Cell Catalysts,” Andrzej Wieckowski, Lajos Gancs, Matthew McGovern, Guo-Qiang Lu, Radoslav Atanasoski, and Mark K. Debe, presented at the American Chemical Society meeting, Anaheim, CA, March 29-April 2, 2004.

59. L. Rivard, D. Pierpont, H. Freemeyer, A. Thaler and S. Hamrock, “ Development of a new electrolyte membrane for PEM fuel cells,” 2003 Fuel Cell Seminar, Miami Beach, FL, November 3-7, 2003, Abstract Book p. 73.

60. This contract’s “Annual Report” in Hydrogen, Fuel Cells, and Infrastructure Technologies FY2003 Progress Report, page 442.

61. M. K. Debe, A. J. Steinbach, K. A. Lewinski, G. M. Jaugen, G. D. Vernstrom, R. T. Atanasoski, A. E. Hester, P. L. Turner, R. J. Ziegler, J. M. Larson, M. T. Hicks and P. E. Serim, “Activities of Low Pt Loading, Carbon-less, Ultra-thin Nanostructured Film-Based Electrodes for PEM Fuel Cells, and Perfoermances in Roll-good Fabricated MEA’s ini Single Cells and Stacks,” 2003 Fuel Cell Seminar, Miami Beach, FL, November 3-7, 2003.

5.2 Patent Applications

1. US 20060063054 “Durable Fuel Cell”, Frey, Matthew H.;Hamrock, Steven J.; Haugen, Gregory M.; Pham, Phat T. (Published 2006).

2. US 20060063055 “Fuel Cell Durability”, Frey, Matthew H.;Hamrock, Steven J.; Haugen, Gregory M.; Pham, Phat T. (Published 2006).

3. US 20060127729 “Fuel Cell” Roscoe, Stephen B.; Rakow, Neal A.; Atanasoski, Radoslav; Jackson, Eric R.; Thomas, John H. III; McIntosh, Lester H. (Published 2006).

4. US 20060147791 “Platinum Recovery from Fuel Cell Stacks,” Debe, Mark K.; Hamilton, Jr., Clayton (Published 2006).

5. US 20060144791 “Platinum Recovery from Fuel Cell Stacks,” Debe, Mark K.; Hamilton, Jr., Clayton (Published 2006).

6. US 20070082814 “Ternary Nanocatalyst and Method of Making,” Debe, Mark K.; Hendricks, Susan M.; Vernstrom, George D.; Hester, Amy E. (Published 2007).

7. US 20070082256 “Fuel Cell Nanocatalyst,” Debe, Mark K.; Hendricks, Susan M.; Vernstrom, George D.; Schmoeckel, Alison K; Atanasoski, Radoslav; Hamilton, Jr., Clayton (Published 2007).

8. US20070099053 “High durability fuel cell components with cerium salt additives” Frey; M. H.; Pierpont; D. M.; Hamrock; S. J. (Published 2007).

9. US20070099052 “High durability fuel cell components with cerium oxide additives” Frey; M. H.; Pierpont; D. M.; Hamrock; S. J. (Published 2007).

10. US20070065699 “Fuel cell electrolyte membrane with basic polymer” Larson; J. M.; Pham; P. T.; Frey; M. H.; Hamrock; S. J.; Haugen; G. M.; Lamanna; W. M. (Published 2007).

5.3 Products Developed Under the Award

Both the 3M PFSA membrane with additives developed in part as discussed in section 2.2 of this report, and the NSTF ternary catalyst coated membranes, developed in part as discussed in sections 2 and 4, have been and continue to be sampled or sold to customers.

Appendix

Contents

Appendix I

Dalhousie/3M publication
J. Electrochemical Soc. 153(10) A1835-A1846 (2006)

Journal of The Electrochemical Society, **153** (10) A1835-A1846 (2006)
0013-4651/2006/153(10)/A1835/12/$20.00 © The Electrochemical Society

Dissolution of Transition Metals in Combinatorially Sputtered $Pt_{1-x-y}M_xM'_y$ (M, M′ = Co, Ni, Mn, Fe) PEMFC Electrocatalysts

A. Bonakdarpour,[a,*] R. Löbel,[a] R. T. Atanasoski,[b,*] G. D. Vernstrom,[b] A. K. Schmoeckel,[b] M. K. Debe,[b,*] and J. R. Dahn[a,*,z]

[a]*Department of Physics, Dalhousie University, Halifax, Nova Scotia B3H 3J5, Canada*
[b]*3M Company, St. Paul, Minnesota 55144-1000, USA*

The stability of Pt-based or other metallic alloys under the corrosive working conditions of proton exchange membrane fuel cells (PEMFCs) is an important factor to consider in the search for improved PEM electrocatalysts. The dissolution of transition metals (Co, Ni, Mn, Fe) from $Pt_{1-x-y}M_xM'_y$ electrocatalysts after operation in PEM hydrogen fuel cells or after treatment in 1 M H_2SO_4 at 80°C is reported. Catalyst libraries were prepared by combinational sputtering on nanostructured thin-film supports that were used directly in fuel cells and for acid testing. In each library the Pt mass loading was kept fixed at 0.1 mg cm^{-2} while the amounts of M and M′ varied with position. The transition metal content of all compositions of all libraries, determined by electron microprobe, was significantly reduced in the same way after fuel cell or acid testing. Samples with $x + y \geqslant 0.25$ before fuel cell or acid testing were found with $x + y \approx 0.25$ after exposure due to the dissolution of transition metals, independent of the choice of M and M′ for the elements studied here. We suggest that the composition $Pt_{1-x-y}M_xM'_y$ with $x + y \approx 0.25$ is near the percolation limit for diffusion of transition metals from the interior of the alloy. The acid treatment described here mimics fuel cell testing from a corrosion standpoint and hence can be used as a simpler, ex situ test for PEM electrocatalysts.
 [DOI: 10.1149/1.2221868]

Manuscript submitted January 30, 2006; revised manuscript received May 3, 2006. Available electronically August 1, 2006.

At present, polymer electrolyte membrane fuel cells (PEMFCs) are under intense research because they provide one avenue for "green" electricity production. However, prior to the successful commercialization of hydrogen fuel cells, besides fuel-related issues, numerous other shortcomings need to be addressed.[1-3] Materials challenges for the fuel cell include low-cost proton conducting membranes, as well as economical high-performance catalysts for both fuel and oxidant electrodes. For the cathode catalyst, where the oxygen reduction reaction (ORR) takes place, improvement of the kinetic activity is highly desired because an overvoltage of about 400 mV, or about 70% of the total losses in a typical PEMFC, occurs at this electrode. Although the effects of numerous factors like catalyst composition, catalyst grain size, crystalline facets, support structures, etc., on the ORR have been studied, details of the ORR mechanism still remain elusive.[4-8]

Current ORR catalysts consist of nanometer-size Pt particles supported on carbon black. When the dispersion of Pt particles on high-surface-area carbon supports reaches its limits, further improvements in activity, durability, and cost reduction can be achieved by new catalyst formulations such as Pt alloys, non-Pt-based catalysts, and/or the development of new support structures.[9-12] Other current ideas that are actively explored in improving the catalytic activity and lowering the Pt content involve Pt monolayers on active alloy cores, metal oxides and strong metal-support interactions, and additives such as heteropolyacids.[13-17]

Binary and ternary Pt transition metal alloys have been studied and developed for the phosphoric acid fuel cell (PAFC) applications,[18] so their use in PEMFCs seems natural. Several groups have reported increased activity of Pt alloys with 3d transition metals toward the ORR.[19-21] Thompsett in particular provides a thorough review of research conducted by Johnson Matthey on carbon-supported Pt/M (M = Ti, Co, Ni, etc.) alloys in the mid 1990s.[21] In these alloys the cathode overpotential is reduced by about 20–40 mV compared to pure Pt at low current densities.

The gain in the catalytic activity upon alloying has been attributed to changes in the geometric and/or electronic properties of the alloys. The electronic contributions generally stem from the structure of the d-band electrons, as is common in many theories of heterogeneous catalysis. Dispersed Pt alloys on carbon support show increased vacancies in their d-band, which leads to a weaker adsorption of intermediates like OH.[22,23] Recently, using a thermochemical ab initio approach, Norskov et al. have calculated a volcano-like behavior for ORR on different metals and have shown correlations between adsorption energies of oxygen and hydroxyl and the rate of ORR.[24] Similar arguments, apparently, hold for the alloy catalysts when the surface layers lose their surface transition metals. That is, the Pt skin layer formed on the Pt alloy cores would have modified d-band structure and consequently weaker oxygen/hydroxyl adsorption and better ORR kinetics.[20,24-27]

Stability of catalysts and catalyst supports are as important as catalytic performance.[3,28] Dissolution and loss of Pt, Pt agglomeration and loss of surface area, poisoning of the anode and cathode catalysts, peroxide formation, and carbon support corrosion are all being actively studied.[3,29-35] Although corrosion of Pt and Pt-alloy catalysts have been studied by several research groups, there have been few thorough published reports on the corrosion of transition metals in Pt alloy electrocatalysts when used in the PEMFC. In phosphoric acid fuel cells, where the working environment is more corrosive, corrosion of Pt–Co catalysts was studied in the past.[36] Recently, we reported detailed results on the characterization of binary $Pt_{1-x}Ni_x$, $Pt_{1-x}Fe_x$ ($0 \leqslant x \leqslant 1$) electrocatalysts prepared by combinatorial sputtering.[37] The structure and composition of these films were studied before and after treatment in a variety of acidic conditions. For all compositions we observed surface leaching of Ni and Fe, as has been reported elsewhere.[37] For higher concentration of transition metals ($x \geqslant 0.6$) lattice expansion after acid treatment was observed, indicating that transition metals were removed from the bulk of the grains. Furthermore, we reported on the close agreement between the composition of the alloys after acid treatment and after fuel cell testing, showing that the acid treatment (1 M, 80°C, 10 days) could simulate the corrosion that occurs in the typical working environment of the PEMFC.

In this article, we present similar studies made on a much wider range of binary and ternary Pt–M (M = Ni, Co, Mn, Fe) alloys, prepared by combinational sputtering. It is our belief that detailed corrosion studies of Pt alloys (binary and higher order) are very useful for developing high-performance, low-cost, and stable ORR catalysts for PEMFC. Combinatorial mappings, as presented here, facilitate the task of catalyst synthesis and characterization.

* Electrochemical Society Active Member.
z E-mail: jeff.dahn@dal.ca

Experimental

Combinatorial sputtering of $Pt_{1-x-y}M_xM'_y$ (M,M′ = Co, Ni, Mn, Fe) films.— The combinatorial sputtering method used has been developed at Dalhousie during the past five years for performing combinatorial materials science (CMS). Detailed information about our approach can be found elsewhere.[38] This method was initially applied to metal-based negative electrode materials for Li-ion batteries[39] and now has been extended to other areas such as fuel cell electrocatalysts. For more applications of CMS in the field of fuel cell electrocatalysts see Refs. 40-43.

The samples were prepared by a Corona Vacuum Coaters V3T multitarget magnetron sputtering machine, modified in-house for combinatorial film growth. The targets were 2 in. diameter disks of pure Pt (99.9%), Mn (99.9%), Co (99.9%), and Ni (99.9%) or grade 1008 low carbon steel (less than 0.08% carbon by weight, balance Fe) sputtered by Advanced Energy MDX-1 K dc power sources. The sputtering chamber reached a typical base pressure of about 1×10^{-7} Torr. The substrates were mounted on a rotating table facing the sputtering targets and consisted of silicon (110 oriented) wafers for X-ray diffraction (XRD), Al foil disks, and nanostructured thin-film (NSTF) substrates for acid leaching and fuel cell testing.[12]

The NSTF technology has been developed and implemented at 3M company. This new class of support contains oriented nanometer-sized crystalline organic whisker structures that are obtained by thermal sublimation and subsequent annealing of a red organic pigment, N,N-di(3,5-xylyl)perylene-4:9,10bis(dicarboximide) (called perylene red or PR) on polymer substrates like polyimide. In the case of the NSTF substrates used here, a 300 Å thick Pt "sublayer" was deposited on the polyimide support before the whiskers were applied. This Pt sublayer was used as an internal standard during XRD measurements. These chemically and thermally stable NSTF substrates, with their high number density and their nanometer-sized dimensions, form ideal supports for PEM catalysts. Details of the growth and physical characterizations of these nanometer-sized whiskers can be found elsewhere.[44,45] Further information on Pt-coated whisker supports, fabrication of membrane electrode assemblies, and early results of fuel cell performance can be found in Ref. 12.

To produce composition variations in libraries of materials, specially designed masks were positioned opposite each target near to the rotating substrate. The details of the mask design and the capabilities of the system are provided elsewhere.[38] The Ar pressure during sputtering was about 3.0 mTorr and the sputtering table was kept at 25°C during the growth. The amount of material deposited was determined gravimetrically, by weighing 1.3 cm diameter Al disks before and after deposition using a precision (0.1 ug) Cahn 29 electrobalance. In all growths the amount of Pt was kept constant (0.1 mg cm^{-2}) throughout the library.

Two types of libraries were prepared: Type I: $Pt_{1-x}M_x$ or $Pt_{1-x}[M_yM'_{1-y}]_x$ where a constant thickness Pt layer alternated with a wedge-shaped layer of transition metal M or metals $M_yM'_{1-y}$, with y constant throughout the library (Libraries 1–6), and Type II: $Pt_{1-x}[M_yM'_{1-y}]_x$ where constant thickness layers of Pt were modulated by mixed compositionally graded layers of $M_yM'_{1-y}$. In Type II libraries, x was kept approximately constant and $0 \leqslant y \leqslant 1$ (Libraries 7–12). These two types of libraries were produced to allow for the alternative layering sequences in Fig. 1 to be created.

Figure 1a shows a schematic of two bilayers of a Type I library. To fabricate this film, the sputtering table rotated slowly (1 rpm) and the target powers were adjusted so as to deposit the desired thickness of Pt and M or $M_yM'_{1-y}$ during each pass of the library under the sputtering targets. To grow the Type II libraries, where M and M′ were homogeneously mixed (Fig. 1b), a rapid table rotation (10 rpm or higher) was needed. The machine software was altered to allow for turning the plasma power sources on or off as desired during the growth. The films prepared and studied here are summarized in Table I. The total thickness of Pt was 500 Å in all libraries. The total number of bilayers were chosen to obtain the desired film compositions in each library. For example, in the Type II libraries, the number of bilayers were about 60, 80, and 120 for $x = 0.3$, 0.5, and 0.7, respectively. Thus, the total film thicknesses on flat Si wafer substrates were approximately 600, 800, and 1200 Å, assuming bulk densities for all the deposited metals.

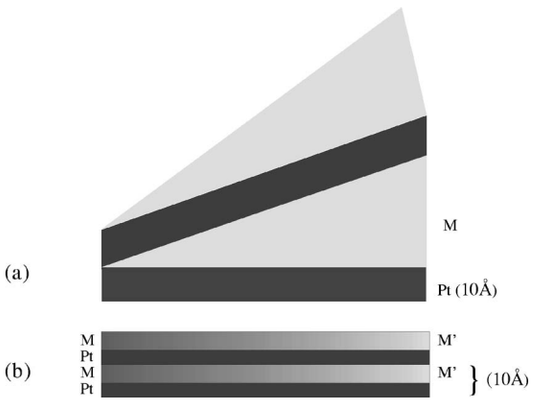

Figure 1. Fabrication of the Type I: $Pt_{1-x}M_x$ or $Pt_{1-x}[M_yM'_{1-y}]_x$ and Type II: $Pt_{1-x}[M_yM'_{1-y}]_x$ libraries: (a) In the Type I libraries, constant thickness layers of Pt are separated by layers of transition metal M or $M_yM'_{1-y}$ (with y constant) which vary linearly in thickness. (b) In the Type II libraries constant thickness Pt layers alternate with constant thickness $M_yM'_{1-y}$ ($0 \leqslant y \leqslant 1$) layers, where M and M′ vary linearly in thickness in opposite directions. The shading in the figure is an indication of the variations in the composition. For the Type II libraries, the bilayer thickness was kept at about 10 Å; however, the ratio of Pt to transition metals (Pt/M + M′) was varied in different libraries (see Table I).

Using the combinatorial techniques described above, a wide range of artificial superlattice structures with composition variations

Table I. Summary of the films deposited. The stoichiometries are ideal. The actual film compositions, in some cases, were slightly different. The actual compositions were obtained by electron microprobe data and shown in the figures.

Library	Sample ID	Type	Composition	Figures
1	SPI4	I	$PtMn_x$, $(0 \leqslant x \leqslant 3)$	3, 8, and 12-15
2	SPI84	I	$Pt_{1-x}Ni_x$ $(0 \leqslant x \leqslant 1)$	15
3	SPI44	I	$Pt_{1-x}Fe_x$, $(0 \leqslant x \leqslant 1)$	15
4	SPI24	I	$Pt_{1-x}[Mn_{0.375}Fe_{0.625}]_x$, $(0 \leqslant x \leqslant 0.75)$	4, 8, 12-14, and 16
5	SPI40	I	$Pt_{1-x}[Mn_{0.167}Fe_{0.833}]_x$, $(0 \leqslant x \leqslant 0.75)$	17
6	SPI42	I	$Pt_{1-x}[Mn_{0.5}Ni_{0.5}]_x$, $(0 \leqslant x \leqslant 0.75)$	8 and 18
7	SPI139	II	$Pt_{0.7}[Co_{1-y}Ni_y]_{0.3}$, $(0 \leqslant y \leqslant 1)$	8, 10, 13, 14, and 19
8	SPI134	II	$Pt_{0.5}[Co_{1-y}Ni_y]_{0.5}$ $(0 \leqslant y \leqslant 1)$	8, 10, 13, and 14
9	SPI133	II	$Pt_{0.3}[Co_{1-y}Ni_y]_{0.7}$ $(0 \leqslant y \leqslant 1)$	3, 8-10, 13, 14, and 20
10	SPI140	II	$Pt_{0.7}[Co_{1-y}Mn_y]_{0.3}$ $(0 \leqslant y \leqslant 1)$	8, 11, 13, 14, and 19
11	SPI141	II	$Pt_{0.5}(Co_{1-y}Mn_y)_{0.5}$ $(0 \leqslant y \leqslant 1)$	4, 8, 11, 13, 14, and 19
12	SPI143	II	$Pt_{0.3}[Co_{1-y}Mn_y]_{0.7}$ $(0 \leqslant y \leqslant 1)$	4, 8, 11, 13, 14, and 20

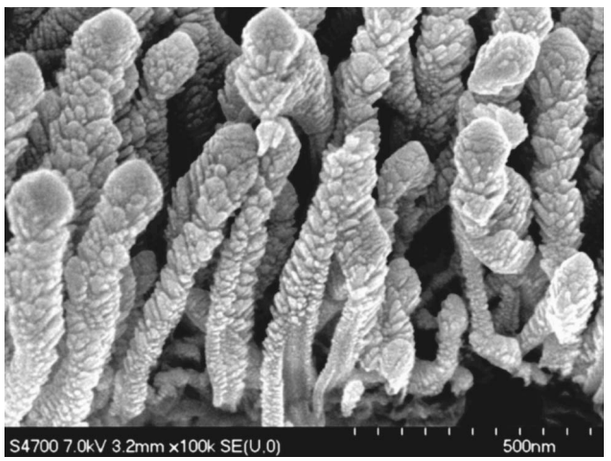

Figure 2. SEM of a typical NSTF support layer coated by $Pt_{0.7}Ni_{0.3}$ electrocatalyst.

can be produced on smooth flat substrates.[46] Superlattice structures were produced in the libraries deposited on the Si wafer substrates, but random alloys were the result of the depositions on the NSTF substrates. This is because the NSTF films have a surface area about 15 times the geometric surface area so a 1 nm layer deposited on a smooth planar surface is less than a monolayer thick on the surfaces of the PR whiskers. Therefore, alternating 1 nm layers of Pt and M give a superlattice structure when deposited on smooth Si but a random alloy (by XRD) when deposited on the NSTF substrates, as we show in detail in the Results section.

Bulk structural and compositional characterization by XRD and electron microprobe.— The bulk structure and composition of the samples, prior to and after acid treatment, were studied by XRD and electron microprobe. The composition of the films was determined quantitatively by a JEOL JXA-8200 Superprobe equipped with one energy dispersive (EDS) spectrometer and five wavelength dispersive (WDS) spectrometers. The metal content (Pt, Ni, Fe, Mn, Co, and Si substrate), was measured by EDS and the oxygen content was analyzed by WDS. The real count time was about 1 min for each measurement. The optical autofocus feature of the microprobe was used for the films deposited on the Si wafer. For the rougher NSTF substrate films, selected points were manually focused and the beam was operated in the scanning mode (covering an area of 150 $\times$ 110 μm) to obtain accurate results. Measurements on libraries deposited on smooth Si wafers and on the NSTF substrates showed the same stoichiometry variation with position in the library. The sputter-coated whiskers are sufficiently absorbing so that the Pt sublayer does not contribute to the EDS signals.

Point by point XRD patterns of the libraries on Si wafer and NSTF substrates were measured by an Inel curved position sensitive detector (CPS 120) and a PW-1720 Phillips X-ray generator using Cu Kα radiation. The size of the X-ray beam spot on the library was about 1×1 mm. A composition variation, $0 \leq x \leq 1$ or $0 \leq y \leq 1$ in $Pt_{1-x}[M_yM_{1-y}]_x$, occurred over a distance of 75 mm in our libraries.

Acid treatment of the $Pt_{1-x-y}M_xM'_y$ (M, M′ = Co, Ni, Mn ,Fe) libraries.— All the acid treatments were performed on the electrocatalyst libraries on the NSTF supports. A number of Type I and Type II libraries were selected for acid treatment. For a typical treatment, a 75 mm long $\times$ 6 mm wide NSTF strip containing the entire library was soaked in 25 mL of 1 M H_2SO_4 (Reagent grade) and was kept in a sealed glass vial at 80°C for 10 days. After treatment, the samples were washed with deionized water and dried in air before further study. Special care was always taken so as not to damage the micrometer-long whiskers on the films during handling. In the case of Pt–Fe and Pt–Ni, studied previously, atomic absorption measurements of the acid solution showed no detectable trace of dissolved Pt to within its detection limit.[37]

Fuel cell measurements of the $Pt_{1-x-y}M_xM'_y$ (M, M′ = Co, Ni, Mn, Fe) libraries.— Details of the membrane electrode assembly (MEA) construction for NSTF catalysts are provided by Debe.[12] Using a decal process, the NSTF catalyst was transferred from the initial substrate web to a 3M fabricated Nafion PEM (30 μm thick) to make a catalyst coated membrane (CCM). The Pt sublayer is not transferred in this process. Fuel cell performance measurements were carried out in 50 cm^2 Fuel Cell Technologies test cells with quadserpentine flow fields. The CCMs were sandwiched, without lamination, between two gas diffusion layers (GDLs). The MEAs were tested on a Fuel Cell Technologies fuel cell test station. For the combinatorial libraries, two half-CCMs with catalyst coated on only one side were used. This allowed the anode and cathode components of the MEA to be easily separated for analysis after fuel cell testing. Electrochemical characterization tests (such as surface area measurements and ac impedance) as well as polarization curves under oxygen were performed at room temperature and 75°C under humidified gasses using a segmented MEA in an eight-segment cell. Tests continued for several days until performance reached a steady level. After testing, the cathode CCM was separated and subjected to electron microprobe studies to determine the changes in bulk stoichiometry.

Results and Discussion

Composition and structure of the libraries prepared.— Figure 2 shows an SEM micrograph of a typical NSTF support layer sputtered with Pt–Ni electrocatalyst. The electrocatalyst grains are about 10 nm or so in size. Figure 3 shows the composition variation vs

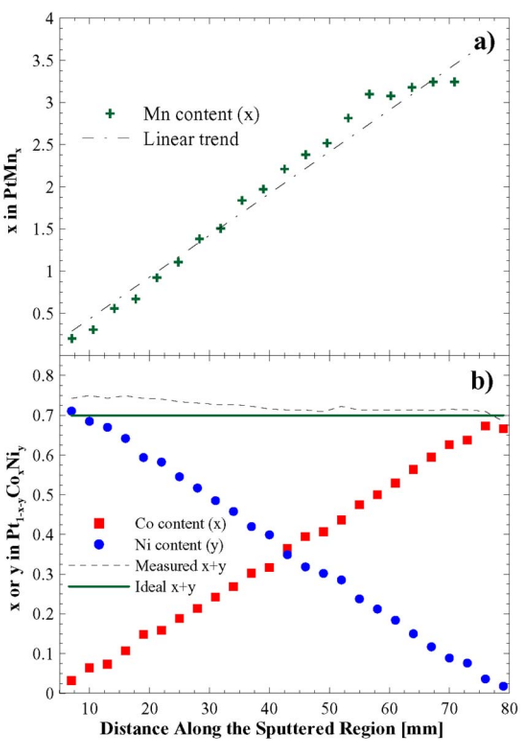

Figure 3. (Color online) Composition of films described in Fig. 1 along the sputtered region as obtained by electron microprobe: (a) Type I library: the intended composition variation was achieved for $PtMn_x$ ($0 \leq x \leq 4$), Library 1. (b) Type II library: the composition of $Pt_{1-x-y}Co_xNi_y$, Library 9, along the sputtered region. The measured transition metal content, $x + y$, is close to the desired value everywhere in the library.

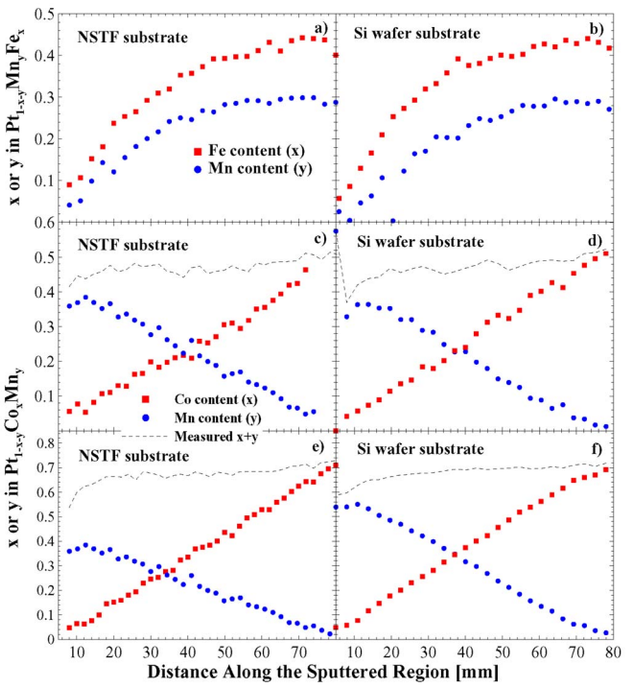

Figure 4. (Color online) Composition of several libraries as measured on NSTF (a, c, e) and Si wafer (b, d, f) substrates. The composition of the films deposited on the two different substrates are in good agreement.

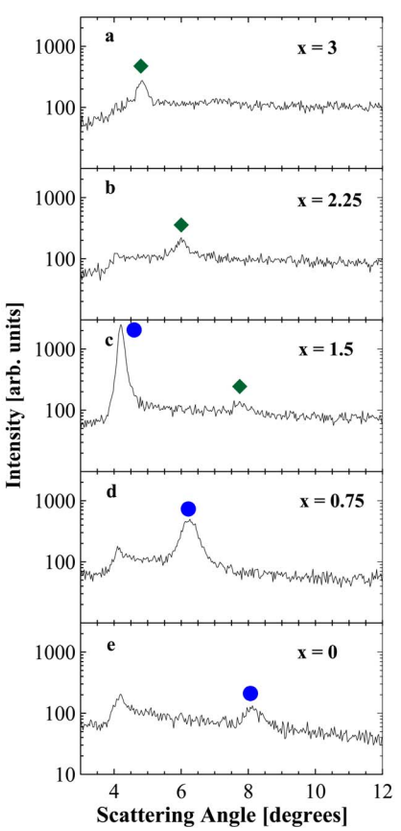

Figure 5. (Color online) Small-angle XRD pattern of selected positions of $PtMn_x$, Library 1. Movement of the superlattice peaks to lower scattering angles indicate that the bilayer thickness is increasing. The diffraction patterns were taken at equal intervals along the library. The corresponding composition for each pattern (x in $PtMn_x$) is indicated on the plot.

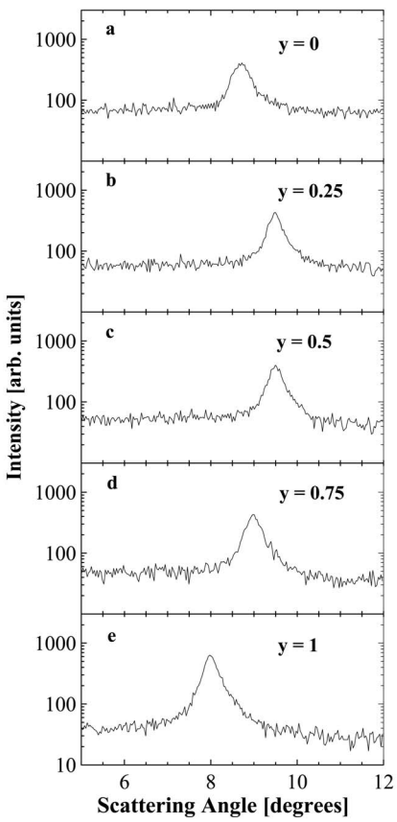

Figure 6. Small-angle XRD pattern of selected positions of $Pt_{0.3}[Co_{1-y}Ni_y]_{0.7}$, Library 9, with y values indicated on the plot. The superlattice peak is nearly stationary across the library.

position for examples of Type I and Type II libraries. Figure 3a shows the linear variation of Mn content in $PtMn_x$ along the film, and Fig. 3b shows the opposing linear changes in Co and Ni content in $Pt_{1-x-y}Co_xNi_y$ for libraries deposited in Si wafer substrates. The variation in the composition of the films with position on the NSTF and Si wafer substrate libraries is similar. Figure 4 shows the composition of $Pt_{1-x}[Co_{1-y}Mn_y]_x$ ($x = 0.5, 0.7$; $0 \leqslant y \leqslant 1$), Libraries 11 and 12, and $Pt_{1-x}[Mn_{0.375}Fe_{0.675}]_x$ ($0 \leqslant x \leqslant 0.75$), Library 4, deposited on the NSTF support and on Si wafer. The agreement between the compositions of the libraries deposited on the two different substrates is very good.

What is the crytallographic structure of these wide composition-range platinum-transition metal libraries? The crystal structure depends on the choice of substrate used to grow the films and can be determined by small-angle and wide-angle XRD. Figures 5 and 6 show the measured low-angle superlattice peaks observed for $PtMn_x$ ($0 \leqslant x \leqslant 3$), Library 1, and $Pt_{0.3}[Co_{1-y}Ni_y]_{0.7}$ ($0 \leqslant x \leqslant 1$), Library 9, deposited on a Si wafer substrate, respectively. In Fig. 5, the movement of the diffraction peaks to lower scattering angles indicates that the thickness of the bilayers is increasing as the Mn content increases, as expected based on Fig. 1a. Figure 6 shows that the superlattice peaks measured for $Pt_{0.3}[Co_{1-y}Ni_y]_{0.7}$ ($0 \leqslant y \leqslant 1$), Library 9, are almost stationary, i.e., the bilayers have constant thickness across the sample, as expected based on Fig. 1b. Using the Bragg law, the superlattice periodicities vs position for these two libraries were determined and are shown in Fig. 7. Similar superlattice peaks were observed in all other libraries deposited on Si wafers. The superlattice peaks depend only on the bilayer thickness and are independent of the composition.

When a flat substrate like Si wafer is used, multilayered, super-

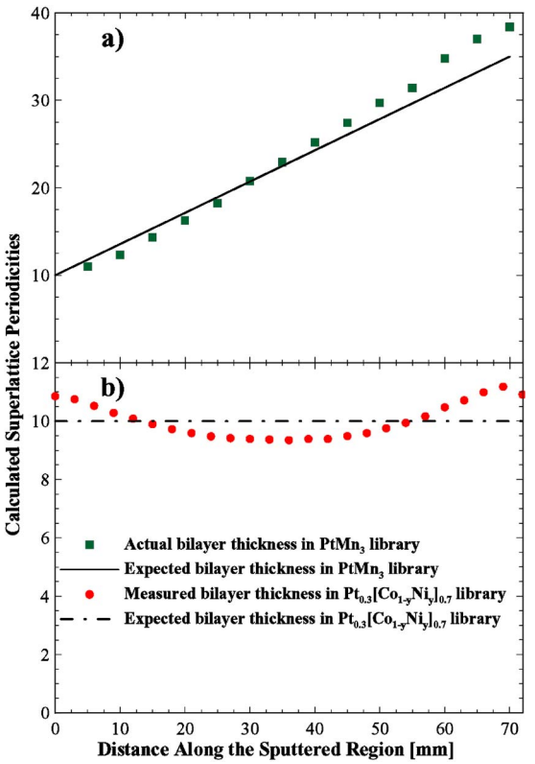

Figure 7. (Color online) Bilayer (Pt-metal) thickness of Type I $PtMn_x$, Library 1, and Type II $Pt_{1-x-y}Mn_xCo_y$, Library 9, obtained from SAX: (a) The linear increase of the bilayer thickness of the $PtMn_x$ film and (b) the nearly constant bilayer thickness of $Pt_{1-x-y}Mn_xCo_y$. The agreement between the expected and actual bilayer thickness is good.

lattice structures are formed. On the NSTF substrates, however, which have an approximate 15-fold increase in surface area, well-mixed, random face-centered cubic (fcc) alloys (not multilayer superlattice structures) form. An exception to the fcc alloy structure-type is $Pt_{1-x}Fe_x$ with $x \geq 0.73$, which is a random bcc alloy.

Figure 8 shows the small-angle X-ray (SAX) data for a number of libraries deposited on NSTF substrate. Panels a–e in the left column of Fig. 8 show the absence of superlattice peaks for a few different values of x in $PtMn_x$ ($0 \leq x \leq 3$), Library 1, and $Pt_{1-x}[Mn_{0.375}Fe_{0.625}]_x$ ($0 \leq x \leq 0.75$), Library 4. The next two columns in Fig. 8, panels f–j and k–o, show the SAX scattering region of Type II, Libraries 7–12, for a number of different compositions. Note that unlike the libraries deposited on Si wafers, no low-angle superlattice peaks are observed for any libraries deposited on NSTF.

A further clue into the crystallographic structure of the libraries deposited on NSTF can be obtained by examining the fcc Bragg peaks. Figure 9 shows the XRD patterns collected across $Pt_{0.3}[Co_{1-y}Ni_y]_{0.7}$ ($0 \leq y \leq 1$), Library 9. Broad diffraction peaks of nanosized, fcc-structured crystallites are observed for all compositions. Similar fcc patterns were seen on all the libraries deposited on NSTF substrates.

Platinum-transition metal alloys generally show a shift of lattice constant with composition, which is taken as an evidence of alloy formation. The (111) and (220) Bragg peaks for $Pt_{1-x}[Co_{1-y}Ni_y]_x$ ($x = 0.3, 0.5, 0.7$; $0 \leq y \leq 1$), Libraries 7, 8 and 9, are shown in Fig. 10a, b, and c, respectively. The bottom XRD pattern in Fig. 10a-c corresponds to the bare NSTF substrate with the 300 Å thick Pt sublayer. Each diffraction pattern corresponds to a change in composition of about $\Delta y \approx 0.06$. In Fig. 10a, all the fcc (111) peaks are shifted to higher angles compared to the Pt 111 position of the base NSTF support. This shift is more pronounced in Fig. 10b and c, where the transition metal content is higher ($x = 0.5$, 0.7). When $x = 0.5$ or 0.7, a doublet of fcc (111) peaks can easily be observed. The higher angle (111) peak corresponds to the Pt–M–M′ alloy, and the lower angle (111) peak is that of the Pt sublayer. When the transition metal content is low ($x = 0.3$), the two fcc (111) peaks

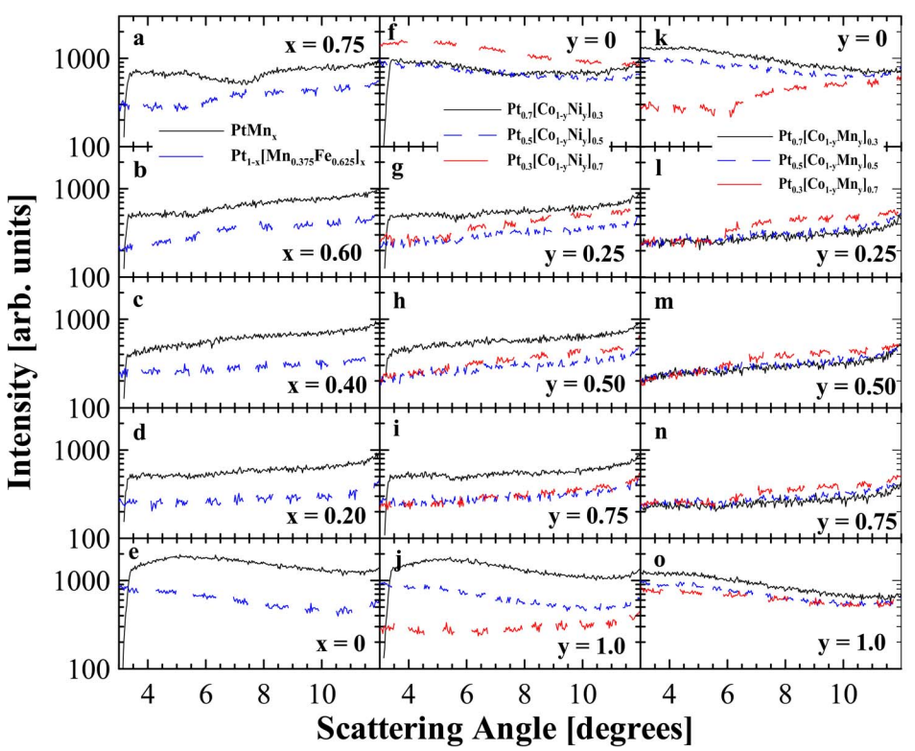

Figure 8. (Color online) Small-angle XRD patterns of selected positions of (a–e) Type I $Pt_{1-x}Mn_x$ and $Pt_{1-x}[Mn_{0.375}Fe_{0.625}]_x$ ($0 \leq x \leq 0.75$), Libraries 1 and 4, and (f–o) Type II $Pt_{1-x}[Co_{1-y}M_y]_x$ (M = Ni,Mn; $x = 0.3, 0.5, 0.7$; $0 \leq y \leq 1$), Libraries 7–12. The values of x and y are indicated in the figure. No superlattice peaks are observed in any library.

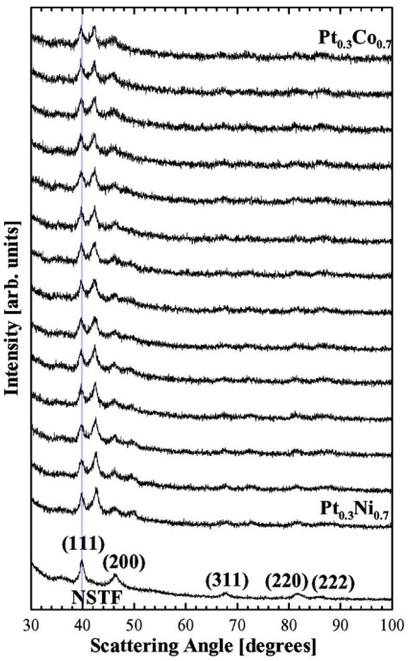

Figure 9. (Color online) Wide-angle XRD patterns of type II $Pt_{0.3}[Co_{1-y}Ni_y]_{0.7}$ ($0 \leqslant y \leqslant 1$), Library 9. The bottom pattern is that of a bare NSTF support, showing the diffraction of X-rays from the Pt sublayer beneath the organic whisker structures. No other crystalline phases are observed.

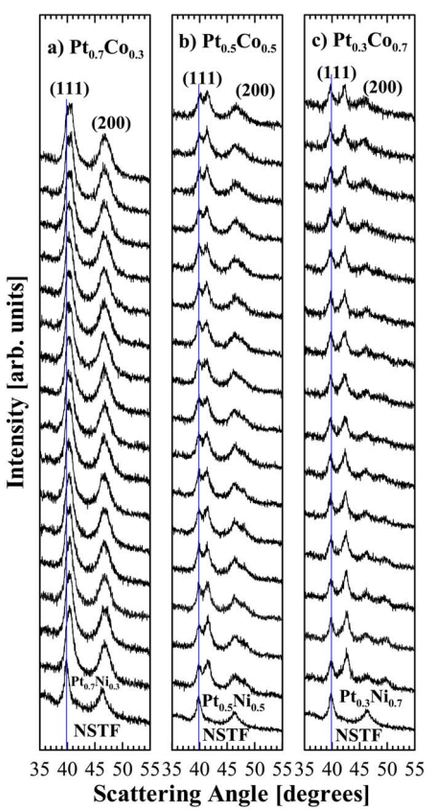

Figure 10. (Color online) Diffraction patterns of $Pt_{1-x}[Co_{1-y}Ni_y]_x$ ($x = 0.3,0.5,0.7$; $0 \leqslant y \leqslant 1$), Libraries 7–9, showing a clear movement of the alloy fcc peaks to higher angles. The shift of the (111) peaks is greater for larger values of x.

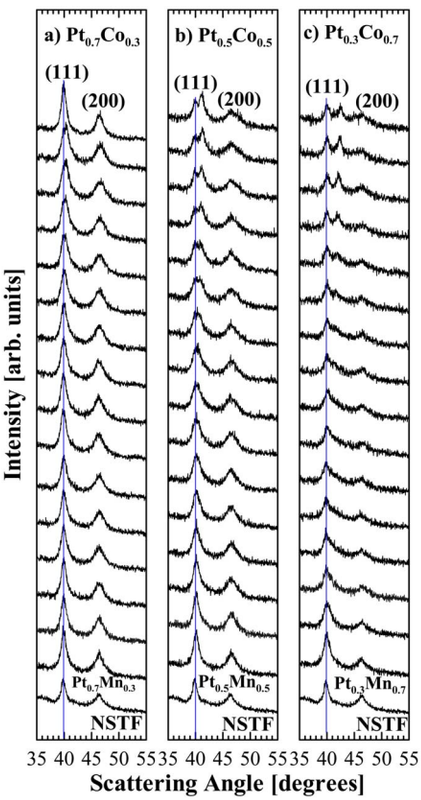

Figure 11. (Color online) Diffraction patterns of $Pt_{1-x}[Co_{1-y}Mn_y]_x$ ($x = 0.3,0.5,0.7$; $0 \leqslant y \leqslant 1$), Libraries 10–12, showing a clear movement of the alloy fcc peaks to higher angles. The shift of the (111) peaks is greater for larger values of x and smaller values of y (i.e., Pt–Co end) in the library.

overlap and are not resolved in our measurements. Note that the shift of the (111) Bragg peak for a given value of x is constant for all the y values, which suggests that Ni and Co contract the fcc lattice to an equal extent.

Figure 11a-c shows XRD patterns for $Pt_{1-x}[Co_{1-y}Mn_y]_x$ ($x = 0.3,0.5,0.7$; $0 \leqslant y \leqslant 1$) Libraries 10–12, deposited on NSTF. Each diffraction pattern corresponds to a change in composition of about $\Delta y \approx 0.06$. The shift of the diffraction peaks to higher angles becomes more noticeable as y increases, i.e., as the Mn content decreases in the library. When $y \approx 0$, i.e., at $Pt_{1-x}Co_x$ ($x = 0.5,0.7$), a similar shift of the (111) peak as in Fig. 10 is observed. The fcc lattice size for $Pt_{1-x}[Co_{1-y}Mn_y]_x$ ($x = 0.3,0.5,0.7$; $0 \leqslant y \leqslant 1$), Libraries 10–12, depends on the values of both x and y.

Figure 12a and b shows the (111) peak in $Pt_{1-x}Mn_x$ and $Pt_{1-x}[Mn_{0.375}Fe_{0.625}]_x$ ($0 \leqslant x \leqslant 0.75$), Libraries 1 and 4, deposited on NSTF support. Each diffraction pattern corresponds to a composition change of $\Delta x \approx 0.05$. The shift of the (111) peaks in $Pt_{1-x}Mn_x$ ($0 \leqslant x \leqslant 0.75$), Library 1, to higher angles is difficult to see because of peak overlap with the Pt sublayer. Furthermore, as mentioned before, the change in the lattice constant of the Pt–Mn phases is not substantial. This shift is more noticeable in $Pt_{1-x}[Mn_{0.375}Fe_{0.625}]_x$ ($0 \leqslant x \leqslant 0.75$), Library 4, because Fe impacts the lattice size more than Mn. The separation between the (111) peaks of the Pt sublayer and the $Pt_{1-x}[Mn_{0.375}Fe_{0.625}]_x$ alloy increases as x approaches 0.75.

For a quantitative analysis of the XRD patterns, the (111) and (200) peaks in all the data shown before in Fig. 10-12 were fitted and lattice constants were extracted for different compositions in each library. The peaks were fitted with a homemade nonlinear least-squares fitting program, which allows for a linear mixing of

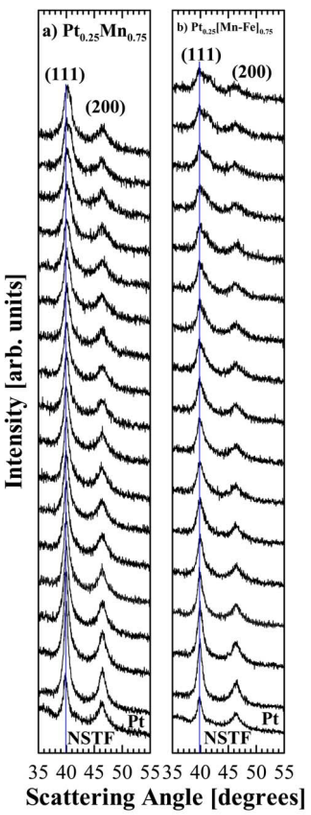

Figure 12. (Color online) Diffraction patterns of $Pt_{1-x}Mn_x$ and $Pt_{1-x}[Mn_{0.375}Fe_{0.625}]_x$ ($0 \leqslant x \leqslant 0.75$), Libraries 1 and 4. The Pt–Mn peaks are slightly shifted to higher angles. Here the Bragg peaks from the Pt sublayer on the NSTF support and the alloyed Pt–Mn peaks overlap. The (111) peaks of $Pt_{1-x}[Mn_{0.375}Fe_{0.625}]_x$, Library 4, show a more noticeable shift to higher angles as x increases.

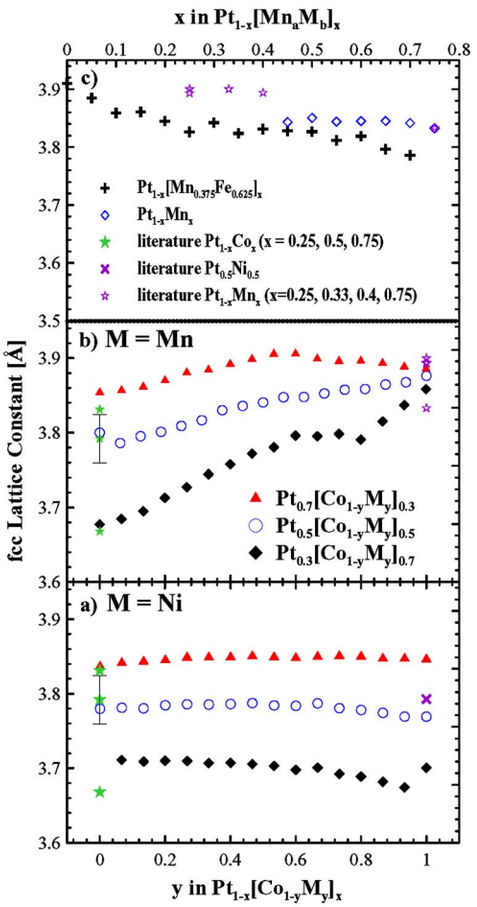

Figure 13. (Color online) Lattice constants derived from the diffraction patterns shown in Fig. 10-12 (a, b) vs y in $Pt_{1-x}[Co_{1-y}M_y]_x$ (M = Ni,Mn; x = 0.3,0.5,0.7; $0 \leqslant y \leqslant 1$), Libraries 7–12 and (c) vs x in $Pt_{1-x}Mn_x$ and $Pt_{1-x}[Mn_{0.375}Fe_{0.625}]_x$ ($0 \leqslant x \leqslant 0.75$), Libraries 1 and 4.

Lorenzian–Gaussian peak shapes (pseudo-Voigt shape). When the fcc (111) peaks of the NSTF substrate and the sputtered alloys were easily resolved, for example in $Pt_{0.3}[Co_{1-y}Ni_y]_{0.7}$ ($0 \leqslant y \leqslant 1$), Library 9, both (111) peaks were fitted for each diffractogram. When the (111) peaks were unresolved, for example in the case of $Pt_{0.7}[Co_{1-y}Mn_y]_{0.3}$ ($0 \leqslant y \leqslant 1$), Library 10, peak deconvolution was performed by first fitting the Pt sublayer (shown as the bottom diffractogram in Fig. 10-12) and including the results in fitting of the diffraction patterns of the libraries. The position, width, and shape of the Pt sublayer peaks were kept fixed in fitting the patterns, wherever the Pt sublayer and the alloy peaks were unresolved. Although the deconvolution was generally not straightforward, and the obtained parameters had higher uncertainties, reliable estimates were nevertheless achieved. An estimate of the grain size for the different alloy compositions was obtained using Scherrer equation.[47]

Figure 13a-c show the variation of the fcc lattice constant with composition in all the libraries discussed above. Figure 13a shows the lattice constants vs y in $Pt_{1-x}[Co_{1-y}Ni_y]_x$, Libraries 7–9, for x = 0.3, 0.5, and 0.7. The contraction of the cubic lattice increases as x increases, i.e., as the total content of transition metals increases; however, it remains approximately constant for the entire range of $0 \leqslant y \leqslant 1$, because Ni and Co have similar atomic radii. Figure 13a also shows the lattice constant of several equilibrium intermetallic phases of Pt–Co and Pt–Ni. Pt–Co shows a number of ordered ($AuCu_3$-like) and randomly ordered (Cu-like) fcc structures.[48-53] These phases are generally prepared at about 1000°C under an inert atmosphere. The three literature data points shown in Fig. 13a for $Pt_{1-x}Co_x$ correspond to x = 0.25, 0.5, and 0.75. The $Pt_{0.5}Co_{0.5}$ data point is an average of several values reported in the literature.[48-51,53] The literature value reported for $Pt_{0.5}Ni_{0.5}$ is also an average of reported literature values for equilibrium phases.[49,54]

Figure 13b shows similar information as Fig. 13a, but for $Pt_{1-x}[Co_{1-y}Mn_y]_x$ (x = 0.3,0.5,0.7; $0 \leqslant y \leqslant 1$), Libraries 10–12. Note that the data for the Co end of the libraries (or $y = 0$ in $Pt_{1-x}[Co_{1-y}Mn_y]_x$) is in good agreement with the Co-end of $Pt_{1-x}[Co_{1-y}Ni_y]_x$ (x = 0.3,0.5,0.7), Libraries 7–9 shown in Fig. 13a. Unlike Pt–Co–Ni libraries, the lattice dimension does not remain constant for $0 \leqslant y \leqslant 1$ in $Pt_{1-x}[Co_{1-y}Mn_y]_x$ for a given value of x. The change in the Pt lattice constant is much smaller at the Mn end of the libraries than it is at the Co end or Ni end of libraries. The equilibrium intermetallic phases of Pt–Mn also do not show a pronounced change in lattice constant compared to pure Pt. In general, two types of crystal structures are observed for the equilibrium Pt–Mn phases: tetragonal (AuCu-like) and fcc (Cu or $AuCu_3$-like). The literature values of the lattice constant for fcc $Pt_{1-x}Mn_x$ (x = 0.25, 0.33, 0.4, and 0.75) are shown in Fig. 13b for comparison.[48,55-57] Figure 13c shows the lattice constant vs composition of $Pt_{1-x}Mn_x$ and $Pt_{1-x}[Mn_{0.375}Fe_{0.625}]_x$, Libraries 1 and 4. Only values for $x \geqslant 0.5$ in $Pt_{1-x}Mn_x$ are shown, because the peak positions for smaller values of x could not be unambiguously determined.

Figure 14 shows the grain size of the Pt–M–M′ alloys sputtered on the NSTF libraries determined from the full-width-half-medium (fwhm) of the (111) peaks. For $Pt_{1-x}[Co_{1-y}Ni_y]_x$ (x = 0.3,0.5,0.7;

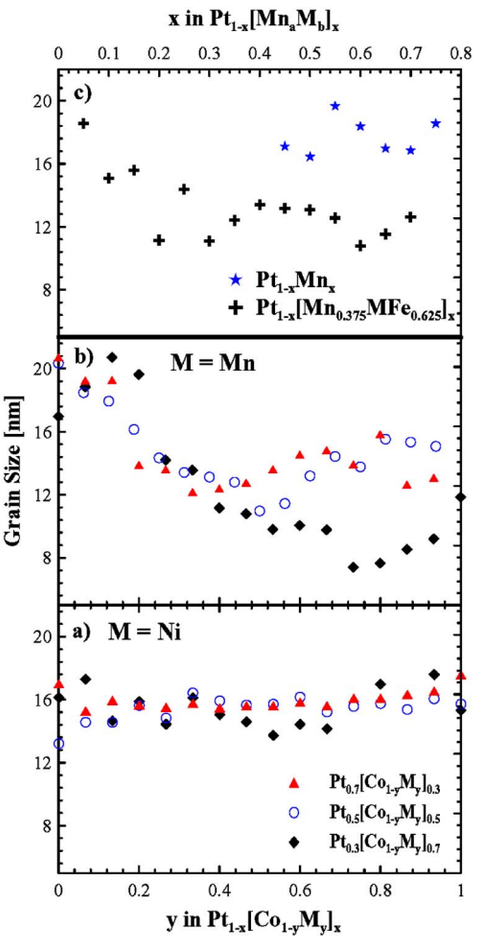

Figure 14. (Color online) Grain sizes obtained from the diffraction patterns shown in Fig. 10-12 (a, b) vs y in $Pt_{1-x}[Co_{1-y}M_y]_x$ (M = Ni,Mn; x = 0.3,0.5,0.7; $0 \leqslant y \leqslant 1$), Libraries 7–12, and (c) vs x in $Pt_{1-x}Mn_x$ and $Pt_{1-x}[Mn_{0.375}Fe_{0.625}]_x$ ($0 \leqslant x \leqslant 0.75$), Libraries 1 and 4.

$0 \leqslant y \leqslant 1$), Libraries 7–9, the grain size is about 15 nm and quite constant for all x and y values. For the Mn-based libraries, (panels b and c), the scatter in the grain size data is much larger. This is largely due to the difficulty of deconvoluting the (111) peaks of the Pt sublayer and the Pt alloy; however, on average the grain sizes are about 12 nm.

Given the evidence in Fig. 10-14, it is clear that randomly ordered, nanocrystalline, substitutional fcc alloys of Pt with Co, Ni, Fe, and Mn are formed on these NSTF supports in the libraries prepared. The observed changes in the lattice constants are in good agreement with those of previously reported equilibrium phases in the literature.

Composition of the libraries after exposure to the fuel cell environment and after acid treatment.— Results for Type I $Pt_{1-x}M_x$ (M = Mn, Ni, Fe), Libraries 1–3.— The composition x in $Pt_{1-x}M_x$, Libraries 1–6, at the same set of positions in the libraries were measured before and after fuel cell testing and before and after acid treatment. For Type I libraries a convenient way to display the compositional changes that take place in the libraries due to corrosion is to plot the composition after treatment, x_{after}, vs the composition before treatment, x_{before}, for the same position in the library. Figure 15 shows such results for $Pt_{1-x}M_x$ (M = Mn, Ni), Libraries 1–3, before and after treatment. The composition of the electrocatalysts after acid treatment ($x = x_{after}$ in $Pt_{1-x}M_x$) vs the M content of

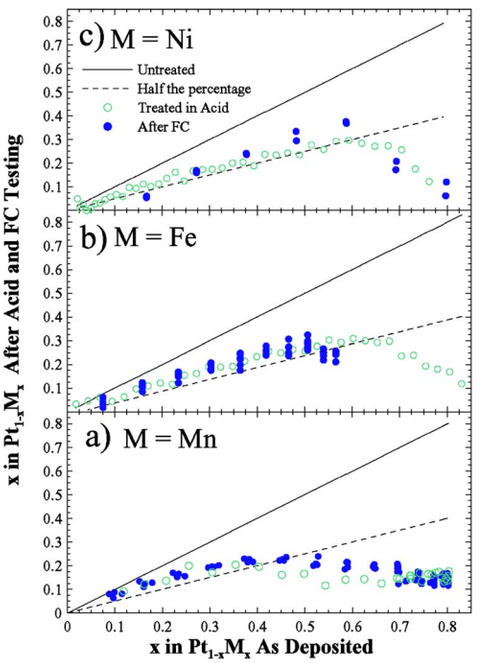

Figure 15. (Color online) Composition of Type I $Pt_{1-x}M_x$ (M = Mn,Ni,Fe), Libraries 1–3, after fuel cell testing and acid treatment vs the composition of the as-deposited films.

the as-deposited films ($x = x_{before}$ in $Pt_{1-x}M_x$) show the same trends that we reported previously in the case of $Pt_{1-x}M_x$ (M = Fe, Ni, $0 \leqslant x \leqslant 1$) libraries.[37] For low initial M content ($x_{before} \leqslant 0.6$) x_{after} is reduced to about half of x_{before}, but the dissolution of M intensifies for higher initial values of x ($x_{before} \geqslant 0.6$). This increased leaching was attributed to bulk dissolution of M because the fcc lattice constant after treatment increased over its value before treatment for $x_{before} \geqslant 0.6$.[37] A similar dissolution mechanism is likely to happen here. For $x_{before} \leqslant 0.6$, transition metals are dissolved primarily from the surface layers, whereas for $x_{before} \geqslant 0.6$ or so, bulk dissolution occurs also. The value of x_{before} in $Pt_{1-x}Fe_x$, Library 2, tested in the fuel cell and shown in Fig. 15, spanned the range $0 \leqslant x_{before} \leqslant 0.5$. Notice the remarkable agreement between the postfuel cell and postacid treated compositions for $Pt_{1-x}M_x$ (M = Mn, Ni, Fe), Libraries 1–3. These results show that the leaching of Mn, Ni, and Fe, which occur in a PEMFC, can be rather accurately mimicked by a 10 day soaking in 1 M H_2SO_4 solution at 80°C.

Results for Type I Pt–MnFe and Pt–MnNi, Libraries 4–6.— Three other libraries of Type I electrocatalysts were prepared and their compositions before and after fuel cell testing and acid treatment were studied by electron microprobe. The initial libraries were designed to be $Pt_{1-x}[Mn_{0.375}Fe_{0.625}]_x$, $Pt_{1-x}[Mn_{0.167}Fe_{0.833}]_x$, and $Pt_{1-x}[Mn_{0.5}Ni_{0.5}]_x$, with ($0 \leqslant x \leqslant 0.75$). These are Libraries 4–6. We learned that the Mn/Fe and Mn/Ni ratios in these libraries did not remain constant during treatment, so we therefore display the compositions in these libraries as x and y in $Pt_{1-x-y}Mn_yFe_x$ and $Pt_{1-x-y}Mn_yNi_x$. Before treatment, the ratio y:x is designed to be constant throughout the libraries and is nominally 0.6, 0.2 and 1.0, respectively, for the three libraries. Figure 16 shows the results of the composition changes after fuel cell testing and after acid treatment for $Pt_{1-x}[Mn_{0.375}Fe_{0.625}]_x$, Library 4.

Figure 16a shows the Mn and Fe contents, y_{before} and x_{before}, before fuel cell testing and the Mn and Fe contents, y_{after} and x_{after}, after fuel cell testing, plotted vs the total transition metal content, $x_{before} + y_{before}$, before fuel cell testing. Figure 16a clearly shows that both Fe and Mn contents are reduced at all points of the library

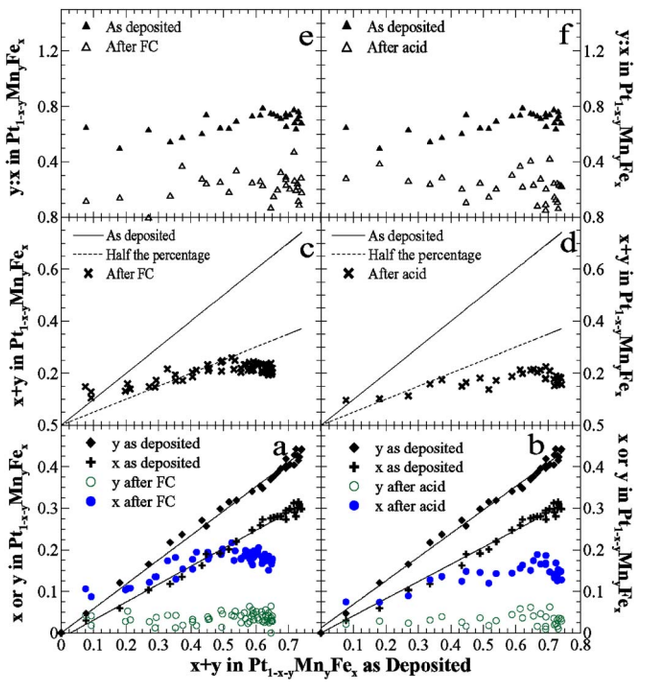

Figure 16. (Color online) Composition of the Type I $Pt_{1-x-y}Mn_yFe_x$, Library 4, with an initial Mn/Fe ratio = 0.65 after (a–c) fuel cell testing and (d–f) acid treatment vs the composition of the as-deposited film. Panels a and b show the individual metal contents (x and y), panels c and d show the total transition metal content ($x + y$), and panels e and f show the ratio of Mn to Fe (y:x).

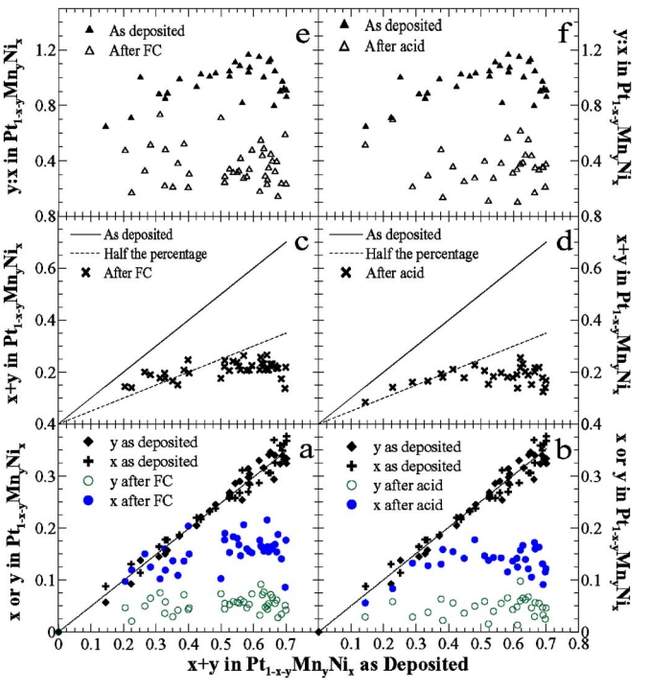

Figure 18. (Color online) Composition of Type I $Pt_{1-x-y}Mn_yNi_x$, Library 6, with an initial Mn/Ni ratio = 1.0 after (a, c, e) fuel cell testing and (b, d, f) acid treatment vs the composition of the as-deposited film. Panels a and b show the individual metal contents (x and y), panels c and d show the total transition metal content ($x + y$), and panels e and f show the ratio of Mn to Ni (y:x).

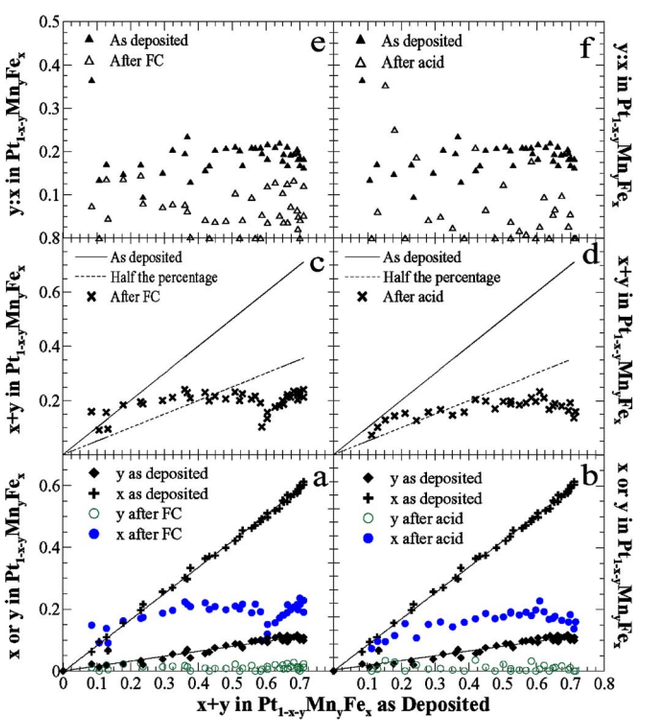

Figure 17. (Color online) Composition of Type I $Pt_{1-x-y}Mn_yFe_x$, Library 5, with an initial Mn/Fe ratio = 0.2 after (a–c) fuel cell testing and (d–f) acid treatment vs the composition of the as-deposited film. Panels a and b show the individual metal contents (x and y), panels c and d show the total transition metal content ($x + y$), and panels e and f show the ratio of Mn to Fe (y:x).

and that the change in the Mn content is larger than the change in the Fe content. Figure 16c shows the total transition metal content after fuel cell testing, $x_{after} + y_{after}$, plotted vs the total transition metal content, $x_{before} + y_{before}$, before fuel cell testing. After fuel cell testing, the total transition metal content is no more than $x_{after} + y_{after} = 0.25$ for any position in the library. Figure 16e shows the measured ratio of Mn to Fe content before fuel cell testing y_{before}:x_{before} and after fuel cell testing y_{after}:x_{after} plotted vs the total transition metal content, $x_{before} + y_{before}$, before fuel cell testing. Figure 16e shows that the Mn content is reduced by about a factor of three relative to Fe for all positions in the library during fuel cell testing. The panels on the right hand side of Fig. 16 show analogous information for an identical library treated in acid. Note the similarities in the compositions of the acid treated libraries vs the libraries after fuel cell testing.

Figure 17 shows analogous results to Fig. 16 collected on $Pt_{1-x-y}Mn_yFe_x$, Library 5, with an initial ratio, y:$x = 0.2$. The ratio y:x after acid treatment and fuel cell testing was reduced to below 0.1. The acid-treated and postfuel cell compositions again compare well. Figure 18 shows results on $Pt_{1-x-y}Mn_yNi_x$ with an initial ratio y:$x = 1$ presented in the same way as in Fig. 16 and 17. The ratio y:x reduces to about 0.3, a three-fold decrease. After both fuel cell testing and acid treatment, the maximum transition metal content, $x_{after} + y_{after}$, is about 0.25, regardless of the initial transition metal content for both libraries studied in Fig. 16-18.

The results in Fig. 16-18 can be summarized as follows: (i) acid treatment and fuel cell testing lead to the same compositional changes, point by point, in these electrocatalyst libraries, (ii) Mn is selectively leached compared to either Fe or Ni, and (iii) provided the initial transition metal content, $x_{before} + y_{before} \geqslant 0.25$, after fuel cell testing or acid treatment the maximum transition metal content is reduced to about $x_{after} + y_{after} = 0.25$.

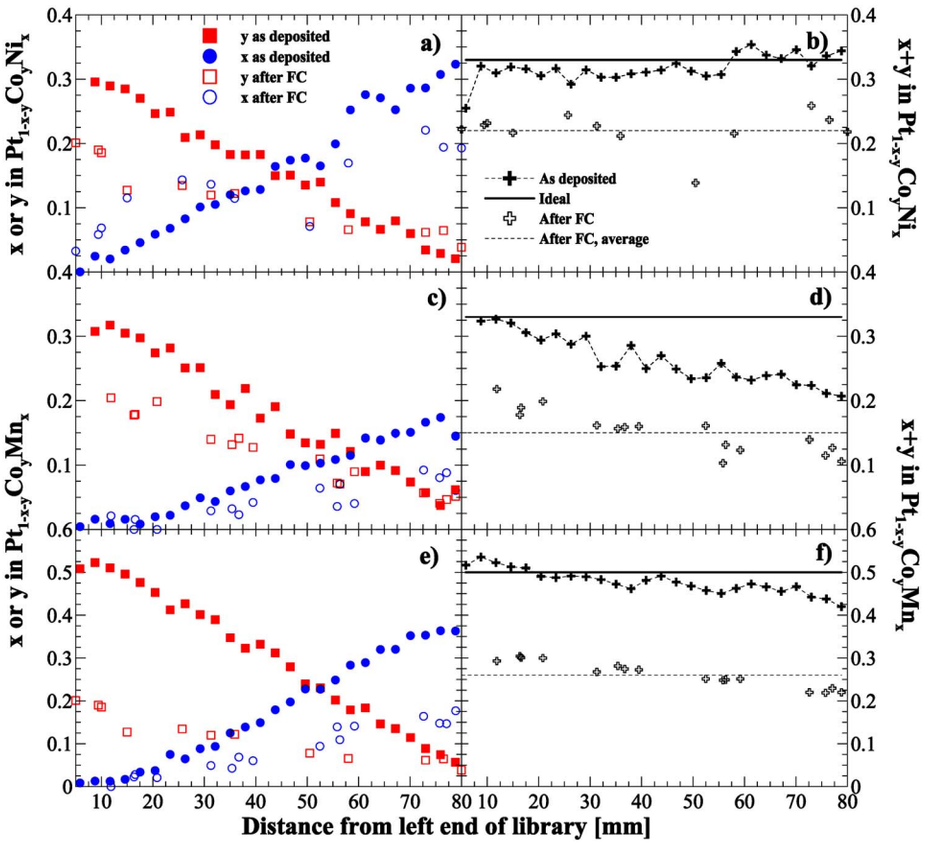

Figure 19. (Color online) Results for three Type II libraries $Pt_{0.7}[Co_{1-y}Ni_y]_{0.3}$, $Pt_{0.7}[Co_{1-y}Mn_y]_{0.3}$, and $Pt_{0.5}[Co_{1-y}Mn_y]_{0.5}$ $(0 \leqslant y \leqslant 1)$. These are Libraries 7, 10, and 11, respectively. The composition of the catalysts, designated as x and y in $Pt_{1-x-y}M_yM'_x$ before and after fuel cell testing are shown in the left panels (a, c, and e). The overall transition metal content, $x + y$, before and after fuel cell testing is given in the right panels (b, d, and f).

Results for Type II $Pt_{1-x}[M_{1-y}M'_y]_x$, $(M = Co,\ M' = Ni, Mn;\ 0 \leqslant y \leqslant 1)$, Libraries 7–12.— Figure 19 shows electron microprobe results for Libraries 7, 10, and 11 having nominal compositions, $Pt_{0.7}[Co_{1-y}Ni_y]_{0.3}$, $Pt_{0.7}[Co_{1-y}Mn_y]_{0.3}$, and $Pt_{0.5}[Co_{1-y}Mn_y]_{0.5}$, with $0 \leqslant y \leqslant 1$. The composition of the catalysts, designated as x and y in $Pt_{1-x-y}M_yM'_x$ before and after fuel cell testing, are shown in the left panels (Fig. 19a, c and e). The overall transition metal content, $x + y$, before and after fuel cell testing is given in the right panels (Fig. 19b, d and f). For the three libraries described by Fig. 19, the content of both transition metals is reduced during fuel cell testing and the overall transition metal content is reduced by about 50%. In no case is the final transition metal content greater than $x_{after} + y_{after} = 0.25$.

Figure 20 shows the composition changes of two further Type II libraries that initially have higher transition metal contents than the libraries described by Fig. 19 and which have been subjected to both acid and fuel cell testing. Figure 20a-d shows results for $Pt_{0.3}[Co_{1-y}Ni_y]_{0.7}$, Library 9, and Fig. 20e-h shows results for $Pt_{0.3}[Co_{1-y}Mn_y]_{0.7}$, Library 12. The left panels of Fig. 20 show the compositions x and y as well as the sum, $x + y$, in $Pt_{1-x-y}Co_yMn_x$ and in $Pt_{1-x-y}Co_yNi_x$ before and after fuel cell testing. The right panels show analogous information after acid treatment. The compositions that are attained at all points of the libraries after fuel cell testing and after acid treatment show the same trends, although the acid treatment removed substantially more transition metals than did the fuel cell testing. For the fuel-cell-tested libraries, the transition metal atomic fraction is reduced from 0.7 to about 0.3 and for the acid-treated libraries, the transition metal content is reduced to about 0.2. Mn is removed preferentially from the Mn-containing alloy compared to Co, as seen in Fig. 20a and b. Both Ni and Co are removed to about the same extent from the $Pt_{1-x-y}Co_yNi_x$ library in both fuel cell and acid testing.

The Pourbaix diagrams for the transition metals studied here (Fe, Ni, Co, Mn) show that these pure elements dissolve under the typical potential/pH conditions encountered in working PEMFCs.[58] We have shown here and in our previous work that these transition metals also dissolve to some degree when they are alloyed with Pt. When the initial transition metal atomic fraction is less than about 0.6, dissolution is primarily from the surface of the alloy and when the initial transition metal fraction is greater than 0.6, both bulk and surface dissolution occurs. The surface depletion of transition metals in Pt alloys has been discussed in the literature.[20]

Selective leaching or dealloying of the transition metals from the $Pt_{1-x-y}M_xM'_y$ libraries studied here is probably similar to the widely known dezincification process of brass and the graphitic corrosion of cast iron.[59] In brass, for example, Zn which is more active (lower redox potential) is preferentially leached out when the alloy is exposed to corrosive environments, leaving behind a porous structure. During this corrosion Cu is also thought to dissolve but later redeposit on the grains. In the case of Pt–Co catalysts in hot phosphoric acid, Watanabe proposed a corrosion mechanism where Co and Pt dissolve and Pt redeposits onto grains with lower surface energy, leading to formation of a Pt skin layer.[36] In all the samples studied here, more active transition metals corrode more extensively. In the case of Pt–MnFe and Pt–MnNi, we observed a stronger dissolution of Mn over either Fe or Ni. This may be explained by the lower reduction potential of Mn [−1.18 V vs standard hydrogen electrode (SHE)] than Fe (−0.44 vs SHE) or Ni (−0.26 V vs SHE), which would make Mn thermodynamically more active for corrosion.

The average particle size of the catalysts studied here is about 10–12 nm, that is, larger than the typical 2–4 nm particles found in carbon-supported Pt catalysts. The NSTF-supported Pt catalysts are different from carbon-supported catalysts in that they exhibit a larger specific activity (similar to bulk Pt crystals) and a much better

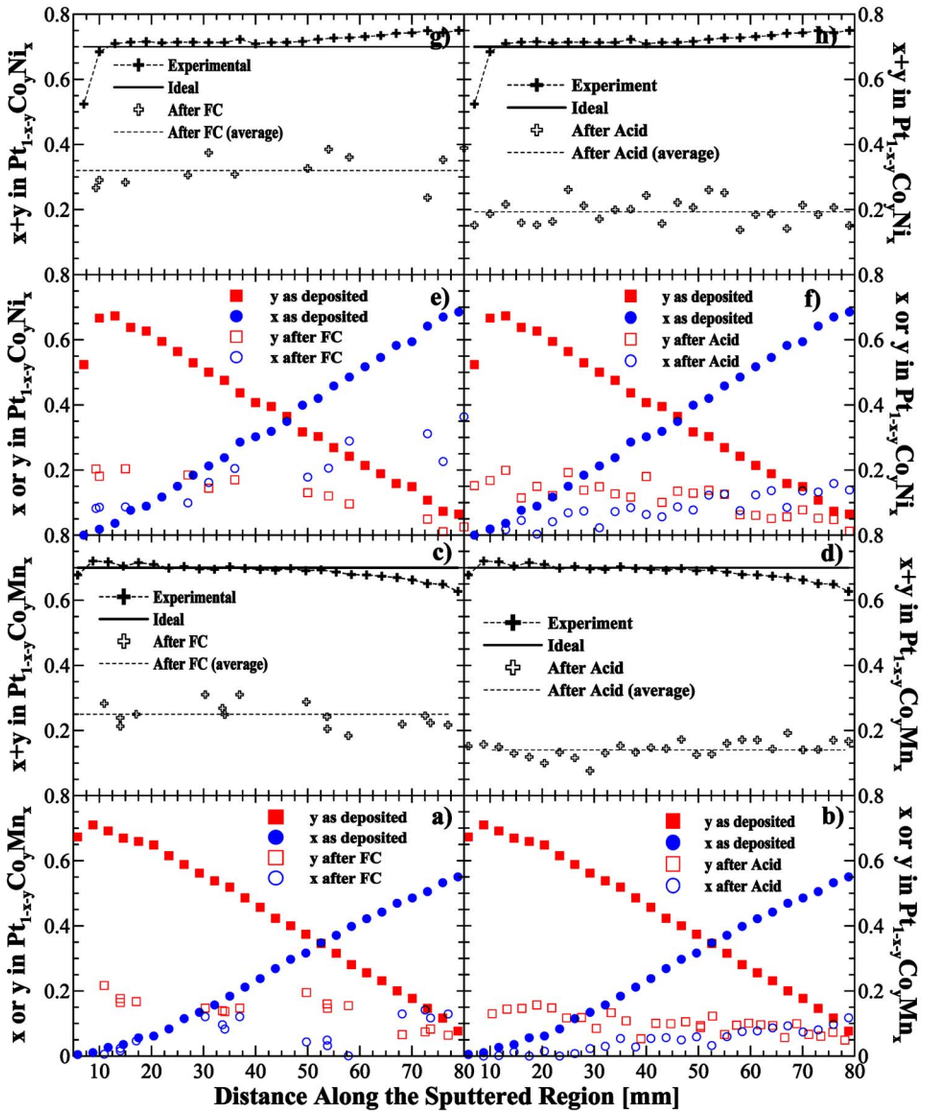

Figure 20. (Color online) Results for two Type II libraries, $Pt_{0.3}[Co_{1-y}Ni_y]_{0.7}$ and $Pt_{0.3}[Co_{1-y}Mn_y]_{0.7}$ $(0 \leqslant y \leqslant 1)$. These are Libraries 9 and 12. The composition of the catalysts, designated as x and y in $Pt_{1-x-y}M_yM'_x$ before and after fuel cell or acid testing are shown in panels a, b, e, and f. The overall transition metal content, $x + y$, before and after fuel cell or acid testing is given in panels c, d, g, and h.

Pt dissolution stability.[35,60-62] The Pt grains in these NSTF-based catalysts are already "coarsened" and hence, surface area degradation occurs more slowly. Corrosion stability of transition metals in the NSTF-supported Pt alloys would thus be closer to bulk-like alloys, whereas smaller grain-size alloys are likely to lose larger fractions of transition metals.

Conclusions

We have shown that in $Pt_{1-x-y}M_xM'_y$ alloys (M = Ni, Co, Mn, Fe) corrosion of the transition metal elements occurs when the electrocatalysts are subjected to 1 M H_2SO_4 at 80°C and also when they are utilized under the typical working conditions of a PEMFC. The composition changes that occur during the acid treatment mimic those that occur during fuel cell testing very closely. Regardless of the initial overall transition metal atomic fraction, the average transition metal atomic fraction is reduced to at most a value of about 0.3. This suggests that it is difficult for the transition metal atoms to diffuse from the cores of the grains when the atomic fraction is less than 0.3. In all cases, for all the libraries studied, it is very likely that there is a significant loss of transition metals at the alloy surface. This explains why the average transition metal content is reduced even for alloys where the initial transition metal atomic fraction is less than 0.3.

Acknowledgments

The authors acknowledge the financial support of NSERC and 3M for this work. A.B. acknowledges NSERC, Killam and Sumner Foundations for scholarship support. R.L. acknowledges the Stiftung der Deutschen Wirtschaft e.V. for scholarship support. This research was supported in part by the Hydrogen, Fuel Cells, and Infrastructure Technology Program in the Office of Energy Efficiency and Renewable Energy at the U.S. Department of Energy. This research was supported in part by the Department of Energy, cooperative agreement no. DE-FC36-02AL67621.

Dalhousie University assisted in meeting the publication costs of this article.

References

1. N. P. Brandon, S. Skinner, and B. C. H. Steele, *Annu. Rev. Mater. Res.*, **33**, 183 (2003).
2. B. C. H. Steele and A. Heinzel, *Nature (London)*, **414**, 345 (2001).
3. M. F. Mathias, R. Makharia, H. A. Gasteiger, J. J. Conley, T. J. Fuller, C. J. Gittleman, S. S. Kocha, D. P. Miller, C. K. Mittelsteadt, T. Xie, S. G. Yan, and P. T. Yu, *Electrochem. Soc. Interface*, **14**, 24 (2005).
4. R. Adzic, in *Electrocatalysis*, 1st ed., J. Lipkowski and P. N. Ross, Editors, p. 197, Wiley-VCH, New York (1998).
5. S. Mukerjee and S. Srinivasan, in *Handbook of Fuel Cells: Fundamentals, Technology and Applications*, 1st ed., W. Vielstich, A. Lamm, and H. A. Gasteiger,

Editors, Vol. 2, p. 502, John Wiley & Sons, Chichester (2003).
6. M. Gattrell and B. MacDougall, in *Handbook of Fuel Cells: Fundamentals, Technology and Applications*, 1st ed., W. Vielstich, A. Lamm, and H. A. Gasteiger, Editors, Vol. 2, p. 444, John Wiley & Sons, Chichester (2003).
7. K. Kinoshita, *J. Electrochem. Soc.*, **137**, 845 (1990).
8. N. Markovic, H. Gasteiger, and P. N. Ross, *J. Electrochem. Soc.*, **144**, 1591 (1997).
9. A. Ishihara, K. Lee, S. Doi, S. Mitsushima, N. Kamiya, M. Hara, K. Domen, K. Fukuda, and K. Ota, *Electrochem. Solid-State Lett.*, **8**, A201 (2005).
10. F. Jaouen, S. Marcotte, J. P. Dodelet, and G. Lindbergh, *J. Phys. Chem. B*, **107**, 1376 (2003).
11. M. Lefevre, J. P. Dodelet, and P. Bertrand, *J. Phys. Chem. B*, **106**, 8705 (2002).
12. M. K. Debe, in *Handbook of Fuel Cells: Fundamentals, Technology and Applications*, 1st ed., W. Vielstich, A. Lamm, and H. A. Gasteiger, Editors, Vol. 3, p. 576, John Wiley & Sons, Chichester (2003).
13. J. Zhang, Y. Mo, M. B. Vukmirovic, R. Klie, K. Sasaki, and R. R. Adzic, *J. Phys. Chem. B*, **108**, 10955 (2004).
14. J. Zhang, M. B. Vukmirovic, K. Sasaki, F. Uribe, and R. R. Adzic, *J. Serb. Chem. Soc.*, **70**, 513 (2005).
15. P. J. Bouwman, W. Dmowski, J. Stanley, G. B. Cotten, and K. E. Swider-Lyons, *J. Electrochem. Soc.*, **151**, A1989 (2004).
16. P. J. Kulesza, K. Karnicka, K. Miecznikowski, M. Chojak, A. Kolary, P. J. Barczuk, G. Tsirlina, and W. Czerwinski, *Electrochim. Acta*, **50**, 5155 (2005).
17. B. R. Limoges, R. J. Stanis, J. A. Turner, and A. M. Herring, *Electrochim. Acta*, **50**, 1169 (2005).
18. P. Stonehart, *J. Appl. Electrochem.*, **22**, 995 (1992).
19. S. Mukerjee, S. Srinivasan, M. P. Soriaga, and J. McBreen, *J. Electrochem. Soc.*, **142**, 1409 (1995).
20. T. Toda, H. Igarashi, H. Uchida and M. Watanabe, *J. Electrochem. Soc.*, **146**, 3750 (1999).
21. D. Thompsett, in *Handbook of Fuel Cells: Fundamentals, Technology and Applications*, 1st ed., W. Vielstich, A. Lamm, and H. A. Gasteiger, Editors, Vol. 3, p. 467, John Wiley & Sons, Chichester (2003).
22. S. Mukerjee, S. Srinivasan, M. P. Soriaga, and J. McBreen, *J. Phys. Chem.*, **99**, 4577 (1995).
23. V. Stamenkovic, T. J. Schmidt, P. N. Ross, and N. M. Markovic, *J. Electroanal. Chem.*, **554**, 191 (2003).
24. J. K. Norskov, J. Rossmeisl, A. Logadottir, L. Lindqvist, J. R. Kitchin, T. Bligaard, and H. Jonsson, *J. Phys. Chem. B*, **108**, 17886 (2004).
25. J. R. Kitchin, J. K. Norskov, M. A. Barteau, and J. G. Chen, *J. Chem. Phys.*, **120**, 10240 (2004).
26. J. L. Zhang, M. B. Vukmirovic, K. Sasaki, A. U. Nilekar, M. Mavrikakis, and R. R. Adzic, *J. Am. Chem. Soc.*, **127**, 12480 (2005).
27. V. Stamenkovic, T. J. Schmidt, P. N. Ross, and N. M. Markovic, *J. Phys. Chem. B*, **106**, 11970 (2002).
28. H. A. Gasteiger, S. S. Kocha, B. Sompalli, and F. T. Wagner, *Appl. Catal., B*, **56**, 9 (2005).
29. P. J. Ferreira, G. J. la O, Y. Shao-Horn, D. Morgan, R. Makharia, S. Kocha, and H. A. Gasteiger, *J. Electrochem. Soc.*, **152**, A2256 (2005).
30. K. Yasuda, A. Taniguchi, T. Akita, T. Ioroi, and Z. Siroma, *Phys. Chem. Chem. Phys.*, **8**, 746 (2006).
31. M. Dowlapalli, P. Atanassov, J. Xie, and G. L. Rice, Paper 1169 presented at The Electrochemical Society Meeting, Los Angeles, CA, Oct 16–21, 2005.
32. F. H. Garzon, J. Davey, and R. Borup, Paper 1179 presented at The Electrochemical Society Meeting, Los Angeles, CA, Oct 16–21, 2005.
33. Z. Siroma, A. Taniguchi, T. Akita, K. Yasuda, K. Ishii, M. Tanaka, M. Inaba, and A. Tasaka, Paper 1181 presented at The Electrochemical Society Meeting, Los Angeles, CA, Oct 16–21, 2005.
34. D. A. Stevens and J. R. Dahn, *Carbon*, **43**, 179 (2005).
35. M. K. Debe, A. K. Schmoeckel, S. K. Hendricks, G. D. Vernstrom, G. M. Haugen, and R. T. Atanasoski, *Electrochem. Soc. Trans.*, **1**(8), 51 (2006).
36. M. Watanabe, K. Tsurumi, T. Mizukami, T. Nakamura, and P. Stonehart, *J. Electrochem. Soc.*, **141**, 2659 (1994).
37. A. Bonakdarpour, J. Wenzel, D. A. Stevens, S. Sheng, T. L. Monchesky, R. Lobel, R. T. Atanasoski, A. K. Schmoeckel, G. D. Vernstrom, M. K. Debe, and J. R. Dahn, *J. Electrochem. Soc.*, **152**, 1 (2005).
38. J. R. Dahn, S. Trussler, T. D. Hatchard, A. Bonakdarpour, J. R. Mueller-Neuhaus, K. C. Hewitt, and M. Fleischauer, *Chem. Mater.*, **14**, 3519 (2002).
39. M. D. Fleischauer, T. D. Hatchard, A. Bonakdarpour, and J. R. Dahn, *Meas. Sci. Technol.*, **16**, 212 (2005).
40. Y. Yamada, A. Ueda, H. Shioyama, and T. Kobayashi, *Appl. Surf. Sci.*, **223**, 220 (2004).
41. S. Guerin, B. E. Hayden, C. E. Lee, C. Mormiche, J. R. Owen, A. E. Russell, B. Theobald, and D. Thompsett, *J. Comb. Chem.*, **6**, 149 (2004).
42. P. Strasser, Q. Fan, M. Devenney, W. H. Weinberg, P. Liu, and J. K. Norskov, *J. Phys. Chem. B*, **107**, 11013 (2003).
43. E. Reddington, A. Sapienza, B. Gurau, R. Viswanathan, S. Sarangapani, E. S. Smotkin, and T. E. Mallouk, *Science*, **280**, 1735 (1998).
44. M. K. Debe and R. J. Poirier, *J. Vac. Sci. Technol. A*, **12**, 2017 (1994).
45. M. K. Debe and A. R. Drube, *J. Vac. Sci. Technol. B*, **13**, 1236 (1995).
46. D. A. R. Barkhouse, A. Bonakdarpour, M. Fleischauer, T. D. Hatchard, and J. R. Dahn, *J. Magn. Magn. Mater.*, **261**, 399 (2003).
47. B. D. Cullity, S. R. Stock, and S. Stock, *Elements of X-Ray Diffraction*, p. 170, Prentice Hall, Upper Saddle River, NJ (2001).
48. K. H. Buschow, P. G. van Engen, and R. Jongebreuer, *J. Magn. Magn. Mater.*, **38**, 1 (1983).
49. C. Leroux, M. C. Cadeville, V. Pierron-Bohnes, G. Inden, and F. Hinz, *J. Phys. F: Met. Phys.*, **18F**, 2033 (1988).
50. J. C. Woolley, J. H. Phillips, and J. A. Clark, *J. Less-Common Met.*, **6**, 461 (1964).
51. E. Gebhardt and W. Koster, *Z. Metallkd.*, **32**, 253 (1940).
52. A. H. Geisler and D. L. Martin, *J. Appl. Phys.*, **23**, 375 (1952).
53. B. van Laar, *J. Phys. (Paris)*, **25**, 600 (1964).
54. U. Esch and A. Schneider, *Z. Elektrochem. Angew. Phys. Chem.*, **50**, 268 (1944).
55. D. E. G. Williams and A. Jezierski, *J. Magn. Magn. Mater.*, **59**, 41 (1986).
56. E. Raub and W. Mahler, *Z. Metallkd.*, **46**, 282 (1955).
57. E. Kren, G. Kadar, L. Pal, J. Solyom, P. Szabo, and T. Tarnoczi, *Phys. Rev.*, **171**, 574 (1968).
58. M. Pourbaix, *Atlas of Electrochemical Equilibria in Aqueous Solutions*, p. 72, NACE International, (1974).
59. D. A. Jones, *Principles and Prevention of Corrosion*, p. 20, Prentice Hall, Upper Saddle River, NJ (1996).
60. K. J. J. Mayrhofer, B. B. Blizanac, M. Arenz, V. R. Stamenkovic, P. N. Ross, and N. M. Markovic, *J. Phys. Chem. B*, **109**, 14433 (2005).
61. M. K. Debe, A. K. Schmoeckel, R. T. Atanasoski, and G. D. Vernstrom, Paper 64 presented at the Fuel Cell Seminar, Palm Springs, CA, Nov 14–18, 2005.
62. M. K. Debe, A. K. Schmoeckel, G. D. Vernstrom, and R. T. Atanasoski, *J. Power Sources*, Submitted.

Appendix II

Dalhousie - Paper on PtCoMn RRDE Activities (in press)

Oxygen Reduction Activity of Pt and Pt-Mn-Co Electrocatalysts Sputtered on Nano-structured Thin Film Support

Arman Bonakdarpour, Krystal Stevens, George D. Vernstrom[a], Radoslav Atanasoski[a], Alison K. Schmoeckel[a], Mark K. Debe[a], and Jeff R. Dahn*

Department of Physics, Dalhousie University, Halifax, Nova Scotia, B3H 3J5, Canada

[a]3M Fuel Cell Components Program, 201-2N-19, 3M Center, St. Paul, MN 55144, USA

Abstract

We report on extensive measurements of oxygen reduction activity of Pt and Pt-Co-Mn electrocatalysts using the rotating ring-disk electrode (RRDE) method. The electrocatalysts were prepared by sputtering from Pt or Pt, Co, and Mn targets onto 3M's nano-structured thin film support (NSTF) structures. The area-specific activity of Pt/NSTF, measured in 0.1 M $HClO_4$ and at room temperature, is similar to that of bulk Pt. The area-specific measurements show a 20 mV reduction in the Pt-Co-Mn/NSTF overpotential compared to Pt/NSTF. The corresponding kinetic gain in the area-specific activity of the ternary alloy is about a factor of two. This ORR enhancement factor observed in the ternary Pt-Co-Mn/NSTF by RRDE measurements is similar to the results obtained in 50 cm^2 H_2/Air fuel cells.

---

keywords: nano-structured thin film support, ternary Pt-Co-Mn alloy, oxygen reduction, RRDE

*corresponding author: jeffdahn@dal.ca, Tel: 1-902-494-2991, fax: 1-902-494-5191

Introduction

Currently, significant research is focused on improving the properties of the materials used in hydrogen proton exchange membrane fuel cells (PEMFC) in order to facilitate their commercialization. In particular, much effort is directed towards improving the Pt-based electrocatalysts that are used for the hydrogen oxidation and oxygen reduction reactions occurring in a PEMFC. Besides the long-term need for fuel cell vehicle commercialization to reduce the amount of the expensive Pt used, there is a more critical near-term need to improve the stability and durability of both the catalyst and its support. Dissolution and agglomeration of Pt nano-particles, which lead to a loss of active surface area and corrosion of the carbon support has been reported by numerous groups [1-7]. These failure modes, in addition to catalyst poisoning effects, all contribute to reducing the electrocatalyst's activity and the overall cell performance.

Numerous approaches have been taken in recent years to improve the kinetic activity of Pt catalysts, lower their loading and improve their durability. Some of these include alloying of Pt with other transition metals, core-shell type electrocatalysts, corrosion-induced strains in Pt-alloys, and overlayers such as polyoxometallates or Au clusters [8-14]. As for the carbon support, improvements in the stability against corrosion have been observed by using more graphitic carbon [7]. Alternative support materials, which are typically conductive metal oxides, such as Magneli phases of Ti-oxides, and more recently In-Sn-oxides, have been reported in the literature [15-17].

For the past 12 years, 3M has been developing a third basic type of fuel cell electrocatalyst after Pt blacks and dispersed Pt on carbon blacks. It utilizes an alternative support system consisting of a single layer of self-assembled crystalline whiskers- that grow by a screw-dislocation mechanism when a vacuum-deposited organic pigment (CAS #PR149) film is annealed at 250-270°C [18]. Typical individual whiskers are about 1000 nm in length and about 50 nm in diameter, with an areal

number density of 3-4 billion per cm^2 [18]. The desired catalyst (Pt or Pt-alloy) is then deposited on these support structures in a single physical vapor deposition step. More details on NSTF fabrication, their physical properties, catalyst deposition, and MEA lamination procedures can be found elsewhere [18-20]. In short, the NSTF-based electrocatalysts used for the cathode provide up to ten times higher area specific activity than conventional state-of-the-art Pt/C or PtCo/C catalysts and 50% higher mass activity values in 50 cm^2 fuel cell tests, using current standard NSTF whisker supports [21].

To further characterize the oxygen reduction activity and H_2O_2 yield of these catalysts, samples of Pt/NSTF and Pt-Co-Mn/NSTF, were studied by RRDE and the results are reported here. The ternary alloy of Pt-Co-Mn/NSTF showed superior performance compared to Pt/NSTF in PEMFC testing [22], including a 2.5× gain in area specific activity. The activities observed by RRDE are consistent with those of the PEMFC measurements, that is Pt-Co-Mn/NSTF provides a kinetic gain of about two times over Pt/NSTF.

Experimental Methods

a) Sample Preparation

Preparation of NSTF supports are explained in more detail by Debe [18-20], as well as procedures for forming catalyst coated membranes for fuel cell testing. The electrocatalysts were deposited onto NSTF supports using a multi-target sputtering system. For the samples investigated in this paper, only one type of NSTF support was utilized. The depositions aimed to produce films of 0.15 $mg \cdot cm^{-2}$ Pt and 0.17 mg of Pt-Co-Mn per cm^{-2}. The Pt content of Pt-Co-Mn was also 0.15 $mg \cdot cm^{-2}$ giving a weight ratio of Pt:(Pt+Co+Mn) of 88%; hence a chemical composition of $Pt_{0.68}Co_{0.3}Mn_{0.02}$. In order to evaluate the NSTFC using RRDE, the catalyst coated whiskers were carefully brushed

off of the original substrate web. Precautions were taken to avoid any contaminations of the catalyst with impurities, mechanical or otherwise. The procedure for applying the NSTF onto a glassy carbon support for the RRDE measurements is discussed below.

d) Bulk Composition, Crystal Structure, and Surface Morphology

The X-ray diffraction patterns were collected using a Siemens 5000 diffractometer equipped with Cu Kα radiation and an incident beam monochromator. The lattice constants and grain sizes were calculated using the Bragg and Scherrer equations, respectively, by fitting Gaussian profiles to the measured data [23].

The film composition was measured by a JEOL JXA-8200 Superprobe electron microprobe system equipped with one energy dispersive (EDS) spectrometer and five wavelength dispersive (WDS) spectrometers. The morphology of deposited electroctalaysts on the glassy carbon (GC) disks were imaged by a Hitachi S-4700 field emission scanning electron microscope.

g) Electrochemical Measurements

All the rotating ring disk electrode (RRDE) measurements were performed using a Pine rotator (AFMSRX), a Pine bipotentiostat (AFCBP1), a Pt-wire counter electrode, and a Cl^--free Koslow Hg/Hg_2SO_4 [with H_2SO_4 filling solution] (MMS) reference electrode. The electrolyte was about 125 mL of 0.1 M $HClO_4$, a non-adsorbing acid, prepared from doubly-distilled $HClO_4$ (GFS Chemicals) and 18 MΩ Barnstead nanopure water. Extreme care was taken to ensure the cleanliness of the glassware, cell parts, and the samples during handling, and to maintain a minimum leakage current in the ring assembly for all the measurements. All the potentials mentioned in this article are referenced to the reversible hydrogen electrode (RHE). The RHE scale for the MMS electrode was established by purging H_2 in the solution and measuring the open circuit

voltage of the cell using both disk and the ring electrodes. The OCV values of disk and ring, always within 5 mV or less, were averaged and used as the RHE scale for the measurements. This reference calibration was performed for each individual disk assembly. The reported currents were normalized by either the geometric electrode area or the electrochemical surface area (ECSA), as explained later.

Several different concentrations of slurries containing nano-pure water and Pt/NSTF or Pt-Co-Mn/NSTF were prepared. No Nafion was used. The slurry concentrations were adjusted to provide catalyst mass density loadings of 20, 40, 60, 80, and 100 $\mu g \cdot cm^{-2}$ when a 15 μL drop was placed on a GC disk. The deposited catalyst slurry was dried under flowing Ar. For all measurements the adhesion of the electrocatalyst to the GC disk was excellent and no loss of electrocatalyst occurred during the measurements. To ensure repeatability of the measurements, each slurry concentration was measured simultaneously in two different Pine rotator setups: one equipped with an RDE and the other with an RRDE.

The technique of RRDE has been developed to a point where state-of-the-art literature-quality CV's and ORR curves of sputtered Pt films and polycrystalline Pt (Pine RDE) are routinely obtained [24-26]. Briefly, the integrated charges of the H_{ads}/H_{des} regions of the CVs were used to obtain the electrochemically active surface area (ECSA) of each sample. The capacitive currents (the current measurements in the Ar-purged cell) were subtracted from the ORR data. The diffusion-limited current was read directly from the ORR data for each corresponding rotation speed and the kinetic currents were obtained using the Koutecky-Levich relation. H_2O_2 detection and quantification were made by measuring the Pt ring current. More details and equations used for the data analysis are given elsewhere [26].

Results and Discussion

Electron microprobe measurements of the catalyst indicated a composition about $Pt_{0.64}Co_{0.32}Mn_{0.04}$ with experimental errors of about 2%, which is close to the nominal values mentioned in the experimental section.

Figure 1 shows X-ray diffraction patterns of Pt/NSTF and Pt-Co-Mn/NSTF. Broad Bragg peaks, indicating the nanometric dimensions of the Pt and Pt-Co-Mn grains, show formation of fcc structured crystallites. From the peak broadening the grain size of Pt/NSTF and Pt-Co-Mn/NSTF are estimated to be 11 and 8 nm, respectively. The fcc lattice constants of the Pt/NSTF and Pt-Co-Mn/NSTF are 3.92 and 3.86 Å, respectively. Contraction of the fcc lattice in the case of Pt-Co-Mn, evident by shifting of fcc peaks to higher angles, is a proof of alloy formation. Average values of reported bulk lattice constants are about 3.79 ± 0.04 Å for fcc $Pt_{0.5}Co_{0.5}$, and 3.83 Å for fcc $Pt_{0.75}Co_{0.25}$ [27-29]. Thus Pt-Co-Mn/NSTF shows, to a very good degree, formation of an alloy. The fcc lattice constant is much less sensitive to the Mn content as reported in the bulk Pt-Mn phases, where values of 3.90 to 3.89 Å are reported for the phases with up to 25% Mn [30, 31].

Figure 2a-e shows slurry depositions on the tip of the GC electrodes for different loadings. Figure 2f shows a higher magnification view of the individual whiskers on a GC disk. Uniform depositions to the eye and in a 40× optical microscope were always achieved.

Figure 3 shows the cyclic voltammograms of Pt/NSTF and Pt-Co-Mn/NSTF for different loadings. A CV of a polycrystalline-Pt disk is also shown for comparison, which provides a signal close to that of the lowest loading (20 $\mu g_{Pt}.cm^{-2}$). Figure 4 shows a comparison of Pt/NSTF and Pt-Co-Mn/NSTF CVs. Note that essentially the CVs show similar features, and are very similar to that of polycrystalline-Pt. There is substantial discussion, based on experimental data and theoretical considerations on the role of OH adsorption as a hindering effect in the kinetics of ORR. In

particular it has been shown that modifying the electronic properties of Pt, by alloying with transition metals like Ni, shifts the onset of OH adsorption to higher potentials and leads to an enhancement in the rate of ORR [8, 32]. For both Pt and Pt-Co-Mn we observe OH onsets which are similar to that of the polycrystalline-Pt disk (Figure 4). Mayerhofer et. al. have shown that onset of OH adsorption shifts to higher potentials, because of a shift in the potential of zero charge ($E_{\sigma=0}$), as the Pt grain size increases [33]. The shift of $E_{\sigma=0}$ to higher potentials is attributed to the change in the surface potential component of the $E_{\sigma=0}$. The onset of OH adsorption for these catalysts and that of polycrystalline-Pt is higher than Pt/C [33].

Surface enhancement factors (SEF) were obtained by dividing the ECSA by geometric area and are plotted vs. the Pt mass loading for Pt/NSTF and Pt-Co-Mn/NSTF in Figure 5. The SEF factor is about 10 for 0.1 $mg_{Pt} \cdot cm^{-2}$, close to values obtained in PEMFC [18]. Both samples show a linear growth of SEF as the Pt content is increased, although at different rates. The ratio of the slopes of the linear fits to the data in Figure 5 shows that the Pt-Co-Mn electrocatalysts have about 15% higher surface area compared to Pt/NSTF. This could be caused by the additional volume imparted by the Co and Mn since the SEF per unit mass of Pt is being compared. There could also be a higher roughness factor due to Co and Mn dissolution.

The ORR curves of Pt/NSTF and Pt-Co-Mn/NSTF, taken at 900 rpm, are shown in Figures 6a and b. The data for poly-Pt is also shown for comparison. Diffusion limited currents are reached at all loadings, except at the lowest loadings, where the number of actives sites (Pt content) is the limiting factor, not the oxygen diffusion rate.

To assess the kinetic behavior of these catalysts, their Tafel region is considered in Figure 7. The currents densities were corrected for double layer capacitive currents, and are normalized by the ECSA. Figure 7a shows the Tafel lines of Pt/NSTF for various loadings. Note that, at best, they

mostly overlap with the Tafel data of the polycrystalline-Pt disk. Duplicate measurements are shown for repeatability. Figure 7b shows similar data for Pt-Co-Mn/NSTF, again with several duplicate measurements. The activities are now similar or better than the poly-Pt data. On average there is about a 20 mV kinetic gain in Pt-Co-Mn/NSTF over Pt/NSTF. This is shown more clearly in Figure 8 where Pt/NSTF and Pt-Co-Mn/NSTF are compared to each other.

This overpotential reduction translates into a kinetic gain of about two times in the specific current density at a given potential. The area specific current density of Pt/NSTF is similar to that of polycrystalline-Pt and is about five times higher than that of Pt/C [34]. For comparative RRDE measurement of several different (TKK and E-TEK) Pt/C samples see Figure 10 in Gasteiger et. al. [10]. These results are consistent with what has been observed in the PEMFC measurements using these electrocatalysts [21, 22]. Comparisons to state-of-the-art dispersed catalysts can be made at the same loading of 0.2 $mg_{Pt} \cdot cm^{-2}$. Using GM recommended conditions for measuring specific and mass activity of 80°C, saturated H_2/O_2 at 150 kPa (abs), at 900 mV (15-20 min average), roll-good fabricated NSTF PtCoMn CCM generate specific activities of 2.93 $mA \cdot cm^{-2}_{Pt}$, and mass activities of 0.18 $A \cdot mg^{-1}_{Pt}$. These specific activities are ~ 10× better than state-of-the-art TKK PtCo dispersed onto corrosion resistant (CR) carbon (0.3 $mA \cdot cm^{-2}_{Pt}$) and ~ 12× higher than 47 wt% Pt/C [35, 36]. This NSTFC mass activity is 38% higher than the TKK PtCo/CR-Carbon and 80% higher than the Pt/C [35, 36]. This enhancement in the specific activity has a contribution from the larger grain size of Pt/NSTF and subsequent higher adsorption potential of OH [33]. The same properties, i.e. larger grain size and their contiguous morphology in the polycrystalline film form, is thought to be largely responsible as well for the excellent corrosion stability of Pt/NSTF in this class of electrocatalysts.

The formation of hydrogen peroxide is a very important phenomenon in the reduction of oxygen, since it is known that peroxides break down into OH radicals, which then attack the PFSA

membrane. Figure 9 shows the hydrogen peroxide yield of Pt/NSTF and Pt-Co-Mn/NSTF, and a sputtered Pt film for comparison. The production of H_2O_2 on both samples having the same loading is essentially the same. What is interesting to note however, is the increased amount of H_2O_2 observed when loading is at its lowest level in both cases. In the case of Pt/C electrocatalysts, Inaba et. al. have reported an increasing amount of H_2O_2 when the loading on the GC disk decreased and/or the particle size was reduced [37]. The loading experiments presented here do not go any lower than 20 $\mu g_{Pt} \cdot cm^{-2}$. Further work is currently underway to study the impact of electrocatalyst loading on the production of H_2O_2.

Conclusions

Pt/NSTF and Pt-Co-Mn/NSTF catalysts were studied by the RRDE method. Results of the RRDE studies reported here are fully consistent with the specific activities measured in fuel cells with Pt/NSTF electrocatalysts. For the first time, these RRDE measurements also demonstrate a two-fold kinetic gain for Pt-Co-Mn/NSTF over Pt/NSTF, consistent with a 2.5× gain seen in working fuel cells.

Acknowledgements

The Dalhousie authors acknowledge the financial support of NSERC and 3M for this work. AB acknowledges the Killam and Sumner Foundations for scholarship support.

List of Figures:

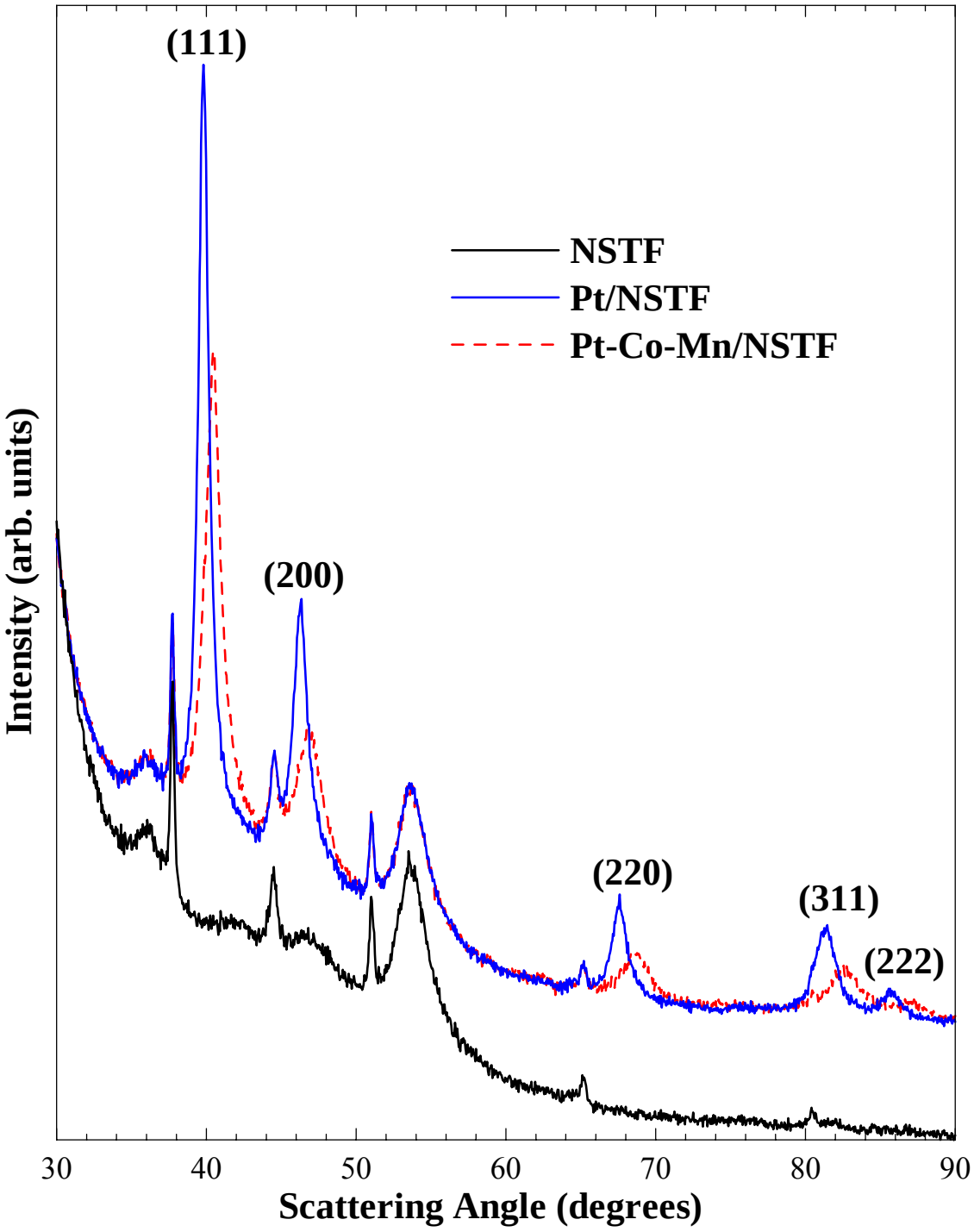
(111)
(200)
(220)
(311)
(222)
NSTF
Pt/NSTF
Pt-Co-Mn/NSTF
Intensity (arb. units)
30
40
50
60
70
80
90
Scattering Angle (degrees)

Figure 1

Figure 2

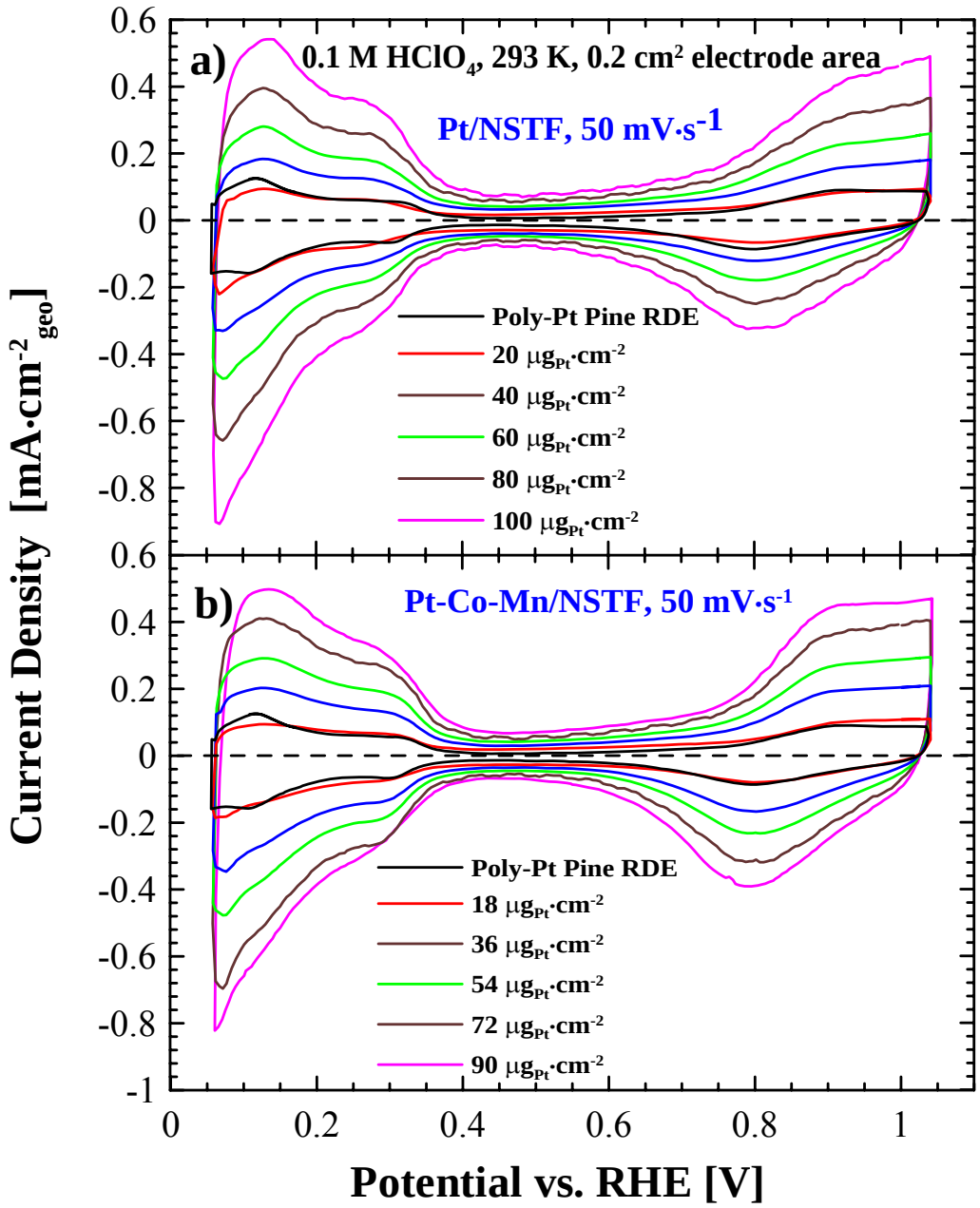
a)
0.1 M HClO4, 293 K, 0.2 cm² electrode area
Pt/NSTF, 50 mV·s-1
Poly-Pt Pine RDE
20 μgPt·cm-2
40 μgPt·cm-2
60 μgPt·cm-2
80 μgPt·cm-2
100 μgPt·cm-2
b)
Pt-Co-Mn/NSTF, 50 mV·s-1
Poly-Pt Pine RDE
18 μgPt·cm-2
36 μgPt·cm-2
54 μgPt·cm-2
72 μgPt·cm-2
90 μgPt·cm-2
Current Density [mA·cm-2geo]
Potential vs. RHE [V]

Figure 3

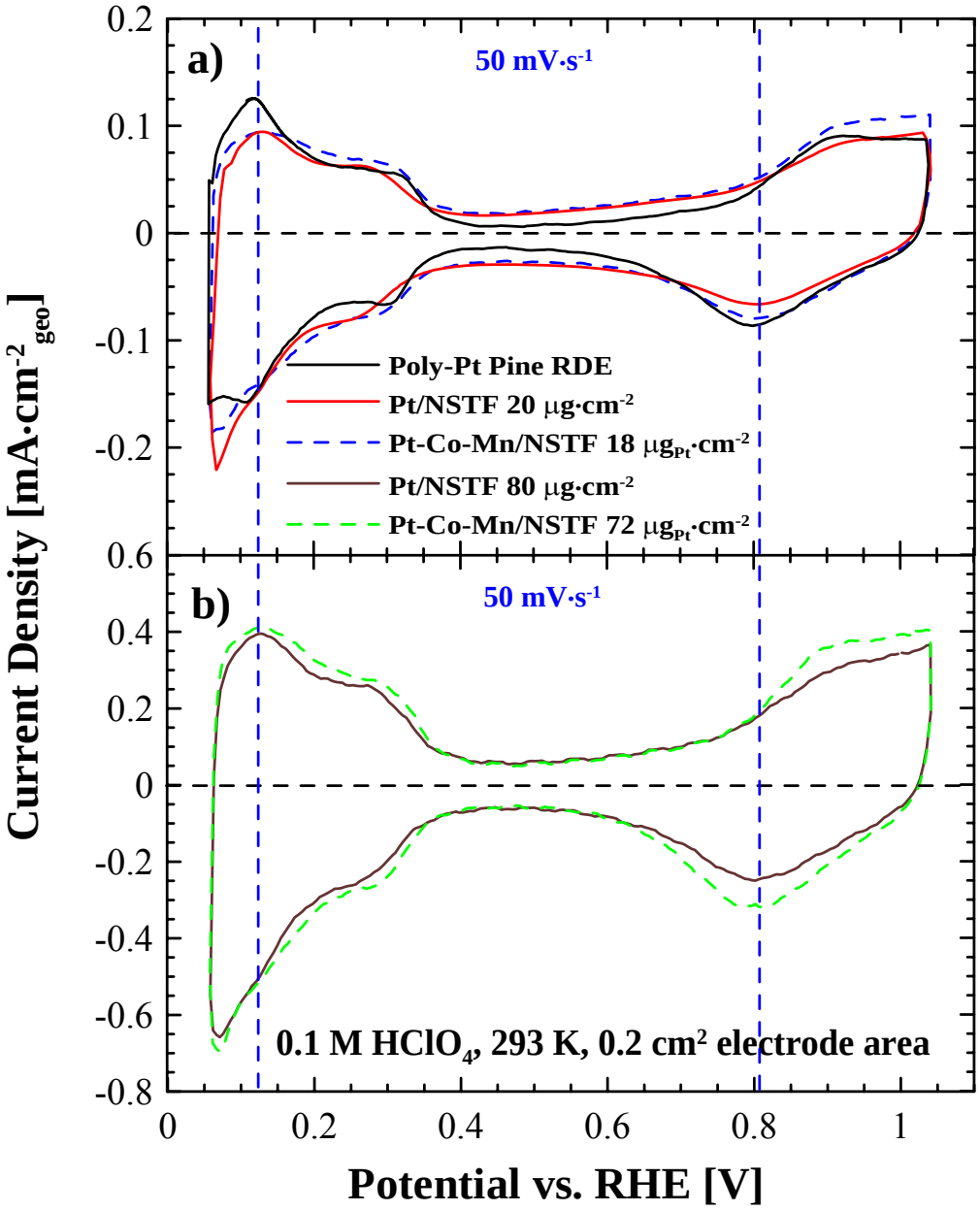
a)
50 mV·s-1
b)
50 mV·s-1
Poly-Pt Pine RDE
Pt/NSTF 20 μg·cm-2
Pt-Co-Mn/NSTF 18 μgPt·cm-2
Pt/NSTF 80 μg·cm-2
Pt-Co-Mn/NSTF 72 μgPt·cm-2
0.1 M HClO4, 293 K, 0.2 cm2 electrode area
Current Density [mA·cm-2geo]
Potential vs. RHE [V]

Figure 4

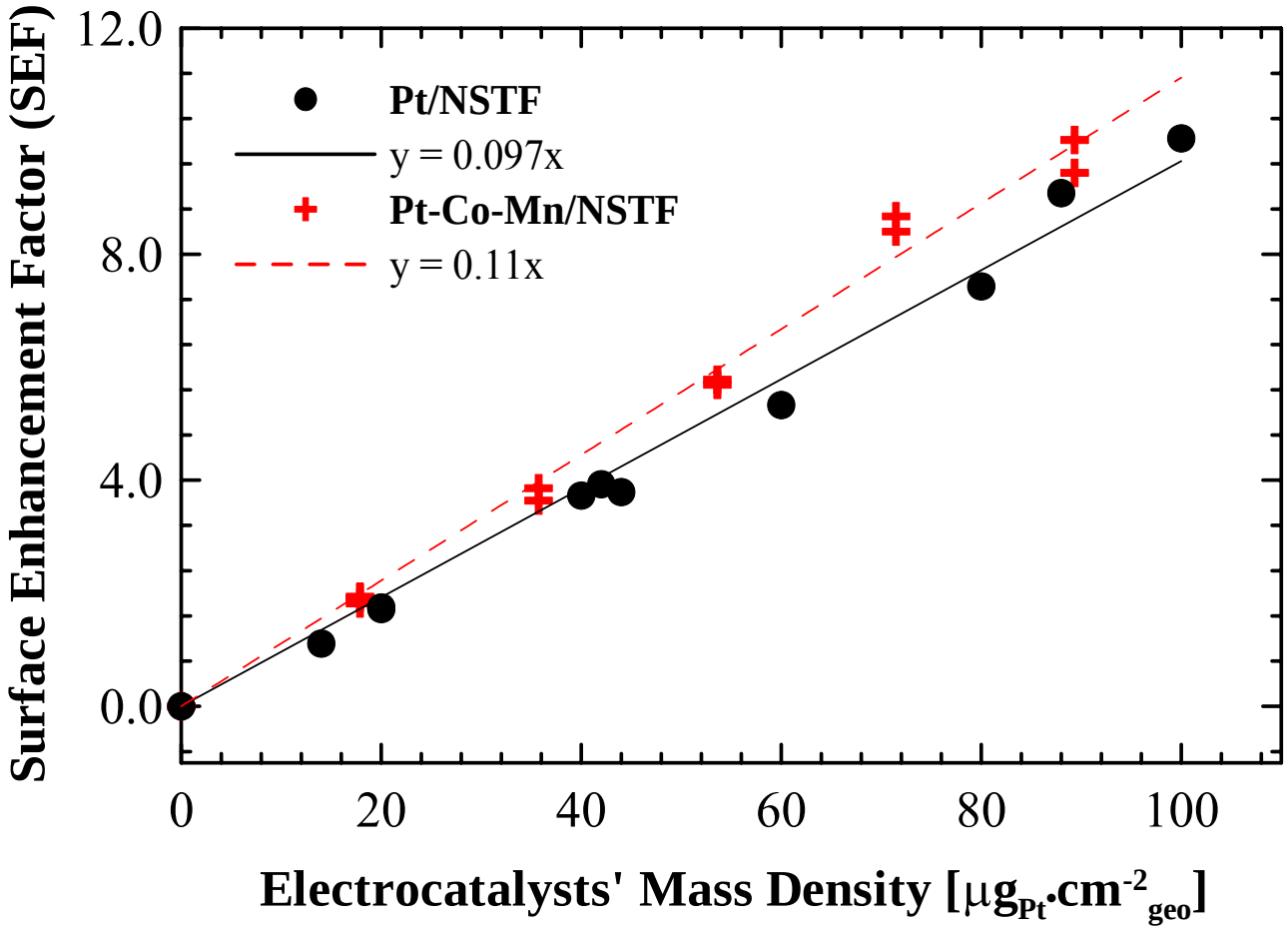
Surface Enhancement Factor (SEF)
12.0
8.0
4.0
0.0
Pt/NSTF
y = 0.097x
Pt-Co-Mn/NSTF
y = 0.11x
0
20
40
60
80
100
Electrocatalysts' Mass Density [μg$_{Pt}$.cm^{-2}$_{geo}$]

Figure 5

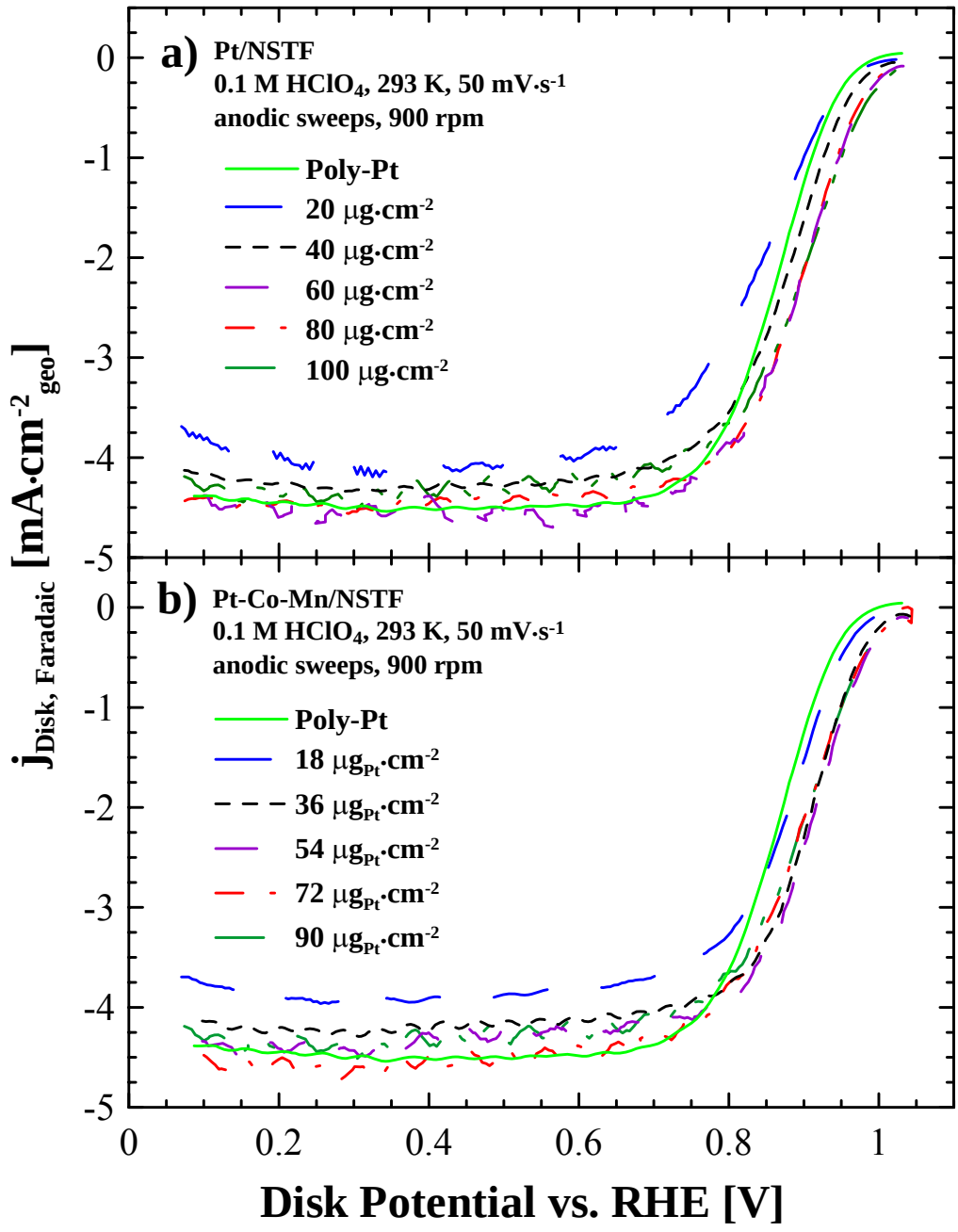
a)
Pt/NSTF
0.1 M HClO4, 293 K, 50 mV·s-1
anodic sweeps, 900 rpm
Poly-Pt
20 μg·cm-2
40 μg·cm-2
60 μg·cm-2
80 μg·cm-2
100 μg·cm-2
b)
Pt-Co-Mn/NSTF
0.1 M HClO4, 293 K, 50 mV·s-1
anodic sweeps, 900 rpm
Poly-Pt
18 μgPt·cm-2
36 μgPt·cm-2
54 μgPt·cm-2
72 μgPt·cm-2
90 μgPt·cm-2
jDisk, Faradaic [mA·cm-2geo]
Disk Potential vs. RHE [V]
0
-1
-2
-3
-4
-5
0.2
0.4
0.6
0.8
1

Figure 6

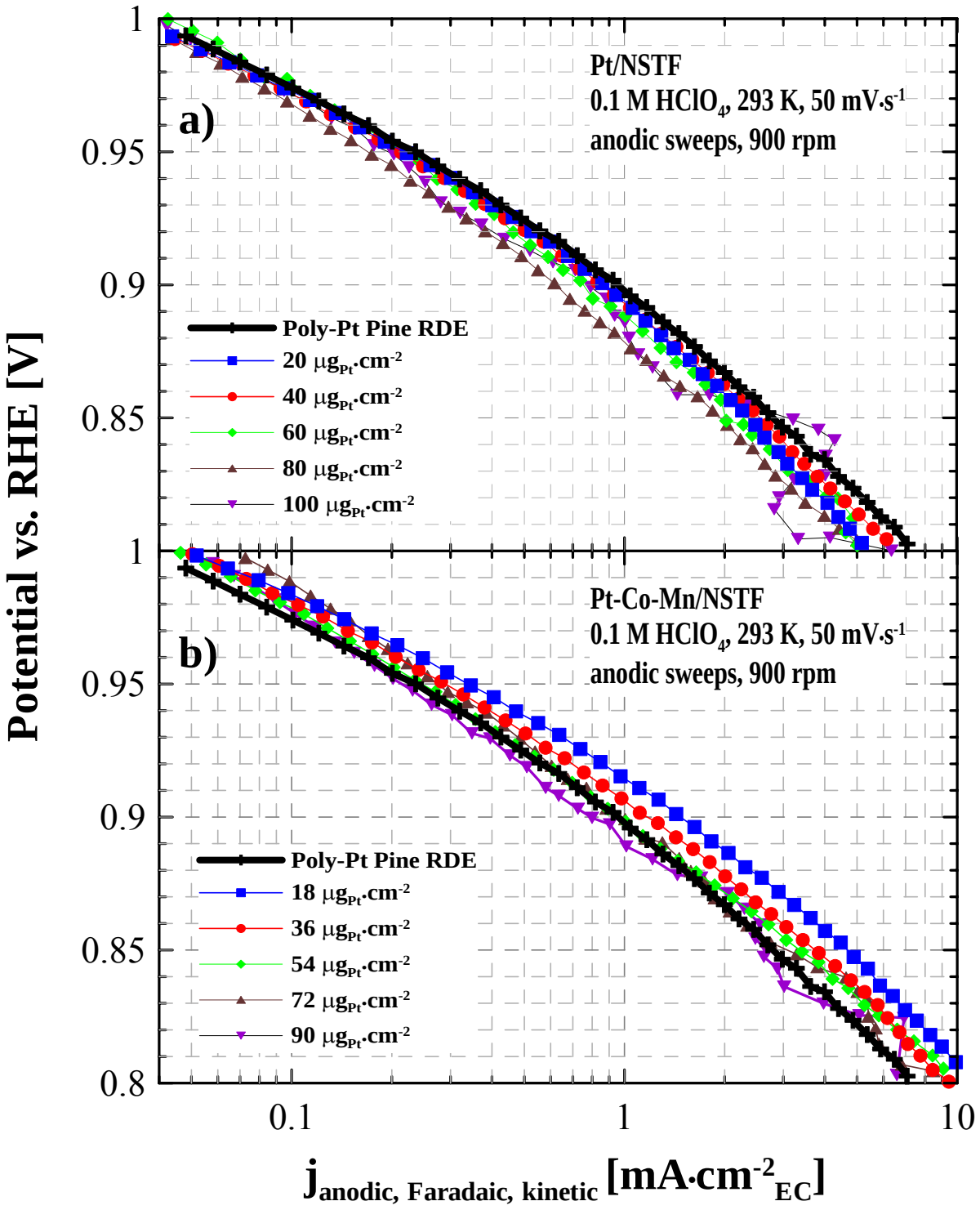
a)
Pt/NSTF
0.1 M HClO4, 293 K, 50 mV·s-1
anodic sweeps, 900 rpm
Poly-Pt Pine RDE
20 μgPt·cm-2
40 μgPt·cm-2
60 μgPt·cm-2
80 μgPt·cm-2
100 μgPt·cm-2
b)
Pt-Co-Mn/NSTF
0.1 M HClO4, 293 K, 50 mV·s-1
anodic sweeps, 900 rpm
Poly-Pt Pine RDE
18 μgPt·cm-2
36 μgPt·cm-2
54 μgPt·cm-2
72 μgPt·cm-2
90 μgPt·cm-2
Potential vs. RHE [V]
1
0.95
0.9
0.85
0.8
0.1
1
10
janodic, Faradaic, kinetic [mA·cm-2EC]

Figure 7

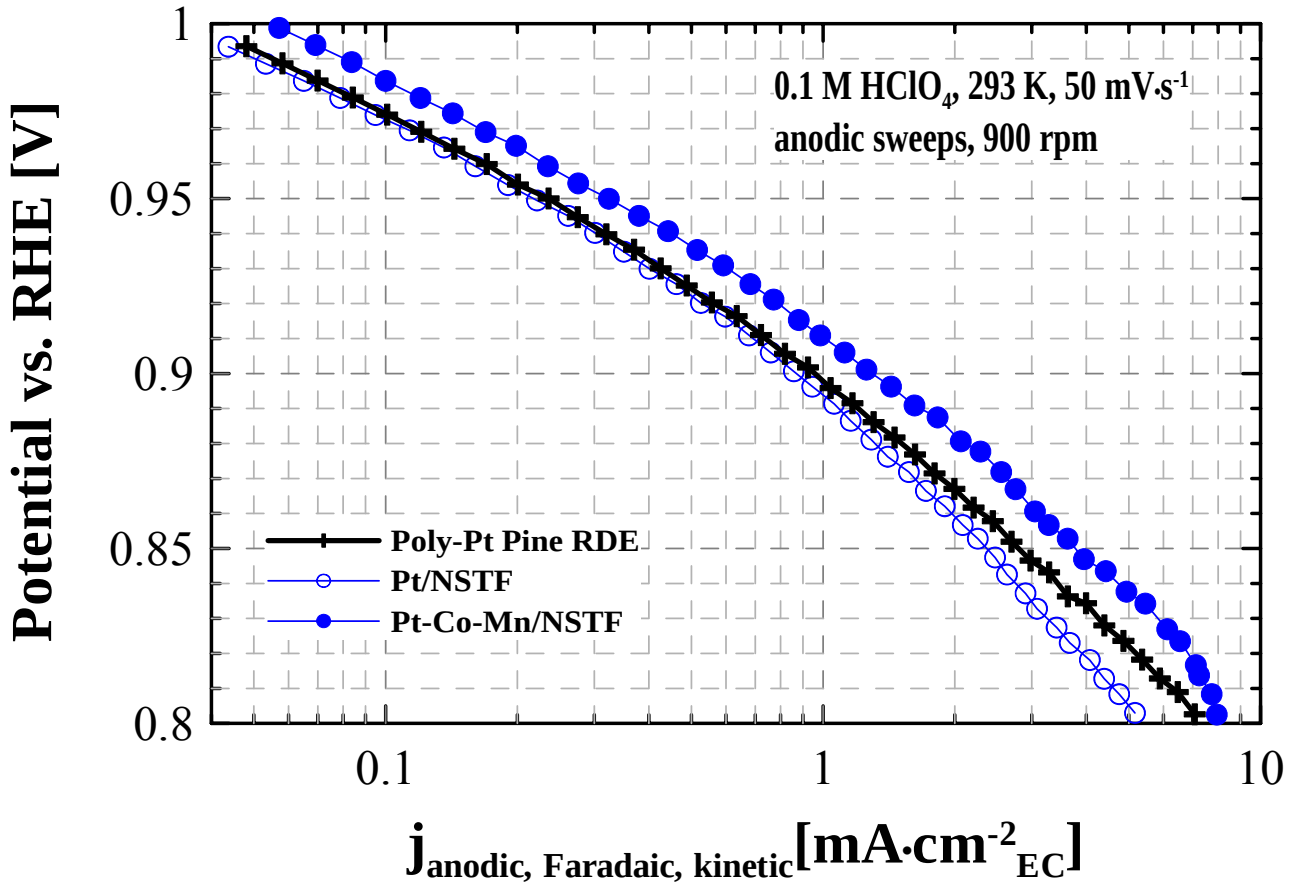
Potential vs. RHE [V]
1
0.95
0.9
0.85
0.8
0.1
1
10
0.1 M HClO4, 293 K, 50 mV·s-1
anodic sweeps, 900 rpm
Poly-Pt Pine RDE
Pt/NSTF
Pt-Co-Mn/NSTF
janodic, Faradaic, kinetic[mA·cm-2EC]

Figure 8

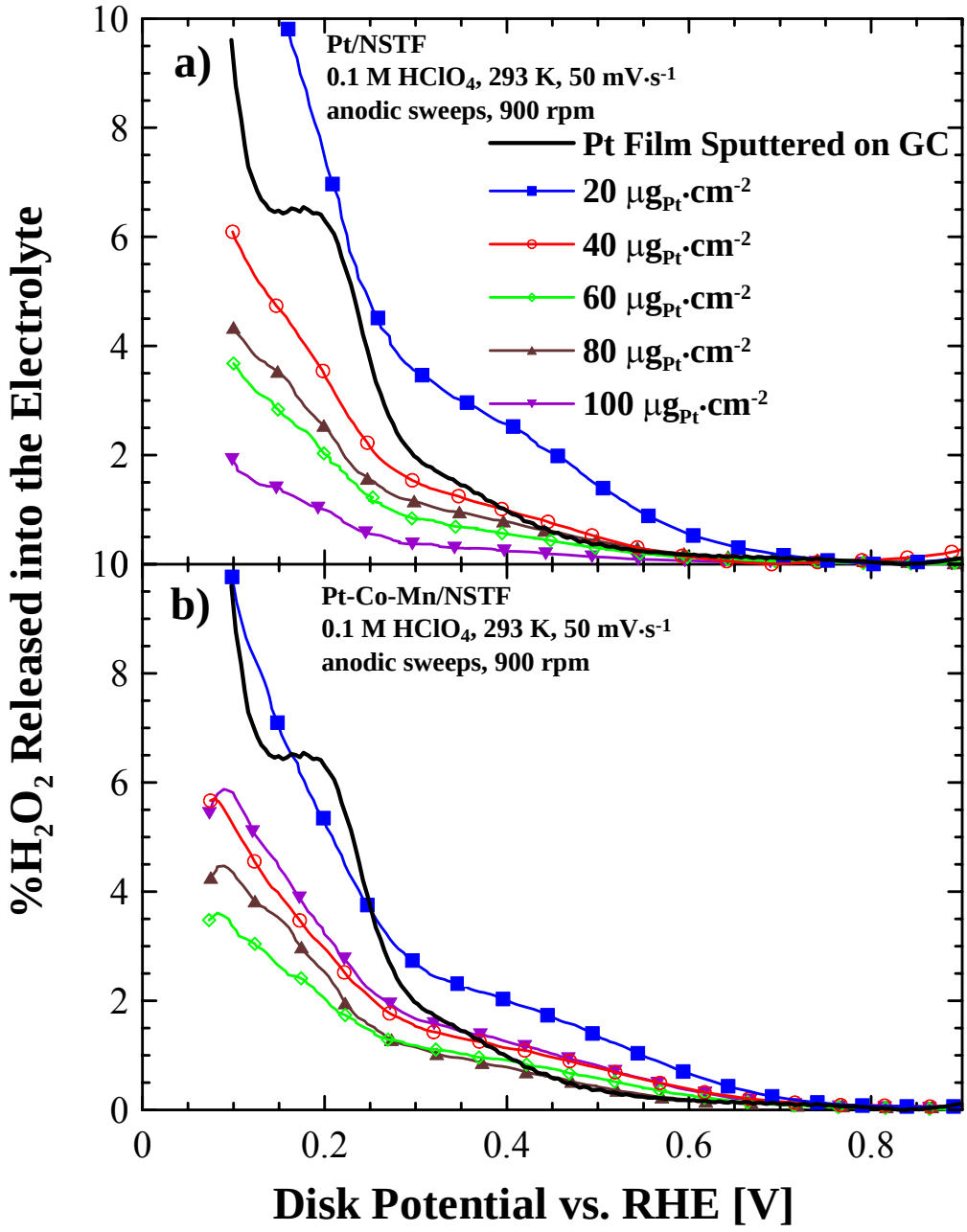
a)
Pt/NSTF
0.1 M HClO4, 293 K, 50 mV·s-1
anodic sweeps, 900 rpm
Pt Film Sputtered on GC
20 μgPt·cm-2
40 μgPt·cm-2
60 μgPt·cm-2
80 μgPt·cm-2
100 μgPt·cm-2
b)
Pt-Co-Mn/NSTF
0.1 M HClO4, 293 K, 50 mV·s-1
anodic sweeps, 900 rpm
%H2O2 Released into the Electrolyte
Disk Potential vs. RHE [V]
0
2
4
6
8
10
0.2
0.4
0.6
0.8

Figure 9

References

1. P. J. Ferreira, G. J. la O, Y. Shao-Horn, D. Morgan, R. Makharia, S. Kocha and H. A. Gasteiger, J. Electrochem. Soc. 152 (2005) A2256.

2. E. Guilminot, A. Corcella, F. Charlot, F. Maillard and M. Chatenet, J. Electrochem. Soc. 154 (2007) B96.

3. L. M. Roen, C. H. Paik and T. D. Jarvic, Electrochem. Solid State Lett. 7 (2004) A19.

4. D. A. Stevens and J. R. Dahn, Carbon 43 (2005) 179.

5 S. Kawahara, S. Mitsushima, K. Ota and N. Kamiya, The Electrochemical Society (Proton Exchange Membrane Fuel Cells 6), Cancun, Mexico, Oct. 29 - Nov. 3, 2006.

6 T. Okada, M. Sugiura and G. Xie, The Electrochemical Society (Proton Exchange Membrane Fuel Cells 6), Cancun, Mexico, Oct. 29 - Nov. 3, 2006.

7 P. T. Yu, W. Gu, R. Makharia, F. T. Wagner and H. A. Gasteiger, The Electrochemical Society (Proton Exchange Membrane Fuel Cells 6), Cancun, Mexico, Oct. 29 - Nov. 3, 2006.

8. V. R. Stamenkovic, B. Fowler, B. S. Mun, G. Wang, P. N. Ross, C. A. Lucas and N. M. Markovic, Science 315 (2007) 493.

9. U. A. Paulus, A. Wokaun, G. G. Scherer, T. J. Schmidt, V. Stamenkovic, V. Radmilovic, N. M. Markovic and P. N. Ross, J. Phys. Chem. B 106 (2002) 4181.

10. H. A. Gasteiger, S. S. Kocha, B. Sompalli and F. T. Wagner, Appl. Catal. B-Environ. 56 (2005) 9.

11. J. Zhang, M. B. Vukmirovic, K. Sasaki, F. Uribe and R. R. Adzic, J. Serb. Chem. Soc. 70 (2005) 513.

12 P. Strasser, N. T. Hahn and S. Koh, The Electrochemical Society (Proton Exchange Membrane Fuel Cells 6), Cancun, Mexico, Oct. 29 - Nov. 3, 2006.

13. P. J. Kulesza, K. Karnicka, K. Miecznikowski, M. Chojak, A. Kolary, P. J. Barczuk, G. Tsirlina and W. Czerwinski, Electrochim. Acta 50 (2005) 5155.

14. J. Zhang, K. Sasaki, E. Sutter and R. R. Adzic, Science 315 (2007) 220.

15. J. R. Smith, F. C. Walsh and R. L. Clarke, J. Appl. Electrochem. 28 (1998) 1021.

16. G. Y. Chen, S. R. Bare and T. E. Mallouk, J. Electrochem. Soc. 149 (2002) A1092.

17. H. Chhina, S. Campbell and O. Kesler, J. Power Sources 161 (2006) 893.

18 M. K. Debe, in: W. Vielstich, A. Lamm and H. A. Gasteiger (Eds.), Handbook of Fuel Cells: Fundamentals, Technology and Applications, vol. 3, John Wiley & Sons, Chichester, England, 2003, ch. 45.

19. M. K. Debe and R. J. Poirier, J. Vac. Sci. Technol. A 12 (1994) 2017.

20. M. K. Debe and A. R. Drube, J. Vac. Sci. Technol. B 13 (1995) 1236.

21 M. K. Debe, 3rd International Hydrogen and Fuel Cell Expo Proceedings, Tokyo, Japan, Feb. 7-9, 2007.

22 M. K. Debe, A. K. Schmoeckel, R. T. Atanasoski and G. D. Vernstrom, Paper 583 presented at the Fuel Cell Seminar, Honolulu, HI, Nov. 13-17, 2006.

23. B. D. Cullity, S. R. Stock and S. Stock, Elements of X-Ray Diffraction, Prentice Hall, Upper Saddle River, NJ, 2001.

24. V. Stamenkovic, T. J. Schmidt, P. N. Ross and N. M. Markovic, J. Electroanal. Chem. 554 (2003) 191.

25. A. Bonakdarpour, R. Lobel, S. Sheng, T. L. Monchesky and J. R. Dahn, J. Electrochem. Soc. 153 (2006) A2304.

26. A. Bonakdarpour, K. Lake, K. Stevens and J. R. Dahn, submitted to the Journal of the Electrochemical Society.

27. C. Leroux, M. C. Cadeville, V. Pierron-Bohnes, G. Inden and F. Hinz, J. Phys. F: Met. Phys. 18F (1988) 2033.

28. E. Gebhardt and W. Koster, Z. Metallkd. 32 (1940) 253.

29. A. H. Geisler and D. L. Martin, J. Appl. Phys. 23 (1952) 375.

30. K. H. Buschow, P. G. van Engen and R. Jongebreuer, J. Magn. Magn. Mater. 38 (1983) 1.

31. D. E. G. Williams and A. Jezierski, J. Magn. Magn. Mater. 59 (1986) 41.

32. V. Stamenkovic, T. J. Schmidt, P. N. Ross and N. M. Markovic, J. Phys. Chem. B 106 (2002) 11970.

33. K. J. J. Mayrhofer, B. B. Blizanac, M. Arenz, V. R. Stamenkovic, P. N. Ross and N. M. Markovic, J. Phys. Chem. B 109 (2005) 14433.

34 M. K. Debe, A. K. Schmoeckel, R. T. Atanasoski and G. D. Vernstrom, Paper 64 presented at the Fuel Cell Seminar, Palm Springs, CA, Nov. 14-18, 2005.

35 F. T. Wagner, H. A. Gasteiger, R. Makharia, K. C. Neyerlin, E. L. Thompson and S. G. Yan, The Electrochemical Society (Proton Exchange Membrane Fuel Cells 6), Cancun, Mexico, Oct. 29 - Nov. 3, 2006.

36. K. C. Neyerlin, W. B. Gu, J. Jorne and H. A. Gasteiger, J. Electrochem. Soc. 153 (2006) A1955.

37. M. Inaba, H. Yamada, J. Tokunaga and A. Tasaka, Electrochem. Solid State Lett. 7 (2004) A474.

Appendix III

University of Miami - Modeling Report

Model Calibration Results for the Ultra-thin Catalyst Layer
11/15/04
Tianhong Zhou and Hongtan Liu
University of Miami

This report contains two major parts:
1. The comparison of the dispersed case-and the nano-cases
2. The calibration efforts

In this calibrating effort, the values have been changed according to recent emails from Thomas. In the dispersed case, the thickness of GDL is changed from 210.84 micron (8.3 mil) to 147.574 micron (5.81 mil), the porosity of GDL is changed from 0.795 to 0.69 when compression is considered. In the nano-case, the thickness of GDL is 8.925 mil or 226.695 micron, GDL porosity is set as 0.7, and the membrane thickness is 30.5 micron.

1. The comparison of the dispersed case-and the nano-cases

The comparisons have been conducted from two aspects: (a) the potential losses in the catalyst layer, (b) and the temperature rise and heat generation in the catalyst layer.

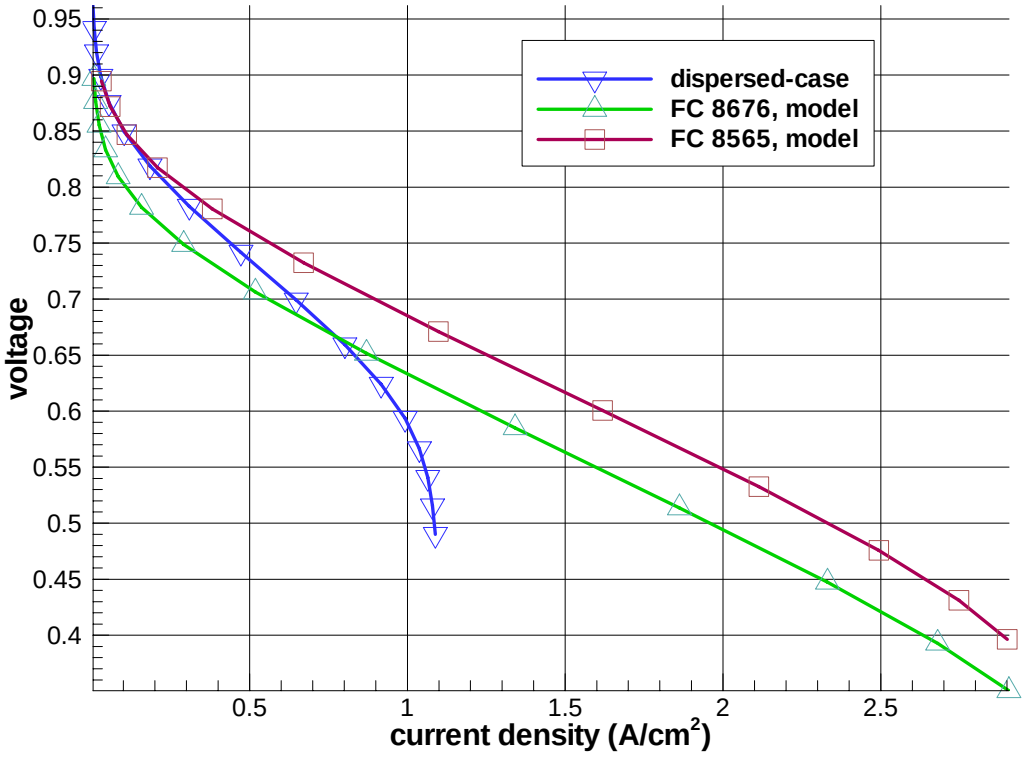

Figure 1 The comparison of polarization curves for dispersed-case and nano-cases FC 8565 and 8676.

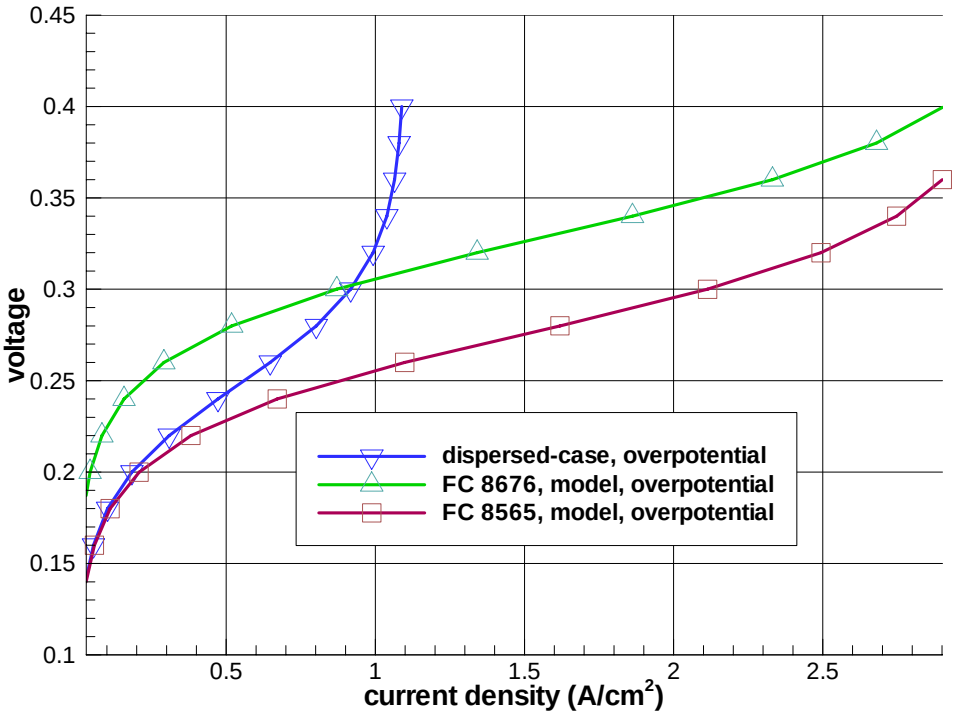

Figure 2 The comparison of overpotential losses

This figure shows the dispersed case has larger overpotential loss due to activation loss and mass transfer resistance.

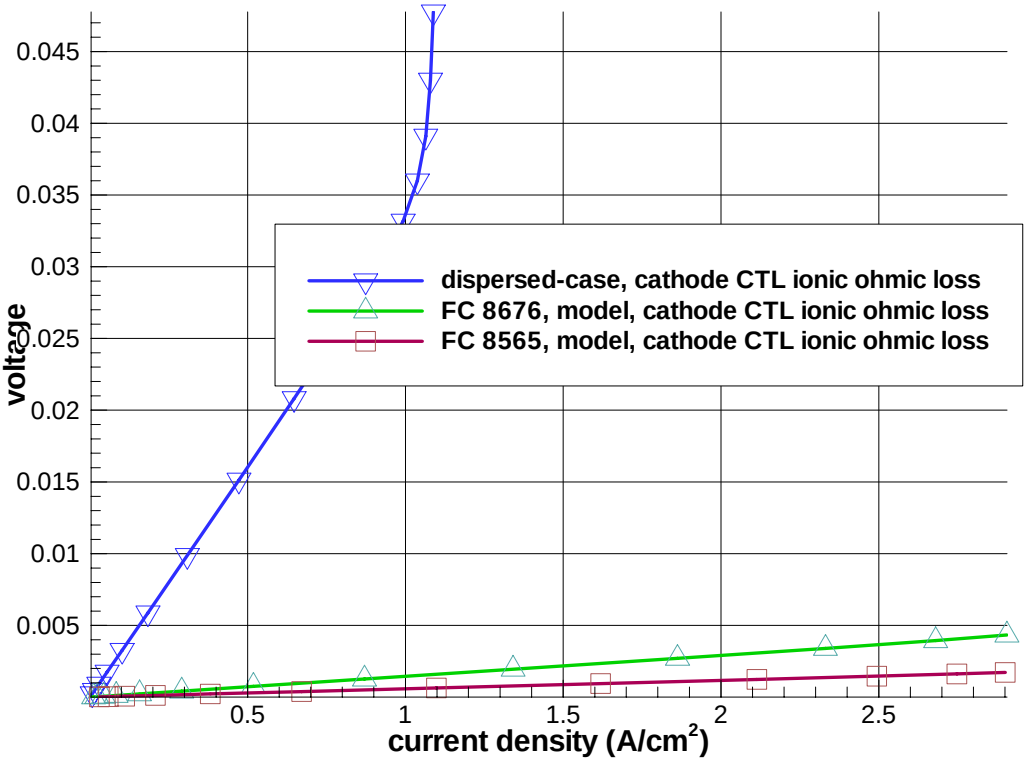

Figure 3 The comparison of cathode CTL ionic ohmic losses

This figure shows larger ionic ohmic loss in the dispersed case due to much thicker catalyst layer and lower ionic conductivity (due to lower Nafion fraction). The CTL in the dispersed case has Nafion fraction of 16%, while this value in nano-cases is about 70%.

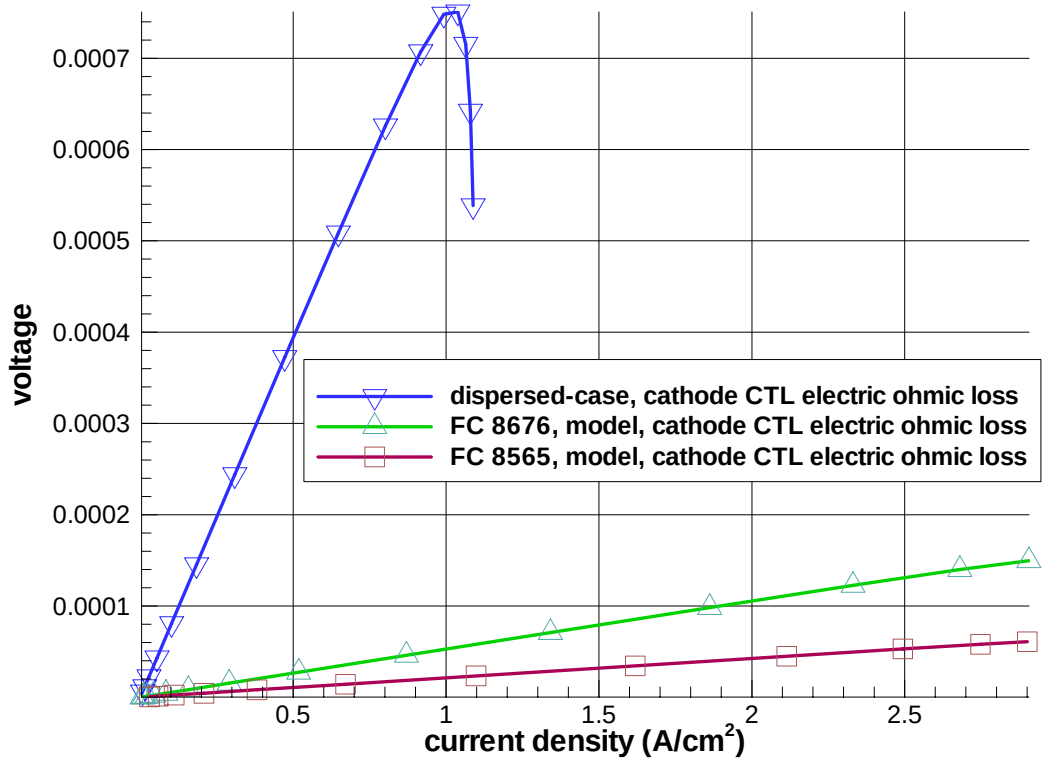

Figure 4 The comparison of cathode CTL electric ohmic losses

The larger electric ohmic loss in dispersed case is because of the thicker layer.

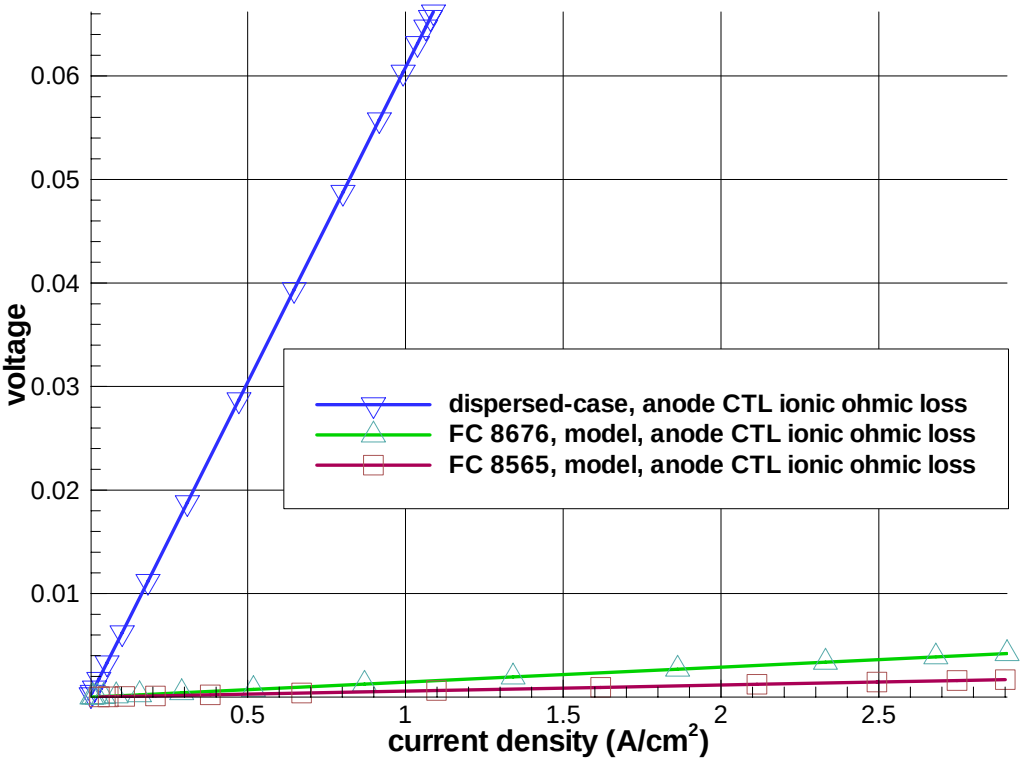

Figure 5 The comparison of anode CTL ionic ohmic losses

Larger CTL thickness and lower ionic conductivity leads to greater ionic ohmic loss in the dispersed case.

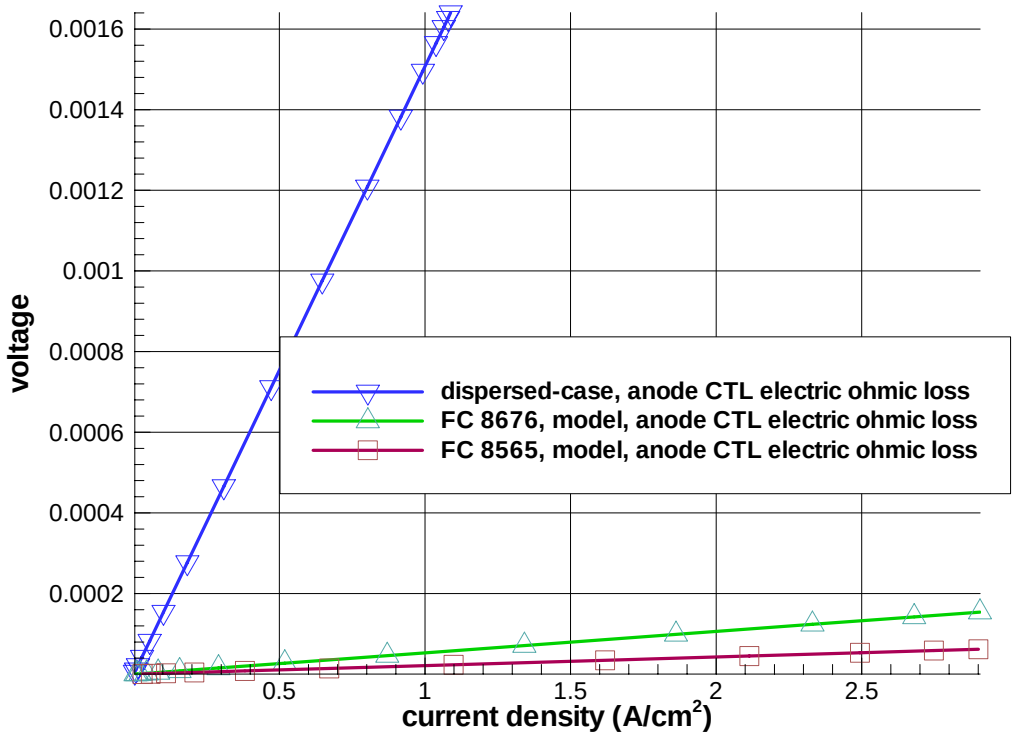

Figure 6 The comparison of anode CTL electric ohmic losses

Larger CTL thickness leads to greater electric ohmic loss in the dispersed case.

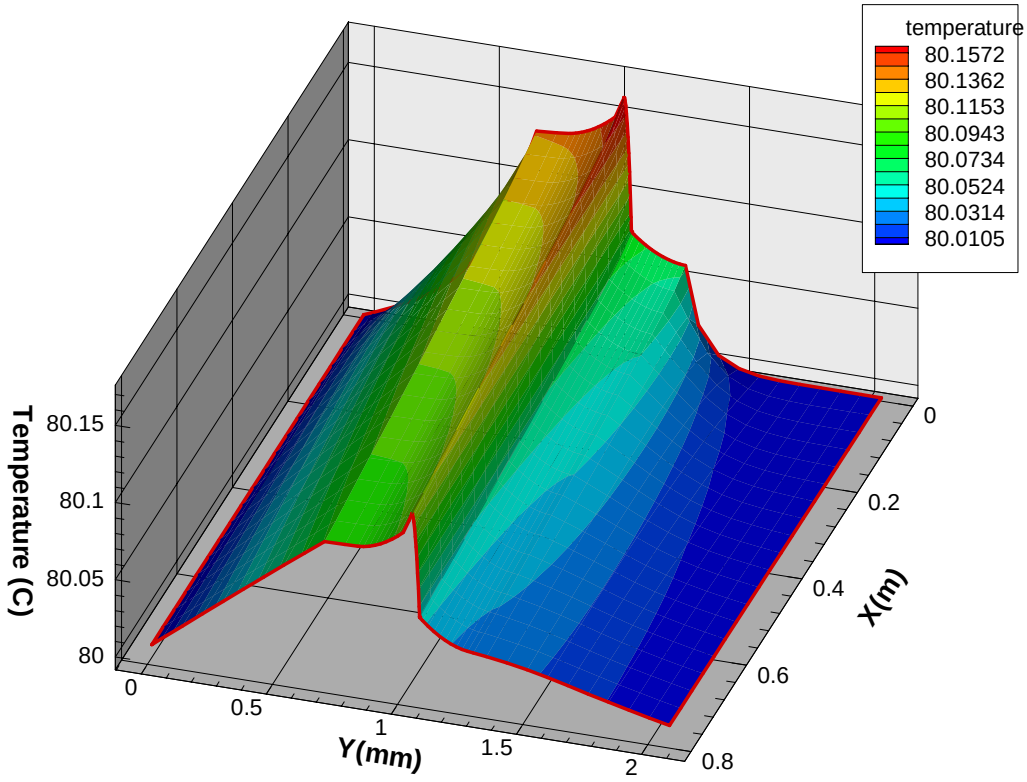

Figure 7. The temperature distribution for FC 8565. Current density = 1.06 A/cm^2.

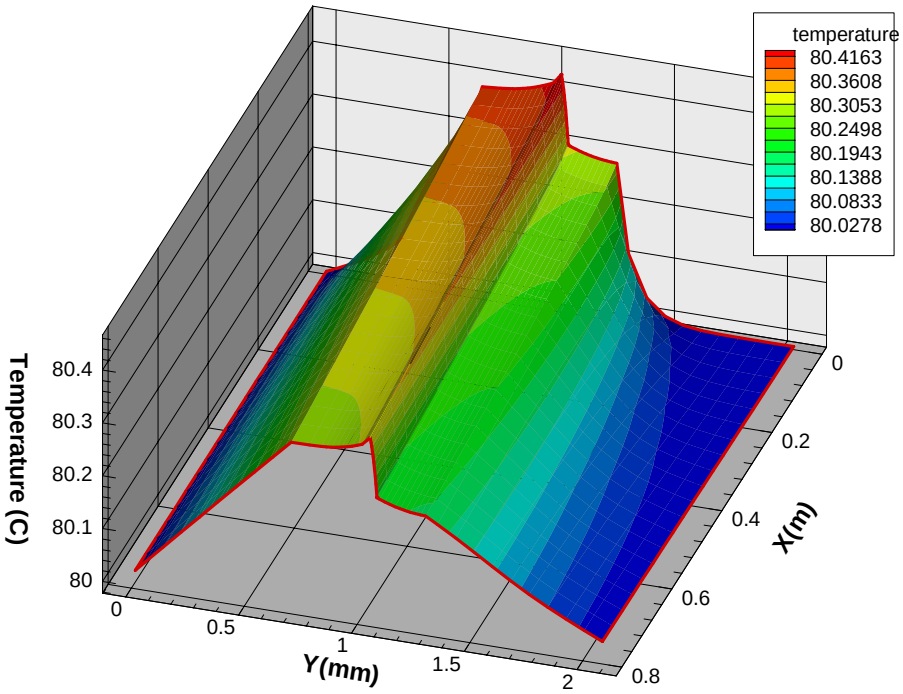

Figure 8. The temperature distribution for FC 8676. Current density = 1.04 A/cm^2.

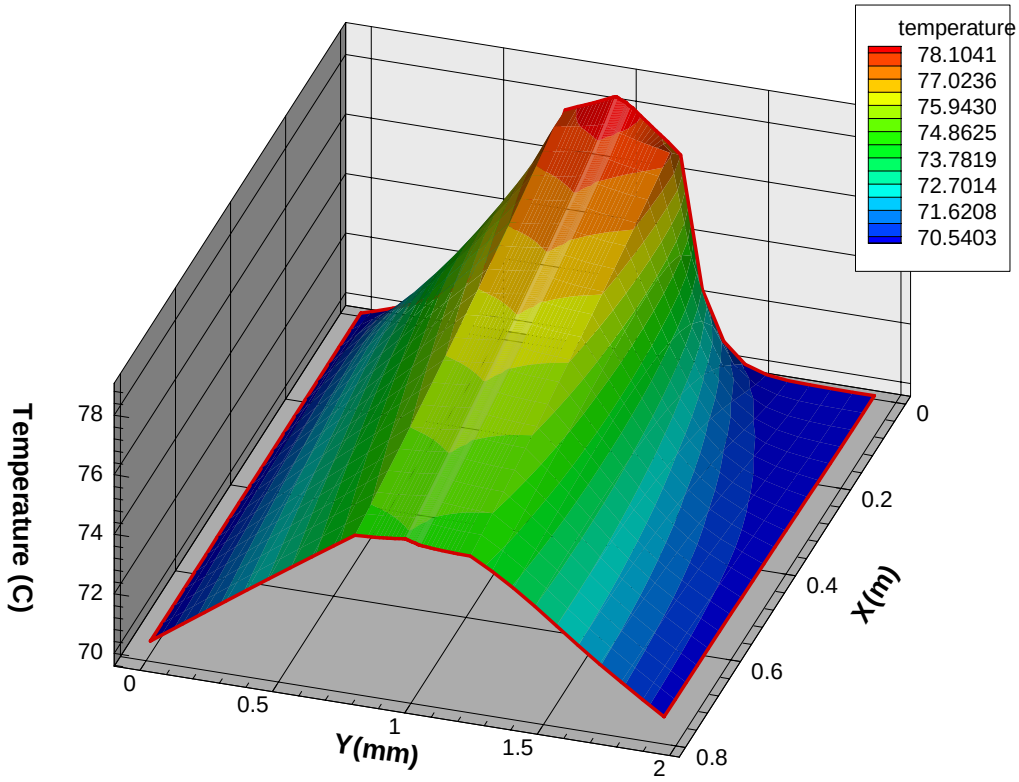

Figure 9. The temperature distribution for dispersed case. Current density = 1.03 A/cm^2.

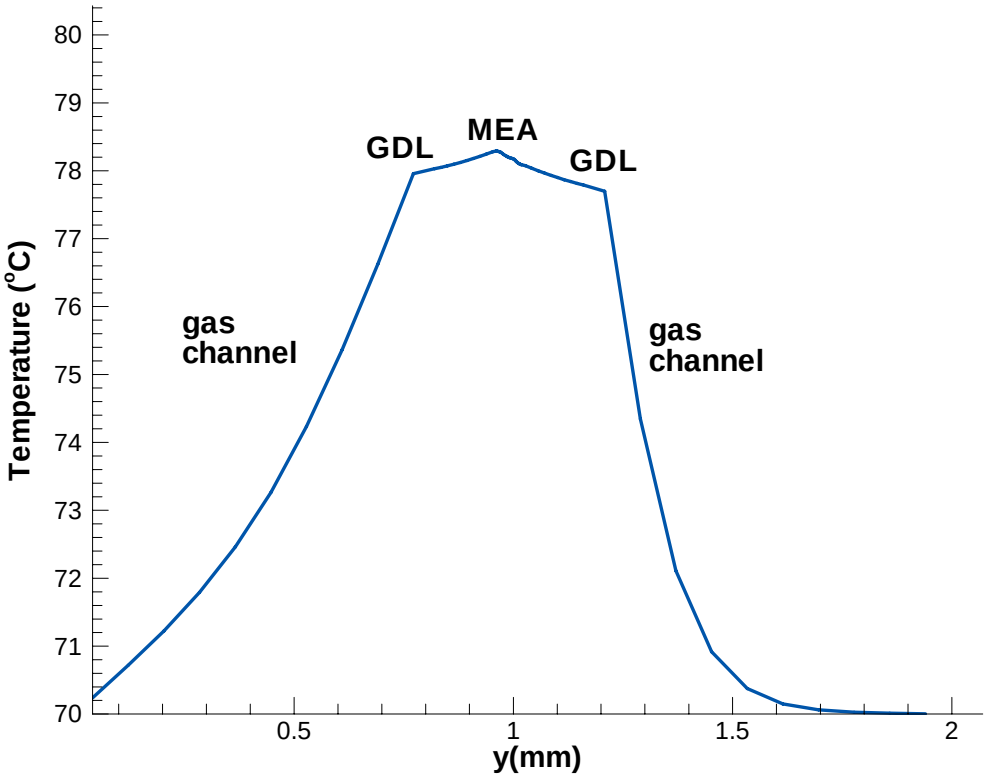

Figure 10. The temperature profile for dispersed case. Current density = 1.03 A/cm^2.

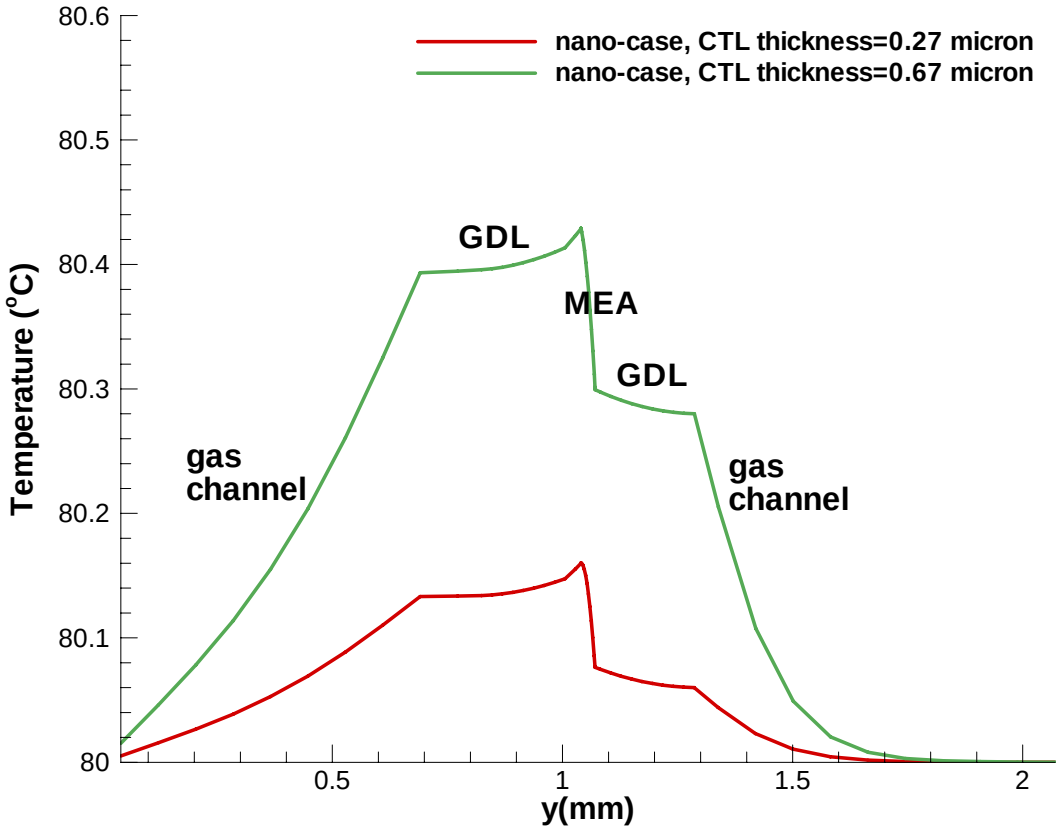

Figure 11. The temperature distribution for the nano-cases.

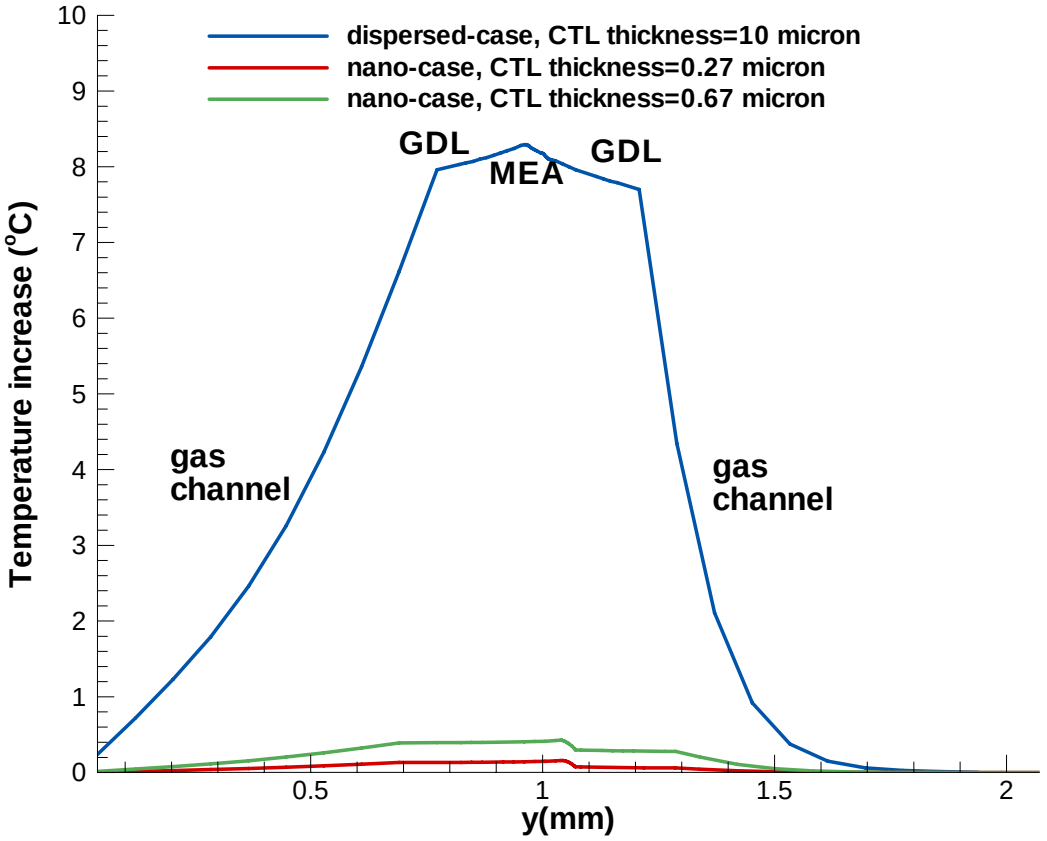

Figure 12. The temperature increase profiles for the three cases.

The nano-cases have very small temperature rise. The smaller temperature rise in nano-case may be attribute the following reasons:

1) the thermal resistance is greatly reduced with the nano-case since,

$$\text{thermal resiance} \propto \frac{\text{layer thickness}}{\text{thermal conductance}}$$

Thus with the very thin catalyst layer, the thermal resistance is greatly reduced and the generated heat within the fuel cell catalyst layer can be transferred out more efficiently

2) The thermal conductance is also much larger as pore volume of the catalyst layer is reduced. In the dispersed case, the effective thermal conductivity is estimated as porous media with larger pores filled with air, while in nano-case, this effective thermal conductivity is estimated as porous media with smaller pore volumes filled with Nafion.

3) Lower heat generation rate from the chemical reaction as the activation loss is lower for the nano cases as shown by Figure 2. Thus less heat is generated with nano-cases as shown by Figure 13. As the layer thickness is different, here the nondimentionlized distance is used in Figures 13-18.

4) less Joule heating inside the both anode and catalyst layer in nano-cases. In addition to the small layer thickness leading to lower total Joule heating inside the catalyst layer, the ionic conductivity is also increased as Nafion fraction is increased. These comparisons of heat generation are shown in Figures 14-18.

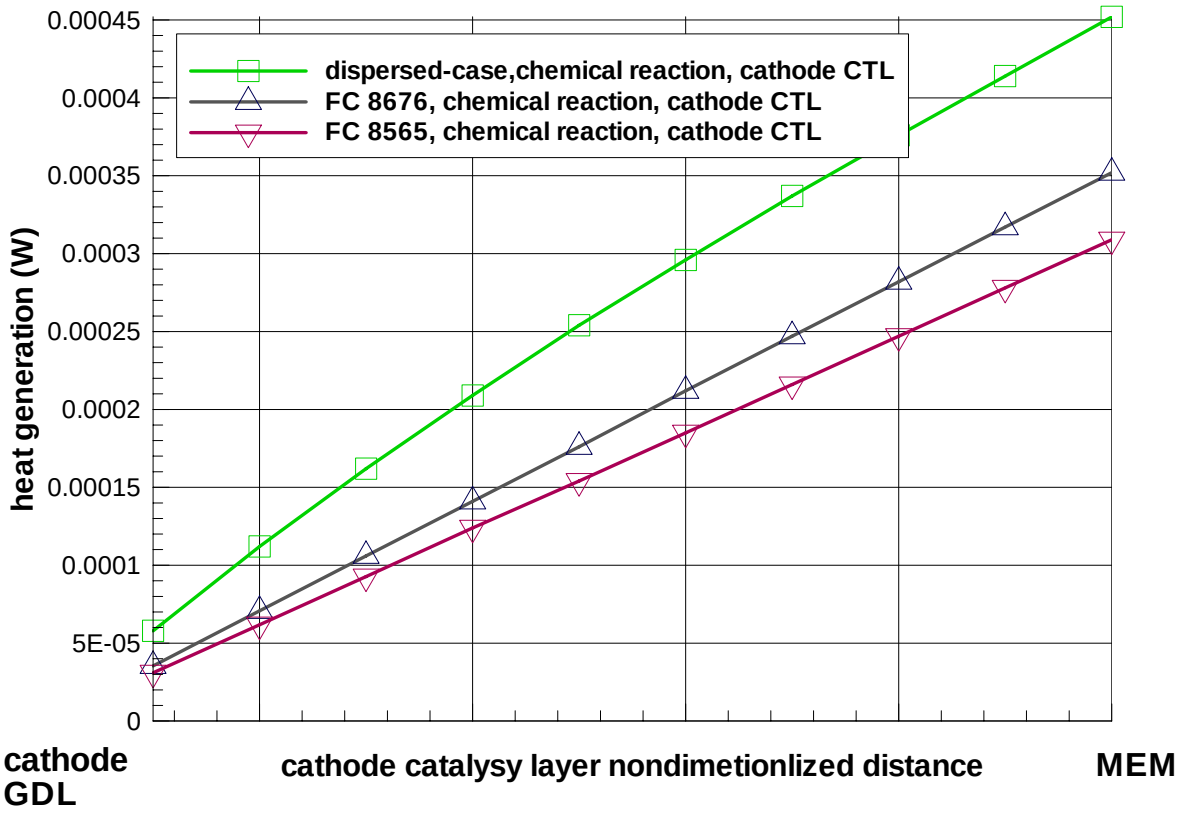

Figure 13 heat generation from chemical reaction inside the cathode catalyst layer for the three cases.

The current density is about 1.04 A/cm2 for the three cases. Heat generated from chemical reaction is the largest in the dispersed-case as the activation has to be larger in the dispersed case.

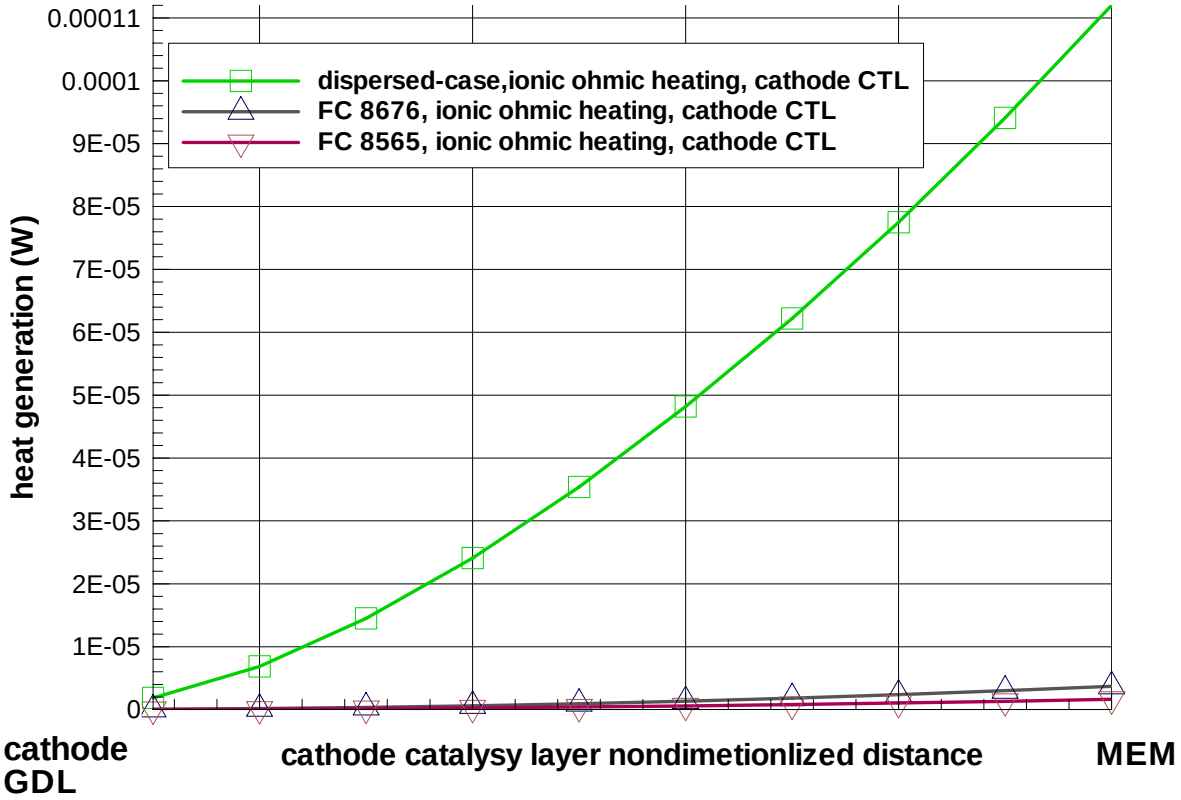

Figure 14. Heat generation from ionic ohmic heating inside the cathode catalyst layer for the three cases.

This heat generation is the largest in the dispersed-case as the layer thickness is larger. It is also because the ionic conductivity is larger as the ionic conductivity is proportional to the nafion amount which is about 70% in nan-case, while in dispersed-case, this value is only about 17%.

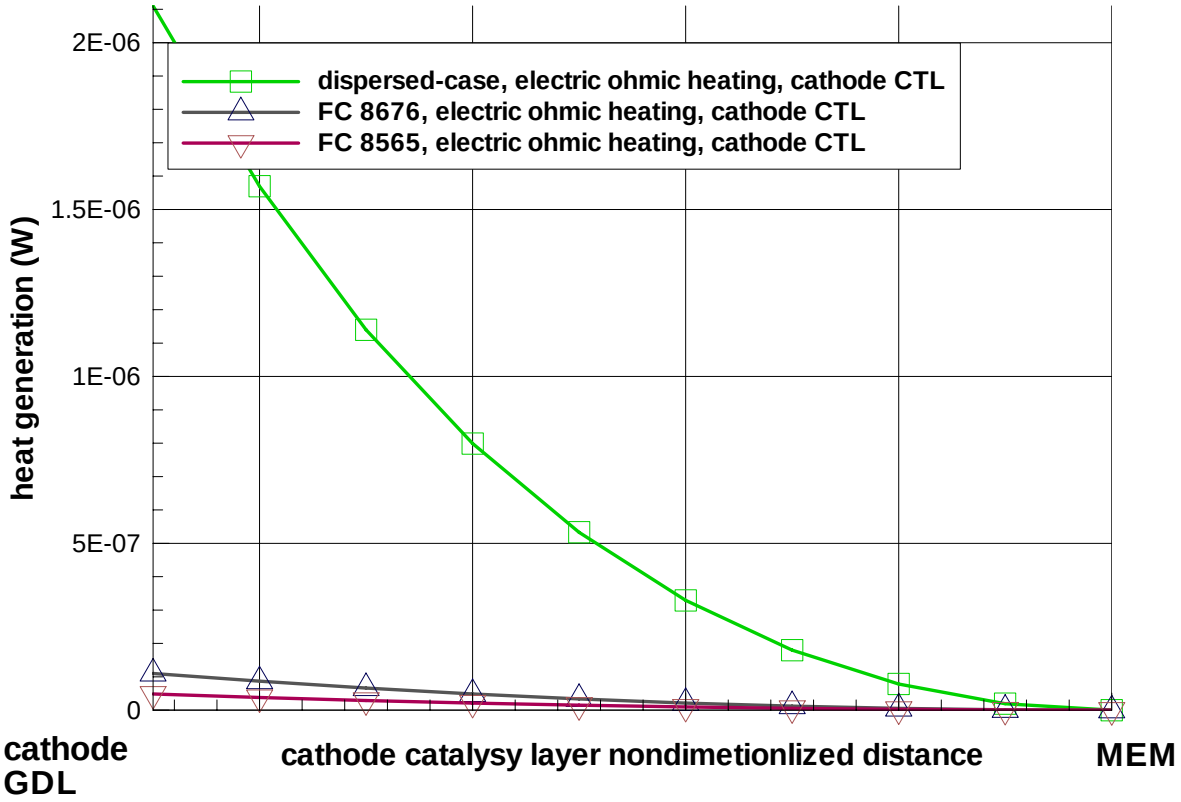

Figure 15 Heat generation from electric ohmic heating inside the anode catalyst layer for the three cases.

This heat generation is the largest in the dispersed-case as the layer thickness is larger.

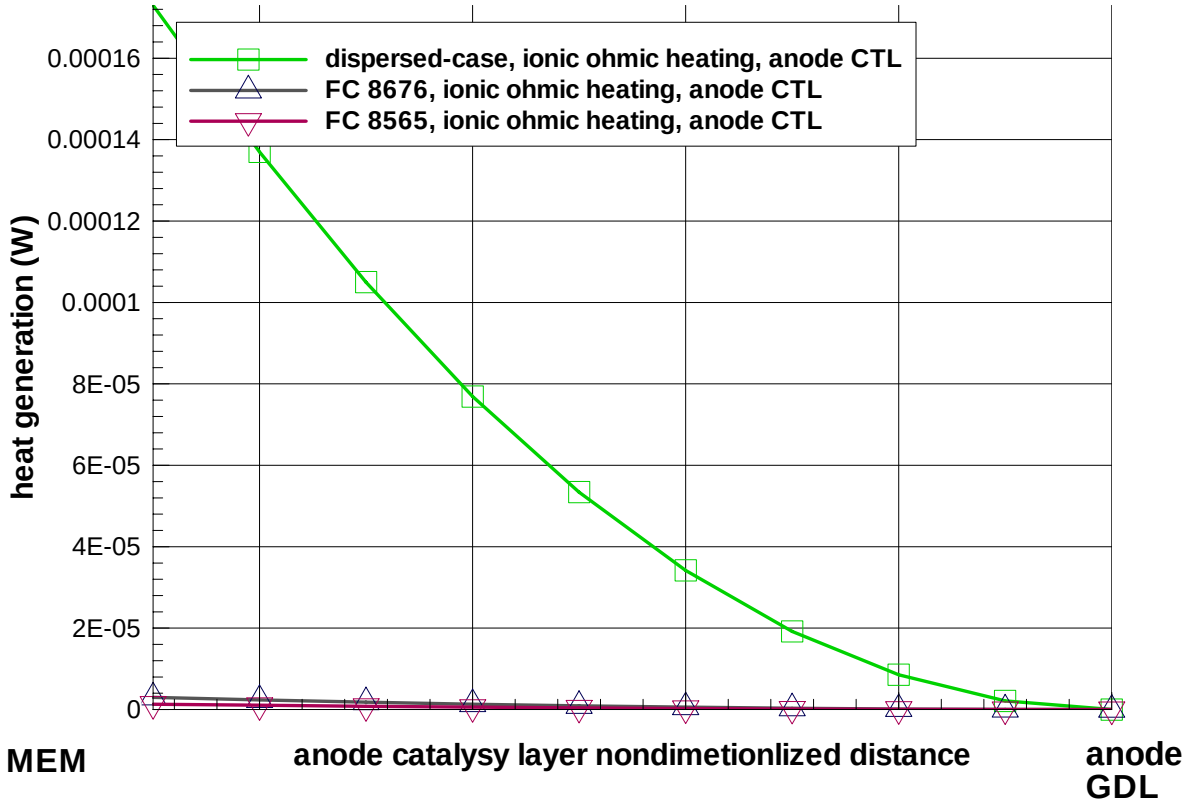

Figure 16 Heat generation from ionic ohmic heating inside the anode catalyst layer for the three cases.

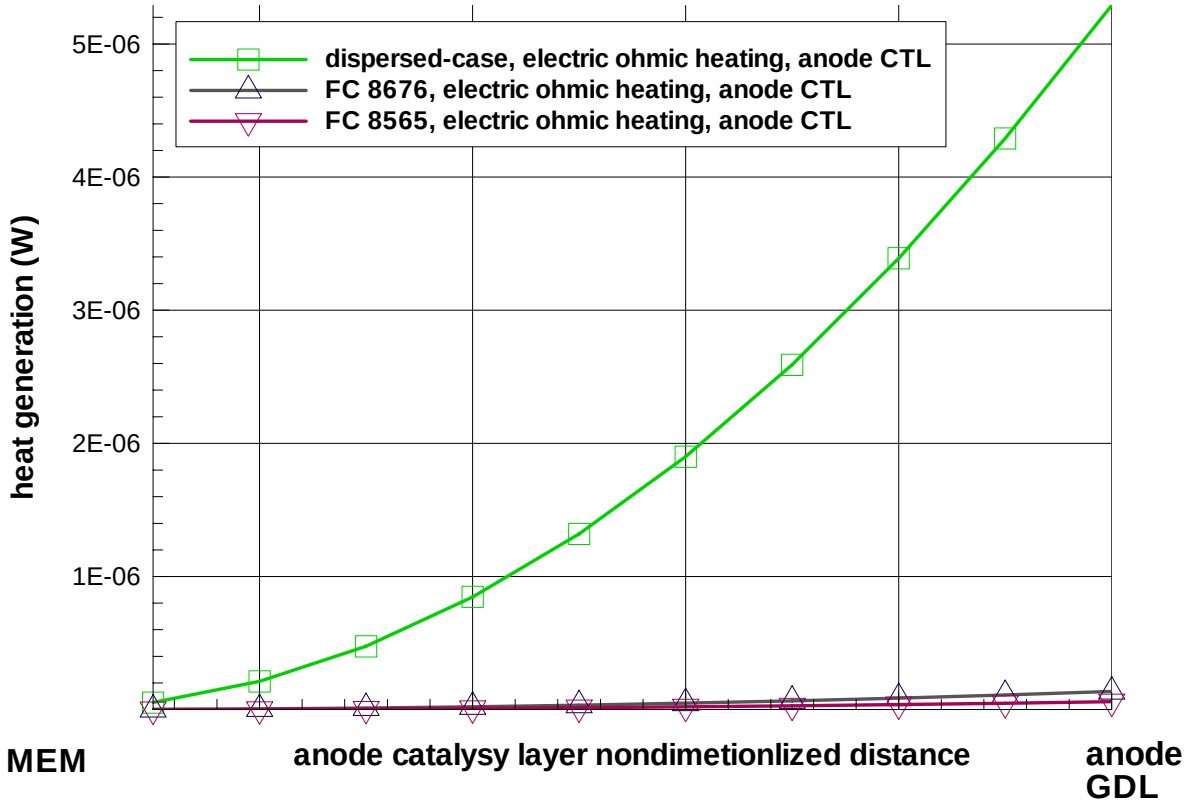

Figure 17 Heat generation from electric ohmic heating inside the cathode catalyst layer for the three cases.

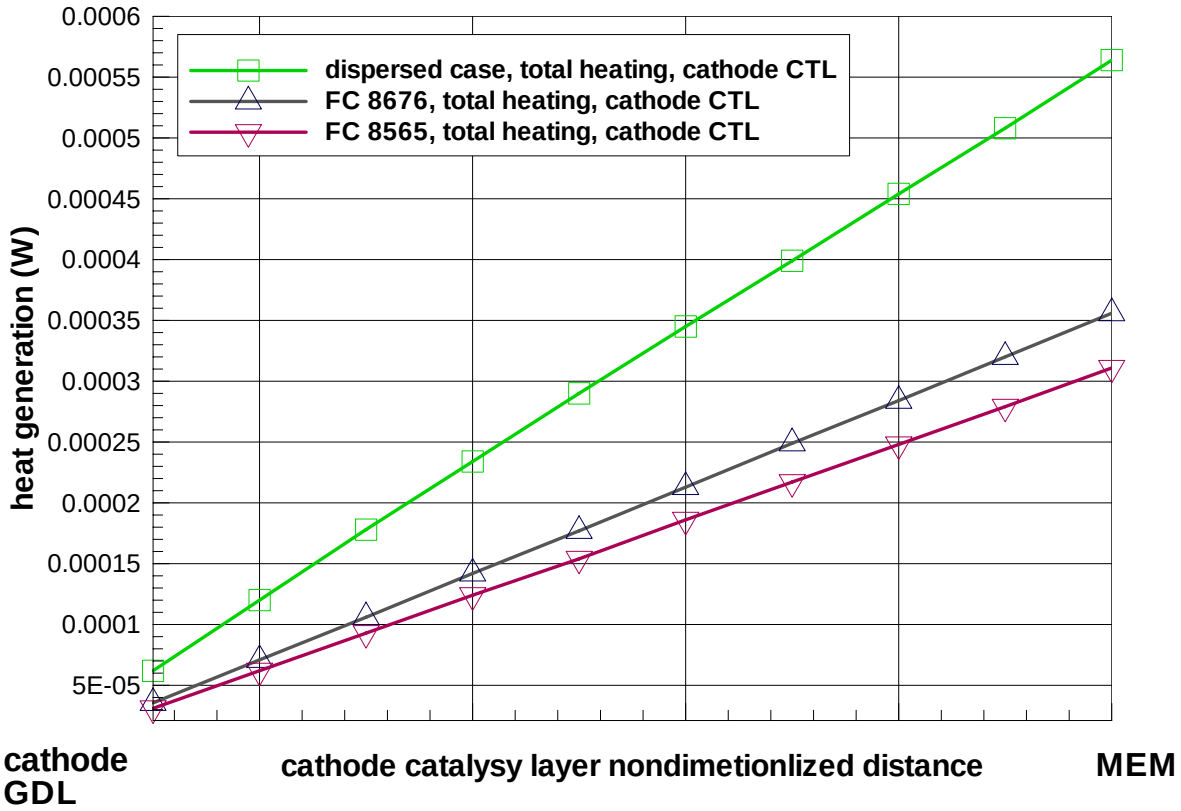

Figure 18. The total heat generation in the catalyst layer

The table below shows the percentages of the three heat generation components in the total heat generation inside the catalyst layer. It is shown that in the dispersed case, the heat generation by ionic ohmic heating can amount to near 20%, while in the nano cases, the ohmic heating can not amount to 1%. Thus the extremely small ohmic heating in the nano- cases also contribute to the small increase of temperature.

	dispersed case			FC 8676			FC 8565		
Grid	chemical	ionic	electric	chemical	ionic	electric	chemical	ionic	electric
1	93.61%	2.97%	3.41%	99.59%	0.11%	0.31%	99.79%	0.05%	0.16%
2	92.99%	5.70%	1.30%	99.67%	0.21%	0.12%	99.83%	0.11%	0.06%
3	91.20%	8.16%	0.64%	99.62%	0.32%	0.06%	99.81%	0.16%	0.03%
4	89.35%	10.30%	0.34%	99.54%	0.42%	0.03%	99.77%	0.21%	0.02%
5	87.61%	12.21%	0.18%	99.45%	0.53%	0.02%	99.73%	0.27%	0.01%
6	85.91%	13.99%	0.10%	99.36%	0.63%	0.01%	99.68%	0.32%	0.01%
7	84.38%	15.57%	0.05%	99.26%	0.73%	0.00%	99.63%	0.37%	0.00%
8	82.90%	17.09%	0.02%	99.16%	0.84%	0.00%	99.58%	0.43%	0.00%
9	81.48%	18.52%	0.00%	99.06%	0.94%	0.00%	99.53%	0.47%	0.00%
10	80.14%	19.86%	0.00%	98.96%	1.04%	0.00%	99.48%	0.53%	0.00%

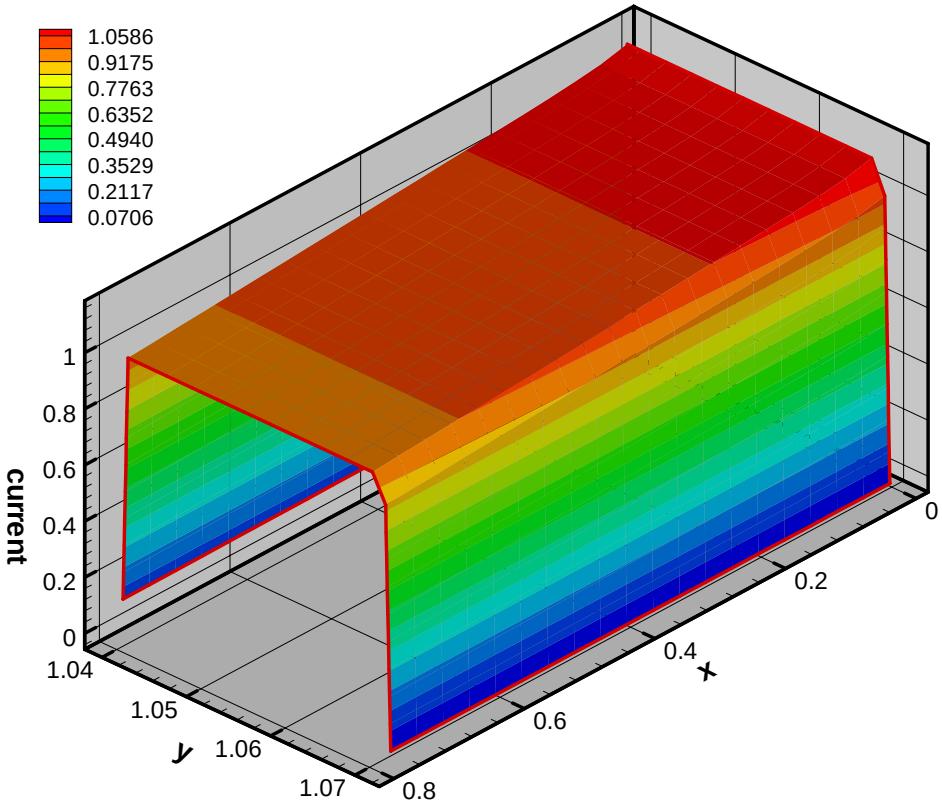

Figure 19. The current density distribution for FC 8565. Current density = 1.07 A/cm^2.

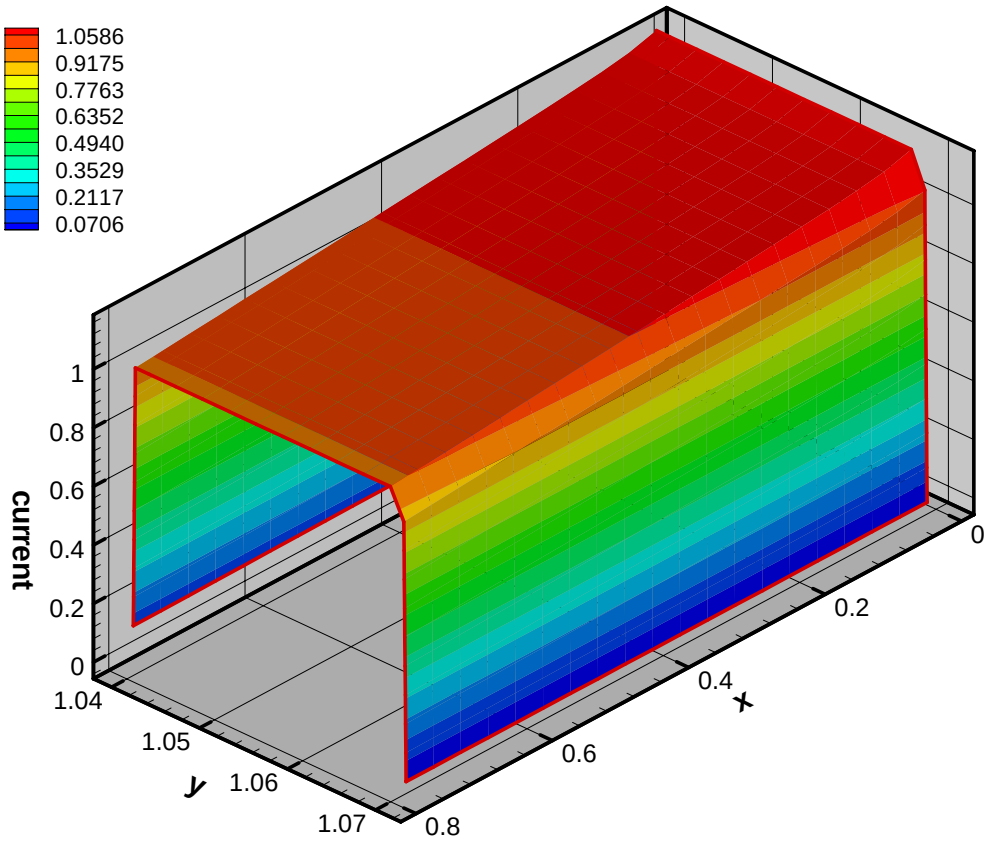

Figure 20. The current density distribution for FC 8676. Current density = 1.04 A/cm^2.

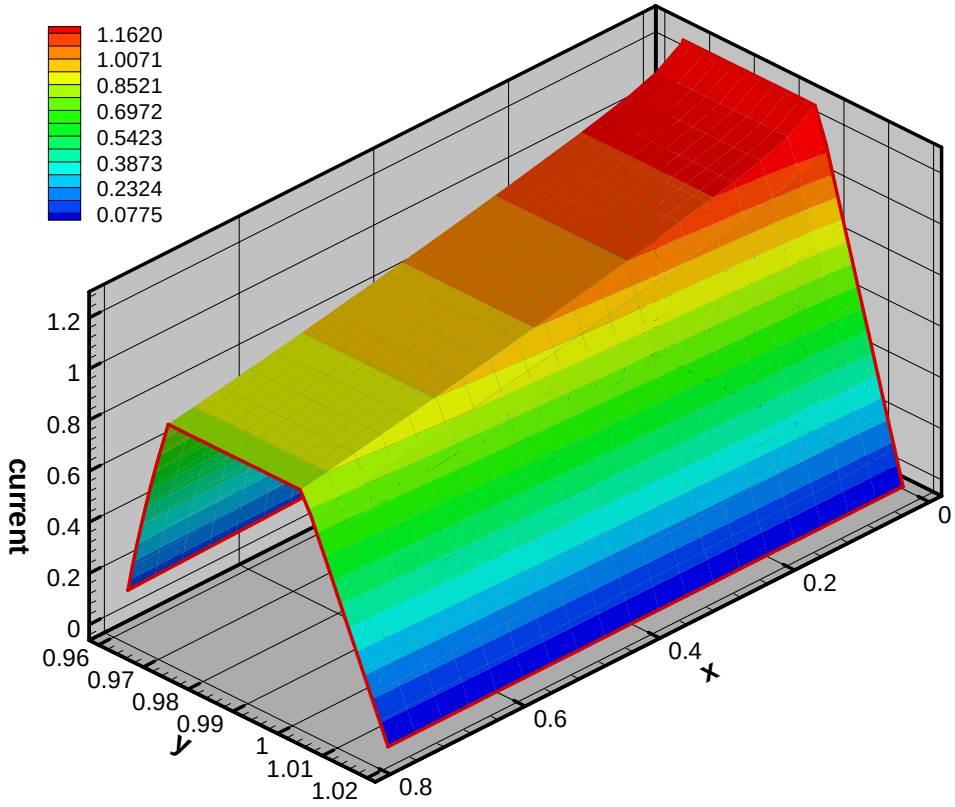

Figure 21. The current density distribution for dispersed case. Current density = 1.04 A/cm^2.

2. The calibration efforts

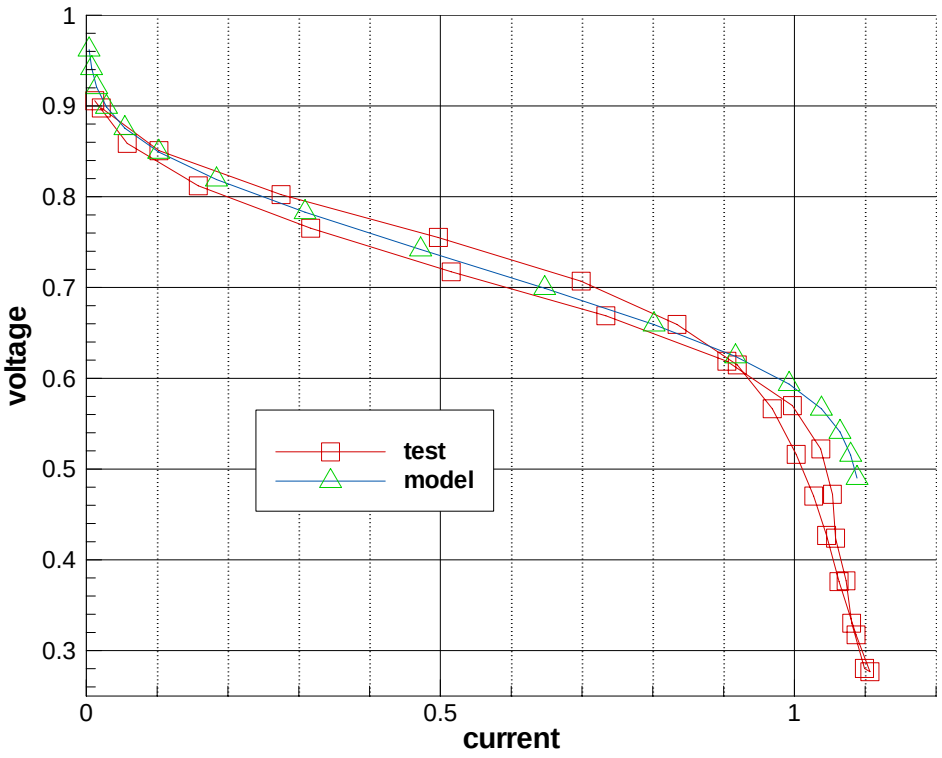

Figure 22. The newly calibrated polarization curve for dispersed case

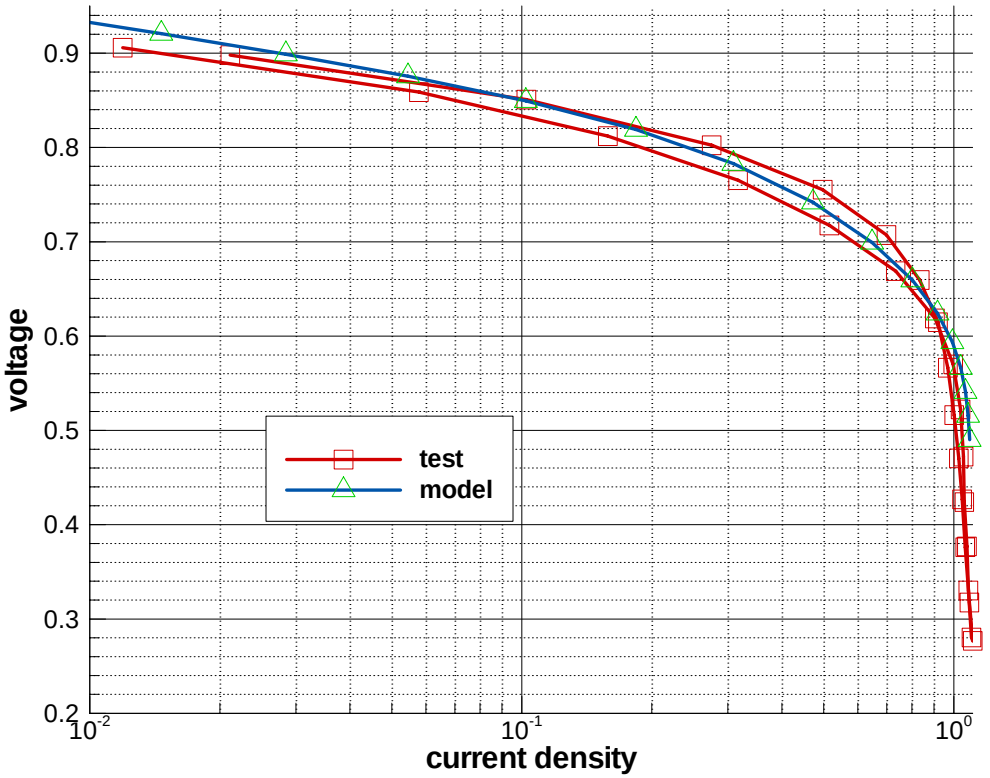

Figure 23. The newly calibrated polarization curve for dispersed case in log scale

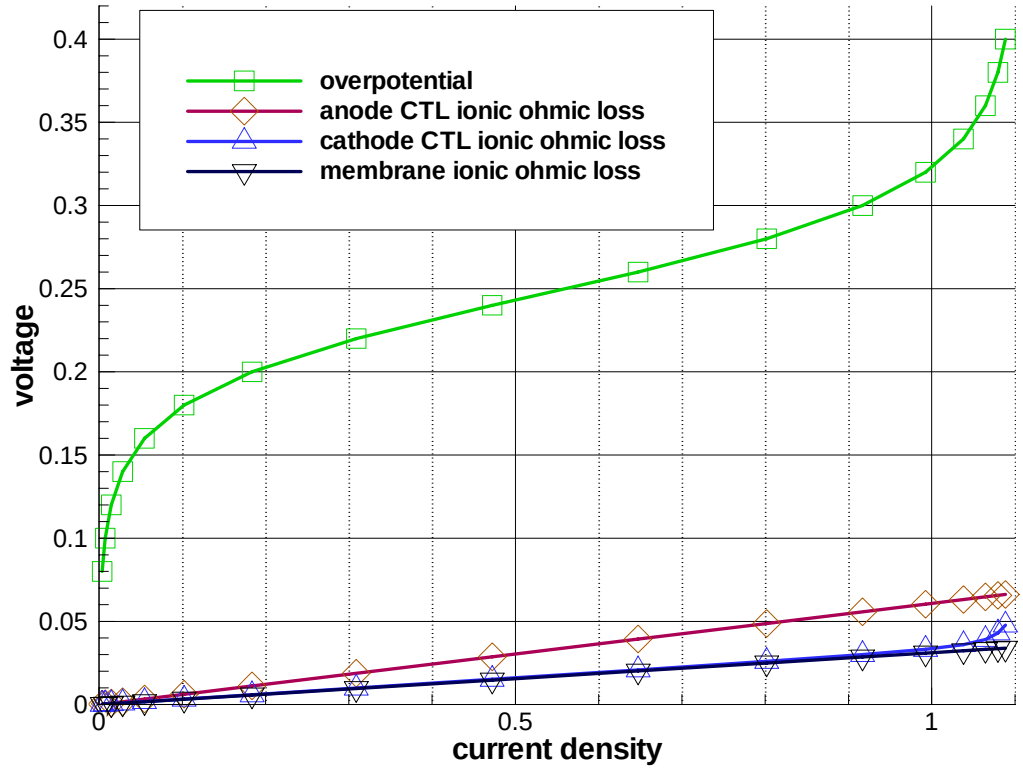

Figure 24. The overpotential loss and ohmic losseses

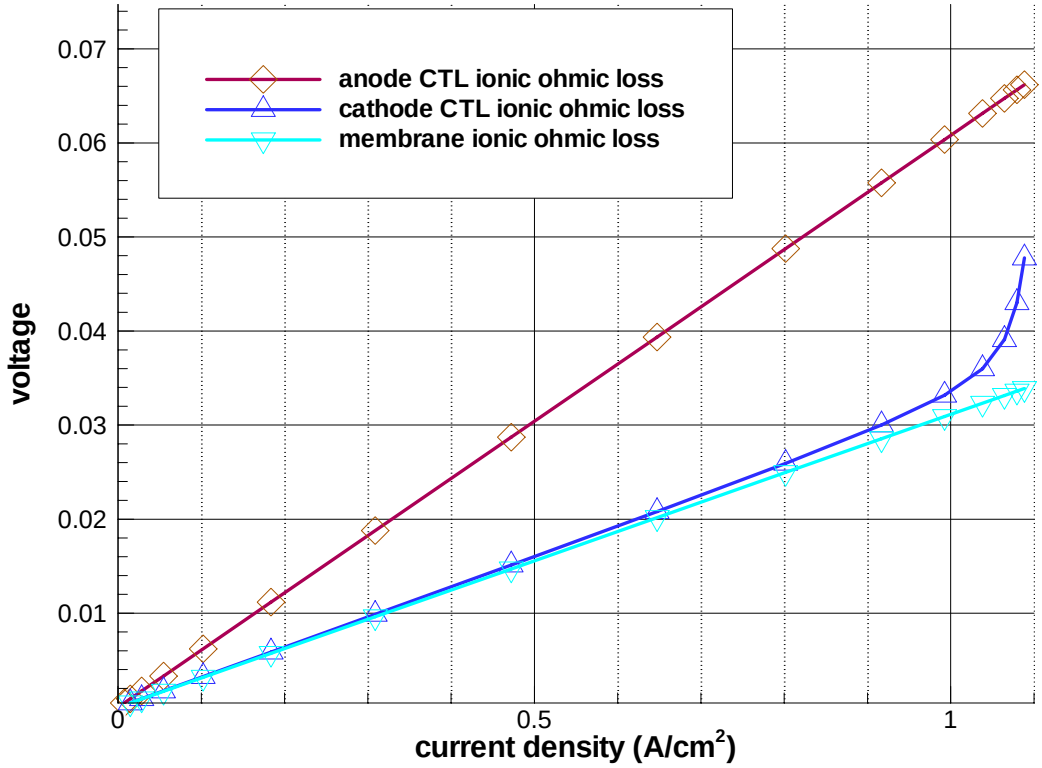

Figure 25. The ionic ohmic losses

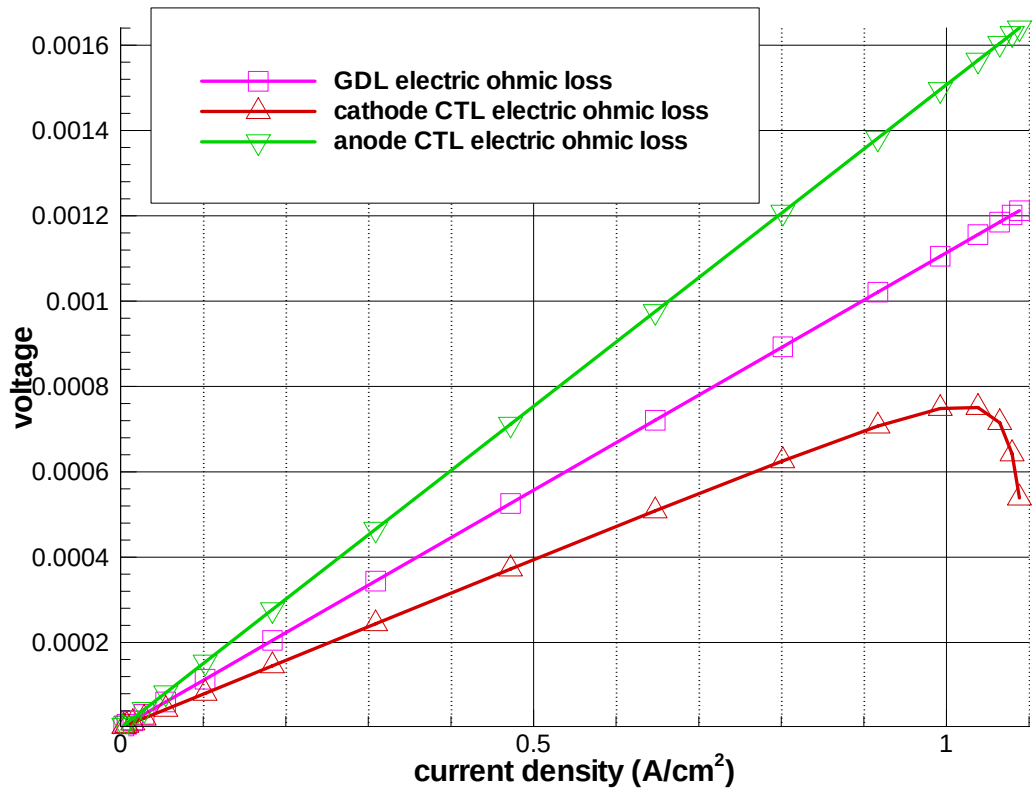

Figure 26. The electric ohmic losses

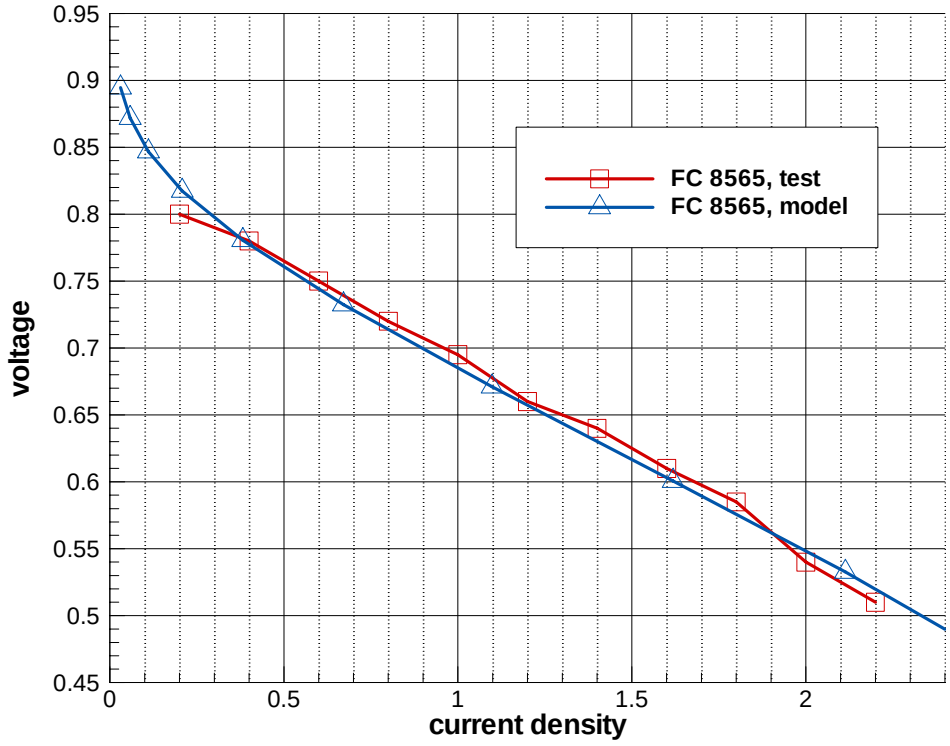

Figure 27. The newly calibrated polarization curve for FC 8565

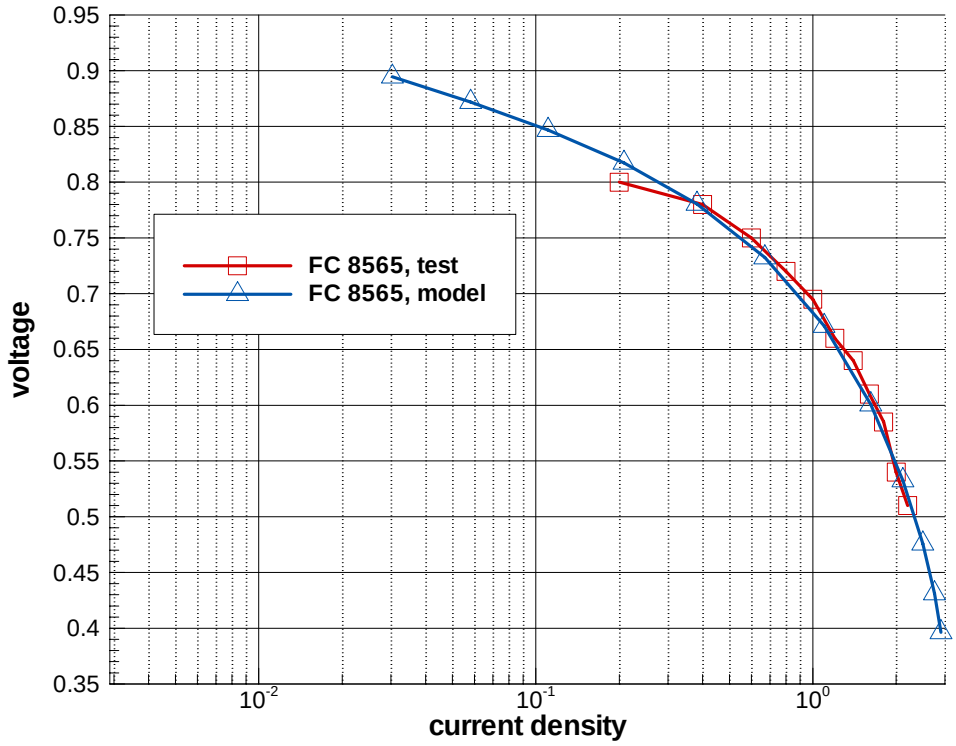

Figure 28. The newly calibrated polarization curve for FC 8565 in log scale

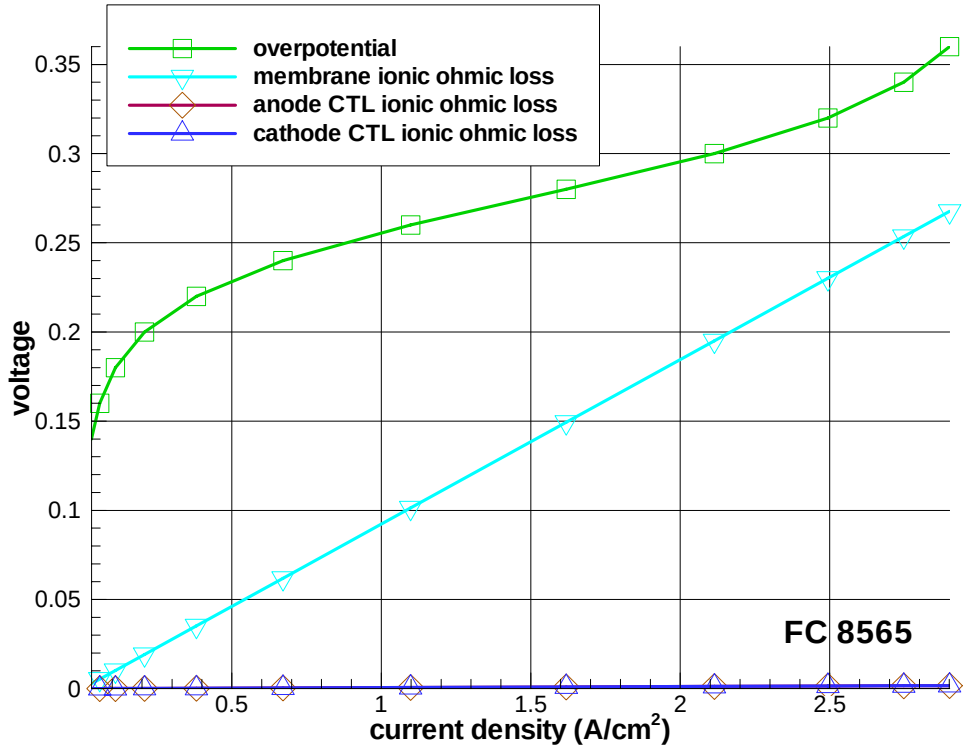

Figure 29. The overpotential and ionic ohmic losses for FC 8565

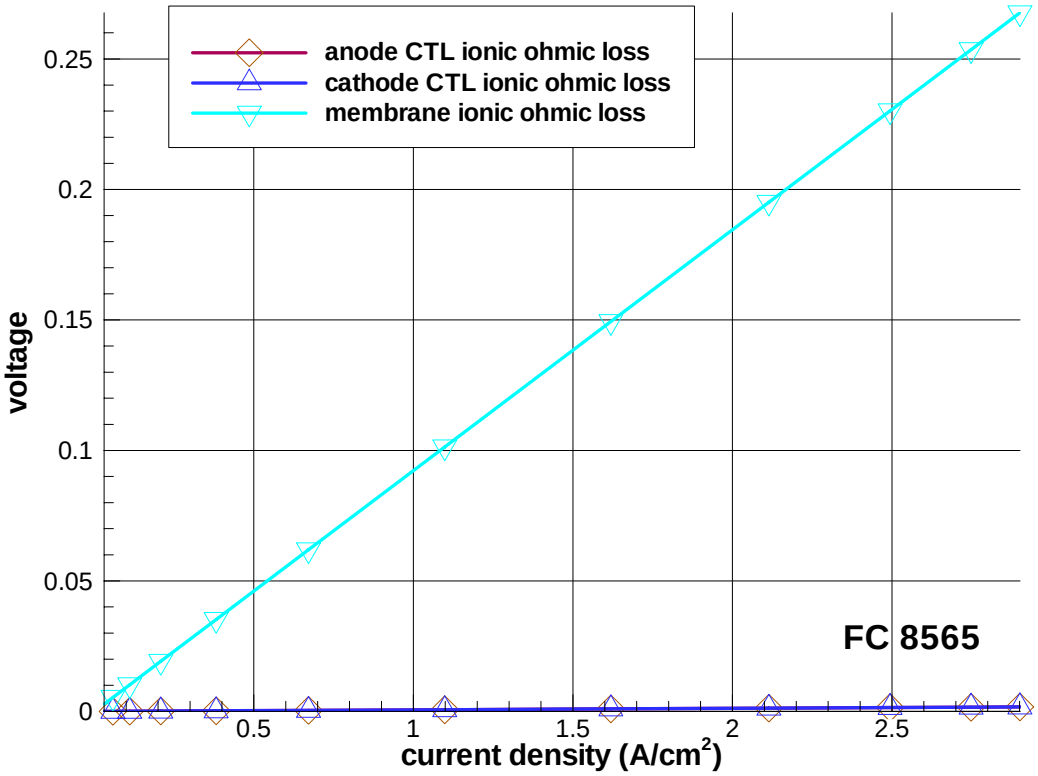

Figure 30. The ionic ohmic losses for FC 8565

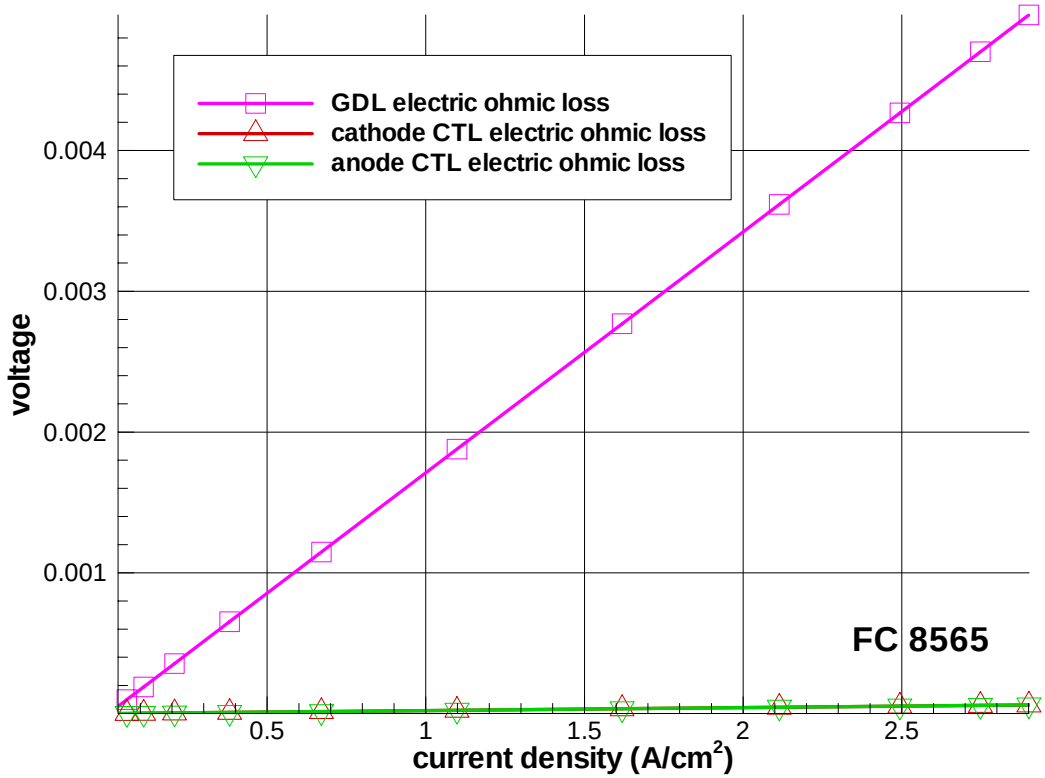

Figure 31. The electric ionic ohmic losses for FC 8565

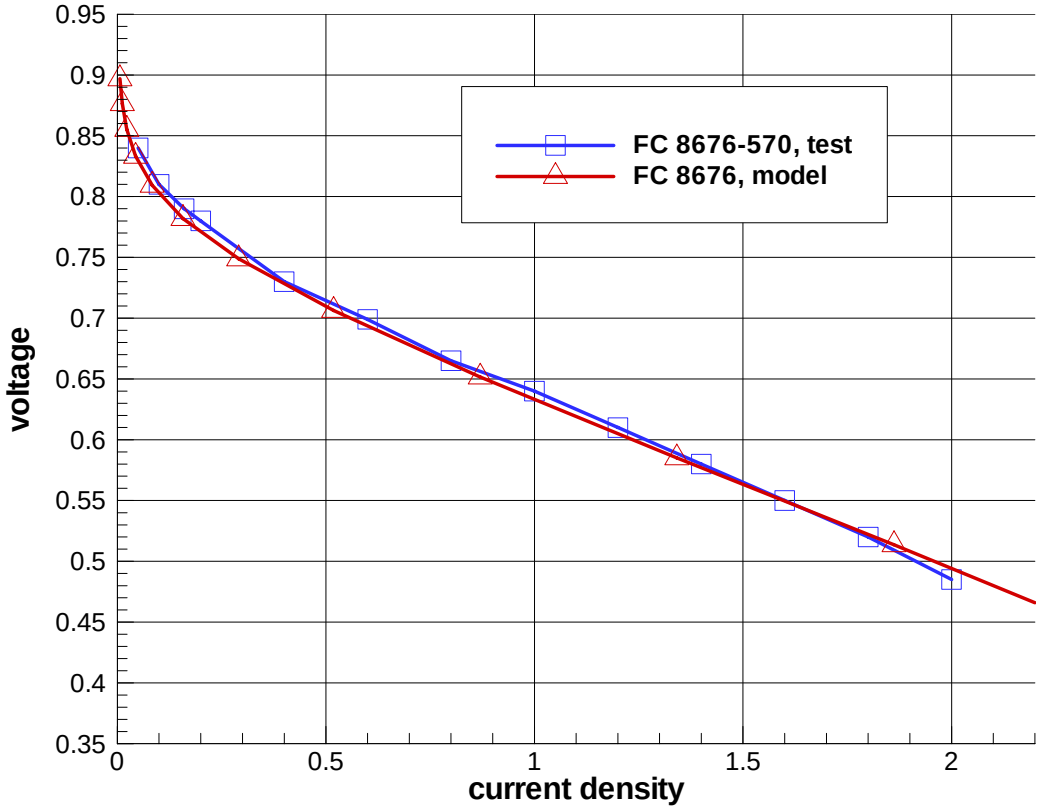

Figure 32. The newly calibrated polarization curve for FC 8676

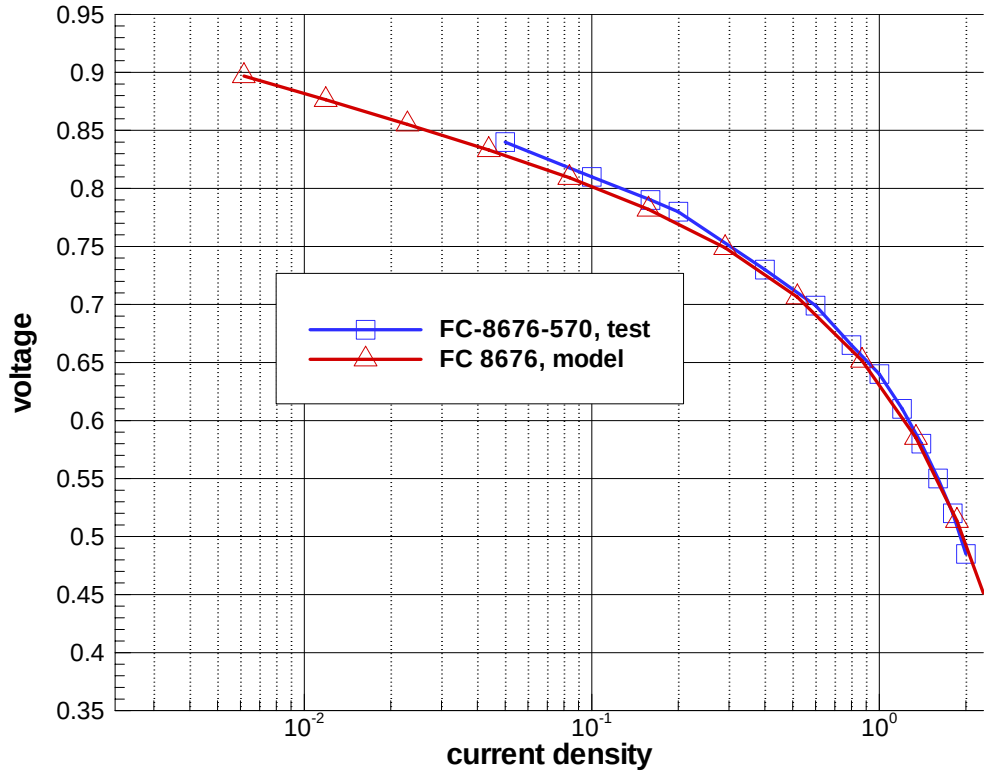

Figure 33. The newly calibrated polarization curve for FC 8676 in log scale

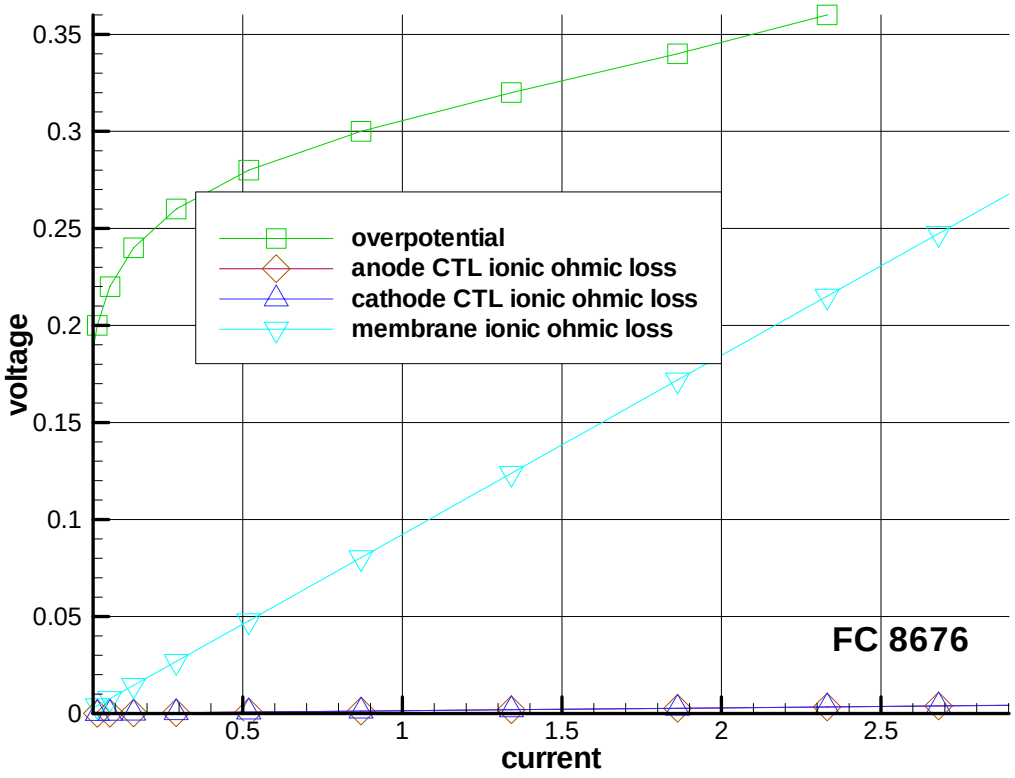

Figure 34. The overpotential and ionic ohmic losses for FC 8676

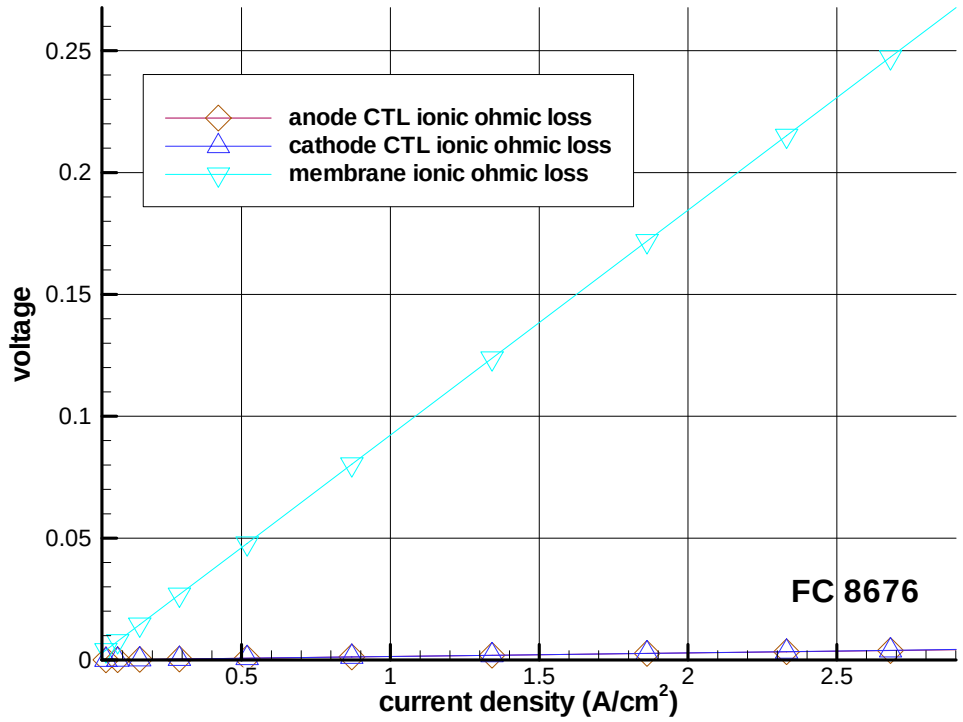

Figure 35. The ionic ohmic losses for FC 8676

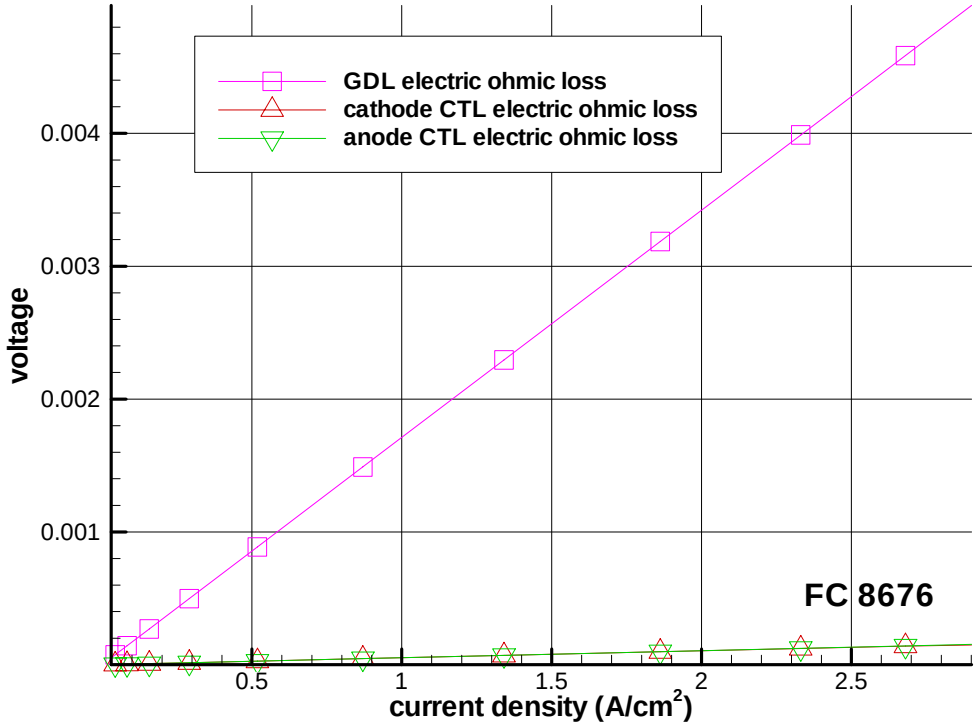

Figure 36. The electric ohmic losses for FC 8676

Appendix IV

Colorado School of Mines - Final Report

Colorado School of Mines – Final Report.

Andrew M. Herring
Tel: (303) 384-2082; Fax: (303) 273-3730; Email: aherring@mines.edu

Contributors: *Steven F. Dec*[x], *Fanqin Meng*,[*] and *James Horan*[x], and in part *Niccolo Aieta*,[*] *Mei-Chen Kuo*, and *Jennifer L. Malers*.[*]

Department of Chemical Engineering[*] and
Department of Chemistry and Geochemistry[x]
Colorado School of Mines
Golden, CO 80401-1887

Table of Contents

1.0 Executive Summary

Whilst many improvements have been made to PFSA ionomers they still require humidification to achieve adequate proton conductivity and so their use under elevated temperature and drier operating conditions is limited. The heteropoly acids, HPAs, are a large class of inorganic super acids that have been shown to give interesting properties to composite PFSA ionomers containing them. In this work we investigated the effect of doping the 3M ionomer with 1 or 5 wt% HPA, where the HPA was 12-phospho, silico or zinco tungstic acid. It was shown that under dry condition that the HPA lowered the Ea for proton transport, the opposite was true for wet conditions below 100°C.
Because of their ability to enhance the proton conductivity in the ionomer under dry conditions considerable effort was placed in trying to immobilize them in the ionomer. Three approaches were taken: 1. the formation of HPA silica particles ex-situ, 2.

attempts to bind the HPA to pre-formed silica particles, and 3. the formation of silica particles in-situ in the ionomer. All of these approaches used silicon based lacunary HPA and silica derived from TEOS and other precursors. While considerable progress was made the robustness of the silica linkage under hot acidic conditions was called in to question.

2.0 Introduction

It is desirable to operate proton exchange membrane, PEM, fuel cells at temperatures >100 °C, so that higher levels of carbon monoxide in the hydrogen feed from the reforming of hydrocarbons can be tolerated, and combined heat and power applications can utilize higher quality heat. The DOE target for vehicular applications is an operating temperature of ≤120°C so that the fuel cell stack can utilize existing radiator technology for heat exchange. In addition humidification of the fuel cell stack represents a significant parasitic load on the system and introduces significant system complexity and so it is desirable that the PEM operate under drier conditions. For stationary applications the target can be up to 165 °C, a temperature at which the platinum anode catalyst is not poisoned by CO levels <2 %. This higher level of 2 % CO in the reformate hydrogen feed allows a significantly cheaper and less complicated reformer to be utilized in which the partial oxidation, PrOx, reactor can be eliminated.

Currently PEM fuel cells based on perfluorosulfonated ionomers such as Dupont's Nafion™ and competing PFSA polymers produced by 3M and Solvay-Solexis need to be operated under humidified conditions to achieve high proton conduction. Practically this equates to an operating temperature of 80 °C, above this temperature the fuel cell system must be pressurized to achieve practical proton conduction, which results in further system complexity and parasitic losses. In addition Nafion™ like materials are degraded by the hydroxyl radicals formed at the cathode of a fuel cell membrane electrode assembly, MEA, and at higher temperatures loose the sulfonic acid groups necessary for proton conduction as the membrane becomes more anhydrous. In order to operate a PEM fuel cell at elevated temperatures, > 100 °C, the perfluorosulfonated ionomers must either be improved or replaced with another material.

Our approach is to add inorganic additives to these perfluorosulfonated ionomers which may be synthetically tailored to enhance the proton conductivity and overall stability of the material. The heteropoly acids, HPAs, are a large and varied class of inorganic proton conducting solids which have been of interest for fuel cell applications for at least two decades. These materials are reported to have proton conductivities as high as 0.2 Scm^{-1} at room temperature and are stable to at least 200 °C. HPA consist of a central heteroatom, which may be almost any element, surrounded by a shell of typically 12 or more tungsten or molybdenum oxygen octahedra. One, two or three of these tungsten or molybdenum oxygen octahedral may be removed to form a lacunary HPA and replaced either by another transition metal or by an organosilane or similar organic functionality to create a hybrid material. In this way the redox chemistry of the HPA and its solubility can be controlled.

Research in our laboratory has demonstrated that the most suitable HPA for fuel cell applications are the heteropolytungstates, HPWs, although these materials are too water soluble when used as the only ionomer component and the high fuel cell performance observed at room temperature in a pure HPA PEM fuel cell is lost as the material dissolves. When the HPW were used to dope Nafion™ we generally observe large increases in current density especially at higher temperatures as compared to the

undoped materials. In Nafion™ 112 we observe an apparent increase in the OCV which we attribute to the hydrogen and oxygen that permeate the membrane being catalytically converted to water internally, resulting in less apparent cross over. In Nafion™117 some of the doped membranes are actually thinner than the control which is in keeping with other evidence that suggests that the HPW form strong hydrogen bonded interactions with the sulfonic acid groups. This leads to variable temperatures of sulfonic acid decomposition, as measured by TGA, and so could be used to add stability to the membrane. So not only do the HPW enhance proton conduction in Nafion™ with their intrinsic conductivity but they also create a self hydrating membrane. It is important, therefore, that the ionomer also be optimized to allow enough permeation of hydrogen and oxygen to maintain proton conductivity through internal hydration but not so much that the overall efficiency of the fuel cell is compromised to unacceptable levels. In addition the HPA have an extensive but still poorly understood chemistry with hydroxyl radical, so an HPA could be tailored to decompose the damaging hydroxyl radical.

Some of these ideas of catalytic hydroxyl radical decomposition and water generation have been previously demonstrated with platinum colloids deposited in the membrane. This is clearly not practical for a MEA designed for terrestrial applications as one overall goal is the production of less expensive fuel cell components by the reduction in the use of precious platinum catalysts in the MEA. The HPA therefore offer an economic and practical alternative to the use of platinum. There are, however, a number of barriers that must be overcome, including understanding the chemistry of HPA/ionomer interactions, tailoring the redox and catalytic activity of the HPA and immobilizing the HPA in the membrane. We have only just begun to unravel the complex chemistry that occurs when an HPA is used to dope sulfonated ionomers.

Most studies to date have used the four commercially available HPA, in our group, which includes a synthetic inorganic chemistry capability, we have begun to synthesize a library of some of the other hundreds of structures available, funded by a DOE Science Initiative grant, for initial screening in Nafion™ or similar materials. As the HPA are strongly hydrogen bound to the sulfonate groups we can compare HPA doped materials and learn which structures are required for optimum operating conditions in short term studies. The HPA are still likely to leach out of the membrane in long term studies and so they must be immobilized. Our strategies for this include creating hybrid HPA where the organic part of the molecule is designed to render the HPA insoluble either through its bulk or by using a monomer that can be polymerized in-situ to create a networked system of immobilized HPA. We also believe that a large HPA may also be immobile and that simply attaching an HPA to an inorganic colloid may also be effective.

In this project we fabricated membranes using novel HPA synthesized at CSM and ionomers supplied by 3M either by imbibing or by recasting the materials with appropriate amounts of added HPA. In some cases we supplied 3M with HPAs for inclusion in ionomers at 3M. The membranes were characterized by IR, NMR, TGA and SAXS and the proton diffusion coefficients were measured by pulse field gradient spin echo NMR from RT up to 150 °C. The work reported here represents the first steps to systematically develop a HPA/ionomer system for use in practical high temperature, <100 °C, low humidity PEM fuel cells.

3.0 Synthesis and Characterization

In order to immobilize the HPA two approaches were taken: 1) HPA were combined with silica precursors *ex-situ* and then blended with the ionomer, 2) immobilized HPA silica systems were prepared *in-situ* in the ionomer. The HPA may be immobilized by entrapment where a large amount of a silica precursor is used to surround the HPA in

silica or by bonding the HPA covalently to the silica by using a lacunary HPA. A lacunary HPA is one in which 1, 2, or 3 of the metal oxygen octahdra surrounding the central heteroatom are removed. The vacancies created can be substituted with functionalities designed to immobilize the HPA.

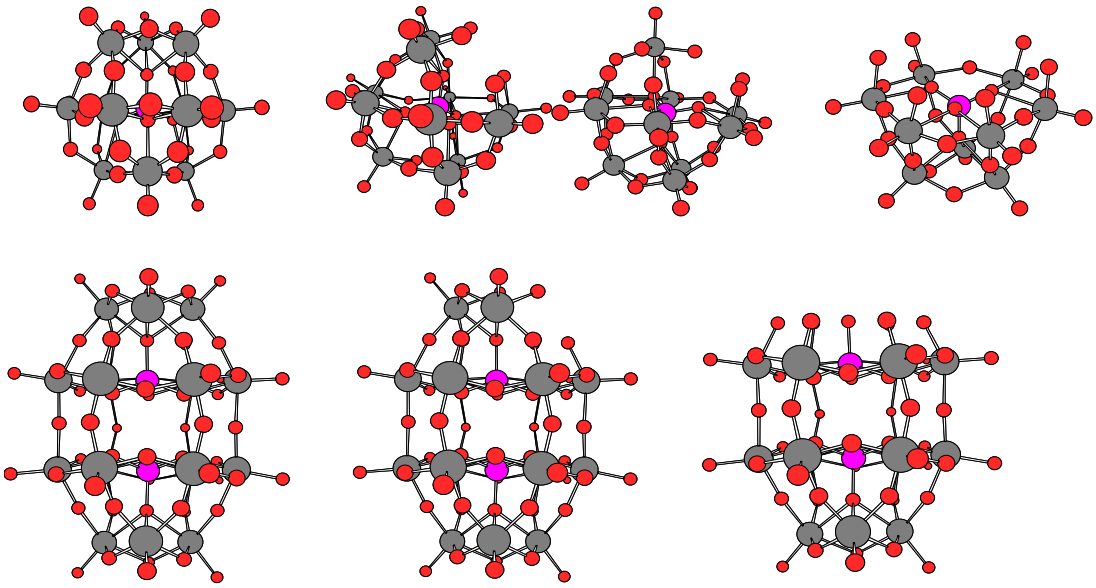

Figure 1. HPA and lacunary HPA based on them; top row Keggin structure, ***e.g.*** **[PW12O40]3-, bottom row, Dawson structure, e.g. [P2W18O62]6-.**

3.1. HPA acronyms

Keggin structures
12-borotungstic acid, HBW
12-silicotungstic acid, HSiW
12-phosphotungstic acid, HPW
12-zinctungstic acid, HZnW
Lacunary Keggin structures,
11-phosphotungstic acid, HPW_{11} etc
Dawson structures
18-diphosphotunsgtic acid, HP2W
Lacunary Dawson structures,
17- diphosphotunsgtic acid, $HP2W_{17}$
Other HPA
21-diphosphotungstic acid, $HP2W_{21}$

3.2. HPA doped 3M ionomer

Baseline data was obtained for doped 3M ionomer samples by mixing the appropriate amount of HPA wit the casting solution of the ionomer prior to casting. The HPA in these membranes is not immobilized and might be expected to wash out during fuel cell operation under conditions under which the membrane would be subjected to liquid water. The most extensive data sets were collected for the 3M ionomer doped with the HPW, HSiW and HZnW at the 1% and 5% doping levels.

3.2.1. ATR – IR

It has been reported that heat treating HPA doped PFSA membranes immobilizes the HPA by the cross links formed by the decomposition of the sulfonic acid groups. All membranes were subjected to a heat treatment at 160 °C for 4 hours and then were soaked in deionized water for 24 hours. The membranes turned dark gray after such treatment, losing their original reddish tint. The ATR spectrum of each sample was taken before and after the above procedure to see the effect pf the HPA on the spectrum and to determine if any HPA had been retained. All ATR samples were dried in air and then under vacuum for a few hours right before the spectra were taken, Figure 2-Figure 7. Additional peaks are present for the 5wt% doped membranes but it is not clear whether or not any HPA has been retained after the heat treatment.

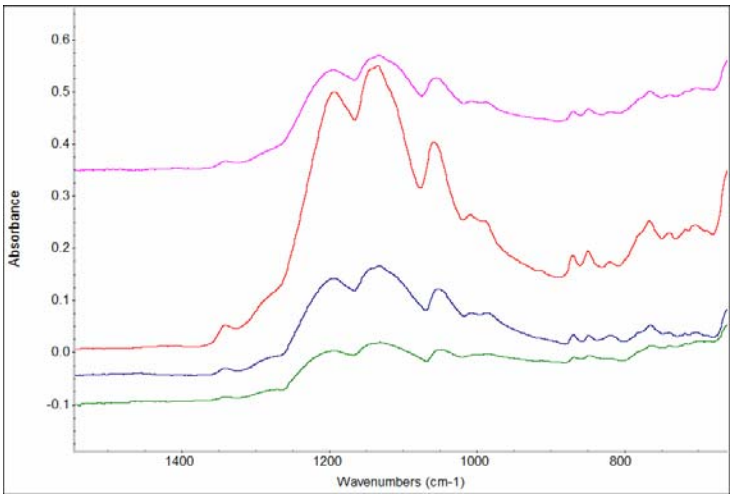

Figure 2. From top to bottom, ATR spectra of 1. Heat-treated 1% HPW-doped membrane, 2. Heat-treated control membrane, 3. untreated 1% HPW-doped membrane, 4. untreated control membrane.

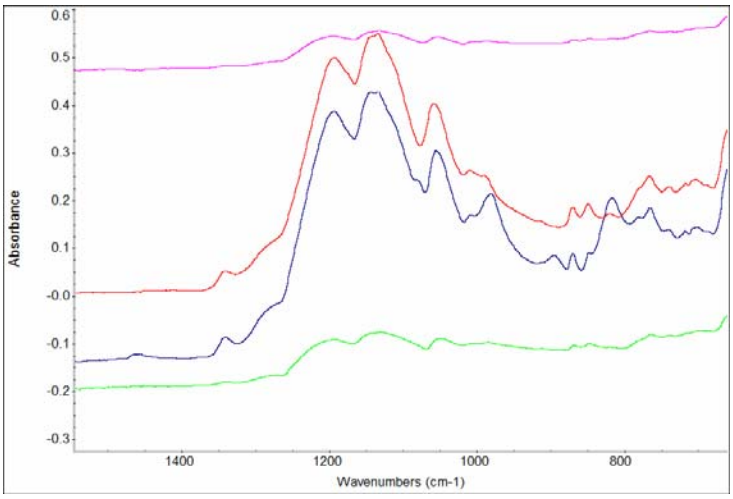

Figure 3. From top to bottom, ATR spectra of 1. Heat-treated 5% HPW-doped membrane, 2. Heat-treated control membrane, 3. untreated 5% HPW-doped membrane, 4. untreated control membrane.

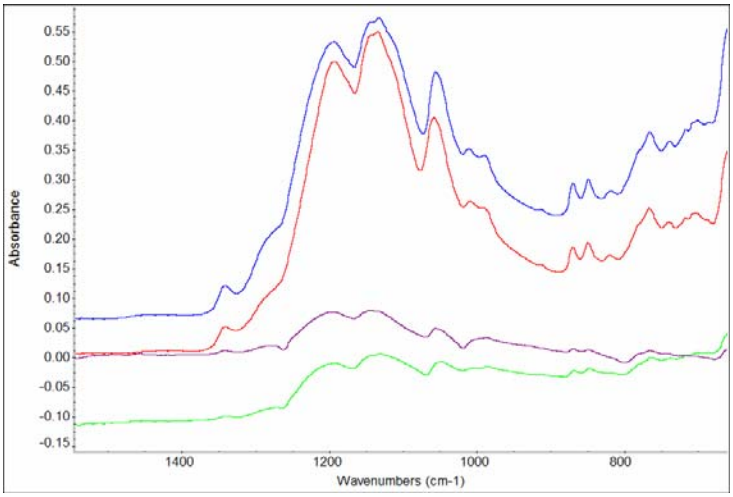

Figure 4. From top to bottom, ATR spectra of 1. Heat-treated 1% HSiW-doped membrane, 2. Heat-treated control membrane, 3. untreated 1% HSiW-doped membrane, 4. untreated control membrane.

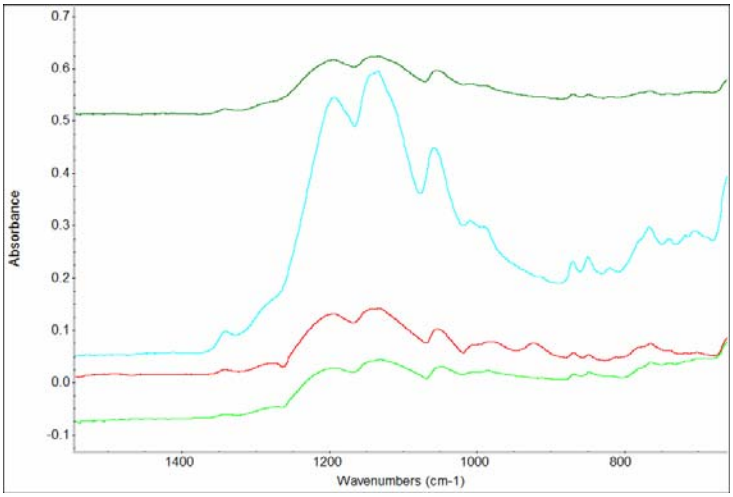

Figure 5. From top to bottom, ATR spectra of 1. Heat-treated 5% HSiW-doped membrane, 2. Heat-treated control membrane, 3. untreated 5% HSiW-doped membrane, 4. untreated control membrane.

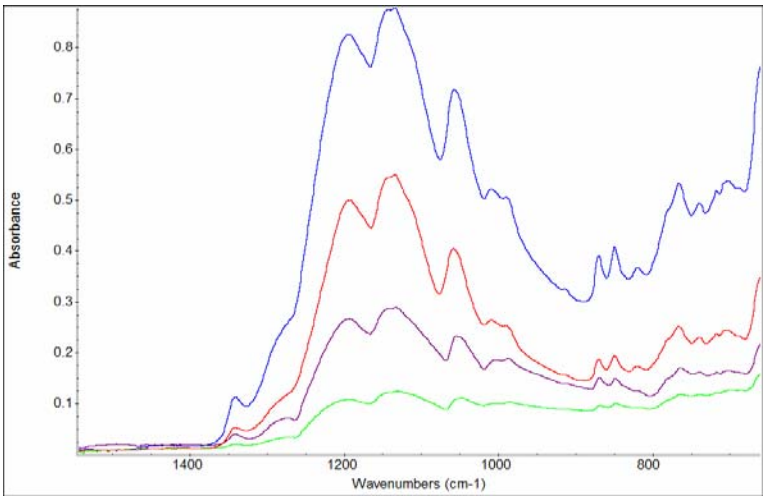

Figure 6. From top to bottom, ATR spectra of 1. Heat-treated 1% HZnW-doped membrane, 2. Heat-treated control membrane, 3. untreated 1% HZnW-doped membrane, 4. untreated control membrane.

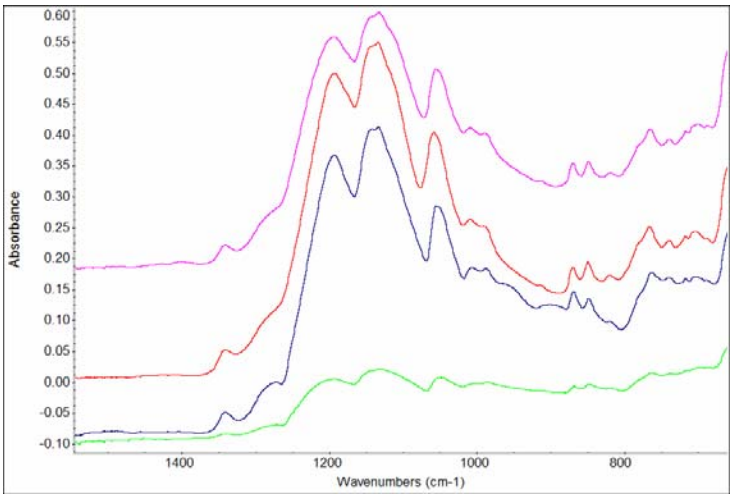

Figure 7. From top to bottom, ATR spectra of 1. Heat-treated 5% HZnW-doped membrane, 2. Heat-treated control membrane, 3. untreated 5% HZnW-doped membrane, 4. untreated control membrane.

3.2.2. SAXS

Small-angle X-ray scattering studies were carried out under He or vacuum conditions. To investigate the effect of hydration state on the scattering properties of the membranes, “water bag experiments” were performed, where the membranes were heat-sealed in an air-tight plastic bag with two drops of water in it. The wet membranes were taken out of the bag, dried under vacuum and then put in the SAXS instrument to observe the change of their scattering properties.

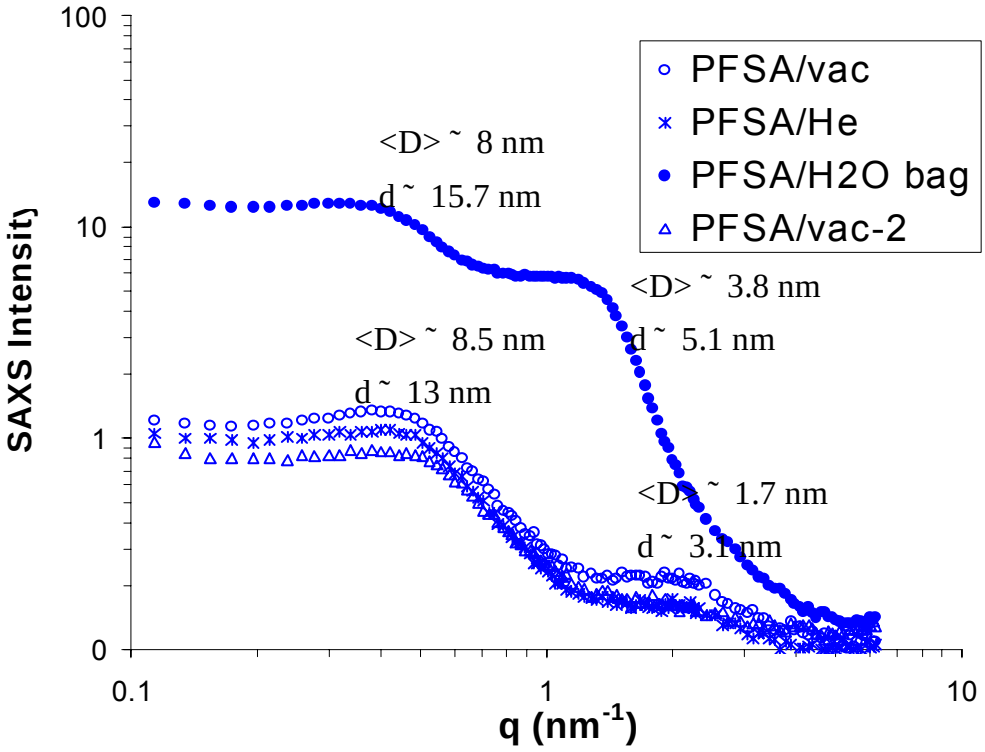

<D> - average cluster size

d – intercluster distance

Figure 8 shows the SAXS spectra of SAXS spectra of the un-doped control membrane under He, vacuum, water bag and vacuum conditions. Under dry conditions, the membrane shows two scattering features, indicated by the two shoulders (or so-called "peaks") in the spectra. The peak at lower q (corresponding to lower 2θ, scattering angle) are fitted by a spherical particle model to have the weighted average particle size of *ca.* 8.5 nm in diameter, and the intercluster distance was calculated by the equation d=2□/q to be approximately 13 nm. Similarly, the smaller structural feature has an average diameter of 1.7 nm, and is 3.1 nm from each other. When the sample was tested under wet conditions, as in the water bag experiment, a dramatic increase in scattering intensity was observed. Compared to the dry sample, the larger structural feature shrank to 8 nm in diameter, while interparticle spacing increased. In contrast, the smaller feature swelled by over 200%. The sample returned to almost exactly its original state after the vacuum drying according to the spectrum taken afterwards.

In the literature, a lot of scattering studies have been done on Nafion™117 or Nafion™112 membranes, and the results consistently show that only one type of scattering centers with a average diameter around 1.5 - 2 nm were observed. The scattering center has been determined to be the hydrophilic clusters of the Nafion™. In our work, apparently two types of scattering centers have been observed, one hydrophilic, the smaller feature which dramatically expands upon water absorption, and the other clusters are the hydrophobic fluorinated backbone which are not swollen by water, but "squeezed" into slightly smaller particles.

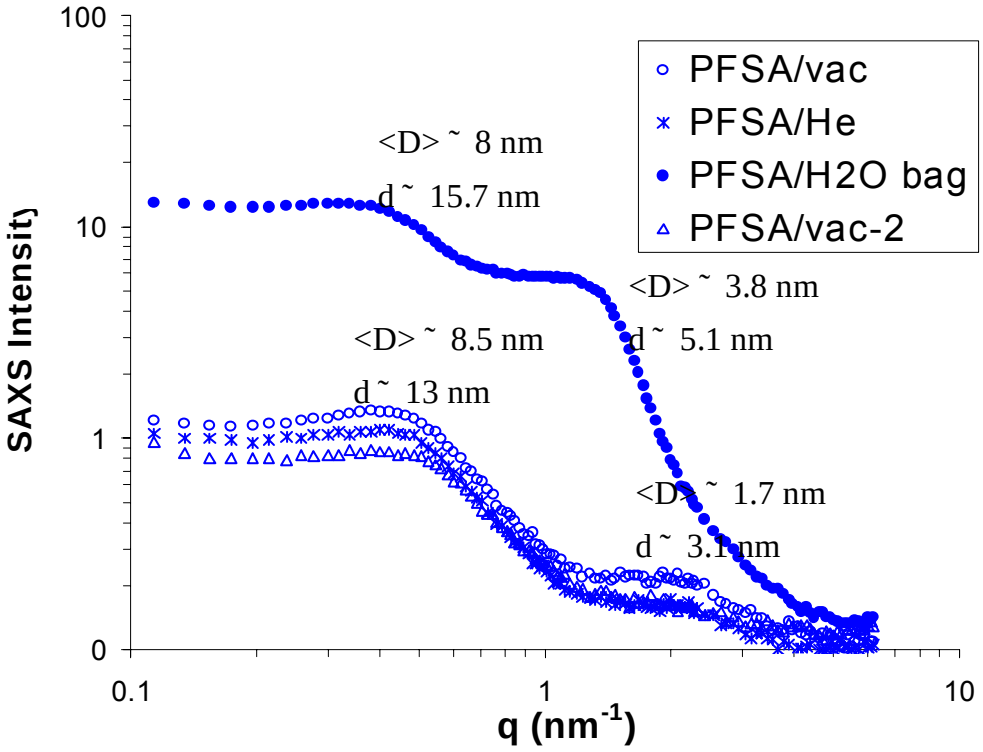

<D> - average cluster size

d – intercluster distance

Figure 8. SAXS spectra of the control membrane under He, vacuum, water bag and vacuum conditions.

As shown in Figure 9, the HPW-doped membranes showed much higher scattering intensity. Under dry conditions, two changes are very noticeable as compared to the control. First, the low-angle scattering feature was stretched out, corresponding to a wide size distribution. Second, a new peak (Bragg peak) started to form (in the case of 5% HPW, the peak is actually evident) at the very high angle of the experiment, presumably due to appreciable crystallinity - long-range ordering of small molecules. The hydrophilic clusters remain shown with approximately the same size and spacing as the control. The Bragg peak in the 5% HPW sample corresponds to a d-spacing of approximately 12 Å, according to Bragg equation (d = □/2sin□. This d spacing is consistent with the d spacing of the 100 planes (12.173 Å) in the cubic Keggin structure. When the samples were put in a water bag, the scattering behavior changed dramatically; the two scattering features seen in the control re-appeared, and the low-angle Bragg peak was gone. The SAXS spectra taken after the samples were dried again almost returned to its original shape with an appreciable intensity drop. This interesting phenomenon can be explained as that the HPW crystallites originally formed in the sample dissolved in the water bag and may have partially leached out of the sample. When the samples were dried again, the HPW molecules recrystallized.

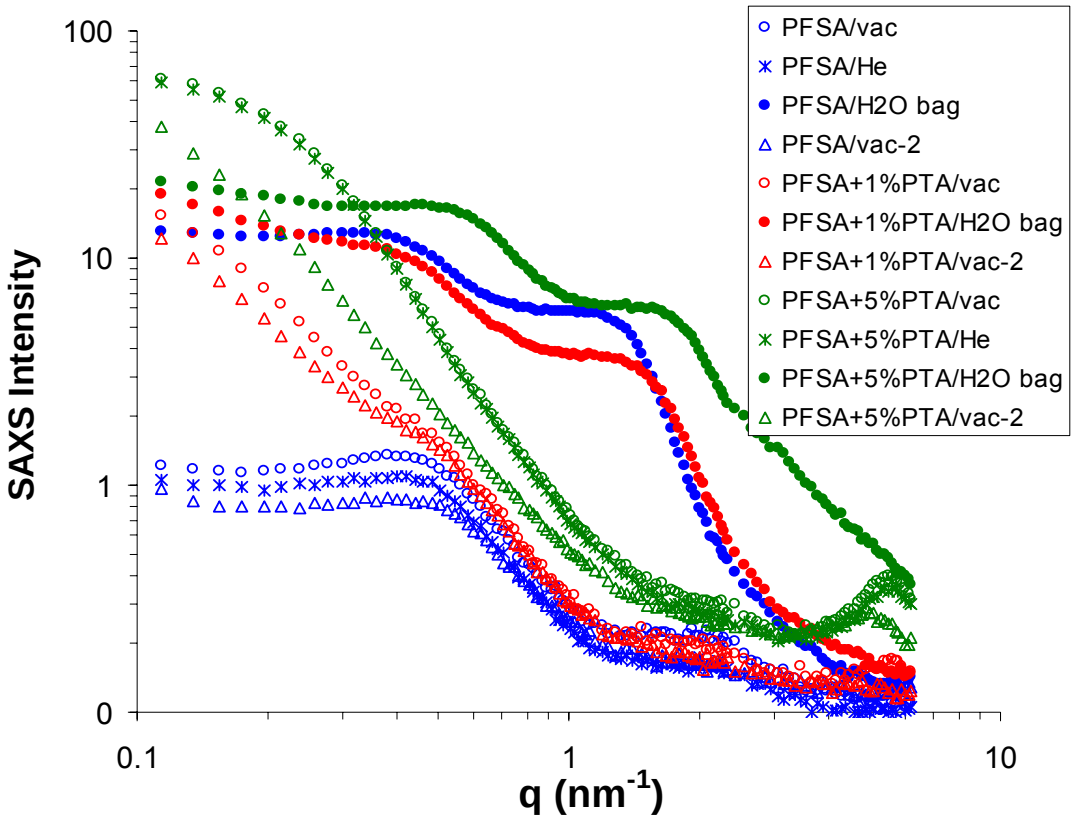

Figure 9. SAXS spectra of the control membrane and HPW (PTA)-doped membranes under He, vacuum, water bag and vacuum conditions.

To get an idea of HPA leaching problem of the membranes, the 1% HPW and 5% HPW samples were soaked in water overnight and the water solutions were checked for tungsten by ICP. The final PTA loading turned out to be 0.65% and 2.70% after the soaking, meaning that roughly 1/3 of the PTA leached out.

The same type of experiments were performed on the HSiW and HZnW membranes and similar results were obtained, as shown in

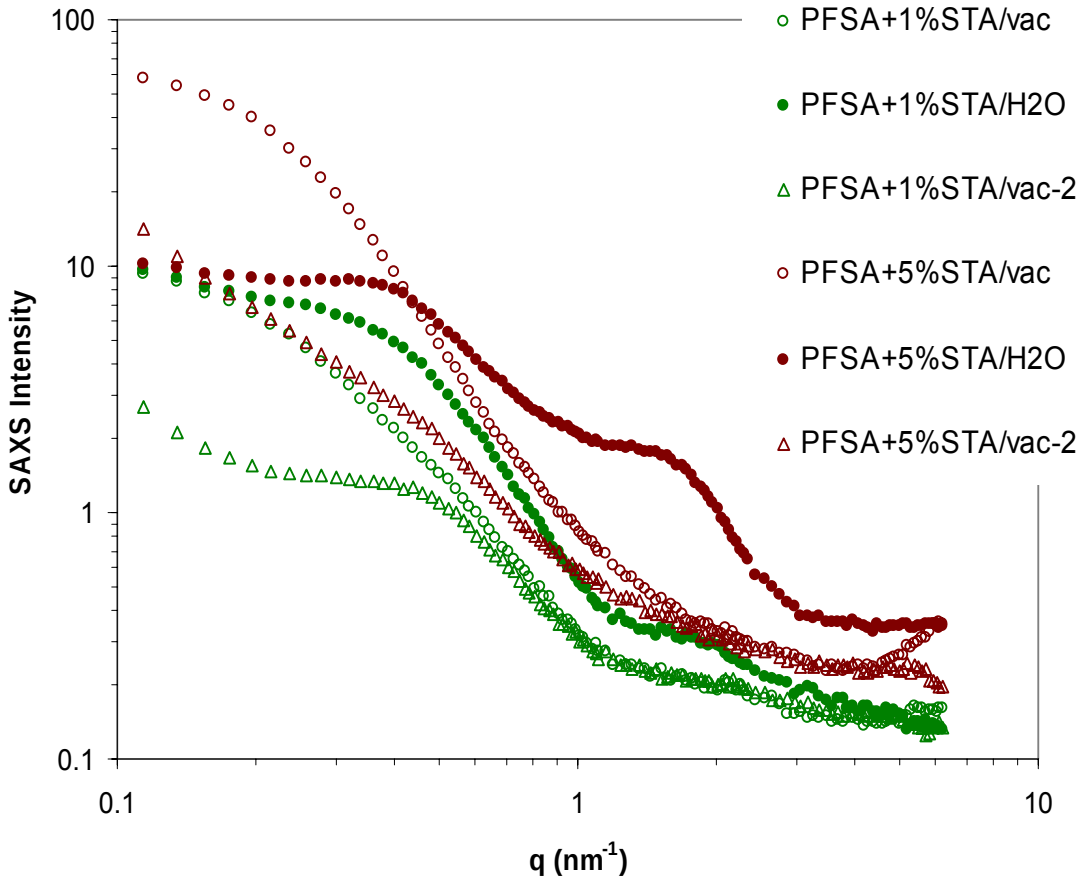

Figure 10. SAXS spectra of the control membrane and HSiW (STA)-doped membranes under vacuum, water bag and vacuum conditions.

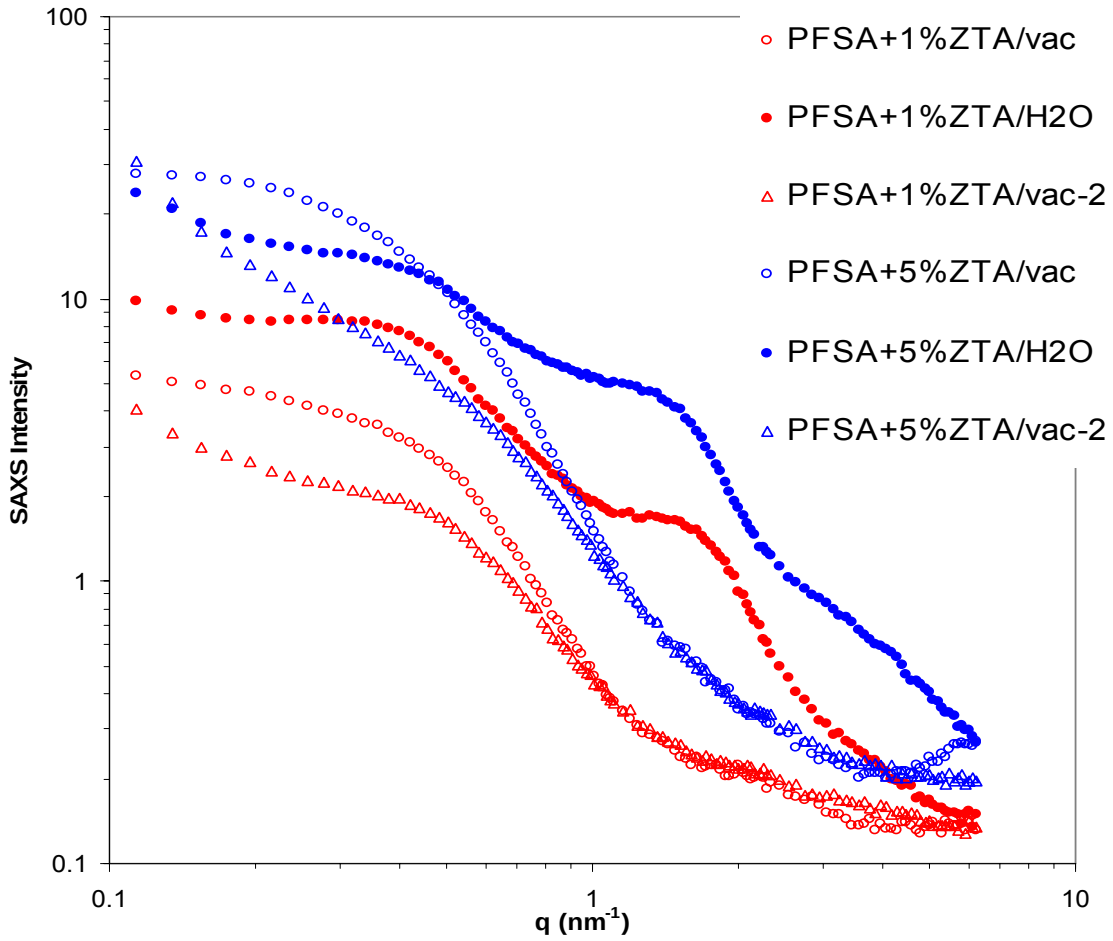

Figure 11. SAXS spectra of the control membrane and HZnW (ZTA) -doped membranes under vacuum, water bag and vacuum conditions.

3.3. Ex-situ synthesis of HPA-silica particles

3.3.1. Using precursor silicon containing species

HPA were mixed with tetraethylorthosilicate, TEOS, and then water to produce HPA in a solid stare silica matrix. The lacunary heteropoly anions [□-$SiW_{11}O_{39}$]$^{8-}$ and [□-$SiW_{10}O_{36}$]$^{8-}$ are much better retained in silica than the Keggin type anions [$PW_{12}O_{40}$]$^{3-}$ due to the formation of Si-O-W bonds between the SiO_2 matrix and the HPA anion. A calculation of the HPA content in the hybrid was reported based on the weights of the products. The ICP analysis was performed to give accurate information on the composition of the insoluble HPA-SiO_2 hybrid materials. Table 1 lists the HPA contents of each hybrid material based on the ICP results, and the calculated numbers based on the weights of the products were included in the parentheses. The trend is more clearly seen in Figure 12, consistent between the calculated and experimental values, although the experiments values turn out considerably lower.

Starting HPA:TEOS (mol/mol)	HPA = HPW (Commercial)	HPA = $K_8[\square\text{-}SiW_{10}O_{36}]$	HPA = $K_8[\square\text{-}SiW_{11}O_{39}]$
1:53	15.4 (23)	35.4 (46)	27.2 (44)
1:30	3.7 (0)	18.8 (44)	42.9 (55)
1:20	3.2 (0)	54.7 (69)	51.7 (64)
1:15	- (0)	49.4 (72)	39.6 (52)
1:10	- (0)	38.2 (70)	42.5 (45)
1:8	- (0)	24.7 (60)	36.4 (33)

Table 1. HPA retention rates in inorganic silica with various ratios of the starting materials. Results are expressed as wt% of HPA anion remained in the insoluble hybrid products. The numbers in the parentheses are previous results based on weights for comparison.

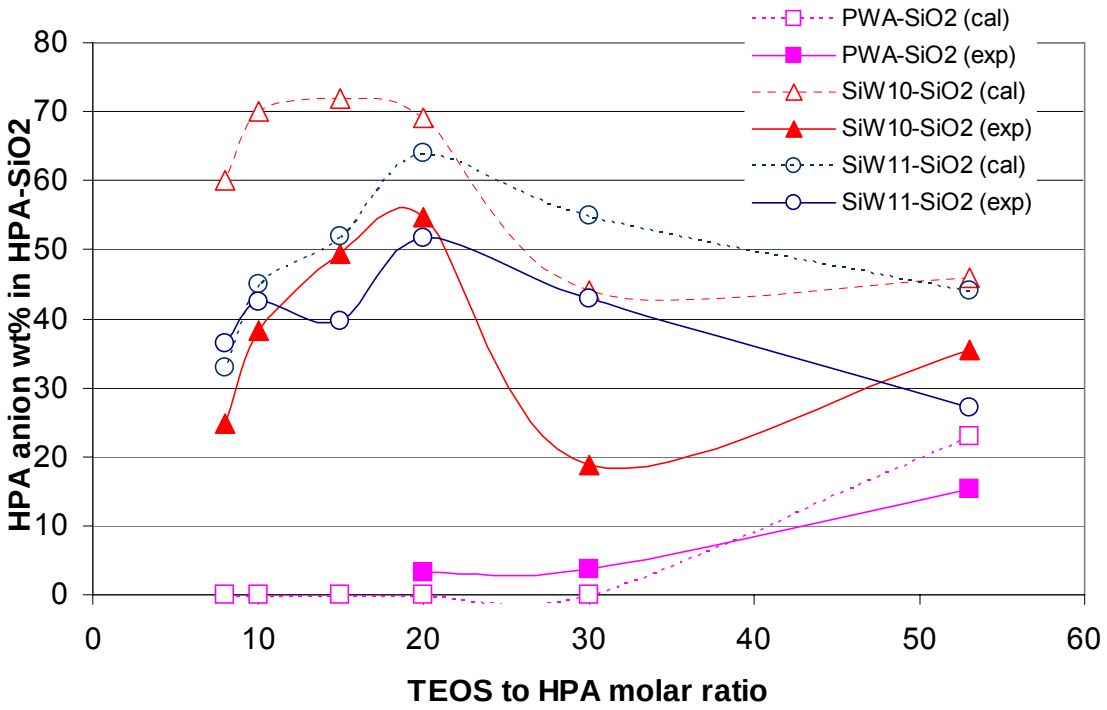

Figure 12. HPA retention rates in inorganic silica with various ratios of the starting materials.

The most effective composition for the starting materials in terms of incorporating the most HPA is 1:20 HPA:TEOS for both the SiW_{10} and SiW_{11} species. In comparison, the same treatment washed out *ca.* 85%

^{29}Si MAS NMR was performed on the HPA-SiO_2 materials to confirm the incorporation of the HPA with the silica framework. One material with the highest HPA loading was chosen from each of the three HPA-SiO2 hybrids, as well as a blank SiO_2 made from TEOS in a similar fashion without any HPA.

Peak positions (ppm) and their respective assignments for the SiO_2 control are as follows. The peak at -110.6 ppm is due to the Si within the bulk SiO_2, where its four neighbors are all (OSi) groups, also conventionally written as $Si^*(OSi)_4$, Q^4. The peaks at -101.5 and -93.0 ppm are designated as $Si^*(OSi)_3(OH)$, Q^3, and $Si^*(OSi)_2(OH)_2$, Q^2,

meaning that these Si atoms are at the surface and bonded to three OSi and one OH, or two OSi and two OH groups, respectively. These peaks are typical for solvent synthesized silica. The SiW_{10}-SiO_2 and SiW_{11}-SiO_2 materials both show additional peaks, at -85.6 and -84.7 ppm respectively, characteristic of the central SiO_4 units within the HPA anions, confirming the incorporation of these anions into the materials. Not surprisingly, incorporation of PWA did not change the ^{29}Si spectrum of the SiO_2 matrix, except for the relative intensity of the peaks perhaps due to different surface properties.

TGA analyses were done on selected hybrid materials in comparison to the SiO_2 control and the free HPA. The TGA curves are presented in Figures 3 – 5. Figure 13 shows that weight loss, presumably due to water, is much slower for the $HSiW_{10}$ doped silica and significant water is retained to 200°C. This is also true for the $HSiW_{10}$ doped silica, Figure 14. The effect is very much less dramatic for the HPW doped silica, Figure 15.

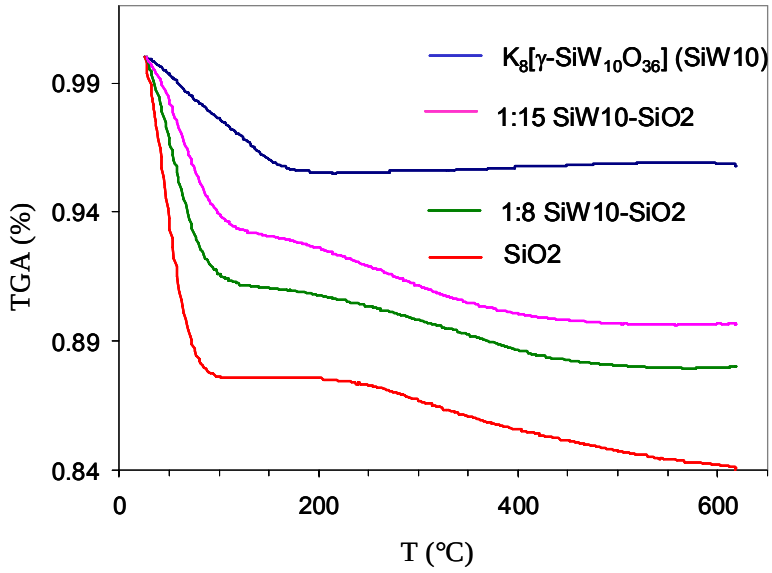

Figure 13.TGA curves of the SiW10-SiO2 in comparison to KSiW10 and SiO2.

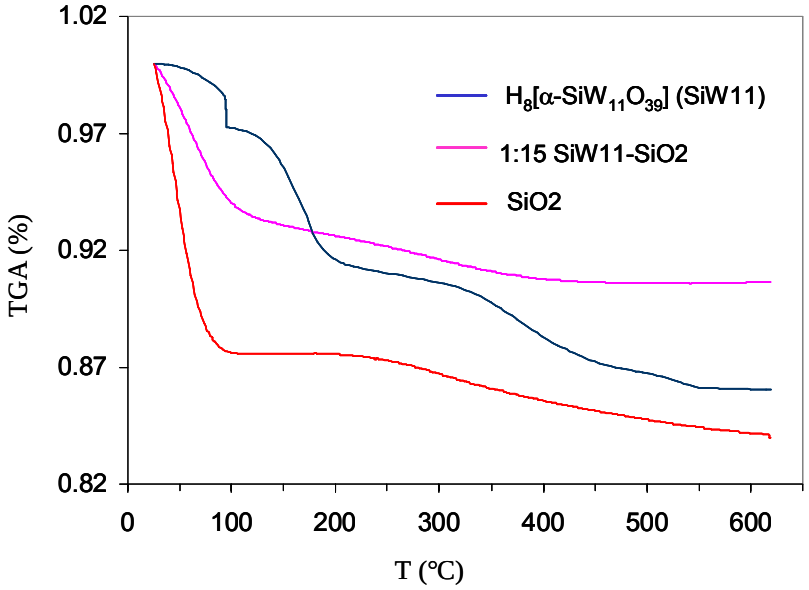

Figure 14. TGA curves of the SiW11-SiO2 in comparison to HSiW11 and SiO2.

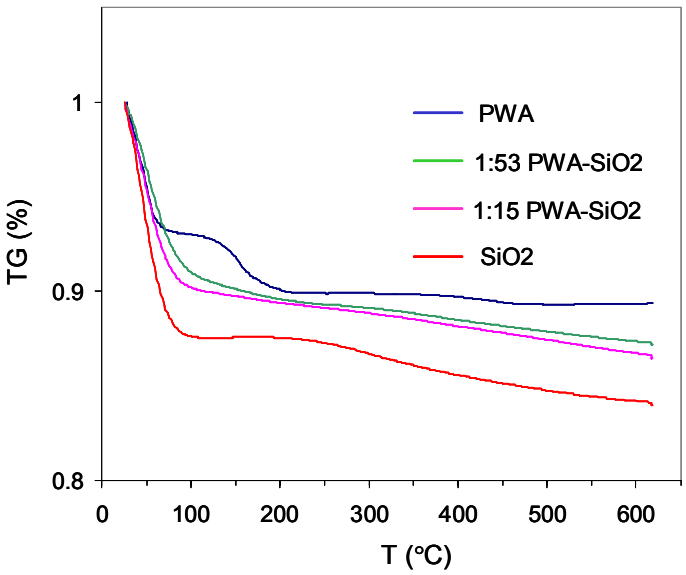

Figure 15. TGA curves of the PWA-SiO2 in comparison to PWA and SiO2.

Difficulty was found in using these SiO_2-HPA particles made by the *ex-situ* method in membrane casting due to the large particle sizes. The goal was to make small size particles with a narrow distribution that can be used as membrane additives. One approach was to introduce monophenyltriethoxysilane (MPh) to the TEOS-$HSiW_{10}$ reaction, hoping to terminate the TEOS hydrolysis and condensation (to form 3-dimensional SiO_2 network) at a certain level so as to yield smaller particles. On the other hand, the bulky phenyl groups on the surface of SiO_2 particles may lesson the aggregation of individual particles in the solution upon solidification.

5 g of $K_8[g\text{-}SiW_{10}O_{36}]\cdot 14H_2O$ was suspended in a mixture of 20 mL H_2O and 15 mL EtOH, to which were added 4 g of TEOS and 2 g of MPh successively. Upon adding 2 mL of concentrated HCl, the suspension became clear. The reaction mixture was stirred for 3 hours till no oily droplets from the silane were observable. This solution was then divided into three portions.

Tetrabutylammonium (TBA) bromide (0.5 g) was added to the first portion of solution (1 g) to obtain a white suspension. Separation of the solid was achieved by centrifugation, which was rinsed twice with 10 mL of H_2O. The solid is a white powder, which tends to stick to the ceramic mortar and pestle. SEM images (Figure 16) of the sample show that the solid has a flaky texture and is composed of loosely packed micron- and submicron-size particles, which may be easily re-dispersed into appropriate solvent. EDEX indicated the solid contains mainly W and Si.

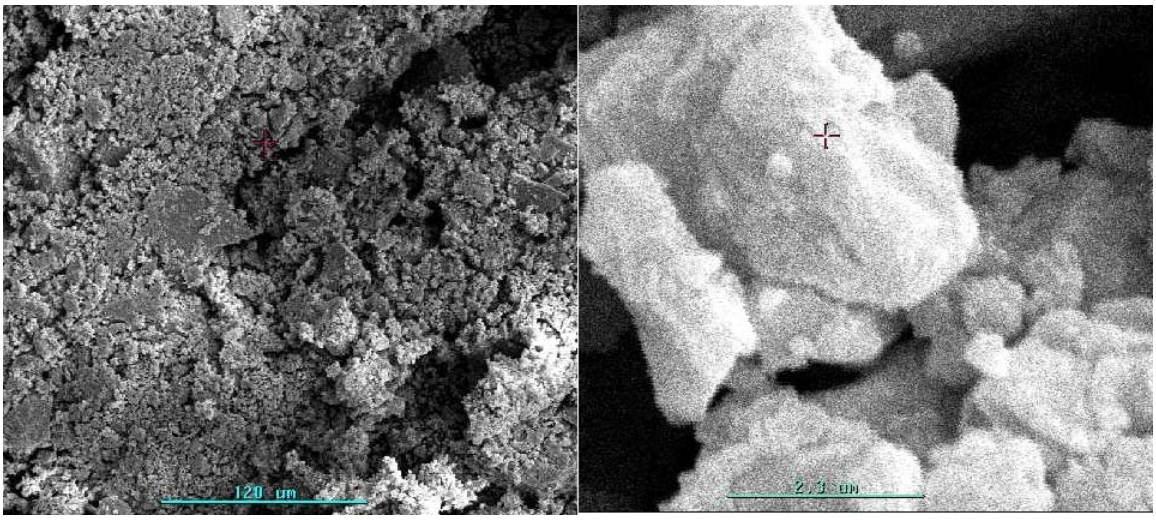

Figure 16. SEM image of the SiO2-Mph-HSiW10 hybrid in the TBA form. Scale bars are 120 (right) and 2.3 m (left), respectively.

The second portion of the solution was dried on an ultrasonic bath till the free solvent was all gone, leaving an off-white paste. Two apparently different solid phases were obtained; one is a white crystalline and fibrous formation, Figure 17, the other phase appeared to be yellow chunks, Figure 18, which turned out to consist of micron-size balls and flakes imbedded in an otherwise featureless matrix under SEM. According to EDEX, the white fibrous crystals are mainly KCl and the chunky material contains mainly W and Si. The fact that small discrete particles were obtained, although at a low yield, is an encouraging sign that Mph may indeed have played a critical role as speculated. The third portion was simply dried in air without ultrasonication or stirring and the solid looked like irregular chunks with a wide distribution of sizes.

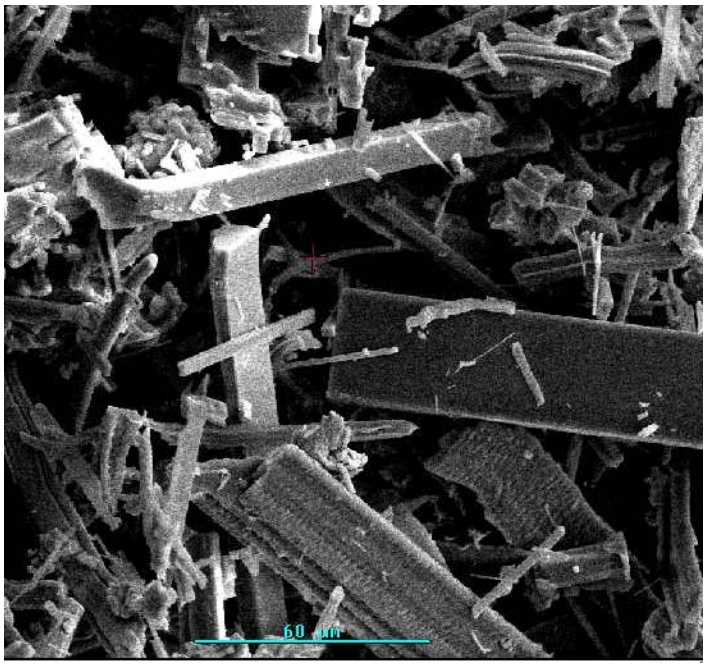

Figure 17. SEM image of the fibrous crystals of the SiO2-Mph-HSiW10 hybrid, scale bar 60 m.

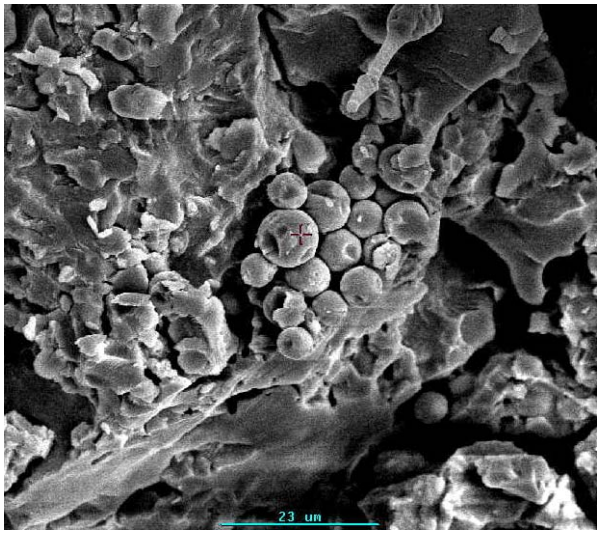

Figure 18. SEM image of the chunky solid of the SiO2-Mph-HSiW10 hybrid, scale bar 23 m.

3.3.2. Using pre-formed silica particles

While the in-situ method may provide a good chance of chemical bonding formation between HPA and the resultant silica, appropriate particle sizes and uniformity, two important properties for the membrane fuel cell performance, seem to be more readily achievable by using colloidal nanosized silica directly. Work done by the 3M team has shown that Keggin type HPA can be well retained in colloidal silica-PFSA composite films, as determined by the film weight losses upon washing. Lacunary HPAs were tested at CSM. Three types of colloidal silica were used: 5 nm (diameter) particles in basic (pH 9) aqueous media (ID 2326), 20 nm particles in basic aqueous media (ID 2327), and 20 nm particles in acidic media (ID 1042).

To carry this investigation further, parallel tests with the addition of a small amount of TEOS were performed. Since all the three colloidal SiO_2 particles and HPA anions are negatively charged, the HPA-SiO_2 interaction is electrostatically unfavorable and there is no driving force for the HPA-SiO2 hybridization to occur at the silica surface. TEOS was added in the hope that it may serve as a linker between HPA and the colloid particles: TEOS could react with both the lacunary HPA and the SiO_2 surface. A. Stein and coworkers reported using bis(silyl)ethane as a linking molecule between bulk silica and SiW10 (*Chem. Mater.* 2001, 13, 1074). The amount of TEOS is four equivalents of HPA anions that were calculated to form monolayer coverage on the colloidal silica surface by close packing. Note that the actual HPA concentration in the film is much less than that calculated for monolayer close packing coverage.

Room temperature water leaching results are summarized in

and Figure 19. Two trends appear to be prominent. First, colloid 2327 and 1042 (20 nm particles) retain HPA much better than 2326 (5 nm particles), shown as the solid bars in Figure **19**. Second, contrary to the desired linking effect, TEOS worsened the HPA leaching, more dramatically for the colloid 2327 and 1042, shown as the crossed bars. A possible reason for this is that TEOS did not bind to the silica surface, instead, it reacted with HPA to form hybrid particles that were soluble or easily dispersible.

Sample Composition	HPA wt%	SiO2 wt% From TEOS	SiO2 wt% From Colloid	HPA leaching%
2326-SiW11	4.9	0.0	8.7	71.5
2326-TEOS-SiW11	4.7	2.9	8.4	84.8
2327-SiW11	4.8	0.0	8.6	20.2
2327-TEOS-SiW11	4.9	0.6	9.0	84.5
1042-SiW11	4.8	0.0	8.8	9.7
1042-TEOS-SiW11	4.8	0.6	9.1	75.7

Table 2. Leaching results of ex-situ SiO_2-HPA containing membranes.

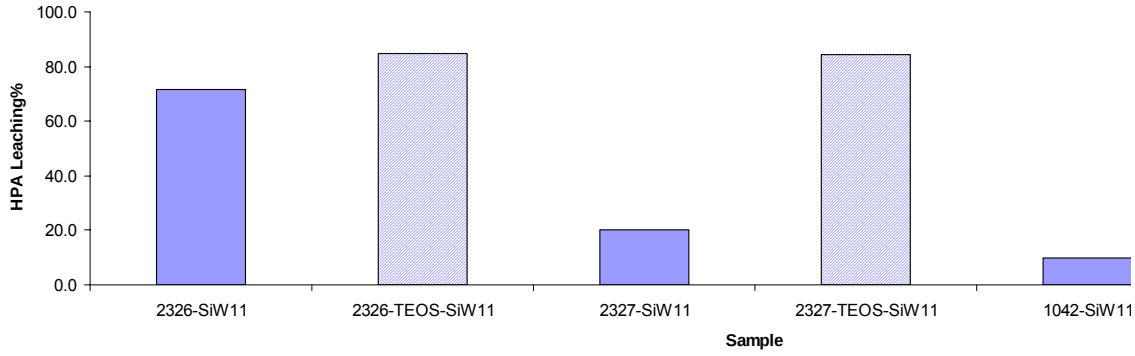

Figure 19**. Leaching results of ex-situ SiO2-HPA containing membranes**

3.4. In-situ synthesis of HPA-silica particles

The objective of this work is to develop composite membranes that most effectively immobilize HPA. To immobilize highly soluble HPA in the PFSA membrane, silica has been used as an anchoring reagent because of its demonstrated capability to entrap HPA. In general, two synthetic approaches have been employed. First, silica particles are produced from in-situ hydrolysis of tetraethoxysilane (TEOS) and

phenyltriethoxysilane (PhTEOS), and according to the reported coordination chemistry between lacunary HPA and silane, covalent bonding between HPA and silica may be formed thus effectively immobilizing the HPA molecules, as shown in Scheme 1. The other approach is to use colloidal nano-sized SiO_2 particles to physically entrap HPA. The effectiveness of the two immobilization methods was tested by washing the resultant membranes or hybrid solids with water and measuring the HPA concentration in the solution.

Scheme 1. Hybridization between lacunary HPA (e.g. $SiW_{10}O_{36}^{8-}$) and TEOS.

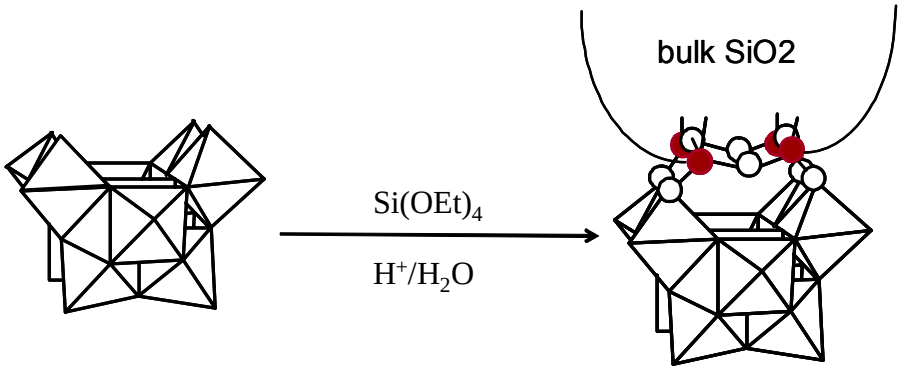

HPA-SiO_2-PFSA composite casting solutions were prepared by first mixing the HPA and the silica source materials (TEOS, PhTEOS, or colloidal SiO_2) for several hours to allow possible reaction between the two species, and then adding a desired amount of PFSA ionomer dispersion. Two readily available lacunary HPAs, $[SiW_{11}O_{39}]^{8-}$ (SiW11) and $[SiW_{10}O_{36}]^{8-}$ (SiW_{10}) have been chosen for this study. However, SiW_{10} can only be made in its salt form (K^+), which has a low solubility in water, therefore the film forming ability is much poorer than the SiW_{11} free acid. $H_4SiW_{12}O_{40}$, parent of the above two lacunary species, which does not have vacant coordination site for the silane hybridization chemistry to occur, was studied as a control.

One promising approach tried involved *in-situ* preparation of the silica particle with a phenyl silane to try and limit particle size, $HSiW_{10}$-SiO_2-Mph particles in the Nafion™ or the 3M ionomer during the membrane casting process. In the initial trials, the loading compositions of all the materials are approximately as follows, $H_8[\gamma\text{-}SiW_{10}O_{36}]$/Nafion™ = 5~8%, SiO_2/Nafion™ = 2~ 3%, Mph/Nafion™ = ~4%. The $HSiW_{10}$-SiO_2-Mph was first mixed and reacted for a few hours, and then the mixture was mixed with Nafion™ or the 3M ionomer solution under stirring and/or ultrasonication which was in turn cast into membrane. Membranes were annealed and subjected to rinsing with H_2O, 1N H_2SO_4 and H_2O in order to remove KCl and acidify the membrane. Preliminary ICP analysis of the wash solution indicated that the hybrid silica materials may have been all washed out, perhaps due to the "solubility" of SiO_2 or the hybrid under the rinsing conditions. Further investigation is underway to find the suitable conditions of the composite system. Recent work has focused on recasting 3M ionomer in the presence of HPA and silica, formed in-situ from tetraethoxysilane (TEOS) and phenyltriethoxysilane (Mph). Preliminary tests of the retention of HPA/SiO_2 in the composite film were carried out by soaking the membrane with DI water, 1 N H_2SO_4, and DI water at 80 °C up to boiling, and then by ICP analysis of the above washing solutions. Tapping mode AFM and ESEM were used to study the morphology and particle sizes. Currently we have just started to use nano-sized colloidal silica instead of TEOS to make composite membranes.

3.4.1. Membrane preparation

This optimized conditions for membrane casting were to spread with an applicator to yield controlled thickness (*ca.* 1.2 mil for final films), heated at 80 °C for 20 minutes, followed by 20 minutes' annealing at 160 °C. The general casting procedure for membranes using Ph end caps are described as follows.

(1) Make the hybrid solution: Suspend a small amount of potassium salt of $HSiW_{10}$ in 70/30 1-PrOH/H_2O mixture (the same solvent used to disperse the ionomer), add appropriate amount of TEOS and MPh, and then add HCl. The suspension cleared up after the addition of HCl.

(2) Mix the hybrid solution with ionomer solution: The clear solution of the above hybrid reaction mixture is mixed with the 3M ionomer solution. Shake, stir or ultrasonicate (for ~ one hour) to obtain a uniform mixture, wait till no bubbles are seen to cast.

Composition of the mixture is equivalent to: $H_8[SiW_{10}O_{36}]$/3Mion = 5 wt%, SiO_2/3Mion = 1.3 wt%, $PhSiO_3$/3Mion = 3.2 wt%. Starting material stoichiometry is: $K_8[SiW_{10}O_{36}]$/TEOS = 1:11 mol/mol, $K_8[SiW_{10}O_{36}]$/Mph = 1:10 mol/mol, consistent with the optimum $HSiW_{10}$ to TEOS loading (1:20) as determined in previous work.

(3) Cast films: Film casting was first done by directly pouring the solution on a glass plate, which resulted in thick and cracked membranes. Later a multiple clearance applicator (with 20 and 25 □m gaps) has been used to apply the casting solution and thin clear films are formed. Solution is dried at 80 °C for 10 min and annealed at 160 °C for 15 minutes.

3.4.2. HPA and SiO_2 retention in the composite membranes

Some thick membrane samples (made without the applicator), with 2 and 5% $HSiW_{10}$ loadings, were soaked in hot (80°C to boiling) DI water, 1 N H_2SO_4, and DI water for one hour each respectively. The wash solutions were analyzed by ICP for K, W and Si concentration, and the general observations are:

(1) For the 5% $HSiW_{10}$ samples, above 90% of all $HSiW_{10}$ anions were washed out after the 3-step (H_2O-H_2SO_4-H_2O) process, more (*ca* 2/3) in the first step with H_2O only. However, a sample loaded with 2% $HSiW_{10}$ showed that only 50% of $HSiW_{10}$ was washed out. This significant $HSiW_{10}$ loss is consistent with the observation that the film became less brittle after washing.

(2) Less than 5% of K^+ cations were washed out in the first H_2O rinsing step, while the rest leached out to the H_2SO_4 solution. This observation suggests that K^+ cations are strongly associated with the sulfonic groups in the ionomer and are exchangeable with protons.

(3) Compared to $HSiW_{10}$, silica are much better retained in the membrane; assuming no Si loss from Mph, 50 – 80% of SiO_2 from TEOS remained in the membrane after the three-step rinsing.

3.4.3. Tapping mode AFM

Morphology of a number of samples was studied by tapping mode AFM, TMAFM, images shown in Figure 20 - 23. Height images were taken in the hope of distinguishing HPA/SiO_2 particles from the polymer matrix; however, surface roughness may give the same affect. Phase imaging has the benefit of locating interfaces within the composite.

Figure 20 shows the height and phase images of as-received 3M control membrane (made at 3M) at the 500 × 500 nm scale. The image quality is low due to improperly applied tapping force so fine features have been damped out to some extent and some streaking occurred. But the phase image still shows distinguishable darker and lighter regions, which can be interpreted as the hydrophilic and hydrophobic domains of the ionomer, respectively. The fine worm-like lines through the image are mostly likely due to instrumental artifacts.

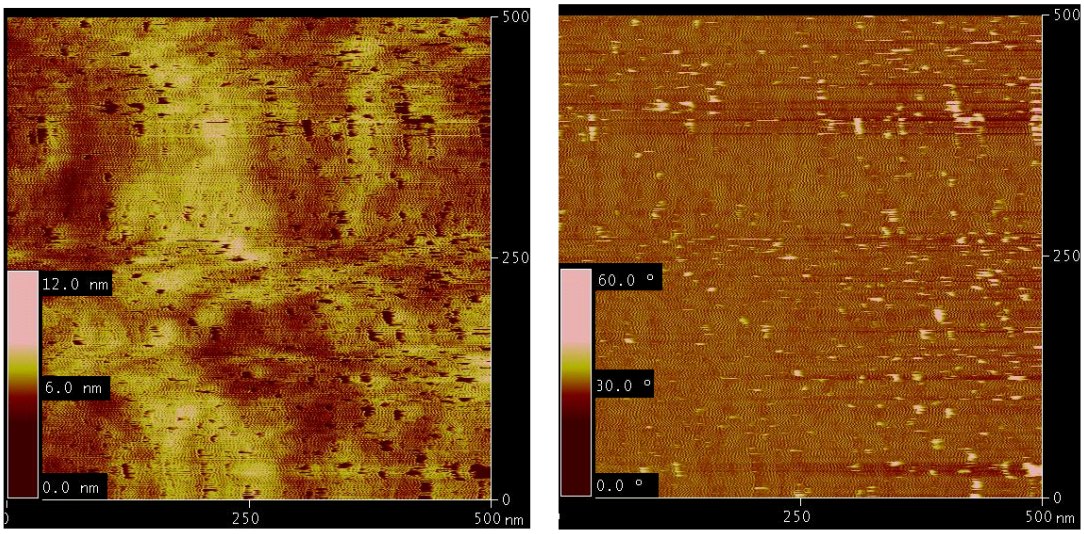

Figure 20. Height (left) and phase (right) images of 3M control membrane, made at 3M.

Figure 21 is of a recast 3M ionomer membrane prepared at CSM, which was washed with H_2O-H_2SO_4-H_2O. Although casting techniques may have affected the surface morphology, the main feature to be emphasized is the more distinguishable hydrophilic and hydrophobic domains in this sample than in the 3M control.

Figure 22 and Figure 23 are of membranes doped with 1 and 5% of HPW, both made at 3M. According to the phase images, higher PTA concentration seems to have resulted in more ordered arrangement of the hydrophilic/hydrophobic domain structures. Figure 22 shows the images of a $HSiW_{10}$-SiO_2 containing membrane before and after washing. Similar to the controls (Figure 20, Figure 21), washing the membrane resulted in a higher degree of the hydrophilic/hydrophobic phase separation.
The AFM of the HPA silica particles prepared in-situ from $HSiW_{10}$ is shown in Figure 24. The washed films shows some significant structural differences from the as prepared film. AFM study of the membranes is still very preliminary. More experiments will be done to verify the current observations and provide further information.

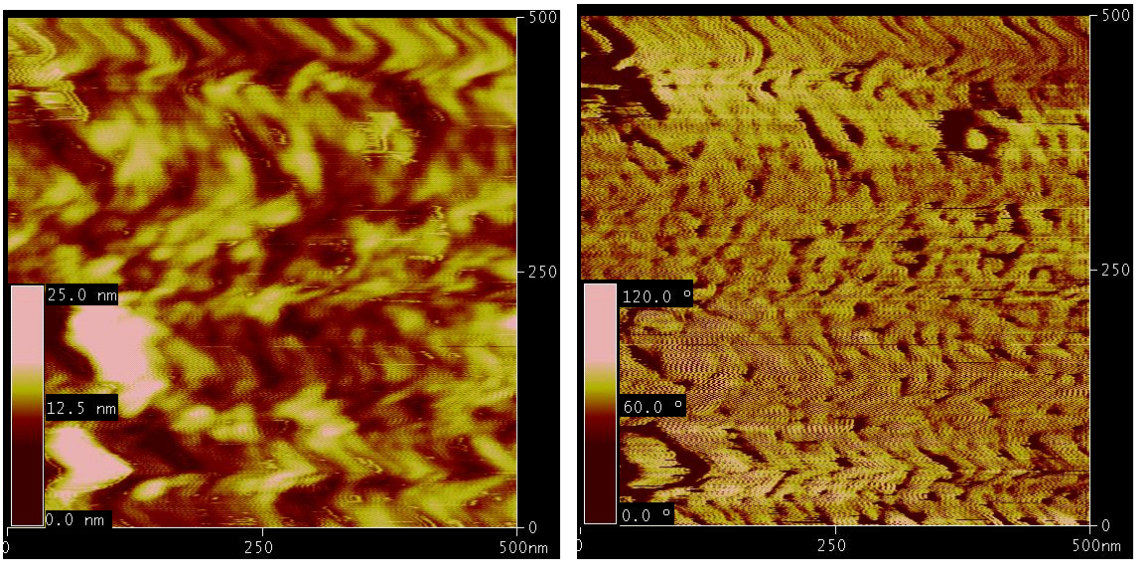

Figure 21. Height (left) and phase (right) image of 3M recast membrane, made at CSM, washed with H2O-H2SO4-H2O.

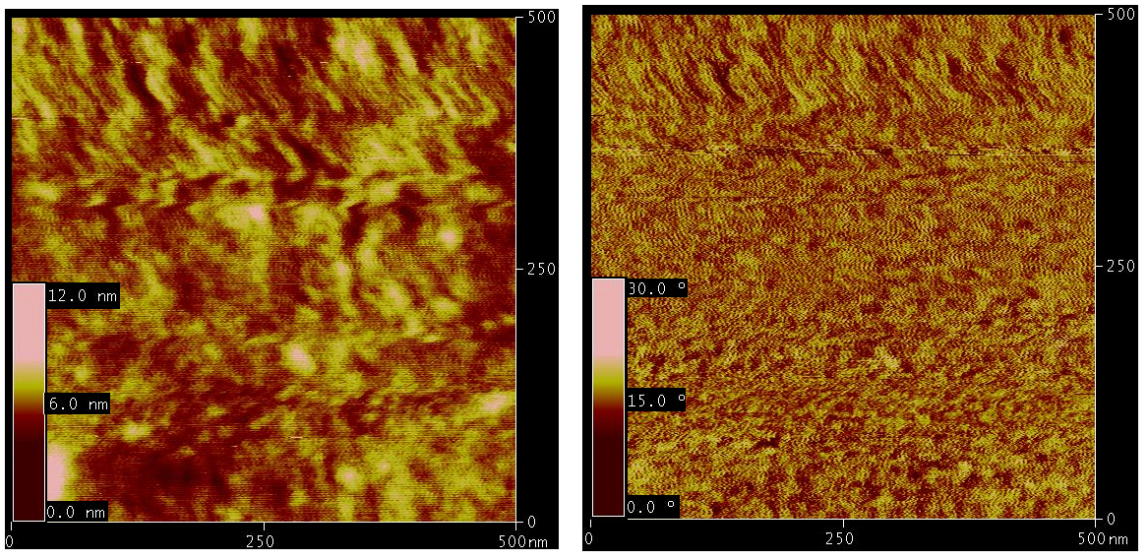

Figure 22. Height (left) and phase (right) image of 3M ionomer doped with 1% HPW, made at 3M.

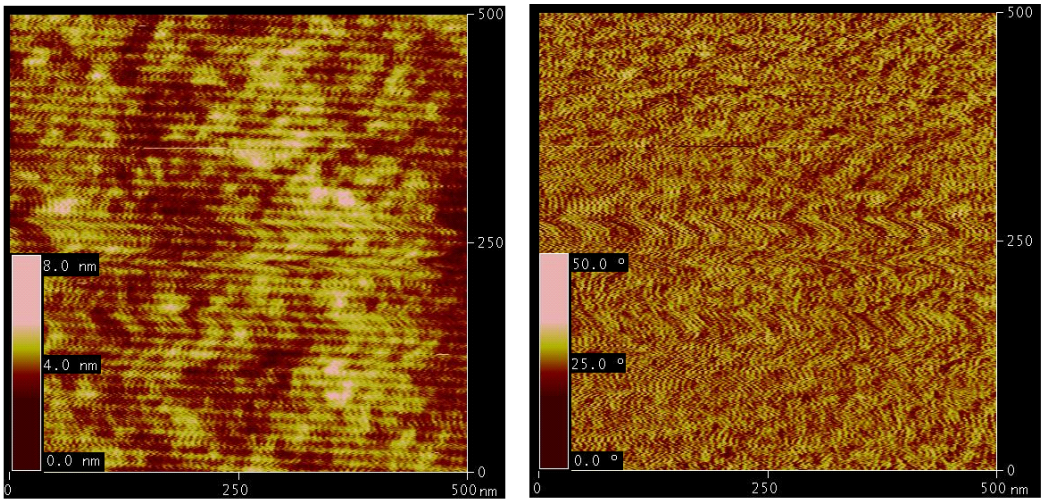

Figure 23. Height (left) and phase (right) image of 3M ionomer doped with 1% HPW, made at 3M.

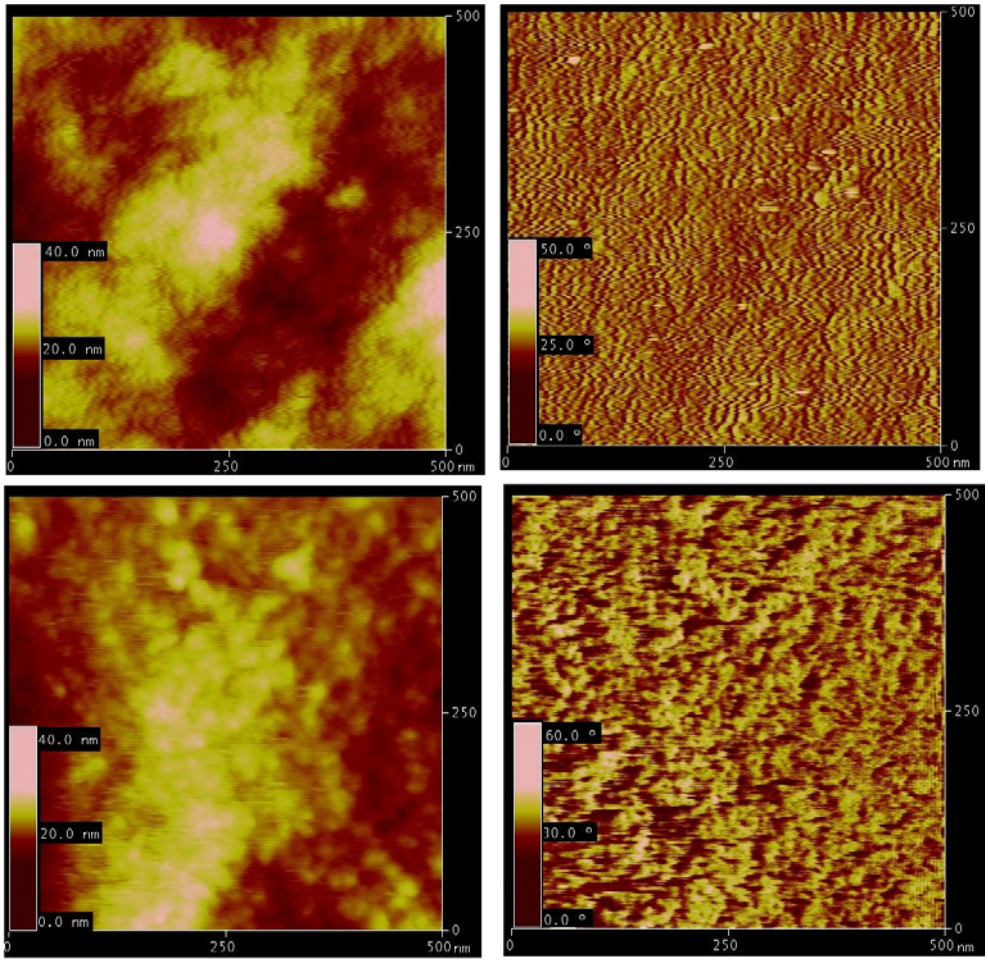

Figure 24. Height (left) and phase (right) image of 3M ionomers incorporated with HSiW10 and silica, made at CSM, as prepared film (top) and washed film (bottom).

3.4.4. ESEM

3M control, 3M recast membranes both look smooth under the microscope for up to 2000 magnification (higher magnification caused the membrane to burn instantly). Holes of a few microns in diameter were observed in a $HSiW_{10}$-SiO_2-PFSA composite film, as shown by the back scattering image, Figure 25. The surface of a SiW_{11}/SiO_2 containing membrane became from smooth to rough after the sample was subjected to H_2O-H_2SO4-H_2O rinsing. Only the rough surface is shown in Figure 26.

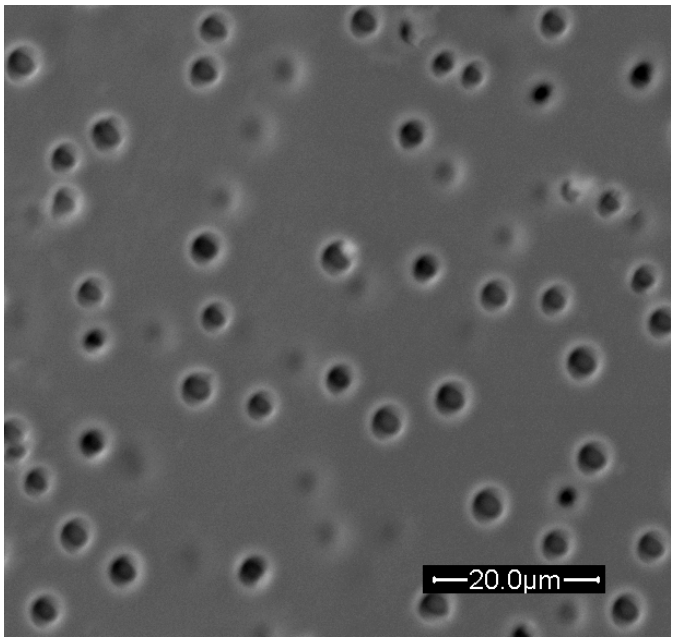

Figure 25. Back scattering image of a composite membrane containing HSiW10/SiO2.

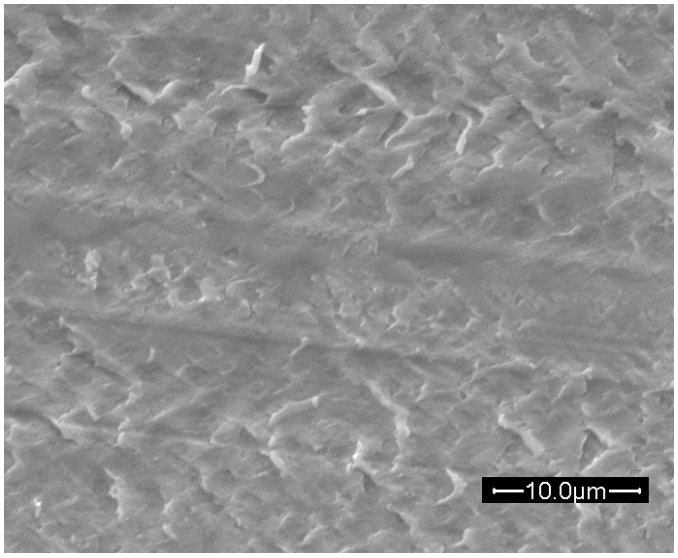

Figure 26. ESEM image of a HSiW11/SiO2-containing composite membrane washed with H2O-H2SO4-H2O.

3.4.5. Leaching experiments Ph capped

Membranes with the following compositions were prepared, percentages based on 100% ionomer by weight: HPA – (1) 1%; (2)5%; SiO_2 – (1) 5%, solely from TEOS or from a mixture of TEOS and PhTEOS; (2) 10%, solely from TEOS or from a mixture of TEOS and PhTEOS; (3) 10%, all from colloidal SiO_2 or from colloidal SiO_2 and TEOS.

Because of the large excess of TEOS and PhTEOS relative to HPA on the molar basis, the following reaction stoichiometry was used in calculating the concentration of silica and phenylated silica in the resultant films.

$Si(OEt)_4 + 2\ H_2O = SiO_2 + 4\ EtOH$

$PhSi(OEt)_3 + 3/2\ H_2O = PhSiO_{3/2} + 3\ EtOH$

Leaching experiments were performed by soaking the membranes in room temperature water (approximately 100 grams of water per gram of membrane) under mild agitation for one hour, and analyzing the tungsten concentration in the solution by ICP. A summary of typical film compositions (as loaded) and HPA leaching results is given in Table 3.

No.	HPA	HPA wt%	SiO2 wt%	PhSiO3/2 wt%	HPA leaching%
1A	SiW10	1.1	2.9	2.6	18
1B	SiW10	1.3	5.9	0.0	44
2A	SiW11	1.4	2.9	2.5	2
2B	SiW11	1.0	5.6	0.0	60
3A	SiW11	4.9	3.0	2.2	21
3B	SiW11	4.3	5.0	0.0	60
4A	SiW11	1.0	5.1	3.4	9
4B	SiW11	1.0	8.9	0.0	86
5A	SiW11	4.8	5.1	3.5	16
5B	SiW11	4.9	8.7	0.0	88
6A	SiW12	1.3	3.3	3.0	7
6B	SiW12	1.3	5.4	0	71
7A	SiW12	5.3	2.9	2.4	15
7B	SiW12	5.2	5.0	0	86
8	SiW12	5.0	0	0	85

Table 3. Summary of HPA leaching results of typical in-situ membranes

Loading composition of the film including the HPA identification, HPA weight percentage, and the converted SiO_2 and $PhSiO_{3/2}$ weight percentages are given. Samples 1A through 7A contain silica and phenylated silica, while 1B – 7B contain the inorganic silica only. Sample 8 was made by mixing 5% of SiW12 (HSiW) in the ionomer without the addition of any silica. There is a clear trend that the membranes with $PhSiO_{3/2}$ (the A's) leach out much less HPA than their counterparts without $PhSiO_{3/2}$ (the

B's). This trend is more easily seen in

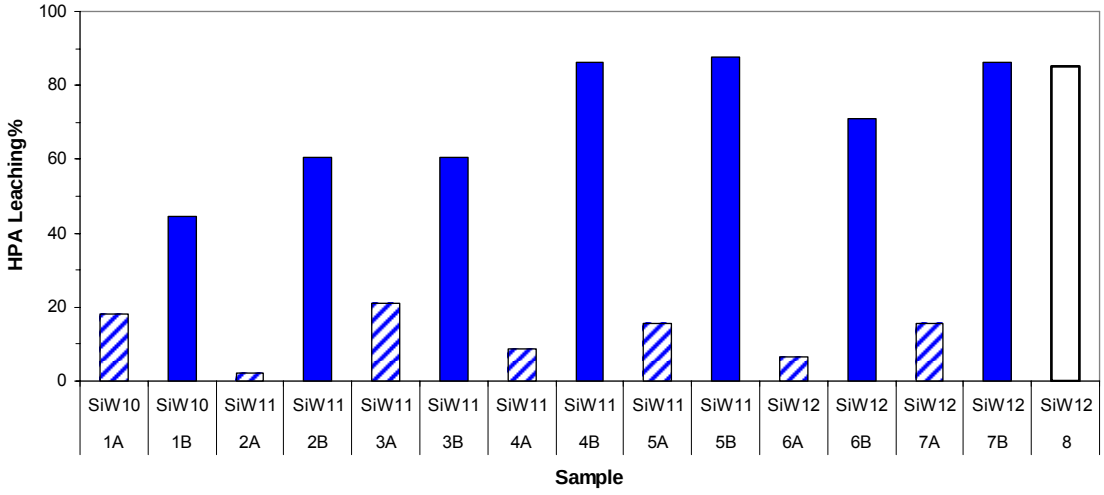

Figure 27 27, where the crossed bars are the ones with $PhSiO_{3/2}$ and solid bars without $PhSiO_{3/2}$.

Based on the existing literature, we have assumed that the hybridization chemistry would occur to the same extent for both TEOS and PhTEOS. The dramatically higher HPA retention capability of PhTEOS than TEOS can be explained as a result of the hydrophobicity introduced by the phenyl functional group. However, no evidence of the Si-O-W covalent bonding has been seen by ^{29}Si NMR in case of the ex-situ TEOS-HPA system where no ionomer was used. We haven't looked into the PhTEOS system for such information but it is suspected that PhTEOS may have reacted with lacunary HPA more completely, while TEOS may prefer self-condensation to hybridization under the sample preparation conditions.

Samples 6-8, doped with SiW12, were intended to show the advantage of lacunary HPA over Keggin type HPA, but the same trend was observed. The open bar in

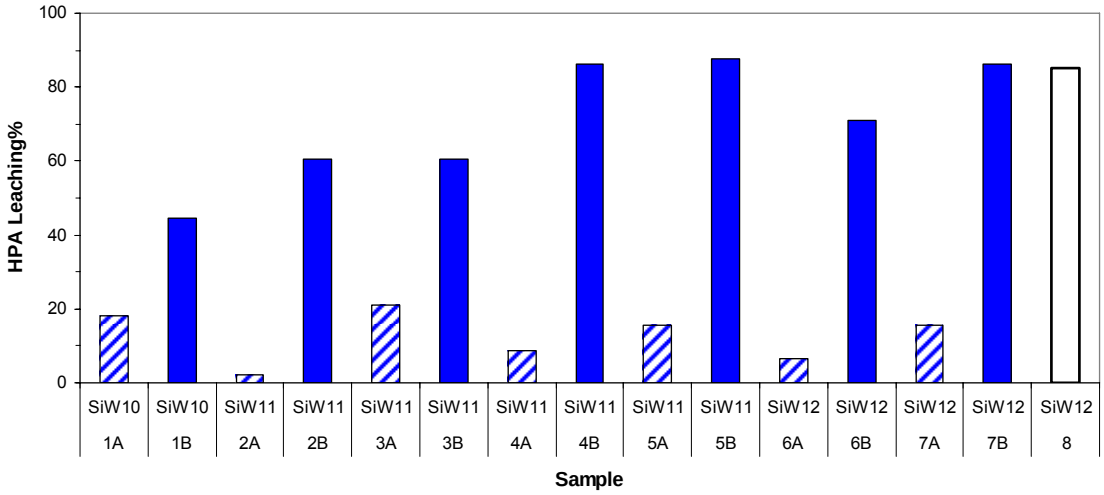

Figure 27 27 is a SiW12 doped sample without any silica, and the HPA leaching rate is approximately the same as sample 7B which has 5% in-situ generated SiO_2. These

observations strongly suggest that SiW12 may have undergone degradation to lacunary species under the membrane preparation conditions. Further analysis is needed to back up this speculation.

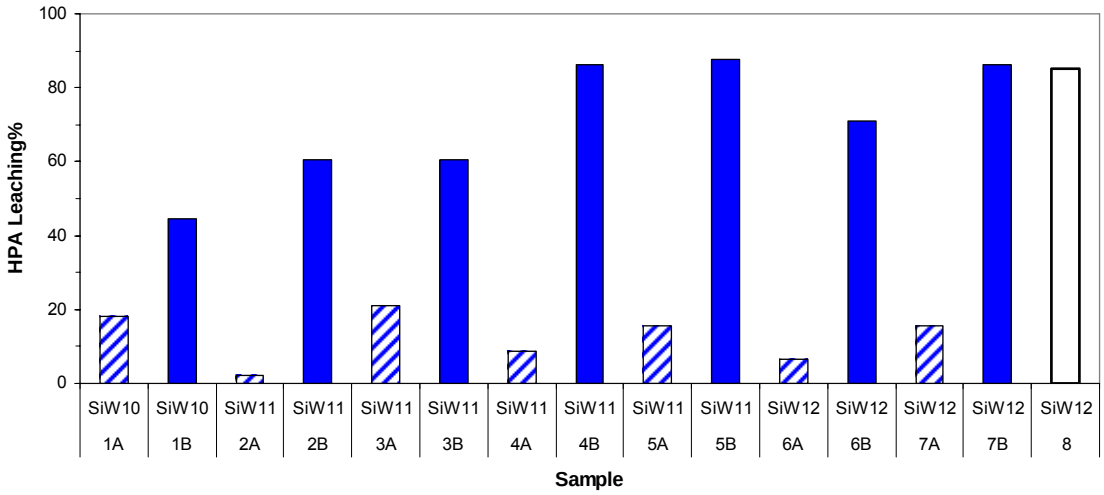

Figure 27. Bar chart of HPA leaching results of typical in-situ membranes.

3.4.6. Leaching experiments without Ph end caps

Leaching tests were performed on composite membranes fabricated by casting a solution mixture of lacunary silicotungstic heteropoly acids (HPA), tetraethoxysilane (TEOS), and a solution of 3M-ionomer onto a glass plate. After casting, the membranes were dried in an oven at 80°C for 20 minutes and then annealed in an oven at 160°C for 15-20 minutes. The HPA compounds used were $K_8[\gamma\text{-}SiW_{10}O_{36}]\bullet 14H_2O$, ($SiW_{10}$), and $H_8[\alpha\text{-}SiW_{11}O_{39}]\bullet 14H_2O$, ($SiW_{11}$). A prescribed amount of SiW_{10} or SiW_{11} was weighed out so that the final membrane composition of the HPA was 1-10 wt.% of the composition of the 3M-ionomer. The target mass of 3M-ionomer in the membranes cast was ~5 g. The solid HPA was dissolved in a minimum amount of a 70/30 mixture of 1-propanol/water. In the case of SiW_{10} a few drops of sulfuric acid (conc.) was added as a catalyst. To this mixture, a small amount of TEOS was added so that the molar ratio of TEOS / HPA was about 15/1, 20/1, 25/1 or 50/1. This mixture was stirred overnight. Then about 5 g of a 21-25% 3M-ionomer casting solution was added to the mixture and stirred for another hour. This solution was cast onto a glass plate using a membrane spreader and then dried and annealed as described above. The mass of each membrane was recorded and the average thickness was determined from 12 thickness measurements spread over the membrane.

Membrane compositions are described by the following code: #.#.#.#

1st number: 1=SiW_{10}, 1=SiW_{11}

2nd number: wt.% of HPA

3rd number: TEOS/HPA molar ratio

4th number: PHTEOS/HPA molar ratio

Note: In the membranes prepared for this study, no phenyl tetraethoxysilane (PHTEOS) was added to the membranes.

Leaching experiments were performed by immersing the membrane in 150 mL of water for one hour at either room temperature or boiling temperature with stirring from a magnetic stir bar. The pH of the solution was measured before and after the leaching

test. Samples of the leaching solution were analyzed using ICP-AES to determine the concentrations of Silicon, Tungsten and Potassium that leached into the water from the membrane. From these values, the amount of HPA and TEOS leached from the membrane was determined. The value for HPA mass loss was determined from the tungsten concentration in the leached solution, since the tungsten only can come from HPA. The values for TEOS mass loss was determined from the silicon concentrations in the leached solution. This is based on the assumption that the contribution of Si into the leached solution from TEOS is much greater than the contribution of Si from HPA and therefore the contribution of Si from the HPA is negligible.

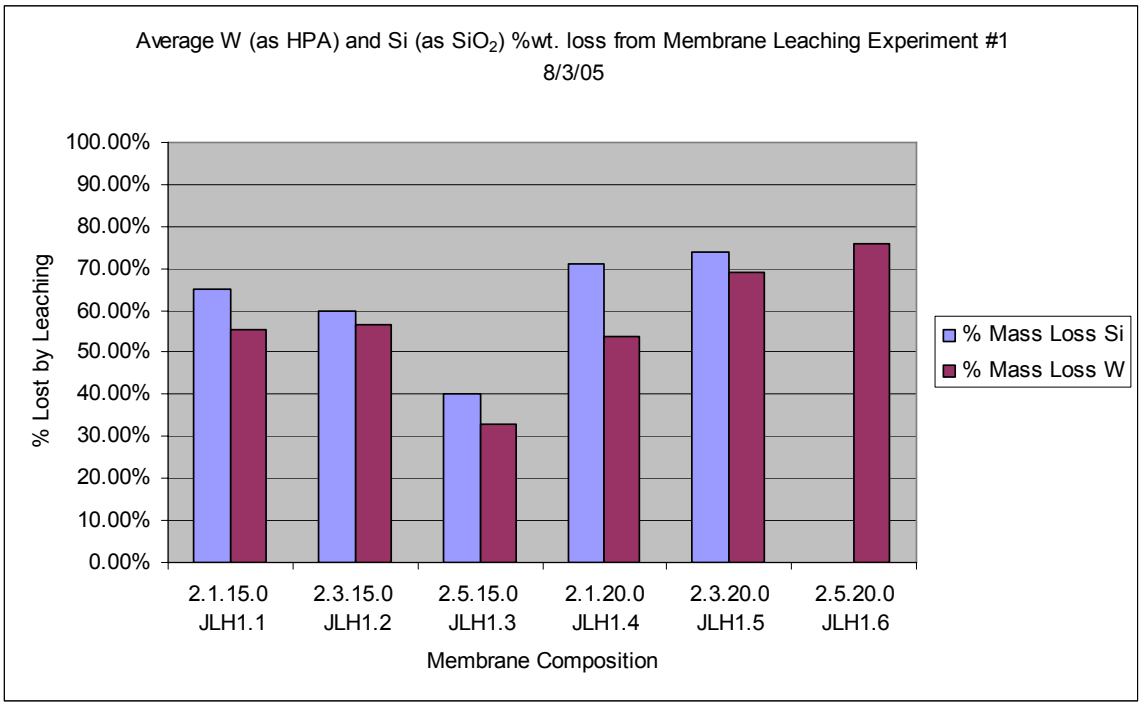

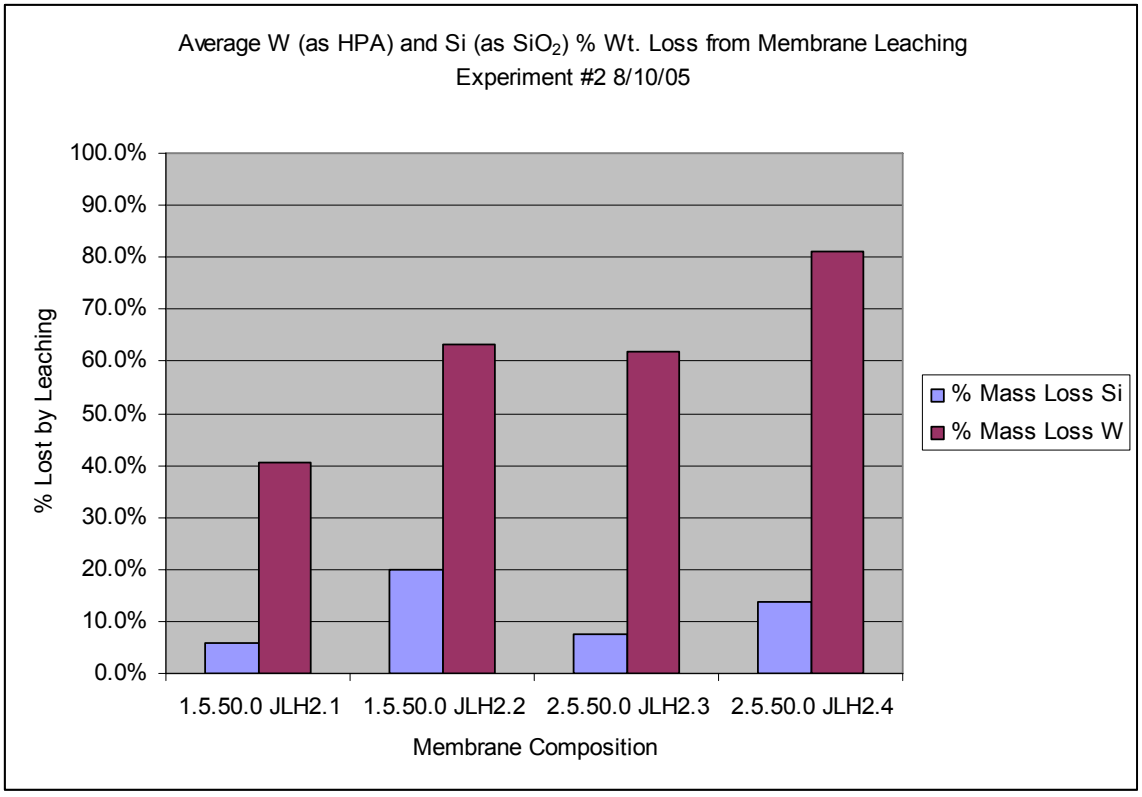
Average W (as HPA) and Si (as SiO_2) % Wt. Loss from Membrane Leaching Experiment #2 8/10/05
100.0%
90.0%
80.0%
70.0%
60.0%
50.0%
40.0%
30.0%
20.0%
10.0%
0.0%
% Lost by Leaching
1.5.50.0 JLH2.1
1.5.50.0 JLH2.2
2.5.50.0 JLH2.3
2.5.50.0 JLH2.4
Membrane Composition
% Mass Loss Si
% Mass Loss W

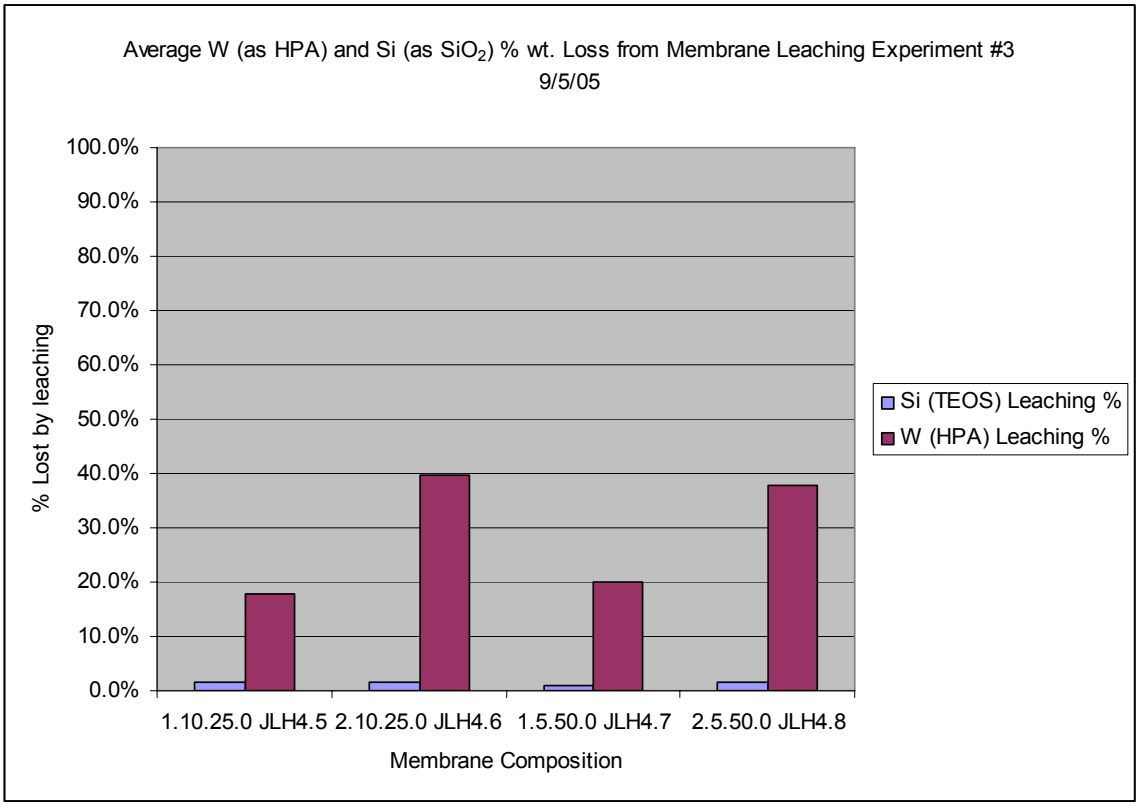
Average W (as HPA) and Si (as SiO_2) % wt. Loss from Membrane Leaching Experiment #3 9/5/05
100.0%
90.0%
80.0%
70.0%
60.0%
50.0%
40.0%
30.0%
20.0%
10.0%
0.0%
% Lost by leaching
1.10.25.0 JLH4.5
2.10.25.0 JLH4.6
1.5.50.0 JLH4.7
2.5.50.0 JLH4.8
Membrane Composition
Si (TEOS) Leaching %
W (HPA) Leaching %

Conclusion

- In all leaching experiments, very little (<2%) potassium was found in the leached solution. The ionic character of this ion tends to hold it in the membrane, probably attached to the sulfonic acid groups.
- Membranes JLH1.1 to JLH1.6 were annealed for only 15 minutes. The rest of the membranes were annealed for 20 minutes. The membranes annealed for longer periods seemed to show somewhat less tungsten leaching and much less silicon leaching.
- In general, membranes with a higher wt.% of HPA compared to 3-M ionomer in them show less silica leaching.
- Membranes with higher mole ratios of TEOS to HPA also show less silica leaching.

3.5. Comparison of retention of HPA by silica

HPA retention was also investigated in standalone silica-HPA (80:20 by weight) hybrid powders and the results are given in Table 4 and In the powder form, the colloidal silica particles will agglomerate and form large grains (micron and above), while in the membrane, it is more likely that the particles agglomerate to a much lesser extent or are even mono dispersed. The leaching experiments do show a difference than the corresponding membrane; HPA retention is considerably less, as shown by the higher solid bars than in the membrane, Figure 28.

Prompted by the same idea as for the ex-situ membrane system, the effect of TEOS in the colloid system was investigated. And the same result was obtained: addition of TEOS in the colloidal SiO2-HPA mixture worsened HPA leaching.

The two in-situ silica-HPA hybrids, where the silica came solely from TEOS, exhibited much better HPA retention than all the other solids that involves colloidal silica. This again is consistent with the covalent bonding formation between TEOS and lacunary HPA, while colloid system is simple entrapment governed by electrostatic interactions.

Composition (80%SiO2-20%HPA)	[HPA anion] leached %
1042-SiW10	80
1042-TEOS-SiW10	81
1042-SiW11	100
1042-TEOS-SiW11	99
2326-SiW10	50
2326-TEOS-SiW10	89
2326-SiW11	52
2326-TEOS-SiW11	97
2327-SiW10	62
2327-TEOS-SiW10	94
2327-SiW11	86
2327-TEOS-SiW11	108
TEOS-SiW10	21
TEOS-SiW11	1

Table 4. Leaching results of ex-situ and in-situ SiO2-HPA solids.

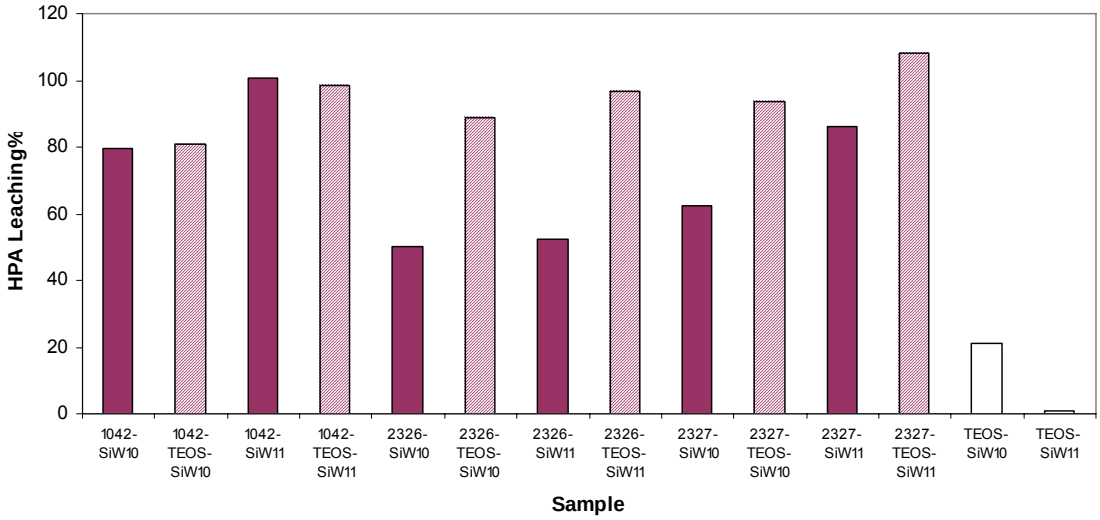

Figure 28. Leaching results of ex-situ and in-situ SiO_2-HPA solids.

In summary, three general trends have been observed.

1. PhTEOS, compared to TEOS, can effectively improve HPA retention in membranes probably due to more complete hybridization with the lacunary HPA as well as reduced hydrophilicity of the resultant hybrid.
2. Larger (20 nm) colloidal silica is better than the smaller (5 nm) colloid in retaining HPA in membranes.

3. Without the addition of PFSA ionomer, the in-situ generated SiO_2 is clearly much more effective in immobilizing HPA than colloidal SiO_2, consistent with the reported organosilane-HPA hybridization chemistry.

3.6. NMR Charcterization

Solid-state ^{29}Si cross-polarization, magic-angle spinning (CPMAS) NMR experiments were performed on five different samples of TEOS containing PTA, $KSiW_{10}$, and $KSiW_{11}$ heteropoly acids to form the various silicate solids. The hypothesis is that the ^{29}Si CPMAS spectra will provide evidence for a heteropoly acid silicate matrix covalent bond. The CPMAS NMR experiment is inherently non-quantitative because the rate of magnetization transfer (cross-polarization) from the protons to the ^{29}Si depends on the structure of the material. Crudely, the rate of the magnetization transfer to the ^{29}Si nuclei depends on the number of protons near that ^{29}Si. Quantitative information can be obtained by performing a variable contact time (cross-polarization time) experiment as shown in Figure 29 for the 1:15 K-SiW_{10}-TEOS solid

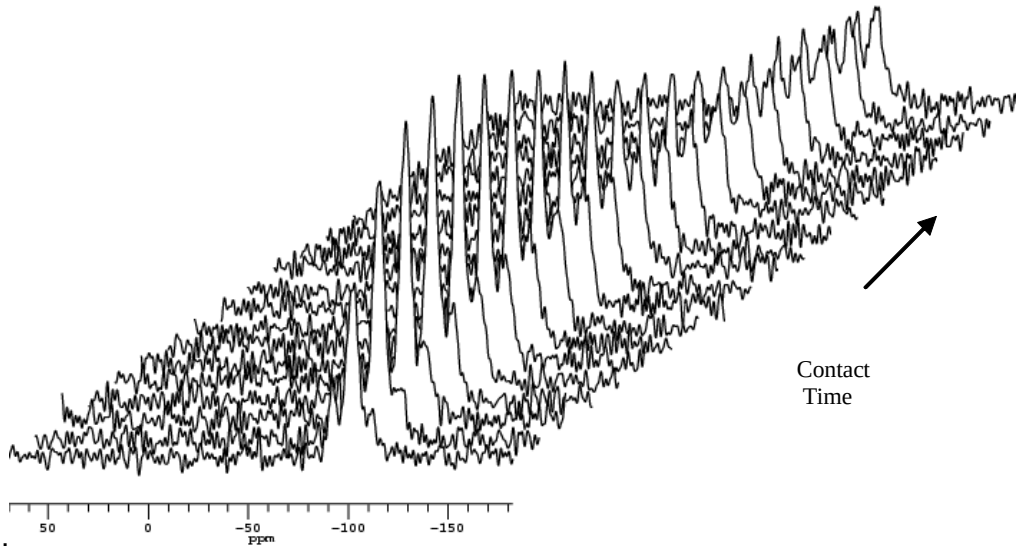

Figure 29. 79.4 MHz 29Si variable contact time CPMAS NMR of 1:15 SiW10-TEOS solid.

From experiments similar to that shown in Figure 29, plots of Intensity versus Contact Time can be made for each sample; a typical example is shown in Figure 30.

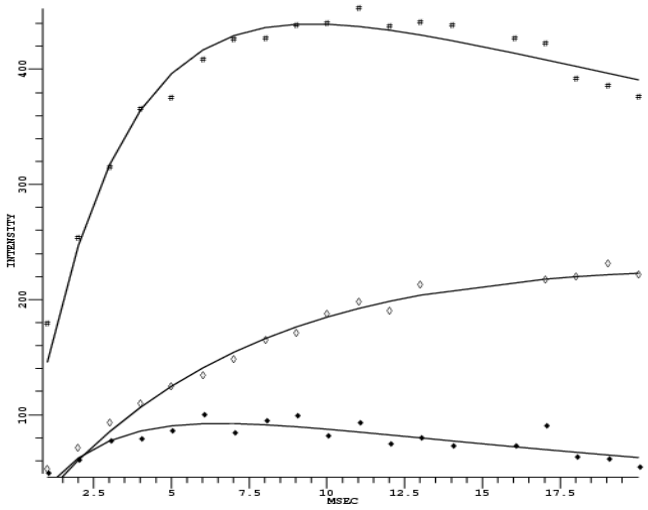

Figure 30. Plot of Intensity versus Contact Time for a 29Si variable contact time CPMAS NMR experiment for solid obtained from TEOS hydrolysis.

The Intensity versus Contact Time data are fit to the following equation:

$$I(\tau) = (I^*)\left[\frac{T_{1\rho H}}{T_{1\rho H} - T_{SiH}}\right]\left(e^{\left(-\tau/T_{1\rho H}\right)} - e^{\left(-\tau/T_{SiH}\right)}\right)$$

where I(□) is the observed intensity at contact time □, I* is the corrected intensity, $T_{1□H}$ is the ^1H spin-lattice relaxation time in rotating frame, and T_{SiH} is the Si-H cross-relaxation rate.

Based on the observation that the ^{29}Si chemical shift of the tetrahedral silicon site in a Keggin anion, with local structure $Si(OW)_4$, is about –85 ppm and using an analogy with ^{29}Si NMR of aluminosilicates, one can estimate that substitution of one OSi unit by one OW unit amounts to a chemical shift change of (110 – 85)/4 = 6.25 ppm where –110 is the ^{29}Si chemical shift of silicon with local structure $Si(OSi)_4$. Thus, the postulated local chemical structure of the Keggin anion to TEOS of $Si(OSi)_2(OW)_2$ should have ^{29}Si chemical shift of about –110 + 6.25 + 6.25 = -97.5 ppm, a value very close to that of ^{29}Si with local structure $Si(OSi)_2(OH)_2$ found in pure TEOS. Thus, one would expect that the intensity of the ^{29}Si peak at this chemical shift value to increase as the number of Keggin anion and TEOS linkages increase. That this is not the case is seen in a quasi-quantitative way in Figure 31 where ^{29}Si CPMAS NMR with a contact time of 5 ms spectra of various Si-heteropoly acid and TEOS solids are shown. The peak with a chemical shift at about –98 ppm decreases as the amount of heteropoly acid increases A quantitative picture is shown in Figure 32 where the corrected ^{29}Si intensities of the $Si(OSi)_4$, $Si(OSi)_3OH$, and $Si(OSi)_2(OH)_2$ peaks are shown. The intensity of the silanol and geminal silanol peaks decrease with the addition of heteropoly acid indicating that the heteropoly acid promotes hydrolysis of the TEOS, i.e., there is no evidence indicating the formation of a Keggin anion – TEOS chemical bond.

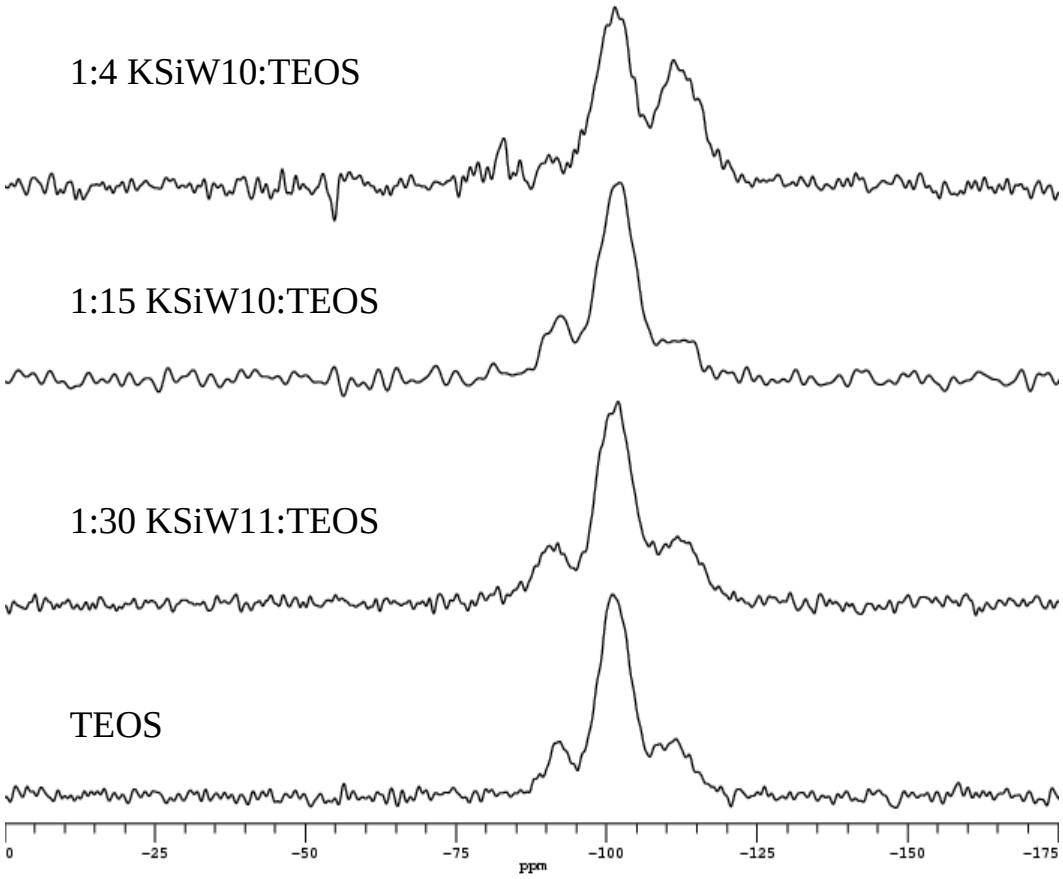

Figure 31. 79.4 MHz 29Si CPMAS NMR spectra of various heteropoly acid and TEOS solids obtained with a contact time a 5 ms.

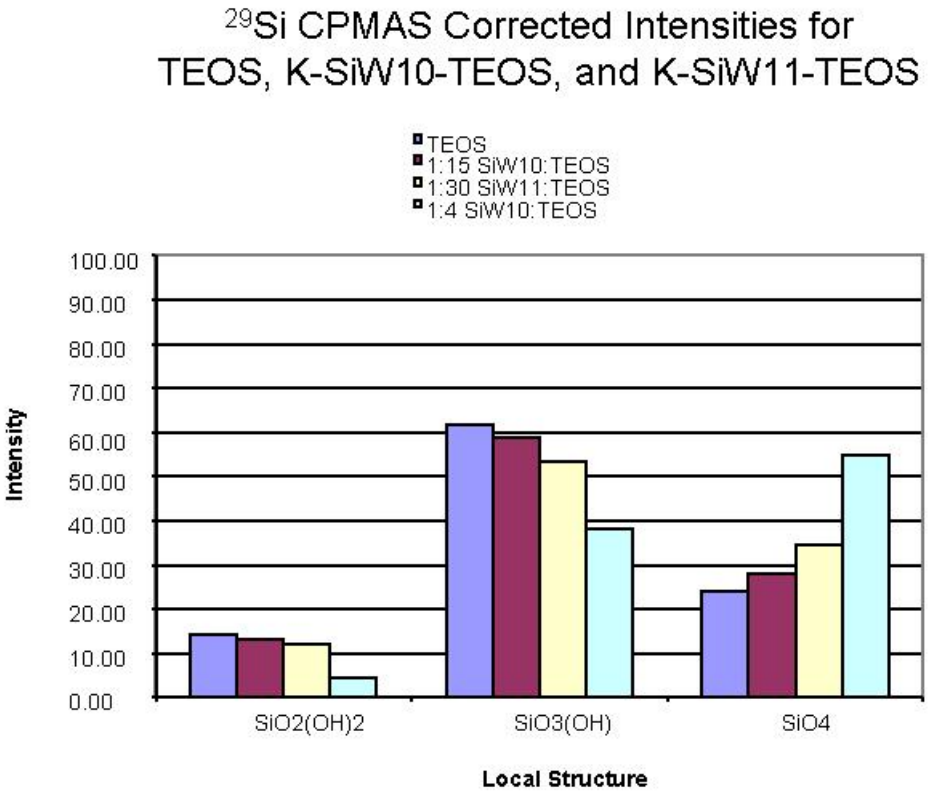

Figure 32. Plot of corrected 29Si intensity from 29Si CPMAS NMR experiments for silicon sites with local structures Si(OSi)4, Si(OSi)3OH, and Si(OSi)2(OH)2.

4.0 NMR Proton transport Measurements

A large amount of time was spent using NMR to focus on the temperature dependence and relative humidity (RH) dependence of diffusion coefficients of PFSA and PFSA-HPA membranes. In addition ^{1}H chemical shift measurements of the PFSA and PFSA-HPA membranes were obtained. The ^{1}H diffusion and chemical shift measurements were recorded using samples prepared in a sealed NMR tube as shown in Figure 33. This is the so-called dry method or a sample with about 0% RH.

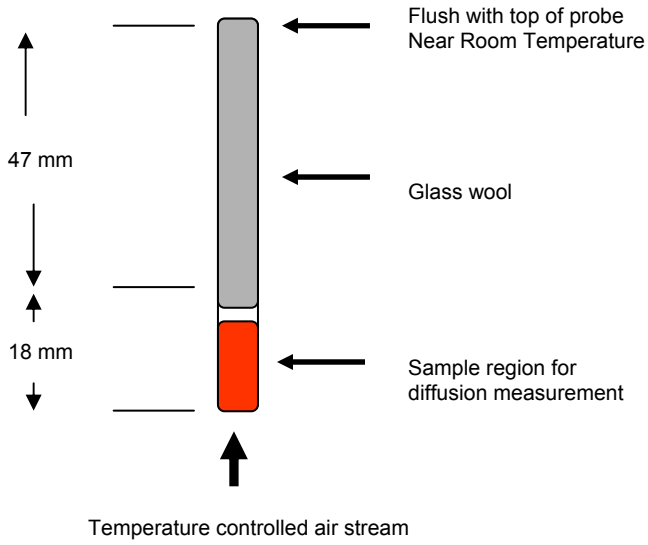

Figure 33**.** Sample cells for diffusion measurements, dry method.

Diffusion coefficient measurements were performed using Pulsed-Field Gradient Spin-Echo (PGSE) NMR using the Stimulated-Echo pulse sequence (J.E. Tanner, *J. Chem. Phys*., 52, 2523 – 2526 (1970)) shown in Figure 34. The parameters δ and Δ are time intervals and g is the amplitude of the applied pulse-field gradient magnetic field. Before we discuss diffusion coefficients obtained using this pulse-sequence, note that an experiment performed without the gradient pulses acts as a chemical shift filter, that is, not all protons present in the sample are necessarily observed. Hence, chemical shift measurements obtained on the various samples using the Stimulated-Echo pulse sequence of Figure 34 with the applied gradient amplitude equal to zero should provide chemical shift information on those protons for which diffusion coefficients are measured.

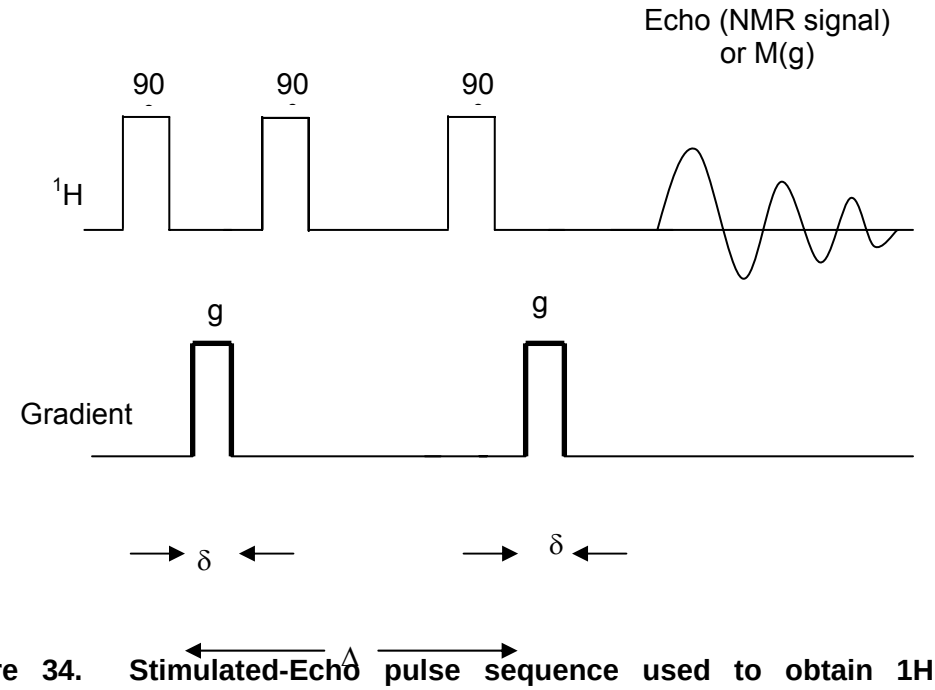

Figure 34. Stimulated-Echo pulse sequence used to obtain 1H diffusion coefficients using Pulsed-Field Gradient Spin-Echo (PGSE) NMR.

The ^{1}H NMR spectra obtained for the 0% RH PFSA-HPW, PFSA-HSiW, and PFSA-HZnW membranes are shown in Figure **35**, Figure 36, and Figure 37.

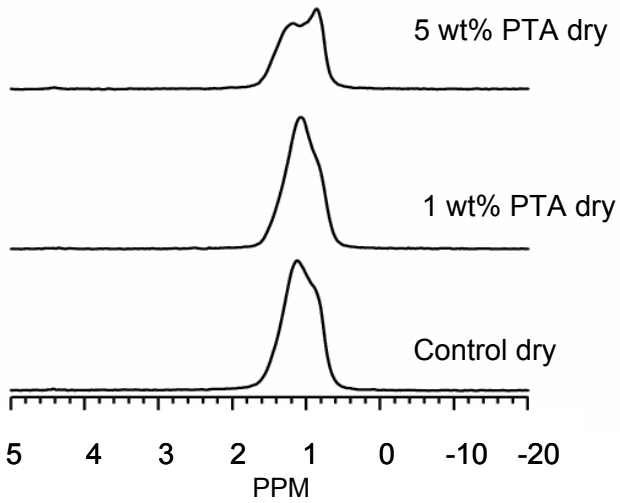

Figure 35**. 400 MHz ^{1}H NMR Spectra of Dry HPW Samples at 25 ^{o}C.**

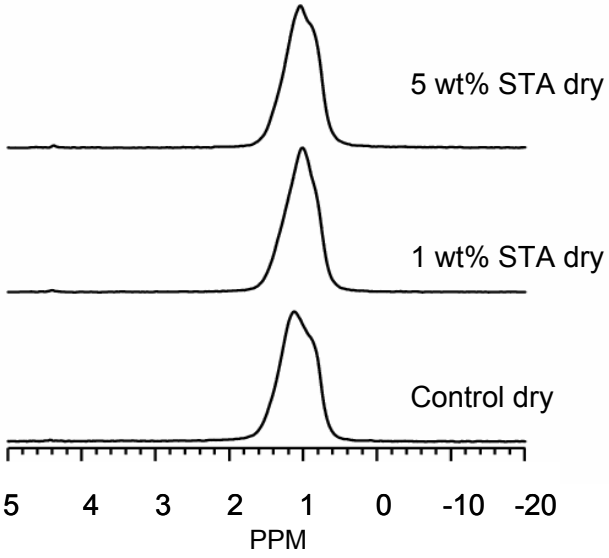

Figure 36**. 400 MHz ^{1}H NMR Spectra of Dry HSiW Samples at 25 ^{o}C.**

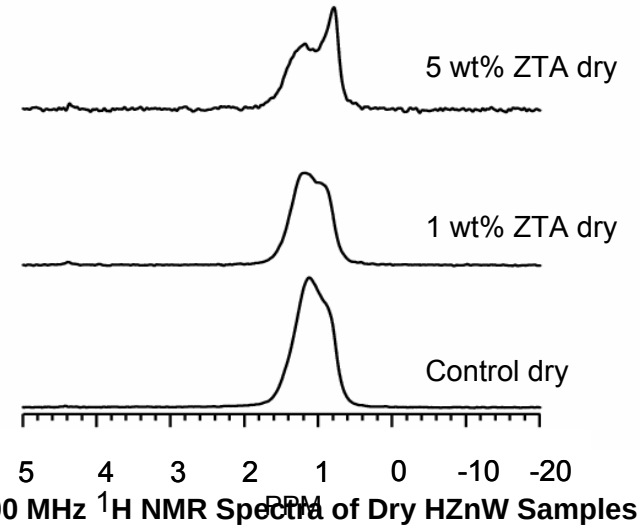

Figure 37.400 MHz ^{1}H NMR Spectra of Dry HZnW Samples at 25 ^{o}C.

All of the spectra shown in Figure 35, Figure 36, and Figure 37 have the same general appearance, that is, there is evidence of two overlapping, broad resonance lines with ^{1}H chemical shifts the order of 10 ppm. Some physical insight into the meaning of the observed ^{1}H chemical shifts can be obtained by defining the average chemical shift, $\langle\delta\rangle$, as

$$\langle\delta\rangle = \sum_i p_i \delta_i$$

where p_i is the probability that the proton is in site i with chemical shift δ_i. The p_i values are obtained from integration of the ^{1}H NMR spectra. A plot of $\langle\delta\rangle$ for each of the PFSA-HPW, PFSA-HSiW, and PFSA-HZnW samples is shown in

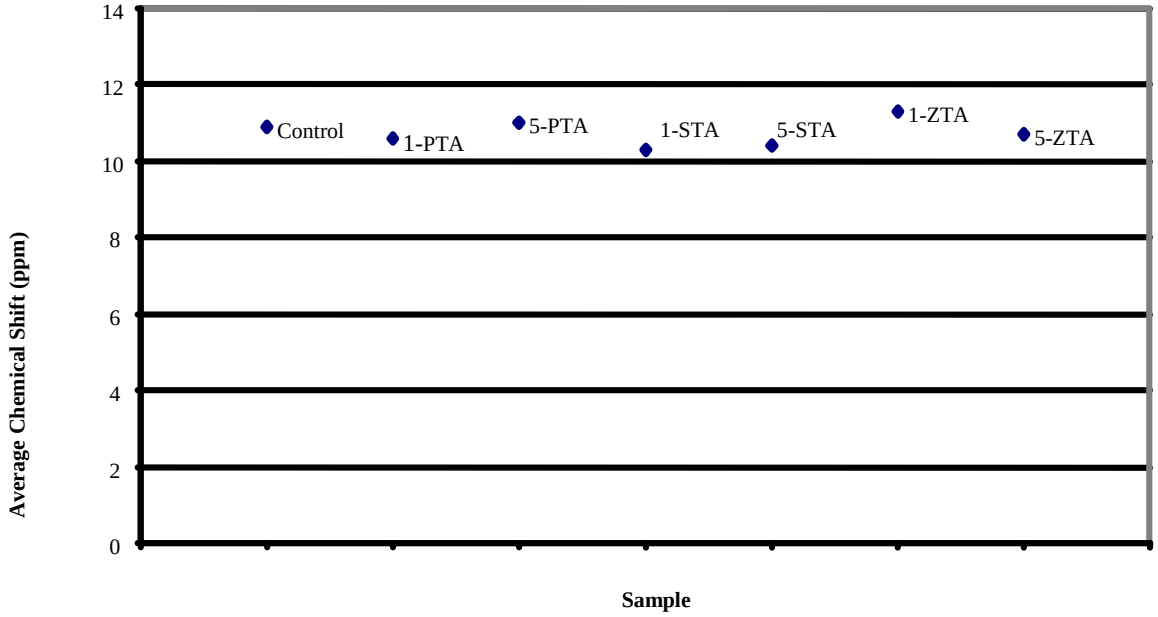

Figure 38. The average ^{1}H chemical shift for each sample is about 11 ppm. It should be noted that higher values of $\langle\delta\rangle$ correspond to more acidic protons.

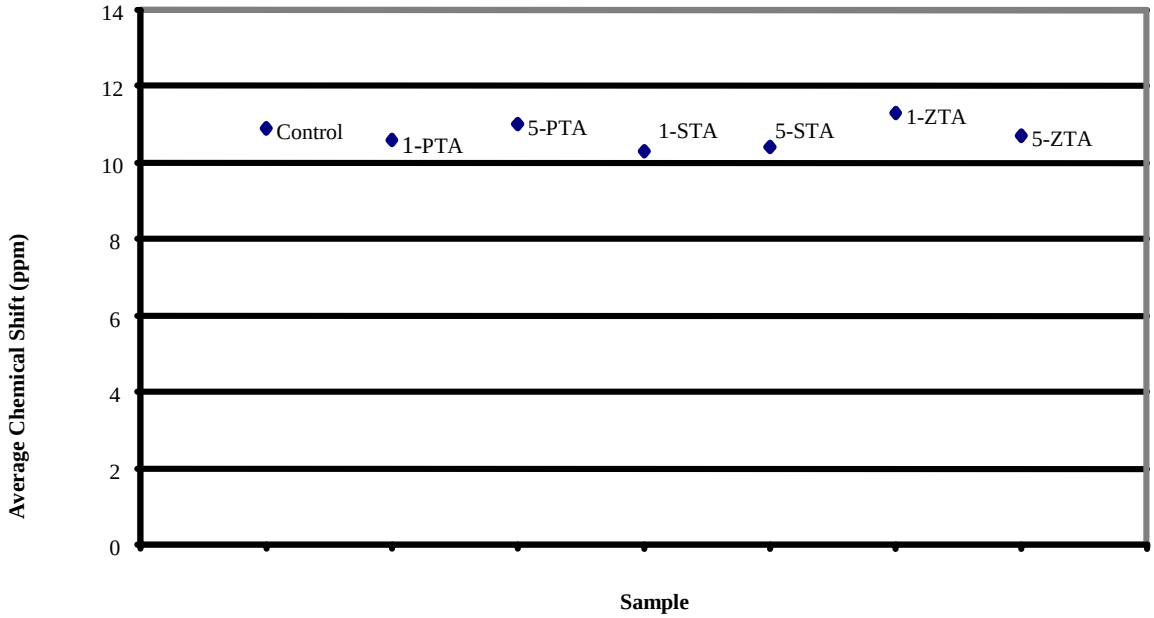

Figure 38.Average Chemical Shifts for Dry PFSA-HPW, PFSA-HSiW, and PFSA-HZnW Samples.

The NMR signal, M(g), obtained in the PGSE experiment described in Figure 34 is given by the following equation:

$$M(g) = M(0)e^{-\gamma^2 D\delta^2(\Delta-\frac{1}{3}\delta)g^2}$$

In this equation γ is the gyromagnetic ratio and D is the diffusion coefficient. If the protons diffuse during the time Δ then a set of spectra similar to that shown in Figure 39 will be obtained. A plot of the integrated intensities obtained in Figure 39 versus g is shown in Figure 40. The best fit of the data to a Gaussian function permits the value of D to be obtained from the expression for M(g) above.

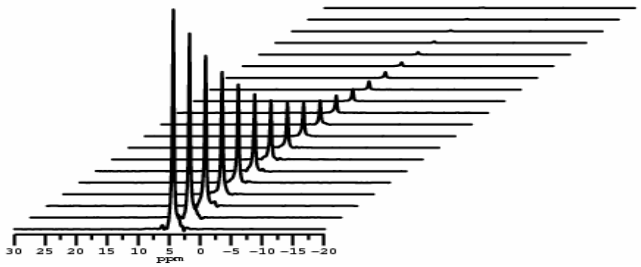

Figure 39.NMR Spectra versus Pulsed-Field Gradient Amplitude g.

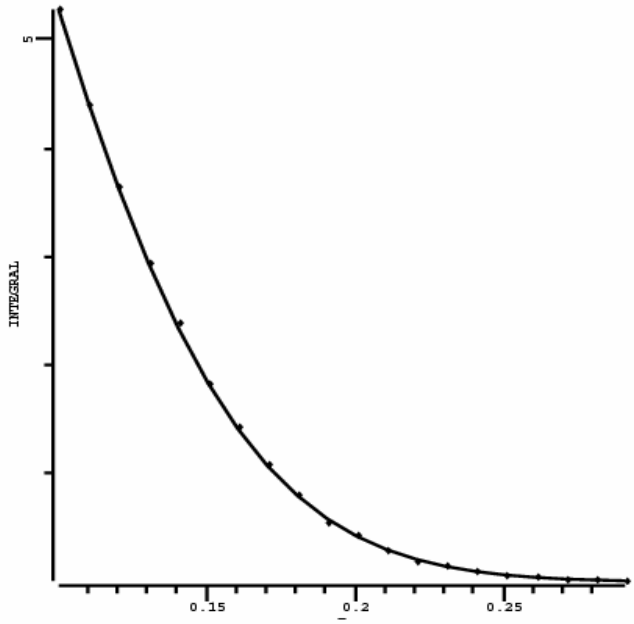

Figure 40. Intensity versus Pulsed-Field Gradient Amplitude g.

Generally, the temperature dependence of diffusion coefficients will exhibits an Arrhenius behavior, that is, the D value is given by

$$D(T) = Ae^{-E_a/RT}$$

Where T is the absolute temperature, A is a constant, E_a is the activation energy, and R is the universal gas constant. This equation predicts that D(T) will increase as T increases. If this behavior is not observed then this indicates that the sample has changed; for the PFSA-HPA samples this probably means that the sample has dehydrated.

Plots of D(T) versus T are shown in Figure 41 and Figure 42. All samples show evidence of dehydration at temperatures above 70 ^{o}C. All samples with PTA or STA show larger D values than the control. The D values for the PTA membranes are independent of loading level while the 5 wt% STA membrane has larger D values than the 1 wt% STA membrane. Generally, the D values for all samples are the order of 10^{-7} cm^2 s^{-1}. This description of the D values is more readily seen in Figure 43.

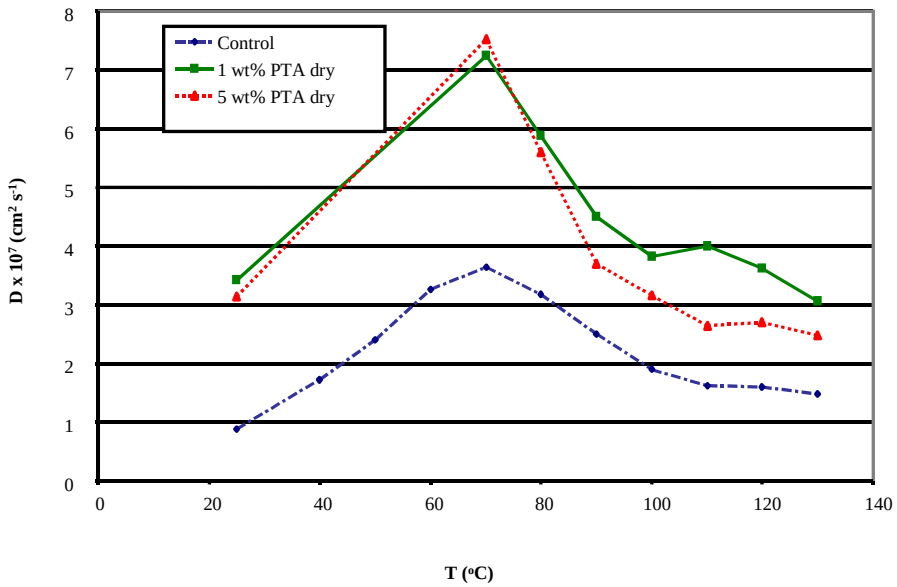

Figure 41.Diffusion Coefficients of PFSA PTA Samples versus Temperature Dry Method.

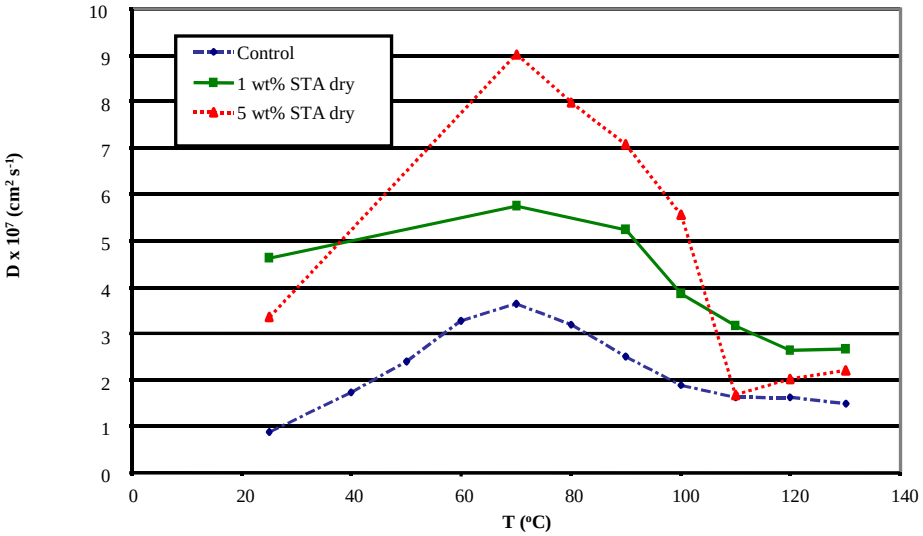

Figure 42.Diffusion Coefficients of PFSA STA Samples versus Temperature Dry Method.

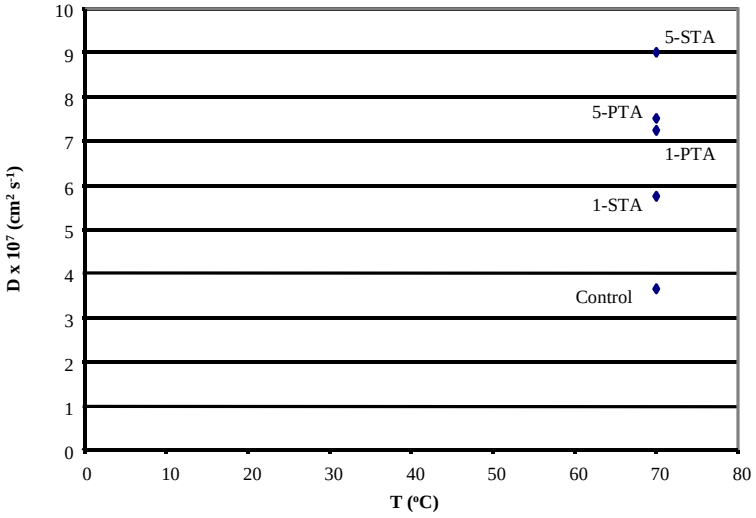

Figure 43.Maximum Diffusion Coefficient versus Temperature Maximum for Dry PTA and STA Samples.

The effect of hydration on the PFSA-HPW, PFSA-HSiW, and PFSA-HZnW samples was also investigated. The sealed sample configuration is shown, Figure 44. Note that 100% RH at all temperatures investigated is achieved by adding sufficient water to the NMR tube at in the position indicated in but because of the temperature gradients along the axis of the tube, the 100% RH condition is not maintained at elevated temperatures (see discussion of the temperature dependence of the diffusion coefficients below).

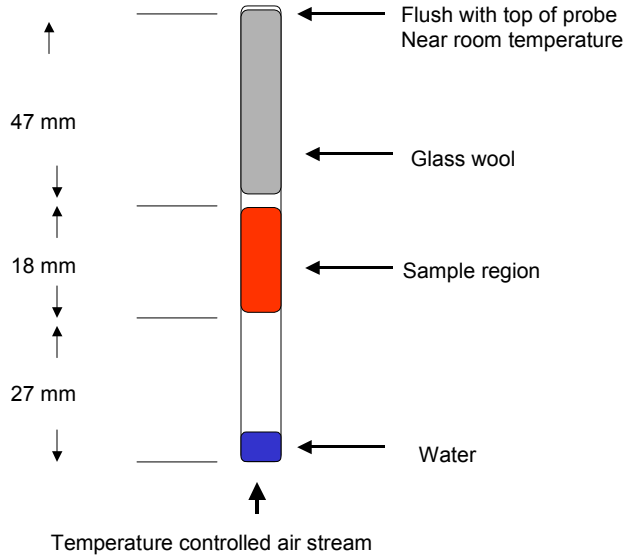

Figure 44. Sample cells for diffusion measurements using hydration method. **The pulse sequence shown in** Figure 34 **with g = 0 was used to obtain 1H NMR spectra of the 100% RH PFSA-HPW, PFSA-HSiW, and PFSA-HZnW membranes as shown in** Figure 45**,** Figure 46**, and** Figure 47**. Except for the 1 wt% PFSA-HPW sample, all the 1H NMR spectra of the 100% RH samples have the same general appearance, that is, two broad, overlapping resonance lines are observed. The two resonance lines for the 1 wt% PFSA-HPW sample are nearly resolved to the baseline and will therefore be treated individually. The average chemical shift for the 100% RH samples is graphically displayed in** Figure 48**. The addition of water to the samples lowers the chemical shift of all resonance lines relative to the 0% RH samples, with the exception of the 1 wt% PFSA-STA sample, indicating that the protons in each sample are now less acidic. This is caused by rapid chemical exchange of H+ from PFSA, PTA, STA, or ZTA acidic sites and water in the membrane.**

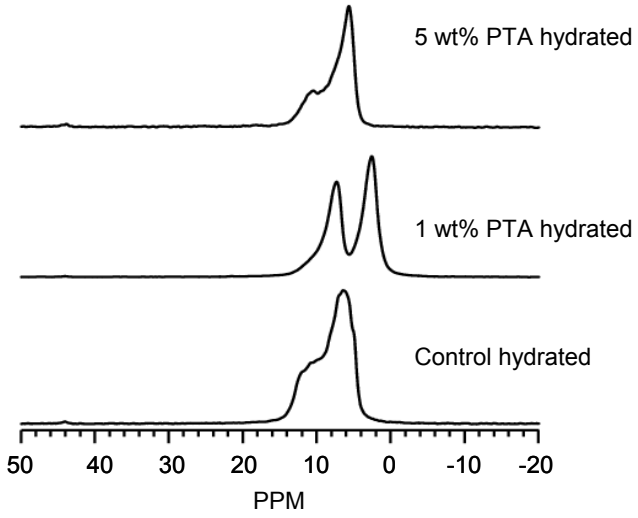

Figure 45. 400 MHz ^{1}H NMR Spectra of Hydrated HPW Samples at 25 ^{O}C.

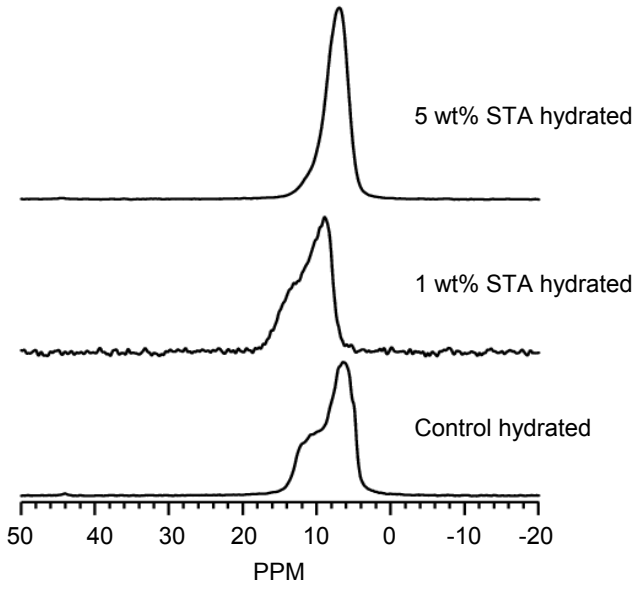

Figure 46. 400 MHz ^{1}H NMR Spectra of Hydrated HSiW Samples at 25 ^{O}C.

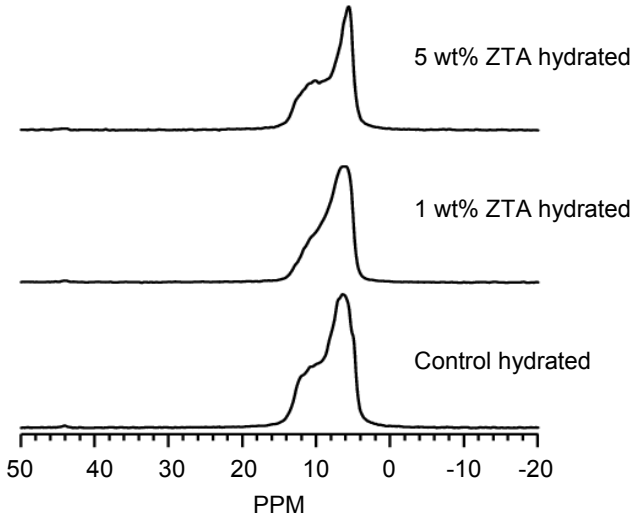

Figure 47. 400 MHz ^{1}H NMR Spectra of Hydrated HZnW Samples at 25 ^{O}C.

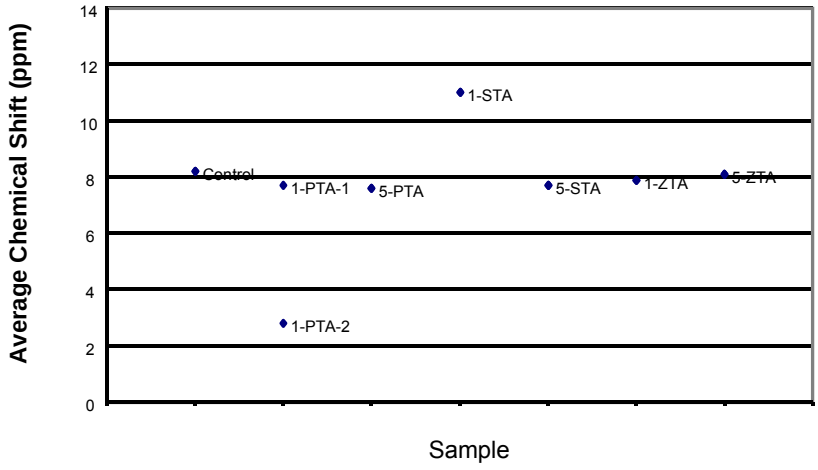

Figure 48. Average Chemical Shifts for Hydrated Samples. Figure 49 shows a plot of D versus T for the 1wt% 100% RH PFSA-HZnW sample as a function of time (Note that D was not measured for the 0% RH PFSA-HZnW samples). Trial 1 shows the expected

behavior of D(T) for a sample that does not change as the temperature is increased while Trials 2 and 3 indicate that the sample dehydrates over time.

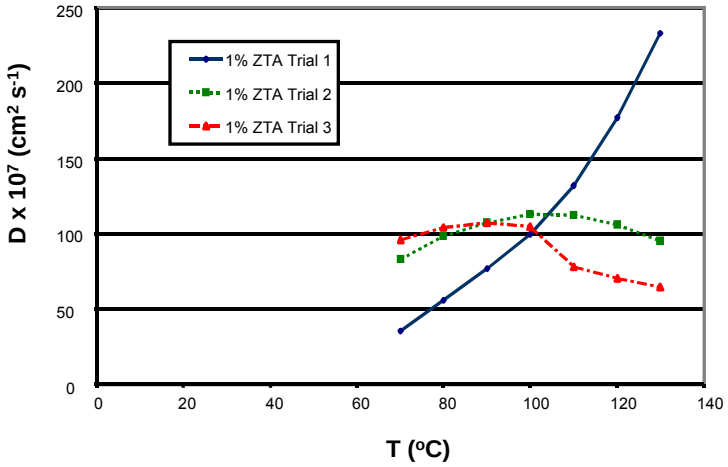

Figure 49.Diffusion Coefficients of PFSA 1 wt% HZnW versus Temperature of Hydrated Samples.

Figure 50 compares D versus T plots for the hydrated Control (PFSA), 1 wt% PFSA-HZnW, and 5 wt% PFSA-HZnW samples. The Control and 5 wt% PFSA-HZnW samples have a maximum D at about 70 ^{o}C while the 1 wt% PFSA-HZnW sample has a maximum D value near 90 ^{o}C. All samples show D decreasing at elevated temperatures indicating the samples dehydrate at these elevated temperature.

For all samples, Control, 1 wt% PFSA-HZnW, and 5 wt% PFSA-HZnW, the D values are 10^{-6} cm^2 s^{-1} or greater indicating that some level of hydration improves the proton transport properties of the membranes.

Figure 51 compares D versus T values for the 0% RH and 100% RH 1 wt% PFSA-HPW and 5 wt% PFSA-HPW samples. All 100% RH samples show much greater D values at all temperatures. The 5 wt% PFSA-PTA sample has the largest D values at elevated temperatures and its maximum D is reached at a higher temperature than the 100% RH 1 wt% PFSA-PTA, 0% RH 1 wt% PFSA-HPW, and 0% RH 5 wt% PFSA-HPW samples.

Figure 52 compares D versus T values for the 0% RH and 100% RH 1 wt% PFSA-HSiW and 5 wt% PFSA-HSiW samples. All 100% RH samples show much greater D values at all temperatures. The 5 wt% PFSA-HSiW sample has the largest D values at elevated temperatures and its maximum D is reached at a higher temperature than the 100% RH 1 wt% PFSA-HSiW, 0% RH 1 wt% PFSA-HSiW, and 0% RH 5 wt% PFSA-HSiW samples.

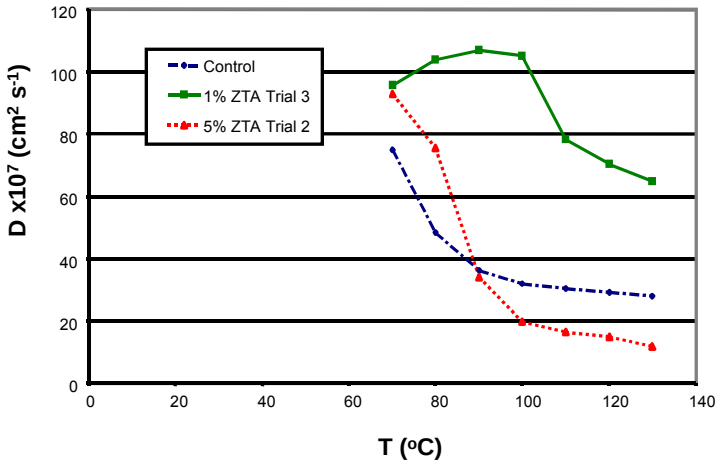

Figure 50. Diffusion Coefficients of PFSA HZnW Samples versus Temperature of Hydrated Samples.

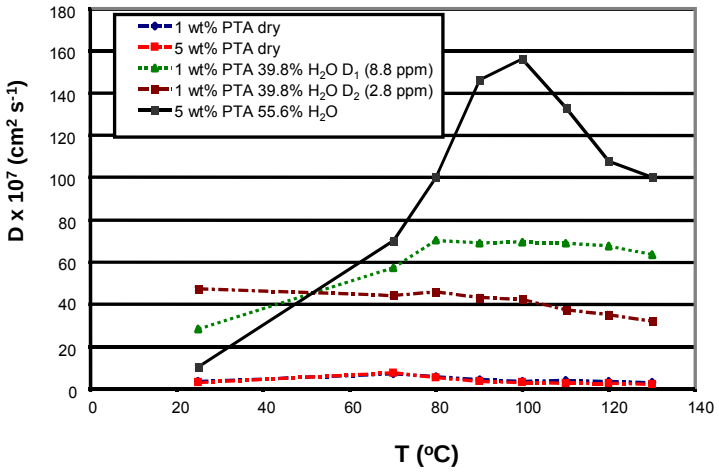

Figure 51. Diffusion Coefficients of PFSA HPW Samples versus Temperature.

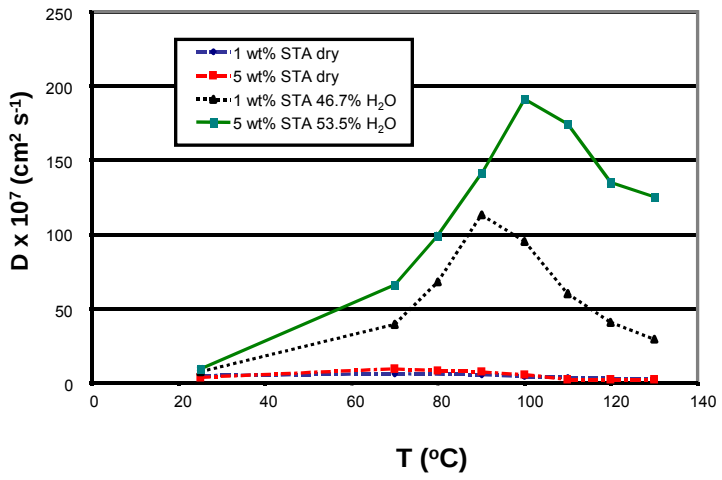

Figure 52.Diffusion Coefficients of PFSA HSiW Samples versus Temperature.

Figure 53 plots the maximum D value versus the temperature at which it occurs for the hydrated Control, 1 and 5 wt% PFSA-PTA, 1 and 5 wt% PFSA-STA, and 1 and 5 wt% PFSA-ZTA samples. There is no obvious trend but all maximum D values are 10^{-6} cm^2 s^{-1} or greater and the maximum temperature is in the range of 70- 100 ^oC.

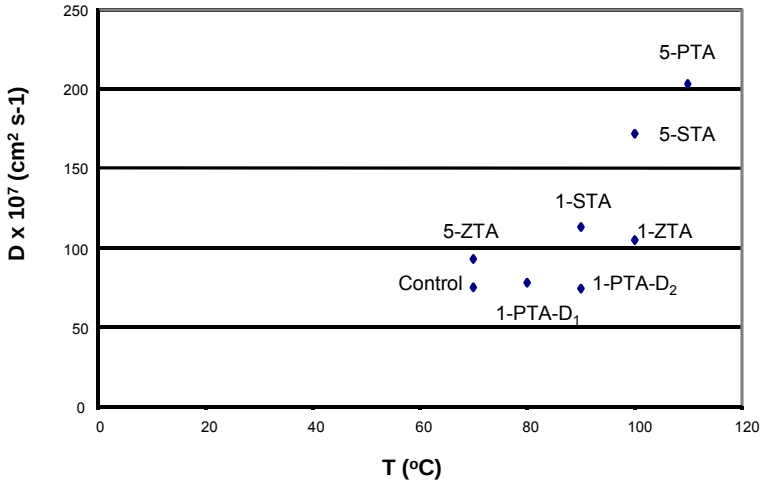

Figure 53. Maximum Diffusion Coefficient versus Temperature Maximum for Hydrated HPW, HSiW, and HZnW Samples.

Proton diffusion coefficient (D) measurements were repeated on the Control, HPW, HSiW, and HZnW doped PFSA membrane samples with an improved procedure that insures that the membrane sample cell was under 100% RH for all temperatures employed. The membrane sample cell configuration for the 100% RH samples is shown in Figure 54.

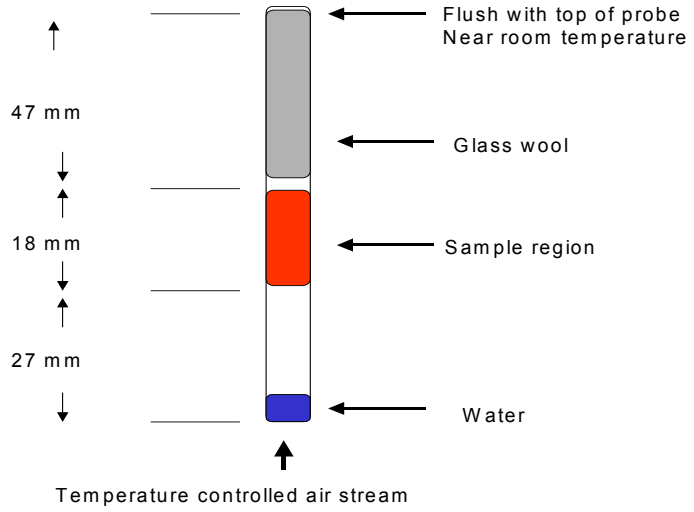

Figure 54. Sample cells for diffusion measurements using hydration method.

Proton diffusion coefficients for the Control, 1% HPW, and 5% HPW samples are shown in
Figure 55. Proton diffusion coefficients for the Control, 1% HSiW, and 5% HSiW samples are shown in Figure 56. Proton diffusion coefficients for the Control, 1% HZnW, and 5% HZnW samples are shown in Figure 57.

The HPW and HSiW filled PFSA samples show the same trend, that is, the order of diffusion is such that the Control > 1% HPW > 5% HPW and Control > 1% HSiW > 5% HSiW while the HZnW sample has an anomalous trend with 5% HZnW > Control > 1% HZnW. The HPW and HSiW filled samples also have D values that approach the Control D values at temperatures near 100 ^{o}C and all samples shown a leveling effect at about 120 ^{o}C. Even though the samples are under 100% RH at all temperatures, this leveling effect indicates that the samples are beginning to dehydrate around 120 °C; note, however, that the D values are still rather large at these elevated temperatures for all the samples.

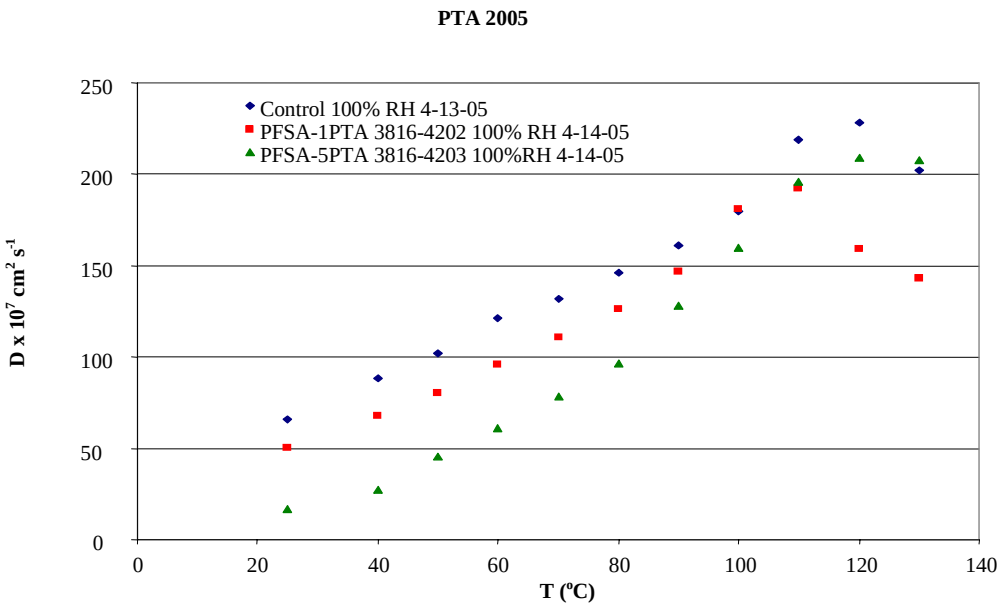

Figure 55. Proton diffusion coefficients versus temperature T for Control, 1%HPW, and 5%HPW PFSA samples.

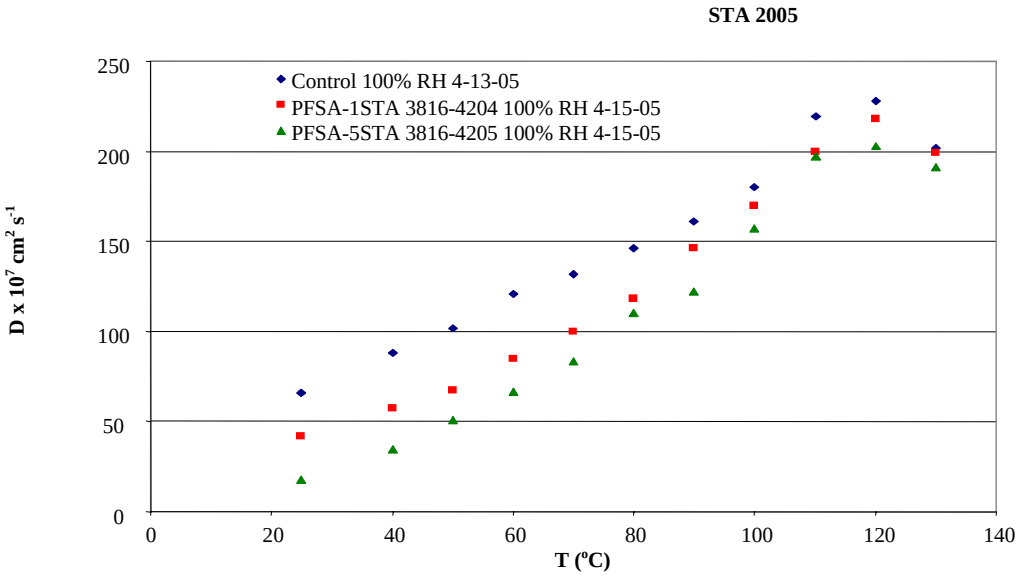

Figure 56. Proton diffusion coefficients versus temperature T for Control, 1% HSiW, and 5% HSiW PFSA samples.

The HZnW doped PFSA samples show an anomaly with the 5% HZnW sample, that is, the 5% HZnW have bigger D values than either the Control or 1% HZnW samples and the 5% HZnW sample exhibited two diffusion coefficients. Only one D value is shown in the interests of clarity. In addition, the D values for the 5% HZnW samples do not exhibit the leveling effect near 120 °C as observed for all other samples but rather appear to grow at a rather large rate for the highest temperatures studied. The D values

for the HZnW samples should be measured again in order to determine the reproducibility of the results.

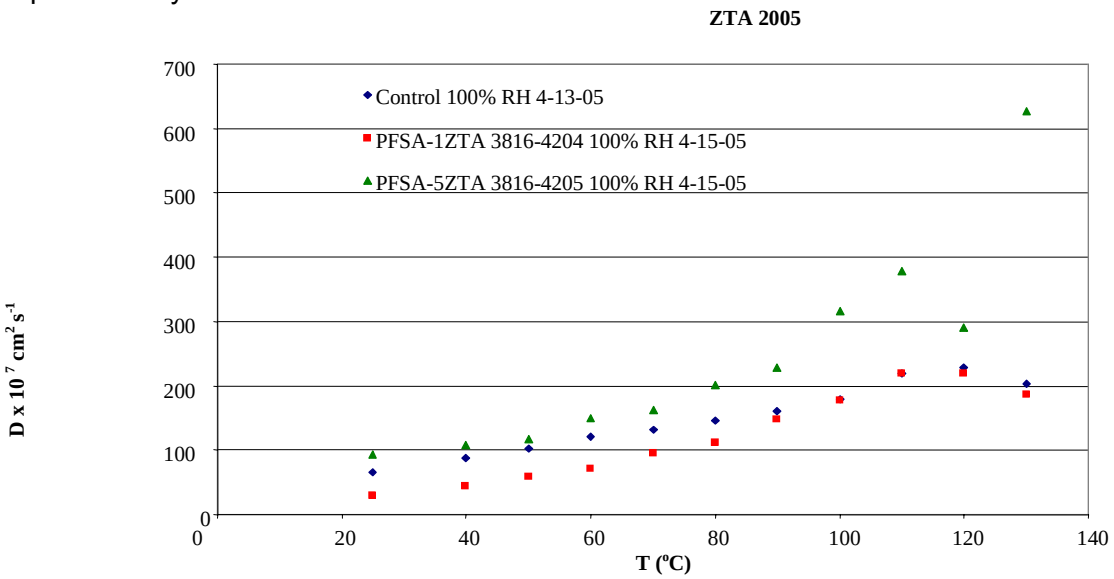

Figure 57. Proton diffusion coefficients versus temperature T for Control, 1% HZnW, and 5% HZnW PFSA samples.

In contrast to the trends observed in the diffusion coefficients values, notably the anomalous 5% HZnW data, the activation energies (E_a) determined from the temperature dependent D values show the same trend for the HPW, HSiW, and HZnW samples. The results are shown in Figure 58. The main feature to note is that as the loading level increases, Ea increases. To a first approximation, each sample may be considered to have the same level of hydration. Therefore, and increase in Ea as the loading of HPW, HSiW, or HZnW increases indicates that the protons are more strongly bound as, presumably, the acidity of the material increases.

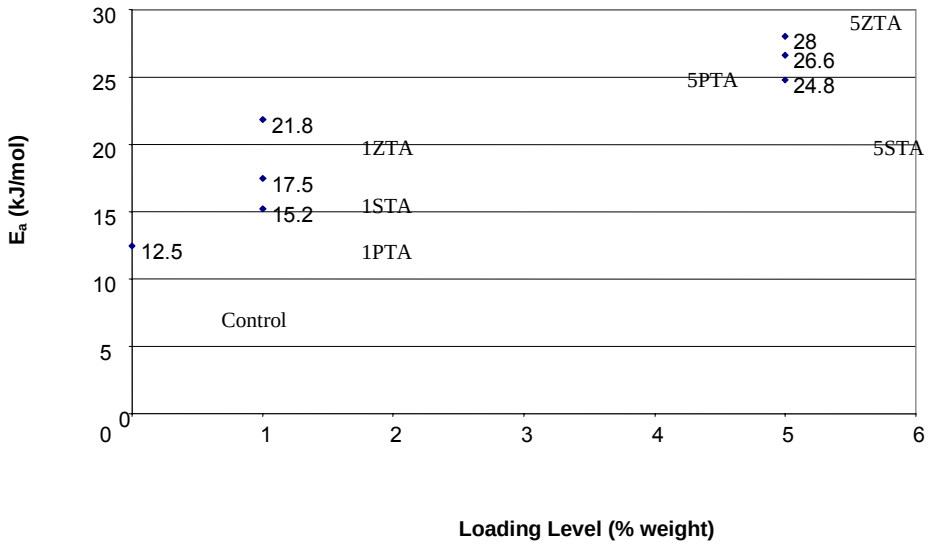

Figure 58. Activation energies for diffusion for various HPA doped PFSA samples.

Appendix V

Case Western Reserve University - Final Report

Case Western Reserve University – Final Report.

Thomas Zawodzinski Jr.
F. Alex Nason Professor of Engineering
Ohio Eminent Scholar in Fuel Cells
Director, Case Advanced Power Institute

email: taz5@case.edu
office: A.W. Smith, Room 124A
tel: (216) 368-5547

Contributors: *Hayley Every, Jessica Kurasch, Derek Lebzelter, Jennifer Levin*

Department of Chemical Engineering
Case Western Reserve University
Cleveland, Ohio, 44106

Task 2.1 Membranes for use at 120ºC or above.

A. Electrochemistry

The primary objective of this work was an examination of the feasibility of fuel cell electrocatalysis reactions in this non-aqueous medium. Typically, it has been found that the ORR does not proceed to a full four-electron process under such conditions.

1. Cyclic Voltammetry

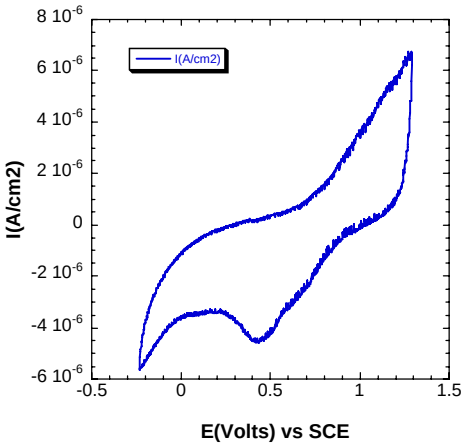

Cyclic voltammograms were obtained for neat EMIm $N(SO_2CF_3)_2$. For both measurements, a platinum disk electrode (geometric area = 0.20cm^2), was the working electrode, a platinum wire was the counter electrode and a saturated calomel electrode was used as a reference (standard potential, +0.2412 V). The reference electrode was separated from the other electrodes via a salt bridge. The ionic liquid was used as the electrolyte in both the measurement and reference cells as well as the salt bridge. Cyclic were measured after purging the cell with nitrogen or oxygen respectively. The scan rate was 20 mV/s in both cases. The cyclic voltammogram obtained is shown at left. The CV indicates a single oxidation process with onset occurring at ~ 0.8V vs. SCE (1.04 V vs. RHE), a complex reduction process with a peak at ~ 0.45V vs. SCE (0.69 V vs. RHE) and a shoulder occurring at ~ 0.7V vs. SCE (0.94 V vs. RHE), and the onset of a reduction process at ~ -0.25V vs. SCE (-0.01 V vs. RHE). These processes suggest that a small amount of

adventitious water is present. The oxidation feature then would correspond to formation of oxide on the Pt surface, with the high voltage reduction peak due to stripping of the oxide to reform water and the low voltage oxidation corresponding to hydrogen evolution from water.

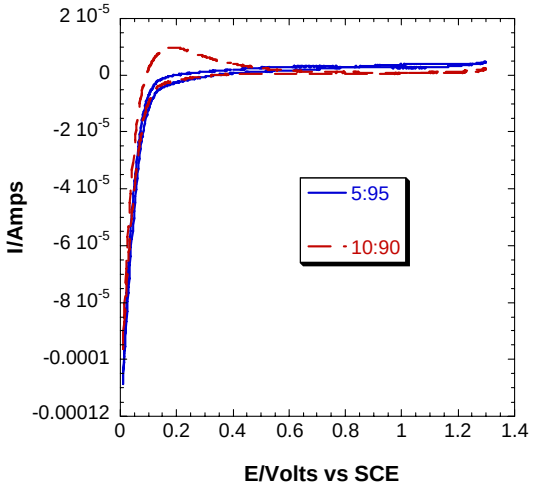

Cyclic voltammograms were obtained for EMIm $N(SO_2CF_3)_2$ containing the corresponding acid. The setup is the same as for the previous experiments. The ratios of acid to ionic liquid were 5:95 and 10:90. The cyclic voltammograms obtained are shown below. The voltammogram for the 5:95 sample is quite featureless except for the low voltage oxidation while a reduction feature coupled to the low voltage oxidation is seen for the 10:90 sample. The latter is quite common in situation when hydrogen is evolved and probably corresponds to a small amount of gas in the vicinity of the electrode. The voltammogram certainly does not have the characteristic structure associated with adsorbed hydrogen.

Two other qualitative aspects emerge upon comparison of the two figures shown. First, the acid-containing sample has a much higher current scale than does the background curve. Second, the acid-containing sample has no indication of any of the features associated with oxide formation or stripping. Our interpretation of these results is as follows. In the first case, the aprotic electrolyte, we strongly suspect that that there is a small aqueous impurity. However, the acid-containing sample seems to have been much more rigorously purified. The current scale—roughly one order of magnitude lower in the hydrogen evolution region for the aprotic ionic liquid with water impurity—suggests that the water is present at the level of 0.5 to 1%. The evolution of hydrogen from water is likely to require some additional activation and thus the potential of hydrogen evolution is more negative for the aprotic ionic liquid with water impurity.

Perhaps the most important finding from this work is what is NOT present in the voltammetry. There is no indication whatsoever of a feature that can be reliably associated with oxygen reduction. This is not promising from the point of view of using these liquids as media for fuel cell reactions.

2. RDE Voltammetry

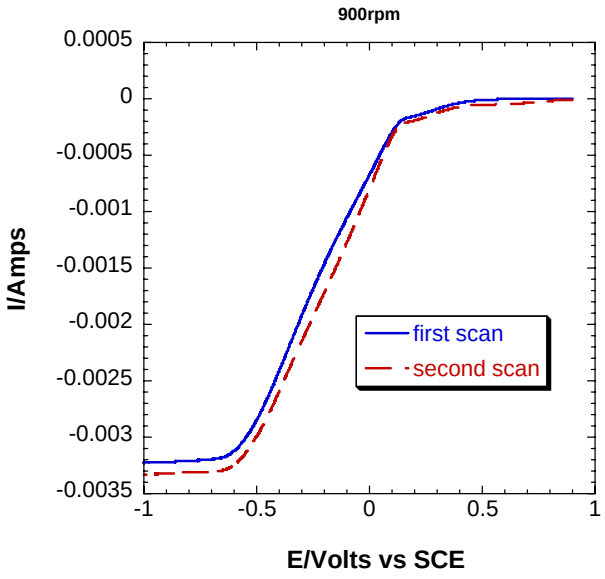

The rotating disk voltammograms were measured for each sample at room temperature. Rotation rates were limited to 2500rpm as above this rotation rates, there was too much turbulence. The voltammograms were different to those seen for the neat ionic liquid: a distinct limiting current was observed and at much larger currents than previously measured. A sample RDE voltammogram is shown at left. There is some evidence to suggest the presence of another limiting current at lower currents (around 0V), but upon analyzing the data, this 'limiting current' showed no variation with rotation rate.

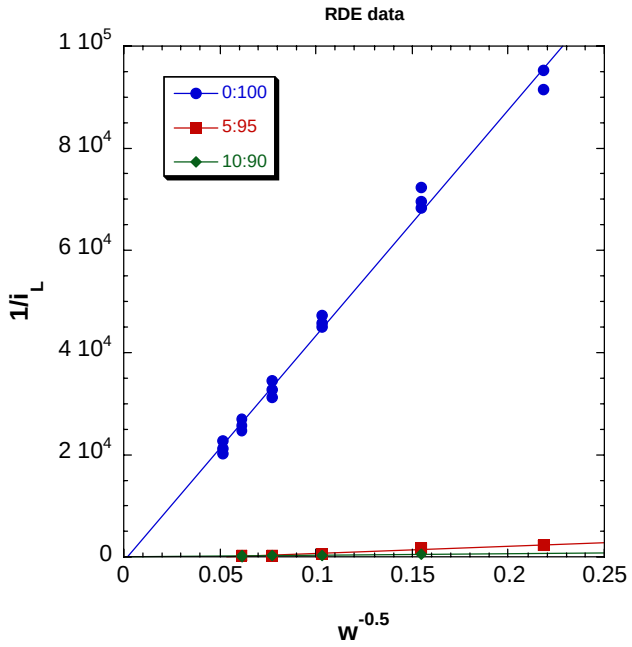

Koutecky-Levich plots for the neat ionic liquid and the acid containing solutions are shown below. The slope for the neat ionic liquid is substantially larger that than observed for either of the acid containing solutions. The results for the acid containing solutions are shown in the next

figure. Upon fitting the data with a linear function, neither sample extrapolates through the origin of the graph. Furthermore, at low rotation rates (large $\omega^{-0.5}$), there is some deviation from the linear fit. One possible explanation for this discontinuity in the results is that the solution undergoes shear thinning at the higher rotation rates. Shear thinning is the apparent decrease in viscosity experienced by complex viscous liquids in response to an applied shearing stress. The RDE experiment would be a perfect environment for complex liquids to display shear thinning.

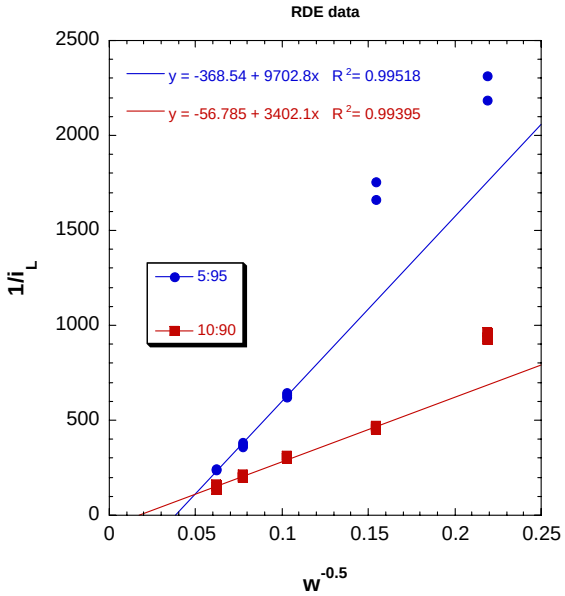

The equations corresponding to the linear fits of the Koutecky-Levich plots are also shown on the above graph. The slope of these fits is proportional to the concentration of electroactive species in the electrolyte (C_X^*), its diffusion coefficient ($D_X^{2/3}$) and the kinematic velocity of the electrolyte ($\nu^{-1/6}$), as given by:

$$slope = \left(0.62nFAC_X^* D_X^{2/3} \nu^{-1/6}\right)^{-1}$$

F is the Faraday constant and A is the area of the electrode, both of which are constant for these experiments. The value n is the number of electrons involved in the reaction; for these materials, the nature of the reaction pathway is not known. The viscosity has been measured for some of these materials and can be extrapolated for some of the other compositions. However, the slope is dependent on the kinematic viscosity, which is the viscosity divided by the density. It is not known how the density varies with composition, but for this purpose, the density is assumed to be constant with a value of 1.55gcm^{-3} (from previous work by Every and coworkers*).

Based on these assumptions, the following table provides some information about the variation of the parameters with composition. These results correspond to a one-electron reduction process, but can be easily determined for a two-electron process. The saturation concentration of X seems to increase with as the acid content increases. Furthermore, the molar concentration (1000 times the tabulated value) of species is fairly consistent with that of the proton in these systems. Given the (approximate) density mentioned about, the total salt concentration in the ionic liquid is roughly 4 to 5M. Thus, the two proton-containing solutions, with ~5.3% and ~11% acid, would have roughly 0.2 and 0.5 M acid concentration. These numbers are quite consistent with those reported in the table and provide a solid indication that we are simply reducing protons.

Acid:Ionic	KL slope	Viscosity/P	Diffusion	Concentration of

Liquid			coefficient/cm^2s^{-1}	electroactive species/$molcm^{-3}$
0:100	43700	0.25	1.8500e-06	5.5922e-06
5:95	9702	0.36	1.6040e-06	0.00021551
10:90	3402	0.44	1.6810e-06	0.00061328

*Hayley A. Every, Andrea G. Bishop, Douglas R. MacFarlane, Greger Oradd and Maria Forsyth, Phys. Chem. Chem. Phys., 2004, 6, 1758 – 1765.

B. NMR Studies

1. T1's

Spin-lattice (T_1) relaxation times are an indicator of the local environment and rotational characteristics of the nuclei, providing information about the local mobility of the ions. Both protons and fluorine relax via a dipolar process, whereby energy is transferred through interactions with the fluctuating magnetic fields of neighboring nuclei. The strength of the interaction is dependent on the nature of the interacting nuclei and the distance separating them. Any motion in within the system will alter these factors, affecting the strength of the interaction and thus facilitating relaxation. Short T_1 relaxation times are indicative of effective relaxation processes, where the nuclear magnetic field fluctuations and interactions are at an optimum and the transfer of energy occurs readily. An increase in nuclear (ion) mobility will result in inefficient energy transfer (relaxation) and thus longer relaxation times.

Several comments are in order with respect to interpretation of the data. First, the observed relaxation times arise from the coupling of motion to a combination of inter- and intramolecular interactions that are difficult to separate. The relative contribution from each is likely to be similar as composition varies, so some qualitative conclusions can be drawn. Also, relaxation times by themselves cannot be used to compare dissimilar nuclei (such as ^1H and ^{19}F, as below). Finally, the motion reflected by relaxation is rotational and translational in nature. These are in general tensor properties dependent on the rotational moment of inertia about given axes. Thus, protons in various positions on the imidazolium ring would not necessarily have the same behavior is motion in one direction is constrained. These factors add up to a need to interpret the data described below rather conservatively.

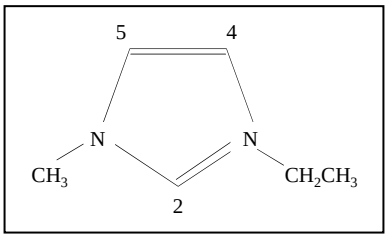

Figure 1 Ethyl Methyl Imidazolium

The T_1 relaxation times for the acid proton, the imidazolium protons and the anion (^{19}F) as a function of acid content are shown below for the different temperatures. The peak numbers refer to the proton peaks from the NMR spectrum and are labeled as such: Peak 1 – acid-proton; Peak 2 – proton in 2 position on the imidazolium ring; Peak 3 and 4 – protons on 4 and 5 positions on the imidazolium ring; Peak 5 – CH_3 protons from N-methyl group; Peak 6 – CH_2 protons from ethyl group; Peak 7 – CH_3 protons from ethyl group.

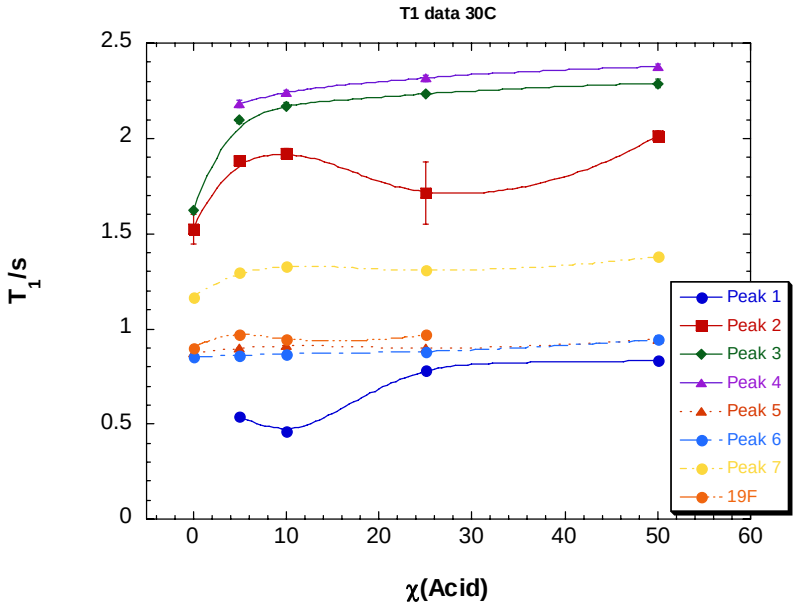

Figure 2. T_1 relaxation times for System 1 at 30°C.

The general trend shows an initial increase in the relaxation times associated with the imidazolium ion and anion upon adding the acid, followed by a leveling off beyond the 10% composition. This is possibly related to an increase in the mobility of the imidazolium ion and anion upon adding the acid. These data should be compared to the observed viscosity of the solution. In contrast, the relaxation of the acid-proton shows a minimum at 10 mol% acid.

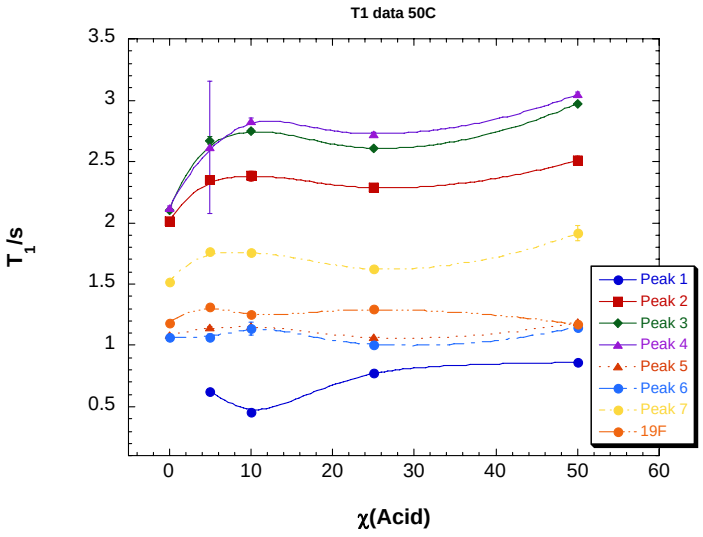

Figure 3. T_1 relaxation times for System 1 at 40°C.

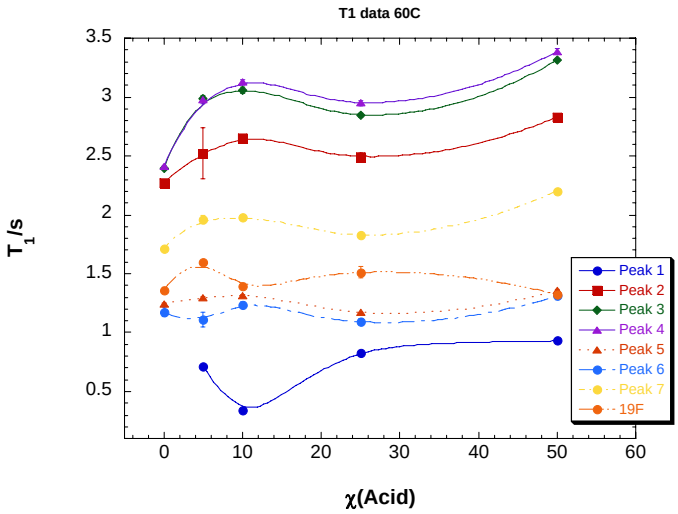

Figure 4. T_1 relaxation times for System 1 at 50°C.

Figures 3 through 4 show the behavior of the relaxation times at various temperatures. Most peaks show a uniform increase with temperature, as might be expected: higher temperature leads to lower viscosity and more rapid motion. However, the behavior of the free proton is notable: the depth of the minimum at 10% seems to increase with temperature.

2. Diffusion

Diffusion coefficients for the acid-proton, the imidazolium ring and the anion (^{19}F) as a function of composition are shown in Figures 5 to 8. Through multiple measurements, an average diffusion value was determined for the imidazolium cation (as a unit entity) with the standard deviation shown as error bars. Upon adding a small amount of the acid, a slight drop in the ring diffusion coefficient is observed at most temperatures. A 'sinusoidal' dependence on acid concentration is apparent with a local maximum in ring diffusion seen at a composition of 10mol% acid, though this should be regarded with some suspicion since few points were measured. The acid-proton diffusion follows a similar trend; the anion diffusion exhibits weaker concentration dependence at higher temperatures.

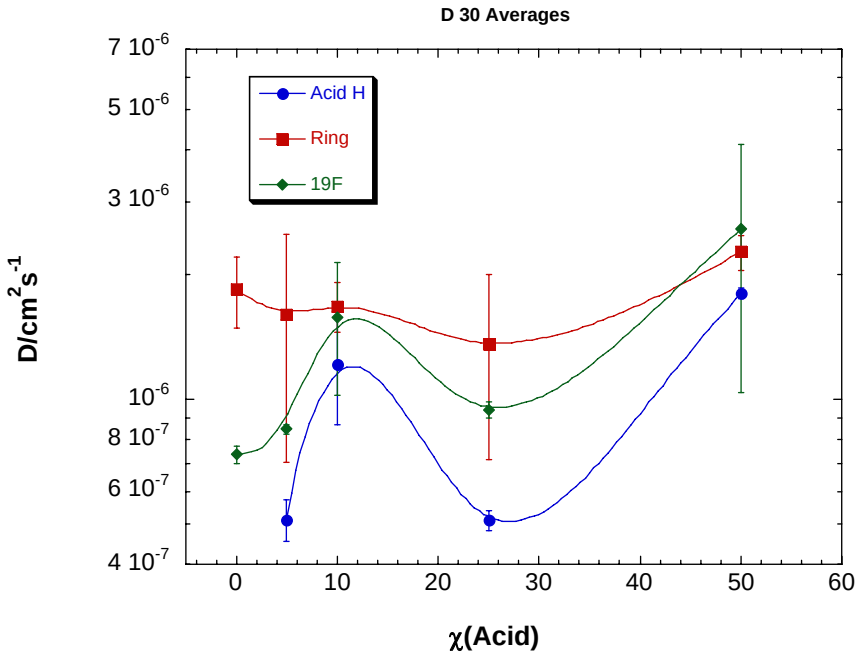

Figure 5. Diffusion coefficients for System 1 at 30°C.

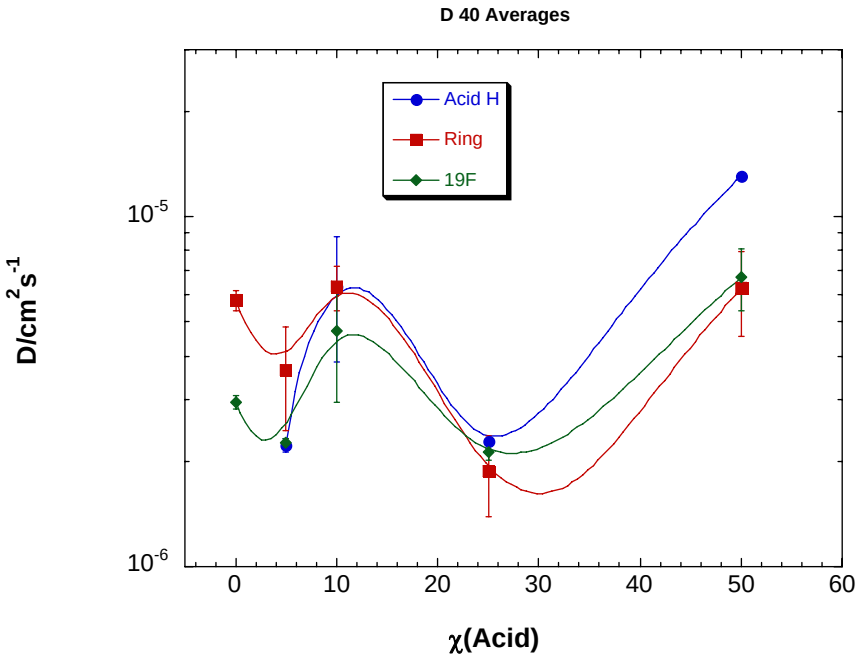

Figure 6. Diffusion coefficients for System 1 at 40°C.

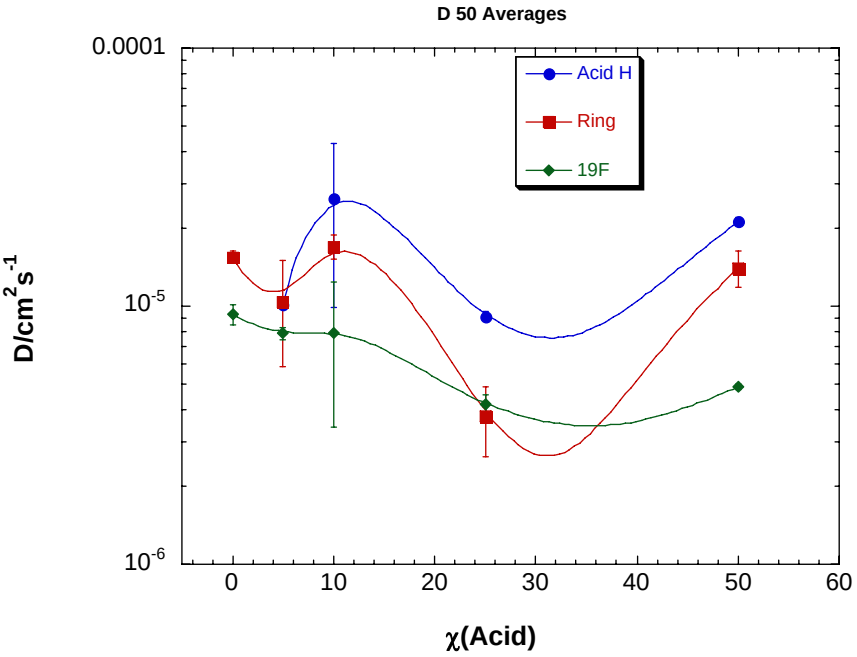

Figure 7. Diffusion coefficients for System 1 at 50°C.

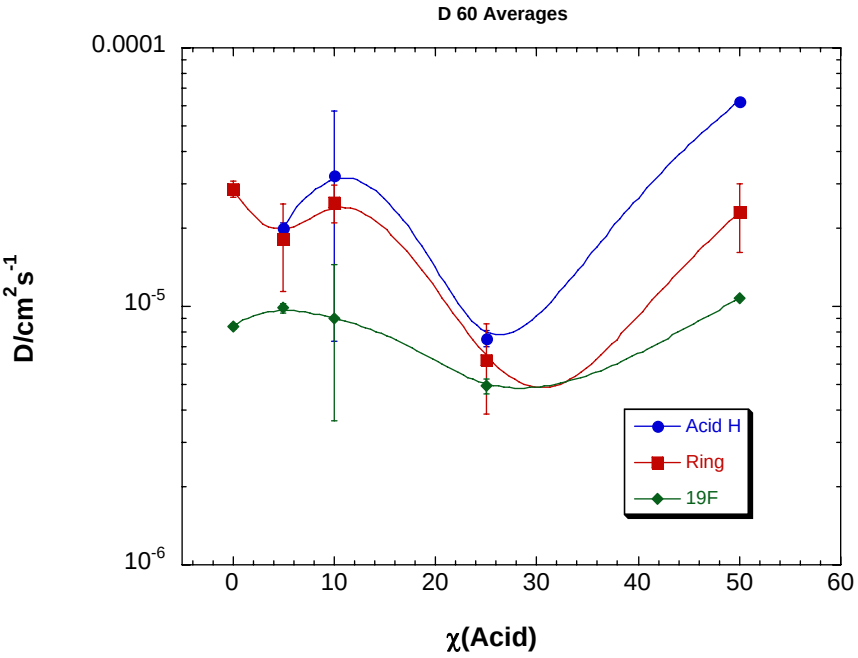

Figure 8. Diffusion coefficients for System 1 at 60°C.

The acid-proton diffusion coefficients typically show greater temperature dependence than the imidazolium ring and the anion, as shown in the following figures (lines are a guide only). A simple Arrhenius temperature dependence does not appear

to hold for most of the curves, suggesting a more complex activation process for diffusion.

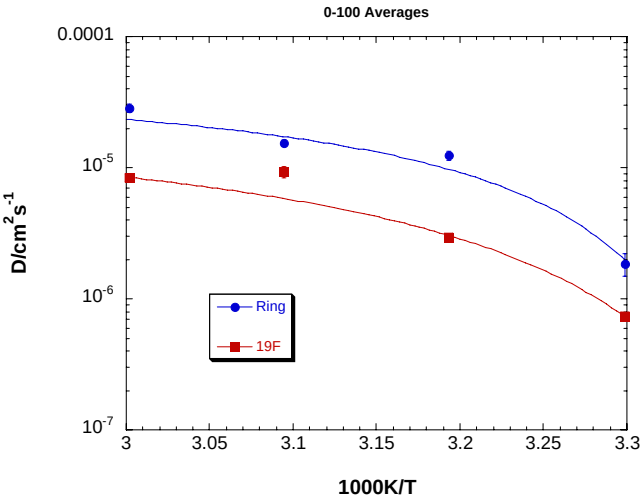

Figure 9. Imidazolium ring and anion diffusion coefficients for the neat ionic liquid as a function of temperature.

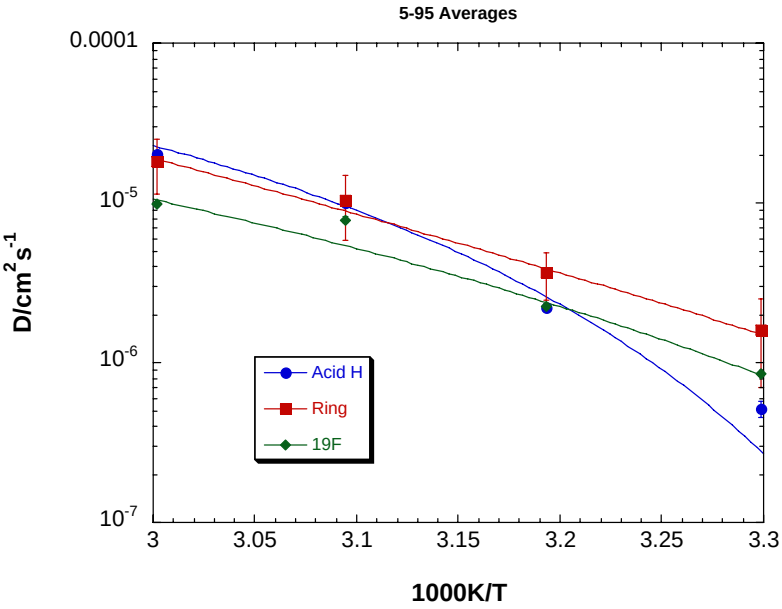

Figure 10. Acid proton, imidazolium ring and anion diffusion coefficients for System 1 as a function of temperature. The acid to ionic liquid ratio is 5:95.

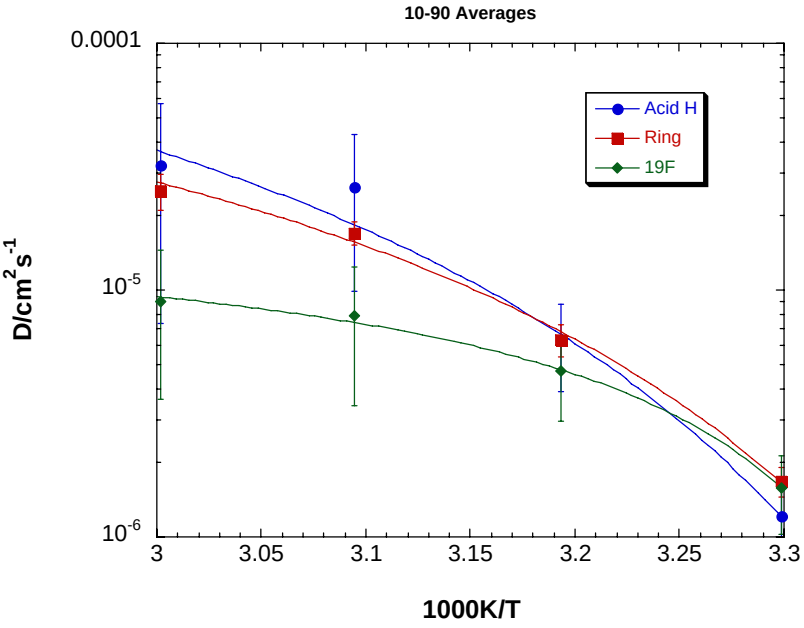

Figure 11. Acid proton, imidazolium ring and anion diffusion coefficients for System 1 as a function of temperature. The acid to ionic liquid ratio is 10:90.

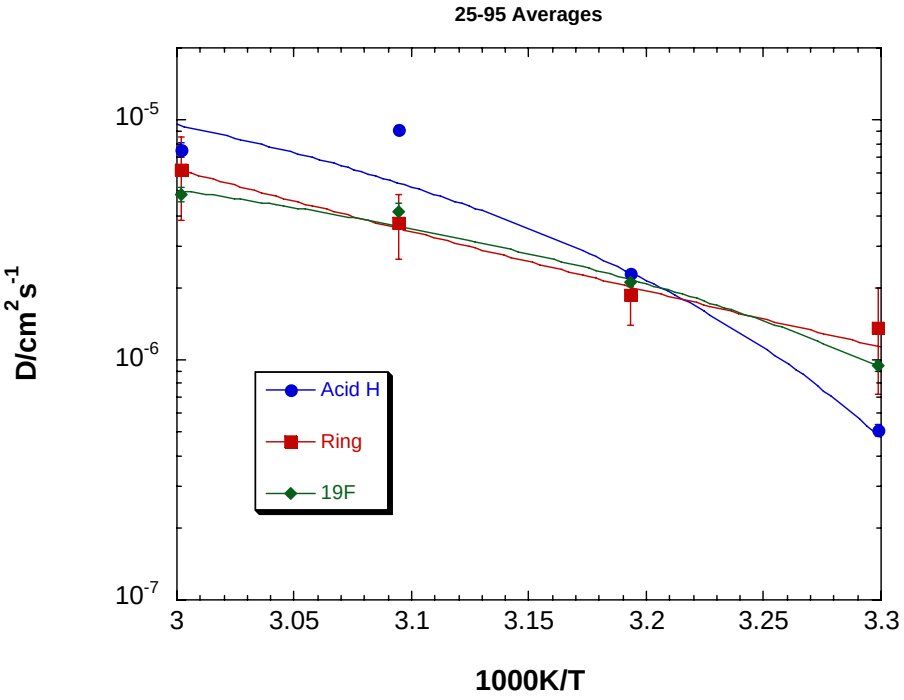

Figure 12. Acid proton, imidazolium ring and anion diffusion coefficients for System 1 as a function of temperature. The acid to ionic liquid ratio is 25:75.

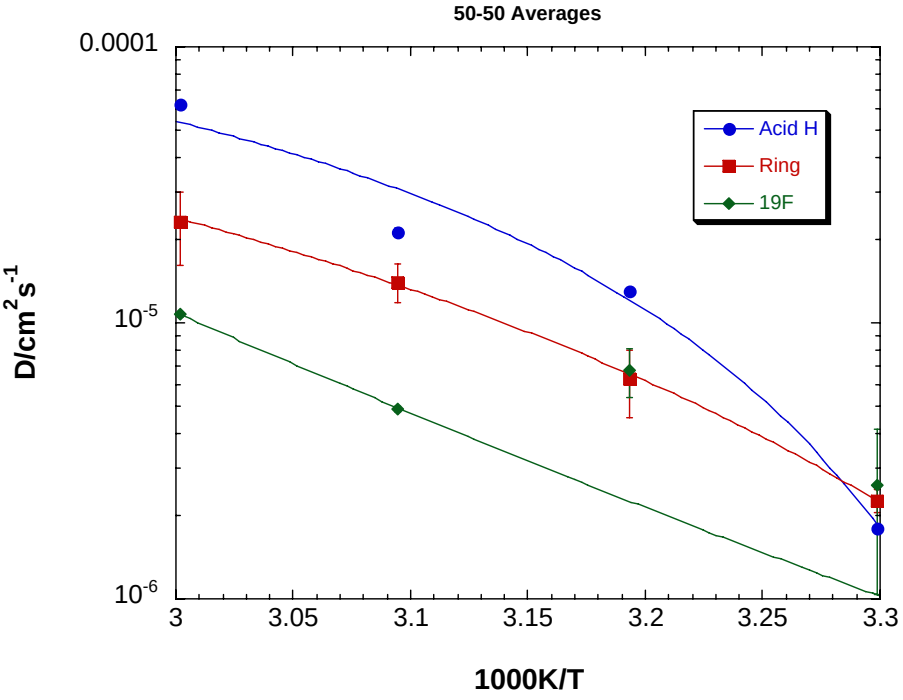

Figure 13. Acid proton, imidazolium ring and anion diffusion coefficients for System 1 as a function of temperature. The acid to ionic liquid ratio is 50:50.

3. Interpretation

In comparing the T_1 relaxation and diffusion coefficients as a function of composition, the 10:90 mole ratio presents some interesting features. At this composition, the imidazolium cation and imide anion typically show a maximum T_1 value, while the acid-proton displays a minimum. Furthermore, all three ions generally exhibit a maximum diffusion coefficient at this same composition.

The minimum in T_1 for the acid-proton indicates that the relaxation mechanism is most effective at this composition. This could suggest that the acid-proton is closely associated with one or both of the ionic species, which might also indicate some level of local order or structure within this material. However, on the face of it, this runs counter to expectations from the diffusion coefficient data, which suggests the highest long-range mobility for protons at this composition.

The temperature dependence of the measured parameters shows that (1) proton diffusion is more strongly affected by temperature than are other ions and (2) the relaxation mechanism at the minimum becomes increasingly less effective at increasing T. Regarding point (1), at low T proton D values are smallest at all compositions while at higher T's protons become the most rapidly diffusing species.

The conductivity is also a maximum at the 10:90 composition, as was seen in the results from 3M. This is consistent with the maximum in the diffusion coefficients. Based on these observations, the 10:90 composition seems to provide an appropriate acid-proton to imidazolium ion ratio that facilitates effective ion transport.

A possible explanation that is consistent with all observations is as follows: A primary difficulty in achieving significant proton mobility arises from the difficulty in achieving proton dissociation in a 'solvent-free medium. The molten salt is fairly highly associated and can be regarded as a perturbed lattice of anions and cations. The incorporation of acid initially introduces defects into the structure. At low acid

concentration, perhaps the protons are initially complexed tightly by pairs of anions, with the protons trapped between anions. The protons are not incorporated into the 'lattice' within icebergs of ordered anions and cations, but rather the acid finds peripheral anionic sites (preferably) or cationic sites. Thus, the acid proton exhibits high mobility. At higher T, the icebergs 'melt'—becomes less ordered—and the proton interacts with more cations more weakly. Thus, transport is strongly activated by T (higher D) even while through-space interactions with other dipolar spins (fluorines on the anions) increases (deeper T_1 minimum). At higher concentrations of acid, the acid is increasingly incorporated into the ionic lattice and transport occurs via percolation through the lattice of alternating anions and cations—the proton moves as a small cation in this system.

To summarize, at any given temperature, the highest mobility for protons is achieved at a composition at which the greatest number of weak interactions occur; above this composition, the proton is trapped in a lattice with a smaller number of strong interactions. The effect of temperature is to create increasing disorder in the liquid structure, driving an increased possibility for protons to find multiple interacting anions below the composition at which it is incorporated into the more regular lattice.

Task 1.4 Membranes for use below 120ºC

In this part of the project, we investigated the water uptake and transport properties of the new 3M ionomer, hereafter referred to as 3M-ion. The uptake of water by 3M-ion 900 as a function of activity (relative humidity) at 30°C is shown in Figure 14. The shape of the curve is typical for PFSA membranes. However, the water uptake at high relative humidity is somewhat less than that of Nafion, which takes up 14 waters per sulfonate under equivalent conditions.

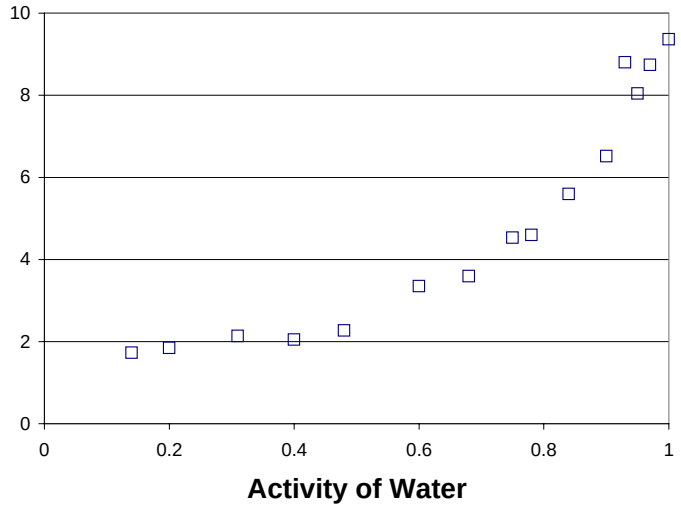

Figure 14: Sorption of water by 3M-ion 900
Also, the low RH end of the curve is remarkably flat.

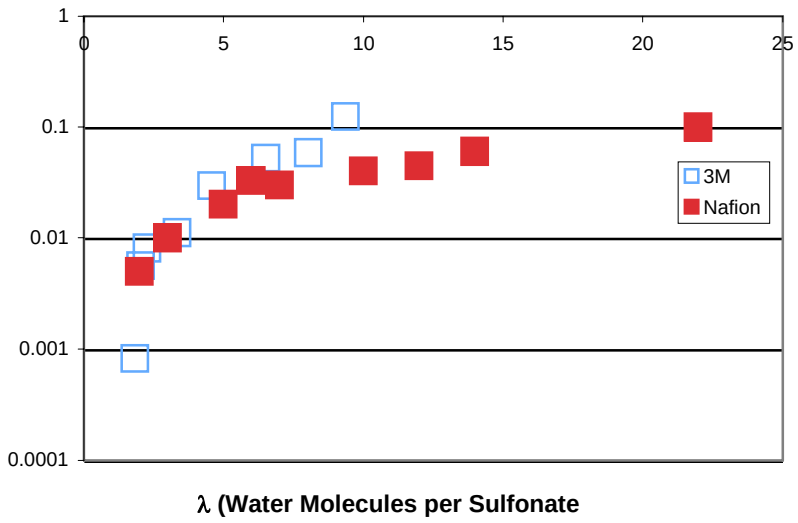

Figure 15, the conductivity of 3M-ion as a function of water content at 30°C

In Figure 15, the conductivity of 3M-ion as a function of water content at 30°C is shown with a similar curve for Nafion included for comparison. Surprisingly, the conductivity of 3M-ion increases sharply at the highest water content: the conductivity at λ =10 matches or even exceeds slightly that of Nafion 1100 at λ =14 (RH =100%, vapor) and λ =22 (RH= 100%, liquid). To investigate further the mobility of species in the membrane, NMR diffusion and relaxation studies were carried out as a function of water content. The results are shown in Figures 16 through 18. As seen in Figure 16, the diffusion of water once again is high relative to that of Nafion. In Figure 17, data are presented for various equivalent weight 3M-ion samples. All water diffusion measurements are consistent: the strong increase at high RH is repeated throughout. In Figure 18, the ^{2}H relaxation rate is shown as a function of water content. In this case, the relaxation rate is similar to that in Nafion at all water contents.

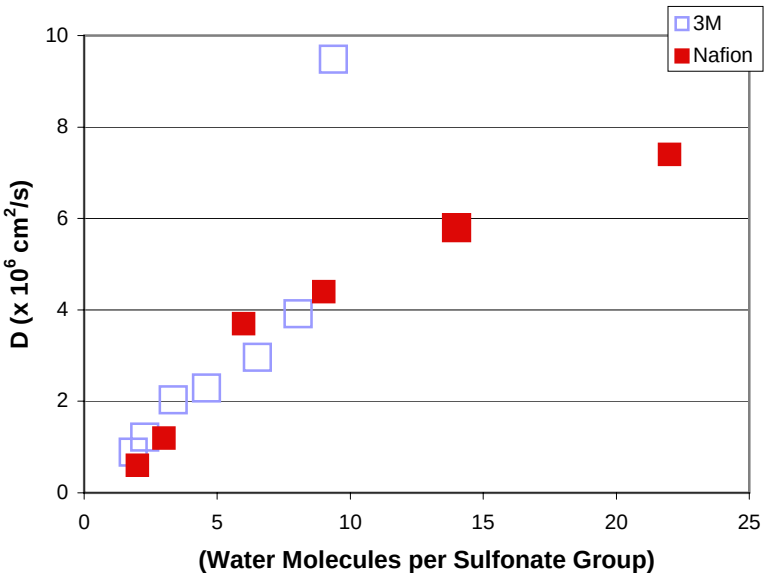

Figure 16 Diffusion of water vs. Lambda for 3M ionomer and Nafion™

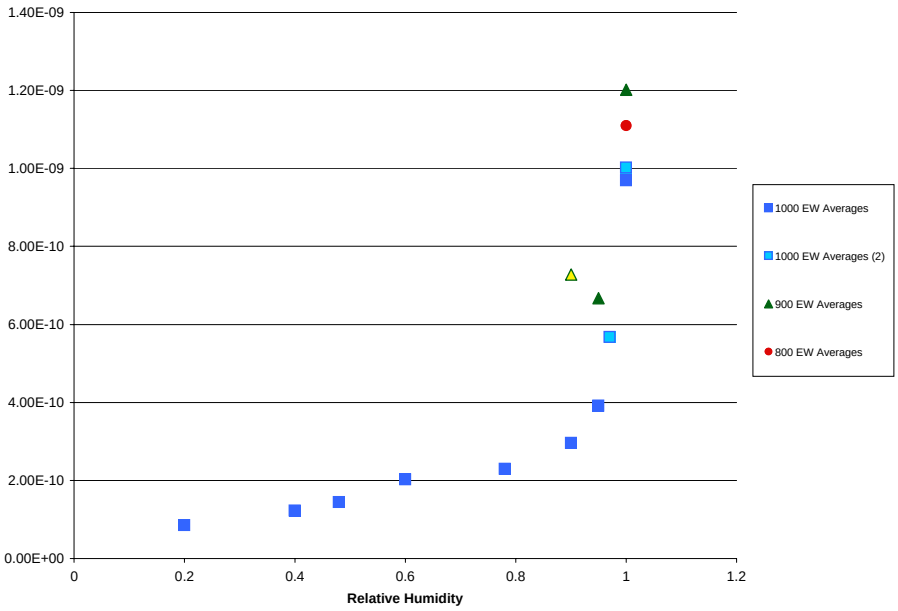

Figure 17 Diffusion data for various equivalent weight 3M-ion samples

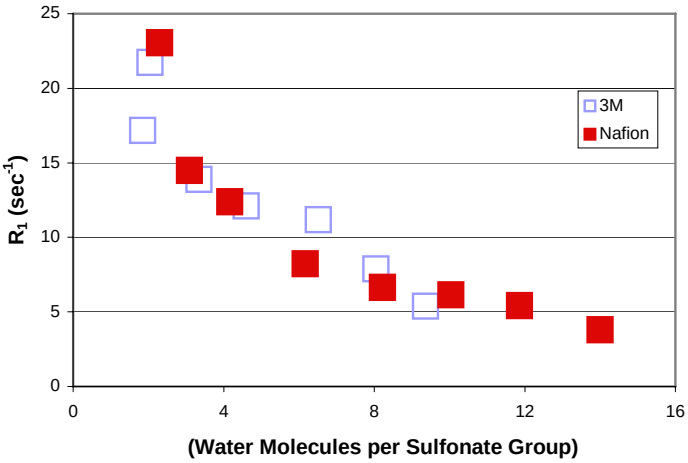

Figure 18 ^{2}H relaxation rate as a function of water content

The substantial increase in conductivity and diffusion rates at high RH and the significant deviation in behavior and values from those found in Nafion are of some interest. The relaxation behavior, which is similar between the two systems, provides a clue concerning the origin of this behavior. Relaxation rates reflect local motions and thus the local chemical interactions. To a good approximation, these are identical for Nafion and 3M-ion. As shown previously by theoretical studies of PFSAs, the interaction of water with the membrane is almost exclusively with the sulfonic acid site and not with the sidechain.

For long-range motions, the underlying chemical interactions are convoluted with the tortuosity of the diffusion path, that is by the morphology of the structure. Thus, we conclude that the differences in observed behavior probably arise from differences in

structure of the polymer at length scales exceeding the nanometer scale. Our findings suggest that, at least for the samples tested, a greater long-range connectivity is developed in 3M-ion compared to Nafion.

An interesting possibility emerges when one also considers the water sorption behavior. Water uptake at high relative humidity levels is determined by the ability to swell the polymer matrix. The uptake level reflects the balance between the chemical potential increase associated with higher water activity with the free energy decrease associated with mechanical distension of the polymer. The 3M-ion material is apparently stiffer than Nafion, with a higher T_g. The additional mechanical strength of the material may be associated with a greater degree of organization of the ionic clusters in the material. This would be consistent with the finding from transport measurements of relatively high transport rates with smaller amounts of water present.

Appendix VI

Universitiy of Minnesota – Final Report

Modeling Proton Transport in HTFSI-TFSI-EMI Mixtures

Lingling Jia, Dat Nguyen, J. W. Halley
School of Physics and Astronomy, University of Minnesota, Minneapolis, MN 55455

Phat Pham, William Lamanna, Steven Hamrock
3M Company, St. Paul, MN 55144

(Dated: June 7, 2007)

We report measurements of the conductivity of a series of mixtures of ionic liquids and acids. We find in particular that a mixtures of 1-ethyl-3-methylimidazolium (EMI, $C_6H_{11}N_2$)-bis(trifluoromethylsulfonyl)imide (TFSI, $(CF_3SO_2)_2N$) with the acid H-TFSI have promising conduction properties for applications to fuel cell membranes. However these mixtures have a peculiar dependence of conductivity on acid concentration. We present a series of model calculations at coarse grained and molecular dynamics levels which suggest that the observed nonmonotonic dependence of conductivity on acid concentration arises because of proton clustering in the mixtures and possibly of phase separation at the higher acid concentrations.

PACS numbers: PACS numbers:

I. INTRODUCTION

Interest in membrane materials for polymer electrolyte membrane (PEM) fuel cells has recently increased because of the international effort to improve fuel cell performance, particularly for automotive applications and the move toward a possible hydrogen economy[1] . In particular, there are strong engineering reasons[2] to seek a proton conducting membrane which will work at higher temperatures (up to 120^o C) and/or at lower water content than possible with the polyperfluorosulfonic acid polymers being used today, such as Dupont's Nafion (TM). Membranes of this type are highly dependent on water for proton conduction. At higher temperatures ($> 90^o$ C) or lower cell humidification levels, the membrane water content is much lower and the conductivity drops dramatically so these two goals are closely related. Though a variety of other polymeric membrane materials have been explored, none have yielded the desired improvements in performance[3].

For these reasons, another membrane material, possibly containing a nonaqueous, nonvolatile plasticiser with a high conductivity would be desirable. There has been some previous work reporting studies of ionic liquids as possible additives to fuel cell electrolytes[5–7]. Somewhat similar systems containing polymers, ionic liquids and lithium salts [8, 9] have been investigated for use in lithium polymer batteries. Here we report experimental and computational studies of ionic liquids as possible additives for fuel cell membranes. We find in particular that 1-ethyl-3-methylimidazolium (EMI, $C_6H_{11}N_2$)-bis(trifluoromethylsulfonyl)imide (TFSI, $(CF_3SO_2)_2N$) has high conductivity at the target temperature at certain acid-salt ratios. (Figures 1, 2).

The dependence of conductivity on the acid salt ratio is unexpected and we report computational and theoretical studies which seem to account for the experimental results.

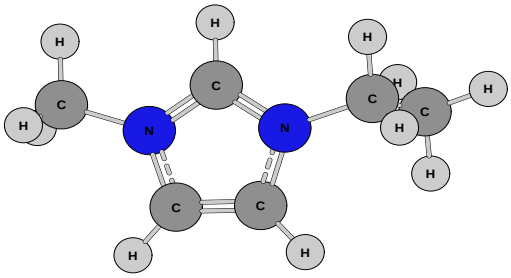

FIG. 1: Cation EMI (1-ethyl-3-methylimidazolium) in the ionic liquid with the best conductivity

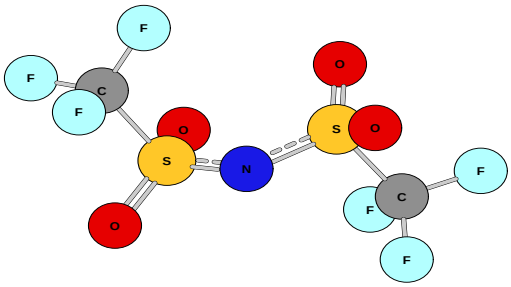

FIG. 2: Anion TFSI (bis(trifluoromethylsulfonyl)imide) in the ionic liquid with the best conductivity

II. EXPERIMENTS

The symmetrical components, including the outer endplates, current collectors and flow fields from a Fuel Cell Technologies 50 cm^2 fuel cell were used to build a liquid conductivity cell (Figure 3), which contains a three-way glass cell with a volume of about 25 ml for liquid elec-

trolyte testing. Two bottom sides of the three-way glass cell separated by a length of 4 cm had attached circular dispersed catalyst (Pt on carbon, 0.4 mg/cm^2) / gas diffusion layers with an active area of 3.0 cm^2. Gaskets attached to glass plates with holes served as leakage protection. A flexible electric heating tape was wrapped around the glass cell for heating. A thermometer and a pressure release adapter were connected to the top of the glass cell. Every component of the liquid cell was cleaned and dried before assembling and then placed in a dry-box, which was continuously pursed with N_2. All the ionic liquids and acids were dried under vacuum at high temperature. For each experiment, more than 20 ml of ionic liquid was charged into the glass cell. Then a measurement of conductivity was made on the neat ionic liquid. Then a measured quantity of acid was added and another conductivity measurement was carried out and so on with a series of incremental additions of acid to obtain the conductivity as a function of acid concentration in the ionic liquid- acid mixture. All the material charges and measurements were carried out in a dry-box. There were no indications of chemical instability of the ionic liquid at either electrode during any of the experiments.

To make the conductivity measurements, prepurified hydrogen gas was bubbled through the liquid cell through the flow fields and catalyst-coated layers on both sides of the cell. Bubbling the hydrogen on both sides of the cell allows equilibrium to be maintained for the $H_2 \leftrightarrow 2H^+ + 2e^-$ reaction at both electrodes so that the open circuit voltage (OCV) is zero. (This procedure is called a 'hydrogen pump' experiment in the literature[4].) Applying a direct current to the cell, hydrogen is consumed at the anode and generated at the cathode. The DC resistances were measured from the slopes of the current-voltage curves (from -1.0 to 1.0 V). The current- voltage curves were scanned using Z-Corrware software, a potentiostat (PAR, 273A), and a frequency response analyzer (Solatron, 1260). Each concentration was measured several times over a period of up to 60 minutes until a stable result was obtained. The conductivity was then calculated from the average DC resistance using the formula: Conductivity = (1/R) L/A, where R is the electrolyte resistance, L is the distance between the two electrodes and A is the active surface area of electrodes.

Using the cell just described, conductivities of the series of ionic liquid-acid mixtures were measured (Table 1). Materials were prepared in anhydrous form were stored and handled in a dry box to prevent adsorption of water. The ionic liquids were prepared according to the procedures described in patent US 6,372,829. The imide acids were prepared according to procedures described in patent US 5,874,616. The methide acids were prepared according to the procedures described in patent US 5,554,664.

The conductivity results shown in Figure 4 indicate that the EMI-TFSI + H-TFSI is the best conducting mixture, followed by EMI-TFSI + H-N$(SO_2C_2F_5)_2$ and EMI-TFSI + H-C$(SO_2CF_3)_3$. Most combinations suggest that very high levels of ionic liquid with lower levels of acid are needed to achieve the highest possible proton conductivity (between 80 to 90 mole%). The only exception is ImH-TFSI + H-TFSI for which the conductivity peaked at 50 mol % ionic liquid. EMI-TFSI has a low viscosity at room temperature, a low melting point (-18^{o}C) and thermal stability up to at least 350^{o}C The proton conductivity is more than 10^{-2} S/cm when 10 mol% of H- TFSI is added to 90 mole % of EMI-TFSI . That is a significant improvement when compared to the very low (or zero) proton conductivity of H-TFSI without ionic liquid additive.

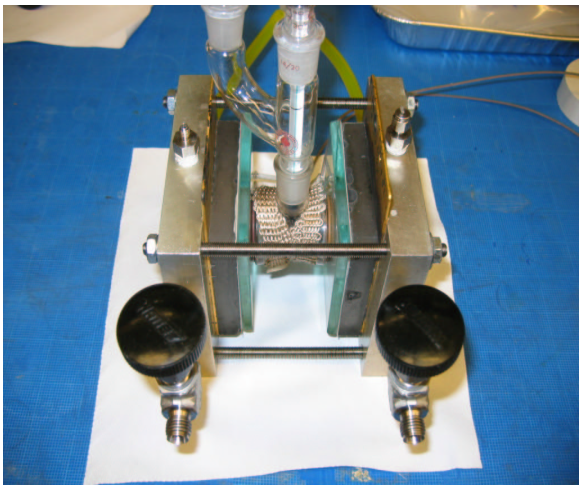

FIG. 3: The liquid cell.

The temperature dependence of the conductivity was measured for several of these systems with results shown in Figure 5. Plotted as $\ln\sigma$ versus $1/T$, most of these data showed linear behavior (as shown for example in Figure 6) corresponding to an activated conduction process with an activation energy of about 0.2eV .

TABLE I:

Ionic Liquid	Acid
EMI-TFSI	H-N$(SO_2CF_3)_2$ (H-TFSI)
EMI-$(C_2F_5SO_2)_2$N (BETI)	H-TFSI
$C_3N_2H_5$ (ImH)-TFSI	H-TFSI
$(C_4H_9)_3N(CH_3)$(Bu3NMe)-TFSI	H-TFSI
EMI-TFSI	H-N$(SO_2C_2F_5)_2$
EMI-TFSI	H-$SO_3C_4F_9$
EMI-$SO_3C_4F_9$	H-$SO_3C_4F_9$
EMI-TFSI	H-C$(SO_3CF_3)_3$
EMI-C$(SO_3CF_3)_3$	H-C$(SO_3CF_3)_3$

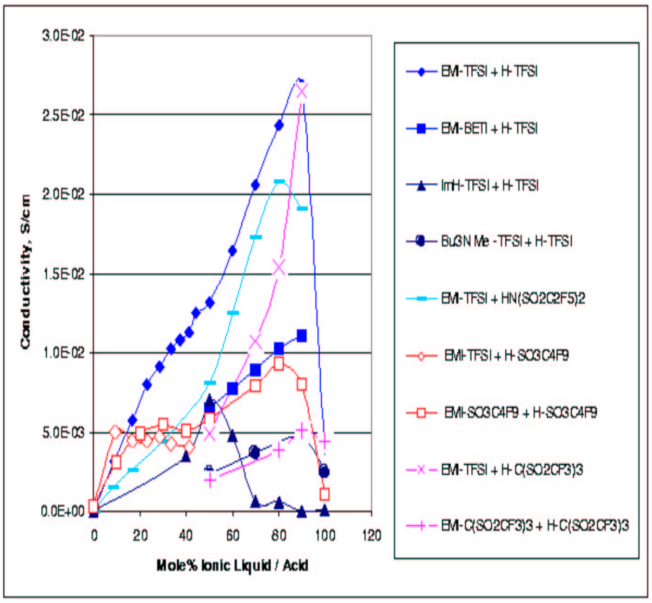

FIG. 4: Data from room temperature measurements of the conductivity of the indicated salts (see Table 1 for key) as a function of mole percent ionic liquid.

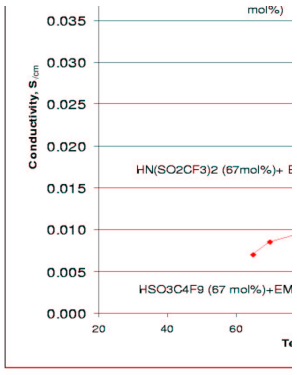

FIG. 5: Conductivity versus T for several of the systems in Figure 3

III. THEORY AND COMPUTATION

To account for the experimental results, and in particular to try to understand the unexpected dependence of the measured conductivity on the acid-salt ratio, we made models and carried out numerical simulations at

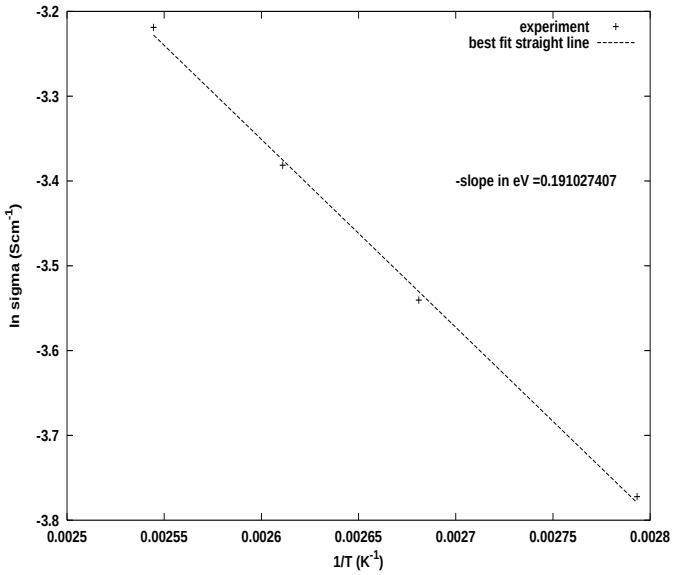

FIG. 6: Log of the conductivity versus $1/T$ For EMI-TFSI (90 mol %), H-TFSI (10 mol %). Straight line is best fit with a slope of 0.2eV.

several levels. At the macroscopic level we made kinetic Monte Carlo simulations to try to understand, at a qualitative level, how the dependence of the conductivity on acid salt ratio might arise. Secondly we performed first principles calculations on small clusters to determine the local energetics and force fields. We then performed molecular dynamics simulations to study the mechanism of transport. Finally, we returned to coarse grained models to further explore the mechanism of transport. We assume in all these modeling studies that ,in the steady state in the experiments, current is entirely carried by the protons, by which we mean that for every electron passing from the cathode to the solution, a proton is reduced and similarly all electrons transferred from the solution to the anode oxidize protons. By simple charge and mass conservation considerations, this will be the case in steady state (dc) as long as there are no Faradaic reactions occuring at the electrodes involving the cation or anion of the ionic liquid. This is believed to be the case to a good approximation in the proton pump experiment described above. The point is discussed somewhat further in the discussion section.

A. General considerations and preliminary Monte Carlo simulations

Note that the experimental conductivity data reported above implies strong collective effects: If the protons diffused or drifted independently of one another then the conductivity would be of form $\sigma = n_H \mu_H |e|$ where n_H is the number density of protons and μ_H is the mobility

which, under the assumption that each proton moves independently of the others, would be independent of n_H. But the expression $\sigma = n_H \mu_H |e|$ then implies a *negative* slope in the data of Figure 4 , whereas a strong *positive* slope is observed over most of the range of acid-salt ratios for the EMI-TFSI,H-TFSI mixtures.

The simplest type of collective effect would be steric blocking of one proton by another. We can roughly model this effect with a lattice model, in which each proton can reside on a lattice site and hops to neighboring sites with a fixed probability at each time step in a Monte Carlo simulation, but with the proviso that the hopping does not occur if the site to which the proton is trying to hop is already occupied by a proton. However, as shown below, such a steric blocking model does not account, even qualitatively, for most of the results shown in Figure 4. To explore the possibilities, we studied two additional models as summarized below. The second model changes the equilibrium distribution of protons due to clustering while retaining steric blocking. In the third model, the kinetic hopping rate depends on the local proton concentration:

Rule 1: Protons hop at a fixed rate and double occupancy is not allowed. Rates are independent of environment and there is not tendency to proton clustering

Rule 2: Same as 1. but protons tend to cluster

Rule 3: Same as 1. But the hoping rate depends on the environment: More protons in the environment slows down the rate.

Characteristic results from Monte Carlo simulations of these three models in three dimensions on a simple cubic lattice are shown in Figures 7-9. (Some details regarding the Monte Carlo simulations appear in Appendix A.) One sees that only rule 3 reproduces the qualitative features of the EMI-TFSI,H-TFSI system. Rule 2 produces conductivity versus concentration curves qualtitatively similar to those found experimentally for EMI-$SO_3C_4F_9$, H-$SO_3C_4F_9$, while Rule 1 results are somewhat like those found for C_2N_2H (ImH)-TFSI, H-TFSI experimentally. The other systems for which data are shown in Figure 4 have dependencies of proton conductivity on acid concentration which are qualitatively intermediate between these three cases. The models have very few parameters which could be varied to fit the data reasonably well in each case. However we regard these Monte Carlo results as having mainly qualitative significance. They indicate that the dependence of proton conductivity on acid concentration requires collective effects in which the protons are not moving independently. A simple blocking effect (Rule 1) cannot account for the data (except possibly in the case of C_2N_2H (ImH)-TFSI, H-TFSI). Clustering of the protons (Rule 2) may account for the data for EMI-$SO_3C_4F_9$,H-$SO_3C_4F_9$. However for the most promising

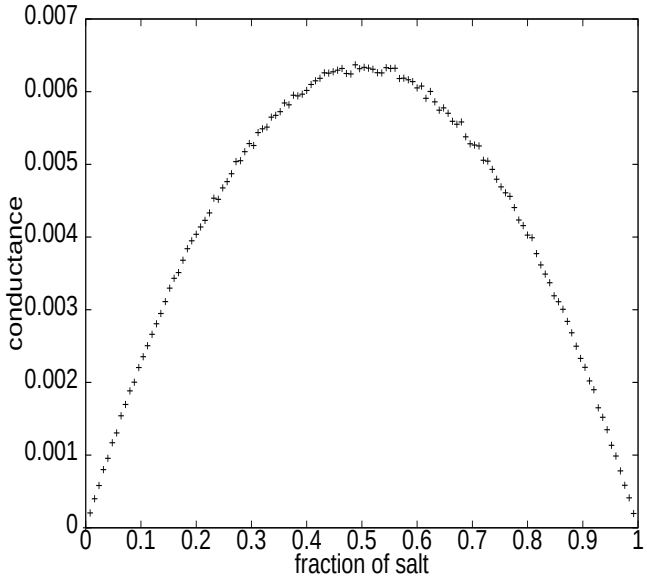

FIG. 7: Monte Carlo results from model obeying rule 1.

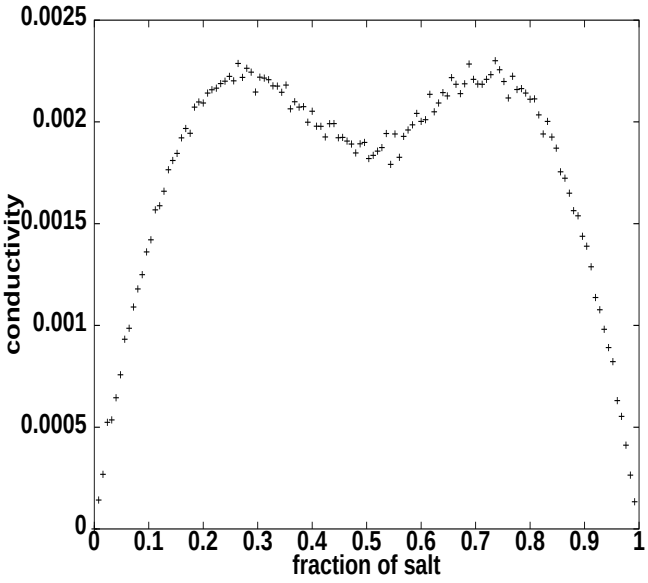

FIG. 8: Monte Carlo results from model obeying rule 2.

EMI-TFSI,H-TFSI system, we seem to need a kinetic collective effect in which the local concentration of protons determines the hopping rate.

B. First principles calculations and development of a molecular dyanmics model

To obtain a more complete picture of the transport mechanism, we developed an atomistically detailed model of the EMI-TFSI,H-TFSI system. The first step in this development was to carry out a number of first principles calculations on small clusters of the constituents

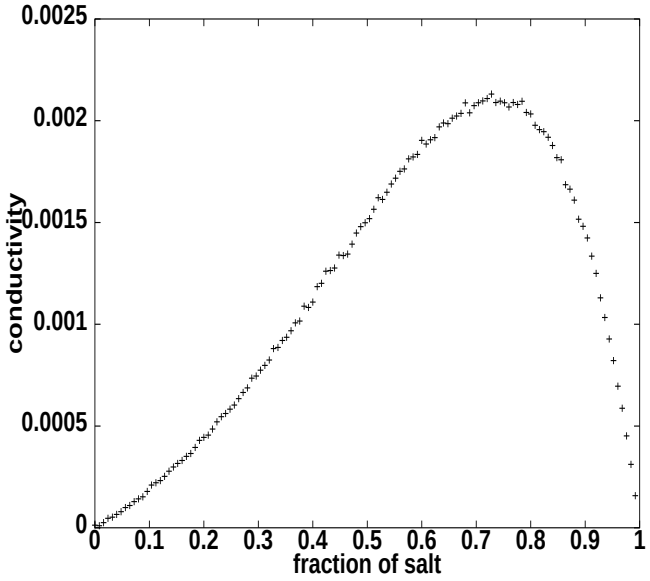

FIG. 9: Monte Carlo results from model obeying rule 3.

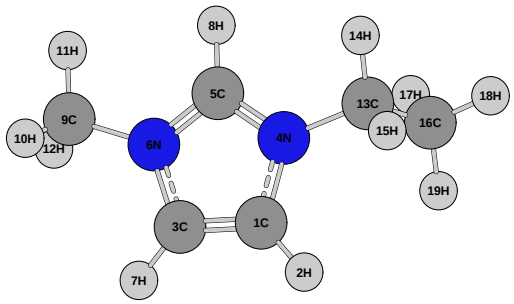

FIG. 10: Structure of EMI cation

of the system. These first principles calculations had two purposes. They provided a data base for development of a quantitatively realistic molecular dynamics model (for which results are described in the next section) and they provided some insight into possible microscopic proton hopping mechanisms. (It is of some precautionary general interest that at least one of the hopping mechanisms suggested by the small cluster calculations was later shown by the larger scale MD calculations to be less important than another mechanism only made possible by the stabilizing Coulombic effects of larger numbers of atoms than we could treat in first principles.) First principles calculations using the Gaussian suite of codes [10] were made for a number of structures of atomic conformations of the EMI and TFSI ions individually, for a proton placed at various positions along a line between the nitrogens of two TFSI anions and for a proton placed at various positions along a line between the nitrogen and an oxygen of two TFSI anions.

TABLE II: Structural parameters for an isolated EMI cation from the first principles calculations, the fitted MD model and X-ray experiments

	Geometry	QM calcd.	MM calcd.	X-ray[a]
Bond Length (Å)	C_1C_3	1.34	1.35	1.38
	C_1N_4	1.38	1.38	1.41
	C_3N_6	1.38	1.38	1.39
	N_6C_5	1.32	1.32	1.30
	N_4C_5	1.31	1.32	1.27
	C_4C_{13}	1.48	1.48	1.55
	$C_{13}C_{16}$	1.52	1.54	1.43
	N_6C_9	1.47	1.47	1.48
Angles(°)	$N_4C_5N_6$	109.9	110.0	110.0
	$C_5N_6C_3$	108.0	107.8	111.0
	$C_5N_4C_1$	108.0	107.7	109.0
	$N_6C_3C_1$	107.0	107.1	104.0
	$N_4C_1C_3$	107.2	107.4	106.0
	$C_5N_6C_9$	126.3	126.9	126.0
	$C_5N_4C_{13}$	126.1	126.8	130.0
	$N_4C_{13}C_{16}$	112.1	109.0	104.0
Dihedral Angles(°)	$C_{16}C_{13}N_4C_5$	106.4	106.4	
	$C_{16}C_{13}N_4C_1$	72.6	76.1	

[a]Taken from *J. Mol. Struct.* **1989**, 213, 25

We compare structural parameters for the isolated ions of the ionic liquid as obtained from first principles, the fitted molecular dynamics model and x-ray experiment in Tables 2 and 3(See Figures 10 and 11 for label and serial number of atoms in cation and anion). We show first principles energies and the fit of the molecular dynamics model to them for the TFSI-H^+-TFSI cluster in Figures 12 and 13 .

Some details of the fitting procedures and the forms of the molecular dynamics force field potentials as well as a listing of the fitted parameters appear in Appendix B.

We note from figures 12 and 13 that in the TFSI-H^+-TFSI cluster, the position of the proton is bound to the nitrogen and Figure 12 might suggest a hopping mechanism from N to N as a likely one for describing the proton transport. However, we found, as described in the next section that, in the presence of many anions and cations, the proton is actually solvated mainly by the oxygen of the TFSI ions.

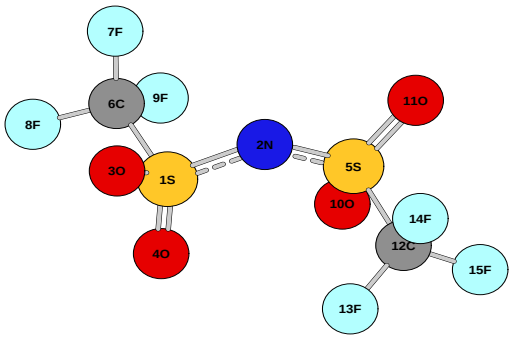

FIG. 11: Structure of TFSI anion

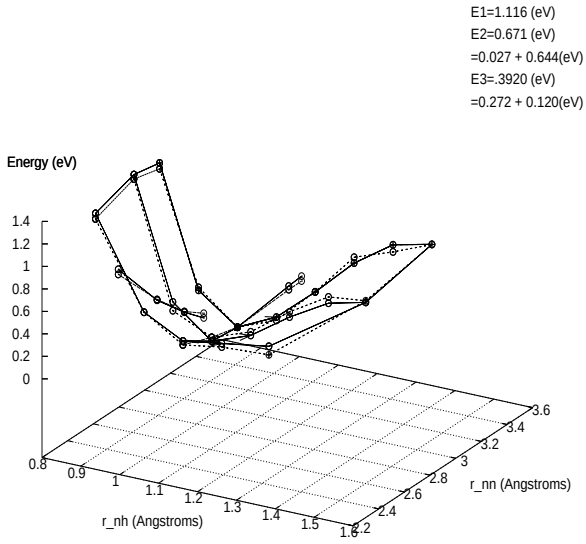

FIG. 12: Energy of the TFSI-H^+-TFSI cluster as a function of the H-N and N-N distances. The H^+ was fixed on a line between the two N and the H-N and N-N distances were fixed while all the other atomic positions were relaxed. Both the first principles results(solid lines) and the molecular dynamics fit to them(dotted lines) are shown.

TABLE III: Structural parameters for an isolated TFSI anion from the first principles calculations, the fitted MD model and X-ray experiments

	Geometry	QM calcd.	MM calcd.	Exp.[a]
Bond Length (Å)	C_6F_7	1.32	1.32	1.30
	C_6F_8	1.32	1.32	1.31
	C_6F_9	1.31	1.30	1.25
	C_6S_1	1.83	1.82	1.81
	S_1O_3	1.43	1.43	1.42
	S_1O_4	1.43	1.43	1.41
	S_1N_2	1.57	1.57	1.58
Angles(°)	$S_1C_6F_7$	111.4	109.6	110.9
	$S_1C_6F_8$	109.7	110.3	110.7
	$S_1C_6F_9$	111.4	111.0	110.6
	$O_3S_1O_4$	118.6	118.7	119.4
	$O_3S_1N_2$	109.2	108.6	107.8
	$C_6S_1N_2$	102.6	101.2	104.0
	$S_1N_2S_5$	128.3	129.3	125.0
	$O_4S_1N_2$	116.3	117.3	116.0
Dihedral Angles(°)	$O_3S_1N_2S_5$	155.8	163.0	
	$O_4S_1N_2S_5$	18.3	24.9	
	$C_6S_1N_2S_5$	-95.0	-87.8	

[a]Taken from *Inorg. Chem.* **1996**, 35, 1918.

C. Molecular Dynamics Simulations

Using the model defined and parametrized as described in the last section and in Appendix B, we first explored its predictions for the neat ionic liquid in the absence of acid. We studied a system of 108 TFSI anions and 108 EMI cations (3672 atoms) in a cubic box of dimensions 36.00 Åx36.00 Åx36.00 Å, which was chosen to give the experimental density of 1.52g/cm^3 at 295K[11]. The pressure in the simulation as measured using the virial was about 20 atm. To interpret the results we first measured the radial distribution functions of the ion centers of mass, in order to get an idea of the liquid structure. We show TFSI-TFSI,TFSI-EMI and EMI-EMI radial distribution functions and running coordination numbers as calculated from the MD model in Figures 14, 15 and 16. The anion-cation correlations are significant. There are approximately 6 anion neighbors in the first solvation shell of each cation and vice versa. The anion- anion correlations are less significant but definitely present whereas, except for steric effects, the cation positions do not appear to be correlated at all. Unfortunately, we did not find any experimental data with which to compare this simulation data on the ionic liquid structure.

Because the EMI cations have a planar structure, it seemed possible that there might be some orientational correlations of the molecules in the liquid, and that these could have some effect on the proton conductivity. Accordingly, we measured the following orientational correlation function in the model liquid.

$$f_{\rm ocf}(r) = (1/(4\pi r^2\rho)) \sum_{i\neq j} \left\langle ((\hat{n}_i \cdot \hat{n}_j)^2 - (1/3))\delta(r - r_{ij}) \right\rangle \quad (1)$$

Here i and j run over cations or anions depending on whether we are calculating partial anion-anion, anion-cation or cation-cation correlation functions. $\hat{n}_i$ is a unit vector in the direction of that principal axes of the ion i which has the largest moment of inertia. The angular brackets indicate a time average. ρ is the number density of the ions of one charge sign and r_{ij} is the distance between the centers of mass of the ions i and j. Numer-

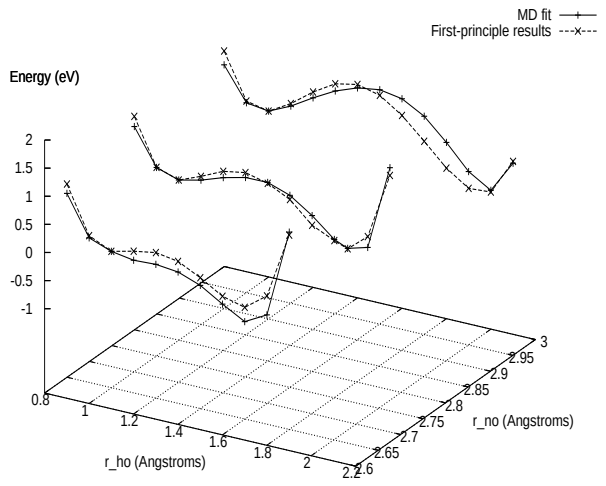

FIG. 13: Energy of the TFSI-H^+-TFSI cluster as a function of the H-O and N-O distances. The H^+ was fixed on a line between the N on one TFSI and O on the other TFSI and the H-O and N-O distances were fixed while all the other atomic positions were relaxed. Both the first principles results and the molecular dynamics fit to them are shown.

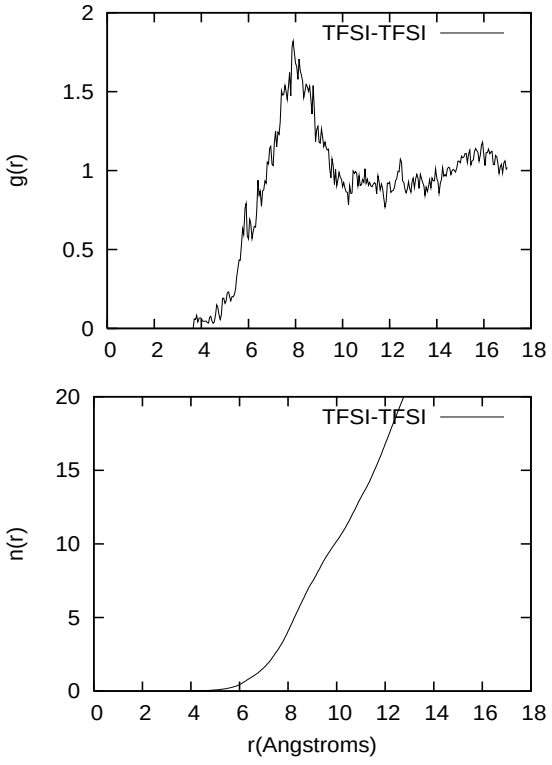

FIG. 14: Top:Calculated radial distribution function for the centers of mass of the TFSI ions in the ionic liquid TFSI-EMI at 300K. Bottom: Running coordination number.

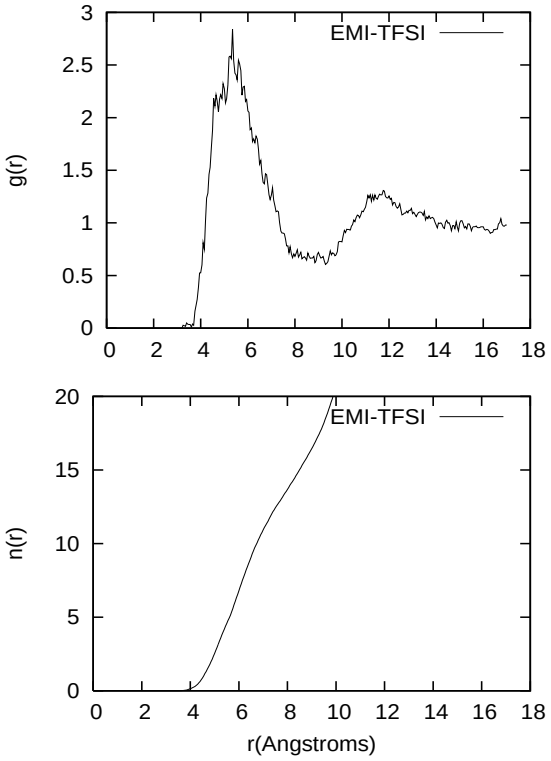

FIG. 15: Top:Calculated EMI-TFSI radial distribution function for the centers of in the ionic liquid TFSI-EMI at 300K. Bottom: Running coordination number.

ically, the delta function is approximated by a Heaviside function so that the correlation function is approximated by

$$f_{\rm ocf}(r) \approx (1/(\rho 4\pi r^2 \Delta r)) \sum_{i\neq j such\ that\ r-\Delta r/2<r_{ij}<r+\Delta r/2} \quad (2)$$

$$\left\langle ((\hat{n}_i \cdot \hat{n}_j)^2 - (1/3)) \right\rangle$$

We show EMI-TFSI,TFSI-TFSI and EMI-EMI orientational correlation functions as calculated from the MD model in Figures 17,18 and 19. From the Figures 17,18 and 19, we conclude that at 300K local orientational order exists in the neat ionic liquid, but no long range order is found.

D. Calculations of proton conductivity in the MD model

To calculate proton conductivities in the ionic liquid acid mixtures, protons were introduced into the MD model for the ionic liquid. (Cations were removed, and protons were substituted for them.) Some calculated radial distributions for oxygen and nitrogen around the protons are shown in Figure 20. The protons are typ-

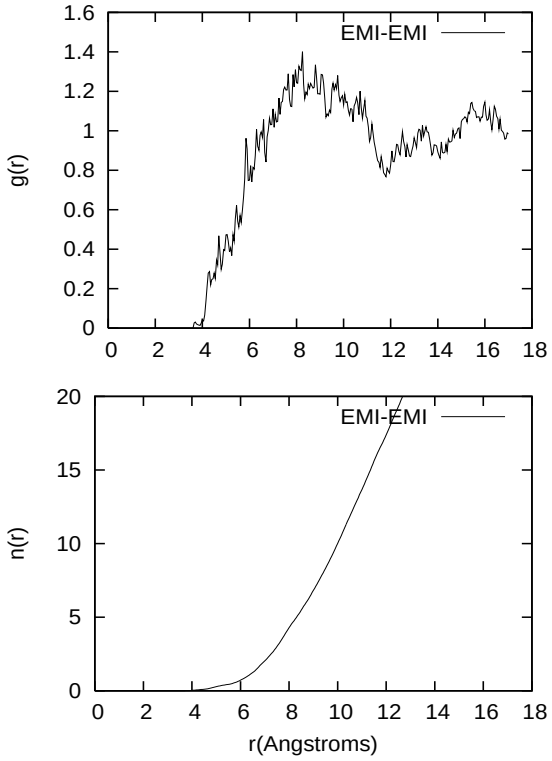

FIG. 16: Top:Calculated radial distribution function for the centers of mass of the EMI ions in the ionic liquid TFSI-EMI at 300K. Bottom: Running coordination number.

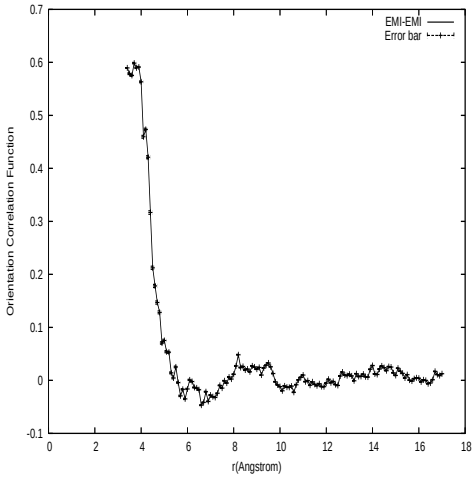

FIG. 17: Calculated orientational correlation function for the principal axis with the largest momentum of inertia of the EMI ions in the ionic liquid TFSI-EMI at 300K.

ically bound to one oxygen and have about 3 other oxygen neighbors as well as two nitrogen neighbors a little farther away at about 3-4 Angstroms. Several anions are involved in this solvation structure. A snapshot of the local structure is also shown in Figure 21.

To study proton transport in the molecular dynamics

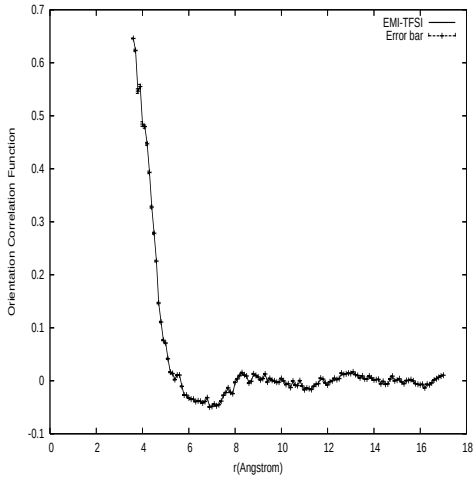

FIG. 18: Calculated orientational correlation function for the principal axis with the largest momentum of inertia of the EMI ions and TFSI ions in the ionic liquid TFSI-EMI at 300K.

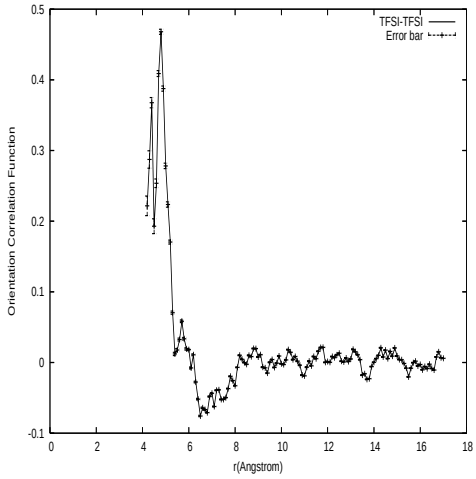

FIG. 19: Calculated orientational correlation function for the principal axis with the largest momentum of inertia of the TFSI ions in the ionic liquid TFSI-EMI at 300K.

model, we directly calculated the conductivity at finite frequencies by using the following well known relation:

$$\sigma(\omega) = \frac{1}{3k_BT}\int_0^\infty e^{-i\omega t}\left\langle \sum_H q_H \vec{u}_H(\tau)\cdot\sum_j q_j\vec{u}_j(t+\tau)\right\rangle dt \quad (3)$$

The sum on H is over protons (charge q_H)and the sum on j runs over protons and all the atoms of each ion (charge q_j). The brackets indicate an average over the times τ. To analyse the conduction mechanism, we split the sum in the equation (3) into parts containing the proton-proton and proton-TFSI and proton-EMI current-current correlation functions.

As an example, we show results in Figure 22 for the calculated frequency dependent conductivity for the sys-

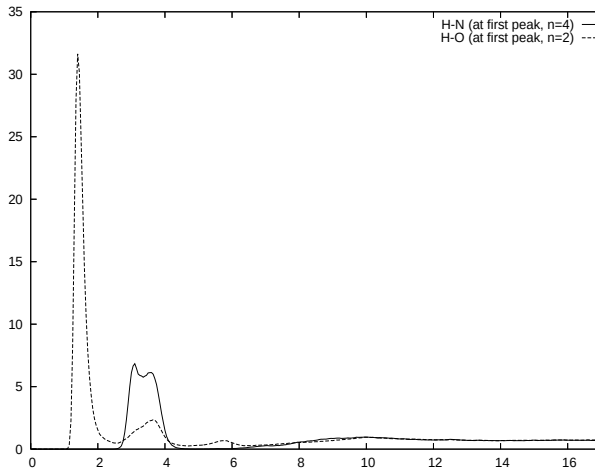

FIG. 20: The radial distribution functions $g_{HO}(r)$ and g_{H} from the molecular dynamics model for 108 TFSI, 93 EMI 15 protons. The protons are trapped by one O and ha other O next nearest neighbors.

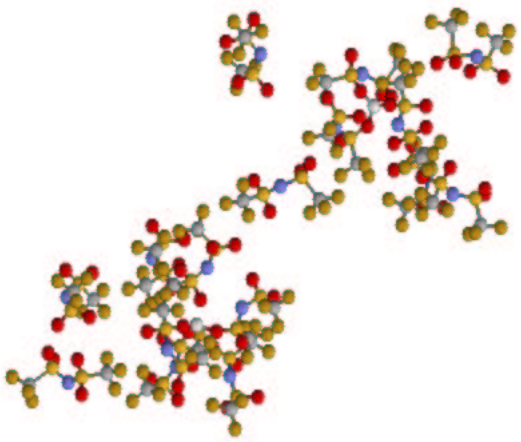

FIG. 21: Snapshot of a part of the simulation with 15 protons, 93 EMI and 108 TFSI. The EMI are not shown. H is white, O is red, C is gray, S is yellow and F is brown. There are two protons in this picture and each of them is 4 fold coordinated with O with one of the 4 bonds much shorter than the other three.

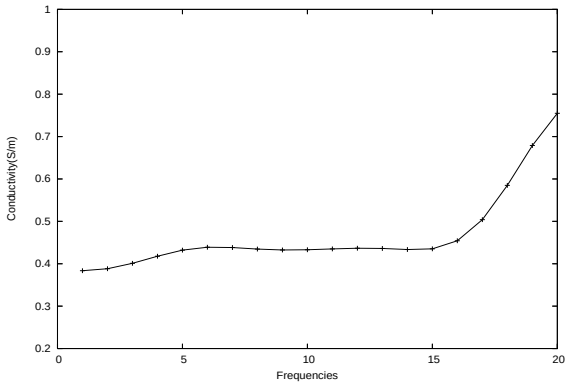

FIG. 22: Conductivity calculated from the proton-proton current-current correlation function as a function of frequency for the system containing 5 protons at T=385K

tem containing 5 protons at 385K.

To estimate the zero frequency proton conductivity from such data we fit the conductivity to the formula $\sigma(\omega) = \sigma(0) + b\omega^2$ to extrapolate to zero frequency. The results of this procedure depended on the maximum frequency which was used in the data base which was fit to the form $\sigma(\omega) = \sigma(0) + b\omega^2$. To find the best value of the maximum frequency to use we calculated the variance (the maximum frequency used is ω_{N_f})

$$(1/N_f)\sum_{i=1}^{N_f}(\sigma(0) + b\omega_i^2 - \sigma^{MD}(\omega_i))^2 \tag{4}$$

and the variance of the mean

$$\sqrt{\frac{1}{N}\sum_i\left(\frac{\sigma_i}{\bar{\sigma}_j} - 1\right)^2} \tag{5}$$

of the data set from the fit as a function of the maximum frequency and used the maximum frequency which gave the smallest variance of the mean, as illustrated in Figure 24. With this procedure we extrapolated all the partial conductivities to zero frequency. Using this procedure and quite long simulation runs (2 ns) we found reproducible values of the dc conductivity at most of the acid concentrations for which calculations were done. However in the 18 proton computational sample (16.7 mol % acid) we found large sample-to-sample fluctuations in the calculated conductivity. Accordingly, we report results for the average calculated conductivity and the variance for 10 computational samples at each proton concentration in Figure 25. In that figure, a correction, described in Appendix C, has been applied, using the calculated partial conductivities, to take account of the fact that in the experiment, the anion and cationic currents are not allowed to flow. Taking this constraint into account, the effective proton conductivity measured is

$$\sigma_{eff} = \sigma_{HH} - \sigma_{OH}^2/\sigma_{OO}$$

where σ_{HH} is the portion of the conductivity calculated from the proton-proton current-current correlation function, σ_{OH} is the contribution to the unconstrained conductivity arising from the proton-current other(cation

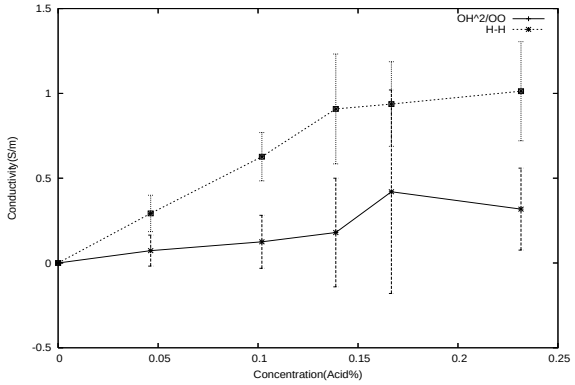

FIG. 23: H-H Conductivity and corrections as a function of proton concentration at T=385K

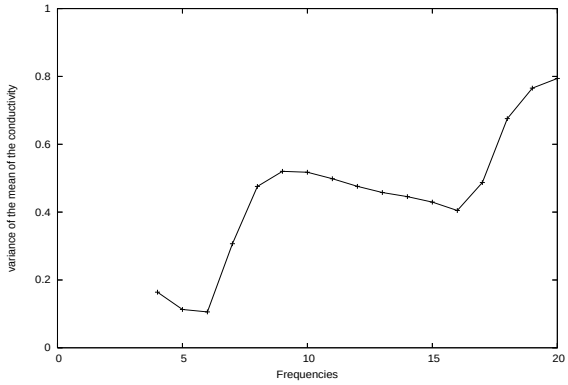

FIG. 24: Variance of the mean fit error as a function of maximum frequency used in the fit for the system containing 5 protons at T=385K

and anion)-current correlation function and σ_{OO} is the other current-other current contribution to the unconstrained conductivity.

The results for the average calculated proton-proton conductivities and corrections and the variance for 10 samples at each proton concentration are shown in Figure 23.

As noted, the variances (indicated by the error bars) are small except in the case of the 18 proton (16.7 mol % acid) system. One sees from the figure that the experimentally observed nonmonotonicity in the proton conductivity as a function of concentration is qualitatively reproduced. The proton concentration at which the calculated peak in conductivity occurs is close to the experimentally observed one, though the magnitude of the calculated conductivity is less than the magnitude of the experimentally observed conductivity by a factor of 4 to 5. A very small error in the activation energy of the relevant processes could account for the discrepancy in magnitude. We regard this as reasonable agreement, probably indicating that in the calculations, a process similar to the one occurring in the real fluid is determining the proton conductivity.

To try to understand the origin of the change at 17% acid concentration , we made a more detailed exploration of the configurations of the protons in the samples. We discovered that, in the calculations, some of the protons are paired in the computational samples with higher concentrations of protons. This pairing effect is visible in the proton-proton pair radial distribution functions for the 15-proton and 18-proton systems as shown in Figures 26 - 28 (shown for one of the computational samples).

The pairing phenomenon can also be described in terms of the potential of mean force $W_{mf} = -k_B T \ln g_{HH(r)}$ as shown for example in Figures 29 and 30 . Minima are seen at around 2 Å in simulations with 18 protons and more. In the simulations with 15 and less protons minima appear at proton-proton distance ≥ 4Å.

To try to understand the origin of the large fluctuations in calculated conductivity from one computational sample to another, in the case of the 18 proton system, we

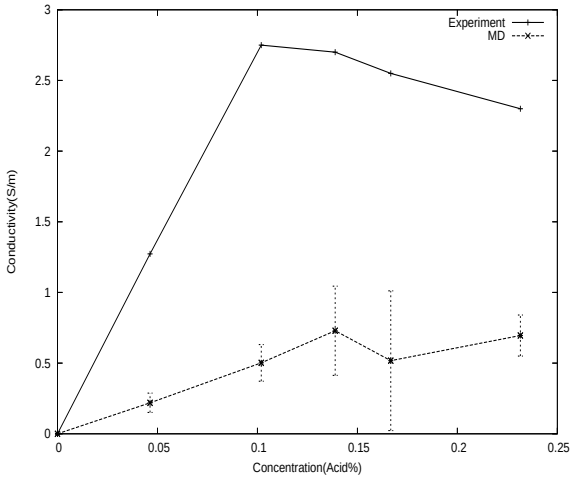

FIG. 25: Calculational results for the d c proton conductivity of the EMI-TFSI, H-TFSI mixture compared with the experimental results.

calculated the proton-proton radial distribution function for each of the ten computational samples. The results were qualitatively similar except in one case, in which a triplet of three bound protons was observed.

IV. DISCUSSION AND CONCLUSIONS

Clearly there are multiple ions present in these mixtures capable of contributing to the measured conductivity. For these materials to be useful in a fuel cell electrolyte, it is necessary that protons account for a sufficient fraction of the conductivity to allow the device to perform at high currents, and that other ions are not being transported in large quantities, which can create concentration gradients and degrade performance. In these DC, hydrogen pump measurements, the fact that no electrochemical reduction or oxidation of the electrolyte is observed during the experiments strongly suggests that

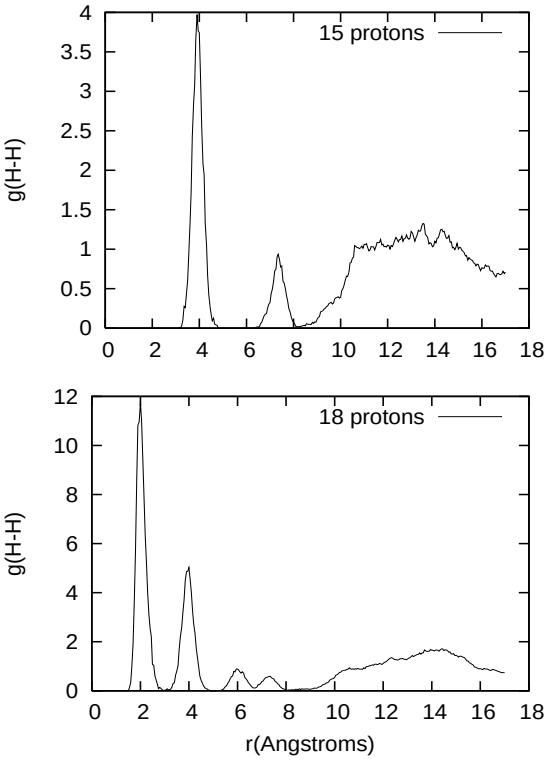

FIG. 26: Radial distribution functions of 15-proton system and 18-proton system.

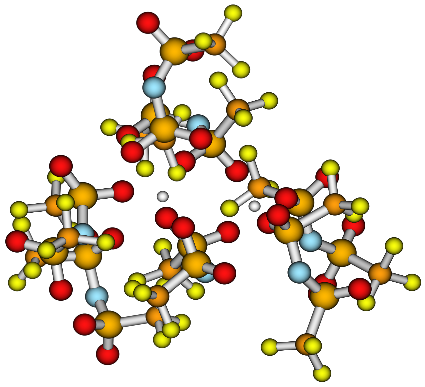

FIG. 27: Snapshot of a part of the simulation with 15 protons, 93 EMI and 108 TFSI. The EMI are not shown. There are two protons in this picture.

most of the current is due to proton transport in these experiments. However it does not rule out contributions to the measured conductivity from other ions as a result of the low frequency variations in the field during the measurements, or as a result of very slow electrolyte reactions which could be occurring at the electrodes. It is possible that electrolyte concentration gradients are present during the measurements. On the other hand, the large

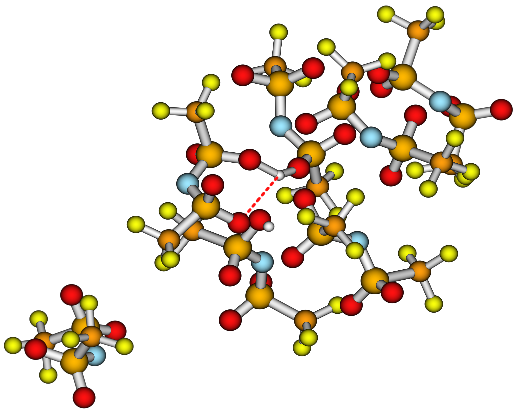

FIG. 28: Snapshot of a part of the simulation with 18 protons, 90 EMI and 108 TFSI. The EMI are not shown. There are two protons in this picture.

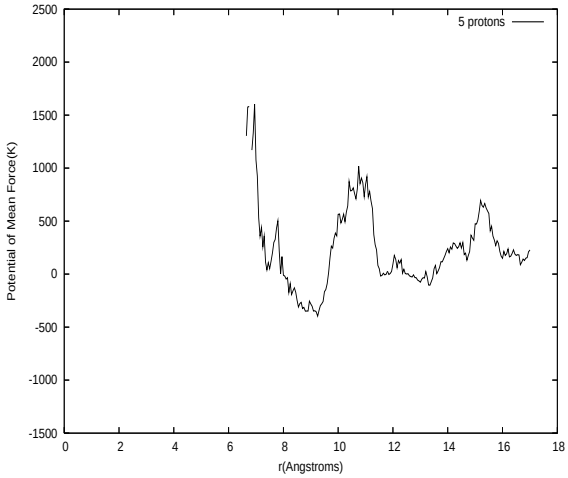

FIG. 29: Potential of the mean force for the systems containing 5 protons

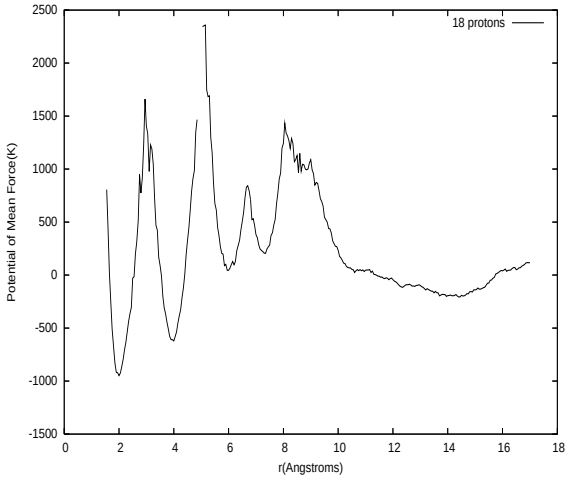

FIG. 30: Potential of the mean force for the systems containing 18 protons

increase in conductivity seen in the presence of the added acids compared to the pure ionic liquid strongly suggests that protonated species are responsible for the bulk of the charge transport. In the computations, if we assume that the EMI and TFSI are completely absorbed at the electrodes then we get a substantially different conductvity than if, as described in Appendix C, and in the text, we impose the constraint that no EMI or TFSI current flows. This emulates the situation in the experiment, in which a concentration gradient is expected to reduce the net ionic currents to zero if the ions do not participate in Faradaic reactions at the electrodes. From Figure 23, where the effect of the constraint on the calculated conductivity is shown, one can see that the effect is small but not completely negligible.

Of the various ionic liquids on which experiments were done, the EMI-TFSI system showed the most promising conductivity for fuel cell applications. Our molecular dynamics simulations reproduce the nonmonotonic behavior of the acid-ionic liquid system H-TFSI, EMI-TFSI as a function of ionic liquid concentration reasonably well (Figure 25). However this comparison does not fully explain the origin of the nonmonotonic behavior without further analysis. A hint of what may be happening is provided by the snapshots of the ion positions during the simulation after the proton conductivity has begun to decrease with increasing proton conductivity (Figure 28). One sees some evidence that the protons are pairing. Looking more closely, Figure 28, we find that some paired protons are surrounded by an overscreening shell of TFSI anions. If the cluster of proton pair and screening anions acted like a kind of superanion, whose current was negatively correlated with the EMI current, such negative superanions would move against an applied electric field, carrying the embedded protons with them and causing a decrease in the proton conductivity. One can make a simple model capturing this possibility as follows. Consider the reaction

$$2H^+ + nA^- \leftrightarrow (H_2A_n)^{2-n} \tag{6}$$

where $n > 2$ and A^- is the anion (here TFSI). In equilibrium

$$[H^+]^2[A^-]^n/[(H_2A_n)^{2-n}] = K' \tag{7}$$

and if y is the molecular per cent ionic liquid

$$y = 1 - [H^+] - 2[(H_2A_n)^{2-n}] \tag{8}$$

so that, solving for $[H^+]$

$$[H^+] = (K/4)\left[\sqrt{1 + (8./K)(1-y)} - 1\right] \tag{9}$$

where $K = K'/[A^-]^n$ is constant as y is varied because the ionic liquid and the acid have the same anion. Now we model the proton conductivity as

$$\sigma_p = q\mu[H^+] - 2q\mu'[(H_2A_n)^{2-n}] \tag{10}$$

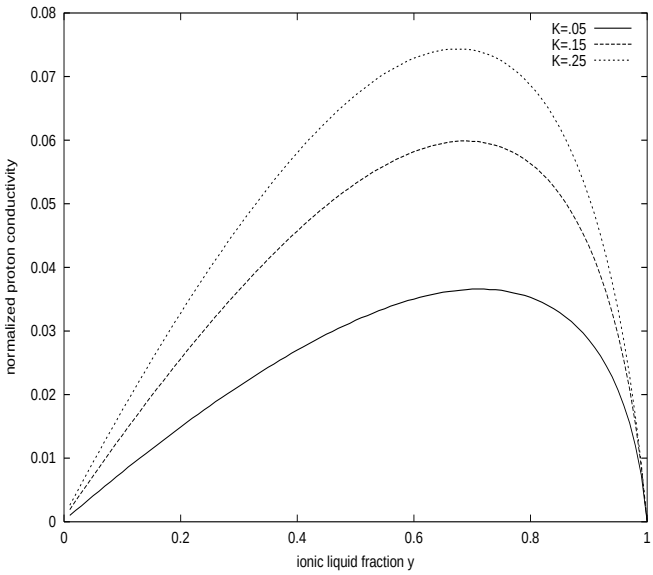

FIG. 31: Form of the proton conductivity in a model in which the protons form a negative complex with the anions. y is the mol concentration of ionic liquid. The parameter K is a renormalized equilibrium constant defined in the text. The renormalized conductivity is $\sigma_p/q\mu$ as defined in the text.

assuming, as in the discussion above, that the negative complex moves against the field with a mobility μ'. This is rewritten

$$\sigma_p/q\mu = [H^+](1 - R[H^+]) \tag{11}$$

where $R = 2\mu'/\mu K$. The proton conductivity is only positive in this model if $R < 1/[H^+]$. In fact, it is possible for the protons to move against the field in this model so negative proton conductivities could occur. However no such phenomenon is observed experimentally so we illustrate this model with values of R chosen just below the upper limit of this range. We plot the resulting values of the proton conductivity for some values of the two parameters K and R in Figure 31 . The assymmetric peak is reproduced, though we did not find values of the parameters which gave a peak at the value of $y \approx 0.9$ which is observed in experiment.

A similar, but somewhat different possibility is that at higher proton concentrations, the acid and the ionic liquid in these systems might be starting to phase separate. One can imagine a phase diagram in y-T space (y is the ionic liquid molar concentration and T is the absolute temperature) as sketched in Figure 32. As one crosses into the two phase region as the proton conductivity is increased, the system separates into an ionic liquid rich and an acid rich phase. Because the acid has low proton conductivity, one expects the proton conductivity to be dominated by the ionic liquid rich phase, but as one gets deeper into the two phase region, less and less of the mixture consists of ionic liquid rich phase and the total conductivity would decrease, as observed. It is unlikely that our MD simulations are large enough to

explicitly simulate such a phase separations and it is possible that the proton clustering we see in the simulations is a microscopic signature of it. One can make a simple mean field type model of the proton conductivity in such a phase separation model. Suppose that near the y=1 part of the phase diagram, in the ionic liquid rich one-phase region, the proton conductivity follows the usual form $(1-y)\mu_H n$ associated with uncorrelated motion of protons. μ_H is the proton mobility and n is the average ionic density. When, with decreasing y at fixed T, the concentration reaches the 2 phase region, the proton conductivity of the ionic liquid rich region is assumed to remain at $(1-y_1)\mu_H n = \sigma_1$ while y continues to decrease. The total contribution of the ionic liquid rich fraction of the two phase mixture in that two phase region is $\sigma_1(y-y_2)/(y_1-y_2)$ where y_2 is the other, ionic liquid poor end of the constant temperature 'tie line' in the assumed phase diagram. If the proton conductivity in the ionic liquid rich phase is much larger than the proton conductivity in the acid rich phase (which is consistent with the experiments) then the proton conductivity would have the form shown in Figure 33, which is qualititatively consistent with several features of the experiments. The simple model does not take account of the requirement that the ionic liquid phase must contain a continuous conducting path across the sample. Because the densities of the two phases are likely to be different, if full equilibrium were achieved, then the higher density phase would be on the bottom of the container in unstirred equilibrium and such a path would exist. However, no indications of such phase separation are evident in the samples prepared for this experiment, even after they were stored for several months. Various bicontinuous phases might be imagined though their stability over such a wide range of concentrations seems unlikely.

In summary, though the phase separation model may be consistent with the simulations and provides a conduction concentration function much like the experimental ones, qualitative observation does not encourage the idea that these systems are phase separating and something like the other model as described above seems more likely to account for the observations. Though that, monomer-dimer equilibrium, model did not give as satisfactory an account of the shape of the concentration versus conductivity relation (though it was qualitatively correct), the model could be elaborated, for example by including equilibria between larger clusters as well. This will be explored further.

Another interesting outstanding issue is the question of the origin of the attraction which is causing proton pairing in the simulations, as well as the question of whether evidence of such pairing can be observed experimentally. With regard to the former issue, there is a substantial literature on possible mechanisms of attraction of charged species of the same charge attracting each other in complex media. Mechanisms include entropic ones as well as mechanisms based on subtle complex screening effects. With regard to experimental observability of the pairs, we will explore the possibility that there presence might be detected in NMR experiments.

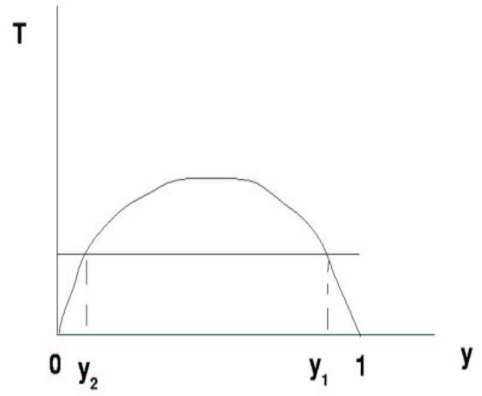

FIG. 32: Form of the phase diagram in a phase separation model. y is the mol concentration of ionic liquid. The region under the curve is a two phase region. The horizontal line indicates the temperature at which an experiment measuring proton conductivity is carried out while varying y. When $y_2 < y < y_1$ the system consists of a mixture of ionic liquid rich and acid rich phases.

V. ACKNOWLEDGEMENTS

We would like to thank Dr. Radoslav Atanasoski and Mr. Gregory Haugen for useful discussions and assistance with the design of the conductivity cell. This research was supported in part by the U.S. Department of Energy, Cooperative Agreement No. DE-FC36-02AL67621 and by the The Minnesota Supercomputing Institute. DOE support does not constitute an endorsement by DOE of the views expressed in this presentation.

VI. APPENDIX A: MONTE CARLO MODELS

In the preliminary simulations described in section III.A, entities ('protons') were initially distributed at random on a simple cubic lattice with multiple occupancy forbidden. The model which described the simulated dynamics can be described by

$$dn_i/dt = \sum_\delta (-W_{i,i+\delta} n_i + W_{i+\delta,i} n_{i+\delta})$$

in which, for Rule 1: $W_{i+\delta,i} = 0$ unless $i+\delta$ is occupied and i is unoccupied, $W_{i+\delta,i} = 0.5$ if the neighbor δ is in

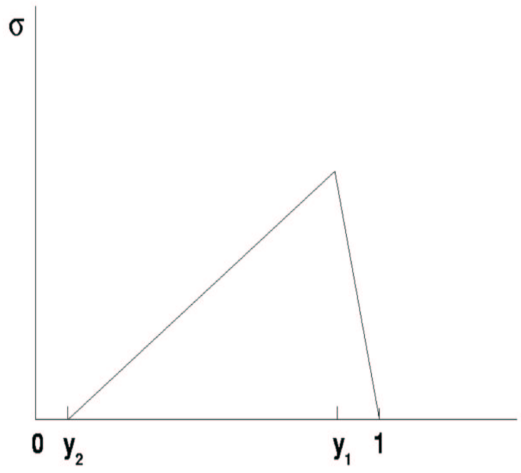

FIG. 33: Form of the proton conductivity in a phase separation model. y is the mol concentration of ionic liquid. The region between y_2 and y_1 is a two phase region. The acid proton conductivity is assumed to be much less than the proton conductivity of the ion-liquid rich phase in the two phase region.

a direction transverse to the field, $W_{i+\delta,i} = D/(1+D)$ if the neighbor δ is in the direction along the field and $W_{i+\delta,i} = 1/(1+D)$ if is in the direction opposite to the field, with similar definitions for the $W_{i,i+\delta}$. One may think of the field as proportional to $\ln D$. For each concentration of 'protons', we ran 230000 steps (about 1064/site) on a 6x6x6=216 site lattice in which, in each step, a site was selected at random. If it contained a proton, a neighbor was selected at random and, if the neighboring site was empty, the proton was moved to the neighboring site with probability $W_{i,i+\delta}$. If the site did not contain a proton and a randomly selected neighboring site was occupied then the proton on the neighboring site was moved to the site with probability $W_{i+\delta,i}$. Periodic boundary conditions were employed for the dynamics and the current was monitored by counting protons which moved in and out of the faces of the simulation box which were perpendicular to the field. Conductivities were determined by fitting the current data as a function of $\ln D$ which were accurately linear, to a straight line. For rule 2, the values of $W_{i+\delta,i}$ became $D'/(1+D')$ where $D' = exp(s\Delta n)D$ (forward hops),$D' = exp(s\Delta n)/D$ (backward hops) and $D' = exp(s\Delta n)$ (transverse hops). Here s is a parameter and Δn is the difference between the number of occupied neighbors of $i+\delta$ and the number of occupied neighbors of i. For rule 3, all the hopping rates W were reduced by a factor $exp(-f*\Sigma N)$ where f was a parameter and ΣN was the sum of the number of occupied neighbors of $i+\delta$ and the number of occupied neighbors of i. For the models discussed in the last section, half of the lattice was occupied by 'anions', placed at random and various numbers, depending on 'acid' concentration, of 'protons' were then placed at random on the occupied anion sites. During the dynamics, the allowed moves were anion without proton to empty site, proton to a neighboring site occupied by an anion (but not occupied by a proton) and anion plus proton to an empty site (without field bias). For the 'correlated' model in the last section, the rates were biased by the sum of the number of protons on the starting and target sites, as in Rule 3.

VII. APPENDIX B: MOLECULAR DYNAMICS MODEL

The force field model can be described in the following functional form:

$$\begin{aligned} E \;=\; & \sum_{\text{bonds}} K_r(r-r_{\text{eq}})^2 + \sum_{\text{angles}} K_\theta(\theta-\theta_{\text{eq}})^2 + \\ & + \sum_{\text{dihedrals}} K_d[1+\cos(n\theta-\gamma)] + \\ & \sum_{i=1}^{N-1}\sum_{j>i}^{N}\left\{4\epsilon_{ij}\left[\left(\frac{\sigma_{ij}}{r_{ij}}\right)^{12}-\left(\frac{\sigma_{ij}}{r_{ij}}\right)^{6}\right]+\frac{q_iq_j}{r_{ij}}\right\} \end{aligned}$$

where the first three terms are for intramolecular interactions, including bond streching, bending and torsion terms, and the last two terms are for non-bonded interactions, including Lennard-Jones and coulomb interactions terms. In our model, the Lennard-Jones and Coulomb interactions are calculated between atoms in different molecules and between atoms in same molecule but seperated by at least three bonds. Lennard-Jones parameters for interactions between different atom types are obtained by use of the Lorentz-Berthelot mixing rule.

For both EMI cation and TFSI anion, atom type and preliminary force field parameters were first taken from [14]. Starting with these parameters carried out a refinement by fitting the MD model to the results of first principles calculations on a set of atomic configurations of the anion and cation. The procedure was:

1. Generate 500 different configurations for a single cation and anion.

2. Calculate the first principles energy E_G for each atomic configuration using first-principle method at HF/6-31G* level.

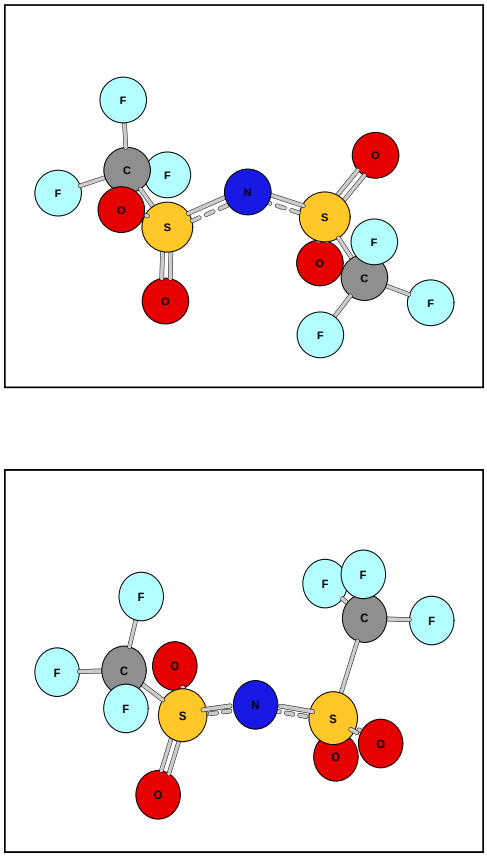

FIG. 34: Top:The structure of TFSI anion with C2 symmetry. Bottom:The structure of TFSI anion with C1 symmetry

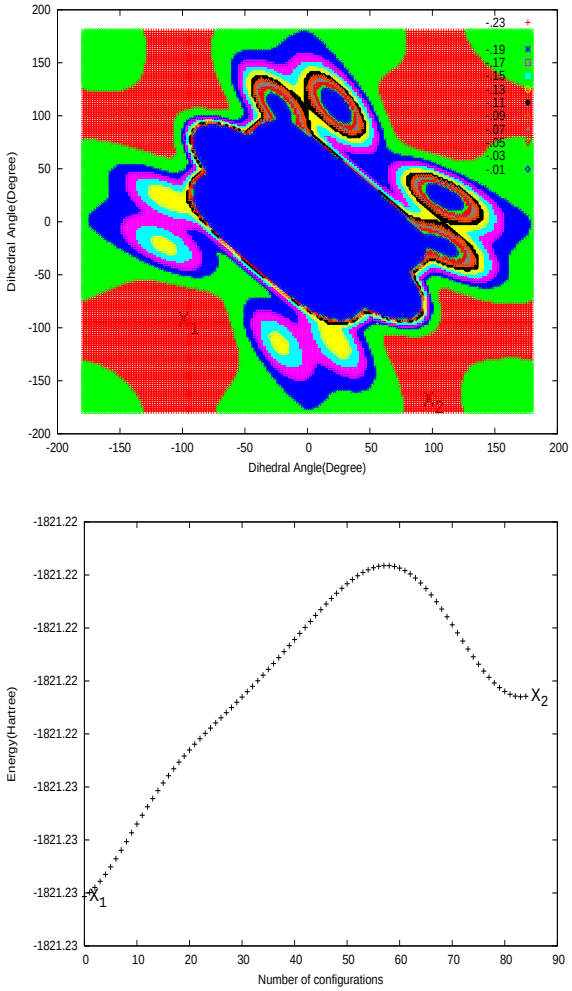

FIG. 35: Top:Energy surface for the TFSI anion through rotations about the two N-S bonds calculated at HF/6-31G*. Bottom:Direct path from X1 to X2 in the energy surface

3. Calculate energy E_{ff} using force field model.

4. Minimize the sum of $(E_G - E_{ff})^2$ as a function of the force field parameters to get the best set of parameters.

The isolated TFSI anion has an interesting feature [12]. It has two minimum energy structures shown in Figure 34, where as the top figure has C2 symmetry and the bottom one has C1 symmetry.

An energy surface for the TFSI anion has been calculated through rotations about the two central N-S bonds by using first principles HF/6-31G* basis set. There are two unique local minima labled with X1 and X2 in the energy surface. From the energy surface we extract the direct transition path from point X1 to point X2. Both the energy surface and the energy diagram for the direct path from X1 to X2 are shown in Figure 35. We included the configurations of TFSI ion in the direct transition path into our database for fitting, so in the resulted MD model both *trans* and *cis* TFSI anions exist.

Figures 36 and 37 define atom types for the cation and anion. The description of atom types are listed in Table 4. All the fitted force field parameters for both cation and anion used in present study are listed in Tables 5-9.

The partial charges on each atom were obtained by first principles calculations at HF/6-31G* level followed by standard RESP [13] fitting approach. In order to represent the most adequate charge distribution for the condensed phase, we carried out first principle calculations on EMI-TFSI ion pair instead of isolated ions. The computed total charges on EMI and TFSI are +0.67 and -0.67, respectively. The charge on proton was adopted to be +0.67 to keep the whole system neutral. The calculated partial charges on each atom are listed in Table 10.

Our molecular dynamics simulation was performed with 108 EMI cations and 108 TFSI anions at fixed particle number N, volume V, and energy E(NVE ensemble), using the primitive "thermostat" to keep the ki-

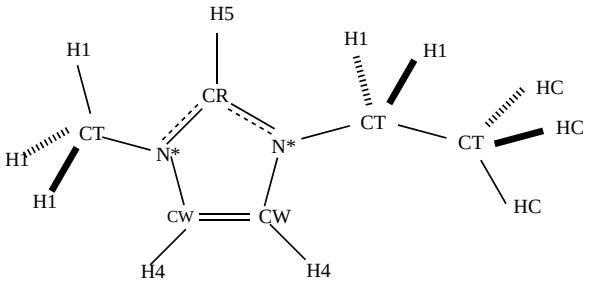

FIG. 36: Definitions of atom types in the tables for the EMI cation.

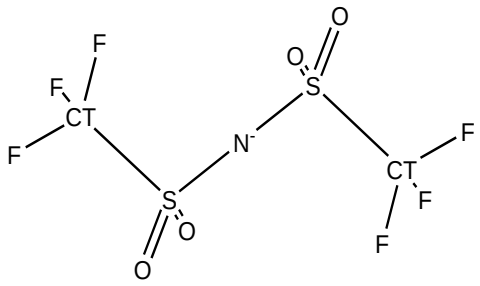

FIG. 37: Definitions of atom types in the tables for the TFSI anion.

TABLE IV: Description of Atom Types

Atom Type	description
CT	any sp^3 carbon
CR	sp^2 aromatic in 5-membered ring next to two nitrogens
CW	sp^2 aromatic in 5-membered ring next to carbon and NH
HC	H attached to aliphatic carbon with no electron-withdrawing substituents
H1	H attached to aliphatic carbon with one electron-withdrawing substituent
H4	H attached to aromatic carbon with one electronegative neighbor
H5	H attached to aromatic carbon with two electronegative neighbors
N*	sp^2 nitrogen in 5-membered ring with carbon substituent
N	sp^2 nitrogen in amides
S	sulfur
O2	sp^2 oxygen in anionic acids
F	Fluorine

netic energy near 300K. The relaxation simulation continued until the thermostat stopped rescaling the velocities and the average values of the internal potential energy stopped changing. In the simulation, equations of motion were integrated by using Verlet algorithm, and periodic boundary conditions were applied. To improve efficiency, a non-bonded neighbour list method was used , and the cutoff was set to 13.5 Angstrom. For the long range Coulomb interactions, standard Ewald summation was used.

To model the interactions of proton and anion, we introduced a Morse potential between protons and the nitrogen and oxygen atoms in the TFSI ions.

$$V = D * (1 - e^{-a(r-r_0)})^2 \tag{12}$$

Three parameters D, a, r_0 of each interaction(H-O and H-N) were obtained from fitting the calculated energies from the molecular dynamics model for the TFSi-H^+-TFSI cluster to the energies calculated from first principles for the same clusters. Our first principles calculation was carried out in the following way.

For each calculation, the distance R_{NN} between the atoms of the two TFSI anions was fixed and the proton was fixed in position on a line between the two nitrogens, a distance R_{NH} from one of the nitrogen atoms. However, with these two parameters(R_{NN} and R_{NH}) fixed, the postions of all the other atoms in the anions were relaxed. Then we repeated the calculations at several different R_{NN} and R_{NH}. The result is the energy surface as a function of R_{NN} and R_{NH}. Using the same method, the energy surface as a function of R_{NO} and R_{OH} was calculated.

Both the first principles energies and the fit of the molecular dynamics model to them for the TFSI-H^+-TFSI cluster were shown in Figures 12 and 13. The fitted parameters are listed in Table IX.

VIII. APPENDIX C: CORRECTION FOR THE CONSTRAINT OF ZERO ANION AND CATION CURRENT

In the experiments, the EMI and TFSI ion currents are not collected. A steady state is established in which the protons carry current but EMI and TFSI ions do not. We impose the condition of zero EMI and TFSI current

TABLE V: Bond Potential Parameters

Bond	K_r(Kcal.mol^{-1}.Å^{-2})	r_{eq}(Å)
CT-H1	330.068	1.084
CT_1-N*	327.051	1.460
CR-N*	470.152	1.320
CR-H5	357.934	1.073
CW-CW	540.176	1.346
CT-CT	318.761	1.520
CW-N*	433.390	1.383
CW-H4	366.413	1.071
CT-HC	333.403	1.083
CT_2-N*	330.459	1.480
CT-F	571.087	1.311
CT-S	308.445	1.828
S-N	509.948	1.574
S-O	812.880	1.427

TABLE VI: Angle Potential Parameters

Angle	K_θ(Kcal.mol^{-1})	$\theta_{eq}(^o)$
H1-CT-H1	36.036	110.092
H1-CT-N*	48.240	109.240
CR-N*-CT	70.909	126.219
CW-CW-N*	69.721	107.424
CW-CW-H4	36.138	130.417
CT-CT-H1	54.311	111.936
CT-CT-HC	45.011	110.240
CT-CT-N*	50.167	111.792
N*-CR-N*	74.854	109.209
N*-CR-H5	32.826	125.989
CR-N*-CW	65.000	107.787
N*-CW-H4	30.957	121.654
CW-N*-CT	69.959	125.193
HC-CT-HC	39.480	108.000
S-N-S	57.795	127.509
O-S-N	65.218	108.905
O-S-O	73.381	118.896
CT-S-N	68.445	102.335
O-S-CT	63.389	104.677
F-CT-S	53.815	110.010
F-CT-F	38.752	108.626

TABLE VII: Dihedral Potential Parameters

Dihedral	K_d(Kcal.mol^{-1})	$\gamma(^o)$	n
CT-CR-N*-CT	1.858	180	2
CT-N*-CR-H5	1.562	180	2
CW-N*-CR-H5	2.464	180	2
N*-CR-N*-CW	2.442	180	2
X-CW-CW-X	6.825	180	2
CW-CW-N*-CR	1.826	180	2
CW-CW-N*-CT	1.842	180	2
H4-CW-N*-CR	1.366	180	2
H4-CW-N*-CT	1.787	180	2
X-CT-CT-X	0.068	0	3
X-X-CT-N*	1.293	180	2
X-X-CR-H5	0.819	180	2
X-X-CW-H4	0.819	180	2
F-CT-S-N	3.323	0	3
CT-S-N-S	2.217	0	2

TABLE VIII: Nonbonded Potential Parameters

Atom Type	R*(Å)	ε(Kcal.mol^{-1})
CT	1.908	0.110
CR	1.940	0.083
CW	1.931	0.075
HC	1.433	0.018
H1	1.400	0.012
H4	1.377	0.012
H5	1.311	0.018
N*	1.793	0.160
F	1.745	0.068
CT	1.908	0.110
N	1.801	0.151
S	2.075	0.221
O	1.598	0.216

by envisioning carrying out the calculation in the presence of an extra term in the Hamiltonian of the system, which is the product of a constant times the polarization arising from the EMI and TFSI ions. The constant, which has the dimensions of an electric field E' , may be regarded as a Lagrange multiplier to be used in the standard manner to impose a constraint in the application of the principle of least action to determine the equations of motion of the fluid in the presence of a (real) electric field E. More physically, the field E' takes account in the simulation of the effects of the concentration gradients in the anions and cations which result from the constraint, so that the competition of drift (due to E) and diffusion (taken into account in the simulation by E') results in zero anion and cation current. It turns out that no molecular dynamics calculation in the presence of an extra field is required. We can determine the correction to the calculated conductivity from features of the zero field molecular dynamics calculation as follows: Let the polarization operator of the protons be $\vec{P}_H = \sum_H q_H \vec{r}_H$ and the polarization of the other ions (here EMI and TFSI be $\vec{P}_O = \sum_O q_O \vec{r}_O$. (Only time derivatives of these operators appear in the expressions for the conductivity so we need not be concerned with issues arising concerning the zeroes of the displacement vectors.) In the canonical ensemble in the presence of the field $\vec{E}$ and the Lagrange multiplier $\vec{E}'$, the expectation value of the current den-

TABLE IX: Morse Potential Parameters

Type	D(Kcal.mol^{-1})	a(Å^{-1})	r_0(Å)
N-H	30.960	4.303	0.980
O-H	45.336	1.802	1.187

TABLE X: Atomic Charges for EMI-TFSI Pair

Atomic Serial Number	q(e)/EMI	q(e)/TFSI
1	-0.1572	0.7481
2	0.2286	-0.2968
3	-0.2278	-0.4743
4	-0.2001	-0.4743
5	0.4597	0.7481
6	-0.0002	0.4592
7	0.2336	-0.1492
8	-0.1427	-0.1492
9	-0.0714	-0.1492
10	0.0894	-0.4743
11	0.0894	-0.4743
12	0.0894	0.4592
13	0.2771	-0.1492
14	0.0012	-0.1492
15	0.0012	-0.1492
16	-0.0643	
17	0.0229	
18	0.0229	
19	0.0229	

sity $\vec{j}_O$ arising from the other ions is

$$< \vec{j}_O >=< (1/V) \sum_O q_O \vec{v}_O >=$$

$$\beta < \vec{j}_O \vec{E} \cdot (\vec{P}_H + \vec{P}_O) > + \beta < \vec{j}_O \vec{E}' \cdot (\vec{P}_O) >$$

$$= E(\sigma_{OO} + \sigma_{OH}) + E' \sigma_{OO}$$

where we assumed that the fields are small and linearized in them. $\sigma_{\mu\nu}$ are components of the conductivity associated with species μ and ν as calculated from equation 3 with appropriate subscripts. (The conductivity tensors are assumed to be diagonal in cartesian indices.) Setting $< \vec{j}_O >= 0$ we solve for E'

$$\vec{E}' = -\vec{E} \left(\frac{\sigma_{OO} + \sigma_{OH}}{\sigma_{OO}} \right)$$

Using this value of E', we calculate the proton current in the same approximations:

$$< \vec{j}_H >= \vec{E}(\sigma_{HH} - \sigma_{OH}^2/\sigma_{OO})$$

so that the effective proton conductivity in the presence of the constraint is

$$\sigma_{eff} = \sigma_{HH} - \sigma_{OH}^2/\sigma_{OO}$$

[1] P. Zegers, Journal of Power Sources 154, 497 (2006); F. Mark, M. F. F. Mathias, R. Makharia, H.A. Gasteiger, J. Conley, T. J. Fuller, C. J. Gittleman, S. S. Kocha, D. P. Miller, C. K. Mittelsteadt, T. Xie, S. G. Yan, P. T. Yu P. T. Interface 14, 24-35 (2005)

[2] Y.-L. Ma, J. S. Wainright, M. H. Litt, R. F. Savinell, Journal of the Electrochemical Society 151, A8 (2004); M. V. Williams, H. R. Kunz, J. M. Fenton, Journal of Power Sources 135, 122 (2004); D. A. Masten, A. D. Bosco, , Handbook of Fuel Cells: Fundamentals, Technology and Applications, Vol 4, W. Vielstien, H. A. Gasteiger, A. Lamm, Eds. John Wiley & Sons: West Sussex, UK, 714-724 (2003)

[3] Steven J. Hamrock and Michael A. Yandrasits , , Polymer Reviews 46, 219 244 (2006)

[4] G. M. Haugen, F. Meng, N. V. Aieta, J. L. Horan,M.-C. Kuo, M. H. Frey, S. J. Hamrock, A. M. Herring Electrochem. Solid-State Lett., 2007 10, B51-B55 (2007)

[5] R. F. de Souza, J. C. Padilha, R. S. Goncalves, J. Dupont, Electrochemistry Communications 5, 728 (2003)

[6] M. Doyle, S. K. Choi, G. Proulx, Journal of the Electrochemical Society 147 34 (2000)

[7] S. Mitsushima, K. Kudo, R. Sakamoto, A. Noda, Y. Takeoka, N. Kamiya, M. Watanabe, M.K. I. Ota, K. I. Electrochemical Society Proceedings 19, 124-133 (2002)

[8] J. Sun, D. R. MacFarlane, M. Forsyth, Solid State Ionics, Diffusion & Reactions 147, 333 (2002)

[9] J. H. Shin, W. A. Henderson and S. Passerini, J. Electrochem. Soc. 152, A978 (2005); W. A. Henderson and S. Passerini, Chem. Matt 16, 2881 (2004) ;M. Castriota, T.Caruso, R. G. Agostino, E. Cazzanelli, W. Henderson, and S. Passerini, , Journal of Physical Chemistry A 109, 92-96 (2005);J. H. Shin, W. A. Henderson and S. Passerini, Electrochemical and Solid State Letters 8, A125-A127 (2005)

[10] http://www.compuchem.com/gaussref.htm

[11] P. Bonhote, A. Dias, N. Papageorgiou, Inorg. Chem. 1996, 35, 1168-1178

[12] P. Johansson, S. P. Gejji, Electrochimica Acta, 43(10-11), 1375-1379, 1998

[13] C. I. Bayly, P. Cieplak, W. D. Cornell, P. A. Kollman, J. Phys. Chem. 1993, 97, 10269-10280

[14] Wendy D. Cornell, et al, J. Am. Chem. Soc. 117, 5179-5197 (1995)

Appendix VII

ANL Report to DOE - 3M Stack Testing

Summary Report

PERFORMANCE AND LIFE OF A 5-KW FUEL CELL STACK FROM 3M

Prepared for the
U.S. Department of Energy
Hydrogen, Fuel Cells and
Infrastructure Technologies Program

Prepared by
L. Walker and I. Bloom
Electrochemical Technology Program
Argonne National Laboratory

August 2007

FOREWORD

This work was performed under the auspices of the US Department of Energy, Office of Hydrogen, Fuel Cells and Infrastructure, under Contract No. DE-AC02-06CH11357. The program manager was Nancy Garland. The tests were conducted at the 3M fuel cell test laboratory in Menomonie, Wisconsin, in fullfillment of the 3M/DOE Contract No. DE-FC36-02AL67621.

EXECUTIVE SUMMARY

A 5kW stack was delivered to Argonne National Laboratory for performance and durability testing of the 3M membrane electrode assemblies (MEA's). The components of the prototype stack were as follows.

- The catalyst was the 3M NSTF ternary catalyst, PtCoMn, with a Pt loading of 0.2 mg/cm^2 on both the cathode and anode. The same material was used on both the anode and cathode.
- The PEM was the 3M PFSA PEM, equivalent weight of ~850, with no additives or supports of any kind for enhanced durability.
- The GDL's were based on commercially-available, non-woven carbon paper to which 3M then applied a hydrophobic coating and microporous layer. (This GDL was optimized for 3M's dispersed catalyst based MEA's not NSTF MEA's.)
- The overall MEA active area size was 312.5 cm^2 and the gaskets were integrated into the MEA at 3M using 3M manufacturing technology. The NTSF MEA was designed to operate in the range of 80-105^{o}C stack temperature.
- The manifolds were sized for a 17.5kW module, and, thus, the mass and volume of the manifolds are larger than actually needed for the 5kW, short-stack version under test.
- The stack design and hardware was not developed under any 3M/DOE contract. The stack separator plates were made of 0.050-in-thick stainless steel. Gold plating was used to reduce plate corrosion effects.

The stack consisted of 22 PEM cells. Cell 1 was the most anodic, and cell 22, the most cathodic. The stack was oriented horizontally for operation, making cell 1 also the gravitational bottom of the stack.

The point of the test was to gauge the performance and durability of the MEAs and not necessarily to compare stack performance to DOE's technical targets. The initial performance of stack is summarized in Table E-1.

Table E-1. Initial performance of the prototype stack.

Parameter	Units	Value
Stack Efficiency at 25% of Rated Power	%	61.9
Stack Efficiency at Rated Power	%	46.7

The durability cycling test was conducted at 90^{o}C and was limited to 560 h to get data before DOE's contract with 3M expired. During this test, the cumulative stack voltage loss was 6.5% at 1.3 A/cm^2 immediately following the durability cycling, which was reduced to 3% at 1.3 A/cm^2 after three shutdown/restart cycles were done and no additional durability cycles were accumulated. Impedance increases accounted for most of the non-reversible performance loss after the durability stress tests, with kinetic and mass transport losses accounting for less than 10 μvolts/hour of decay per cell.

INTRODUCTION

As part of the Department of Energy's (DOE) Hydrogen, Fuel Cells and Infrastructure Technologies Program, the Electrochemical Analysis and Diagnostics Laboratory (EADL) at Argonne National Laboratory evaluated the short-stack performance of MEA's developed at 3M under the 3M/DOE contract DE-FC36-02AL67621 . The testing was originally to be performed at the EADL, but due to delays in facility upgrades, testing was performed at 3M's fuel cell testing lab in Menomonie, Wisconsin so that it could be completed before the end of 3M's DOE contract. The stack hardware used was developed at 3M for non-DOE contract purposes. The stack required external gas supplies, cooling, and control.

The stack consisted of 22 cells which were electrically connected in series. Cell 1 was the most negative and cell 22 was the most positive. The stack was oriented so the cells were horizontal; this made cell 1 the gravitational bottom of the stack. The active area of the cells was 312.5 cm^2. The stack was originally delivered to ANL during the week of November 27, 2006. It is shown in Fig. 1.1 after being removed from the shipping container.

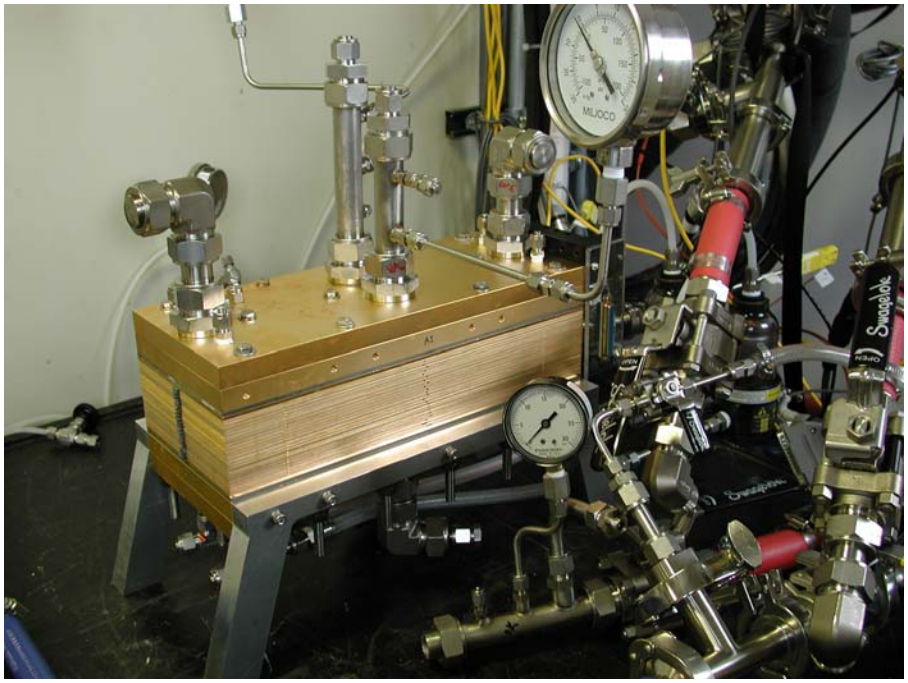

Fig. 1.1. Photograph of the 3M 5-kW stack.

The components of the MEA's and prototype stack were as follows.

- The catalyst was the 3M NSTF ternary catalyst, PtCoMn, with a Pt loading of 0.2 mg/cm^2 on both the cathode and anode. The same material was used on both the anode and cathode.
- The membrane was the 3M PFSA PEM, equivalent weight of ~850, with no additives or supports of any kind for enhanced durability.

- The GDL's were based on commercially-available, non-woven carbon paper to which 3M then applied a hydrophobic coating and microporous layer. (This GDL was optimized for 3M's dispersed catalyst based MEA's not NSTF MEA's.)

- The overall MEA active area size was 312.5 cm^2 and the gaskets were integrated into the MEA at 3M using 3M manufacturing technology. The NTSF MEA was designed to operate in the range of 80-105^oC stack temperature.

- The stack manifolds were sized for a 17.5kW module, and, thus, the mass and volume of the manifolds were larger than would actually be needed for the 5kW, short-stack version under test.

- The stack design and hardware was not developed under any 3M/DOE contract. The stack separator plates were made of 0.050-in-thick stainless steel. Gold plating was used to reduce plate corrosion effects.

The test plan, given in Appendix I, was developed to characterize the performance of the MEA's at a variety of operational set points, such as temperature, humidification levels, and stoichiometric ratios. The plan included a constant power stability test at 33% rated power and durability testing using the Dynamic Stress Test (DST) duty cycle. Changes in MEA performance were gauged by a reference performance test (RPT), which consisted of a sequential polarization curve.

The MEA's required higher temperatures than the EADL cooling system could provide. A cooling system upgrade project began in November 2006.

Testing began the week of November 27, 2006 in the presence of a representative from 3M, but was halted when a false alarm from the CO monitoring system for the EADL Fuel Cell Test Facility (FCTF) suspended testing. The stack was put into long term storage, using the 3M procedure and under the direction of the 3M representative. Testing was scheduled to resume in March 2007 after facility upgrades to the cooling system were complete. However, due to delays in the upgrade project, the stack was sent to 3M's fuel cell testing lab in Menomonie, WI, to be characterized prior to the resumption of testing at Argonne. The MEA's showed noticeable degradation, with cell 1 exhibiting severe degradation. 3M deemed the stack unsuitable for testing. 3M decided to rebuild the stack and to deliver the new stack at the beginning of May 2007. Delays in the cooling system upgrade project, and higher than expected degradation rates observed in duplicated single cell tests at EADL, required that testing be resumed at 3M in Menomonie, WI, so that the evaluation could be completed prior to the conclusion of the DOE contract with 3M. Testing resumed in Menomonie on May 21, 2007 in the presence of an ANL representative.

1 RESULTS

The performance and durability of the stack were evaluated in terms of DOE's technical targets. These results are summarized in Table 2.1. The results from the individual tests are discussed below. Graphs of performance and other figures are given in Appendix II as Figs. 1 to 21.

The point of the test was to gauge the performance and durability of the MEAs and not necessarily to compare stack performance to DOE's technical targets. The initial performance of stack is summarized in Table 1.

Table 1. Initial performance of the prototype stack.

Parameter	Units	Value
Stack Efficiency at 25% of Rated Power	%	61.9
Stack Efficiency at Rated Power	%	46.7

Performance Characterization

Sequential Polarization Curves in the Temperature Range of 80 to 90^{o}C (Figs. 1, 2, and 3) – A total of ten individual sequential polarization curves were measured. The intent was to measure the response of the fuel cell stack to changes in operating conditions. The conditions used are given in Table 2.2. From the data in Table 2.2, the fuel stoichiometry was constant at 2; that for air was an experimental variable. The anode inlet pressure was adjusted from 0 to approximately -15% from the nominal value to minimize anode-to-cathode overpressure due to high cathode pressure drop with the stack's flow field design.

Table 2.2. Operating conditions for the polarization curves. The format for each entry is as follows. T1/T2/T3; P1/P2; fuel:air stoichiometric ratios, where T1=stack coolant outlet temperature, ^{o}C, T2=anode inlet dewpoint, ^{o}C, T3=cathode inlet dewpoint, ^{o}C, P1=fuel inlet pressure, atm-abs, P2=air inlet pressure, atm-abs.

Expt. No.	Condition
7.1 a (a)	80/77/77; 1/1 outlet; 2:2.5
7.1 a (b)	80/76/76; 1/1 outlet; 2:2
7.1 a (c)	85/80/80; 1.51/1.51; 2:2.5
7.1 a (d)	85/78/78; 1.51/1.51; 2:2
7.1 a (e)	90/83/83; 2.02/2.02; 2:2.5
7.1 a (f)	90/81/81; 2.02/2.02; 2:2
7.1 a (g)	90/78/78; 2.02/2.02; 2:1.7
7.1 a (h)	90/79/79; 2.56/2.56; 2:2.5
7.1 a (i)	90/75/75; 2.56/2.56; 2:2
7.1 a (j)	90/70/70; 2.56/2.56; 2:1.7

Fig. 1 shows the polarization curves for the initial performance tests. There were dramatic differences in the curves from one condition next, most

notably as the current density increases. At 1.0-A/cm^2, the stack voltage ranges from 10.61 to 14.36 V (see Table 2.3); this is an average increase of 170 mV/cell from experiment number 7.1 a (b) to 7.1 a (h). In all cases, the higher air stoichiometries and pressures produced better stack performance.

Table 2.3. Stack potential as a function of cell operating conditions.

Expt. No.	Stack potential at 1.0 A/cm^2, V	Cell Temp., ^{o}C	Relative humidity, %	Fuel inlet pressure, atm-abs	Air inlet pressure, atm-abs	Air stoichiometry
7.1 a (a)	12.00	80	88.5	1.00	1.00	2.5
7.1 a (b)	10.61	80	84.9	1.00	1.00	2
7.1 a (c)	11.70	85	81.9	1.51	1.51	2.5
7.1 a (d)	11.35	85	75.5	1.51	1.51	2
7.1 a (e)	13.52	90	76.3	2.02	2.02	2.5
7.1 a (f)	13.22	90	70.4	2.02	2.02	2
7.1 a (g)	12.91	90	62.3	2.02	2.02	1.7
7.1 a (h)	14.36	90	64.9	2.56	2.56	2.5
7.1 a (i)	14.09	90	55.0	2.56	2.56	2
7.1 a (j)	13.82	90	44.5	2.56	2.56	1.7

Fig. 2 shows the power output of the stack as a function of the current density for the ten different conditions. The maximum power attained was 5.5-kW at 1.5-A/cm^2 for experiment number 7.1 a (h). The conditions in 7.1 a (i) will be used for future RPTs in subsequent tests.

An additional test was performed to show the effect of humidity on the performance of the stack. At a stack temperature of 90^{o}C, reactant gas inlet pressures of 2.51 atm-abs (23 psig), and fuel:air stoichiometries of 2:2, the potential of the stack was measured as the dewpoint temperature was changed. The dewpoint temperatures were 70, 75, and 80^{o}C (relative humidity: 44.5, 55.0 and 67.6%, respectively). Fig. 3 shows the average cell voltage as a function of the dewpoint temperature. At a dewpoint temperature of 70^{o}C, the average cell voltage was 0.565 V at 1.3 A/cm^2; at 75^{o}C, it decreased to 0.555 V; and, at 80^{o}C, it increased to 0.557 V. From these data, the sensitivity of the stack potential to humidity decreases markedly after the dewpoint reached 75^{o}C (55.0% relative humidity).

2.1.2 Sequential Polarization Curves at Higher Temperatures (Figs. 4 and 5). Two additional sequential polarization curves were measured to judge MEA performance at high temperature. A third one was planned at 105^{o}C, but, due to the limitations of the test stand at 3M, was not completed. The conditions used are given in Table 2.4.

Table 2.4. Conditions used in high-temperature polarization experiments

Expt. No.	Conditions*
7.1 d (a)	95/87/87; 2.56/2.56; 2:2.5
7.1 d (b)	100/95/95; 2.56/2.56; 2:2.5

*See Table 2.2 for definition.

Fig. 4 shows the polarization curves for three different sets of operating conditions, those given in Table 2.4 and in Table 2.2, experiment 7.1 a (h). The performance of the stack under these conditions is summarized in Table 2.5. From the data in Table 2.5, there was a 60-mV increase in stack potential at 100°C as compared to the other conditions.

Table 2.5. Stack performance at 1 A/cm^2 from high-temperature polarization tests.

Expt. No.	Stack potential at 1 A/cm^2, V	Temp., °C	Relative humidity, %	Fuel inlet pressure, atm-abs	Air inlet pressure, atm-abs	Air stoichiometry
7.1 a (h)	14.36	90	64.9	2.56	2.56	2.5
7.1 d (a)	14.36	95	73.9	2.56	2.56	2.5
7.1 d (b)	14.42	100	83.4	2.56	2.56	2.5

Fig. 5 shows a comparison of the power output of the stack for the three conditions shown in Table 2.5. The power output levels under these operating conditions were almost identical, 4.79 (at 1.1 A/cm^2), 4.77, and 4.79 kW for 90°C, 95°C, and 100°C, respectively.

2.1.3. Random Polarization Curve (Fig. 6). A random polarization curve was generated to determine if the sequential polarization experiments introduced humidification artifacts that would mask the true performance of the stack. At the high current densities in the current-increasing portion of the measurement, the membrane would become well-humidified and, hence, more conductive. In turn, this would make the values from the current-decreasing portion of the measurement higher than they should be.

Using the conditions described in Table 2.3, experiment number 7.1 a (i), the current density was varied randomly in the range of 0 to 1.2 A/cm^2. Each current density was held for three minutes to allow the performance to stabilize. Fig. 6 shows a comparison between the random polarization curve and the sequential polarization curve generated from experiment 7.1 a (i). The curves are almost identical.

2.1.4. Constant Power Test (Fig. 7 to Fig. 9). Originally, the test plan specified a 50-hour test at 25% of the rated power. However, due to the limitations of the test stand at 3M, the power level was changed to 36% of the

rated power. The test was performed using the conditions described in Table 2.3, experiment number 7.1 a (i) and a current density of 0.35-A/cm^2. An RPT was done before the test began. After the test, a shutdown/restart cycle was done before the concluding RPT.

Fig. 7 shows the average cell voltage versus time during this test. The average cell voltage was initially ~0.75 V and, after 50 h, decreased to ~0.71 V. The average cell voltage decay rate was 0.64 mV/h. Fig. 8 shows the stack power versus time. Initially, the power output of the stack was 1.8 kW, and, with time, the power output decreased to 1.71 kW. The power output decreased linearly at a rate of 1.55 W/h.

Fig. 9 shows a comparison between the RPT performed before the constant power test and the one performed after the test. From Fig. 9, the performance of the stack was unchanged by the constant power test. Fig. 9 also shows that the apparent loss in stack performance was recoverable after a shutdown/restart cycle.

Durability

The durability consisted of voltage-cycling duty cycle called the Dynamic Stress Test (DST). Fig. 10 shows the DST profile that was initially used. The values for the current were derived from the initial polarization curve. However, due to limitations in the test equipment at 3M, the profile was modified. The test stand could not accommodate the high current slew rate inherent in the DST profile. A slew rate of 20 A/s was used to allow the test equipment to maintain the proper operating conditions for the fuel cell stack. Fig. 11 shows the modified DST profile used. The original profile was 382 s long; the modified profile was 429 s long.

The stack was characterized before beginning durability test by an RPT, which consisted of a sequential polarization curve using the conditions from 7.1 a (i) given in Table 2.3. RPTs were performed every Monday and Friday during this test in the presence of an Argonne representative. After the first RPT, a hydrogen pump experiment was added to the RPT to measure the ohmic resistance of the cells in the stack. The hydrogen pump experiment consisted of using hydrogen on both anode and cathode sides of the stack and an external power supply to pass current through the stack.

Cycling began on May 29, 2007 and finished on June 25, 2007. 560 h of test time were accrued.

2.2.1. Changes in stack performance with cycling (Figs. 12 to 20). Fig. 12 shows the polarization curves from the RPTs performed during cycling. The overall trend seemed to be a decrease in performance from one RPT to the next, but this was not always true. An example of this is the RPT conducted on June 11; the performance of the stack seemed to have degraded greatly from the

previous RPT, but, in reality, this was an artifact of how the test was performed. The temperature of the stack was not allowed to equilibrate before the polarization curve was begun; this, in turn, skewed the data.

An explanation for the degradation and recovery on June 22 has not been determined. The overall improvement for the curve on June 29 was due to the stack being shutdown on June 25 and three shutdown/restart cycles on June 28 with no DST cycles between these dates.

Fig. 13 shows the polarization curves for the average cell voltage from the RPTs performed during the durability test. The error bars are the standard deviation from the mean; the standard deviation increases as the current density increases. These data are plotted in Fig. 14 as power output of the stack vs. current density.

Fig. 15 shows the stack potential at 1.0-A/cm^2 and 1.3-A/cm^2 as a function of the accumulated time. The data points are from the RPT polarization curves. For both curves, the stack showed a decrease in potential over time. The voltage decreased at rates of 1.3 mV/h and 1.7 mV/h at current densities of 1.0-A/cm^2 and 1.3-A/cm^2, respectively, from a regression analysis of the data.

Fig. 16 shows the area-specific impedance (ASI) values for each cell calculated from the hydrogen pump experiments. Many of the cells showed a linear growth of the ASI with time. Several, however, exhibited a higher growth rate in the ASI values, with cell numbers 13 and 19 showing the most dramatic growth rates. The cell with the greatest resistance growth was cell 19 which began life with a resistance of 75 mΩ-cm^2 and finished with 108 mΩ-cm^2. This growth seemed to be exponential whereas that for the other cells seemed linear.

Fig. 17 shows the ASI growth of cells 13 and 19 compared with cell 07. The performance of cell 07 is typical of the other cells in the stack. Cell 07 had an ASI growth rate of 15.6 μΩ–cm^2/h compared to 36.7 μΩ–cm^2/h for cell 13 and 44.3 μΩ–cm^2/h for cell 19. This led to a greater voltage drop across cells 13 and 19 due to the increased ohmic resistance.

These data were then used to approximate the voltage loss due to the materials at 1.3 A/cm^2. The results of this calculation were then subtracted from the observed voltage loss at 1.3 A/cm^2 in each cell. The last group of data, called remaining voltage loss, is shown in Fig. 18 against cycling time. From Fig. 18, the remaining voltage loss for cell 07 does not change markedly with time, whereas those from the other two cells do.

The combined irreversible and recoverable loss in the stack voltage was 6.5% at the conclusion of the durability test. The amount of irreversible loss was 3% after the stack underwent three additional shutdown/restart cycles. Of this

irreversible loss, the majority was due to increases in the area-specific impedance (see Fig. 19).

Figs. 19 and 20 compare the as-measured and *iR*-free, averaged polarization curves taken at the start and after completion of the durability stress tests. The as-measured performance curve taken after the stress testing was taken after additional thermal cycles were completed to recover any non-permanent performance loss. The average hydrogen-pump-derived, area-specific resistance was used to correct the curves. Fig. 20 shows an expanded view of the *iR*-free curves. From this figure, it can be seen that the changes in combined kinetic and mass transport losses, due to non-reversible performance changes, were less than 10 μvolts/hr.

2 INFERENCES

Characterization. From the data, there were four parameters that affected initial stack performance: stack/cell temperature, humidity and gas stoichiometries and pressure. As these parameters increased, the stack performance increased. The interaction of these parameters with the cell thermodynamics, kinetics and materials properties is very complex. A full treatment of these interactions is beyond the scope of this report.

The average, apparent resistance of the cells in the stack was calculated from the observed *iR* loss at 1 A/cm^2 data under the conditions given in Table 2.3. These resistance values were calculated from (*OCV*-*V*)/(1 A/cm^2), where *OCV* is the stack open-circuit potential under a set of experimental conditions, *V* is the observed potential at 1 A/cm^2. These values are not purely ohmic in nature; they contain contributions from the electrochemical reactions. An Arrhenius plot of these values is given in Fig. 3.1.

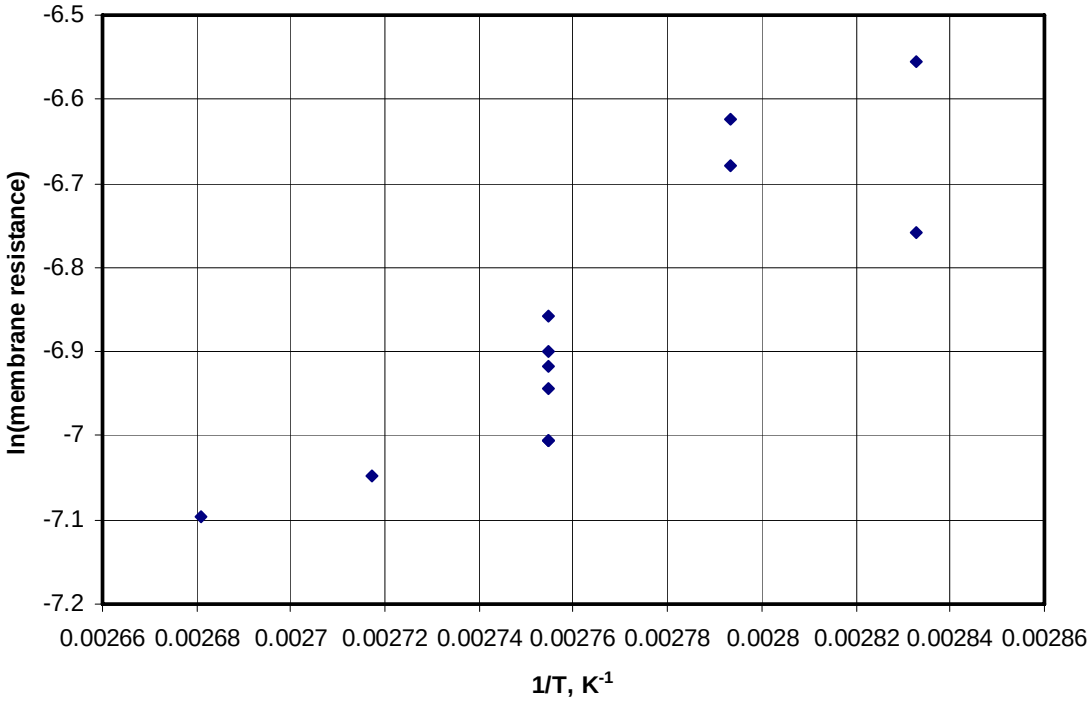

Fig. 3.1. Arrhenius plot of the apparent cell resistance.

(Ira, you may want to change the label on the y-axis to say ln(apparent resistance)

The plot indicates that the apparent resistance seems to follow an Arrhenius-like relationship despite the scatter in the data.

Durability. A total of 560 hours of cycling was accumulated with RPTs every 65 to 92 hours. The performance of the stack decreased with cycle time. Much of the loss was recoverable, but some was not. Some of the performance recovered after a shutdown/restart procedure was completed. One aspect of the performance that seemed to not recover as dramatically as the stack potential was the maximum current density. At the beginning of the durability test, the maximum current density was 1.5 A/cm^2; at the conclusion of the test the current density had decreased to 1.3-A/cm^2.

In the fuel cell, the observed potential, E_{obs}, can be given by $E_{obs} = E^0 - iR_{materials\ only} - \eta_{H2} - \eta_{O2} - \eta_{MT}$, where E^0 is the thermodynamic potential of the cell, $iR_{materials\ only}$ is the voltage loss due to the materials (ionomer, etc.), and η_X is the kinetic or mass transport overpotential for the reaction of gas species 'X'. As a first approximation, η_{H2} will be considered small enough to ignore. The hydrogen pump experiment provided impedance values for the proton- and electron-conducting materials. The remaining (~ iR-free) voltage loss can primarily be associated with changes in the oxygen reduction overpotential (η_{O2}) and mass transport overpotential (η_{MT}.) From Fig. 18, the apparent rates of these combined overpotential increases were 2.6, 119 and 155 μV/h for cells 7 (average), 13 and 19 (worst), respectively.

According to 3M, the performance loss due to impedance increase is what they typically observe when the MEA's are contaminated with cations. After disassembly of the first 22-cell build of the stack, noticeable corrosion of the gold plating on the stainless steel plates was observed. Although not proven, this corrosion of the stack separator plates may provide transition metal cations which can poison the MEA's.

Appendix I.

DOE / ANL TEST PLAN FOR

3M 5-kW PEM FUEL CELL STACK

[Created: 07-Nov-2006]
[Revised: 07-Jun-2007]

Approved: ....
Amy Manheim, DOE **Date**

Acknowledged: ....
Nancy Garland, DOE **Date**

Acknowledged: ....
Jason Marcinkoski, DOE **Date**

Acknowledged: ....
Andy Steinbach, 3M **Date**

Acknowledged: ....
Ira Bloom, EADL **Date**

DOE / ANL TEST PLAN FOR

3M 5-kW PEM FUEL CELL STACK

1.0 Purpose and Applicability

This document outlines a series of tests to assess the performance and life of a 5-kW fuel cell stack by 3M, which contains roll-good fabricated MEA's made with proprietary catalyst and membrane materials. The system is designed for automotive applications and will undergo performance and life evaluations using the procedures developed by ANL and 3M. The stack will be tested at Argonne National Laboratory (ANL).

2.0 References

3 Test Procedures for the Argonne National Lab Fuel Cell Test Facility, Revision 0, March 2001

4 Fuel Cell Power Systems Performance Test Codes, ASME PTC 50-2002, November 2002

3.0 Equipment

Existing ANL-EADL equipment will be used to conduct these tests. Measurements will include:

- Stack Voltage
- Stack Current
- Individual Cell Voltages
- Coolant Inlet and Outlet Temperature
- Coolant Inlet Pressure
- Coolant Flow
- Coolant Conductivity
- Fuel Inlet and Outlet Temperature
- Fuel Flow
- Fuel Inlet Pressure
- Fuel Relative Humidity
- Fuel Outlet Pressures
- Oxidant Inlet and Outlet Temperature
- Oxidant Flow
- Oxidant Inlet Pressure
- Oxidant Relative Humidity
- Oxidant Outlet Pressures

4.0 Prerequisites and Pre-Test Preparations – Incoming Inspections

4.1 The stack will be visually inspected for signs of shipping or other damage. The actual weight of the stack as received will be recorded. Digital photographs will be taken before and after setup.

4.2 Prior to the start of testing, a pre-test readiness review will be conducted using the released version of this test plan and the associated test procedures. The readiness review should be attended by the project engineer (or designee), the test laboratory manager, and the test engineer assigned to the test. An external readiness review involving the DOE Technology Manager may be required at his/her discretion, and it may be in addition to or in lieu of an internal review.

4.3 Representatives from 3M will be present during the installation and initial testing of the stack.

5.0 Stack Specifications

5.1	Stack Construction	22 PEM fuel cells
5.2	Stack Nominal Voltage	19.8 ± 0.66 V OCV; TBD V at full power
5.3	Stack Operating Temperature	see test plan
5.4	Stack Weight	___ kg (dry, maximum)
5.5	Active Area	312 cm^2
5.6	Stack Internal Resistance	TBD Ω
5.7	Limiting Conditions	
	Lowest Cell Voltage	< 0.4 V

At this voltage, testing will suspend.

5.8 Operational Procedure and Limits

Maximum constant current	500 A
Minimum voltage	0.8 V OCV; 0.3 V/cell at full power

If these limits are reached, testing should be halted and 3M consulted.

5.9 End-of-Testing Criterion: Stack testing will last approximately 1000 h unless otherwise agreed.

6.0 Safety Concerns and Precautions

- The unit must be kept out of water.
- The unit should be stored and used in an area that is shielded from accidental exposure to personnel.
- Since hydrogen is in use, a sign stating "Hydrogen in Use" will be posted on the laboratory door. There will be proof of adequate

ventilation before testing begins.

7.0 Tests to be Performed under this Test Plan

The stack will be subjected to the performance test sequence given below. In the tests described below, the anode inlet pressure will be adjusted as a function of current to avoid large anode/cathode pressure differentials, as the cathode pressure drop can approach 40kPa at high current.

Prescribed anode inlet pressure set points for each test, as a function of current, are provided in Table 1.

A constant coolant flow rate of 20L/min should be used for all testing, to maintain coolant ΔT of $7^{o}C$ or less.

When testing is interrupted for short times (3-15 minutes), the stack should be held at OCV with test-specified operating pressures, temperatures, and humidities, with gas flows appropriate for 31A (or whatever minimum flow is achievable with the station). Preferably, N2 should be flowed on the cathode instead of air during this period, but air is acceptable if necessary. Upon resumption of testing, current should be increased slowly (~5A/sec) back to target conditions to allow the stack to rehumidify if drying has occurred

When testing is interrupted for more than 15 minutes but less than 8 hours (e.g., a few hours for humidifier temperatures to re-equilibrate to new conditions), the "3M Stack Short-Term Shutdown and Restart 111506" procedure given in Appendix A is to be used. Holding the stack at OCV with sub-saturated gases flowing for periods longer than 15 minutes leads to excessive oxide formation on the cathode catalyst and excessive drying of the MEAs.

When testing is interrupted for periods of 8 hours-3 days (e.g., overnight, over weekends), the stack will be shutdown during this period using the "Shutdown" section of the procedure given in Appendix B. Upon resumption of testing, the stack will be restarted using the "Restart" section of the procedure.

When testing is interrupted by periods of time greater than 3 days, the procedure given in Appendix C will be followed.

During testing, if the minimum test cell voltage of 0.4V is reached and this occurs during periods when the stack is being actively monitored by ANL personnel, the test station may automatically implement the procedure outlined above for test interruptions for short times (3-15 minutes). Once detected, ANL personnel should attempt to resume testing under the conditions where the problem initially occurred. If the problem persists, no further testing at that current or higher should be performed under those conditions.

During testing, if the minimum test cell voltage of 0.4V is reached and this occurs during periods when the stack is **not** being actively monitored by ANL personnel, the procedure outlined in Appendix A should be followed. Once detected, ANL personnel should attempt to resume testing under the conditions where the problem initially occurred. If the problem persists, no further testing at that current or higher should be performed. The 3M representative should be contacted.

Table 1. Anode Inlet Pressures

1) Anode Inlet Pressures in kPag

2) Values based on measurements with 8-cell 3M stack. These values should be adjusted to ensure that the average anode pressure ((inlet+outlet)/2) is within 5-10kPa of the average cathode pressure

Stack Current (A)	Test 7.1a(a)	Test 7.1a(b)	Test 7.1a(c)	Test 7.1a(d)	Test 7.1a(e)	Test 7.1a(f)	Test 7.1a(g)	Test 7.1a(h)	Test 7.1a(i)	Test 7.1a(j)	Test 7.1d(a)	Test 7.1d(b)	Test 7.1d(c)
500	x	x	x	x	x	x	X	130	x	x	x	x	x
468.75	x	x	x	x	x	x	X	130	135	x	x	x	x
437.5	x	x	x	x	x	x	X	130	135	140	x	x	x
406.25	x	x	x	x	80	80	X	135	135	140	130	x	x
375	x	x	x	x	80	85	90	135	140	140	135	130	130
343.75	x	x	25	30	80	85	90	135	140	145	135	130	130
312.5	25	20	25	35	85	90	90	140	140	145	135	135	135
281.25	25	20	25	35	85	90	95	140	140	145	140	135	135
250	20	20	30	40	90	90	95	140	145	150	140	140	140
218.75	20	15	35	40	90	95	95	145	145	150	140	140	140
187.5	15	15	40	40	90	95	100	145	145	150	140	145	145
156.25	15	10	40	45	95	95	100	145	145	150	145	145	145
125	10	10	45	45	95	100	100	150	150	150	145	145	145
93.75	10	10	45	45	95	100	100	150	150	150	145	150	150
62.5	5	5	50	50	100	100	100	150	150	150	150	150	150
31.25	0	0	50	50	100	100	100	150	150	150	150	150	150
0	0	0	50	50	100	100	100	150	150	150	150	150	150

Sequence Number	Test	Approximate Test Time [hours]	# of Iterations
7.0	**Checkout / Verification Tests** The stack will be manually cycled between current levels sequentially from 0A to 312A under the conditions given in 7.1a (b) to verify proper integration of the unit and test equipment.	8	1
7.1a	**Initial Performance Tests** The following polarization curves will be attempted when the unit arrives at Argonne. The current will be varied over the entire rated range sequentially. The current levels will be between 0A and the maximum designated for each condition, in 31A increments. Each current level will be held for 3 min; the current interrupted for 15 s (OCV) and the current turned back on for 1 min. The current will then be sequentially decreased. The format for each entry is as follows. T1/T2/T3; P1/P2; fuel:air stoichiometric ratios, where T1=stack coolant outlet temperature, ^{o}C T2=anode inlet dewpoint, ^{o}C T3=cathode inlet dewpoint, ^{o}C P1=fuel inlet pressure, psig P2=air inlet pressure, psig a. 80/77/77; 0/0 outlet; 2:2.5; 313 A max b. 80/76/76; 0/0 outlet; 2:2; 313 A max. c. 85/80/80; 7.5/7.5; 2:2.5; 344 A max. d. 85/78/78; 7.5/7.5; 2:2; 344 A max. e. 90/83/83; 15/15; 2:2.5; 406 A max. f. 90/81/81; 15/15; 2:2; 406 A max. g. 90/78/78; 15/15; 2:1.7; 375 A max.	48-50	1

	h. 90/79/79; 23/23; 2:2.5; 500 A max. i. 90/75/75; 23/23; 2:2; 469 A max. j. 90/70/70; 23/23; 2:1.7; 438 A max.		
7.1b	**High-temperature Performance** Sequential polarization curves, as described in 7.1a(h) will be performed, except the conditions will be as follows. (a) 95/87/87; 23/23; 2:2.5; 406 A max (b) 100/95/95; 23/23; 2:2.5; 375 A max. (c) 105/102/102; 23/23; 2:2.5; 375 A max.	12-16	1
7.1c	**Other polarization tests** ANL Model		
7.2	**Random Polarization Curve** Current levels between 0 and 375 A will be attempted. Each current level will be held for 3 min; the current interrupted for 15 s (OCV) and the current turned back on for 1 min. The current levels will be chosen at random. Each current level will occur twice in the sequence and the same current level will not occur sequentially. This test may be repeated, if necessary. The stack will be held at OCV for no more than 2 minutes. The conditions will the same as in 7.1a(i).	4	1
7.3	**Constant Power** The unit will be held at 25% of rated power for a period of 50 h under the conditions specified in 7.1a(i). Upon completion of this test, the stack will be shut-down, restarted, shut-down, and restarted using the procedure given in Appendix B.	50	1
7.4	**Driving Duty Cycle** After completing the test described in Section 7.3, the unit will be undergo a reference performance test and then be subjected to a driving duty cycle. The profile is given as Fig. 1 and Table 1 in Appendix D. The 6-minute profile will be repeated continuously. The stack will be operated with 90°C coolant outlet, 20L/min coolant flow, 90°C anode and cathode dewpoint, 135/150kPag (inlet) H_2/Air, with constant reactant flows equivalent to 2/2 H2/Air stoichiometry at the maximum current point	500+	1

	(step 12, C_{60}). Reference performance tests, as described in Section 7.5, will be performed to gauge system performance with time on test. A suggested timetable for the cycling-RPT process is given in Table 2.		
7.5	**Reference Performance Tests (RPTs)** The procedure given in Appendix B will be followed, performing a shut-down and restart of the stack before the RPT is performed. Reference performance tests will be conducted on a periodic basis during the tests in Sections 7.3 and 7.4 to gauge the change in performance of the unit. The reference performance test will consist of a hydrogen pump experiment and the same sequential polarization curve that was used in Section 7.1a(i). The interval for the reference performance test is approximately 65-75 h.	4-5	12-14

Table 2. Suggested, typical timetable for cycling-RPT process

Day,Time	Action	Comment
Mon 8am	Shutdown	
Mon 10am	Restart	
Mon noon	RPT	Reference performance test
Mon 4pm	Cycling	Mon 4pm - Thurs 2pm: 70hrs
Tue	Cycling	
Wed	Cycling	
Thurs 2pm	Shutdown	Let sit overnight
Fri 8am	Restart	
Fri 10am	RPT	Reference performance test
Fri noon	Cycling	Fri Noon - Mon 8am: 68 hrs
Sat	Cycling	
Sun	Cycling	
Mon 8am	Shutdown	
	.....	

8.0 Anticipated Results

8.1 Performance and Durability Testing

The goal of these tests is to provide an unbiased basis for the comparison of the 3M stack with other polymer electrolyte fuel cell technologies. The results will also help model the performance of the unit under steady state and transient

conditions and under long-term operation. For this purpose, using laboratory control of the experimental conditions is mandatory.

8.2 Deliverables

Monthly summary reports will be sent to DOE. A final report will be sent to DOE.

9.0 Contacts

Company	Name	Phone	Email
3M	Andy Steinbach	651-737-0103	ajsteinbach2@mmm.com
EADL / ANL	Ira Bloom	630-252-4516	Ira.Bloom@anl.gov
US DOE	Amy Manheim	202-586-7425	Amy.manheim@ee.doe.gov

Appendix A.

Overview:

- This document outlines the 3M recommended procedure for shutting down and restarting the 3M stack, when the shutdown period is between 15 minutes and 8 hours.
- The procedure involves two primary phases, a "Shutdown" phase and a "Restart" phase:
  - Shutdown:
    1. Remove load, reduce gas flows and set pressures to ambient (if applicable), and halt gas and coolant flows.
  - Restart:
    1. Resume coolant flow, resume low gas flows and resume reactant pressurization (if applicable), resume target gas flows, re-establish load.

Usage:

- This procedure can be used as often as needed.

Equipment:

1. Test station

Generic Procedure (specific procedure TBD during initial 3M visit to ANL)

Shutdown

1. Start with the stack at operating conditions.
2. Set load to open circuit
3. (If under pressurized conditions): set flows to 30/30SLM H2/Air and slowly reduce anode and cathode pressures to ambient pressure, keeping the anode and cathode pressures within 10kPa of each other.
4. Halt gas flows and coolant flow.
    a. Note: If cell OCVs remain at 0.7V or higher for more than 15 minutes, remove the ½" plug from the Tee at the stack's anode reactant inlet to allow H2 to escape and air to diffuse into the stack anode.

Restart

1. (If applicable) reinstall the anode ½" plug on the anode inlet reactant inlet manifold.
2. Restart coolant flow.
3. Restart gas flows of 30/30 SLM H2/Air. OCVs should quickly re-establish
4. (If applicable) pressurize stack to target conditions.
5. Set flows to target gas flows and resume load.
6. Wait 5 minutes for re-equilibration
7. Stack is ready for further testing.

Appendix B.

Overview:

- This document outlines the 3M recommended procedure for shutting down and restarting the 3M stack, when the stack is to be kept idle for periods of 8hours-3 days.
- The procedure involves two primary phases, a "Shutdown" phase and a "Restart" phase:
  - Shutdown:
    1. Fill the reactant chambers and reactant flow fields of the stack with 18Mohm-cm DI water
    2. Cool the stack to room temperature
  - Restart:
    1. Reheat the stack to operational temperature
    2. Remove the DI from the reactant chambers of the stack
    3. Resume reactant flows; OCV check.
    4. Resume normal operation

Usage:

- This procedure can be used as often as desired with little/no deleterious effect.

Equipment:

3M to include items 1, 2, 3, 4, 5, 6, 8, 9, 10, and 11 with delivery of stack. 3M may include a small coolant system to partially satisfy item 12.

2. 2 1" Swagelock 316SS Tees, installed as close as possible to the stack anode and cathode reactant outlets
3. 2 1"->1/4" Swagelok 316SS adapters, one connected to each Tee
4. 2 1" Swagelok 316SS shutoff valves, installed between the stack reactant outlet Tees and the station reactant return lines.
5. 2 ¼" 316SS Checkvalves, installed to the ¼" adapters on the tees
6. 2 ALLDOS diaphragm pumps (~0.5-1gph), connected to the ¼" check valves
7. 10' of ¼" OD PTFE or FEP tubing, used to connect the diaphragm pumps to the check valves
8. ~2 gallons of 18Mohm-cm DI water
9. 2.5 gallon HDPE bottle, with 2 ¼" 316SS adapters, to feed ALLDOS pumps
10. 2 1" Swagelock 316SS Tees, with adapters down to 1/2" Swagelok, installed as close as possible to the stack anode and cathode reactant inlets
11. 2 ½" Swagelok plugs, to be connected to the ½" Swagelok adapters on the 1" Tees installed on the reactant inlets
12. 2 3/8" 316SS Swagelok plugs (used for disabling/enabling the reactant manifold drains).
13. Hardware and equipment for rapid cooling of the stack.
14. Miscellaneous 1", 3/8", and ¼" 316SS Swagelok fittings (port connectors, caps, plugs, tees, elbows, nuts, ferrules)

Generic Procedure (specific procedure TBD during initial 3M visit to ANL)

See included diagrams for clarification of hardware setup.

Shutdown

1. Prepare for shutdown
    a. Start with the stack at operating conditions.
    b. Set load to open circuit ("idle" mode)
    c. (If under pressurized conditions): set flows to 30/30SLM H2/Air and slowly reduce anode and cathode pressures to ambient pressure, keeping the anode and cathode pressures within 10kPa of each other.
    d. Set flows to 30/30SLM N2/Air.
    e. Halt gas flows and halt coolant flow (safe mode)
2. Prepare for water injection
    a. On the backside of the panel behind stack, disconnect the station's reactant lines and connect the purge water overflow lines.
        i. IMPORTANT! FAILURE TO CONNECT THE PURGE OVERFLOW LINES CAN RESULT IN INADVERTENT STACK PRESSURIZATION BY THE PRESSURIZED DI SOURCE, AND POSSIBLE STACK DAMAGE.
    b. Close the designated valves on the stack reactant outlets, to force the DI flush water through the stack.
    c. (Optional). Disable the stack manifold drains by disconnecting the 3/8" lines from the stack reactant drain fittings and install plug.
    d. In the software, disable the gas supply, humidity, reactant pressure control, coolant pressure control, and reactant line heaters.
    e. In the software, disable the cell voltage and stack voltage alarms.
    f. If desired, begin logging data.
3. Fill stack reactant manifolds and flow field channels with DI
    a. Slowly open the DI flush water valves (anode and cathode) until 3psig is read on each. Watch the reactant pressure gauges to ensure that the pressure does not exceed 3psig (this is a check to make sure that the stack is not being inadvertently pressurized).
    b. Wait ~ 1 minute. Water should be coming out the purge overflow lines.
4. Cool stack to room temperature
    a. Switch station to idle mode. Coolant will begin to flow. Set the coolant to 20C.
    b. Wait 45 minutes.
    c. Close DI flush water valves to halt DI water from flowing into the stack and switch station to safe mode to halt coolant flow.
    d. Halt data logging, if enabled.
    e. If testing is complete for the day or week, allow stack to sit idle overnight or over the weekend. If stack to remain idle longer than 3 days, please see "3M Stack Long-Term Storage Procedure 111506" document.

Restart

1. Reconfigure station for operation
    a. Close DI water purge valves, if not already off.
        i. IMPORTANT: FAILURE TO CLOSE BOTH VALVES CAN RESULT IN REACTANT GASES MIXING (EXTERNAL "CROSSOVER").
    b. Reconnect reactant drains to stack
    c. Open valves on station reactant exhaust lines, located near the stack reactant outlets
        i. IMPORTANT! FAILURE TO OPEN THE VALVES CAN CAUSE STACK FAILURE DUE TO OVER-PRESSURIZATION ONCE REACTANT GAS FLOW IS RESUMED.
    d. Disconnect DI water purge overflow drain lines from backside of panel behind stack, and reconnect station reactant lines, ensuring lines are tight.
    e. Remove ½" Swagelok caps from reactant inlets near stack; this helps prevent inadvertent pressurization of stack upon restart of gas.
    f. In the software, disable the gas supply, humidity, reactant pressure control, coolant pressure control, and reactant line heaters
    g. In the software, ensure that 30/30SLM N2/Air is specified as minimum flows and gas type.
    h. In the software, load the "DOE3_Startup_052007" loadtable (default values for flows, temperatures, pressures, …). Make sure no overrides are enabled.
    i. In the software, enable the cell and stack voltage alarms.
    j. In the software, start data logging
2. Remove DI from reactant manifolds and cell flow fields
    a. In the software, switch to idle mode (starts station, gas flows and coolant)
    b. Reinstall the ½" Swagelok caps on the reactant feed lines, making sure that the pressure doesn't build beyond 5psig. This step acts as a double check that the reactant exhaust valves are open.
3. Introduce reactant gases; OCV check
    a. Switch to 30/30SLM H2/Air. Wait until H2/Air OCV (~0.88-0.94V) is established on each cell (~10-30 seconds, depending upon volume between station flow controllers and the stack).
        i. If OCVs of any cells do not achieve > 0.85V with 30/30SLM H2/Air gas flows, increase gas flows to 80/80SLM and wait 10-30 seconds. If OCVs of >0.85V are still not established, shutdown the stack by halting gas and coolant flows and contact 3M for diagnostics.
4. Warmup
    a. Increase anode gas flow to 50SLM H2, wait 10 seconds, then increase to 95SLM H2.
    b. Increase cathode gas flow to 100SLM, wait 10 seconds, then increase to 200SLM, wait 10 seconds, then increase to 225SLM.
    c. Validate the following conditions in the load table
        i. Anode and cathode dewpoint: 70C
        ii. Coolant temperature (outlet): 75C
        iii. Reactant inlet heaters +15/+25C (A/C) (above dewpoint)

iv. Coolant flow: 20SLM
v. Anode and cathode pressures: 0/0kPag
vi. Coolant pressure: 0kPag
vii. Cell voltage safeties: 0.3V (warn), 0.2V (alarm)

d. Switch station to manual mode (current draw now allowed)
e. Begin increasing current slowly, in nominally 2A/step, 5s/step increments until any of the cells reaches 0.4-0.5V.
f. As the stack warms, the cell voltages will increase. Increase the current stepwise to keep the stack at as high of current as possible while still keeping all cells above 0.4V; allowable current step sizes will be small initially (2A) while the stack is still cool, but can be increased to as much as 20A as the stack warms. During this period, periodically (every 3-5 minutes) cycle the stack from its current load level to OCV then back down to the initial load level. As the stack approaches 75C, ~312A of current (1A/cm2) should be achieved with all cells above 0.4V. The coolant may overheat slightly (2-3C); this is ok.
g. Allow the stack to operate at 312A for 15 minutes, again cycling to OCV every ~5 minutes.
h. The stack is ready for testing, or further shutdown/restart cycles.

Appendix C.

Overview:

- This document outlines the 3M recommended procedure for preparing the 3M stack for periods when the stack will be left idle for 3 days or more.
- The procedure involves two primary phases, a "MEA Drydown" phase and a "Coolant Removal" phase:
  - MEA Drydown:
    1. Hold the stack at temperature and flow 100SLM nitrogen to both anode and cathode at 50% RH for 60 minutes.
    2. Halt gases and cooldown
  - Coolant removal:
    1. Disconnect stack from station.
    2. Tip stack on side, allowing coolant to drain out
    3. Flow ~50L/min N2 into the coolant inlet until moisture is appreciably removed.

Equipment:

1. Test station
2. 1" and 3/8" Swagelok plugs

Generic Procedure (specific procedure TBD during initial 3M visit to ANL)

See included diagrams for clarification of hardware setup.

MEA Drydown

1. Start with the stack at operating conditions used immediately prior to shutting down.
2. Set load to open circuit
3. (If under pressurized conditions): set flows to 30/30SLM H2/Air and slowly reduce anode and cathode pressures to ambient pressure, keeping the anode and cathode pressures within 10kPa of each other.
4. If coolant temp > 80C, cool stack down to anywhere between 70-80C (whatever is convenient). If cooling the stack is required, halt gas flows during this period.
5. Adjust dewpoints for 50% RH for the target temperature noted in the previous step. Keep flows off while humidifier setting is attained.
6. Flow 100SLM of nitrogen on anode and cathode, with dewpoint sufficient for 50% RH for 1 hour.
7. Halt gas flows.
8. Halt coolant flow. Allow stack to cool to room temperature by convection or a "rapid cooldown" method TBD by 3M and ANL.
    f. ANL coolant system can be used to cool the stack if it can cool the stack to room temperature in < 6 hours.

Coolant Removal

1. Start with stack at room temperature.

2. Disconnect gas, coolant, and electrical leads from stack (leave voltage sense assembly attached to the stack).
    i. **DO NOT** disconnect or adjust any of the Swagelok fittings which are threaded directly into the stack. PTFE tape was used to protect the stack's coating, so disturbing these fittings could result in small bits of PTFE tape entering the stack!
3. Tip stack on narrow side, opposite of the voltage sense assembly. Some coolant will drain out, so place a catch pan if necessary.
4. Connect the station's cathode reactant feed to the coolant inlet. Flow ~100SLM of dry N2 to blow out excess water (flow should be adjusted to keep inlet pressure < 50kPag). Allow this to occur until no more appreciable water is removed.
5. Install Swagelok plugs on all open stack fittings, a little less than finger-tight. This will prevent any debris from entering the stack, while allowing the stack to remain at atmospheric pressure with any temperature changes.

Appendix D.

Figure 1 Dynamic Stress Test

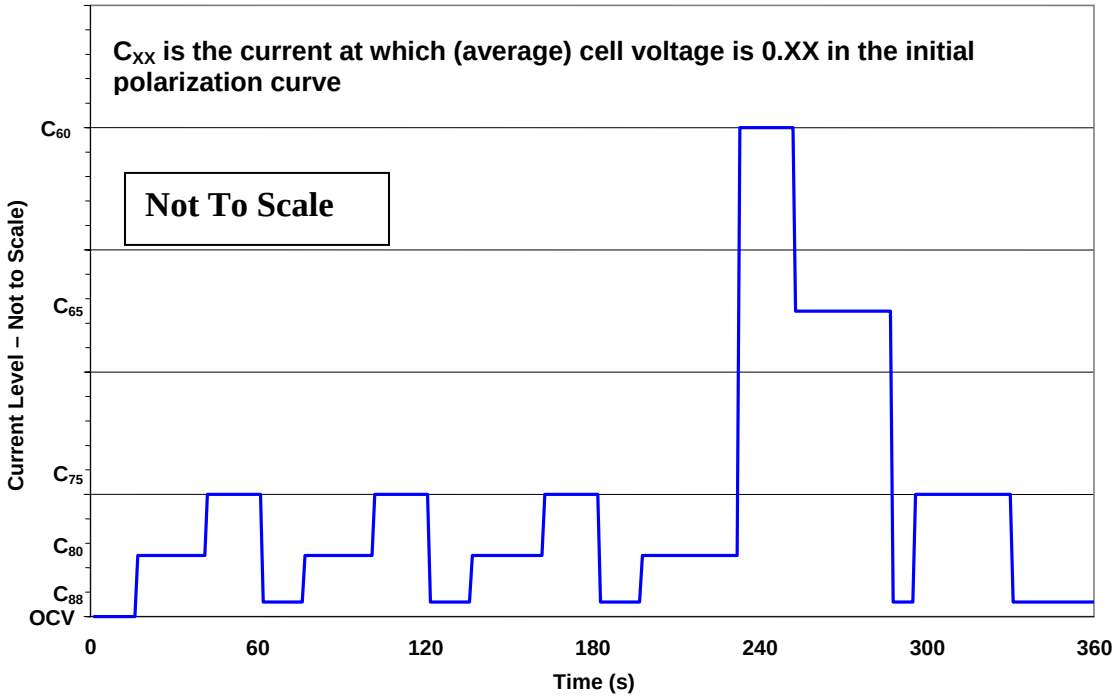

Table 1 – Current Density vs Time for the Cycle Profile						
Step	**Duration sec**	**C_{XX}**		**Step**	**Duration sec**	**C_{XX}**
1	**15**	**OCV**		9	20	C_{75}
2	25	C_{80}		10	15	C_{88}
3	20	C_{75}		11	35	C_{80}
4	15	C_{88}		12	20	C_{60}
5	24	C_{80}		13	35	C_{65}
6	20	C_{75}		14	8	C_{88}
7	15	C_{88}		15	35	C_{75}
8	25	C_{80}		16	40	C_{88}

Appendix II.

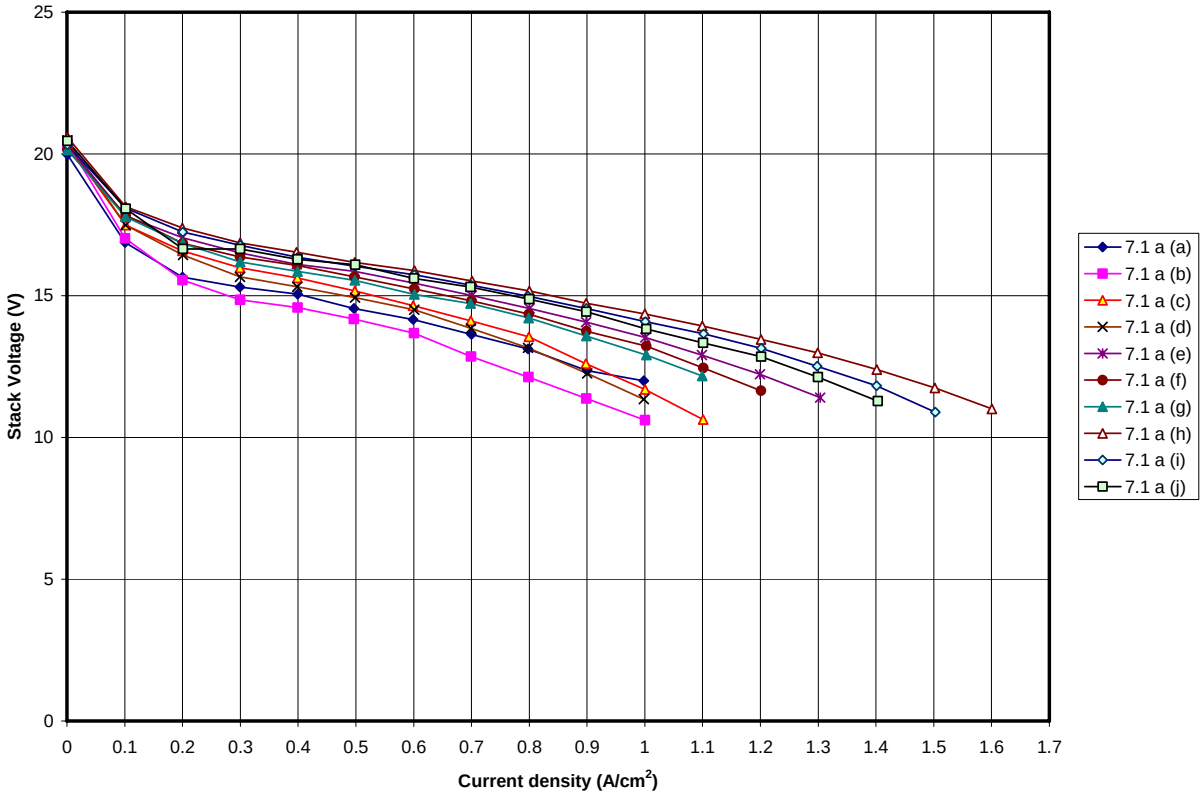

Fig. 1. Stack voltage vs. current density at initial performance tests. See text for description of the conditions used.

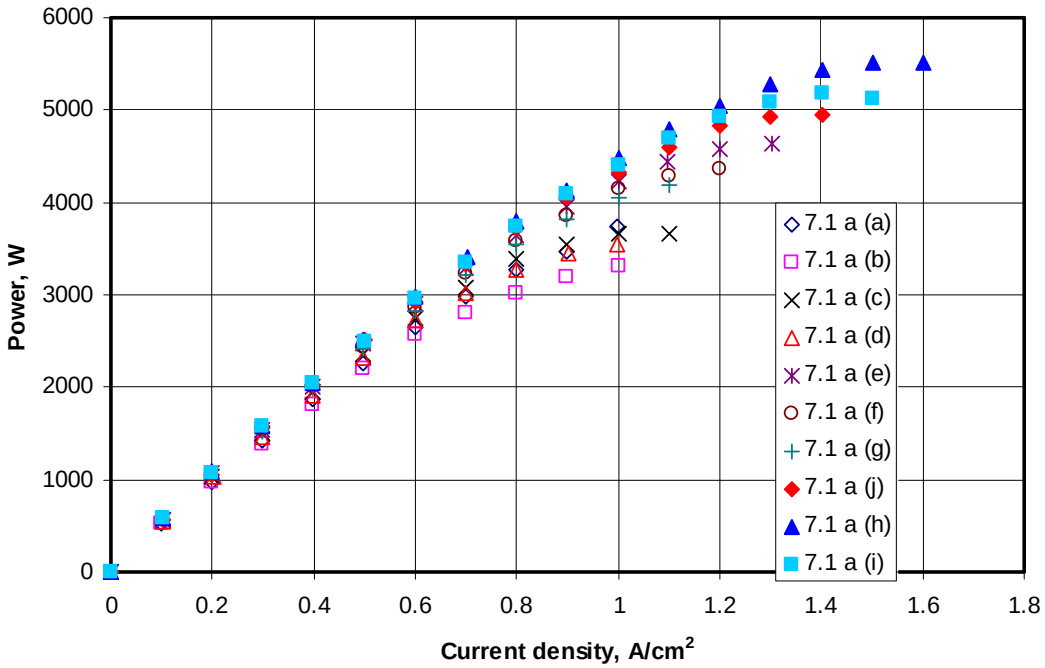

Fig. 2. Power vs. current density at initial performance tests.

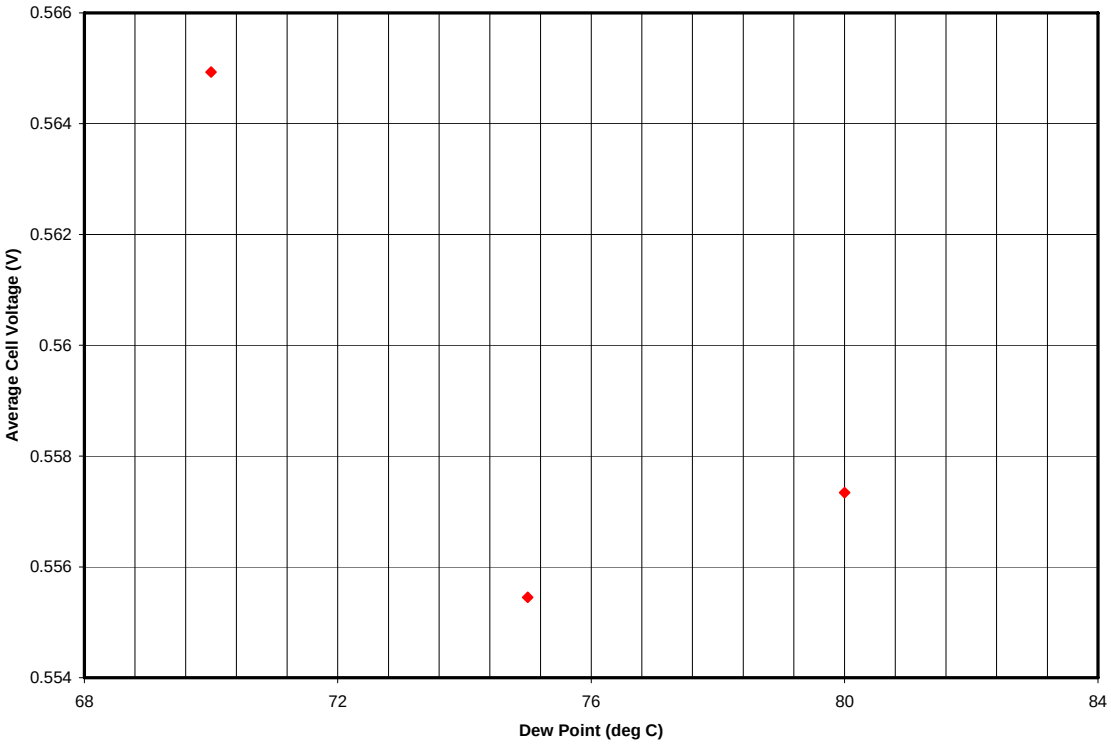

Fig. 3. Average cell voltage vs. dewpoint for humidity sensitivity test.

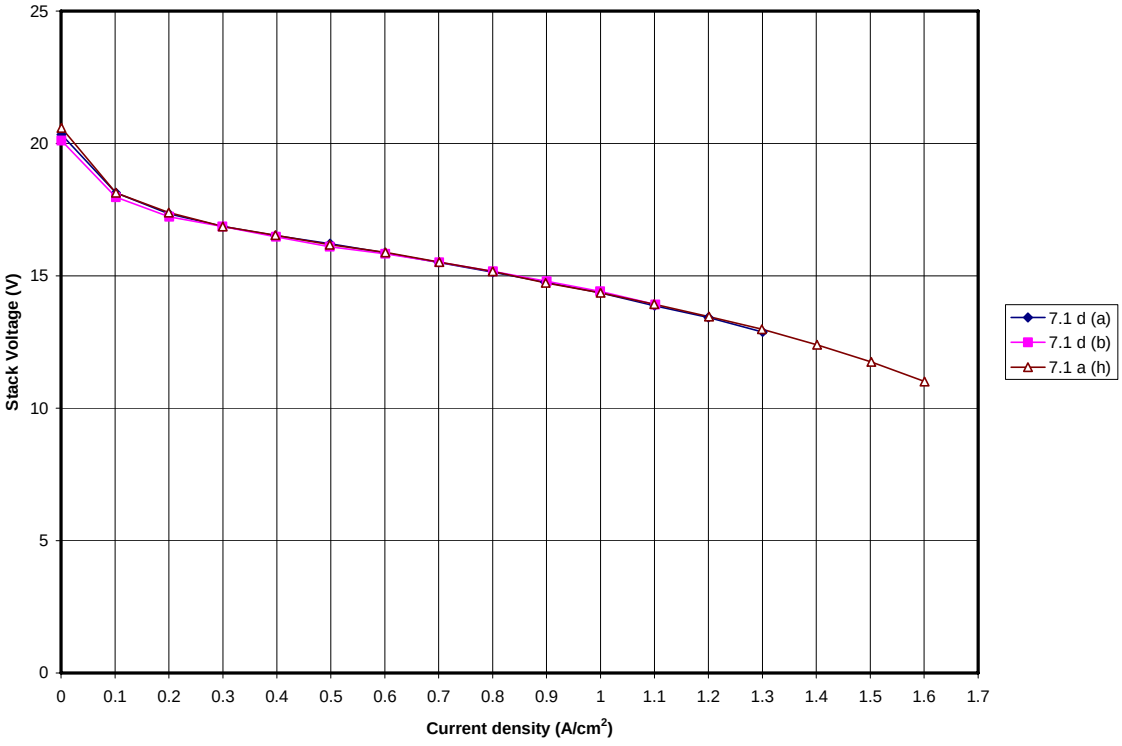

Fig. 4. Stack voltage vs. current density in high temperature performance tests

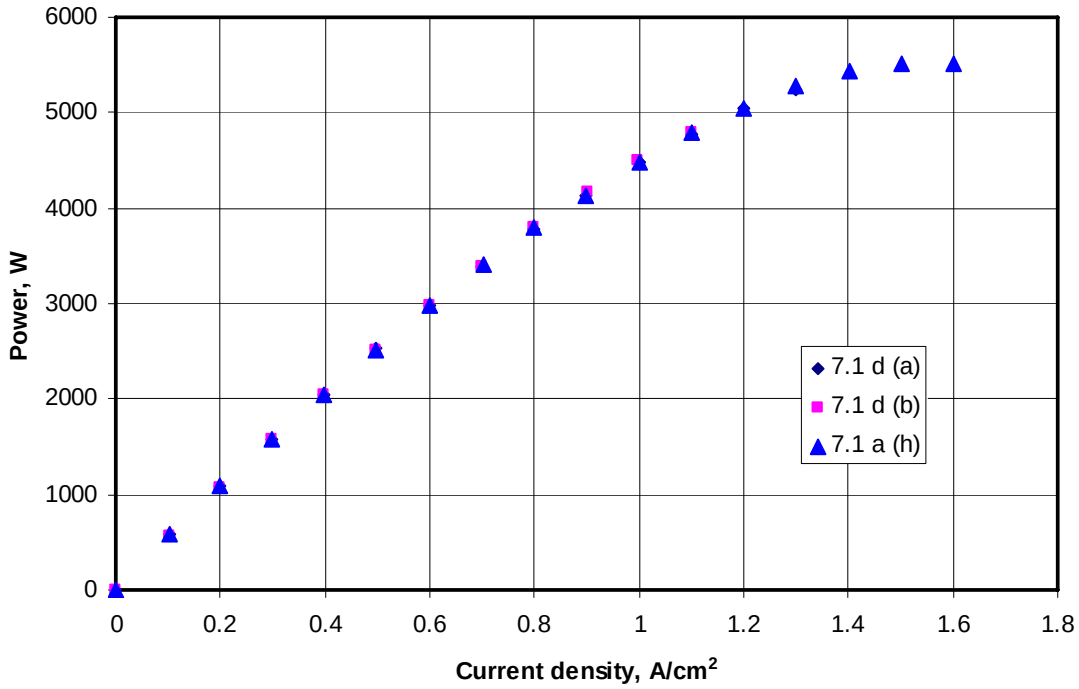

Fig. 5. Stack power vs. current density for high temperature operation.

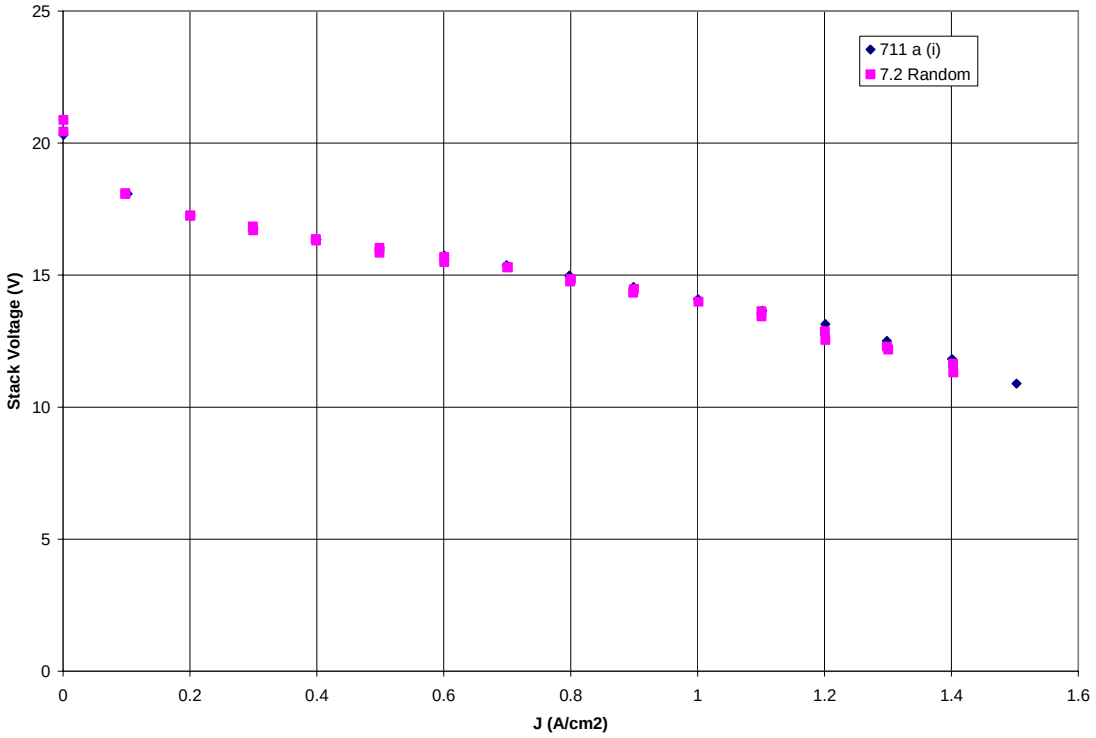

Fig. 6. Stack voltage vs. current density, random compared with sequential polarization.

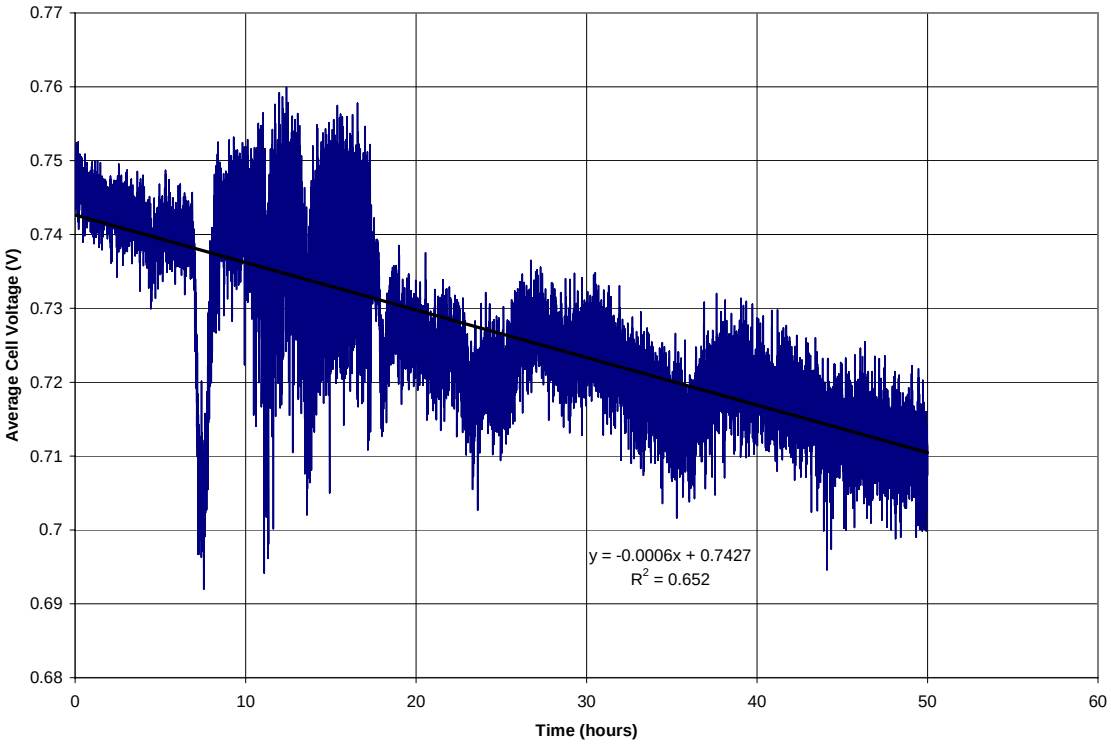

Fig. 7. Average cell voltage vs. time in the constant power test.

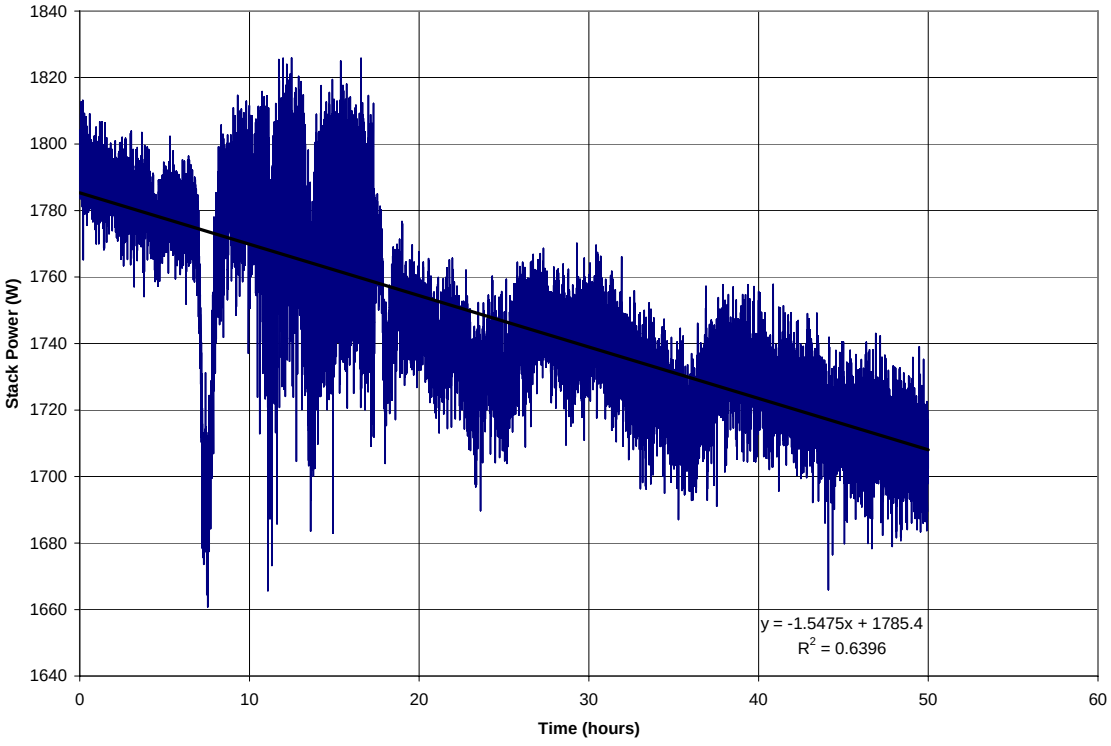

Fig. 8. Stack power vs. time in constant power test.

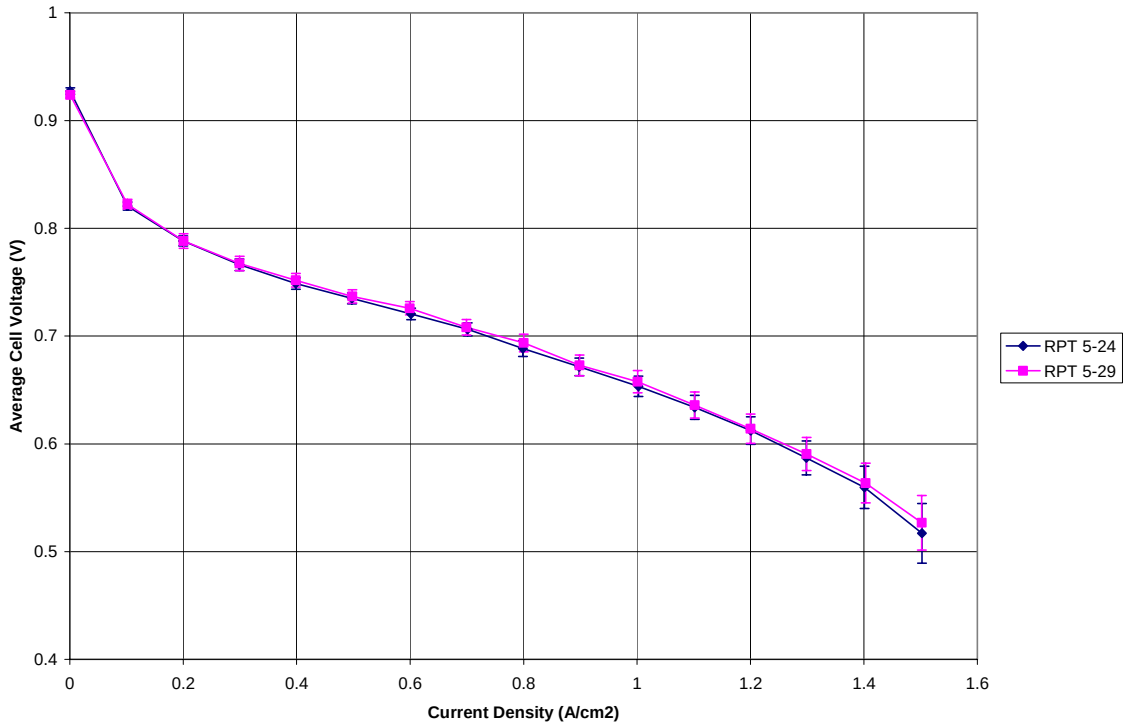

Fig. 9. RPT polarization curves from before and after 50 hours constant power test.

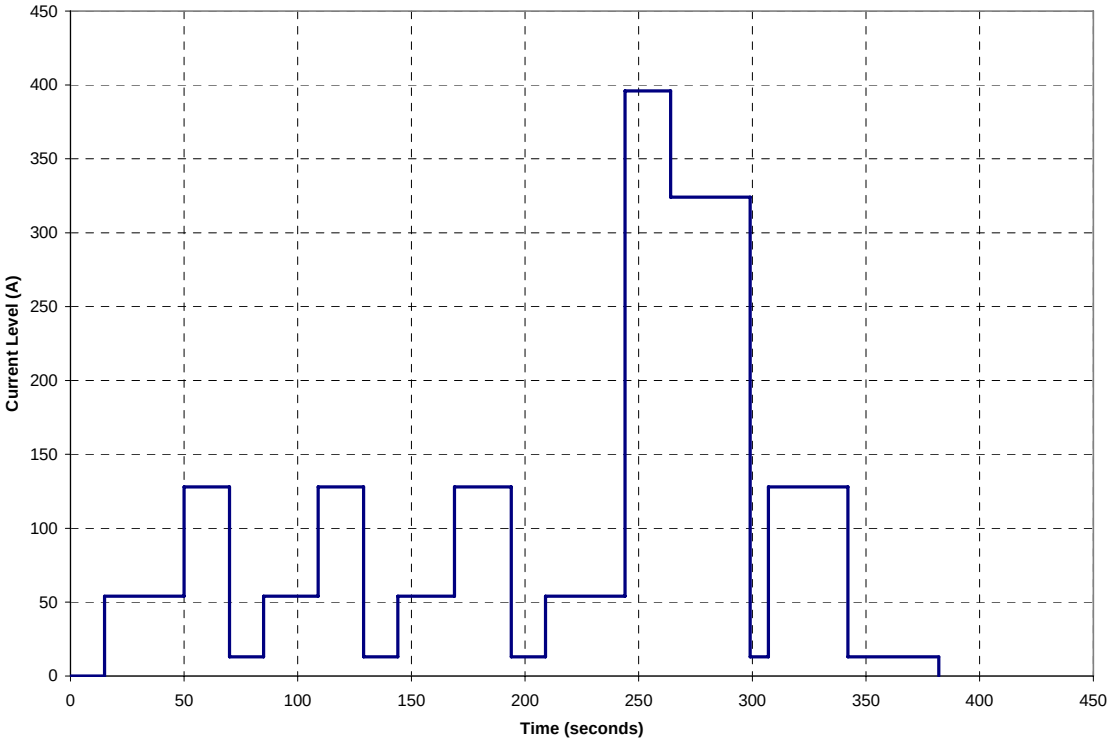

Fig. 10. Ideal scaled DST profile for durability cycling.

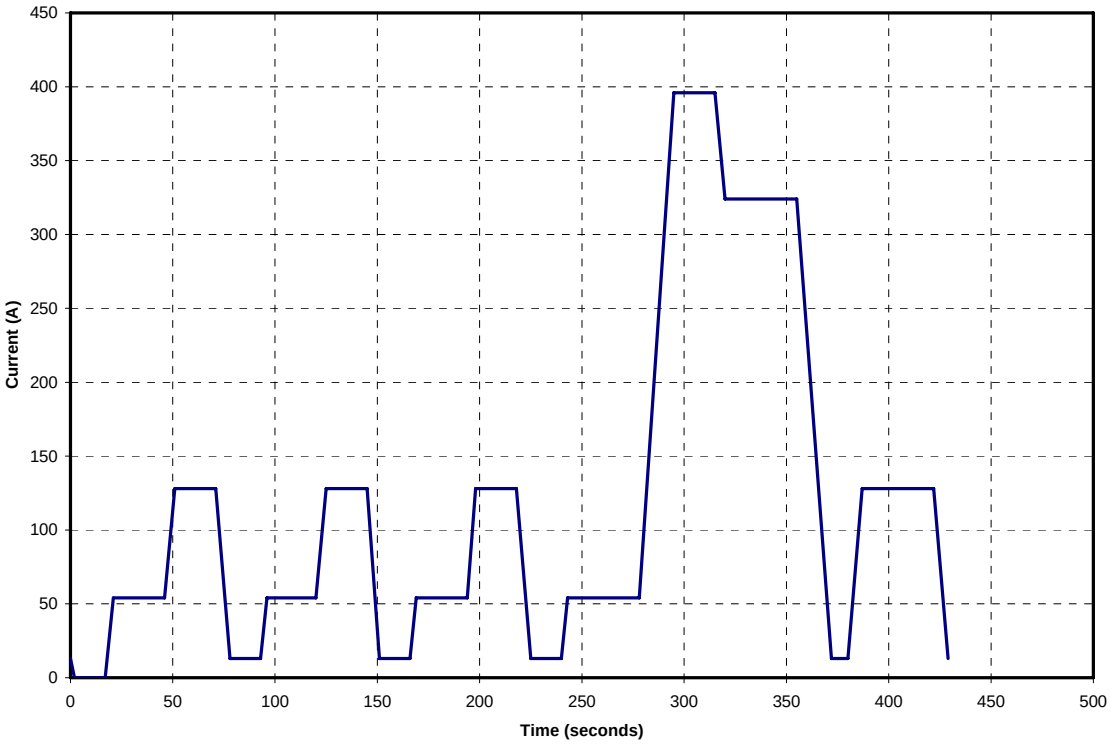

Fig. 11. Adjusted DST profile for durability cycling.

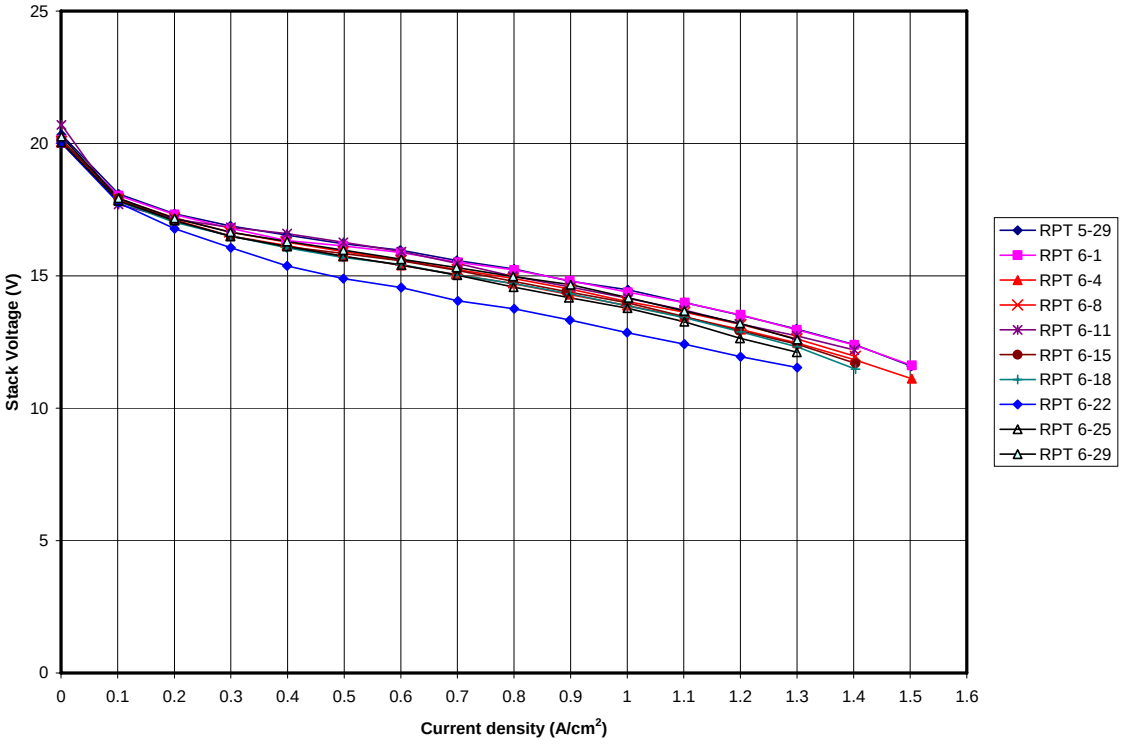

Fig. 12. Stack voltage vs. current density, polarization curves from DST RPTs.

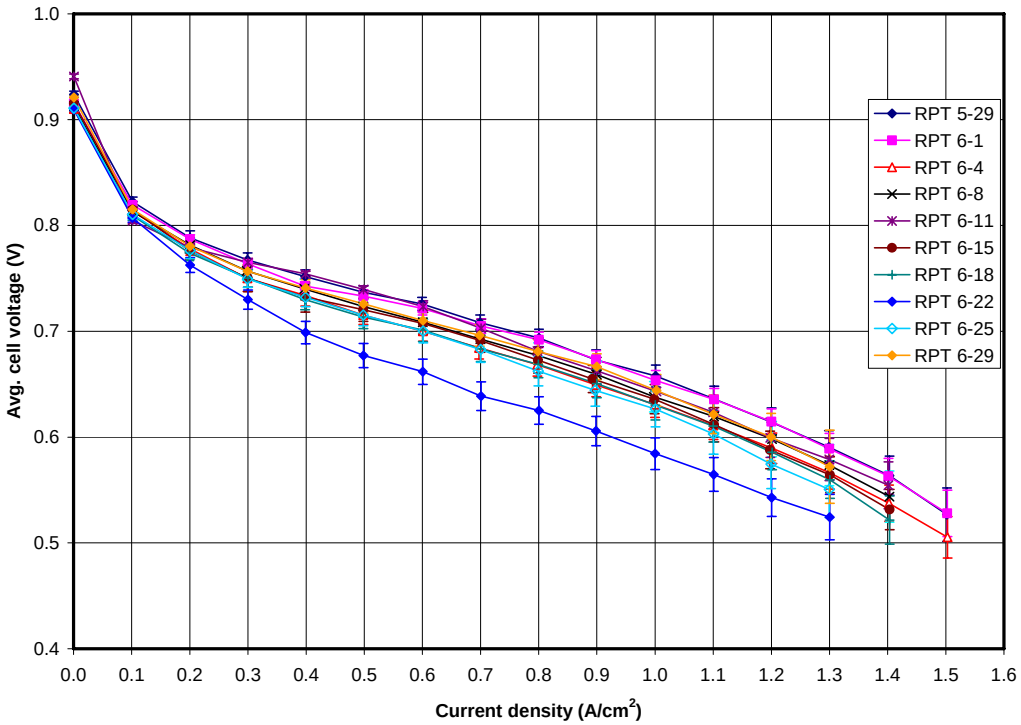

Fig. 13. Average cell voltage vs. current density, polarization curves from DST RPTs.

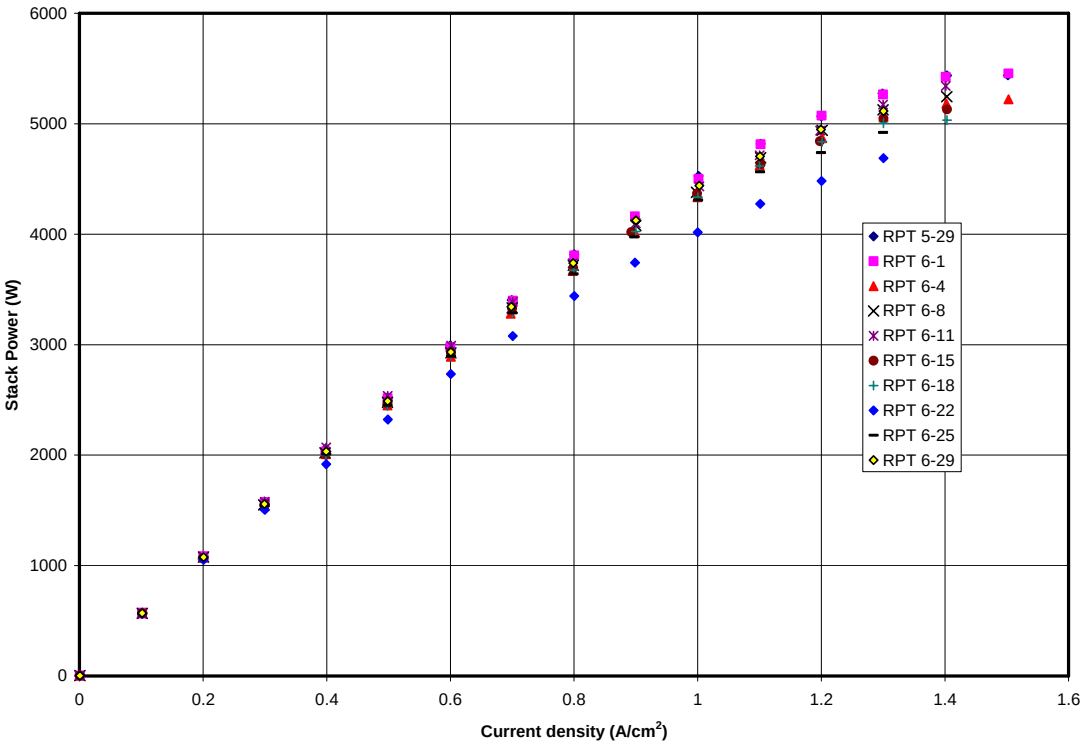

Fig. 14. Stack power vs. current density, from DST RPTs.

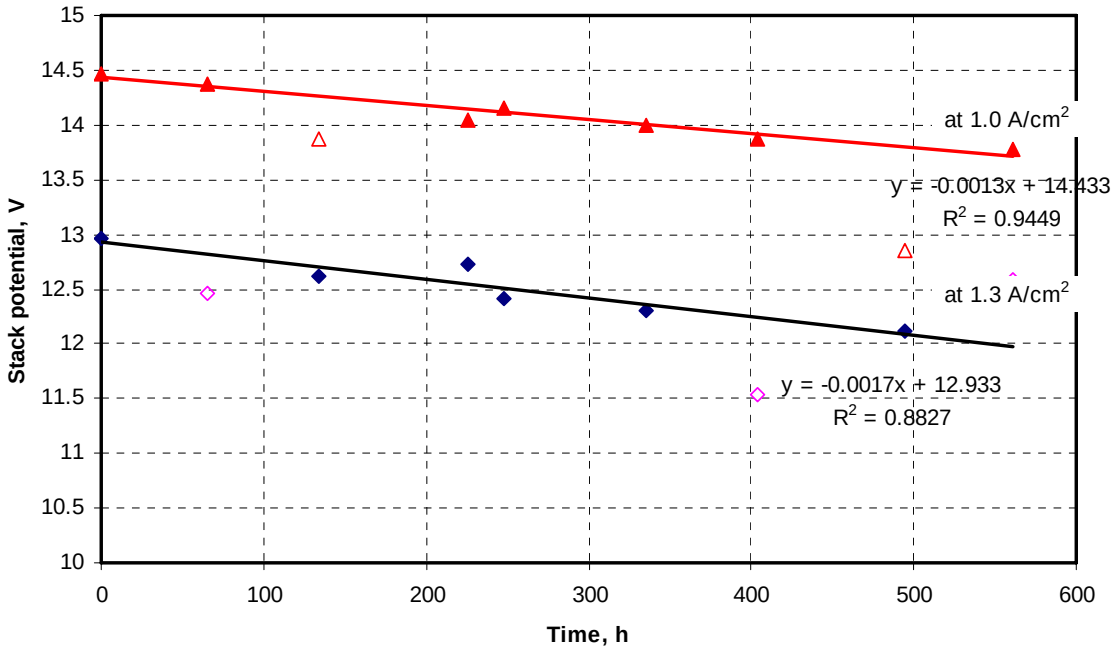

Fig. 15. Stack potential vs. accumulated cycle time from durability cycling.

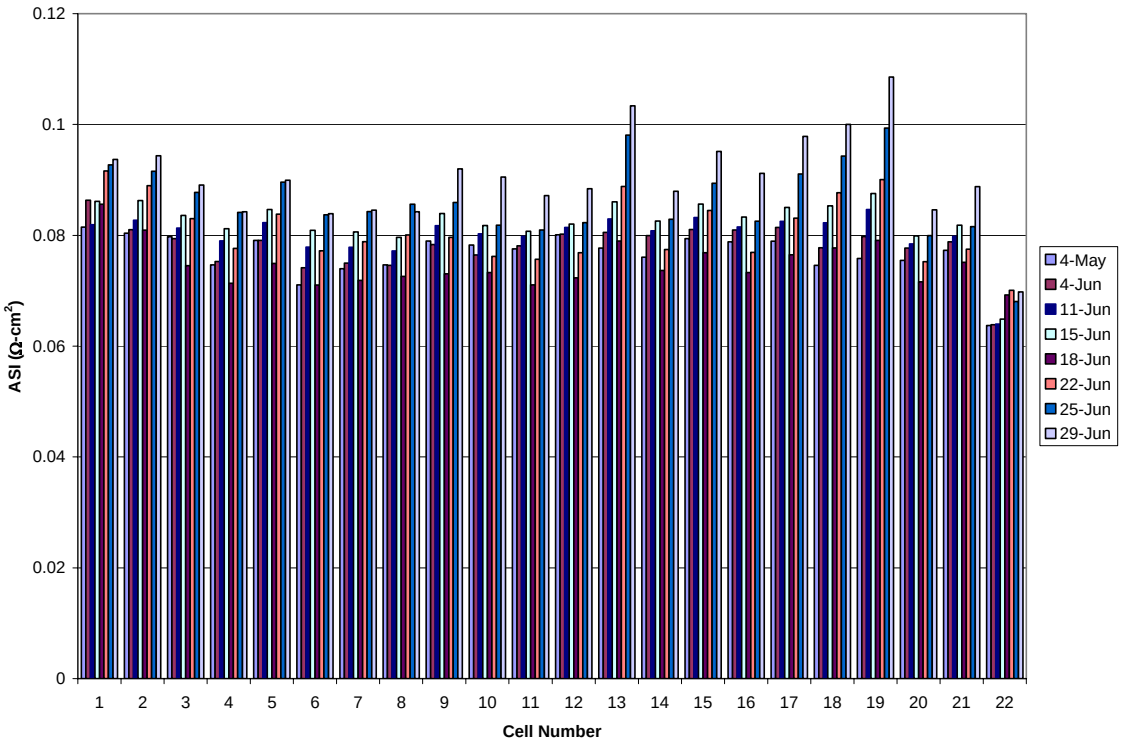

Fig. 16. Measured ASI for each cell from each hydrogen pump experiment.

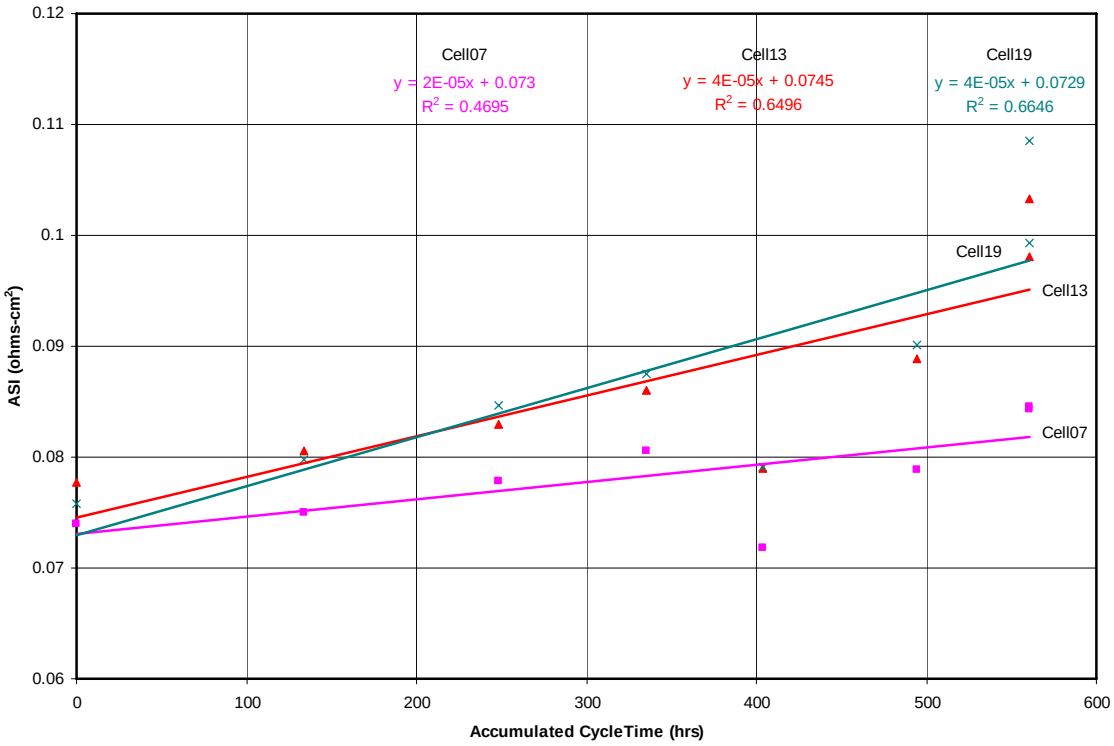

Fig. 17. ASI vs. accumulated cycle time for three cells from the hydrogen pump experiment.

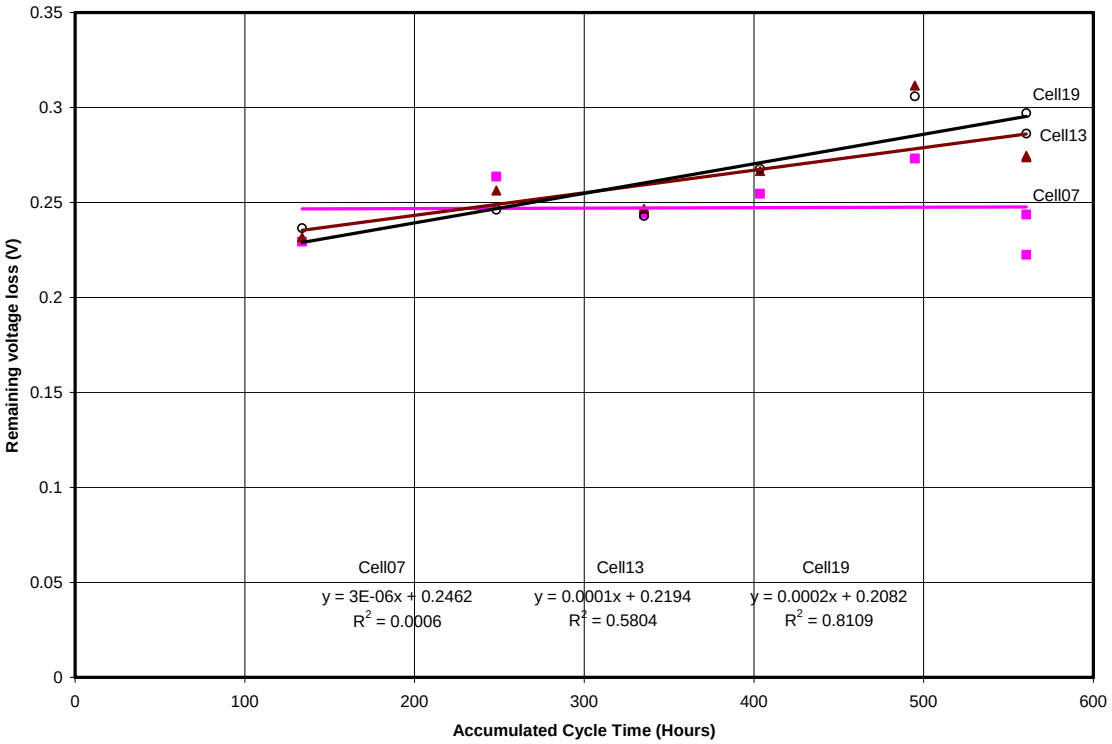

Fig. 18. Remaining voltage loss vs. time. See text for more details.

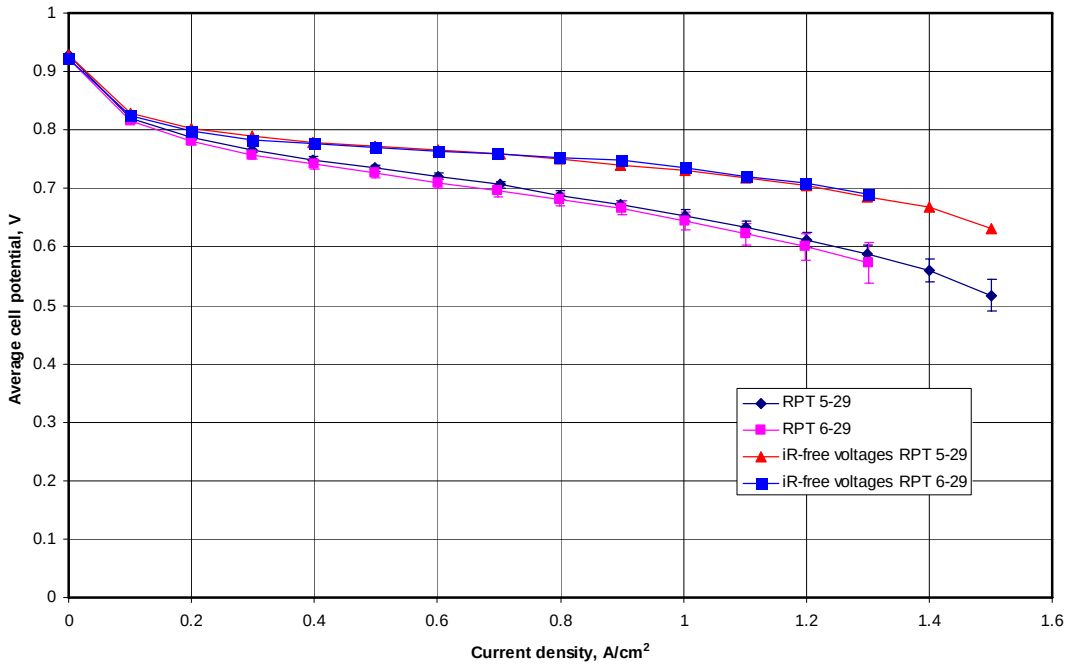

Fig. 19. Comparison of as-measured and iR-free polarization curves taken at the start and after completion of the durability stress tests. The final, as-measured performance curve was taken after further thermal cycles were completed to recover any non-permanent performance loss. The average hydrogen-pump-derived specific resistances were used to correct the curves for iR losses. Fig. 20 shows an expanded view of the iR-free curves.

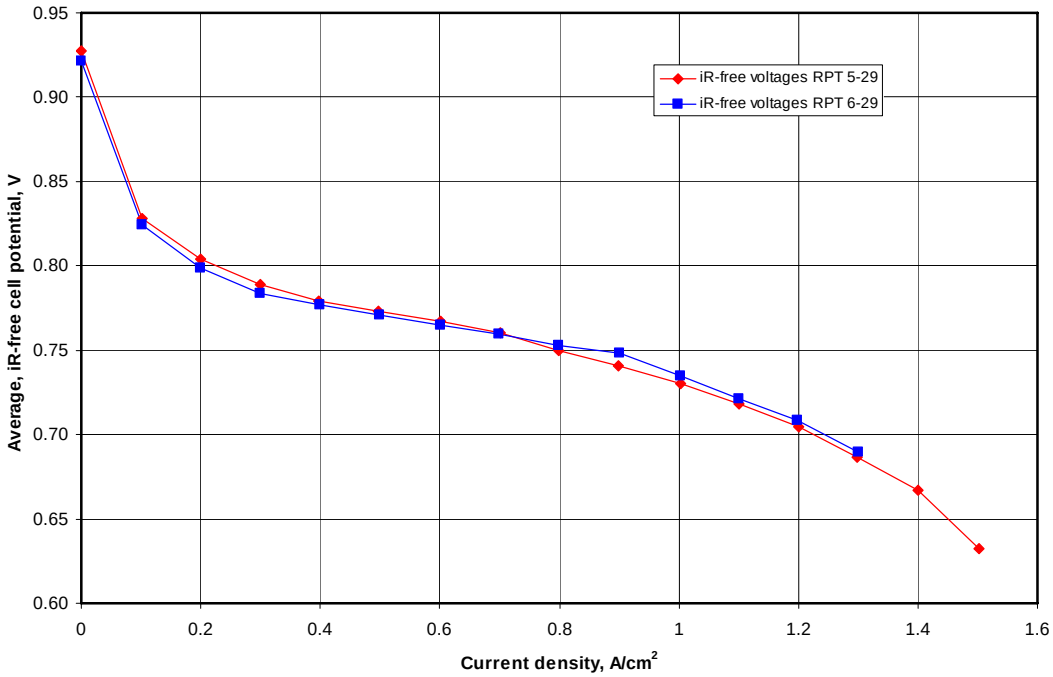

Fig. 20. Expanded view of Fig. 19 showing the iR-free performance change in the 3M NSTF MEA's after the durability tests. The remaining non-iR changes are due to a combination of kinetic and mass transport overpotential changes.

Appendix VIII

ANL Report – Status of Automotive Fuel Cell Systems

Argonne NATIONAL LABORATORY

… for a brighter future

Status of Automotive Fuel Cell Systems

R.K. Ahluwalia and X. Wang

April 23, 2007

U.S. Department of Energy

UChicago ▶ Argonne LLC

A U.S. Department of Energy laboratory managed by UChicago Argonne, LLC

Argonne 2007 Reference Fuel Cell System

- Modified PFSA membrane for enhanced durability at low humidity
- 3M NSTF ternary-alloy catalyst for low Pt loading, diminished ECSA loss with potential cycling, stability at high potentials
- Higher cell temperature to help with heat rejection

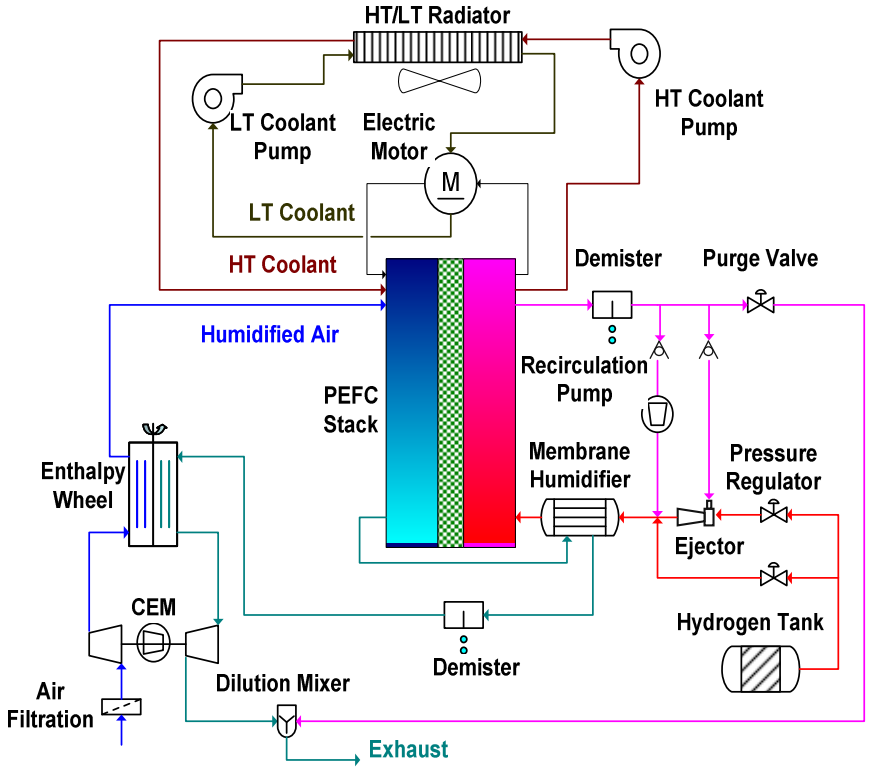

2005 Status

- Difficult to meet 50% η_s target at acceptable Pt loading
- 1 g-Pt/kW loading for 46% η_s
- Durability of finely dispersed Pt catalyst and PFSA membrane
- Heat rejection is an issue at 80°C stack temperature

Argonne 2007 FCS Configuration – S2

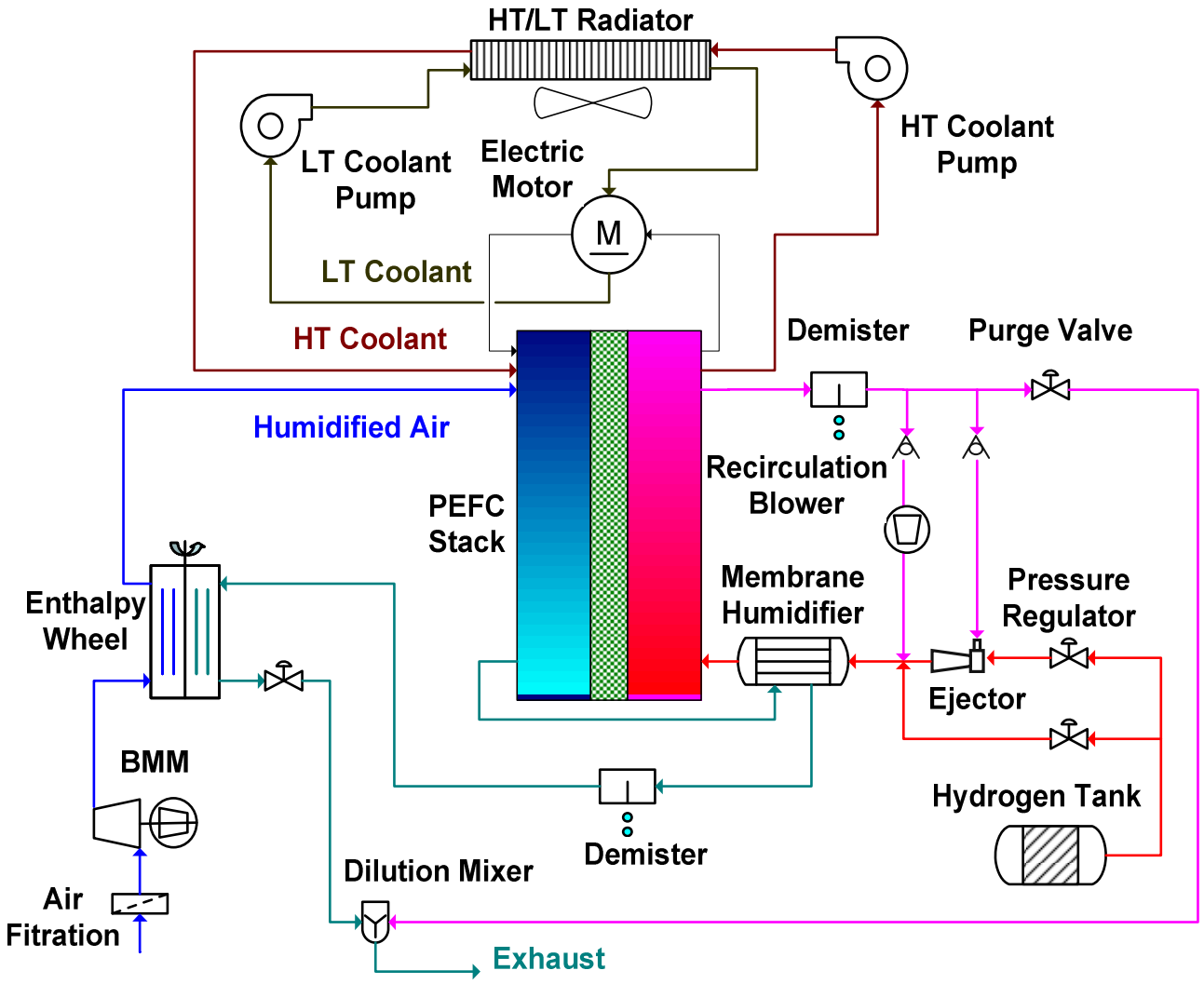

Changes from FCS 2005

MEA

- Catalyst: Ternary Pt alloy
- 3M's NSTFC
- Organic whisker support
- 3M PFSA membrane
- 80°C

AMS

- Low Pressure: BMM

WMS

- External humidification
- Dry gases

TMS

- Advanced radiator

FMS

- FC quality H_2

S2 Parameters

PEFC Stack

- 1.5 atm at rated power
- 50% O_2 utilization
- 70% H_2 consumption per pass
- Cell voltage at rated power: 0.684
- 30-µm 3M membrane at 80°C
- Pt loading: 0.2/0.1 mg/cm^2 on cathode/anode
- GDL: 275-µm non-woven carbon fiber
- 2-mm expanded graphite bipolar plates, each with cooling channels
- 10 cells/inch

Fuel Management System

- Hybrid ejector-recirculation pump
- 40% pump efficiency
- 2 psi pressure drop at rated power

Air Management System

- Restricted vane blower
- Liquid-cooled motor
- Efficiencies at rated power: 81% compressor, 92% motor, 92% controller
- Turn-down: 10
- 5 psi pressure drop at rated power

Heat Rejection System

- Two circuits: 75°C HT, 55°C LT coolant
- 75% pump + 92% motor efficiency
- 60% blower + 92% motor efficiency
- 10 psi pressure drop each in stack and radiator

Water Management System

- EWH for air, 65% RH at rated power
- MH for H_2, 65% RH at rated power

S2: Integration of Air, Water and Stack Subsystems

Variable P, SR & T_{dp}

- As P↑, V↑, but P_{cp}↑
- As SR↑, V may ↑, but P_{cp}↑
- If T_{dp} is too high, V↓ because of flooding
- If T_{dp} is too low, V↓ because of membrane dry out

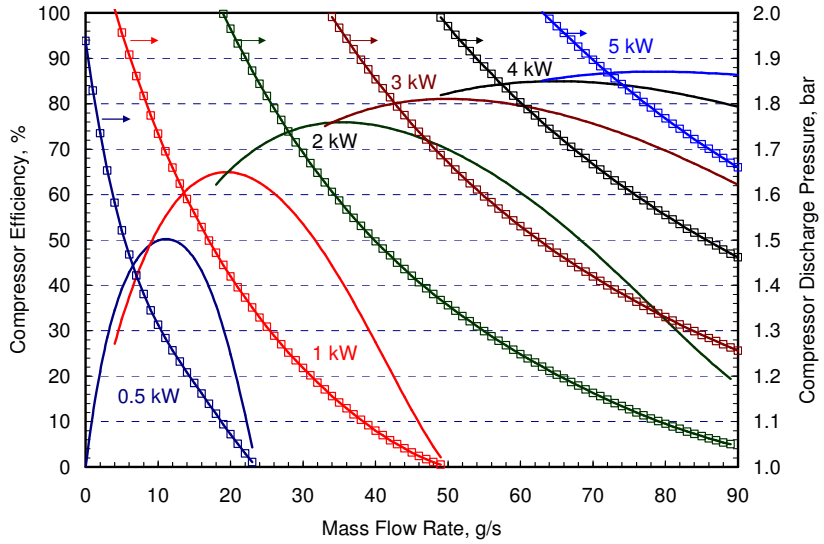

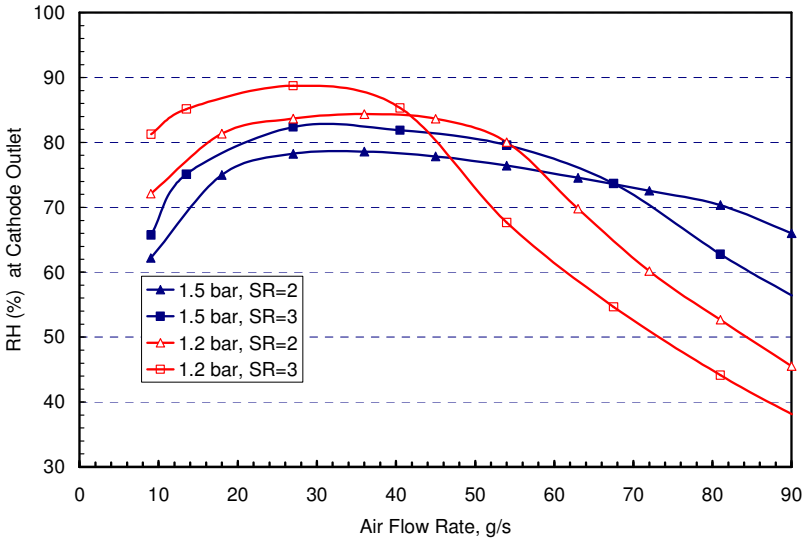

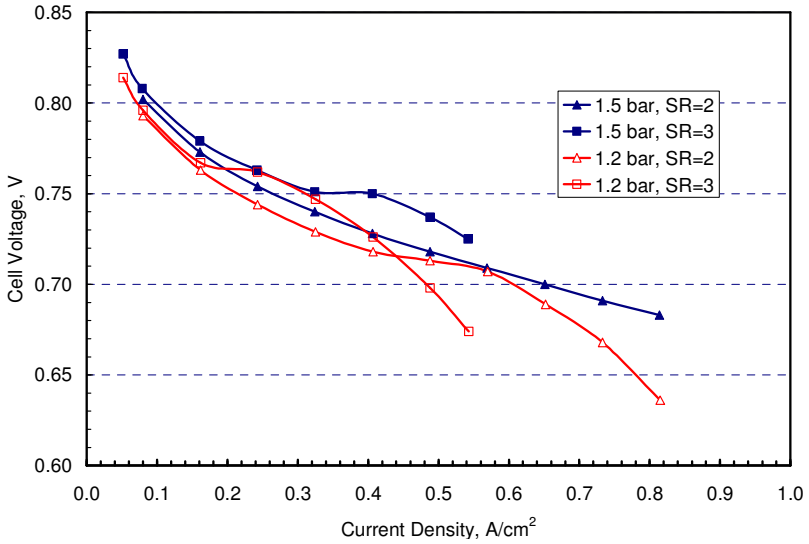

S2 Operating Map

- Operating maps constructed assuming no bypass of humidifier
- Higher stoichiometry at low loads to prevent flooding
- Stack cell voltage is not necessary maximum at the optimum operating conditions

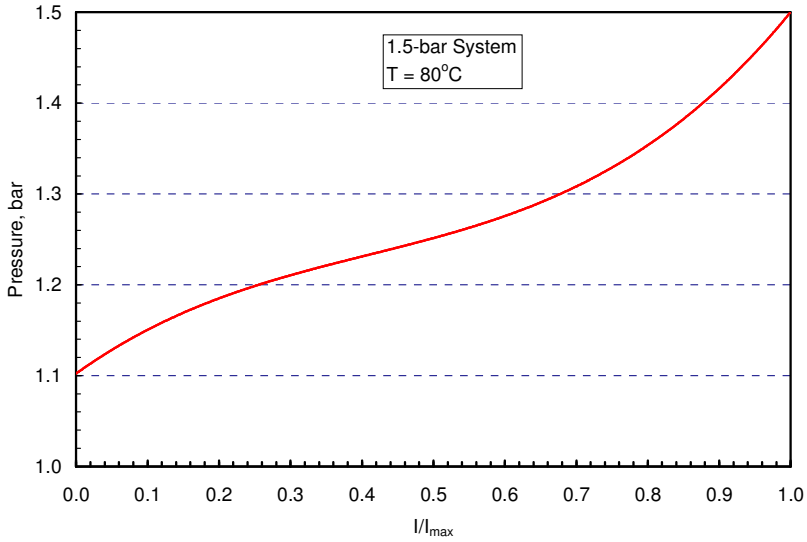

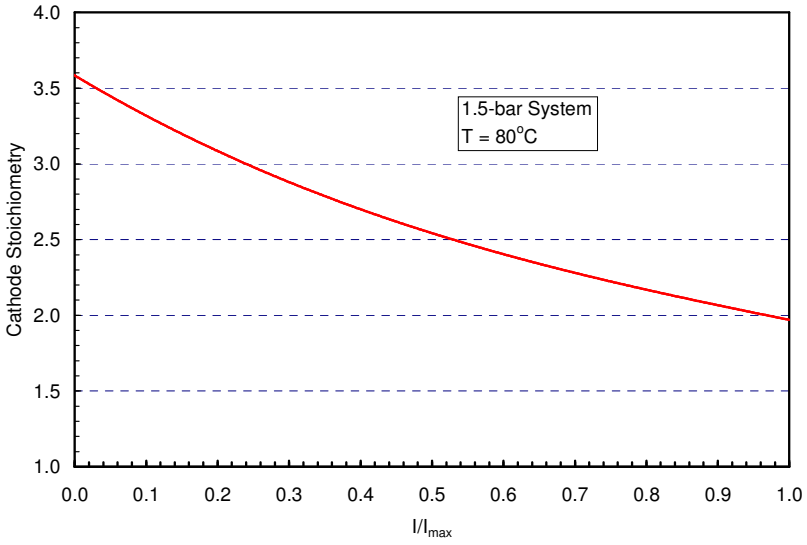

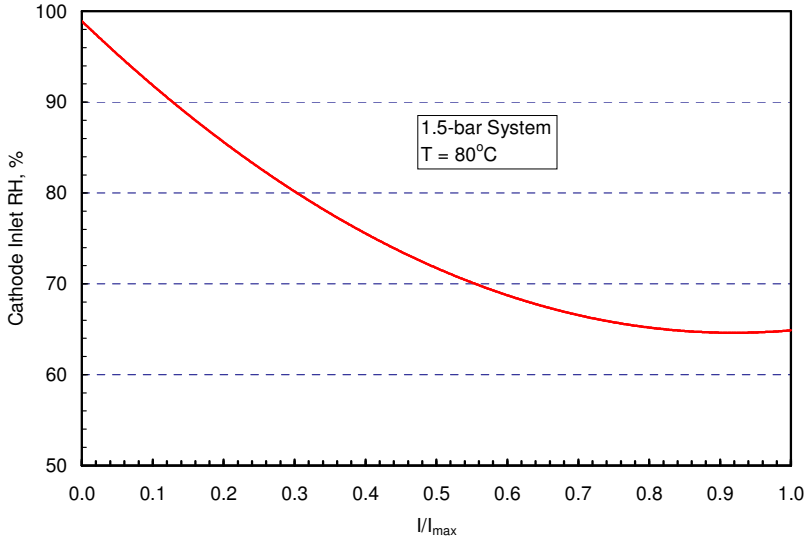

S2 Heat Rejection

- Heat rejection most challenging at 55 mph on 6.5% grade
- Frontal area reduced by allowing the stack temperature to rise
- To prevent dry out, operate at $P>P_{opt}$, $SR<SR_{opt}$

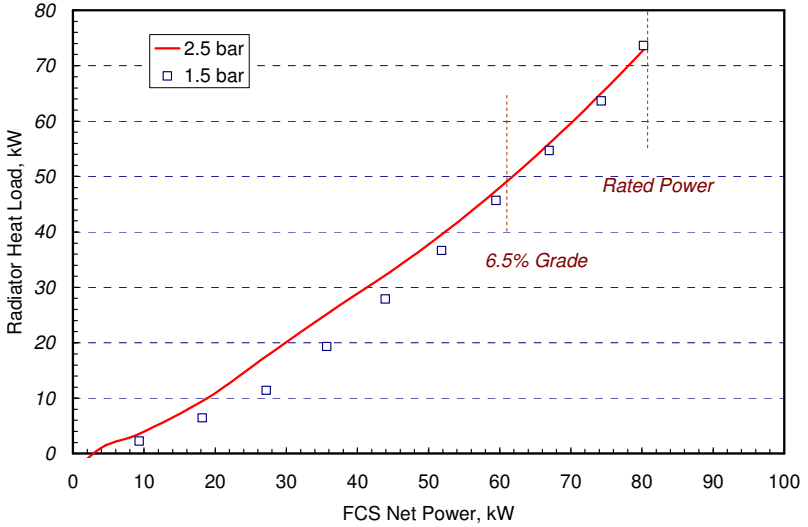

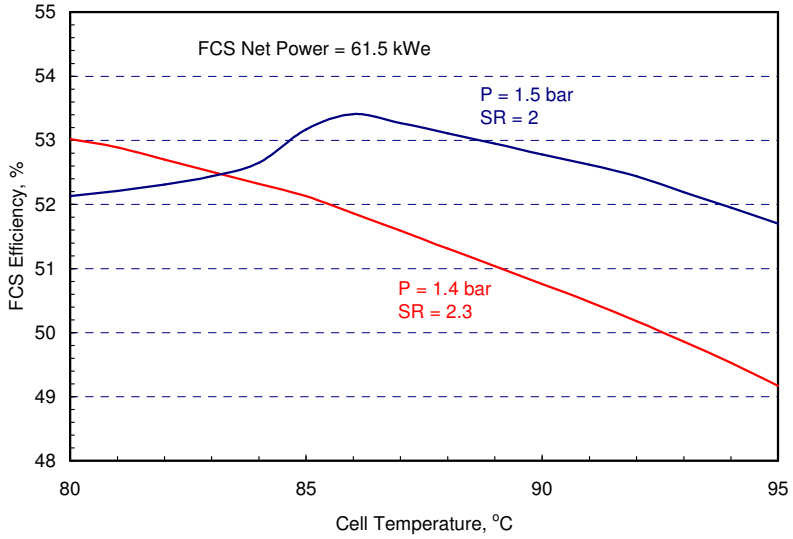

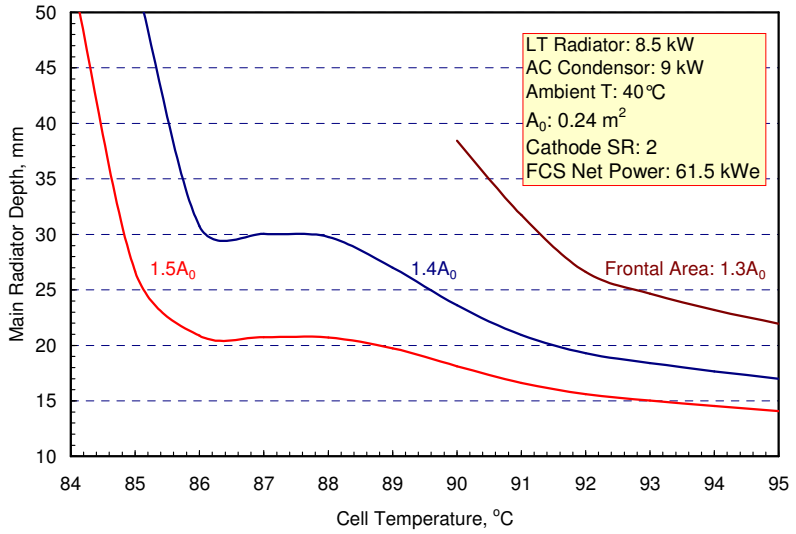

Argonne 2007 FCS Configuration – S1

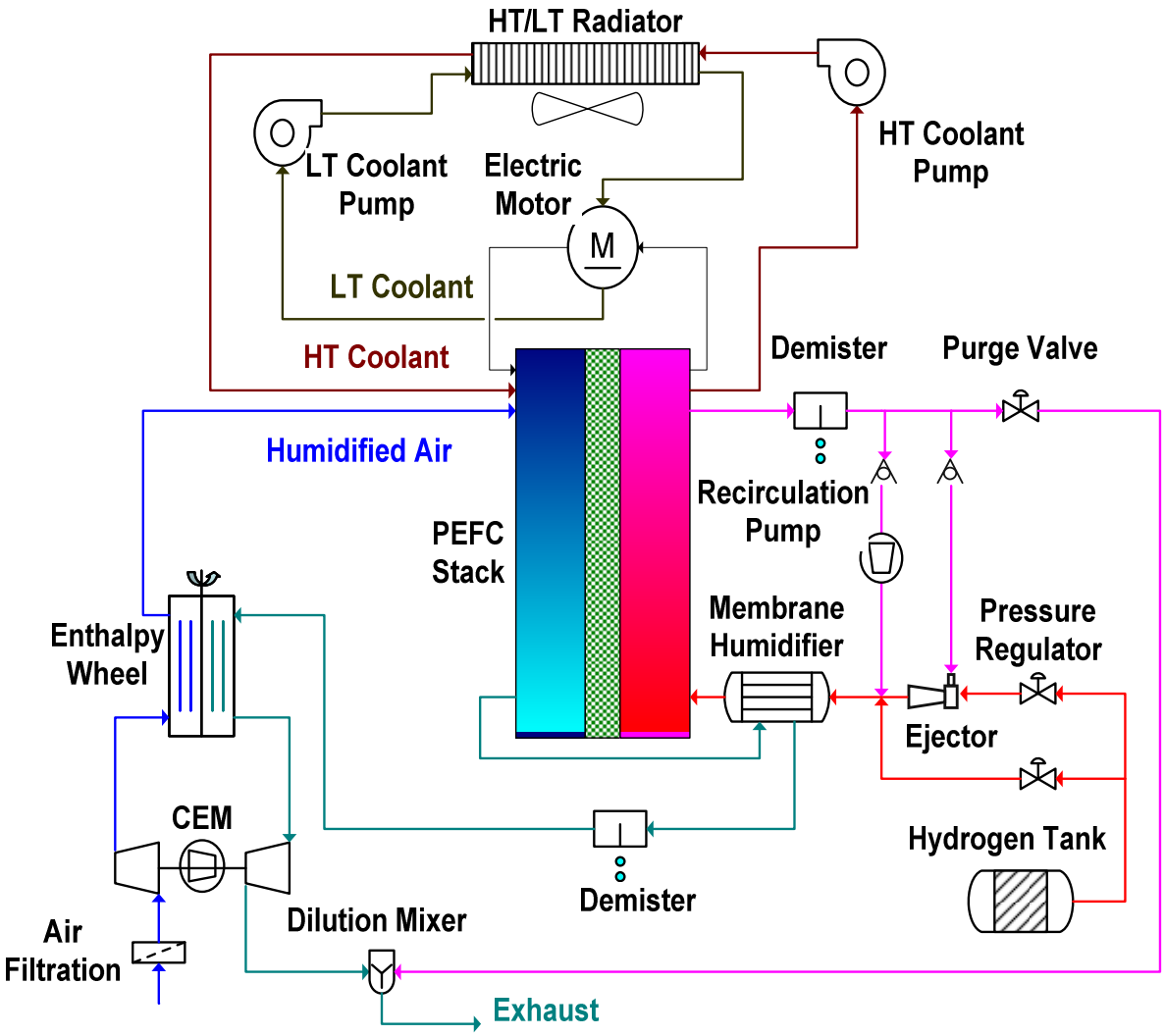

Changes from FCS 2007

MEA
- No Change
- 90°C

AMS
- CEMM: 2.5 bar

WMS
- No change

TMS
- No change

FMS
- No change

S1 Operating Map

- With compressor and expander on a single shaft, pressure is uniquely determined by I/I_{max}.
- Optimum SR>5 at low loads, even higher below the maximum turn-down of the compressor.
- At the optimum operating conditions, the spent gases are just saturated although liquid water may exist in the catalyst layers.

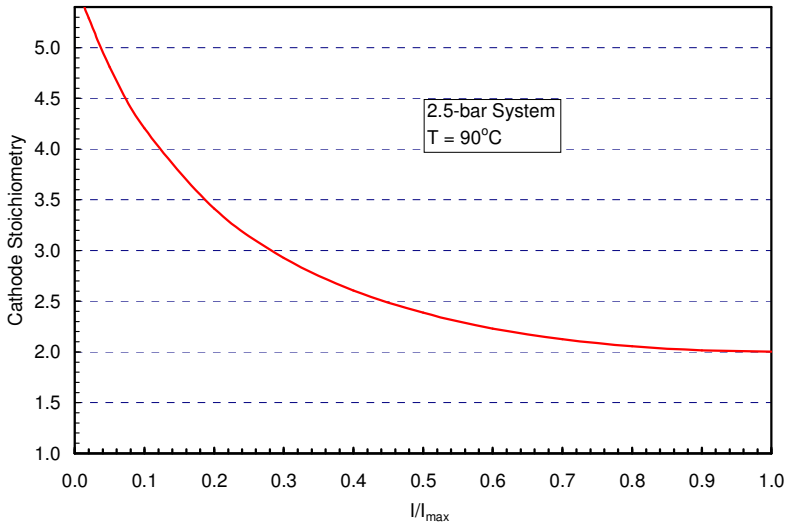

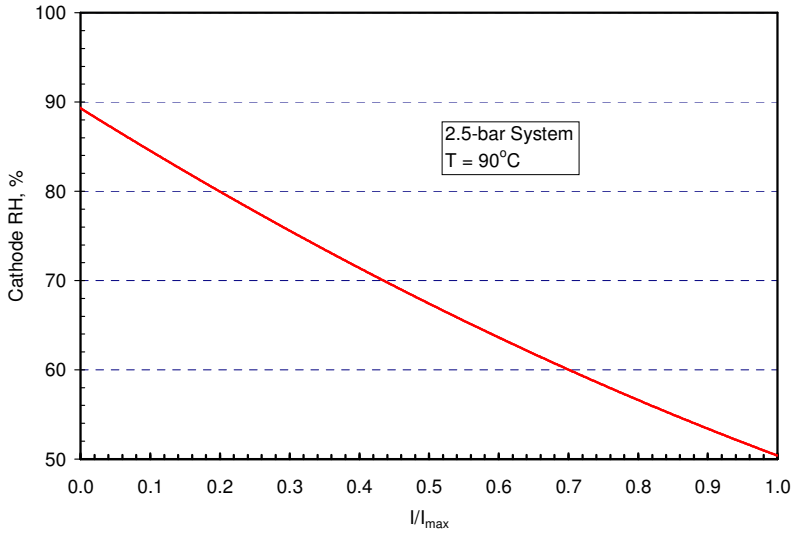

S1 Parameters

PEFC Stack

- 2.5 atm at rated power
- 50% O_2 utilization
- 70% H_2 consumption per pass
- Cell voltage at rated power: 0.685
- 30-µm 3M membrane at 90°C
- Pt loading: 0.2/0.1 mg/cm^2 on cathode/anode
- GDL: 275-µm non-woven carbon fiber
- 2-mm expanded graphite bipolar plates, each with cooling channels
- 10 cells/inch

Fuel Management System

- Hybrid ejector-recirculation pump
- 40% pump efficiency
- 2 psi pressure drop at rated power

Air Management System

- Compressor-expander module
- Liquid-cooled motor
- Efficiencies at rated power: 78% compressor, 82% expander, 92% motor, 92% controller
- Turn-down: 20
- 5 psi pressure drop at rated power

Heat Rejection System

- Two circuits: 85°C HT, 55°C LT coolant
- 75% pump + 92% motor efficiency
- 60% blower + 92% motor efficiency
- 10 psi pressure drop each in stack and radiator

Water Management System

- EWH for air, 51% RH at rated power
- MH for H_2, 51% RH at rated power

S1 Heat Rejection

- Cathode stoichiometry must decrease in order to allow the stack temperature to rise (otherwise membrane dries out).
- The allowable temperature is < 94°C with 1.3 A_0 frontal area and 25-mm depth.
- The frontal area can be smaller if the ambient temperature is <40°C for driving on grade

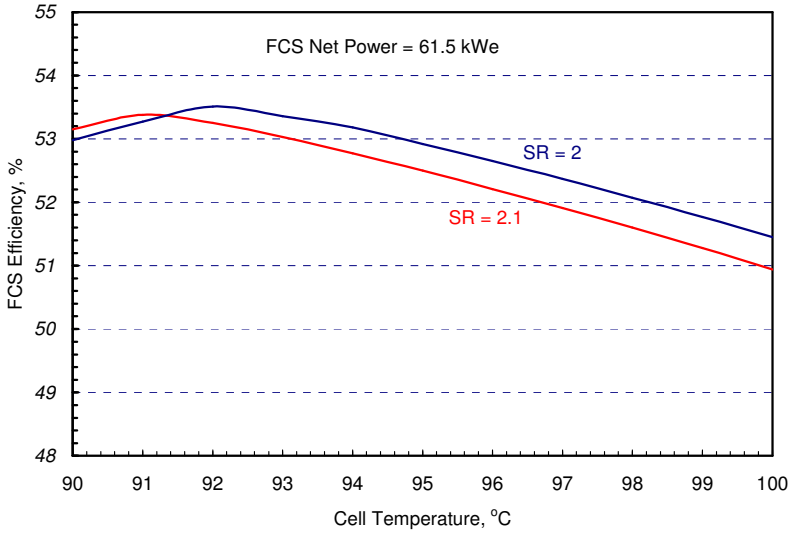

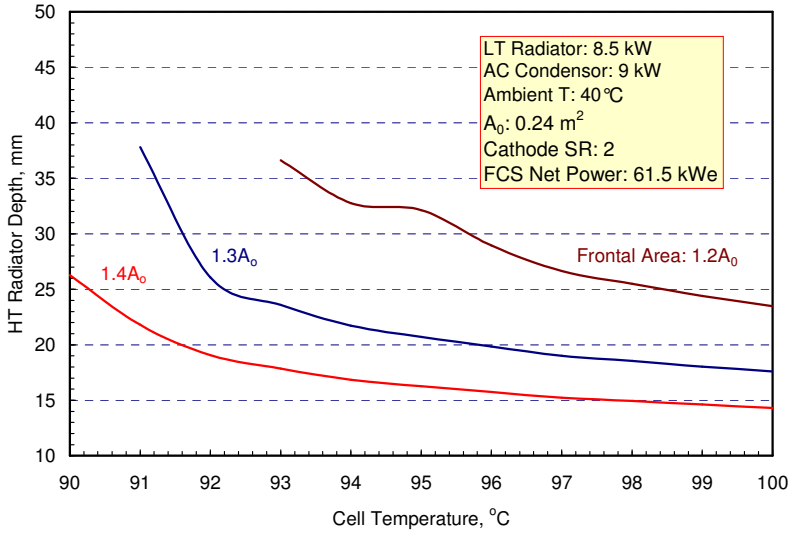

Stack Subsystem

- 3-M PFSA membrane with or w/o chemical additives, EW=825
- 3M's ternary $Pt/Co_x/Mn_y$ alloy NSTFC, Pt:TM = 3:1
- Catalyst supported on organic whiskers: $5*10^9/cm^2$, 1 μm H, 50 nm ϕ

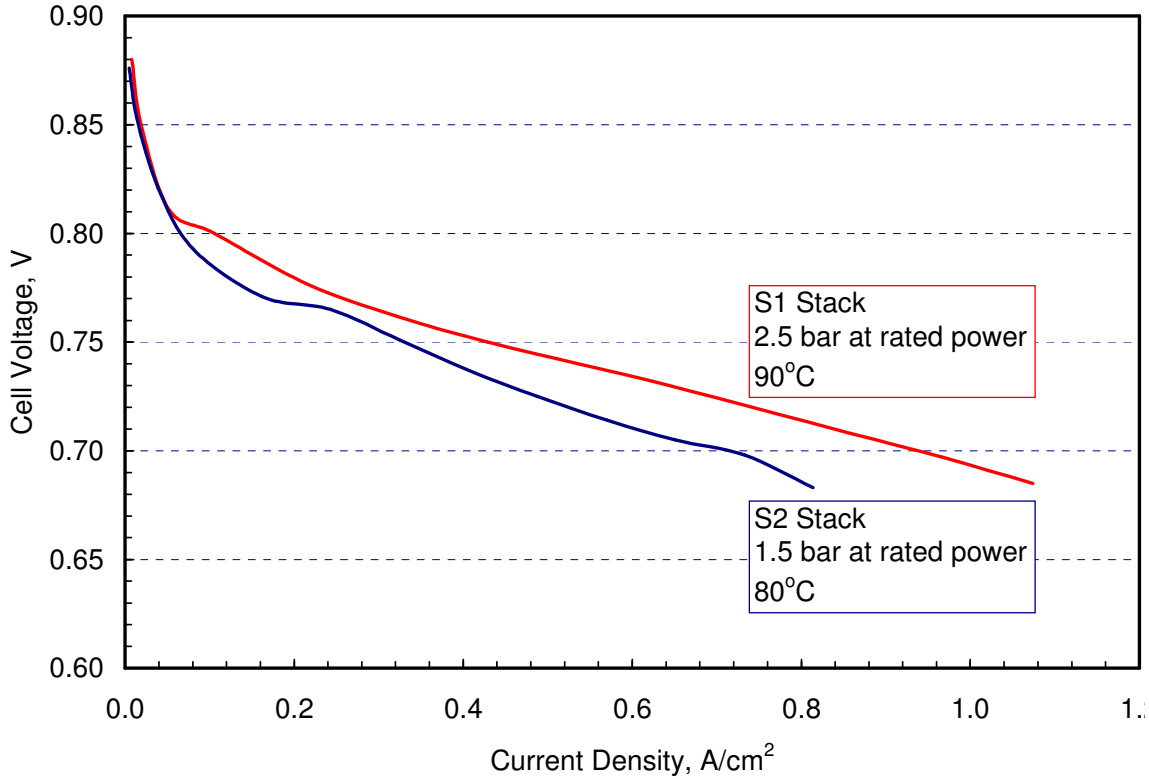

- Preliminary results from a stack model developed on the basis of data supplied by M Debe, A Steinbach and S Hamrock of 3M

PEFC Stack

Bipolar plates account for ~65% of total stack volume and 50% of total stack weight.

- 2 stacks
- 85% active cell area
- 300 V at rated power
- 2-mm bipolar plate

	S1		S2	
	W(kg)	V (L)	W(kg)	V (L)
MEA Total	5.6	6.6	7.3	8.7
Bipolar Plate	23.1	27.7	30.5	36.6
Gaskets	0.4	0.3	0.5	0.5
Frame Seal	1.2	1.9	1.6	3.3
Endplate	2.7	2.5	3.6	3.3
Current Collector	2.4	0.1	3.1	0.2
Insulator	1.1	0.6	1.5	0.8
Outer Wrap	3.4	1.9	3.9	2.2
Tie Bolts	6.0	0.8	6.0	0.8
Stack Total	46	42	58	56

Stack Performance

- S1 may meet DOE's 2010 targets of 2000 W/L and 2000 W/kg.
  - May satisfy 2010 PGM target of 0.4 g/kW but 5500-h durability remains to be demonstrated.
- Model being developed to determine EOL stack performance

	Units	S1	S2
Cell V at rated power	mV	685	684
Stack power	kW	87.0	86.9
Active membrane area	m^2	11.8	15.6
Pt loading	g/kW	0.41	0.54
Current density	A/cm^2	1.1	0.8
Power density	mW/cm^2	740	560
Stack specific power	W/kg	1900	1500
Stack power density	W/L	2070	1560

Stack Efficiency

- Stack efficiency defined as the DC power produced divided by the LHV of H_2 fed. It accounts for H_2 losses due to crossover of H_2 and O_2 and purge.
- Effect of fuel impurities to be simulated

	Units	S1	S2
Cell V at rated power	mV	685	684
N_2 crossover	%	0.02	0.01
H_2 crossover	%	0.37	0.23
O_2 crossover	%	0.04	0.02
Crossover current	mA/cm^2	20	9
Purge fraction	%	1	1
H_2 utilization	%	99	99
Stack efficiency	%	54.6	54.4

Air Management System

S2 AMS (Variex design)

- Restricted vane compressor
- Brushless DC motor
- Liquid cooled motor & controller
- Turn-down: 10:1

S1 AMS (Honeywell design)

- High speed centrifugal machines: 110,000 max rpm
- Air foil bearing: 36,000 rpm idling speed
- Mixed flow axial compressor
- Radial inflow variable nozzle turbine
- Liquid cooled motor & controller
- Turn-down: 20:1

	Units	S1	S2
Air Flow Rate	g/s	90.4	90.4
Compressor Power	kW	11.2	4.6
Expander Power	kW	6.4	0.0
CEM Motor Power	kWe	5.7	5.4
Volume	liter	15	10
Weight	kg	17.5	15.0

Heat Rejection System

- A/C condenser (9 kW), LTR (8.5 kW) and HTR (73 kW)

	Units	S1	S2	Comments
Coolant Pump				
Flow rate	kg/s	3.5	3.5	ΔP = 20 psi
Power	kWe	0.7	0.7	70% combined pump and motor efficiency
Volume	L	3	3	
Weight	kg	2	2	
Radiator Fan				
Air flow rate	kg/s	2	2	55 mph at 6.5% grade
Fan head	Pa	125	125	55% combined fan and motor efficiency
Fan power	kWe	0.5	0.5	
Volume	L	10	10	
Weight	kg	2	2	
Radiator				
Heat duty	kW	49	50	55 mph at 6.5% grade
Frontal area	m^2	0.31	0.34	Fin pitch = 985/m
Fin area	m^2	13.2	14.2	Fin thickness = 75µm
Depth	cm	2.5	2.5	
Volume	L	19.9	23.0	Advanced automotive design, 90/93 ℃ Stack T
Weight	kg	8.4	9.5	

Water Management System

- Demister upstream of EWH but downstream of MH

	Units	S1	S2	Comments
Enthalpy Wheel				
Mass transfer	g/s	8.2	14	Dessicant coated 400-cpi cordierite monolith, 4-mil thick walls
Core	inch	Ø6.2 x 6	Ø7 x 6	
Cartridge	inch	Ø8 x 9	Ø8 x 9	
Cartridge volume	L	6.1	7.5	
Cartridge weight	kg	5.7	6.5	
Motor power	W	30	30	Ø8"x6" motor/manifold
Total volume	L	10	12	Includes 4 L motor
Total weight	kg	8	9	Includes 2 kg motor
Membrane Humidifier				
Mass transfer	g/s	0.67	2.2	ID=1 mm, OD=1.12 mm
No of Nafion Tubes		600	1440	
Membrane area	m^2	0.30	1.01	
Core	inch	Ø2.5 x 5	Ø4 x 8	
Housing	inch	Ø3x11	Ø4.5 x 15	
Volume	L	1.2	3.2	
Weight	kg	1.2	2.4	

Fuel Management System

Hybrid system: ejector + hydrogen recirculation blower

- Ejector can recirculate spent anode gas for 25-100% flow
- Some H_2 bypasses ejector between 25-100% flow
- Recirculation blower needed at low flows (data from www.h2systems.net)

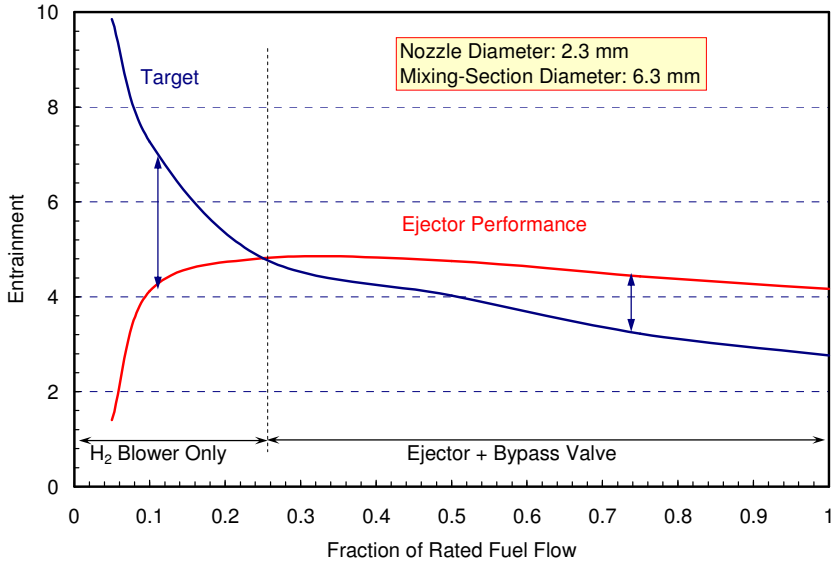

	Units	S1	S2	Comments
Recirculation rate	L/s	5.8	9.4	ΔP = 2 psi
Power	We	200	325	40% peak efficiency
Volume	L	5	5	Includes controller
Weight	kg	3	3	Air-cooled, 24 or 42 V

System Efficiency at Part Load

- With a CEM turndown of 20, peak in efficiency at 5-10% of rated power.
- Difficult to meet the DOE's 60% efficiency target at 25% rated power.

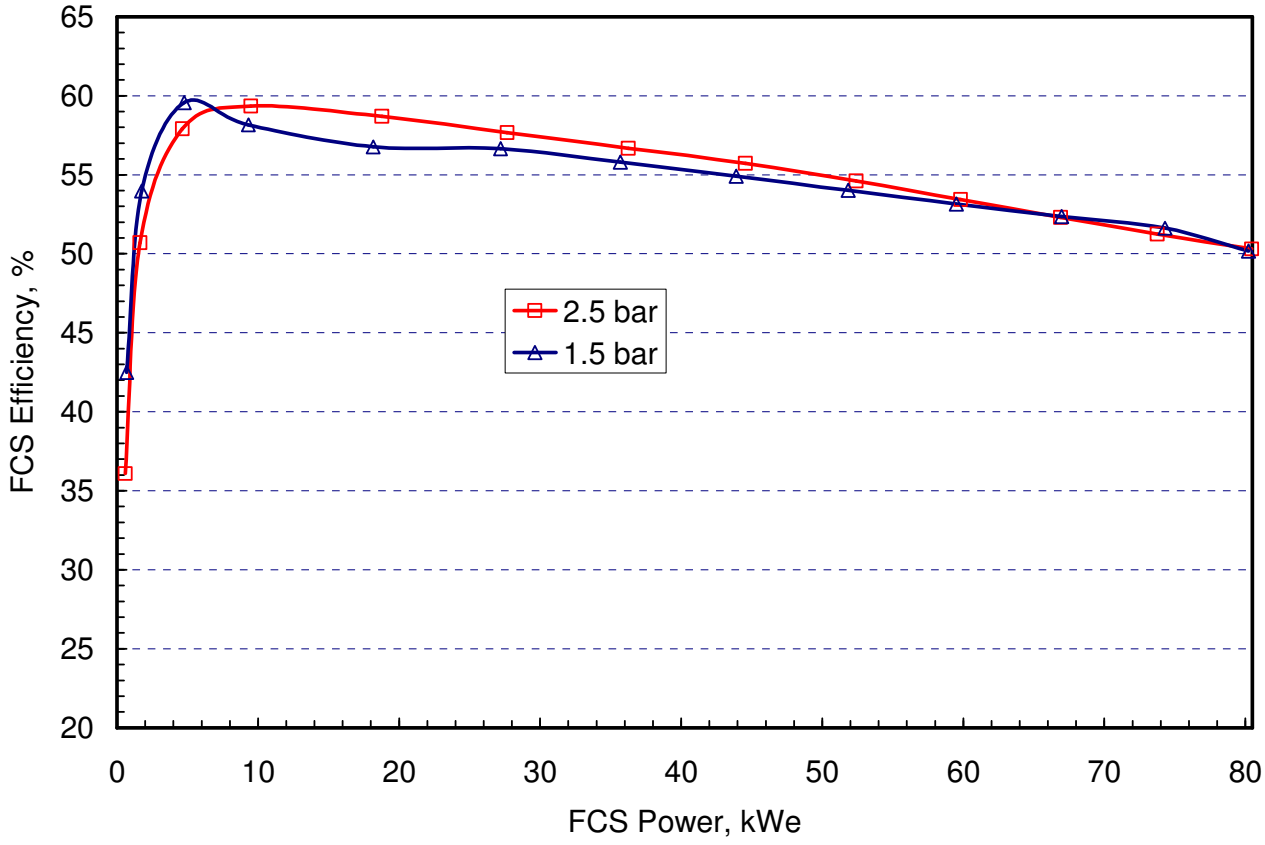

Parasitic Losses and System Efficiency

Listed efficiency values are for comparison purposes only.

- Depending on degree of hybridization, FCS cannot be operated continuously at rated power.
- Radiator fan runs intermittently.
- H_2 recirculation pump is not always needed.
- CEM motor may be overloaded or not powered.

	Units	S1	S2
Cell V at rated power	mV	685	684
PEFC Stack	kWe	87.0	86.9
CEM motor	kWe	5.5	5.2
Enthalpy wheel motor	We	30	30
Radiator fan	kWe	0.5	0.5
Coolant pump	kWe	0.8	0.8
H_2 recirculation pump	We	200	325
FCS efficiency	%	50	50

Summary: FCS Specific Power and Power Density

- S1 may meet the DOE's system target of 650-W/kg specific power and 650-W/L power density
- A/C condenser weight & volume not included but affect weight, volume & parasitic power
- Effects of fuel impurities and durability being addressed

	S1		S2	
	W (kg)	V (L)	W (kg)	V (L)
PEFC stack	46	42	58	56
Air management system	18	15	15	10
Fuel management system	7	9	7	9
Heat rejection system	12	36	14	34
Water management system	9	11	11	15
Miscellaneous	9	11	10	12
Total	101	124	115	136
FCS specific power (We/kg)	790		700	
FCS power density (We/L)	640		590	